

PPM 2013

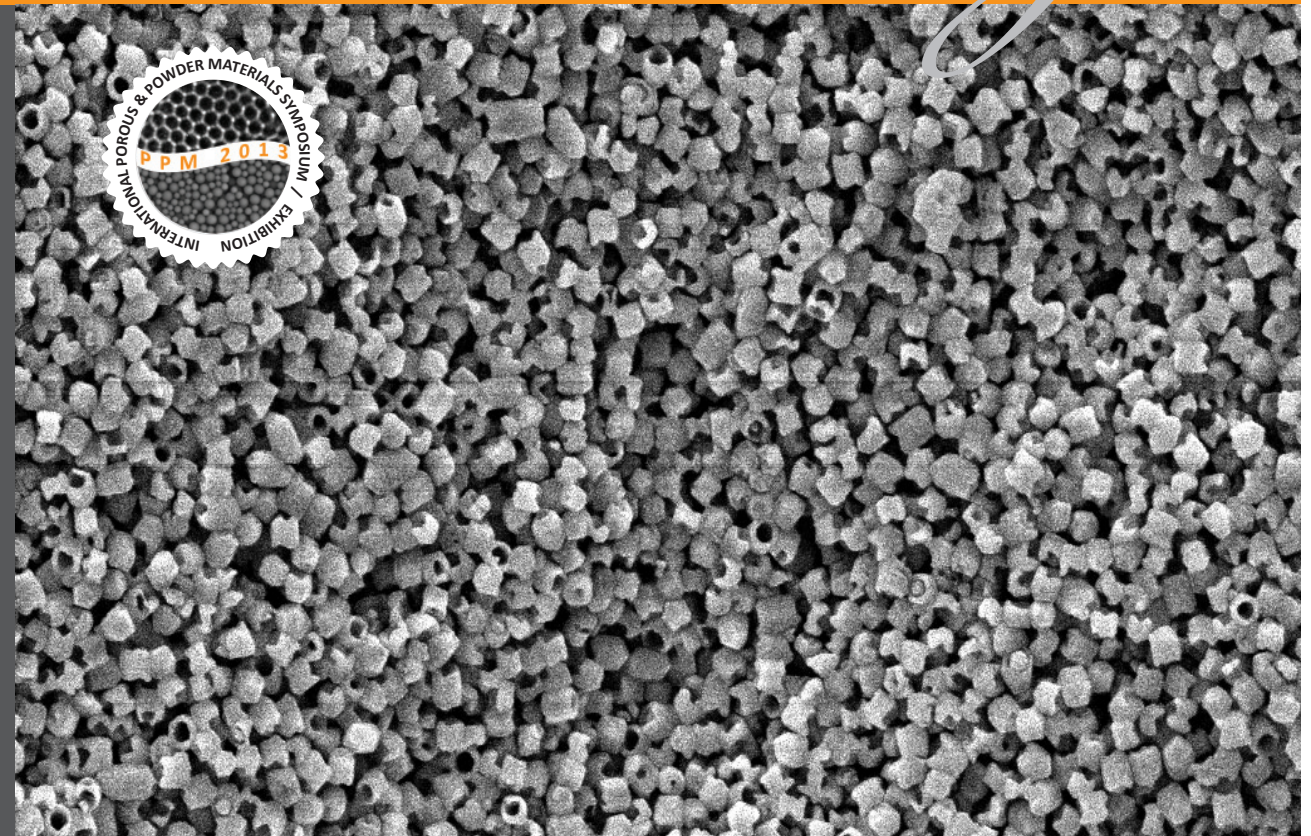
Proceedings

Proceedings

PPM 2013

EDITORS : Sevgi KILIC OZDEMIR, Mehmet POLAT & Metin TANOGLU

INTERNATIONAL POROUS
& POWDER MATERIALS
SYMPOSIUM & EXHIBITION



ISBN: 978-975-6590-05-8



INTERNATIONAL POROUS
& POWDER MATERIALS
SYMPOSIUM & EXHIBITION

3-6 September 2013

İzmir Turkey

EDITORS
OZDEMIR
POLAT
TANOGLU

3-6 September 2013
İzmir Turkey

PPM 2013

3-6 September 2013

İzmir Turkey

INTERNATIONAL & POROUS POWDER MATERIALS SYMPOSIUM & EXHIBITION

Published By:
The Organizing Committee of
The International Porous and Powder Materials Symposium and Exhibition

Assist. Prof. Dr. Sevgi KILIC OZDEMIR
Symposium Secretary
Izmir Institute of Technology, Department of Chemical Engineering
Urla Izmir Turkey
sevgikilic@iyte.edu.tr
+90 232 750 6647

Mehmet POLAT
Symposium Chair
Izmir Institute of Technology, Department of Chemical Engineering
Urla Izmir Turkey
mehmetpolat@iyte.edu.tr
+90 232 750 6693

Metin TANOGLU
Symposium Chair
Izmir Institute of Technology, Department of Mechanical Engineering
Urla Izmir Turkey
metintanoglu@iyte.edu.tr
+90 232 750 6693

Editorial Board:

Aybike Nil OLCAY, Izmir Institute of Technology Environmental Engineering Program, Urla Izmir Turkey
Elif Suna SOP, Izmir Institute of Technology Chemical Engineering Program, Urla Izmir Turkey
Serkan KANGAL, Izmir Institute of Technology Mechanical Engineering Program, Urla Izmir Turkey

Printed by:



Üç Adım Printing House
Shop: 2824 Sok. No 41 Sanayi Sitesi Izmir Turkey / Tel +90 232 458 35 13
Office: 8001 Sok. No 8/1 Cigli Izmir Turkey / Tel +90 232 376 16 39
ucadimmatbaa@hotmail.com

Cover Design:

Mutfak: theBRANDkitchen
Mecidiye Kuyu Sk. , Ozdemir Apt. No:18/5, Mecidiyekoy, Sisli, Istanbul Turkey
Tel: +90 532 614 3854 / +90 212 264 0858
www.markamutfakta.com

ISBN: 978-975-6590-05-8

The Proceedings of
the 1st International
**Porous and Powder Materials
Symposium and Exhibition
PPM 2013**



**3-6 September 2013
Çeşme Izmir-TURKEY**

**Edited by
Sevgi KILIC OZDEMIR
Mehmet POLAT
Metin TANOGLU**

SCIENTIFIC COMMITTEE

Seniz Akin	TUBITAK	Erol Kaya	Dokuz Eylul University
Gokhan Aksoy	Ege University	Seda Keskin	Koc University
S. Alsoy Altinkaya	Izmir Institute of Technology	J. L. Lopez-Lacomba	University Complutense
Sabri Altintas	Bogazici University	Christos N. Likos	University of Vienna
Gursoy Arslan	Anadolu University	Arzu Marmarali	Ege University
Vedat Arslan	Dokuz Eylul University	M. P. Ginebra Molins	Univ. Politecnica de Catalunya
Alper Arslanoglu	Izmir Institute of Technology	Keshavan Niranjana	University of Reading
Levent Artok	Izmir Institute of Technology	M. Lutfi Ovecoglu	Istanbul Technical University
Ali Ata	Gebze Inst. of Technology	Orhan Ozturk	Izmir Institute of Technology
Devrim Balkose	Izmir Institute of Technology	Gulnur Ozyuzer	Izmir Institute of Technology
Yusuf Baran	Izmir Institute of Technology	Aysegul Pala Iyilikci	Dokuz Eylul University
Ergin Basar	Akzo Nobel	Ferda Soyer	Izmir Institute of Technology
Hasan Boke	Izmir Institute of Technology	Nurettin Sahiner	Onsekiz Mart University
Volga Bulmus	Izmir Institute of Technology	Gamze Tanoglu	Izmir Institute of Technology
M. Sabri Celik	Istanbul Technical University	H. Ibrahim Unal	Gazi University
A. Erdem Senatalar	Istanbul Technical University	Serife Yalcin	Izmir Institute of Technology
Osman Ersoy	Arcelik Inc.	Talat Yalcin	Izmir Institute of Technology
Ayhan Ezdesir	PETKIM PetroChemicals Inc.	Ismail Ozgur Yaman	Middle East Technical Univ.
Hasan Gocmez	Dumlupinar University	Yuda Yurum	Sabancı University
Sasidhar Gumma	Indian Institute of Technology	Hadi Zareie	Gediz University
Sebnem Harsa	Izmir Institute of Technology	Haifei Zhang	University of Liverpool
Cengiz Kaya	Yildiz Technical University		

LOCAL ORGANIZING COMMITTEE

Mehmet Polat	Symposium Chair, Izmir Institute of Technology
Metin Tanoglu	Symposium Chair, Izmir Institute of Technology
Sevgi Kilic Ozdemir	Symposium Secretary, Izmir Institute of Technology
Ozgenç Ebil	Izmir Institute of Technology
Nuran Elmaci	Izmir Institute of Technology
Tahir Kemal Erdem	Izmir Institute of Technology
Ayten Nalbant	Izmir Institute of Technology
Devrim Pesen Okvur	Izmir Institute of Technology
Engin Ozcivici	Izmir Institute of Technology
Ekrem Ozdemir	Izmir Institute of Technology
Banu Ozen	Izmir Institute of Technology
Fehime Ozkan	Izmir Institute of Technology
Hurriyet Polat	Izmir Institute of Technology
Yusuf Selamet	Izmir Institute of Technology
Selahattin Yilmaz	Izmir Institute of Technology

ACADEMIC ORGANIZING COMMITTEE

Halil Bakan	TUBITAK Marmara Research Center
Erdal Celik	Director, Nanotechnology Center, Dokuz Eylul University
Mustafa Demir	Director, Materials Research Center, Izmir Institute of Technology
Mustafa Demircioglu	Chemical Engineering, Ege University
Can Erkey	Chemical Engineering, Koc University
Gultekin Goller	Metallurgical and Materials Engineering, Istanbul Technical University
Mustafa Guden	Rector, Izmir Institute of Technology
Uner Ipekoglu	Mining Engineering, Dokuz Eylul University
Hasan Mandal	Vice Rector, Sabanci University
Salih Okur	Dean, Faculty of Engineering and Architecture, Katip Celebi University
Lutfi Ozyuzer	Applied Quantum Research Laboratory, Izmir Institute of Technology
Kambiz Ramyar	Vice Dean, Faculty of Engineering, Ege University
Ender Suvaci	Vice Rector, Anadolu University
Funda Tihminlioglu	Dean, Faculty of Engineering, Izmir Institute of Technology
Suleyman A. Tuncel	Chemical Engineering, Hacettepe University
Mehmet Turker	Vice Rector, Gazi University
Ahmet Yemenicioglu	Director, Biomaterials Research Lab., Izmir Institute of Technology

INSTITUTIONAL ORGANIZING COMMITTEE

Sedat Guldogan	Deputy Undersecretary, Undersecretariat for Defence Industries
Erguder Can	General Secretary, Izmir Development Agency
Bahadir Tunaboylu	Manager, Materials Institute, TUBITAK Marmara Research Center
Yalcin Yilmazkaya	Aerospace Clustering Association
Necmi Sadikoğlu	Istanbul Chemicals and Chemical Products Expoters' Association
Arslan O. Erdinc	President, Aegean Mine Exporter Union
Saadet Caglin	President, Izmir Chamber of Chemical Engineers
Muhammet Yildiz	President, Izmir Chamber of Mining Engineers
Erol Paksu	President, Ege PLASDER
Suleyman Temizci	Association of Natural Isolation Materials
Yusuf Usta	President, Turkish Powder Metallurgy Association

INDUSTRIAL ORGANIZING COMMITTEE

Adnan Altas	R&D Manager, Eczacibasi ESAN
Levent Gokce	General Director, Weber Saint-Gobain Turkey
Cagri Gurbuz	Deputy General Manager, Sentebir Inc.
Cagan Heris	Deputy General Manager, Akdeniz Kimya Inc.
Nafiz Karabudak	Sr. Manager, Technology Initiatives, Lockheed Martin Corp., USA
Saim Kirgiz	R&D Manager, Bosch Thermotechnology
Sanal Limoncuoglu	General Manager, Akzo Nobel Paint Inc.
Murat Muduroglu	Development Manager, Adacal Industrial Minerals Inc.
Osman Okyay	Technical General Manager, Kale Holding Inc.
Goksel Paker	CEO, Inci Aku Inc.
Arslan Salman	General Manager, EastChem Inc.
Mustafa Sezer	R&D Technology Group Leader, Materials Technologies, Arcelik Inc.
Emre Tutuncu	General Manager, Cimstone Inc.
Ugur Uzgan	Product Manager, AKG Gazbeton Inc.
A. Murat Yildirim	R&D Manager, Tupras Turkish Petroleum Refineries Co.

FOREWORD

We welcome you to the first of the International Porous and Powder Materials Symposium and Exhibition, PPM 2013.

The idea of organizing a symposium on porous and powder materials owes its germination to the curiosity about the ‘other side of the fence’. We are all familiar of the mild surprise when we come accross with a research paper from a totally unrelated field written in a completely different terminology but describing something pleasantly familiar. Just imagine the elation of a PhD student in ceramics who is trying to optimize the stability and plasticity of the green body reading about the double layer around a protein, of an environmental engineer who is attempting to flocculate a nasty sludge coming accross with the concept of aggregation of micellar structures or of a researcher in chemical engineering who is looking for the perfect catalyst seeing the SEM pictures of porous nanoparticles developed for drug delivery. The list could be extended with much better examples by the readers of this book. But the best set of words to describe these feelings is an awareness of wholeness and solidarity.

PPM 2013 aims to focus on and amplify this awareness which will in turn help to forge pathways between different fields of science and technology, as well as creating a familiarity for the work of each other. Porous and Powder Materials Symposium is intended to bring us together around a topic which we all deal with in our proliferiated research fields.

This ambitious aim in mind, the symposium was structured around the following themes:

- Theme A: Development and Characterization
- Theme B: Catalytic Aspects
- Theme C: Environmental and Hygenic Aspects
- Theme D: Biological and Medical Aspects
- Theme E: Transport and Surface Chemistry
- Theme F: Modeling and Simulation
- Theme G: Industrial Applications

Both the Oral Sessions and the Proceedings Book are constructed around these themes. We are proud to say that, for a symposium which has the *first* in its title, what emerged was astounding with number of abstract submissions reaching eight hundreds. The submissions were distilled to 175 oral presentations and 300 posters. The Symposium venue, Cesme Sheraton Hotel in Izmir, will host around 600 participants from over 40 countries. The proceedings book that you are holding in your hands contains 185 full papers.

It is obvious that the symposium have adressed a need for those of us who work with porous and powder materials. A need which arises from the curiosity about what is happening beyond the fence. We believe that this healty curiosity will make Porous and Powder Materials Symposium and Exhibition a regular and respected gathering in the field for years to come.

Hope to get together in both sense of the word in future PPM's.

With our best regards.

Mehmet Polat and Metin Tanoglu, Symposium Chairs
Sevgi Kilic Ozdemir, Symposium Secretary

CONTENT

Plenary Papers	1
Advanced Technology Needs for New Multifunctional Materials with Controlled Functional Nanostructure	2
Designing Porosity in Polymer-Derived-Ceramics Nanostructure	9
SECTION A: Development and Characterization	15
Study On Nanostructured Silicon Carbon Thin Films Deposited by PECVD	16
3D Characterization, Analysis, and Simulation of Multiphase Systems using High Resolution X-ray Micro Tomography	25
Polymer Based and Inorganic Monosized-Porous Beads: Synthesis and Cromotographic Applications	35
Characterisation of powder mixtures using morphologically directed Raman spectroscopy	39
Characterization of Porous Coatings on Az31 Mg Alloy by Plasma Electrolytic Oxidation	42
Effect of Pore Wall Microstructure on the Mechanical Properties of Low Alloy Steel Foams	47
Mechanical Properties of Sinter-Hardened Cu-Ni-Mo Based Steels	52
Abrasive Wear Behavior of Powder Metallurgy Cusn10-Graphite Metal Matrix Composites Produced By Powder Metallurgy	58
Characterization of Porous Hydroxyapatite Produced on Ti6Al4V by Plasma Electrolytic Oxidation	63
An Experimental Study on Hot Formability of Closed Cell Metallic Foams	68
Influence of Zeolite LTA Morphology on Their Bulk Properties	73
The Transverse Rupture Strength of Hot Pressed Segments with B4C	77
Microstructure and Electrical Properties of Cu-Tic Composites Produced by Hot Pressing Method	82
Usage of Boric Acid as an Alternative Activating Agent to Produce Porous Carbons by Microwave Induced Carbonization	88
Investigation on Manufacturability, Repeatability, and Mechanical Properties of Lightweight Polylactic Acid Bcc-Z Cellular Lattice Structures Fabricated by Fused Deposition Modeling	92
Electro Ceramic Compositions with the Improved Properties on the Basis of Local Mineral Raw Material.....	98
Synthesis of Mandelic Acid from Benzaldehyde using Third-Liquid Phase System with Immobilized Peg Phase Transfer Catalyzed under Ultrasonic Irradiation Combination.....	105
Synthesis and Characterization of Acidic Cesium Salt of 12-Tungstophosphoric Acid.....	109

Wear Behaviour Of Powder Injection Molded Ti-6Al-4V Alloy.....	114
Effect Of Highly Porous Expanded Silica Gel Addition on the Properties of SiC-C Based Composite Ablation Material	119
Uniaxial Stress-Strain Behavior of Aluminum Foams and Aluminum Foam Based Composite Sandwiches.....	123
Dynamic Behavior Analysis of Fml/Aluminum Foam Sandwich Structures Under Simulated Blast Test.....	128
Al-Si Based Syntactic Foams by Using Porous Silica Gels via Vacuum Casting: Cell Size vs Strength and Energy Absorbance Behaviour	133
Microwave Absorption Properties of Co,Mn Spinel Ferrite–Acrylated Epoxy Nanocomposites	137
Dielectric and Magnetic Properties of Co-Mn Spinel Ferrites	139
Synthesis and Electromagnetic Absorbing Properties of Spinel Ferrites and Paraffin Nanocomposite Structures.....	142
Investigation of the Compaction Behaviour of AG8ZNO Composite Produced by Mechanical Alloying	145
Microstructure and Characterization of B4C Reinforced Al2024 Alloy Matrix Composites Produced by Mechanical Alloying Technique.....	150
Examination of Abrasive Wear Behaviour in Al 2014-SiC Composites	155
Preparation and Characterization of the Composites With Ha/ZrO2/Poly(Methyl Methacrylate)	160
Development of Novel Boron Nitride Nanotube Synthesis Method.....	164
Swelling Behavior in Microwave Sintering of Fe–Al Mixtures.....	168
Sinterability Comparison of the Al/SiC and Al/MoSi2 Powder Systems under Microwave Sintering Conditions.....	171
Effect of Tic Particle Size on Some Properties of Cu-Al/TiC Composites Produced using Hot Pressing Process.....	175
Effects of the Sintering Parameters on Mechanical Properties of Fe-Based Powder Metal Parts.....	180
Investigation of Weldability of Produced by Powder Metallurgy Method of Ni-Ti Composite with Stainless Steel Couple	186
Synthesis of Fe/WC-Co Bi-Layered Carbide Cutting Materials by Powder Metallurgy	190
The Distribution Analysis of Aluminum and TiH2 Powders in the Powder Metallurgy Foaming Process.....	195
One-Pot and Template-Free Synthesis of Magnetite Porous/Hollow Nanostructure.....	199
Applications of Image Processing for the Analysis and Characterization of Porous Media	202
Plasma Sprayed and Annealed Calcium Titanate Dielectrics	207
Influence of Rheological Properties on the Foaming Process of Polylactide.....	212

Preparation and Characterization of Uniform Tio ₂ Membrane on Porous 316l Stainless Steel Substrate	216
Obtaining and Characterisation of Hydroxyapatite–Zirconia Powders by Chemical Precipitation	222
Relationship Between Cell Wall Morphology and Energy Absorption Behavior of Aluminum Foams Produced via Melt Route	227
X-Ray Microtomography of Geological Soft Sediment Samples: Reduction of Motion Artifact by Resin Consolidation	232
Processing and Characterization of Porous Tini Alloys.....	237
Development of Anticorrosion Composite Polymer Materials and Coatings Based on Them with Using Powdery Wastes of Various Productions	242
Production and Characterization of Chitosan/Peo Polymer Nanofibers Using Electrospinning Technique	248
Composite Membrane Synthesis for Pervaporation Membrane Bioreactor	253
Characterization and Formation of Porous Surface on Magnesium Coated by Plasma Electrolytic Oxidation	258
The Effect of Structural Characteristics on the Reflectivity of Porous Silicon.....	263
The Estimation of Pore Anisotropy and its Relationship with Morphometric Properties of Porous Solids	268
Grain Size Assessment in Supercoarse Hardmetals With Cobalt And Nickel Based Matrices	274
Application of Nano-Sized Up-Conversion Phosphors Doped With Rare-Earth Elements in Polymer Photonics.....	278
Tensile Properties of Ground Colemanite Filled Polypropylene Homopolymer	283
The Effect of Thermal Cycles on Fracture Behaviour of Filled Calcium Carbonate Polypropylene Random Copolymer	288
Synthesis and Characterization of ZSM-5 Zeolite From Wheat Hull Ash.....	292
Zeolite Filled Polyvinylalcohol Membrane Preperation and Alcohol Dehydration by Pervaporation.....	297
Surface Roughening of Stainless Steel Plates by Electrochemical Etching Techniques Used for Porous P/M Applications	301
Synthesis and Characterization of Hydroxyapatite	306
Synthesis and Characterization of Pr ³⁺ Doped Yttrium Aluminum Garnet (Yag) Nanophosphors	310
Electrodeposition of Layered Manganese Oxides under Hydrothermal Conditions.....	315
Mesoporous Materials from a Novel Silica Source.....	320
Superacidic Mesoporous Sulfated Titania-Silicates for Dehydration of Fructose	325
Mechanical Proporties of a Composite Produced by using Electroless Ni Plated Fe-Co-Cr Powders	331

Controlled Crystallization of 0.25Li ₂ O.2SiO ₂ -0.75BaO.2SiO ₂ Glass	336
Vickers Microhardness (HV) and Indentation Fracture Toughness (KIC) of 25Li ₂ O.2SiO ₂ -0.75BaO.2SiO ₂ Glass and Glass-Ceramic	339
Synthesis and Surface Properties of Ga-Te Co-Doped ZnO NanoroDS	342
Synthesis and Surface Properties of Ga-Te Co-Doped ZnO NanoroDS	342
Statistical Analysis of Indentation Fracture Toughness (Kic) of 0.25Li ₂ O.2SiO ₂ - 0.75BaO.2SiO ₂ Glass And Glass-Ceramic	345
Effects of Modified ZnO Nano Powder on The Mechanical and Anticorrosion Properties of Polyester Powder Coatings	348
Sytnthesis of Metallic Copper Nanowires at Low Temperature.....	352
Experimental Investigation of the Effect of Thermal Conductivity of Density in EPS	354
 SECTION B: Catalytic Aspects	 360
Mesoporous Materials With Ordered Pore Structures Catalytic Applications.....	361
Photocatalytic Activity of Film Structures Comprising Titania Xerogel in Porous Anodic Alumina	366
Development of Three Way Catalytic Converters for Elimination of Hydrocarbons, Carbon Monoxide and Nitric Oxide in Automotive Exhaust.....	371
Photocatalytic Activities of ZnO And Pd-ZnO Doped by Borohydride Reduction Method	377
Use of Metal Doped Zsm-5 Zeolite Catalysts in Methylation of 2-Methylnaphthalene	382
Sodium Borohydride Hydrolysis for Hydrogen Production over a Highly Efficient Co- B/Pani Catalyst.....	387
Synthesis of Sol-Gel Derived TiO ₂ Xerogel Supported Metal Boride Catalysts for Hydrogen Generation by Hydrolysis of Alkali Sodium Borohydride	391
 SECTION C: Environmental And Hygenic Aspects	 396
Characterizing the Adsorption Properties of Nanoporous Materials for Gas Storage and Separation Technology	397
Photovoltaics Based on Semiconductor Powders.....	405
Production of Activated Carbon from Biochar by Chemical Activation using Potassium Hydroxide.....	417
Study of Adsorption Capacity Recovery in Different Adsorbents for Nitrogen Removal from Diesel	422
Cu-Btc /Graphite Oxide and Cu-Btc/Aminated Graphite Oxide Composites as Superior Adsorbents of Co ₂ at Ambient Conditions	433
Nickel Removal by using Immobilized Macro Fungus: Batch Biosorption Studies	438

Application of Oxidized and Reduced Activated Carbon for Para-Nitrophenol Removal.....	443
Removal of the Ampicillin Antibiotic in Aqueous Solution By Photo-Fenton/Ultrasonic-Fenton Processes	449
Adsorption of Methylene Blue onto Activated Carbon Produced by Microwave Assisted Chemical Activation of Filter Coffee Waste	452
Adapting Nanoporous Silica Materials for Molecular Filtration and Thermal Insulation	457
Optimization of Process Parameters for Arsenic Removal by Iron Containing Adsorbents Using Box-Behnken Design	463
Biosorption of Reactive Red 2 By Ctab-Modified Powdered Biomass: Isotherm Studies	467
Purification of Alcohol Containing Mesh With Powder Filtering Materials	472
Research and Development of Surface-Active Powder Composite Material Based On Viscous-Flow Waste.....	475
Production Chemically Activated Carbon from Industrial Waste Material and Its Adsorption Behavior in the Dye Removal	481
CO ₂ Adsorption on Zeolite X	486
Crystallization of Sodium Organic Salts Produced in Partial Wet Oxidation of Black Liquor	489
Disintegration&Stabilization of Mechanically Dewatered Industrial Sludge Through Semiconductor Based Heterogeneous & Thin Film Methods	495
Capture of Low Molecular Weight Organic Contaminant within Micelle Structures in Meuf	502
Identification and Treatment of Heavy Metals from Soil.....	506
Purification of Slime Phosphoric Acid From Fe ²⁺ Cations by Natural Zeolite	511
Removal of Copper from Dilute solutions using SDS AIDID Active Carbon Adsorption	514
Modification of Natural Zeolite to Enhance its Neutralizing Capacity in Lactic Acid Medium.....	520
SECTION D: Biological and Medical Aspects	524
Importance of Porous and Colloidal Structures in Biomedical Applications.....	525
Nanostructuring of Bioimplants through Chemical Mechanical Polishing.....	534
Fabrication of Hollow Hydroxyapatite Microspheres by Spray Drying	539
Evaluation of Magnesium-Aluminum Metasilicate and Silica Carriers for Improving Oral Bioavailability of Poorly Soluble Drug.....	545
Alginate Nanoparticles for Cancer Therapy: Effect of Crosslinker Type on Drug Activity.....	550
Fabrication of Scaffold for Cartilage with Subchondral Bone Regeneration by Lamination of Hydroxyapatite/Collagen Nanocomposite and Collagen	555

Morphology of Micellar Structures in Simulated Body Fluid for Drug Delivery Purposes	559
In-Vitro Release of Theophaylline Through Cellulose Acetate Membranes Modified by N-SiO ₂	563
Non-Degradable Porous Poly(Vinyl Alcohol) Hydrogels for Cartilage Tissue Engineering	569
Characterization and Determination of Biofilm Forming Potential of a Waste Sericin-Rich Protein Mixture	572
Titanium-Based Composite For Biomedical Applications.....	577
Design Of Nanostructured Surfaces of the DNA-Active Film-Like Acrylamide/N-(2-Dibenzylamino-Ethyl)-Acrylamide	581
Anti-Inflammatory and Chemical Composition of Two Plants Family Asteraceae Growing in Saudi Arabia	586
Amino Acids Adsorbed onto Cellulose as a Way to Increases the Cellulose'S Oxidation by Supported Y Zeolite to Costly Compounds.....	593
Porous Polylactide as Medical Scaffold	598
Fabrication and Characterization of Porous Bioglass Ceramic.....	602
Nano-Sized Upconversion Phosphors for Deep Optical Imaging of Biological Tissues	606
Silver and Zinc Oxide Based Nano Powders and their Polymer Based Nanocomposites for Antibacterial Application	611
Analysis of the Growth of Alpha-Lactalbumin Protein Nanotubes Functional for Food Applications.....	616
Elemental Release Comparison of Selective Laser Sintering Method and Conventional Dental Casting Alloys Usingicp-Ms	620
DNA Adsorption onto Silica Aerogel	624
SECTION E: Transport and Surface Chemistry	628
Changes in Magnetic Properties from Particles to Atomic Clusters	629
Investigation of Hydroxyapatite (Ha) Coatings Wear Behaviour Created on the Surface of Ti6al4v Materials After Different Activation Procedures	635
Study of Transport of Liquids Through Glassy Polymers by New Express Dynamic Technique	638
Adsorption Kinetics Of Steam Methane Reformer (Smr) off Gas on Mil-53(Al)	642
Experimental and Theoretical Study on StyraX Officinalis Activated Carbon Adsorption of Lead and Zinc from Aqueous Solution	646
Hydraulic Conductivity and Suction Characterization of Gördes Zeolite Blocks.....	651
Enhanced Photo- and Under X-Ray Luminescence from Xerogels Embedded in Mesoporous Anodic Alumina.....	656

Investigation of Solubility and Transport of Boric Acid in Ethanol at Subcritical and Supercritical Conditions	659
Analysis of Multiphase Transport Processes and Fluid Dispersion in Sintered Porous Structures	664
Synthesis, Crystal Structure, and Nitrogen-Gas-Adsorption Property of Chain Complex of Dinuclear Rhodium(Ii) Benzoate and Ethylenediamine.....	669
Procedure for Contact Detection Between Platy Cohesive Particles	674
Morphology of Micelles and Micellar Aggregates as a Function of Electrolyte Valence and Concentration.....	680
The Dispersion Properties of Micronized Marble Suspensions in the Presence of Inorganic and Polymeric Dispersants.....	686
Adsorption of Lead (Ii) Ions from Aqueous Solution on Porous and Crystalline Hap	693
Experimental Investigation of the Selective Permeability of Hollow Glass Microspheres With Nanostructured Shell	697
SECTION F: Modeling and Simulation	702
Computational Structure Characterization Tools for the Era of Material Informatics.....	703
Analysis of Swelling Behaviour of Clay Minerals by Discrete Numerical Simulation	713
Artificial Neural Network Approach to Predict of Effect of Process Control Agent on the Microhardness of Al-Al ₂ O ₃ Composite Powders Produced by Mechanical Alloying	722
A Study for Anisotropy of Porous and Powder Materials from a Different Perspective: ‘Use of Orthonormal Parts of Elastic Constant Tensor’	727
Discrete Element Modeling of Spherical Copper Powder Compaction Process.....	732
Kinetic Monte Carlo Simulation of Semiconductor Heteroepitaxy on Featured Substrates.....	737
Simulation of Flow through Open Cell Copper Foams using Microtomography Structure	746
Continuum Simulation of the Discharge of Powders In Silos with and without Inserts	752
Modeling Thermal Energy Storage using Porous Adsorbents	757
SECTION G: Industrial Applications	761
Nanoporous Aerogels and their Composites for Thermal Insulation Applications.....	762
Natural Porous Lightweight Aggregates and Their Industrial Future	770
The Advantages of Using Nano PCC (Precipitated Calcium Carbonate) in Production of Coated Carton.....	781
Relation Between Rheological Properties and Pore Structure of the Fly Ash/Cement Based AAC Mortar and Product Properties	788

Investigation on Utilization of Bioplastics in Turkey	792
The Effect of the Porous Bentonite-Alcni Material in the Turbine Efficiency Preservation.....	796
Effects of Different Process Control Agent on Characteristics of Mechanically Milled Al ₂ O ₃ Powders.....	804
Fabrication of Fe–Al Intermetallic Coatings Using mechanical Milling Technique	809
Fabrication of Bulk Ytria Stabilized Zirconia-Alumina Composite Filters by Different Foaming Methods	814
High Temperature Mechanical Properties of Cement Prepared by Addition of Waste Foundry Sand.....	819
The Production of Hard Porcelain in Low Temperatures.....	823
Comparisons of Fine Dry Grinding of Two Different Porous Powders: Amorphous Silica and Diatomite	828
Evaluation of Phosphogypsum Powder as an Additive in the Production of Plaster.....	836
Utilization of Activated GBFS and Perlite in Porous Lightweight Composite Material	839
Technical Properties of Sepiolite Fiber-Reinforced AAC.....	844
Bio-Pitch: A Novel Precursor for Carbon Foam Production.....	848
Production of Porous Ceramic Material from Kaolin Doped Porcelain Polishing Waste	853
Utilization of Polishing Porcelain Stoneware Waste With Talc Addition in the Production of Porous Ceramic Bodies	857
Magnesia Based Castable Refractory Production and Utilization Areas	862
Cement-Based Composites Modified Low Basic Clinkers	867
Research and Development of Composite Powder Polymer Materials and Production of Cotton Machine Parts on Their Bases	871
Research and Development of New Powder Colorific Compositions Based On Salts of Polyvalent Metals for Dyeing the Natural and Synthetic Fibers and Textile Materials on Their Bases	877
Research and Development of Technologies of Obtaining the Mechanically Activated Powder Based on Natural Ingredients and Dune Sand for Production of Sealing Composite Cements and Composite Materials for Various Purposes	883
Research and Development of Technologies of Obtaining the Composite Metal Materials from Powder Poor and Off-Balanced Ores	889
Research and Development of Composite Powder Materials Based Industrial Wastes for Use in Drilling of Oil and Gas Wells	894
Production of Copper Foam by Carbamide Space Holder	900
The Effects of Porosity Ratio of The Welded Tuffs on Sound and Heat Insulation.....	905

Using of Photoluminescent Tile for Evacuation of the Buildings During Electrical Failure.....	910
Silica Based Shear Thickening Fluids (Stfs) for Personal Protection	913
Energy Effective Granule Preparation in Porcelain Tile Production	918
Effect of Usage of Fly Ash and Silica Fume at Concrete Production over Quality and Cost of Concrete	921
The Effect of Waste Marble Powder on the Fresh State and Mechanical Properties of Self- Compacting Mortars	926
Tribological and Thermo-Mechanical Properties of Glass Fiber Reinforced Composites Containing Tungsten Based Nanofillers.....	931
Natural Juglon Dye as a Photosensitizer for Dye-Sensitized Solar Cells.....	939
Simple Silicon Vapor Etching Technique to Form Thin SiO _x /Si/SiO _x Structures.....	942
AUTHOR INDEX.....	946

Plenary Papers

ADVANCED TECHNOLOGY NEEDS FOR NEW MULTIFUNCTIONAL MATERIALS WITH CONTROLLED FUNCTIONAL NANOSTRUCTURE

Edward H “Ned” Allen¹ and Luke A. Uribarri^{2a}

1. Lockheed Martin Corporation, Corporate Engineering and Technology, Bethesda MD USA

2. Lockheed Martin Corporation, Advanced Technology Laboratory, Arlington, VA, USA

a. Corresponding author (luke.uribarri@lmco.com)

ABSTRACT: A survey of 21st century advanced materials with controlled functional structure, from the macro scale to the nanoscale, is presented. Novel advanced materials, which draw on both classical and quantum properties in order to achieve new functions, are overcoming such long-standing limitations as the diffraction limit in imaging optics and efficiency limitations in photovoltaic cells. The design and applications of engineered metamaterials are discussed across a wide size range, from earthquake mitigation for buildings to quantum cloaks at the nanoscale. In similar fashion, the intersection between biotechnology, biofabrication, and functional nanostructured materials is considered. Special attention is paid to the role of new manufacturing techniques for these advanced materials, the importance that manufacturing will play in their commercialization, and the role of powdered and porous materials in enabling both the manufacture of engineered metamaterials across many scales and the application of new catalytic materials in flow applications. Finally, some desired applications for these new classes of materials are presented as promising directions for research.

1. INTRODUCTION

One of the most astonishing things about materials science is the similarity in material functions over many orders of magnitude of size scales, and across functional disciplines. This similarity is not necessarily immediately obvious, nor does it obscure the truly bewildering variety of material properties and functions that exist. But the very existence of similar functionality from the macro to the nano scale gives the researcher pause, and invites the question to be asked at every step: if such-and-such a function is possible at this scale, is it possible at every other scale as well? Hence we talk of molecular machines or meta-atoms, phrases that represent real pairings of scale and functionality, but whose nouns and adjectives are drawn from opposite ends of the size scale in order to make their uses clear by analogy.

In this paper, we begin by making a few observations on the state of materials science generally, spanning from the classical to the quantum regime; we then move on to discuss engineered functional materials, giving emphasis to particularly promising directions in the state-of-the-art; finally, we finish with a discussion of applications to which new multifunctional materials can make a significant contribution and can enhance the overall capability of our technoculture to meet both established and emerging challenges.

2. THE CLASSICAL, SEMI-CLASSICAL AND QUANTUM REGIMES

Fascinating materials functionality exists on both the classical and the quantum scales, and in between at the semi-classical scale. “The so-called Bohr correspondence principle asserts that quantum mechanics is a kind of

generalization of classical mechanics in the sense that one should be able to recover the classical properties of a system by making some approximations of its quantum properties. The goal of the semiclassical mechanics is to study the quantum behavior when the mass of the particle becomes big with respect to the Planck constant h , in this case h tends to 0” [Baghli and Zanoun, 2009]. Thus we begin with the classical secondary properties of response to light waves (reflection, refraction, absorption), to electrostatic and magnetic fields separately (polarization and emission, magnetism, etc.), and to mechanical dynamics evidenced in the response to sound, temperature, mechanical impact and abrasion, etc. We then move down the scale to where h is no longer negligible, ending in the quantum regime where the physics is counterintuitive but the applications are often still recognizable.

2.1. The Classical Regime

In recent years there has been a great deal of work on so-called *metamaterials*, whose functional properties derive more from the structure of the material than from its composition (though the material composition always plays some part in the function, through its conductivity, electromagnetic or acoustic wave impedance, tensile strength, etc.). These metamaterials can be structured to have properties that do not exist in natural materials, such as left-handedness (or negative refractive index), photonic bandgaps, non-physical material properties such as negative permeability or negative mass density, anisotropy in any of these properties, and chirality. For materials comprised of complex molecules, chirality is the rule rather than the exception and materials with a single chirality, or a selected mix of chiralities will exhibit different properties depending upon how they are excited.

These meta-properties of the engineered materials, accessible to the designer by way of structural changes, will allow us to tune these materials for particular applications more finely. Already they are demonstrating their utility as lenses, waveguides, cloaks, and energy traps; we suspect that the application space has only barely begun to open. [Liu and Zhang, 2011].

2.2. The Semi-Classical Regime

Metamaterials, and their fascinating properties, are not the only notable materials to have made progress in recent years. Non-linear materials are also of increasing interest for their applications in measurement devices, transmitters, photovoltaics, etc. The non-linearity of these materials is often treated in a semi-classical fashion: a classical oscillator interacts with photons, for example, or a quantum oscillator with a classical field. Frequency doubling in non-linear optics, in which two photons are combined through the nonlinear action of the material into a single one of greater energy, shares some of these properties. Not just photons, but any quantum phenomenon, can take advantage of such materials, properly produced: photons, phonons, excitons, plasmons, polarons, etc. Applications to all these different energy packets are nascent or not yet even conceived; but the richness of the phenomena invites further exploration and will demand ever-increasing control over the composition and structure of materials.

These kinds of materials are considered “semi-classical” because their behavior seems to break the classical rules but does not yet evidence or make use of the distinguishing elements of “quantum weirdness”—superposition, uncertainty, and entanglement, for example—as do the class of quantum materials.

2.3. The Quantum Regime

The purely quantum materials exhibit secondary properties that are the hallmarks of the quantum regime. Perhaps the defining characteristic of the quantum regime is indistinguishability. A.J. Leggett gives a rigorous definition of what constitutes a quantum material: it is "...a many-particle system in whose behavior not only the effects of quantum mechanics, but also those of quantum statistics, are important" [Leggett 2006]. For quantum materials to exist properly then, the thermal energy of the system ($k_B T$) must in general be smaller than the relevant energy quanta ($n^{2/3} \hbar^2/m$), which generally requires the key features of the system be of nanoscale size or very cold or both. In these conditions, though, certain well-known quantum materials emerge: Bose-Einstein condensates of atoms and Cooper pairs of electrons, which exhibit such behavior as superconductivity and superfluidity. The effective mass of particles can become infinite; their effective size large compared with their normal physical dimensions; and with such properties, how many potential applications must there be? Magnetic levitation is among the several common superconductor applications; but for other phenomena, a rich variety of electrical, mechanical, and optical devices must lie within an application space that is still largely unexplored.

3. FUNCTIONAL MATERIALS FROM THE MACRO SCALE TO THE NANO SCALE

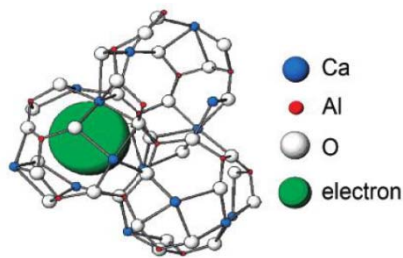
We now return to discussing functional materials; in particular, we wish to show that by thinking across size scales and disciplines, new applications for functional materials may be conceived, and that for these new materials, new synthesis methods will be necessary.

3.1. Functional Materials with Periodic Structure

Classical metamaterials, in which the properties of the substances composing the material are of secondary importance to the structure of the material, are built upon a set of concepts that scales across 12 orders of magnitude in size. The reason for this wide scaling is that metamaterials exhibit their special properties when interacting with waves; and wave properties are similar across physical phenomena and across length scales. Metamaterials were originally conceived to manipulate electromagnetic fields. These may have wavelengths from many meters (RF) to hundreds of nanometers (visible light). But the concepts work both up and down in size: it has been proposed that a metamaterial cloak might be embedded in the ground around buildings, to deflect the energy carried by in-plane elastic waves—whose wavelength may be on the order of a kilometer—during earthquakes [Brun *et al.* 2009]; it has also been proposed [Lee and Lee, 2013] that a properly patterned nanoparticle with a hollow core can be used to shield its contents from the quantum effects of its surroundings—essentially, providing a shield against atoms, electrons, photons, or anything else that is defined by a wavefunction. In one case, we see the structure interacting with a very large acoustic wave; in the other, with a very small probability wave. In between these scales are sound waves, vibrations, RF and microwave communications signals, photons, phonons and so forth; and in principle the metamaterial approach can be used to control any of these phenomena.

In some ways, the history and nature of metamaterials at all scales shares many attributes with porous materials. Some of the earliest electromagnetic metamaterials were porous materials: dielectric sheets drilled with patterns of

holes. The difference in permittivity and permeability between the dielectric and the air in the holes provided the property contrast that made the metamaterial work [Yablonovich, 2001]. The seismic metamaterial can be accomplished using cylindrical pores in the ground around the building, filled with an absorber such as water [Kim and Das, 2012]. And at the nano scale, certain clathrate materials (also called “host-guest” materials), in which molecular “cages” are built around cavities containing atoms or electrons, the cage structure of the material deforms the wavefunctions of the guest particles, either allowing or denying them the ability to jump from cage to cage [Sushko *et. al.*, 2007]. This is just transport through a porous medium, played out at the quantum scale. The fundamental cage structure of one such material is



shown in Fig. 1.

Figure 1: The unit cell of C12A7 (Mayenite), a host-guest material demonstrated to transport a number of particles through its lattice, including electrons and oxygen atoms [Kim *et. al.*, 2007].

Fabricating functional metamaterials is a challenging process, for reasons that differ along the size spectrum. At the scale of acoustic waves, vibration, and RF and microwave electromagnetic wavelengths (from 1 meter to 1 millimeter), the challenge is primarily structural: many of the structures that are designed using computer software such as ANSYS or COMSOL—and which can

interact with these waves in extraordinarily sophisticated ways—simply are not manufacturable with standard subtractive machining techniques, and therefore often must be assembled by hand out of many pieces. This is both tedious and inexact, and the quality of the metamaterials suffers for it. The development of sophisticated 3D printing techniques, which are now approaching accuracies on the sub-millimeter scale, presents new opportunities to develop structures that are impossible to machine, using many different materials, with a speed and precision that will make metamaterials practical for many purposes. Because the most precise method for 3D “additive” manufacturing involves laser sintering of sequential layers of powdered materials to form the structure, we anticipate that there will be a great demand in the near future for powdered materials of every conceivable composition, of high purity, and well-defined mechanical characteristics. It is likely that the future of metamaterials on this scale depends upon these advances in manufacturing. An early prototype, 3D printed at MIT to focus RF radiation, is shown in Fig. 2.

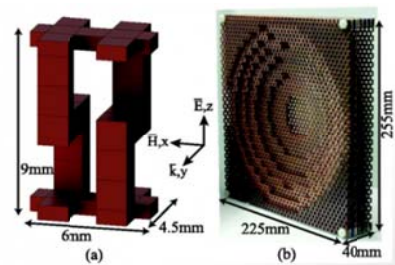


Figure 2: An RF metamaterial lens with negative index of refraction. On the left is the unit cell; on the right, the roughly 10 inch by 10 inch structure, 3D printed in polymer and copper coated [Ehrenberg *et. al.*, 2012].

At the nanoscale, additive manufacturing is not a viable option for creating periodic structures. For larger nanostructures, photolithography continues to make advancements, with typical feature sizes

of about 20 nm now possible. It is very difficult, however, to create complex 3D structures in this way—it can be compared to creating macroscopic metamaterials without the benefit of 3D printing.

At the molecular scale, the challenge becomes even greater. Whereas for macroscopic metamaterials, the composition of the material is less important than the structure of the material, at the molecular scale *the composition defines the structure*. Carbon, for example, readily forms nanotubes and graphene because its electron affinity of +4 allows it to form one double bond and two single bonds with three other carbon atoms; it also forms diamond by forming four single bonds to four other carbon atoms. It cannot, however, be used to create arbitrarily shaped structures, for the repulsion of the chemical bonds dictates either the planar hexagonal or the tetrahedral configurations. Forming other structures requires use of other elements with different bonding patterns. Therefore the design problem—not to mention the manufacturing problem—is much greater when dealing with the tiniest structures.

3.2. Materials with Engineered Moieties

In chemistry, a moiety, or a functional group, is a group of atoms or molecules that exhibits some form of chemical response regardless of the macromolecule to which it is attached. Biological processes are full of functional groups that make life possible: hemoglobin, for example, contains several functional groups that are responsible for the uptake and release of oxygen in the bloodstream; hydrophobic functional groups are essential to the formation of the bilipid layers that form cell walls. There has been a great uptick in interest recently in the field of synthetic biology, which

seeks to exploit the functions of normally biological molecules to engineer surfaces with defined properties, highly selective reaction catalysts, or “living foundries” to manufacture biomolecules.

These biomaterials are fundamentally molecular level entities, and so share the manufacturing difficulty of the molecular-level metamaterials just discussed; often the functionality of a molecule, such as a protein, is entirely defined by its structure, which is in turn defined not only by the covalent bonds of the atoms within the molecules, but also by the complex mix of polar, ionic, and van der Waals forces found in such large molecules. Nevertheless, because biology also provides a great number of functioning templates, it is possible to reverse-engineer molecules already found in nature, and then modify their functional groups to new ends. For example, a protein known to bind to nickel atoms was recently modified to instead bind to uranyl (UO_2) molecules [Wegner *et al.*, 2009]; similarly modified functional groups can target toxic and environmentally hazardous materials, to function as either sensors or part of a cleanup strategy. The first such protein created for uranyl selectivity is diagrammed in Fig. 3.

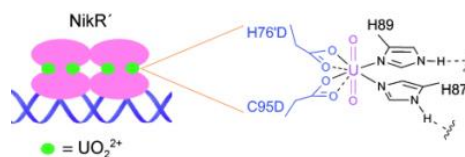


Figure 3: The first uranyl-selective DNA-binding protein was designed using a protein that was originally nickel-responsive. Modifications to the composition adjust the shape of the protein, giving it high selectivity to the target [Wegner *et al.*, 2009].

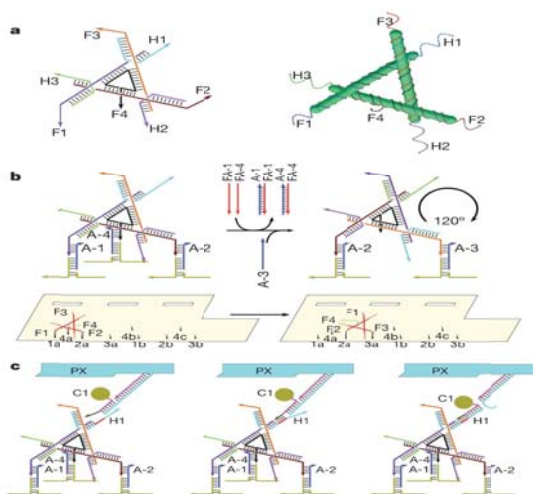
Synthetic construction of such molecules can in theory be done with the tedious use of atomic force microscopy to manipulate individual atoms; but this is impractical

for molecules of any significant size. On the other hand, recent advances in understanding the composition and function DNA and RNA, and their role in encoding protein structure and facilitating protein manufacture, have enabled researchers to use these organic molecules as machines in assembly lines, not only to fit together all the components of the desired proteins, but also to affix the finished product to a surface being functionalized [Gu *et. al.*, 2010]. A diagram of a DNA-based cargo mover for such an assembly line is shown in Fig. 4.

In fact, in the most extreme cases the use of the “bio-” prefix (as in biomaterials, biomolecules, etc.) is more a homage to the inspiration for the processes used to create the materials, than it is to the source of the materials themselves. When an RNA molecule—specifically assembled to create a protein that does not exist in nature—is used as a manufacturing tool to create, for example, nanoparticles of inorganic composition, to what extent are we still speaking of biology? At this level of detail, the boundaries between nanoscience, molecular biology, and

collecting and delivering gold nanoparticles as part of a molecular manufacturing system [Gu *et. al.*, 2010].

Frequently the moieties manufactured in synthetic biology have some catalytic end in mind. This may be stripping elements off of an organic molecule, breaking down a hydrocarbon into smaller chains, or neutralizing pathogens in a ventilation or water system. For catalytic applications, the speed at which the desired reaction takes place is usually directly proportional to the functionalized surface area available; for a working fluid in the gas or liquid states, the best way to achieve contact with a large catalytic surface is to filter it through a powder, or force it through a porous material. We expect, therefore, as new applications come online that make use of synthetic or bio-derived catalysts, demand will increase for powdered materials that can easily host functional groups; and perhaps more critically, for processes that can sinter those powders into porous materials without losing the functional groups. Highly catalytic porous materials will find many applications in gas and liquid processing for energy, healthcare, agriculture, and transportation.



physical chemistry begin to dissolve.

Figure 4: A DNA-based “walker” designed to move along a track,

4. SOME SAMPLE APPLICATIONS FOR ADVANCED MATERIALS

The application space opened by the materials discussed here is very large, and a few sample applications will serve to illustrate how significantly these materials, and others like them, will affect a number of industries. For example:

- A nonlinear material capable of absorbing solar energy (mostly visible) or earthshine (mostly infrared) and converting it directly to RF would dramatically reduce the complexity and weight of balloons and airships with communications requirements.

- Materials that could convert acoustic energy to electromagnetic energy and back (meta-piezoelectrics) would increase the capability and reduce the space, weight, and power requirements of sonar and ultrasound equipment.
- An acoustic cloak metamaterial that rejects certain bands of vibrational frequencies would provide excellent protection to vibration-sensitive electronics and sensing equipment on airborne, ground-based, and ocean platforms.
- Metamaterial antennas, which can receive and transmit more power than conventional antennas and overcome the diffraction limit, are achievable today but only become practical on large scales when advanced manufacturing techniques are employed to create economies of scale.
- Novel synthetic catalysts with moieties that reconfigure hydrocarbons to enhance their energy density or combustion properties would be employed to create new synthetic fuels and enhance the energy efficiency of existing transportation and industrial equipment. The efficiency of such processes would depend upon large catalytic surfaces being available to process large volumes of working fluid.
- A quantum cloak used to shield an atom or electron from lattice vibrations within a solid would extend the coherence time for quantum states of the particle and allow solid-state quantum computers to operate at higher temperatures and qubit densities than currently possible.

This short list of applications illustrates the wide variety of fields that are likely to be impacted by new advances in materials science within the near future.

Enabling these materials to be manufactured is a serious challenge in its own right, and the scientific community that creates the raw materials, usually beginning in powdered form, will play a significant role in realizing these and many other applications.

REFERENCES

- Baghli, N and A. Zanon. "Mathematical methods for physics: Semiclassical regime." *Adv. Stud. Theor. Phys.*, 3(1) 2009, p. 179
- Brun, M., S. Guenneau and A. B. Movchan. "Achieving control of in-plane elastic waves." *Applied Physics Letters* 94, 061903 2009.
- Ehrenberg, I. M., S. E. Sarma, and B.-I. Wu. "A three-dimensional self-supporting low loss microwave lens with a negative refractive index." *J. Appl. Phys.* 112, 073114, 2012.
- Gu, H., J. Chao, S.-J. Xiao and N. C. Seeman. "A proximity-based programmable DNA nanoscale assembly line." *Nature* v. 465, p. 202, 2010.
- Kim, S.-H. and M. P. Das. "Seismic Waveguide of Metamaterials." <http://arxiv.org/abs/1202.1586>
- Kim, K.-B., M. Kikuchi, M. Miyakawa, H. Yanagi, T. Kamila, M. Hirano and H. Hosono, "Photoelectron Spectroscopic Study of C12A7:e- and Alq3 Interface: The Formation of a Low Electron-Injection Barrier," *Journal of Physical Chemistry C*, vol. 111, p. 8403, 2007.
- Lee, J. Y. and R.-K. Lee. "Hide the interior region of core-shell nanoparticles with quantum invisible cloaks." <http://arxiv.org/abs/1306.2120>
- Leggett, A. J., *Quantum Liquids*. Oxford University Press. 2006.
- Liu, Y. and X. Zhang. "Metamaterials: a new frontier of science and technology." *Chem. Soc. Rev.*, 40(5) 2011 p. 2494
- Sushko, P.V., A. L. Shluger, M. Hirano and H. Hosono, "From Insulator to Electride: A Theoretical Model of Nanoporous Oxide 12CaO 7Al2O3," *Journal of the American Chemical Society*, vol. 129, p. 942, 2007.
- Wegner, Seraphine V., Boyaci, H., Chen, H., Jensen, Mark P. and He, C. (2009), Engineering A Uranyl-Specific Binding Protein from NikR. *Angew. Chem. Int. Ed.*, 48: p. 2339. 2009.
- Yablonovitch, Eli. "Photonic Crystals: Semiconductors of Light." *Scientific American*. December 2001, p. 47.

DESIGNING POROSITY IN POLYMER-DERIVED-CERAMICS

Paolo Colombo^{1,2,a}

1. University of Padova, Department of Industrial Engineering, Padova, Italy

2. The Pennsylvania State University, Department of Materials Science and Engineering, University Park, PA, USA

a. Corresponding author (paolo.colombo@unipd.it)

ABSTRACT: This paper reviews the main methods for the fabrication of highly porous ceramics from preceramic polymers. Different processing techniques can be employed to produce components with a pore size ranging from a few nanometers to a few millimeters in size, and with a very varied morphology.

1. INTRODUCTION

Highly porous ceramics, also called cellular ceramics when the total porosity is about ≥ 70 vol%, have found applications in several engineering fields because of their unique combination of favorable properties [Green, 2003]. Different applications require different pore architectures, in terms of cell size and size distribution, cell shape, presence of pores interconnecting the cells, size of the interconnecting pores, distribution of the porosity within the entire body (e.g. graded structures), presence of pores in multiple dimensional scales (i.e. ceramics with hierarchical porosity, with pores ranging from a few nm to hundreds of micrometers) [Colombo, 2008a; Colombo, 2010a]. Clearly, it is necessary to use different processing approaches to fabricate ceramics possessing such a wide range of morphological features [Colombo, 2006].

Preceramic polymers are a specific class of polymers that convert into a ceramic material upon heat treatment. Carbide (SiC), nitride (Si₃N₄, BN), mixed carbide-nitride (SiCN), oxycarbide (SiOC) and oxynitride ceramics (SiON) can be produced, as well as oxide ceramics. The range of compositions can be expanded by the addition of suitable fillers, either inert (i.e. not reacting with the preceramic polymer) or active (i.e. reacting with the decomposition products

of the preceramic polymer and/or the heating atmosphere) [Chae, 2009; Colombo, 2013].

The resulting ceramics are nano-structured, possessing amorphous and crystalline (e.g. β -SiC, Si₃N₄, BN), domains a few nanometers in size, and possess very interesting chemical, thermal and functional properties. Because of their polymeric nature, preceramic polymers can be processed in a great variety of ways, also employing techniques typical of conventional polymer processing (e.g. resin transfer molding, melt spinning, blowing, injection molding, etc.) [Colombo, 2010b]. Therefore, they represent a very versatile class of materials in which a large volume of tailored porosity can be embedded following several different processing approaches.

2. EXPERIMENTAL

Commercially available preceramic polymers were used in the experiments. Specifically: polymethylsilsesquioxane, polymethylphenylsilsesquioxane (MK and H44, Wacker-Chemie GmbH, München, Germany), poly(methylvinyl)silazane (Ceraset VL20, Clariant, USA) and polycarbosilane (PCS Type S, Nippon Carbon Co. Ltd., Yokohama, Japan). Poly(methylmetacrylate) micro-sized beads of different diameters

(Aldrich Chemical Company Inc., USA) were used as sacrificial filler, while azodicarbonamide (ADA, Sigma-Aldrich, USA) was used as physical blowing agent. Samples were heated in different atmospheres (air, Ar, N₂) at various temperatures, depending on which phases were designed to be obtained. Nano-sized or micro-sized fillers were also added in order to modify the composition of the resulting porous ceramics. Further processing details can be found in the cited literature.

3. RESULTS AND DISCUSSION

First of all, one should make a distinction between the fabrication of components possessing a micro-cellular or a macro-cellular structure. The first ones comprise porous ceramics in which the cell size is typically below 50 μm, while in the second ones the cell size ranges from ~50 μm up to several hundred microns or a few millimeters [Colombo, 2008b].

For the production of micro-cellular ceramics, the use of sacrificial fillers (e.g. dense or hollow/expandable polymeric micro-beads) or electro-hydrodynamic spraying is most suited, but emulsion techniques can be used (also in conjunction with micro-fluidics) [Vakifahmetoglu, 2009; Kim, 2004; Nangrejo, 2009; Bakumov 2009; Vakifahmetoglu, 2011; Ye, 2010]. Supercritical CO₂ has also been demonstrated to be a very promising way for developing porous ceramics with cell densities >10⁹ cells/cm³ and cell size < 10 μm [Kim, 2003].

In Figure 1 is shown the morphology of SiOC micro-cellular components fabricated using a silicone resin and different processing techniques. Graded porosity or closed cells can also be fabricated, by modifying the layout and amount of the sacrificial fillers. The advantage of employing a micro-cellular

ceramic over a macro-cellular one lies in the fact that the mechanical strength of ceramic foams increases with decreasing the dimension of the cells, because the strut size decreases [Colombo, 2004]. Moreover, the geometric surface that is present in a component possessing micro-sized cells is much higher in comparison to that of a component with macro-sized cells, and this surface can be exploited by chemical functionalization or the creation of additional porosity in the cell walls, with pore sizes of the order of a few nanometers [Colombo, 2010a].

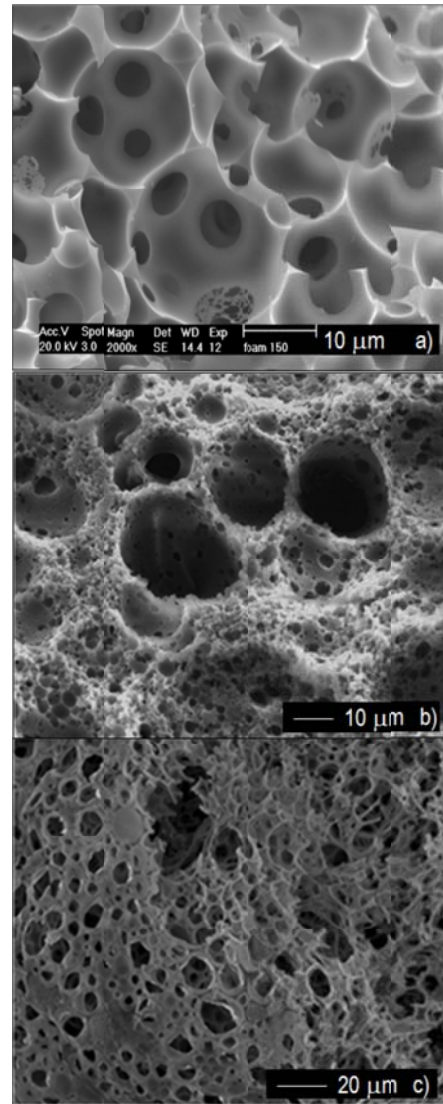


Figure 1. SiOC micro-cellular foams produced by: a) sacrificial templates; b)

electro-hydrodynamic spraying; c) micro-fluidic processing of emulsions.

Macro-cellular ceramics can be produced by direct foaming, using for instance polyurethane precursors as foaming agents, or a solvent with low boiling temperature [Colombo, 2002], or suitable chemicals (such as ADA) that decompose at temperatures ranging from about 150 to 250°C developing a large amount of gas [Idesaki, 2012], (Figure 2). In particular, the latter method is very versatile, enabling the fabrication of components containing a large volume of macroscopic pores (>70 vol%) from different preceramic polymers, such as silicones [Takahashi, 2003], silazanes [Vakifahmetoglu, 2009] and carbosilanes [Fukushima, 2012a]. Depending on the viscosity of the polymeric precursor used, some residual closed porosity can be retained in the components [Idesaki, 2012]. Freeze casting of preceramic polymers using camphene has also been proposed, leading to the formation of parts possessing highly aligned macropores [Yoon, 2007]. Mixing preceramic polymers with different molecular architectures (i.e. branched/cage structures or linear molecules), that possess a different ceramic yield after pyrolysis, also provides a very simple route for the production of macro-cellular ceramics with a large amount of open porosity, from solutions that can be cast in any shape [Vakifahmetoglu, 2008]. Another versatile approach enabling the production of both highly porous monoliths or micro-sized porous beads (diameter ranging from ~100 to ~700 μm), is the use of emulsified solutions (water/oil or water/oil/water), in which the preceramic polymer is dissolved in the oil phase [Vakifahmetoglu, 2011]. Albeit open cell foams find more applications because they allow fluid transport throughout the structure, closed cell foams can be fabricated by using suitable surfactants or advanced

processing control [Colombo, 2002; Kim, 2003; Kim, 2004].

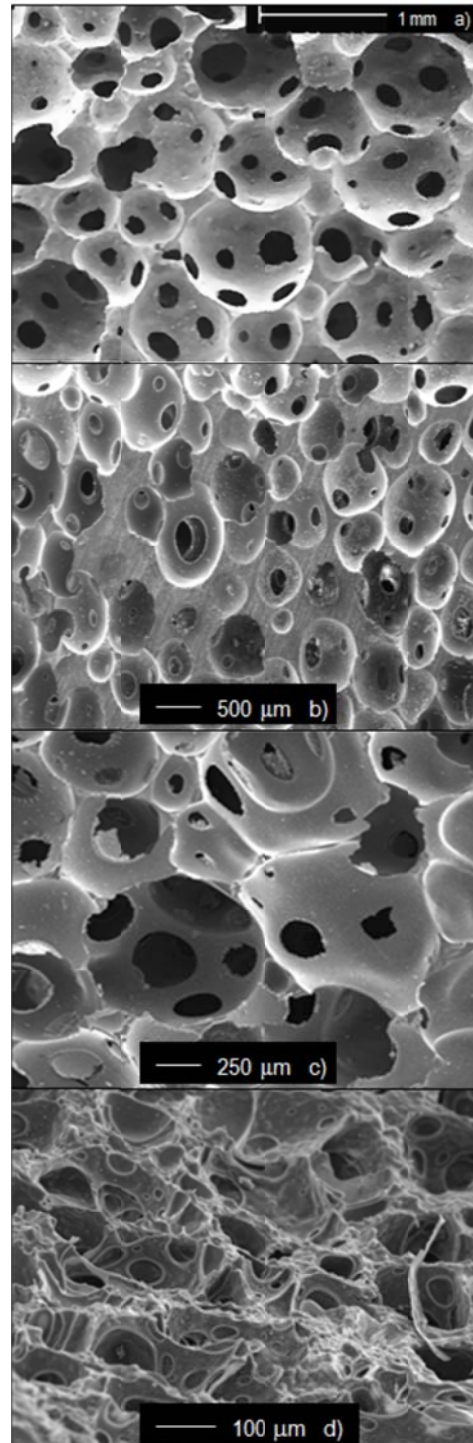


Figure 2. Macro-cellular foams produced by direct foaming: a) mixing with polyurethane precursors (SiOC); b) using pentane (SiOC); c) using ADA (SiCN); d) mixing preceramic polymers with different molecular architecture (SiOC).

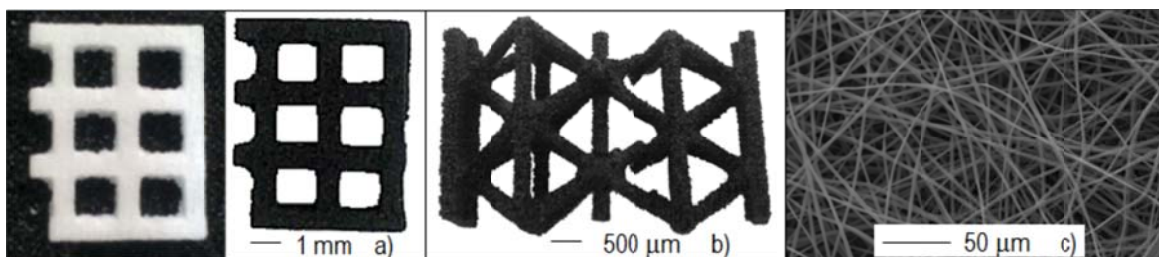


Figure 3. Porous structures produced by: indirect printing, a) 2D structure (left, before pyrolysis; right, after pyrolysis); b) 3D octahedral structure (after pyrolysis); or by electrospinning, c) fiber mat (after pyrolysis).

The addition of suitable fillers enables the production of ceramics possessing different additional functionalities, besides porosity, such as electrical conductivity [Colombo, 2001] or magnetic properties [Biasetto, 2008a], that further extend the range of possible applications. Furthermore, reactive fillers (such as calcium carbonate) can be mixed with silicone resins to fabricate bioceramic scaffolds for biomedical applications [Bernardo, 2012].

Pre-ceramic polymers can also be shaped into highly porous components by using additive manufacturing technologies (AMTs), such as indirect printing or fused deposition. This research is just in its beginnings, but very promising results have already been obtained [Zocca, 2013]. The advantage of AMTs is the possibility of precisely controlling the shape and dimension of the porosity to be embedded in a component, as well as its distribution throughout the body, enabling the fabrication of parts with complex pore architecture and a morphology not achievable using other processing methodologies. Moreover, highly porous components with an open-interconnected-network structure can be obtained by electrospinning of pre-ceramic polymer solutions [Guo, 2013]. In Figure 3 are shown the images of porous structures built by indirect printing or by electrospinning of a silicone resin.

Finally, all the cellular structures produced from pre-ceramic polymers using the different processing techniques briefly illustrated before can be further modified by the addition of micro- and meso-pores, resulting in cellular ceramics with hierarchical porosity. Such components possess a large amount of specific surface area (SSA, expressed in m^2/g) and display improved properties over single-mode porous components. In fact, the macroporous framework ensures the chemical and mechanical stability and good mass transport properties (lower pressure drop, higher rate of external transfer of mass, greater turbulence and increasing convective heat transfer in comparison to parts containing only micro- and/or meso-pores), while the smaller pores provide the functionality for a given application (e.g. enhanced catalytic properties or the selective binding of a specific molecule) [Colombo, 2010a].

Suitable strategies for the creation of micro- (i.e. with a size < 2 nm) or meso- (i.e. with a size from 2 to 50 nm) pores include: the controlled thermal treatment of (foamed) pre-ceramic polymers [Schmidt, 2001], the addition of high SSA fillers to pre-ceramic polymers before foaming [Vakifahmetoglu, 2010a], the deposition of high SSA coatings [Costacurta, 2004], the infiltration into foams of high SSA materials (e.g. aerogels), chemical etching (HF , Cl_2) [Biasetto, 2008b; Yeon, 2010], and the *in*

situ growth of 1D nanostructures (such as nanowires) [Vakifahmetoglu, 2010a; Fukushima, 2012b]. The SSA values achievable range from a few tens of m²/g to 2600 m²/g, depending on the processing procedure adopted.

Micro- and meso-pores can also be created in preceramic polymers using procedures such as self-assembly or nanocasting in sacrificial templates [Malenfant, 2007; Wang, 2013; Alauzun, 2011]. Moreover, preceramic polymers can be used for the fabrication of ceramic membranes for the efficient separation of gases [Iwamoto, 2005].

4. CONCLUSIONS

Designing porosity in polymer-derived-ceramics involves the utilization of a wide range of processing approaches, which include direct foaming, emulsions, the use of sacrificial templates, additive manufacturing technologies, freeze casting, electro-hydrodynamic spraying, electrospinning, the use of microfluidic devices, self-assembly or nanocasting. In this way, it is possible to fabricate porous ceramic components from preceramic polymers with a porosity higher than 70 vol %, and possessing a very varied set of characteristics, with pore sizes ranging from a few nanometers to a few millimeters and specific surface area as high as 2600 m²/g.

Acknowledgements: The author gratefully acknowledges the significant contribution and collaboration of several researchers for the development of highly porous components from preceramic polymers (E. Bernardo, M. Edirisinghe, M. Fukushima, C.M. Gomes, J. Guenster, A. Guo, C. Martinez, M. Modesti, C. Vakifahmetoglu, A. Zocca).

REFERENCES

Alauzun, J.G., Ungureanu, S., Brun, N., Bernard, S., Miele, P., Backov, R., Sanchez, C., 2011. Novel monolith-type boron nitride hierarchical foams obtained through

integrative chemistry. *J. Mater. Chem.*, 21, 14025.

Bakumov, V., Schwarz, M., Kroke, E., 2009. Emulsion processing of polymer-derived porous Si/C/(O) ceramic bodies, *J. Europ. Ceram. Soc.*, 29, 2857.

Bernardo, E., Colombo, P., Cacciotti, I., Bianco, A., Bedini, R., Pecci, R., Pardun, K., Treccani, L., Rezwan, K., 2012. Porous Wollastonite-Hydroxyapatite Bioceramics from a Preceramic Polymer and Micro- or Nano-sized Fillers, *J. Europ. Ceram. Soc.*, 32, 399.

Biasetto, L., Francis, A., Palade, P., Principi, G., Colombo, P., 2008a. Polymer-Derived Microcellular SiOC Foams with Magnetic Functionality, *J. Mater. Sci.*, 43, 4119.

Biasetto, L., Peña-Alonso, R., Sorarù, G.D., Colombo, P., 2008b. Etching of SiOC Ceramic Foams, *Adv. Appl. Ceram.*, 107, 106.

Chae, S.-H, Kim, Y.-W., Song, I.-H., Kim, H.-D., Narisawa, M., 2009. Porosity control of porous silicon carbide ceramics, *J. Europ. Ceram. Soc.*, 29, 2867.

Colombo, P., Gambaryan-Roisman, T., Scheffler, M., Buhler, P., Greil, P., 2001. Conductive Ceramic Foams From Preceramic Polymers, *J. Amer. Ceram. Soc.*, 84, 2265.

Colombo, P., Hellmann, J.R., 2002. Ceramic foams from preceramic polymers, *Mat. Res. Innovat.*, 6, 260.

Colombo, P., Bernardo, E., Biasetto, L., 2004. Novel Microcellular Ceramics from a Silicone Resin, *J. Am. Ceram. Soc.*, 87, 152.

Colombo, P., 2006. Conventional and novel processing methods for cellular ceramics, *Phil. Trans. R. Soc. A*, 364, 109.

Colombo, P., 2008a. In Praise of Pores, *Science*, 322, 381.

Colombo, P., 2008b. Engineering Porosity in Polymer-Derived Ceramics, *J. Europ. Ceram. Soc.*, 28, 1389.

Colombo, P., Vakifahmetoglu, C., Costacurta, S., 2010a. Fabrication of Ceramic Components with Hierarchical Porosity, *J. Mat. Sci.*, 45, 5425.

Colombo, P., Mera, G., Riedel, R., Sorarù, G.D., 2010b. Polymer-Derived-Ceramics: 40 Years of Research and Innovation in Advanced Ceramics, *J. Am. Ceram. Soc.*, 93, 1805.

Colombo, P., Bernardo, E., Parciannello, G., 2013. Multifunctional Advanced Ceramics from Preceramic Polymers and Nano-sized Active Fillers, *J. Europ. Ceram.*, 33, 453.

Costacurta, S., Biasetto, L., Pippel, E., Woltersdorf, J., Colombo, P., 2004. Hierarchical Porosity Components via

- Infiltration of a Ceramic Foam, *J. Am. Ceram. Soc.*, 90, 2172.
- Fukushima, M., Colombo, P., 2012a. Silicon carbide-based foams from direct blowing of polycarbosilane, *J. Europ. Ceram. Soc.*, 32, 503.
- Fukushima, M., Yoshizawa, Y., Colombo, P., 2012b. Decoration of ceramic foams by ceramic nanowires via catalyst-assisted-pyrolysis of preceramic polymers, *J. Am. Ceram. Soc.*, 95, 3071.
- Green, D.J., Colombo P., 2003. Cellular Ceramics: Intriguing Structures, Novel Properties, and Innovative Applications, *MRS Bull.*, 28, 296.
- Guo, A., Roso, M., Modesti, N., Liu, J., Colombo, P., 2013. Preceramic Polymer-derived SiOC Fibers by Electrospinning, *J. Appl. Polym. Sci.*, in press.
- Idesaki, A., Colombo, P., 2012. Synthesis of a Ni-Containing Porous SiOC Material From Polyphenylmethylsiloxane by a Direct Foaming Technique. *Adv. Eng. Mater.*, 14, 1116.
- Kim, Y.-W., Kim, S.-H., Wang, C., Park, C.B., 2003. Fabrication of Microcellular Ceramics Using Gaseous Carbon Dioxide. *J. Am. Ceram. Soc.*, 86, 2231.
- Kim, S.-H., Kim, Y.-W., Park, C.B., 2004. Effect of inert filler addition on pore size and porosity of closed-cell silicon oxycarbide foams. *J. Mater. Sci.*, 39, 3513.
- Malenfant, P.R.L., Wan, J., Taylor, S.T., Manoharan, M., 2007. Self-assembly of an organic-inorganic block copolymer for nano-ordered ceramics. *Nat. Nanotechnol.*, 2, 43-46.
- Nangrejo, M., Farook, U., Ahmad, Z., Bernardo, E., Colombo, P., Stride, E., Edirisinghe, M., 2009. Electrohydrodynamic Forming of Porous Ceramic Capsules from a Preceramic Polymer, *Mater. Lett.*, 63, 483.
- Schmidt, H., Koch, D., Grathwohl, G., Colombo, P., 2001. Micro-Macro Porous Ceramics From Preceramic Precursors, *J. Amer. Ceram. Soc.*, 84, 2252.
- Takahashi, T., Colombo, P., 2003. SiOC Ceramic Foams through Melt Foaming of a Methylsilicone Preceramic Polymer, *J. Porous Mat.*, 10, 113.
- Vakifahmetoglu, C., Colombo, P., 2008. A Direct Method for the Fabrication of Macro-Porous SiOC Ceramics from Preceramic Polymers, *Adv. Eng. Mater.*, 10, 256.
- Vakifahmetoglu, C., Menapace, I., Hirsch, A., Biasetto, L., Hauser, R., Riedel R., Colombo, P., 2009. Highly Porous Macro- and Micro-Cellular Ceramics from a Polysilazane Precursor, *Ceram. Inter.*, 35, 3281.
- Vakifahmetoglu, C., Pauletti, A., Fernandez Martin, C., Babonneau, F., Colombo, P., 2010a. SiOC ceramic monoliths with hierarchical porosity, *Inter. J. App. Ceram. Tech.*, 7, 528.
- Vakifahmetoglu, C., Colombo, P., Carturan, S., Pippel, E., Woltersdorf, J., 2010b. Growth of 1D-Nanostructures in Porous Polymer Derived Ceramics by Catalyst-Assisted-Pyrolysis. Part II: Cobalt Catalyst, *J. Am. Ceram. Soc.*, 93, 3709.
- Vakifahmetoglu, C., Balliana M., Colombo, P., 2011. Ceramic foams and micro-beads from emulsions of a preceramic polymer, *J. Europ. Ceram. Soc.*, 31, 1481.
- Ye, C., Chen, A., Colombo, P., Martinez, C., 2010. Ceramic Micro-particles and Micro-capsules via Microfluidic Processing of a Preceramic Polymer, *Roy. Soc. Interf.*, 7, S461.
- Yeon, S.-H., Reddington, P., Gogotsi, Y., Fischer, J.E., Vakifahmetoglu, C., Colombo, P., 2010. Carbide-Derived-Carbons with Hierarchical Porosity from a Preceramic Polymer, *Carbon*, 48, 201.
- Yoon, B.-H., Lee, E.-J, Kim, H.-E., Koh, Y.-H., 2007. Highly Aligned Porous Silicon Carbide Ceramics by Freezing Polycarbosilane/Camphene Solution, *J. Am. Ceram. Soc.*, 90, 1753.
- Iwamoto, Y., Sato, K., Kato, T., Inada, T., Kubo, Y., 2005. A hydrogenpermselective amorphous silica membrane derived from polysilazane. *J. Eur. Ceram. Soc.*, 25, 257.
- Wang, J., Oschatz, M., Biemelt, T., Lohe, M.R., Borchardt, L., Kaskel, S., 2013. Preparation of cubic ordered mesoporous silicon carbide monoliths by pressure assisted preceramic polymer nanocasting, *Microporous Mesoporous Mater.*, 168, 142.
- Zocca, A., Gomes, C.M., Guenster, J., Staude, A., Bernardo, E., Colombo, P., 2013. SiOC ceramics with ordered porosity by 3D-printing of a preceramic polymer, *J. Mater. Res.*, in press.

SECTION A

Development and Characterization

STUDY ON NANOSTRUCTURED SILICON CARBON THIN FILMS DEPOSITED BY PECVD

D.K. Basa^{1a}, G. Ambrosone,^{2,3} U. Coscia^{3,4}

¹Utkal University, Department of Physics, Bhubaneswar, India

²CNR-SPIN, Napoli, Italy

³Naples University "Federico II", Dipartimento di Fisica, Napoli, Italy

⁴CNISM Unita' di Napoli, Italy

a. Corresponding author (basa@iopb.res.in)

ABSTRACT: Ever since the discovery of room temperature visible photoluminescence in porous silicon, the porous materials like nanostructured silicon based materials, composed of silicon nanocrystallites embedded in amorphous matrix of different kind, have generated considerable interest both fundamentally and technologically for the new generation optoelectronic and micro electric devices because of their tunable properties and efficient room temperature visible photoluminescence. Powder, amorphous and crystalline silicon have been grown by plasma enhanced chemical vapour deposition (PECVD) system. Microcrystalline and nanocrystalline silicon phases in the amorphous matrices have been grown under very similar deposition conditions in PECVD system. Therefore, a clear picture regarding their phase transition is necessary to determine the growth conditions to obtain nanostructured films with suitable properties for device applications. Further, both silicon nanocrystallites and the amorphous silicon carbon matrix are responsible for the room temperature visible photoluminescence but their role concerning the said photoluminescence is not well studied in spite of the importance of these materials. Accordingly, we have undertaken a detailed study on the structural and optical properties of hydrogenated silicon carbon films prepared by varying rf power in PECVD system using silane and methane gas mixture highly diluted in hydrogen and have not only demonstrated that the transition from microcrystalline to nanocrystalline phase is smooth, but also have discussed the contributions of the Si nanocrystallites and amorphous silicon carbon matrix to the room temperature visible photoluminescence.

1. INTRODUCTION

Ever since the discovery of room temperature visible photoluminescence (PL) in porous silicon, there has been a flood of activity in the porous materials like nanostructured silicon based materials that are composed of silicon nanocrystallites embedded in dielectric matrix of different kind such as silicon oxide (SiO₂), silicon nitride (Si₃N₄) and silicon carbide (SiC). Because these materials offer the possibility of tunable opto-electronic properties as well as efficient room temperature visible

photoluminescence (PL), they have generated considerable interest both fundamentally and technologically for the future generation micro-electronic and opto-electronic devices [Canham, 1990, Lehmann and Gosele, 1991, Ball, 2001, Canham, 2000, Lu et al., 1995, Allan 1997, Park et al., 2001, Draeger, 2003, Basa et al., 2008, Coscia et al., 2008, Wang et al., 2012, Voyles et al., 2001, Green, 2003]. The SiC dielectric matrix has lower band gap and lower barrier height, as compared to SiO₂ and Si₃N₄ matrices, which is much favorable for the carrier transport because of the enhanced

tunneling probability of carriers and accordingly have opened up great possibilities for the new generation tandem solar cells [Green, 2003, Conibeer, 2006].

Among the deposition techniques the plasma enhanced chemical vapour deposition (PECVD) has the advantages of obtaining large area devices at low cost. Powder, amorphous and crystalline silicon have been prepared by PECVD technique under different deposition conditions. However, in PECVD system [Fontcuberta, 2001] nanostructured and microcrystalline silicon carbon have been grown near the onset of crystallization, therefore, a study regarding the microcrystalline to nanocrystalline phase transition is necessary to establish the deposition conditions of the nanostructured films. Furthermore, it is known that both amorphous hydrogenated silicon carbon matrix ($a\text{-Si}_{1-x}\text{C}_x\text{:H}$) as well as silicon nanocrystallites can be responsible for the room temperature visible photoluminescence in these materials [Coscia et al., 2008, Wang et al., 2010], however their respective contributions are not yet completely clear. Accordingly, in this manuscript, we have undertaken a detailed study on the structural and optical properties of the hydrogenated silicon carbon films prepared by varying rf power in PECVD system using silane (SiH_4) and methane (CH_4) gas mixtures highly diluted in hydrogen (H_2), to address these issues.

2. EXPERIMENTAL DETAILS

The hydrogenated silicon carbon films were prepared in a 13.56 MHz capacitively coupled high vacuum PECVD system, using silane and methane gas mixture highly diluted in hydrogen. The films were grown by varying rf power (w) from 15 W to 100 W (power density from 65 to 325 mW/cm^2) while the other deposition parameters were maintained constant as

follows: substrate temperature at 250 °C, pressure at 226 Pa, total gas flow rate at 300 SCCM (cubic centimeter per minute at standard temperature and pressure), methane fraction $\text{CH}_4/(\text{CH}_4 + \text{SiH}_4)$ at 0.50 and hydrogen dilution $\text{H}_2/(\text{CH}_4 + \text{SiH}_4)$ at 250. Films were deposited simultaneously onto different substrates: 7059 Corning glass for X-ray diffraction (XRD), Raman, optical and PL and c-Si $\langle 100 \rangle$ for FTIR and nuclear measurements. The discharge chamber was pumped down to 10^{-5} Pa prior to the deposition of the films.

X-ray diffraction measurements were carried out in the grazing incident geometry (incident angle of 0.7) for the structural measurement. The XRD setup consists of a Bruker D5000 diffractometer equipped with a Cu target and a solid state detector to collect the scattered rays. A Gobel mirror was used to collimate and select the K_α incident beam. Raman spectra were obtained in 200-2000 cm^{-1} range using a micro Raman Renshaw spectro-photometer equipped with a cooled CCD detector and an argon laser excitation at 514.5 nm. IR absorption measurements in the range 400-4000 cm^{-1} were carried out with a Fourier transform infrared (FTIR) Perkin-Elmer spectrophotometer having resolution of 1 cm^{-1} . Rutherford back scattering, nuclear reaction analysis and the elastic recoil detection analysis were used to determine the atomic density of silicon, carbon and hydrogen respectively. The optical absorption in 200-2500 nm range were obtained by using a dual beam Perkin-Elmer 900 spectrophotometer to determine the optical band gap (E_{04}), corresponding to absorption coefficient $\alpha = 10^4 \text{ cm}^{-1}$. Photoluminescence spectra were obtained at room temperature by exciting the sample with the 514.5 nm line of an argon laser at power density of 25 mW/mm^2 . The emitted light was collected in a single monochromator with

a focal length of 20 cm coupled to a cooled back illuminated CCD camera.

3. RESULTS AND DISCUSSION

The composition of the deposited films was determined by nuclear techniques. Fig. 1 displays the variations of Si, H and C atomic percentages as a function of rf power w : Si atomic percentage decreases while H and C atomic percentages increase.

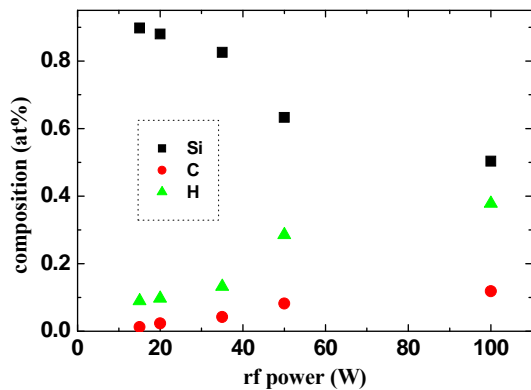


Figure 1: Si, C and H atomic percentages as a function of rf power w .

Fig. 2 displays the XRD spectra of the films deposited with different rf power values. Three peaks located at 28.4° , 47.2° and 56° , assigned to $\langle 111 \rangle$, $\langle 220 \rangle$ and $\langle 311 \rangle$ reflection planes respectively of crystalline silicon are observed for the films deposited with rf power $w \leq 25$ W. The spectrum of the samples deposited at $w = 35$ W exhibits only a feeble protuberance, while no crystalline peaks are visible for the films with higher rf power. The intensity of the XRD peaks are observed to decrease while the full width at half maximum (FWHM) of the XRD peaks are found to increase with increase in rf power, indicating the decrease of crystallinity degree. The average grain size in $\langle 111 \rangle$ direction, δ , calculated from the well known Scherrer formula [Klug and Alexander, 1974], is shown as a function of w in the inset in Fig. 2: δ decreases from 14.3 to 7.7 nm in the 15-35 W range. Neither SiC nor C

crystalline peaks are found to be present for these films indicating that carbon is incorporated only in the amorphous matrix.

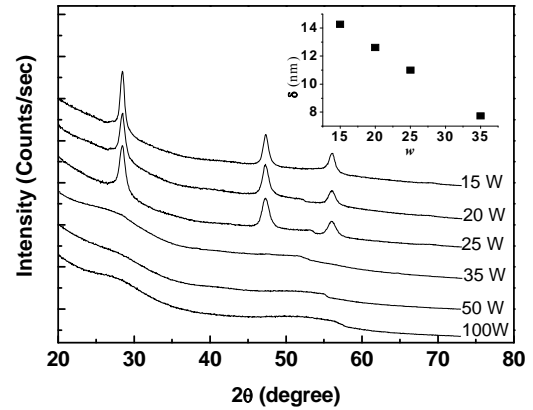


Figure 2: XRD spectra of films deposited at different rf power w . In the inset the average grain size δ vs. w .

Raman spectroscopy was also used to investigate the structural evolution of the films. The Raman spectra of the films deposited with different rf power are shown in Fig. 3. The sharp Raman peak at 520 cm^{-1} which is the characteristic of crystalline silicon, is observed for the films deposited with $w < 25$ W. Raman peak for the film deposited with $w = 25$ W is not only observed to downshift to 517 cm^{-1} but also found to be broadened. The downshift and the broadening of this peak indicate the size reduction of the silicon crystallites [Iqbal et al., 1981]. The Raman spectra of the films deposited with $w \geq 35$ W show little difference from each other. Although they do not provide the signature of large crystallites they show an asymmetric peak centered at $\sim 483\text{-}484 \text{ cm}^{-1}$, suggesting the presence of very small silicon crystallites embedded in the amorphous matrix [Zhang et al., 2006]. Further, neither Raman peak due to SiC or C crystallites are observed for the films which is consistent with XRD results. XRD and Raman measurements have established

conclusively the presence of microcrystalline phase for the films deposited with low rf power. The Raman measurements however, strongly suggest the presence of nanocrystallites of smaller size in the films deposited with $w \geq 35$ W.

The FTIR spectra of the films deposited at 15, 35 and 100 W in the 400 - 4000 cm^{-1} range, shown in Fig. 4, present the following absorption bands.

- i. The band from 2800 to 3000 cm^{-1} , scarcely visible only for the film deposited at highest w , ascribed to C-H stretching (s).
- ii. The absorption band from 2000 to 2200 cm^{-1} assigned to Si-H (s).
- iii. The region from 600 to 1200 cm^{-1} attributed to the superposition of four vibration modes: Si-H rocking/wagging at 640 cm^{-1} , Si-C stretching (s) around 760-780 cm^{-1} , Si-H bending near 800-900 cm^{-1} and C-H wagging at 1000 cm^{-1} respectively.

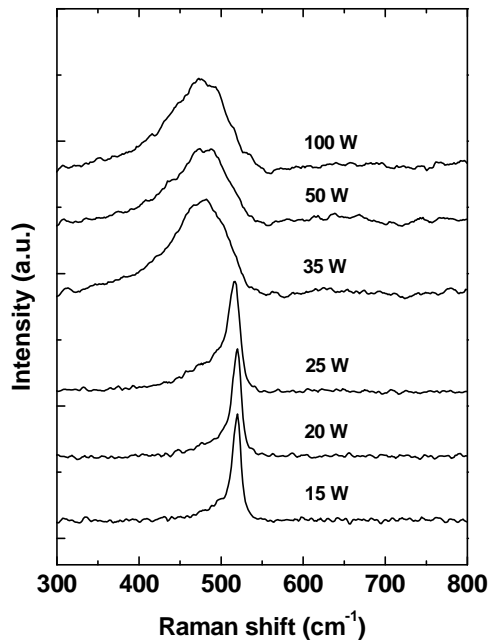


Figure 3: Raman spectra of films deposited at different rf power values.

Because the Si-C stretch mode provides information about network bonding and ordering, this mode was investigated in

detail. In Fig. 4 the deconvoluted Si-C stretch mode, obtained using Lorentzian curve, is also displayed for each spectrum. The bond density of Si-C(s) mode, evaluated by using the appropriate inverse cross-section [Basa and Smith, 1990] as reported in Fig. 5, increases as function of w . The FWHM of Si-C(s) peak, also displayed in Fig. 5, increases from 126 cm^{-1} to 137 cm^{-1} with increase in w from 15 W to 35 W, then keeps decreasing with increase in rf power and reaches the value of 131 cm^{-1} for $w = 100$ W.

It is interesting to note that from the data analysis the following picture on the structure of the films can be obtained.

It is well established [Basa and Smith, 1990, Kerdiles et al., 2000, Oliveira and Carreno, 2006] that a Gaussian line shape indicates a Gaussian distribution of bond lengths and bond angles, typical of amorphous phase, while Lorentzian line shape reflects a smaller bond angle distribution and a narrower bond length distribution, indicating a more uniform and ordered environment which is the characteristic of the crystalline phase. Because the line shape of Si-C(s) mode remains Lorentzian for all the films, this demonstrates that crystalline character is retained even for the samples deposited with $w \geq 35$ W, confirming the inference of Raman measurements.

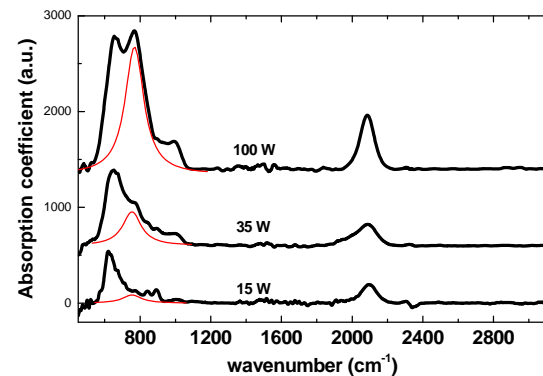


Figure 4: IR spectra of films deposited at 15, 35 and 100 W (thick lines). The Si-C

stretch peak deconvoluted using Lorentzian curves are represented by thin lines. The nuclear measurements, on the other hand, reveal that the carbon content as well as the hydrogen content increase with increase in rf power and due to chemical ordering [Mui et al., 1987a, Mui et al., 1987b] carbon is bonded to silicon, resulting in the increased formation of Si-C bonds. Because of the near absence of C-H modes for the studied films, hydrogen is mostly bonded to silicon, as a result of which Si-H bonds increase with increase in hydrogen content. Therefore, the increased formation of Si-C bonds as well as Si-H bonds result in the decreased formation of Si-Si bonds. In addition, the increase in the number of Si-C bonds is responsible for making more extended amorphous silicon carbon regions, that surround the silicon crystallites, while the formation of more Si-H bonds tends to terminate the network. These, in turn, result in the formation of small but more numerous silicon nanocrystallites with increase in rf power. The increase in the number of nanocrystallites as well as the decrease in their size with increase in rf power have been demonstrated in silicon carbon films by [Suendo et al., 2006] through HRTEM measurements which corroborates our conclusion.

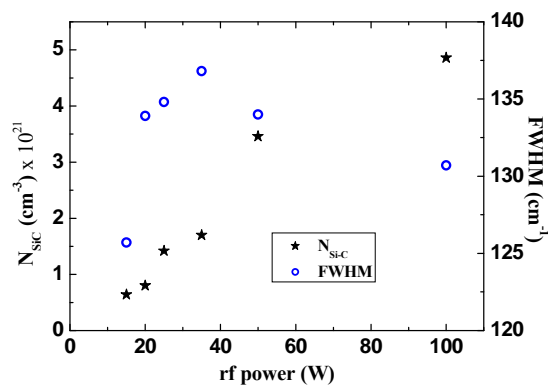


Figure 5: The bond density of Si-C(s) peak, N_{Si-C} , and FWHM of Si-C(s) peak vs. the rf power.

It is reported [Voyles et al., 2001, Zhang et al., 2006] that order in the system increases with increase in the number of nanocrystallites of smaller size and also that FWHM of Si-C(s) peak increases with decrease in order in the network [Basa and Smith, 1990, Basa, 2002]. Thus the observed increase in FWHM of Si-C(s) from 126 cm^{-1} to 137 cm^{-1} with increase of rf power from 15 W to 35 W (see Fig. 5) is attributed to the decrease in order, caused by the decrease in the size of microcrystallites which is also consistent with XRD results. The observed decrease of FWHM of Si-C(s) peak for $w > 35\text{ W}$ is attributed to the increase in order due to the increase in the number of nanocrystallites of smaller size. Clearly, the formation of nanocrystallites, established for the films deposited with rf power $w \geq 35\text{ W}$, implies medium range order in the system since this has been demonstrated conclusively in hydrogenated silicon films by fluctuation electron microscopy measurements [Voyles et al., 2001]. Furthermore, the smooth variation in the FWHM of the Si-C(s) peak with rf power indicates the absence of an abrupt transition from microcrystalline to nanocrystalline phase, quite different from an abrupt order-disorder transition [Sarott, 1982], i.e. from long range order to short range order.

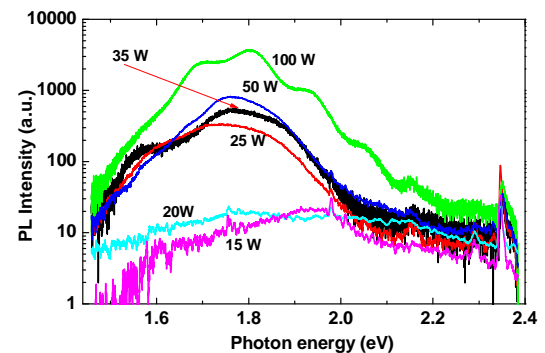


Figure 6: Room temperature PL spectra of the films deposited at different rf power values.

The presence of increased number of nanocrystallites of smaller size is further confirmed from the fact that the films deposited with high rf power exhibit strong room temperature visible photoluminescence, contrary to what happens for films deposited with low rf power as revealed in Fig. 6. The carbon content ($x = C/(C+Si)$), PL peak position (E_{PL}), FWHM of PL peak (Δ_{PL}), the integrated area of the PL peak (A_{PL}), the optical band gap (E_{04}) and ($E_{04} - E_{PL}$) for various rf power are shown in Table 1.

Table 1. Compositional and optical properties.

w is the rf power, x is the $C/(C+Si)$ carbon content, E_{04} is the optical band gap, E_{PL} is the position of PL peak, Δ_{PL} is the FWHM of PL peak and A_{PL} is the integrated area of PL peak.

w	x	E_{04}	E_{PL}	Δ_{PL}	A_{PL}	$E_{04} - E_{PL}$
W		eV	eV	meV	a.u.	eV
25	0.039	1.95	1.74	107.1	38.8	0.21
35	0.049	2.20	1.75	77.41	52.7	0.45
50	0.115	2.23	1.77	69.44	67.7	0.46
100	0.190	2.30	1.81	72.28	297	0.49

The observed increase of PL intensity and the blue shift of PL peak position as a function of carbon content can be attributed either to Si nanocrystallites [Coscia et al., 2008, Wang et al., 2010, Tong et al., 2012] or to the $a-Si_{1-x}C_x:H$ matrix [Tessler and Solomon, 1995, Giorgis et al., 2000]. However, in the $a-Si_{1-x}C_x:H$ alloys with the increase in carbon content the FWHM of PL peak increases while for the studied films the FWHM of the PL peak decreases. Thus the PL phenomena have to be primarily attributed to the increase in the number of Si nanocrystallites of smaller size.

In order to better evaluate the contribution of Si nanocrystallites and $a-Si_{1-x}C_x:H$ matrix to the process, the PL peak position as a function of x for the

studied films along with E_{PL} of the amorphous silicon carbon films of corresponding carbon content reported in the literature [Ambrosone et al., 2002] is shown in Fig. 7. It is seen that E_{PL} data of the studied films are strongly shifted towards higher energy as compared to the amorphous samples, thus demonstrating that the $a-Si_{1-x}C_x$ matrix cannot play a dominant role in the PL process and that PL phenomena can be attributed mainly to Si nanocrystallites

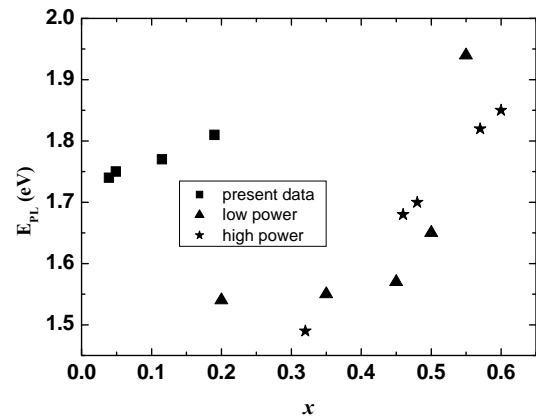


Figure 7: PL peak position, E_{PL} , as a function of carbon content x . squares: E_{PL} of present work; triangles and stars: E_{PL} of $a-Si_{1-x}C_x:H$ films of ref. [Ambrosone et al., 2002].

In order to confirm this further, the variation of PL peak position vs optical band gap (E_{04}) for the studied films as well as for the $a-Si_{1-x}C_x:H$ films of corresponding E_{04} reported in the literature [Ambrosone et al., 2002] is shown in Fig. 8. Clearly, for the studied films the PL peak position is strongly shifted as compared to amorphous samples, thus corroborating that nanocrystallites are playing dominant role in the PL phenomena of the nanostructured silicon carbon films. The increase in the PL intensity with increase in rf power can be ascribed to the increase in the radiative recombination of generated carriers through the localized

surface states that increases with increase in the number of nanocrystallites [Islam and Kumar, 2003].

Finally, it must be emphasized that ($E_{04} - E_{PL}$) increases from 0.21 to 0.45 eV with increase in rf power from 25 to 35 W and thereafter remains almost constant with further increase in rf power (Table 1), which indicates similar cause for the increase in optical band gap as well as for the blue shift of the PL peak position. Since the blue shift of the PL peak is shown to be due to the reduction in the size of the nanocrystallites [Wang et al., 2010], therefore, the same can be attributed to the increase of the optical band gap, in accordance with the results of others [Park et al., 2001, Ambrosone et al., 2012, Sancho-Parramon et al., 2009].

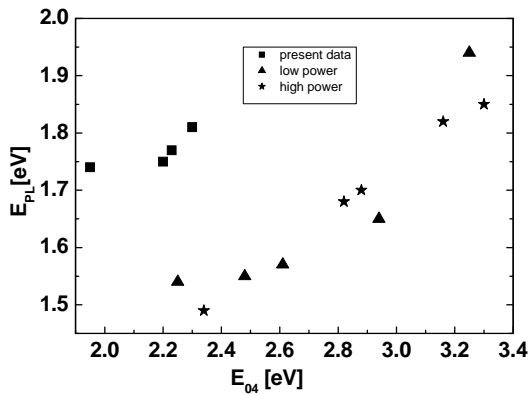


Figure 8: PL peak position, E_{PL} , as a function of optical band gap E_{04} . squares: E_{PL} of present work; triangles and stars: E_{PL} of $a\text{-Si}_{1-x}\text{C}_x\text{:H}$ films of ref. [Ambrosone et al., 2002]

4. CONCLUSIONS

The important conclusions of the study are:

1. Microcrystalline to nanocrystalline silicon phase transition has been demonstrated conclusively in the hydrogenated silicon carbon films prepared from silane and methane gas mixture highly diluted in hydrogen in PECVD system by varying rf power. The

transition from long range order to medium range order is shown to be smooth, rather than abrupt as in the order-disorder transition. Further, it is found that in the investigated deposition conditions nanostructured silicon carbon films can be obtained for $w \geq 35$ W.

2. The room temperature visible photoluminescence is demonstrated to be primarily due to the silicon nanocrystallites embedded in the amorphous silicon carbon matrix. The $a\text{-Si}_{1-x}\text{C}_x\text{:H}$ matrix has been shown to play an important role in the formation of nanocrystalline phase because the increase of Si-C bonds facilitates the increase in the number of nanocrystallites of smaller size. The increase in the PL intensity, the blue shift of the PL peak position and the decrease in the FWHM of PL peak as well as the increase in the optical band gap are established to be mainly due to formation of increased number of nanocrystallites of smaller size.

REFERENCES

- Allan, G., Delerue, C. and Lannoo, M., 1997, Electronic structure of amorphous silicon nanoclusters, *Phys. Rev. Lett.*, 78, 3161.
- Ambrosone, G., Coscia, U., Giorgis, F., Ferrero, S., Mandracci P. and Pirri, C.F., 2002, Structural and optical properties of amorphous silicon-carbon grown by plasma enhanced chemical vapour deposition at different rf powers, *Philos. Mag. B*, 82, 35.
- Ambrosone, G., Basa, D.K., Coscia, U. and Passacantando, M., 2012, Evolution of structural and optical properties of nanostructured silicon carbon films deposited by plasma enhanced chemical vapour deposition, *Thin Solid Films*, 520, 4875.
- Ball, P., 2001, Let there be light, *Nature*, 409, 974.
- Basa, D.K. and Smith, F.W., 1990, Annealing and crystallization processes in a hydrogenated amorphous silicon-carbon alloy film, *Thin Solid Films*, 192, 121.
- Basa, D.K., Ambrosone, G. and Coscia, U., 2008, Microcrystalline to nanocrystalline silicon phase transition in hydrogenated silicon carbon alloy films, *Nanotechnology*, 19, 415706.

- Basa, D.K., 2002, Correlation between optoelectronic and structural parameters in amorphous semiconductors, *Thin Solid Films*, 406, 75.
- Canham, L.T., 1990, Silicon quantum wire array fabrication by electrochemical and chemical dissolution of wafers, *Appl. Phys. Lett.*, 57, 1046.
- Canham, L.T., 2000, Gaining light from silicon, *Nature*, 408, 411.
- Conibeer, G., Green, M., Corkish, R., Cho, Y. and Cho, E.C., Jiang, C.W., Fangsuwannarak, T., Pink, E., Huang, Y.D., Puzzer, T., Trupke, T., Richards, B., Shalav, A. Lin, K.L., 2006, Silicon nanostructures for third generation photovoltaic solar cells, *Thin Solid Films*, 511-512, 654.
- Coscia, U., Ambrosone, G. and Basa, D.K., 2008, Room temperature visible photoluminescence of silicon nanocrystallites embedded in amorphous silicon carbide matrix, *J. Appl. Phys.*, 103, 063507.
- Draeger, E.W., Grossman, J.C., Williamson and A.J., Galli, G., 2003, Influence of synthesis conditions on the structural and optical properties of passivated silicon nanoclusters, *Phys. Rev. Lett.*, 97, 167402.
- Fontcuberta i Morral, A. and Roca i Cabarrocas, P., 2001, Shedding light on the growth of amorphous, polymorphous, protocrystalline and microcrystalline silicon thin films, *Thin Solid Films*, 383, 161.
- Giorgis, F., Vinegoni, C. and Pavese, L., 2000, Optical absorption and photoluminescence properties of α -Si_{1-x}N_x:H films deposited by plasma-enhanced CVD, *Physical Review B*, 61, 4693.
- Green, M.A., 2003, *Third Generation Photovoltaic: Ultra-High Efficiency at Low Cost* Springer-Verlag, 2003.
- Iqbal, Z., Vepřek, S., Webb, A.P. and Capezzuto, P., 1981, Raman scattering from small particle size polycrystalline silicon, *Solid State Commun.*, 37, 993.
- Islam, M.N. and Kumar, S., 2003, Influence of surface states on the photoluminescence from silicon nanostructures, *J. Appl. Phys.*, 93, 1753.
- Lehmann, V. and Gosele, U., 2001, Porous silicon formation - a quantum wire effect, *Appl. Phys. Lett.*, 58, 856.
- Lu, Z.H., Lockwood, D.J. and Baribeau, J.M., 1995, Quantum confinement and light-emission in SiO₂/Si superlattices, *Nature*, 378, 258.
- Kerdiles, S., Berthelot, A., Goubilleau, F. and Rizk, R., 2000, Low temperature deposition of nanocrystalline silicon carbide thin films, *Appl. Phys. Lett.*, 76, 2373.
- Klug H.P. and Alexander E., 1974, *X-ray Diffraction Procedure for Polycrystalline and Amorphous Materials*, Wiley, New York.
- Mui, K., Basa, D.K., Smith, F.W. and Corderman, R., 1987, Optical-constants of a series of amorphous hydrogenated silicon-carbon alloy-films - dependence of optical-response on film microstructure and evidence for homogeneous chemical ordering, *Phys. Rev. B*, 35, 8089.
- Mui, K., Basa, D.K., Corderman, R. and Smith, F.W., 1987, Optical-constants and microstructure of amorphous hydrogenated silicon-carbon alloy-films, *J. Non-Cryst. Solids*, 97&98, 999.
- Oliveira, A.R. and Carreno M.N.P., 2006, Post thermal annealing crystallization and reactive ion etching of SiC films produced by PECVD, *J. Non-Cryst. Solids*, 353, 1392.
- Park, N.M., Choi, C.J., Seong, T.Y. and Park, S.J., 2001, Quantum confinement in amorphous silicon quantum dots embedded in silicon nitride, *Phys. Rev. Lett.*, 86, 1355.
- Sancho-Parramon, J., Gracin, D., Modreanu, M. and Gajovic, A., 2009, Optical spectroscopy study of nc-Si-based p-i-n solar cells, *Solar Energy Materials & Solar Cells*, 93, 1768.
- Sarott, F.A., Iqbal, Z. and Vepřek, S., 1982, Effect of substrate bias on the properties of microcrystalline silicon films deposited in a glow discharge, *Solid State Commun.*, 42, 465.
- Suendo, V., Patriarche, G. and Roca i Cabarrocas, P., 2006, Influence of deposition parameters and post-deposition plasma treatments on the photoluminescence of polymorphous silicon carbon alloys, *J. Non-Cryst. Solids*, 352, 1357.
- Tessler, L.R. and Solomon, I., 1995, Photoluminescence of tetrahedrally coordinated α -Si_{1-x}C_x:H, *Physical Review B*, 52, 10962.
- Tong, G.B. Muhamad, M. R. and Rahaman, S.A., 2012, Photoluminescence and structural properties of silicon nanostructures grown by layer-by-layer deposition *Opt. Mater.* 34, 1282.
- Voyles, P.M., Gerbi, J.E., Treacy, M.M.J., Gibson, J.M. and Abelson, J.R., 2001, Absence of an abrupt phase change from polycrystalline to amorphous in silicon with deposition temperature, *Phys. Rev. Lett.*, 86, 5514.
- Wang, J.Z., Suendo, V., Abramov, A., Yu, L.W. and Roca i Cabarrocas, P., 2010, Strongly enhanced tunable photoluminescence in polymorphous silicon carbon thin films via excitation-transfer mechanism, *Applied Physics Letters*, 97, 221113.

- Wang, J.Z., Yu, L.W., Abolmasov, S.,
http://apps.webofknowledge.com/OneClickSearch.do?product=WOS&search_mode=OneClickSearch&colName=WOS&SID=R1bKCnPOC2jdepIo8dE&field=AU&value=Kim,%20KH and Roca i Cabarocas, P., 2012.
Strong visible and near-infrared electroluminescence and formation process in Si-rich polymorphous silicon carbon, J. Appl. Phys., 111, 053108.
- Zhang, S., Liao, X., Raniero L., Fortunato, E., Xu, Y., Kong, G. , Aguas, A., Ferreira, I. and Martins, R., 2006, Silicon thin films prepared in the transition region and their use in solar cells, Solar Energy Mater. & Solar Cells, 90, 3001

3D CHARACTERIZATION, ANALYSIS, AND SIMULATION OF MULTIPHASE SYSTEMS USING HIGH RESOLUTION X-RAY MICRO TOMOGRAPHY

J.D. Miller^a and C.L. Lin

Department of Metallurgical Engineering, College of Mines and Earth Sciences, University of Utah, 135 South 1460 East, Room 412, Salt Lake City, Utah, 84112, U.S.A.
a. Corresponding author (Jan.Miller@utah.edu)

ABSTRACT: Further advancement in the development of advanced materials technology can be facilitated by a more detailed understanding of multiphase systems. 3D characterization, analysis, and simulation of complex multiphase systems will help to provide a fundamental basis for the design of improved technology. In this regard, developments in X-ray computed tomography (CT) afford the opportunity for multiscale imaging of multiphase systems in 3D, including packed particle beds and porous structures. Such developments include X-ray milli-, micro-, and nano-CT systems with voxel size resolution extending from the mm range down to 50 nm.

During the past 10 years point-projection X-ray micro CT systems have been used for 3D visualization and quantitative analysis of multiphase systems. Analysis of packed particle beds containing as many as 30,000 particles can be accomplished in less than 3 hours with special software to establish the 3D spatial characteristics of each multiphase particle in the population and the spatial organization of the packed particle bed. Now, due to advances in X-ray optics, the resolution afforded with point-projection micro CT systems has been improved by at least an order of magnitude using a lens-based X-ray micro CT system. Software tools for the 3D characterization, analysis, and simulation of packed particle beds and porous structures using high resolution X-ray micro tomography (HRXMT) are being developed. Examples to be discussed include the properties of mineral particles (size, shape, and composition) and the properties of engineered materials including pore network structures (packed particle beds, porous structures). Based on 3D image data from HRXMT, both fluid flow and mechanical strength simulations will be presented using the LB method of computational fluid dynamics and finite element analysis respectively.

1. INTRODUCTION

Since the first commercial introduction of the conventional cone beam X-ray micro computed tomography (micro CT) in the late 1990s, micro CT has provided the foundation for advanced research in the 3D characterization and analysis of multiphase particle properties (such as size, shape, and composition) and pore network structures (packed particle beds and engineered porous structures). As shown in Figure 1, most of the commercial cone beam x-ray micro CT systems are based on the principle of

point projection of an x-ray source through the sample onto a detector. In this design, the achievable resolution is both a function of the x-ray source size, and the detector resolution. Commonly the resolution is thought to be driven by the x-ray source spot size. Practical resolution of conventional micro CT systems is generally limited to a few microns. Data obtained from the conventional point projection micro CT system (XMT) at low resolution (20 μm) provides insufficient information for detailed quantitative analysis of

multiphase systems.

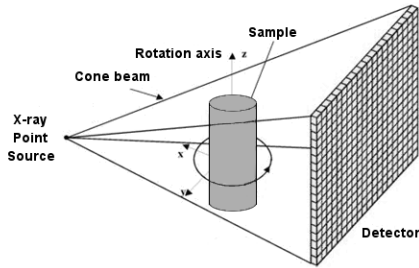


Figure 1: Conventional cone beam x-ray micro CT system based on point-projection geometry with point source and a flat panel detector.

The solution is to utilize an x-ray detector with high resolution. In fact, by using a high resolution x-ray detector, an imaging resolution better than the x-ray source spot size can be realized for sources with spot sizes larger than the x-ray detector resolution. Such a system is the High-Resolution X-ray Micro Tomography (HRXMT) from Xradia, which employs an x-ray detector with sub-micron resolution combined with a microfocus x-ray source. In this HRXMT system working distances between source, sample and detector are typically around 100 mm, so that full tomography even for larger samples can be achieved. The basic layout of the HRXMT system is shown in Figure 2.

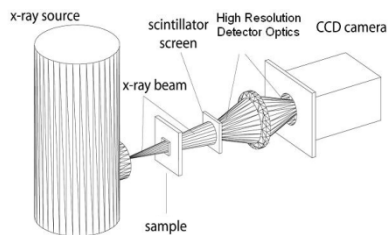


Figure 2: The Xradia's High-Resolution X-ray Micro Tomography (HRXMT) system uses a microfocus x-ray source with 150 kV acceleration voltage. High resolution is achieved with a proprietary x-ray detector with an effective detector pixel size < 1 micron.

In this paper, the HRXMT system made by Xradia with a voxel resolution of less than 1 micron is being used for the characterization of multiphase particle properties. In this way, direct 3-D determination of size, shape and composition of multiphase mineral particles which vary from 40 mm down to 100 microns in size have been studied at a voxel resolution of a few microns. With HRXMT data, and based on micro finite element analysis (microFE) the mechanical properties of porous engineered materials are simulated.

Flow simulation in the complex pore geometry of a packed particle bed is a challenging subject and is the last topic discussed. In this regard, the Lattice Boltzmann method (LBM) was used to directly simulate the flow through pore network structures obtained from HRXMT data.

2. PARTICLE PROPERTIES

In the processing industries, it is well known that geometric particle properties, such as size, shape, and composition are important factors which determine the behavior of particulate systems. For example, system properties of technological significance including rheology, suspension stability, agglomeration, packing, permeability ...etc, are affected by particle shape. The analysis of mechanical and transport problems involving particulate materials will generally use a multitude of correlations to predict the behavior of particles with regular shape, particularly in the case of spheres. In practice, the particulate process industries are concerned with particles that are far from being of a regular shape and generally cover a wide range of particle size. In this regard, characterization and analysis of particle shape is essential for more detailed understanding and improved development of particulate processes. In

general, it is clear that the behavior of these systems depends on the statistical characteristics of particle properties. Remarkably few techniques exist to predict the mechanical and hydrodynamic behavior of an irregularly shaped particle or a population of irregularly shaped particles for that matter. The lack of models and correlations can be attributed to the wide variety and complexity of particle shapes, the difficulty of defining shape descriptors suitable for modeling, the limitations of measuring shape, and the lack of classifying techniques to characterize particle shape.

3D quantitative analysis of particle properties including size and shape, as well as composition can be accomplished using HRXMT.

2.1. Particle Size and Shape Analysis

Geometrical particle properties, such as size and shape, can be analyzed directly in 3D based on a three-dimensional digital map of the density spectrum of a particle or particle population using HRXMT. The 3D gray scale image obtained from HRXMT can be thresholded to a black and white image by recovering the volume of the particles in the sample. Then, geometric parameters of particle (size and shape) can be determined based on the mathematical analysis using either the boundary method or the assemblage method. Details of this technique and be found in the literature [Lin and Miller, 2005].

X-ray microtomography is suitable for surface analysis and the acquisition of three-dimensional shape information from a particle assemblage. Surface reconstruction is an important step in geometric modeling (three dimensional shape analysis) for generating surfaces from data points captured for actual irregularly shaped particles. Directed

three-dimensional digital map of the density spectrum of a particle or particle population can be obtained using HRXMT. Figure 3 shows the reconstructed CT images obtained from three kinds of particle samples, namely glass beads (0.85x0.71mm), quartz sand (0.85x0.71 mm) and rock particles (2.0x1.18 mm).

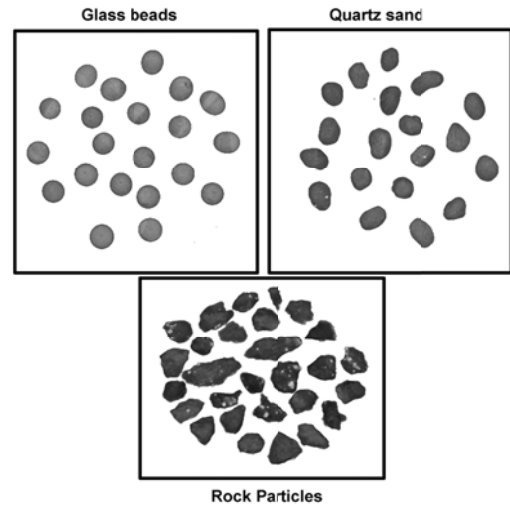


Figure 3: Reconstructed images of glass beads (0.85x0.71 mm), quartz sand (0.85x0.71 mm) and rock particles (2.0x1.18 mm) obtained from X-ray microtomography.

Based on the Marching Cube method [Lewiner, et al, 2002], volume, surface area, aspect ratio of the three major principal axes, and sphericity [Lin and Miller, 2005] were determined to describe particle shape. It is evident that the particle shape is similar for glass beads and quartz sands, however, rock particles are the extreme case, in which variations of particle volume, surface area and shape factor (sphericity) are significantly different for the same size class as shown in Table I. Figure 4 shows the surface morphology of selected reconstructed particles (glass beads, quartz sand and rock particles) based on the Marching Cube method.

Table 1: Volume, surface area and sphericity of rock particles (2.0x1.18 mm), shown in Figure 3, based on the Marching Cube method.

Particle No.	Volume (mm ³)	Surface Area (mm ²)	Sphericity
1	3.1378	12.7560	0.8126
2	2.6385	13.8446	0.6670
3	2.3348	13.7736	0.6179
4	2.1629	9.6288	0.8400
5	2.0079	9.6754	0.7955
6	1.8576	9.1428	0.7993
7	1.8535	10.7868	0.6765
8	1.7520	8.4078	0.8359
9	1.5446	7.4624	0.8659
10	1.4361	8.3303	0.7389
11	1.4052	7.6987	0.7881
12	1.3435	8.1570	0.7219
13	1.3407	9.0752	0.6479
14	1.3223	7.2254	0.8063
15	1.3128	6.8646	0.8446
16	1.3009	7.1112	0.8104
17	1.2839	6.9187	0.8257
18	1.1872	6.5235	0.8312
19	1.1735	7.2562	0.7415
20	1.1180	6.0257	0.8645
21	1.0543	7.6929	0.6512
22	1.0002	6.6045	0.7323
23	0.9297	5.9129	0.7791
24	0.9076	6.3633	0.7124
25	0.8881	6.4323	0.6947
26	0.8730	5.3351	0.8280
27	0.7108	5.6680	0.6795
28	0.6990	5.0051	0.7610

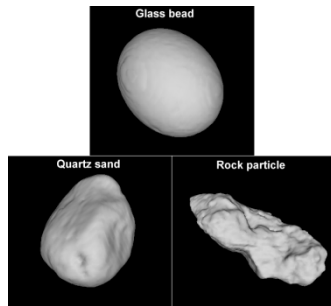


Figure 4: Surface morphology of the reconstructed glass bead (0.85x0.71 mm), quartz sand (0.85x0.71 mm) and rock particle (2.0x1.18 mm) based on the Marching Cube method using HRXMT image data.

Sphericity (or compactness) is one of the important shape factors to be considered for the classification and reconstruction of 3D-particle shape. In this regard, Figure 5 shows the log-log plot of surface

area versus volume for the three particle types. Regression based on the formula: Surface Area = $A_0 (\text{Volume})^{2/3}$ is also included in Figure 5. The theoretical value of 2/3 is set based on the surface area and volume of particles being a function of 2nd and 3rd power of particle size. The compactness term, A_0 , for a sphere ($\sqrt[3]{36\pi}$) is included for comparison. The sphericity values for each particle type can be determined as $\frac{\sqrt[3]{36\pi}}{A_0}$.

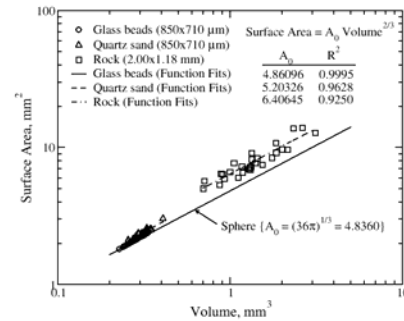


Figure 5: Surface area versus volume for glass beads, quartz sands and rock particles as shown in Figure 3 and Table 1.

2.2. Particle Composition Analysis

In order to illustrate the reliability of the HRXMT measurements a single particle from a copper ore sample of known composition was analyzed by Scanning Electron Microscopy (SEM) and by HRXMT. The single copper ore particle of approximately 6 mm in diameter consisted of chalcopyrite (CuFeS_2), chalcocite (Cu_2S) and gangue minerals was selected for this study. Figure 6 shows the 3D reconstructed image (top left hand side) and the sectional view of this particle by removing the top portion of the particle (top right). Then, the small particle was embedded in epoxy and after an adequate curing time the HRXMT analysis was run. Once a 3D digitalized image was acquired, a diamond saw was used to cut the sample in half, leaving a surface of the sample exposed for SEM

analysis. This surface and a plane of the 3D reconstructed image at the same location are compared in order to determine if the features and mineral phases present at the polished surface are in agreement with the 2D HRXMT section at the same location.

Results from the same selected section of the particle by HRXMT and SEM are shown in the bottom of Figure 6. Excellent agreement of the phases and grain locations is evident. Even though the HRXMT image has a lower resolution when it is compared with the SEM polished section image, we see that both images show the major features, a matrix of chalcocite (light grey color) with chalcopyrite grains (dark grey color) in both images.

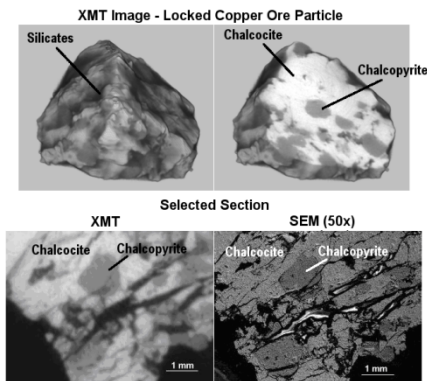


Figure 6: Top – 3D reconstructed image and sectional view of 6-mm locked copper ore particle. Bottom – HRXMT and SEM comparison of selected section.

Figure 7 illustrates the ability of the HRXMT system for quantitative analysis to determine the 3D spatial distribution of mineral phases in multiphase particles from a copper rougher feed, concentrate and tailing samples (45x25 μm). The image elements in the reconstruction are cubic, so the spacing between planes equals the voxel resolution which in this case corresponds to 1.09 μm . Here the gray scale levels of the images indicate the relative attenuation coefficient present in the bulk of the sample. Based on the

magnitude of the x-ray attenuation coefficient, differentiation of mineral phases within the sample is possible. For example, light gray color identifies pyrite, the bright white color identifies chalcopyrite, and the dark gray identifies silicate minerals. In this way, each particle in the population of more than 10,000 particles can be described with respect to the spatial distribution of mineral phases.

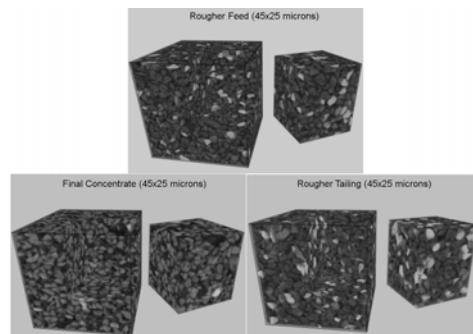


Figure 7: Comparison of 3D rendering images from the three dimensional HRXMT reconstruction of a packed bed of 325x500 mesh multiphase ore particles (45x25 μm) for rougher feed, concentrate and tailing samples.

3. ENGINEERED MATERIAL

Porous engineered material of metals, polymers, and other materials are in common use. Polymer foams, namely ROHACELL, consist of a substantial amount of porosity which leads to very low density, on the order of 0.1 g/cm^3 . Besides the light-weight of the foam material, the ROHACELL also provides very unique material properties such as very high specific strength, specific energy absorption, and acoustic damping. ROHACELL has been used in many interesting applications and is frequently used as the core for composite layered structures.

Two important parameters, namely the microstructure of the foam and the properties of the polymer wall material have a significant influence of the mechanical properties of the foam.

The methodology involving the coupling of 3D microCT data with microFE analysis allows for modeling the mechanical properties of similar microstructures to design, produce, and optimize the performance of engineered cellular material. In this regard, the complex 3D geometries of ROHACELL foams with different densities were analyzed using HRXMT. The microstructures obtained from HRXMT are converted to hexahedra mesh for compression simulation using the micro finite element method (microFE). The relationship between mechanical properties and relative density was investigated and validated with experimental results from compression tests.

3.1. Microstructure of ROHACELL Foams in 3D

Figure 8 presents a 2D slice, and split 3D volume rendering images for the ROHACELL (RC 51 IG) sample. The 3D image consists of 992x1005x970 voxels. The size of each voxel is 5.77 x 5.77 x 5.77 μm .

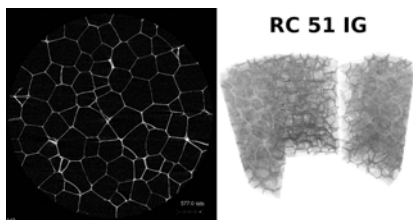


Figure 8: 2D section image (left), and split 3D volume rendering image (right), of the ROHACELL (RC 51 IG) sample.

A watershed algorithm [Videla et al, 2006] was used to patch the broken cell walls and to determine the 3D closed cell size distributions. Figure 9 shows the volume rendering image for the separated cell sizes of RC 51 IG foam.

3.2. Simulation of Compression

The microstructures obtained from HRXMT are converted to hexahedra mesh for compression simulation using the micro finite element method (microFE). The relationship between

mechanical properties and relative density was investigated and validated with experimental results from compression tests.

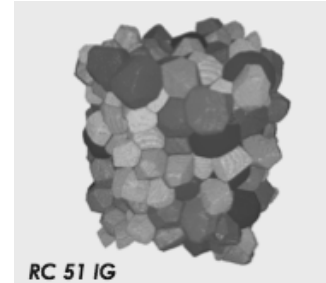


Figure 9: Volume rendering images of the separated cell size of RC 51 IG sample from 3D-image analysis using a 3D-watershed algorithm from HRXMT scans (5.77 μm resolution).

Uni-axial compression tests were simulated using FEBio [Maas et al, 2012]. The following conditions were set for the numerical simulations: Young's modulus $E = 2.9 \text{ GPa}$, Poisson's ratio $\nu = 0.33$, and 20 time steps to 10% compression. Figure 10 shows 3D views of the simulation of foam (RC 51 IG, 256x256x256 voxels) undergoing compression (0%, and 5.8% compressive strains). The nodes of the material are shaded according to their effective (von Mises) stress in GPa.

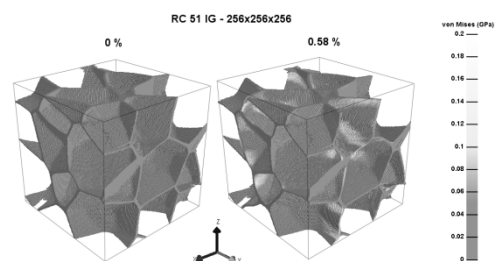


Figure 10: 3D views of foam (RC 51 IG, 256x256x256 voxels) in compression (un-deformed, and 5.8% compressive strain) from FEBio simulation using PostView. Gray scale bar indicates the effective (von Mises) stress (GPa).

The solid line in Figure 11 shows the stress-strain curve obtained from the compression tests on a cylindrical sample

of RC 51 foam. Results obtained from numerical simulations at two sizes (200x200x200, and 256x256x256 voxels) using FEBio are also included in Figure 11 for comparison. The experimental modulus was 28.1 MPa while the simulations moduli were 29.2 MPa at 200 voxel size and 30.5 MPa at 256 voxel size. Excellent agreement between experiment and simulation based on HRXMT data and FEBio software was obtained.

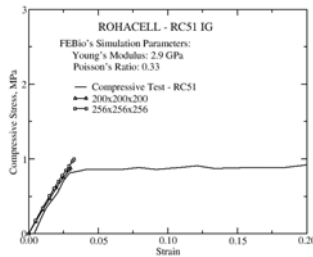


Figure 11: Comparison of stress-strain curves (linear elastic region) obtained from numerical simulation using HRXMT and FEBio with experimental data (ROHACELL RC 51 IG).

3.3. Texture Analysis in 3D

Another example of an engineered porous structure is gypsum wallboard. The 3-D geometrical texture of the gypsum wallboard structure was analyzed including: spatial organization of the complex structure as revealed from 3-D images, porosity analysis (including the bulk porosity and the porosity of the wall structure), air bubble size distribution, and wall thickness distribution [Lin, et al. 2010b]. These features of the gypsum wallboard sample were analyzed based on calibration of the x-ray linear attenuation coefficient, use of a 3-D watershed algorithm [Videla, et al., 2006], and use of a 3-D skeletonization procedure [Lindquist, et al., 1996]. Typically a subset (with size of about 6x6x6 mm³) of the undisturbed reconstructed 3-D images was sampled for characterization, with respect to porosity, air bubble size distribution, and wall thickness distribution.

Figure 12 shows the 3D volume rendering images and the 2D sliced images from the reconstructed CT data for subsets of 2 gypsum wallboard samples, namely samples A and B with large and small air void distributions, respectively. The 3D images consist of 300x300x300 voxels (volume elements) and the size of each voxel is 20x20x20 μm .

It is noted, as shown in Figure 12, that many of the air bubbles are in contact as indicated from the reconstructed image. Using the 3D watershed algorithm [Videla, et al., 2006], such air bubbles were separated. Then, the 3D air bubble size distribution was determined. Figure 13 shows the volume rendered images of the separated air bubbles. Total air bubbles counted are about 1200 and 25000 for samples A and B, respectively.

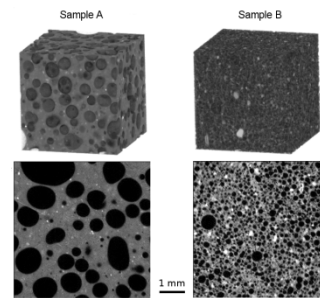


Figure 12: 3D volume rendering images and 2D sliced images of two gypsum wallboard samples (size of the samples: 6x6x6 mm³ with each voxel 20 μm in size).

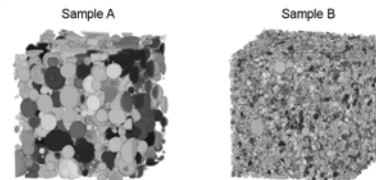


Figure 13: 3D volume rendering images of separated air bubbles from two gypsum wallboard samples using 3D-watershed algorithm.

Understanding the mechanical property-porosity relationship involving different pore geometries and crystal orientation is

important for improved engineering of porous materials. Particularly, it is important to understand how processing conditions influence the porous microstructure. In this regard, the structure depends on the dispersion and type of raw material, water to stucco ratio, temperature, employment of modifiers, etc. The resulting shape of crystallites can be needle-like or layer-like with the diameter about 1 micron, depending on the magnitudes of the above-mentioned factors and their combination. For characterization and analysis of gypsum crystals, nano CT is needed to acquire the needle-like structures. Figure 14 shows the 3D characteristics of randomly oriented gypsum crystals obtained from high resolution X-ray micro tomography and X-RAY nano tomography with resolution of 1.5 μm and 50 nm, respectively. The nano CT image on the right represents the wall material from gypsum board.

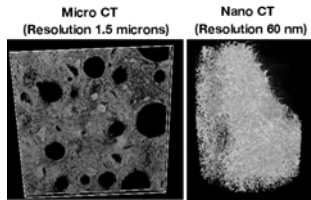


Figure 14: 3D volume rendering images of gypsum crystals obtained from micro CT and nano CT with resolution of 1.5 μm and 50 nm, respectively.

4. FLOW IN POROUS STRUCTURES

In the last decades the subject of numerical simulation, and in particular computational fluid dynamics (CFD) simulation, has increasingly become a very popular approach to resolve complex practical problems in engineering and science. Specifically, the study and analysis of fluid flow and transport phenomena in porous media. In this regard, the coupling of the X-ray microtomography (XMT) technique with LBM allows for fast and easy construction of the pore network structure

and determination of the fluid flow regime.

Figure 15 shows a packed bed of sand particles and its pore network structure as obtained by the micro CT system. The particle size is between 300 and 425 μm , the resolution of each voxel is 20 μm in length and the size of the image is 200x200x200 voxels. It is possible to observe how image processing of the digital data allows a clear separation between the sand particles and the air present in the pores due to the distinct difference in attenuation coefficients. This technique easily obtains the pore network structure for the packed particle bed by filtering and thresholding. During simulation, the fluid flows through this network structure having a specific connectivity with well-defined pore dimensions not only to determine the local flow but also the overall permeability of the sample.

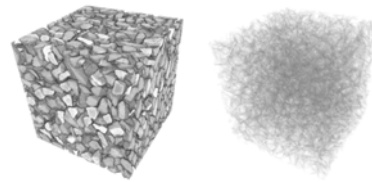


Figure 15: 3D image reconstruction of a packed bed of sand particles (300x425 μm). The voxel resolution is 20 μm and the image size contains 200x200x200 voxels. The left-hand side image shows the packed particle bed and the right-hand side image shows the pore network structure.

The images of pore network structures for packed particle beds reveals why the LBM method is more suitable for this kind of problem than the standard CFD mesh methods. The standard solution with a CFD solver requires the construction of a grid, the definition of the boundary conditions in the boundary nodes, and the solution of the Navier–Stokes equation at each node. The standard CFD methodology, therefore,

will require an enormous amount of time for grid construction and also for computer simulation.

X-ray micro CT has been used to define the pore network structure of packed particle beds. In this way, fluid flow in the pore space is simulated using the Lattice Boltzmann method (LBM) of computational fluid dynamics. From such an approach the permeability of packed particle beds can be determined [Lin, et al., 2005; Videla et al., 2008]. Also, in the case of filtration, conditions for breakthrough can be established and the residual moisture calculated from the filtration simulation.

4.1. Filtration

Application of the single component multiphase flow LBM known as the He-Chen-Zhang model coupled with XMT analysis to define the complex pore geometry allows for simulation of flow in porous media [Lin, et al., 2010a]. The model is used for simulation of fluid penetration into porous samples and the analysis of capillary phenomena. At present, the LBM has been applied to 3D simulations of filtration for a packed bed of coal particles digitalized by XMT. Results from LBM simulations are shown in Figure 16.

4.2. Heap Leaching

Understanding the behavior of fluid flow through packed particle beds is important to enhance the performance of heap leaching from both design and operating considerations. The microstructure and connectivity of pore space are important features to describe detailed fluid flow phenomena in heap leaching operations. In this regard, both milliCT and microCT can be used to determine the complex pore structure of the packed particle beds. The 3D reconstructed images of complex pore structures obtained from the CT scans allow for the analysis of multiphase

fluid transport phenomena through packed particle beds. On this basis the Lattice-Boltzmann (LB) method can be used to simulate in detail multiphase flow inside the packed particle beds.

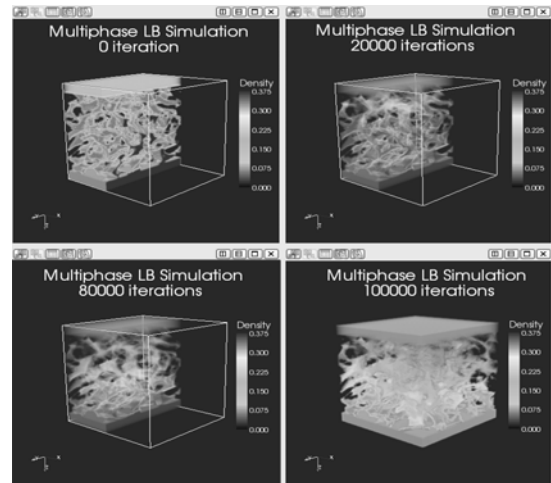


Figure 16: Results of LB simulation of multiphase flow through a packed bed of coal particles (0.850x0.589 mm).

Figure 17 illustrates the 3D view of the LB simulation for saturated flow through the pore space of packed beds both before and after leaching. Once we remove the solid particles, the middle sections of Figures 17 show the nature of the flow channels. Zoom view of the bottom of the column is shown on the right-hand side of Figure 17. The main thing to notice is that most of the flow occurs in a small fraction of the available pore space. Clearly, fewer flow channels in the central portion are observed after leaching due to compression of the bed and transport of fine particles which accumulate in the center. Solid particles are white, and solution velocity ranges from black for no flow, dark gray, and finally light gray for the highest flow rate. The estimated permeabilities from LB simulation of flow in the column before and after leaching were found to be $1.34 \times 10^{-3} \text{ cm}^2$ and $4.60 \times 10^{-4} \text{ cm}^2$, respectively.

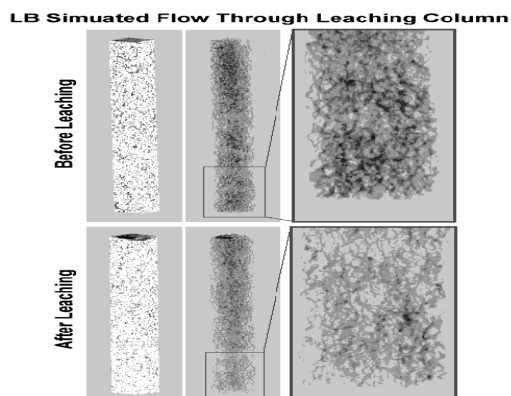


Figure 17: 3D views of LB simulated flow through packed column before and after leaching. Left-hand side image indicates the data sets with solid phase as white, the middle image are data sets with transparent solid phase, and right-hand side image is the zoom view at the bottom of the column [Lin, et al., 2005].

5. CONCLUSIONS

3D characterization, analysis, and simulation of complex multiphase systems will help to provide a fundamental basis in the design of improved technology for process operations and for the design of engineered materials. In this regard, developments in X-ray computed tomography (CT) afford the opportunity for multiscale imaging of multiphase systems in 3D, including packed particle beds and porous structures. Such developments include X-ray milli-, micro-, and nano-CT systems with voxel size resolution extending from the mm range down to 50 nm.

The technology, based on the HRXMT imaging and the developed software tools, allows for the determination of particle properties (size, shape, compositions) and pore network structures (packed particle beds, engineered porous structures). For example, the mechanical property of the engineered porous structure can be simulated based on the 3D image data from HRXMT coupling with the finite

element analysis.

Finally, from HRXMT imaging, complex pore network structures can be determined for packed particle beds and with this information flow can be simulated to describe mineral processing operations such as filtration and heap leaching.

REFERENCES

- Lewiner, T., Lopes, H., Vieira, A.W., Tavares, G., 2002, Efficient implementation of marching cubes' cases with topological guarantees, *Journal of Graphics Tools*, 8 (2), 1.
- Lin, C.L. and Miller, J.D., 2005. 3D Characterization and analysis of particle shape using X-ray microtomography (XMT), *Powder Technology*, 154, 61.
- Lin, C.L., Miller, J.D. and Garcia, C., 2005. Saturated flow characteristics in column leaching as described by LB simulation, *Minerals Engineering*, 18, 1045.
- Lin, C.L., Videla, A.R., and J.D. Miller, J.D., 2010a, Advanced 3D multiphase flow simulation in porous media reconstructed from X-ray micro tomography data using the He-Chen-Zhang Lattice Boltzmann model, *Flow Measurement and Instrumentation*, 21, 255.
- Lin C.L., Videla, A.R., Yu, Q, and Miller, J.D., 2010b, Characterization and analysis of porous, brittle solid structures by X-ray micro computed tomography, *Journal of Metal*, 62, 86.
- Lindquist, W.B., Lee, S.M, Coker, D.A, Jones, K.W. and Spann, P., 1996, Medial axis analysis of three dimensional tomographic images of drill core samples, *Journal of Geophysical Research*, 101B, 8297.
- Maas, S.A., Ellis, B.J., Atheshian, G.A., Weiss, J.A., 2012, FEBio: Finite elements for biomechanics, *Journal of Biomechanical Engineering*, 01105-1.
- Videla, A.R., Lin, C.L. and Miller, J.D., 2006, Watershed functions applied to a 3D image segmentation problem for the analysis of packed particle beds, *Particle and Particle System Characterization*, 23, 237.
- Videla, A.R., Lin, C.L. and Miller, J.D., 2008, Simulation of saturated fluid flow in packed particle beds – the Lattice-Boltzmann method for the calculation of permeability from XMT images, *Journal of Chinese Institute of Chemical Engineers*, 9, 117.

POLYMER BASED AND INORGANIC MONOSIZED-POROUS BEADS: SYNTHESIS AND CHROMATOGRAPHIC APPLICATIONS

Ali Tuncel

Hacettepe University, Chemical Engineering Department and Division of Nanotechnology and Nanomedicine, Beytepe, Ankara, Turkey
a. Corresponding author (atuncel@hacettepe.edu.tr)

ABSTRACT: Our recent research on the synthesis and applications of organic and inorganic based monosized-porous beads was reviewed. Polyacrylate based spherical beads in the size range of 2-8 μm were obtained by newly established staged-shape template polymerization protocols. The reactive functionalities on the polymer beads allowed the synthesis of various support materials functionalized with different ligands via one-pot and simple derivatization procedures. New synthetic protocols were also developed for monodisperse-porous and micron-size beads of inorganic materials like silica and titania. For this purpose, staged-shape template hydrolysis and condensation protocols were established by starting from the strong anion/cation exchanger forms of both types of polymer beads. The functionalized forms of both polymer based and inorganic beads were evaluated as either stationary media for different micro-high performance liquid chromatography modes or active support for various catalytic applications.

1. INTRODUCTION

Various methods were developed for the synthesis of both polymer based and inorganic spherical-porous beads in the monosized form. Monosized-porous poly(styrene-co-divinylbenzene), poly(S-co-DVB) beads are one of the firstly synthesized members of this family. The seeded polymerization method developed by Ugelstad's group (Ugelstad *et al.*, 1983), the staged shape template polymerization protocol proposed by Svec's group (Galia *et al.*, 1994) are the pioneering studies for the synthesis of these beads. Monosized-porous Poly(glycidyl methacrylate-co-ethylene dimethacrylate), poly(GMA-co-EDMA) and poly(4-chloromethylstyrene-co-divinylbenzene), poly(CMS-co-DVB) beads were also obtained as reactive starting materials for the preparation of various chromatographic supports (Li *et al.*, 1999 and Smigol *et al.*, 1994). The presence of functional groups (i.e. epoxypropyl of poly(GMA-co-EDMA) and chloromethyl of poly(CMS-co-DVB)

beads) allowed the tailoring of starting beads with different functional groups. Hence, the chromatographic stationary phases or the ion-exchanger materials carrying different functional groups were successfully synthesized by starting from poly(CMS-co-DVB) and poly(GMA-co-EDMA) beads (Xu *et al.*, 2003; Unsal *et al.*, 2006; Hao *et al.*, 2011). Hence, the monosized-porous beads carrying functional groups like octadecyl, carboxyl/diethylamine and quaternary ammonium were successfully used as stationary media in various chromatographic modes like reversed phase, ion-exchange and hydrophilic interaction chromatography (Xu *et al.*, 2003; Unsal *et al.*, 2006; Hao *et al.*, 2011).

Various synthetic protocols were also developed for the synthesis of porous-monosized beads in the form of metal oxides (Shchukin *et al.*, 2004; Wang *et al.*, 2007; Drisko *et al.*, 2010; Meyer *et al.*, 2012). By using these methods,

particularly silica, titania and zirconia beads were obtained. These beads were also successfully tried as stationary phase particularly in reversed phase and hydrophilic interaction chromatography applications.

The synthetic protocols were mostly developed for the monosized-porous beads relatively hydrophobic in nature. The synthesis of hydrophilic beads in the monosized-porous form can be still evaluated as a gap in the literature. Hence our recent research was focused on the synthesis of poly(acrylate) based hydrophilic, monosized porous beads that could be utilized as a reactive starting material for the preparation of stationary media particularly for the reversed phase and hydrophilic interaction chromatography modes. The reactive poly(acrylate) beads were also used as template for the synthesis of monosized-porous beads in the form of metal oxides. Hence, monosized-mesoporous titania and silica beads were obtained.

2. RESULTS AND DISCUSSION

For the synthesis of polyacrylate based, monosized-porous beads, 3-chloro-2-hydroxypropyl methacrylate (HPMA-Cl) was selected as the main monomer. The monosized-porous beads ca 5 μm in size were obtained by the multistage-microsuspension copolymerization of HPMA-Cl with different acrylate based crosslinking agents. For this purpose, ethylene dimethacrylate (EDMA), glycerol dimethacrylate (GDMA) and diurethane diacrylate (DUDA) were selected as the crosslinking agents. The porous properties (i.e. porosity, mean pore size and specific surface area) were adjusted by changing polymerization conditions. The reactive monosized-polyacrylate beads with the specific surface areas up to 180 m^2/g and the porosities up to 45 % were achieved (Kip *et al.*, 2013). The use of different

crosslinking agents allowed to synthesize poly(HPMA-Cl) based beads with different polarities. Lower contact angle values were obtained with the beads using DUDA and GDMA as the crosslinking agent.

Various methods were tried to attach different chromatographic ligands onto the surface of polyacrylate beads via chloropropyl moiety. Octadecylamine (ODA), triethylamine (TEA) and triethanolamine (TEA-OH) were covalently attached onto the beads using the direct reaction between chloropropyl and amine moieties. ODA, TEA and TEA-OH attached-poly(HPMA-Cl-co-EDMA) beads were successfully used as stationary phase in reversed phase, ion chromatography and hydrophilic interaction modes with the plate heights up to 40 μm .

Terminal bromine moiety was introduced into the chloropropyl functionalized beads and zwitterionic molecular brushes were generated via the surface initiated-atom transfer radical polymerization of 2-(methacryloyloxy)ethyl] dimethyl-(3-sulfopropyl) ammonium hydroxide (MESH) on the bromine functionalized beads. The beads carrying zwitterionic molecular brushes exhibited good chromatographic performance in the hydrophilic interaction chromatography mode in micro-liquid chromatography system (Çelebi *et al.*, 2013).

Monodisperse-porous titania beads in the size range of 3-6 μm and with the specific surface areas up to 80 m^2/g were obtained using both sulfonic acid and triethylamine attached-poly(HPMA-Cl-co-EDMA) beads as templates. Porous titania beads were also comparatively synthesized using monosized poly(S-co-DVB) beads as template material. The results indicated that the porosity and the specific surface area of resulting titania

beads were correlated with those of starting template.

Poly(HPMA-Cl-co-EDMA) beads were reacted with cysteamine and gold nanoparticles (GNP) ca 10 nm in size were covalently attached onto their surface via the reaction between gold surface and covalently linked –SH groups on the beads. The photocatalytic performance of the GNP attached-monosized-porous titania beads was comparatively investigated in batch fashion for the removal of polar organics in aqueous media.

3.CONCLUSION

HPMA-Cl carrying monosized-porous beads were successfully synthesized and tailored with different chromatographic ligands in the form of single small molecule or molecular brush (Gölgelioğlu *et al.*, 2011; Kip *et al.*, 2013). Both types of beads exhibited satisfactory chromatographic performance in size exclusion, reversed phase and hydrophilic interaction modes in micro-liquid chromatography system (Gölgelioğlu *et al.*, 2011; Gökaltun *et al.*, 2013; Çelebi *et al.*, 2013).

Monosized-porous titania beads in the size range of 3-6 µm and with the specific surface areas up to 80 m²/g were obtained by using poly(HPMA-Cl-co-EDMA) beads functionalized with both positively and negatively charged groups as the template material (Nazlı *et al.*, 2013). These beads were functionalized with gold nanoparticles and successfully tried as photocatalyst in the degradation of dye molecules in aqueous media. The comparative catalytic performance is still under-investigation and will be documented during the presentation.

Acknowledgements: This study is supported by both Turkish Academy of Sciences (TÜBA) and TUBİTAK-

Chemistry and Biology Research Group. The financial support provided is gratefully acknowledged.

REFERENCES

- Cao, Q., Xu, Y., Liu, F., Svec, F., Frechet J.M.J., 2010, Polymer Monoliths With Exchangeable Chemistries: Use of Gold Nanoparticles as Intermediate Ligands for Capillary Columns With Varying Surface Functionalities. *Anal. Chem.* 82, 7416.
- Çelebi B., Kip, Ç., Özen, M.B., Tuncel, A., 2013, A stationary medium for semi-micro-hydrophilic interaction chromatography: Polyacrylate based hydrophilic, monosized-porous beads with zwitterionic molecular brushes, Manuscript in preparation.
- Drisko, G. L., Kimling, M. C., Scales, N. , Ide, A., Sizgek, E., Caruso, R. A. and Luca, V. , 2010, One-Pot Preparation and Uranyl Adsorption Properties of Hierarchically Porous Zirconium Titanium Oxide Beads using Phase Separation Processes to Vary Macropore Morphology, *Langmuir* 26 (22), 17581.
- Galia, M. Svec, F. Frechet, J.M.J., 1994. Monodisperse Polymer Beads as Packing Material for High-Performance Liquid Chromatography: Effect of Divinylbenzene Content on the Porous and Chromatographic Properties of Poly(styrene-co-divinylbenzene) Beads Prepared in Presence of Linear Polystyrene As A Porogen, *Journal of Polymer Science Part A: Polymer Chemistry*, 32 (11), 2169.
- Gökaltun, A., Çelebi B., Arman, E., Tuncel, A., 2013, Polyethylenimine attached-poly(3-chloro-2-hydroxypropyl methacrylate-co-ethylene dimethacrylate) beads as a new stationary phase for hydrophilic interaction chromatography, *J. Sep. Sci.*, Submitted.
- Hao, J., Wang, F., Dai, X., Gong, B., 2011, Preparation of Poly(vinyltetrazole) Chain-Grafted Poly(glycidyl methacrylate-co-ethylenedimethacrylate) Beads by Surface-Initiated Atom Transfer Radical Polymerization for the Use In Weak Cation Exchange and Hydrophilic Interaction Chromatography, *Talanta* 85 (1), 482.
- Gölgelioğlu C, Bayraktar A, Celebi B, Uğuzdoğan E, Tuncel A., 2012, Aqueous Size Exclusion Chromatography in Semimicro and Micro-columns by Newly Synthesized Monodisperse Macroporous Hydrophilic Beads As a Stationary Phase, *J. Chromatogr. A*, 1224 (1), 43.

- Kip Ç., Maraş, B., Evirgen, O., Tuncel A., 2013, Synthesis and characterization of new hydrophilic, monosized, porous and reactive polyacrylate beads, Manuscript in preparation.
- Li, W.H., Li, K., Stöver, H. D. H., 1999. Monodisperse Poly(chloromethylstyrene-*co*-divinylbenzene) Microspheres by Precipitation Polymerization, *Journal of Polymer Science Part A: Polymer Chemistry*, 37 (14), 2295.
- Lv Y., Lin Z., Svec F., 2012, Hypercrosslinked Large Surface Area Porous Polymer Monoliths for Hydrophilic Interaction Liquid Chromatography of Small Molecules Featuring Zwitterionic Functionalities Attached to Gold Nanoparticles Held in Layered Structure, *Anal. Chem.* 84, 8457.
- Meyer, U., Larrison, A., Hentze, H.P., Caruso, R.A., 2012, Templating of Porous Polymeric Beads to Form Porous Titania and Silica Spheres, *Advanced Materials*, 14 (23), 1768.
- Nazlı, K.Ö., Çelebi, B. Tuncel, A., 2013, Synthesis and characterization of Monosized-Porous Titania beads Using Different Polymer Beads as Templates, Manuscript in preparation.
- Shchukin, D. G., Caruso R. A., 2004, Template Synthesis and Photocatalytic Properties of Porous Metal Oxide Spheres Formed by Nanoparticle Infiltration, *Chem. Mater.* 16, 2287.
- Smigol, V., Svec, F., Frechet, J. M. J., 1994. High-Performance Liquid Chromatography of Complex Mixtures Using Monodisperse Dual-Chemistry Polymer Beads Prepared by a Pore-Size-Specific Functionalization Process. A Single Column Combination of Hydrophobic Interaction and Reversed-Phase Chromatography, *Anal. Chem.*, 66 (13), 2129.
- Ugelstad, J., Söderberg, L., Berge, A., Bergström, J., 1983. Monodisperse Polymer Particles: A Step Forward For Chromatography, *Nature* 303, 95.
- Unsal, E., Elmas, B., Çağlayan, B. , Tuncel, M., Patir, S., Tuncel, A., 2006 Preparation of an Ion-Exchange Chromatographic Support by A “Grafting From” Strategy Based on Atom Transfer Radical Polymerization, *Anal. Chem.*, 78 (16), 5868.
- Xu M., Peterson D. S., Rohr T., Svec F., Fréchet, J. M. J., 2003. Polar Polymeric Stationary Phases for Normal-Phase HPLC Based on Monodisperse Macroporous Poly(2,3-dihydroxypropyl methacrylate-*co*-ethylene dimethacrylate) Beads, *Anal. Chem.*, 75 (4), 1011.
- Wang, M.L., Wang, C. H., Wang, W., 2007, Porous Macrobeads Composed of Metal Oxide Nanocrystallites and With Percolated Porosity, *J. Mater. Chem.*, 17, 2133.

CHARACTERISATION OF POWDER MIXTURES USING MORPHOLOGICALLY DIRECTED RAMAN SPECTROSCOPY

Deborah Huck-Jones, Carl L. Levoguer, Lisa Makein and Ulf Willén^a

Malvern Instruments Limited, Grovewood Road, Malvern, Worcestershire. WR14 1XZ, UK
a. Corresponding author (Ulf.Willen@malvern.com)

ABSTRACT: Many products and intermediates may consist of a mixture of different types of particulate materials. Traditional particle characterization methods are unable to differentiate between components in a mixture unless they have extremely different physical properties. For example a particle size measurement such as laser diffraction will give the particle size distribution of all components within a mixture. The only way to characterize the individual components is to do this prior to mixing/blending, however this does not take into account any changes that occur within the sample during the mixing process, such as particle attrition or agglomeration. In this presentation we will consider the use of a novel technique, which combines automated particle imaging and Raman spectroscopy to allow characterization of individual components within a powder mixture.

1. METHODS

The target sample was a powder blend consisting of several different chemical entities. It was characterised using the Morphologi G3-ID (Malvern Instruments Ltd). The complete analysis is made up of three parts, sample dispersion, morphological analysis and chemical analysis. The complete three step analysis can be run as a single standard operating procedure (SOP).

A volume of 5mm³ of powder was dispersed using the instrument's integrated sample dispersion unit at 4 bar using the high pressure option in order to maximise separation of fine particle agglomerates.

The morphological analysis was performed using a 50x objective which provided size and shape data as well as images of every particle analysed.

A representative sample of more than 2500 particles with circular equivalent diameter (CED) of 1-10 µm were selected for chemical analysis. Raman spectra were automatically collected from the centre of each of the selected particles with an acquisition time of 30 seconds.

Separately, a spectral library was constructed using Raman spectra

acquired from each of the components of interest. The spectra acquired from the dispersed blend were compared to the spectra from the library and a correlation calculation performed. The correlation score calculated provided an indication of the match of the particle spectra to the library spectra. A score close to 1 indicates a good match of the target particle to the reference whereas a score close to 0 means no match.

The particles for which spectra had been acquired were chemically classed using these correlation values. Particles falling into each chemical class were isolated allowing component specific size distributions (PSD) to be compared. Particles that did not fit any of the classes were identified and many were found to be agglomerates.

2. RESULTS

The morphological part of the analysis recorded an image of every particle analysed. Particles that were in the 1 – 10 µm size range were targeted for chemical analysis. Figure 1 shows images of some of the particles from which a spectrum was acquired during the measurement.

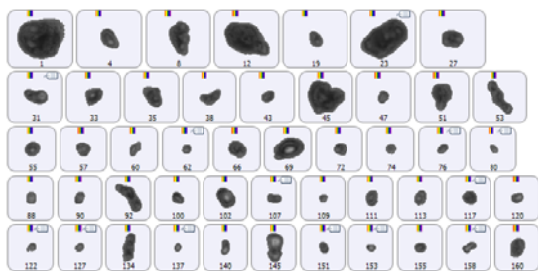


Figure 1: Images of some of the particles that were targeted for chemical analysis.

The components of interest shared very similar morphology but gave a different Raman spectrum. This made it possible to identify the particles of interest from the remainder of the mixture based on chemical information. The populations were classed based on the Raman correlations to the library spectra of the 2 drug components. It was possible to visualise the two drug populations of interest using the scattergram of correlation to component 1 vs correlation to component 2 shown in figure 2. Figure 2 also shows the reference spectra for the two components of interest.

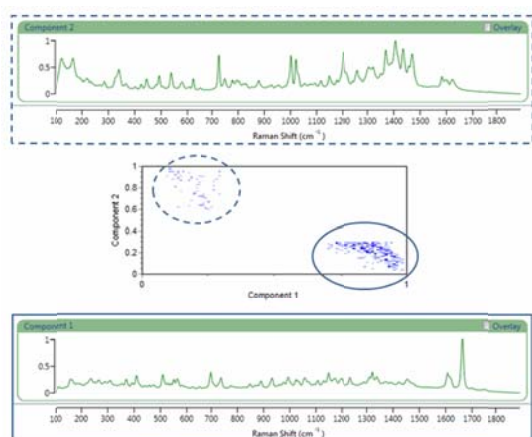


Figure 2: Scattergram showing the relationship between the chemical results for the two drug components in the blend.

Particles of each component were classed to isolate them and to obtain the component specific particle size distributions. Figure 3 shows the overlay

of the circular equivalent diameter distributions for the two drug components. It can be seen that component 1 contains larger particles than component 2.

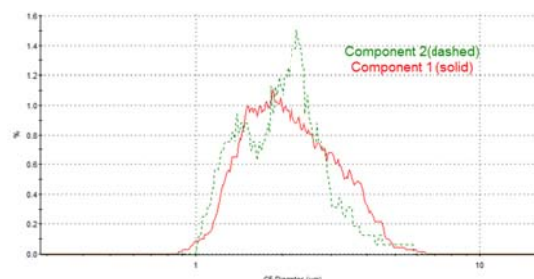


Figure 3: Overlay of the particle size distributions for the 2 drug components in the blend.

Some particles were found to correlate relatively highly to more than one component in the blend. The spectrum for such a particle, (particle 177) was viewed along with the reference spectra. Figure 4 shows how this particle's spectrum contains features relative to both library components. This particle is clearly an agglomerate of the components and was classed as such.

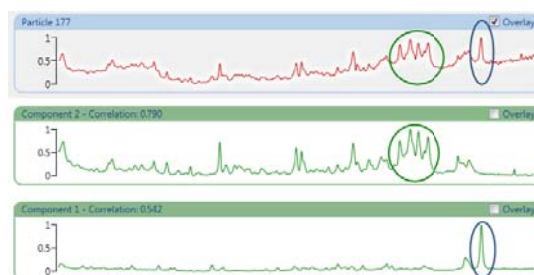


Figure 4: Reference spectra for components 1 and 2 and a spectrum from an agglomerate particle containing both components.

The proportion of each component and the agglomerates present in the sample is reported in the classification chart shown in figure 5. Here it can be seen that in the 1-10 µm size range analysed, component 1 is the most abundant at 85 % by number. Component 2 is only present in

an un-agglomerated form at approximately 2 % by number.

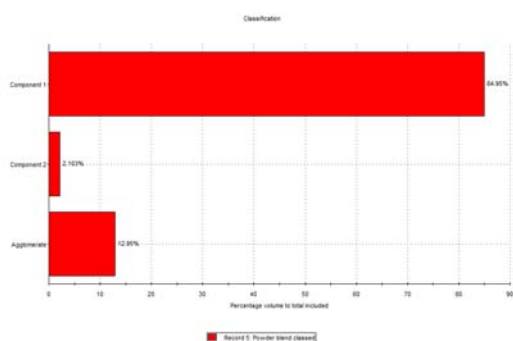


Figure 5: Classification chart showing the proportion of each of the 2 drug components and the agglomerates found in the blend.

3. CONCLUSION

The component specific particle size distributions for the two components within mixture of different types of particulate materials were successfully measured using morphologically directed Raman spectroscopy. Some particles that did not correlate to a specific reference uniquely were found to be agglomerates. This technique may be applied to a wide range of formulated particulate products in either powder or suspension form and provide valuable information which cannot be obtained by conventional particle characterization techniques.

CHARACTERIZATION OF POROUS COATINGS ON AZ31 MG ALLOY BY PLASMA ELECTROLYTIC OXIDATION

Salim Levent Aktuğ^{1,a}, Salih Durdu², Işıl Kutbay³, Aysun Demirtaş⁴, Selin Bayramoğlu⁵,
Metin Usta⁶

1,2,3,4,5,6. Gebze Institute of Technology, Kocaeli, Turkey
a. Corresponding author (saktug@gyte.edu.tr)

ABSTRACT: In this study, AZ31 Mg alloy produced by twin roll casting was coated by plasma electrolytic oxidation (PEO) in solutions, consisting of 4 g/L Na₂SiO₃.5H₂O + 1,5 g/L KOH (called as E1) and 8 g/L Na₂SiO₃.5H₂O + 1,5 g/L KOH (called as E2) electrolytes at 0,14 A/cm² current density for 60 minutes. The average coating thicknesses are 73 to 68 µm for E1 and E2, respectively. XRD results indicated that Mg₂SiO₄ (Forsterite) and MgO (Periclase) phases were formed on the surface of the coated magnesium alloy. Average hardnesses of coatings were measured as 735 HV for E1 and 795 HV for E2, while the hardness of substrate is 70 HV. Surface roughnesses of coatings were measured as 5.75 and 6.23 µm for E1 and E2, respectively. PEO coatings exhibited superior wear resistance. The wear resistance of coating produced in E1 is greater than the one in E2.

1. INTRODUCTION

Magnesium and magnesium alloys have been used for a number of applications such as aerospace and automotive industries, transportation, mobile communication devices and personal computers [Yerokhin *et al.*, 2004] owing to their excellent physical and mechanical properties, such as low density, high specific strength, good castability, good weldability, relatively good electrical conductivity, high thermal conductivity, high dimensional stability and good electromagnetic shielding characteristics [Guo *et al.*, 2006; Guo and An, 2005]. However, the magnesium and its alloys have poor corrosion resistance because of low chemical stability and high negative electric potential [Guo and An, 2005; Wu and Zheng 2007, Lee and Lee, 2008]. In addition, the magnesium alloys have inferior wear resistance [Abbas *et al.*, 2006]. Therefore, the practical usage of the magnesium and its alloys need coating to improve the poor corrosion and wear resistance. Many researchers have attempted to develop anticorrosive and

high wear-resistance strategies [Lv *et al.*, 2009; Zhang *et al.*, 2008].

PEO is an eco-friendly and practical process to make high-quality oxide coatings on the surfaces of light metals such as aluminum, titanium, magnesium and their alloys [Lee and Lee, 2008]. In addition to those superior physical and chemical properties such as wear resistance, corrosion resistance, electrical insulation, micro hardness, PEO can uniformly form an oxide film which strongly adheres to a substrate with complex geometries. Therefore, wide applications of this technique are expected in many fields [Guo and An, 2005; Lee and Lee, 2008].

In current study, the different electrolytes from the literature was used and the effect of these on the structural and mechanical behavior of the coating such as hardness, adhesion strength, wear resistance at the same current density and the same time was investigated.

2. EXPERIMENTAL PROCEDURE

2.1. Analysis of samples

Coating thicknesses were measured using eddy current method by Fischer Dualscope MP20 device. Surface morphologies of coatings were scanned by using SEM (Philips XL300 SFEG). Phase structures on the coating were detected by X-ray diffraction (Bruker D8 Advance). Hardness of the substrate and the coating via distance were measured by using Vickers tester (Anton Paar MHT-10). Adhesion strengths of the coatings were measured by using scratch tester (Nanovea Series). Wear rates of the coatings and base metal were carried out by using ball-on disc mechanism tribometer (CSM Instrument). Wear tracks generated on the coatings and substrate material were measured using profilometer (Veeco Dektak 8) after the wear tests.

2.1. Sample preparation

AZ31 Mg alloy produced by twin roll cast was used as substrates. Chemical composition of alloy is given in weight percent in Table 1. All samples were ground to grits of 400, 800, and 1200 by SiC paper and then cleaned by distilled water and acetone. AZ31 Mg alloys were coated by the plasma electrolytic oxidation in the solutions E1 and E2, consisting of 4 g/L $\text{Na}_2\text{SiO}_3 \cdot 5\text{H}_2\text{O}$ + 1,5 g/L KOH (called as E1) and 8 g/L $\text{Na}_2\text{SiO}_3 \cdot 5\text{H}_2\text{O}$ + 1,5 g/L KOH (called as E2) electrolytes at 0,14 A/cm^2 current density for 60 minutes. Fig. 1 illustrates the electrode process in aqueous solutions [Yerokhin *et al.*, 1999].

Table 1: Chemical composition of AZ31 Mg alloys.

Element	Composition (% wt)
Al	2.65
Zn	1.03
Mn	0.31
Si	0.15

Fe	0.003
Sn	0.002
Ni	0.0002
Mg	Balance

PEO system of 100 kW composed of stainless steel container, cooling and stirring equipment was run with alternative current (AC). Mg sample was used as an anode, whereas stainless steel container was used as a cathode.

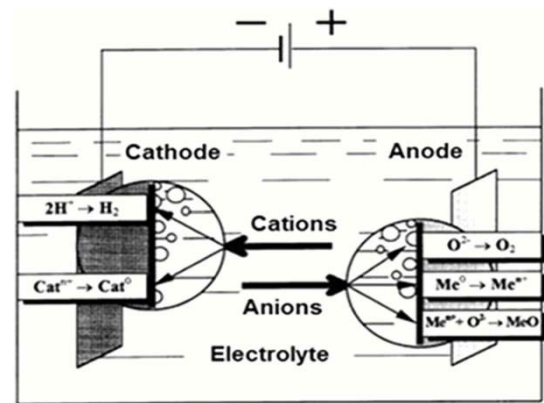


Figure 1: Electrode processes in aqueous solutions [Yerokhin *et al.*, 1999].

3. RESULTS AND DISCUSSION

3.1. Coating Thickness

Average coating thickness is given in Table 2.

Table 2: The Coating Thickness

E1	73.3 μm ±2.3
E2	67.6 μm ±3.6

Micro discharge channels are formed on the surface with losing of dielectric stability due to causing high voltage in PEO process. Anions in the electrolyte penetrate into micro discharge channels owing to the existence of electrical field. AZ31 Mg alloy reacts with anionic compounds oxides in the micro discharge channels. Ions from the electrolyte are drawn into oxide layers and the layer is modified by these ions. At the end of this process, the oxide in contact with electrolyte quickly solidifies because the

electrolyte is colder than the oxide surface. The ions from the substrate react with ions from electrolyte in micro discharge channels and they form new layer on the surface. This kinetic event repeats itself as long as the process continues. [Guangliang *et al.*, 2002, Jin *et al.*, 2006]. So it should have expected that coating thickness of E2 solution would have been higher than E1 solution due to the amount of ions in the solution which was greater than E1. However, there are some cracks on the surface of the coating during this process and one more point, diminishing power of the coating kinetic cause loss of coating layer on the surface. So the E2 coating thickness is less than E1 solution even though the ions volume are greater.

3.2. Phase structure of coatings

Fig. 2 shows the phase structures of PEO coatings produced on the AZ31 Mg alloys in the silicate solutions E1 and E2. The dominant phases of spinal Mg_2SiO_4 (Forsterite) and MgO (Periclase) are detected by X-ray diffraction. In Fig. 2, E1 and E2 electrolytes show mostly similar characteristic peak intensities with each other due to the same ingredients in the electrolytes. One noticeable difference in the XRD result is the peak intensity of MgO phases which is greater in E1 solution.

3.3. Surface morphology

Fig. 3 shows the surface morphology of coatings produced by PEO. Typically, the coatings produced by PEO method have very porous and rough surface structure due to the existence of micro discharge channels. These pores are called as micro discharge channels in PEO process. Pore size and surface morphology depend on the applied voltage, current value and duration time. Coating surface becomes much porous with increasing duration time. The number of pores decreases due to growing of micro discharge channels

with increasing duration time; however the size of pores increases. Increasing in the diameter of the micro discharge channels is balanced by reducing of the pressure in the micro discharge channels through process [Sundararajan and Rama, 2003].

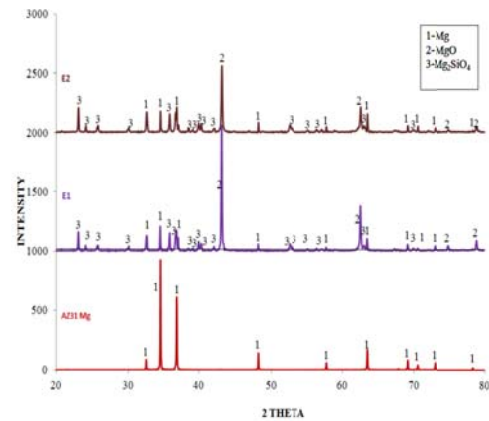


Figure 2: X-ray diffraction patterns of E1, E2 and AZ31 Mg

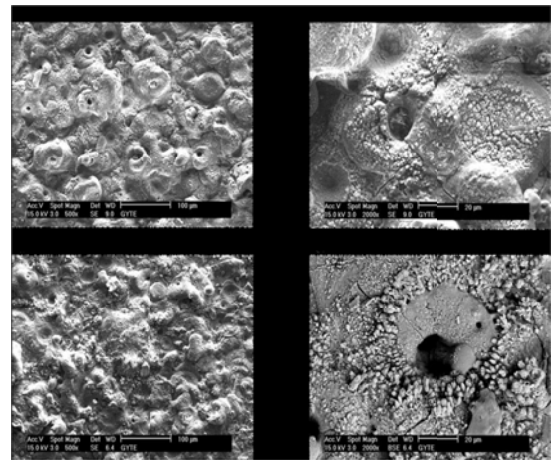


Figure 3: SEM images of surface morphology of coatings: (a) E1 surface (b) E1 discharge Channel (c) E2 surface and (d) E2 Discharge Channel.

3.4. Hardness of coating

The coating hardness of E2 is harder than that obtained E1 in Table 3. High value of coating hardness depends on the development of phase structure of coating. This is because, depending on the concentration of the increase in the amount of the phases. Mg_2SiO_4

(forsterite) phase appeared to be greater in the E2 solution in XRD result.

Table 3: The hardness of the Coating

E1	734 HV
E2	797 HV

3.5. Adhesion strength of coatings

Micro scratch tester is used to evaluate the adhesion strength of coatings. The scratch test results for coatings are given in Table 4. The critical load results measured by the scratch test are characteristic values for each coating. The adhesion strength of coatings increases with increasing critical load. L_c refers to critical load required to fail the coating.

Table 4: Critical loads on the coatings

Solution	Coating Thickness	Critical load L_c (N)
E1	73.3 $\mu\text{m} \pm 2.3$	145.01
E2	67.6 $\mu\text{m} \pm 3.6$	143.67

According to this result, the critical load depends on coating thickness, the amount of phase structure and coating hardness. Also, the higher critical load value, the higher load carrying capacity of coating is. The critical load required to damage the coating increases with coating thickness because the inner layer is denser and harder than the outer layer.

Table 5: Critical loads on the coatings

Solution	Surface roughness (μm)	Wear rate $\times 10^4$ ($\text{mm}^3/\text{N}/\text{m}$)
Untreated AZ31 Mg	0.15	35.0
E1	5.75	1.86
E2	6.23	2.89

Also, porous surface forms in PEO process. The coated layer consists of different regions in terms of compactness of the layer. There is a greater porosity in the region away from the substrate than in the region close to the substrate as seen in Figure 4.

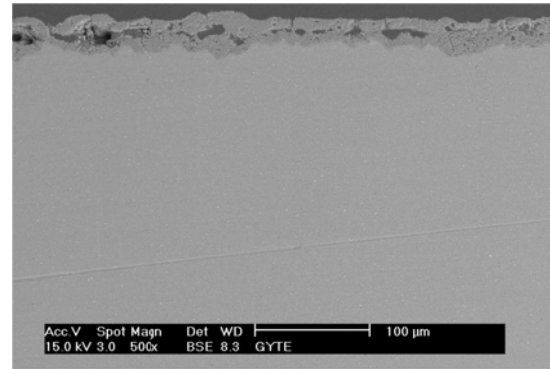


Figure 4: Cross Section image of E2 Coating

4. CONCLUSIONS

1. Coating thicknesses varies according to the ion concentration in the solution. E1 thickness is greater than E2's.

2. XRD results indicated that the coatings consist of Mg_2SiO_4 (Forsterite) and MgO (Periclase) phases for E1 and E2.

3. Hardness and surface roughness increase with increasing additives amount. Hardness is proportional to $\text{Na}_2\text{SiO}_3 \cdot 5\text{H}_2\text{O}$ volume in the solution.

4. Wear rates of the coatings are lower than AZ31 Mg alloy. In addition, wear rates of coatings increase because of forming of much more rough and porous surface.

REFERENCES

- Yerokhin AL, Shatrov A, Samsonov V, Shashkov P, Leyland A, Matthews A 2004. Fatigue properties of Keronite[®] coatings on a magnesium alloy, Surf Coat Tech; 182:78-84.
- Guo H, An M, Xu S, Huo H 2006. Microarc oxidation of corrosion resistant ceramic

- coating on a magnesium alloy, *Mater Lett*;60:1538-41.
- Guo HF, An MZ 2005. Growth of ceramic coatings on AZ91D magnesium alloys by micro-arc oxidation in aluminate-fluoride solutions and evaluation of corrosion resistance, *Appl Surf Sci*; 246:229-38.
- Wu K, Wang YQ, Zheng MY 2007. Processing maps for hot working of ZK60 magnesium alloy, *Mater Sci Eng A*;447:227-32.
- Lee YK, Lee K, Jung T 2008. Study on microarc oxidation of AZ31B magnesium alloy in alkaline metal silicate solution, *Electrochem Commun*;10:1716-9.
- Abbas G, Li L, Ghazanfar U, Liu Z 2006. Effect of high power diode laser surface melting on wear resistance of magnesium alloys, *Wear*; 260:175-80.
- Lv G, Chen H, Li L, Niu E, Pang H, Zou B, et al 2009. Investigation of plasma electrolytic oxidation process on AZ91D magnesium alloy, *Curr Appl Phy*;9:126-30.
- Zhang WX, Jiang ZH, Li GY, Jiang Q, Lian JS 2008. Electroless Ni-P/Ni-B duplex coatings for improving the hardness and the corrosion resistance of AZ91D magnesium alloy, *Appl Surf Sci*; 254:4949-55.
- Yerokhin AL, Nie X, Leyland A, Matthews A, Dowey SJ 1999. Plasma electrolysis for surface engineering, *Surf Coat Tech* 122:73-93
- Guangliang Y, Xianyi L, Yizhen B, Haifeng C, Zengsun J. J 2002. The effects of current density on the phase composition and microstructure properties of micro-arc oxidation coating, *Alloy Compound*; 345:196-200.
- Jin F, Tong H, Li J, Shen L, Chu PK 2006. Structure and mechanical properties of magnesium alloy treated by micro-arc discharge oxidation using direct current and high-frequency bipolar pulsing modes, *Surf Coat Tech*;201:292e5.
- Sundararajan G, Rama KL 2003. Mechanisms underlying the formation of thick alumina coatings through the MAO coating technology, *Surf Coat Tech*; 167:269-77.

EFFECT OF PORE WALL MICROSTRUCTURE ON THE MECHANICAL PROPERTIES OF LOW ALLOY STEEL FOAMS

Nuray BEKÖZ^{1,a} and Enver OKTAY¹

1. Istanbul University, Metallurgical and Materials Engineering Department, Istanbul, Turkey
a. Corresponding author (nbekoz@istanbul.edu.tr)

ABSTRACT: Mechanical behaviour of metal foams is not only affected by porosity level, pore shape and pore size but also depend on properties of pore wall material. This study primarily concerns the role of pore wall microstructure which influences mechanical behaviour of steel foams. Three low alloy steel foams having rather similar porosity and pore structure but differences in pore wall microstructure were produced by space holder-water leaching technique in powder metallurgy. Pre-alloyed steel powders with different Cu-Ni-Mo contents were mixed with space holder (carbamide), and then compacted at 200 MPa. The spacer in the green compacts was removed by water leaching at room temperature. The green specimens were sintered at 1200 °C for 60 min in hydrogen atmosphere. The microstructural and mechanical property variations resulting from the use of steel powder containing different alloying elements were discussed.

Keywords: Steel foam, Powder metallurgy, Microstructure, Mechanical properties.

1. INTRODUCTION

During the last years a number of studies have demonstrated the remarkable properties of metal foams and their potential for a variety of applications [Michailidis *et al.*, 2011]. The excellent combination of good mechanical properties and low weight is the prime advantage for such class of materials and in particular for steel foams. In recent years space holder-water leaching technique in powder metallurgy has been used to manufacture steel foams. This technique is rather cost effective, flexible and leads to desired foam properties [Bakan, 2006]. The process and deformation behaviour of steel foams have been the subject of numerous studies that mainly focus on the strength properties during compression [Bram *et al.*, 2000; Zhang and Zhao, 2008; Bekoz and Oktay, 2012]. However, the mechanical behaviour of the foams is not only affected by the structure and pore morphology of the foam, but also depend on the properties of the pore wall material [Markaki and Clyne, 2001; Jiang *et al.*, 2005]. The details of the mechanical properties should be further examined in

order to use steel foam material in a large scale. There are not enough studies on the effect of pore wall microstructure on compressive properties of the steel foams. The selection and use of pre-alloyed powders have many advantages over mechanical properties of sintered materials. Low alloyed steel powders commercially known as Distaloy AB, Distaloy AE and Astaloy Mo are a partially pre-alloyed iron powder containing different copper, nickel and molybdenum contents. The powders consist of very pure iron powder to which finely divided alloying elements are diffusion bonded. In this way the extremely high compressibility of the powder is maintained. The fine alloying additives are well utilized and the risk of segregation is minimized. Other advantages of these alloys include good green strength and dimensional stability [Höganäs, 2004].

Comparing of steel foams containing different alloying elements should be required to characterize the influence of pore wall microstructure on the properties

of steel foams. In this study, three low alloy steel foams having rather similar porosity and pore structure but differences in pore wall microstructure were produced by space holder-water leaching technique in powder metallurgy. The microstructural and mechanical property variations resulting from the use of steel powder containing different alloying elements were investigated.

2. EXPERIMENTAL PROCEDURES

Low alloy steel foams were produced using steel powders commercially known as Distaloy AE, Distaloy AB and Astaloy Mo, which is a registered trademark of Höganäs Company, Sweden. The powder premixes consisted of 0.8 wt.% zinc stearate as lubricant, and 0.2 wt.% carbon was added as fine graphite (UF4). The binder for green strength was polyvinyl alcohol (PVA), supplied by Merck, Germany. Carbamide particles were used as space holder for its advantage of ease of removal in water. Spherical carbamide particles were crushed and sieved to obtain the fraction of 710-1000 μm with irregular shape. The chemical compositions of the powder mixes prepared are given in Table 1. The average particle sizes of Distaloy AE, Distaloy AB and Astaloy Mo powders were found to be about 90 μm , 112 μm and 109 μm , respectively and a rounded but irregular shape.

Table 1: The chemical composition of the powder mixes (wt.%).

Base powder	Cu	Ni	Mo	C	Lub.	Fe
Distaloy AE	1.5	4.0	0.5	0.2	0.80	Bal.
Distaloy AB	1.5	1.75	0.5	0.2	0.80	Bal.
Astaloy Mo	-	-	1.5	0.2	0.80	Bal.

Initially, 2.5 wt.% PVA solution was added to the steel powder as a binder. Mixing of the steel powder and carbamide particles was performed in a Turbula type mixer. The coated carbamide particles with the

steel powder were then compacted uniaxially at 200 MPa into cylindrical shapes with a 12 mm diameter and height of about 18 mm. The green specimens were immersed in distilled water at room temperature to leach the carbamide. The PVA in the green specimens was thermally removed as part of sintering cycle, which consisted of heating at a ramp rate of 5 $^{\circ}\text{C min}^{-1}$ to 450 $^{\circ}\text{C}$ with a dwell time of 30 min, followed by heating at a rate of 10 $^{\circ}\text{C min}^{-1}$ to sintering temperature. The specimens were sintered at 1200 $^{\circ}\text{C}$ for 60 min under high purity hydrogen in a tube furnace (Lenton, UK).

The sintered foam specimens' density and porosity content were determined by Archimedes' principle in a Sartorius precision balance equipped with a density-determination kit. Fractions of open and closed porosity were determined by weight measurements prior to and after dipping the specimens in boiling paraffin at 150 $^{\circ}\text{C}$. The pore morphology of the foams was examined by scanning electron microscopy (SEM). Pore size distributions were determined by quantitative image analyses using commercial image analyzer software, Clemex Vision PE. The specimens' pores were filled with a cold-hardening epoxy resin then etched in 2% Nital solution for optical examination. The foam specimens' mechanical properties were studied using the compression test performed on a Zwick-Roell Z050 materials testing machine. Compression tests were conducted at a crosshead speed of 0.5 mm min^{-1} .

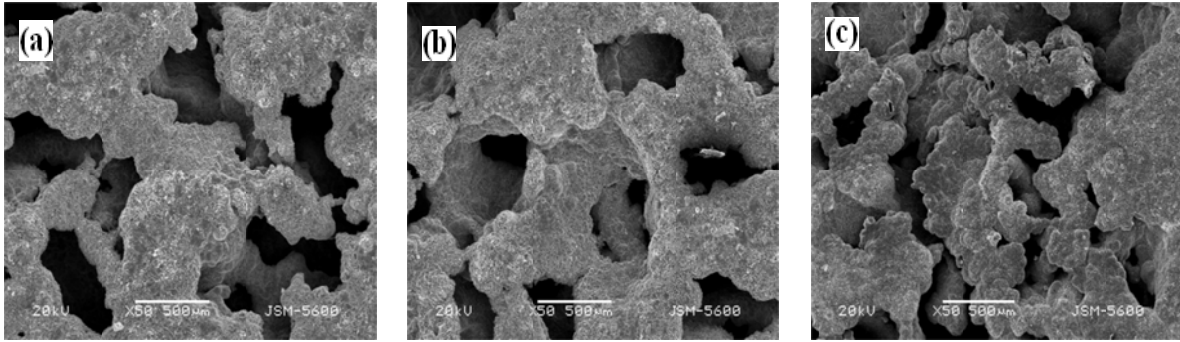


Figure 1: SEM images of foams: (a) Astaloy Mo, (b) Distaloy AB and (c) Distaloy AE.

3. RESULTS AND DISCUSSION

Three low alloy steel foams have about %70 porosity. The total porosity of the specimens consists of 62.1-65.7% open and 5.5-8.1% closed porosity. Sintering caused 7.11% to 7.21% volumetric shrinkage in the specimens. The SEM images of the surfaces of the foams are given in Figure 1. The specimens have a relatively uniform pore distribution. Cell walls separating each pore from its neighbors can be clearly seen. The morphology of the final pores was similar to that of the carbamide particles for all the specimens. This suggests that the pore structures can be designed by using proper size, shape and content of the carbamide particles.

The foams were observed to contain mainly two types of pores: macropores obtained as a result of spacer, and micropores on the cell walls due to incomplete sintering of the steel powders. Quantitative metallographic studies showed that the mean micropore sizes of Astaloy Mo, Distaloy AB and Distaloy AE foams were 156 μm , 134 μm and 118 μm , respectively. Mean macropore sizes of Astaloy Mo, Distaloy AB and Distaloy AE foams were 678.3, 658.5 μm and 667.4 μm , respectively. Carbamide particles' mean size was determined to be 812.6 μm . The decrease in size was attributed to the carbamide particle crushing during pressing and moistening prior to the mixing. Figure 2 shows the optic microscope images taken from cell walls of Astaloy Mo, Distaloy

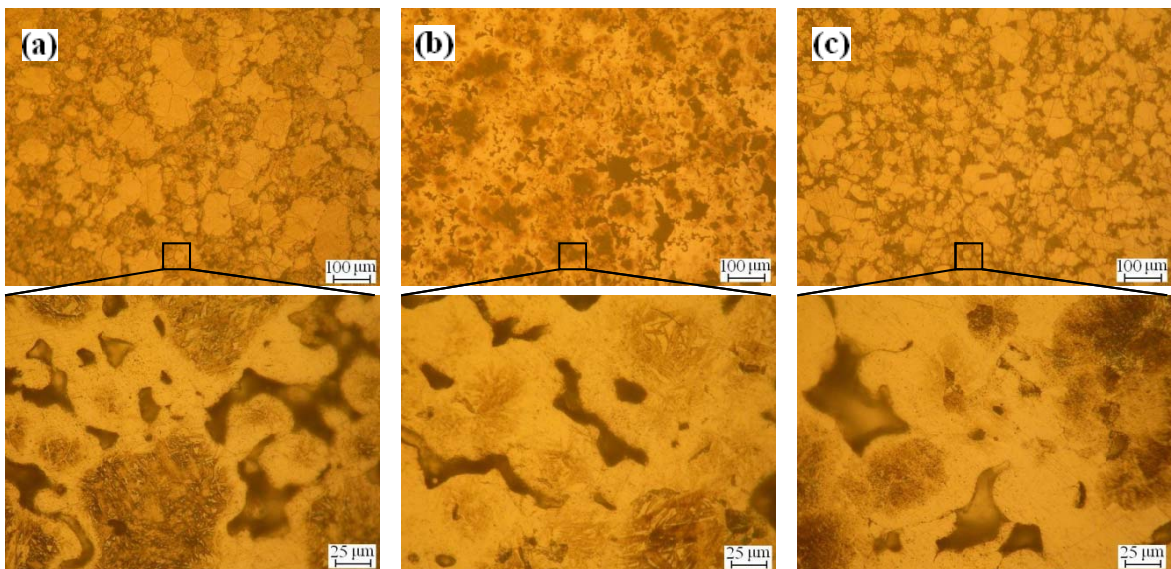


Figure 2: Microstructure images from the cell walls of (a) Astaloy Mo, (b) Distaloy AB and (c) Distaloy AE foams.

The foams were observed to contain mainly two types of pores: macropores obtained as a result of spacer, and micropores on the cell walls due to incomplete sintering of the steel powders. Quantitative metallographic AB and Distaloy AE foam specimens at different magnifications.

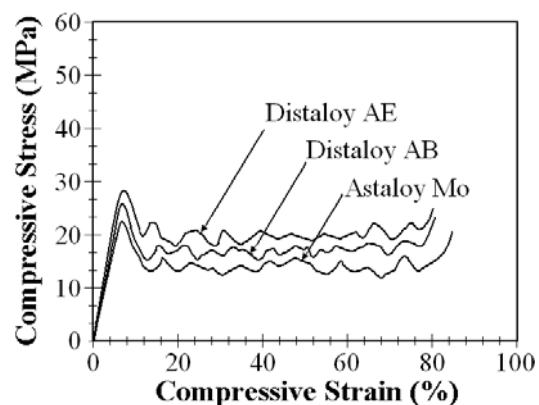
The sintered specimens consisted of ferrite, pearlite, austenite, bainite and a small amount of martensite phases. The microstructural images of Distaloy specimens showed that copper was accumulated in the grain boundaries as a result of sintering. In the micrograph, bright regions are martensite, darker regions are bainite plus pearlite, brown regions are austenite and black regions are micropores between the steel particles. The alloys that contained Ni had nickel-rich areas in the grain boundaries due to the heterogeneous distribution of nickel, especially in Distaloy AE specimens. Several researchers reported that the microstructure of Distaloy specimens consisted of pearlite, martensite and nickel-rich phases [Chawla and Deng, 2005; Ivanuş and Branduşan, 2007].

The compressive stress-strain curves of the foam specimens are illustrated in Figure 3. Three distinct regions characterized the curves: an elastic region where cell walls bending occurred; a large plateau region and finally a densification region where the flow stress increases rapidly. The stress, after a first maximum, drops significantly as a result of the collapse of a pore layer. The deformation mode, resulting from repeatable failure of the pore layers, gives rise to very uneven character of the stress-strain curve. At the end of the plateau region, stress starts to increase since the pores at the deformation zone have flattened and the material shows bulk-like properties under compression. During compression, the cell walls tend to crack and fracture in a brittle manner, a probable consequence of the micropore content of

the cell walls. The deformed structure exhibited extensive cell wall failures.

Compressive yield stress values of Astaloy Mo, Distaloy AB and Distaloy AE foams were 22 MPa, 24 MPa and 26 MPa, respectively. Differences in pore wall microstructure did not significantly affect the length of the plateau region, but slightly increased the compressive strength of the specimens.

Figure 3: Compressive stress-strain curves of the foam specimens.



The present results demonstrated that the compressive strength of both Distaloy foams is higher than that of the Astaloy foams. An explanation for this discrepancy may be due to the effect of the alloying elements, where it was found that the presence of copper as an alloying element in the chemical composition of Distaloy powder reduces micropores in the cell walls. This has positive effect on the compressive strength due to the liquid phase absence during sintering. Liquid phase is one of the most successful methods to accelerate the sintering mechanism for processing the sintered low alloyed steels. A similar improvement has been reported by the use of boron as an additive for liquid phase sintering of the stainless steel foams [Bakan, 2006; Gülsoy and German, 2008]. The compressive strength of the Distaloy AE which contained high Ni is higher than the other two foams. Gething et al. [Gething *et al.*, 2005] studied the effects of Ni addition on

the mechanical properties of Fe-0.85Mo-0.4C, and also reported that Ni as alloying element increased the strength of sintered compacts.

4. CONCLUSIONS

- Mechanical properties of the foams are sensitive to the cell wall structure. As a result of steel powder containing different alloying elements, bainite and martensite phases form in the cell wall structure of the foams. This is the reason for the increase in the compressive yield stress of the foam specimens.
- The strength values of Astaloy Mo foams were lower than Distaloy foams' strength values. The reason for this is the difference in chemical composition and the production technique of Astaloy Mo powder.
- Distaloy AE foams had higher strength values than the other foams as a result of formation of nickel-rich phases in the cell-wall microstructure.

Acknowledgements: This work was supported by Scientific Research Projects Coordination Unit of Istanbul University, Project number T-1431. It was partially based on a Ph.D. thesis pursued by Nuray Beköz.

REFERENCES

- Bakan, H.I., 2006. A novel water leaching and sintering process for manufacturing highly porous stainless steel, *Scripta Mater.*, vol.55, 203.
- Bekoz, N., Oktay, E., 2012. Effect of carbamide shape and content on processing and properties of steel foams, *J. Mater. Process. Tech.*, vol.212, 2109.
- Bram, M., Stiller, C., Buchkremer, H.P., Stöver, D., and Baur, H., 2000. High porosity titanium, stainless steel and superalloy parts, *Adv. Eng. Mater.*, vol.2, 196.
- Chawla, N., Deng, X., 2005. Microstructure and mechanical behavior of porous sintered steels, *Mat. Sci. Eng. A*, vol.390, 98.
- Gething, B.A., Heaney, D.F., Koss, D.A., Mueller, T.J., 2005. The effect of nickel on the mechanical behavior of molybdenum P/M steels, *Mat. Sci. Eng. A*, vol.390, 19.
- Gülsoy, H.Ö., German R.M., 2008. Sintered foams from precipitation hardened stainless steel powder, *Powder Metall.*, vol.51, 350.
- Höganäs Handbook for Sintered Components, 2004. Höganäs Iron and Steel Powder for Sintered Components, Höganäs AB, Sweden.
- Ivanuş. R., Branduşan, L., 2007. Effect of carbon content and post-sintering cooling rate on mechanical properties of Fe-Ni-Cu-Mo-C high density sintered steel, *Advanced Materials Research*, vol.23, 79.
- Jiang, B., Zhao, N.Q., Shi, C.S., Li, J.J., 2005. Processing of open cell aluminum foams with tailored porous morphology, *Scripta Mater.*, vol.53, 781.
- Markaki, A.E., Clyne, T.W., 2001. The effect of cell wall microstructure on the deformation and fracture of aluminium-based foams. *Acta Mater.*, vol.49, 1677.
- Michailidis, N., Stergioudi, F., Tsouknidas, A., Pavlidou, E., 2011. Compressive response of Al-foams produced via a powder sintering process based on a leachable space-holder material, *Mater. Sci. Eng. A*, vol.528, 1662.
- Zhang, L.P., Zhao, Y.Y., 2008. Fabrication of high melting-point porous metals by lost carbonate sintering process via decomposition route, *Proc IMechE Part B – J Eng Manuf.*, vol.222, 267.

MECHANICAL PROPERTIES OF SINTER-HARDENED Cu-Ni-Mo BASED STEELS

Nuray BEKÖZ

Istanbul University, Metallurgical and Materials Engineering Department, Istanbul, Turkey
a. Corresponding author (nbekoz@istanbul.edu.tr)

ABSTRACT: Sinter hardening is an attractive technique for the manufacturing of high hardness powder metallurgy parts which eliminates secondary heat treatment by increasing the post-sintering cooling rate, thus significantly reducing processing costs. In this study, the effect of sinter hardening on the mechanical properties of steel specimens produced using pre-alloyed Cu-Ni-Mo powders with addition 0.5% C was investigated. Powder mixtures were pressed uniaxially at 650 MPa in order to obtain cylindrical compacts, and then sintered at 1130 °C for 20 min under cracked ammonia atmosphere. After the sintering step, the specimens were rapidly cooled directly from sintering temperature. As-sintered specimens were sinter-hardened at two different cooling rates (2 °C/sec and 3 °C/sec). Mechanical properties (macrohardness, microhardness and compressive strength) of as-sintered and sinter-hardened specimens were determined and the results discussed in light of the microstructure of the specimens. The study showed that sinter hardening enhanced the mechanical properties of the specimens as a consequence of microstructure strengthening.

1. INTRODUCTION

Powder metallurgy (PM) is one of the most competitive methods to produce components with complicated shapes and large in quantity. Many sintered components need to be heat treated in order to improve their mechanical properties. Due to the fact that PM parts contain many pores that can accelerate the corrosion effect inside the treated parts in case of water quenching, oil quenching has to be applied during heat treatment. The assimilated oil during quenching process has to be removed from the treated parts for effective tempering, which costs much not only for the equipment and energy but also for the environment [Hatami *et al.*, 2010]. Sinter hardening is a cost effective manufacturing route for production of high performance sintered parts. Sinter hardening combines both sintering and hardening in one process to produce martensite as the major phase in the microstructure of the sintered

components. Sinter hardening has been more and more applied in the PM component manufactures worldwide, due to its pronounced advantages: good hardening effect, cost saving, better dimensional control and environmental friendly [Engström *et al.*, 2006; L'Esperance *et al.*, 1996].

The selection and use of pre-alloyed powders have many advantages over mechanical properties of sintered materials. Low alloyed steel powders commercially known as Distaloy AB and Distaloy AE are a partially pre-alloyed iron powder containing copper, nickel and molybdenum. With additions of graphite, high strength can be obtained after sintering. Copper forms a liquid phase during sintering and increases the strength. Molybdenum and nickel are commonly used in low alloy PM steel powders because their oxides are easily reduced during the annealing treatment of water atomized powders. Molybdenum is

very efficient for increasing the strength and hardenability of steel while nickel increases the hardenability, strength and toughness [Chagnon and Trudel, 1996]. The powders consist of very pure iron powder to which finely divided alloying elements are diffusion bonded. In this way the extremely high compressibility of the powder is maintained. The fine alloying additives are well utilized and the risk of segregation is minimized. Other advantages of this alloy include good green strength and dimensional stability. It can be sintered at relatively low temperature [Höganäs, 2004]. Pre-alloyed Distaloy powders are widely used in sinter hardening studies. The pre-alloying process is known to decrease the compressibility of the powders. However, the pre-alloyed powders are preferred in sinter hardening because of the fact that pre-alloyed powders are much more homogenous than admixed powders [German, 1994; Hatami *et al.*, 2010]. Sinter hardening behaviour of pre-alloyed steel powders has been investigated by a few researchers [Öge *et al.*, 2012; Hafizoğlu *et al.*, 2012; Bocchini *et al.*, 2004]. These studies showed that the martensitic structure can be achieved by sinter hardening with a considerable increase in mechanical properties. In this study, the effect of sinter hardening on the mechanical properties of steel specimens produced using pre-alloyed Cu-Ni-Mo powders with addition 0.5% C was investigated. Mechanical properties of as-sintered and sinter-hardened specimens were determined and the results discussed in light of the microstructure of the specimens.

2. EXPERIMENTAL PROCEDURES

Low alloy steel specimens were produced by powder metallurgy method using steel powders commercially known as Distaloy AB and Distaloy AE, which is a registered trademark of Höganäs Company, Sweden. Both the powders are

diffusion alloyed. The powder premixes consisted of 0.8 wt.% zinc stearate as lubricant at the pressing process, and 0.5 wt.% carbon was added as fine graphite (UF4) to increase the hardness of the steel. The powder mixtures were prepared by weighing samples in Sartorius balance with 0.01 g sensitivity and then mixed homogeneously in a laboratory scale mixer for 30 min. The chemical compositions of the powder mixes prepared are given in Table 1. The pre-alloyed powders had a rounded but irregular shape. The average particle size of the powders was measured by low angle laser light scattering method (Malvern-Mastersizer). The average particle sizes of Distaloy AB and Distaloy AE powders were found to be 109 μm and 90 μm , respectively. Typical morphologies of Distaloy AB and Distaloy AE steel powders revealed by scanning electron microscopy (SEM) are given in Figure 1.

Table 1: The chemical composition of the powder mixes (wt.%).

Base powders	Cu	Ni	Mo	C	Lub.	Fe
Distaloy AB	1.5	1.75	0.5	0.5	0.80	Bal.
Distaloy AE	1.5	4.0	0.5	0.5	0.80	Bal.

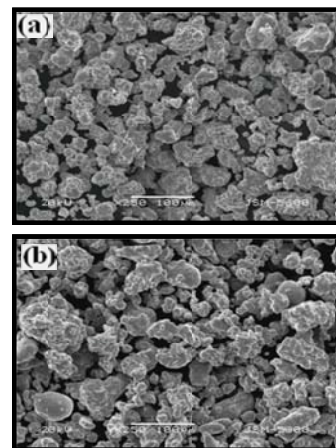


Figure 1: SEM images of the steel powders: (a) Distaloy AB and (b) Distaloy AE.

Powder mixtures compacted uniaxially at 650 MPa in a steel die using a hydraulic press into cylindrical specimens that have about 6.9 g cm^{-3} green densities with a diameter of 10 mm and height of about 10 mm. The specimens were sintered at 1130 °C for 20 minutes in an industrial continuous pusher furnace under 25% N₂-75% H₂ (cracked ammonia) atmosphere. After the sintering step, the specimens were cooled with a cooling rate of 0.5 °C/sec which correspond to normal sintering cycle, and with higher cooling rates of 2 °C/sec and 3 °C/sec for sinter hardening process. The carbon contents of as-sintered specimens were determined using a C/S analyzer instrument (Leco CS-255). Green and sintered densities of the specimens were determined from measurements of weight and dimensions of the specimens. Dimensional change was calculated from green to as-sintered and the mean of five measurements. Microstructural characterization and mechanical tests of as-sintered and sinter-hardened specimens were performed. The specimens were grinded and polished in cloths with alumina and pure water then etched in 3% Nital solution for optical examination. Olympus PME3 optical microscope was used for microstructural examination. Rockwell B (HRB) scale was used to measure the macrohardness of the specimens in Zwick hardness testing machine. The microhardness measurements were taken on Vickers scale with a Tukon microhardness machine. Three different locations were selected on the surface of the specimens and the average of those values was used as the hardness measure of samples. Compression test of the specimens were investigated at room temperature using the Zwick-Roell Z250 materials-testing machine fitted with a 250 kN load cell operating at the displacement control mode, with a strain rate of 0.05 mm sec^{-1} . Grease oil was used between the samples and the compression loads to minimize

the friction. Each test was repeated three times to ensure the repeatability of the results.

3. RESULTS AND DISCUSSION

A small quantity of carbon losses took place in the specimens after sintering due to reaction of the carbon with the oxygen in the powder and the surrounding atmosphere. The carbon contents of as-sintered Distaloy AB and Distaloy AE specimens were determined to be 0.46 and 0.45 wt.%, respectively. Table 2 shows the influence of increased cooling rate on dimensional change. Shrinkage decreased slightly when raising the cooling rate from 2 °C/sec to 3 °C/sec. In as-sintered and sinter-hardened specimens, shrinkage of the Distaloy AE specimens increased due to the high nickel content.

Table 2: Influence of cooling rate on dimensional change.

Cooling rates	Dimensional change, %	
	Distaloy AB	Distaloy AE
Sintering (0.5 °C/sec)	0.78	0.84
Sinter hardening (2 °C/sec)	0.76	0.81
Sinter hardening (3 °C/sec)	0.73	0.78

The microstructures of as-sintered, sinter-hardened with cooling rates of 2 °C/sec and 3 °C/sec for Distaloy AB and Distaloy AE specimens at different magnifications are shown in Figure 2 and Figure 3, respectively. The pores formed in the specimens due to the melting of Cu particles at the sintering temperature 1130 °C. These pores are much smaller and more uniformly distributed in Distaloy AE specimens which higher Ni content due to solid state sintering of Ni during sintering. The as-sintered specimens consisted of ferrite, pearlite, austenite and a small amount of bainite phases. The microstructural images of the specimens showed that copper was

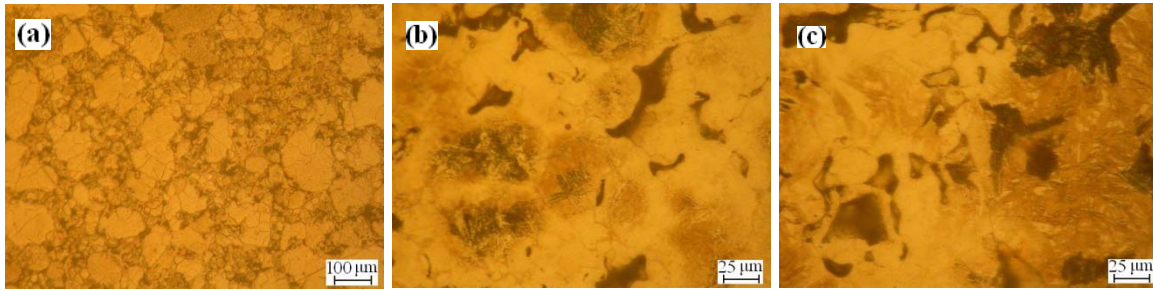


Figure 2: Microstructure of Distaloy AB specimens: (a) as-sintered, sinter-hardened with cooling rates of (b) 2 °C/sec and (c) 3 °C/sec.

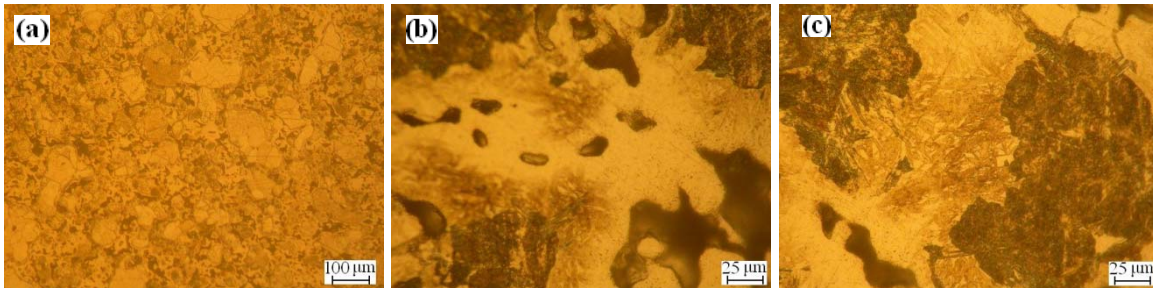


Figure 3: Microstructure of Distaloy AE specimens: (a) as-sintered, sinter-hardened with cooling rates of (b) 2 °C/sec and (c) 3 °C/sec.

accumulated in the grain boundaries as a result of sintering. Martensite phase is not observed in the microstructure of the as-sintered specimens due to furnace cooling step of sintering cycle. The microstructure of sinter-hardened specimens consisted of pearlite, bainite and martensite phases as a result of rapid cooling. In the micrograph, bright regions are martensite, darker regions are bainite plus pearlite, brown regions are austenite and black regions are micropores between the steel particles. The alloys that contained Ni had nickel-rich areas in the grain boundaries due to the heterogeneous distribution of nickel, especially in Distaloy AE specimens. As it can be seen in Figure 3, the reason for is the higher Ni content which resulted in nickel-rich areas in the microstructure. Chawla et al. [Chawla *et al.*, 2001]; showed that the microstructure of Distaloy AB consisted of pearlite, martensite and nickel-rich phases. Chawla and Deng [Chawla and Deng, 2005] reported that the microstructure of Fe-0.85Mo-2Ni-0.6C were porous and consisted of pearlite, bainite, nickel-rich

areas. The present results demonstrated for the specimens with the cooling rate of 3 °C/sec, a large amount of martensite formation in the structure was observed as a result of rapid cooling. The macrohardness and the compressive yield strength values of as-sintered and sinter-hardened specimens are given in Table 3. Compressive yield strength and macrohardness values of the sinter-hardened specimens increased with increase in cooling rate after sintering. As a result of high cooling rate, the amount of pearlite and bainite phases increased and the martensite phase formed in the structure. This is the reason for the increase in the mechanical properties of sinter-hardened specimens. Increase in the compressive yield stress values of the specimens with the cooling rates of 2 °C/sec and 3 °C/sec were about 21% and 32% for Distaloy AB and about 25% and 34% for Distaloy AE, respectively. The specimens with the cooling rates of 2 °C/sec and 3 °C/sec, about 24% and 44% for Distaloy AB and about 26% and 45% for Distaloy AE, respectively, increase in macrohardness value were achieved with sinter hardening. The mean

microhardness values of as-sintered and

properties of Fe-0.3Ni-1.5Cu-0.5Mo, and

Table 3: The macrohardness and compressive yield strength of as-sintered and sinter-hardened specimens.

Mechanical properties of the specimens	Distaloy AB		Distaloy AE	
	Macrohardness (HRB)	Compressive yield strength (MPa)	Macrohardness (HRB)	Compressive yield strength (MPa)
Sintering (0.5 °C/sec)	89 ±6	385 ±25	96 ±4	397 ±35

sinter-hardened specimens are given in Table 4.

Table 4: The microhardness of as-sintered and sinter-hardened specimens.

Microhardness of the specimens	Distaloy AB	Distaloy AE
	Microhardness (HV0.1)	Microhardness (HV0.1)
Sintering (0.5 °C/sec)	233 ±45	267 ±37
Sinter hardening (2 °C/sec)	297 ±38	336 ±42
Sinter hardening (3 °C/sec)	356 ±47	387 ±36

Increase in the microhardness values of the specimens with the cooling rates of 2 °C/sec and 3 °C/sec were about 27% and 53% for Distaloy AB and about 26% and 45% for Distaloy AE, respectively. Sinter hardening led to increase in microhardness due to formation of martensite and bainite. In as-sintered and sinter-hardened specimens, mechanical properties of the Distaloy AE specimens which contained high Ni are higher than Distaloy AB specimens. Gething et al. [Gething *et al.*, 2005] studied the effects of Ni addition on the mechanical properties of Fe-0.85Mo-0.4C, and reported that Ni as alloying element increase hardenability in the steels, increase in cooling rate after sintering led to the hard structure in the microstructure. Ivanuş and Branduşan [Ivanuş and Branduşan, 2007] studied the effects of cooling rate on the mechanical

found the formation of bainite and martensite by raising cooling rate from 1 °C/sec to 3.5 °C/sec increased strength and apparent hardness.

4. CONCLUSIONS

- The sinter hardening process enhanced the mechanical properties of the specimens, as a consequence of microstructure strengthening. The amount of pearlite and bainite phases increased and the martensite phase formed in the structure, as a result of high cooling rate.
- The use of higher cooling rates after sintering led to higher the macrohardness and the compressive yield strength values which are due to the formation of bainite and martensite in the microstructure.
- The maximum compression strength was found at Distaloy AE alloy for all cooling rates. The reason for is the higher Ni content which resulted in nickel-rich areas in the microstructure.

Acknowledgements: The author is grateful to Sintek Powder Metallurgy Industry and Trade Joint-Stock Company, and especially to Hazar Yaranuş, for their support.

REFERENCES

- Bocchini G.F., Rivolta G., Silva G., Poggio E., Pinasco M.R., Ienco M.G., 2004. Microstructural and mechanical characterization of some sinter hardening alloys and comparisons with heat treated PM steels, Powder Metall., vol.47, 343.

- Chagnon, F., Trudel Y., 1996. Designing low alloy steel powders for sinterhardening applications, The 1996 World Congress on Powder Metallurgy&Particulate Materials, June 16-21, Washington.
- Chawla, N., Murphy, T.F., Narasimhan, K.S., Kopman, M., Chawla, K.K., 2001. Axial fatigue behavior of binder-treated versus diffusion alloyed powder metallurgy steels, *Mat. Sci. Eng. A*, vol.308, 180.
- Chawla, N., Deng, X., 2005, Microstructure and mechanical behavior of porous sintered steels, *Mat. Sci. Eng. A*, vol.390, 98.
- Engström, U., Milligan, D., Klekovkin, A., 2006. Mechanical properties of high performance chromium materials, *Advances in Powder Metallurgy&Particulate Materials*, vol.7, 21.
- German, R.M., 1994. *Powder Metallurgy Science*. MFIF Princeton New Jersey: The Pennsylvania State University.
- Gething, B.A., Heaney, D.F., Koss, D.A., Mueller, T.J., 2005. The effect of nickel on the mechanical behavior of molybdenum P/M steels, *Mat. Sci. Eng. A*, vol.390, 19.
- Hafizoğlu, H., Durlu N., Ataş., A, Özdural, H., 2012. Mechanical properties of sinter hardened Astaloy CrA powder alloys, 16th Int. Metallurgy & Materials Congress, 13-15 September 2012, TÜYAP Fair, Convention & Congress Center, Istanbul-Turkey, 112.
- Hatami S., Malakizadi A., Nyborg L., Wallin D., 2010. Critical aspect of sinter-hardening of prealloyed Cr-Mo steel, *J. Mater. Process. Tech.*, vol.210, 1180.
- Höganäs Handbook for Sintered Components, 2004. Höganäs Iron and Steel Powder for Sintered Components, Höganäs AB, Sweden.
- Ivanuş. R., Branduşan, L., 2007. Effect of carbon content and post-sintering cooling rate on mechanical properties of Fe-Ni-Cu-Mo-C high density sintered steel, *Advanced Materials Research*, vol.23, 79.
- L'Esperance, G., Duchesne, E., Rege, A., 1996. Effect of materials and process parameters on the microstructure and properties of sinter hardening alloys, *Advances in Powder Metallurgy and Particulate Materials*. MPIF.
- Öge, A.M., Durlu N., Bozacı C., Johansson, P., 2012. Mechanical properties of sinter hardened Astaloy Mo and Distaloy DH powder alloys, 16th Int. Metallurgy & Materials Congress, 13-15 September 2012, TÜYAP Fair, Convention & Congress Center, Istanbul-Turkey, 73

ABRASIVE WEAR BEHAVIOR OF POWDER METALLURGY CUSN10-GRAPHITE METAL MATRIX COMPOSITES PRODUCED BY POWDER METALLURGY

A. Canakci^{a*}, H. Cuvalci^a, T. Varol^a, F. Erdemir^a, S. Ozkaya^a, E.D. Yalcin^b

^aDepartment of Metallurgical and Materials Engineering, Engineering Faculty,

^bAbdullahKanca Vocational School of Higher Education

Karadeniz Technical University, Trabzon, Turkey.

a. Corresponding Author (aykut@ktu.edu.tr)

ABSTRACT: In this study, CuSn10 metal matrix composites (MMCs) reinforced with 0, 1, 3 and 5 vol.% graphite particulates, respectively, were produced by powder metallurgy. SiC abrasive papers of grit size 400, having an average particle size of 38 μm , were used. The applied loads were selected as 60N. The tests were carried out under sliding speeds of 0.8 m/s. In all tests, the sliding distances were chosen in the range of 50-500m. The effects of sliding distance and graphite particle content on the abrasive wear properties of the composites have been evaluated. The microstructure evolution of composites and the main wear mechanisms were identified using a scanning electron microscope. A decrease in hardness and density of the sintered CuSn10-graphite composites was observed with increase in graphite content. According to results, the abrasive wear resistance of metal matrix composites could be increased by incorporation of graphite particles.

1. INTRODUCTION

Metal-matrix composites (MMCs) have received substantial attention from the aerospace and automotive industries because of their improved strength, high elastic modulus and increased wear resistance over conventional monolithic base alloys during the last decade. Improvements in mechanical properties and wear resistance of MMCs have already been demonstrated for a variety of reinforcements [Kök, 2006; Canakci, 2011; Abachi et al. 2006; Srivastava and Das; Veeresh Kumar et al. 2012; Cui et al. 2012]. These composites are usually supplied through the conventional engineering processes of powder metallurgy, leading to complicated microstructures that comprise copper, graphite, binder carbon, and sintering-induced micropores, even if they look like macroscopically uniform [Futami et al. 2008]. Graphite as solid lubricants is widely used because of low cost and

excellent lubrication performance. The lubrication roles of graphite were extensively investigated and entirely understood [Lu et al. 1999; Zhan et al. 2004; Chen et al. 2008]. However, solid lubricants having similar structures possess different lubrication roles and their lubrication degrees were not identical in a way. The principal objective of this investigation was to produce CuSn10-graphite composites by powder metallurgy, evaluate the abrasive wear behavior of CuSn10 alloy and its composite under two-body abrasive wear testing condition and examine the effect of graphite content, applied load, sliding distance and abrasive grid size on the abrasive wear behavior of the composites as compared to that of the CuSn10 matrix alloy.

2. EXPERIMENTAL PROCEDURE

In this study, CuSn10 alloy powders ($d_{50}=30\mu\text{m}$) and graphite particles ($d_{50}=28\mu\text{m}$) were used as the matrix

material and reinforcement particles, respectively. The powder mixtures were sealed in tungsten carbide vial together with tungsten carbide balls in a ratio of 10:1 and milled for 0.5h with rotation speed of 200rpm in a Fritsch “Pulverisette 7, Premium line” planetary ball mill. The samples for abrasive wear tests produced from CuSn10-graphite particles mixtures containing various amounts of graphite particles as well as the unreinforced CuSn10alloy powders by cold pressing in a steel die having the internal dimensions of 10x10x40 mm at 700 Mpa. The compacted green bulks were sintered at 800 °C for 2h under protective pure argon gas in a tube furnace.

A pin-on-disc with emery paper apparatus was used to investigate the wear characteristics of composites and CuSn10 alloy, as shown in Fig. 1. SiC papers with 38µm size, fixed on a rotating 155 mm diameter and 10 mm thick steel disc with the help of four rectangular clamps, were employed as abrasive mediums. The tests were carried out in air at room temperature at a load of 60N. The ends of the specimens were sequentially polished with abrasive paper of grades 600, 800 and 1000. Wear tests were conducted in dry conditions in order to avoid effect of lubricating medium. A fixed track diameter of 100mm was used in all the tests.

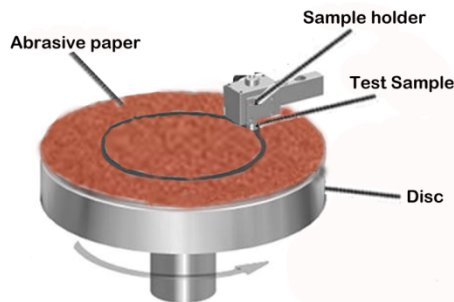


Fig. 1: The schematic view of the abrasion wear test apparatus.

3. RESULTS AND DISCUSSIONS

3.1. Microstructural Observation

SEM image of CuSn10-graphite composites reinforced with 3 wt% graphite particles is shown in Fig. 2. In images, light grey areas indicate CuSn10 alloy matrix and dark areas indicate the graphite particles. Particles which dispersed in CuSn10 matrix semi-homogeneously, generally stuck between points of contact of CuSn10 matrix powders. If reinforcement particles in the composites do not disperse uniformly, this affects mechanical and electrical properties of composites negatively.

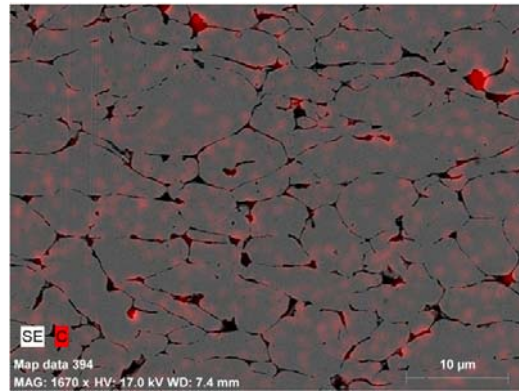


Fig. 2: Scanning electron micrographs of the CuSn10-3 vol. % graphite composite.

The values of relative density, porosity and hardness of unreinforced CuSn10 alloy and composites are presented in Table 1. It is seen that the porosity content of the unreinforced compact are considerably lower than the composites. The relative density of unreinforced CuSn10 alloy was determined as 98.5%. The results showed that the density of composites decreased from 97.5 to 92 % with increasing the graphite particle volume fraction from 1% to 5%. This is due to the density of graphite particles being much lower than that of CuSn10 powders. In spite of the good interfacial bonding between CuSn10 and graphite, graphite particles between CuSn10 matrix

powders prevents the contact of particle and particle due to agglomeration of

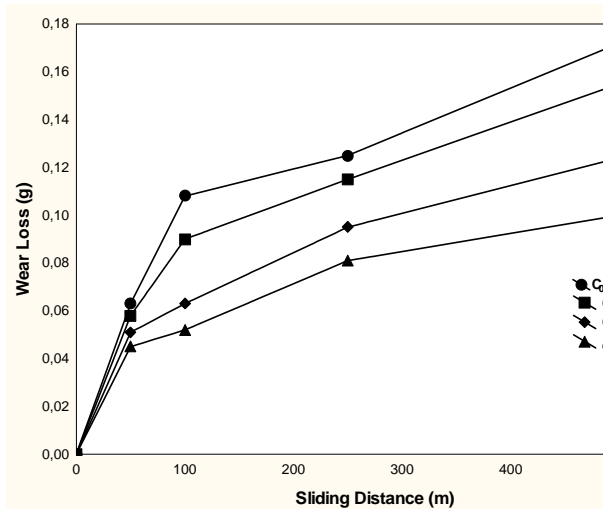
Table 1. Physical characteristics of the CuSn10 alloy and CuSn10-graphite composites.

Code	Composition (vol.%)	Density (g/cm ³)	Porosity (%)	Hardness (BSD)
C ₀	CuSn10 Alloy	8.57	1.5	112
C ₁	CuSn10-1% graphite	8.41	2.5	108
C ₂	CuSn10-3% graphite	8.1	5	105
C ₃	CuSn10-5% graphite	7.6	8	100

graphite particles during the consolidation process. As can be seen from the Table 1, composite hardness decreased with increasing the graphite content. This is a result of the decrease in density.

Fig. 3 show the effect of sliding distance on the average wear loss of the composites with SiC abrasive. It was observed that the wear loss increases with increasing sliding distance (Fig. 3) for all the materials studied. In the case of higher graphite content composites (5 vol.%),

the graphite smears out at contact surface. This reduces the metal to metal contact. Due to the inherent self lubricity of smeared out graphite film, the composites with higher graphite exhibited lower wear rates. Though 1vol% graphite composites are having availability of graphitic film at the contact surface is scarce, which results in reduced lubrication effects and thereby results in higher wear rate. However, with 5vol% graphite composite, the amount of graphite addition is sufficient enough to produce the self lubricative effect.



sliding direction on the worn surfaces are deep in the graphite reinforced composites (Fig. 4). The worn out surface of the composites suggests that the wear mechanism is by the plowing of the surface by SiC abrading particles. SEM images exhibited that wear progressed by grooving action of the abrasive particles.

The SiC abrasive particles with sharp edges cause micro-ploughing and grooving in the surface of CuSn10 alloy. Material in the form of chips is removed from the grooves.

Fig. 3: Variation of the weight loss of CuSn10-graphite composites containing different graphite content at the sliding distance of 500m with the given abrasive grit size of 400 and a load of 60N.

Fig. 4 shows the wear surfaces of the CuSn10-graphite composites. In image, an arrow mark is shown to indicate the sliding direction. The continuous longitudinal grooves parallel to the

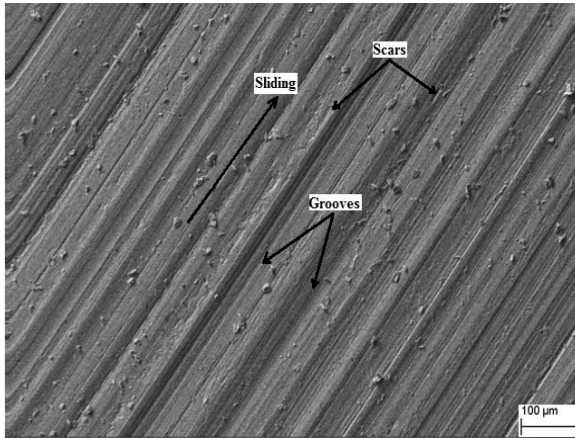


Fig. 4: SEM images of worn surfaces of CuSn10-graphite composites

Fig. 5 shows typical SEM micrographs of wear debris morphology of the CuSn10-graphite composites at 60N and 500m. The wear debris is in the form of fine particles and ribbon-type metallic chips, as shown in Fig.4. The formation of fine debris may be due to continuous rubbing action of samples on the wear track while ribbon-type debris are the characteristics of cutting and ploughing action of hard abrasive particles [4].

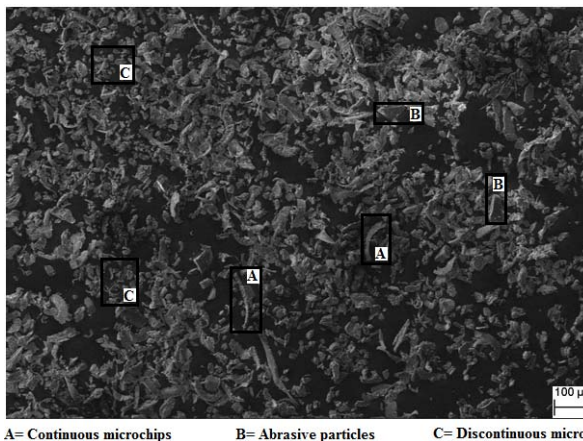


Fig. 5: SEM images of the wear debris of CuSn10-graphite composites

4. CONCLUSIONS

1- A decrease in hardness and density of powder metallurgy CuSn10-graphite composites were observed with increase in graphite content. The increase in amount of graphite leads to a decrease in densification of materials during

consolidation process due to agglomeration of graphite particles during the consolidation process.

2-The wear resistance of powder metallurgy CuSn10-graphite composites was found to be considerably higher than that of the unreinforced CuSn10 alloy and increased with increasing particle content.

3- Plastic deformation (micro cutting and microploughing) was identified as the main wear mechanism operating on the worn surfaces of the composites studied. The wear loss of the matrix alloy and the composites increased with increasing the sliding distance.

Acknowledgments

The authors are grateful to the Karadeniz Technical University Research Fund for financially supporting this research (No: 2010.112.0105).

REFERENCES

1. Kök, M., 2006. Abrasive wear of Al₂O₃ particle reinforced 2024 aluminum alloy composites fabricated by vortex method. *Composites: Part A*, 37, 457.
2. Canakci, A., 2011. Microstructure and abrasive wear behavior of B₄C particle reinforced 2014 Al matrix composites, *Journal of Materials Science*, 46, 2805.
3. Abachi, P., Masoudi, A. and Purazrang, 2006. K. Dry sliding wear behaviour of SiCp/QE22 magnesium alloy matrix composites, *Materials Science and Engineering A*, 435-436, 653.
4. Srivastava, A.K. and Das, K. 2010. The abrasive wear resistance of TiC and (Ti,W)C-reinforced Fe-17Mn austenitic steel matrix composites, *Tribology International*, 43, 944.
5. Veeresh Kumar, G.B., Rao C.S.P., and Selvaraj, N. 2012. Studies on mechanical and dry sliding wear of Al6061-SiC composites, *Composites: Part B*, 43, 1185.
6. Cui, G., Bi, Q., Zhu, S. et al., 2012. Tribological properties of bronze-graphite composites under sea water condition, *Tribology International*, 53, 76.
7. Futami, T., Ohira, M., Muto, H. et al., 2008. "Indentation contact behavior of copper-graphite particulate composites: Correlation

- between the contact parameters and the electrical resistivity,” *Carbon*,46,671.
8. Lu, D., GuM., and Shi,Z., 1999.“Materials transfer and formation of mechanically mixed layer in dry sliding wear of metal matrix composites against steel,” *Tribology Letters.*, 6, 57-
 9. ZhanY.and Zhang,G.“Friction and wear behavior of copper matrix composites reinforced with SiC and graphite particles,” *Tribology Letters*,17, 91(2004).
 10. Chen,B., Bi, Q., Yang,J., et al., 2008. “Tribological properties of solid lubricants (graphite, h-BN) for Cu-based P/M friction composites,”*Tribology International*, 41, 1145.

CHARACTERIZATION OF POROUS HYDROXYAPATITE PRODUCED ON Ti6Al4V BY PLASMA ELECTROLYTIC OXIDATION

Salih Durdu^{1,a}, Işıl Kutbay¹, Metin Usta¹

1. The Department of Materials Science and Engineering, Gebze Institute of Technology, 41400, Gebze/TURKEY

a. Corresponding author (sdurdu@gyte.edu.tr, durdusalih@gmail.com)

ABSTRACT: In this study, hydroxyapatite (HAp) and calcium apatite based ceramic composite coatings were produced on Ti6Al4V alloy by plasma electrolytic oxidation (PEO) in the electrolyte consisting of calcium acetate (CA) and β -calcium glycerophosphate (β -Ca GP) at 0.140 A/cm² current densities for 1, 2, 3, 4, 5, 20, 40 and 60 minutes. The phase structure, surface morphology of the coatings and functional groups of the molecules were characterized by X-ray diffraction (XRD), scanning electron microscope (SEM) and energy dispersive spectroscopy (EDX-mapping), respectively. The XRD results indicated that anatase-TiO₂, rutile-TiO₂, Ca₃(PO₄)₂ (TCP), CaTiO₃ (perovskite) and Ca₁₀(PO₄)₆(OH)₂ (HAp) phases were formed on the surface of the coated titanium alloy. The PEO coatings have very porous surface structure due to the existence of micro discharge channels during process. According to the EDS mapping results, uniform Ca and P elements were observed on the surface of PEO coatings.

1. INTRODUCTION

Titanium and its alloys are widely used in dental and orthopedic fields owing to their excellent properties, good corrosion resistance, including high strength-to-weight ratio, low toxicity, and favorable mechanical properties [Kung et al., 2010; Stojadinovic et al., 2013]. However, these materials cannot bond efficiently with living bone and present poor ability to facilitate new tissue formation on their surfaces at the early stage of implantation due to the absence of bioactivity on their surfaces, which would delay the healing time of the operation and even result in the failure of implantation [Hanawa, 2010; Zhang et al., 2013]. Hydroxyapatite which is similar to dental and bone mineral has good bioactivity and biocompatibility is an important mineral to connect chemically with bone tissue [Durdu et al., 2013]. Bioactive ceramic materials such as hydroxyapatite (HAp) and bioactive glass ceramics have widely used in biomedical applications [Katti,

2004; Wei et al., 2007]. Unfortunately, these biomaterials are not suitable for load-bearing conditions owing to their poor mechanical properties [Liu et al., 2004].

The plasma electrolytic oxidation (PEO), is also known micro arc oxidation (MAO), is a relatively convenient and effective technique to deposit ceramic coatings on the surfaces of Ti, Al, Mg and their alloys [Yerokhin et al., 1999]. Plasma electrolytic oxidation of titanium and its alloys represents a versatile surface modification technology with the capability of producing porous biofunctional coatings that can find applications in the field of biomedical engineering [Necula et al., 2011]. The PEO coatings are both porous and firmly adhere to the substrate, wear-resistant oxide coatings, with fine-scale interconnected porosity which is beneficial for the biological performance while Ti and Ti-6Al-4V are implanted in

a human body (Curran and Clyne, 2006; Liu et al., 2010).

The aim of this study was to produce hydroxyapatite and calcium apatite-based coatings that are bioactive and biocompatible to be used as a biomaterial in biomedical applications by PEO method.

2. EXPERIMENTAL DETAILS

The plasma electrolytic oxide coatings were produced on the Ti6Al4V specimens using plasma electrolytic oxidation (PEO). The PEO equipment (100 kW) was composed of an AC power supply, a stainless steel container as well as cooling and stirring systems. The titanium substrate was used as the anode, while the stainless steel container as the cathode. The PEO was carried out at constant current density (0.140 A/cm^2) for 1, 2, 3, 4, 5, 20, 40 and 60 minutes in the electrolyte consists of calcium acetate ($(\text{CH}_3\text{COO})_2\text{Ca}$) (Alfa Aesar), β -calcium glycerophosphate ($\beta\text{-C}_3\text{H}_5(\text{OH})_2\text{PO}_4\text{Ca}$) (Alfa Aesar) and pure water mixture.

The phases on the PEO coating surface were detected by X-ray diffraction (XRD; Bruker D8 Advance) using $\text{Cu-K}\alpha$ radiation ($\lambda = 1.54 \text{ \AA}$) between 20° and 80° angles with a step size $0.02^\circ/\text{min}$. The surface morphologies of the coatings were investigated by scanning electron microscope (SEM; Philips XL30 SFEG). The elemental mappings of the coatings were analyzed by energy dispersive spectroscopy (EDX)

3. RESULTS AND DISCUSSION

3.1. Phase Structure of the Coatings

Figure 1 and 2 illustrate the XRD patterns of the PEO coatings produced at low and high treatment times, respectively. According to the XRD patterns; titanium, anatase, rutile, TiP_2 , TCP, perovskite and

HAp phases were detected on the PEO coated surfaces by XRD analysis.

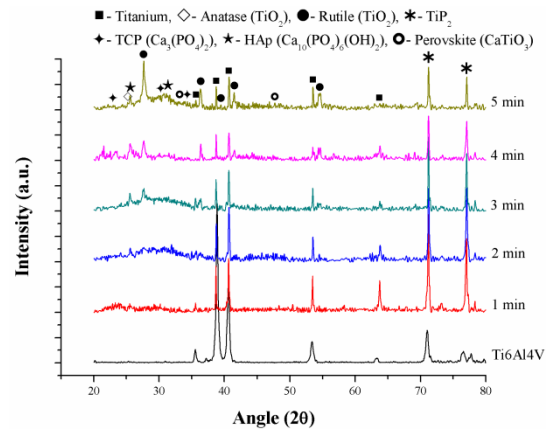


Figure 1: XRD patterns of the PEO coatings produced at low treatment times and uncoated Ti6Al4V alloy

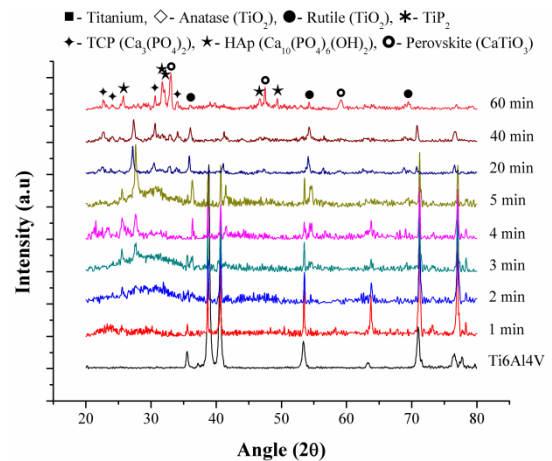


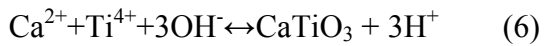
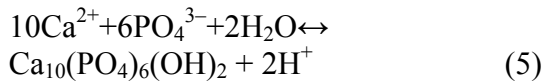
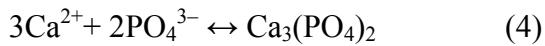
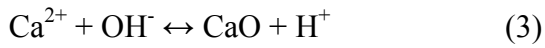
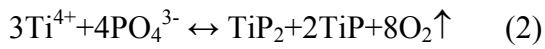
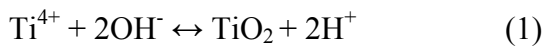
Figure 2: XRD patterns of the PEO coatings produced at all treatment times and uncoated Ti6Al4V alloy

The amount of TiO_2 , calcium apatite and hydroxyapatite based phases is very low at the coating produced at low treatment times. Especially, calcium apatite and hydroxyapatite based phases begin to form on the surface after 5 min. Perovskite and hydroxyapatite are major phases for the coating produced at 60 min.

For the coatings produced at low duration times (from 1 to 5 min), amorphous TiO_2 ,

calcium apatite and hydroxyapatite based phases was observed on the PEO surfaces. The PEO coatings produced at low duration times have amorphous phases because the time is not enough to crystallize of phases. Amorphous phases transformed into crystalline phases under high temperature and high pressure in micro discharge channels as increased treatment time. As a result, the amount of these crystalline phases increased with increasing time. It was stated in the literature (Han et al., 2008) that the outer layer of the PEO coating consists of HAp and TCP although the inner layer of the PEO coating is composed of TiO₂ and perovskite phases.

The formation mechanisms of the phases occurred on the PEO coatings are below (Durdu et al., 2013; Han et al., 2008):



3.2. Surface Morphology of the Coatings

Figure 3 shows the surface morphologies of the PEO coatings. The surface of the PEO coatings is very porous and rough due to the existence of micro discharge channels as seen in Figure 3. There are many randomly distributed pores with different sizes and shapes appearing as dark circular spots on the PEO coating surfaces. The pore serves as a micro discharge channel during PEO process. The pores which are surrounded by

molten oxide are rapidly solidified by electrolyte. The porous feature strongly depends on discharging nature involved in the PEO mechanism (Polat et al., 2010).

The surface morphologies of the PEO coatings depend on the various parameters such as electrolyte composition, applied voltage and treatment times. The micro sparks grow up gradually as the number of micro sparks decrease with increasing treatment time. As a result, the number of the pores decreases while the size of the pores increases with increasing treatment time.

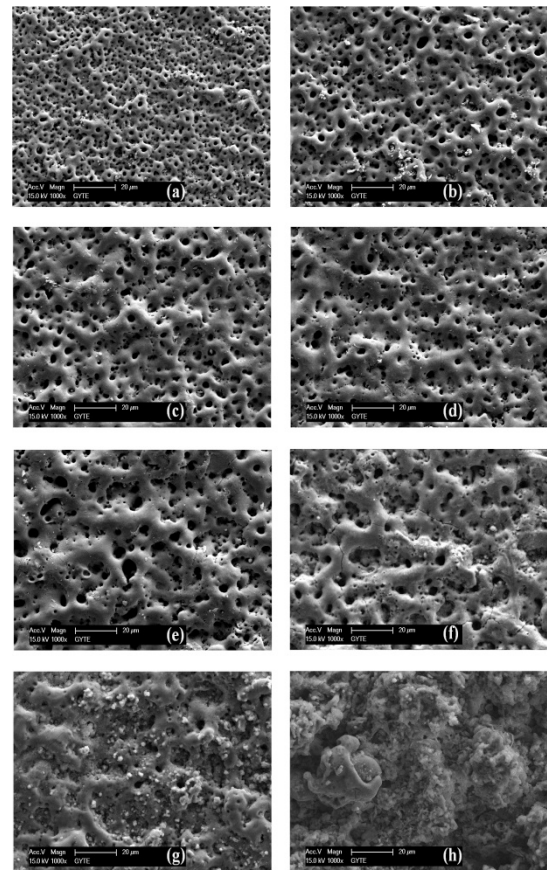


Figure 3: The surface SEM morphologies of the PEO coatings: (a) 1 min, (b) 2 min, (c) 3 min, (d) 4 min, (e) 5 min, (f) 20 min, (g) 40 min and (h) 60 min

3.3. Elemental Distribution of the Coatings

Figs. 4a, 4b, 4c, 4d, 4e, 4f, 4g and 4h show the elemental mapping results of the PEO coatings produced at 1, 2, 3, 4, 5, 20, 40 and 60 minutes, respectively. Ti, O, Ca, P and Al are observed on the coatings. The concentrations of Ca and P increase with increasing duration time as seen in Figs. 4a-h.

The Ca and P elements in the electrolyte consisting of CA and β -Ca-GP ionize due to the existence of electrical field during PEO process and they react with each other in micro discharge channels. The Ca and P, which are required to form hydroxyapatite (HAp), enter into the coating structure with increasing time and react with each other and oxygen.

The Ca and P exist as amorphous structure on the outer coating surface owing to the rapid cooling rate of melted compounds during PEO process (Durdu et al., 2013; Han et al., 2002). The Ca and P are uniformly distributed in the coating surfaces as seen in Figs. 4a-h. The Ca and P cause the formation of HAp and calcium apatite-based phases as major phases with increasing duration time because they exist as dominant elements in the coating. As a result of these mapping images, it can be concluded that HAp and calcium apatite-based phases are homogeneously distributed on the PEO coating surfaces.

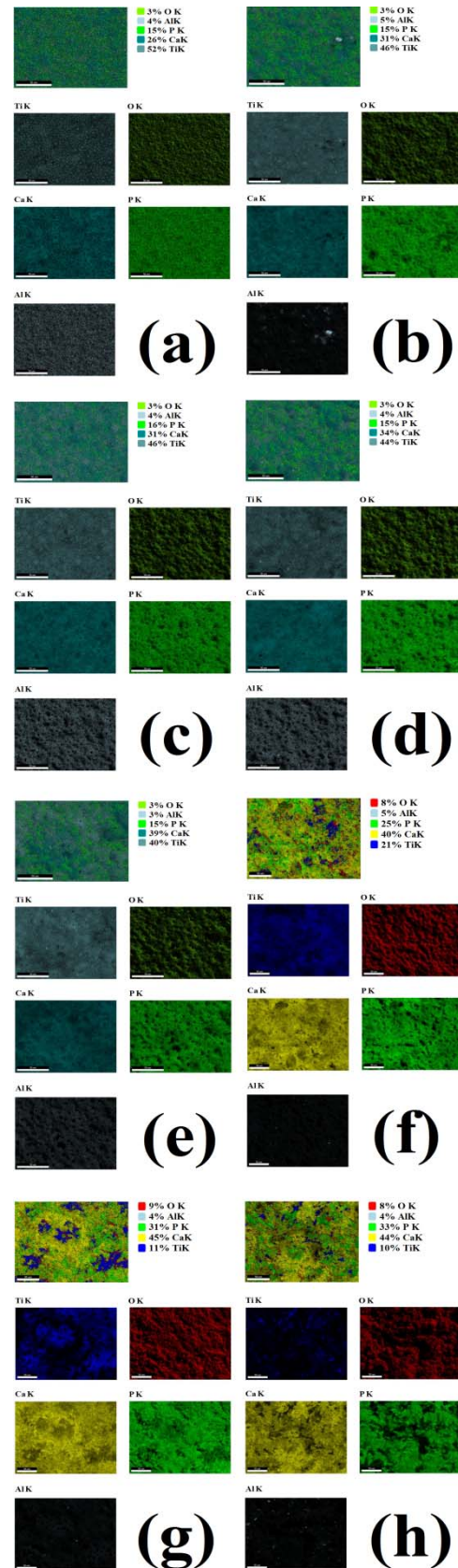


Figure 4: The elemental mapping results of the PEO coatings produced at different duration times

4. CONCLUSIONS

Hydroxyapatite (HAp) and calcium apatite-based phases such as TCP and perovskite - CaTiO_3 were coated on Ti6Al4V alloy at different duration times in the electrolyte consisting of CA and β -Ca-GP by PEO method. The following results were obtained as below:

1. The PEO coatings produced at all treatment times contained TiO_2 , TiP_2 , TCP ($\text{Ca}_3(\text{PO}_4)_2$), perovskite CaTiO_3 and HAp ($\text{Ca}_{10}(\text{PO}_4)_6(\text{OH})_2$) phases. Especially, the amount and the intensity of HAp and calcium apatite-based phases increased with increasing duration time. HAp and calcium apatite-based phases were observed as major phases at the coating produced at 60 min.
2. The coatings produced by PEO method have very porous and rough surface. Especially, this porous surface beneficially helps to cell attachment and bone growth in biomedical applications.
3. According to the EDX mapping results, Ca and P elements were uniformly distributed on the PEO surface and the amount of them increased with increasing duration time

Acknowledgments

The authors would like to thank Mr. A. Nazım for running Scanning electron microscopy (SEM) and Mr. S. Levent Aktug for running X-ray diffractometer (XRD) at Gebze Institute of Technology.

REFERENCES

- Curran JA, Clyne TW (2006). Porosity in plasma electrolytic oxide coatings. *Acta Materialia* 54(7):1985-1993.
- Durdu S, Deniz OF, Kutbay I, Usta M (2013). Characterization and formation of hydroxyapatite on Ti6Al4V coated by plasma electrolytic oxidation. *Journal of Alloys and Compounds* 551(422-429).
- Han Y, Hong SH, Xu KW (2002). Porous nanocrystalline titania films by plasma electrolytic oxidation. *Surface & Coatings Technology* 154(2-3):314-318.
- Han Y, Sun J, Huang X (2008). Formation mechanism of HA-based coatings by micro-arc oxidation. *Electrochemistry Communications* 10(4):510-513.
- Hanawa T (2010). Biofunctionalization of titanium for dental implant. *Japanese Dental Science Review* 46(2):93-101.
- Katti KS (2004). Biomaterials in total joint replacement. *Colloids and Surfaces B: Biointerfaces* 39(3):133-142.
- Kung K-C, Lee T-M, Lui T-S (2010). Bioactivity and corrosion properties of novel coatings containing strontium by micro-arc oxidation. *Journal of Alloys and Compounds* 508(2):384-390.
- Liu F, Xu J, Wang F, Zhao L, Shimizu T (2010). Biomimetic deposition of apatite coatings on micro-arc oxidation treated biomedical NiTi alloy. *Surface and Coatings Technology* 204(20):3294-3299.
- Liu X, Chu PK, Ding C (2004). Surface modification of titanium, titanium alloys, and related materials for biomedical applications. *Materials Science and Engineering: R: Reports* 47(3-4):49-121.
- Necula BS, Apachitei I, Tichelaar FD, Fratila-Apachitei LE, Duszczuk J (2011). An electron microscopical study on the growth of TiO_2 -Ag antibacterial coatings on Ti6Al7Nb biomedical alloy. *Acta Biomaterialia* 7(6):2751-2757.
- Polat A, Makaraci M, Usta M (2010). Influence of sodium silicate concentration on structural and tribological properties of microarc oxidation coatings on 2017A aluminum alloy substrate. *Journal of Alloys and Compounds* 504(2):519-526.
- Stojadinovic S, Vasilic R, Petkovic M, Kasalica B, Belca I, Zekic A *et al.* (2013). Characterization of the plasma electrolytic oxidation of titanium in sodium metasilicate. *Applied Surface Science* 265(226-233).
- Wei D, Zhou Y, Jia D, Wang Y (2007). Characteristic and in vitro bioactivity of a microarc-oxidized TiO_2 -based coating after chemical treatment. *Acta Biomaterialia* 3(5):817-827.
- Yerokhin AL, Nie X, Leyland A, Matthews A, Doney SJ (1999). Plasma electrolysis for surface engineering. *Surface & Coatings Technology* 122(2-3):73-93.
- Zhang P, Zhang Z, Li W, Zhu M (2013). Effect of Ti-OH groups on microstructure and bioactivity of TiO_2 coating prepared by micro-arc oxidation. *Applied Surface Science* 268(0):381-386.

AN EXPERIMENTAL STUDY ON HOT FORMABILITY OF CLOSED CELL METALLIC FOAMS

Emrah ERSOY^{1,a}, Yusuf ÖZÇATALBAŞ² ve Ersin BAHÇECİ³

1. Gazi University, Graduate School of Natural and Applied Science, Ankara, Türkiye
 2. Gazi University, Technology Faculty, Metallurgical&Materials Engineering Dept., Ankara, Türkiye
 3. Kastamonu University, Cide VHS, Kastamonu, Türkiye
- a. Corresponding author (emrahersoy06@gmail.com)

ABSTRACT: The purpose of this study is to investigate formability of Al based closed cell metallic foams at high temperature. Rectangular section foam specimens were produced from AlMg1Si0.6TiH₂0.8 alloy preform material under stationary experimental conditions. By means of a mechanism placed in foaming furnace, free bending test with the effect of gravity and force bending test were performed to foam specimens. As a result of force bending test applied in different deformation rates in 600 and 625 °C, specimens ruptured after angular deformation of nearly 11°. In free bending tests which lasted up to 75 minutes in 635-656 °C temperature intervals, high deformation rates could be achieved. During this test, the time-angular deformation relationships based on temperature were determined. Angular deformation of 82° was achieved without macro defect at 656 °C temperature via free bending method. The importance of a critical temperature and deformation rate was emphasized in maintaining the deformation.

Keywords: Metallic foam, Closed cell, Al alloy, Hot deformation.

1. INTRODUCTION

Metallic foams are known for their mechanical and physical characteristics such as good energy absorption feature, high compression strength, low specific gravity and high rigidity. Forming the foam material was not a preferable situation until recently due to the errors encountered frequently in its structure. The solution of this problem is formalizing the foam material under high temperature. Thus, formability limits increase while shear stress decreases under temperature [Merklein and Geiger, 2002].

The purpose of this study is to determine formability of foam materials produced from preform material at high temperatures by forming force bending test and free bending test with the effect of gravity.

2. MATERIAL and METHOD

In the experimental study, Al alloy preform material (foaming primer material) whose chemical composition is AlMg1Si0.6TiH₂0.8 and dimensions are 5x20x200mm was used.

Preform material was foamed in foaming mold in the dimensions of 17x22x200mm at 730 °C furnace temperature.

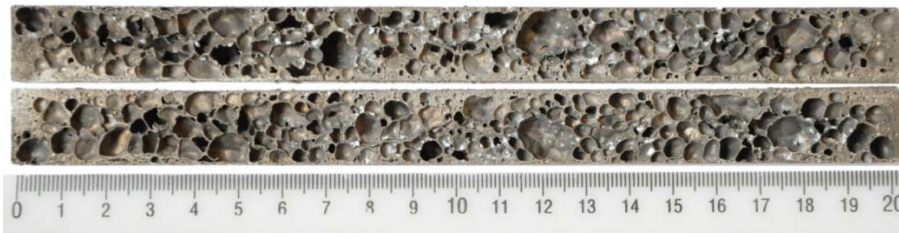


Figure 1: Longitudinal section and cell structure of foam specimen.

Figure 1 illustrates longitudinal section of the foam specimen produced. Foam specimens were produced in the density of approximately $0,7\text{g/cm}^3$. Metallic foam specimens were firstly subjected to force bending tests by applying force from outside of furnace by means of bending test apparatus mounted to foaming furnace shown in Figure 2. Force bending tests were performed to the specimens at 600 and 625 °C from the edge of the specimen, which was placed on bending cylinder, by the load arm proceeding in 0.01, 0.1 and 6.8 mm/sec rates. By using thermocouple, which was in contact with specimen, specimen temperatures were kept under control.

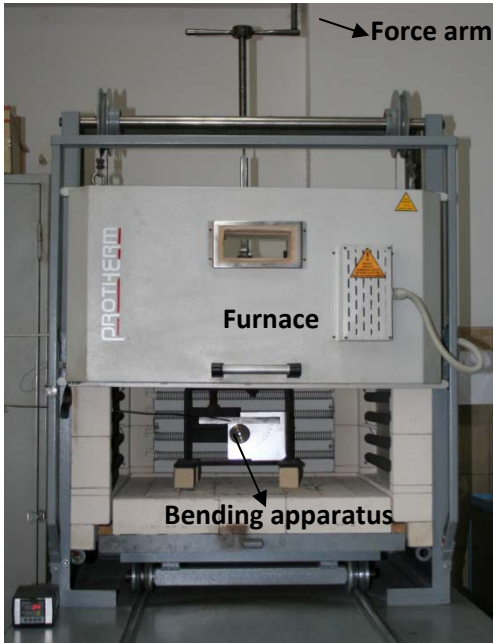


Figure 2: Bending test apparatus.

Procedures of free bending test with the effect of gravity were performed in the apparatus illustrated in Figure 3. Center of specimen was placed as overlapping with center of the bending cylinder $\varnothing 50\text{mm}$. Thus, bending inner diameters of the specimens, which were bent, remained the same. An angular scale which determines the angular deformation (bending) was placed in the back of specimen. In this way, angular

deformation of specimens according to time was determined. Furthermore, deformation process was analyzed by recording tests in video. Free bending tests were performed at 635, 640, 645, 650 and 656 °C maximum temperatures for maximum 75 minutes.

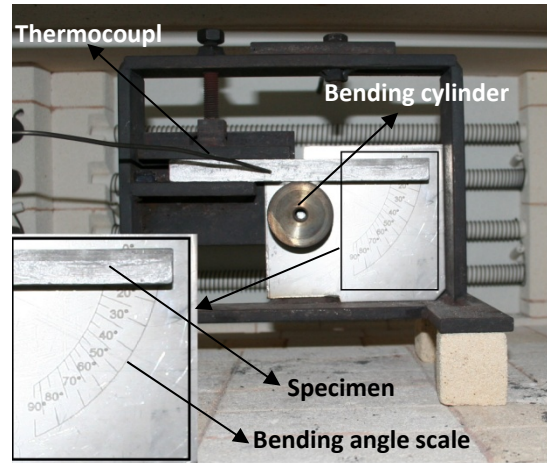


Figure 3: Free bending test apparatus.

3. EXPERIMENTAL RESULTS AND DISCUSSION

Deformation rate being high or low affected the deformation process in force bending tests performed in 600 and 625 °C. Angular deformation quantity decreased due to early crack formation with the increase of deformation rate in both temperatures in Table 1. Approximately same angular deformation values were obtained in rates greater than 0.1 mm/sec load arm speed. After this deformation amount, cracks and then a rupture occurred in the locations where maximum moment took place on the top surfaces of specimens because of the load applied.

Table 1: Change of angular deformation based on load arm speed

Temperature (°C)	Load arm speed, V (mm/s)		
	0.01	0.1	6.8
600	13	11	11
625	16	11	rupture

In free bending test, specimens were placed in the apparatus in room temperature and Figure 4 illustrates angular deformation based on time when they reached to 620, 635, 640, 645, 650 and 656 °C deformation temperatures.

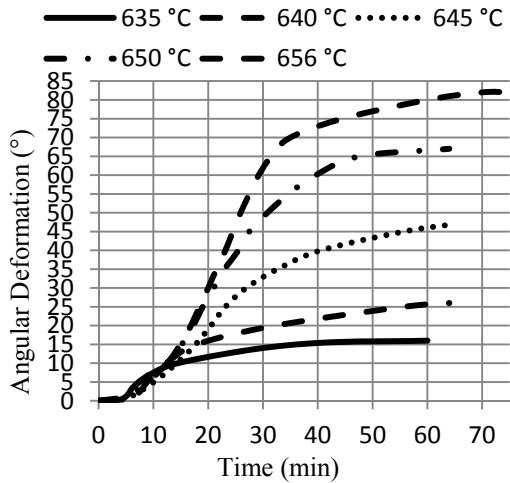


Figure 4: Angular deformation change of free bending specimens based on time.

A 5° angular deformation was observed in specimen within minute 7 at 635 °C deformation temperature (Figure 4). Moment effect occurring in bending point of specimen decreased with the increase in angular deformation. 15° angular deformation was observed within minute 36. Thereafter, only 1° increase was observed until minute 60. The reason for this could be associated with the fact that the force, which specimen applied in the center of the specimen in horizontal position in the beginning, could not able to respond shear stress of the material with the increasing angular deformation.

Generally angular deformation increases within 60 min as the deformation temperature increases. The specimen in 650 °C deformation temperature exhibited an increasing tendency in specimen temperature until the deformation time in 45 min. In the other decreasing deformation periods, there was an increase until the deformation

times less than 20 min and then it became fixed (Figure 4). The increase of deformation temperature increased angular deformation in short times.

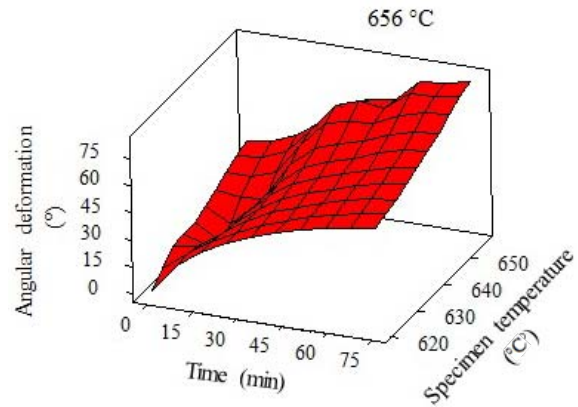


Figure 5: Surface curve of angular deformation change of free bending specimen in 656 °C based on time and temperature.

Figure 5 illustrates the effect of temperature and time on angular deformation of the specimen on which free bending was performed in 656 °C. It shows the increase in deformation based on time for a fixed temperature. In addition, it was determined that deformation rate in unit of time also increased with the increase in temperature. The increase in temperature and time provided maximum angular deformation with 82° angle.

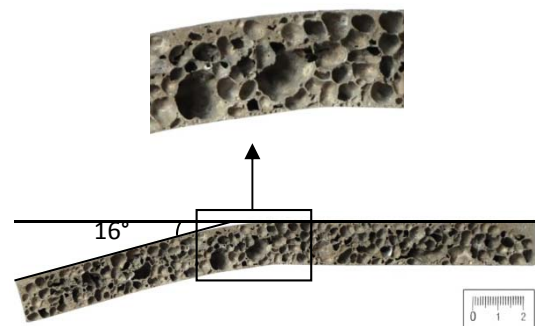


Figure 6: The specimen, on which free bending was performed in 635 °C.

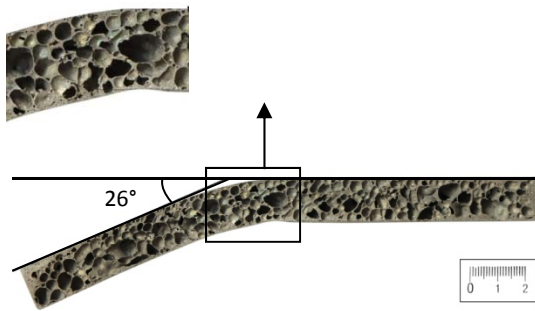


Figure 7: The specimen, on which free bending was performed in 640 °C.

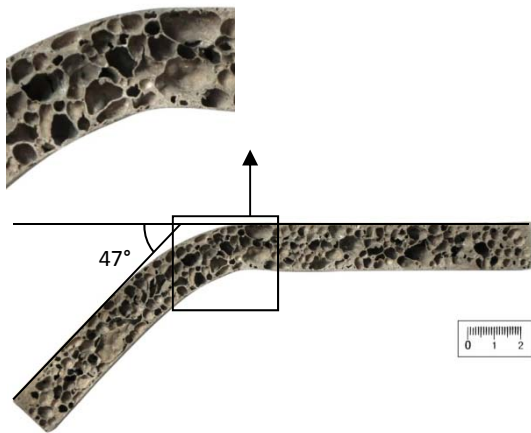


Figure 8: The specimen, on which free bending was performed in 645 °C.

In free bending tests, angular deformation increased with the increase in the deformation temperature. (Figure 6, Figure 7, Figure 8 and Figure 9). The bending angle is a function of the forming temperature and the time foam remains at this forming temperature [Merklein and Geiger, 2002].

Figure 9 illustrates two-dimensional image of foam material deformed with free bending in 650 °C after the form change. During emergence of form change; tension has occurred in the upper side of material while a compression behavior was observed in its lower part. It is clearly seen that as long as the deformation temperatures increased, the cells got deformed with the effect of elongation and contraction as a result of

being exposed to deformation in the direction of tension and compression without having any crack and as being compatible with each other. Angular deformation up to 69° occurred with free bending in material at the end of period of 64 minutes (Figure 9).

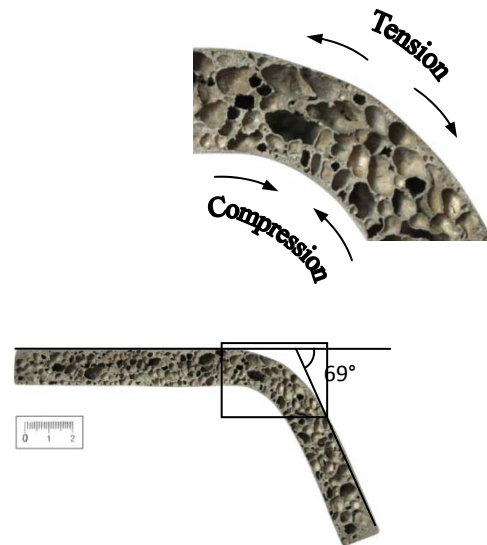


Figure 9: The specimen, on which free bending was performed in 650 °C.

Figure 10 illustrates maximum angular deformation of 82° in the specimen on which free bending process was applied in 75-min waiting time. An increase in length of the specimen was also observed at the end of deformation applied at high temperature. In addition, as well as cell orientation in the direction of tension deformation, a decrease in thickness in deformation area was observed. The cell deformation effect seen in the specimen in 650 °C was also observed in this specimen and cells changed their shapes as elongation in areas of tensile stress and contraction in cell dimensions in areas of compressive stress. Also, especially wall thickening in the upper side of the specimen is remarkable. In this zone, it is possible that cells close to upper side shrink by elongating and increase the wall thickness by closing. Form change which occurred without crack in these free bending tests performed at high

temperature could be explained with grain boundary sliding mechanism. Typical grain boundary sliding behavior was observed both in metallic foams and bulk materials [Andrews *et al.*, 1999].

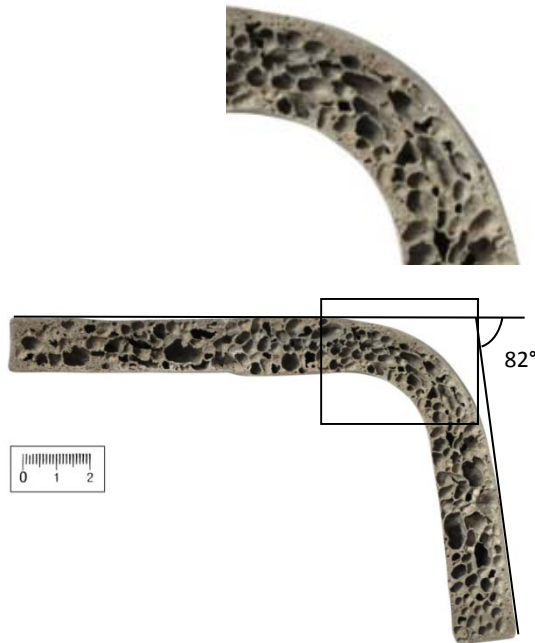


Figure 10: The specimen, on which free bending was performed in 656 °C.

4. RESULTS

As a result of the experimental study conducted, following conclusions are obtained:

- In force deformation; increasing deformation rates resulted in early

crack formation and the rupture of specimen.

- In free bending experiments; as deformation temperature and time increased, angular deformation also increased.
- It was observed that as deformation temperature increased, cells were exposed to plastic deformation without any cracking as being compatible with each other.
- With free bending method, an angular deformation of 82° was achieved at 656 °C temperature and in the areas, where deformation was intense, the thickening effect was observed in exterior walls of foam.

Acknowledgement: Authors thank to Gazi University providing support as being the 07/2012-16 coded project.

REFERENCES

- Andrews, E. W., Huang, S. And Gibson, L., J., 1999, “Creep Behavior of a Closed-Cell Aluminum Foam”, *Acta mater.* vol. 47, No. 10, pp. 2927-2935, 1999
- Merklein, M., Geiger, M.,2002.“New materials and production technologies for innovative lightweight constructions”, *Journal of Materials Processing Technology*, (125-126), 532-536.

INFLUENCE OF ZEOLITE LTA MORPHOLOGY ON THEIR BULK PROPERTIES

Tomaž Fakin^{1,a}, Alenka Ristić¹, Venčeslav Kaučič¹

1. National Institute of Chemistry, Hajdrihova 19, 1000 Ljubljana, Slovenia
a. Corresponding author (tomaz.fakin@ki.si)

ABSTRACT: Among the most important parameters of powdered zeolitic materials are also bulk and tapped densities. These properties of powders can be controlled by changing the morphology of the zeolite crystals. Crystal sizes, particle size distribution and the shape of the crystals play an important role as well as they control the density of materials, flowability, permeability, etc. In the present study we investigated the influence of synthesis parameters such as the molar ratio of reactants, the preparation of the reactants, the crystallization time and temperature, the addition of crystallization seeds, the mixing of reaction gel, the gel aging and heating rate of reaction gel on the morphology of the as-synthesized zeolite LTA and consequently on their bulk and tapped densities.

1. INTRODUCTION

Zeolites are crystalline, hydrated aluminosilicates with a three-dimensional structure which contains many voids and channels. [Cejka *et al.*, 2005]. Zeolites can be used in the detergent industry as water softeners and in separation processes, as molecular sieves for gas cleaning. Due to the reversible adsorption and desorption of water in the pores of zeolites, they are used as desiccants. Rapidly developing field of applications of zeolites is their use as catalysts in the processes of heterogeneous catalysis in the petrochemical industry. Especially interesting are recent and evolving uses of zeolites for heat storage purposes and for the removal of heavy metals from contaminated soils and waste water.

Bulk and tapped densities are a properties of powders, granules, and other solids are defined as the mass of many particles of the material divided by their total occupied volume. The total volume includes particle volume, inter-particle void volume, and internal pore volume. Bulk density is not an intrinsic property of a material; it can change depending on how the material is handled. For example, a powder poured in to a cylinder will

have a particular bulk density; if the cylinder is disturbed, the powder particles will move and usually settle closer together, resulting in a higher bulk density. For this reason, the bulk density of powders is usually reported both as bulk density (or poured density) and tapped density, where the tapped density refers to the bulk density of the powder after a specified compaction process, usually involving vibration of the container. [Buckman *et al.*, 1960]. Many of today's modern zeolites applications in adsorption processes, gas purification technology, catalysis, etc. require the use of compacted shapes of zeolites, in forms of spheres or extrudates.

Some properties of compacted zeolites such as: bulk density of compacted forms, intragranular porosity, diffusion limitations inside the granules and extrudates are directly related to the bulk and tapped densities of zeolite powder from which they are made. Changing the bulk and tapped densities of powdered zeolites can be done in two ways. The first process requires the use of usually organic compounds which reduce the

attractive forces between the individual crystals, but does not affect the other physico-chemical properties of the zeolite such as adsorption capacity, ion exchange capacity, etc... The second process for variation of bulk and tapped densities of zeolites requires changes in the shape and size of the crystals, so that they can be more or less effective in the moving side by side and thus in creating more or less dense distribution of the particles.

2. EXPERIMENTAL

In the first part of the study, we used the conventional zeolite type 4A, manufactured by Silkem Ltd. Powdered zeolite was again remixed with water so that the obtained slurry has the desired density. Various amounts of an anionic surfactant (ethoxylated alcohol) were added to the prepared slurry. Slurry was then stirred for 1 h and then dried in a pilot spin-flash type dryer at the output air temperature of 110°C - 115°C. Samples were collected with a bag filter, and cooled to room temperature before analysing.

In the second part of the study, zeolite type 4A were synthesized in the pilot 1300 L reactor. 4A zeolite was prepared from sodium water glass as a source of silicon and sodium aluminate as the source of aluminum. By varying the synthesis parameters, influence of the individual parameters were studied such as the size of the zeolite particles and their shape on the bulk and tapped densities of the prepared zeolite powder. Synthesized slurry was then filtered and washed with water on the pilot filter-press to the desired pH value and density of the zeolitic slurry. So prepared slurry was then dried in a pilot spin-flash type dryer at the output air temperature of 110°C - 115°C. Samples were again collected with a bag filter, and cooled to room temperature before analysing. Bulk densities were measured using cylinder

and device for free flowing filling of the cylinder. Tapped densities were measured on the same sample with tapping machine.

3. RESULTS

Addition of an anionic surfactant in the zeolite slurry was carried out on the same sample of the powdered zeolite. Addition of an anionic surfactant was increased from 0.1% to 1% by weight of the dry zeolite. The results of measured bulk and tapped densities are shown on the figure below.

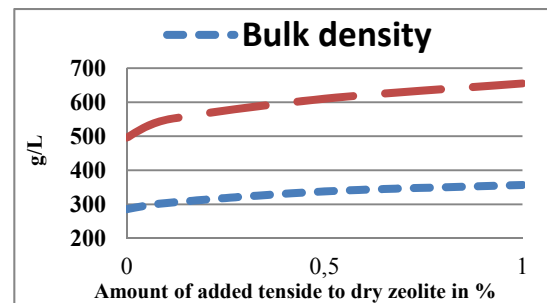


Figure 1: Influence of anionic tenside addition on bulk and tapped densities of powdered zeolite 4A.

The average size (d50) of zeolite crystals was changed by varying the synthesis parameters such as zeolite gel aging time, the gel temperature and the heating rate of the zeolite gel to the crystallization temperature. The crystal size impact on the bulk and tapped densities as shown in Figure 2 and Figure 3 were determined.

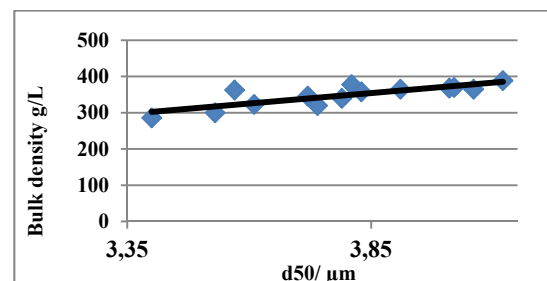


Figure 2: Influence of zeolites mean particle sizes on bulk density of powdered zeolite 4A.

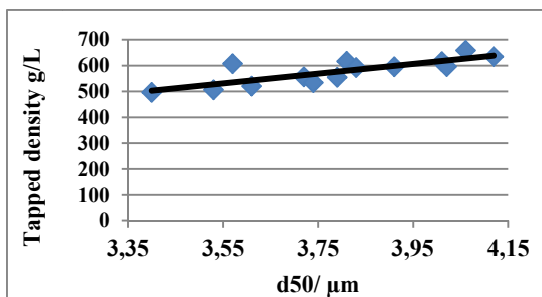


Figure 3: Influence of zeolites mean particle sizes on tapped density of powdered zeolite 4A.

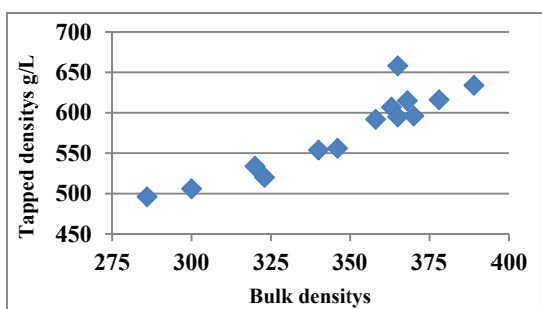


Figure 4: Relationship between bulk and tapped densities of powdered zeolite 4A.

We were interested in the impact of zeolite crystals shape on bulk and tapped densities of zeolite 4A. From the literature it is known that the $\text{SiO}_2/\text{Al}_2\text{O}_3$ ratio can affect the shape of zeolite crystals in terms of higher or lower crystals sphericity. (Subotić et al, 2009). Results and comparison of bulk and tapped densities are shown on Figure 5 and the zeolite crystals SEM images on Figure 6.

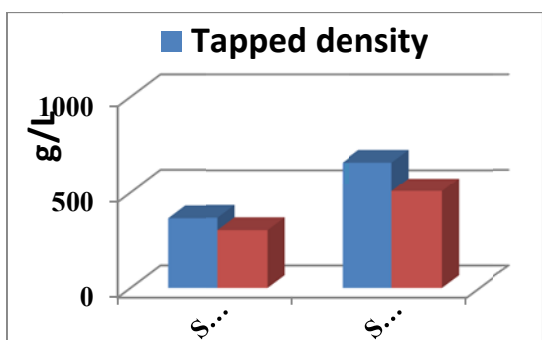


Figure 5: Influence of $\text{SiO}_2/\text{Al}_2\text{O}_3$ ratio on zeolite crystals and consequently on the shape of powdered zeolite 4A for bulk and tapped densities.

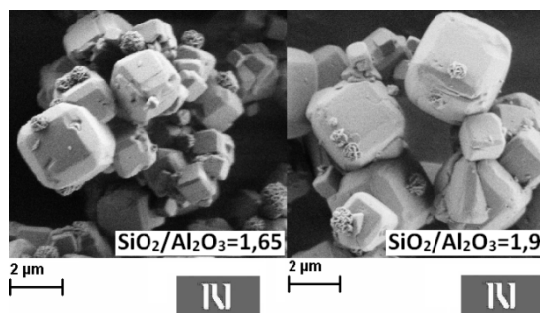


Figure 6: SEM images of zeolite crystals with different $\text{SiO}_2/\text{Al}_2\text{O}_3$ ratio.

4. DISCUSSION

Within research, the influence of anionic surfactant addition on the bulk and tapped densities of dried zeolite 4A was examined. It should be noted that the addition of anionic surfactant has completely opposite effect in the case of dry zeolite and zeolite slurry. The molecules of the anionic surfactant are distributed on the surface of the zeolite crystals, which can cause certain repulsive forces between them and consequently between zeolite crystals. In the aqueous medium, this result in a stable zeolitic suspension where no settling of zeolitic particle is observed, is completely different in the case of zeolite slurry without added anionic surfactant. In dried form, the anionic surfactant effects in the way, that they reduce the resistance between the zeolite particles, thereby enabling a better sliding of particles, thus increasing bulk and the taped density of zeolite powder. Any negative impact of anionic surfactant addition to the 4A zeolite to other physico-chemical properties of zeolite 4A, such as calcium exchange capacity, water adsorption capacity etc. was detected.

Especially interesting are the results from the second part of our research, where we investigate the effect of the particle size of the synthesized zeolites on bulk and tapped densities. The particle size was varied by varying the zeolite gel heating

rate and the final temperature of crystallization. Particular attention was paid to the prevention of sodalite formation, which occurs at elevated temperatures of crystallization and may interfere with determination of bulk and tapped densities. In Figure 2 it can be observed the bulk density of zeolite powders as a function of their mean particle sizes. Bulk density of zeolite 4A increases proportionally with the average particle size. Figure 3 shows the tapped density dependence of the mean particle sizes. We found out proportionality between tapped density and the zeolites mean particle sizes. If the comparison between bulk and tapped density is done for each sample we get a graph shown in Figure 4. It shows the direct link between the bulk and tapped density of zeolite 4A for different mean particle sizes samples.

Figure 5 shows the impact of different $\text{SiO}_2/\text{Al}_2\text{O}_3$ ratios in the bulk and tapped densities of synthesized zeolites. The synthesis parameters are in both cases exactly the same, but the bulk density and tapped density are quite different. The reason may be found in a different mean particle size, since the mean particles of as-synthesized zeolite 4A with a higher $\text{SiO}_2/\text{Al}_2\text{O}_3$ ratio are larger than those with a lower ratio of $\text{SiO}_2/\text{Al}_2\text{O}_3$. In addition to the larger mean particle size effect, higher tapped density may be attributed also to slightly more spherical crystals of zeolite 4A as shown in Figure 6.

5. CONCLUSIONS

In the present study, the factors that affect the bulk and tapped densities of the powdered zeolite type 4A were investigated. In the first part of the study, zeolite bulk and tapped densities changes using anionic tenside were investigated. A considerable increase of bulk and tapped densities at 1% addition of anionic

tenside to the zeolite 4A without having a negative impact on the physical and chemical properties of zeolite powder was found. Effect of the mean particle size of zeolite 4A on the bulk and tapped densities was studied and almost linear mean particle size dependence on the bulk and tapped density of zeolite 4A powder was found. In the last part of the research the $\text{SiO}_2/\text{Al}_2\text{O}_3$ ratio was changed and found a significant reduction in bulk and tapped densities for zeolite 4A with lower $\text{SiO}_2/\text{Al}_2\text{O}_3$ ratio.

Acknowledgements: This research was supported by the Slovenian Research Agency (research program Nanoporous materials, P1-0021-0104).

REFERENCES

- Buckman, H. O., Brady, N. C., 1960, *The Nature and Property of Soils - A College Text of Edaphology* (6th ed.), New York: MacMillan Publishers, New York, 50.
- Cejka, J., van Bekkum J., 2005, *Zeolites and Ordered Mesoporous Materials: Progress and Prospects; Studies in Surface Science and Catalysis 157C*; Elsevier: Amsterdam.
- Subotić, B., Kosanović, C., Bosnar, S., Antonič, Jelič, T., Bronić, J., Igrec, I., 2009: *Chemical controlled morphology of zeolite A crystals*, Proceedings of 2nd Slovenian-Croatina Symposium on Zeolites, Ljubljana.

THE TRANSVERSE RUPTURE STRENGTH OF HOT PRESSED SEGMENTS WITH B4C

Serkan Islak^{1,a}, Durmuş Kır², Halis Çelik³

1. Kastamonu University, Faculty of Eng. and Architecture, Dep. of Materials Sci. and Nanotech. Eng., Kastamonu, Turkey
2. Kocaeli University, Hereke Vocational High School, Kocaeli, Turkey
3. Firat University, Faculty of Technology, Dep. of Metallurgy and Materials Eng., Elazig, Turkey
a. Corresponding author (serkan@kastamonu.edu.tr)

ABSTRACT: In this paper, the effect of sintering temperature on transverse rupture strength (TRS) of diamond cutting segments with boron carbide produced using hot pressing process was investigated. The boron carbide addition quantity was changed as 2, 5 and 10 wt %. The hot pressing process was carried out under a pressure of 35 MPa, at 600, 650 and 700 °C, and for a sintering time of 3 minutes. The TRS of segments were determined using three-point bending test. A Scanning Electron Microscopy was used to analyze the fractured surfaces of the segments. With increasing of the sintering temperature, the TRS values of segments increased.

Keywords: Sintering temperature, diamond cutting segments, boron carbide, hot pressing

1. INTRODUCTION

Diamond cutting tools are commonly used for cutting, drilling, grinding, and polishing natural stone [Konstanty, 2005]. In general, these tools include circular saws, cores, diamond wires, and drills [Xu, 2009]. Diamond cutting tools are comprised of a metallic matrix and cutting grain. In general, Fe, Co, Ni, Cu, CuSn, and their alloys are used as the metallic matrix, and synthetic diamond is used as the cutting grain. The hot pressing method enables the synthetic diamond to bond with the metallic matrix [Zeren and Karagöz, 2006; Tilmann, 2000]. The two basic functions of the metallic matrix are to hold the diamond tight and to wear at a rate compatible with the diamond loss. The wear resistance of the matrix has to correspond with the abrasiveness of the work piece material, so that neither the diamond grits protrude insufficiently nor they are lost prematurely [Konstanty, 2005; Xipeng et al., 2007]. Carbides were added to the matrix in order to increase the wear resistance of the metallic matrix. The number of subject-related studies in

literature is limited. Meszaros and Vadasdi [Meszaros and Vadasdi, 1996] produced Co-2% WC matrix diamond cutting tools. The study reported that WC controlled the weight loss of the matrix with abrasion and ultimately increased the wear resistance. Oliveira et al. [Oliveira et al., 2007] used Fe-Cu-SiC powders as a matrix for diamond cutting tools. There was a 14% rate of increase at the hardness level that has a controlling effect on the rate of wear with the addition of SiC. In this investigation, the effect of boron carbide content, known to be the hardest material with the best mechanical properties after diamond and cubic boron nitride [Pierson, 1996; Jiang et al., 2009; Ma et al., 2010], and the sintering temperature on the bending strength of diamond cutting segments were studied.

2. EXPERIMENTAL STUDIES

Pure The raw materials used in experiments were bronze powder (Cu-15 wt.% Sn, purity 99.9%, grain size 45-50 µm), boron carbide powder (purity 99.5%, grain size 20 µm), and synthetic diamond grain (grain size 40/50 US

mesh). B_4C grains were added to the bronze at the amount of 2, 5 and 10 wt.% percents. The amount of diamond was selected as concentrations of 30 (1.32 carat/cm³). Bronze, boron carbide powders and diamond grain were mixed together in mixer. Then, the mixture was hot-pressed in graphite moulds for 3 min at 600, 650 and 700 °C with an applied pressure of 35 MPa on an automatic hot pressing machine. The relative densities of segments were measured by Archimedes' principle. Hardness measurements were performed using a Brinell scale with a ball diameter of 2.5 mm and a load of 62.5 kg. The three-point bending tests were performed using an Instron 4411 universal testing machine to determine the transverse rupture strength (TRS) of the segments. A scanning electron microscope (SEM) fitted with an energy dispersion X-ray spectroscopy (EDS), an X-ray diffractometer were used to investigate microstructure of segments.

3. RESULTS AND DISCUSSION

3.1. Microstructure

The segments containing B_4C were successfully produced using the hot pressing method together with a sintering time of three minutes at 600, 650, and 700 °C, under a pressure of 35 MPa. Fig. 1 illustrates the XRD pattern of the segments manufactured in the present study. As illustrated, α -Cu, ϵ -bronze (Cu_3Sn) and B_4C phases formed in the microstructure of the segment matrix.

Fig. 2 illustrates the SEM images of the microstructure of segments without boron carbide. As illustrated, the amount of pores in the segments sintered at 600 °C was more in comparison to that of 700 °C. The amount of pores decreased at a high sintering temperature, which lead to high speed solid-state diffusion [Rahimian et al., 2009].

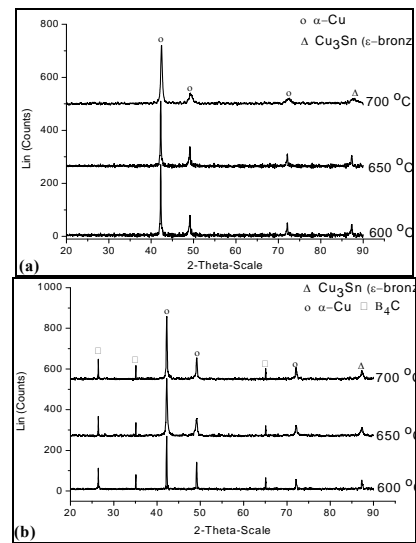


Figure 1: XRD pattern of the segments: (a) bronze and (b) 5 wt.% B_4C

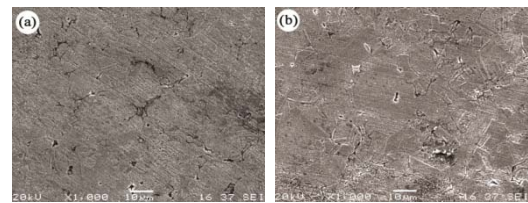


Fig. 2: The SEM image of CuSn (no B_4C added) segment, (a)600 °C and (b)700 °C

Fig. 3 illustrates the SEM images of the segments produced by adding 2%, 5%, and 10% B_4C in weight to bronze powder. The B_4C grains were relatively homogeneously distributed throughout the microstructure, and surrounded by bronze. In micrographs, light grey areas indicate bronze matrix, and the dark grey and cornered shapes indicate the reinforcement component B_4C . As illustrated in Fig. 3, as the sintering temperature and B_4C addition increases, B_4C grains spread towards the bronze grain boundaries, like a homogenous network. The XRD patterns illustrate that there was no chemical reaction between bronze and B_4C . Pores formed at the grain borders in the microstructure of bronze- B_4C segments. The level of porosity increased together with the increased rate of boron carbide because boron carbide had an adverse effect on

sinterability. Table 1 illustrates the EDS analysis of regions identified in the SEM images illustrated in Fig. 3. The region 1, 2, and 3 illustrate B_4C , CuSn and Cu_3Sn phases, respectively.

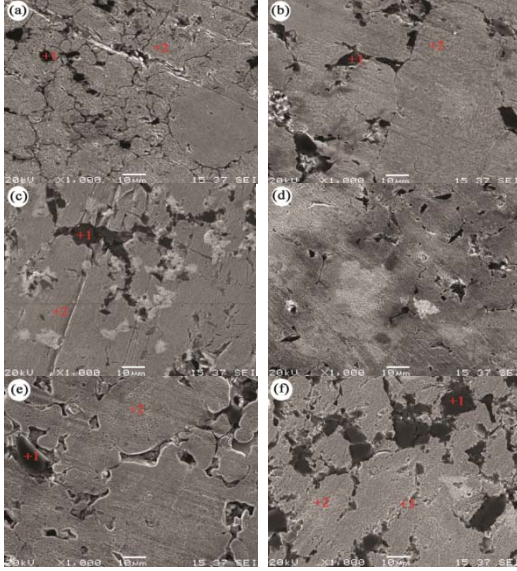


Fig. 3: SEM images of the segments: (a) 2 % B_4C - 600 °C, (b) 5 % B_4C - 600 °C, (c) 10 % B_4C - 600 °C, (d) 2 % B_4C - 700 °C, (e) 5 % B_4C - 700 °C and (f) 10 % B_4C - 700 °C

Table 1: EDS analysis of microstructures in Fig. 3

Regions	Chemical Composition (wt.%)			
	B	C	Cu	Sn
1	79.18	19.80	0.00	1.02
2	0.00	0.00	85.89	14.11
3	0.00	0.00	62.28	37.72

3.2. Density and Hardness

Table 2 illustrates the effect of sintering temperatures and boron carbide on densities of segments. The sintered and theoretical densities of segments were used to determine their relative density.

When boron carbide was introduced to the CuSn, it decreased the sintered density. This was due to the fact that the density of boron carbide was lower than that of bronze. The density of B_4C was 2.52 g/cm^3 , while the density of bronze was 8.68 g/cm^3 . Relative density also

decreased as the amount of added boron carbide increased. This was due to the fact that the increased rate of added boron carbide had an adverse effect on sinterability. Another reason was the fact that there was a great difference in the melting points of the bronze and the boron carbide, and boron carbide may have an inhibiting effect in the rearrangement of the grains during sintering [Rahimian et al., 2009]. At higher sintering temperatures, a denser structure was formed due to higher diffusion rates. The difference between theoretical and sintered densities decreased with the increase in sintering temperature (Table 2).

Table 2: The effect of sintering temperature and B_4C content on the densities of the segment

No	Sintered density (g/cm^3)			Relative density (%)		
	600	650	700	600	650	700
0	8.59	8.60	8.61	98.96	99.07	99.19
1	7.58	7.73	7.96	88.55	90.30	93.02
2	7.20	7.34	7.55	86.02	87.69	90.16
3	6.50	6.68	6.93	80.55	82.78	85.77

*) (0) CuSn, (1) 2 % B_4C , (2) 5 % B_4C , (3) 10 % B_4C

As temperature increased, the two adjacent grains formed a good bond by diffusion in a solid-state bonding process, the relative and sintered densities of the segments increased [Lima et al., 2003]. The highest densification for boron carbide added segments was obtained for the CuSn-2 % B_4C segment and at 700 °C sintering temperature, with a relative density of approximately 93.02 %.

Fig. 4 illustrates hardness as a function of the sintering temperature and the B_4C content in the segments. Hardness of the segments increased with increasing B_4C content. The increase in the hardness of segments by adding B_4C can be attributed to the dispersion strengthening effect

[Min et al., 2007]. The matrix hardness increased with the increase in sintering temperature. This was due to the same reason of the good bonding between the grains of the composites at a high sintering temperature [Lima et al., 2003].

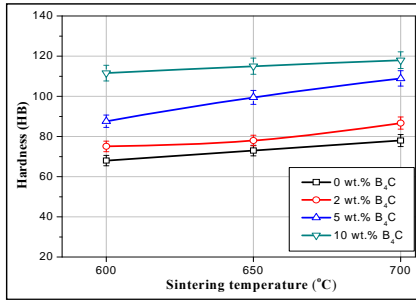


Figure 4: The hardness of segments.

3.3. Transverse Rupture Strength (TRS)

The TRS for each segment was determined using a three-point bending test. The three-point bending test was repeated five times for every segment. Fig. 5 illustrates the effect of sintering temperature and boron carbide content on the TRS. The TRS of the segments decreased together with the increase in the amount of boron carbide. This situation can be explained as the increase of boron carbide grains lead to the increase of the total area of the weakly bonded interface, which results in the decrease of the TRS [Jin et al., 2009]. In addition, the difference in thermal expansion coefficient between B₄C and CuSn contributes to the interfacial stress. This stress may cause the TRS to decrease [Samuel et al., 1995]. Furthermore, the level of porosity affects the TRS [Dwan, 2007]. With increasing of the sintering temperature, the TRS values of segments increased. This was due to good bonding between the bronze and B₄C/diamond grains in case of high temperature.

Fig. 6 illustrates the SEM images of the fracture surface of segments having bronze matrix sintered at different

temperatures. It is obvious that the bonding between the bronze and diamond was weak for the segment sintered at 600 °C. The gaps between the diamond and matrix illustrate that the interface bonding was weak (Fig. 6a). The failure behavior of the matrix was the ductile fracture. The bonding between the bronze and diamond for segments sintered at 700 °C was stronger than segments sintered at 600 °C (Fig. 6b). A denser segment was achieved with increasing sintering temperature. The diamond holes and pores were observed on the fracture surface. This situation proves that the sintering temperature was lower than the desired level.

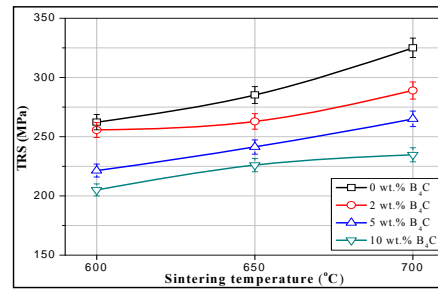


Figure 5: TRS of segments with B₄C.

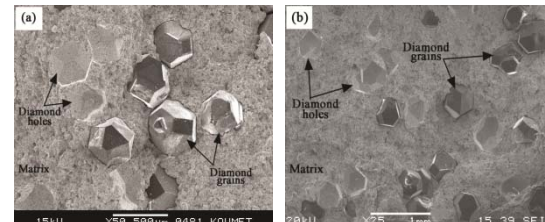


Fig. 6: The fracture surfaces of the segments with bronze matrix: (a) at 600 °C and (b) at 700 °C

Fig. 7 illustrates the SEM images taken from the fracture surfaces of the segments containing 5wt.% B₄C. There was weak bonding between matrix and diamond. B₄C grains adversely affected the bonding of diamond-matrix by getting bronze and diamond. This situation proved the presence of B₄C grains in the diamond holes. The weak bonding was due to insufficient sintering conditions. The quality of bonding between diamond

and matrix can be improved by changing sintering conditions.

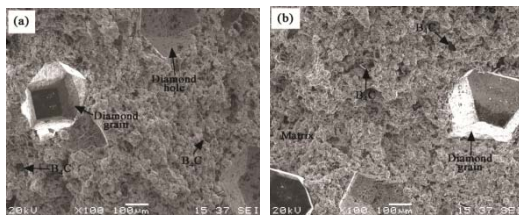


Fig. 7: The SEM images of the fracture surfaces of the segments having bronze-5 wt.% B₄C matrix: (a) sintered at 600 °C and (b) sintered at 700 °C

4. CONCLUSIONS

Microstructure observation demonstrates a relative homogenous distribution in bronze of B₄C particulates. The increase in B₄C content increased the amount of pores. The amount of pores decreased at high sintering temperature. Relative density of segments decreased as B₄C content increased. The highest densification for bronze/B₄C segments was obtained in the bronze – 2 wt. % B₄C segment sintered at 700 °C, with a relative density of approximately 93.01%. Hardness of segments was increased as the sintering temperature and amount of B₄C grains increased. The highest hardness value was 118 HB, obtained by adding 10 wt. % B₄C. The TRS of the segments decreased together with the increase in the amount of B₄C, while it increased with increasing sintering temperature.

Acknowledgements

The research was supported by the Firat University Scientific Research Projects Unit (Project no: TEF.10.01).

REFERENCES

Dwan, J., 2007. Fracture toughness determination of diamond impregnated PM cobalt, *Ind. Diamond Rev.*, 1, pp. 33-36.
 Jin, X., Wu, L., Sun, Y., Guo, L., 2009. Microstructure and mechanical properties of ZrO₂/NiCr functionally graded materials, *Mater. Sci. Eng. A.*, 509, pp. 63-68.

Jiang, T., Jin, Z., Yang, J., Qiao, G., 2009. Investigation on the preparation and machinability of the B₄C/BN nanocomposites by hot-pressing process, *J. Mater. Proc. Technol.*, 209, pp. 561-571.
 Konstanty, J., 2005. *Powder Metallurgy Diamond Tools*, Elsevier Ltd, The Metal Powders Technology Series.
 Lima, W.M., Velasco, F.J., Abenojar, J., Torralba, J.M., 2003. Numerical approach for estimating the elastic modulus in MMCs as a function of sintering temperature, *J. Mater. Proc. Technol.*, 143-144, pp. 698-702.
 Ma, Q.C., Zhang, G.J., Kan, Y.M., Xia, Y.B., Wang, P.L., 2010. Effect of additives introduced by ball milling on sintering behavior and mechanical properties of hot-pressed B₄C ceramics, *Ceram. Int.*, 36, 167.
 Meszaros, M., Vadasdi, K., 1996. Process and equipment for electrochemical etching of diamond-containing Co-WC tools and recovery of diamond from used steel tools, *J. Refract. Metals Hard Mater.*, 14, pp. 229-234.
 Min, K.H., Lee, B.H., Chang, S.Y., Kim, Y.D., 2007. Mechanical properties of sintered 7xxx series Al/SiCp composites, *Mater. Lett.*, 61, pp. 2544-2546.
 Oliveira, L.J., Bobrovitchii, G.S., Filgueira, M., 2007. Processing and characterization of impregnated diamond cutting tools using a ferrous metal matrix, *J. Refract. Metals Hard Mater.*, 25, pp. 328-335.
 Pierson, H.O., 1996. *Handbook of Refractory Carbides and Nitrides*, William Andrew Pub..
 Rahimian, M., Ehsani, N., Parvin, N., Baharvandi, H.R., 2009. The effect of sintering temperature and the amount of reinforcement on the properties of Al–Al₂O₃ composite, *Mater. Des.*, 30, pp. 3333-3337.
 Samuel, A.M., Gotmare, A., Samuel, F.H., 1995. Effect of solidification rate and metal feedability on porosity and SiC/Al₂O₃ particle distribution in an Al–Si–Mg (359) alloy, *Compos. Sci. Technol.*, 53, pp. 301-315.
 Tillmann, W., 2000. Trends and market perspectives for diamond tools in the construction industry, *J. Refract. Metals Hard Mater.*, 18, pp. 301-306.
 Xipeng, X., Xiaorui, T., Hairong, W., 2007. The effects of a Ti coating on the performance of metal-bonded diamond composites containing rare earth, *J. Refract. Metals Hard Mater.*, 25, pp. 244-249.
 Xu, X.P., 1999. Friction studies on the process in circular sawing of granite, *Tribol. Lett.*, 7, 221.
 Zeren, M., Karagoz, Ş., 2006. Defect characterization in the diamond cutting tools, *Mater. Charac.*, 57, pp. 111-114.

MICROSTRUCTURE AND ELECTRICAL PROPERTIES OF Cu-TiC COMPOSITES PRODUCED BY HOT PRESSING METHOD

Serkan Islak^{1,a}, Soner Buytoz², Özkan Eski³ and Durmuş Kır⁴

1. Kastamonu University, Faculty of Engineering and Architecture, Dep. of Materials Science and Nanotech. Eng., Kastamonu, Turkey
 2. Firat University, Faculty of Technology, Dep. of Metallurgy and Materials Eng., Elazığ, Turkey
 3. Kastamonu University, Faculty of Eng. and Architecture, Dep. of Mech. Eng., Kastamonu, Turkey
 4. Kocaeli University, Hereke Vocational High School, Kocaeli, Turkey
- a. Corresponding author (serkan@kastamonu.edu.tr)*

ABSTRACT: The TiC particle reinforced Cu matrix composite materials were successfully produced using hot pressing method. The TiC quantity was changed as 1 wt.%, 3 wt.%, 5 wt.%, 10 wt.% and 15 wt.%. Cu and Cu-TiC powder mixtures were hot-pressed for 4 min at 700 °C under an applied pressure of 50 MPa. Phase composition, microstructure, relative density, hardness, and electrical conductivity of the hot pressed composites were investigated. Phase composition and microstructure of the composites were characterized by X-ray diffraction, scanning electron microscope, and optic microscope techniques. Microstructure studies revealed that TiC particles were distributed uniformly in the Cu matrix. With the increasing addition of TiC, hardness of composites changed between 58.6 HV_{0.1} and 87.8 HV_{0.1}. The highest electrical conductivity for Cu-TiC composites was obtained in the Cu-1 wt.% TiC composite, with approximately 81.2 % IACS.

Keywords: Hot pressing, Cu-TiC, microstructure, electrical conductivity

1. INTRODUCTION

Copper is commonly used as electrical contact material today due to its high electrical and thermal conductivity, corrosion resistance, low cost and easy production [ASM Handbook, 1990 and Deshpande and Lin, 2006]. However, low hardness, strength and low wear resistance restrict usage area of pure copper. Mechanical characteristics and wear resistance of the copper are generally enhanced with two ways; age hardening mechanism or addition of hard secondary phases [Tjong and Lau, 2000 and Dong et al., 2001]. During age hardening, addition of small quantities of chromium and zirconium into copper causes precipitation of secondary hard phases, which could not be dissolved in the copper at low temperatures. Alloys hardened by this ageing process lose their

strengths at temperatures above 500 °C with grain coarsening of precipitated hard

phases due to structural instability [Correia et al., 1997]. On the other hand, in the second method, Cu matrix composite materials are produced by adding carbide, oxide, and boride into copper. Characteristics of the copper could be improved by producing particle reinforced Cu matrix composite materials [Alpas et al., 1993].

Ceramic reinforced metal matrix composite materials are used for structural applications in wear industry due to super toughness and wear resistance. Especially alumina and silicon carbide based composite materials do not lose their hardness and wear resistances during high temperature applications [Chang and Lin, 1996; Upadhyaya and

Upadhyaya, 1995; Ritasalo et al., 2011]. Cu matrix composite materials are alternative materials when high electrical/thermal conductivity and good wear resistance are required. Considering carbide reinforced copper composite materials; studies conducted with SiC in the literature are remarkable. Efe et al. fabricated Cu-SiC composites via cold pressing technique by making addition of SiC at various ratios into copper and subsequently sintering the mixture at different temperatures. It was determined that as a result of increasing SiC addition, a great quantity of porosity appeared in composites produced via cold pressing and consequently values of electrical conductivity decreased [Çelebi Efe et al., 2011]. Zhan and Zhang coated SiC particles with nickel using electroplating method in order to obtain a stronger bonding on Cu and SiC interface in Cu-SiC composites. While relative densities of coated composites were higher compared to uncoated composites, the electrical conductivity remained almost the same. However, mechanical features of coated composites came out good due to strong interface bonding [Zhan and Zhang, 2003]. In this study, TiC between 0-15 wt.% was added into copper. Microstructure and electrical features of composites produced using hot pressing technique were investigated.

2. EXPERIMENTAL STUDIES

Pure copper powder (in averagely 20 µm grain size) and titanium carbide powder (in averagely 10 µm grain size) were used in the experiments. TiC was added at 1, 3, 5, 10, and 15 wt.% rates into Cu matrix. Figure 1 illustrates SEM images of copper and titanium carbide powders. While copper powder had a dendritic structure, titanium carbide powder had a sharp-edged structure.

Copper and titanium carbide powders were mixed using powder mixing

machine at 20 rpm/min for 30 minutes in such a way that the mixture would become homogenous. The powder mixture was put into graphite moulds and pressed using an automatic hot pressing machine for 4 minutes at 700 °C sintering temperature under pressure of 50 MPa. Relative densities of samples were measured according to Archimedes' principle. Micro-hardness measurements of pure copper and Cu-TiC composites were performed using a Vickers hardness instrument under a load of 100 gf. The electrical conductivity of Cu and Cu-TiC composites was evaluated with eddy current instruments in accordance with ASTM standard E1004-02 [ASTM E1004-02]. The electrical conductivity measured by this equipment is usually expressed as a percentage of the conductivity of the International Annealed Copper Standard (% IACS). Minimum five readings were taken for each sample. The average electrical conductivity value of % IACS was converted into SI unit (S/m) by multiply by 0.58×10^6 , as the 100% IACS equals to 0.58×10^8 S/m. For metallographic study, the samples were prepared according to standard metallographic procedure. An optical microscopy, scanning electron microscope, and X-ray diffractometer were used to investigate microstructure and phase composition of composites.

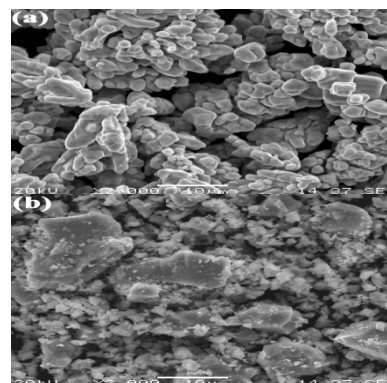


Figure 1: SEM micrographs of (a) Cu and (b) TiC powders.

3. RESULTS AND DISCUSSION

3.1. Microstructure

Figure 2 illustrates optical images of Cu and Cu-TiC composites produced via hot pressing. When the microstructure is examined, three different structures draw the attention. Gray and sharp-edged grains represent TiC, dark gray areas represent porosities, and finally yellowish areas represent Cu matrix. TiC particles distributed uniformly in the Cu matrix. Lee et al stated that if reinforced particles do not distribute homogeneously, this situation would affect mechanical and electrical features of the composite negatively [Lee et al., 2001]. TiC particles were positioned as embedded since they were within grain borders of ductile Cu matrix. SEM images demonstrate that quantity of TiC in the microstructure increased depending on addition quantity of TiC.

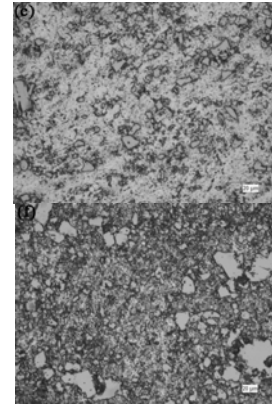
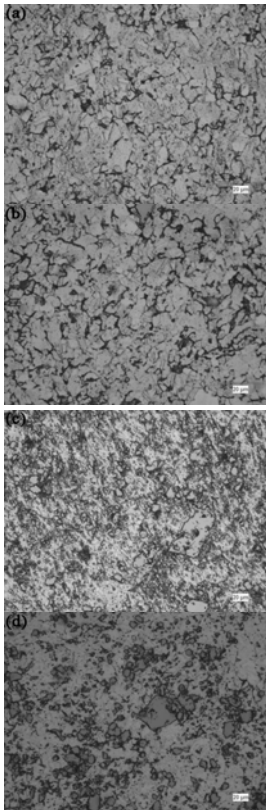


Figure 2: Optic micrographs of Cu-TiC composites: (a) un-reinforced, (b) 1 wt% TiC, (c) 3 wt% TiC, (d) 5 wt% TiC, (e) 10 wt% TiC and (f) 15 wt% TiC

The XRD analysis was performed for each composite in order to determine whether a phase formed to provide bonding in the interface of copper (matrix) and titanium carbide (reinforcement) particles or not. Figure 5 illustrates XRD graphics of the composites. It is seen from graphics that Cu and TiC phases formed. Any phase did not form between Cu and TiC. This situation demonstrated that there was no chemical reaction between Cu and TiC. It is evidently seen from graphics that there was an increase in peaks of TiC phase based on increasing titanium carbide rates. Furthermore, XRD graphics obviously show that no oxide phase formed in Cu-TiC composites.

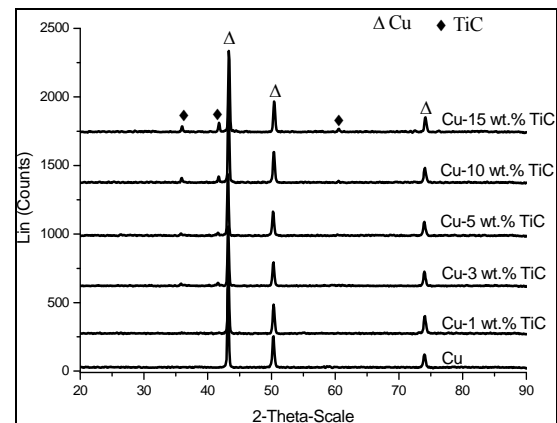


Figure 3: XRD diffraction patterns of Cu-TiC

3.2. Density and Hardness

Figure 4 illustrates effect of TiC addition on relative density and hardness of Cu-TiC composites produced via hot pressing. Relative densities of the composites were determined according to Archimedes' principle. With increasing TiC addition, relative densities decreased. In consideration of addition of TiC up to 15 wt.%, relative densities decreased from 98.6 % to 78.8 %. This decrease in the relative densities could be associated with the fact that increasing rate of TiC affected the sintering adversely [Rahimian et al., 2009]. Another reason is that huge difference between melting points of matrix and reinforcing member, namely Cu and TiC was an inhibiting factor in the rearrangement of particles during sintering. Moreover, the fact that density of TiC is lower than density of copper is another reason for the decrease in the relative densities.

Hardness of Cu-TiC composites produced with addition of TiC significantly increased. While hardness of pure copper produced via hot pressing method was 47.5 HV_{0.1}, hardness of composites with addition of TiC ranged from 58.6 HV_{0.1} to 87.8 HV_{0.1}. This hardness increase was caused by dispersion strengthening effect of boron carbide. Additionally, the increase in addition of TiC caused an increase in dislocation density in the Cu matrix and consequently it is thought that hardness of composites increased.

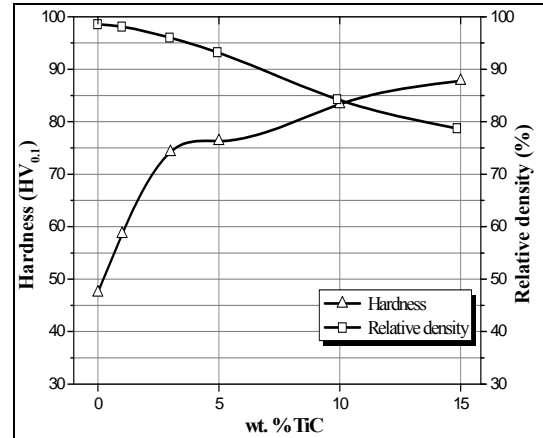


Figure 4: Hardness and relative density of Cu-TiC composites

3.3. Electrical Conductivity

Figure 5 illustrates results of electrical conductivity test of Cu-TiC composites, produced via hot pressing method, based on content of titanium carbide. With the increase in addition rates of titanium carbide, the electrical conductivity of composites decreased. While the electrical conductivity of Cu with no addition was measured as 88.7 % IACS, the electrical conductivity of composites with 1, 3, 5, 10 and 15 % TiC addition was measured as 81.3 % IACS, 74.3 % IACS, 72.2 % IACS, 64.9 % IACS and 58.2 % IACS, respectively. Porosity and oxidation could be asserted as the reason for low electrical conductivity of pure copper [Randal, 2005]. Interaction between free electrons and nucleus is weak in the metals. Therefore, electrons easily move and accordingly electrical conductivity of metals is good. However, electrons are firmly bonding to the nucleus in the carbides and electrons do not move. For this reason, electrical conductivity of carbides is weak [Pierson, 1996]. Since rate of Cu matrix in TiC addition in the Cu-TiC composite material decreased, it is an expected result that electrical conductivities of the composites would decrease with increasing addition of TiC. Reinforced TiC particles in the composite exhibited

an effect inhibiting the movement of Cu electrons.

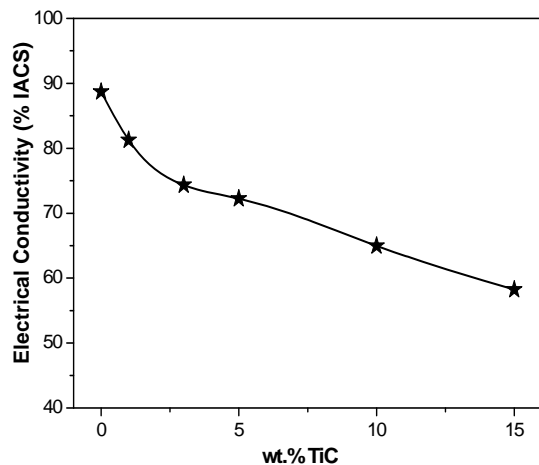


Figure 5: Electrical conductivity of Cu-TiC composites

4. CONCLUSIONS

Cu-TiC composites were successfully produced using a hot pressing method together with 4-minute sintering at 700 °C, under pressure of 50 MPa. Microstructure studies revealed that TiC particles were distributed uniformly in the Cu matrix. The presence of Cu and TiC was confirmed by X-ray diffraction analysis. XRD analysis showed that there was no formation of copper oxide which affected electrical properties of composites negatively. With the increasing addition of TiC, the hardness of composites increased while relative density decreased. High TiC contents decrease the electrical conductivity of Cu-TiC composites as expected. The highest electrical conductivity for Cu-TiC composites was obtained in the Cu-1 wt.% TiC composite, with approximately 81.2 % IACS.

ACKNOWLEDGEMENTS

This research was financially supported by Kastamonu University Scientific Research Projects Coordination Unit (Project no: KUBAP-01/2012-15).

REFERENCES

- Alpas, A.T., Hu, H. and Zhang, J. 1993. Plastic deformation and damage accumulation below the worn surfaces, *Wear* 162–164, 188.
- ASM Handbook: Properties and Selection: Nonferrous Alloys and Special-Purpose Materials, Vol.2, 10th ed., 1990.
- ASTM E1004-02, Standard practice for determining electrical conductivity using the electromagnetic (eddy-current) method.
- Chang, S. and Lin, S. 1996. Fabrication of SiC_w reinforced copper matrix composite by electroless copper plating, *Scripta Materialia*, 35, 225.
- Correia, J.B., Davies, H.A. and Sellars, C.M. 1997. Strengthening in rapidly solidified age hardened Cu-Cr and Cu-Cr-Zr alloys, *Acta Materialia*, 45, 177.
- Celebi Efe, G., Yener, T., Altinsoy, I., Ipek, M., Zeytin, S. and Bindal, C. 2011. The effect of sintering temperature on some properties of Cu-SiC composite, *Journal of Alloys and Compounds*, 509, 6036.
- Deshpande, P.K. and Lin, R.Y. 2006. Wear resistance of WC particle reinforced copper matrix composites and the effect of porosity, *Materials Science and Engineering: A*, 418, 137.
- Dong, S.R., Tu, J.P. and Zhang, X.B. 2001. An investigation of the sliding wear behavior of Cu-matrix composite reinforced by carbon nanotubes, *Materials Science and Engineering: A*, 313.
- Lee, D.W., Ha, G.H. and Kim, B.K. 2001. Synthesis of Cu-Al₂O₃ nano composite powder, *Scripta Materialia*, 44, 2137.
- Pierson, H.O. 1996 *Handbook of Refractory Carbides and Nitrides*, William Andrew Pub., Noyes.
- Rahimian, M., Ehsani, N., Parvin, N. and Baharvandi, H.R. 2009. The effect of particle size, sintering temperature and sintering time on the properties of Al-Al₂O₃ composites, made by powder metallurgy, *Journal of Materials Processing Technology*, 209, 5387.
- Randal, M.G. 2005 *Powder Metallurgy & Particulate Materials Processing*, Metal Powder Industry.
- Ritasalo, R., Liua, X.W., Söderberg, O., Honkola, A.K., Pitkänen, V. and Hannula, S-P. 2011. The Microstructural Effects on the Mechanical and Thermal Properties of Pulsed Electric Current Sintered Cu-Al₂O₃ Composites, *Procedia Engineering*, 10, 124.
- Tjong, S.C. and K.C Lau. 2000. Tribological behaviour of SiC particle-reinforced copper matrix composites, *Materials Letters*, 43, 274.

Upadhyaya, A. and Upadhyaya, G.S. 1995. 1995. Sintering of copper-alumina composites through blending and mechanical alloying powder metallurgy routes, *Materials & Design*, 16, 41.

Zhan, Y. and Zhang, G. 2003. The effect of interfacial modifying on the mechanical and wear properties of SiC_p/Cu composites, *Materials Letters*, 57, 4583.

USEAGE OF BORIC ACID AS AN ALTERNATIVE ACTIVATING AGENT TO PRODUCE POROUS CARBONS BY MICROWAVE INDUCED CARBONIZATION

Gamzenur ÖZSİN¹, Murat KILIÇ¹, Ersan PÜTÜN², Ayşe Eren PÜTÜN*¹

¹Chemical Engineering Department, Anadolu University, TURKEY

²Materials Science and Engineering Department, Anadolu University, TURKEY

a. Corresponding author: (aeputun@anadolu.edu.tr)

ABSTRACT: Porous carbon materials, especially those containing micropores or mesopores, are extensively being used in important applications such as adsorption and energy storage. Among porous carbons, activated carbon has come into prominence with its unique surface properties for decades. Basically, activated carbon can be produced by carbonization and activation processes which involve the steps of decomposition, evolution of tarry and gaseous products, and finally formation of a solid porous matrix. In recent years, microwave induced production of activated carbon studies draw attention because of the good adsorptive properties of resultant carbon since microwave induced heating processes are different from the conventional ones in the way the heat is generated. There are many studies conducted with different activating agents using microwave activation such as phosphoric acid, potassium hydroxide and potassium carbonate. The objective of this study is to produce of chemically activated carbon from an agricultural waste using boric acid. The novelty of this work arises from using the combination of a new technique as microwave activation and a new activation agent as boric acid to produce activated carbon.

1. INTRODUCTION

Activated carbon is considered as the most commonly used and most effective adsorbent due to its high specific surface area. In recent years activated carbon production via microwave heating has paid attention because the advantages related to decrease production costs.

Microwave induced heating processes are different from the conventional ones in the way the heat is generated. In the microwave heating device, the microwaves supply energy directly to the carbon bed. Energy transfer is not by conduction or convection as in conventional heating, but energy is readily transformed into heat inside the particles by dipole rotation and ionic conduction in the case microwave heating [Yağmur *et al.*, 2008]. As a consequence, bulk temperature of the material rises rapidly and uniformly by microwave

irradiation. Thereby, activated carbon prepared with microwave heating has been introduced as a substitute to conventional heating and has unique pore structure. In addition, both reduction of the processing time and selective heating of raw material and activating agent would lead to a reduction in energy consumption for the activation process [Kubota *et al.*, 2009; Zaini and Kamaruddin, 2013].

In the activated carbon production numerous studies have also been devoted to investigate the effects of several activating agents on pore development. Whereas, a few of chemical agents such as phosphoric acid, zinc chloride, potassium hydroxide has been widely accepted from the feasibility point of view of the production process.

In the presented study, boric acid activation together with microwave

radiation is performed to investigate activating effect of this agent. Because it is well known that boric acid inhibits the release of combustible gases from burning cellulosic materials and is used as flame retardant due to this feature. The primary flame retardant mechanism of boric acid consists of the formation of an impenetrable coating on the solid surface, which traps the volatile pyrolysis products, hinders oxygen diffusion and prevents the propagation of exothermic combustion reactions. Also boric acid is known to increase the amount of char formed upon acid catalyzed dehydration reactions during carbonization [Blasi *et al.*, 2007].

Because of the reasons stated, the objective of this study is to produce of chemically activated carbon from an agricultural waste using boric acid using microwave radiation and is to investigate the effects of different parameters. Besides, the preparation conditions of activated carbon were optimized for the methylene blue adsorption using response surface methodology (RSM). There are several researches carried out for optimization of influential factors on activated carbon production via conventional methods. Whereas there is not enough published work using RSM along with microwave radiation for activated carbon production [Hesas *et al.*, 2013]. Considering the lack of optimization of factors affecting microwave assisted activated carbon production, RSM applied and methylene blue uptake and BET surface areas of the produced activated carbons were evaluated as responses.

2. EXPERIMENTAL

2.1. Preparation of Activated Carbon

The walnut shells were selected as precursors to be experimented, crushed and sieved in order to get a standardized particle dimension prior to carbonization and activation steps (Figure 1).

Ground and sieved walnut shells were treated with boric acid with in different impregnation ratios. The impregnation ratio was calculated as the ratio of the weight of boric acid to the weight of the precursor and varied between 0.25 and 1.25 (wt. / wt.) After mixing of the shells with boric acid and deionized water, microwave treatment were done for 2 to 10 min in order to investigate effects of microwave time and impregnation ratio.

After microwave treatment, carbonization and activation of shells were performed in a fixed bed stainless steel reactor and heated in a furnace to 500 °C under N₂ flow of 100 cm³/min for 1 h. After cooling the resulting activated carbons were then washed by hot distilled water and dried overnight at 105 °C.

The dried products were then kept in tightly closed bottles for subsequent characterization and adsorption experiments.

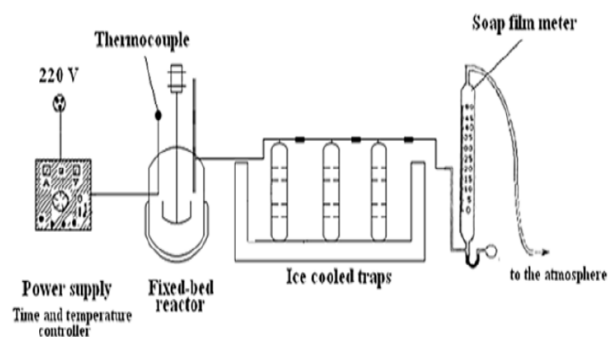


Figure 1: Experimental set-up for carbonization and activation experiments

2.2. Characterization Methods

For observing the thermal behavior of raw walnut shells, thermogravimetric analysis of were performed by a TGA (Seteram Labsys Evo) which performed under N₂ atmosphere with a heating rate of 10 °C/min up to 1000 °C.

N₂ adsorption isotherms of produces were measured using a surface area analyzer (Quantachrome-Autosorb) at 77 K. Samples were outgassed at 200 °C for approximately 6 h to remove any moisture or volatiles within the existing pores of the material. The specific surface area of the samples were then determined from the adsorption isotherm using the multipoint BET (Brunauer, Emmett, and Teller) theory.

2.3. Batch Adsorption Studies

In order to evaluate adsorptive properties of produced carbon, methylene blue (MB) was chosen as a model adsorbate to study in batch adsorption.

MB (Figure 2) is an organic dye which has a heterocyclic aromatic chemical structure with a formula of C₁₆H₁₈N₃ and a molecular weight of 319.85 g/mol. Stock solution of MB were prepared by mixing 1g of the solid with 1 liter of double-distilled water. The stock solution was diluted as required to obtain standard solutions.

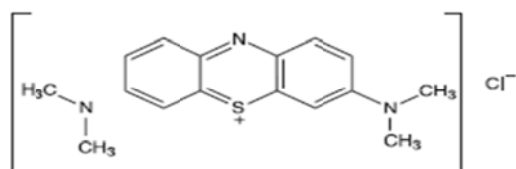


Figure 2: Chemical structure of methylene blue

Adsorption experiments on prepared carbon were conducted using known masses of each sample (0.3 g) mixed with 200 ml of 200 mg/l MB solution. After

the adsorption process, all the samples were filtered and the residual concentrations of methylene blue in the filtrate were found by detecting the absorbance by a double-beam UV-visible spectrophotometer.

The adsorbed MB per unit mass of AC, q_t (mg/g), and % removal of MB were calculated according to:

$$q_t = \frac{(C_i - C_t)}{W} \quad (1)$$

$$Adsorption(\%) = \frac{(C_i - C_e)}{C_i} \quad (2)$$

Response surface methodology (RSM) is then used as an empirical statistical modeling technique to evaluate the effects of microwave time and impregnation ratio on the quantitative data obtained from the methylene blue adsorption experiments.

3. RESULTS AND DISCUSSION

Boric acid impregnated shells were primarily evaluated in terms of methylene blue uptake or in other words the adsorbed MB per unit mass of carbon.

Accordingly, best result was obtained using carbon produced with an impregnation ratio of 1.25 (wt./wt.) and microwave time of 6 min. Maximum % removal and q_e values were obtained as 47.1 % and 62.8 mg/g, respectively. And hence, effect of activation temperature was investigated using 1.25 (wt./wt.) impregnation ratio and 6 min microwave time as constants. It is concluded that increasing activation temperature tend to increase methylene blue adsorption amount and at 700 °C methylene blue adsorption efficiency had reached a maximum value.

Characterization of products revealed the pore formation due to boric acid

activation. According to SEM analysis (Figures 3a-b), products have a porous network with channels. In the micrograph of raw walnut shells' a non-porous, heterogeneous surface is noticeable. On the other hand, the products' BET surface areas exceed $700 \text{ m}^2/\text{g}$ due to boric acid activation.

Moreover, an experimental design was done to study the effects of two variables on activated carbon production: microwave radiation time and impregnation ratio. Through process optimization, methylene blue uptake and BET surface area were evaluated as a model sorbate on the produced carbons and three-dimensional graphics of response surface were interpreted (Figure 4).

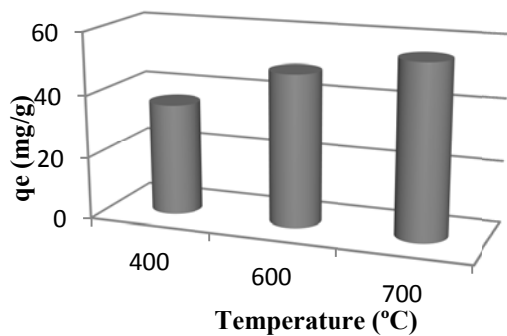


Figure 4: Effect of activation temperature on methylene blue uptake

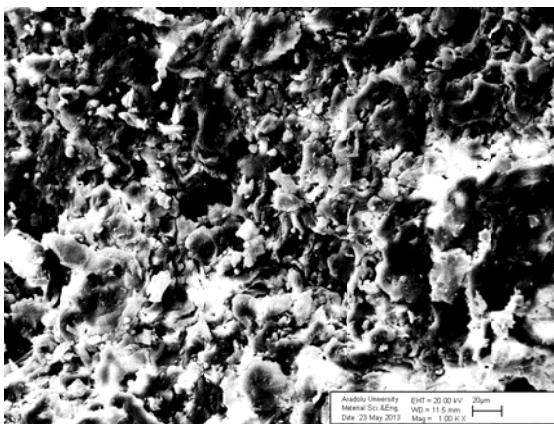


Figure 3a: SEM micrograph of raw walnut shells (1000X)

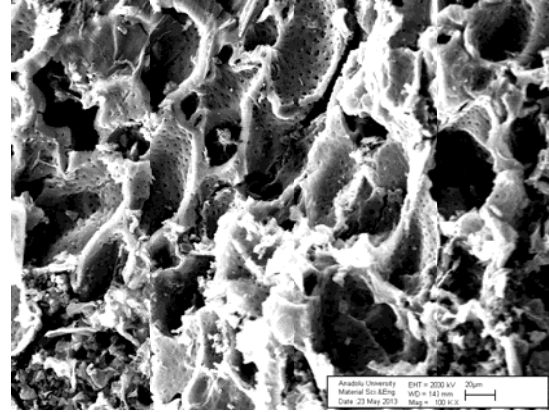


Figure 3b: SEM micrograph of boric acid activated carbon (1000X)

4. CONCLUSIONS

All in all, this study revealed the potential of boric acid as a suitable candidate for activating agent in activated carbon production using microwave activation which needs to be further developed by studying the effects of different production conditions.

REFERENCES

- Blasi, C. D., Branca, C., Galgano, A., 2007, Flame retarding of wood by impregnation with boric acid – Pyrolysis products and char oxidation rates, *Polymer Degradation and Stability*, Volume 92, Issue 5, 752.
- Hesas, R. H., Niya, A. A., Daud, W. M.A.M. , Sahu, J.N., 2013, Preparation of granular activated carbon from oil palm shell by microwave-induced chemical activation: Optimisation using surface response methodology, *Chemical Engineering Research and Design*, Article in Press
- Kubota, M., Hata, A., Matsuda, H., 2009, Preparation of activated carbon from phenolic resin by KOH chemical activation under microwave heating, *Carbon*, Volume 47, 2805.
- Yagmur, E., Ozmak, M., Aktas, Z., 2008, A novel method for production of activated carbon from waste tea by chemical activation with microwave energy, *Fuel*, Volume 87, 3285.
- Zaini, M. A. A., Kamaruddin, M. J., 2013, Critical issues in microwave-assisted activated carbon preparation *Journal of Analytical and Applied Pyrolysis*, Volume 101, 238.

INVESTIGATION ON MANUFACTURABILITY, REPEATABILITY, AND MECHANICAL PROPERTIES OF LIGHTWEIGHT POLYLACTIC ACID BCC-Z CELLULAR LATTICE STRUCTURES FABRICATED BY FUSED DEPOSITION MODELING

M.R Karamooz Ravari^{1,a}, R. Rezaei¹, M. Kadkhodaei¹ and M. Badrossamay¹

1. Department of Mechanical Engineering, Isfahan University of Technology, Isfahan, Iran
a. Corresponding author (m.karamoozravari@me.iut.ac.ir)

ABSTRACT: Cellular lattice structures are of high interest, due to their high strength in combination with low weight, and can be used in various industries such as aerospace and automotive. Besides, if a biocompatible material is utilized, these cellular structures can be employed for load bearing applications in tissue engineering. Accordingly, assessing their manufacturability, repeatability and mechanical properties are very important. In this paper, these issues are investigated for Polylactic Acid as a biocompatible and biodegradable material. A cellular lattice structure with more than 90% porosity is fabricated by fused deposition modeling (FDM) process. To do so, some benchmarks are designed and fabricated to find suitable manufacturing processing parameters as well as the structure dimensions. A number of fabricated cellular lattices are then tested in compression to obtain the force-displacement curves. These curves are very similar to each other with a good resolution indicating the repeatability of the mechanical properties of the manufactured structures. The elastic modulus of the built structure and its load-carrying capacity are found to be about 43 MPa and 150 kg respectively whereas its weight is about 5.2 gr. Accordingly, this paper suggests a method to fabricate strong and lightweight cellular lattice structures with a laboratory low cost FDM machine.

1. INTRODUCTION

Cellular lattice structures (CLS) have been receiving considerable attention for few decades due to their significant benefits over dense materials including high strength accompanied by relatively low mass, and highly porous internal structure [Gumruk *et al.*, 2013]. CLS are extensively used in various engineering and medical application areas such as energy absorbers, packaging, automotive parts, scaffold in tissue engineering, heat exchanger, heat transfer, sound and thermal insulation [Kooistra *et al.*, 2007; Wadley *et al.*, 2007; Babaei *et al.*, 2012; Yan *et al.*, 2012; Gumruk *et al.*, 2013].

Nowadays, additive manufacturing (AM) processes allows to obtain innovative parts with complex geometries directly from three-dimensional computer aided design (3D CAD) models [Sun *et al.*,

1996; Yan *et al.*, 2012; Cerardi *et al.*, 2013]. In addition, these techniques can be used to fabricate prototypes as well as end-use parts having acceptable mechanical properties and geometrical details [Yan *et al.*, 2012; Cerardi *et al.*, 2013]. Consequently AM processes have been applied to fabricate lightweight and strong porous structures which are of interest in several industries [Murat tekin, 2009; Cerardi *et al.*, 2013].

Kooistra *et al.* [2004] fabricated lattice structures using perforated aluminum alloy sheets and carried out some experimental compression tests. A number of Ti6AL4V scaffolds were fabricated through selective laser melting (SLM) and characterized mechanically and geometrically to investigate their repeatability [Bael *et al.*, 2006]. Kooistra *et al.* [2007] introduced a new method to

use sheet material in making lattice structures efficiently. Wadley and Queheillalt [Wadley *et al.*, 2007] investigated hollow truss structures to improve the mechanical strength as well as the efficiency of heat transfer capability. To assess the influence of processing parameters on the mechanical properties of lattice structures, Tsopanos *et al.* [Tsopanos *et al.*, 2010] fabricated BCC micro-lattice structures using SLM and reported the stress-strain curve of the micro struts. These curves were calibrated using finite element simulations. Three different cellular core types, fabricated in the University of Liverpool, were investigated by Labeas and Sunaric [Labeas *et al.*, 2010]. A methodology was also developed to predict mechanical properties and deformation behavior of the structure using finite element method. The obtained results were compared with experimental measurements [Tsopanos *et al.*, 2010]. The influence of unit cell size on the possibility of manufacturing and mechanical properties of lattice structures fabricated by SLM were investigated by Yan *et al.* [Yan *et al.*, 2012]. Ceradi *et al.* [2013] derived a correlation between yield strength and relative density of parts fabricated by selective laser sintering (SLS) process. Gumruk and Mines [2013] investigated mechanical properties of stainless steel lattice structures fabricated by SLM process.

The catastrophic failure of space shuttle Columbia on February 1, 2003, shows that the manufacturability of cellular materials is very important [Altenbach *et al.*, 2010]. One of the most important issues, which can affect the manufacturability, is the complex internal structure of lattice structures. Such complexity may cause the need of support structures to prevent overhanging and deformation. Removing these

temporary structures are very difficult and time-consuming [Yan *et al.*, 2012]. Accordingly, it is very important to investigate limitations of the process before designing and fabricating parts [Santorinaios *et al.*, 2006].

In this study, the manufacturability and repeatability of a biocompatible and biodegradable material, Polylactic Acid, BCC-Z cellular lattice structures fabricated by fused deposition modeling (FDM), an extrusion-based AM processes, are investigated. Initially, some benchmarks are designed to obtain the minimum value of strut diameter, diagonal struts angles and fabrication speed. Based on the findings of benchmark studies, a number of BCC-Z CLS's are then fabricated and tested in mechanical compression to assess their repeatability. The results show that these specimens have almost the same stress-strain curves.

The fabricated CLS is capable of carrying about 150 kg compressive load at its ultimate point while its weight is about 5.2 gr. So, this paper presents a lightweight structure with a high load-to-weight ratio which can be manufactured with a low cost process. Such a lattice structure can be used in sandwich panels for aerospace and automotive industries.

2. MATERIALS AND METHODS

2.1. Specimen Design and Fabrication

To evaluate the manufacturability of FDM for fabrication of Polylactic Acid CLS, first a BCC-Z lattice structure is modeled. This structure is used to have a good performance due to vertical struts which enable the structure to carry higher loads [Smith *et al.*, 2013]. The structure is generated through ABAQUS 6.11-1 software using a set of vertexes and connections among which (

Figure 1). It should be noted that, in this model, no diameter has been assigned to the struts and the appropriate diameter will be found in the following steps.

Generally a BCC-Z CLS is defined by the strut distances, angle of diagonal struts, diameter of the struts, and the whole structure height. Its manufacturability, however, depends on the strut distances, diameter of the struts, and angle of diagonal struts.

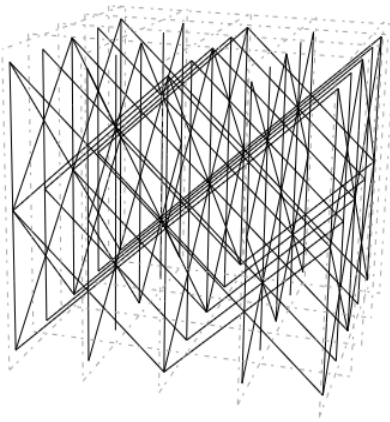


Figure 1: The lattice cellular structure designed in ABAQUS.

RAPMAN 3.2 FDM machine, a low-cost laboratory desktop AM apparatus, with 5 mm Polylactic Acid polymer filament is used to fabricate the CLS. The processing parameters used in this study are as follows: the layer thickness is 0.125 millimeter; the maximum extrusion temperature for material is 195°C, and the laboratory temperature is about 25 °C.

Considering the model presented in Figure 1, three types of benchmarks are designed and fabricated with FDM. The first benchmark is designed to obtain a suitable diameter for vertical struts. It contains six columns of struts whose diameters are 1.5, 2, 2.5, and 3 millimeters (Figure 2 (a)). The second benchmark is designed to find the achievable strut diameter and corresponding angle for diagonal struts.

Four columns of struts with the angles of 35, 40, 45, and 50 degrees respect to the horizontal axis were fabricated (Figure 2 (b)) for each strut diameter obtained using the first benchmark. Accordingly, proper angle and diameter are determined using these two benchmarks.

The fast movement of the machine nozzle may cause severe vibration leading to difficulties during the fabrication. Another benchmark is designed to find suitable parameters in which the effects of vibration are negligible. This benchmark has two unit cells with the obtained dimensions as illustrated in Figure 2 (c).

A plate is designed under the benchmarks as well as the CLS to repel the poor base attachment of the struts and the raft (Two layers fabricated by FDM under the part that allows the operator to separate it from the base plate of the machine). Although fabrication of less inclined struts is easier, fabrication time increases by increasing in the total height of the structure. Since the FDM machine is designed for laboratorial purposes, it is necessary to consider the overall built time of the test parts. As result, it is preferable to design the diagonal struts with the minimum possible angle, because the higher strut's angle causes higher structure's height.

Figure 3 shows the final version of the structure with the finalized dimensions obtained based on the benchmarks outputs. The final STL file is generated through Autodesk Inventor Professional 2012 commercial software. This file is then used as the input file of AXON 2.0 for generating the G-CODE to be used by the FDM machine.

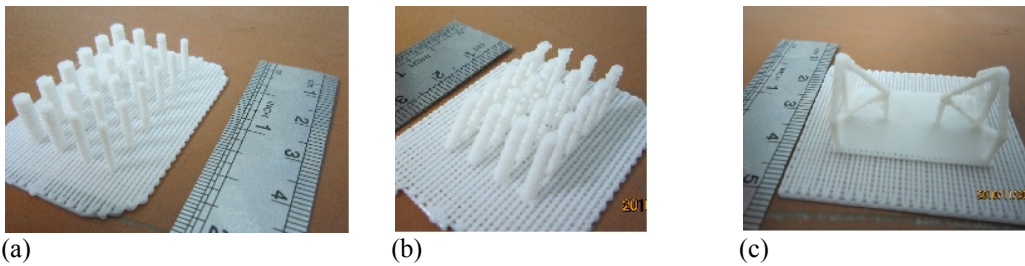


Figure 2: Three designed benchmarks to obtain a) the minimum diameter, b) the minimum angle of struts, and c) the processing parameters

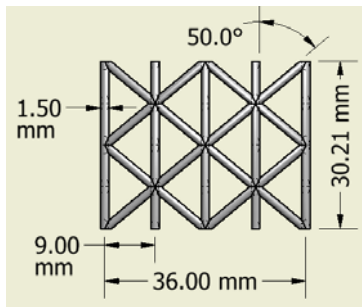


Figure 3: The dimensions of the final version of the cellular lattice structure

Three specimens with the dimensions of $36 \times 36 \times 30.21 \text{ mm}^3$ are built on the base plate and then are cut off from the base plate using a removal tool.

Figure 4 depicts one of the final fabricated CLS's.



Figure 4: Cellular lattice structures fabricated by the FDM.

2.2. Mechanical Characterization

The capacity of carrying the mechanical compression loads is the most promising characteristics of the cellular structures.

So, the compression tests are carried out to obtain the stress- strain curves of the CLS's. The measurements are carried out on a tension and compression test machine (SANTAM, STM-50). The first CLS is tested with the strain rate of about $10^{-4} \text{ (S}^{-1}\text{)}$. But the deformation is localized near the moving platen indicating that the loading on the structure is dynamic. So, the velocity of the upper platen should be decreased. For other specimens the strain rate has been reduced to $10^{-5} \text{ (S}^{-1}\text{)}$ and a more uniform deformation in the struts of the structure is observed meaning that the loading is quasi-static. The compression tests are carried out using this value of strain rate for all specimens, and the average stress-strain curve is reported.

3. RESULTS AND DISCUSSION

3.1. Mechanical Properties

The CLS specimens are compressed at $\dot{\epsilon} = 10^{-5} \text{ 1/s}$. The force- displacement of the structure (not presented here) shows the load carrying capacity of the structure is about 150 kg, which is impressive compared to the weight of the fabricated CLS that is about 5.2 gr.

Figure 5 shows the stress- strain curve of the CLS. The stress is calculated by dividing the applied force to the area parallel to the loading direction, and the strain is calculated by dividing the deformation of the CLS in the loading direction by the CLS's height.

As the obtained curves are nonlinear even in small strains, the method presented in ASTM D695 which is suitable for elastomeric foams with high nonlinear stress- strain curves is used [Kinney *et al.*, 2001]. In this method, a piecewise polynomial is fitted to the stress-strain curves. Then the maximum value of the derivative of the polynomial is assumed to be the Young's modulus. Using the above-mentioned method, the elastic modulus is calculated to be about $E_{CLS}=43.07\pm 0.13$ MPa.

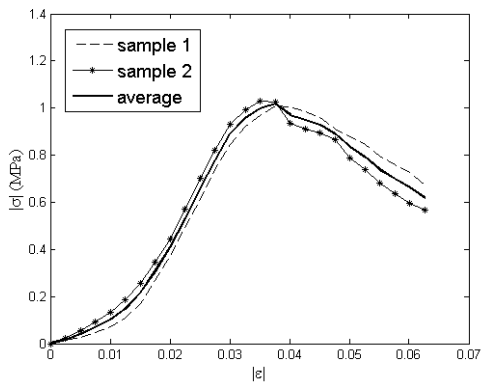


Figure 5: Stress- strain curve of the CLS

3.2. Porosity Measurement

The CLS porosity is measured using the Archimedes' principle [Yan *et al.*, 2012]. In this paper, one specimen is used to measure the porosity. This specimen is tested three times and the average value of the porosity is obtained to be about 90% while the CAD model predicts the amount of 92.68%.

4. CONCLUSIONS

In this study, the manufacturability and repeatability of polyamide BCC-Z CLS's fabricated by FDM is investigated. To do so, some benchmarks are designed to obtain the suitable value of strut diameter, diagonal struts angles and fabrication speed. Three BCC-Z CLS's are fabricated using the results of the benchmarks. The mechanical compression test is performed on CLS's

and the stress- strain curves are obtained. The results show that these specimens have almost the same stress- strain curves which illustrate the repeatability of the fabrication process. Furthermore, the elastic modulus is calculated using the method presented for elastomeric foams to be about 43.07 MPa.

The force- displacement curve shows the fabricated CLS is capable of carrying about 150 kg while its weight is about 5gr as well. So, this paper suggests a method to fabricate strong and lightweight cellular lattice structures with a laboratory low cost FDM machine.

REFERENCES

- Altenbach, Holm and Andreas Öchsner 2010. Cellular and Porous Materials in Structures and Processes. NewYork, Springer,Wien, NewYork.
- Babae, Sahab, Babak Haghpanah Jahromi, et al. 2012. Mechanical Properties of Open-Cell Rhombic Dodecahedron Cellular Structures. Acta Materialia, (60(6-7)), 2873.
- Bael, Simon Van, Ben Vandenbroucke, et al. 2006. Design and Production of Bone Scaffolds with Selective Laser Melting.
- Cerardi, A., M. Caneri, et al. 2013. Mechanical Characterization of Polyamide Cellular Structures Fabricated Using Selective Laser Sintering Technologies. Materials & Design, 46, 910.
- Gumruk, R and Mines RAW, 2013. Compressive Behaviour of Stainless Steel Micro-Lattice Structures. International Journal of Mechanical Sciences.
- Kinney, J.H. and et al., 2001. Three-Dimensional Imaging of Large Compressive Deformations in Elastomeric Foams. Journal of Applied Polymer Science, (80), 1746.
- Kooistra, G., 2004. Compressive Behavior of Age Hardenable Tetrahedral Lattice Truss Structures Made from Aluminium. Acta Materialia 52(14), 4229.
- Kooistra, Gregory W. and Haydn N. Wadley G., 2007. Lattice Truss Structures from Expanded Metal Sheet. Materials & Design, (28), 507.
- Labeas, G. N. and Sunaric M. M., 2010. Investigation on the Static Response and Failure Process of Metallic Open Lattice Cellular Structures. Strain, (46), 195.
- Murat tekin, Cevdet 2009. Mechanical Characterization and Modeling of Porous

- Polymeric Materials Manufactured by Selective Laser Sintering. Master of science, Middle East Technical University.
- Santorinaios, M., W. Brooks, et al. 2006. Crush Behaviour of Open Cellular Lattice Structures Manufactured Using Selective Laser Melting. (1), 481.
- Smith, M., Z. Guan, et al. 2013. Finite Element Modelling of the Compressive Response of Lattice Structures Manufactured Using the Selective Laser Melting Technique. International Journal of Mechanical Sciences.
- Sun, C. and R. Vaidya 1996. Prediction of Composite Properties from a Representative Volume Elemen. Composites Science and Technology, (56), 171.
- Tsopanos, S. , R. A. W. Mines, et al. 2010. The Influence of Processing Parameters on the Mechanical Properties of Selectively Laser Melted Stainless Steel Microlattice Structures. Journal of Manufacturing Science and Engineering, (132), 041011.
- Wadley, Haydn N. G. and Douglas T. Queheillalt 2007. Thermal Applications of Cellular Lattice Structures Materials Science, (539).
- Yan, Chunze, Liang Hao, et al. 2012. Evaluations of Cellular Lattice Structures Manufactured Using Selective Laser Melting. International Journal of Machine Tools and Manufacture, (62), 32.

ELECTRO CERAMIC COMPOSITIONS WITH THE IMPROVED PROPERTIES ON THE BASIS OF LOCAL MINERAL RAW MATERIAL

Raisa Abdullaeva¹, Soyibjon Negmatov¹, Vasila Tulyaganova¹, Surayo Yulchieva¹, Djura Islamov¹

1. GUP "Science and Progress" Under Toshkent State Technical University,
a. Corresponding author: (polycomft2005@rambler.ru)

ABSTRACT: The present research work is devoted to study of structures, properties of mineral raw materials, development of structure and technology of reception magnesium containing of electro ceramic materials on their basis. With the purpose of development of structure steatite, forsterite, cordierite of electro ceramics on the basis of local mineral raw materials.

On the basis of raw materials kaolin, bentonite, talk, burnt talk, kuartzcontaining of a withdrawal (waste) the structure steatite of ceramics is developed. By researches is established, that samples steatite of ceramics burnt at optimum temperature have dense fine-grained structure. The basic crystal phase is metacilikate magnesium ($MgO \cdot SiO_2$) his (its) contents makes 50-55 %, besides structure of a researched material contains quartz, kristobalite, forsterite and some grains mullite, and about 30-35% glassy a phase.

Established, that the received material has dense, homogeneous structure, contained 80-82 of % forsterite ($2MgO \cdot SiO_2$) size of grains 1-18 microns, $N_g = 1,668$; $N_p = 1,636$, glassy a phase 10-18 % and magnesium met silicate, quartz, mullite in insignificant quantity. Besides on a basis kaolin, bentonite, pegmatite, aluminum and quartz we develop a high-voltage electro ceramic material on which properties meets the requirements the standard

1. OBJECT AND METHODS OF THE STUDY

As object of the study us are chose talc Sultanuizdagskogo, kaolin Angrenskogo, bentonite Kattakurganskogo, Leykokrato granitest Ingichkinskogo field, quartzcontained departure. At study characteristic experienced masses others and sample used the traditional methods physico-chemical analysis chemical, petrografical, rengenografichesky, electronic-microscopic, differential-termal, accounting and others.

Petrograficheskoe study were executed

on polarization microscope on sample in the manner of transparent sections and powder by way to immersions.

Rentgenofazovyy analysis conducted on diffraction-metre Dron-4 with copper radiation and nickel filter. Termograficheskoe study were conducted on hungarian derivatograf Erdey-Poulik. Electronic-microscopic analysis were conducted electronic-microscope "Emma-4".

2. RESULTS OF RESEARCHES AND THEIR DISCUSSION

The present research work is devoted to study of structures, properties of mineral raw materials, development of structure and technology of reception magnesium containing of electro ceramic materials on their basis.

Chemical-mineralogical composition, property, the physic-chemical processes occurring at firing of mineral raw materials investigated comprehensively. In the table №1 the chemical structures of raw materials are given. The purpose of the present work was the development of structure magnesium containing electro ceramic materials on a basis of the above given raw materials.

Table 1 The chemical composition of raw materials

Naimeno va-set of indicators	Oxide content, %										
	SiO ₂	Al ₂ O ₃	Fe ₂ O ₃	CaO	MgO	Na ₂ O	K ₂ O	P ₂ O ₃	nnn	Ti O ₂	SO ₃
Angren kaolin	51,0	35,7	0,28	0,44	0,14	0,12	0,24	-	11,85	-	-
Kattakurg an-sky bentonite	59,6 3	17,6 0	3,68	0,69	1,9	1,44	1,92	0,1 1	12,01	0,9 0	-
Talc	38,0 6	7,69	7,95	4,2	27,35	0,57	0,18	-	13,03	Сл. .	Сл.
Quartz- bearing waste	81,4 0	13,7 6	1,68	1,42	1,25	0,34	0,15	-	0,23	-	0,24
Leykokrat o granitest	73,3	12,0 8	0,71	2,2	0,36	3,26	4,25	-	3,18	-	0,01 4
Dolomite deposits of the "Sypko"	36,8	-	0,98	19,6	16,0	0,01	0,01	-	27,18	0,0 1	-
Glinozem so- containin g waste	0,37	85,9 5	0,07	1,53	0,64	Сл.	Сл.	-	11,56	Сл. .	1,48

With the purpose of the decision of the put task we were based on known of literary data the diagram of a condition 3 component of system MgO-Al₂O₃- SiO₂.

With the purpose of development of structure steatite, forsterite, cordierite of electro ceramics on the basis of local mineral raw materials, were based on their chemical structures, hoped it structures in the field of concerning steatite, forsterite, cordierite of materials.

On the basis of raw materials kaoline, bentonite, talk, burnt talc, quarts containing of a withdrawal(waste) the structure steatite of ceramics is developed. The skilled weights and samples from them are prepared, the ceramico- technological properties of the dried up and burnt samples are investigated, which results are given in table 2. As is known from the table 3, molding the humidity of weight makes

20-21 %, the firing shrinkage 9,6-9,8 %.
On the ceramic - technological properties

samples from weight M-4, M-5, M-6 differ.

Table 2. Ceramic-technological properties of prototypes soapstone electro ceramics

Naimenovaset of indicators	Ед.изм.	M ₁	M ₂	M ₃	M ₄	M ₅	M ₆	M ₇
Humidity	%	20	21	20	20	21	21	21
Air shrinkage at 105-110 ⁰ S	%	13,2	13,0	13,6	13,7	13,5	13,7	13,8
The firing shrinkage	%	9,6	9,7	9,5	9,8	9,8	9,9	9,8
Flexural	МПа	194	182	186	190	192	194	182
Water absorption	%	0,012	0,023	0,016	0,009	0,012	0,016	0,014
Bulk density	г/см ³	2,60	2,62	2,62	2,63	2,65	2,66	2,60
Density	г/см ³	2,82	2,83	2,84	2,86	2,86	2,86	2,84
The dielectric loss 20 ⁰ S	·10 ⁴	22	23	19	218	20	21	19
Specific volume electric resistance	·10 ¹³ ОМ·см	6,2	6,1	6,3	6,2	6,5	7,0	6,4
Dielectric strength	кВ/мм	41	40	39	38	39	40	38
Resistance to thermal shock	⁰ C	130	129	128	131	125	124	129

Dielectrically of property steatite of materials depends on many factors. Is established, with increase of temperature обжига the specific volumetric electrical resistance decreases, that with increase of temperature the specific volumetric electrical resistance of a material decreases, that these properties are increased with increase of temperature and decrease with increase of frequency of a current.

Operational properties electro ceramics of materials depends on their phase structure, therefore skilled samples were exposed petrograficheskyy, rengenograficheskyy, and differentially -thermal analyses. By researches is established, that samples steatite of ceramics burnt at optimum temperature have dense fine grained structure. The basic crystal phase is met silicate magnesium

(MgO SiO₂) his(its) contents makes 50-55 %, besides structure of a researched material contains quartz, kristobalite, forsterit and

some grains mullite, and about 30-35 % glassy phase. Contained metasilicate magnesium gives steatite to ceramics high durability and low dielectrical of loss.

From the references it is known, that metasilicate magnezium has polymorphic transformations, and there are 3 updatings: protoenstatite, klinoenstatite and ensttite. At researched samples metasilicate magnezium is present as protoenstatite by the size of grains 2-6мкм, with a parameter of refraction N=1,520.

In the table 1 are given settlement chemical structure of skilled samples steatite of ceramics. On the basis of the received results is developed the following technological

circuit of reception steatite of electro ceramics.

In the second part of research the basic purpose was the development forsterite of

electro ceramics on a basis kaoline, bentonite, talk, magnezite.

In the table 3 the ceramic-technological properties of skilled samples forsterite of electro ceramics are given.

Table 3 Ceramic-technological properties of prototypes forsterite electro ceramics

Naimenova-set of indicators	Ед.изм.	Φ-1	Φ-2	Φ-3	Φ-4	Φ-5	Φ-6	Φ-7
Humidity	%	20	20	21	21	20	20	20
Air shrinkage	%	13,5	12,2	12,0	12,6	12,7	12,5	12,4
The firing shrinkage	%	10,6	10,7	10,5	10,8	10,8	9,9	9,8
Flexural	МПа	204	202	200	190	192	179	174
Water absorption	%	0,017	0,028	0,018	0,005	0,006	0,012	0,016
Bulk density	г/см ³	2,90	2,95	2,96	2,96	2,98	3,0	3,0
Density	г/см ³	2,92	2,92	2,89	2,94	2,92	2,86	2,86
Dielectric loss tangent	10 ⁴	2,3	2,2	2,0	2,1	2,1	2,0	2,0
Permittivity		5,6	5,4	5,8	6,2	6,8	6,9	6,9
Specific volume el.soprotivlenie	·10 ¹³ ом·см	4	6	5	8	9	10	12
Dielectric strength	кВ/мм	34	34	35	36	37	39	40
Thermal coefficient of linear expansion of 10 ⁻⁶	°C ⁻¹	7,4	7,6	7,7	7,8	7,7	7,8	7,9

Established that by high parameters ceramic - technological and dielectrically of properties samples from weight Φ-4, Φ-5, Φ-6 have.

The results of the differentially - thermal analysis have shown, that on ДТА of curve weight Φ-5, at heating at temperature 125-175⁰C is observed weak endothermic effect, it is connected to removal (distance) hygroscopic of a moisture, thus occurs losses of weight of weight, and exothermically of effect is not observed.

Phase structure forsterite electro ceramics were investigated petrografical and rengenografichesky by methods of the analyses, as a result of which is established, that the received material has dense, homogeneous structure, contained

80-82 of % forsterite (2 MgO SiO₂) size of

grains 1-18 microns, Ng =1,668; Np=1,636, glassy phase 10-18 % and metasilicate magnezium, quartz, mullite in insignificant quantity (amount).

In the third part of researches the works till development of structure and technology of reception cordierite of electro ceramics with use of local raw material are carried out (spent). Cordierite ceramics use basically for manufacturing details high- voltage of switches with magnetic blast, high-voltage air of switches, low-voltage equipment etc.

Cordierite the ceramics has low meaning (importance) ТКЖП, therefore is widely

applied as a heat-resistant element. To raw materials for cordierite of electro ceramics it is required the rigid requirements concerning stability, uniformity of structure and their cleanliness. Taking into account these requirements as initial raw material have chosen: kaoline, bentonite, talk,

cremnizium containing a withdrawal(waste) of an industry, leykokrato granitest.

In the table 4 are given ceramic-technological of property of skilled samples cordierite of electro ceramics.

Table 4: Ceramic-technological properties of prototypes cordierite electro ceramics

Naimenovas et of indicators	Name of mass										
	ЕД из м	K-1	K-2	K-3	K-4	K-5	K-11	K-12	K-13	K-14	K-15
density	г/с м ³	2,25	2,30	2,32	2,33	2,32	2,32	2,34	2,31	2,30	2,28
humidity	%	5,81	6,21	6,16	6,09	6,03	7,95	7,78	7,01	7,89	7,93
Water absorption	%	15,46	15,3	15,3	15,3	15,5	16,1	14,8	12,8	9,60	15,6
Total shrinkage	М Па	85,8	83,8	80,8	79,9	72,9	89,7	88,6	81,2	78,4	73,3
porosity	%	11,5	11,8	12,0	12,5	12,2	11,7	11,3	12,2	12,4	12,2
Flexural	⁰ С	550	525	565	570	580	595	610	605	610	614
Thermal coefficient of linear expansion of 10 ⁻⁶	⁰ С	3,0	2,8	3,1	2,7	2,9	3,0	3,1	3,2	3,3	3,4
Dielectric strength	кВ/мм	14,3	14,2	14,6	15,5	14,8	15,2	15,6	15,5	15,4	15,3
Resistance to thermal shock		23	22	24	23	24	20	21	20	22	22
Specific volume el. soprotivlenie	·10 ¹³ Ом·см	5,1	4,5	6	5,4	5,8	6,2	6,4	6,8	6,6	6,9
Dielectric strength		6,8	6,5	6,4	7,0	6,9	7,1	7,2	6,9	6,8	7,1

As it is visible from the table 4, the application 4 % bentonite in structure of skilled weights in exchange 18 %-fire-resistant clays is provided sufficient plasticity and dried samples have sufficient mechanical durability. The high plasticity of weight facilitates process molding of large-sized products. Dried and burnt samples on ceramic -technological and dielectrical to properties meet the requirements the standard.

The analysis of the received results show, that skilled samples have low Water absorption, high density and mechanical durability at temperature 1200- 13000C, the maximal meanings(importance) dielectrical of properties have samples burnt at 13000C. Is established, that skilled samples from weight K-1, K-2, To - 11, To - 12 have high parameters of properties and optimum temperature burnt 1200-1300⁰ C.

Phase structure of burnt skilled samples were defined (determined) petrografichesky and rengenografichesky by the analyses.

Samples burnt at 1200⁰C have non-uniform, coarse-grained structure, the plenty pores contains. In structure contain metakaolinit, metatalk (Ng =1,575; Np=1,540), quartz with Ne = 1,552; No= 1,540, oxide calcium and magnezium. Oxide calcium and magnezium is formed at the expense of disintegration dolomite.

Samples burnt at 1250⁰C have non-uniform grained, porous structure. Structure contains glassy phase, grains mullite by the size 2- 3 мкм, quartz by the size 25-35мкм, cordierite in small quantity(amount).

Cordierite has 2 updatings: high-temperature - and low-temperature The form. In researched samples cordierite has. The form with Ng =1,524; Np=1,528; grains of quartz Ne =1,552; No=1,540 at high temperature passes in α - kristobalite.

At temperature 1250⁰C magnezium oxide it is not revealed, they joining with metasilicate magnesium is spent for formation (education) cordierite.

Samples burnt at temperature 1300⁰C have grained non-uniform structure, decreased pores, 50-55 % cordierite by the size 1- 2мкм (Np=1,528) contains, seldom meet metasilicate magnesium, also quartz, kristobalite, glassy phase.

Besides on a basis kaolin, bentonite, pegmatite, aluminum and quartz we develop a high-voltage electro ceramic material on which properties meets the requirements the standard.

By research is established, what skilled samples burnt at temperature 1250⁰C contain in the structure. Quartz, kristobalite, mullite. The contents of quartz decreased, crystal lattice feldspar disruption.

In samples burnt at 1300⁰C the part of quartz passed in kristobalite (d = 0,314; 0,243), quantity(amount) mullite were increased, i.e. intensity of peaks mullite were increased.

In samples burnt at temperatures 1350⁰C the quantities (amount) of quartz decreased at the expense of transition in kristobalite, the quantities (amount) mullite were increased.

3. CONCLUSIONS

Thus, on the basis of the carried out (spent) researches it is possible to make the following conclusions:

tg δ by increase of temperature up to 300⁰C grows slowly, is higher 300⁰C grows by the accelerated rates;

- Dielectric the permeability of skilled samples is increased of directly proportional dependence on temperature:

- With increase of the contents of clay materials in structure of weight,

decreases $\tan\delta$. At the expense of increase of the contents alkaline oxide:

- The specific volumetric electro resistance decreases with increase of temperature:

- Dialectical the permeability decreases with increase of frequency of an electrical current up to certain temperature, then is increased:

- The structure and technology of reception steatite, forsterite, cordierite of electro ceramics is developed on the basis of local raw material:

- Skilled samples of the created electro ceramic materials on the properties answer the requirements of the standard:

- The created technology of reception of electro ceramic materials gives economic benefit at the expense of decrease (reduction) of temperature burnt.

REFERENCES

- Abdullaeva, R.I., Negmatov, S.S., Abdullaev, G.Z., Isroilova, G.B., Tulaganova, V.S., Yulchieva, S.B., A Pushes contion electroceramical compositions with high properties, Gourn of "Compozite materials" 2005 g, №1 page-7-8.
- Moroz, T.H., Maslennikova G.W., Termicheskie prevpasheniya kremnezyoma, Gourn "Steklo and ceramica", 1985, №2 c 21-23

SYNTHESIS OF MANDELIC ACID FROM BENZALDEHYDE USING THIRD-LIQUID PHASE SYSTEM WITH IMMOBILIZED PEG PHASE TRANSFER CATALYZED UNDER ULTRASONIC IRRADIATION COMBINATION

Elif Ödeş AKBAY^{1a}, Nilüfer ÖZ², Didar YAZHANOV³

1. Anadolu University, Dept. of Chemical Engineering, Eskişehir, Turkey

2. Anadolu University, Dept. of Chemical Engineering, Eskişehir, Turkey

3. Anadolu University, Dept. of Chemical Engineering, Eskişehir, Turkey

a. Corresponding author (eodes@anadolu.edu.tr)

ABSTRACT: Mandelic acid has cosmetic, pharmaceutical, and antibacterial activities and is used in urinary antiseptic medicines. The present work focuses on synthesis of mandelic acid by L–L–L PTC reaction of chloroform with benzaldehyde in the presence of PEG and PEG supported with silica gel. The effects of parameters such as amount of PTC and sodium hydroxide, temperature, without and with ultrasonic irradiation and stirring combinations, reactant mole ratio on the reaction rate will be study.

1. INTRODUCTION

Phase transfer catalysis (PTC) has been used in more processes, particularly as liquid–liquid (L–L) and solid–liquid (S–L) systems for the past 40 years. However, only recently the importance of liquid–liquid–liquid (L–L–L) PTC has been demonstrated as a powerful method in the relation to biphasic PTC in commercially relevant reactions. The conversion of L–L PTC into L–L–L PTC gives several benefits. [1]

In L–L–L PTC, the middle phase is the catalyst-rich phase which is the main locale of the reaction into which both aqueous and organic phase reagents are transferred from the two interfaces. A typical L–L–L PTC consists of an organic phase dispersed as spherical drops, surrounded by a thin film of catalyst phase, within an aqueous continuous phase. There could be another situation where the inner phase is aqueous and the outer phase organic depending on density difference. The reaction rate depends on the concentration of the reacting species in the organic droplet and in the catalyst film at the middle at any instant of

consideration. L–L–L PTC facilitates easier recovery and reuse of the catalyst-rich phase, enhancement in reaction rate, improvement in selectivity, and also reuse of the aqueous phase, leading to considerable reduction of waste and overall process intensification. [1]

The current work focuses on the production of mandelic acid by L–L–L PTC reaction of dichlorocarbene with benzaldehyde. Dichlorocarbene is generated in situ by the reaction of chloroform and sodium hydroxide in the presence of poly ethylene glycol (PEG) as the catalyst. Mandelic acid is an important ingredient in urinary antiseptic medicines. Further, its cosmeceutical and antibacterial properties make it a product of considerable commercial significance. PEGs and their derivatives have been extensively used as phase transfer agents. PEG is very cheap, non-toxic and easily biodegradable. PEGs are also more stable at higher temperature and show higher stability to acidic and basic conditions than quaternary onium salts. [2,3]

2. EXPERIMENTALS

2.1. Materials

Benzaldehyde, chloroform, hexane, m-xylene, benzene, sodium hydroxide, and hydrochloric acid (37%) and PEG 800, 1000, 4000 and 6000 were obtained from Sigma-Aldrich Chemie, Turkey.

Synthesis of mandelic acid using L-L-L PTC was studied in a spherical jacketed glass batch reactor with a 500 cm³ total capacity and 5 cm inner diameter. Typical runs were conducted at 55°C with organic phase (0.025 mole benzaldehyde, 0.05 mole chloroform, 10 µL m-xylene as internal standard dissolved in hexane to make the volume of organic phase to 50 cm³) and aqueous phase (0.4 mole sodium hydroxide dissolved in water to make up volume of aqueous phase to 50 cm³) with 0.00175 mole PEG as the catalyst.

Firstly, the sodium hydroxide solution was heated to 55°C with a stirring and then the PEG and organic phase added to the reactor respectively. The reactor was equipped with atmosphere opened condenser and magnetically stirrer stick. Typically the reaction was carried out at 55°C and under atmospheric pressure for 90 minute, after that the organic phase was removed from aqueous phase and catalyst-rich middle phase. The reaction was continued another 2 hours between catalyst rich phase and aqueous phase which was improve the selectivity of the mandelic acid. The last procedure was done because the conversion of α -chloro acid to a mandelic acid was slow.

The product mandelic acid appeared in the aqueous phase as sodium salt of mandelic acid. The aqueous phase neutralized with 5N HCl solution and evaporated at 60°C under vacuum through the overnight. Then the solid mixture of mandelic acid was extracted from NaCl with hot benzene. The mandelic acid is separated from the ammonium chloride by extraction with hot benzene.

This was best done by dividing the solid mixture into four approximately equal parts. One of these portions was placed in a flask with 400 cm³ of boiling benzene. After a few minutes the hot benzene solution was decanted through a suction funnel. The filtrate was cooled in an ice bath and the mandelic acid that crystallizes was filtered with suction. The benzene is returned to the extraction flask containing the residue from the first extraction, and a new portion of the sodium chloride-mandelic acid mixture was added and extracted as before. The process was repeated until the mandelic acid is completely removed from the sodium chloride.

After the product purification, mandelic acid analysis with NMR. Spectrum is shown in Figure 3.1. Mandelic acid MNR spectrum is very similar to the literature spectrum [5]. These procedures were done for each of PEGs (PEG 600, 1000, 4000, 6000) and for immobilized PEG 4000 with silica gel.

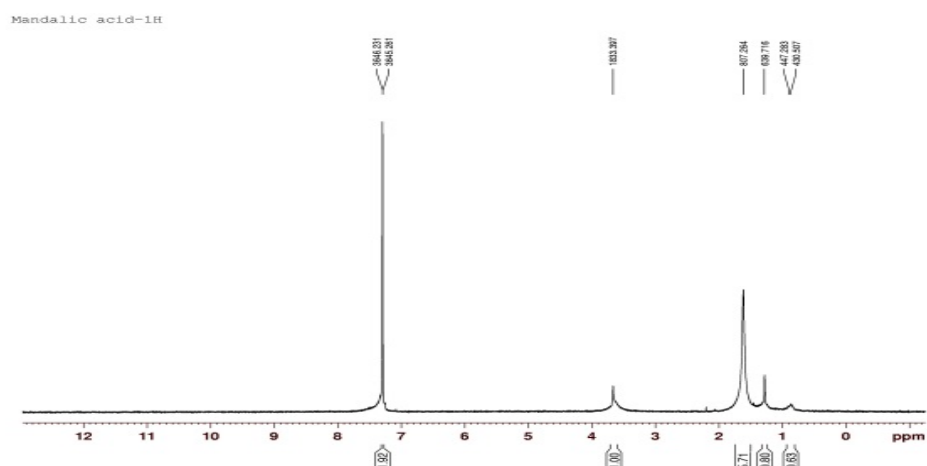


Figure 1: Mandelic Acid NMR spectrum

2.2. Synthesis of Silica gel supported PEG

Silica gel was activated by treatment with HCl (5N) and dried in vacuum at 120°C. PEG was heated at 80°C under vacuum for 30 min before use to remove traces of moisture.

An oven dried 250 mL flask equipped with a magnetic stirrer is charged with dried activated silica gel (20g) under nitrogen atmosphere. Then freshly distilled SOCl₂ (45 mL) was added slowly to the flask through an addition funnel and the reaction mixture was stirred at room temperature. Evolution of copious amounts of HCl and SO₂ occurred instantaneously. After stirring for 4h, the excess unreacted thionyl chloride was distilled out and the resulting grayish silica chloride was flame dried, stored in airtight container and used as it is for the reactions [4].

To a well-stirred silica chloride (20g) in dry CH₂Cl₂ (40mL) was added dropwise PEG (10g) under nitrogen atmosphere and at room temperature. HCl was instantaneously evaluated. After stirring for 2h, the obtained silica gel supported PEG was removed by filtration. For elimination of any additional PEG, the PTC was washed several times by

acetone (3x30 mL). Silica gel supported PEG was dried in a vacuum oven overnight.

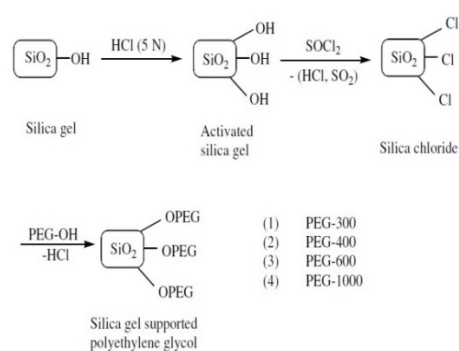


Figure 2: Preparation of silica-grafted PEG [4]

3. RESULTS AND DISCUSSIONS

Several experiments were conducted to understand the critical parameters for maintaining three immiscible phases at 55°C temperature with a different agitation speeds (rpm) from 300 to 1000. The formation of third phase occurred between the aqueous phase, which was saturated with sodium hydroxide and organic phases of hexane as solvent, when the catalyst concentration was beyond a critical concentration. During agitation, the reaction mass had droplets of organic phase surrounded by a thin film of catalyst-rich phase in a pool of

aqueous phase, which was the continuous phase.

Experimental data are given at Table 4.1 and from there it can be easily decide the maximum yield of mandelic acid reached at 1000 rpm agitation and with PEG 4000 catalyst. Yield were practically the same at PEG 4000 and PEG1000-SiO₂. But it is very low increases of yield between PEG 1000 and immobilized PEG 1000.

Table 1: Yields % of the Mandelic Acid with different PEGs and agitation speeds

PEG	Agitation Speed (rpm)			
	300	500	700	1000
600	55	62	76	82
1000	60	68	79	88
4000	68	72	83	90
6000	65	70	81	89
PEG1000SiO ₂	63	71	83	91

Ultrasonic irradiation effects on yield is examined in presence of PEG and immobilized PEG phase transfer catalyst. Results are given in Table 3.2. It shows that irradiation effect is not strong compared from under agitation. The yield of the mandelic acid in presence of PEG and immobilized PEG was very close to which was found without irradiation.

REFERENCES

- [1] Sowbna, P. R., Yadav, Ganapati, D., 2012, Population Balance Modeling and Simulation of Liquid-Liquid-Liquid Phase Transfer Catalyzed Synthesis of Mandelic Acid from Benzaldehyde, *AIChE Journal*.
- [2] Yadav, Ganapati, D., Sowbna, P.R., 2012, Process intensification and waste minimization in liquid-liquid-liquid phase transfer catalyzed selective synthesis of mandelic acid, *IChemE*.
- [3] Sanjeev, D. Naik, Doraiswamy, L. K., 1998, Phase Transfer Catalysis: Chemistry and Engineering, *AIChE Journal*, Volume 3, Page 612.

Table 2: Yields % of the Mandelic Acid with ultrasonic irradiation and immobilized PEG

PEG4000	84
PEG1000-SiO ₂	92

4. CONCLUSION

Synthesis of mandelic acid with L-L-L PTC is more convenient then the L-L PTC and the PEG also most useful then ammonium salt as catalyst because of their renewable capability, non-toxicity and low cost. Separation of catalyst was very easy and it could be reused several times. There is 92% yield of mandelic acid due to the creation of the third phase. The creation of third phase allows high conversion with high yield and quality. Also using the PEG as catalyst the environmental problems can be forgotten from the point of view of catalyst waste.

Acknowledgements: Special thanks to our thesis professor for support, Anadolu University.

- [4] Kiasat, A., R., Zayadi, M., 2008, Polyethylene glycol immobilized on silica gel as a new solid-liquid phase-transfer catalyst for regioselective azidolysis of epoxides in water: An efficient route to 1,2-azido alcohols, *Elsevier*.

[5]http://www.hmdb.ca/spectra/nmr_one_d/1488#spectrum-image

SYNTHESIS AND CHARACTERIZATION OF ACIDIC CESIUM SALT OF 12-TUNGSTOPHOSPHORIC ACID

Elif Ödeş AKBAY^{1a}, Gülberk DEMİRKILIÇ²

1. Anadolu University, Dept. of Chemical Engineering, Eskişehir, Turkey

2. Anadolu University, Dept. of Chemical Engineering, Eskişehir, Turkey

a. Corresponding author (eodes@anadolu.edu.tr)

ABSTRACT: Acidic Cs salt, $\text{Cs}_{2.5}\text{H}_{0.5}\text{PW}_{12}\text{O}_{40}$, exhibits high catalytic activity for various kinds of acid-catalyzed reactions. This excellent catalysis of $\text{Cs}_{2.5}\text{H}_{0.5}\text{PW}_{12}\text{O}_{40}$ is attributed to the strong acidity, hydrophobicity, unique pore structure, etc. In this study, acidic cesium salts, $\text{Cs}_{2.5}\text{H}_{0.5}\text{PW}_{12}\text{O}_{40}$, were prepared by the impregnation method. Then obtained acidic cesium salts have been characterized by X-ray powder diffraction (XRD), Fourier transform infrared spectroscopy (FT-IR) and BET analysis.

1. INTRODUCTION

Nanoparticles have emerged as sustainable alternatives to conventional materials, as being robust, high surface area heterogeneous catalysts and catalyst supports [1]. The nano-sized particles increase the exposed surface area of the active component of the catalyst, thereby enhancing the contact between reactants and catalyst dramatically and mimicking the homogeneous catalysts. However, their insolubility in reaction solvents renders them easily separable from the reaction mixture like heterogeneous catalysts, which in turn makes the product isolation stage effortless. Also, the activity and selectivity of nano-catalyst can be manipulated by tailoring chemical and physical properties like size, shape, composition and morphology [2].

Catalysis by heteropoly acids (HPAs) and related polyoxometalate compounds is a field of increasing importance, attracting increasing attention worldwide, in which many new and exciting developments are taking place in both research and technology [3].

Interesting acidic cesium salt of heteropoly compounds, $\text{Cs}_{2.5}\text{H}_{0.5}\text{PW}_{12}\text{O}_{40}$, has high surface area and thus acidic Cs salt, ,

$\text{Cs}_{2.5}\text{H}_{0.5}\text{PW}_{12}\text{O}_{40}$, exhibits high catalytic activities for various kinds of acid-catalyzed reactions [4-6]. This excellent catalysis of $\text{Cs}_{2.5}\text{H}_{0.5}\text{PW}_{12}\text{O}_{40}$ is attributed to the strong acidity, hydrophobicity, unique pore structure, etc. [7]. It was demonstrated that many reactions were effectively catalyzed by $\text{Cs}_{2.5}\text{H}_{0.5}\text{PW}_{12}\text{O}_{40}$ in a solid-liquid reaction system. $\text{Cs}_{2.5}\text{H}_{0.5}\text{PW}_{12}\text{O}_{40}$ is an interesting candidate for use as a 'water-tolerant' catalyst because of its insolubility in organic and aqueous media, in contrast with $\text{H}_3\text{PW}_{12}\text{O}_{40}$ [8]. Aim of this study, determine the best method for synthesis of 12-tungstophosphoric acid cesium salt (Cs-TPA).

2. EXPERIMENTALS

2.1. Materials

The chemicals used in the preparation of catalysts, 12-tungstophosphoric acid hydrate ($\text{H}_3\text{PW}_{12}\text{O}_{40}\cdot x\text{H}_2\text{O}$) were purchased from Merck and cesium carbonate (Cs_2CO_3) were also purchased from Alfa Aesar. Distilled water used in the preparation of solutions.

2.2. Synthesis of Cs-TPA

0.1 M aqueous solution of Cs_2CO_3 and 0.08 M aqueous solution of 12-

tungstophosphoric acid hydrate were prepared. Then, aqueous solution of Cs_2CO_3 (20 cm^3) was added to aqueous solution of 12-tungstophosphoric acid hydrate (20 cm^3) with a constant rate of about $1 \text{ cm}^3/\text{min}$ and $0.1 \text{ cm}^3/\text{min}$ at room temperature, under vigorous stirring. Applied methods for each flow rate is shown in Table 1.

2.3. Characterization of Cs-TPA

The crystallinity and the phase purity of synthesized samples were analyzed by X-ray diffraction (XRD) patterns using X-ray diffractometer (Rigaku Rind 2000, Japan), and $\text{Cu-K}\alpha$ (1.54 \AA) radiation. The BET (Brunauer–Emmett–Taller) specific surface area was obtained from N_2 adsorption–desorption isotherm measured at 77 K in an automatic adsorption apparatus (ASAP2010; micromeritics). Prior to measurement, samples were degassed at 100°C for about 2 h . FTIR studies of the catalysts were conducted by using a Bruker IFS-66 single channel Fourier transform spectrophotometer.

3. RESULTS and DISCUSSIONS

3.1. X-ray Diffraction Analysis (XRD)

All synthesized Cs-TPA and TPA have been characterized by using XRD

Table 1: Different synthesis methods for Cs-TPA

Number	Sample Name	Flow rate (ml/min)	Synhtesis Method
1	01G50E	0.1	aging overnight drying with drying-oven at 50°C
	1G50E	1	
2	01G50V	0.1	aging overnight drying with vacuum oven at 50°C
	1G50V	1	
3	01G110V	0.1	aging overnight drying with vacuum oven at 110°C
	1G110V	1	
4	01110V	0.1	drying with vacuum oven at 110°C
	1110V	1	
5	01110V473K	0.1	drying with vacuum oven at 110°C calcination at 200°C
	1110V473K	1	

patterns due to basic analytical techniques. Diagrams obtained from analysis is shown in Figure 1.

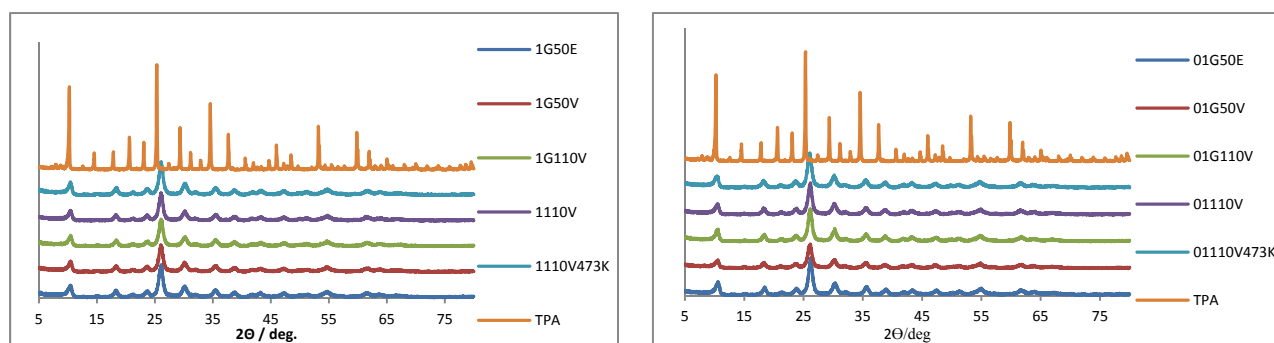


Figure 1: XRD diagrams for a) synthesized catalysts with $1 \text{ ml}/\text{min}$ flow rate b) synthesized catalysts with $0.1 \text{ ml}/\text{min}$ flow rate

Fig. 1 shows that the powder XRD patterns of all synthesized Cs-

tungstophosphoric acid salts is in the 2θ range of $5\text{--}80^\circ$. It is seen that all Cs-

TPAs are identical with each other. The patterns for the Cs salts, $\text{Cs}_{2.5}\text{H}_{0.5}\text{PW}_{12}\text{O}_{40}$, exhibit the characteristic lines of HPW structure and are in agreement with published data [9,10]. It can be seen that the location of XRD peaks of Cs-TPA is very similar to that of pure TPA; indicating that the Cs salt has similar crystalline structure as the pure TPA. However, the main peaks depicting TPA are shifted toward slightly higher angles in Cs-TPA [11].

3.2. Fourier Transform-Infrared Spectroscopy Analysis (FT-IR)

Cs-TPAs was characterized by using FT-IR to investigate structure of catalysts as shown in Fig. 2 Basic structure of synthesized Cs-TPAs were tried to explain by comparing with TPA

absorbance bands using FT-IR analysis. FT-IR bands of pure TPA seen at Fig. 2, have six characteristic peaks of its Keggin structure observed at 1080 cm^{-1} (P-O in central tetrahedral), 990 cm^{-1} ($\text{W}=\text{O}_f$ terminal oxygen in the Keggin structure), 882 cm^{-1} and 804 cm^{-1} ($\text{W}-\text{O}_c-\text{W}$), 582 and 516 cm^{-1} , which coincides with those referred in the literature [10;12-15]. The FT-IR spectrum of Cs-TPA salt exhibits similar characteristic bands compared with bands of bulk acid TPA. Also, all Cs-TPAs have very similar FT-IR bands with each other. However, the typical vibration of the $\text{W}=\text{O}_f=990\text{ cm}^{-1}$ on acidic form splits into two components at 985 cm^{-1} .

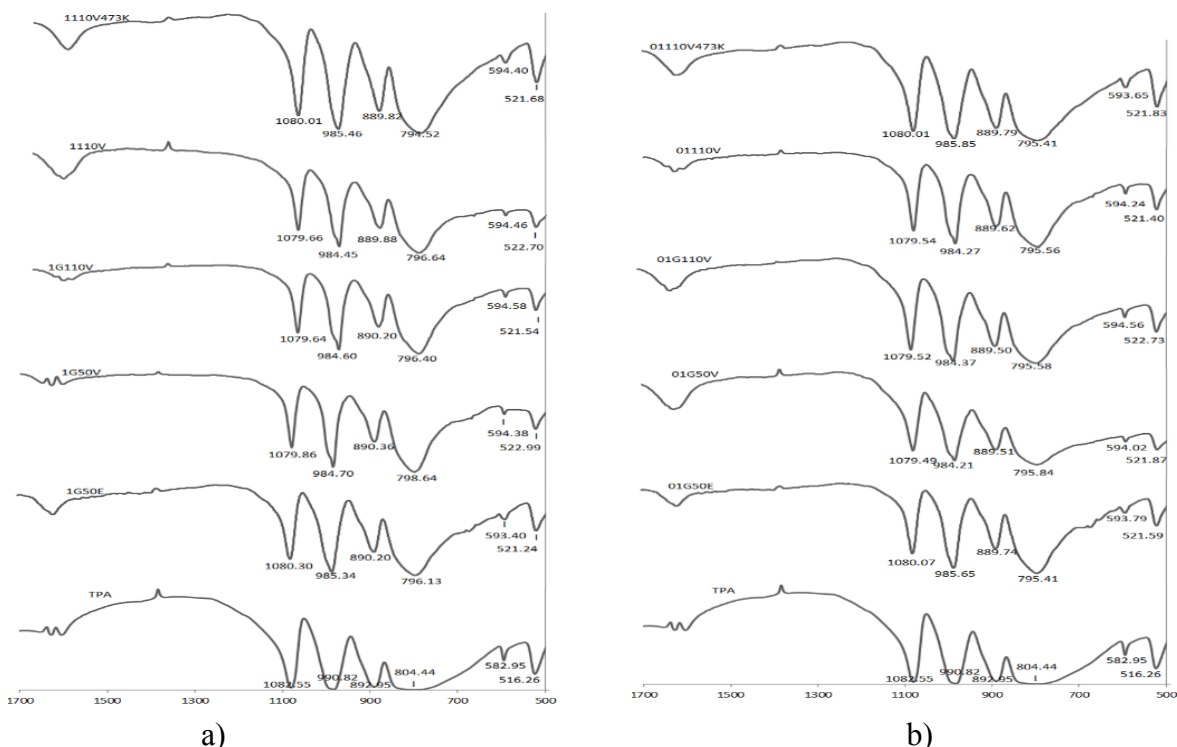


Figure 2: FT-IR spectrums for a) synthesized catalysts with 1ml/min flow rate b) synthesized catalysts with 0.1 ml/min flow rate

This shows the interaction of Cs^+ ions with $\text{W}=\text{O}$ (Doğan et al., 2010). From the FT-IR results, it can be inferred that the Keggin structure remains intact

during the incorporation of cesium into the heteropoly cage structure [16].

3.3. BET Analysis

Single and multipoint BET areas, average pore diameters and pore

volumes determined by N₂ adsorption analysis results is given in Table 2.

Table 2: N₂ adsorption analysis results of Cs-TPA catalysis

Sample Name	Surface Area (m ² /g)			Pore Diameter (Å)		Pore Volume (cm ³ /g)		
	BET (multi point)	BET (single point)	S _{BJH}	d _{adsorption}	d _{BJH}	V _t	V (single point)	V _{BJH}
1G50E	88.739	143.399	95.983	57.671	40.961	0.01608	0.12794	0.09829
01G50E	93.482	140.106	98.523	59.658	45.651	0.01759	0.13942	0.11244
1G50V	90.644	147.895	94.975	64.874	48.307	0.01939	0.14701	0.11469
01G50V	96.801	148.538	102.054	54.599	40.013	0.01903	0.13213	0.10208
1G110V	91.641	147.005	99.964	59.143	42.236	0.01623	0.13549	0.105552
01G110V	87.850	137.023	93.640	67.918	51.998	0.01696	0.14916	0.12172
1110V	87.685	145.033	95.307	76.338	57.351	0.01748	0.16734	0.13665
01110V	58.166	90.570	64.395	55.583	39.491	0.00999	0.08083	0.06357
1110V473K	86.401	142.792	94.750	60.552	42.739	0.01524	0.13079	0.10123
01110V473K	91.918	140.328	99.613	54.431	39.449	0.01544	0.12508	0.09824

It is seen that surface areas, pore volumes, average pore diameters, of obtained Cs-TPAs by different synthesis conditions have different values. The sample coded by 01G50V showed the highest surface area in all synthesized Cs-TPA. Although the sample coded by 01110V is obtained by the same methods the results of BET analysis is not correspond to our expectation. Therefore, it is thought that BET analysis of this sample has to be repeated.

4. CONCLUSIONS

In this study, synthesis and characterization of acidic cesium salt of

12-tungstophosphoric acid is investigated. The XRD and FT-IR

analysis show that there is no significant difference between synthesis methods of all synthesized Cs-TPA's. However, the differences have been observed at the results of N₂ adsorption/desorption isotherms analysis. The highest BET area have been found for the sample coded by 01G50V.

Acknowledgements: Special thanks to our thesis professor for support, Anadolu University.

REFERENCES

- [1] Polshettiwar, V. and Varma, R.S., 2010, Green chemistry by nano-catalysis, *Green Chem.*, 12, 743–754.
- [2] Somorjai, G.A., Frei H. and Park J. Y., 2009, *J. Am. Chem. Soc.*, 131, 16589.
- [3] Kozhevnikov, I.V., 1995, *Heteropoly Acids and Related Compounds as Catalysts for Fine Chemical Synthesis*, *Catal., Rev. – Sci. Eng.*, 37(2), 311-352.
- [4] Na, K., Okuhara, T., Misono, M., 1995, *J. Chem. Soc. Farad. Trans.*, 91, 367.
- [5] Essayem, N., Couduurier, G., Fourier, M., Vedrine, J.C., 1995, *Catal. Lett.* 34 223.
- [6] Okuhara, T., Nishimura, T., Watanabe, H., Misono, M., 1992, *J. Mol. Catal.*, 74 247.
- [7] Okuhara, T., Nishimura, T., and Misono, M., 1996, *Novel Microporous Solid "Superacids": Cs_xH 3-xPW 12O₄₀ (2 ≤ X ≤ 3)*, 101, 581-589.
- [8] Kimura, M., Nakato, T., Okuhara, T., 1997, *Water-tolerant solid acid catalysis of Cs_{2.5}H_{0.5}PW₁₂O₄₀ for hydrolysis of esters in the presence of excess water*, 165, 227-240.
- [9] Volkova, G. G.; Plyasova, L. M.; Salanov, A. N.; Kustova, G. N.; Yurieva, T. M.; Likholobov, V. A. *Catal. Lett.*, 2002, 80, 175–179.
- [10] Dias J.A., Caliman E., Sias SCL., 2004, *Effects of cesium ion exchange on acidity of 12-tungstophosphoric acid.*

- Microporous Mesoporous Mater, 76, 221-32.
- [11] Doğan, H., Inan, T.Y., Unveren, E., Kaya, M., 2010, Effect of cesium salt of tungstophosphoric acid (Cs-TPA) on the properties of sulfonated polyether ether ketone (SPEEK) composite membranes for fuel cell applications, 35, 7784-7795.
- [12] Choi, S., Wang, Y., Nie, Z., Liu, J., Peden, C.H.F., 2000, Cs-substituted tungstophosphoric acid salt supported on mesoporous silica, 55, 117-124.
- [13] Essayem N., Holmqvist A., Gayraud P.Y., Vedrine J.C., Ben T.Y., 2001, In situ FTIR studies of the protonic sites of H₃PW₁₂O₄₀ and its acidic cesium salts M_xH_{3-x}PW₁₂O₄₀. J Catal, 197, 273-80.
- of used vegetable oils with a Cs-doped heteropolyacid catalyst in supercritical methanol, 96, 572-578.
- [14] Zhaoa D., Yia BL. Zhagn HM., Yuc HM. Wang L., Ma YW., 2009, Cesium substituted 12-tungstophosphoric (Cs_xH_{3-x}PW₁₂O₄₀) loaded on ceria-degradation mitigation in polymer electrolyte membranes. J Power Sources, 190, 301-6.
- [15] Ghanbari-Siahkali A., Philippou A., Dwyer J., Anderson MW., 2000, The acidity and catalytic activity of heteropoly acid on MCM-41 investigated by MAS NMR, FT-IR and catalytic tests. Appl Catal A, 192, 57-69.
- [16] Shin, H.Y., An, S.H., Sheikh, R., Park, Y.H., Bae, S.Y., 2012, Transesterification

WEAR BEHAVIOUR OF POWDER INJECTION MOLDED Ti-6Al-4V ALLOY

Hamit Özkan Gülsoy¹, Zeynep Taşlıçukur²
Gözde Sultan Altug^{2,a}, Tuba Karahan², Sunullah Özbek²

1. Marmara University, Technology Faculty, Metallurgical and Materials Engineering, Istanbul, Turkey.

2. Gedik University, Department of Metallurgical and Materials Engineering, Istanbul, Turkey.

a. Corresponding author (gozde.altug@gedik.edu.tr)

ABSTRACT: Titanium and its alloys which are widely used in aerospace, biomedical and chemical applications, producing very good combination of properties, including high specific strength, low density, good corrosion resistance and exceptional biocompatibility. Nowadays, it is possible to fabricate Ti alloy components by powder injection molding (PIM) technique for unique mechanical properties. However, the use of titanium alloys in sliding applications is restricted because of their poor tribocharacteristics. In this study, the wear behavior of Ti6Al4V (Ti64) alloy was investigated under dry sliding condition against 100Cr6 steel. In the first stage of the study, Ti64 powders spherical in shape was injection molded with wax based binder. After molding and debinding stage, all samples sintered at 1150 °C, 1200 °C and 1250 °C for 1h under high vacuum level. The microstructures of sintered samples were determined with optical microscope. In the second stage, wear tests were carried out using “ball-on-disc” type tribometer. In the wear test, the load, total distance and sliding velocity were selected as 20 N, 500 m and 1 m/s, respectively. All worn surfaces were examined by scanning electron microscope and wear characteristics were evaluated as a function of sintering temperatures.

1. INTRODUCTION

Titanium and its alloys which are widely used in aerospace, biomedical and chemical applications, exhibit an excellent combination of properties, including high specific strength, low density, good corrosion resistance and exceptional biocompatibility [Sidambe *et al.*, 2012 and Sarkar *et al.*, 2011]. Currently, Ti6Al4V alloy is the most widely used titanium alloy among others in the world, and no other titanium alloys can threaten its dominant position [Casalina *et al.*, 2005]. Ti6Al4V alloy presents very attractive properties with inherent workability which provides it to be produced in all kinds of mill products, in both large and small sizes and these can be made in to parts with complex shapes. [Bayha, 2001].

Despite all the attractive characteristics, the application of titanium and its alloys to large, high load bearing structures has been limited due to difficulties associated with making titanium into large structural shapes. Nowadays it is possible to produce Ti alloy components by fabrication technique for highly required mechanical properties with cost advantages. Although Ti alloys produced by conventional techniques such as casting, wrought (forging/milling from ingots), powder metallurgy, relatively new processing methods by direct digital manufacturing such as direct metal laser sintering (DMLS), laser-engineered net-shaping (LENS) and ultrasonic consolidation (UC) has emerged [Murr *et al.*, 2009 and Shi-bo *et al.*, 2006]. Between these methods, powder injection molding (PIM) which is derived from plastic injection molding is

highly useful for producing Ti alloys with complex shapes and more homogeneous microstructure [González et al., 2006 and Alagic *et al.*, 2011].

However, the use of titanium alloys in sliding applications is restricted due to their low resistance to plastic shearing and the low protection exerted by the surface oxides. Thus, the application of these alloys in the areas related with wear and friction can be limited. [Straffellini et al, 1999 and Alam *et al.*, 2002]. In this study, the wear behavior of Ti6Al4V (Ti64) alloy was investigated under dry sliding condition against 100Cr6 steel.

2. EXPERIMENTAL STUDY

2.1. Materials

The spherical shape Ti64 powder (Ti-5.9Al-3.9V-0.19Fe-0.12O-0.01C-0.01N-0.004H) provided by SOLEA Corp. (France) was selected as the experimental alloy. Specimens were fabricated by Powder Injection Molding for obtaining homogeneous microstructures. Ti64 powders spherical in shape were injection molded with wax based binder. After molding and debinding stage, all samples sintered at 1150 °C, 1200 °C and 1250 °C for 1h in an atmosphere controlled vertical recrystallised alumina tube furnace under high vacuum level (10^{-3} Pa). The microstructures of sintered samples were determined with optical microscope. The densities of the sintered samples were measured by means of the Archimedes water-immersion method. The densities of the samples produced were measured as %93.5, %95.9, % 96.4 respectively.

2.2 Wear Test Under Dry Sliding Condition

For tribological characterization wear tests were performed under dry sliding condition. 100Cr6 steel ball was used as counterpart material. Friction behaviour

and wear characteristics were then determined based on wear-induced loss amounts. Wear tests were realized using a “ball-on-disc” type tribometer (Nanovea). Related test parameters are listed in Table 1.

Table 1: Parameters used in wear tests.

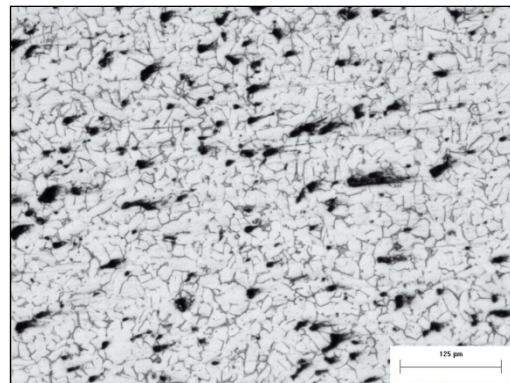
Counterpart material	100Cr6
Counterpart hardness	65 HRC
Friction Velocity	0,1m/s
Normal load	20 N
Total sliding distance	500 m
Surrounding atmosphere	Ambient air
Lubrication method	None

3. RESULTS AND DISCUSSION

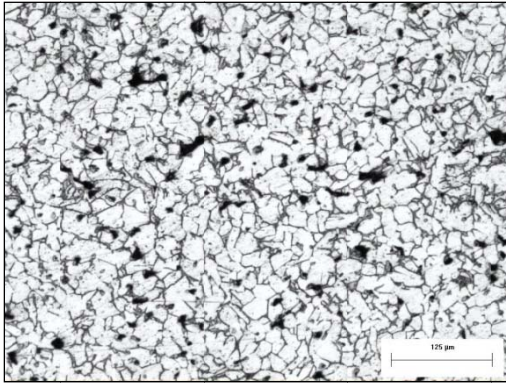
3.1. Microstructural Examination

Figure 1 shows the microstructures of produced from spherical Ti6Al4V alloy powder in 100x magnification, etched with Kroll reagent.

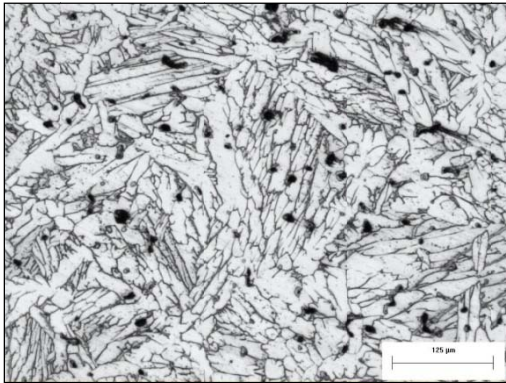
Due to the increase in sintering temperature, the amount of the porosity in the samples decreased, as seen from the result of the densities. The sample sintered at 1250 °C is characterized by the highest relative density of %96.37 while the sample sintered at 1150 °C is characterized by the lowest relative density of %93.5.



(a)



(b)



(c)

Figure 1: The microstructures of produced from spherical Ti6Al4V alloy powder alloy in 100x magnification, etched with Kroll reagent (3 ml HF, 6 ml HNO₃ in 100 ml H₂O); (a) sample sintered at 1150 °C, 1 h., (b) sample sintered at 1200 °C, 1h., (c) sample sintered at 1250 °C, 1h.

3.2. Evaluation of Wear Test Data

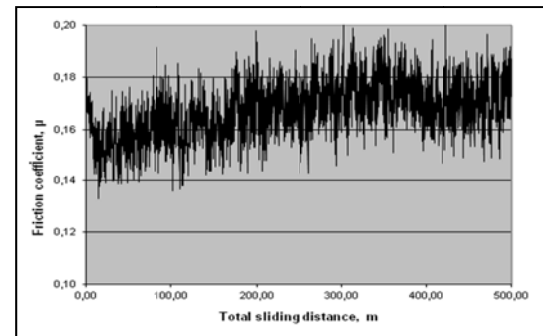
The results were evaluated using the friction coefficient-distance diagram and loss in weight. Table 2 shows the loss in weight of the sintered samples before and after wear tests. The lowest loss in weight was obtained as 16.6 mg for the sample sintered at 1250 °C.

Figure 2 shows the friction coefficient values as a function of sliding distance for the samples sintered at 1150, 1200 and 1250 °C. In the diagram a, friction coefficient value was obtained within the range of about 0.14-0.20. For the diagram b, friction coefficient value directly increased from 0.12 to 0.18. For the

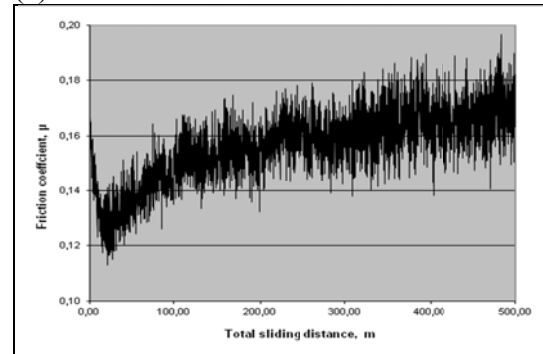
diagram c, friction coefficient value increased and then came to steady-state within the range of from 0.14 to 0.18.

Table 2: Loss in weight of the samples before and after wear tests.

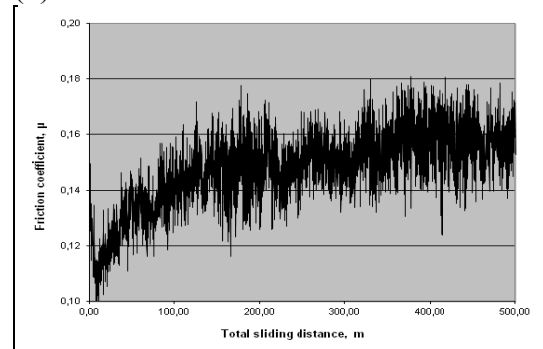
Sample Sintered at	Initial weight (g)	Final weight (g)	Loss in weight (mg)
1150 °C	11.3980	11.3786	19.4
1200 °C	11.5251	11.5027	19.9
1250 °C	18.2068	18.1906	16.2



(a)



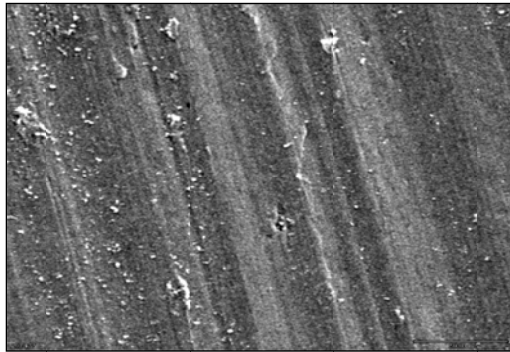
(b)



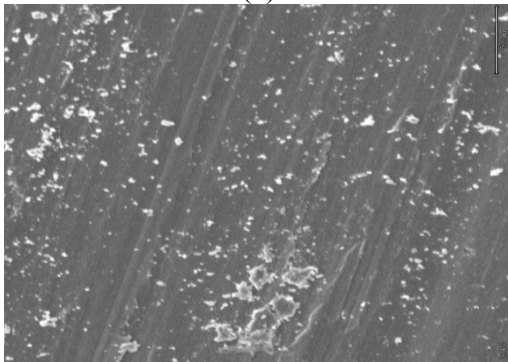
(c)

Figure 2: The diagrams showing the friction coefficient as a function of distance for the samples; (a) sintered at 1150 °C, (b) sintered at 1200 °C, (c) sintered at 1250 °C.

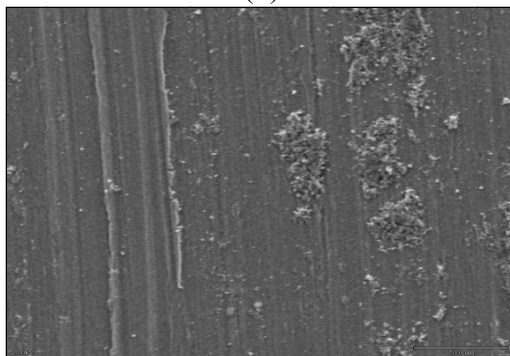
SEM microstructures of the worn surfaces are given in Figure 3. Abrasive layers takes place on the worn surfaces of the samples sintered at 1150 °C (Figure 3a). As it can be seen in the Figure 4b and 4c, in addition to abrasive layers, in the direction of sliding some wear debris adhering to the worn surfaces.



(a)



(b)



(c)

Figure 3: The SEM microstructures of powder injection molded Ti6Al4V alloy produced from spherical Ti6Al4V alloy powder in 500x magnification after wear test. (a) sample sintered at 1150 °C, 1 h., (b) sample sintered at 1200 °C, 1h., (c) sample sintered at 1250 °C, 1h.

4. CONCLUSIONS

The effects of the sintering temperature (1150, 1200 and 1250 °C) on the wear properties of Ti6Al4V (Ti64) alloy produced by PIM technique were investigated in this study. The conclusions can be given as follows:

- The densities of the samples sintered at 1150, 1200 and 1250 °C were measured as %93.45, %95.91, % 96.37 respectively.
- The lowest loss in weight was obtained as 16,6 mg for the sample sintered at 1250 °C.
- The sample sintered at 1150 °C has the friction coefficient value within the range of about 0.14-0.20 while the sample sintered at 1250 °C has the friction coefficient value within the range of from 0.14 to 0.18.

Acknowledgement

The authors wish to acknowledge Metallurgy and Materials Department of Kocaeli University and Yildiz Technical University for their support during experimental test and analysis.

REFERENCES

- Sidambe A.T., Figueroa I.A., Hamilton H.G.C., Todd I., 2012. Metal injection moulding of CP-Ti components for biomedical applications, *Journal of Materials Processing Technology* Volume (212), 1591.
- Sarkar A., Roy S., Suwas S., 2011. X-ray diffraction line profile analysis of deformation microstructure in boron modified Ti-6Al-4V alloy, *Materials Characterization* Volume (62), 35.
- Casalino G., Curcio F., Memola Capece Minutolo F., 2005. Investigation on Ti6Al4V laser welding using statistical and Taguchi approaches, *Journal of Materials Processing Technology* Volume (167), 422.
- Bayha T.D., 2001. Howmet Design Allowables Program Up-date, Mil-Handbook-5 Committee Meeting.
- Murr L.E., Quinones S.A., Gaytan S.M., Lopez M.I., Rodela A., Martinez E.Y., Hernandez D.H., Martinez E., Medinac F., Wickerc R.B., 2009. Microstructure and mechanical

- behavior of Ti-6Al-4V produced by rapid-layer manufacturing, for biomedical applications, *Journal of the Mechanical Behavior of Biomedical Materials* Volume (2), 20.
- Shi-bo G., Xuan-hui U., Jun-huai X., Rong-fa A., Xiang-ming H., Ming-sheng L., Shu-wang D., Wen-hi L., 2006. Effect of annealing processing on microstructure and properties of Ti-6Al-4V alloy by powder injection molding, *Trans. Nonferrous Met. SOC. China* Volume (16), 701.
- González-Gutiérrez J., Stringari G. B., Emri I., 2012. Powder Injection Molding of Metal and Ceramic Parts, Some Critical Issues for Injection Molding, ISBN: 978-953-51-0297-7.
- Alagic' C., Cvijovic' Z., Mitrovic S., Panic' V., Rakinb M., 2011. Wear and corrosion behaviour of Ti-13Nb-13Zr and Ti-6Al-4V alloys in simulated physiological solution, *Corrosion Science* Volume (53), 796.
- Straffelini G., Molinari A., 1999. Dry sliding wear of Ti-6Al-4V alloy as influenced by the counterface and sliding conditions, *Wear* Volume (236), 328.
- Alam M. O., Haseeb A.S.M.A., 2002. Response of Ti-6Al-4V and Ti-24Al-11Nb alloys to dry sliding wear against hardened steel, *Tribology International* Volume (35), 357.

EFFECT OF HIGHLY POROUS EXPANDED SILICA GEL ADDITION ON THE PROPERTIES OF SiC-C BASED COMPOSITE ABLATION MATERIAL

M.Serhat Başpınar¹

1. Afyon Kocatepe University, Technical Education Faculty, Turkey
a. Corresponding author (sbaspınar@aku.edu.tr)

ABSTRACT: The main objective of this study was to investigate the processing of SiC-C based ablation material and optimization potential of the properties by the addition of highly porous expanded silica gel beads. SiC powders were bonded by Phenol formaldehyde type Novolac resin with hardener Hexamethylenetetramine (Hexamin) under single axis pressing. Samples were cured at 200 °C and graphitized at 1300 °C. To increase the carbon yield of the resin after graphitization, carbon flakes were added to the mixtures. Expanded silica gel beads which have different size and porosity were added to the mixtures at different amounts. Physical and mechanical properties of the composite were examined. Microstructural development were investigated and related with properties. Ablation rate of the samples were also measured under high velocity oxy-gas flame. Lowest bulk density of 1.56 gr.cm⁻³ composites were produced by this method. Addition of the porous expanded silica gel beads decreases the ablation rate of the composite. However, this behaviour strongly depends on the mineralogical composition of the beads especially cristobalite content.

1. INTRODUCTION

Ceramics being used for aerospace and missile take off area must withstand high heat fluxes thus ceramic composites with good oxidation and thermal shock resistance, dimensional stability and ablation resistance are requested. Ablation is an erosive phenomenon with a removal of material by a combination of thermo-mechanical, thermo-chemical, and thermo-physical factors from high temperature, pressure, and velocity of combustion flame [Yan *et al.*, 2009]. Silicon carbide-Carbon composites (designated as C/SiC) possess good high temperature strength, high hardness, low thermal expansion, high thermal conductivity, good thermal shock, especially outstanding ablation resistance property up to 1700 °C due to the formation of a layer of protective SiO₂ glass that inhibits ablation atmosphere diffusion to the parent materials [Wang *et*

al.,2010]. Phenolic resins are known for their excellent thermal properties and

chemical stability. In the field of advanced composite materials, phenolic based composites are known for their excellent flame resistance and are excessively used in the rocket industry because of their ablative characteristics [Srebrenkoska *et al.*, 2009]. Novolac type phenol-formaldehyde resin binder is extensively used for the refractory applications at high temperatures due to the high carbon yield during service [Aneziris *et al.*, 2007]. Silica gel is a granular, vitreous, highly porous form of silica made synthetically from sodium silicate. Despite its name, silica gel is a solid. Silica gel is fireproof and highly heat resistant, chemically stable and, highly hygroscopic and has a large specific surface area. Because of these characteristics, silica gel is often applied as a drying agent and catalyst carrier. Although silica gel has a very high melting temperature (1600 °C), it loses its chemically-bound water molecules and hygroscopic properties when heated above 300 °C. Sodium silicate, the main raw

material for the silica gel, is intumescent. Otaka and Asoka, 2002 proved that intumescent materials swell as a result of heating. Expanded silica gel (ESG) beads are highly porous and refractory spherical granules which can be used for several purposes [Başpınar and Kahraman, 2011]. The main purpose of this study was to investigate the processing of SiC-C composite which was produced from SiC powder and phenol formaldehyde type Novolac resin as a binder phase. Since the porous expanded silica beads have heat sink potential, effect of its addition on the technical properties of the SiC-C composite and ablation behaviour were investigated.

2. EXPERIMENTAL

The expansion process of the silica gel beads were discussed in detail in previous study [Başpınar and Kahraman, 2011]. The density of the beads strongly depends on the heating regime. In this study, 1-3 mm beads were used which were expanded at 1100 °C. The mineralogical structure of the beads were mainly amorphous silica and cristobalite. Properties of the beads like mineralogical structure and density-strength depends on the expansion process. The bulk density of the beads which were used in his study were measured as 0,217 gr.cm⁻³. 240 Grit 240 (ANSI) SiC particles (average particle size 47-53µm) were used in the samples preparation. Chopped carbon fibers (grade 400 gr/km, 1,78 gr.cm⁻³) were used. SiC particles, graphite, hexamine, beads and resin were mixed in Hobart type mixer until homogenous mixture was obtained. Then the mixtures were put into the cylindrical steel mould. All of the samples were pressed to 40x40 mm (diameter x height) under 10 MPa pressure. Shaped samples were cured at 200 °C for 1 hour. Samples were graphitized at 1300 °C for 1 hour under normal atmosphere but samples were put into the alumina crucible and covered by both graphite and SiC powders. Density of the samples decreased after the

graphitization process. Table 1 shows the base composition and the test results of the sample series. Bulk density of the samples were measured from simple weight-volume ratio after graphitization. Thermal conductivity values were derived after the measurement of effusivity values of the samples. Ablation rate of the samples were measured by exposing the samples to the oxy-acetylene flame where the flow rate of the oxygen and acetylene fixed constant at each test. Each sample was exposed to the flame for 20 sec. Surface temperature of the samples were also measured under specially design heating set-up. Than percent weight loss of the samples were measured and normalized to 1 minute exposure time.

3. RESULTS AND DISCUSSIONS

Physical and mechanical properties of the samples were given n Table 1.

Table 1: Base composition of the series (wt%) and properties. (BD: bulk density, CS: compression strength, Thermal conductivity, AR: ablation rate, mass loss %·min⁻¹)

Series and Properties				
Components	A	B	C	D
SiC	75	70	87,4	82,4
Resin	10,4	10,4	5,2	5,2
Graphite	13,5	13,5	6,8	6,8
Hexamin	1,1	1,1	0,6	0,6
ESG	---	5	---	5
C-Fiber	---	0,12	---	0,12
BD (gr.cm ⁻³)	1,80	1,56	2,07	1,83
CS (MPa)	27,1	19,35	21,3	9,44
TC (W/mK)	5,57	4,50	4,61	3,76
AR (loss%.min ⁻¹)	0,84	0,52	1,04	1,30

Experiments showed that the pressing pressure greater than 10 MPa resulted in the cracking of the beads in the sample. Fractured surface of the sample is given in Figure 1.



Figure 1: Fractured surface of the sample.

Ablation measurement set-up is given in Figure 2. Samples were put into the refractory board and fixed. Temperature of the cold site was measured and recorded. Temperatures were measured between the range of 225 to 262 °C (20 sec. results) depending on the sample type.



Figure 2: Ablation test set-up.

SEM images showed that the beads and the resin bonded SiC matrix are in good contact and there isn't any gaps between them. Figure 3 shows that graphite phase provides good bonding of the beads with matrix.

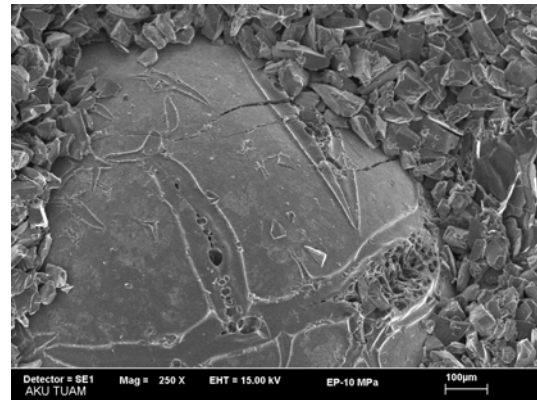
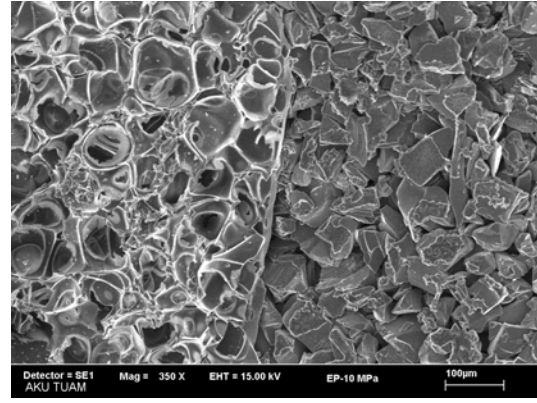
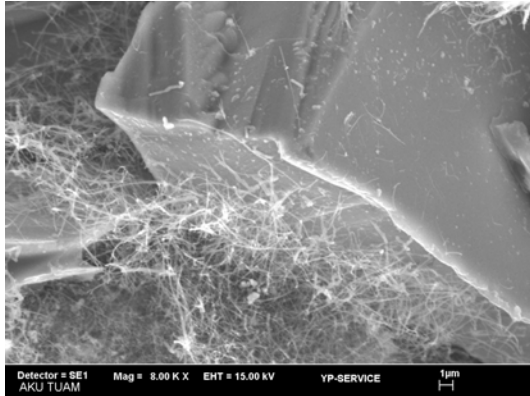


Figure 3: Interface structure of the samples.

The difference between A and B series is the binder resin content. When the resin content decreased bulk density increased. However, strength and thermal conductivity of the samples decreased with decreasing resin and graphite content. Ablation rate increased with decreasing resin and graphite content. When expanded silica gel beads were added to the samples with C fibers, bulk densities of the samples were decreased drastically. Refractory porous silica based beads addition are very effective for the conductivity decrease. Addition of the C fibers was not able to compensate the conductivity decrease. When the expanded porous silica gels were added to the lower resin sample C, strength was decreased drastically. Lowering the carbonaceous phases and introducing the refractory beads lead to decrease in the thermal conductivity in sample D. Combined effect of decreasing the binder phase and introducing the silica beads increased the ablation rate drastically.

SEM investigation after the ablation test showed that nano sized C fibers were grown over and between the SiC grains. Figure 4 shows the fibrous formations on the SiC surface after flame exposure.



It was thought that; the nano carbon fiber formations during the flame ablation test useful for the thermal conductivity. However, transformation of carbonaceous matrix to the weak fiber matrix is thought to be negative effect on the ablation rate due to the loss of bonding between the SiC grains. Addition of porous expanded silica gel beads found to be useful for decreasing the ablation rate. However, when porous beads used carbonaceous binder phase amount must not be decreased.

4. CONCLUSIONS

Defect free SiC-C composite with lowest bulk density of $1,56 \text{ gr.cm}^{-3}$ were successfully produced by using resin binder and followed by graphitization process. It was concluded that the amount carbonaceous phases is the key factor for the properties of the ablation material. Addition of the porous silica gel beads decreased the ablation rate when the carbonaceous phases presents in proper amount. It was concluded that heat sink behaviour of the porous expanded silica

gel beads, which have closed pore structure, are the main reason for the decrease in the ablation rate. Sudden absorption of the heat in the beads resulted in the decrease of the carbonaceous binder phase and prevent oxidation. For the improved ablation resistance, addition of antioxidants to the SiC-C system can be studied in the future studies.

Acknowledgements: The author wish to thanks to the Kümaş Refractory Co. and Ezcacıbaşı Esan Raw Material Co. for their contributions during the supplements of the materials.

REFERENCES

- Aneziris, C.G., Hubalkova, J., Barabas R., 2007. Microstructure evaluation of MgO-C refractories with TiO₂- and Al-additions. *Journal of the European Ceramic Society* 27, 73.
- Başpınar, M.S., Kahraman, E., 2011. Modifications in the properties of gypsum construction element via addition of expanded macroporous silica granules. *Construction and Building Materials* 25, 3327.
- Otaka, T., Asoka, Y., 2002. Thermal intumescent characteristics of heated sodium silicate. *ASME International mechanical engineering congress proceedings (IMECE)*, vol. 1, New Orleans, Louisiana, USA, pp. 205
- Srebrenkoska, V., Bogoeva-Gaceva, G., and Dimeski, D., 2009. Composite material based on an ablative phenolic resin and carbon fibers. *Journal of Serbian Chemical. Society* 74 (4), 441.
- Yan, B., Zhaofeng, C., Jianxun, Z., Jianzhong, Z. and Yun, J., 2009. Effects of ablation at different regions in three-dimensional orthogonal C/SiC composites ablated by oxyacetylene torch at 1800 °C, *Journal of materials processing technology*, 209, 3438.
- Wang Y., Xu Y., Wang Y., Cheng L., and Zhang L., 2010. Effects of TaC addition on the ablation resistance of C/SiC. *Materials Letters* 64, 2068.

UNIAXIAL STRESS-STRAIN BEHAVIOR OF ALUMINUM FOAMS AND ALUMINUM FOAM BASED COMPOSITE SANDWICHES

S. Bahar Baştürk^{1,a}, Metin Tanoglu²

1. Celal Bayar University, Department of Materials Engineering, Manisa, Turkey

2. İzmir Institute of Technology, Department of Mechanical Engineering, İzmir, Turkey

a. Corresponding author(*bahar.basturk@cbu.edu.tr*)

ABSTRACT: Cellular metals, particularly aluminium (Al) foams, have great potential to be used in various engineering applications due to their high specific stiffness and strength, fire resistance, noise reduction, vibration damping and cost efficiency. The microstructural properties as well as densification behavior significantly affect the mechanical performance of Al foams under various loading conditions. In this study, the mechanical characterization of the ALULIGHT-AFS™ panels with three different thicknesses (8, 20 and 30 mm) was carried out by uniaxial compression, tension and shear tests. Based on the compression test results of as-received Al foams, the specimens with higher elastic modulus usually exhibited higher collapse strength for each thickness set of foams. It was found that the foam thickness increase generally resulted in collapse strength decrease. As the thickness increases, the structural defects are expected to increase and the lower strength values of thicker foams are attributed to this. Similar trend was also observed for the tension and shear test results and 8 mm foams showed the highest strength values. The foams mentioned above were also integrated with skins composed of Al sheet and glass fiber reinforced polypropylene (GFPP) composite fibre/metal laminates. The mechanical characteristics of these composites fabricated with different techniques were also investigated within this study.

1. INTRODUCTION

Sandwich structures are the combination of different materials that provide stiffness and strength with a lightweight composition compared to the traditional materials. The distinctive properties of the sandwiches are obtained by the contribution of each component's superior feature into the whole system. Characteristically, sandwiches consist of three main components: the face-sheets (skin), the core and the adhesive for the integration of constituents [Sarzynski and Ochoa, 2003]. The main goal of the core material is to enhance the flexural stiffness of the sandwich structures. Usually, core materials have lower density in order to decrease the total weight of the sandwich panel [Gupta, 2003]. Metallic foams have various remarkable features for acting as cores in

sandwich structures such as good stiffness and strength to weight ratios, good sound damping, electromagnetic wave absorption, high thermal insulation and non-combustibility. Among the metallic foams, the popularity of aluminum foams is growing up in transport (aerospace, ship building, etc.), sport and biomedical industries. Relatively recent studies related with aluminum foam have revealed the impact performance of sandwich structures with composite skins. The researchers observed that the significant impact energy is absorbed through buckling and crushing of cells throughout the foam core [Styles, 2008]. Under compressive loads, aluminum (Al) foams show characteristic stress-strain behavior. Compressive stress-strain curve consists of three distinct regions: linear elastic

region, collapse region and densification region [Gibson and Ashby, 2000]. The present work reports the microstructural characterization of as-received aluminum foams with various thicknesses (8, 20 and 30 mm). Uniaxial compression, tension and shear properties of these foams were evaluated according to the corresponding standards. The FML systems including Al metal layer and glass fiber reinforced polypropylene (GFPP) composite were integrated with Al foams to manufacture the sandwich panels. Both compression and flexural behavior of Al foam based sandwiches were investigated and their energy absorption capacities were determined. The flexural characteristics of the Al foam sandwiches were evaluated as a representative case in this paper.

2. MATERIALS AND METHODS

Aluminum (Al) sheet and aluminum foam with various thicknesses were used to produce sandwich structures in this study. The physical and geometrical properties of the materials used in the experiments are tabulated in Table 1. The closed-cell aluminum foam material (supplied by Shinko Wire Company™ Ltd., Austria) with the trade name ALULIGHT-AFS® was employed as core material, as shown in Figure 1. The non-crimp commingled glass fiber/PP fabrics (0/90⁰ biaxial glass) were used to manufacture thermoplastic based composite structures. Polypropylene (PP) and glass fibers were used as a matrix and reinforcement components, respectively. The non-crimp fabrics used in this study were developed in collaboration with TELATEKS™ A.Ş.

2.1. Production of Layered Structures

The non-crimp fabrics consisting of commingled glass and polypropylene fibers (GFPP) with a glass fiber volume fraction of 34.5 % were stuck between Al sheet and Al foam as an intermediate layer for

producing hybrid Al sheet/GFPP/Al foam sandwich structures. In the present study, the adhesion at the composite/metal interface was achieved by surface pretreatment of Al components with amino based silane coupling agent, incorporation of PP based film containing 20 wt. % a maleic anhydride modified polypropylene (PP-g-MA). In order to increase the effect of bonding between the components of the sandwich samples, the combination of silane treatment and PP-g-MA/PP based film addition was also investigated.

Table 1: Physical and geometrical properties of materials used in mechanical test (mean value ± standard deviation)

	Thickness (mm)	Density (gr/cm ³)
	(+/- std. dev.)	(+/- std. dev.)
Al Foam	8 (0.2)	0.409 (0.006)
	20 (1.05)	0.395 (0.003)
	30 (0.1)	0.456 (0.007)
GFPP	0.65 (0.2)	1.254 (0.04)
Al Sheet	2.01 (0.2)	2.7 (0.01)



Figure 1: As-received ALULIGHT™ AFS Al foam panels with 8, 20 and 30 mm thickness.

2.2. Mechanical Testing of Foams and Foam Based Sandwiches

The flatwise compression tests were applied to the samples in order to characterize the compression behavior of

as-received Al foams. Tensile tests were performed according to the ASTM C 365-03 standard to determine the flatwise tensile properties of the foams parallel to the skin. The specimens were adhesively bonded to a specially prepared T-shape steel sections using Bison[®] bond epoxy adhesive. Both compression and tension test samples were prepared with about 50 mm x 50 mm by sectioning from larger panels. The shear properties of the Al foam cores were determined for each thickness and the test coupons had a constant rectangular cross-section and the length-to-thickness ratio was 12 as recommended by ASTM C273-61. The specimens were adhesively bonded to specially prepared Al/Cr alloy plates by Bison[®] high bond epoxy matrix. At least three specimens were tested and force versus stroke values was recorded. All tests were conducted at room temperature with 250 kN loading cell using the Shimadzu[™] universal test machine. The crosshead speed of compression test specimens was 2 mm/min while the tensile and shear tests were performed at 0.5 mm/min. The three point bending test (3PB) according to the ASTM C 393-62 standard was applied to the prepared sandwiches in order to measure the flexural properties such as core shear strength, face-sheet strength and collapse loads. At least three specimens for each type of bonding were tested and force versus stroke values was recorded using a 100 kN capacity Devotrans[®] universal test machine at a crosshead displacement rate of 2 mm/min.

3. RESULTS AND DISCUSSIONS

The compressive stress-strain behavior of as received (monolithic) Al foams up to 60% deformation were recorded and typical representative data for each thickness set of foams are plotted in Figure 2. It is obvious from the Figure 2 that the stress-strain curves initially increase almost linearly up to a specific

value of the compressive stress and then the stress remained almost constant up to a certain value (plateau region). The densification region started as the completion of the plateau region. The collapse of foam cells ends and they start to densify at a specific strain.

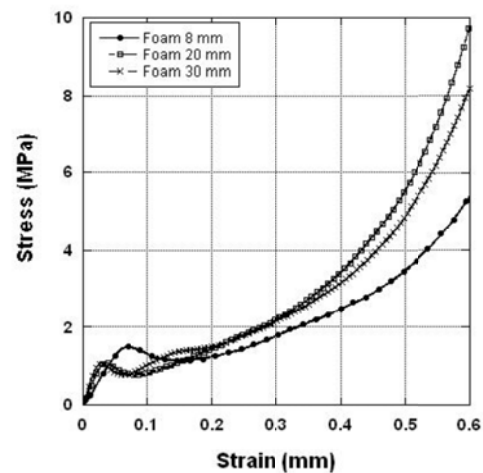


Figure 2: Compressive stress vs. strain curves of as received Al foams.

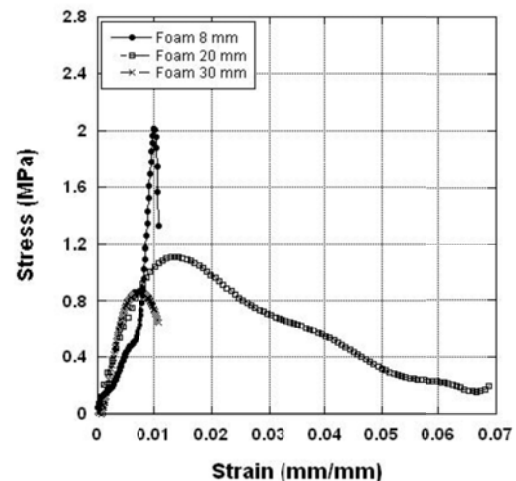


Figure 3: Tensile stress vs. strain curves of as received Al foams.

The typical tensile stress-strain behavior of Al foams are shown in Figure 3. Based on this figure, the curves show linear elastic behavior at a strain rate of roughly 0.01, smaller than in compression followed by plastic yielding. For the

closed cell Al foams, bending of cell edges are accompanied by stretching of the cell faces during compression. However, in tension test, the foams show local fracturing and failed at low applied strains due to the highly defective and thin cell faces.

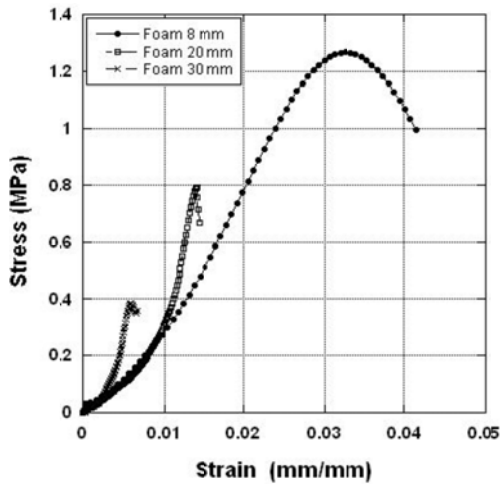


Figure 4: Shear stress vs. strain curves of as received Al foams

As it is known, the generation of pure shear is rather difficult on the cellular materials. In this study, the shear stress testing was performed by the application of tensile stress from the loading plates and Figure 4 shows the typical stress-strain relationship of tested Al foams. The foams showed an initial linear behavior followed by yielding with a subsequent peak load. After the material reaches its peak load, the load carrying ability drops dramatically. A small group of shear samples exhibited a short stress plateau after reaching the peak load, however, high percentage of foams showed a sharp drop in load after initial failure. The modulus and collapse/yield strength values of Al foams with respect to their thickness were tabulated in Table 2. The foam thickness increase resulted in the increase of compressive elastic modulus for the as-received Al foams. It was found that the foam thickness increase generally resulted in collapse

strength decrease. As the thickness increases, the structural defect probably increases and the lower strength values of thicker foams are attributed to this. For tension test, it was found that the foam thickness increase resulted in the decrease of yield strength and increase of elastic modulus. As compared to the compressive strength results, the ultimate tensile strength magnitudes decreased for each thickness set of foams. The shear strength and shear modulus values of the 8 mm Al foams are significantly higher as compared to the thicker foams (20 mm and 30 mm). The increase of foam thickness led to the decrease of yield strength between the magnitudes of 30%-60% compared to the tension test.

Table 2: Physical and geometrical properties of as-received Al foam test samples (average values are given with standard deviations).

	8 mm foam	20 mm foam	30 mm foam
Compressive Modulus (MPa)	29.06 (4.79)	36.21 (4.48)	54.61 (10.85)
Tensile Modulus (MPa)	92.58 (47.3)	170.65 (52.4)	239.7 (22.61)
Shear Modulus (MPa)	51.12 (9.68)	18.57 (6.60)	20.02 (3.22)
Comp. Collapse Strength (MPa)	2.07 (0.46)	1.11 (0.06)	1.15 (0.66)
Tensile Yield Strength	2.01 (0.3)	1.21 (0.19)	0.87 (0.15)
Shear Strength (MPa)	1.21 (0.21)	0.83 (0.02)	0.39 (0.01)

The flexural response of sandwich structures bonded with PP-g-MA/PP based film after silane treatment is plotted as a representative case in Figure 5. The

sandwiches exhibited an initial linear elastic region with a subsequent non-linear part resulted in the decrease of slope near to the maximum force. The foam thickness increase led to the increase of both equivalent flexural rigidity and the slope of linear elastic region. The force level after maximum force values showed some differences among the samples. Regardless of the bonding type and the core thickness, some sandwich structures showed a smooth force drop while some of them exhibited a sudden drop followed by a plateau region in which the foams fail by buckling of the cell walls and edges.

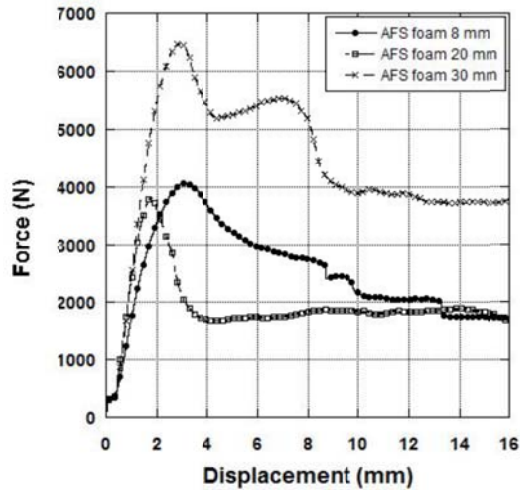


Figure 5: Force-displacement graphs of Al foam sandwiches bonded with PP-g-MA/PP based adhesive film after silane surface treatment of Al surfaces.

4. CONCLUSIONS

Based on the compression test results of as-received Al foams, the specimens with higher elastic modulus usually exhibited higher collapse strength for each thickness set of foams. It was found that the foam thickness increase generally

resulted in collapse strength decrease. As the thickness increases, the structural defect probably increases and the lower strength values of thicker foams are attributed to this. Similar trend was also observed for the tension and shear test results and 8 mm foams showed the highest strength values. The flexural behaviors of Al foam based sandwiches integrated with PP-g-MA/PP were characterized by three point bending test. The samples modified with silane coupling agent and consolidated with PP-g-MA/PP based film showed the highest performance among all the bonding types. The damage progression appeared to be steady and consistent with the increase of displacement and the core shear and debonding were found to be the major failure mechanisms observed during the flexural tests.

Acknowledgement: The financial support provided by the Scientific and Technological Research Council of Turkey (TUBITAK)-107A15 Project is gratefully acknowledged.

REFERENCES

- Sarzynsky, M.D. and Ochoa, O.O., 2005. Carbon Foam Core Composite Sandwich Beams: Flexure Response, *Journal of Composite Materials*, Volume (39), 1067.
- Gupta, N., 2003. Characterization of Synthetic Foams and Their Sandwich Composites: Modeling and Experimental Approach, Phd Thesis, Louisiana State University, USA.
- Styles, M., 2008. Characterization of the flexural behavior of aluminum foam Composite sandwich structures, Phd Thesis, Australian National University, Australia.
- Ashby, M.F. and Gibson, L.J. 2000. *Metal Foams: A Design Guide*, Butterworth-Heinemann, USA.

DYNAMIC BEHAVIOR ANALYSIS OF FML/ALUMINUM FOAM SANDWICH STRUCTURES UNDER SIMULATED BLAST TEST

Bahar Baştürk^{1,a}, Metin Tanoglu²

1. Celal Bayar University, Materials Engineering, Manisa, Turkey

2. İzmir Institute of Technology, Department of Mechanical Engineering, İzmir, Turkey

a. Corresponding author(*bahar.basturk@cbu.edu.tr*)

ABSTRACT: In this work, the sandwich structures using thermoplastic fiber/metal laminate (FML) skins and metal foam cores were manufactured for the anti-blast applications. The FML system consists of glass fiber/PP fabrics (GFPP) and aluminum (Al) metal sheet act as the skin component and closed cell Al foams with various thicknesses act as the core component in the sandwich panels. The blast responses of the sandwiches were predicted by the application of “simulated blast test”. The principle of this test allows us to simulate the blast loading effects on the panels. For the air blast analysis, the applied force shows dynamic characteristics, however, in the simulated blast test the sandwich panel was assumed as a single-degree of freedom mass spring system to include the dynamic effect. Based on this approach, the light-weight sandwich composites were subjected to compression loading with a very special test apparatus. Liquid soap filled rubber sack below the sandwich panels simulated the characteristics of blast loading with simply supported boundary conditions under quasi-static compressive forces. Based on the pressure-time graphs of the blast waves depending on the explosive amount and stand-off distance, the blast characteristic time (T) was determined. By the calculation of natural frequency (ω) of the panel and characteristic time parameters, the $f(T\omega)$ product was determined. The peak deflection (δ_{peak}) of the sandwich structure under blast loading was predicted by considering the dimensionless deflection ($\delta_{peak} / \delta_{static}$) - $f(T\omega)$ graph.

1. INTRODUCTION

In the recent decade, the application of composite sandwiches as anti-blast systems has been increasingly growing. The performance of such material systems has great importance in order to sustain the safety and survivability. There are a number of studies dealing with the response of composite structures under dynamic loading. Both experimental and numerical characterizations of these systems are investigated by many researchers in the literature. Ballistic pendulum is generally used to generate micro-scale blast loading in order to determine the performance of materials. In addition, drop tower tests are commonly employed for the evaluation of energy absorption characteristics of structures. However, the presences of these equipment's are not as common as quasi-static loading test machines [Zhu,

2008]. Andrews *et al.*, (2009) focused on the situation of air blast loading of lightweight foam core sandwich panels. The compressive quasi-static loading was carried out and dynamic effect was included in the analysis by considering the panel as a single degree of freedom mass-spring system. Variable design parameters such as sandwich thickness, skin/core thickness or core density can be altered and this analysis can help designers to evaluate these differences with a relatively easy way. This approach was based on the theory described in the book written by W. Baker and his co-workers. The damage response of a loaded structure is almost always dynamic. Thus, the structural response or damage usually depend on both static and dynamic properties of the applied system such as the magnitude of the amplitude

(peak overpressure) of the blast loading, the loaded area, mass or inertia of the structure and the duration of the transient pressure loading. These concepts can be adopted into simple dynamic mechanical systems as shown in Figure 1 [Baker *et al.*, 1983].

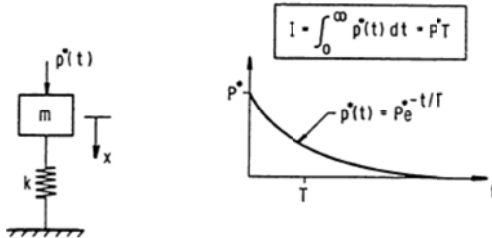


Figure 1: Linear oscillator loaded by a blast wave [Baker *et al.*, 1983].

In the present study, prediction of the blast response of the prepared sandwich systems were investigated by applying “simulated blast tests”. In this test, compressive quasi-static loading was carried out and the sandwiches were assumed as single degree of freedom mass-spring systems in order to include the dynamic effect. The blast performances of hybrid material systems were predicted based on the modified formulations presented by Baker *et al.*, (1983) and Andrews *et al.*, (2009).

2. MATERIALS AND METHODS

In this study, the Fiber-Metal Laminates (FMLs) containing glass fiber reinforced polypropylene (GFPP) and aluminum (Al) sheet were bonded together with Al foam cores for composing the sandwich panels. A closed-cell aluminum foam material (supplied by Shinko Wire Company Ltd, Austria) with the trade name ALULIGHT-AFS[®] was chosen as the core material. The foam panels contained about 0.6 mm thick non-porous Al skin that was produced during manufacture of the foam. The Al sheet/GFPP FML system and Al foam were integrated with PP-g-MA/PP based film under 200°C and 1.5 MPa pressure. The sandwich panels with 30 mm

thickness are given as representative specimens in Figure 2.



Figure 2: 30 mm thick Al/Al foam / GFPP sandwich panels fabricated.

2.1. Experimental Set Up for Panel Analysis under Simulated Blast Testing

In this study, the quasi-static loading was applied to the sandwich panels with three foam thicknesses (8, 20 and 30 mm). The 500 mm x 500 mm Al foam structures were sectioned from larger panels and the Al sheet/GFPP FML system was integrated with PP based film under 200°C and 1.5 MPa pressure. The produced sandwich structure was cut with a jigsaw and divided into four equal parts with the dimension of 250 mm x 250 mm. The sandwich was considered as a single degree of freedom mass-spring system that allows simulating the effect of blast loading on the panels. The simply supported boundary conditions were assumed in the analysis. The system had three main components: upper support frame, a liquid soap filled rubber bladder and a lower frame. The sandwiches were located in the lower frame and the support frame acting as simple support boundary condition to the samples. The liquid soap filled rubber bladder was placed under the aluminum foam sandwich to provide uniformly distributed load over the surface of the panel. The linear variable differential transformer (LVDT) was used in order to detect the central deflection of the panels under compressive loading. An extra

apparatus was manufactured to protect the LVDT measurement system and placed upon the upper support frame. A rigid steel plate was also located on to the LVDT protection apparatus for homogeneously distribute the load from the compression test head to the whole system and the manufactured test rig is shown with its components in Figure 3.

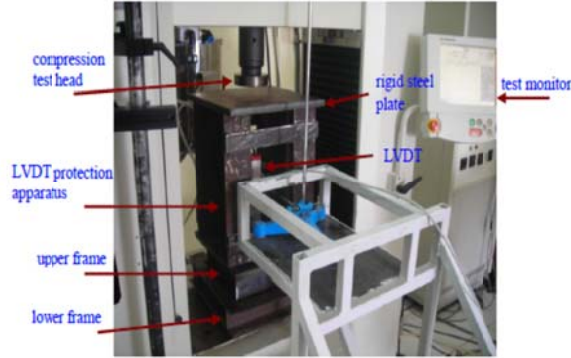


Figure 3: Simulated blast test apparatus

2.2. The Blast Response Evaluation of Sandwich Panels under Simulated Blast Test

In the simulated blast test analysis, natural frequency (ω) for the lowest mode of the panel should be considered. Other parameters like θ and ρ^* can be calculated by using the equations (1) and (2). The constants L_1 and L_2 , E_f , h_f , h_c , d , ν_f , G_c , ρ_c and ρ_f represent panel dimensions, face-sheet elastic modulus, face-sheet thickness, core thickness, face-sheet and core thickness summation, face-sheet Poisson ratio, core modulus, core density and face-sheet density, respectively.

$$\omega = \pi^2 \left[\left(\frac{L_2}{L_1} \right)^2 + 1 \right] \sqrt{\frac{E_f h_f d^2}{2\rho^* L_2^4 (1-\nu_f^2)}} \quad (1)$$

$$\theta = \frac{E_f h_f h_c}{2G_c L_2^2 (1-\nu_f^2)} \quad \rho^* = \rho_c h_c + 2\rho_f h_f \quad (2)$$

Compliance expression of the panel has critical importance and this term is defined as the ratio between the central

deflection of the panel and corresponding applied pressure, which is called as p_0 . The effective compliance of the panel denoted as C_p can be formulated by implementing both bending (w_b) and shear deflection (w_s) terms as in equation (3). In our analysis, total deflection terms (w_t) of the panels were determined from the sensitive LVDT measurements and these results were used to determine the final deflections under blast loading conditions [Andrews *et al.*, 2009].

$$C_p = \frac{(w_b + w_s)}{p_0} = \frac{w_t}{p_0} \quad (3)$$

Based on the analysis of the differential equation controlling this simple system, the peak deflection δ_{peak} of the panel under the dynamic pressure loading is equal to the quasi-static deflection that would be seen under the blast pressure P_{blast} , multiplied by $f(T\omega)$ product. The “ T ” is the blast characteristic time and the static deflection, δ_{static} , can be determined from the panel compliance and the known blast pressure P_{blast} . Thus we may write the peak deflection as in equation (4) [Andrews *et al.*, 2009]. The dimensionless deflection $\delta_{peak}/\delta_{static}$ (function f) is plotted as a function of the product $T\omega$ and shown in Figure 4.

$$\delta_{peak} = \delta_{static} f(T\omega) \quad (4)$$

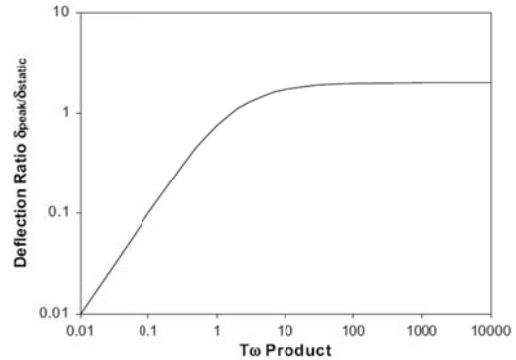


Figure 4: Characteristic function of SDOF system under blast loading [Andrews, 2009].

3. SIMULATED BLAST TEST ANALYSIS OF SANDWICH PANELS

The peak deflections of the panels under blast loading were predicted based on the analysis described below.

- Identification of the failure pressure (P_{fail}) and corresponding failure deflection (w_{fail}) under quasi-static compression test.
- Evaluation of the panel compliance (C_p) by means of LVDT measurements.
- Determination of panel natural frequency (ω).
- Determination of maximum blast pressure (P_{blast}) and blast characteristic time (T) parameters depending on the TNT amount and stand-off distance.
- Calculation of panel deflection (δ_{static}) under maximum blast pressure (P_{blast}) by considering panel compliance.
- Evaluation of $T\omega$ product and determination of peak deflection (δ_{peak}) under maximum blast pressure.

The central deflection-force data of Al foam sandwich panels during quasi-static tests were recorded and the stress was calculated by considering the area acting over the support frame. The typical sandwich panels for each thickness set of foam based sandwiches were selected as representative cases and their stress versus deflection behavior are given in Figure 5. For 8 mm Al foam sandwich, three distinct regions are visible on the graphs. In the first region, a linear deflection behavior is observed at low pressures. In the second zone, in spite of the stress increase, the central deflection is almost constant and in addition, thicker Al foam sandwich structures (20 mm and 30 mm foams) show extra regions. In the plots, the sample with 20 mm Al foams continue into 4th region at around 1.5 MPa pressure and the central deflection value is slightly changing. Similarly, the panel with 30 mm core exhibited five different zones during the test.

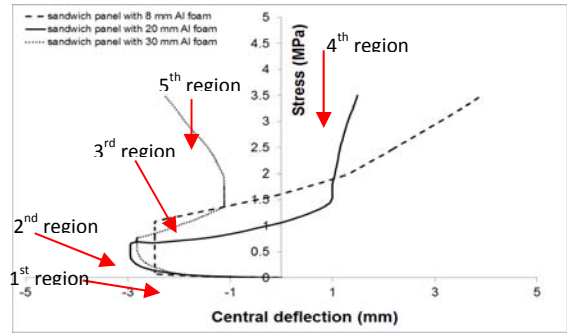


Figure 5: Stress vs. central deflection graph of Al sheet/GFPP/Al foam sandwiches with various thicknesses during simulated blast test.

Core shear and core crushing were the main failure mechanisms observed in the panels after simulated blast tests. In spite of the debonding between the FML components during the initial stages of the test, the protection of the core was performed by GFPP composite. Therefore, debonding of FML is not considered as the dominant failure mechanisms such as skin wrinkling or core shear. Independent of core thickness, all the samples exhibited similar type of deformation patterns and 8 mm foam sandwich panel is given in Figure 6 as a representative case. Both front face and back face views are presented and 8 mm foam structures showed relatively uniform deformation profile. The back face of the samples exhibited dome-shaped deformation moving out from the center, changing a more quadrangular shape towards the supported edges. The effective compliance (C_p) term of structures were determined by considering the central deflection (w_l) and compressive stress (σ_{fail}) values associated with core-crushing failure.

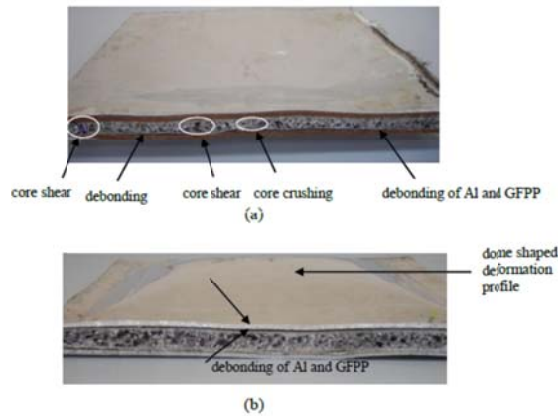


Figure 6: Deformation patterns of Al/GFPP/Al foam sandwich panel with 8 mm Al foam and loaded up to 200 kN: (a) front face view (b) back face view.

The real central deflection values of the samples were calculated by subtracting the compliance deflection values of individual bladder and sandwich system from the simulated blast test deflection values. Core material properties significantly affected the natural frequency of the structures. The maximum natural frequency was calculated as 3283.8 N/m.kg for 8 mm Al foam sandwich panel. The numerical analyses performed by LS Dyna CONWEP module were used to determine the pressure-time ($P-t$) history of the blast loading according to the explosive amount and stand-off distance parameters. Eight different TNT weights (12, 10, 8, 6, 4, 2, 1.37 and 1 kg) and six stand-off distances (0.2, 0.3, 0.4, 0.5, 0.6 and 0.7m) were selected as representative cases for the determination of blast parameters. Both blast characteristic time (T) and maximum blast pressure (P^*) were obtained based on these analyses and the maximum blast pressure was calculated as 15.645 MPa for 12 kg TNT explosive. The increase of TNT amount led to the increase of blast pressure, static and peak deflection parameters, as expected. The 20 mm and 30 mm Al foam sandwich panels showed the highest peak deflections of 241.049 mm and

219.720 mm for 12 kg TNT explosive, respectively. However, the deflection of 8 mm sandwich structure for the same weight was calculated as 181.546 mm. The maximum blast pressure was calculated as 14.89 MPa when the distance between the panel and the explosive center was 0.2 m. The increase of stand-off distance resulted in the decrease of blast pressure, as expected. The 20 mm Al foam panel exhibited highest peak deflection of 226.619 mm when the stand-off distance was 0.2 m. The minimum deflection was calculated as 24.163 mm for 8 mm foam structure at 0.7 m stand-off distance.

4. CONCLUSIONS

Core shear and core crushing were the main failure mechanisms observed in the panels after simulated blast tests. Independent of core thickness, all the samples exhibited similar type of deformation patterns. As compared with the static and peak deflections of the panels for the same explosive weights or stand-off distances, the 8 mm foam sandwich panel showed minimum values while the panel with 20 mm foam exhibited maximum deflections.

Acknowledgement: The financial support provided by the Scientific and Technological Research Council of Turkey (TUBITAK)-107A15 Project is gratefully acknowledged.

REFERENCES

- Zhu, F., 2008. Impulsive Loading of Sandwich Panels with Cellular Cores, Phd Thesis, Swinburn University of Technology, Australia.
- Andrews, E.W. and Moussa, N.A. 2009. Failure Mode Maps for Composite Sandwich Panels Subjected to Air Blast Loading, International Journal of Impact Engineering, Volume (36), 418.
- Baker, W., Cox, P., Westine, P., Kulesz, J., and Strehlow, R. (1983). Explosion Hazards and Evaluation, New York, Elsevier.

Al-Si BASED SYNTACTIC FOAMS BY USING POROUS SILICA GELS via VACUUM CASTING: CELL SIZE vs STRENGTH AND ENERGY ABSORBANCE BEHAVIOUR

İbrahim Yavuz¹, M.Serhat Başpınar^{2,a} and Hüseyin Bayrakçeken³

1. Afyon Kocatepe University, Technical Education Faculty, Automotive Edu.Dept. Afyonkarahisar, Turkey
2. Afyon Kocatepe University, Technical Education Faculty, Metal Edu. Dept., Afyonkarahisar, Turkey
3. Afyon Kocatepe University, Faculty of Engineering, Automobile Eng.Dept, Afyonkarahisar, Turkey
a. corresponding author (sbaspınar@aku.edu.tr)

ABSTRACT: There has recently been an increase in interest in the use of cellular materials in various structural and functional applications. Syntactic foams defined as a composite material with hollow or porous ceramic particles embedded in a continuous polymer or metal matrix. Metal matrix syntactic foams are a relatively new class of material with higher densities than traditional open or closed-cell metallic foams produced. They are not only used for structural applications but also used in functional applications such as low density heat sink and heat exchangers. In this study, the processing of aluminum-based syntactic foams by a newly developed vacuum casting method was studied. Macroscale (larger than 1 mm diameter) fillers (space holders) were used rather than the powder fillers of previous syntactic foam studies. This paper presents SiO₂-based porous expanded silica gels used as fillers in the processing of syntactic foams by a vacuum-based infiltration method. Effect of cell-size (space holder diameter) on the density-strength relations and energy absorbance behaviour were investigated. Lowest relative density was measured as 0.31 gr.cm⁻³. It was concluded that; expanded silica gel density and size determines the strength-density relation. It also effect the cell wall thickness and shape.

1. INTRODUCTION

Today, growing industrial needs and new research and development studies resulted in new material groups. Most recent subject of materials science is the metallic foams and several researches are conducted on it. Although metallic foams are not natural materials, due to the similar structure of the foam it is called as foam. There has recently been an increase in interest in the use of cellular materials in various structural and functional applications. Banhart [2001] detailed metallic foam production by a variety of casting and powder metallurgy routes. Syntactic foams are recently developed materials. These foams are different than the conventional metallic foams. Density of the foam reduced by addition of the second materials which are very low density. Usually micro scale second

phase added into the metal and polymer matrixes. Syntactic foams were first introduced in 1960s. [Chittineni 2009]. Syntactic foams are some kind of composite materials where the matrix and a second functional phase exist [Egidio et al. 2000]. Syntactic foams usually defined as matrix with low density fillers [Chittineni 2009]. Filler materials can be glass, ceramic or metal with different sizes [Ashida 1995]

2. EXPERIMENTAL

Silica gel is a granular, vitreous, highly porous form of silica made synthetically from sodium silicate. Despite its name, silica gel is a solid. Silica gel is fireproof and highly heat resistant, chemically stable and, highly hygroscopic and has a large specific surface area. Because of these characteristics, silica gel is often

applied as a drying agent and catalyst carrier. Although silica gel has a very high melting temperature (1600 °C), it loses its chemically-bound water molecules and hygroscopic properties when heated above 300 °C. Sodium silicate, the main raw material for the silica gel, is intumescent. Başpınar and Kahraman [2011] showed that it is possible to produce foam-like, very low density, high temperature resistant and spherical functional filler materials from ordinary silica gel. The density and strength of the expanded silica gel depend strongly on the processing conditions used (heating-cooling regime and expansion temperature). Industrial grade, non-indicating, non-toxic, food and drug quality, 1–3 mm diameter silica gel beads (2.1 g.cm^{-3}) were selected to produce expanded light weight beads. The SiO_2 content of the silica gel is over 99.5%. Because expanded silica gels are fragile and have very thin and dense outer shells, a different expansion regime than that used in a previous study conducted by Başpınar and Kahraman [2011] was used. Therefore, the collapse of silica gels during high temperature vacuum casting process was prevented. A heating rate of $10 \text{ }^\circ\text{C.min}^{-1}$ was used. Silica gels were held one hour at the maximum expansion temperature, before being cooled in the furnace. Differential scanning calorimetric (DSC) analysis showed that 12.5 % weight loss was observed upon heating up to 1200 °C. Absorbed free water left the granules at 100 °C with a corresponding endothermic peak in the DSC profile. A continuous and broad exothermic peak was observed to commence at 1000 °C. XRD studies showed that the original crystal structure of the silica gel was amorphous. However, a cristobalite phase was formed due to the heat input to the system during the expansion process. Because such amorphous to crystalline phase changes are exothermic, a broad

exothermic peak was observed in the DSC analysis. Expanded silica gel has a very low density, lower than that of water, which is why conventional water immersion techniques are inadequate for measuring the silica gel bulk density. Because the expanded silica gel granules were almost spherical in shape, bulk density of the granules were calculated by simply measuring their weight and dividing it by the volume of the spheres. The lowest density granules were produced by processing at 1100 °C. Higher expansion temperatures resulted in increased densities due to increased sintering activity at higher temperatures for a given expansion conditions. After the expansion process, expanded silica gels were classified according to their particle size by simple screening process. -4 mm, +2 mm, -4,75mm,+4mm, -5,6 mm+4,75mm size range particles were used for the sample preparation. Figure 1 shows the casting system and the moulds. After making some trials on the vacuum level, -0,6 bar was used for the suction of the molten metal into the expanded silica gels. Figure 1b shows the effect of increasing vacuum level on the size of the successful sample production. Al-12Si alloy was used. Before the casting both mould and the gels were preheated to different temperatures according to the gel size.



Figure 1: Vacuum casting system and casting mould.

Table 1 shows the series codes and used expanded silica gel sizes. Compression test applied to the samples. Relative

densities of the samples were calculated and presented.

3. RESULTS AND DISCUSSIONS

Table 1 shows the strength and density relations of the different foams. When the diameter of the gels increased plastic collapse strength (σ_p) decreased. Compression tests shows that produced syntactic foams shows similar deformation behaviour as in the case of regular metallic foams (Figure 2).

As the expanded silica gel diameter increased, the density of the foams decreased. Depending on the increase in the gel sizes, the cell wall thicknesses were decreased (Figure 3).

Table 1: Series and the properties.

Series	Gel Size (mm)	σ_p (Mpa)	Relative Density ρ^*/ρ_s
AS 241	2,00-4,00	22	0,37
AS 471	4,00-4,75	19	0,35
AS 561	4,75-5,60	16	0,31

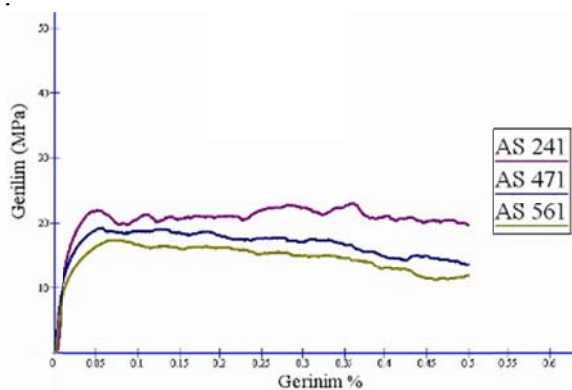
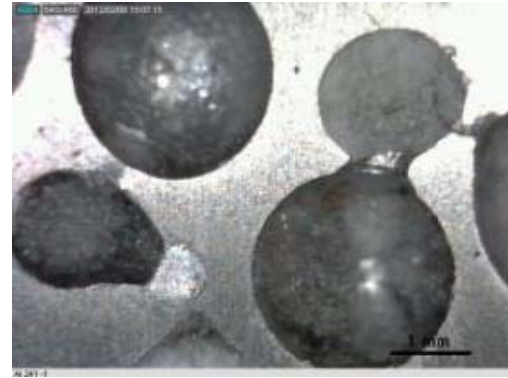
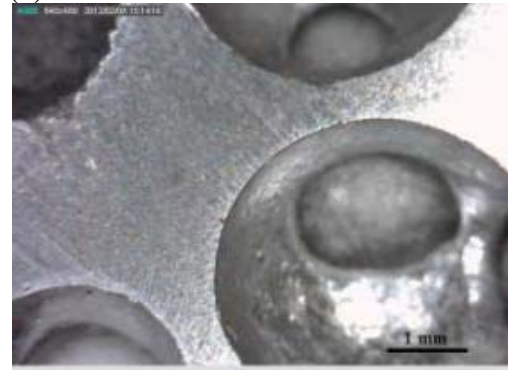


Figure 2: Stress vs Strain diagram during the compression test.



(a)



(b)



(c)

Figure 3: Cell structure and size of the produced syntactic foams. (a: AS241, b: AS471, c: AS561)

According to the compression test, densification region was not observed. Densification regions in the deformation curves are usual behaviour. In this experiments, samples were broken until 50% deformation due to the fragile nature of the cell walls. It was concluded that, such a behaviour should be due to the dissolution of the silica in aluminum matrix. Therefore cell wall compositions changed to the higher content of silicium.

4. CONCLUSIONS

New production technology for the production of syntactic foams were successfully introduced. Cell size and the density of the foam strongly depending on the expanded silica gel density and size. Minimum relative density of 0,31 gr.cm^{-3} was obtained. Although this value is higher than the conventional metallic foams (its around 0,2-0,25 gr.cm^{-3}), reached densities were much lower than the conventional syntactic foam densities. As a conclusion, expanded silica gels found to be effective for the production of metallic foams.

Acknowledgements: Authors wish to thanks to Afyon Kocatepe University Research Grant which allows the financial support to this project.

REFERENCES

- Banhart, J., 2001. Manufacture, characterisation and application of cellular metals and metal foams. *Progress in Materials Science*, 46: 559–632.
- Chittineni, K., 2009. Ally Gradient Syntactic Foams. Jawaharlal Nehru Technological University, Master of Science, India
- Egidio, R., Enrico, P., Alberto, C., 2000. Mechanical behaviour of a syntactic foam: Experiments and Modelling. *Int. J. of Solids and Structure*. 37: 5773-5794
- Ashida, K., 1995. Handbook of Plastic Foams: Types, Properties, *Manufacture and Applications*, Noyes Publications, 147-163.
- Başpınar, M.S., Kahraman, E., 2011. Modifications in the properties of gypsum construction element via addition of expanded macroporous silica granules. *Construction and Building Materials*. 25, 3327–3333.

MICROWAVE ABSORPTION PROPERTIES OF CO,MN SPINEL FERRITE–ACRYLATED EPOXY NANOCOMPOSITES

Harun Bayrakdar

Çanakkale Onsekiz Mart University, Faculty of Engineering, Department of Materials Science and Engineering, ÇANAKKALE, TURKEY

a. Corresponding author (h.bayrakdar@comu.edu.tr)

ABSTRACT: We have investigated the electromagnetic (EM) characteristics of $\text{Co}_x\text{Mn}_{1-x}\text{Fe}_2\text{O}_4$ spinel ferrite (where $x = 0.0, 0.5$ and 1.0) nanoparticles (NPs) / acrylated epoxy nanocomposite material at 8-20 GHz. $\text{Co}_x\text{Mn}_{1-x}\text{Fe}_2\text{O}_4$ NPs. have been synthesized by cetyltrimethylammoniumbromide (CTAB) assisted hydrothermal route using NaOH. A reflection loss (RL) of -59.60 dB was found at 12 GHz for an absorber thickness of 2 mm. $\text{Co}_x\text{Mn}_{1-x}\text{Fe}_2\text{O}_4$ may be attractive candidates for EM wave absorption materials.

1. INTRODUCTION

In recent years, the number of applications of electromagnetic (EM) wave in the high GHz ranges, which are wireless telecommunication systems, radar, local area network, medical equipment, etc., [1-4]. With together applications of electromagnetic (EM) wave in the high GHz ranges, the electromagnetic interference (EMI) problems have been attracting more attention recently due to the extensive growth in the application of electronic devices and security such as computer local area networks, mobiles phones, laptops, microwave oven etc[5-7]. Ferrites serve as better electromagnetic interference (EMI) suppressors compared to their dielectric counterparts on account of their excellent magnetic properties. Ferrite materials exhibit various electrical and magnetic properties of which the complex permeability and the complex permittivity, in particular, are important in determining their high frequency characteristics [8–13].

2. EXPERIMENTAL

2.1. Preparation of Nano-Particles $\text{Co}_x\text{Mn}_{1-x}\text{Fe}_2\text{O}_4$

Nanoparticles of $\text{Co}_x\text{Mn}_{1-x}\text{Fe}_2\text{O}_4$ have been prepared nanoparticles using

surfactant-assisted hydrothermal process by using CTAB. According to this method, 0.003 mol. surfactant cetyltrimethylammonium (CTAB) was dissolved in 35 ml. deionized water to form a transparent solution. The synthesize processes have been presented in detail by Bayrakdar [7].

2.2. $\text{Co}_x\text{Mn}_{1-x}\text{Fe}_2\text{O}_4$ Nanoparticles and Acrylated Epoxy Composite Process

Powders of $\text{Co}_x\text{Mn}_{1-x}\text{Fe}_2\text{O}_4$ and Acrylated epoxy are taken in weight ratio of 5:x:1 (x is not disclosed) and thoroughly mixed powders, Acrylated epoxy and silver hexafluoroantimonate, which was used initiator for polymerization process, in the glass bottle in the oven at 150°C . It was mixed and waited 2 days for polymerization process. After his polymerization process was finished, this polymer was homogenized in mortar and then poured in the mould which is $a = 19.4$ mm, d (cross section length) = 21.5 mm and c (thickness) = 2 mm and waited 20 min. at room temperature [7].

3. MICROWAVE MEASUREMENTS

Measurements were made rectangular waveguide technique. Samples was put into a rectangular shape of size $a = 19.4$

mm, d (cross section length) = 21.5 mm and c (thickness) = 2 mm to fit in rectangular waveguides and connected between two waveguides [7,12]. Figure shows the measured absorption spectra for prepared polymer. In the present studies, optimized thickness is 2 mm for sample. This sample shows maximum reflection loss of -59.60 dB. The reflection loss for sample thickness of 2 mm in the frequency range of 8–20 GHz was made for prepared these composites [7,12].

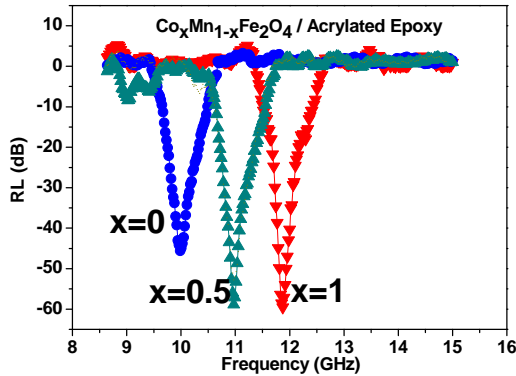


Figure 1: Absorption spectra of samples.

4. CONCLUSION

It has been successfully synthesized ferrite-polymer nanocomposite structures. These microwave absorbers are using synthesized prepared composite has been fabricated, and successfully demonstrated for a maximum reflection loss of -59.60 dB at 12 GHz with a bandwidth of approximately 2 GHz in a sample thickness of 2 mm. Our results indicate that the nanocomposite structures exhibit good absorption performances. This reflection loss is measured very high and this bandwidth is higher than normally reported. It can be said that this samples will provide great benefits for electromagnetic applications and EMI shielding characteristics.

Acknowledgments

The author are grateful to the The Scientific and Technological Research Council of Turkey (TUBİTAK, Contract no: 112E044) for financial support of this study.

REFERENCES

- [1] Wickenden B.V.A, and W.G. Howell, 1st Conf. Roc. Military Microwaves, 1978, 310.
- [2] Abbas S.M., Dixit A.K., Chatterjee R., Goel T.C., J. Magn. Magn.Mater.2007, 309, 20.
- [3] Maeda T., Sugimoto S., Kagotani T., Tezuka N., Inomata K., J MagnMagn Mater, 2004, 281, 195.
- [4] Jing L., Wang G., Duan Y., Jiang Y., J. of All. and Com., 2009, 475, 862.
- [5] Lim K.M., Kim M.C., Lee K.A., Park C.G., IEEE Trans. Magn. 2003, 39, 1836.
- [6] Sugimoto S., Okayama K., Kondo S., Mater. Trans., JIM. 1998, 39, 1080.
- [7] Bayrakdar H., J MagnMagn Mater, 2011, 323, 1882.
- [8] Zabetakis D., Dinderman M., Schoen P., Adv. Mater.2005, 17, 734.
- [9] Da Silva J.B, Mohallem N.D.S., J MagnMagn Mater, 2001, 226, 230.
- [10] Arshak K.I., Ajina A., Egan D., Microelectron J, 2001, 32, 113.
- [11] Hwang Y., Mater Lett 2006, 60, 3277.
- [12] Bayrakdar H., PIER, 2012, 269.

DIELECTRIC AND MAGNETIC PROPERTIES OF CO-MN SPINEL FERRITES

Harun Bayrakdar^a

Çanakkale Onsekiz Mart University, Faculty of Engineering, Department of Materials Science and Engineering, Çanakkale, Turkey

a. Corresponding author (h.bayrakdar@comu.edu.tr)

ABSTRACT: We have synthesis ferrite nanoparticles and ferrite-polymer nanocomposite structures, theoretically and experimentally investigated magnetic and dielectric behavior of ferrite nanoparticles. Variation of complex dielectric permittivity at room temperature with frequency in the range 1MHz–3GHz has been studied. Magnetization measurements showed that coercivity increasing with decreasing temperature and with increasing some particles.

Keywords: Nanoparticles, Magnetic properties, Dielectric properties.

1. INTRODUCTION

The physical properties of ferrites are related the structure of solids. They belong to a large class of compounds which have spinel structure. The spinel unit cell consists of a cubic array of 32 oxygen anions, 16 Fe⁺³ ions 8 Fe⁺² ions. A total 24 metal cations are distributed among eight tetrahedral interstices and sixteen octahedral interstices [Gorteret *al.*, 1954; Selimet *al.*, 1999].

Ferrites have vast applications, from microwave to radio frequencies. They exhibit relatively high resistivity at carrier frequency, sufficiently low losses for microwave applications and a wide range of other electric properties [Shinde and Jadhav, 1998; Sawatakyet *al.*, 1968].

The technological importance of AFe₂O₄ (A = Ni, Co, Zn, Mn...ext) has motivated several studies on the synthesis as well as the physical properties of this material. Shortly, ferrite nanoparticles have been prepared by mechanical-milling [Rondinoneet *al.*, 2000], hydrothermal method [Pallaiet *al.*, 1996; Skomski, 2003; Ramankutty and Sugunan, 2001; Reddy and Manorama, 1999], microwave route [Candlishet *al.*,

1992; Skandanet *al.*, 1994; Kishimotoet

al., 1994; Li *et al.*, 2004], sol–gel method [Goya and Rechenberg, 1999], surfactant-assisted route [Kasapogluet *al.*, 2007; Baykal *et al.*, 2008].

Spinel ferrites are technologically important group of materials. So, they can be easily used optical, magnetic, electrical and electromagnetic absorbing materials. To give some examples for these materials to use as electrodes in energy storage devices, in magnetic storage devices, as catalysts, RADAR absorbing media, etc. [Sertkolet *al.*, 2009; Bayrakdar, 2011; Bayrakdar and Pier, 2012; Bayrakdar and Esmer, 2010].

In this work, we have synthesis, theoretically and experimentally investigated magnetic and dielectric behavior of ferrite nanoparticles. Theoretical and experimental investigations of dielectric properties of samples were investigated using LCR Meter.

2. SYNTHESIS OF NANOPARTICLES

NPs of Co_xMn_{1-x}Fe₂O₄ (where x=0.0, 0.5 and 1.0) were prepared using the surfactant-assisted hydrothermal process using CTAB. According to this method, a 0.003 mol surfactant CTAB was dissolved in 35 ml deionized water to from a transparent solution. The synthesis

processes are presented in detail by reference [Bayrakdar, 2011; Bayrakdar 2012; Bayrakdar and Esmer, 2010].

3. CHARACTERIZATION

3.1 Magnetization measurements

The influence of different hydrolyzing agents on the particle size and magnetic behavior of $\text{Co}_x\text{Mn}_{1-x}\text{Fe}_2\text{O}_4$ NPs were investigated. This method is very useful for solid state powder technology. XRD results of powders of $\text{Co}_x\text{Mn}_{1-x}\text{Fe}_2\text{O}_4$ showed that nanoparticles indicate high phase purity, crystalline and inverse spinel ferrites. Magnetization measurement of $\text{Co}_x\text{Mn}_{1-x}\text{Fe}_2\text{O}_4$ sample hydrolyzed by NaOH was performed using the VSM technique and the M-H curves of the sample were investigated at room and 10 K. Coercivity and the magnetization of $\text{Co}_x\text{Mn}_{1-x}\text{Fe}_2\text{O}_4$ NPs increase with the decrease in temperature. Also, the coercivity and the magnetization decrease with the increase in Co. These results can be explained that Co content attributed to the anisotropic properties of Mn. These samples can be used very successfully the magnetic recording, electromagnetic absorbing technologies applications.

3.2. Dielectric measurements

The complex dielectric permittivity, $\epsilon = \epsilon' - i\epsilon''$, where ϵ' is the reel part, and ϵ'' is the imaginary part of dielectric constant, was measured by Agilent 4287 A RF LCR Meter at room temperature in the frequency range of 1 MHz-3 GHz. The real part of dielectric constant was calculated from the equation $\epsilon' = C_p d / (\epsilon_0 A)$, where C_p is the parallel capacitance, d is the inter electrodes distance, ϵ_0 is the permittivity of free space, A is cross-sectional area (the space area).

4. CONCLUSIONS

The dielectric response of $\text{Co}_x\text{Mn}_{1-x}\text{Fe}_2\text{O}_4$ NPs have been studied in the frequency range of 1 MHz to 3 GHz and at room temperatures. Dielectric measurements showed that the complex permittivity of composites was significantly modified by the incorporation of nanoparticles with different Co/Mn ratios. With increasing Co/Mn ratio, the increase of the real and imaginary part of permittivity as well the resonance peak of real and imaginary part of permittivity shifts to higher frequencies. We observed a resonance peak in the curves of both the real and imaginary parts of complex permittivity can be interpreted as different compositions of Mn-Co ratio that is atomic polarization.

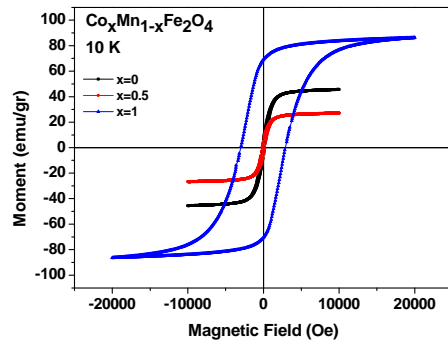
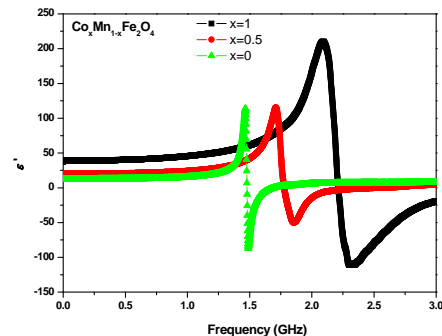


Figure 1: Magnetization loop of $\text{Co}_x\text{Mn}_{1-x}\text{Fe}_2\text{O}_4$ NP hydrolyzed by NaOH at 10K.

(a)



(b)

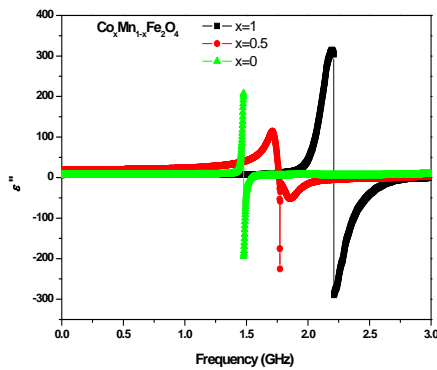


Figure 2: Dependency of real and imaginary part of permittivity on frequency for (a) and (b).

REFERENCES

- E.W. Gorter, 1954. Saturation magnetization and crystal chemistry of ferrimagnetic oxides, Philips Res. Repts. 9, 295.
- M.S. Selim, G. Turkey, M.A. Shouman, G.A. El-Shobaky, 1999. Effect of Li^{2+} O doping on electrical properties of CoFe_2O_4 , Solid State Ionics, 120, 173.
- S.S. Shinde, K.M. Jadhav, 1998. Electrical and dielectric properties of silic on substituted cobalt ferrites, Materials Letters, 37, 63.
- G.A. Sawatky, F. Van Der Woude, A.H. Morrish, 1968. Cation Distributions in Octahedral and Tetrahedral Sites of the Ferrimagnetic Spinel CoFe_2O_4 , J. Appl. Phys. 39, 1204.
- A.J. Rondinone, A.C.S. Samia, Z.J. Zhang, 2000. Characterizing the magnetic anisotropy constant of spinel cobalt ferrite nanoparticles, Appl. Phys. Lett., 76, 3624.
- V. Pallai, D.O. Shah, 1996. Synthesis of high-coercivity cobalt ferrite particles using water-in-oil microemulsions, J. Magn. Mater., 163, 243.
- R. Skomski, 2003. Nanomagnetism, J. Phys. Condens. Matter., 15, R841.
- C.G. Ramankutty, S. Sugunan, 2001. Surface properties and catalytic activity of ferrosinels of nickel, cobalt and copper, prepared by soft chemical methods, Appl. Catal. A, 218, 39.
- C.V.G. Reddy, S.V. Manorama, V.J. Rao, 1999. Effect of Mo_2N on the gas-sensing characteristics of SnO_2 -based sensors, Sens. Actuators B: Chemical, 55, 90.
- I.E. Candlish, B.H. Kear, B.K. Kim, 1992. Nanostuct. Mater, 1, 119.
- G. Skandan, H. Hahn, M. Roddy, W.R. Cannon, 1994. Ultrafine-Grained Dense Monoclinic and Tetragonal Zirconia, J. Am. Ceram. Soc., 77, 1706.
- M. Kishimoto, Y. Sakurai, T. Ajima, 1994. Magneto-optical properties of Ba-ferrite particulate media, J. Appl. Phys., 76, 7506.
- F. Li, J.J. Liu, D.G. Evans, X. Duan, 2004. Stoichiometric synthesis of pure MFe_2O_4 (M = Mg, Co, and Ni) spinel ferrites from tailored layered double hydroxide (hydrotalcite-like) precursors, Chem. Mater., 16, 1597.
- G.F. Goya, H.R. Rechenberg, 1999. Ionic disorder and Néel temperature in ZnFe_2O_4 nanoparticles, J. Magn. Mater., 196, 191.
- N. Kasapoglu, B. Birsoz, A. Baykal, Y. Koseoglu, M.S. Toprak, 2007. Synthesis and magnetic properties of octahedral ferrite $\text{Ni}_{1-x}\text{Co}_x\text{Fe}_2\text{O}_4$ nanocrystals, Cent. Eur. J. Chem., 5(2), 570.
- A. Baykal, N. Kasapoglu, Y. Koseoglu, M.S. Toprak, H. Bayrakdar, 2008. CTAB-assisted hydrothermal synthesis of NiFe_2O_4 and its magnetic characterization, J. Alloys Compounds, 464, 514.
- M. Sertkol, Y. Koseoglu, A. Baykal, H. Kavas, A. Bozkurt, M.S. Toprak, 2009. Microwave synthesis and characterization of Zn-doped nickel ferrite nanoparticles, J. Alloys Compounds, 486, 325-329.
- Bayrakdar H., 2011. Complex permittivity, complex permeability and microwave absorption properties of ferrite-paraffin polymer composites, J. Magn. Mater. 323 1882-1885.
- Bayrakdar H., 2012. Electromagnetic Propagation and Absorbing Property of Ferrite-Polymer Nanocomposite Structure, Progress In Electromagnetics Research M, 25, 269-281.
- Bayrakdar H. and Esmer K., 2010. Dielectric characterization of $\text{Ni}_x\text{Co}_{1-x}\text{Fe}_2\text{O}_4$ nanocrystals thin film over a broad frequency range (1 MHz–3 GHz), J Appl Phys., 107, 044102.

SYNTHESIS AND ELECTROMAGNETIC ABSORBING PROPERTIES OF SPINEL FERRITES AND PARAFFIN NANOCOMPOSITE STRUCTURES

Harun Bayrakdar^a

Çanakkale Onsekiz Mart University, Faculty of Engineering, Department of Materials Science and Engineering, Çanakkale, Turkey

a. Harun Bayrakdar (h.bayrakdar@comu.edu.tr)

ABSTRACT: We have synthesis ferrite nanoparticles and ferrite-polymer nanocomposite structures, theoretically and experimentally investigated electromagnetic propagation, absorption properties of these nanocomposite materials at 8-20 GHz in microwave guides. Microwave absorbing measurements was made by transmission line method for an absorber thickness of 2 mm. These nanocomposites can be attractive candidates for microwave absorption materials.

Keywords: Nanocomposites, Microwave properties, Electromagnetic Interference, Microwave propagation

1. INTRODUCTION

The technological importance of AFe_2O_4 (A = Ni, Co, Zn, Mn...ext) has motivated several studies on the synthesis as well as the physical properties of this material. Shortly, ferrite nanoparticles have been prepared by mechanical-milling [Pallai *et al.*, 1996], hydrothermal method [Skomski, 2003; Ramankuttyand Sugunan, 2001 Reddy *et al.*, 1999], microwave route [Candlish *et al.*, 1992; Skandanet *al.*, 1994; Kishimotoet *al.*, 1994; Li *et al.*, 2004], sol-gel method [Goya *et al.*, 1999], surfactant-assisted route [Kasapoglu *et al.*, 2007; Baykal *et al.*, 2008].

Spinel ferrites are technologically important group of materials. So, they can be easily used optical, magnetic, electrical and electromagnetic absorbing materials. To give some examples for these materials to use as electrodes in energy storage devices, in magnetic storage devices, as catalysts, RADAR absorbing media, etc. [Sertkol *et al.*, 2009; Bayrakdar and Pier, 2012].

In this work, cetyltrimethylammonium bromide (CTAB) assisted hydrothermal route using NaOH was used to synthesize

$Co_xMn_{1-x}Fe_2O_4$, nanoparticles (NPs) and prepared $Co_xMn_{1-x}Fe_2O_4$ / Paraffin nanocomposite materials. The synthesized nanocrystalline samples were characterized the electromagnetic properties of samples were investigated using Network analyzer.

2. EXPERIMENTAL

2.1. Preparation of nano-particles $Co_xMn_{1-x}Fe_2O_4$

Nanoparticles of $Co_xMn_{1-x}Fe_2O_4$ have been prepared nanoparticles using surfactant-assisted hydrothermal process by using CTAB. According to this method, 0.003 mol. surfactant CTAB was dissolved in 35 ml. deionized water to form a transparent solution. Then ferric chloride hexahydrate ($FeCl_3 \cdot 6H_2O$) of 0.004 mol. added to solution and mixed 10 min. After 10 min. stirring, stoichiometric amount of $CoCl_2 \cdot 6H_2O$ and $MnCl_2 \cdot 6H_2O$ was introduced into mixed solution under vigorous stirring. Deionized water added to make the solution for a total volume 40 ml. and pH of the solution mixture was adjusted to 11. Before being transferred to teflon lined auto clave of 50 ml. capacity, the solution mixture was pretreated under an ultrasonic water bath for 40 min.

hydrothermal synthesis was carried out at 130°C for 15 h. in an electric oven without shaking or stirring. Afterwards, the autoclave was allowed to cool to room temperature gradually. The black precipitate collected was washed with distilled water several times in an ultrasonic bath to remove any possible impurities. The solid was then heated at 100°C and dried under vacuum for 5 h [Bayrakdar, 2011; Bayrakdar and Pier, 2012].

2.2. Composite preparation

Powders of $\text{Co}_x\text{Mn}_{1-x}\text{Fe}_2\text{O}_4$ and paraffin are taken in weight ratio of 5:x:1 (x is not disclosed) and thoroughly mixed powders and paraffin in the glass bottle. The mix was homogenized in mortar and then poured in the mould which is a = 19.4 mm, d (cross section length) = 21.5 mm and c (thickness) = 2 mm and waited 20 min. at room temperature [Bayrakdar, 2011; Bayrakdar and Pier, 2012].

3. ELECTROMAGNETIC ABSORBING MEASUREMENTS

Measurements were made rectangular waveguide technique. Samples was put into a rectangular shape of size a = 19.4 mm, d (cross section length) = 21.5 mm and c (thickness) = 2 mm to fit in rectangular waveguides and connected between two waveguides. Figure shows the measured absorption spectra for prepared nanocomposites [Bayrakdar, 2011; Bayrakdar and Pier, 2012].

4. CONCLUSION

It has been successfully synthesized ferrite-polymer nanocomposite structures. Theoretically and experimentally were investigated the electromagnetic propagation, absorption properties of these nanocomposite materials at 8-20 GHz in microwave guides. The microwave absorption, magnetization, EMI shielding, of spinel ferrites/ paraffin nanocomposite were analyzed. These

microwave absorbers are using synthesized prepared composite has been fabricated, and successfully demonstrated for a maximum reflection loss of ~-50 dB at 12 GHz with a bandwidth of approximately 2 GHz in a sample thickness of 2 mm.

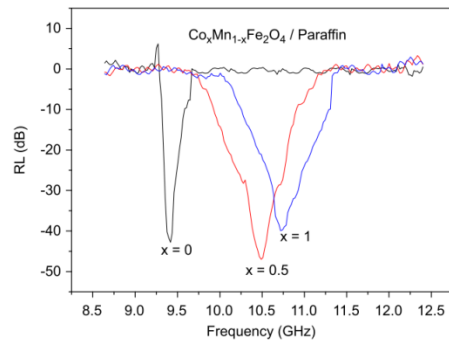


Figure 1: Absorption spectra of nanocomposite samples.

Acknowledgments

The author are grateful to The Scientific and Technological Research Council of Turkey (TUBITAK, Contract no: 112E044) for financial support of this study

REFERENCES

- V. Pallai, D.O. Shah, 1996. Synthesis of high-coercivity cobalt ferrite particles using water-in-oil microemulsions, *J. Magn. Mater.*, 163, 243.
- R. Skomski, 2003. Nanomagnetism, *J. Phys. Condens. Matter.*, 15, R841.
- C.G. Ramankutty, S. Sugunan, 2001. Surface properties and catalytic activity of ferrosinels of nickel, cobalt and copper, prepared by soft chemical methods, *Appl. Catal. A*, 218, 39.
- C.V.G. Reddy, S.V. Manorama, V.J. Rao, 1999. Effect of Mo_2N on the gas-sensing characteristics of SnO_2 -based sensors, *Sens. Actuators B: Chemical*, 55, 90.
- I.E. Candlish, B.H. Kear, B.K. Kim, 1992. Processing and Properties of Nanostructured WC-Co, *Nanostuct. Mater.*, 1, 119.
- G. Skandan, H. Hahn, M. Roddy, W.R. Cannon, 1994. Ultrafine-Grained Dense Monoclinic and Tetragonal Zirconia, *J Am. Ceram. Soc.*, 77, 1706.

- M. Kishimoto, Y. Sakurai, T. Ajima, 1994. Magneto-optical properties of Ba-ferrite particulate media, *J. Appl. Phys.*, 76, 7506.
- F. Li, J.J. Liu, D.G. Evans, X. Duan, 2004. Stoichiometric synthesis of pure MFe_2O_4 ($M = Mg, Co, \text{ and } Ni$) spinel ferrites from tailored layered double hydroxide (hydrotalcite-like) precursors, *Chem. Matter.*, 16, 1597.
- G.F. Goya, H.R. Rechenberg, 1999. Ionic disorder and Néel temperature in $ZnFe_2O_4$ nanoparticles, *J. Magn. Magn. Matter.*, 196, 191.
- N. Kasapoglu, B. Birsoz, A. Baykal, Y. Koseoglu, M.S. Toprak, 2007. Synthesis and magnetic properties of octahedral ferrite $Ni_{\chi}Co_{1-\chi}Fe_2O_4$ nanocrystals, *Cent. Eur. J. Chem.*, 5(2), 570.
- A. Baykal, N. Kasapoglu, Y. Koseoglu, M.S. Toprak, H. Bayrakdar, 2008. CTAB-assisted hydrothermal synthesis of $NiFe_2O_4$ and its magnetic characterization, *J. Alloys Compounds*, 464, 514.
- M. Sertkol, Y. Koseoglu, A. Baykal, H. Kavas, A. Bozkurt, M.S. Toprak, 2009. Microwave synthesis and characterization of Zn-doped nickel ferrite nanoparticles, *J. Alloys Compounds*, 486, 325-329.
- Bayrakdar H., 2011. Complex permittivity, complex permeability and microwave absorption properties of ferrite-paraffin polymer composites, *J. Magn. Magn. Mater.*, 323, 1882-1885.
- Bayrakdar H., 2012. Electromagnetic Propagation and Absorbing Property of Ferrite-Polymer Nanocomposite Structure, *Progress In Electromagnetics Research M* 25, 269.

INVESTIGATION OF THE COMPACTION BEHAVIOUR OF Ag₈ZnO COMPOSITE PRODUCED BY MECHANICAL ALLOYING

Serkan BIYIK^{1,a}, Murat AYDIN²

¹Karadeniz Technical University, Department of Metallurgical and Materials Engineering, Trabzon, Turkey

²Karadeniz Technical University, Department of Mechanical Engineering, Trabzon, Turkey

a. Corresponding author (serkanbiyik@ktu.edu.tr)

ABSTRACT: In this study, silver and zinc oxide powders were processed by mechanical alloying and powder metallurgy techniques to obtain Ag₈ZnO composite, and the green density, porosity and microhardness values of this composite at different compaction pressures were investigated. Planetary type ball mill was used to achieve homogeneous distribution of the reinforcement (zinc oxide) in the matrix (silver). For this reason, particle size and morphology at different milling times were determined, and the relationship between particle size and milling duration was examined. The optimum ball-milling time is approximately 0.5 h. In addition, four different pressure values, namely 40, 60, 80 and 100 bars, were selected to investigate the effect of compaction pressure on green density, hardness and porosity ratio. The compaction was performed separately for each pressure level, and the green compacts produced by this way were analyzed by using SEM coupled with energy dispersive X-ray spectroscopy (EDX). The experimental results showed that the highest green density and microhardness values were obtained with the compaction pressure of 100 bar. Besides, the porosity ratio constantly decreases with increasing compaction pressure, and reaches its minimal at 100 bar. The EDX map characterization showed that zinc oxide distribution was homogeneous in the silver matrix.

1. INTRODUCTION

Electric contact, which is mainly used for electrical and electronic applications and responsible for controlling one or more electric circuits by making or breaking the circuit, is one of the most important components of electromagnetic switches. Electrical contact materials should possess a good combination of electrical and thermal conductivities, wear performance and resistance to erosion and welding. Otherwise, the contact erosion which is defined as the material loss at the contact surfaces, for example, due to material evaporation by an arc, will occur [Gurevich, 2005]. However, none of the materials may have all of these properties by itself, and there is no such thing as a universal contact. Fine (unalloyed) silver is a soft, malleable and ductile metal, and it has the highest electrical and thermal conductivities among all the metals [Schwartz, 2002]. Therefore, it is used extensively in electromagnetic switches

such as relays and contactors. However, silver has some drawbacks such as low melting and boiling points, low mechanical strength, possible contact welding and a tendency to form sulfide films (tarnishing) [Braunovic *et al.*, 2006]. Due to the reasons mentioned above, it is necessary to form a composite containing metal oxide in order to increase strength against arc erosion and minimize welding. Hence, different types of silver-based composite electrical contact materials have been developed in order to meet the requirements for various applications [Swingler *et al.*, 2011]. The most common metal oxides used in electrical contacts are cadmium oxide (CdO), tin dioxide (SnO₂) and zinc oxide (ZnO).

The main aim of this study based on developing novel materials for electrical contacts used in electromagnetic switches is to optimize the manufacturing process

parameters for a specific electrical contact material. In this content, conventional powder metallurgy technique is combined with mechanical alloying process. The main reason of using the MA process is just for improvement of homogeneity with finer particle sizes.

In this study, the influence of compaction pressure on the microstructure and physical properties such as density, porosity and hardness of Ag8ZnO composites is investigated.

2. EXPERIMENTAL PROCEDURES

Silver was used as the matrix material and zinc oxide as the reinforcement for this study. As starting materials, very fine commercial elemental silver having particle size of 45 μm and 99.99 % purity and zinc oxide having particle size of 45 μm and 99.999 % purity powders were used for mechanical alloying experiments. Both silver and zinc oxide powders were supplied by Goodfellow Corporation.

The morphology of the starting powders was investigated by means of scanning electron microscopy (SEM) by Zeiss Evo LS 10 (Fig.1).

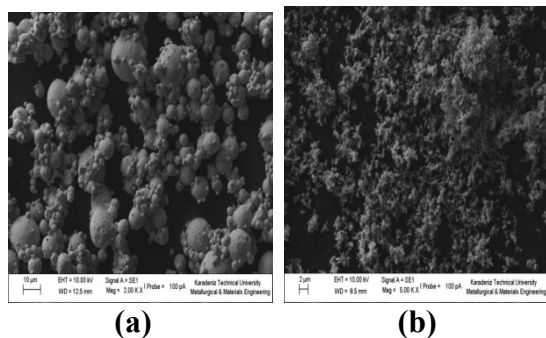


Fig. 1: Morphology of as-received powders: a) Silver powder, b) Zinc oxide powder

Planetary type ball mill (Fritsch Pulverisette 6) is used to carry out the milling experiments. Both the milling container and the grinding balls are made of tungsten carbide (WC). The diameter of the balls (Φ) is 10 mm. ZnO powders were added to silver powders in the amount of 8 % in weight. The milling was carried out at

a speed of 300 rpm and a ball-to-powder ratio (BPR) of 10:1. No process control agent (PCA) was used during milling. The starting powders were ball-milled separately for six different test durations between 0.5 to 10 h. For each test, the fresh powder charge was installed into the vial. After each test, the powder samples were taken for particle size measurements. Particle size distribution of the powders was analyzed using Malvern Mastersizer 2000. The variation of average particle sizes with milling duration was also investigated by using SEM. After MA experiments, the composite powders were processed to bulk solid pieces by conventional powder metallurgy route. For this reason, the Ag8ZnO composites were consolidated in the form of green compacts of approximately 6 mm diameter and 2 mm thickness by hydraulic press under the various pressure levels of 40, 60, 80 and 100 bars in a single action steel die.

The microstructure of the Ag8ZnO composite produced by MA was characterized by using SEM. The green compacts pressed at different compaction pressures were also studied by both secondary and backscattered electron modes of SEM to determine the porosity ratio for each condition. Hardness measurements were carried out by using a Microvickers hardness tester applying load of 4.904 N and loading period of 15 seconds. The EDX map characterization was performed to evaluate the homogeneity of the green compacts.

3. RESULTS AND DISCUSSION

3.1. Particle Size Evaluation and Morphology of Milled Powder

The effect of milling time on the average particle size of the Ag8ZnO composite powders is shown in Fig. 2. The analysis report containing average particle sizes for all specimens is presented in Table 1.

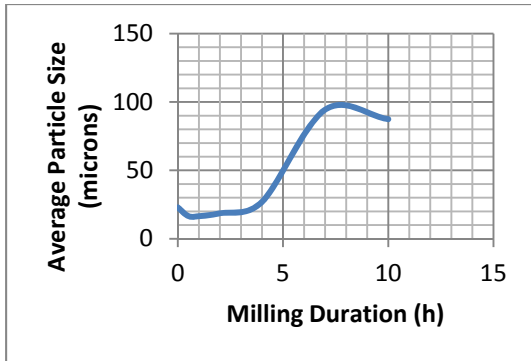


Fig. 2: The variation of average particle size with milling duration for Ag8ZnO composite powder

Table 1: Average particle sizes of the powders milled.

Milling duration (h)	Average particle size, μm		
	d_{10}	d_{50}	d_{90}
0	11.243	22.879	44.757
0.5	2.641	16.544	54.265
1	4.485	16.495	51.744
2	6.058	18.653	105.916
4	7.926	26.957	224.279
7	12.095	94.352	345.285
10	16.019	87.435	303.769

It can be seen from Fig. 2 and Table 1 that the average particle size was reduced in the first test duration (0.5h), and slightly increased up to 3 h, and then increased significantly. It is known that the powder charge contaminates with the prolonged milling durations [Suryanarayana, 2004]. Taking into account all of these factors, approximately 0.5 h of milling duration was determined as optimum milling time. However, the same process should be repeated for any specific composition as the optimum milling time depends on initial particle sizes of both matrix and reinforcement, and of course the MA conditions [Zoz *et al.*, 1999; Rehani *et al.*, 2009; Soni, 1999].

Particle size distribution and SEM micrograph of the Ag8ZnO composite formed after 0.5 h of milling duration is given in Figs. 3-4, respectively. It can be seen from Fig. 3 that average particle size

(APS) of Ag8ZnO composite powder is 16.544 μm (d(0.5)).

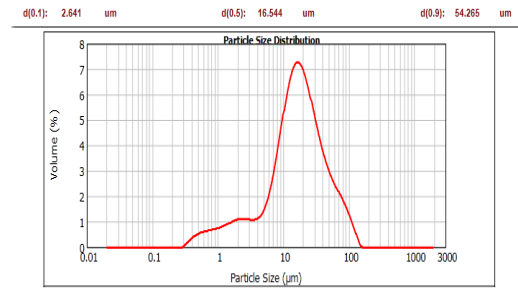


Fig. 3: Particle size distribution curve of Ag8ZnO composite powders

Fig. 4 represents that the Ag and ZnO powders being the constituents of Ag8ZnO composite are homogeneously mixed after the milling duration of 0.5 h.

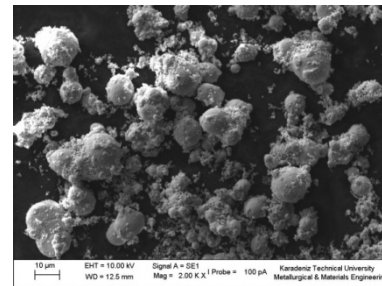


Fig. 4: Microstructure of the Ag8ZnO composite powders produced by ball-milling for 0.5 h.

3.2. Green Density of the Samples

The green density values of the samples increased with the increasing compaction pressure, and maximum value (9.307 g/cm^3) was obtained at the pressure of 100 bar as seen in Fig. 5. During densification in the die compaction, the compaction pressure increases as the resistance of the metal powder compact increases. Since particle sliding is dominant mechanism at low compaction pressures, large increases in density occur. As compaction continues, particle deformation takes place, and high pressures are required to exceed flow stress of the powder particles. Therefore, the rate of densification reduces with increasing pressure at further pressure levels. Hence, the increase in the green density is not remarkable above 100 bar pressure level.

Consequently, the pressure levels above 100 bar are deliberately eliminated.

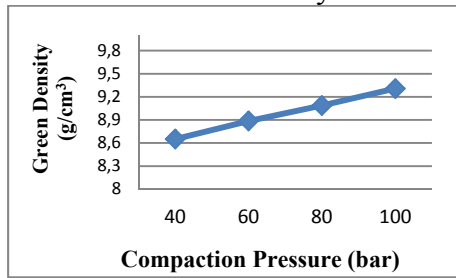


Fig. 5: The variation of green density vs. compaction pressure

It is known that the characteristic of green strength is very important [Upadhyaya, 1998]. The green compacts should maintain their size and shape during handling prior to sintering. Therefore, the pressure levels below 40 bar are deliberately eliminated as the pressure levels below 40 bar are insufficient to maintain the original shape. On the other hand, green density is also related to the size reduction and homogenization of composite powders. Reducing the average particle size increases particle surface area, and thus provides more sites for mechanical interlocking. Considering all pressure levels, the total contact area between powder particles is maximum at 100 bar. Furthermore, the green density is increased by minimizing surface oxidation and contamination. The contamination of the powders is macroscopical in the long-term milling. That is why the powders were no longer milled. Hence, the milling duration of 0.5 h at which the minimal particle size and contamination determined, was selected to manufacture green compacts.

3.3. Porosity

The porosity ratio gradually decreases and reaches its minimal at 100 bar as well (Fig. 6). At this pressure level, the porosity ratio calculated as approximately 5%.

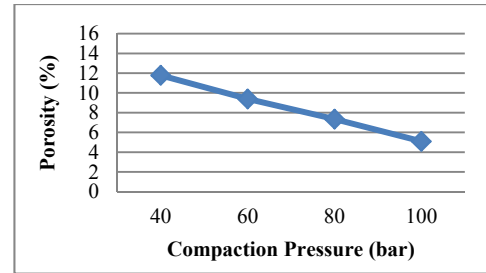


Fig. 6: The variation of porosity vs. compaction pressure

The porosity distribution of the samples was also characterized by using SEM in the backscattered electron mode as seen in Fig. 7. The SEM micrographs in Fig. 7 also confirm the decrease in porosity ratio with increasing compaction pressure.

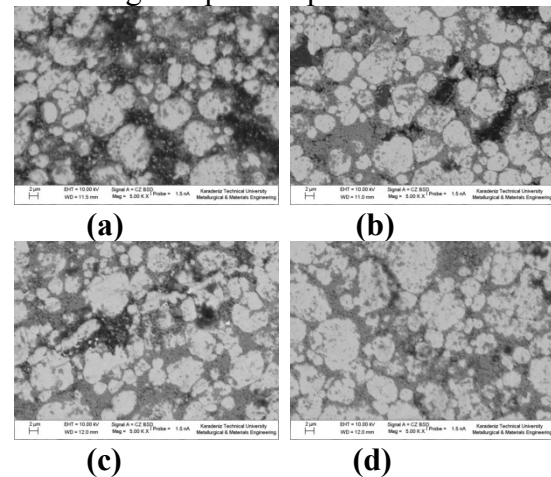


Fig. 7: SEM backscattered images of porosity distributions of Ag8ZnO composites pressed at different compaction pressures: a) 40 bar, b) 60 bar, c) 80 bar, d) 100 bar.

3.4. Hardness

It can be seen from Fig. 8 that the hardness increases gradually with increasing compaction pressure. The highest value of hardness was determined at 100 bar, and measured as 94.25 Vickers (HVN). This is because, the hardness of the silver matrix is increased by reinforcement phases via dispersion hardening. These brittle secondary phase particles minimize the welding phenomena of the contact surfaces by reducing the silver-to-silver contact area.

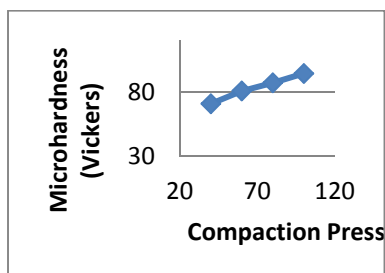


Fig. 8: The variation of microhardness vs. compaction pressure

3.5. Chemical Analysis (EDX)

The EDX map characterizations were investigated for assessing homogeneity of the composites produced at different pressures. It was determined that the ZnO distribution was homogeneous in each condition. As example of this, the EDS analysis and mapping report of Ag₈ZnO compacts pressed at 100 bar were given in Figs. 9 and 10, respectively.

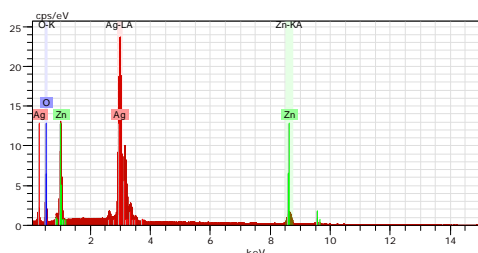


Fig. 9: EDS analysis of Ag₈ZnO green compact pressed at 100 bar.

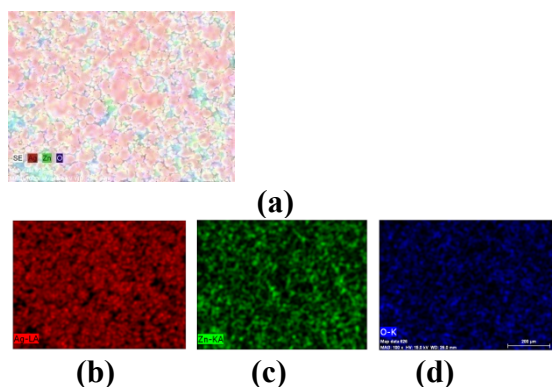


Fig. 10: Mapping analysis report of the Ag₈ZnO composite: a) selected area for EDX mapping, b) Ag element mapping, c) Zn element mapping, d) O element mapping

4. CONCLUSION

The following conclusions can be drawn for this investigation:

1. Mechanical alloying allows obtaining fine and homogeneous dispersion of the reinforcement (zinc oxide) phase in the matrix (silver).
2. Green density values increases with increasing compaction pressure.
3. Porosity ratio decreases up to 5 % with the increasing compaction pressure.
4. Hardness of the specimens increases with the increasing compaction pressure.

ACKNOWLEDGEMENT

This work has been supported by the Scientific Research Fund of Karadeniz Technical University (KTUBAP, Under Grant No:1073).

REFERENCES

- Braunović, M., Myshkin, N. K., Konchits, V. V., 2006. "Electrical Contacts: Fundamentals, Applications and Technology", CRC Press.
- Gurevich, V., 2005. "Electric Relays: Principles and Applications", CRC Press.
- Rehani, B. R., Joshi, P. B., Kaushik, V. K., 2009. "Nanostructured silver-graphite electrical contact materials processed by mechanical milling", Indian Journal of Engineering & Materials Sciences, 16, pp. 281-287.
- Schwartz, M., 2002. "Encyclopedia of Materials, Parts, and Finishes", CRC Press.
- Soni, P.R., 1999. "Mechanical Alloying: Fundamentals and Applications", Cambridge International Science.
- Suryanarayana, C., 2004. "Mechanical Alloying and Milling", CRC Press.
- Swingler, J., 2011. "Performance and arcing characteristics of Ag/Ni contact materials under DC resistive load conditions", IET Science, Measurement and Technology, 5, 2, pp. 37-45.
- Upadhyaya, G. S., 1998. "Powder Metallurgy Technology", Cambridge International Science.
- Zoz, H., Ren, H., Späth, N., 1999. "Improved Ag-SnO₂ Electrical Contact Material Produced by Mechanical Alloying", Metall, 53, pp. 423-428.

MICROSTRUCTURE AND CHARACTERIZATION OF B₄C REINFORCED Al2024 ALLOY MATRIX COMPOSITES PRODUCED BY MECHANICAL ALLOYING TECHNIQUE

T. Varol¹ and A. Canakci^{1,a}

1. Department of Metallurgical and Materials Engineering, Engineering Faculty
Karadeniz Technical University, Trabzon, Turkey.

a. Corresponding author (aykut@ktu.edu.tr)

ABSTRACT: In this study, Al2024 composite reinforced with B₄C particles was produced by mechanical alloying. Al2024 and B₄C powders were mixed mechanically and milled at different times (0.5, 1, 2, 5, 7 and 10h) to achieve Al2024-5 wt.%B₄C, Al2024-10 wt.%B₄C and Al2024-20 wt.%B₄C composite powders. The microstructure of Al2024-B₄C composites was investigated using a scanning electron microscope. The mechanical and physical properties of the composite specimens were determined by measuring the density, hardness and tensile strength values. The results showed that relatively homogeneous distribution of B₄C reinforcement in the matrix was obtained by mechanical alloying technique after 5h. The hardness of the composites increased with increasing the weight percentage of the B₄C particles, while the relative density of the composites decreased with increasing the weight percentage of the B₄C.

1. INTRODUCTION

Al alloys with superior mechanical and physical properties are promising materials for several industrial components where lightweight is required. One of the emerging technologies for the production of these alloys is the development of Al matrix composites. Mechanical properties of Al composites can be improved by dispersion of ceramic particles into the metal matrix [Hernandez Rivera et al., 2012; Wang et al., 2010]. Several methods such as squeeze casting [Miserez et al., 2002], semi-solid mechanical stirring [Qin et al. 2004] and mechanical alloying [Tousi et al. 2009] have been used for the production Al-based composites. Mechanical alloying (MA) has been proved to be a process that overcomes some drawbacks (for example segregation phenomena) that commonly occur in composites produced from liquid processes [Arik, 2008; Sivasankaran et al., 2010; Alizadeh and Aliabadi, 2011]. The aim of this study was to produce Al2024 alloy matrix reinforced with B₄C

by the mechanical alloying technique. B₄C reinforced Al2024 alloy matrix composites were synthesized at milling durations up to 10h and their microstructural characterization and mechanical properties were investigated.

2. EXPERIMENTAL PROCEDURE

To produce Al2024/B₄C composites, Al2024 powders with average particle size of about 75µm and B₄C powders with particle size of 5µm were used. The mixtures were milled using a planetary ball mill (Fritsch “Pulverisette 7, Premium line”) at different milling times (0.5, 1, 2, 5, 7 and 10 h). A ball to powder weight ratio of 10:1 was kept constant in the tungsten carbide vials. Methanol (2 wt.%) was used as a process control agent. The rotational speed was controlled at 400 rpm.

The above mixtures milled 0.5, 1, 2, 5, 7 and 10h were loaded into a steel die and cold pressed at 200MPa and then hot-pressed at 400 °C at a pressure of 400MPa. The microstructure of composites was characterized by means of scanning electron microscopy

(SEM). The density (δ) of compacts was determined by the Archimedes method. The hardness of all samples was measured by the Brinell hardness method and mean of at least five readings was taken at a load of 31.25 kgf. Tensile test was performed using an MTS model 45 electromechanical test instrument at room temperature on plate specimens with a cross-head speed of 0.5 mm min^{-1} . At least three samples were tested for each material.

3. RESULTS AND DISCUSSION

3.1. Microstructure

The presence of reinforcement particles mixed with Al2024 alloy powders changes the mechanical alloying/milling classification to a ductile/ brittle component system [Fogagnolo et al., 2003; Canakci et al., 2012]. It is proposed one possible scheme of the mechanical alloying process of this system in Fig. 1. To evaluate the distribution of B_4C particles in Al2024 matrix, SEM images were used. Fig. 2 shows the distribution of B_4C particles in Al2024 matrix in the powders containing 20 wt.% B_4C .

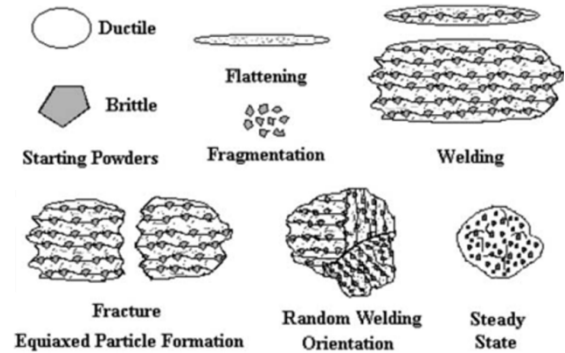


Fig. 1: The various stages of a ductile-brittle system during mechanical alloying.

It was observed that B_4C particles accumulated in the regions between the Al2024 matrix powders in the first stage of 0.5h milling (Fig. 2a). Fig. 2b shows the milling time less than 5h is not suitable to produce uniform composite. Therefore to investigate the particle distribution, the 10h milled samples are studied and the effect of weight percentage of B_4C is investigated. It was showed that increase in milling time resulted in the fragmentation of hard particles due to the impacts of balls. Moreover, the increase in milling time caused the homogenous distribution of reinforcements in the matrix (Fig. 2b). Finally, there was a balance between welding and fracturing of powders resulting in the homogenous distribution of particles (Fig 2c and 2d).

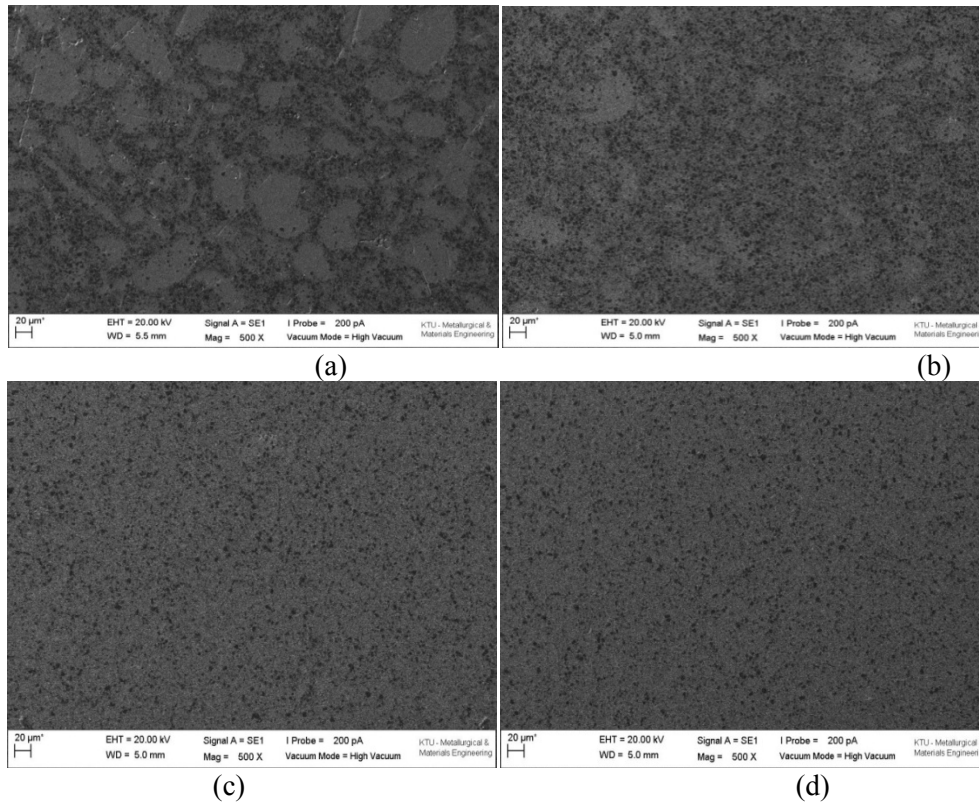


Fig. 2: Secondary electron images of the Al2024-20 wt% B₄C composite: (a) 0.5h, (b) 2h, (c) 5h, (d) 10h.

3.2. The Properties of the Composites

As can be seen in Fig.3a, the relative density of the composite decreased with increasing B₄C content. The presence of reinforcement particles decreased the relative density in mechanically alloyed composite. The relative densities for pressed samples decreased with increasing milling time, until reached a minimum value after 10h. Decreasing the relative density is due to the work hardening effect of MA and hence lower deformation capacity during pressing. MA promotes work hardening and homogeneous dispersion of B₄C particles which in turn decrease the powder deformation capacity.

Fig. 3b shows the hardness of the consolidated specimens. The hardness of the B₄C-reinforced composites is higher when compared to that of the unreinforced Al2024 samples. The hardness was found to also increase with increasing both milling time and B₄C

content. The increase in hardness of the nanostructured composites compared to nanostructured Al2024 samples is ascribed to the Orowan strengthening mechanism triggered by the B₄C particles. It can be seen from Fig. 3c that ultimate tensile strength of the Al2024-10 wt.% composites are higher than those of the other composites and unreinforced samples. With increasing the B₄C content from 0 to 10 wt.%, the tensile strength of composites increased as a result of increased interfacial area between the matrix and B₄C particles. In general, as the volume fraction of the B₄C particles increases, the interfacial area between the B₄C particles and matrix also increases, and more load can be transferred from the Al2024 matrix to the hard B₄C particles. At the same time, the increase in the volume fraction of the B₄C particles also nucleates more thermal induced dislocations in the Al2024 matrix

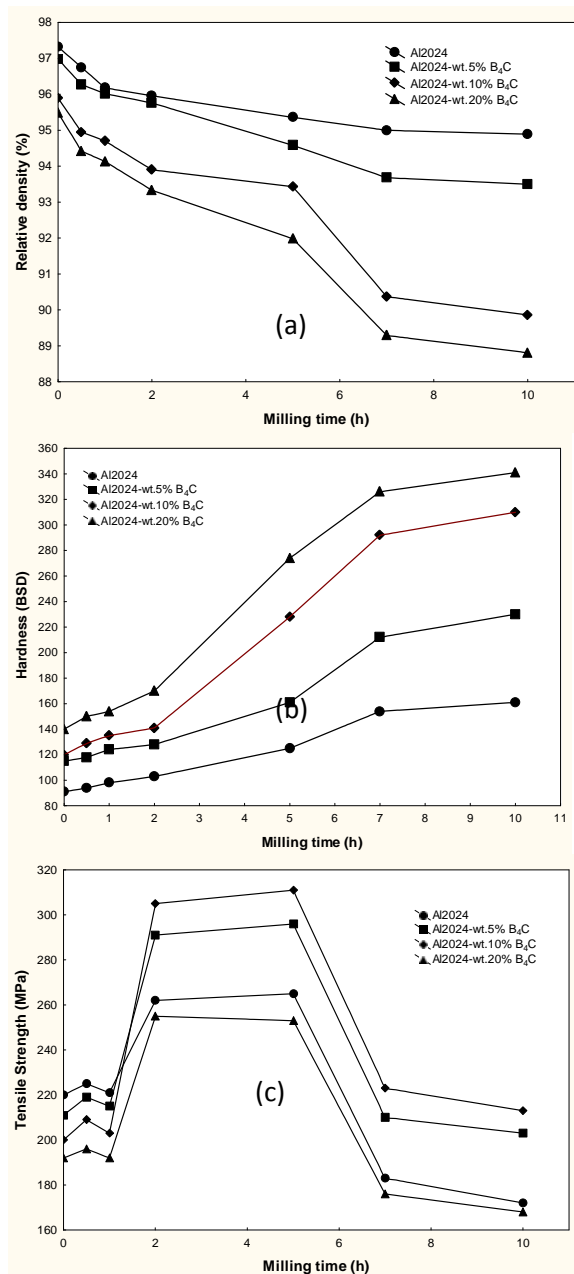


Fig. 3:(a) Relative density, (b) Hardness, (c) Tensile strength

4. CONCLUSION

A homogeneous distribution of B₄C particles in the Al2024 matrix was obtained by mechanical alloying technique. Increasing the milling time and B₄C content caused the relative density of composites to decrease. Increasing the milling time and amount of B₄C particles brought about high hardness in the consolidated samples. The

tensile strength of composites was improved as the milling time increased to 5h, and then decreased with further increasing the milling time.

Acknowledgements

The authors are grateful to the Karadeniz Technical University Research Fund for financially supporting this research (No: 2010.112.010.4). The researchers would also like to thank the GundogduExotherm Service for providing the Al2024 powders.

REFERENCES

- Hernandez Rivera, J.L., Cruz Rivera, J.J., Angel, V.P., Febles, V.G., Alonso O.C., and M Sanchez, R., 2012. Structural and morphological study of a 2024 Al–Al₂O₃ composite produced by mechanical alloying in high energy mill, *Materials Design*, 37, 96.
- Wang, Z., Song, M., Sun, C., Xiao, D. and He Y., 2010. Effect of extrusion and particle volume fraction on the mechanical properties of SiC reinforced Al–Cu alloy composites, *Materials Science and Engineering A*, 527, 6537.
- Miserez, A., Stucklin, S., Rossoll, A., Marchi C.S., and Mortensen A., 2002. Influence of heat treatment and particle shape on mechanical properties of infiltrated Al₂O₃ particle reinforced Al–2 wt-% Cu, *Materials Science and Technology*, 18, 1461.
- Qin, X.H., Jiang D.L. and Dong S.M., 2004. Nanometer, submicron and micron sized aluminum powder prepared by semi-solid mechanical stirring method with addition of ceramic particles, *Materials Science and Engineering A*, 385, 31.
- Tousi, S.S., Rad, R.Y., Salahi, E., Mobasherpour I. and Razavi, M. 2009. *Powder Technology*, 192, 346.
- Arik H., 2008. Effect of mechanical alloying process on mechanical properties of α -Si₃N₄ reinforced aluminum-based composite materials, *Materials Design*, 29, 1856.
- Sivasankaran S., Sivaprasad K., Narayanasamy R. and Iyer V.K., 2010. An investigation on flowability and compressibility of AA 6061100 – x-x wt.% TiO₂ micro and nanocomposite powder prepared by blending and mechanical alloying. *Powder Technology*, 201, 70.
- Alizadeh, M. and Aliabadi, M.M., 2011. Synthesis behavior of nanocrystalline Al–Al₂O₃ composite during low time mechanical milling

- process, *Journal of Alloys and Compounds*, 509, 4978.
- Fogagnolo, J.B., Velasco, F., Robert and Torralba J.M., 2003. Effect of mechanical alloying on the morphology, microstructure and properties of aluminium matrix composite powders, *Materials Science and Engineering A*, 342, 131-143.
- Canakci A, Ozsahin S, Varol T., 2012. Modeling the influence of a process control agent on the properties of metal matrix composite powders using artificial neural Networks, *Powder Technology*, 228, 26-35.

EXAMINATION OF ABRASIVE WEAR BEHAVIOUR IN Al 2014-SiC COMPOSITES

Niyazi Selçuk CİLASUN^{1a}, Recep ÇALIN², Osman BİCAN², Muharrem PUL²

¹Kırıkkale University, Department of Mechanical Engineering, Kırıkkale, TURKEY

²Kırıkkale University, Department of Metallurgical and Materials Engineering, Kırıkkale, TURKEY
a. Corresponding author (niyazicilasun_s@hotmail.com)

ABSTRACT: In this study, the effects of reinforcement volume fractions on abrasive wear behaviour were examined in Al-SiC reinforced metal matrix composites (MMCs) of 3%, 6% and 12% reinforcement – volume (R-V) produced by melt stirring. Abrasive wear tests were carried out by 320 mesh sized Al₂O₃ abrasive papers and pin-on-disc wear test apparatus under 10 N, 20 N and 30 N loads at 0.2 m/s⁻¹ sliding speed. The mechanical properties of composite specimens such as hardness and fracture strength were determined. Subsequent to the wear tests, the microstructures of worn surfaces were examined by Scanning Electron Microscope (SEM) and EDS analyses. While increased SiC reinforcement volume fraction in the composite resulted increased hardness, fracture strength was determined to decrease. Additionally, it was found that increased SiC reinforcement volume fraction in the composite was accompanied with increased wear loss and porosity as well as R-V were identified to be significant determinants of abrasive wear behaviour.

Keywords : Metal matrix composite, SiC, Abrasive wear, Scanning electron microscopy

1. INTRODUCTION

In recent years, depending upon the development of technology and the rising needs of industry, the number of research and development studies about the production of composites have increased. There are several reasons for the increase in the area of use of composites which are their reproducibility at different compositions and different characteristics, their resistance feature for fatigue, toughness and high temperature, and their high level of oxidation and abrasion resistance [1].

Examination of wear behaviour of composite materials is an important research subject. Use of reinforcing components in composite materials increases toughness as well as strength by creating hard phases within the soft structure. Abrasion resistance changes depending on the amount, dimension, distribution of hard parties, hardness of matrix and reinforcing components, and

fracture toughness [2, 3]. Production of composites with Al matrix is realized through casting, infiltration or the techniques of powder metallurgy. Melt stirring method which is one of the production techniques of Particle Reinforced Composites with Metal Matrix (MMCs) is preferred due to low cost at general purposed applications.

Many researchers studied about the friction and wear behaviour of composites with Al metal matrix. Eventually, they identified that hard particle reinforced composites resist much higher degree of abrasion than matrix alloy [4]. Wear ratio, slip velocity, particle size, hardness, applied load are impressed by chemical composition of matrix material and volume of reinforcing material and its distribution within the structure [5 - 8]. In literature, it is stated that wear increases with the increase in volume

and particle size of hard phases [9 - 11]. In this study, the effects of R-V and applied wear load on micro structure of composites and wear behaviour in composites produced at the ratio of 3%, 6% and 12% SiC Reinforcement-Volume (R-V) has been studied with melt stirring method.

2. EXPERIMENTAL STUDY

2.1. Production of Composite Samples

99.5% purity grade Aluminium (Al 2014) as liquid matrix material and SiC as reinforcing component have been utilised for the production of composite samples. Chemical compositions and mechanical properties of the matrix material Al 2014 and reinforcing component SiC added into the ladle at 92.3 μm particle size are shown in Table 1 and Table 2.

Table 1: Mechanical and chemical properties of Al 2014

Density [g/cm ³]	Tensile strength [MPa]	Rupture elongation [%]	Hardness [VSD]
2,8	186	18	45
Content %	Al [%]	Cu [%]	Si [%]
	93.1	4.50	0.80
	Mn [%]	Mg [%]	Zn [%]
	0.80	0.50	0.20

Table 2: Mechanical and chemical properties of SiC

Density [g/cm ³]		Hardness [mohs]	
3.20		>9.5	
SiC [%]	C [%]	Fe ₂ O ₃ [%]	Cl [%]
98	0.15	0.20	<50 ppm

For the production of composite samples; the liquid matrix material Al 2014 has been placed into the ladle and melting process has been started, which is continued until the temperature of liquid

matrix material reached 800 °C. The apparatus prepared for mixing the liquid matrix material has been dipped into liquid metal and mixing process has been started. Increasing the mixing speed gradually to 500 r/min; and the SiC particles, of which amount is predetermined as per reinforcing has then been included into the liquid metal during the mixing process. After the addition of reinforcing component SiC into liquid matrix material Al is complete, mixing process has been continued at 500 r/min for 4 minutes for the purpose of providing homogenous distribution of SiC particles inside the mixture. After the mixing is complete, the ladle has been taken out of furnace and poured into the prepared mould and left to cool down at room temperature. The same processes have been applied separately for each R-V.

Scanning Electron Microscope (SEM) photographs have been taken for the purpose of analysing the microstructures of the obtained composite samples. The view of the melt stirring testing apparatus is shown in Figure 1.

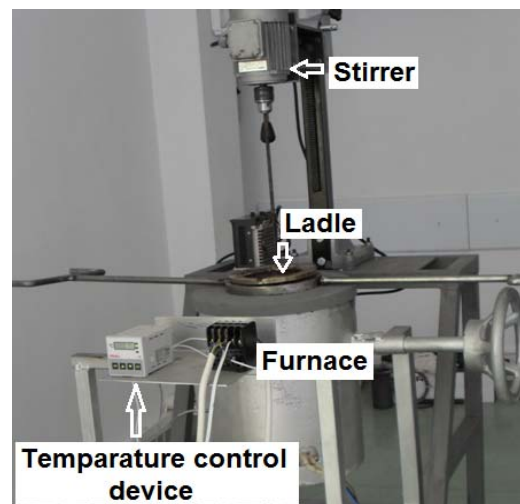


Figure 1: Melt stirring testing apparatus

Afterwards, test samples of 6 mm diameter and 25 mm length have been prepared for the purpose of determining the abrasive wear values of composite

materials produced at 3%, 6% and 12% SiC R-V.

2.2. Abrasive Wear Tests

Wear tests have been conducted under dry and unlubricated sliding conditions at room temperature on pin-on-disc type wear device by using aluminium oxide (Al_2O_3) abrasive sandpaper of 320 mesh particle size. The composite samples on abrasive sandpaper have been moved perpendicular to wear direction, providing constant contact of samples with new sandpaper surfaces at all times. Tests have been performed by applying three different loads of 10 N, 20 N and 30 N at 0.2 ms^{-1} sliding speed and 10 m sliding distance. By applying three different loads separately on composite materials of 3%, 6% and 12% SiC R-V, a total of 9 abrasion tests have been conducted. By weighting on a scale with 0.1 mg measurement sensitivity before and after each testing, the wear amounts of composite samples have been recorded.

SEM views corresponding to wearing surfaces have been obtained and assessed after the wear tests. The view of the testing apparatus on which the abrasive wear tests were performed is shown in Figure 2.

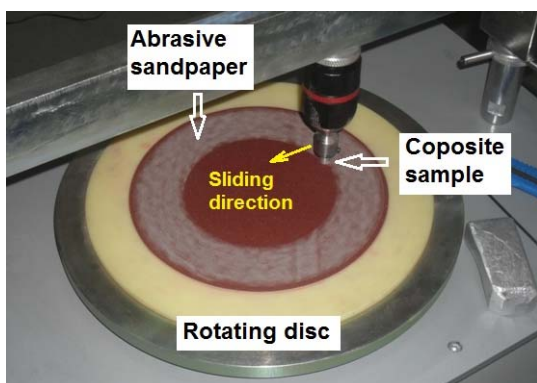


Figure 2: The view during abrasion test

3. RESULTS AND DISCUSSIONS

3.1. Assessment of Microstructures

The SEM views obtained for MMK samples produced at different R-V through melt stirring method are shown in Figures 3 a), b) and c).

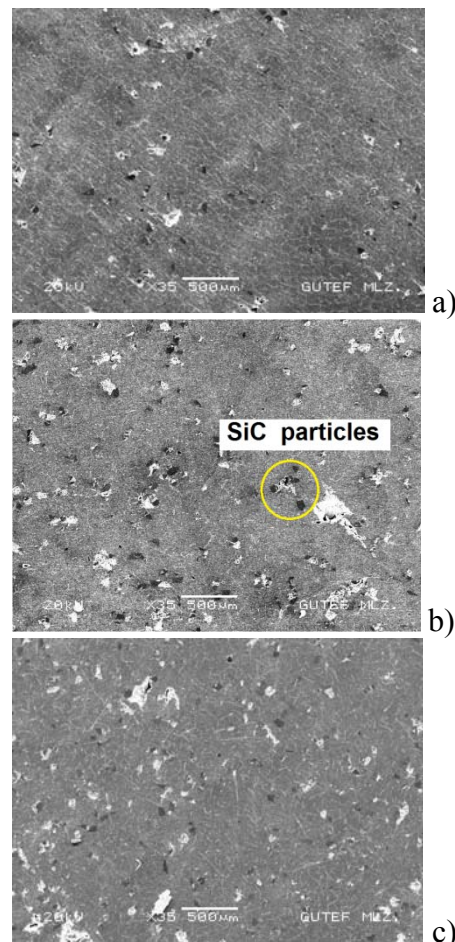


Figure 3: a) 3% SiC, b) 6% SiC c) 12% SiC reinforced composite microstructure views

Examining the SEM views, it is observed that increasing the R-V also increases the homogenous distribution of SiC particles inside the produced composites. It is seen that the reinforcing agent is not distributed homogeneously inside the 3% SiC reinforced composite (Figure 3 a)). It is considered that this situation is brought out by the sweeping of low R-V SiC particles during mixture and their local aggregations. It is also seen that the least homogenous distribution is observed in

the sample with 3% R-V , the distribution is somewhat improved with 6% R-V (Figure 3 b)), and a homogenous particle distribution near the desired level can be seen with 12% R-V (Figure 3 c)). In a similar study conducted by M. Pul *et al.* [12], the same results have been obtained.

3.2. Assessment of Abrasive Wear Tests

The values corresponding to the abrasion amounts of composite samples produced with 3%, 6% and 12% SiC reinforcement are shown in Table 3 and the graph in Figure 4.

Table 3: The wear amounts from the wear tests of composite samples

Reinforcement Amount	Applied Loads		
	10 N	20 N	30 N
3% SiC	0.054	0.094	0.079
6% SiC	0.051	0.040	0.019
12% SiC	0.072	0.053	0.009

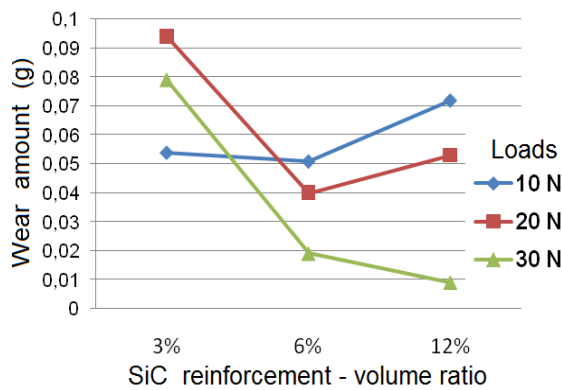


Figure 4: Wear amounts of composites produced with 3%, 6% and 12% SiC R-V in result of 4 minutes mixing at 500 cycle/min. and 800 °C temperature in tests done with 320 mesh particle sized abrasive under 10 N, 20 N and 30 N loads

When Figure 4 is examined, it is observed that volume loss increased in tests conducted under 10 N load, while the volume loss decreased in tests conducted under 20 N and 30 N loads.

This situation points out that the effective wearing mechanism is abrasion at loads up to 10 N, and adhesion at 20 N and 30 N levels. When the SEM views obtained from surfaces worn in result of the tests are examined, it is seen that more smearing layers were formed on material surfaces at 20 and 30 N loads. In other words, the wearing particles adhere on the Al layer smeared on surface at loads over 10 N due to pressure effect and form a further smearing layer along with Al [Figure 5 a), b) and c)]. Therefore, a certain decrease has been observed in the loss of volume with increased loads. Similar results have been revealed in the study conducted by O. Bican [12].

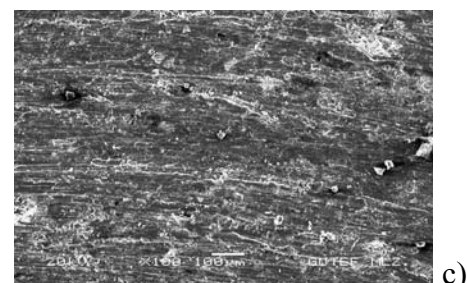
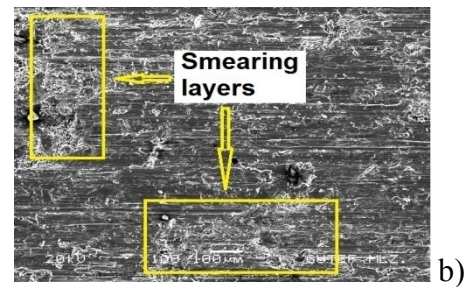


Figure 5: Wearing effect SEM views of composites produced in result of 4 minutes mixing at 500 r/min, 800 °C temperature and 6% R-V , under a) 10 N, b) 20 N and c) 30 N loads

4. CONCLUSIONS

The conclusions obtained in this study are summarised below:

- It has been determined that, the homogenous distribution of SiC particles within the composites increased with the increase of R-V inside composite structure.
- It has been observed that volume loss increased in tests conducted under 10 N load, while the volume loss decreased in tests conducted under 20 N and 30 N loads. This situation points out that the effective wearing mechanism is abrasion at loads up to 10 N, and adhesion at 20 N and 30 N levels.
- Considering R-V, the highest wearing has occurred in 12% SiC reinforced samples and the least wearing has occurred in 3% SiC reinforced MMC samples.

REFERENCES

- [1] Sur G., Şahin Y., ve Gökaya H., 2005. Ergimiş Metal Karıştırma Ve Basınçlı Döküm Yöntemi İle Alüminyum Esaslı Tanecik Takviyeli Kompozitlerin Üretimi, Gazi Üniv. Müh. Mim. Fak. Der. Cilt 20, No 2, sayfa 233-238.
- [2] Özey Ç. ve Haşçalık A., 2004. T/M Yöntemi İle Üretilen Cu-C-Al₂SiO₅ Kompozitinin Abrasiv Aşınma Dayanımı, Dumlupınar Üniv. Fen Bilimleri Enstitüsü Dergisi, Sayı 6, sayfa 175- 184.
- [3] Akbulut, H., Durman, M., Yılmaz F., 1993. SiC Seramik Partikül Takviyeli Alüminyum Silisyum Metal Esaslı MMK'lerin Üretimi ve Özelliklerinin İncelenmesi, 7. Uluslararası Metalurji ve Malzeme Kongresi, Ankara, sayfa 1183- 1194.
- [4] Candan, E., Ahlatci, H. and Cimenoglu, H., 2001. Abrasive wear behaviour of Al-SiC composites produced by pressure infiltration technique, Wear, 247, Pages 133-138.
- [5] Mondal, D.P., Das, S., Jha, A.K. and Yegneswaran, A.H., 1998. Abrasive wear of Al alloy-Al₂O₃ particle composite: a study on the combined effect of load and size of abrasive, Wear, 223, Pages 131-138.
- [6] Sahin, Y., 2003. Preparation and some properties of SiC particle reinforced aluminum alloy composites, Materials and Design, 24, Pages 671-679.
- [7] Shorowordi, K.M., Haseeb, A.S.M.A. and Celis, J.P., 2004. Velocity effects on the wear, friction and tribochemistry of aluminum MMC sliding against phenolic brake pad, Wear, 256, Pages 1176-1181.
- [8] Acilar M. ve Gul F., 2007. Effect of the reinforcement particle size on the abrasive wear behaviour of the Al-SiCp composites produced by pressure infiltration technique, J. Fac. Eng. Arch. Gazi Univ., Vol. 22, No 2, Pages 323-327.
- [9] Buytoz, S. ve Eren H., 2007. A209 Al Metal Matris Kompozitlerin Abrasiv Aşınma Performansına Takviye Elemanlarının Etkisi, Fırat Üniv. Fen ve Müh. Bil. Dergisi, 19 (2), sayfa 209-216.
- [10] Özey Ç., ve Haşçalık A., 2004. T/M yöntemi ile üretilen Cu-C-Al₂SiO₅ kompozitinin abrasiv aşınma dayanımı, Dumlupınar Üniv. Fen Bilimleri Enstitüsü Dergisi, 6, sayfa 175-184.
- [11] Ramadan J. Mustafa., 2010. Abrasive Wear of Continuous Fibre Reinforced Al And Al-Alloy Metal Matrix Composites, JJMIE Jordan Journal of Mechanical and Industrial Engineering, Vol. 4, Number 2, March, Pages 246 – 255.
- [12] Çalın R., Pul M., Çıtak R., Şeker U., 2011. The effect of reinforcement ratio on the composite structure and mechanical properties in Al-MgO composites produced by the melt stirring method” Advanced Composites Letters, Vol. 20, Iss. 4, Pages 91-96.
- [13] Bican, O., 2010. ‘Bakır ve Silisyum İçeren Al-25Zn Esaslı Alaşımların Dökülmüş ve Isıl İşlem Görmüş Durumdaki Yapısal, Mekanik ve Tribolojik Özelliklerinin İncelenmesi, Doktora Tezi, Karadeniz Teknik Üniversitesi Fen Bilimleri Enstitüsü, Trabzon.

PREPARATION AND CHARACTERIZATION OF THE COMPOSITES WITH HA/ZrO₂/POLY(METHYL METHACRYLATE)

Ileana Cojocaru^{1a}, Stanca Boboia², Viorica Saplontai³, Doina Prodan², Laura Silaghi Dumitrescu² and Marioara Moldovan²

1. University of Craiova, Craiova, Romania;

2. Babes Bolyai University - Raluca Ripan Chemistry Research Institute, Cluj-Napoca, Romania;

3. Technical University of Cluj-Napoca, Romania

a. Corresponding Author (i_cojocaru2005@yahoo.com)

ABSTRACT: The materials properties of conventional organic–inorganic hybrid materials produced by mixing or dispersing inorganic materials in organic polymers are mainly determined by the nature of the interface between the organic and inorganic components, as well as by the size and dispersibility of the inorganic filler material. ZrO and hydroxyapatite nanoparticles of various sizes have been incorporated by compounding in a poly(methyl methacrylate) (PMMA) matrix to enhance its mechanical properties. SEM and XRD were used to determine component and morphology of the composite. Results indicated that HA and Zr particles were dispersed well in PMMA matrix, The mechanical properties of the composite were evaluated by using flexural strength (LOYD LR5K Plus). It was found that the flexural strength. The addition of HA can also reduce the ratio of water absorption of composite, which postponed the retention of mechanical properties of composite under moisture condition. The possibility of combining properties of organic and inorganic materials have been explored some years ago. One aspect was the development of composite membranes using a ceramic porous support and a selective top layer of an organic or hybrid polymer.

1. INTRODUCTION

There have been many attempts using various techniques to develop high performance organic–inorganic hybrid materials, which combine the features of inorganic and organic substances. Such hybrid materials have been investigated at various scales from the level of microscale order to molecular order. [Zulfikar *et al.*, 2006] Organic polymer materials exhibit excellent flexibility, toughness, moldability, and adhesiveness, but their heat resistance properties are inferior to those of inorganic materials. [Landry *et al.*, 1992], [Cheng *et al.*, 1990], [Shen *et al.*, 1985], [Cojocaru *et al.*, 2009].

The materials properties of conventional organic–inorganic hybrid materials produced by mixing or dispersing inorganic materials in organic polymers

are mainly determined by the nature of the interface between the organic and inorganic components, as well as by the size and dispersibility of the inorganic filler material. [Laachachi *et al.*, 2005]

From the above reason, many researches have enrolled with composites dealing with the combination of ceramics and polymers in order to improve some properties, especially mechanical properties. [Doyen *et al.*, 1996], [Shen *et al.*, 1985]

The purpose of the present study was the preparation of hydroxyapatite-ZrO₂/poly(methyl methacrylate) (HA-ZrO₂/PMMA) composites by interpenetrating polymerization of methyl methacrylate (MMA) monomer in the nanoporous HA-ZrO₂ templates.

2. MATERIALS

Experiments were made on the obtaining of nanoparticles HA-ZrO₂ through sol-gel method (synthesized at UBB-ICCRR- Cluj-Napoca). HA was prepared by coprecipitation of calcium hydroxide (Ca(OH)₂) and phosphoric acid (H₃PO₄). The sol of ZrO₂ (35 % in water) was added to the hydroxyapatite gel, reheated to 120°C. The powders were annealed at 1000°C(2h).HA-ZrO₂/poly(methyl methacrylate) composites were prepared by interpenetrating bulk polymerization of methyl methacrylate (MMA) monomer in porous structures. The porous HA-ZrO₂ templates were prepared by mixing their calcined powders with poly(vinyl alcohol) (PVA) solution, shaping by uniaxial pressing and then firing at 1000°C. The templates were soaked in the solution mixture of MMA monomer and 0.1 mol% of benzoyl peroxide (BPO) for 24 h. The pre-composites were then bulk polymerized at 85°C for 24 h under nitrogen atmosphere. The flexural strength was determined by using the expression $FS = 3xFxl/2xbxh^2$, where l is the distance between props, b is the thickness of the test piece and h is the height of the test piece. The tests were carried out on a universal testing system LOYD LR5K Plus. The scanning electron microscope (SEM) QUANTA 133 from FEI Company was used for the examination of the samples by electronic microscopy.

3. RESULTS AND DISCUSSION

Polymers capable of forming spherical structures in solution has been shown critical in forming these films. [Widawski *et al.*, 1994]

The mechanical properties are the improved with the increase of the filler concentration and vary according to the composition of the filler. This improvement of the mechanical properties is due to a good insertion of

hydroxyapatite and zirconium nanoparticles in the polymeric matrix, as well as to the creation of chemical bonds between the organic phase and the inorganic one. In figure 1. we have a values flexural strength for 5 samples: **1.** 20%wtHA-ZrO/80%wtPMMA; **2.** 30%wt HA-ZrO/70 %wt PMMA; **3.** 65 %wt HA-ZrO / 35 %wt PMMA; **4.** 40%wtHA-ZrO/60 %wt PMMA; **5.** 50%wt HA-ZrO /50 %wtPMMA;

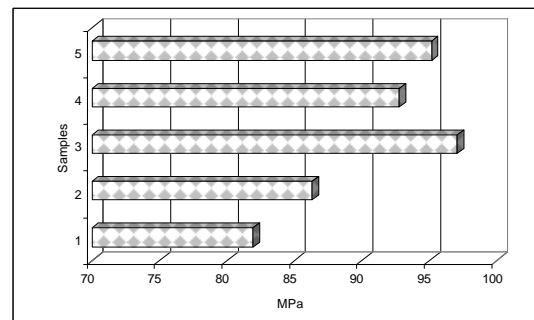


Figure 1: Flexural Strength Values

Method for synthesis of nanoscopic particles is very important. For example, mesoporous hydroxyapatite agglomerates which is generally very hygroscopic in nature and contain adsorbed water, so the connection between nano-fillers and organic matrix may be compromised. The results of this study showed differences in flexural strength values of composites when experimental variation between HAZrO/PMMA under the same polymerization conditions. The high values are obtained for samples **3** to 65% by weight of HA-ZrO could be explained by a good bond between the polymer and filler particles, and the particles hydroxyapatite appropriate the filler content, size, type, and distribution, as well as coupling between particles and matrix are factors that influence mechanical properties.

SEM micrographs of the obtained samples are shown in Figure 2. Scanning electron microscopy (SEM) was used to

monitor the particle size and size distribution.

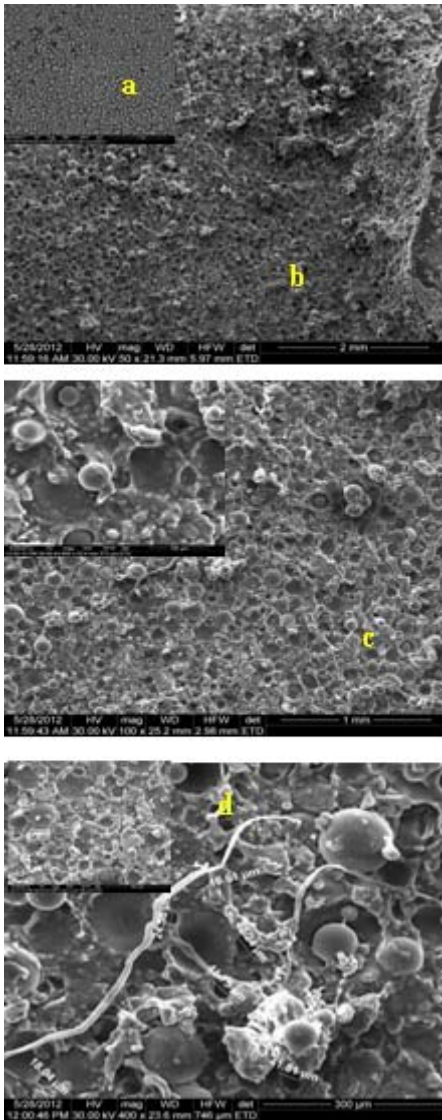


Figure 2: (a) SEM micrograph of as-received PMMA particles; (b) sample 1; c) sample 3; d) sample 5

Generally, a uniform distribution of macro porous throughout the polymer matrices is found, but a solid film of polymer (skin layer) is observed over the majority of the sample surface. SEM pictures have shown that no external porosity was apparent in the beads (Fig. 2), although no accessible internal porosity is likely present. On the contrary, PMMA polymer modified with

MMA macro monomer have shown external porosity clearly evidenced by visual observation of SEM micrographs (Fig. 2b,c,d). Possibly, the presence of the macro monomer reduced polymer mobility and partially prevented the formation of the outer skin.

The mixing of nanofillers and polymers is difficult to achieve due to the large surface energy of nanometric particles. Zirconia (ZrO_2) is an important biomaterial due to its excellent biocompatibility and high mechanical strength. Hydroxyapatite (HA) is a major inorganic component consisting of human hard tissues, such as bones and teeth, and its content determines their microstructures and physical properties.

However, this mechanical mixing would cause low sintering density and/or non-uniform zirconia phase distribution in the sintered HA matrix due to the large particle size and/or segregation of zirconia particles. Non-uniform distribution of the zirconia phase in the HA matrix would seriously deteriorate the mechanical properties of HA/ ZrO_2 composites. On the other hand, the chemical co-precipitation technique can allow the preparation of a homogeneous mixture of nanoscale HA and ZrO_2 nanoparticles, which would be the most suitable approach for the preparation of HA/ ZrO_2 composites with superior mechanical properties. Improvement of the mechanical properties can be achieved by the incorporation into resistant oxide phase, e.g. Zirconia partially stabilized by calcia. The preparation of homogeneously distributed zirconia- hydroxyapatite composites can be accomplished using a co-precipitation process of precursor reagent solutions.

HA- ZrO_2 nanoparticles behave as load carriers leading to good mechanical properties if they are distributed homogeneously in the cement. The shape and the size of the particles have a

preponderant influence on the charging degree, which is experimentally determined so as to ensure an adequate consistency and obvious plastic properties for the nanocomposite mixture. We may specify that the bond between the filler and the organic matrix is the most important for a nanocomposite with appropriate properties, and, from this point of view, it is easy to justify why the break of the bond between the fillers and the organic matrix could be the first destruction mechanism that appears in the process of composite degradation. However their low strength and brittle nature limits their potential applications to principally non-load-bearing applications. The mixing of nanofillers and polymers is difficult to achieve due to the large surface energy of nanometric particles. Evidently, the concurrent occurrence of the different steps in the final process will induce differences in the obtained composite material.

4. CONCLUSIONS

The use of inorganic fillers consisting of rational mixtures of fractions with different particle size increase packing density and filler content, improve the good flexural strength. The possibility of combining properties of organic and inorganic materials have been explored some years ago. One aspect was the development of composite membranes using a ceramic porous support and a selective top layer of an organic or hybrid polymer. With the help of SEM a series of biofilms and nanocomposites have been characterised. To investigate the role of HA-Zr in mixing with PMMA, causes the significant changes of nanocomposites structure. The addition of HA-Zr to PMMA (up to 65 wt%) did not changed significantly the flexural properties.

Acknowledgements: Funding from the Romanian Ministry of Education and

Research, National project PNII no: 165/2008, is gratefully acknowledged.

REFERENCES

- Widawski, G.; Rawiso, M.; Francois, B. 1994, Self-organized honeycomb morphology of star-polymer polystyrene films organized Nature 369, 387.
- Doyen, W., W. Adriansens, B. Molenberghs, and R. Leysen, 1996, A Comparison Between Polysulfone, Zirconia and Organo-mineral Membranes for Use in Ultrafiltration, J. Membrane Sci., 113, 247.
- Landry, C.J.T., B. K. Coltrain, and B. K. Brady, 1992a, In situ Polymerization of Tetraethoxysilane in Poly(methyl methacrylate): Morphology and Dynamic Mechanical Properties, Polymer, **33**:7, 1486.
- Zulfikar, M. A., A. W. Mohammad, A. A. Khadum, and N. Hilal, 2006a, Synthesis and Characterization of Poly(methyl methacrylate)/SiO₂ Hybrid Membranes: Effect of Solvents on Structural and Thermal Properties, J. App.Polym. Sci., **99**, 3163.
- Cheng, W., Miller, G., Manson, J., and Hertzberg, R. W., 1990, "Mechanical Behaviour of Polymethylmethacrylate, Part 1. Tensile Strength and Fracture Toughness," Journal of Materials Science, 25, 1917.
- Shen, J., Chen, C. C., and Sauer, J. A., 1985, "Effects of Sorbed Water on Properties of Low and High Molecular Weight PMMA: 1. Deformation and Fracture Behavior," Polymer, Vol. 26, pp. 511
- Cojocaru I., Moldovan M., Trif M., Prodan D., Popescu G.L., Constantinescu I., 2009, "The influence of some alumina and titanium nanoparticles on the mechanical properties of the composites based on poly (methyl methacrylate)", Materiale Plastice, MPLAAM, , 46(4), 383-386
- Laachachi A, Leroy E, Cochez M, Ferriol M, Lopez-Cuesta, 2005, Thermal Stability and Degradation Kinetics of Poly(methyl Methacrylate)/Layered Copper Hydroxy Methacrylate Composites, JM. Polym Degrad Stab, , 89:344.

DEVELOPMENT OF NOVEL BORON NITRIDE NANOTUBE SYNTHESIS METHOD

Şaban Kalay¹, Zehra Yılmaz¹ and Mustafa Culha^{1,a}

1. Department of Genetics and Bioengineering, Yeditepe University, Atasehir, Istanbul, Turkey
a. Mustafa Culha (mculha2@gmail.com)

ABSTRACT: In this study, the synthesis of BNNTs are achieved from a boron ore and Fe catalyst under NH₃ atmosphere for the first time. The synthesized BNNTs have single crystalline hexagonal boron nitride lattice, multi-walled and randomly oriented at uniform structure at 10-30 nm outer diameter and 5 nm wall thickness. High-resolution transmission electron microscopy revealed that the distance between the BNNT walls is 3.4 Å.

1. INTRODUCTION

Boron nitride nanotubes (BNNTs) known as the structural analogues of carbon nanotubes (CNTs) are more superior than CNTs due to their robust structure that resists to high temperature and harsh chemical conditions [Golberg *et al.*, 2010], high hydrogen storage capacity [Okan *et al.*, 2012] and electronic properties that depend on ionic nature of B-N bond.

First obtained BNNTs by Chopra *et al.* in 1995 were synthesized with arc-discharge method [Chopra *et al.*, 1995]. Up to date, several methods were developed for the synthesis of BNNT. The arc-discharge, chemical vapor deposition (CVD) and laser ablation can be given as examples to these methods. In most of the synthesis methods, amorphous boron, boric acid, borazine or CNTs were used as starting materials [Huang *et al.*, 2011]. The use of BNNTs is foreseen in a wide range of applications including preparation of polymer composites, microfluidic devices, superhydrophobic surfaces, and biomedical devices [Wang *et al.*, 2009].

In this study, the BNNTs were synthesized for the first time from a boron ore, colomenite, with CVD method at 1280⁰C. The reaction parameters such as the amount of boron ore, the type and amount of catalysts, the reaction temperature and duration were optimized.

2. RESULTS

2.1. Effect of Catalyst Type to the BNNT Synthesis

Boron ores can be used for the synthesis of BNNTs since it contains B₂O₃ in its structure (Figure 1).

Three types of catalyst, ZnO, Al₂O₃, Fe₃O₄, and Fe₂O₃, were investigated for their performances and samples were analyzed by scanning electron microscopy (SEM). Iron oxides were used as the catalysts, the formation of BNNTs was dramatically improved to compare others (Figure 2).

(Boron Ore)

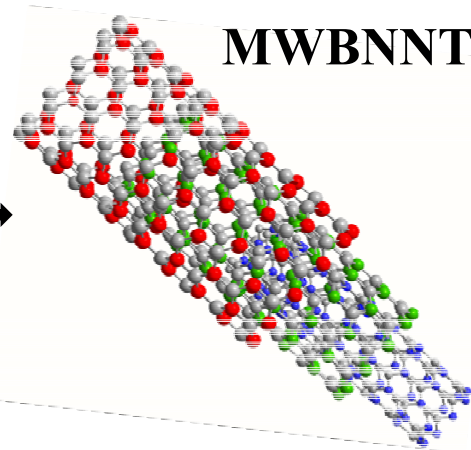
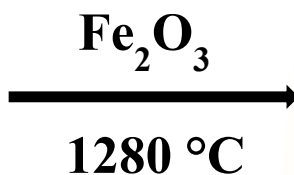


Figure 1: Direct synthesis of BNNT from boron ore.

2.2. Effect of Reaction Time to the BNNT Synthesis

The reaction time on the yield and the size of BNNTs were investigated. The reaction was set to 30, 60, 120 and 150 min. Then, the obtained BNNTs were analyzed by SEM.

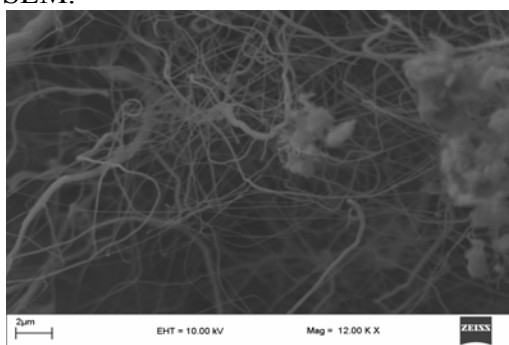


Figure 2: BNNT synthesis in the presence of Fe_2O_3 .

We concluded that the ideal reaction time for high yield BNNT formation was 120 min (Figure 3).

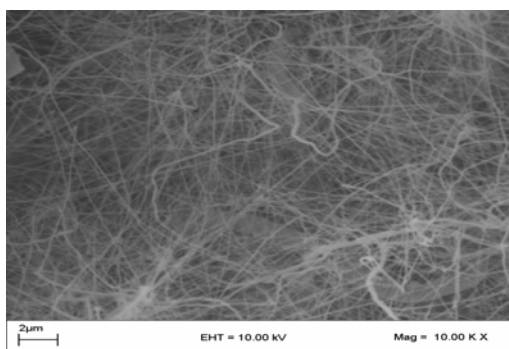


Figure 3: BNNT synthesis in the presence of Fe_2O_3 and reaction time is 120 min.

2.3. TEM and HRTEM Analysis

The structure of BNNTs was further analyzed with TEM (Figure 4). As seen on TEM images, the BNNTs are multi-walled, single-crystal and have an outer diameter ranging from 10 nm to 30 nm. The Fe_2O_3 catalyst was not observed on the tip of BNNTs and they were open-ended. The wall thickness of these BNNTs ranges from 5 nm to 6 nm. The diffraction image of the selected area showed that the distance between the walls was 0.34 nm and the sidewalls were well-crystallized h-BN (002).

The BNNTs were analyzed with UV-Vis, FT-IR and Raman spectroscopic techniques.

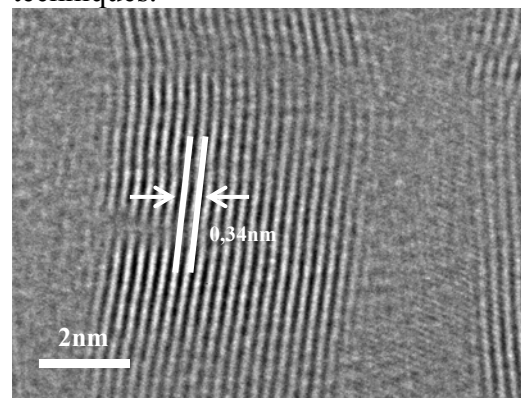


Figure 4: TEM image of BNNT.

2.4. UV-Vis Analysis of BNNTs

The UV-Vis spectrum of BNNT, a band-gap transition peak at 200 nm was observed. In addition, an absorption peak in the form of shoulder that is caused by Van Hove Singularities was detected at 273 nm (Figure 5).

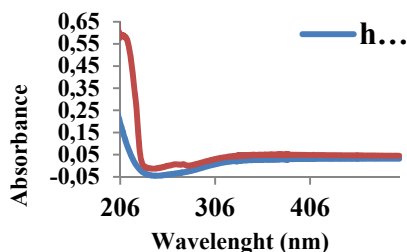


Figure 5: UV-Vis spektrum of BNNT

2.5. Raman Spectroscopy Analysis of BNNTs

The BNNTs give a sharp peak at 1368 cm^{-1} on Raman spectrum. This peak shows the E_{2g} in-plane model of h-BN structure and it is due to the bond vibration between B and N, which is located on the same plane (Figure 6)

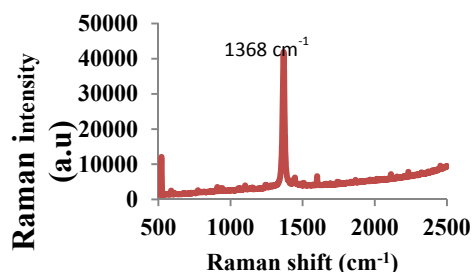


Figure 6: Raman spektrum of BNNT.

2.6. FT-IR Analysis of BNNTs

The pure BNNTs were also analyzed by FT-IR. The B-N-B in-plane bonding vibration peak at 1327 cm^{-1} and the secondary absorption peak at 758 cm^{-1} were observed (Figure 7). It was consistent with the reported FT-IR spectrum of BNNTs in the literature [Zong *et al.*, 2011].

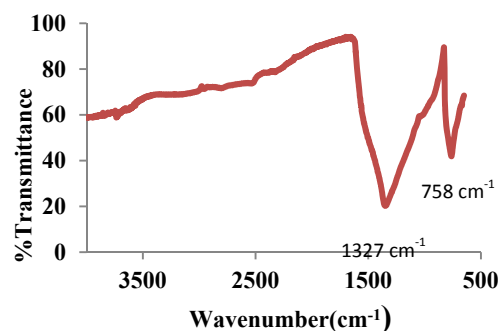


Figure 7: FT-IR spectrum of BNNT

2.7. XRD-Pattern Analysis of BNNT

XRD pattern result of pure BNNT indicates the presence of single and dominant h-BN phase (Figure 8). Peaks were observed 2θ angles of 26.8° and 41.8° belonging to hexagonal BN. There are not any crystalline phase peaks originating from substrate and Fe_2O_3 catalystr.

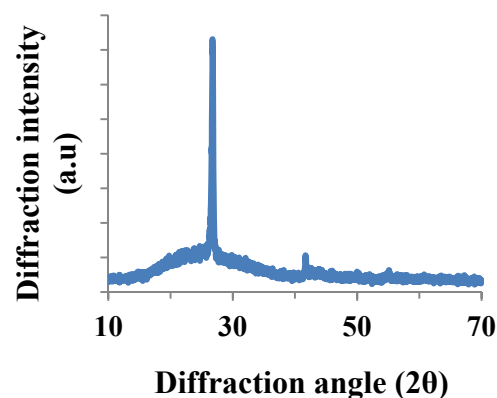


Figure 8: XRD pattern analysis of BNNT.

3. CONCLUSION

In our study, the BNNTs were synthesized from directly a boron ore, colemanite, for the first time in the presence of Fe_2O_3 catalystr and under the NH_3 atmosphere $1280\text{ }^\circ\text{C}$ using CDV technique. The finding suggests that for high-yield synthesis of BNNTs boron ore/catalystr ratio is 12/1 (w/w). In conclusion, large scale and pure BNNTs can be obtained using this novel synthesis approach. The obtained BNNTs are expected to be used in many applications including specific ion retention, hydrogen storage, improving mechanical and chemical durability of polymer composites.

4. Acknowledgements

This study was supported by Scientific and Technological Research Council of Turkey (TUBITAK) (Project No: 112M480).

REFERENCES

- Golberg, D., Bando, Y., Huang, Y., Terao, T., Mitome, M., Tang, C., Zhi, C., 2010. *ACS Nano*, 4, 2979.
- Okan, B. S., Kocabas, Z. O., Ergun, A. N., Baysal, M., Papst, I. L., Yurum, Y., 2012. *Ind. Eng. Chem. Res.*, 51, 11341.
- Chopra, N. G., Luyken, R. J., Cherrey, K., Crespi, V. H., Cohen, M. L., Louie, S. G., Zettl, A., 1995. *Science*, 269, 966.
- Huang, Y., Lin, Y., Tang, C., Bando, Y., Zhi, C., Zhai, T., Dierre, B., Sekiguchi, T., Golberg, D., 2011. *Nanotechnology*, 1.
- Wang, J., Lee, C. H., Bando, Y., Golberg, D., Yap, Y. K., 2009. *Lecture Notes in Nanoscale Science and Technology*, 23.
- Zong, B., Huang, X., Wen, G., Yu, H., Zhang, X., Bai, H., 2011. *Nanoscale Res Lett*, 6, 1.

SWELLING BEHAVIOR IN MICROWAVE SINTERING OF FE-AL MIXTURES

Mehmet ÇAKMAKKAYA¹, Şükrü TALAŞ²

1. Afyon Kocatepe University Technology Faculty, Department of Automotive Engineering, Afyonkarahisar.

2. Afyon Kocatepe University Technology Faculty, Department of Metallurgy and Materials Engineering, Afyonkarahisar

ABSTRACT: Iron aluminides are intermetallics composites that are potentially suitable for applications such as high temperature corrosion. There are different manufacturing methods which can be applied for this composite. From these, P/M could be remarked as a highly effective and economic method compared with other alternatives. Sintering of elemental powders of Fe and Al can be an alternative manufacturing method for Fe aluminides. Nevertheless, the swelling problem is always observed in a stress-free reactive sintering of iron-aluminum elemental powder mixtures, even in a microwave sintering of iron-aluminum elemental powder mixtures. Present study on the stress-free vacuum quartz tube sintering of Fe-26at. % Al compacts showed that the eliminating swelling behavior is possible under vacuum.

1. INTRODUCTION

Lately, due to the cost of material and the preservation of strategic elements, ordered Fe₃Al intermetallic compound were of interest to researchers [Change-Jiu, Li. *et al.*, 2008]. They exhibit less density than steel and good strength for relatively high temperature up to about 600 °C, also excellent oxidation and corrosion resistance owing to from the protective oxides scales in hostile environments such as oxidizing and sulfurizing atmospheres [Chen-Ti, Hu. *et al.*, 2005]. The iron aluminates have been produced by a number of processing methods, including melting-casting and mechanical alloying [Lou Baiyang. *et al.*, 1998]. In recent studies, much attention has been paid to the powder metallurgy processing that has the advantages of controlling microstructure and improving general properties.

The present investigation intends to study the dimensional change and thermal behavior during sintering of elemental Fe-Al mixture in order to find out the

possible cause of swelling problem [Schneibel H.J., and Deevi S.C., 2004].

2. EXPERIMENTAL PROCEDURE

The atomized iron powder (>99.9% purity, and average diameter about 45µm, and atomized aluminum powder with purity of 99.9% particle size 75µm were purchased from Alfa Aesar for the present investigation.

The weighed Fe and Al powder according to the composition of Fe-26 at [Kimura T. *et al.*, 2001]. Al were completely blended in a laboratory mixer at a speed of 90 rpm for 60 min. The mixed powder were cold-rolled to 60% reduction in cross-section area with a rolling mill and put through a heating process at various temperatures by a vacuum Quartz tube. The maximum sintering temperatures of 550, 600 and 700 °C for min were selected to investigate the phase transformation in the cold-rolled Fe 26at. %Al compacts [Chen-Ti, Hu. *et al* 2004].

The phase change of the variously heated specimens was examined with X-ray

diffractometer. The microstructural study was conducted with SEM, and a solution of 13 vol.% HCL, 7 vol. % HNO₃ and balanced H₂O was used as the etching agent.

3. RESULTS AND DISCUSSION

Fe and Al powders were mixed and compacted to obtain a high density compact containing required amounts of Fe and Al. The SEM pictures show morphology of Fe+at.%Al compacts in Fig. 1.

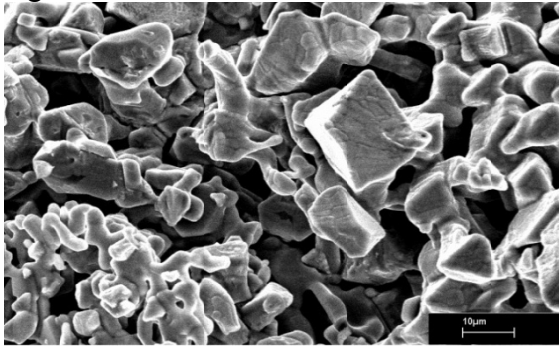


Fig. 1: The SEM micrographs of mixed iron and aluminum powder

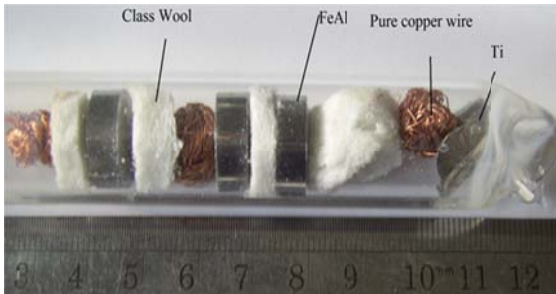


Fig. 2: Sintering at 550 °C for 60 min of Fe-26, 30, 33 at% Al compacts in vacuum quartz tube

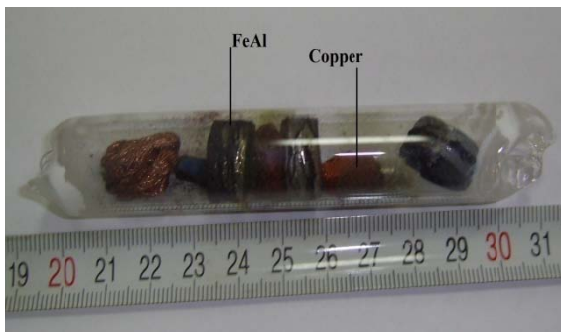


Fig. 3: Sintering of Fe-26, 30, 33 at% Al compact at 600 °C for 60 min in vacuum quartz tube

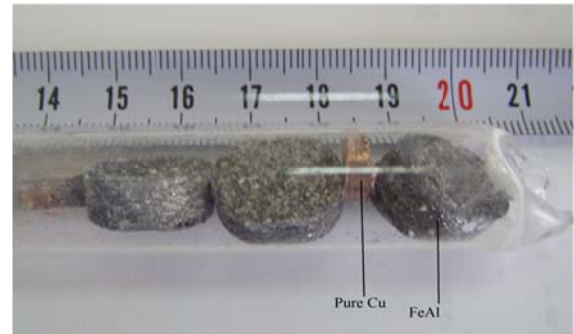


Fig. 4: Sintering at 700C for 60 min of Fe-26, 30, 33 at% Al compact in vacuum quartz tube

Fig. 5 shows XRD patterns of the Fe-Al composite deposit obtained after quenching from the temperatures of 600 °C and 700 °C. The result obtained after the sintering at a temperature of 600 °C indicated that the formation of intermetallic phases, D03 and B₂ and Fe₂Al₅ occurred. The temperature rising to 700 °C, the intensive reaction between Fe and Al took place because the liquid Al phase quickly covered the free iron surface through capillary action [Lou B. Y. *et al.*, 1999].

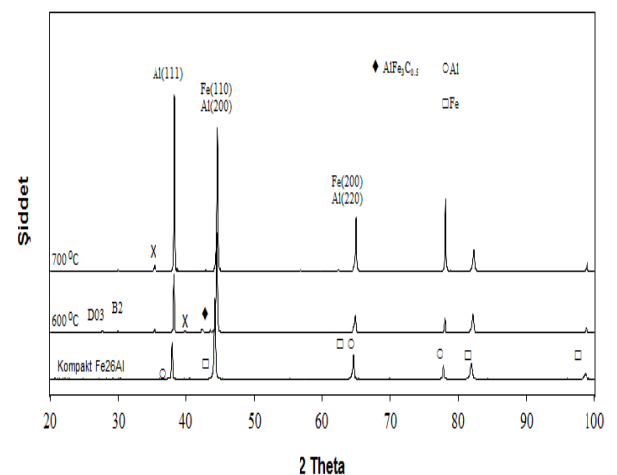


Fig. 5: The XRD result of Fe-26 at% Al compacts after heat treatments at 600 and 700 °C for 60 min.

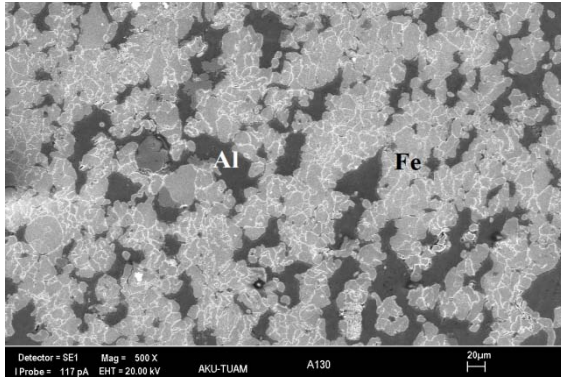


Fig. 6: The microstructure of Fe-26 at% Al compacts sinter treated at 550°C for 60 min.

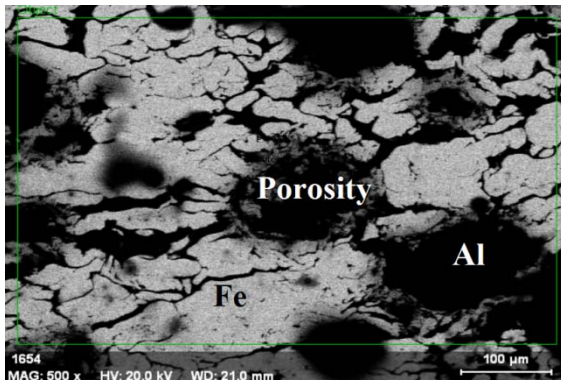


Fig. 7: The 600 °C 60 min sintered Fe-26 at% Al displays a weary porous and sponge-like microstructure

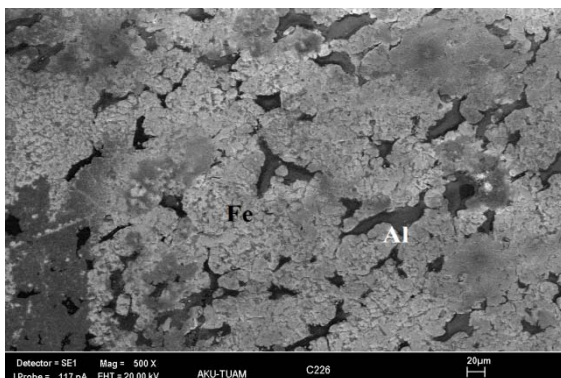


Fig. 8: The 700 °C 60 min sintered Fe-26 at% Al displays a weary swelling sponge-like microstructure

REFERENCES

- Change-Jiu, Li. *et al.*, 2008 Cold Spraying of Fe/Al Powder Mixture: Coating characteristics and Influence of Heat Treatment on the phase Structure, *Applied Surface Science*, 255, 2538-2544.
- Chen-Ti, Hu. *et al.*, 2004 Swelling behavior in Reactive Sintering of Fe-Al Mixtures, *Materials chemistry and Physics*, 88, 264-272.
- Chen-Ti, Hu. *et al.*, 2005 The Role of pre-Formed Fe₂Al₅ in P/M Processing of Fe₃Al, *Materials Science and Engineering A308*, 360-366.
- Lou Baiyang. *et al.*, 1998 Effects of Mn on Fracture Behavior of D₀₃, Fe₃Al-based Intermetallic Alloy, *Journal of Materials Science*, 33, 1481-1486.
- Lou B. Y. *et al.*, 1999 TEM Observation of D₀₃ structure in Fe₃Al Alloy with Mn Addition, *Journal of Materials Science*, 34, 1025-1030.
- Kimura T. *et al.*, 2001 Microwave Synthesis of Yttrium Aluminum Iron Garnet Powder, *Journal of Materials Science and Processing*, 9, 2.
- Schneibel H.J., and Deevi S.C., 2004 Processing and Mechanical Properties of Iron Aluminide Composites Containing Oxides Particles, *Materials Science and Engineering A364* 166-170

SINTERABILITY COMPARISON OF THE Al/SiC AND Al/MoSi₂ POWDER SYSTEMS UNDER MICROWAVE SINTERING CONDITIONS

Mehmet Çakmakkaya^{1a}, M.Serhat Başpınar², Ahmet Yönetken³ and Ayhan Erol⁴

1. Afyon Kocatepe University, Faculty of Technology, Automotive Eng. Dept., Turkey

2. Afyon Kocatepe University, Technical Education Faculty., Metal Education. Dept., Turkey

3. Afyon Kocatepe University, Engineering Faculty, Department of Electric Engineering, Turkey

4. Afyon Kocatepe University, Faculty of Technology, Metallurgy and Material Sci.Dept., Turkey

a. Corresponding author (cakmakkaya@aku.edu.tr)

ABSTRACT: Aluminum cooler panels were extensively used in micro scale electronic and also in macro scale electrical power systems. Conventionally used aluminum cooler systems fails under excessive heating and cooling cycles. Therefore, Al/SiC systems replaced instead of it where critical conditions exists. Although SiC is good in heat conductivity, it lowers the heat conductivity of the Al/SiC system. The main objective of this study was to investigate the sintering behavior of Al/MoSi₂ where MoSi₂ is more conductive than SiC. Atmosphere controlled microwave sintering technique was used for the sintering process. Two main powder system were prepared with different SiC and MoSi₂ addition (5, 10, 15% vol.) with aluminum. After the preliminary studies it was concluded that the wetting of the MoSi₂ powder surface with aluminum is problem and non-homogeneous sintering surfaces was obtained. In order to solve this problem MoSi₂ powder surfaces were coated with Ni by electroless coating technique. It was concluded that Al/MoSi₂ powder system with Ni coating has better sintering and densification behavior than the other powder systems.

1. INTRODUCTION

In order to effective working of Si transistors in electronic packaging, it has to provide effective cooling to stay in the safe operating temperature limit. Effective cooling of the packaging increases the reliability of the components. Al/SiC plates are made for power modules and SiC gives good thermal conductivity. Small scale of the cooler parts are produced by powder metallurgy technique. However, sintering products which are formed between Al and SiC interface is problem (Al₄C₃ formation) [Rodriguez *et al.* 2006]. There exist many solution for this problem. Coating of the SiC surfaces is one of the solution. By this way, a diffusion barrier is formed at the contact interface of the aluminum and SiC powders. Electroless nickel plating has found wide uses in many fields, because the technique of electroless plating was invented and the high performance product with high hardness, wear resistance and corrosion resistance were produced.

Several advantages like low cost, easy formation of a continuous and uniform coating on the surface of substrate with complex shape, and capability of depositing on either conductive or nonconductive parts have attracted a lot of interests from the academy and the industry [1]. Early studies on the sintering couple of Aluminum powder and MoSi₂ powders showed that, Wettability of the MoSi₂ powders with aluminum is not good [Ramasesha and Shobu, 1998]. Therefore, aluminum bubbles were occurred on the surface of the samples after the sintering under conventional sintering systems. Another approach for the prevention of the interface product formation is using more efficient sintering method like microwave sintering. Microwaves (MWs) are electromagnetic waves with frequencies ranging from 300 MHz to 300 GHz, and wavelengths ranging from a few cm to a few mm. Unlike conventional heating, the

penetration of microwaves into materials gives rise to a volumetrically distributed heat source. Consequently, microwave processing makes it possible to rapidly heat both small and large samples with greater uniformity when compared with conventional heating [Talaş Ş., and Çakmakkaya M., 2012]. The main objective of this study was to compare the sinterability of two powder system after coating of the SiC and MoSi₂ powders with Ni as a diffusion barriers.

2. EXPERIMENTAL

In this study, Aluminum powders, silicon carbide (SiC, density: 3,2 gr.cm⁻³), molybdenum disilicide (MoSi₂, density:6,2 gr.cm⁻³) were used. SiC powders with 10 µm grain size and 99.5% purity, MoSi₂ powders with -100µm grain size and 99.5% purity. The aim of this study was to coat the SiC and MoSi₂ powders with Ni and observe the sintering behavior in Al powder system. It was thought that Ni powders obtained through plating with nickel chloride (NiCl₂.6H₂O) used in electroless nickel plating bath. The preparation of the samples consist of two main part. In the first part SiC and MoSi₂ powders were coated with nickel by electroless plating technique. In the second part coated SiC and MoSi₂ powders were mixed with aluminum powders and set of specimens were produced by powder metallurgy routes. NiCl₂.6H₂O was used for plating as a source of Ni. Electroless plating bath conditions and chemicals used are shown in Table 1. The ratio of approximately 1:1 for Powder:Ni were maintained for sets of specimens. Powder mixtures were homogenized in rotational mixer for 24 hour. Powder compacts were shaped into cylindrical tablet shape (15 mm diameter, 5 mm height) under single axial press with steel mould at 30 MPa pressure without any pressing aid material.

Table 1: The chemicals of Nickel plating bath and their ratios

Chemicals	Amount and Ratio
MoSi ₂	10g
SiC	10g
NiCl ₂ .6H ₂ O	40g
N ₂ H ₄ .H ₂ O	20%
Distilled Water	80%
Temperature (°C)	90-95°C
pH Value	9-10

The sintering of the specimens was performed at the temperature of 900°C under argon atmosphere (0.5 lt/min gas flow rate, 10 °C/min heating rate) both in conventional and microwave furnace for one hour. Following the sintering, specimens were mounted with resin and polished for electron microscopy. Samples were coated with carbon to prevent charging. Images were taken by LEO 1430 VP Scanning Electron Microscopy equipped with Rontec EDX. Density of the samples were calculated from the mass and the volume ratio. In order to identify the sintering effect, density of the samples were first calculated according the simple mixture rule.

3. RESULTS AND DISCUSSION

Density comparisons of the series are given in Table 2. 3 density values were compared in Table 2. Green densities of the samples were measured after shaping. Similarly densities of the sintered samples were also measured by simple mass-volume ratio. For the each series, theoretical densities were also calculated from the volume fraction and the densities of the powders.

Table 1: Measured and calculated theoretical density comparison (in gr.cm^{-3}).

Series	Green Density	Sintered Density	Calculated Density
Al	2,26	2,32	2,7
ASi-5	2,29	2,33	2,73
ASi-10	2,33	2,42	2,75
ASi-15	2,41	2,50	2,78
AMo-5	2,52	2,71	2,88
AMo-10	2,63	2,75	3,05
AMo-15	2,67	2,76	3,23

Defect free sintered samples were obtained for all samples series. Previously encountered Al leakage bubbles were not observed in Ni coated MoSi_2 powders. This showed that, Ni coating of the MoSi_2 powders makes the surface properties of the Al and MoSi_2 powders suitable for the sintering. However, when the densification behavior is discussed, one can say that Al/SiC powder mixture sinterability is better than the Al/ MoSi_2 mixture.

SiC containing samples' densities were more closer to the calculated theoretical densities than the MoSi_2 containing samples. The main reason for this behavior was thought to be due to the more clustering of the MoSi_2 powders than the SiC powders. Therefore, pores in the powder clusters decreased the density. This effect can also be seen in the SEM micrographs. Ni coated SiC surfaces contain stable Ni layer (Figure 1).

Back scattered image of the polished sample declares that the Ni coating layer on the SiC is very stable. Grinding and the polishing operations not affect the layer very much. Mapping results showed that there isn't any Al-C compound formation around the SiC powders.

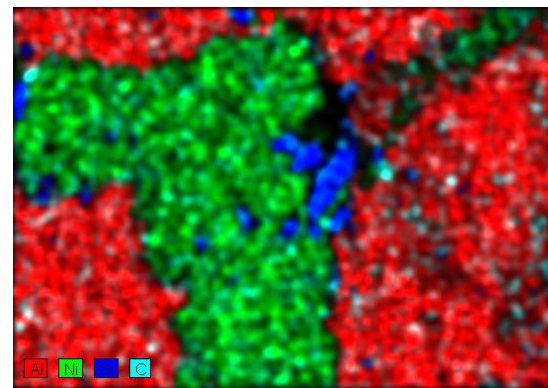
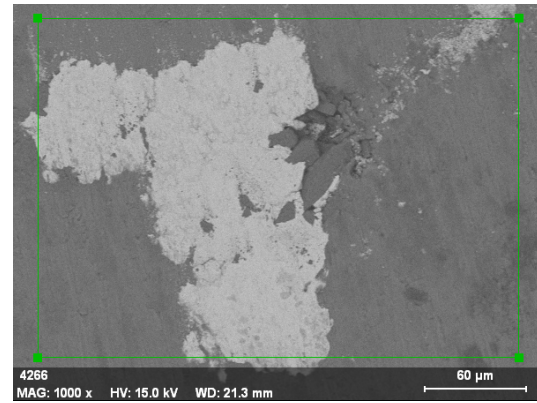


Figure 1: SEM image and element mapping for Al/SiC samples

Opposite to the SiC containing samples, MoSi_2 containing sample pictures showed that the Ni coating layer is not stable enough and worn from the surface after the polishing operation. It is also evident from the Figure 2 that the MoSi_2 powders in the form of cluster and contains small pores. In Figure 2, worn Ni layer is seen and Ni atoms left only on the interface between Al and MoSi_2 interface. Clustering and the combined effect of increase porosity in the MoSi_2 powders resulted in the lower sintered density than the calculated theoretical density.

When the densities in the Table 1 is examined, one can say that depending on the added powder density, composite density changed. Denser MoSi_2 powder addition increase the density more than the SiC powder addition. However, when the density differences of the SiC and MoSi_2 powders considered, one can expect more

density increment when MoSi_2 powders added to the aluminum powder.

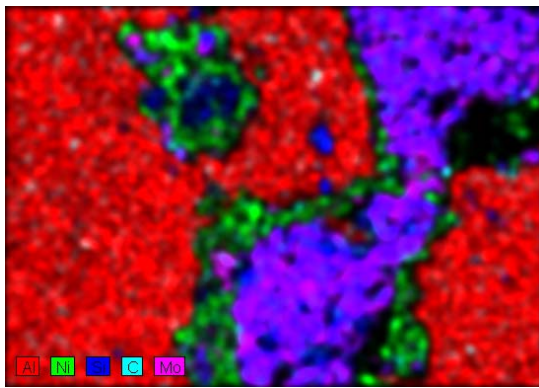
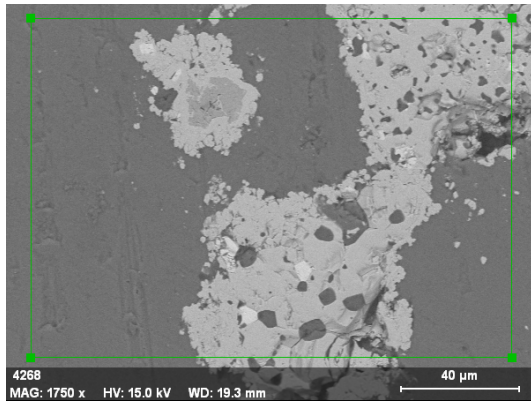


Figure 2. SEM image and element mapping for Al/ MoSi_2 samples.

4. CONCLUSIONS

Defect free sintered samples were obtained. Al bubbles on the surface of the samples after sintering did not observed when the MoSi_2 powders were coated with

Ni. This shows that coated Ni layer act as a good diffusion barrier. Electroless nickel plating of the SiC and MoSi_2 surfaces can be used as a good method for the creating diffusion barrier. However, due the aqueous nature of the process, powders are always in the tendency of agglomeration. Therefore, special care must be paid during the coating operation. Clustering of the powders prevents the targeted densities after the sintering operation. Coating of the SiC with Ni was found to be useful for the prevention of the Al-C compound formation between the SiC- Aluminum interface.

REFERENCES

- Ramasesha, S.K, and Shobu, K.,1998. Reactive Infiltration of Aluminum into Molybdenum Disilicide Preform. *J. Am. Ceram. Soc.*, **81** [3] 730.
- Rodríguez-Reyes, M., Pech-Canul, M. I., Rendón-Angeles, J. C., López-Cuevas, J. (2006). "Limiting the Development of Al_4C_3 to Prevent Degradation of Al/SiCP Composites Processed by Pressureless Infiltration". *Composites Science and Technology*, Vol. 66, No. 7-8, pp. 1056.
- Talaş Ş., and Çakmakkaya M., Mikrodalga ile Sinterlenmiş Fe-26Al, Fe-30Al, Fe-26Al-14Ti ve Fe-30Al-14Ti Toz Karışımlarının Cu Aratabakalı Difüzyon Kaynağı ile Birleştirilmesi, *Gazi Üniversitesi Mühendislik - Mim*, 27, 01, 2012

EFFECT OF TiC PARTICLE SIZE ON SOME PROPERTIES OF Cu-Al/TiC COMPOSITES PRODUCED USING HOT PRESSING PROCESS

Ertuğrul Çelik ^{1,a}, Serkan Islak ² and Durmuş Kır ³

¹Tunceli University, Faculty of Engineering, Department of Mechanical Engineering, Tunceli, Turkey

²Kastamonu University, Faculty of Engineering and Architecture, Department of Materials Science and Nanotechnology Engineering, Kastamonu, Turkey

³Kocaeli University, Hereke Vocational High School, Kocaeli, Turkey

a. Corresponding author (ecelik@tunceli.edu.tr)

ABSTRACT: In this study, the Cu-Al/TiC composite materials were produced using hot pressing process. Effect of TiC particle size (0.2, 4 and 44 μm) on microstructure and hardness properties of these materials was investigated experimentally. Production of Cu-Al/TiC composite was carried out under pressure of 35 MPa, at 700 °C, and for a sintering time of 5 minutes. Optical microscopy studies showed that the TiC grains were relatively homogeneously distributed in the Cu-Al matrix. With the decreasing of TiC particle size, the hardness of composites increased. Moreover, the relative density of composites increased.

1. INTRODUCTION

Nowadays, there is an increasing need worldwide for the advanced materials in order to obtain the desired properties. This is because a single material generally cannot meet the requirements of harsh engineering environments. That is why the need for composites with unique properties is growing every day. Metal matrix composites (MMC) are widely used in different industries because of their high mechanical properties and wear resistance [Sevik and Kurnaz, 2006 and Rahimian *et al.*, 2010].

The particle reinforced metal matrix composites can be synthesized by such methods as standard ingot metallurgy, powder metallurgy, disintegrated melt deposition technique, spray atomization and co-deposition approach. Different method results in different properties. The powder metallurgy (PM) processing route is generally preferred since it shows a number of product advantages. The uniform distribution of ceramic particle reinforcements is readily realized [Kim *et al.*, 2001; Zhang and Wang, 2005]. PM

method consists of the steps of pressing metal powders inside a mould, bonding

powder particles with each other, and sintering. This method is also a large process which several materials are manufactured by pressing-sintering or hot pressing. Not only simple cylindrical shafts, bearings but also complex shaped parts such as filters, gears can be conveniently manufactured through powder metallurgy method [Narayanasamy *et al.*, 2006].

Development of high conductivity and high strength Cu alloys can be achieved by uniformly dispersing fine ceramic particles such as oxides, borides, carbides and nitrides in the Cu matrix. Dispersion strengthened Cu alloys are also known to have better mechanical properties than precipitation hardened Cu alloys at elevated temperatures because of the thermal stability of these dispersoids [Lee *et al.*, 2000].

In this work, TiC particles having 0.2, 4 and 44 μm size are used to reinforce Cu–

Al matrix. A hot pressing method is carried out to prepare Cu–Al/TiC composites. Some properties of the Cu–Al/TiC composites are characterized.

2. EXPERIMENTAL STUDIES

Cu–Al alloys were prepared by blending pure Cu powder (purity 99.9%, particle size 10 μm) and pure Al powder (purity 99.9%, particle size 10 μm) to form the Cu–5 wt% Al. The aim of Al powder addition was to form a liquid phase and aid in densification during hot pressing. Composites based on Cu–5 wt% Al matrix alloy and containing TiC (particle sizes 0.2, 4 and 44 μm) powder were mixed with the addition of a 1 wt.% of paraffin wax, at a speed of 20 rpm, for 30 minutes in an ∞ shape rotary mixer. TiC powders were added to the Cu–Al matrix at the amount of 5 wt.% percents. Then, the mixture was hot-pressed in graphite moulds for 5 min at 700 $^{\circ}\text{C}$ with an applied pressure of 35 MPa on an automatic hot pressing machine. Figure 1 illustrates the flow scheme for composite production.

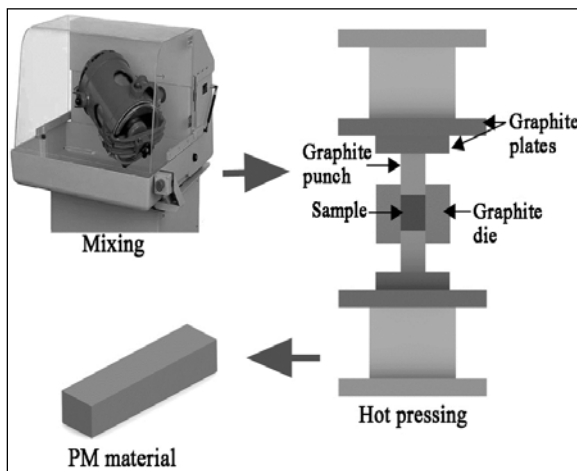


Figure 1: Flow scheme for composite production

The relative density and hardness of the composites were determined. The relative densities of composites were measured by Archimedes' principle. Microhardness of composites was determined using a

Leica model Vickers hardness instrument under an applied load of 100 g. An Optical Microscopy and X-ray diffractometer (Bruker AXS D8 Advanced System, Germany) were used to investigate the microstructure properties of composites.

3. RESULTS AND DISCUSSION

3.1. Microstructure

Cu–Al and Cu–Al/TiC composites were successfully produced using the hot pressing method together with a 5-minute sintering time at 700, under pressure of 35 MPa. Figure 2 illustrates optical microstructure of Cu–Al matrix. Aluminum liquid phase formed due to 700 $^{\circ}\text{C}$ sintering temperature. Al liquid phase is seen as islets in the Cu–Al microstructure. This liquid phase fills the pores in the microstructure. Besides, due to the liquid phase, at the interface of Cu and Al occurred the good wettability.

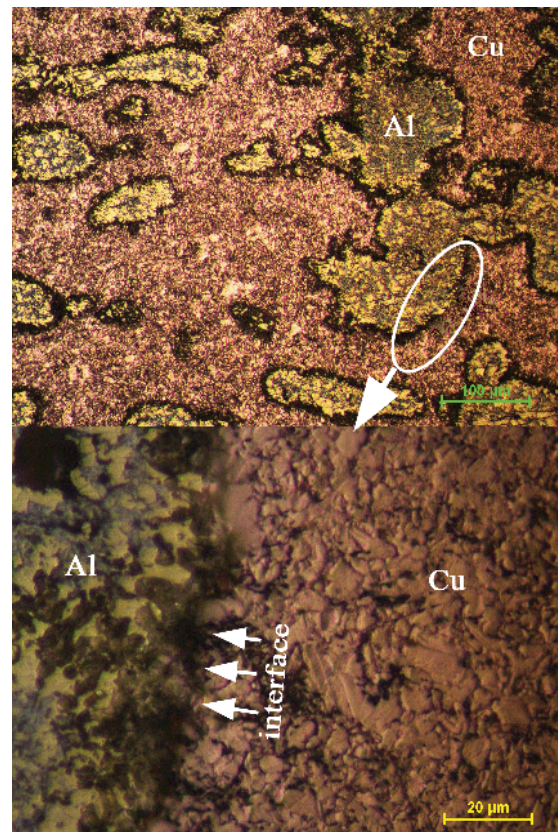


Figure 2: Optical micrograph of CuAl

Figure 3 shows the Optical micrographs of CuAl-TiC composites with three types of the particle size (0.2, 4 and 44 μm). The TiC particles were relatively homogeneously distributed in the microstructure. In micrographs, the reddish areas indicate Cu, the yellowish areas indicate Al, and black and cornered shapes indicate the reinforcement component TiC. The TiC having 0.2 μm particle size distributed in the form of clusters. This situation is due to agglomeration of TiC powder during mixing of powders.

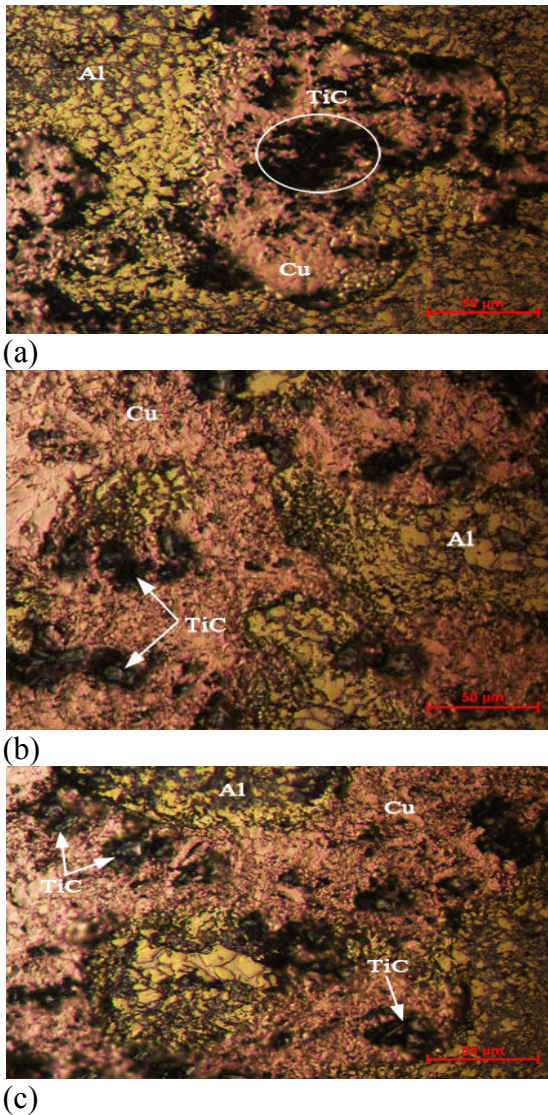


Figure 3: Optical micrographs of CuAl-TiC composites with different particle size: (a) 0.2 μm , (b) 4 μm and (c) 44 μm

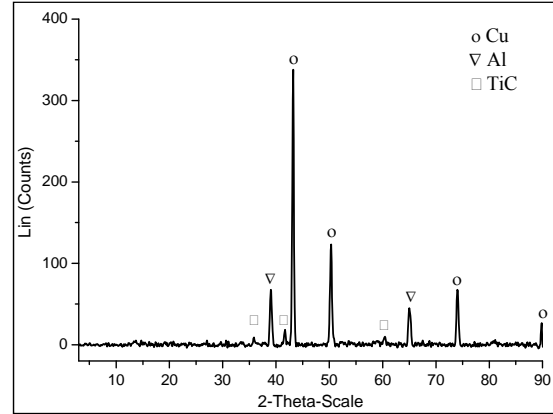


Figure 4: XRD pattern of CuAl-TiC composite

Figure 4 shows XRD patterns of the CuAl-TiC composite. Cu, Al and TiC phases are detected in the microstructure. This implies that no chemical change occurred in the sintered CuAl-TiC composite at 700 $^{\circ}\text{C}$ temperature. As shown in Figure 4, in the composite oxidation was not observed.

3.2. Density and Hardness of Composites

Table 1 illustrates the effect of TiC particle size on densities of composites. The sintered and theoretical densities of composites were used to determine their relative density. When TiC was introduced to the CuAl matrix, it decreased the sintered density. This was due to the fact that the density of titanium carbide was lower than that of CuAl. The density of TiC was 4.93 g/cm^3 , while the density of CuAl was 8.62 g/cm^3 . Relative density of composite decreased as the TiC particle size increased. It can be concluded that two concurrent consolidation mechanisms act between the ceramic phase and the metal one, in which lower TiC particle size leads to the less porosity is achieved. Moreover, large TiC particles reduce the contact area between the matrix particles. For this reason, in the microstructure of composite occurred high porosity. By the addition of more coarse-grained TiC particles to the matrix the relative density

of composites decreases because the presence of porosity is related to density [German, 1998; Min *et al.*, 2005; Rahimian *et al.*, 2009].

Table 1: The effect of TiC particle size on the densities of the composites

Samples	Theoretical density (g/cm ³)	Sintered density (g/cm ³)	Relative Density (%)
M*	8.63	7.87	91.25
M/TiC – 0.2 μm	8.43	7.43	88.18
M/TiC – 4 μm	8.43	7.39	87.67
M/TiC – 44 μm	8.43	7.07	83.85

*M is CuAl

Figure 5 shows the effect of the size of reinforcement particle on the hardness of Cu-Al/TiC composites. Five measurements for each composite specimen were carried out in the hardness test for reproducibility. The hardness of Cu-Al without TiC was measured as 35.5 HV_{0.1}. The hardness of Cu-Al/TiC composites was 51.9 HV_{0.1} for TiC having 0.2 μm particle size, 45.5 HV_{0.1} for TiC having 4 μm and 40.2 HV_{0.1} for TiC having 44 μm particle sizes. Hardness was found to decrease with increasing TiC particle size. This phenomenon can be evaluated at various viewpoints. Some researchers have attributed this to greater interfacial area between the reinforcement particle and the matrix [Sevik and Kurnaz, 2006]. Furthermore, the defects in the coarse-grained particles are more than the fine-grained ones [Rahimian *et al.*, 2010]. The hardness of composites increases with decreasing powder particle size according to Hall-Petch equation which indicates the relationship between the grain size and strength [Angelo and Subramanian, 2008].

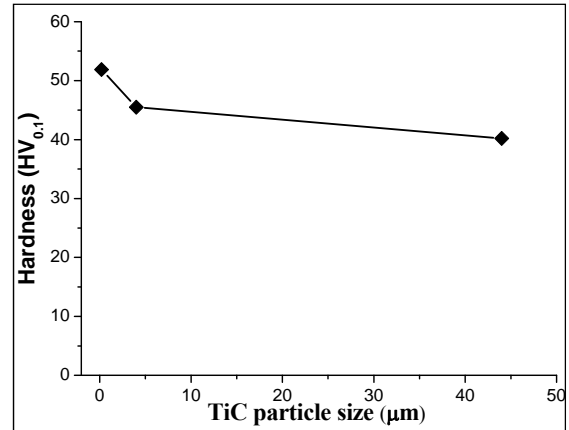


Figure 5: The effect of TiC particle size on composite hardness

4. CONCLUSIONS

- ▶ Cu-Al/TiC composites were successfully produced using the hot pressing method.
- ▶ The TiC particles were relatively homogeneously distributed in the CuAl matrix.
- ▶ Cu, Al and TiC phases are detected in the microstructure according to XRD.
- ▶ With the decreasing of TiC particle size, the hardness and relative density of composites increased.

REFERENCES

- Angelo, P.C., Subramanian, R., 2008. Powder Metallurgy Science: Technology and Applications, Prentice-Hall of India Pvt.Ltd., India.
- German, R.M., 1998. Powder Metallurgy of Iron and Steel. Wiley, USA.
- Kim, B.G., Dong, S.L., Park, S.D., 2001. Effects of thermal processing on thermal expansion coefficient of a 50 vol.%SiCp/Al composite. Mater. Chem. Phys. 72, 42–47.
- Lee, J., Jung, J.Y., Lee, E.S., Park, W.J., Ahn, S., Kim, N.J., 2000. Microstructure and properties of titanium boride dispersed Cu alloys fabricated by spray forming, Materials Science and Engineering: A, 277 (1–2), 274–283.
- Min, K.H., Kang, S.P., Kim, D.G., Kim, Y.D., 2005. Sintering characteristic of Al₂O₃-reinforced 2xxx series Al composite powders. J. Alloys Compd. 400, 150–153.
- Narayanasamy, R. Ramesh, T. Pandey, K.S., 2006. Workability studies on cold upsetting of Al–Al₂O₃ composite material. Materials and Design 27(7), 566–575.

- Rahimian, M., Parvin, N., Ehsani, N., 2010. Investigation of particle size and amount of alumina on microstructure and mechanical properties of Al matrix composite made by powder metallurgy, *Materials Science and Engineering: A*, 527 (4-5), 1031-1038.
- Rahimian, M., Ehsani, N., Parvin, N., Baharvandi, H.R., 2009. The effect of particle size, sintering temperature and sintering time on the properties of Al-Al₂O₃ composites, made by powder metallurgy, *J. Mater. Proc. Technol.*, 209, pp. 5387-5393.
- Sevik, H., Kurnaz, S.C., 2006. Properties of alumina particulate reinforced aluminum alloy produced by pressure die casting, *Materials & Design*, 27(8), 676-683.
- Zhang, R., Wang, H.L., 2005. Spheroid growth during sintering of copper coated silicon carbide particles in the fabrication of nanocomposite. *Key Eng. Mater.* 280–283, 1275–1278.

EFFECTS OF THE SINTERING PARAMETERS ON MECHANICAL PROPERTIES OF FE-BASED POWDER METAL PARTS

Can ÇİVİ^{1,a}, Göksan AKPINAR², Enver ATİK³

1. Celal Bayar University Engineering Faculty Mechanical Engineering Department, Manisa, Turkey

2. Celal Bayar University Engineering Faculty Mechanical Engineering Department, Manisa, Turkey

3. Celal Bayar University Engineering Faculty Mechanical Engineering Department, Manisa, Turkey

a. Corresponding author (can.civi@cbu.edu.tr)

ABSTRACT: Sintering is one of the most important step of the production of powder metal parts, because it brings into desired values the mechanical properties of pressed metal powder according to usage area. Generally sintering of powder metal parts is made classical sintering furnaces. Induction sintering method is an important alternative of classical sintering method because of lack of time and energy consumption in sintering. In this study, changing of mechanical properties of induction sintered Fe based components included Cu and Graphite were investigated according to the exchange of sintering time. For this purpose Vickers hardness, change of volume, mass, and surface roughness values of sintered powder metal parts by induction for 8.4, 15 and 30 minutes were investigated and compared with each other and micro structural investigation was applied to powder metal parts.

1. INTRODUCTION

Powder metallurgy method, day by day becoming more common because of small number of processing step, repeatability, measurement accuracy, and only can be obtaining of some of the materials by this method (for instance materials which hard and have a high degree of melting).

Powders which have different composition are pressed and then sintered at powder metallurgy method. Sintering is one of the most important issues of powder metallurgy because sintering causes significantly an increase in resistance of pressed powders [Randall *et al.*, 2007]. The sintering process is generally performed in the sintering furnaces. It is done in batch furnaces and continuous furnaces [Randall *et al.*, 2007]. In addition, rapid sintering methods such as induction sintering, microwave sintering, plasma sintering, laser sintering and discharge sintering are important alternative to conventional sintering methods [Atikand Çavdar, 2011].

Sintering and additional heat treatments of powder mixtures generate the microstructure to meet the performance as required [Narasimhan, 2001].

Mixtures of elemental iron and graphite powders are commonly used for Powder Metallurgy application. A small amount of copper powder is always added to further strengthen the sintered alloys owing to its relative ease of dissolving and diffusing in the iron matrix upon sintering [Wang, 2005].

Almost all powder metal low alloy steels contain copper. The amount of copper in them varies from approximately 1 to 8% depending upon desirability of end products. At low content it is added to provide strength by age hardening, while at higher concentrations the purpose is to promote liquid phase sintering causing faster densification and homogenization [Ranjan, 2001]. Addition of carbon to iron powder increases the sintering kinetics as it dissolved into the iron

lattice, changing the melting point, surface tension and viscosity of the iron melt formed. Small areas of martensite and tempered martensite are also formed [Shimchi, 2008].

In previous studies in the literature, induction sintering was generally carried out with high frequency induction sintering unit at the same time pressing process. [Dohet *et al.*, 2007], [Khalil and Kim, 2007], [Khalil and Almajid, 2012], [Kim *et al.*, 2004], [Kim *et al.*, “2005], [Kim *et al.*, 2006], [Mazaheriet *al.*, 2009], [Park *et al.*, 2007], [Shonet *al.*, 2009].

Hwan-Cheol Kim *et al.* used a high-frequency induction heated sintering (HFIHS) method, the densification of binderless WC and WC-x wt.%Co (x=8, 10, 12) hard materials were accomplished using an ultra fine powder of WC and WC-Co. They found nearly fully dense WC and WC-Co with a relative density of up to 99.9% could be obtained with a simultaneous application of 60 MPa pressure and induced current (within 2 min) without a significant change in grain size [Kim *et al.*, 2007].

In-Jin Shon *et al.* investigated sintering behavior and mechanical properties of WC-10 wt.%Co, WC-10 wt.%Ni and WC-10 wt.%Fe hard materials. It was produced by high-frequency induction heated sintering (HFIHS) method was accomplished using ultra-fine powder of WC and binders (Co, Ni, Fe). It was shown that highly dense WC-10Co, WC-10Ni and WC-10Fe with a relative density of up to 99% could be obtained with simultaneous application of 60 MPa pressure and induced current within 1 min without significant change in grain size. And they saw the hardness and fracture toughness of the dense WC-10Co, WC-10Ni and WC-10Fe

composites produced by HFIHS were investigated [Shonet *al.*, 2009].

Zongyin Zhang and Rolf Sandström investigated the effects of sintering temperature, time and atmosphere on the properties of sintered steels with these Fe-Mn-Si master alloy powders. Eventually, they found the density of the compacts increases with sintering temperature and time. The ultimate tensile strength and hardness increases with sintering temperature and time mainly due to increasing amounts of bainite and martensite after cooling. Elongation is initially raised with sintering temperature and time probably due to improved bonding between powder particles. And also they saw liquid phase sintering accelerates the sintering process, which leads to improved mechanical properties [Zhang and Sandström, 2004].

In this study, sintering was carried out after pressing process with medium frequency induction unit (30 kHz). Mechanical properties of induction sintered powder metal parts were compared depending on the sintering time. Effects of sintering time on mechanical properties (change of volume, mass, Vickers hardness and surface roughness values) were investigated and microstructural investigation was applied. Developed induction sintering mechanism (Figure 1) provided continuously production and same sintering conditions (sintering time, temperature, etc.) of powder metal parts according to mass production similarly continuous sintering furnaces.



Figure 1: Induction Sintering Mechanism

2. EXPERIMENTAL STUDIES

In this study, Hogenas ASC 100.29 iron powder (%3 Cu, %0,5 Graphite and %1 kenolube lubricant by weight) was used. Metal powder was pressed under 600 N/mm² with uniaxial compression and 10X10X55 mm samples were formed. Samples were sintered with medium frequency induction sintering mechanism (30 Khz) for 8.33, 15 and 30 minutes at 1120°C to compare. Differences in weights and volumes of the samples were measured. Surface roughness measurements, and the micro Vickers hardness measurements were applied to the samples. Also, micro structural investigation was applied to the samples.

3. RESULTS AND DISCUSSION

3.1. MicroVickers Hardness Measurements Results

Micro Vickers Hardness measurements were applied to the sintered samples on six separate points of surfaces. Vickers Hardness measurements results of the samples were shown at Figure 2.

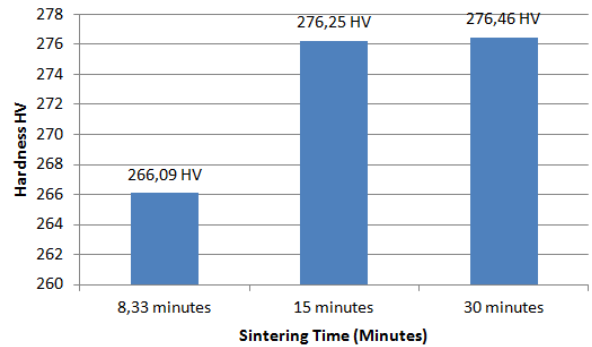


Figure 2: Vickers Hardness Test Results

Micro Vickers hardness of samples were increased with sintering time. This increasing was significantly between 8,33 and 15 minutes sintered samples. Micro Vickers values of 30 minutes sintered samples were increased but this increasing was occurred in a very small amount.

3.2. Weight Changes Results

Weight changes of samples before and after sintering were measured with precision scales. The measurement results are shown in Figure 3.

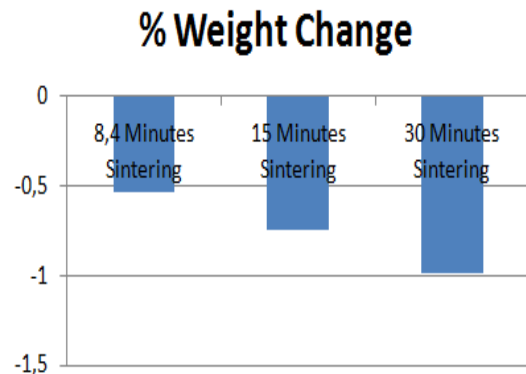


Figure 3: Weight changes results of the samples before and after sintering.

The decreasing in weight was increased with sintering time increase. After sintering along 30 minutes, weights of samples were decreased by the amount of lubricant (%1). All of the lubricant did not evaporate from powder metal sample after 15 and 8,4 minutes sintering.

3.3. Volume Changes Results

Volume changes of samples before and after sintering were measured geometrically with micrometer. The measurement results are shown in Figure 4.

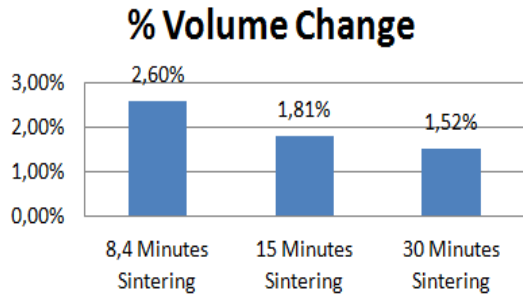


Figure 4: Volume Changes results of sintered samples

The volumes of the samples were increased after sintering process in accordance with the literature [1]. However, increasing of volume is decreased with sintering time increases.

3.4. Surface Roughness Measurements Results

Surface roughness values of samples were shown at figure 5.

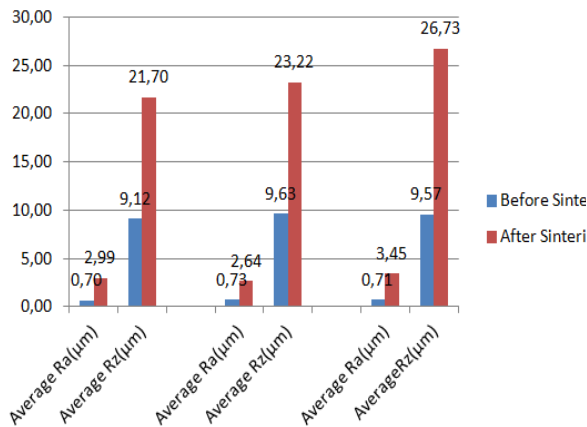


Figure 5: Surface Roughness Values of Samples

Surface roughness values of samples (Ra and Rz) were increased after sintering. Ten-point mean roughness values of samples (Rz) were increased with sintering time. Despite arithmetical mean

roughness values of samples (Ra) were decreased 15 minutes sintering, in general, Ra values of samples were increased with sintering time.

3.5. Microstructural Investigation of Samples

Microstructure pictures of sintered samples were shown at figure 6.

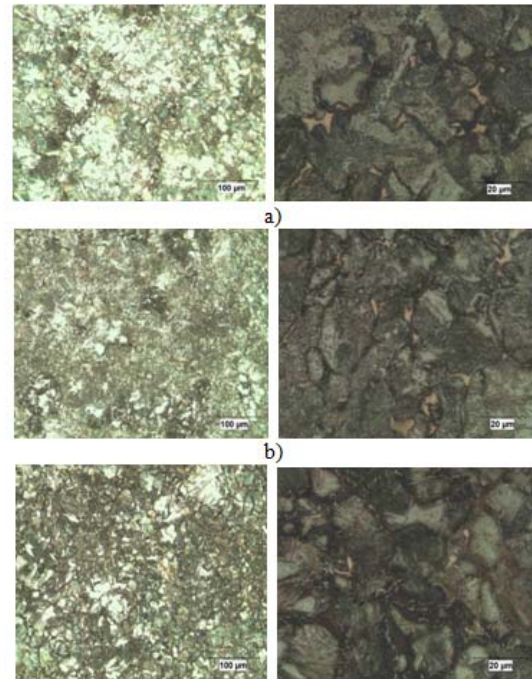


Figure 6: Microstructure Pictures a) 8,4 Minutes, b) 15 Minutes, c) 30 Minutes Sintered Samples with Induction

It can be seen that as the sintering time increased, copper diffused better into the iron particles. Due to relatively short sintering time, copper was melted and not diffused into the matrix of the microstructure of samples which were sintered for 8.4 minutes. As can be seen from the microstructure pictures, copper melted and diffused better into the matrix of samples sintered 15 and 30 minutes.

4. CONCLUSIONS

As a result of this study; Vickers hardness values of the samples were increased by sintering time.

Weights of samples were decreased after sintering and the decreasing was increased with sintering time increase. This was occurred because of evaporating of lubricant of pressed powder with sintering process. It was determined that with 30 minutes induction sintering, all of the lubricant inside of the pressed powder was evaporated and lubricant residues did not remain in the samples.

Surface roughness values (Ra and Rz) of the samples were increased generally with sintering time. This was considered that because of increasing of lubricant outputting and surrounding of iron powders with melted copper.

The volumes of the copper containing samples increase after sintering process at studies in the literature [1]. In this study, volumes of the samples were increased after sintering process in accordance with the literature. However, increasing of volume is decreased with sintering time increases. This was considered that result from the increasing of density with the sintering time.

Our previous study, maximum stress , maximum strain and Rockwell-B Hardness values of the samples sintered by induction of 8,4 minutes were caught and passed samples sintered 30 minutes by classic sintering furnace and these values were increased with induction sintering time [Çivi and Atik, 2009]. In this study, effect of induction sintering time on other mechanical property values was investigated. It was found that despite obtaining of same strength values of classical sintering at lower time at induction sintering, other mechanical properties of samples were increased with induction sintering time and lubricant residues in the sample were decreased.

REFERENCES.

- Atik, E.; Çavdar, U.; 2011, Geleneksel ve Hızlı Sinterleme Yöntemleri, CBÜ Soma Meslek Yüksekokulu Teknik Bilimler Dergisi, Cilt 1, Sayı:15
- Çivi C. Atik E., 2012, "Comparison Of Effect Of Induction And Classical Sintering To Mechanical Properties Of Powder Metal Components." AIP Conference Proceedings; 1476 , 119-122
- Doh, J.M., Jeong, I. K., Kim, H. C., Ko, I. Y. Shon, I. J. ,Yon I. J, 2007, "Rapid sintering of ultra fine WC and WC-Co hard materials by high frequency induction heated sintering and their mechanical properties", Metals And Materials International Volume 13, Number 1, 39-45
- Khalil, K.A., Kim, S.W., 2007 "Mechanical wet-milling and subsequent consolidation of ultra-fine Al₂O₃-(ZrO₂+Y₂O₃) bioceramics by using high-frequency induction heat sintering", Science Press, Trans. Nonferrous Met. Soc. China 17,21-26
- Khalil, A., K.; Almajid, A., A.,2012; "Effect of high-frequency induction heat sintering conditions on the microstructure and mechanical properties of nanostructured magnesium/hydroxyapatite nanocomposites" Materials and Design 36 58–68
- Kim, H.C., Oh, D.Y., Shon, I.J.,2004 "Sintering of nanophase WC-15 vol. %Co hard metals by rapid sintering process", Elsevier, Refractory Metals & Hard Materials 22; 197-203
- Kim, H.C. I. J. Shon, Z. A. Munir, 2006 "Rapid sintering of ultra-fine WC-10 wt % Co by high frequency induction heating", Elsevier, International Journal of Refractory metals & Hard Materials 24 427-431
- Kim H. C., Yoon J. K., Doh J.M., Ko I. Y., Shon I. J.; 2006 "Rapid sintering process and mechanical properties of binderless ultra fine tungsten carbide" Materials Science and Engineering A 435–436 717–724
- Kim, H. C., Shon, I. J., Jeong, I.K., Ko, I.Y., Yoon, J.K., Doh, M.J.; 2007, " Rapid sintering of ultra fine WC and WC-Co hard materials by high-frequency induction heated sintering and their mechanical properties " Metals and Materials International, 13, 1, pp 39-45.
- Mazaheri, M. ,Zahedi, A.M. , M. Haghightazadeh, Sadrnezhad, S.K. ,2009 "Sintering of titaniananoceramic: Densification and grain growth" Ceramics International 35 685–691
- Narasimhan, K. S., 2001 Sintering of powder mixtures and the growth of ferrous powder metallurgy, Materials Chemistry and Physics , Volume 67, Issues 1-3, , Pages 56-65

- Park, H.K., Shon, I.J., Yoon, J.K., Doh, J.M., Ko, I.Y., Munir, Z.A., 2008; "Simultaneous synthesis and consolidation of nanostructured NbSi₂-Si₃N₄ composite from mechanically activated powders by high frequency induction-heated combustion" Elsevier, Journal of alloys and compounds 461; 560-564,
- Randall M. G., Editörler; Durlu, N., Sarıtaş, S., Türker, M., 2007, "TozveParçacıklıMalzemeİşlemleri", p.p. 2-9, 143, 233-273, 279-296, TMMOB, Ankara/Türkiye,
- Ranjan G. S. Upadhyaya, 2001, "Effect of copper and VCN additions on sintering of low alloy steel", Materials & Design, Volume 22, Issue 5, Pages 359-367
- Simchi, A., 2008, "Effect of C and Cu addition on the densification and microstructure of iron powder in direct laser sintering process", Materials Letters Volume 62, Issues 17-18, 30, Pages 2840-2843
- Shon, I. J; Jeong, I. K; Jeong, H.V.; Park, J. H.; Kim, B.R.; Lee, K.T.; 2009, "Effect of Fe₂O₃ addition on consolidation and properties of 8 mol% yttria-stabilized zirconia by high-frequency induction heated sintering (HFIHS) Ceramics International 35 ;363-368
- Shon, In-Jin, In-KyoonJeong, In-Yong Ko, Jung-Mann Doh, Kee-Do Woo, 2009 " Sintering behavior and mechanical properties of WC-10Co, WC-10Ni and WC-10Fe hard materials produced by high-frequency induction heated sintering " Ceramics International 35 339-344.
- Wang, W. F., 2005, "Effect of alloying elements and processing factors on the microstructure and hardness of sintered and induction-hardened Fe-C-Cu alloys", Materials Science and Engineering, Volume 402, Issues 1-2, 15, Pages 92-97
- Zongyin Zhang and Rolf Sandström, 2004 " Fe-Mn-Si master alloy steel by powder metallurgy processing " Journal of Alloys and Compounds 363 194-202.

INVESTIGATION OF WELDABILITY of PRODUCED BY POWDER METALLURGY METHOD OF NI-TI COMPOSITE WITH STAINLESS STEEL COUPLE

Mehmet ÇAKMAKKAYA¹, Fatih ÇOLAK^{2,a}, Ersan MERTGENÇ³, Rıza KARA²

1. Afyon Kocatepe University, Faculty of Technology, Automotive Engineering, Afyonkarahisar, Turkey
2. Usak University, Vocational School of Usak, Welding Technology Programme, Uşak, Turkey
3. Afyon Kocatepe University, Graduate School of Natural and Applied Science, Afyonkarahisar, Turkey
a. Corresponding author (fatih.colak@usak.edu.tr)

ABSTRACT: In this study, a pair of austenitic stainless steel with Ni-Ti composite material combined with TIG welding method. Ni-Ti composite produced by the powder metallurgy (P / M) method. Ni-Ti composite material, 45 µm grain size of 99% purity powders by weight was prepared by mixing the composition of 51% Ni and 49% Ti. This study pairs of materials joining TIG welding method is preferred. Welding process, the Ni-Ti composite material of two stainless steel plate was used. Welding process was carried out with the forehead and blunt 40A. Search for post-merger changes in microstructure that occur on the surface of the source examined by SEM-EDX analysis. In this study has been observed a pair of stainless steel and Ni-Ti composite successful due to the TIG welding method.

Keywords: TIG welding method, Composite materials, Stainless Steel, Microstructure

1. INTRODUCTION

Powder metallurgy method of producing shaped parts for the production of a large number of materials and finished last more competitive manufacturing method according to the production methods. Powder metallurgy method, which is not obtainable with conventional metallurgical methods provides an excellent opportunity to manufacture the materials [Şalak *et al.*, 2005].

Powder metallurgy is one of the composite material production technology [Groover, 2007].

Shaped pieces of metallic and ceramic powders produced by the method finished last. Metal or non-metal powder / powders desired ratio are mixed and subsequently compressed to take their final form in a metal mold. Finally, this compacted powder or mixture of powder is subjected to sintering under vacuum or controlled atmosphere [Waters, 1996].

In recent years the effect of super-elastic NiTi shape memory alloys with shape memory effect, and in recent years has become one of the well-known materials. Due to these characteristics martensitic transformation is activated [Yong *et al.*, 2001].

NiTi shape memory alloys approximately equal atoms and cheaper than other shape memory alloys. The biggest disadvantage of NiTi alloys have many advantages, though high ductility. Therefore the workability of these alloys is low [Dapino *et al.*, 2012].

TIG welding method is one of the methods of welded joint. Method under a protective gas atmosphere consists of an electric arc between the work piece and the tungsten electrode and the merger takes place with the help of this arc. TIG welding can be performed welding metals of different thickness. TIG welding

combined with the different material groups [Fox *et al.*, 2012].

In the study of NiTi shape memory alloy pipe and AISI 304 stainless steel tube with a layer of Ni resulted from the search. TIG welding was used in this study. Fatigues testing of welded samples were applied. Successfully carried out the welding process [Riggs, 2012].

NiTi alloy stainless steel weldability also investigated by laser welding [Wang, 1997] Laser source has been found that this material is a promising source pairs [Hall, 2003].

In this study, the maximum reaction in the transition and the NiTi alloy is stainless steel side by side, the grain growth observed in epitaxial solidification [Eijk *et al.*, 2012].

2. MATERIALS AND METHODS

In this study, the pair of stainless steel weldability with NiTi composite sample investigated. NiTi composite material produced by powder metallurgy method. In this method, % 51Ni and 49Ti% by weight of metal powders were weighed precisely.

The weighed powders are mixed homogeneously. Powder mixtures with uniaxial cold pressing method is shaped under pressure of about 100 to 200 bar. Atmosphere of argon-protected samples were pressed in tube furnace sintered at 950 °C for 30 minutes.

Composite sample was obtained after sintering and austenitic stainless steel TIG welding method stemmed from a 40 amp.

Metallographic samples were then prepared in the welding process. Characterization of welded samples were completed. In this study the applied flow chart in Figure 1 is shown.

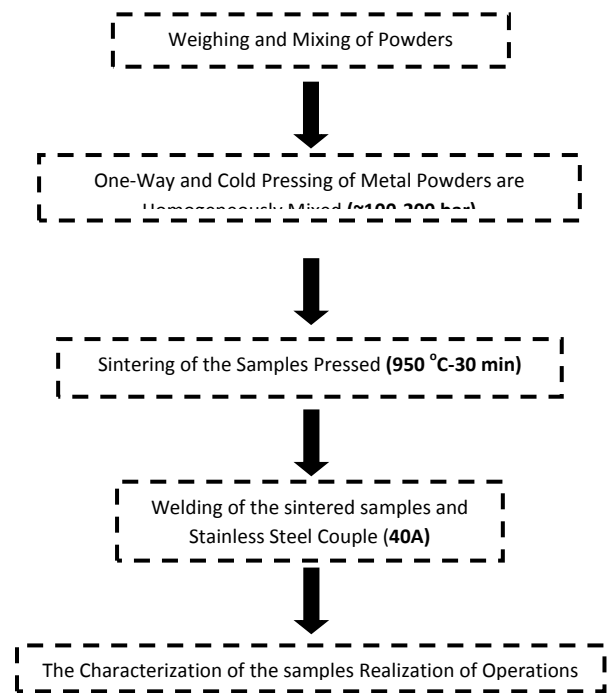


Figure 1: Flow chart

3. RESULTS AND DISCUSSION

3.1. Experimental Results

NiTi composite material and a pair of stainless steel with TIG welding due. SEM analysis image from the welding zone in Figure 2 is shown. The merger has been obtained as a result of the welding process.

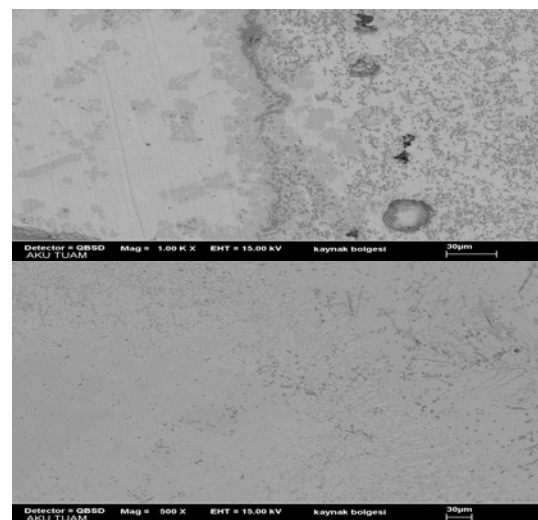


Figure 2: SEM image from the welding zone

On the welding zone, line, and area made SEM-EDX analysis in Figure 3 is shown.

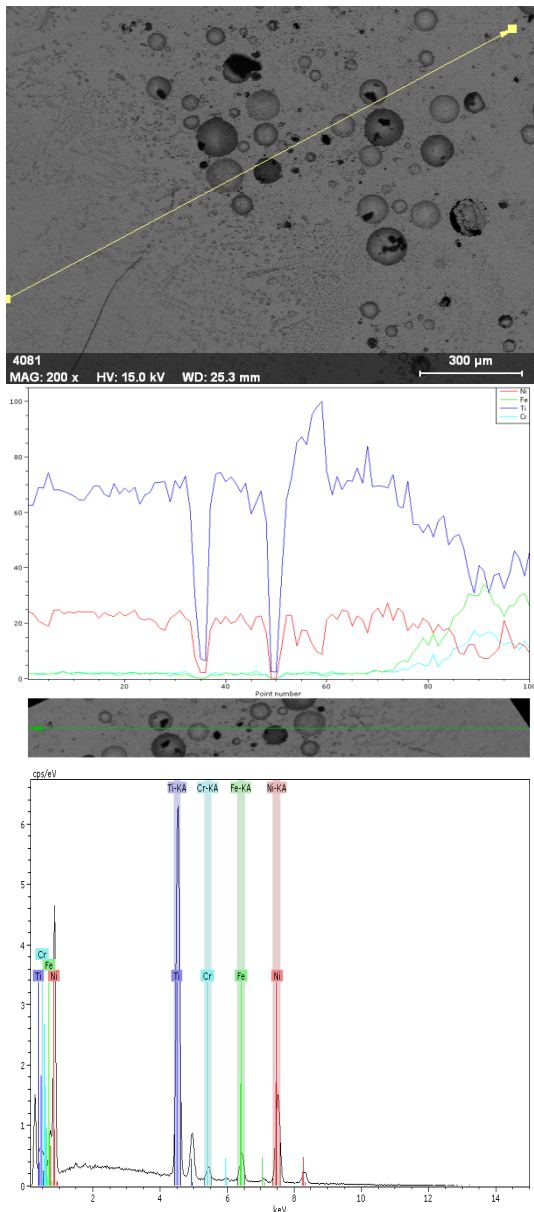


Figure 3: Line EDX analysis of welding zone

Figure 4 shows the EDX analysis of the sample shown in the welding zone. Elements Ni and Ti ratio decreased as a result of analysis of the welding zone. Welding zone is rich with Fe and Cr elements observed.

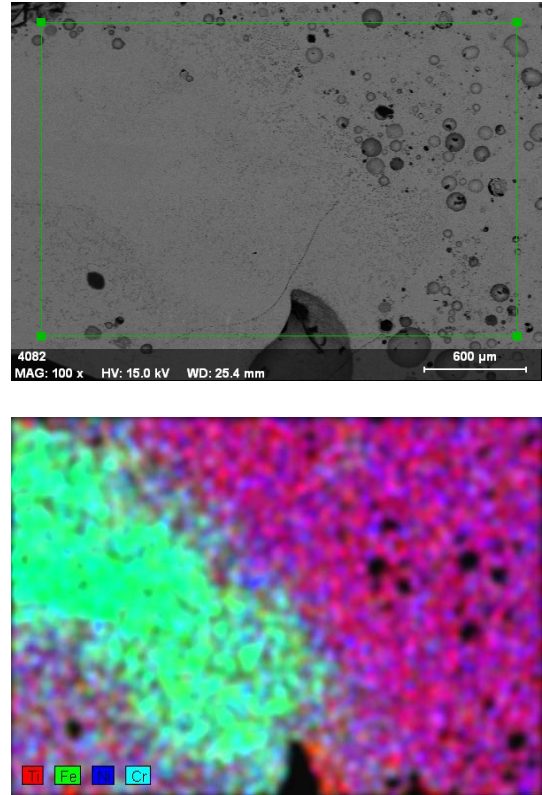


Figure 4: Regional EDX analysis

3.2. Discussion

In this study;

- 1- NiTi alloy powder metallurgy method successfully produced.
- 2- TIG welding of austenitic stainless steel pair of NiTi and successfully combined with the method.
- 3- The pores formed in the welding zone is determined by SEM analysis.
- 4- As a result of EDX analysis of the weld pass part by stainless steel was observed that more of the mixture.

REFERENCES

- Šalak, A., Selecká, M., Danninger, H., "Machinability Of Powder Metallurgy Steels", Cambridge International Science Publishing, 1-23, (2005).
- Groover, M.P., "Fundamentals of Modern Manufacturing: Materials, Process and Systems", Jhon Wiley&Sons, Inc., 3rd Edition, 337-361, (2007).

- Waters, T.F., "Fundamentals of Manufacturing for Engineers", Taylor & Francis Routledge, 173-180, (1996).
- Ertuğ, B., "Sintering Applications", InTech, First Edition, 1-342, (2013).
- Yong, L., Wilson, A.R., Asanuma H., "Proceedings of the Conference on Smart Structures and Materials", SPIE, Newport Beach, CA, p. 92, (2001).
- Dapino, M., and Fox, G. "Design and Analysis of Joints Between Shape-Memory NiTi Torque Tubes and Structural Materials" M.S. Thesis Apr., (2012).
- Fox, G., Hahnen, R., Dapino, M.J., "Fusion welding of nickel-titanium and 304 stainless steel tubes: Part II: tungsten inert gas welding", Journal of Intelligent Material Systems and Structures, 1-11, (2012).
- Riggs, M., "Adhesive and TIG Joining Nickel-Titanium to 304 Stainless Steel", Undergraduate Honors Thesis, The Ohio State University, (2012).
- Wang, G., "Welding of Nitinol to Stainless Steel", Proc. 2nd Int. Conf. Shape Memory and Superelastic Technologies, pp.131-136, (1997).
- Hall, P.C., "Laser welding Nitinol to stainless steel", Proc. Int. Conf. Shape Memory and Superelastic Technologies, pp.219-228, (2003).
- Eijk, C. van der, Fostervoll, H., Sallom, Z., Akselsen, O.M., "Plasma Welding of NiTi to NiTi, Stainless Steel and Hastelloy C276", Int. Conf. Joining of Specialty Materials VI Program, ASM Materials Solutions Conf. & Exposition, Oct. 13-15, (2003).

SYNTHESIS OF FE/WC-CO BI-LAYERED CARBIDE CUTTING MATERIALS BY POWDER METALLURGY

Ayman Elsayed^{1,a}

1. Central Metallurgical Research & Development Institute, Powder Technology lab., Cairo, Egypt
a. Corresponding author (ayman_elsayed_11@yahoo.com)

ABSTRACT: The carbide cutting materials have been widely used in conventional and advanced machining operations. For a cutting tool, they require materials with superior characteristics including high wear resistance, high temperature stability and hardness. However, those properties are usually incorporated with low impact toughness. Therefore, attention was given to improving the toughness of cutting materials. The ability of powder technology to manufacture multi-layered materials has become the motivation for its use to overcome the problem. In this study, cutting materials with cemented carbide-iron based layers were manufactured by powder technology. Mixtures of Co-based tungsten carbide and iron powders were prepared by ball milling and then green-compacted and vacuum sintered into bi-layered tools. The integrity of the tools were then investigated. The microstructure and the mechanical properties have shown that the synthesis was successful to yield a good combination of wear resistance and toughness.

1. INTRODUCTION

The use of cemented tungsten carbides (WC-Co) for material cutting applications has long been established due to their superior combination of properties including hardness, wear resistance and toughness. Different grades of such materials has been developed to meet different application requirements varying from high wear resistance to high fracture toughness, mostly depend on the Co-content [Fan et al., 2013]. These two properties are very difficult to be obtained in a single grade of WC-Co, and thus, trials have been made to combine such properties by novel ways, the most important of which is the fabrication of functionally graded (FG) WC-Co composites [Fang et al., 2005]. FG WC-Co composite rely on the Co-gradient structure to alter properties of the surface and the interior layers of the cutting tools, which technologically faces strong barriers [Zhang et al., 2013]. The key for success in manufacturing such materials is maintaining the Co-gradient during liquid phase sintering [Wang et al., 2013]. This could be done by altering

grain size as well as by carburization [Huang et al., 2008].

Another important method for combining superior properties is the coating of WC-Co cutting materials with extremely high wear resistant layers, with TiCN representing most frequently used coat [Siow et al., 2013]. Further modification was the use of multilayered coating by hybrid PVD to realize higher performance [Nordin et al., 1998] and [Zhong et al., 2009]. Apart from coating, other technological methods included manufacturing multilayered cutting tools by hot pressing of layered powders of different compositions [Jianxin et al., 2010], or by spark plasma sintering [Eriksson et al., 2013]. Both methods aim at manufacturing parts containing different performances of layers. Conventional brazing technique was also used to bond layered materials [Chen et al., 2013], along with more advanced techniques like powder injection molding [Li et al., 2009].

The use of powder metallurgy technique to manufacture layered parts could also be realised with different WC-Co grades bonded together during compaction and sintering [Rosso et al., 1999]. Even the sinterbonding of WC-Co to tungsten heavy alloys could also be done by both hot pressing and pressureless sintering [Rodelas et al., 2009]. To make use of the superior toughness of steel, it was also sinterbonded to different grades of WC-Co, which showed strong success in some grades of WC-Co and partial success in others [Vasilenko et al., 2009]. [Pascal et al., 2009] also studied the microstructure of multilayered steel/WC-Co sinterbonded tools. However, there is not enough data of the steel/WC-Co joint mechanical integrity.

The aim of the present study was to manufacture bilayered cutting tools combining both high toughness and high wear resistance. The iron powder has been chosen to be the base for the tough layer because of its well known toughness as well as its similarity to both Co and Ni which are the main binder elements of WC that is used as the base for the wear resistant layer. The challenge was to sinterbond these two layers together to obtain a cutting tool with sufficient integrity.

2. EXPERIMENTAL WORK

Powders of both tungsten carbide and commercially pure iron were used in this study. Commercially available standard P30 powder having the composition WC-5 wt.% TiC-2 wt.% (Ta, Nb)C-9 wt.% Co with the average particle size of 10 μm and a 99.5 % pure iron with the average particle size of 8 μm were prepared. Also mixture of both powders in each other, namely WC-x% iron (powder A) and iron-x%WC (powder B), with x having the values 10 and 20, were also prepared by planetary ball milling using ball to powder ratio of 3 to 1 using dry milling

for 2 hrs with 800 rpm. These mixtures have been prepared to reduce the shrinkage and thermal expansion coefficient mismatch between WC and iron powders. All types of powders were then inoculated with 1.5 wt.% paraffin wax dissolved in acetone and then dried for 1 hr at 100 °C.

Compaction by single action uniaxial hydraulic press was performed using a rectangular cross-section 30 x 8 mm² die. The layers of powder A (higher density) and then powder B were introduced to the die cavity consecutively, and then pressed using 60 MPa compaction pressure. Also, specimens of both pure iron and tungsten carbide were prepared for comparison. Sintering was done in vacuum furnace at 1300 °C for 1 hr. Holding at various temperatures have been done for dewaxing, homogenization and sintering consecutively, as shown in (Figure 1).

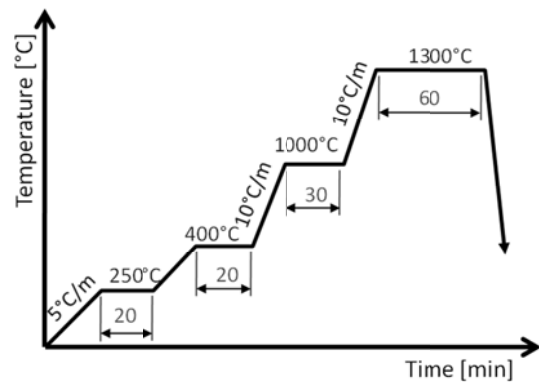


Figure 1: The sintering cycle for all specimens.

Microstructural investigations by both optical and SEM metallography as well as EDS analysis were performed and Vickers hardness of specimens including different layers was measured. The integrity of layered specimens as well as the strength and toughness were evaluated using transverse rupture strength (TRS) test by applying slow loading rate of 0.5 mm/min to the upper

punch, where the specimen width, thickness and span were 8, 4 and 25 mm respectively, as shown in (Figure 2). During test, the load applied on the upper punch is recorded against the relative cross head displacement.



Figure 2: The TRS test setup.

3. RESULTS AND DISCUSSION

As stated earlier, the iron and WC powders were selected to form tough and wear resistant layers in the composite cutting tool based on their well known characteristics. The key factor for manufacturing good composite material is always how its components are distributed together in the structure. Hence, the way by which each constituent was introduced to the other in layers has taken much consideration. The realization of homogeneously distributed powders in both the tough and the wear resistant layers has been the target of the mixing process. The result was evident to be satisfactory after applying planetary ball milling for 2 hrs at 800 rpm, as shown in (Figure 3). The figure shows how the layers are joined together. Very few positions have shown minor bundling like the one at the area between the two layers. Several pre-test trials have been made to adjust both the layer mixture compositions and the sintering conditions. Those trials have shown that 10% mixing (for iron in WC in the wear resistant layer and WC in iron in the tough layer) could give acceptable

structure. Sintering at 1300 °C has also been found to be a good choice as sintering at higher temperatures has resulted in melting the iron based layer while at lower temperatures has shown less than enough sintering of the WC based layer.

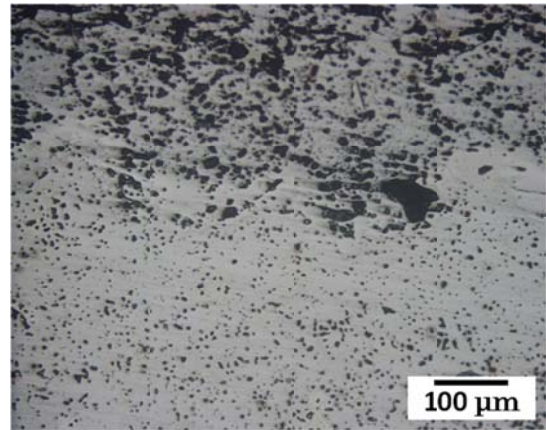


Figure 3: Unetched as-polished surface of the 10% mixing composite cutting tool by optical microscopy.

As the shrinkage mismatch between both layers of the composite was relatively larger in case of 10% mixing specimen, a 20% mixing specimen was also prepared which has shown much better homogeneity, as shown in (Figure 4). This was clear from avoiding the specimen curvature that happened due to the shrinkage mismatch between both layers of the composite. The 20% mixing specimen has also shown an intermediate layer of the thickness about 120 µm that has yielded better bonding and integrity between layers.

It is believed that diffusion of iron during sintering into the WC base layer was responsible for forming the intermediate layer. The composition gradient in multilayered specimens with different mixing concentrations has shown strong influence on the hardness of different layers, as shown in (Figure 5). The 10 % mixing composition specimen has shown higher hardness for the wear resistant

layer and lower for the tough layer than that of 20 % one, which in turn has shown much closer values of layers. The intermediate layer has shown an intermediate hardness value due to the iron diffusion that occurred between layers.

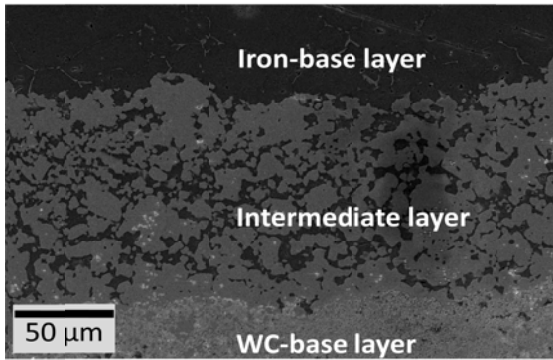


Figure 4: SEM of the surface of 20% mixing cutting tool.

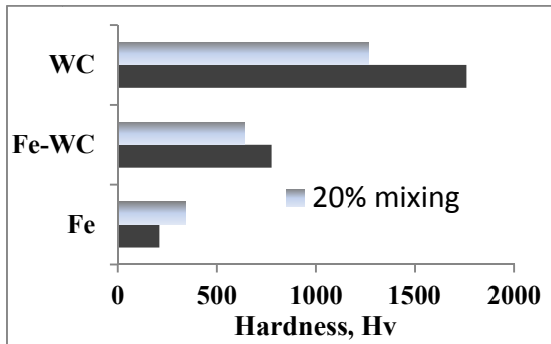


Figure 5: Hardness of different layers in both the 10 % and 20 % mixing parts.

The integrity of the 10 % mixing bilayered specimen was investigated by evaluating its TRS and comparing it to that of both pure iron and WC-Co specimens, as shown in (Figure 6). The very low toughness of the WC-Co specimen is clear from its low TRS value as well as its limited displacement to fracture. On the other hand, the iron specimen has shown the highest TRS with very high displacement to fracture. The bilayered specimen has shown that it could gain much of the advantage of the high toughness of iron.

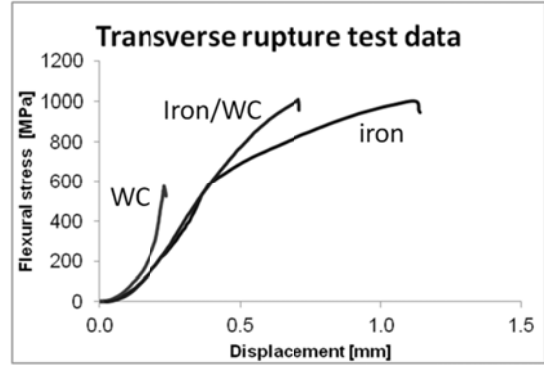


Figure 6: TRS of bilayered specimen compared to both iron and WC-Co ones.

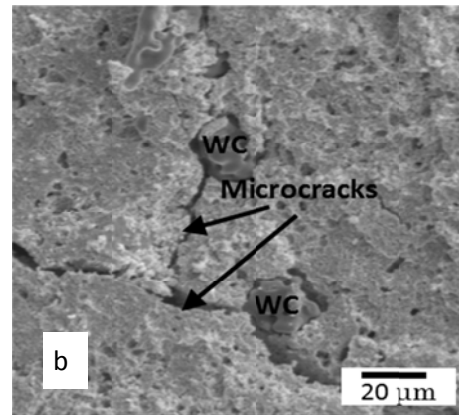
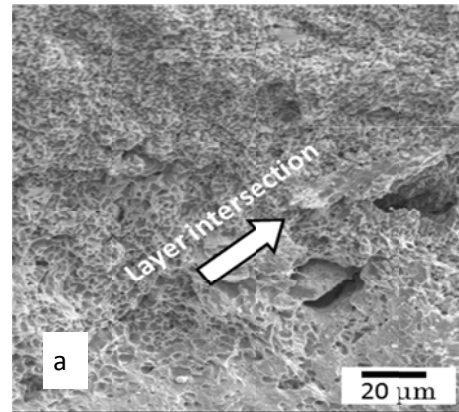


Figure 7: The format for figure heading.

The fractography of the fractured TRS test specimen has shown that no separation has occurred at the layer intersection, which proves enough bonding after sintering, as shown in (Figure 7-a). the layer intersection can be identified between the upper area of dimpled fracture of the iron base layer and the lower area of quasi-cleavage fracture of the WC-Co base layer. On the other hand, it could be shown that micro

cracks has formed at the iron base layer emanating from the WC-Co hard particles due to the hardness mismatch between them and the tough matrix, as shown in (Figure 7-b). These micro cracks have served as starters for the final fracture of TRS test specimens.

4. CONCLUSIONS

Bilayered cutting tool specimens with tough iron base layer and wear resistant WC-Co base layer could be manufactured by powder metallurgy. The properties mismatch between both layers that contributed to the specimen curvature at 10 % mixing could be overcome with higher mixing composition of 20 %, but on the expense of lower maximum hardness of the wear resistant layer. The TRS test has shown that the bilayered specimen could gain very high toughness compared to that of WC-Co specimen and close to that of the tough iron specimen. This result proves that the manufacturing route promises providing high toughness / high wear resistant cutting tools for severe working conditions.

Acknowledgements: The author acknowledges the help of both Engineer Ahmad Osama and Chemist Shaymaa Abulkasem to accomplish this work. Their valuable efforts in preparing powders and surfaces for metallographic investigation are very appreciated.

REFERENCES

- Fan, P., 2013. A Review of Liquid Phase Migration and Methods for Fabrication of Functionally Graded Cemented Tungsten Carbide, *Int. Journal of Refractory Metals and Hard Materials*, 36, 2.
- Fang, Z.Z., 2005. Liquid Phase Sintering of Functionally Graded WC-Co Composites, *Scripta Materialia*, 2005, 785.
- Zhang, L., 2013. Transformation of Cobalt Gradient Structure After Resintering of DP Cemented Carbide, *Int. Journal of Refractory Metals and Hard Materials*, 38, 118.
- Wang, X., 2013. Mechanical Properties and Wear Resistance of Functionally Graded WC-Co, *Int. Journal of Refractory Metals and Hard Materials*, 36, 46.
- Huang, Z., 2008. Finite Element Analysis of Thermal Residual Stresses at Cemented Carbide Rock Drill Buttons with Cobalt-Gradient Structure, *Transactions of Nonferrous Metals Society of China*, 18, 660.
- Siow, P.C., 2013. Characterization of TiCN and TiCN/ZrN Coatings for Cutting Tool Applications, *Ceramics International*, 39, 1293.
- Nordin, M., 1998. Mechanical and Tribological Properties of Multilayered PVD TiN/CrN, TiN/MoN, TiN/NbN and TiN/TaN Coatings on Cemented Carbide, *Surface and Coatings Technology*, 106, 234.
- Zhong, J., 2009. Fabrication of Functionally Graded Ti(C, N)-Based Cermets by Double-Glow Plasma Carburization, *Int. Journal of Refractory Metals and Hard Materials*, 27, 642.
- Jianxin, D., 2010. Fabrication and Performance of Al₂O₃/(W,Ti)C+Al₂O₃/TiC Multilayered Ceramic Cutting Tools, *Materials Science and Engineering A*, 527, 1039.
- Eriksson, M., 2013. Spark Plasma Sintering of WC, Cemented Carbide and Functional Graded Materials, *Int. Journal of Refractory Metals and Hard Materials*, 36, 31.
- Chen, H., 2013. Characterization and Stress Relaxation of The Functionally Graded WC-Co/Ni Component/Stainless Steel Joint, *Journal of Alloys and Compounds*, 557, 18.
- Li, T., 2009. Two-Material Powder Injection Molding of Functionally Graded WC-Co Components, *Int. Journal of Refractory Metals and Hard Materials*, 27, 95.
- Rosso, M., 1999. Studies of Graded Cemented Carbide Components, *Int. Journal of Refractory Metals and Hard Materials*, 17, 187.
- Rodelas, J., 2009. Sinterbonding Cobalt-Cemented Tungsten Carbide to Tungsten Heavy Alloys, *Int. Journal of Refractory Metals and Hard Materials*, 27, 835.
- Vasilenko, A.A., 2009. Cutting Performance of Two-Layered Cutting Tool Tips with Thin M20 and K10 Sintered Carbide Plates Compared to Homogeneous Tips, *Int. Journal of Machine Tools & Manufacture*, 49, 1048.
- Pascal, C., 2009. Design of Multimaterial Processed by Powder Metallurgy: Processing of A (Steel/Cemented Carbides) Bilayer Material, *Journal of Materials Processing Technology*, 209, 1254.

THE DISTRIBUTION ANALYSIS OF ALUMINUM AND TiH₂ POWDERS IN THE POWDER METALLURGY FOAMING PROCESS

Alpay Tamer ERTÜRK^{1,a}, Tülin Şahin²

^{1,2}Kocaeli University, Mechanical Engineering Department, Umuttepe Campus, 41380 İzmit, Turkey
a. Corresponding author (tamererturk@gmail.com)

ABSTRACT: Titanium hydride takes place the source of pure hydrogen for foaming aluminum in powder metallurgy route. The regular mixture of aluminum powder and TiH₂ particles is regarded as a parameter that directly effect on the final aluminum foam product. This research was aimed at determining the mixing parameters that give optimal powder homogeneity. In order to analyze the conditions of the best distributions as a function of mixing time and speed, the titanium hydride powder was mixed with specified amounts of aluminum powders to reach the targeted composition. After the mixing processes optical microscope images were taken with 100 and 200 magnifications. The distributions of average particle size, the aspect ratio and the distribution ratio of titanium hydride particles were analyzed and graphically illustrated by the Clamex-Captiva image capturing and measuring software on the images. After conducting the distribution analysis, we concluded that the mixing process should be carried out with 90 rev/min stirring rate and 90 or 120 min periods to obtain the best particle distribution.

1. INTRODUCTION

Metal foams are required for the production of light-weight structures, and impact energy absorption. Aluminum foams are ultra-light materials with closed or open cell structure [Yang and Nakae, 2000]. Several methods have been used to produce metallic foams but the study is based on the powder metallurgy route [Campana and Pilone, 2008]. In the PM process, metal powders are mixed with a foaming agent, such as TiH₂, and compacted to yield a dense precursor [Esmaeelzadeh *et al.*, 2006].

The PM foaming process is rapid with expansion occurring in only a few minutes and foam product with a usable cellular structure is achieved only seconds before the maximum expansion is obtained [Asavavisithchai and Kennedy, 2006]. Near-net shaped parts can be done by inserting the precursor material into a hollow mold and expanding it by heating [Kennedy, 2002]. Their inhomogeneity is a disadvantage [Koza *et al.*, 2004].

Powder mixing is an important operation routinely used in materials processing techniques whose starting materials are powders. Effective powder mixing can add significant value to the product as the quality of products mostly depends on the degree of mixing of their constituent materials, thereby guaranteeing the homogeneity of the final product. Thorough and uniform mixing is always essential regardless of whether these metals are to form an alloy of certain desired properties, or to remain in the compact as independent constituents while retaining their individual characteristics [Obadele *et al.* 2012].

Our research was aimed at determining the mixing parameters that give optimal powder homogeneity to obtain near the best spherical pore form.

2. EXPERIMENTAL

The aluminum powder and titanium hydride as the foaming agent were mixed for preparing a raw precursor mixture.

The greater number and the bigger size both of these powders play a role in disruptive. The characteristics of the starting materials are summarized in Table 1.

Table 1: Characteristics of the powders.

Powder	Purity (%)	Size (μm)
Al (Gurel Inc, Turkey)	98	200
TiH ₂ (Alfa Aesar, Germany)	99,9	44

2.1. Foaming Procedure

The foaming aluminum is fabricated in the following stages. 1- the TiH₂ powder was spread on a glass plate and heat treated in a pre-heated fan oven at 475°C for 180 min. 2- the heat treated TiH₂ powder (1,5wt %) is added to the Al powder in a tubular mixer and mixed at a set speed and time. 3- pressing: Powder mix is pressed by cold uni-axial compaction. 4- Pressing with induction heating. 5-Holding in a furnace which was pre-heated to 820°C. It was held in the furnace for 5-6 min to allow decomposition of TiH₂ powder. In this stage, hydrogen gas releases in the compact with the holding time until a cellular structure form. The current study, involves the second stage mixing only.

2.2. Mixing Analysis

The mixing parameter researches were carried out by using the following methodologies to analyze the conditions of the best distributions as a function of mixing time and speed, the titanium hydride powder was mixed with specified amounts of aluminum powders to reach the targeted composition. After the mixing processes optical microscope images were taken with 100 and 200 magnifications. The distributions of average particle size, the aspect ratio and the distribution ratio of titanium hydride particles were analyzed and graphically

illustrated by the Clamex-captiva image capturing and measuring software on the images.

3. RESULTS AND DISCUSSION

Regular mixing of aluminum and TiH₂ particles is a parameter affecting the final product directly. For the mixture homogeneous distribution is another desired feature as a homogeneous grain size.

In order to analyze the conditions of the best distribution, aluminum powder mixed with 1% by weight TiH₂ particles at different rotational speeds (22,4-45-63 and 90 RPM) and periods (30, 60, 90, 120 min). Figure 1 graphically illustrates the distribution of particle analysis. Accordingly D10, D50 and D90 indicate the distribution percentage of the total in the group analysis. D50 is the median of the same time.

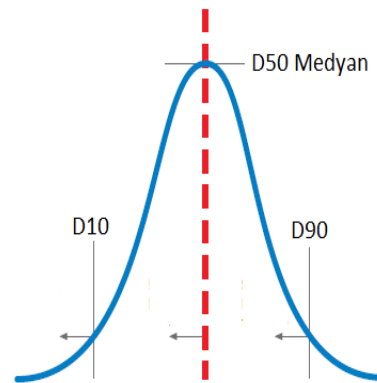


Figure 1: Statistical distribution

The aspect ratio of titanium hydride particles, distribution and dimensional analysis were analyzed separately on the cross sectional each surface of mixtures with optical microscope images. Although severe limitation of optical microscopy is its small depth of focus. Microscopic analyses are the only method in which the individual particles are measured to particle size.

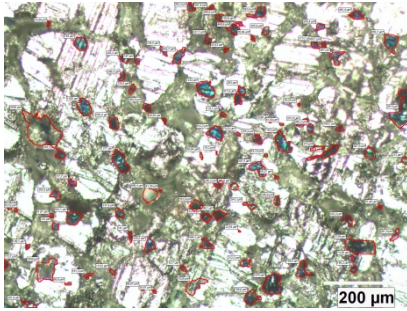


Figure 2: The analysis of particle aspect ratio.

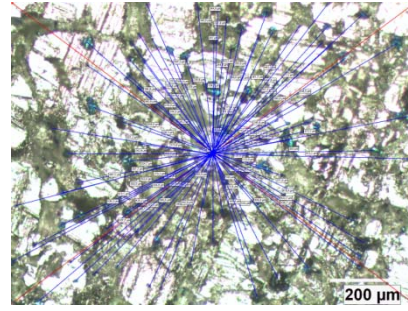


Figure 4: The orientation analysis of titanium hydride particles.

Figure 2—6 shows samples with 100 magnification optical microscope image analyses after the 45 RPM rotational speed and 90 min mixing times. Figure 2 shows the particle aspect ratio analysis. Each of particle aspect ratio was calculated. Thus Figure 3 was generated with data of the count, the curve of cumulative content ratio and aspect ratio span.

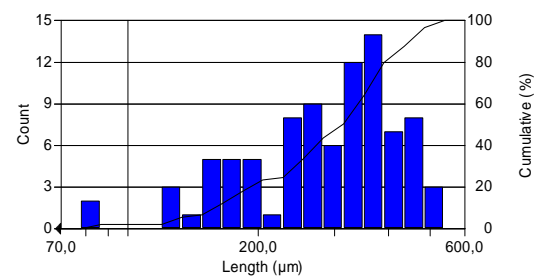


Figure 5: Chart of the titanium hydride particle orientation.

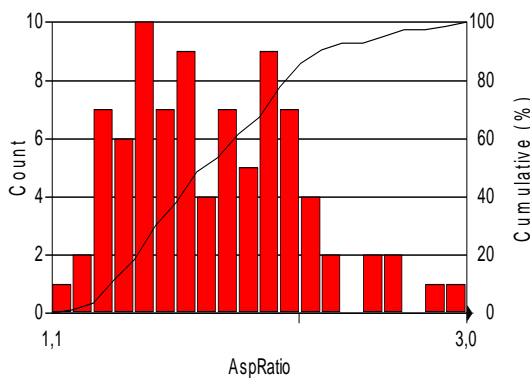


Figure 3: Count and cumulative percent of the titanium hydride particle aspect ratio.

The particle size distribution on the cross section was generated in Figure 6. The average particle size distribution was obtained by examining the each of mixtures particle size analyses. By examining the change in average particle size, it appears to be distributed in the range 32 to 18 μm. It is concluded that the average value of distributions and 25 μm.

Figure 4 shows each of titanium hydride particle orientation. A particle length of the cross sectional image center, count and the curve of the cumulative content were generated on the chart of Figure 5.

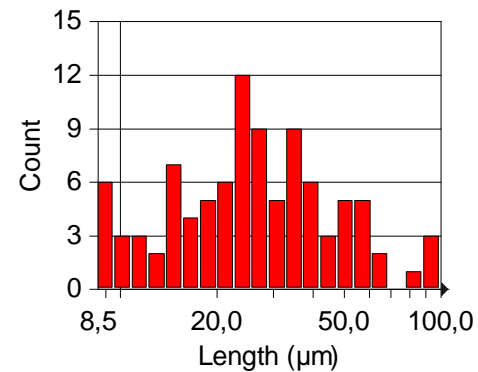


Figure 6: Chart of the titanium hydride particle size distribution.

It was selected as a mixing parameter that D10 and D90 values as close as possible. When the statistical distribution of the aspect ratio is examined at the 90 RPM stirring rate, both of 90 and 120 min mixing times give the desired result.

4. CONCLUSIONS

Titanium hydride particle distributions according to mixing parameters was analyzed. Irregularities are available at the maximum and minimum values of the dispersion at low mixing speeds. It is also obtained that this situation no longer exists at 60 and 90 RPM.

An interesting remark from this study is the effective parameters mixing can influence on foam structure.

Acknowledgements: The study has been supported by The Scientific Research Projects Unit of Kocaeli University (KOU-BAP, 2010/093).

REFERENCES

- Asavavisithchai, S., Kennedy A.R., 2006. Effect of powder oxide content on the expansion and stability of PM-route Al foams, *Journal of Colloid and Interface Science*, Volume (297) 715.
- Campana F, Pilone D., 2008. Effect of wall microstructure and morphometric parameters on the crush, *Materials Science and Engineering: A*, Volume (479) 58.
- Esmaeelzadeh, S., Simchi, A., Lehmhus, D., 2006. Effect of ceramic particle addition on the foaming behavior cell structure and mechanical properties of P/M AISi7 foam, *Materials Science and Engineering*, Volume (424) 290.
- Kennedy, A.R., 2002. The Effect of TiH₂ Heat Treatment on Gas Release and Foaming Al-TiH₂ Preforms, *Scripta Materilia*, Volume (47) 763.
- Koza, E.; Leonowicz, M.; Wojciechowski, S.; Simancik, F. 2004. Compressive strength of aluminium foams. *Materials Letters*, Volume (58) 132.
- Obadele, B.A., Masuku, Z.H., Olubambi P.A., 2012. Turbula mixing characteristics of carbide powders and its influence on laser processing of stainless steel composite

- coatings, *Powder Technology*, Volume (230) 169.
- Yang C.C., Nakae H., 2000. Foaming characteristics control during production of aluminum alloy foam, *Journal of Alloys and Compounds*, Volume (313) 188.

ONE-POT AND TEMPLATE-FREE SYNTHESIS OF MAGNETITE POROUS/HOLLOW NANOSTRUCTURE

Dung The Nguyen¹ and Kyo-Seon Kim^{1,a}

1. Department of Chemical Engineering, Kangwon National University,
Chuncheon, Kangwon-Do, 200-701, Korea

a. Corresponding author (kkyoseon@kangwon.ac.kr)

ABSTRACT: Porous/hollow magnetite nanoparticles are synthesized through a one-pot solvothermal process, using a sole iron precursor ($\text{FeCl}_3 \cdot 6\text{H}_2\text{O}$) and without any template. The product particles show a narrow size distribution, good crystalline and high magnetization saturation. We demonstrate the development of hollow structure of magnetite spheres by characterizing systematically the changes of morphology and crystal structure for different processing times. A detailed process mechanism to form the hollow structure of magnetite spheres is proposed, combining the formation of numerous tiny grains, the spherical assembly of those grains and the chemical conversion of the Fe (III) compounds to generate Fe_3O_4 simultaneously coupled with the Ostwald ripening process within the magnetite spheres.

1. INTRODUCTION

Magnetite Fe_3O_4 nanoparticles are of great interest because of their wide applications which demand nanomaterials of specific sizes, shapes, surface modifications and magnetic properties [Nguyen *et al.*, 2011]. Recently, monodisperse Fe_3O_4 hollow particles have been emerged as an ideal candidate for biomedical applications because they integrate advantages of hollow structures, such as low density, high surface-to-volume ratio, high encapsulating capacity, and magnetic properties. Many methods have been developed so far for the synthesis of Fe_3O_4 porous/hollow nanoparticles. The porous/hollow structures are conventionally prepared through template method which involves precipitation of precursors on the template particles [Caruso *et al.*, 2001; Peng and Sun, 2007]. However, there are difficulties of achieving high product yield, removing the template completely and refilling the hollow interior with functional species [Lou *et al.*, 2008].

In this study, we synthesized monodisperse Fe_3O_4 porous/hollow

nanostructures through through one-pot solvothermal process, using $\text{FeCl}_3 \cdot 6\text{H}_2\text{O}$ precursor and ammonium acetate in ethylene glycol solution without any template. This method showed several advantages. The Fe_3O_4 nanoparticles were prepared by one-pot process and their surfaces were coated by a hydrophilic layer which allows them to be dispersed easily in aqueous media or other polar solvent. Besides, the relatively high reaction temperature favored the synthesis of particles with higher crystallinity as well as higher magnetization.

2. EXPERIMENTAL SECTION

A solution of ethylene glycol ($\text{C}_2\text{H}_4(\text{OH})_2$, J.T.Baker, AR) containing 0.1 M of $\text{FeCl}_3 \cdot 6\text{H}_2\text{O}$ (Sigma-Aldrich, $\geq 98\%$) and 1 M of ammonium acetate ($\text{CH}_3\text{COONH}_4$ or NH_4Ac , Sigma, $\geq 98\%$) was well mixed and then transferred to a Teflon-lined autoclave cell. The autoclave cell was kept inside an oven at 200°C to guarantee the uniform temperature inside the cell. After the scheduled processing time, the autoclave

cell was cooled to room temperature by using tap water. The product particles were obtained by centrifuging and washing with ethanol and water for several times and then were dried in a vacuum oven at 60°C for 6 h before characterization.

2. RESULTS AND DISCUSSION

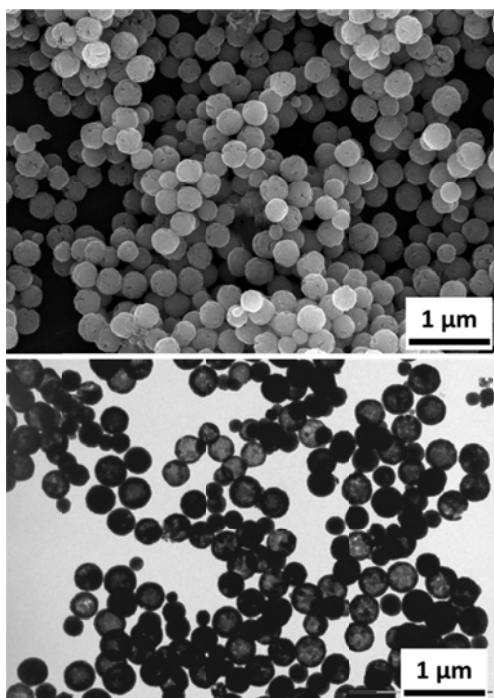
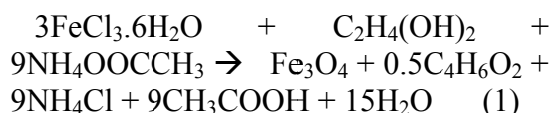


Figure 1: Representative SEM image (a) and TEM image (b) of the Fe₃O₄ porous/hollow nanoparticles.

The morphology and structure of the product particles were investigated by SEM and TEM measurements as shown in Figure 1. Figure 1 shows a formation of a large quantity of spheres with an average diameter of 300 nm. The spheres were composed of many smaller grains. The hollow structure of the product particles was observed by the TEM measurement as shown in Figures 1b. An intensive contrast between the black margin and the bright center of the particles indicates the existence of hollow structure in the resulting spheres. The particles were of uniform hollow spheres with the average shell thickness of 40 nm

from TEM measurements. Compared with other hollow structures with a dense shell wall, our porous and non-sealed hollow nanoparticles can immobilize and encapsulate various moieties with higher loading capacity for controlled drug delivery application.

On the basis of formation of Fe₃O₄ from a sole Fe (III) precursor, a series of chemical conversion processes was proposed. Acetate groups derived from NH₄Ac might coordinate with iron ions derived from FeCl₃ to form Fe (III) acetate compounds. Ethylene glycol could partially reduce the Fe (III) compounds to generate Fe (II) compounds. The respective Fe (III) and Fe (II) compounds were then hydrolyzed to form Fe(OH)₃ and Fe(OH)₂, followed by the generation of Fe₃O₄ nanoparticles via dehydration of these hydroxides. A general chemical reaction can be proposed as follows [Nguyen and Kim, 2013a].



Regarding the formation of the Fe₃O₄ porous/hollow nanostructures, the formation mechanism comprised simultaneous chemical and physical processes including the formation of numerous tiny grains, the spherical assembly of those grains to form the spheres and the chemical conversion coupled with the relocation of the grains within a sphere [Nguyen and Kim, 2013b]. The chemical conversion, as mentioned above, caused the non-uniformities of tiny grains and the empty spaces within the spherical assemblies and thus enhanced the outward migration and relocation of the core grains toward the outer layer, resulting in the formation and expansion of the hollow core structure. The morphologies of Fe₃O₄

porous/hollow nanostructures can be controlled by varying the initial concentrations of iron precursor and ammonium acetate as well as the molar ratio of Fe precursor to ammonium acetate. [Nguyen *et al.*, 2013a].

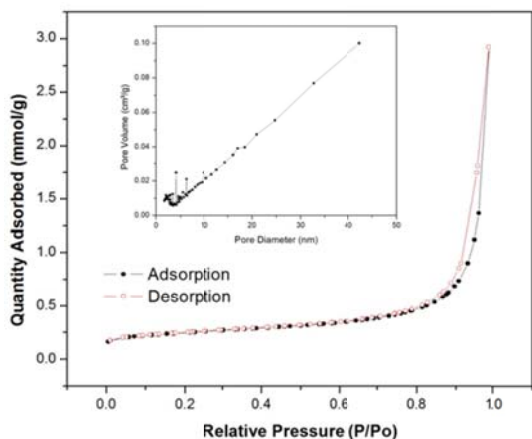


Figure 2: BET measurement (inset: BJH pore size distribution) of the Fe₃O₄ porous/hollow nanoparticles.

Figure 2 shows the nitrogen adsorption-desorption isotherm and Barrett-Joyner-Halenda (BJH) pore size distribution (inset) of the Fe₃O₄ porous/hollow nanostructures. The Fe₃O₄ porous/hollow nanostructures have the BET surface area of 19.6 m²/g and the average pore size based on BJH adsorption of 12.6 nm. The pore size distribution of the Fe₃O₄ porous/hollow nanostructures revealed the micropores was about several nanometers which could be attributed to the void among the grains which built the porous/hollow nanostructures, and also the mesopores with diameters of few tenth nanometers which could belong to the large holes on the surface or the inner empty spaces [Nguyen *et al.*, 2013b].

3. CONCLUSIONS

The magnetite porous/hollow nanostructures with the average diameter of 300 nm and the shell thickness of 40 nm were successfully synthesized through one-pot solvothermal process without any surfactant and template in an

isothermal oven at 200°C for 12 h. The nanostructures consisted of many smaller magnetite nanoparticles. The formation mechanism of the magnetite porous/hollow nanostructures comprised simultaneous chemical and physical processes including the formation of numerous tiny grains, the spherical assembly of those grains and the chemical conversion coupled with the relocation of the grains

Acknowledgements: This work was supported by the Regional Innovation Center for Environmental Technology of Thermal Plasma (ETTP) at Inha University, designated by MKE (2009).

REFERENCES

- Caruso F., Spasova M., Susha A., Giersig M., Caruso R. A., 2001, Magnetic Nanocomposite Particles and Hollow Spheres Constructed by a Sequential Layering Approach *Chem. Mater.* 13, 109.
- Lou X. W., Archer L. A., Yang Z., 2008, Hollow Micro-/Nanostructures: Synthesis and Applications, *Adv. Mater.* 20, 3987.
- Nguyen D. T., Park D.-W., Kim K.-S., 2011, Seed-Mediated Synthesis of Iron Oxide and Gold/Iron Oxide Nanoparticles, *J. Nanosci. Nanotechnol.* 11, 7214.
- Nguyen D. T., Kim K.-S., 2013a, Template-Free Synthesis and Characterization of Monodisperse Magnetite Hollow Nanoparticles through Solvothermal Process, *J. Nanosci. Nanotechnol.*, in publication.
- Nguyen D. T., Kim K.-S., 2013b, Analysis on Development of Magnetite Hollow Spheres through One-Pot Solvothermal Process, *AIChE J*, in publication.
- Nguyen D. T., Park D.-W., Kim T., Kim K.-S., 2013a, Controlled Synthesis of Magnetite Porous/Hollow Nanoparticles through a Template-Free Solvothermal Process, *J. Nanosci. Nanotechnol.*, in publication.
- Nguyen D. T., Charinpanitkul T., Park D.-W., Kim K.-S., 2013b, Preparation of Magnetite Hollow Structure for Drug Delivery Application, *J. Nanosci. Nanotechnol.*, in publication.
- Peng S., Sun S., 2007, Synthesis and Characterization of Monodisperse Hollow Fe₃O₄ Nanoparticles, *Angew. Chem. Int. Ed.* 46, 4155.

APPLICATIONS OF IMAGE PROCESSING FOR THE ANALYSIS AND CHARACTERIZATION OF POROUS MEDIA

Harun Koku^{1,a}

¹Middle East Technical University, Department of Chemical Engineering, Ankara, Turkey
a. Corresponding author (harunk@metu.edu.tr)

ABSTRACT: High resolution microscopy techniques, in tandem with readily available image processing tools offer a unique and insightful look into the microstructure of porous materials. However, one has to be aware of the limitations and drawbacks of such an approach due to limited sampling size, and the possibility of artifact formation during sample preparation, imaging and image processing. Some of these factors are presented and discussed, for a case study of the analysis of porous polymeric materials, with emphasis on their topographic properties such as pore size distribution.

1. INTRODUCTION

The availability of high-resolution imaging techniques, coupled to advances in computational capabilities enable a unique array of methods for the rigorous investigation of material properties and behavior. These direct-imaging based methods are especially useful in relating the observed behavior of materials to microstructure, or for screening studies where the goal is to identify natural or synthetic materials with desired characteristics that ultimately depend on the topography. However, image-based characterizations inevitably involve their own limitations, which should be considered in method development and the subsequent analyses.

This article aims to present examples of image-based analyses for specific case studies of porous polymeric materials used for ion-exchange chromatography, using scanning electron microscopy (SEM) and transmission electron microscopy (TEM) micrographs. Examples include the estimation of properties such as the pore size distribution (PSD), the capacity for a designated probe and the overall pore network. Some of the limitations and trade-offs involved in these analyses are also discussed.

2. METHODS

The results presented in this article are based on several prior studies focusing on the analysis of porous polymeric ion-exchange media. An outline of the methods in these studies is given here and the reader is referred to the referenced articles for the details. The overall image analysis study can be broadly considered as a sequence of three stages: sample preparation, imaging and image processing.

2.1. Sample Preparation and Imaging

For SEM imaging in the backscatter mode, samples of polymeric, porous ion-exchange media were chemically fixed using solutions of glutaraldehyde, paraformaldehyde and osmium tetroxide, infiltrated with resin and heat-cured in an oven [Bowes *et al.*, 2009]. Concurrent automated serial-sectioning and imaging was implemented by a variable pressure field emission SEM equipped with a Gatan 3-View system [Koku *et al.*, 2011].

For preparation of samples to be imaged in the secondary-electron SEM mode, the samples were dehydrated in supercritical carbon dioxide and optionally coated using a palladium-gold support under vacuum [Koku, 2011]. The images were obtained on a Hitachi S4700 FESEM.

2.2. Image Processing

Depending on the information sought, simple processes such as denoising and binarization as well as morphological operations such as erosion and dilation were applied on the raw images. These processes were carried out using scripts written in Matlab[®], the public domain suite ImageJ [Rasband, 1997-2012], and the commercial package Amira[®].

3. RESULTS

3.1. Topography

Example secondary electron and backscatter SEM results for a commercial polymeric ion-exchange material, the CIMTM monolith, are displayed in Figures 1 and 2. Especially at high magnifications, the secondary-electron image (Figure 1) provides detailed qualitative information on the overall microstructure, exposing the fractal-like, complex topography of the material.

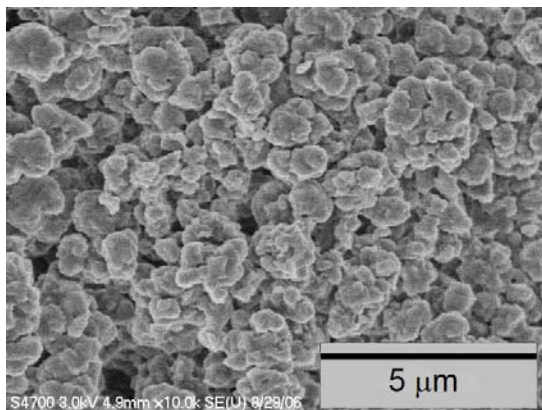


Figure 1: A secondary-electron SEM image of the CIMTM monolith

The backscatter image on the other hand (Figure 2) displays a two-dimensional cross-section and more appropriate for the quantitative analyses of the following sections.

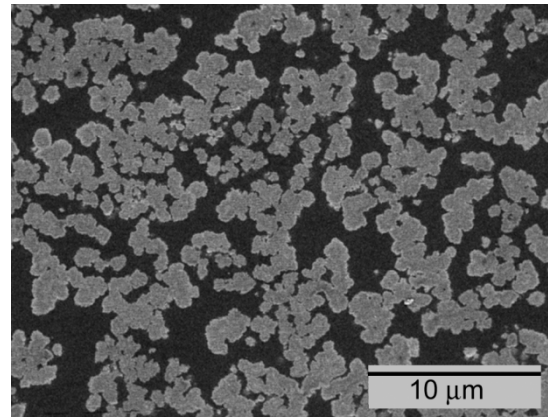


Figure 2: A backscatter SEM image of the CIM monolith.

3.2. Pore Size Distribution

The pore size distribution (PSD) function is one way to characterize the pore volume of a material. There are several methods that can be employed to extract PSD information from images such as Figure 2. One group of procedures is based on image morphology operations [Serra, 1982], which involve processing images by a so-called structuring-element or probe. For PSD, the starting point is that when two of these operations are used in succession, namely first eroding the image by a probe, and then dilating the intermediate image by the same probe, the final image represents the area of the original that is accessible to that probe. This sequence of erosion followed by dilation is also referred to simply as an ‘opening’ operation. By repeating this operation for a number of probes, the variation of the accessible area with respect to probe size, which is equivalent to the *cumulative* PSD, is obtained. The cumulative PSD is differentiated to yield the *differential* PSD.

A two-dimensional (2-D) application of this procedure for the CIM monolith is shown in Figure 3. The first step is to binarize grayscale images such as that of Figure 2, i.e., convert them to black and white by an appropriate thresholding procedure. A filter to improve image definition can be used prior to the binarization. The top panel in Figure 3 is

simply Figure 2 after binarization, with the white regions representing the pore area. Figure 3B displays the result of the opening operation by a $0.66\ \mu\text{m}$ probe, where the result, i.e. the area that remains accessible to the probe, is shown in white.

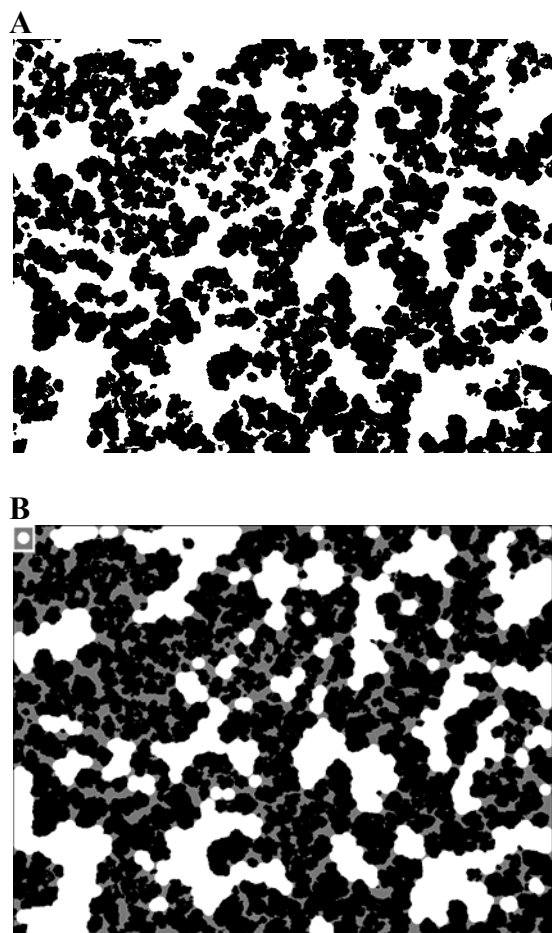


Figure 3: An example calculation of accessible pore space for a circular probe, diameter $0.66\ \mu\text{m}$. (A) The binarized image. Black areas are solid, white regions void. (B) Same image showing the accessible pore space (white) after the opening operation; inaccessible pore space is in gray. The frame in the upper left corner shows the used probe.

It is possible to extrapolate this procedure to three dimensions as well, but since the morphological operations are applied point-wise, the computational demands are intense except for the simplest geometries, and dedicated hardware and software capable of processing massive amounts of data with speed may be needed. The PSD

curve for a 3-D reconstructed monolith sample computed using such a specialized commercial package (Amira) is plotted in Figure 4, alongside the 2D distribution. The latter was obtained as the average of 10 sections.

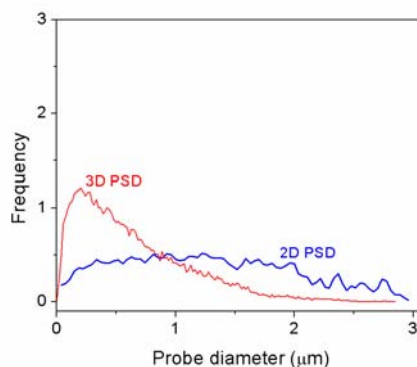


Figure 4: The two- and three-dimensional PSD curves for the CIM monolith.

Note that the 2D and 3D curves are vastly different with respect to their peaks and overall standard deviations.

3.3. Overall 3D Pore Network

The PSD curves are but one way of characterizing the pore space and they do so by binning and averaging the available data. When full high-resolution data is available however, this results in unnecessary loss of information that could provide more insight for the purposes of the investigator. For instance, while the PSD curves provide an idea of the frequency and dispersion of pore sizes within the material, they do not yield information on how these pores are interconnected –knowledge that is crucial in transport processes for example.

For this latter purpose, a more detailed analysis can be carried out directly on a 3D sample. Figure 5A displays such a 3D sample cube from the monolith and the resulting pore network obtained (using Amira) is given in 5B, where the sizes (diameters) of the individual pores are represented by the relative thicknesses of the branches. What the 3D network conveys is that while most of the pores are those of low diameters, there are a few

continuous pore structures of large diameters. Such extremities or ‘defects’ have profound implications for flow and mass-transfer, as observed in simulation studies [Koku *et al.*, 2012].

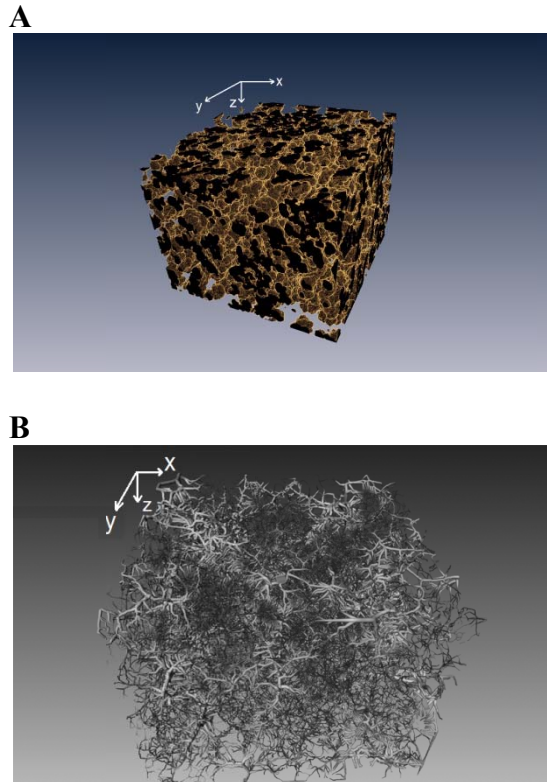


Figure 5. (A) A reconstructed 3D sample from the monolith. (B) The pore network of the sample. Note that the two images are at slightly different orientations.

3.4. Capacity Estimation

One possible extension of the morphological operations mentioned earlier is their use for the estimation of the specific holding capacity of a material for a defined probe. An example application is shown in Figure 6, where $0.66\ \mu\text{m}$ circular probes are ‘bound’ to the solid regions of the image of Figure 3A. If the density of the actual probe and the thickness of the imaged section are known, an estimate for the experimental static capacity of the porous medium can be obtained [Trilisky *et al.*, 2009].

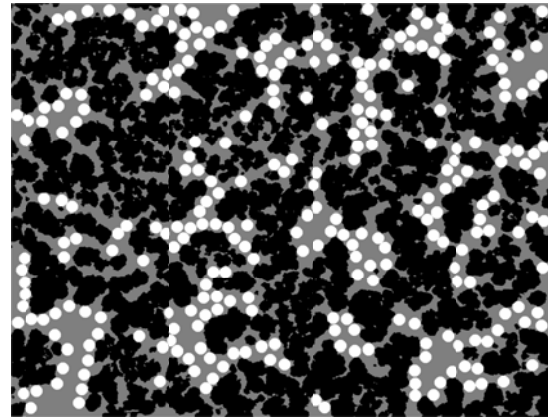


Figure 6. An example of binding capacity prediction using the image of Fig. 3B. The black areas correspond to solid, grey to the pore space, and the white disks are the probes with diameter $0.66\ \mu\text{m}$.

3.5. Limitations of Image Processing

Although the analyses are versatile and rigorous, data obtained via image-processing can be prone to random and systematic deviations from the actual information sought. Some of the factors to consider in order to be aware of, and if possible avoid, such limitations is briefly summarized below.

Reproducibility: All materials exhibit random sample-to-sample variation to some extent. This variability is further amplified by the fact that high-resolution images focus on minute regions which may not ‘represent’ the whole. A careful analysis of the partitioning of variation between and among different samples, sections, blocks and locations could help identify and account for this variability.

Visibility: Image-based analyses depend on the ability to distinguish between the features in an image, regardless of whether this distinction is automated or implemented manually. The upper limit for this capability is the analog resolution of the imaging method, but practical visibility is influenced by additional factors such as the signal-to-noise ratio, contrast and appropriate digitization [Pawley, 2006]. A proper choice of the imaging method

should present an optimum of these factors.

Artifact formation: Once a visible, reproducible feature is observed, the question to be asked is if this information is genuine or an artifact. While artifact formation during imaging (e.g. due to beam-damage) can often be identified ‘on-site’, most high-resolution methods necessitate intensive sample preparation procedures at extreme conditions prior to imaging, some of which can damage the sample. A cross-check imaging study that involves either completely different preparation methods, or better yet a non-destructive technique, even if at lower resolutions, could help confirm that the sample structural integrity has not been compromised by the original method.

4. CONCLUSION

Image-processing methods can be utilized for a diverse array of characterizations in porous media. Provided that their limitations are understood and accounted for, such analyses yield rigorous and useful information.

Acknowledgments: The author thanks his mentor Dr. Abraham M. Lenhoff and the group members at the University of Delaware for the opportunities, support and guidance they have provided. The guidance and help of Dr. Deborah Powell, Ms. Shannon Modla and particularly Dr.

Kirk Czymmek of the Delaware Biotechnology Institute is greatly appreciated. The backscatter imaging of the 3D sample was performed by Gatan Instruments, courtesy of Christel Genoud and Paul Miller. Financial support for the studies this work is based on was provided by the US-NIH grant R01GM75047.

REFERENCES

- Bowes, B. D., Koku, H., Czymmek, K. J., and Lenhoff, A. M. 2009. Protein adsorption and transport in dextran-modified ion-exchange media. I: Adsorption. *Journal of Chromatography A*, 1216(45), 7784.
- Koku, H. 2011. *Microstructure-based Analysis and Simulation of Flow and Mass Transfer in Chromatographic Stationary Phases*. Ph.D. Thesis, University of Delaware, Newark.
- Koku, H., Maier, R. S., Czymmek, K. J., Schure, M. R., and Lenhoff, A. M. 2011. Modeling of flow in a polymeric chromatographic monolith. *Journal of Chromatography A*, 1218(22), 3466.
- Koku, H., Maier, R. S., Schure, M. R., and Lenhoff, A. M. 2012. Modeling of dispersion in a polymeric chromatographic monolith. *Journal of Chromatography A*, 1237.
- Pawley, J. B. (Ed.). (2006). *Handbook of Biological Confocal Microscopy* (3rd ed.). New York: Springer.
- Rasband, W. S. 1997-2012. ImageJ. U. S. National Institutes of Health, <http://imagej.nih.gov/ij/>
- Serra, J. 1982. *Image Analysis and Mathematical Morphology*. London: Academic Press.
- Trilisky, E. I., Koku, H., Czymmek, K. J., and Lenhoff, A. M. 2009. Relation of structure to performance characteristics of monolithic and perfusive stationary phases. *Journal of Chromatography A*, 1216(36), 6365.

PLASMA SPRAYED AND ANNEALED CALCIUM TITANATE DIELECTRICS

Jiri Kotlan^{1,a}, Pavel Ctibor² and Zdenek Pala²

1. Czech Technical University in Prague, Faculty of Electrical Engineering. Department of Electrotechnology, Prague, Czech Republic

2. Academy of Sciences of the Czech Republic, Institute of Plasma Physics, Materials Engineering Department, Prague, Czech Republic

a. Corresponding author (kotlaji1@fel.cvut.cz)

ABSTRACT: This paper studies self-supported CaTiO_3 layers prepared by plasma-spraying technology. Water stabilized plasma gun WSP as well as conventional widely used gas stabilized plasma gun GSP were employed. For both methods of plasma spraying CaTiO_3 in the form of powder with size 63–125 μm was used. Self-supporting layers were obtained by removing the coating from metallic substrates. These specimens were annealed in air atmosphere up to 1170°C. Work is focused on dielectric properties of these specimens. Relative permittivity and loss factor were observed in frequency range 30 Hz to 30 MHz. Microstructure was studied by light microscopy, microhardness and X-ray diffraction. The work deals with influence of annealing on dielectric properties, crystalline structure and porosity of plasma deposited calcium titanate.

1. INTRODUCTION

Plasma spraying has become widely used coating method for different types of materials and takes place in variety of fields including electrical engineering [Sampath, 2010]. This technology is used for improvement of substrate properties and for preparation of self-supporting layers as well. Plasma sprayed coatings are produced by interaction between plasma jet and material in the form of a powder. Materials particles are melted and propelled towards to substrate where a typical structure is formed [Herman, 1988]. All mechanical and electrical properties of plasma coatings depend on chemical and phase composition. Typical lamellar porosity also strongly affects the coatings properties.

Sintered calcium titanate CaTiO_3 is well known dielectric material exhibiting linear character of permittivity [Koller A. – ed., 1994]. Due to high permittivity are dielectrics based on calcium titanate used in electrical engineering like capacitors,

sensors and dielectric parts for high frequency circuits.

2. EXPERIMENTAL

2.1. Powder and spraying

Calcium titanate was obtained in the form of tablets of industrial purity without any additives, which are commonly used for decreasing sintering temperature. Tablets were produced by reactive sintering of calcium carbonate (CaCO_3) and titanium oxide (TiO_2) micro-powders. Final sprayable powder CaTiO_3 was produced by crushing and sieving sintered tablets to correct size for spraying (particularly WSP), 63-125 μm .

A conventional gas stabilized plasma gun F4 was used for spraying one set of samples. This system operated with power 24 kW and working gases Ar/H₂ (65/2.5 slpm). Spray distance, i.e. the distance between the plasma nozzle and the substrate, was set before spraying to 100 mm. These samples are labeled

GSP 100. Other sets of samples were prepared by high feed rate water stabilized plasma spray system WSP (WSP 500, IPP ASCR, Prague, Czech Republic) [Chraska and Hrabovsky, 1992]. This system is operated with power 160 kW. Spray distance was set before spraying to 350 mm and for other spray test to 450 mm. Samples are labeled WSP 350 and WSP 450.

2.2. Thermal annealing

All samples were stripped out of the substrate by method based on different thermal expansion of substrate and coatings and later were annealed in air atmosphere at its normal pressure for 2 hours in variety of temperatures from 530 – 1170⁰C. Typical temperature step was set to 80⁰C, up and down ramps were set to 7⁰C/ min.

3. CHARACTERIZATION

3.1. Dielectric measurements

Aluminum electrodes were sputtered to the ground surface of plan-parallel samples (sample dimension of approximately 10 x 10 x 1.5 mm) in the reduced pressure. Capacity was measured in the frequency range from 30 Hz to 30 MHz. For low frequency measurements (10 Hz - 100 kHz) was used Hioki 3522-50 LCR HiTester. The device was set to four times averaging of all values. Agilent 4285 with materials fixture Agilent 16451B employs frequency range measurements from 75 kHz to 30 MHz. The frequency step was progressively increased and applied AC voltage 1 V kept constant at both devices. Three electrode measuring system was employed. The electric field was applied along the spray direction (i.e., perpendicular to the substrate surface). Relative permittivity ϵ_r was calculated from measured capacities and specimen dimensions.

These same LCR-meters were at the same moment used for the loss factor measurement. Loss factor $\tan \delta$ was measured at the same frequencies as capacity.

3.2. Porosity

Porosity was studied on light microscopy cross-section images taken from 10 randomly selected areas for each sample at 250 magnification. Evaluation was done by image analysis software Lucia G (Laboratory Imaging, Prague, Czech Republic).

3.3. Microhardness

Vickers microhardness of the self-supported layers was measured on polished cross sections by optical microscope (Neophot 2) equipped with a Hanemann head and Vickers indenter. For the test was used 1 N load. The mean value of microhardness was calculated as an average from 20 indentations.

3.4. X-ray diffraction

All annealed samples were analyzed by X-ray diffraction in order to establish whether there exist any changes in phase composition, crystallinity or peak broadening. Measurements were done on D8 Discover Bruker diffractometer using filtered CuK α radiation and 1D LynxEye detector.

4. RESULTS AND DISCUSSION

4.1. Porosity

Results of porosity measurements are shown in Table 1. Circularity (CIR) of pores (planar 2D projections) is equal to zero for a line and to 1 for a circle. This parameter is similar for all samples.

In general, porosity increases with increasing annealing temperature due to thermal expansion of materials which is the cause of new pores up to sintering temperature.

Table 1: Porosity of samples.

Sample	T _{anneal.} [°C]	Porosity [%]	N.Obj. [mm ⁻²]	CIR [-]
WSP 350	-	11.70	1987	0.422
	930	14.16	912	0.492
	1090	14.01	1155	0.436
WSP 450	-	13.60	2033	0.378
	530	11.99	1275	0.430
	930	13.89	965	0.471
	1090	18.01	1378	0.401
	1170	16.87	1196	0.422
GSP 100	-	22.80	2556	0.412
	930	19.37	1832	0.499
	1090	25.30	2202	0.525

Sample WSP 450 exhibit thermal coagulation of pores in the interval between 930 – 1090°C.

The highest porosity with the highest number of pores have samples GSP 100. The lowest porosity has WSP 450 and the lowest number of pores has WSP 350. The micrographs of cross-sections of all coatings are provided (Figure 2)

4.2. X-ray diffraction

Since the sizes of the samples were comparatively small, polycapillary optics with cylinder collimator of 1 mm in diameter was inserted into the primary beam path.

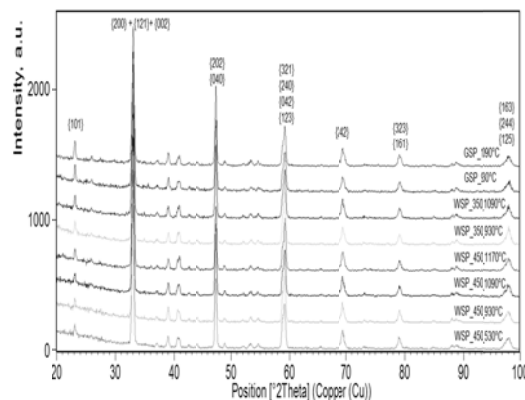


Figure 6: X-ray diffraction patterns.

The obtained diffraction patterns (Figure 1) are characteristic for purely crystalline materials, i.e. the so called “amorphous

halo” is not observed, with only one phase, orthorhombic perovskite, present in the irradiated volume. Furthermore, diffraction profile analysis carried out within the frame of Rietveld method in TOPAS 4.2 software revealed no differences either in preferred orientation, grain size or microstrain.

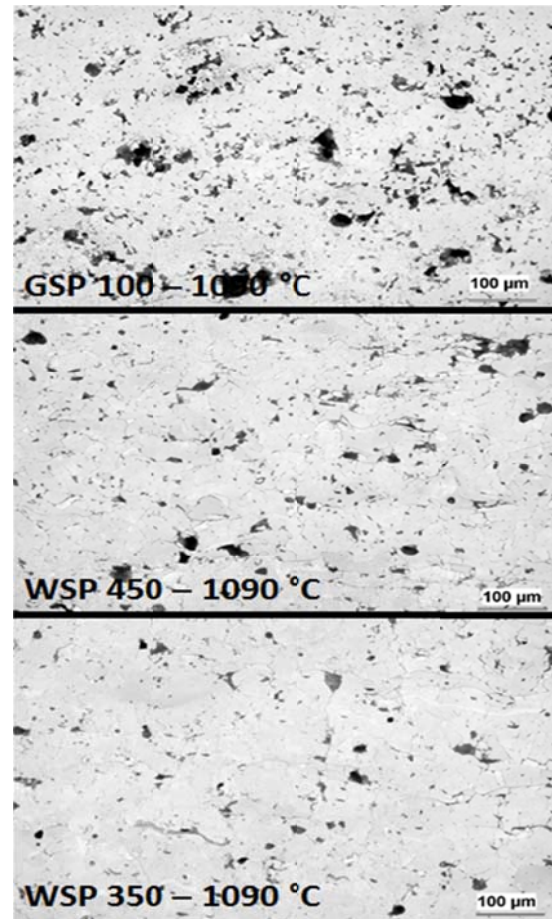


Figure 7: Micrographs of cross-sections.

4.3. Permittivity and losses

Dependence of relative permittivity of SD 350 samples in frequency range 30 Hz to 30 MHz is given (Figure 3). In general it drops with growing frequency, as usual for titanates [Kumar *et al.*, 2013]. The permittivity increased and became more stable with increasing annealing temperature. Sample annealed at 770°C has stable part on permittivity curve below 130 and sample annealed at 1170°C exhibits relative permittivity over

150. The same character of dependence was observed at other sets of samples (SD 450, GSP 100). Non-annealed sample exhibits higher permittivity (not shown in the figure). For 10 kHz the value is 240 and for 100 Hz is permittivity about 330.

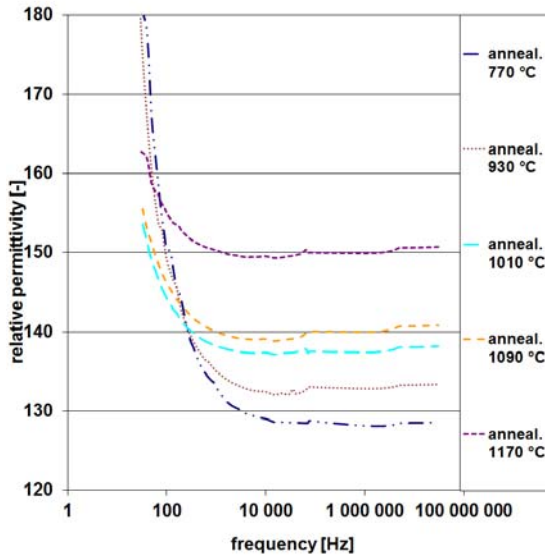


Figure 8: Frequency dependence of relative permittivity for SD 350.

Frequency dependence of dielectric loss factor for SD 350 is shown (Figure 4). Samples annealed to lower temperature have higher losses. The best dielectric properties has sample annealed to 1170°C. For 500 kHz has it the loss factor below 0.005. The non-annealed sample has loss factor much higher. Observed value is about 0.09.

Relative permittivity decreased after thermal annealing but loss factor decreased as well. Due to significant change of dielectric properties the plasma sprayed and annealed CaTiO₃ approached to sintered CaTiO₃ [Ctibor *et al.*, 2003].

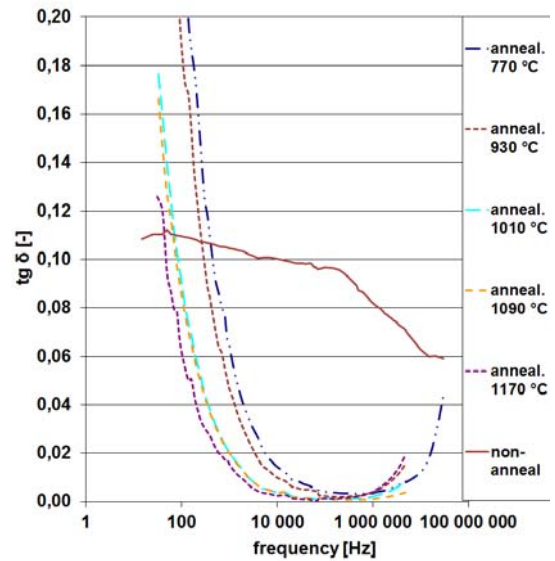


Figure 9: Frequency dependence of dielectric loss factor for SD 350.

4.4. Microhardness

Results are summarized (Table 2). Microhadness mainly increased with increasing annealing temperature except GSP samples where microhardness of non-annealed sample is the highest.

Table 2: Microhardness of samples.

Sample	T _{anneal.} [°C]	HV [GPa]
WSP 350	-	6.80 ± 1.28
	930	6.73 ± 1.10
	1090	6.95 ± 0.72
WSP 450	-	5.80 ± 0.89
	530	7.23 ± 0.98
	930	6.46 ± 1.77
	1090	6.84 ± 0.91
GSP 100	-	7.11 ± 1.27
	930	5.79 ± 0.91
	1090	6.45 ± 0.99

Typical examples of phenomena taking place in plasma sprayed coatings are an increase of the microhardness and reduction of the porosity after annealing, taking place more or less in the case of both WSP coatings. Initial high porosity of GSP samples was influenced by the

fact that the coating was sprayed using rather coarse powder for this technique.

Dielectric properties of the annealed coatings are more stable to tuned frequency [Zhou *et al.*, 2011] and particularly the dielectric loss significantly decreased. This phenomena is related to structural changes. There exists a temperature range where deposit structure appears almost identical to the non-annealed one with a possible exception of some grain growth where particles are in perfect contact (i.e., without inter-lamellar voids) [Bacciochini *et al.*, 2010]. According our experience is it from room temperature up to approx. 0.5 of the melting point; i.e. 600-1000⁰C for CaTiO₃.

When the annealing temperature rises - there exists a temperature range where a structural change is more pronounced - with radical grain growths and diffusion effects at grain boundaries between spherical and flattened particles [Bacciochini *et al.*, 2010]. We consider this interval from approx. 0.5 to 0.7 of the melting point, i.e. 1000-1400⁰C for CaTiO₃. The open void content decreases slightly with temperature increases. This demonstrates that sintering mechanism takes place at the same time than elastic strain relaxation and that open voids are rearranged into closed voids. This process can be named coalescence of voids. Non-reactive sintering in solid state is very likely the involved mechanism [Bacciochini *et al.*, 2010].

5. CONCLUSIONS

This paper studied dielectric properties and selected mechanical properties of annealed plasma sprayed self-supported CaTiO₃. Strong influence of thermal annealing on dielectric properties was observed. The results show that plasma sprayed CaTiO₃ subjected to subsequent annealing has better dielectric behavior

than the non-annealed material. After proper annealing the material has tendency to respond to the electric field like a bulk [Ctibor *et al.*, 2003].

Acknowledgements: This work was supported by the Grant Agency of the Czech Technical University in Prague, grant No. SGS13/195/OHK3/3T/13.

REFERENCES

- Bacciochini, A., Ben-Ettouil, F., Brousse, E., Ilavsky, J., Montavon, G., Denoirjean, A., Valette, S. and Fauchais, P., 2010. Quantification of void networks of as-sprayed and annealed nanostructured yttria-stabilized zirconia (YSZ) deposits manufactured by suspension plasma spraying, *Surface & Coatings Technology* 205 (3), 683.
- Chraska, P. and Hrabovsky, M., 1992. An overview of water stabilized plasma guns and their applications, In *Proceedings of the International Thermal Spray Conference*, ed. C. Berndt, 81.
- Ctibor, P., Sedlacek, J., Neufuss K. and Chraska, P., 2003. Dielectric relaxation in calcium titanate-containing ceramics prepared by plasma spraying, *Ceramics International*, 29 (8), 955.
- Herman, H., 1988. Plasma-Sprayed Coatings, *Scientific American*, 259 (3), 112.
- Koller, A. – ed., 1994. *Structure and properties of ceramics*, Elsevier, 496.
- Kumar, T.S., Bhuyan, R.K. and Pamu, D., 2013. Effect of post annealing on structural, optical and dielectric properties of MgTiO₃ thin films deposited by RF magnetron sputtering, *Applied Surface Science*, 264, 184.
- Sampath, S., 2010. Thermal spray applications in electronics and sensors: past, present, and future, *J. Thermal Spray Technol.*, 19 (5), 921.
- Zhou, L., Zhou, W., Liu, T., Luo, F. and Zhu, D., 2011. Influence of ZnO content and annealing temperature on the dielectric properties of ZnO/Al₂O₃ composite coatings, *Journal of Alloys and Compounds*, 509, 5903.

INFLUENCE OF RHEOLOGICAL PROPERTIES ON THE FOAMING PROCESS OF POLYLACTIDE

Joanna Macyszyn, Marek Kozłowski^a

Wrocław University of Technology, Faculty of Environmental Engineering, Wrocław, Poland
a. Corresponding author (marek.a.kozlowski@pwr.wroc.pl)

ABSTRACT: An experimental study on the influence of rheological properties of two grades of polylactide (PLA) on the foaming process has been carried out. The cellular structure of PLA was obtained during extrusion process using the chemical blowing agent (CBA). The influence of coupling agents on the degree of crystallinity and viscoelastic properties that are critical during the foaming process of polylactide was investigated. Selection of the preferred PLA grade has been correlated with a structure of the polymer.

1. INTRODUCTION

Microcellular materials are gaining increasing attention due to their low density and a lower consumption of raw materials compared to solid materials, good thermal insulation and high damping properties. Foamed polymers use to be produced using chemical (CBA) or physical blowing agents (PBA). Blowing agents provides a gas, which is dissolved in the polymer, which after decompression causes the cells nucleation followed by their growth in the polymer matrix [Baldwin *et al.*, 1996]. The foaming process allows to obtain a microcellular structure in materials, characterized by a cell size in the range of 0.1-10 μm and cell densities in the range of 10^9 - 10^{15} cm^{-3} [Park *et al.*, 1998]. Applications of cellular polymers are numerous, including the automotive, construction sector (insulations) and medicine (scaffolds). Replacement of traditional materials by biodegradable polymers, as well as reducing material costs due to a lower weight of the final product is a current goal of several research institutes and industry.

The best way to solve the problems related to the plastics waste management, high crude oil prices and the gradual exhaustion of fossil resources is the use of polymers derived from renewable

resources. Poly (lactic acid) (PLA) is a bio-based, biodegradable polymer, that is synthesized

from L- and D-lactic acid, being produced by fermentation of sugars belonging to renewable resources [Cabedo *et al.*, 2006]. PLA use to be produced by the ring-opening polymerization of lactide [Carothers and Hill, 1932].

2. EXPERIMENTAL

2.1. Materials

In this study two grades of PLA (3052D, 2003D) supplied by NatureWorks were used. The chain extender (CE) were implemented: Joncryl 4368 (BASF) and IncoMax 100 (Croda Polymer Additives). The general chemical formula for the styrenic-glycidyl acrylate copolymer (Joncryl 4368) is given in Figure 1. Polylactide was dried at 70°C for a minimum of 4 h before processing. A commercial grade blowing agent Hydrocerol CF (Clariant) was used in an amount 0.75 wt%.

2.2. Crystallinity

Structural changes in polylactide caused by the chain extender have been studied with differential scanning calorimetry using DSC apparatus Q20 (TA

Instruments, USA). A thermal ramp running from -20°C up to 250°C at the rate of 10°C min⁻¹ under nitrogen allowed calculations of the percentage of crystallinity according to:

$$\text{Percentage of crystallinity [\%]} = \frac{[\Delta H_m - \Delta H_c]}{\Delta H_m^\circ} \times 100\%$$

where ΔH_m (J/g) is the melting enthalpy, ΔH_c (J/g) is the cold crystallization enthalpy and ΔH_m° is the melting enthalpy of a 100% crystalline PLA reported to be equal to 93 J/g.

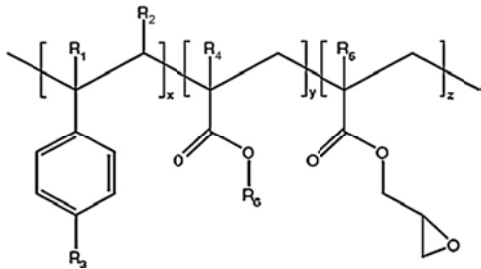


Figure 1: Joncryl 4368 formula [Corre *et al.*, 2011].

2.3. Rheological Properties

The rheological measurements of a molten polymer were carried out with Haake RheoStress 6000 rotational rheometer (Thermo Scientific) in the oscillatory mode, using a plate-plate measuring system and the gap between the plates of 1 mm. The test temperature was 160°C.

2.4. Foaming Process

Cellular structure was obtained during the extrusion process using the single screw extruder Rheomex 252 (Haake) equipped with three heating zones and the extrusion die. The temperature setting was of 150-160-165-145°C. The screw rotation speed was 15 rpm.

2.5. Cellular Morphology

Scanning electron microscopy (SEM) was used to characterize the cellular

morphology of foamed PLA samples. Sputtering with gold was performed prior to the SEM observations which were carried out with VEGA microscope (TESCAN).

3. RESULTS AND DISCUSSION

Thermal analysis showed no significant differences between the two different grades of PLA. Polylactide 3052D and 2003D exhibit semi-crystalline structure, characterized by the glass transition temperature of 62°C, the melting point of 150°C and the degree of crystallinity of about 33% (Table 1). The coupling agent Joncryl has an effect on the degree of crystallinity of polylactide. Epoxy groups of Joncryl can react with the carboxyl and hydroxyl groups in polylactide, which may lead to formation of the branched polymer chains. The presence of branching disturbs a dense packing of the polymer chains, which results in a lower crystallinity. Incromax agent has less impact on the structure of polylactide.

Table 1: DSC results.

	Tg [°C]	Tm [°C]	% of crystallinity [%]
PLA 3052D	62,3	150	32,7
PLA 2003D	62,3	150,1	33,4
PLA 3052D + 1% Joncryl	62,7	150,9	11,9
PLA 2003D + 1% Joncryl	63,4	152,8	12,5
PLA 2003D + 1% Incromax	61,7	151,1	28,9

Polylactide 3052D and 2003D exhibit different viscoelastic properties (Figure 2).

PLA 2003D shows higher viscosity, higher value of storage modulus (G') and loss modulus (G'') compared to PLA 3052D in the whole tested range.

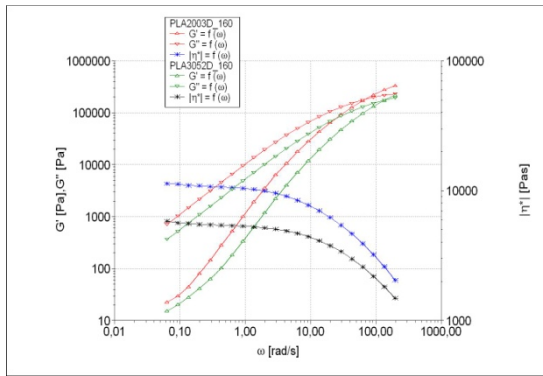


Figure 2: Rheological properties of polylactide 3052D and 2003D.

Addition of a coupling agent Joncryl has a very strong influence on the rheological properties of polylactide. Amount of 1% increased markedly a viscosity of the polymer matrix (Figures 3 and 4). Incromax agent has lower effect on the viscosity of polylactide 2003D compared to the coupling agent Joncryl.

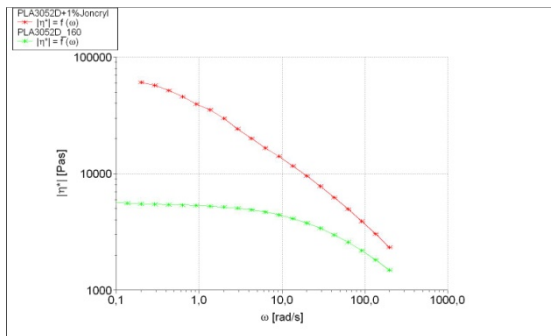


Figure 3: Rheological properties of polylactide 3052D with addition of 1% of Joncryl.

The degree of crystallinity and the viscoelastic properties of the polymer matrix have an essential influence on the quality of the cellular structure which is formed during the foaming process. The foaming extrusion process of polylactide

3052D allowed obtaining pores in the range of 200-250 μm (Figure 5).

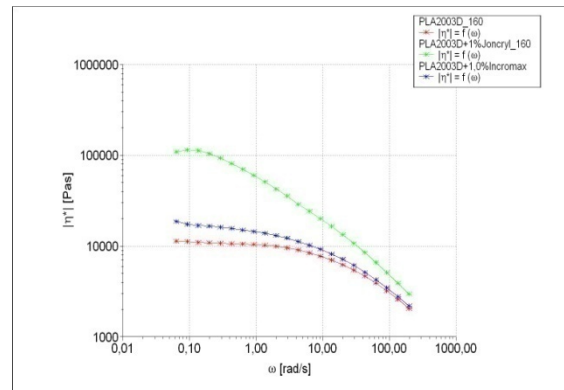


Figure 4: Rheological properties of polylactide 2003D with addition of 1% of Joncryl and Incromax.

Addition of 1% of chain extender has an impact on creation of smaller cells (about 50 μm) in polylactide. High polymer melt viscosity makes difficult the cells to increase during the foaming process (Figure 6).

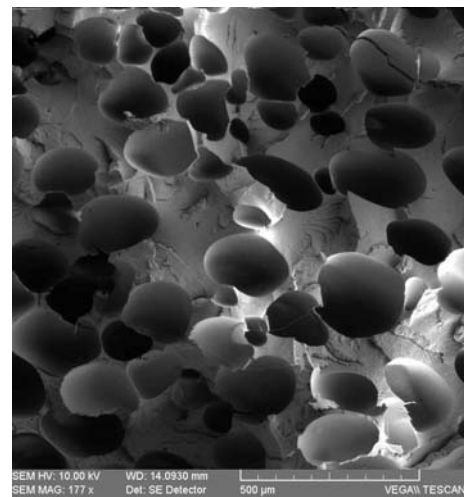


Figure 5: Cellular structure of polylactide 3052D.

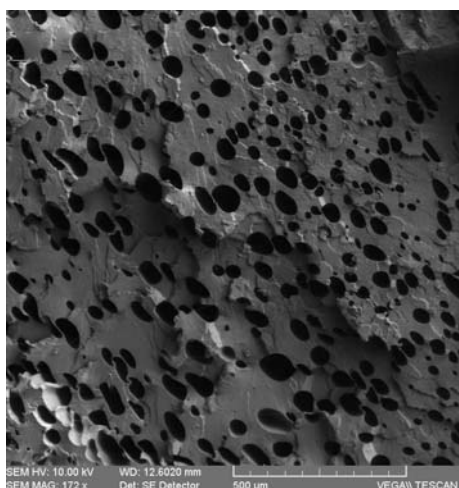


Figure 6: Cellular structure of polylactide 3052D with addition of 1% of Joncryl.

4. CONCLUSION

The effect of coupling agents on the degree of crystallinity and the viscoelastic properties of polylactide has been presented.

Cellular structure in polylactide was created using the foaming extrusion process. Addition of the coupling agent Joncryl has caused creation of smaller pores (about 50 µm) in the PLA matrix.

Acknowledgements: The work was supported by Wrocław Research Centre EIT+ within the project "The Application of Nanotechnology in Advanced

Materials" - NanoMat (POIG.01.01.02-02-002/08) co-financed by the European Regional Development Fund (Operational Programme Innovative Economy, 1.1.2).

The Authors wish to thank Dr S. Frackowiak for his help in rheological measurements and Dr M. Gasior for SEM images.

REFERENCES

- Baldwin D.F., Park C.B., and Suh N.P., 1996. An Extrusion System for the Processing of Microcellular Polymer Sheets: Shaping and Cell Growth Control. *Polymer Engineering & Science*, (36), 1425.
- Park C.B., Behravesh A.H., Venter R.D., 1998. Low Density Microcellular Foam Processing in Extrusion Using CO₂. *Polymer Engineering & Science*, (38), 1812.
- Cabedo L., Luis Feijoo J., Pilar Villanueva M., Lagarón J.M., and Giménez E., 2006. Optimization of Biodegradable Nanocomposites Based on aPLA/PCL Blends for Food Packaging Applications, *Macromolecular Symposia*, 233, 191.
- Carothers W.H., and Hill J.W., 1932. Studies of Polymerization and Ring Formation. XIII. Polyamides and Mixed Polyester-Polyamides, *Journal of the American Chemical Society*, (54), 1566.
- Corre Y-M., Maazouz A., Duchet J., and Reignier J., 2011. Batch Foaming of Chain Extended PLA with Supercritical CO₂: Influence of the Rheological Properties and the Process Parameters on the Cellular Structure, *The Journal of Supercritical Fluids*, (58), 177.

PREPARATION AND CHARACTERIZATION OF UNIFORM TiO₂ MEMBRANE ON POROUS 316L STAINLESS STEEL SUBSTRATE

Fatemeh Mohamadi ^{1, a}, Nader Parvin ¹, Amir_Reza_Azadmehr ¹

1. Department of Mining and Metallurgical Engineering, Amirkabir University of Technology (Tehran Polytechnic), Hafez Street, Tehran, Iran

a. Corresponding author (fmohamadi@aut.ac.ir)

ABSTRACT: In this work the preparation and characterization of a membrane containing a uniform mesoporous Titanium oxide top layer on a porous stainless steel substrate has been studied. The supported membrane was a suitable metallic-ceramic composite membrane which incorporated desirable properties of both ceramic membrane and porous metallic substrate. The 316L stainless steel substrate was prepared by powder metallurgy technique and modified by soaking-rolling and fast drying method. The mesoporous titania membrane was fabricated via the sol-gel method. Morphological studies were performed on both supported and unsupported membranes using scanning electron microscope (SEM) and field emission scanning microscope (FESEM). The membranes were also characterized using X-ray diffraction (XRD) and N₂ –adsorption / desorption measurement (BET analyses). It was revealed that a defect-free anatase membrane with a thickness of 1.6 μm and 4.2 nm average pore size can be produced. In order to evaluate the performance of the supported membrane, single – gas permeation experiments were carried out at room temperature with nitrogen gas. The permeability coefficient of the fabricated membrane was 4×10⁻⁸ lit s⁻¹pa⁻¹cm⁻¹. The prepared titania membrane can be utilized in nano filtration and separation.

1. INTRODUCTION

Pressure-driven membrane processes are among the most mature membrane technologies. They are used for liquid separations. Ceramic membranes have a high application potential due to their chemical, mechanical and thermal stability. Two main classes of membranes can be distinguished: dense and porous membranes. The following classification of pore size has been recommended by IUPAC: macropores Ø>50 nm, mesopores: 2 nm<Ø<50 nm, and micropores Ø<2 nm. Two types of membrane structures may be distinguished: symmetric and asymmetric membranes. The membranes are asymmetrical, in which case the membrane is composed of a thin selective layer and a strong supportive layer giving mechanical strength [Abedini *et al.*,2012].

There are many preparation methods of membranes such as state-particle-sintering, sol-gel and chemical vapour deposition [Kermanpur *et al.*, 2008]. In these methods, state-particle-sintering and sol-gel process are considered to be the practical ones. Silica, alumina, titania and zirconia are considered as the most common porous membrane materials. Among them, titania gained much considerable attention due to its high hydrothermal and chemical stability as well as several unique characteristics such as semi-conductivity, catalysis and photo catalytic behaviors [Li.,2007]. The application of a metallic material as a substrate is advantageous in providing a composite membrane with desirable mechanical properties. Stainless steel is a material of interest in this case due to its

good mechanical strength, flexibility of fabrication and corrosion resistance.

The aim of this paper is to optimize a novel stainless steel supported structure for conventionally used ceramic supported mesopore anatase membrane and to improve its application in nano filtration.

2. EXPERIMENTAL

2.1. Substrate Preparation

To prepare the support, spherical austenitic 316L stainless steel granulate powder was shaped into a disk of 17 mm in diameter and 1.5 mm thickness using a uniaxial press and sintering method. Soaking-rolling-fast drying (SRF) method was applied for surface modification, using a stable colloidal sol including titania particles.

2.2. Titania Membrane Preparation

The method used to prepare the membrane layer, was the sol-gel technique. TiO_2 sol was obtained by hydrolysis of tetra isopropyl orthotitanate ($\text{Ti}(\text{OC}_3\text{H}_7)_4$) (Merck, 8.21895.0250) via the addition of an excess H_2O ($[\text{H}_2\text{O}]/[\text{Ti}] > 4$). A solution of hydroxyethyl cellulose (HEC) and polyvinyl alcohol (PVA) was added to the sol as binders before coating the supports. The layer was formed by dip-coating the support in the prepared sol. The unsupported gel layer was also produced by pouring the prepared sol in a petri-dish. The obtained gel layers were dried at room temperature for 24 h and 30°C for 3h, subsequently calcined for 1 h at 455°C by heating rate of $1^\circ\text{C}/\text{min}$.

2.3. Characterization

The support porosity was measured by Archimedes method according to the ASTM 373-88 standard. The crystal structure was identified using X-ray diffraction technique with $\text{Cu K}\alpha$ wavelength (XRD, INEL France,

Equinox3000). N_2 -sorption measurement was performed to determine the BET information of the unsupported titania layer. Morphological studies were performed on the membranes using scanning electron microscope (SEM, PhillipsXL30) and field emission scanning microscope (FESEM, SEOL AIS-2100). The permeability of the prepared titania membrane was examined with a home-fabricated membrane chamber. This system has been established based on the ASTM S316 standard. The laboratory measured permeability was obtained employing the expression,

$$J = K \frac{\Delta P}{L} \quad (1)$$

Where K is permeability of the membrane, J is the permeated gas flow rate per unit of the membrane surface, L is the membrane thickness, and ΔP is the transmembrane pressure difference.

3. RESULT AND DISCUSSION

3.1. Stainless Steel Substrate Characterization

Archimedes method revealed approximate porosity of 24% for the prepared macroporous support. The fracture cross-section of a sintered stainless steel support is illustrated in Fig.1. It clear that a porous body with adequate bonding between spherical particles and permeable pore paths was produced. Fig.2, represents the N_2 gas fluxes permeated through the prepared stainless steel substrate as a function of pressure difference. Permeability of the support was calculated to be 1.2×10^{-7} lit /s.Pa.cm, using Eq. (1)

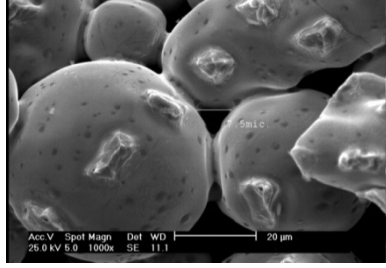


Fig.1: Cross-section of 316L stainless steel support.

together with the substrate thickness, $X_s=0.135$ cm. The permeability of prepared stainless steel support in comparison with the same substrate produced in prior studies [Abedini *et al.*, 2012], [GAO *et al.*,2012] is lower due to used fine stainless steel powder with low formability and applying high pressure in pressing stage.

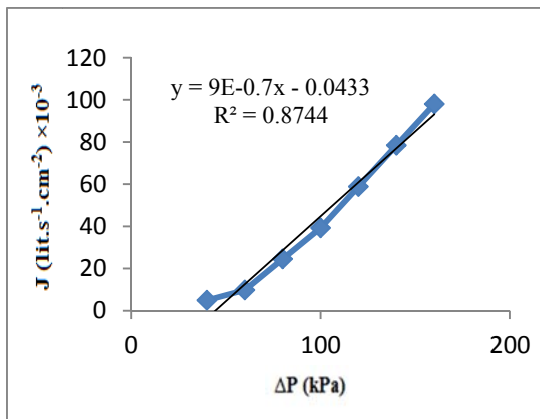


Fig.2: The N₂ gas flux permeation through stainless steel substrate versus its relevant pressure difference.

3.2. Mesopore Titania Membrane Characterization

Fig.3, shows the XRD pattern, obtained for freestanding titania membrane. Phase identification of the samples revealed that the structure of as-synthesized membrane is in accordance with that of anatase. Fig.4 represents the achieved narrow pore size distribution of the prepared membrane and

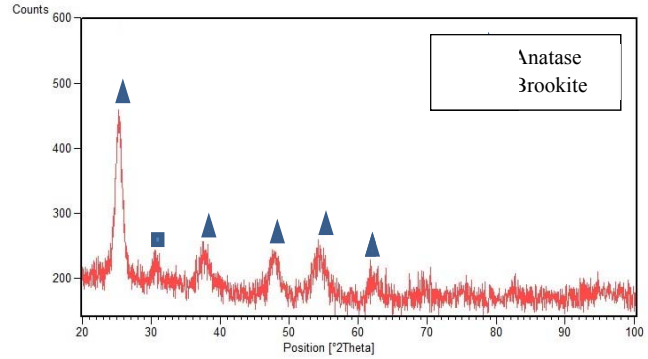


Fig.3: XRD pattern of as-prepared unsupported titania membrane material.

its accordance to the mesopore size range. This is due to the adjusted peptizing and filtering steps of the dip coating sol preparation process which led to small titania particles and a narrow particle size distribution.

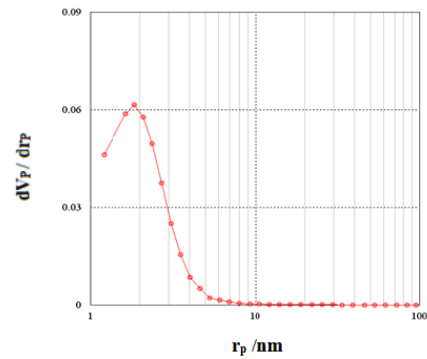


Fig. 4: Pore size distribution of the unsupported titania membrane.

Table1, shows the results of N₂-sorption measurements. The specific surface area measurement was based on the BET model and the pore size was characterized based on the assumption of cylindrical pores.

Table 1: Pore size, pore volume and surface area of the unsupported titania membrane.

BET surface area (m ² /g)	1.2×10^2
Pore volume (cm ³ /g)	0.13
Average pore size (nm)	4.3

3.3. Stainless Steel Supported Mesopore Titania Membran

Fig.5, shows SEM image of the substrate cross-section after membrane layer coating. It is evident that a continuous membrane layer could not be successfully achieved by dip coating due to the penetration of the sol particles into rather large pores of the substrate (1–10 μm). Increasing the size of the coating particles, manufacturing the substrate with smaller average pore size or polishing the substrate surface prior to coating in order to let the larger surface pores to be filled could reduce the penetration effect. However, in these cases the permeability of the substrate would be reduced like the titania substrate. Thus, the substrate modification step with the colloidal titania sol before the subsequent membrane layer coating was utilized in this study. SEM

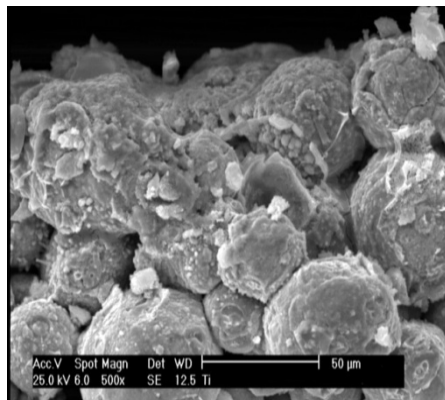


Fig. 5: Cross-section of 316L stainless-steel support after membrane coating.

images of cross - section of the stainless steel substrate after modification by the SRF process for five times are shown in Fig.6(a). It exhibits formation of a uniform defect-free intermediate layer continuously covering the substrate. Only a partial penetration of the titania particles in the support pores was observed, because of the short dipping time selected for the soaking stage of the

SRF process. Thus, decreasing the permeability of the substrate as a result of the particle penetration could be effectively prevented.

FESEM micrograph of the intermediate layer surface is illustrated in Fig.6(b). A typical carrier structure with a mean pore size of about 200 nm can be observed and the pore size is in the desired range for coating with the colloidal Titania sol.

3.3.1. Structural properties

From micrograph given in Fig.7, the graded structure of the finally obtained

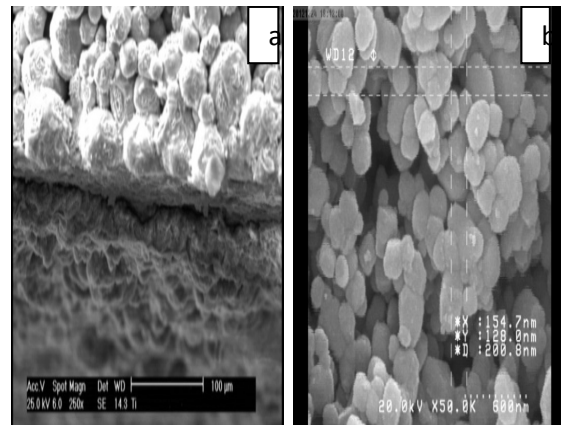


Fig. 6: (a) Cross-sectional SEM images of overview of the modification titania

composite membrane can be clearly observed. Mesopore titania top layer with a thickness of 1.6 μm was prepared on the modified 316L stainless steel support by the explained dip coating method. Moreover, the interfacial adhesion problems in the case of metallic substrate and ceramic layer could be overcome because of the advantages of the selected SRF process for the intermediate layer coating.

3.3.2. Permeability

Permeability of the membrane was measured to evaluate the integrity and the properties of the membrane, as shown in Fig.8. Graph of this figure in comparison with Fig.5 clearly shows that the support has a high permeability. On the other

hand, the permeability of the membrane with a thickness of 1.6 μm exhibited a considerable decrease, compared to the porous stainless steel support. This experiment shows a decrease in the permeability coefficient from 1.2×10^{-7} to 4×10^{-8} lit/s.Pa.cm for the stainless steel support and stainless steel supported anatase composite membrane, respectively. The lower permeability of the membrane is explained by its small pore size. By replacing ceramics support with more permeable stainless steel one, a developed three layer composite structure, with improved properties was achieved for mesopore titania membrane.

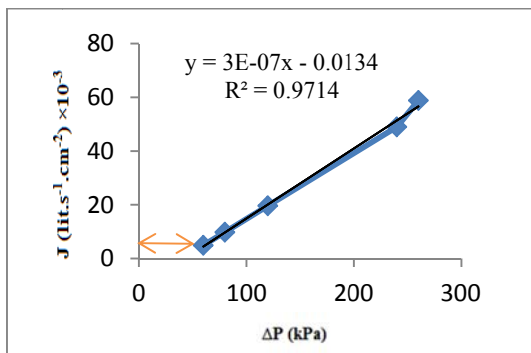
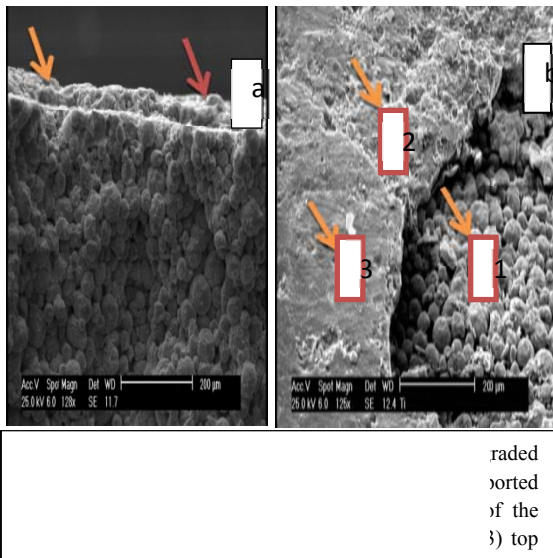


Fig.8: The N_2 gas flux permeated through the finally obtained stainless steel supported anatase composite membrane versus its relevant pressure difference.

4. CONCLUSIONS

In this present work, porous stainless steel substrates with 24% porosity was produced by uniaxial press and sintering method. In order to produce a titania membrane with high permeability and mechanical strength for high pressure application, a full process was adjusted for preparing a high quality mesopore titania membrane with an optimized three-layer stainless steel supported graded structure. A defect-free mesopore anatase membrane with 4.2 nm average pore size and 1.6 μm thickness was finally prepared by sol-gel dip coating method on the modified stainless steel substrate. This was achieved through precautions made in the sol preparation stages of the membrane manufacturing process, like adjusting the pH value and filtering. The stainless steel supported anatase membrane has significant potential for environmental applications and nano filtration processes due to its simultaneous photocatalytic, disinfection, separation functions and mechanical strength.

REFERENCES

- Ali Alem, Hossein Sarpooolaky and Mehrdad Keshmiri, 2009. Titania ultrafiltration membrane—Preparation, characterization and photocatalytic activity, J. of European Ceramic Society 29, 629.
- A. Kermanpur, E. Ghassemali, S. Saleemizadeh 2008. Synthesis and characterisation of microporous titania membranes by dip-coating of anodised alumina substrates using sol-gel method, J. of Alloys and Compounds 461, 331.
- Anita Buekenhoudt, 2008. Stability of porous ceramic membranes, Membrane Science and Technology, 13, 1.
- GAO Hai-yan, HE Yue-hui, ZOU Jin, XU Nan-ping, C.T. LIU, 2012. Tortuosity factor for porous FeAl intermetallics fabricated by reactive synthesis, Trans. Nonferrous Met. Soc. China 22, 2179.
- Sanam Abedini, Nader Parvin, Parviz Ashtarip, 2012. Preparation, characterization and microstructural of a thin γ -alumina membrane on a porous stainless steel

- substrate, *J. of Materials Science and Engineering A* 533, 1.
- Yong Hong Wang, Xing Qin Liu, Guang Yao Meng, 2008. Preparation and properties of supported 100% titaniac ceramic membranes, *Materials Research Bulletin* 43 ,1480.
- Yunfeng Gu, and S.Ted Oyama, 2009. Permeation properties and hydrothermal stability of silica–titania membranes supported on porous alumina substrates, *J. of Membrane Science*, 345,275.
- Zhonghong Li, Nongxue Qiu, Gongming Yang, 2009. Effects of synthesis parameters on the microstructure and phase structure of porous 316L stainless steel supported TiO₂ membranes, *J.of Membrane Science* 326, 533.

OBTAINING AND CHARACTERISATION OF HYDROXYAPATITE–ZIRCONIA POWDERS BY CHEMICAL PRECIPITATION

Marioara Moldovan^{1,a}, Doina Pordan¹, Cristina Prejmerean¹, Codruța Saroși¹, Vasile Eugen² and Aniela Saplontai-Pop³

1. "Babeș Bolyai" University, "Raluca Ripan" Chemistry Research Institute, Cluj-Napoca, Romania;

2. S.C.Metav-Research Development S.A., Bucharest, Romania

3. "Iuliu Hațieganu" University of Medicine and Pharmacy, Cluj-Napoca, Romania

a. mmarioara2004@yahoo.com

ABSTRACT: Hydroxyapatite (HAP) is the most important inorganic phase of the hard tissues of mammals and other organisms. Zirconia (ZrO_2) is an important biomaterial due to its excellent biocompatibility and high mechanical strength. ZrO_2 exhibits the best mechanical properties of oxide ceramics. The combination of two components hydroxyapatite-zirconia shows a promising candidate that can be used as dental materials, with a high impact due to their mechanical properties. HAP-zirconia are new materials that can be used as fillers in the formulation of restorative and endodontic dental materials. The paper presents a study related to the obtaining and characterization of HAP- zirconia nanoparticles. The HAP- zirconia nanoparticles are synthesized by precipitation of HAP in the presence of zirconia. The starting materials were CaO, H_3PO_4 for synthesized HAP and $ZrOCl_2 \cdot 8H_2O$ as precursor for zirconia. Following the precipitation the obtained sol was subjected to heat treatment at 120°C, 400°C, 850°C and 1050°C. X ray diffraction was used in order to study the structural properties of the obtained powder. FT-IR was used in order to evaluate the interactions between HAP and zirconia. Scanning electron microscopy (SEM) was applied to investigate the morphology. The microstructure of the HAP-zirconia products was further observed by transmission electron microscopy (TEM) and high resolution transmission electron microscopy (HRTEM).

1. INTRODUCTION

The growth of research activity in bioceramics especially in the synthesis, processing, characterization and applications of ceramic materials in medicine, are the current status in the field of biomedical applications. Zirconia (ZrO_2) is an important biomaterial due to its excellent biocompatibility and high mechanical strength. Hydroxyapatite (HAP) is a major inorganic component consisting of human hard tissues, such as bones and teeth, and its content determines their microstructures and physical properties [With *et al.*, 1981]. Artificial HAP shows strong biocompatibility and thus it has found broad applications in replacing damaged hard tissues [Dean-Mo *et al.*, 2002, Jia *et al.*, 2003, Kalyana *et al.*, 1998, Kumar *et*

al., 2004]. The artificial HAP, however, suffers from its intrinsic low mechanical properties, and thus cannot sustain heavy load or severe impact. To meet the requirements for the self load-bearing, HAP has been incorporated with other stiff mineral phases such as mullite [Porter and Heuer, 1997, Tyagi *et al.*, 2005] zirconia [Woodward *et al.*, 2006], alumina, wollastonite, leucite, and apatite. Among these composite bioceramics, the combination of HAP and zirconia could be the most desirable for applications to hard tissues exposed under high friction and high impact due to the promising mechanical properties such as high fracture toughness and hardness as well as bioinertness of the zirconia component. The conventional

mechanical mixing of micrometer or even nanometre scale HAP and zirconia powders has been reported for the preparation of HAP/Zirconia composites through sintering [Vasconcelos and Barreto, 2011]. However, this mechanical mixing would cause low sintering density and/or non-uniform zirconia phase distribution in the sintered HAP matrix due to the large particle size and/or segregation of zirconia particles. Non-uniform distribution of the zirconia phase in the HAP matrix would seriously deteriorate the mechanical properties of HAP/ZrO₂ composites. On the other hand, the chemical co-precipitation technique can allow the preparation of a homogeneous mixture of nanoscale HAP and ZrO₂ nanoparticles, which would be the most suitable approach for the preparation of HAP/ZrO₂ composites with superior mechanical properties.

The preparation of homogeneously distributed zirconia-hydroxyapatite composites can be accomplished using a co-precipitation process of precursor reagent solutions. The present study describes the preparation and characterization of fine powders of zirconia and hydroxyapatite submitted at thermal treatment at various temperatures intended for use in medicine. The powders were evaluated using XRD, FT-IR, SEM and TEM. Full utilisation of the unique properties of hydroxyapatite bulk ceramics is, however, possible only after its proper reinforcement, i.e. by preparation of composites.

2. MATERIALS AND METHODS

The HAP- zirconia nanoparticles are synthesized by precipitation of HAP in presence of zirconia. The starting materials was CaO, H₃PO₄ (Aldrich) for synthesized HAP and ZrOCl₂ x 8 H₂O (Aldrich) as precursor for zirconia sol. The mixed sols were subjected to heat treatment at 120°C, 400°C, 850°C and

1050°C respectively. The X-ray diffraction (XRD- standard DRON-3M powder diffractometer) and Fourier Transform Infrared Spectroscopy (FTIR-JASCO-610) techniques were employed to investigate and characterized HAP and zirconia phases' formation. Scanning electron microscopy (SEM FEI-Company) was used in order to study the morphology of the samples and Transmission Electronic Microscopy (TEM, HRTEM - TECNAI F30 G²) was used for the determination of the particles size.

3. RESULT AND DISCUSSIONS

Using precipitation and co-precipitation methods, white powders of HAP and HAP/ZrO₂ were successfully synthesized. XRD patterns of the HAP (to 120⁰C) and HAP/ZrO₂ powder thermal treated at 120°C, 400°C, 850°C and 1050°C for 2h are presented in Figure 1.

The diffraction peaks revealed the presence of the oxide compounds formed during the precipitation and thermal treatments. Diffraction circles marked by diameters correspond to the interplanar distances that are specific to the families of crystalline planes of HAP with hexagonal network that evidenced nanostructured nanoparticles (probale ZrO₂) and bigger particles of 0.1-0.3 μm hydroxiapatite. All samples containing HAP and tetragonal zirconia (t-zirconia) phases and is polycrystalline. The main compound of the system is hydroxyapatite (HAP), but there is also an important content of apatite (AP). XRD patterns of HAP-ZrO₂ compounds presents maximum diffraction angle at 50 degrees and at 34.9 degrees corresponding zirconia oxide. The beta-tricalcium phosphate (β-TCP) phase, which is unstable in human bodies and highly bioresorbable, was also identified in HAP and HAP-ZrO₂ powders. The increasing of the sol temperature up to

120°C had a positive effect on the disappearance of impurity phases. With the increase of the calcinations' temperature up to 850°C, calcium phosphate impurity phases disappeared. Heat treatment caused the appearance of ZrO₂ crystallites.

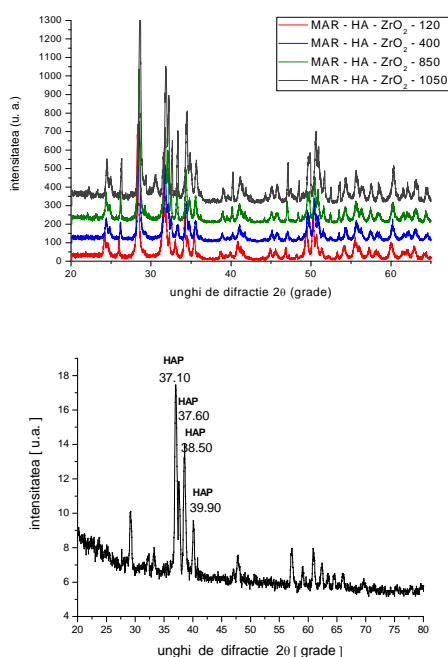


Figure 1: XRD patterns of HAP and HAP-ZrO₂

The FTIR spectra (Figure 2) of HAP-zirconia shows peaks at 1105 cm⁻¹ for the samples treated at 120 and 400°C indicating P-O asymmetric stretching in orthophosphate.

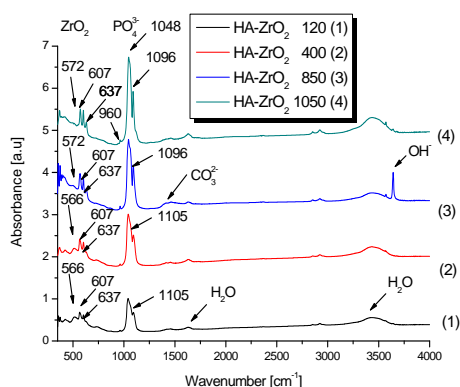


Figure 2: FTIR spectra of HAP-ZrO₂

If the temperature increased at 850 and 1050 cm⁻¹ respectively, the absorption peaks from 1105 cm⁻¹ displaced toward smaller wavenumbers (1096 cm⁻¹). The strong adsorption peak from 1048 cm⁻¹ indicated also P-O asymmetric stretch in orthophosphate, while the sharp very weak band at 960 cm⁻¹ symmetrical valence bond of P-O.

The bands from 607 and 566 cm⁻¹ indicate P-O-P deformation of the PO₄³⁻ ion for the samples treated at 120 and 400°C, while in the case of the sample treated at 850 and 1050 °C the absorption peak from 566 shifts to 572 cm⁻¹, probable due to the interactions between HAP and zirconia. A broad band around 870 cm⁻¹ region can be attributed to the simultaneous presence of P-O-H in HPO₄²⁻ groups and C-O vibrations in CO₃²⁻ groups. The value of 423 cm⁻¹ is attributed to stretching vibrations of Zr-O bond. The IR bands between 785 and 618 cm⁻¹ could be assigned to Zr-O stretching vibrations, while the intense band around 500 cm⁻¹ is the superposition result of stretching Zr-O. The broad peak at 3412-3435 cm⁻¹ and the small one from around 1636 cm⁻¹ represents O-H bonding in water. The small absorption peak from 637 cm⁻¹ and sharp peak from 3645 belong to OH groups from HA.

SEM (Figure 3) has shown better dense and finer powder in case of HAP-ZrO₂ synthesized under our specific conditions than normal condition of synthesis. The SEM observation showed that the HAP-ZrO₂ powders possess particle sizes in the range of micrometers to nanometers in diameter. The micrographs show high crystallinity for HAP and HAP-ZrO₂ nanopowders. The HAP-ZrO₂ nano powders show average particle size of 50–70 nm and a uniform distribution.

SEM micrographs for HAP-ZrO₂ powder reveals the presence of the nanoparticles

in an agglomerated form ZrO_2 crystals dispersed throughout the HAP nano crystals are proved by X-ray diffraction results and IR spectra.

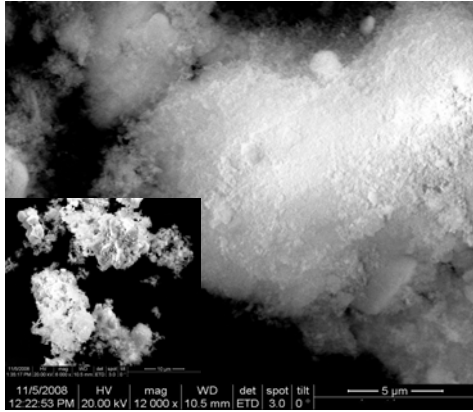


Figure 3: SEM images of HAP- ZrO_2 ($120^\circ C$) and HAP- ZrO_2 ($1050^\circ C$, small)

SEM images revealed that if the thermal treatment was $120^\circ C$ the obtained powder is very fine with uniform particles size distribution looking very aerated. Thermal treatment applied at $1050^\circ C$ leads to the agglomeration of the particles that look denser compared with the powder obtained at $120^\circ C$. For better characterization of the samples of HA- ZrO_2 at a smaller scale we used TEMBF (Figure 4) (Transmission Electron Microscopy Bright Field)

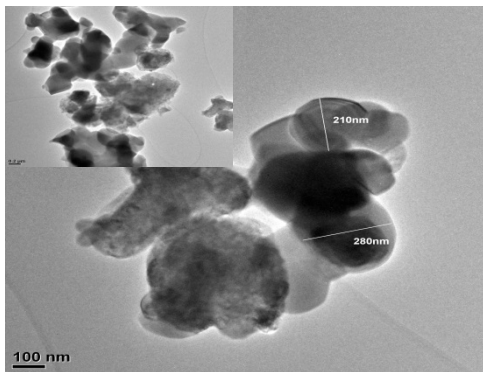


Figure 4: TEMBF image of HA- ZrO_2 micro and nanoparticles

The bright spots belong to big crystallites while the small spots belong to much smaller particles.

The experimental results suggest that the HAP-zirconia nanoparticles may be used as filler for bone tissue restoration, or as nanofiller in polymerized composites because the particles are fine and could assure the obtaining of a very homogenous material.

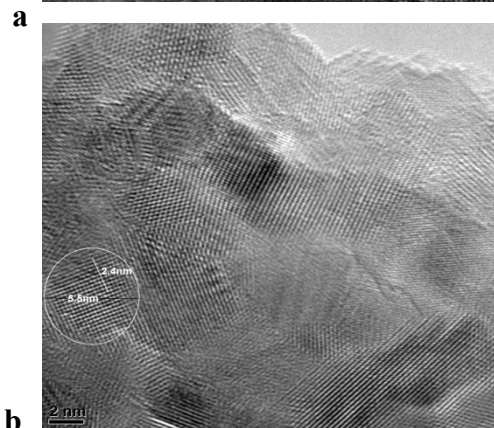
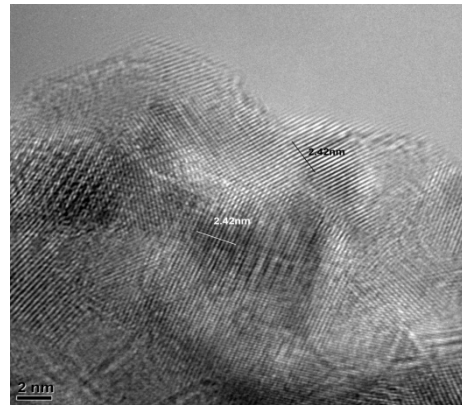


Figure 5: HRTEM images HA- ZrO_2 nanoparticles

In figure 5 (a) observed recorded for the agglomeration of the particles for the interplanar distance of 2.4 \AA , correspond to cubic CaO. The image 5 (b) put into evidence crystallized nanoparticle with sizes of 5-8 nm. Image of bright field electron microscopy (TEMBF) in figure 5 reveals nanostructure particles probably CaO and large particles of 0.1 - 0,3 μm hydroxyapatite. Very bright spots belong to larger crystallites and small spots

correspond to very small nanocrystals. Diffraction circles marked with diameters corresponding to interplanar distances specific crystal plane families (indexed image) of the compound $\text{Ca}_5(\text{PO}_4)_3\text{OH}$ the hexagonal crystal lattice.

4. CONCLUSION

ZrO_2 crystals dispersed throughout the HAP nanocrystals are proved by X-ray diffraction results and IR spectra. SEM micrographs for HAP- ZrO_2 powder reveals the presence of the nanoparticles in an agglomerated form ZrO_2 crystals dispersed throughout the HAP nanocrystals. Image of electron microscopy TEM reveals nanostructure particles probably CaO and large particles of 0.1 - 0.3 μm hydroxyapatite. Very bright spots belong to larger crystallites and small spots correspond to very small nanocrystals. In the future investigations related to physical, mechanical and toxicological properties will be done; both ceramics can be used as implant biomaterials, for example in bone repair.

Acknowledgements: Funding from the Romanian Ministry of Education and Research, National project PNII no: 165/2008, is gratefully acknowledged.

REFERENCES

- Dean-Mo, L., Quanzu, Y., Tom, T. and Wenjea, J. T., 2002. Structural Evolution of Sol-gel-derived Hydroxyapatite, *Biomaterials*, (23), 1679.
- Jia, Y., Wiliana, T., Yun, Z. C., Kam, C. T., Jan, M. and Bernard, S., 2003. Hydroxyapatite Nanostructure Material Derived Using Cationic Surfactant as a Template, *J. Mater. Chem.*, (13), 3053
- Kalyana Sundaram N.T., Vasudevan Suchanek T. W., and Yoshimura M., (1998), Processing and Properties of Hydroxyapatite-based Biomaterials for Use as Hard Tissue Replacement Implants", *J. Mater. Res.*, 13, 94.
- Kumar, R., Prakash, K. H., Cheang, P. and Khor, K. A., 2004. Temperature Driven Morphological Changes of Chemically Precipitated Hydroxyapatite Nanoparticles, *Langmuir*, (20), 5196.
- Porter D. L., Heuer A. H., 1977. Mechanisms of Toughening Partially Stabilised Zirconia (PSZ), *J. Am. Ceram. Soc.*, (60), 183 .
- Tyagi A K , Mangamma G , Kamruddin M , Dash S , Raj Baldev, 2007. *Nanosci Nanotechnol*, 7(6): 2005, Synthesis and characterization of nanocrystalline Cr_2O_3 and ZrO_2 ceramic materials.
- Vasconcelos HC, Barreto MC, 2011, Tailoring the microstructure of sol-gel derived hydroxyapatite / zirconia nanocrystalline composites, *Nanoscale Res Lett*, (6), 1
- With G. D., Van Dijk H. J. A., Hattu N., and Prijs K., 1981. Preparation, microstructure and mechanical properties of dense polycrystalline hydroxyl-apatite, *J. Mater. Sci.*, (16), 1592.
- Woodward JD, Pickel JM, Anovitz LM, Heller WT, Rondinone, 2006. Self-assembled Colloidal Crystals from ZrO_2 Nanoparticles , *J Phys Chem B Condens Matter Mater Surf Interfaces Biophys.*, (110), 19456.

RELATIONSHIP BETWEEN CELL WALL MORPHOLOGY AND ENERGY ABSORPTION BEHAVIOR OF ALUMINUM FOAMS PRODUCED VIA MELT ROUTE

Nima Movahedi^{1,a}, S. Reza Hoseini¹

1. Metallurgy Research and Development Department, soroushsanatCo, Isfahan, Iran
a. Corresponding author (nima.movahedi@gmail.com)

ABSTRACT: A study was carried out to realize the relationship between cell wall morphology of closed cell aluminum foam and mechanical properties of this material as energy absorbant. For this purpose three aluminum foam samples with closed cell structure were prepared via melt route at different molten aluminum temperatures (650, 675 and 700°C) by adding same amounts of granule calcium as thickening agent and titanium hydride as foaming agent. The fabricated aluminum foams were characterized by scanning electron microscope to determine the cell wall morphology and compression tests of these three aluminum foams with different relative density were tested to obtain energy absorption. The results indicate that molten aluminum temperature during holding step of producing aluminum foam has a dominant role on cell wall morphology. By increasing temperature the flow of aluminum foam inside the crucible during holding would be higher and cellular structure changes from ordered to disordered one and mechanical properties will be decreased.

1. INTRODUCTION

Cellular metals owing to their pores possess a set of unusual properties compared with bulk structural materials, they are crushable, they exhibit a plateau stress if compressed, and they exhibit a change in poisson ratio on deformation. The excellent combination of good mechanical properties (mostly strength and stiffness) and low weight is the prime advantage. In addition, cellular metals absorb high impact energies regardless of the impact direction, and are very efficient in sound absorption, electromagnetic shielding and vibration damping [Degischer and Kriszt, 2002]. Process parameters influence the pore morphology of produced aluminum foams and consequently mechanical properties will be affected by changing cell size and shape, much attention should be paid to control of the morphology of the cells during foaming process of an aluminum melt. It is very important to understand the bubble foaming mechanism.

The influence of TiH₂ addition on the cell structure of foamed aluminum has been showed that a TiH₂ addition of 1.0 and 1.5 wt% induces a greater uniformity of spherical cell distribution [Yang and Nakae, 2000]. The effect of cell size on quasi-static and dynamic compressive properties of open cell aluminum foams produced by infiltrating process revealed the elastic modulus and compressive strength of foams not only depend on relative density but also depend on cell size [Xiao-qing et al., 2006]. Some researchers pointed out that during cooling stage the pores elongated in rise direction and cells in longitudinal and transverse direction have different dimensions, in longitudinal direction Al-Si alloy foams can absorb more energy because the plastic collapse of Al-Si alloy foams in longitudinal direction is higher than that in transverse direction [Zu and Yao, 2012]. The effect of foaming temperature on pore size and density has been reported before

[Fushenget *al*,2003].The purpose of this paper is to evaluate the effect of foaming temperature on cell morphology and its effect on energy absorption of samples,for this goalthree different aluminum alloy foams have been manufactured at different foaming temperatures through melt route by using same amounts of calcium granule and TiH₂powder as thickening and foaming agent respectively.

2.RESULT AND DISCUSSION

The materials used for manufacturing of aluminum foams were A356 aluminum alloy(7.56 wt% Si,0.41 wt% Mg), high purity calcium granules (1-3mm in size) as thickening and titanium hydride(40μm) as blowing agents. Aluminum alloys were melted at three different temperatures(650°C,675°C and 700°C) in separate graphite coated steelcrucibles, for each aluminum melt at its specific temperature 2wt% of calcium granule was added and stirred at 500 rpm for 10 minto make the viscose aluminum melt, afterward 1wt% of TiH₂added to the viscose aluminum melt and stirred at 1200 rpm for 1 min, finally holding step was carried out at same time of 180 seconds for three samples and then cooled in air to room temperature. At holding stage due to titanium hydride decomposition cellular structure forms.Figure 1 shows the macroscopicstructure of produced foams at different holding temperatures.

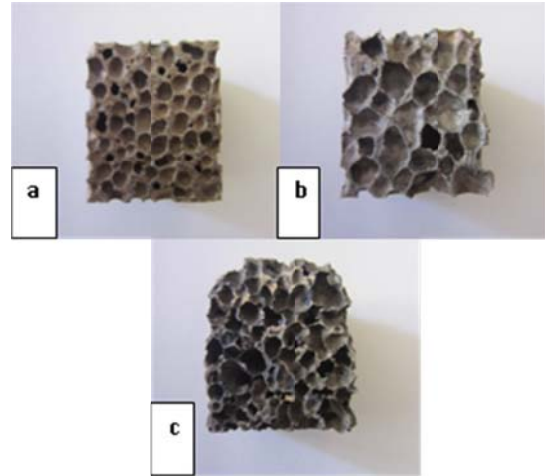


Figure 1: Macrostructure of aluminum foams produced at temperatures of a)650°C,b)675°Cand c)700°C.

It is clearthat with increasing foaming temperature cell morphology has been changed. At low temperatures smaller cell size with round shape is obvious while At high foaming temperature, unfavorable curvature of the foam is observed,it is may be because of this fact that when the temperature raises to around 700°C,the equilibrium hydrogen pressure due to TiH₂ decomposition increases and cause cell wall curvature[Yang and Nakae,2000].

Figure2 shows the SEM micrograph of pores at different foaming temperatures.Figure 3 reveals the cell wall thickness and relative morphology at different foaming temperatures. A comparison of the cell structure shows that at high temperatures cell walls migrate in irregular manner, also cell wall thickness will be reduced at high temperatures because of lower aluminum viscosity at hightemperatures[Deqingand Ziyuan,2003].

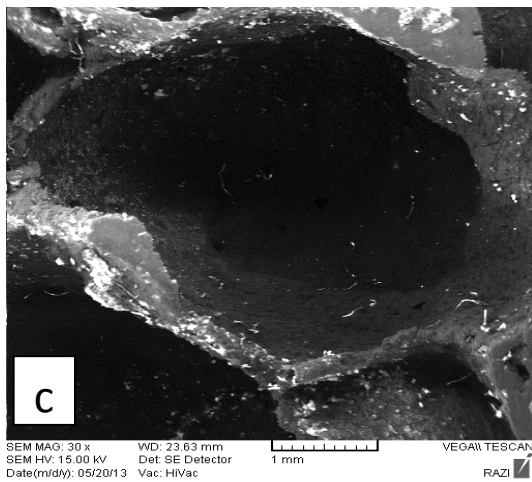
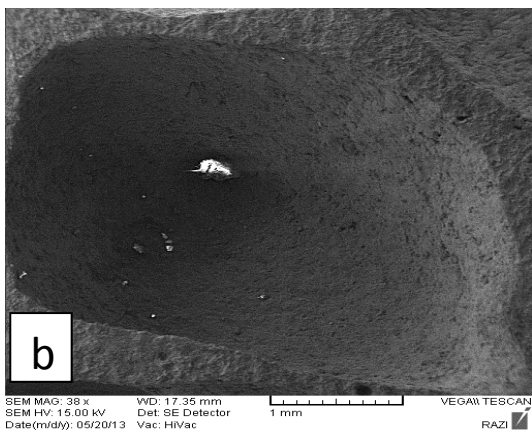
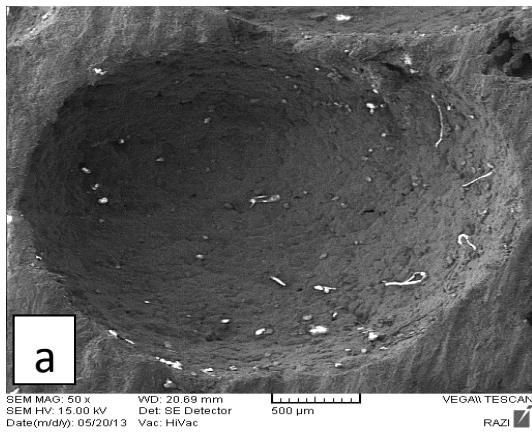


Figure 2: SEM micrograph of pores at different foaming temperature of a)650°C, b)675°C and c)700°C

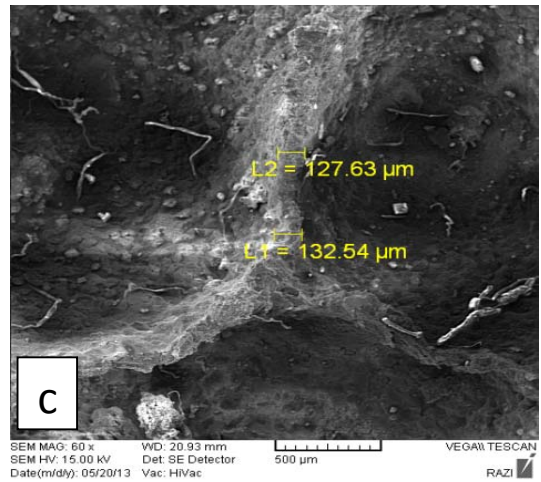
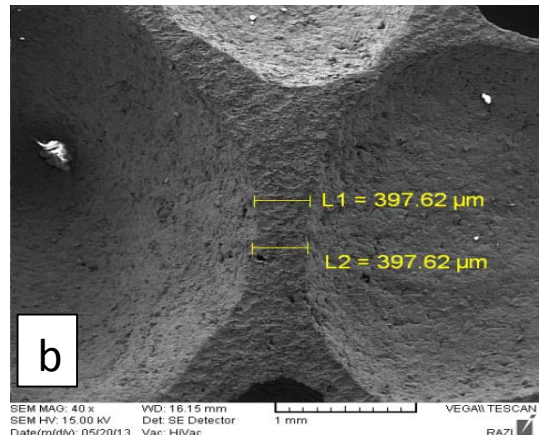
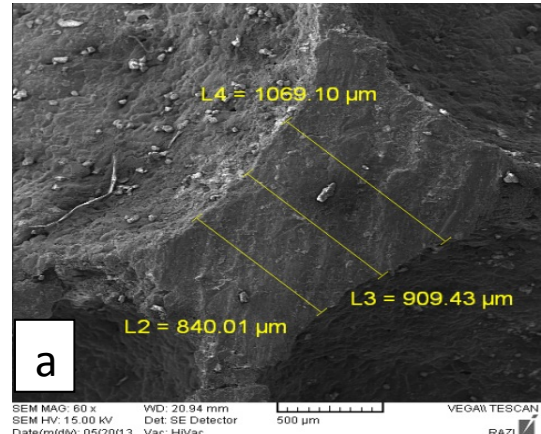


Figure 3: Cell wall morphology and thickness at different foaming temperatures of a)650°C, b) 675°C and c) 700°C.

Foam density (ρ) and total porosity of each specimen were calculated by dividing the mass to volume of three different aluminum foams and by using the below formula respectively [Deqing and Ziyuan, 2003].

$$P = 1 - \rho / \rho_0$$

Where ρ is the foam density and ρ_0 is the density of material which foam is made from it.

The relationship between density, total porosity and holding temperature is shown in figure 4.

By increasing foaming temperature, gas pressure inside the bubbles will be increased and surface tension decreases, so that bubbles nucleate and grow easily, leading to low densities and high porosities [Yang and Nakae, 2000].

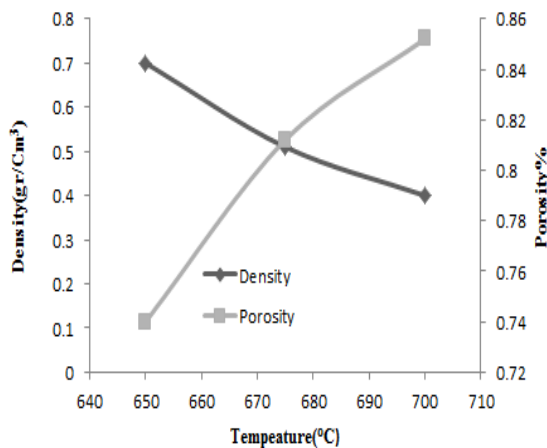


Figure 4: Relationship between foaming temperature, density and porosity.

In order to determine the energy absorption behavior of foamed aluminums, compressive tests were conducted on 25*25*20 (mm) samples at test speed of 1mm/min, as it can be seen from figure 5, by increasing the foaming temperature, compressive strength drops rapidly, this phenomenon is as a result of sharp edges which acts as stress concentration centers

in disordered cells that produced at 700°C, also aluminum foams that produced at this temperature because of having low density has lower ability to absorb energy in comparison with samples have been foamed at lower temperatures.

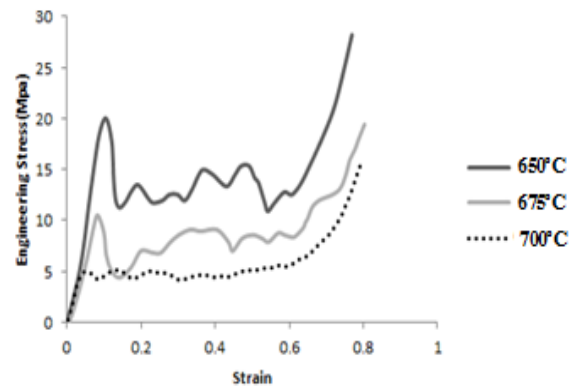


Figure 5: Stress-strain curves of aluminum foams produced at different temperatures.

3. CONCLUSION

Foaming temperature has a dominant role in microstructure and mechanical properties of aluminum foams that produced via melt route and during production of this kind of cellular material is it possible to determine the energy absorption of foams by adjusting foaming temperature for industrial applications.

Acknowledgement

The authors would like to thank the SoroushSanat company for the financial support of this research.

REFERENCES

- Degischer,2002,Handbook of cellular metals production, processing, application.Wiley-VCH verlagGmbH&Co.KGaA.
- Deqing,2003,Effect of ceramicparticles on cell size and wall thickness of aluminum foam, Journal of Materials Science and Engineering A,Volume(361),page 45.
- Fusheng,2003, Effects of process parameters and alloy composition on the pore structure of foamed aluminum, Journal of Materials processing technology,Volume(138),page 505.
- Xiao-qing,2006,Effect of cell size on compressive properties of aluminum foam, Transaction of Nonferrous metals society of China,Volume(16),page 351.
- Yang,2000,Foaming characteristics control during production of aluminum alloy foam, Journal of alloys and compounds,Volume(313),page188.
- Zu,2012,Influence of cell shape anisotropy on the compressive property of closed cell Al-Si alloy,Journal of Materials Engineering and Performance,Volume(21),page 985.

X-RAY MICROTOMOGRAPHY OF GEOLOGICAL SOFT SEDIMENT SAMPLES: REDUCTION OF MOTION ARTIFACT BY RESIN CONSOLIDATION

Yoshito Nakashima

National Institute of Advanced Industrial Science and Technology (AIST),
Central 7, Higashi 1-1-1, Tsukuba, Ibaraki 305-8567, Japan
a. Corresponding author (nakashima.yoshito@aist.go.jp)

ABSTRACT: X-ray microtomography (XRM) is useful to obtain three-dimensional microstructure of powder/porous materials, and has been applied to geological samples. When applied to soft or unconsolidated geological samples (e.g., sea bottom sediments), however, undesirable sample deformation occurs due to the relative displacement of fine sediment particles, for example, during the sample rotation in an X-ray chamber (motion artifact). This sample deformation can be serious because it destroys the original pore structure, reducing the reliability of any post XRM outcomes obtained using the images. As a solution to the problem, sample preprocessing was performed using resin to consolidate the soft samples before the XRM operation. Via alcohol replacement of the pore water in the sediment, the pore space was completely filled with solid resin to increase the rigidity of the sample. This technique was applied to bottom fine sediment samples from Tokyo Bay, Japan, and the three-dimensional XRM images without motion artifact were successfully obtained.

1. INTRODUCTION

The elucidation of the decomposition mechanism of organic matter in the bottom sediments of eutrophicated coastal regions is important in terms of the environmental science [e.g., Sayama, 2001; Sayama *et al.*, 2005; Nielsen *et al.*, 2010]. The matter transport, chemical reactions and biological activities occur within the porous sediments having three-dimensionally complex pore structure. Therefore, the development of three-dimensional imaging technique for the porous sediments is needed to elucidate the various physical, chemical and biological phenomena occurring on the sea floor.

X-ray computed tomography or X-ray microtomography (XRM) is a powerful tool to obtain three-dimensional structure of powder/porous geo-materials [e.g., Nakashima, *et al.*, 2004; Nakashima, *et al.*, 2008; Nakashima and Nakano, 2011; Nakashima, *et al.*, 2011; Nakashima and

Nakano, 2012ab]. However, a serious problem occurs when XRM is applied to soft or unconsolidated geological samples (e.g., sea bottom sediments). Such soft samples readily deform by the relative displacement of weakly glued sediment particles during the transportation from the sampling site to the laboratory and/or the sample rotation in an X-ray chamber (the latter is referred to as the *motion artifact* yielding blurred outlines of the sediment particles in the XRM images). This sample deformation can be serious because it destroys the original pore structure and/or decreases the spatial resolution, reducing the reliability of any post XRM processes (image processing and pore-scale computer simulation) obtained using the images.

Resins or plastics are conventionally used in geology for the preservation of the original sedimentary structures of unconsolidated samples at fields and

laboratories [McMullen and Allen, 1964]. This resin method was applied to make soft sediments rigid before the XRM operation in the present study. Via non-destructive alcohol replacement of the pore water in the sediments, the pore space was completely filled with solid resin to increase the rigidity of the sample [Suzuki *et al.*, 2011], which does not allow the sample deformation. This technique was applied to bottom fine sediment samples, and the three-dimensional XRM images were successfully obtained at a spatial resolution of a few micrometers.

2. EXPERIMENTAL

Unconsolidated fine sediments were sampled from Tokyo Bay, Japan. Because the seasonal variation was reported about the sediment composition [Sayama, 2011], sampling was performed in summer (July 26, 2011) and winter (November 25, 2012). A SEM image of the sample is shown in Fig. 1.

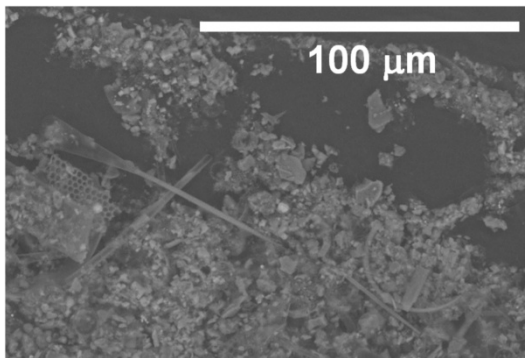


Figure 1: SEM microscopy of a dried sea bottom sediment sampled in summer (July 26, 2011). The sediment is a mixture of planktons and mineral grains (several to several tens of micrometers in particle size).

The two wet sediment samples were processed as follows. Pore water is undesirable for the resin infiltration. Thus, firstly sea water in the pores was replaced with the ethanol (Fig. 2). The pore water was gradually exchanged with

the diffusing ethanol molecules. The supernatant fluid (mixture of the sea water and ethanol) was replaced with pure ethanol (purity, 99.5 %) five times, and it took 3 days to complete the water-ethanol replacement.

Secondly liquid Osteoresin™ (Wako Pure Chemicals Industries, Ltd., Japan) was poured on the sediment to replace ethanol in pores with resin molecules. The sample was put on a vacuum chamber at room temperature to enhance the evaporation of ethanol in the pores. It took about 2 months to complete the polymerization of the Osteoresin™. The rigid sediment sample was cut into a column (Fig. 3) for the XRM experiments.

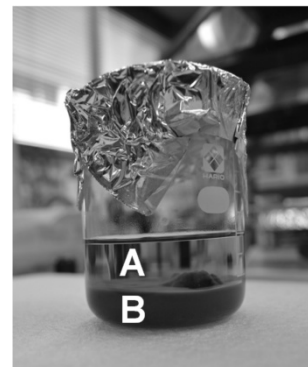


Figure 2: Photo of a single step of the resin consolidation processing. Ethanol (A) was poured on a sediment (B). The beaker was capped with an aluminum foil to prevent from the evaporation.



Figure 3: Consolidated columnar sediment sample (indicated by an arrow, 4mm x 4mm x 15mm in dimensions) on a sample stage for XRM. The sediment was sampled in winter (November 25, 2012) from the 2-4 cm depth interval below the sea floor.

The cut sample was imaged by an XRM apparatus (Shimadzu, SMX-160CT-SV3 with a focus size of 400 nm) at the Center of Materials Research for Low Carbon Emission (National Institute for Materials Science, Tsukuba, Japan). The reconstructed raw XRM images were processed (e.g., trimmed and converted from 16 bit to 8 bit) for further analysis using original programs publicly open at <http://staff.aist.go.jp/nakashima.yoshito/p/roeng.htm>.

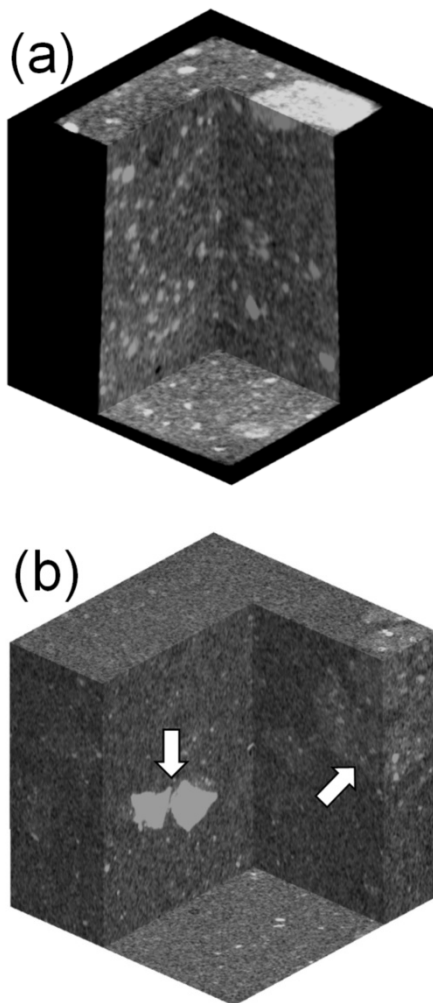


Figure 4: Three-dimensional XRM images of the winter sample of Fig. 3. (a) The image dimension is $5.0^3 \text{ mm}^3 = 180^3$ voxels. Each voxel dimension is $28^3 \mu\text{m}^3$. The black voxels are the ambient air. (b) Zoomed XRM of a portion of (a). The image dimension is $0.84^3 \text{ mm}^3 = 600^3$ voxels. Each voxel dimension is $1.4^3 \mu\text{m}^3$. The high-density grains (bright voxels) and medium-density objects (slightly bright voxels) are clearly seen as shown by arrows.

3. RESULTS AND DISCUSSION

Obtained XRM images are shown in Figs. 4 and 5. The grey level increases with density and atomic number; the resin-filled pore is dark, the ambient air is darkest, and iron-bearing solid minerals are bright in the images. Unfortunately the individual fine grains in Fig. 1 were not clearly imaged due to the finite spatial resolution of the XRM apparatus used. However, the outline of the large iron-bearing mineral grains in the sediment was clearly imaged (Fig. 4b), suggesting that the resin technique is effective to reduce the motion artifact.

Many large iron-bearing minerals having bright voxel-values appear in winter (Fig. 4a) compared with the summer sample (Fig. 5). This can be related to the report that the magnetite-, ferrihydrite- and lepidocrocite-content increase in winter on the sea floor of Tokyo Bay [Sayama, 2011]. Iron-bearing minerals such as magnetite are important for the decomposition of organic matter in eutrophicated coastal marine sediments due to its large electric conductivity [Sayama, 2011]. Thus, the next possible step is the pore-scale electric current simulation [Nakashima and Nakano, 2011; Nakashima *et al.*, 2012] using the winter XRM images of Fig. 4. XRM study coupled with such computer simulations will help to understand the

organic matter decomposition utilizing the extracellular electron transfer.

The main components of the sediments are silicate minerals and diatom planktons that are probably not altered by the injection of ethanol. However the sediments contain a certain fraction of organic matter that may be altered (e.g., dissolved) by the use of ethanol (Fig. 2). As a future problem, this alternation problem should be carefully examined to confirm the reliability of the resin technique.

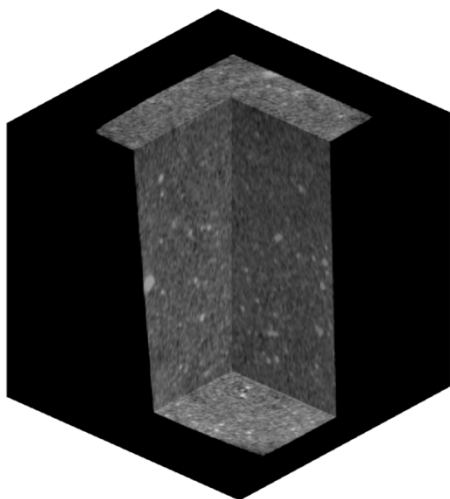


Figure 5: Same as Fig. 4a but for a consolidated sediment sampled in summer (July 26, 2011). The XRM image dimension is $5.0^3 \text{ mm}^3 = 239^3$ voxels. Each voxel dimension is $21^3 \text{ }\mu\text{m}^3$.

4. CONCLUSIONS

The resin technique was applied to the XRM of unconsolidated sea bottom sediments to preserve the original sedimentary structures and to reduce the motion artifact. The three-dimensional micro-structure of the sediments was successfully obtained to demonstrate that the technique is promising.

Acknowledgements: The Tokyo Bay samples were provided by M. Sayama (AIST). The resin consolidation

processing of the sediments were conducted by A. Oowada (Geological Museum, Geological Survey of Japan). The present study was supported in part by JSPS KAKENHI (No. 23241012).

REFERENCES

- McMullen, R.M. and Allen, J.R.L. 1964. Preservation of sedimentary structures in wet unconsolidated sands using polyester resins, *Marine Geology*, 1, 88.
- Nakashima, Y., Nakano, T., Nakamura, K., Uesugi, K., Tsuchiyama, A., and Ikeda, S. 2004. Three-dimensional diffusion of non-sorbing species in porous sandstone: computer simulation based on X-ray microtomography using synchrotron radiation, *Journal of Contaminant Hydrology*, 74, 253. Full text is open at <http://dx.doi.org/10.1016/j.jconhyd.2004.03.002>.
- Nakashima, Y. and Kamiya, S. 2007. Mathematica programs for the analysis of three-dimensional pore connectivity and anisotropic tortuosity of porous rocks using X-ray computed tomography image data, *Journal of Nuclear Science and Technology*, 44, 1233. Full text is open at <http://www.tandfonline.com/doi/abs/10.1080/18811248.2007.9711367>.
- Nakashima, Y., Kamiya, S., and Nakano, T. 2008. Diffusion ellipsoids of anisotropic porous rocks calculated by X-ray computed tomography-based random walk simulations, *Water Resources Research*, 44, article number W12435. Full text is open at <http://www.agu.org/journals/wr/wr0812/2008WR006853/>.
- Nakashima, Y. and Nakano, T. 2011. Accuracy of formation factors for three-dimensional pore-scale images of geo-materials estimated by renormalization technique, *Journal of Applied Geophysics*, 75, 31. Full text is open at <http://dx.doi.org/10.1016/j.jappgeo.2011.06.021>.
- Nakashima, Y., Mitsuhashi, Y., Nishiwaki, J., Kawabe, Y., Utsuzawa, S., and Jinguuji, M. 2011. Non-destructive analysis of oil-contaminated soil core samples by X-ray computed tomography and low-field nuclear magnetic resonance relaxometry: a case study, *Water Air & Soil Pollution*, 214, 681. Full text is open at <http://dx.doi.org/10.1007/s11270-010-0473-2>.
- Nakashima, Y. and Nakano, T. 2012a. Nondestructive quantitative analysis of a

- heavy element in solution or suspension by single-shot computed tomography with a polychromatic X-ray source, *Analytical Sciences*, 28, 1133. Full text is open at <http://dx.doi.org/10.2116/analsci.28.1133>.
- Nakashima, Y. and Nakano, T. 2012b. Steady-state local diffusive fluxes in porous geomaterials obtained by pore-scale simulations, *Transport in Porous Media*, 93, 657. Full text is open at <http://dx.doi.org/10.1007/s11242-012-9976-1>.
- Nakashima, Y., Jinguuji, M. and Sayama, M. 2012. Pore-Scale simulations of the diffusion in the fluid-saturated porous sediments using X-ray microtomographic images, Abstract of the Japan Geoscience Union Meeting 2012.
- Nielsen, L. P., Risgaard-Petersen, N., Fossing, H., Christensen, P. B., and Sayama, M. 2010. Electric currents couple spatially separated biogeochemical processes in marine sediment, *Nature*, 463, 1071.
- Sayama, M. 2001. Presence of nitrate-accumulating sulfur bacteria and their influence on nitrogen cycling in a shallow coastal marine sediment, *Applied and Environmental Microbiology*, 67, 3481.
- Sayama, M., Risgaard-Petersen, N., Nielsen, L. P., Fossing, H., and Christensen, P. B. 2005. Impact of bacterial NO_3^- transport on sediment biogeochemistry, *Applied and Environmental Microbiology*, 71, 7575.
- Sayama, M. 2011. Prevention mechanism of hydrogen sulfide release in eutrophicated coastal marine sediment: possible role of extracellular electron transfer, *Journal of Environmental Biotechnology*, 11, 25 (in Japanese).
- Suzuki, M., Oowada, A., Satou, T., Nagayoshi, K., Inukai, K. and Aoki M. 2011. Preparation of thin section sample of nano-tube aluminium silicate imogolite by a dry method, *Journal of the Clay Science Society of Japan (Nendo Kagaku)*, 50, 63 (in Japanese).

PROCESSING AND CHARACTERIZATION OF POROUS TiNi ALLOYS

G.İpek Nakaş^a, E. Erkan Aşık, Şakir Bor

Middle East Technical University, Department of Metallurgical and Materials Engineering, Türkiye
a. Corresponding author (ipeknakas@gmail.com)

ABSTRACT: In this study, porous TiNi alloys with a porosity content of 64 vol% were processed by sintering with magnesium space holder technique. Prealloyed TiNi powder was used to prevent the formation of brittle secondary intermetallics. Both the powder and porous TiNi alloys were examined by X-ray analyses and SEM studies. According to X-ray analyses, it was found that both powder and processed TiNi foams are fully austenitic (B2) while SEM examination revealed the homogeneously distributed, interconnected, spherical pore structure of TiNi foams. Furthermore, both monotonic and superelastic compression behavior were analyzed at room temperature. It was observed that monotonic compression behavior of TiNi foams was similar to that of cellular metals. On the other hand, TiNi foams were cyclically loaded up to $0.75 \sigma_{\max}$ (75% of ultimate compressive strength) and unloaded to analyze the superelastic response. It was also observed that full recovery of 3% strain was achieved at the end of five cycles of training.

Keywords: *TiNi, foam, compression, superelasticity*

1. INTRODUCTION

TiNi alloys, which were first developed by Naval Ordnance Laboratory, USA, in 1961 [Goldstein, 1978], have attracted considerable attention due to their distinct shape memory and superelasticity properties. While the wide range of applications [Duerig, 1999; Otsuka and Ren, 2005; Petrini, L. and Migliavacca, F., 2011; Kumar and Lakshmi, 2013] of TiNi alloys make them highly appealing, production of TiNi in the porous form further enlarges their application fields [Wen *et.al.*, 2010; Jardine and Cicchi, 2013].

Processing of porous TiNi alloys are generally conducted with powder metallurgical techniques due to their high melting point and highly reactive nature. There are several methods reported in literature for the processing of porous TiNi alloys including hot-isostatic pressing (HIP) [Lagoudas, D.C. and

Vandygriff, E.L., 2002; Yuan *et.al.*, 2006], self-propagating high-temperature synthesis (SHS) [Wisutmethangoon *et.al.*, 2009; Resnina, N. and Belyaev, S., 2011], spark plasma sintering (SPS) [Zhao *et.al.*, 2005], metal injection molding (MIM) [Bram *et.al.*, 2011], sintering with space holder [Bansiddhi, A. and Dunand, D.C., 2007; Nakaş *et.al.* 2011; Zhang *et.al.*, 2013;], etc. The main drawback of the methods such as SHS, which employ elemental powders for processing TiNi foam, is the formation of secondary intermetallics and oxide phases. The secondary intermetallics as well as oxide phases degrade the mechanical response as well as increase the possibility of Ni release during implant applications. The methods such as HIP, MIM and SPS, on the other hand, require high cost equipment for manufacturing. Among the mentioned methods, sintering with space holder technique from prealloyed powder seems to be best for the prevention of unwanted phases in addition to the close control of the shape, size and distribution of pores.

Accordingly, sintering with space holder technique was employed to process Ti-50.8 at%Ni foams in this study. Magnesium (Mg) was employed as the space holder both due to its higher oxygen affinity and lower boiling temperature than that of sintering.

Both powder and porous TiNi alloys were examined by X-ray diffraction (XRD) analyses and scanning electron microscope (SEM) studies. Moreover, produced TiNi foams with 64 vol% porosity were also mechanically characterized with both monotonic compression and compression superelasticity tests.

2. MATERIALS AND METHODS

In this study, porous TiNi alloys with a porosity content of 64 vol% were processed by sintering with Mg space holder technique. Spherical Mg powders (99.82% purity, TangShanWeiHao Magnesium Powder Co. LTD., Tangshan, Hebei Province, China) were sieved to a size range of 250-600 μm . Prealloyed TiNi powder ($\sim 19 \mu\text{m}$, Ti-50.8 at%Ni, 99.9% purity, Nanoval GmbH & Co. KG, Berlin, Germany) was used to prevent the formation of brittle secondary intermetallics.

TiNi powder was mixed with 70 vol% Mg with the aid of 5 wt% polyvinyl alcohol solution (2.5 wt% PVA+ distilled water) as binder and compacted under 400 MPa pressure to obtain cylindrical specimens having 10 mm diameter and aspect ratio of 1.

The compacts were sintered at 1200 $^{\circ}\text{C}$ for 2 hours in an atmosphere controlled vertical tube furnace. High purity (99.999% purity, N₂: 6.2 vpm, O₂: 2.2 vpm, humidity: 2vpm) Argon gas was used for atmosphere control during sintering in order to prevent oxidation.

Porosity content of TiNi foams was measured according to the Archimedes'

principle by use of a precision balance equipped with a density measurement kit. SEM (Jeol JSM 6400, Tokyo, Japan) was utilized for the conformation of raw powder shape as well as the extent of sintering and pore structure of the processed TiNi foams. The phases present at room temperature in as-received TiNi powder as well as processed porous TiNi alloys were determined via XRD analyses using a conventional diffractometer (Cu-K α , Rigaku D/Max 2200/PC, Rigaku Corporation, Tokyo, Japan).

Both monotonic and superleastic compression behavior of processed porous TiNi alloys were analyzed with a 100 kN capacity screw driven mechanical tester (Instron 5582, Instron Co. LTD., Norwood, USA) at room temperature. Strain measurements were conducted with a non-contact video extensometer (Instron 2663-821, Instron Co. LTD., Norwood, USA). All of the mechanical test samples were 10 mm in diameter and height.

3. RESULTS AND DISCUSSION

3.1. Characterization of Powders

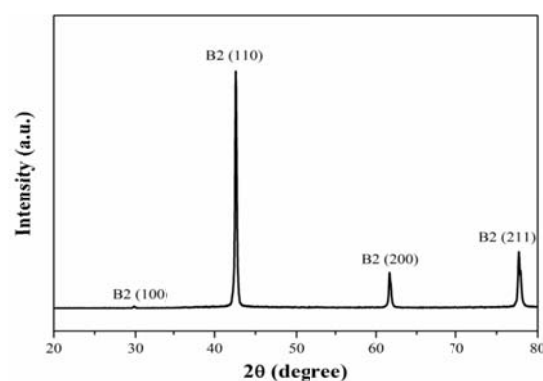
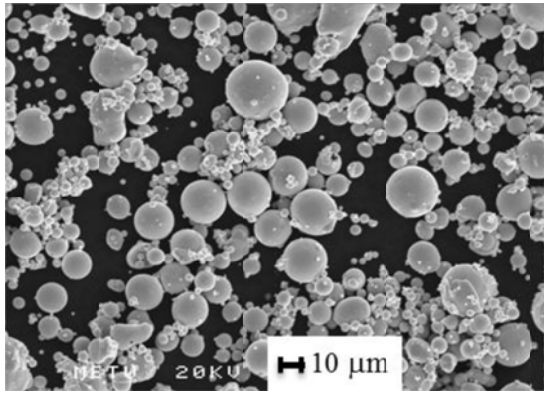
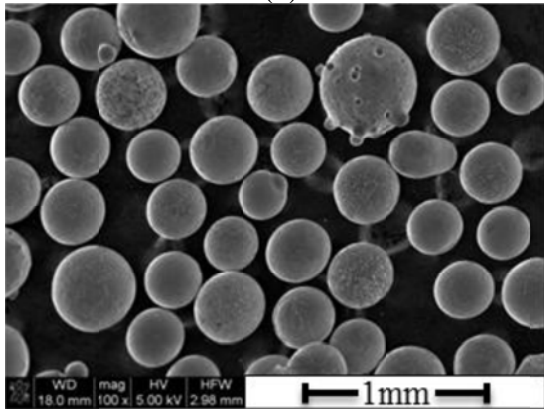


Figure 1: XRD analysis of prealloyed Ti-50.8 at%Ni powders.

XRD analysis indicated that TiNi powder is in fully austenitic state (Figure 1) at room temperature. On the other hand, SEM analyses confirmed that both of the powders have spherical shape (Figure 2).



(a)



(b)

Figure 2: SEM micrographs revealing the morphology of (a) TiNi and (b) Mg powders.

3.2. Characterization of Processed TiNi Foams

Although 70 vol%Mg was added to TiNi powder, it was found that the porosity of the processed TiNi foams was 64 vol%. The lower porosity attained was attributed to the shrinkage of microporosity in the struts (cell walls) during continued sintering resulting in the shrinkage of macropores created by the evaporation of magnesium. The evaporation of magnesium during sintering have resulted in spherically shaped macropores with interconnections as revealed by SEM micrograph (Figure 3).

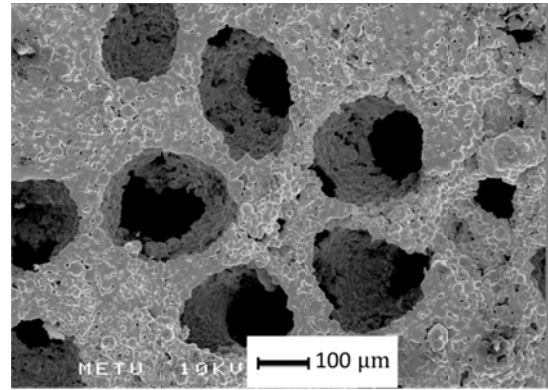


Figure 3: SEM micrograph indicating the interconnections between macropores.

XRD analysis indicated that the processed TiNi foams were in fully austenitic state after sintering while oxidation and/or formation of secondary intermetallics have been found to be prevented (Figure 4). MgO peaks in Figure 4 were found to be due to the residual trapped MgO particles which could be easily removed by a post-sintering dilute HCl treatment without degrading TiNi foam.

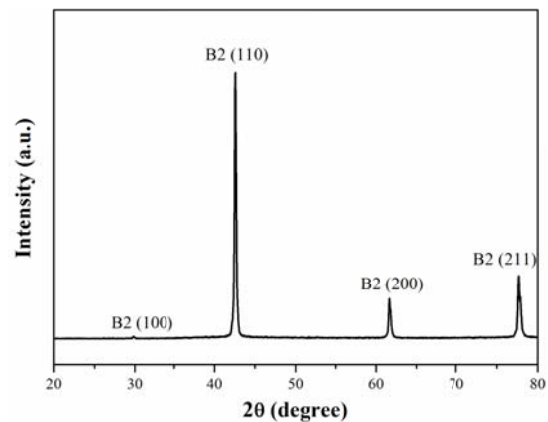


Figure 4: XRD analysis result of sintered Ti-50.8 at%Ni foam.

The monotonic compression tests were conducted by measuring the stress with respect to the strain at a constant crosshead speed of 0.1 mm/min. As given in Figure 5, instead of a sudden collapse of the structure, it was observed that strength was reduced gradually displaying plateaus. The observed deformation behavior is believed to be due to the inhomogeneous deformation, which arose from the differences between the orientation and size of different struts. As the deformation

proceeds, struts and/or strut groups that exceed the ultimate strength due to their favorable orientation and/or size locally collapses, and after the failure of each such struts a small plateau region was reached with the transient stiffening of these regions with lower porosity up to the failure of another strut or strut group.

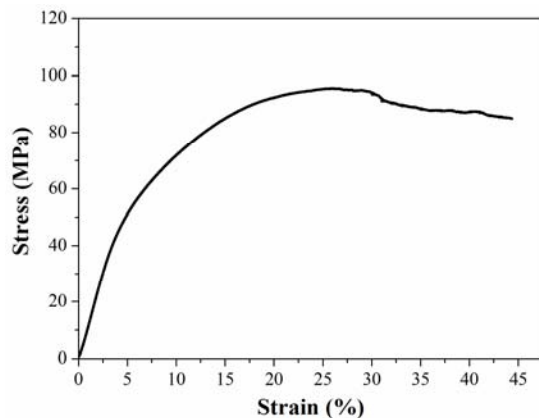


Figure 5: Monotonic compressive behavior of processed TiNi foam.

Superelasticity of porous TiNi alloys, on the other hand, was characterized under compression with load controlled tests via the application of loading-unloading cycles up to 70 MPa (75% of ultimate compressive strength) at a stress rate of 10 MPa/min.

As it is obvious from Figure 6, full recovery of strain cannot be attained at first cycle of loading-unloading. As in the case of monotonic compression, some of the struts undergo to plastic deformation due their misorientation while the other display martensitic transformation under applied loading. Accordingly, full recovery cannot be observed. However, if the loading-unloading cycles are repeated at the same stress level, full recovery can be achieved. These repeated cycles are called as training and the reason behind full recovery after training is that irreversibly deformed regions of the specimen became inoperative at each step so that remaining portions of the specimen exhibit only martensitic transformation upon loading at the later cycles. As it can be seen from

Figure 6, full recovery of 3% strain was achieved after training TiNi foams with 64 vol% at 70 MPa.

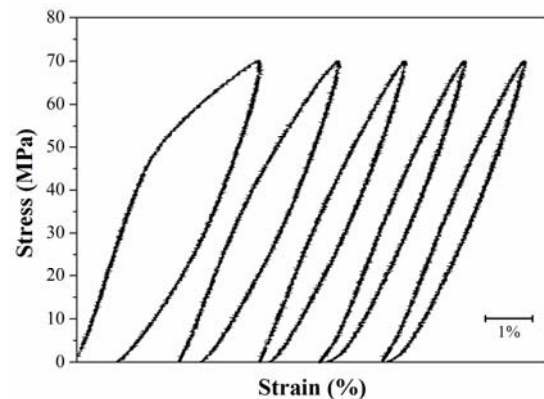


Figure 6: The consecutive stress-strain curves of TiNi foams with 64 vol% porosity indicating the role of training at 70 MPa.

4. CONCLUSIONS

In this study, by sintering with Mg space holder technique was employed to produce porous TiNi alloys with 64 vol% porosity. XRD analysis indicate that processed foams were in fully austenitic state while SEM analyses indicated that pores are in spherical shape with irregular edges and have interconnections between them.

Monotonic compression tests have shown that failure occurs gradually leading to enhanced ductility. Moreover, superelasticity tests revealed that full recovery of 3% can be attained after 5 cycles of training.

REFERENCES

- Bansiddhi, A. and Dunand, D.C., 2007. Shape-memory NiTi foams produced by solid-state replication with NaF, *Intermetallics*, 15, 1612.
- Bram, M., Köhl, M., Buchkremer, H. and Stöver, D., 2011. Mechanical Properties of Highly Porous NiTi Alloys, *Journal of Materials Engineering and Performance*, 20, 522.
- Duerig, T., 1999. An Overview of Nitinol Medical Applications, *Materials Science and Engineering A*, 273-275, 149.
- Goldstein, D., 1978. A Source Manual for Information on NITINOL and TiNi, Naval Surface Weapons Center. NSWC/WOL/TR-78-26.

- Jardine, P. and Cicchi, M., 2013. Foam Nitinol Torque Tubes as High Power Density Actuators, 24th Advanced Aerospace Materials and Processes.
- Kumar, S.M. and Lakshmi, M.V., 2013. Shape Memory Alloys and its Application in MEMS Devices, *International Journal of Current Engineering and Technology*, 3, 292.
- Lagoudas, D.C. and Vandygriff, E.L., 2002. Processing and Characterization of NiTi Porous SMA by Elevated Pressure Sintering, *Journal of Intelligent Material Systems and Structures*, 13, 837.
- Nakaş, G.İ., Dericioğlu, A.F. and Bor, Ş. 2011. Fatigue Behavior of TiNi Foams Processed by the Magnesium Space Holder Technique, *Journal of the Mechanical Behavior of Biomedical Materials*, 4, 2017.
- Otsuka, K. and Ren, X., 2005. Physical Metallurgy of Ti–Ni-Based Shape Memory Alloys, *Progress in Materials Science*, 50, 511.
- Petrini, L. and Migliavacca, F., 2011. Biomedical Applications of Shape Memory Alloys, *Journal of Metallurgy*, 2011, Article ID 501483.
- Resnina, N. and Belyaev, S., 2011. Influence of Annealing on Martensitic Transformations in Porous TiNi-Based Alloys Produced by Self-Propagating High-Temperature Synthesis, *Journal of Alloys and Compounds*, doi:10.1016/j.jallcom.2011.10.118
- Wen, C.E. Xiong, J.Y., Li, Y.C. and Hodgson, P.D., 2010. Porous Shape Memory Alloy Scaffolds for Biomedical Applications: A Review, *Physica Scripta*, T139, 014070.
- Wisutmethangoon, S., Denmud, N. and Sikong, L., 2009. Characteristics and Compressive Properties of Porous NiTi Alloy Synthesized by SHS Technique, *Materials Science and Engineering A*, 515, 93.
- Yuan, B., Chung, C.Y., Huang, P. and Zhu, M., 2006. Superelastic Properties of Porous TiNi Shape Memory Alloys Prepared by Hot Isostatic Pressing, *Materials Science and Engineering A*, 438, 657.
- Zhang, X.X., Hou, H.W., Wei, L.S., Chen, Z.X., Wei, W.T. and Geng, L., 2013. High Damping Capacity in Porous NiTi Alloy with Bimodal Pore Architecture, *Journal of Alloys and Compounds*, 550, 297.
- Zhao, Y., Taya, M., Kang, Y. and Kawasaki, A., 2005. Compression Behavior of Porous NiTi Shape Memory Alloy, *Acta Materialia*, 53, 337.

DEVELOPMENT OF ANTICORROSION COMPOSITE POLYMER MATERIALS AND COATINGS BASED ON THEM WITH USING POWDERY WASTES OF VARIOUS PRODUCTIONS

Sayibjan Negmatov¹, Khamza Shodiev¹, Madina Babakhanova¹,
Jahongir Negmatov¹, Mukhida Babakhanova¹, Malika Negmatova¹,
Bakhodir Sobirov¹, Lola Nosirova¹

1. State Unitary Enterprise "Fan va Taraqqiyot", Tashkent State Technical University, Uzbekistan
a. Corresponding author: (polycomft2005@rambler.ru)

ABSTRACT: The paper demonstrates corrosion composite polymeric materials based on epoxy resin ED-20 and powder coatings using fillers from wastes of various industries, such as phosphogypsum (PG), fosfoshlak (FSH), kaolin, bentonite, gold processing plant waste Marjanbulak Navoi Mining and Metallurgical Combine (OZIF), and as a plasticizer gossipol resin (HS).

During the filling of the active ingredients and the mechanically activated powder is hardening of the polymer matrix, providing a high homogeneity and improves physical, mechanical and performance properties. Inhibition of transport of substances through the film, when filling in the first place, the result of increasing the rigidity of the molecular chains and reduce the rate of relaxation processes. Therefore, corrosion resistance of developed coatings is improved.

Thus it can be concluded that the coating using the mechanically activated powder production waste can significantly improve the physical and mechanical properties and reduce the time of the curing compositions. The use of local raw materials and waste products for corrosion protection coatings enables effective reduction in the cost of anticorrosive protection and operating costs with a high degree of reliability and durability of the equipment required in aggressive environments.

1. INTRODUCTION

Corrosion of metal is essential. Annually due to corrosion is lost a lot of metal. Thus, in Russia annual direct damage caused by corrosion, comes to Rs 15-16 billion in the U.S. - 13-14 billion dollars, Germany - 10-11 billion. Particularly acute problem of corrosion control in process industries where metals and other materials in aggressive environments.

The use of expensive corrosion-resistant materials, alloys and metallization coatings are not always justified because the materials themselves are rather scarce and requires a special expensive equipment for their implementation, and, in addition, these materials only work in

certain corrosive environments and can corrode in other harsh environments.

To prevent corrosion of equipment in the chemical, food and petroleum industries as well as in engineering is widely used various corrosion resistant composite polymeric coating.

The most promising and affordable for corrosion protection of metals production equipment, are anti-corrosion coatings based on polymer materials.

Despite much research in the field of creation of highly corrosion-resistant coatings composite polymeric materials that can be used in hostile environments

studied enough and today remains a very important issue.

Composite polymeric materials based on epoxy resins are common in the industry due to the high physical, chemical and mechanical properties. Depending on the filling, mix the data can be used as anti-corrosion coatings for metal substrates. It is important to establish how it is influenced by the structure of the material.

Therefore, the aim of this work is to study the mechanism and the establishment of the laws of chemical coating damage in harsh environments and development of additional effective anticorrosive composite coatings with the use of local raw materials and powder fillers of various waste facilities, providing high quality with affordability and low cost the coating material.

The object of the study, we chose epoxy oligomer ED-20 (GOST 10587-84), polyethylene polyamine (PEPA).

It is known that epoxy compositions based on ED-20 most commonly used as coatings, varnishes, adhesives. However, the film-forming coatings of non-modified epoxy resins are characterized by low physical-mechanical and thermal performance. Low heat resistance and impact resistance, and the lack of elasticity limit the use of epoxy resins as corrosion and insulating coatings. To address these shortcomings in the epoxy introduced modifiers containing different reactive functional groups that improve operational performance epoxy coatings [Lee H. and Neville, 1973; Chernin, 1982; Paken, 1962].

Improve the performance of the coatings can be addressed by regulatory structure: The optimal heterogeneity is achieved through the introduction of particulate filler and plasticizer.

As fillers used powdered ingredients of phosphogypsum (PG), phosphoshlaka (PS), kaolin, bentonite, gold processing plant waste MarzhanbulakNavoi Mining and Metallurgical Combine (OZIF) and as a plasticizer gossipol resin (GR).

The chemical composition of powder filling in the table.

Phosphogypsum (PG) was used as filler. He is an easy adhesive gray with silky shine, addition - loose, structure - mineral, texture - messy and consists mainly CaO , SO_3 , SiO_2 , and small amounts of other oxides. Phosphogypsum humidity ranges from 30 to 40%. In the cured state phosphogypsum breaks easily and is a powder.

Phosphoshlak - departure Shymkent plant phosphate salts, is a uniform light gray glassy solids. Phosphorus is in the glass slag is sometimes found in small amounts in the form of fluorapatite.

Kaolin - or white clay - a mineral that is the gidratied plate aluminum silicate, having the chemical composition: $\text{Al}_2\text{O}_3 \cdot 2\text{SiO}_2 \cdot 2\text{H}_2\text{O}$. Its structure can be described as alternating between a plate tetrahedral SiO_4 and octahedral Al (O, OH) 6, coupled to each other by hydrogen and dipole interaction. When filled with kaolin resin improves the uniformity of the flow, which allows to obtain composite materials and coatings based on them with more uniform properties.

Bentonite - refers to a group of montmorillonite clay, is dedicated to upper glossy deposits, pH of the aqueous suspension of 7-9. chemical composition of bentonite has several unique features.

Table . The chemical composition of powder fillers based on waste products

Fillers	SiO ₂	Al ₂ O ₃	Fe ₂ O ₃	CaO	MgO	CaPO ₄	P ₂ O ₅	Na ₂ O	K ₂ O	PPP	total
PG	10,17	0,63	след.	32,00	0,80	46,64	2,07	0,07	0,12	7,50	100
PS	42,73	2,38	0,16	45,72	3,20	0,25	1,57	0,65	0,30	1,47	99,25
Kaoline	51,20	43,40	2,22	0,21	0,30	0,25	0,70	0,30	0,25	1,17	100
Bentonite	60,56	17,68	3,20	0,69	1,90	-	-	1,44	1,92	12,04	100
OZIF	67,72	12,52	0,16	13,48	0,94	traces	-	1,78	0,72	2,03	99,35

Gossipolovaya resin (HS) - waste oil and fat production. The distillation of fatty acids isolated from cottonseed soapstock, a complicated process of further transformations of gossypol, in particular their interaction with each other nasyshennymi fatty acids and other co-existing substances. As a result, if the distillation of fatty acids lead to a specific mode at 220-2300S, along with the distillation of fatty acids formed gossipol resin. Gossipol resin use as a plasticizer to replace costly dibutyl phthalate.

Samples for research on aggressive resistance as a hostile environment, in accordance with GOST 4104-77, used the solution and sulfuric (H₂SO₄), hydrochloric (HCl), nitric (HNO₃), and acetic (CH₃COOH) acids.

The resulting coating was performed in the laboratory as follows: weigh out the required amount of epoxy resin and heated to 800 ° C or 60 is kept in a vacuum oven for 30-40 minutes to remove air bubbles from the bulk polymer. With constant stirring (15 parts by weight of polymer) plasticizer (gossipol resin) at 40-600C. Mixing time 6-8 minutes. To add liquid mixture mechanoactivated filler and mix again for 6-8 minutes (until smooth). Hardener (PEPA) is added prior to application to the surface of the metal.

Fillers for mechanical activation was set to - dismembrator [Negmatov, 2000] based on the shock-splitting and abrasive action.

Method for studying the chemical stability is based on the determination of the change in mass, linear dimensions, and physical and mechanical properties of standard samples after keeping them in aggressive solutions for some time [Negmatov, 1975; Karjakin, 1988].

The diffusion penetration of aggressive media in composite films were determined by the method of absorption of oxygen in monometrich set [Karjakin, 1988], which allows to register the absorption of oxygen.

2. RESULTS AND ANALYSIS

To move a number of film-forming into a solid and irreversible condition creating the required structure of the polymer film in the coating material is introduced stabilizers, hardeners, fillers, initiators and promoters. Need to use these components determined by the chemical nature of the film former and conditions of coverage.

Improve the performance of the coatings can be addressed by regulatory structure: The optimal heterogeneity is achieved through the introduction of a dispersed particulate filler and plasticizer.

In this case, there are significant changes in the physical-chemical and mechanical properties of the resulting composites, due to change in the mobility of the macromolecules in the boundary layers, the orienting effect of the surface of the filler, different kinds of interaction between polymers with her, and by the

effect of fillers on the chemical structure and the structure of polymers formed in their the presence of curing and polymerization of the monomers or oligomers. It should be noted that the chemistry of the surface of the fillers is important in determining the nature of the interaction of polymers with filler

Introduction to polymer powder production wastes with certain chemical properties of the surface can lead to an acceleration or inhibition of the various stages of the process of destruction and change the chemistry of these reactions. It is becoming increasingly clear that the particulate fillers act as heterogeneous components of high-temperature chemical processes of polymer degradation occurring at the interface between the polymer-filler.

Great influence on the permeability of coatings have fillers, while important are their nature, volume fraction, particle size and shape, the degree of interaction with film-formers. Inhibition of transport of substances through the film, when filling in the first place, the result of increasing the rigidity of the molecular chains and reduce the rate of relaxation processes.

By mechanical activation of solid carriers have increased the number of free radicals on the surface of the particles. Mechanical activation of solid and liquid systems leads to a significant change of structure-sensitive properties of the activated systems usually occur at the interfaces of mechanical-chemical reactions with atmospheric constituents.

Brittle fracture of crystalline materials (split and grinding) occur mainly along the boundaries of clusters of impurities and defects. Moreover, it can be noted that the newly formed surfaces in brittle

fracture are inactive defect-free areas, accompanied by brittle fracture.

Destruction in aggregates impact type leads to a more active defective surface than the split or milling. The surface is covered with powdered solids coating of impurities, which in the future and focused electrical charges determines the chemical properties of the crushed material. This, obviously, can be explained by the stability properties of substances after mechanical activation. The use of mechanically activated fillers can significantly reduce the time of formulation, providing a high homogeneity of the system and improve the range of their physical and operational properties.

It should be noted that the size reduction of solids, accompanied by the formation of a new surface during grinding, accompanied by friction solid particles from each other. In this case, the active centers on the surface of the crushed material, may occur as a result of splitting particles, and in the process flow of the tribological reactions. This increases the contact matrix with filler (particle size of 5 to 20 microns).

In studying the chemical resistance of composite materials, used as a coating, one of the important criteria of their resistance is to change the adhesive strength in aggressive environments. Especially effective is the use of this criterion in the evaluation of the protective properties of coatings as diffusion permeability and internal stresses.

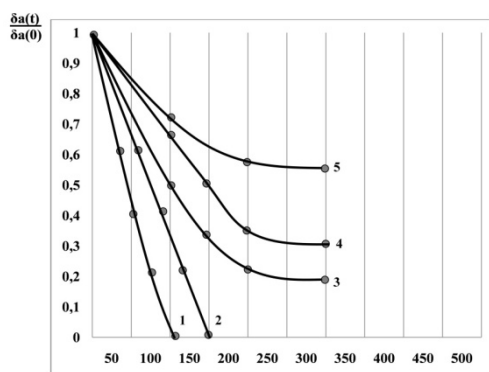
Study of the dependence of adhesive strength unfilled epoxy resin compositions based on ED-20 from the action of aggressive environment showed that the adhesive strength of the coating is reduced in all cases, namely, in sulfuric acid - 40, in the water - at 60, in

hydrochloric acid - 70 % relative to the value of adhesive strength when exposed to these environments, more than 10 days in the air. Cover has completely lost adhesion in nitric and acetic acid for 10 and 6 days, respectively, as a result of degradation of polymers at the interface of polymer-substrate (Figure 1).

Figure 2 shows the change in the adhesive strength of the filled coatings 40 % H_2SO_4 .

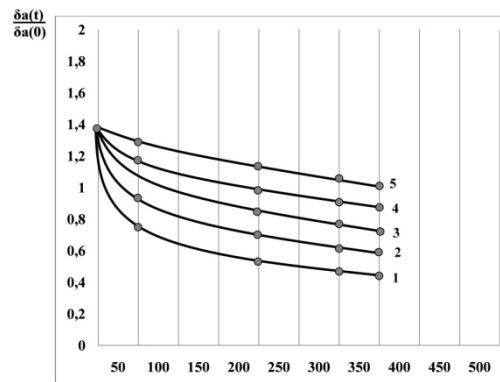
Therefore, analyzing the changes adhesive strength can be judged on the permeability of coatings, the nature of the chemical interaction between the substrate and aggressive media.

The presence of pores and micro-defects in unfilled coatings (they controlled electron microscope) promotes the accelerated penetration of aggressive media in the interior of the material, increasing the area of contact with the medium of film-forming layer, accelerating the flow of the following processes: chemical degradation, sorption components aggressive environment, dissolution sol fraction of film-forming layer desorption of a polymer material of various additives, changes to the physical structure of the material.



1 - 50% - CH_3COOH , 2 - 40% - HNO_3 ; 3-25% - HCl ; 4 - H_2O ; 5-40%- H_2SO_4

Figure 1. Changing the adhesive strength of unfilled coatings based on ED-20 in a variety of harsh environments



1 - Filled with phosphogypsum, 2 - Filled with phosphoshlak; 3 - Filled with kaolin, 4 - Filled with bentonite; 5 - Filled with OZIF

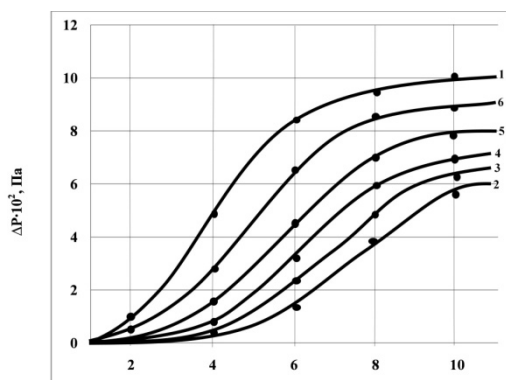
Figure 2. Changing the adhesive strength of the filled coatings based on ED-20 in 40% - H_2SO_4

Under the structure of the activity of powdered filler understand its ability to influence the structure of the polymer, which leads to changes in the characteristics of the supramolecular structure formation at one or more levels of supramolecular organization, or only in the packing density (change in the relationship between disordered and ordered parts of the polymer). Possible effect of the filler on all of the structural characteristics of both. Structural active filler can have a certain orientation (the form of) affect mainly on supramolecular structure and the relative density of packing of the polymer.

In forming coatings of paints filming often takes place with the absorption of oxygen and the release of volatile products. Therefore, in determining the degree of curing of coatings of this type is necessary to continuously measure the amount of oxygen absorbed in the process of film formation and capture volatile oxidation products formed for further qualitative and quantitative analysis.

The kinetics of vapor absorption of hydrochloric acid was investigated by

recording the change in its vapor pressure (Figure 3). For unfilled composites with increasing vapor pressure of HCl absorption rate of its vapor increases. The highest rate of absorption of the vapor pressure of HCl observed at 19-20 kPa. It is seen that in all cases, the rate of oxygen absorption filled sample is less than the unfilled composite. It can be seen that as the concentration of oxygen increases the rate of oxygen absorption.



2 - 25 mass.p.waste (OZIF) 3 - 25 mass.p. bentonite; 4 - 25 mass.p.kaolin, 5 - 25 mass.p.phosphogips; 6-25% phosphoshlak

Figure 3. The kinetics of oxygen uptake during curing compositions based on ED-20 unfilled (1) and filled with a variety of powdered fillers at $T = 293-298K$, $P_{O_2} = 1,9 \cdot 10^4 Pa$

In this case, the rate of vapor absorption of HCl in the reaction increases, so that the curves become S-shaped. Fillers retard the oxidation and the rate of oxygen consumption in the deep stages after the induction period does not change. In forming the coating filled with 25% powdered kaolin, bentonite and OZIFom resin which shows good adhesion, in the layers of coatings, bordering both the substrate and the air, there are structural elements oriented fibrillar type near the filler particles.

In all cases, the rate of oxygen consumption of the filled sample is less than the unfilled sample. When filled

composite with industrial powder wastes stabilization effect is improved.

3. CONCLUSIONS

Thus, we can conclude that with the use of powder coating ingredients of industrial waste can significantly reduce the curing compositions are hardening of the polymer matrix, providing a high homogeneity of the system and improve the physical, mechanical and performance properties. The use of local raw materials and waste products of powder for anticorrosion coatings enables effective reduction in the cost of anticorrosive protection and operating costs with a high degree of reliability and durability of the equipment required in aggressive environments.

REFERENCES

- Lee H., Neville K, Handbook on epoxy resins. trans. from English. / Edited by. Aleksandrova N.V.. - Moscow: Energiya, 1973. - 415 p.
- Chernin I.Z, Smekhov FM, Zherdev Y. Epoxy resins and compositions. - M.: Chemistry, 1982. - 232.
- Paken A.M. Epoxies and epoxy resins. trans from Deutsch. / Edited by. L.S.Efrosa. - L.: Goskhimizdat 1962. - 963 p.
- Negmatov N.S. Developing an effective technology for high-wollastonite filler and creation of multifunctional composite materials applications.: Author. dis ... Candidate of Science. - Tashkent. 2000– 23p.
- Negmatov S. Technology for producing coatings. - Tashkent, Uzbekistan, 1975. – 23p.
- Karjakin M. Testing of coatings and materials. - M.: Chemistry, 1988. – 276p.

PRODUCTION AND CHARACTERIZATION OF CHITOSAN/PEO POLYMER NANOFIBERS USING ELECTROSPINNING TECHNIQUE

Nihan Tuğçe Nergiz^{1,a}, Hande Çelebi²

1. Advanced Technologies Research Unit, Program in Nanotechnology, Anadolu University, Eskişehir, Turkey
2. Department of Chemical Engineering, Anadolu University, Eskişehir, Turkey
a. nnergiz@anadolu.edu.tr

ABSTRACT: Chitosan (CS) is a biodegradable natural polymer that is soluble in concentrated acid solutions. It is difficult to obtain nanofibers from pure chitosan solution, therefore synthetic polymers and surfactants are used in order to improve pure chitosan nanofiber morphology. In this study, poly(ethylene oxide) (PEO) was chosen as a co-spinning agent due to its positive properties such as water-solubility, linear structure, biocompatibility etc. A surfactant and a co-solvent was added to improve the morphology of nanofibers. The effect of CS/PEO blend ratio, applied voltage and flow rate on the morphology of nanofibers was investigated. The eletrospun nanofibers were characterized by using SEM (Scanning Electron Microscopy), DSC (Differential Scanning Calorimetry) and TGA (Thermo Gravimetric Analysis).

1. INTRODUCTION

Electrospinning process allows producing nanofibers from a variety of pure polymer and polymer blend solutions. The electrospun nanofibers are highly porous materials due to their high surface area to- volume ratio. This unique property forms the basis of wide range of applications for nanofibers from textile to electronics.

Chitosan is a polyaminosaccharide with unique properties like biologically renewable, biodegradable, nonantigenic and biocompatible natural polymer. In this study, CS was blended with a synthetic polymer, PEO in order to improve the electrospinnability of chitosan. PEO is also biocompatible and has low toxicity.

2. MATERIALS AND METHODS

2.1. Materials

The coarse ground flakes and powder of chitosan and poly(ethylene oxide) (PEO) ($M_v = \sim 2.000.000$) were obtained from

Sigma-Aldrich. Triton X-100TM for molecular biology was purchased from Sigma. Dimethylsulfoxide (DMSO) ($M_v = 78.13$ g/mol) was supplied from Acros Organics. Acetic acid (Merck Co.) was used as received.

2.2. Solution Preparation

CS/PEO blend solutions were prepared in different compositional weight ratios of 90/10, 75/25 and 50/50. 2 wt.% CS solution in 2 wt. % acetic acid was prepared with 0.5% Triton X-100 and 10% DMSO. The PEO solution (3 wt. %) was prepared in distilled water. Solutions were stirred under magnetic stirring overnight to obtain a homogenous solution.

2.3. Rheological Measurements

The viscosity and conductivity of solutions were determined with Rheometer Bohlin Gemini-200. The viscosity of solutions was measured at 25°C with shear ramp mode at controlled

rate. The conductivity of the solutions was determined at room temperature with Sartorius Professional Meter PP-20. The average of at least three measurements was taken in order to determine the conductivities of the solutions.

2.4. Electrospinning of CS-PEO Solutions

A schematically electrospinning setup is presented in Fig.1.

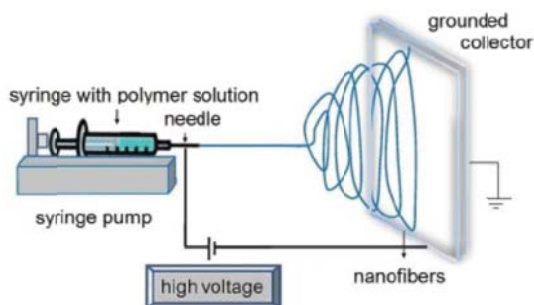


Figure 1: A schematical illustration of electrospinning setup [Rošicet. al. 2012].

The blend solution was loaded in a 5 mL syringe with a metal capillary needle. The DC voltage between 15-30 kV was applied between the syringe tip and the collector covered with aluminum foil. The typical distance between the syringe tip and the grounded collector was ranging between 10-20 cm.

2.5. Morphology of Electrospun Nanofibers

The surface of the electrospun nanofibers were investigated by SEM (Zeiss Evo 50). Electrospun nanofiber surfaces were sputter-coated with Au/Pd before SEM analysis.

2.6. Thermogravimetric Analysis

TGA analysis was carried out with TA Instruments TGA Q500 Analyzer. The experiments were run at a scanning rate of 10°C/min from 25 to 800°C.

2.7. Differential Scanning Calorimetry

DSC measurements of pure CS and blend films were carried out using a TA

Instruments DSC Q2000. The samples were heated from 25 to 250 °C with a heating rate of 10°C/min.

3. RESULTS AND DISCUSSION

3.1. The Effect of the Solution Composition and Surfactants on the Solution Properties

The formation of nanofibers from neat chitosan is a challenging process, therefore PEO was added to CS solution indifferent weight fractions. The solution properties of CS and PEO effects the spinnability and morphology of spinned fibers [Sonet. al., 2004]. The solution properties such as conductivity, surface tension and viscosity show that the interactions of polymer-polymer and polymer-solvent are the major factors in electrospinning process. [Kriegel et. al. 2009]. It is known that the addition of surfactants into the polymer blends, improves the morphology of obtained nanofibers. The viscosity and conductivity values of CS/PEO blend solutions are shown in Table 1 and 2.

Table 1: The viscosity and conductivity values of CS/PEO blend solutions without additive Triton X-100 and DMSO.

CS/PEO blendratio	Conductivity (mS/cm)	Viscosity (Pa.s)
100/0	1.867	1.275
90/10	1.767	1.534
75/25	1.267	1.822
50/50	1.100	1.962
0/100	0.980	2.363

Table 2: The viscosity and conductivity values of CS/PEO blend solutions with additive 0.5% Triton X-100 and 10% DMSO.

CS/PEO blend ratio	Conductivity (mS/cm)	Viscosity (Pa.s)
100/0	3.700	1.198
90/10	1.467	1.562
75/25	1.190	1.745
50/50	1.033	3.063

It is seen that in Table 1, the viscosity of the solutions increases with increasing PEO proportion in blend. And conductivity of blend solutions decreases with increasing PEO. Adding surfactant (Triton X-100) and co-solvent (DMSO) increases the conductivity of pure chitosan solution, on the other side it reduces CS/PEO blend solution. The reason of the decrease in the conductivity may be due to the CS/PEO blends contain less of polyionic polymers (chitosan) and more of the uncharged PEO compared to pure chitosan solution.

Viscosity is an important characteristic of the intermolecular interactions between polymer chains in the polymer solutions. Due to the strong hydrogen bonding between NH₂ and OH groups in chitosan polymer chains, chitosan has high viscosity. With the addition of synthetic polymers like PEO, inter and intramolecular interactions modifies on chitosan backbones. In theory, PEO molecules disrupt the chitosan chains by forming new hydrogen bonding between its OH groups and water molecules [Bhattari *et. al.*, 2005]. Because of the increasing intermolecular interactions between polymers, the viscosities of the solutions are also increases, as seen in Table 1 and 2.

Conductivity is another important factor, which effects electrospinnability. The increase in the PEO content results in the decrease of the conductivity as seen in the Table 1 and 2.

3.2. Electrospinning of the Solutions

The optimized conditions for nanofibers were determined as 20 kV voltage, 20cm tip-collector distance and 0.010 ml/min flow rate.

The SEM images of the electrospun nanofibers are shown in Figures 2-4.

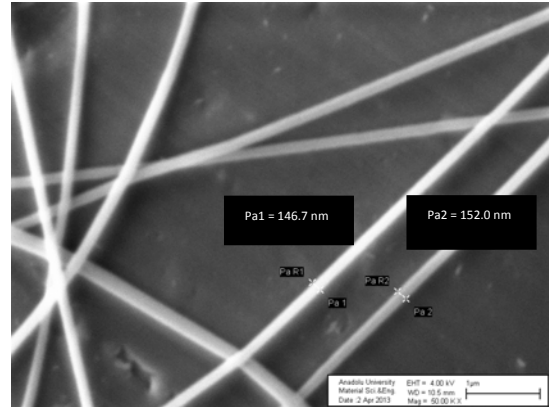


Figure 2: (90/10) CS/PEO nanofibers at magnification 50KX.

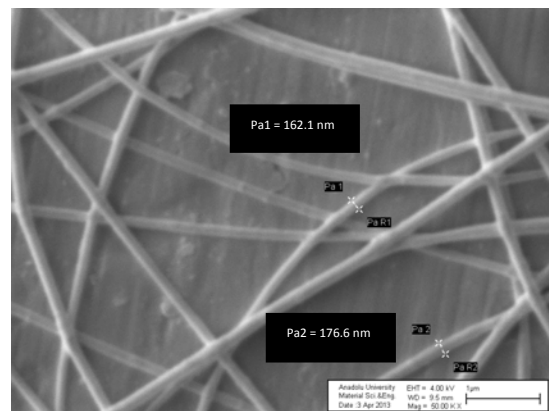


Figure 3: (75/25) CS/PEO nanofibers at magnification 50KX.

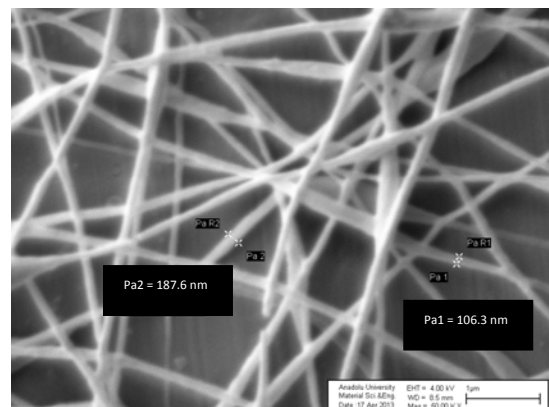


Figure 4: (50/50) CS/PEO nanofibers at magnification 50KX.

It is seen that the morphology of the blend fibers are related to directly to the compositional fractions of solutions. Fiber diameters are increased with increasing PEO content in the blend. As seen in Figure 2, (90/10) CS/PEO nanofibers has the lowest diameter. The

reason was that the addition of chitosan results in a higher charge density on the jet surface because of its ionic character [Abdelrahman *et. al.*, 2012 and Sajeew *et. al.* 2008]. It has been known that the overall tension in the fibers depend on the self-repulsion of the excess charges on the jet. Thus, increasing charge density on the jet leads to the reduced diameter of the blend fibers [Jia *et. al.*, 2008].

3.3. Thermogravimetric Analysis

The TGA analysis confirms the existence of both polymer fractions. Pure chitosan is found to thermally decompose at $\sim 284^{\circ}\text{C}$ and PEO decomposes at $\sim 445^{\circ}\text{C}$. The decomposition degree of blend films shows two distinct peaks. Table 3 represents the decomposition temperatures of samples.

Table 3: Decomposition degrees of pure chitosan, PEO and blend films

Samples	First Decomposing Temperature ($^{\circ}\text{C}$)	Second Decomposing Temperature ($^{\circ}\text{C}$)
Pure Chitosan	284	-
(90/10) Chitosan/PEO	293	439
(75/25) Chitosan/PEO	292	419
(50/50) Chitosan/PEO	289	417
Pure PEO	445	-

As the PEO content increases in the blend solutions, PEO's decomposition temperature slightly decreases. Figure 5 represents the TGA results of prepared samples.

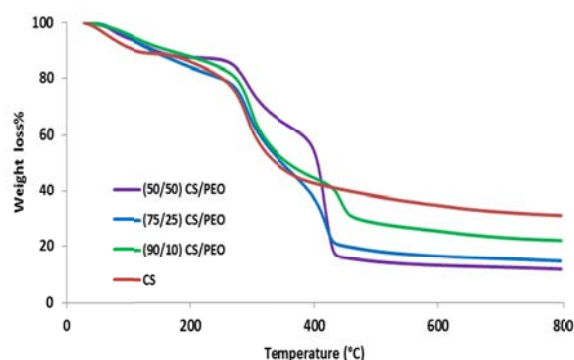


Figure 5: Thermogravimetric analysis of film samples.

3.4. Differential Scanning Calorimetry Analysis

The melting temperature and melting enthalpy values of the samples are shown in the Table 4.

Like chitosan, many polysaccharide do not demonstrate melting but they degrade above a certain temperature. Thus their DSC peaks show broad endotherms which is associated with water evaporation below the degradation [Duan, *et.al.*, 2004]

In DSC investment of samples chitosan and chitosan blend films, it gives a broad peak at $\sim 116^{\circ}\text{C}$. Very similar broad peak also seems at CS-PEO blend films but due to the presence of PEO content, their heat flow datas gives a second peak. All the appeared second peak degrees are below the PEO's melting temperature ($\sim 65^{\circ}\text{C}$) and as PEO content increases, second peak degree is also increases. This may causes from the increasing hydrogen bondings between the chitosan's amino/hydroxyl group and PEO ether groups [Chen *et.al.*, 2008].

Table 4: Melting temperature and melting enthalpy values of pure chitosan, PEO and blend film samples.

Samples	T _{m,1} (°C)	T _{m,2} (°C)	ΔH _{m,1} (J/g)	ΔH _{m,2} (J/g)
Pure CS	116	-	39	-
(90/10) CS/PEO	117	52	80	49
(75/25) CS/PEO	102	52	65	43
(50/50) CS/PEO	98	61	46	50
Pure PEO	65	-	59	-

4. CONCLUSION

Electrospinning is a technique which allows to produce nanofibers from pure and blend solutions. Produced nanofibers are highly porous materials due to their high surface area to- volume ratio. This unique property forms the basis of wide range of applications for nanofibers from textile to electronics. Chitosan is a polyaminosaccharide natural polymer with unique properties like biologically renewable, biodegradable, nonantigenic and biocompatible. Because of the challenging process of producing pure chitosan nanofibers, synthetic polymers are used in blends of chitosan to ease obtaining nanofibers.

In this study, PEO was used as a synthetic polymer due to its biocompatible and low toxicity properties. A variety blend solution CS/PEO was prepared for electrospinning. Solutions were prepared with different weight ratios (90/10, 75/25 and 50/50) of CS and PEO, respectively. After preparing the solutions, their viscosities and conductivities were measured. The results showed that increasing PEO content results in the increment of the viscosity. The nanofibers were characterized by SEM,

TGA and DSC analysis. The morphological analysis showed that the 90/10 CS/PEO nanofibers have the lowest diameter. TGA diagram represented two distinct peaks which lead from the presence of CS and PEO in the samples.

REFERENCES

- Kriegel, C., Kit, K.M., McClements, D.J., Weiss, J., 2009. Influence of Surfactant Type and Concentration on Electrospinning of Chitosan–Poly(Ethylene oxide) Blend Nanofibers, *Food Biophysics* (4), 21
- Son, W.K., Youk J.H., Lee T.S., Park W.H., 2004. The Effects of Solution Properties and Polyelectrolyte on Electrospinning of Ultrafine Poly(ethylene oxide) Fibers, *Polymer* (45), 2959
- Duan, B., Dong, C.H., Yuan, X.Y., Yao, K.D., 2004. Influence of Surfactant Type and Concentration on Electrospinning of Chitosan–Poly(Ethylene Oxide) Blend Nanofibers, *J. Biomater. Sci. Polym. Ed.* 15(6), 797
- Chen, Z., Mo, X., He, C., & Wang, H. 2008. Intermolecular interactions in electrospun collagen–chitosan complex nanofibers. *Carbohydrate Polymers*, (72), 410
- Bhattarai, N., Edmondson, D., Veiseha, O., Matsen, F. A., Zhang, M., 2005. Electrospun chitosan-based nanofibers and their cellular compatibility, *Biomaterials*, (26), 6176
- Rošic, R., Kocbek, P., Baumgartner S., Kristl J. 2012. Electrospun Chitosan/Peo Nanofibers and Their Relevance in Biomedical Application. 5th European Conference of the International Federation for Medical and Biological Engineering IFMBE Proceedings (37), pp 1296.
- Abdelrahman M, Abdelgawad A.M., Hudson S.M., Rojas O.J. (2012). Antimicrobial wound dressing nanofiber mats from multi-component(chitosan/silver-NPs/polyvinyl alcohol) systems. *Carbohydr. Polym.* (in press)
- Sajeev U.S., Anand K.A., Menon D., Nair S. (2008). Control of nanostructures in PVA, PVA/chitosan blends and PCL through electrospinning. *Bull. Mater. Sci.*,(31), 343.
- Jia Y.T., Gong J., Gu, X. H., Kim, H. Y., Dong, J., Shen, X. Y. (2007). Fabrication and characterization of poly(vinyl alcohol)/chitosan blend nanofibers produced by electrospinning method. *Carbohydr Polym.*, (67), 403.

COMPOSITE MEMBRANE SYNTHESIS FOR PERVAPORATION MEMBRANE BIOREACTOR

Filiz Ugur Nigiz^{1,a}, Nilufer Durmaz Hilmioglu¹

1. Kocaeli University, Chemical Engineering Department, Kocaeli, Turkey
a. Corresponding author (filiz.ugur@kocaeli.edu.tr)

ABSTRACT: Bioethanol is sustainable and renewable fuel energy source which is biologically produced by fermentation from biomass. However the production of high purity ethanol has some drawback such as requirement of complex production, separation steps which have high energy consumption. Recently hybrid fermentation – separation processes have been recommended to overcome the cost and efficiency problem. In this system fermentation and ethanol purification steps are carried out simultaneously. This system not only prevents the product inhibition, but also provides high quality ethanol production. In literature there have been numbers of suggested hybrid systems such as azeotropic distillation, extractive distillation and pervaporation coupled by fermentation. Pervaporation is a membrane separation process. The performance of the system is commercially proved by hundreds of alcohol dehydration plant around the world.

Pervaporation membrane bioreactors (PVMBR) is a pervaporation coupled fermentation hybrid process. In PVMBR, ethanol is selectively removed from fermentation broth by polymeric, inorganic or composite membranes. Mostly hydrophobic membrane is preferred to purify the ethanol.

In this study ZSM-5 loaded polydimethylsiloxane composite membrane has been prepared and employed in PVMBR for bioethanol production from molasses. The effect of zeolite loading on ethanol production and purification has been evaluated.

1. INTRODUCTION

Pervaporation (PV) is a membrane-based separation system that ethanol is selectively separated from the fermentation broth [Vane, 2008a, 2008b, Jiang *et al.*, 2008, Sun *et al.*, 2002]. Unlike other membrane processes used in bioreactors, non-porous membranes are used in PV. Therefore, the separation via non-porous membrane depends on the membrane affinity, membrane-solution interaction, hydrogen bonding ability and diffusivities of components into the membrane. PV performance is controlled by the physical structure of membrane, polarity and physicochemical properties of mixture, component-membrane interaction, membrane affinity, and the hydrogen bonding ability [Semenova *et al.*, 1997, Mulder, 1996]. In this system,

driving force is concentration gradient which is maintained by pressure difference.

PV has become an important process since 1982 and it is used commercially followed areas;

- i) dehydration of organic solvents
- ii) removal of dilute organic components from aqueous stream
- iii) organic-organic mixture separation

A basic vacuum PV system has been shown in figure 1.

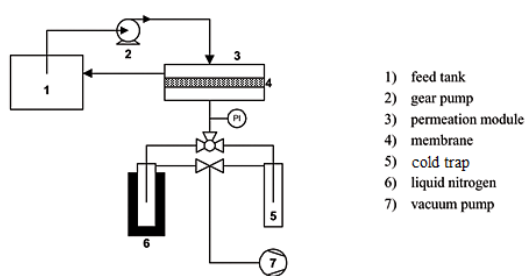


Figure 1: Experimental PV system [Ribeiro *et al.*, 2004]

It consists of vacuum and feed pumps, feed tank, membrane cell and cold traps. The mixture is fed to the membrane cell. One of the components preferentially removed from the mixture due to the affinity of membrane. The component selected by the membrane diffuses through membrane. Selected component which is called as permeate, passes through membrane and desorbed as vapor phase. Then the vapor product condenses in cold traps [Pereira *et al.*, 2005, Liu *et al.*, 2011, Santosh 2010].

Separation via pervaporation with non-porous membrane is mainly determined and explained by the solution-diffusion model.

Sorption depends on the hydrogen bonding interest of water in active channels and the diffusion depends on structural parameters of such as intermolecular channel distribution and diameters. During the membrane separation process the solvent which interact inside, changes the physical and chemical stability of membrane material. It is important that select appropriate membrane to overcome stability problem and increase membrane flux and selectivity. In PV inorganic, polymeric and composite membranes are used. Inorganic membranes are used commercially due to mechanical strength, temperature and chemical stability. Polymeric membranes are cheap, easy to operate, flexible but not have resistance to temperature. The factors that affect the component transition in the polymer

matrix are polymer crystallinity, glass transition temperature, melting point, tortuous pathway (in zeolite filled membrane) and thickness.

Pervaporation membrane bioreactors (PVMBR) is a reactive separation system contains fermentation and pervaporation unit. There are two kind of PVMBR; internal system in which the selective PV membrane is employed inside the fermenter, and external system which the pervaporation is established after the fermenter. Figure 2 and 3 shows the internal and external PVMBR system separately [Ding *et al.*, 2011, Esfahaniana *et al.*, 2012, Chen *et al.*, 2012].

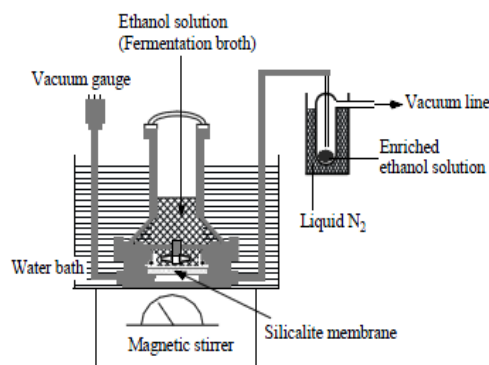


Figure 2: Internal PVMBR [Ikegami *et al.*, 2003]

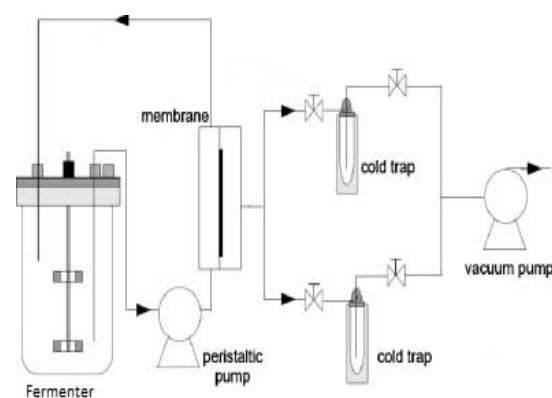


Figure 3: External PVMBR [Modified from Hyder *et al.*, 2009]

In this study, an internal PVMBR system has been used to bioethanol production from molasses and ethanol purification.

Pristine and ZSM-5 filled PDMS membrane have been used to separate ethanol from fermentation broth. *Saccharomyces cerevisiae* has been used as yeast.

2. MATERIALS AND METHODS

2.1 Material

PDMS has been kindly supplied from the Plastics and Rubber Processing Laboratory at Kocaeli University. Toluene, dicumylperoxide have been purchased from Merck Chemicals. Molasses and *Saccharomyces cerevisiae* have been kindly supplied from PAKMAYA, İzmit.

2.2. Membrane Preparation

A desired amount of PDMS dissolved in toluene and stirred for five hours at 50 °C. Pristine and 20, 30 wt. % of ZSM-5 and about 4 wt. % of DCP (respect to the total polymer weight) were added to solution and stirred for two hours. After a homogeneous solution was obtained, it was poured into a Teflon plate and dried over night. Then polymer film was cured in vacuum oven at 180 °C for five hours.

2.3. Pervaporation Membrane Bioreactor

In PVMBR fermentation was carried out for five hours. The diluted molasses [Goksungur *et al.*, 2001] solution was stated at upstream of the membrane, 10 wt. % of yeast respect to the total sugar weight was added to solution and the reaction has been started one hour later.

Effective membrane area was 28.26 cm², the cell capacity was 500 ml. Upstream of the membrane was kept at atmospheric pressure and downstream of membrane was kept 30 mbar. As the fermentation carried out, ethanol was continuously separated from fermentation broth.

Flux (J) and selectivity (α) are calculated as seen in equation (1) and (2);

$$J = W_p/A.t \quad (1)$$

$$\alpha = (P_w/P_{et}) / (F_w/F_{et}) \quad (2)$$

W_p represents the total permeate weight of mixtures, A is the effective area of membrane and t is the time. P_w and F_w are weight % of water in permeate and feed respectively. P_{et} and F_{et} are the weight % of ethanol in permeate and feed respectively [Nunes *et al.*, 2006]. Permeate and feed composition was obtained by a Gas Chromatograph.

3. RESULTS AND DISCUSSION

Pristine and zeolite filled membranes have been employed in internal PVMBR system. Effects of zeolite loading on membrane flux and selectivity have been investigated.

Figure 4 shows ethanol concentration at broth in the internal PVMBR in which the pristine PDMS membrane is used. System has been reached the steady state condition in five hours.

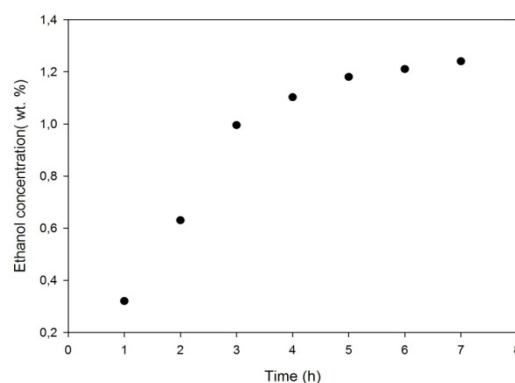


Figure 4: Ethanol concentration in PVMBR

3.1. SEM Analysis

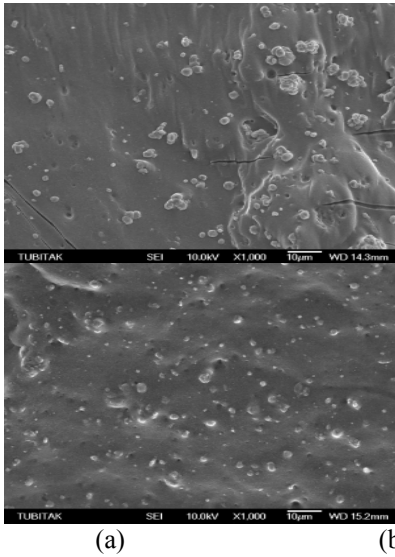


Figure 5: SEM Analysis (Cross-section of 20 wt. % of ZSM-5 (a) and 30 wt. % of ZSM-5 zeolite loaded PDMS)

As seen in figure 5, zeolite particles are homogenously dispersed to PDMS matrix.

3.2. Effect of Zeolite Loading on Flux

Figure 5 shows the total membrane flux change with time and zeolite loading. Due to the hydrophobicity of ZSM-5 total flux has been enhanced as the zeolite loaded increases. Zeolites make the polymeric matrix more durable and stable at the challenging and difficult process conditions. Especially, in biologic reactions in which the microorganism must be used, membrane has to show good resistance to microbial conditions.

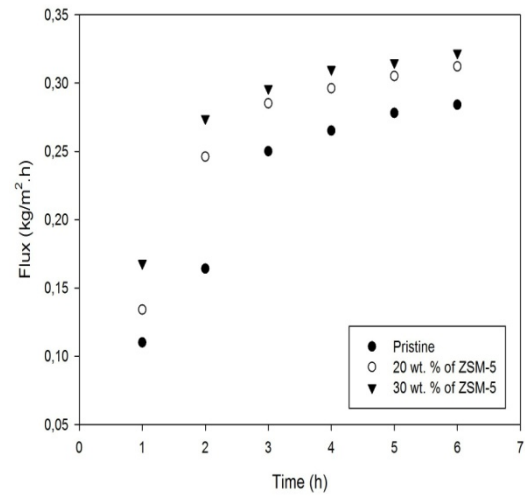


Figure 5: Flux values of PVMBR

3.3. Effect of Zeolite Loading on Selectivity

In most cases, such as alcohol dehydration, selectivity has been enhanced in line with the zeolite loading. The selectivity has been enhanced by the zeolite loading as seen in Figure 6.

Unlike other cases, in this study ethanol production and purification have been carried out simultaneously so they are two factors that affect the membrane selectivity.

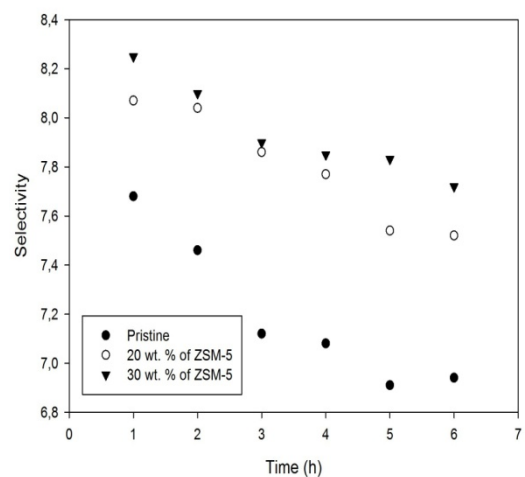


Figure 6: Selectivity values of PVMBR

It is well known that the feed concentration mostly causes an increase in flux and a decrease in selectivity. In

this study ethanol production has been increased with time. Hence a decrease in selectivity can be expected.

4. CONCLUSIONS

In this study innovative PVMBR system has been carried out to produce and purify bioethanol from molasses. Effects of zeolite loading on flux and selectivity have been evaluated. The total flux has been increased by zeolite loading. Moreover, due to the increasing the production of ethanol in broth, selectivity has been decrease by time. These results clearly show the availability of usage of the PVMBR system in practice.

REFERENCES

- C. Chen, X. Tang, Z. Xiao, Y. Zhou, Y. Jiang, S. Fu, 2012, Ethanol fermentation kinetics in a continuous and closed-circulating fermentation system with a pervaporation membrane bioreactor. *Bioresource Technology*. 114, 707–710.
- G. Liu, W. Wei, H. Wu, X. Dong, M. Jiang, W. Jin, 2011. Pervaporation performance of PDMS/ceramic composite membrane in acetone butanol ethanol (ABE) fermentation–PV coupled process. *Journal of Membrane Science*. 373, 121–129.
- H. Jiang, R. Shri, U.W. Tschirner, B.V. Ramarao, 2008. A review of separation technologies in current a future biorefineries. *Separation and Purification Tech.* 62, 1-21.
- J.R. Ribeiro and C.P.. Borges, 2004, Using pervaporation data in the calculation of vapour permeation hollow-fibre modules for aroma recovery. *Braz. J. Chem. Eng.*, 21: 629-640.
- J.R.M. Pereira, A.C. Rufino, R. Habert, L.M.C. Nobrega, C.P. Cabral, C.C. Borges, 2005. Aroma compounds recovery of tropical fruit juice by pervaporation:membrane material selection and process evaluation, *J. Food Engin.*, 66, 77–87.
- K. Santosh, S. Neetu, P. Ram, 2010. Anhydrous ethanol: A renewable source of energy. *Renewable and Sustainable Energy Reviews*. 14, 1830–1844.
- L.M. Vane, 2008a. A review of pervaporation for product recovery from biomass fermentation processes. *Journal of Chemical Technology & Biotechnology*. 80,603-629.
- L.M. Vane, 2008b. Separation Technologies for the recovery and dehydration alcohols from fermentation broths. *Biofuels, Bioproducts and Biorefining*. 2, 553-588.
- M. Esfahaniana, A. H. Ghorbanfarahi , A. A. Ghoreyshi, G. Najafpour, H. Younesi, A. L. Ahmad, 2012, Enhanced Bioethanol Production in Batch Fermentation by Pervaporation Using a PDMS Membrane Bioreactor. *Ije Transactions B: Applications*. 25 (4) 249-258.
- M. Mulder. 1996. Basic Principles of Membrane Technology, Kluwer Academic Press, AA Dordrecht.
- M.N. Hyder, R.Y.M. Huang, P. Chen, 2009, Pervaporation dehydration of alcohol–water mixtures: Optimization for permeate flux and selectivity by central composite rotatable design, *Journal of Membrane Science*, 326:343–353.
- S. Semenova, H. Ohya, K., Soontarapa, 1997, Hydrophilic membranes for pervaporation: An analytical review, *Desalination*, 110, 251-286.
- S.P. Nunes and Klaus-Viktor Peinemann: Membrane Technology in the Chemical Industry, 2006, P:2.
- T. Ikegami , D. Kitamoto, H. Negishi , T. Imura , H. Yanagishit, 2003, Bioethanol production by a coupled fermentation/pervaporation process using silicalite membranes coated with silicone rubbers.
- W. Ding, Y. Wu, X. Tang, L. Yuan, Z. Xiao, 2011. Continuous ethanol fermentation in a closed-circulating system using an immobilized cell coupled with PDMS membrane pervaporation, *J Chem Technol Biotechnol*. 86, 82–87.
- Y. Goksungur, N. Zorlu, 2001. Production of Ethanol from Beet Molasses by Ca-Alginate Immobilized Yeast Cells in a Packed-Bed Bioreactor. *Turk J Biol*. 25, 265-275.
- Y. Sun, J. Cheng, 2002. Hydrolysis of lignocellulosic Materials for Ethanol Production: a review. *Bioresour Technol*. 83 (1), 1-11.

CHARACTERIZATION AND FORMATION OF POROUS SURFACE ON MAGNESIUM COATED BY PLASMA ELECTROLYTIC OXIDATION

Büşra Özkal^a, Doğukan Çetiner, Salih Durdu, Işıl Kutbay, Metin Usta

The Department of Materials Science and Engineering, Gebze Institute of Technology, 41400, Gebze/KOCAELİ

a. Corresponding author (busra_ozkal89@hotmail.com; busraozkal89@gmail.com)

ABSTRACT: In this study, commercial pure magnesium was coated by plasma electrolytic oxidation (PEO) in 4.5 g/L Na₃PO₄ + 1 g/L KOH electrolyte at 0.085 A/cm² current density for 15, 30 and 45 minutes. Coating thickness, phase composition, surface morphology, surface roughness, hardness and wear test were analyzed by eddy current method, X-ray diffraction (XRD), scanning electron microscopy (SEM), surface profilometer, micro Vickers tester and tribometer, respectively. The average coating thicknesses were measured as 34, 55 and 17 µm for 15, 30 and 45 minutes, respectively. The XRD results showed that Mg₃(PO₄)₂ (Farringtonite) and MgO (Periclase) phases were detected on the coating. The PEO coatings have very porous surface structure due to the existence of micro discharge channels during process. Surface roughnesses of coatings were measured as 3.19, 4.21 and 4.08 µm for 15, 30 and 45 minutes, respectively. The PEO coatings exhibited superior wear resistance than uncoated magnesium.

1. INTRODUCTION

Magnesium and its alloys have made effective inroads into areas where aluminum alloys were traditionally the materials of choice and are widely used aerospace and automotive industries, transportation, mobile communication devices and personal computers attempted to develop anticorrosive and high wear-resistance strategies (Lv et al., 2009; Zhang et al., 2008).

There are a number of surface coating techniques that have been considered for the protection of magnesium and its alloys from corrosion such as chemical conversion coatings, electroplating and electroless plating, anodizing etc. [3]. Among these, PEO coatings have more advantages than other coatings (Ghasemi et al., 2008). Plasma electrolytic oxidation (PEO) is a unique surface treatment technology, which developed from conventional anodic oxidation forming that transforms the surface of light alloys such as Mg, Al and Ti

(Cakmak et al., 2010; Durdu et al., 2013b). This coating process can both be used at high temperatures and is environmental friendly. During PEO process, high voltage and complicated reactions occur in the discharge channels. Because of this reasons oxide coatings are broken down (Chen et al., 2010; Durdu et al., 2011). As a result, thick and hard ceramic films with good adhesion, high wear and high corrosion resistance can fabricate on magnesium alloys (Wang et al., 2009).

In this paper, a comparative study is carried out to investigate the mechanical properties of pure magnesium coated by plasma electrolytic oxidation (PEO) at different treatment times in sodium phosphate based solutions.

2. EXPERIMENTAL DETAILS

2.1. Materials

Magnesium blocks with the purity of 99.96% were used as substrates. Coatings were produced on the magnesium specimens using plasma electrolytic oxidation (PEO). The PEO equipment (100 kW) was composed of an AC power supply, a stainless steel container as well as cooling and stirring systems. The magnesium substrate was used as the anode, while the stainless steel container as the cathode. The coatings were made in the solution of Na_3PO_4 and KOH for 15, 30 and 45 minutes.

2.2. Characterization of the Coatings

The thickness of each coating was measured by using Fischer Dualscope MP40. An X-ray diffractometer (Bruker D8 Advance) was used to measure the composition of the coatings. The Vickers hardness tests on the coatings were proceeded by using a microhardness tester (Anton Paar MHT-10). The friction and wear tests on the coatings were carried out on a ball-on-disk tribometer (CSM Instruments) at room temperature. An alumina ball with the diameter of 6 mm was tightly fixed in the ball as the rubbing partner. A normal load of 2 N was applied in all tests. The samples reciprocated against the pin with the maximum linear speed of 1.0 cm/s and amplitude of 8.5 mm. No liquid was added during the tests.

3. RESULTS AND DISCUSSION

Figure 1 illustrates the coating thickness versus the duration time. The average thickness of the PEO coatings produced at 15, 30 and 45 min measured as 33.5, 55 and 17.2 μm , respectively. The thickness of the coatings produced by PEO depends on parameters such as electrolyte, voltage and treatment times (Durdu et al., 2013a). In addition, the kinetics of the PEO coatings is interface

controlled during process. Generally, the thickness of the coatings increases with increasing time or voltage. Up to 30 min, the coating thickness increased with increasing time and then it decreased as seen in Fig. 1. After the thickness of coating produced at 30 min reached maximum value, the loose outer oxide layer was broken down during process (Narulkar et al., 2007). Therefore, the thickness of coating produced at 45 min is lower than the one produced at 30 min.

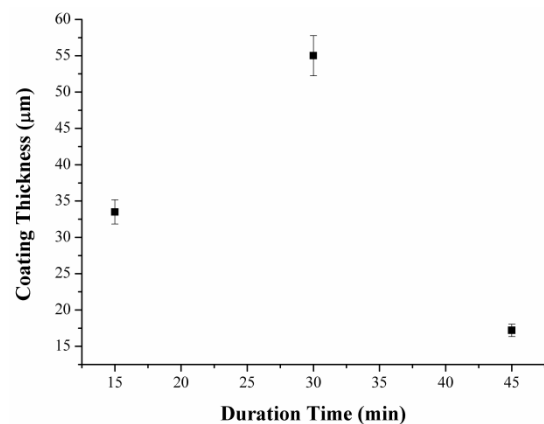


Figure 1: The thickness of the PEO coatings versus the duration time

Figure 2 shows the X-ray diffraction patterns of the PEO coatings. The Mg and MgO phases exist in the coating structure produced at 45 min, while Mg, MgO and $\text{Mg}_3(\text{PO}_4)_2$ phases on the PEO coatings produced at 15 and 30 min were detected by XRD analysis. Depending on coating thickness, the intensities of the MgO and $\text{Mg}_3(\text{PO}_4)_2$ phases increased up to 30 min. Also, MgO phase observed as a major phase on surface as seen in Fig. 2. The formation mechanism of oxide phases at PEO process could be explained by ionization and sintering in micro discharge channels under high temperature and pressure. The ions of Mg^{2+} emigrates from substrate to electrolyte interface and the O^{2-} ions migrates inward from electrolyte to substrate through process. The ions of

Mg^{2+} and O^{2-} react with each other in the micro discharge channels under high pressure and high temperature (Durdu and Usta, 2012). The formation reactions of the phases on the coatings are below:

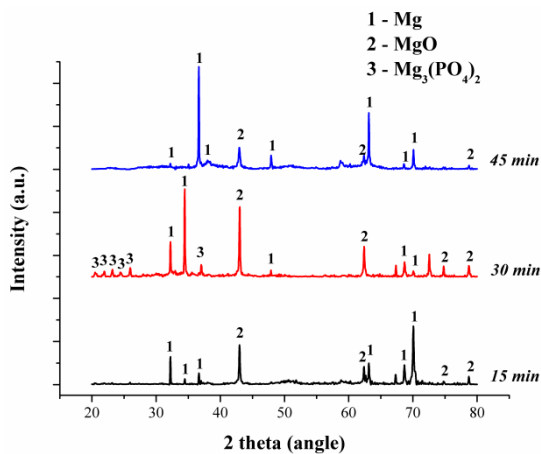


Figure 3: The XRD spectra of the PEO coatings

Figures 3a, 3b and 3c show the surface SEM morphologies of the coatings produced at 15, 30 and 45 min. The coatings produced by PEO are very porous and rough due to the existence of discharge channels through process. The sizes of these pores changes depending on electrolyte composition, voltage and treatment time. Generally, the porosity and the size of the pores increase with increasing time and voltage due to the growing of the intensity of micro sparks. In addition, the electrolyte causes rapid solidification of the melted oxide. Therefore, the thermal cracks forms on the PEO surface owing to the existence of thermal stresses.

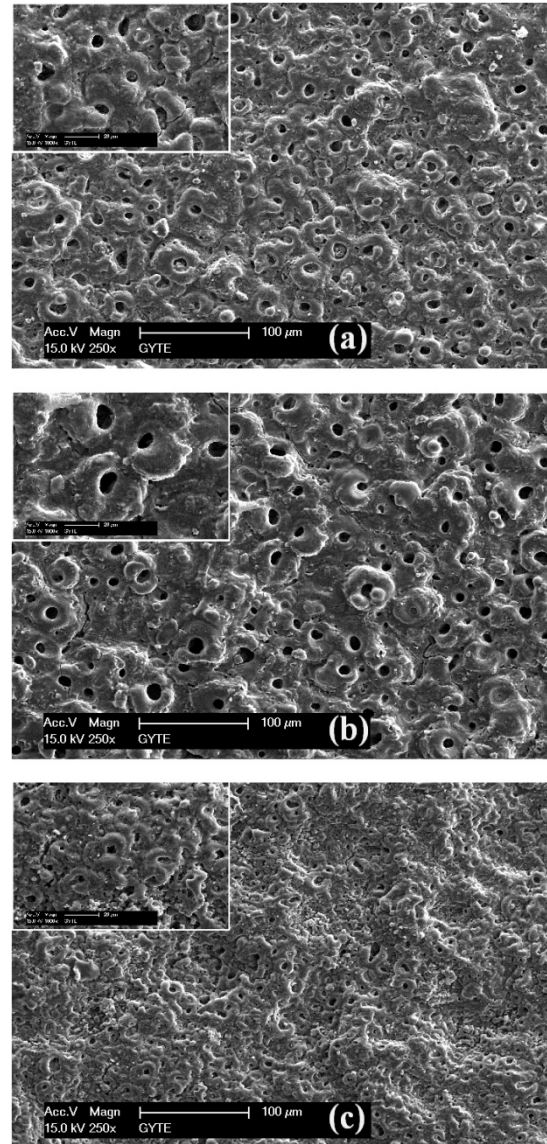


Figure 3: The surface micrographs of the PEO coatings:
(a) 15 min, (b) 30 min and (c) 45 min

Figure 4 illustrates the Vickers hardness of the PEO coatings produced at different duration times. The average hardness of the coatings produced at 15, 30 and 45 min measured as 330, 420 and 130 HV while the average hardness of uncoated magnesium was 40 HV. The hardness of the PEO coatings depends on the phase structure, thickness and compactness of the coating. Therefore, the coating produced at 30 min has maximum hardness due to the presence of oxide phases and high thickness.

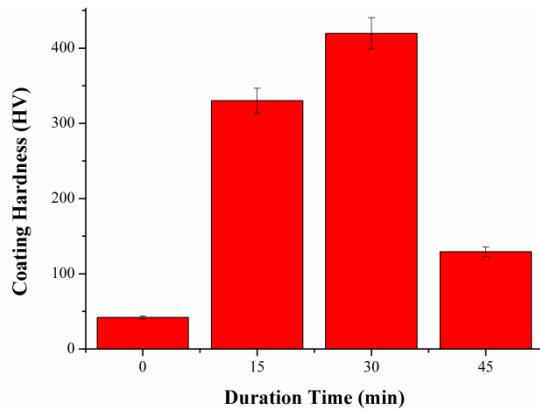


Figure 4: The hardness of the PEO coatings produced at different duration times

The wear rates of the PEO coatings and uncoated magnesium are given in Figure 5. The wear rates of the coatings produced at 15, 30 and 45 min determined as 20×10^{-4} , 1.3×10^{-4} and 23.7×10^{-4} $\text{mm}^3/\text{N}/\text{m}$, respectively. The wear rates of the materials are interested with the value of hardness. According to the results, the wear rates of the PEO coatings are very low compared to uncoated magnesium because the coatings are harder than the uncoated magnesium. In addition, the coating produced at 30 min has greater wear resistance than the ones produced at 15 and 45 min owing to the high amount of oxide phases in the coating.

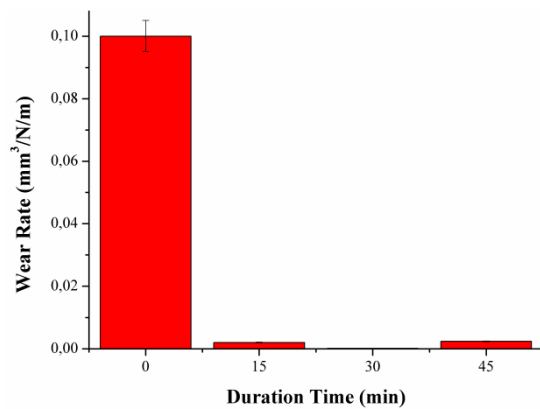


Figure 5: The wear rates of the PEO coatings produced at different duration times

4. CONCLUSIONS

MgO based phases were generated on commercial pure magnesium at different duration times in the electrolyte consisting of sodium phosphate and potassium hydroxide by PEO method. The some experimental results were obtained as below:

1. The thickness of the coating increased up to 30 min, however the thickness of coating produced at 45 min decreased.
2. The Mg, MgO and $\text{Mg}_3(\text{PO}_4)_2$ phases were detected on PEO surfaces, however Mg and MgO phases was observed on the coating produced at 45 min.
3. The PEO coatings are very porous due to the presence of micro discharge channels during process. The porosity and the size of pores increased with increasing treatment time.
4. The hardnesses of the coatings are greater than the one of uncoated magnesium. The coating produced at 30 min has maximum hardness value due to the existence of oxide phases and high thickness.
5. The wear rates of the coatings are lower than the one of uncoated magnesium. The coating produced at 30 min has maximum wear resistance value due to the high hardness in the coating

Acknowledgments

The authors would like to thank Mr. A. Nazım for running SEM and Mr. S. Levent Aktug for running X-ray diffractometer at Gebze Institute of Technology.

REFERENCES

- Cakmak E, Tekin KC, Malayoglu U, Shrestha S (2010). The effect of substrate composition on the electrochemical and mechanical properties of PEO coatings on Mg alloys. *Surface & Coatings Technology* 204(8):1305-1313.

- Chen HA, Lv GH, Zhang GL, Pang H, Wang XQ, Lee H *et al.* (2010). Corrosion performance of plasma electrolytic oxidized AZ31 magnesium alloy in silicate solutions with different additives. *Surface & Coatings Technology* 205(S32-S35).
- Durdu S, Aytac A, Usta M (2011). Characterization and corrosion behavior of ceramic coating on magnesium by micro-arc oxidation. *Journal of Alloys and Compounds* 509(34):8601-8606.
- Durdu S, Usta M (2012). Characterization and mechanical properties of coatings on magnesium by micro arc oxidation. *Applied Surface Science* 261(774-782).
- Durdu S, Bayramoglu S, Demirtas A, Usta M, Ucisik AH (2013a). Characterization of AZ31 Mg Alloy coated by plasma electrolytic oxidation. *Vacuum* 88(130-133).
- Durdu S, Deniz OF, Kutbay I, Usta M (2013b). Characterization and formation of hydroxyapatite on Ti6Al4V coated by plasma electrolytic oxidation. *Journal of Alloys and Compounds* 551(422-429).
- Ghasemi A, Raja VS, Blawert C, Dietzel W, Kainer KU (2008). Study of the structure and corrosion behavior of PEO coatings on AM50 magnesium alloy by electrochemical impedance spectroscopy. *Surface & Coatings Technology* 202(15):3513-3518.
- Guo H, An M, Xu S, Huo H (2006). Microarc oxidation of corrosion resistant ceramic coating on a magnesium alloy. *Materials Letters* 60(12):1538-1541.
- Guo HF, An MZ (2005). Growth of ceramic coatings on AZ91D magnesium alloys by micro-arc oxidation in aluminate-fluoride solutions and evaluation of corrosion resistance. *Applied Surface Science* 246(1-3):229-238.
- Lv GH, Chen H, Li L, Niu EW, Pang H, Zou B *et al.* (2009). Investigation of plasma electrolytic oxidation process on AZ91D magnesium alloy. *Current Applied Physics* 9(1):126-130.
- Narulkar VV, Prakash S, Chandra K (2007). Ceramic coated Y1 magnesium alloy surfaces by microarc oxidation process for marine applications. *Bulletin of Materials Science* 30(4):399-402.
- Song YL, Liu YH, Yu SR, Zhu XY, Wang Q (2008). Plasma electrolytic oxidation coating on AZ91 magnesium alloy modified by neodymium and its corrosion resistance. *Applied Surface Science* 254(10):3014-3020.
- Wang L, Chen L, Yan ZC, Wang HL, Peng JZ (2009). Effect of potassium fluoride on structure and corrosion resistance of plasma electrolytic oxidation films formed on AZ31 magnesium alloy. *Journal of Alloys and Compounds* 480(2):469-474.
- Yerokhin AL, Shatrov A, Samsonov V, Shashkov P, Leyland A, Matthews A (2004). Fatigue properties of Keronite((R)) coatings on a magnesium alloy. *Surface & Coatings Technology* 182(1):78-84.
- Zhang WX, Jiang ZH, Li GY, Jiang Q, Lian JS (2008). Electroless Ni-P/Ni-B duplex coatings for improving the hardness and the corrosion resistance of AZ91D magnesium alloy. *Applied Surface Science* 254(16):4949-4955.

THE EFFECT OF STRUCTURAL CHARACTERISTICS ON THE REFLECTIVITY OF POROUS SILICON

Gulsen Kosoglu¹, Dimitrios Chaliampalias², Aikaterini Breza², Ozhan Ozatay¹, Nikolaos Frangis², Christos Lioutas², Yani Skarlatos¹, Efstathios Polychroniadis^{2a}

1. Bogazici University, Physics Department, Istanbul, Turkey

2. Aristotle University of Thessaloniki, Physics Department, Thessaloniki, Greece

a. Corresponding author (polychr@auth.gr)

ABSTRACT: The reduction in reflectivity of porous silicon layers was investigated as part of an attempt to improve the efficiency of silicon photovoltaic solar cells. The effect of production parameters on the nature of porosity and hence reflectivity was examined with the aid of scanning and transmission electron microscopy. Porosity reduces the reflectivity of polished silicon wafers by a factor of 10 to 20, with larger pore sizes resulting in higher reduction factors. However, intensive etching of the silicon surface in order to increase pore size beyond about 150 nm in diameter, causes flaking on the top of the porous layer, with the remaining lower part displaying smaller pore diameters.

1. Introduction

The main aim in photovoltaic industry is to produce efficient and energy competitive solar cell modules at low cost. Efficient Antireflection Coatings (ARC) improve light collection and thereby increase the current output of solar cells. Broadband ARCs are desirable for efficient application over the entire solar spectrum, and porous silicon as antireflective coating layers provide successful light collection. Porous silicon is one form of silicon nanocrystalline or nano clustered material used in silicon photonics with the ultimate aim of producing photonic devices [Xie *et al.*, 2009], [Bisi *et al.*, 2000].

Photovoltaics constitutes one major group of such devices, [Beard *et al.*, 2007] where solar cells using porous silicon as active material have potential of higher efficiency through blue light harvesting; (converting ultraviolet and blue light into light of lower frequency) reducing reflectance losses because of the irregular surface texture; band gap

tenability; and direct band gap behavior similar to amorphous silicon and gallium arsenide.

Nanoporous silicon solar cells in the form of Schottky diodes made from electrochemically etched silicon wafers back coated with an aluminum or gold film have been produced, and their electrical characteristics have been measured [Martin-Palma *et al.*, 2004].

The electrical characteristics of thick (several microns) porous silicon layers needed for active devices are extremely sensitive to substrate doping profiles and crystalline morphology [Fauchet, 2003]. Therefore, research so far has focused on using the porous silicon layer (in much thinner form) as an antireflection coating [Moreno *et al.*, 2005] or for second carrier generation in a conventional solar cell [Prezioso *et al.*, 2009].

The aim of the present work is to examine the porous silicon forming and

structural parameters that bring about desirable quality of porous silicon in terms of reduced reflectivity as compared to polished crystalline silicon. To this end, porous silicon was formed by anodization on the top surface of p-n junctions, and the reflectivity was measured, while the structure of the pores was examined by scanning and transmission microscopy.

2. EXPERIMENTAL

2.1. Sample Preparation

P-N junctions were produced on n-type (100) silicon wafers doped with boron to a depth of 500 nm by ion implantation¹. The back surface of the diodes was then coated with a few hundred nanometers of vacuum deposited aluminum film to serve as back contact. To achieve a good ohmic contact, the wafers are annealed for 30 minutes. They are then cut into small pieces of approximately 1cm² so as to place them in our etching bath. All wafers were ultrasonically cleaned in distilled water/acetone/isopropanol for 15 min separately, and then dried with nitrogen.

The back electrode was covered with wax temporarily to prevent it from corroding during etching. Subsequently, porous silicon of several micron thicknesses was formed by electrochemically etching of the wafers in a hydrofluoric acid (48%) – ethanol (99.99%) mixture in 1:3 to 2:3 ratios. Teflon was used as the etching bath container because of its resistance to corrosion by HF.

The current density was electronically adjusted during the etching process so as to keep the latter uniform. Current stability is important because some applications showed that high and unstable current values will cause nonuniform and inhomogeneous pore

formation and, even worse, sometimes cracks and device failure.

Anodization time was carefully controlled during the process, and varied between 10 and 20 minutes. After etching, the samples were carefully removed from the etching bath so as to prevent damage to the freshly formed pores.

Eventually, semitransparent electrical contacts of a few tens of nanometers of indium tin oxide (ITO) will be deposited (by sputtering) on the porous side in order to complete the production of the photovoltaic cells and test their performance under various illumination levels. For the present work however, the porous layer was left exposed so that it can be studied in the scanning electron microscope.

Although a multitude of samples was produced in order to test the parameters and standardize the etching process, the relevant parameters for only the four examined in this article are given in Table 1. All these samples are immersed in an acidic solution which 18% of the total concentration is HF.

Table 1: The etching experimental conditions

Sample name	Etching Time min	Current Density mA/cm ²	Applied Voltage V
A	10	40	20
B	10	60	20
C	15	40	20
D	20	40	20

All the samples are illuminated with a light source during the process. The illumination of the silicon surface is an important fact for n-type wafers so as to create holes for the electrochemistry.

¹ Performed at YITAL, TUBITAK in Gebze, Turkey.

2.2 Sample examination with electron microscopy (TEM-SEM)

Preparation of the samples for cross sectional examination with TEM involves particularly difficult and time consuming technical processing, which must be carried out in several careful steps. For reliable structural characterization, sample thickness must vary between a few and a few tens of nanometers. Obviously, the material has to be processed appropriately so that it reaches the required thickness without changing its characteristics to be studied.

The samples of porous silicon that were examined in the electron microscope were of lateral cross section for a side view of the pores. For preparation of such samples the silicon wafer, on which the pores were formed, is diced in sizes of 3mm X 0.5mm. Then the cut chips are bonded in pairs using epoxy glue in such a way as to have the porous faces one against the other. The glue, apart from holding the pairs together, protects the pores throughout the manipulation. Afterwards the sample is then mechanically polished on both sides using sandpapers and special abrasive pastes until the thickness drops to about 50 μm . Finally, the sample is mounted on a copper ring and on an appropriate holder for further thinning with ions. Argon ion bombardment is employed for the latter stage. The accelerating voltage of the ions varies between 3 and 7kV depending on the hardness of the material. To prevent the ions from destroying the sample, the incident beam angle relative to the sample surface is kept at 5–10° (glancing angle). Moreover, the sample is rotated about a axis perpendicular to its surface throughout the bombardment. Polishing is stopped when the ions form a hole near the center of the sample.

After the etching process, selective samples were prepared for cross sectional

electron microscopy observation by mechanical polishing and ion beam milling. After the preparation the samples were studied by TEM using a JEOL 100CX conventional TEM (CTEM) operating at 100 kV. By this way it was possible to examine the morphology and shape of the as formed pores in every anodizing process and correlate the experimental findings with the reflectivity measurements.

The SEM images were taken with a Philips XL 30 ESEM-FEG/EDAX microscope.

2.3. Optical Measurements

Optical reflection measurements were performed by using the setup in which a constant current was fed to a power LED by applying 5V DC voltage from the power supply. The reflectances of the crystalline and the porous samples were measured as the output voltage of a Thorlabs PDA100A-EC Si amplifier photodetector, and their ratio was calculated.

3. RESULTS AND DISCUSSION

The reflectance values for the four samples examined here are given on Table 2. Sample 0 refers to a polished silicon wafer which has not been made porous.

Table 2: Porous silicon sample reflectance relative to polished silicon.

Sample name	Reflectance (V)	Reflectance decrease
0	3.205	0%
A	0.348	89.2%
B	0.235	92.67%
C	0.234	92.66%
D	0.142	95.6%

These low relative reflection values show that the porosity of the surface keeps the incoming light beam inside the bulk material and behaves as a good

antireflecting layer. Etching time duration is important for pore formation, and optical measurements directly show that longer etching times result in higher reflection decrease. For fixed etching time, higher anodization current will produce much deeper porous layers and also reduce reflection. However, the anodization current is limited by the ionic concentration in the solution; therefore, it can not be increased without bound, nor there is a need for such action, since the thickness of the porous layer does not affect the reflectivity. Figure 1 shows the SEM images of samples C (figure 1a) and D (figure 1b) etched at current density values of $40\text{mA}/\text{cm}^2$. Etching time is so important that even for small increase in time it will produce large pore formations inside the bulk silicon. The pores first get deeper inside the bulk structure, and then increase in diameter.

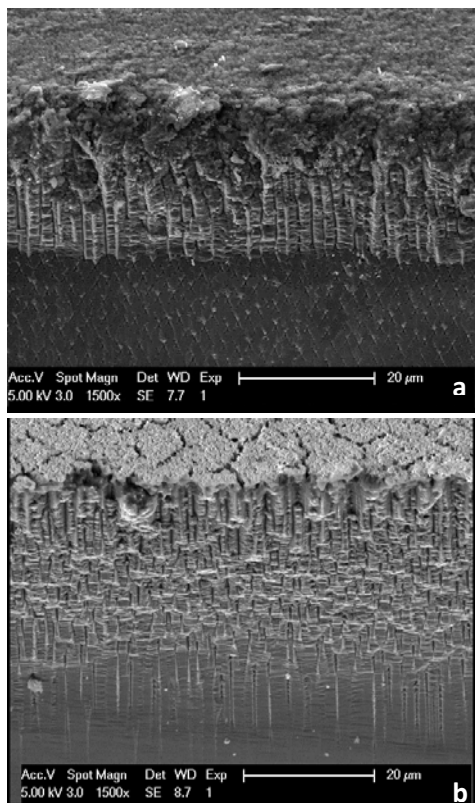


Figure 1: The SEM images of samples C (a) and D (b) both etched at the same current density values

Attention must be focused on the pore structures on the wafer surface for reflection measurements. The acid concentration should not be increased too much because SEM images showed that it may cause cracks on the surface of silicon wafer especially at the first time that pores start forming. The creation of pores is much faster and deeper at high concentrations, but the stability of pore formation on the surface may be problematic and cause pore wall destruction.

The SEM images of Figure 2 belong to samples A (figure 2a) and B (figure 2b). The etching time is fixed at 10 min. The current density is $40\text{mA}/\text{cm}^2$ and $60\text{mA}/\text{cm}^2$ respectively. Increased current density also helps create deeper pores in fixed time duration. The branches at the bottom of the pores may have been formed because of the spontaneous inhomogeneity in current density while the process is terminated.

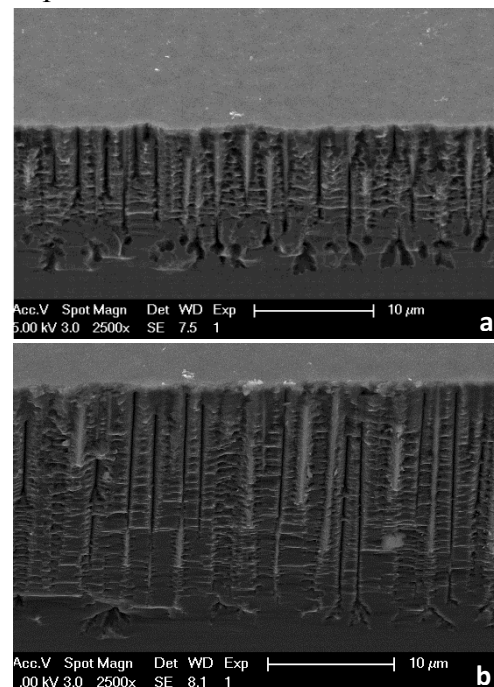


Figure 2 : SEM images of Sample A (a) and sample B (b) having the same etching time.

In figure 3 the TEM micrographs of samples A (figure 3a), B (figure 3b), C

(figure 3c) and D (figure 3d) are presented. Measuring the pore dimensions from the corresponding images it was found that in the case of sample A the pore diameter varies between 650-1500nm (near the surface). The pores formed on sample B have 500-800nm while in sample C the pore width was measured to be 600-700nm. Finally the pore width of sample D was measured to be 550-750nm.

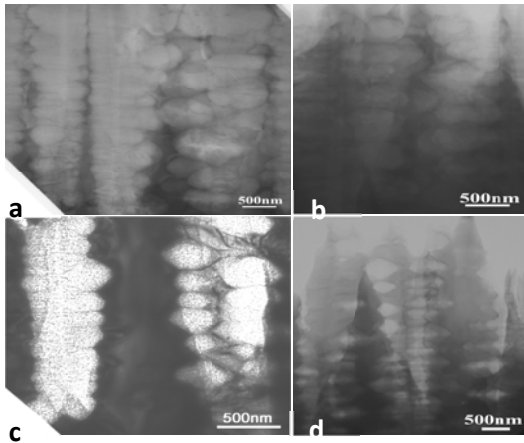


Figure 3: Bright Field TEM micrographs of samples A (a), B (b), C (c) and D (d).

From the above TEM results it is evident that both pore width and length have no remarkable difference. It is concluded that the different etching conditions mostly affect the surface roughness and not the microstructure of the pores. Also, comparing with the results of Table 2, it is deduced that the pore morphology has no significant influence on the reflectivity values. Furthermore, it is revealed that the morphology of the as formed pores, is bubble-shaped with a certain periodicity. The creation of this morphology is most probably due to the stable rate of the bubble formation at the bottom of the pore, resulting from the constant chemical etching conditions of the Si wafers.

4. CONCLUSIONS

The results of the herein examination revealed that the formation of a porous layer on the top surface of a Si solar cell reduces dramatically its reflectivity, with

an analogous increase in captured light. The Si wafer etched for 20min with $40\text{mA}/\text{cm}^2$ was measured to have the highest reflectivity decrease comparing with the other tested conditions. Finally, the morphology of surface has a significant effect on the reflectivity since no such correlation was identified with the pore inner morphology. It remains to be seen what the effect on the overall efficiency of the solar cell will be, as the effects of the porous layer on carrier forming per photon as well as carrier recombination ratios are yet unknown.

Acknowledgements: This work was supported by TUBITAK Grant 209T099, Bogazici University Research Fund Project Nr. 5782P and GSRT 10TUR/5-1-3.

REFERENCES

- Xie, M , Yuan Z., Qian B. , Pavese L. Silicon Nanocrystals, 2009. Enabling Silicon Photonics, Chinese Optics Letters special issue on Silicon Photonics.
- Bisi O., Ossicini S., Pavese L.,2000. Porous Silicon: A Quantum Sponge Structure for Silicon Base Optoelectronic, Surface Science Reports 264, 1-126.
- Beard M.C., Knutsen K.P., Yu P. , Luther J.M., Song Q., Metzger W.K., Ellingson R.J., and Nozik A.J., 2007. Multiple Exciton Generation in Colloidal Silicon Nanocrystals, Nano Lett. 7, 2506
- Martin-Palma RJ, Lemus R.G., Moreno JD , Martinez-Duart JM. 2004. Nano-porous Silicon for Sun Sensors dan Solar Cells, Esa. Muhtiar, Sudiana IN & Anas M.
- Fauchet P. ,2003. Porous Polycrystalline Silicon Thin Film Solar Cells, Subcontractor Report NREL/SR-520-34824
- Moreno J.A. , Garrido B. Pellegrino P., Garcia C., Arbiol J. , Morante J.R. ,2005. Size Dependence of Refractive Index of Silicon Nanoclusters Embedded in Silicon Dioxide, Jour. Appl. Phys. 98, 013523 .
- Prezioso S., Hossain S. M. , Anopchenko A., Pavese L., Wang M., Pucker G. , Bellutti P.,2009. Super-Linear Photovoltaic Effect in Silicon Nanocrystals Based Metal-Insulator-Semiconductor Devices, Appl. Phys. Lett., 94, 062108

THE ESTIMATION OF PORE ANISOTROPY AND ITS RELATIONSHIP WITH MORPHOMETRIC PROPERTIES OF POROUS SOLIDS

Eleni T.Tsaousi¹, Gerasimos S. Armatas² and Philippos J. Pomonis^{1a}

¹Department of Chemistry, University of Ioannina, Ioannina 45110, Greece.

²Department of Materials Science and Technology, University of Crete, Heraklion 71003, Crete, Greece.

a. Corresponding author (ppomonis@cc.uoi.gr)

ABSTRACT: The concept of pore anisotropy $b=L/D$ corresponds to the ratio between the pore length L and diameter D and can be estimated using standard N_2 physisorption data. This work outlines the following points: (i) It will be shown how we can estimate b in porous materials with organized or random nanoporosity. (ii) Since in real materials the pores are connected to, and intercepted by, other pores, forming a complex network, it will be shown how the pore anisotropy b is affected by the mean connectivity c of pores. (iii) Since the length of mesopores is usually intercepted by various micropores, it will be shown how the pore anisotropy b is influenced by the extent of microporosity (%micro) of porous domains. (iv) It will be shown that the methodology for estimating b is directly related to the fractal dimensionality D_s of adsorption – desorption phenomena. (v) A comparison will be attempted between the phenomenology describing the development of surfactant micelles in synthesis of organized mesostructured materials, like MCM and SBA-type silicas, and the mechanism affecting the most common example of anisotropic development in nature, which is the plant cells.

1. INTRODUCTION

Pore anisotropy b is defined as the ratio of the pore length L over its diameter D or radius r , as seen in Figure 1.

$$b = L/D = L/2r \quad (1)$$

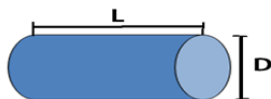


Figure 1: The anisotropy b of a cylindrical pore is defined by the ratio between the pore length L and the pore diameter D .

This article focuses on pore anisotropy of porous solids, especially mesoporous materials with ordered pore structure, like MCM and SBA-type silicas, as well as disordered porosity, like aluminas, silicas

and aluminophosphates [Pomonis and Armatas, 2004]. The text outlines the following points: (i) The method of estimation of b using the adsorption isotherm data obtained by N_2 porosimetry. (ii) The dependence of pore anisotropy b on the mean pore connectivity c . (iii) The influence of microporosity (%micro) on the pore anisotropy b . (iv) The relationship between b and the fractal dimensionality D_s of adsorption. (v) The phenomenological similarity between the anisotropic development of micelles in synthesis of mesoporous materials and the mechanism of anisotropic development of plant cells [Pomonis and Armatas, 2012].

2. THE ESTIMATION OF b

The method of estimating b , based on nitrogen physisorption data, is as follows [Pomonis and Tsaousi, 2009]: At each particular pressure P_i ($=p_i/p_0$) the values of differential specific surface area S_i ($\text{m}^2 \text{g}^{-1}$) and differential specific pore volume V_i ($\text{cm}^3 \text{g}^{-1}$) are estimated using a standard pore-size distribution method, like BJH. At each P_i it is assumed that a number N_i of cylindrical pores with diameter $D_i = 2r_i$ are filled-up. Furthermore, the length L_i of the pores is related to the radius r_i via the scaling relationship $L_i = r_i^{\alpha_i}$, where α_i is a *scaling parameter* whose determination, in combination with pore radius r_i , will enable the estimation of anisotropy. As a result, the pore anisotropy is given by:

$$b_i = L_i / D_i = r_i^{\alpha_i} / 2r_i = 0.5r_i^{\alpha_i-1} \quad (2)$$

Then, the differential specific surface area S_i and the differential specific pore volume V_i corresponding to each relative pressure P_i may be related to that scaling parameter α_i and the number N_i of cylindrical voids via the following relationships:

$$S_i = N_i(2\pi r_i)L_i = N_i(2\pi r_i)r_i^{\alpha_i} = 2\pi N_i r_i^{\alpha_i+1} \quad (3)$$

$$V_i = N_i(\pi r_i^2)L_i = N_i(\pi r_i^2)r_i^{\alpha_i} = \pi N_i r_i^{\alpha_i+2} \quad (4)$$

Relations (3) and (4) can now be used in combination, or independently, for estimating b .

Estimation of the pore anisotropy from the dimensionless ratio $\lambda_i = S_i^3/V_i^2$: From eqs (3) and (4) the following dimensionless ratio λ_i can be obtained:

$$S_i^3/V_i^2 = \lambda_i = 8\pi N_i r_i^{(\alpha_i-1)} \quad (5)$$

and after taking logarithms:

$$\log(\lambda_i) = \log(8\pi N_i) + (\alpha_i-1)\log(r_i) \quad (6)$$

Then plots of $\log(\lambda_i)$ vs. $\log(r_i)$ provide curves with slope $s_{i(SV)} = (\alpha_i-1)$ at each point i . Therefore, according to eq. (2), the anisotropy b_i for each group i of pores can be obtained as:

$$b_{i(SV)} = 0.5r_i^{\alpha_i-1} = 0.5r_i^{s_{i(SV)}} \quad (7)$$

where, the subscript (SV) means that the estimation took place based on both S_i and V_i parameters.

Estimation of the pore anisotropy from the differential surface area: Equation (3) after taking logarithms yields:

$$\log(S_i) = \log(2\pi N_i) + (\alpha_i+1)\log(r_i) \quad (8)$$

Then plots of $\log(S_i)$ vs. $\log(r_i)$ should provide curves with slope $s_{i(S)} = \alpha_i+1$ at each point i . Then according to eq. (2), we obtain the following expression for anisotropy:

$$b_{i(S)} = 0.5r_i^{\alpha_i-1} = 0.5r_i^{s_{i(S)}-2} \quad (9)$$

where the subscript (S) indicates that the estimation took place based only on the specific surface area S_i values.

Estimation of the pore anisotropy from the differential pore volume. In that case, eq. (4) is used which yields:

$$\log(V_i) = \log(\pi N_i) + (\alpha_i+2)\log(r_i) \quad (10)$$

Then plots of $\log(V_i)$ vs. $\log(r_i)$ provide curves with slope $s_{i(V)} = (\alpha_i+2)$ at each point i . Then according to eq. (2), we obtain:

$$b_{i(V)} = 0.5r_i^{\alpha_i-1} = 0.5r_i^{s_{i(V)}-3} \quad (11)$$

where the subscript (V) means that the estimation took place based only on the specific pore volume V_i . Note that the pore anisotropies $b_{i(SV)}$, $b_{i(S)}$ and $b_{i(V)}$ are all identical and their estimation should not be affected by the applied method.

$$b_i = 0.5r_i^{ai-1} = 0.5r_i^{si(SV)} = 0.5r_i^{si(S)-2} = 0.5r_i^{si(V)-3} = b_{i(SV)} = b_{i(S)} = b_{i(V)} \quad (12)$$

Figure 2 shows indeed that this is the case. This Figure compares in a bar-chart plot the estimated anisotropies $b_{i(SV)}$, $b_{i(S)}$ and $b_{i(V)}$ for different mesoporous silicate (OSi) materials containing 1-2 wt% of various metal ions, namely 2% Pt (2Pt/OSi), 1% Ni (Ni/OSi), 1% Fe (1Fe/OSi), 2% Cu (2Cu/OSi), and 1% Mn (1Mn/OSi).

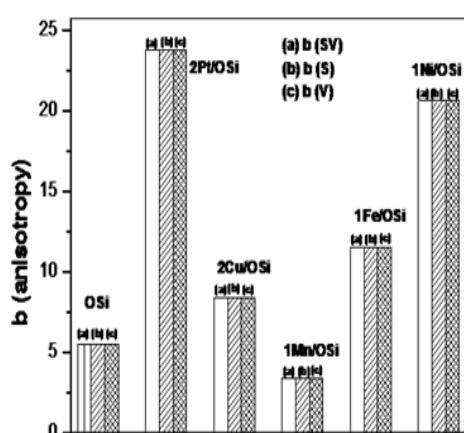


Figure 2: Comparison of pore anisotropies $b_{(SV)}$, $b_{(S)}$ and $b_{(V)}$ for organized and quasi-organized silicate (OSi) solids containing 1-2 wt% of various metal ions.

Figure 3 shows typical results from N_2 physisorption measurements as well as the relevant calculations that have been made to determine $b_{(SV)}$, $b_{(S)}$ and $b_{(V)}$ for the mesoporous OSi sample.

This Figure contains the following information and calculations: (a) The N_2 adsorption – desorption isotherm. (b) The corresponding pore size distribution $dV/dD = f(D)$ according to BJH method. (c) The plot $\log(\lambda_i) = \log(S_i^3/V_i^2)$ vs. $\log(r_i)$ according to equation (6). (d) The anisotropy $b_{(SV)}$ as a function of pore radius r_i according to equation (7). (e) The plot $\log(S_i)$ vs. $\log(r_i)$ according to

equation (8). (f) The anisotropy $b_{(S)}$ as a function of pore radius r_i according to equation (9). (g) The plot $\log(V_i)$ vs. $\log(r_i)$ according to equation (10). (h) The anisotropy $b_{(V)}$ as a function of pore radius r_i according to equation (11).

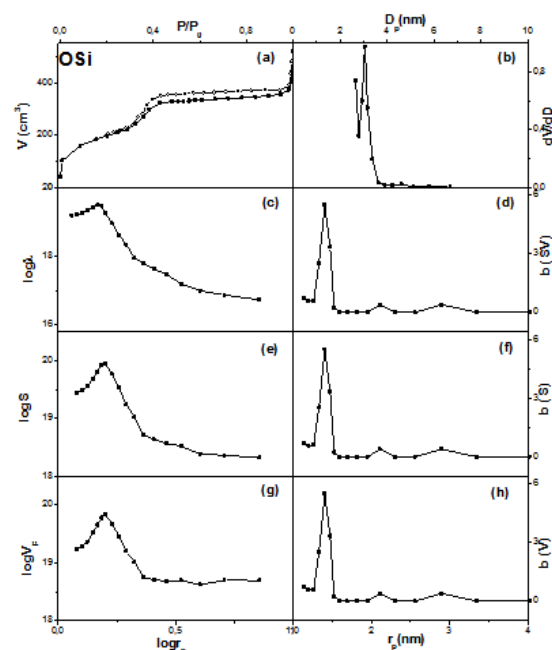


Figure 3: For the estimation of pore anisotropy. For details see text.

3. THE DEPENDENCE OF PORE ANISOTROPY b ON THE PORE CONNECTIVITY c

The logarithm of pore anisotropy b , reduced over the mean pore connectivity c , the standard deviation of the pore size distribution σ_p and the standard deviation of the pore anisotropy distribution σ_b , as a function of mean pore connectivity c for mesoporous $Al_{100}P_XV_Y$ materials bearing random porosity is shown in Figure 4. The justification of this dependence is given by [Pomonis and Armatas, 2012].

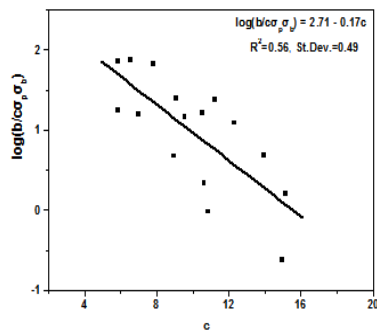


Figure 4: The variation of the logarithm of the reduced pore anisotropy, $\log(b/c\sigma_p\sigma_b)$, with the pore connectivity c for mesoporous aluminophosphate materials.

4. THE INFLUENCE OF MICROPOROSITY ON THE PORE ANISOTROPY

It has been observed [Katsoulidis et al. 2007] that there is a linear relation between the logarithm of pore anisotropy, $\log b$, and percent (%) of microporosity according to eq. (13), which depends on the kind of porous material. An explanation of this dependence is given in by [Katsoulidis, A.P.et al., 2009] and shown schematically in Figure 5.

$$\log b = B - A(\% \text{ microporosity}) \quad (13)$$

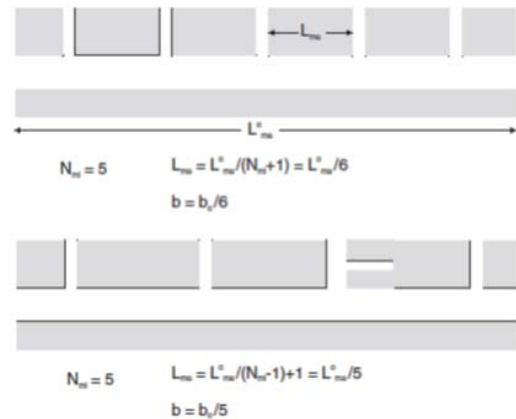
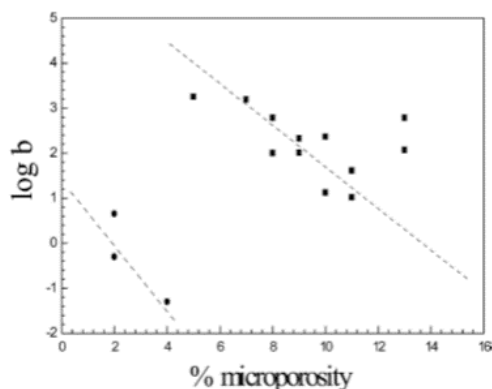


Figure 5: Upper part: The dependence $\log b = B - A$ (%microporosity). Lower part: A schematic representation of the pore anisotropy for regular pore channels with different connectivities. For details see the original articles.

5. THE RELATIONSHIP BETWEEN b AND THE FRACTAL DIMENSIONALITY OF ADSORPTION

In ref. [Pomonis and Tsaousi, 2009], it was shown that the pore anisotropy b , scaled in units of pore radius r , is related to the fractal dimension D of adsorption according to the relationship (14). This is valid for a specific region of the adsorption isotherm, as seen in Fig. 6.

$$b_i = L_i / D_i = 0.5r_i^{-D} \quad (14)$$

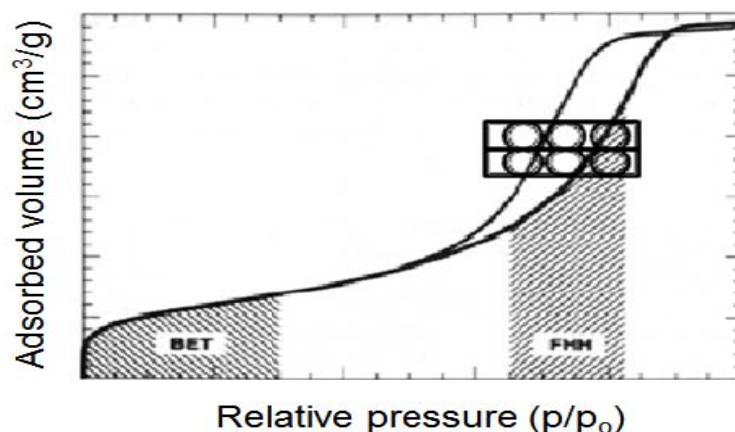


Figure 6: For the explanation of the conjunction that if the pore anisotropy b is scaled in units of pore radius r , then its dimensionality D corresponds to the fractal dimension of the adsorbing space or operation. The shade area at the beginning of the isotherm (left) is the so-called BET range where adsorption takes place in a single monolayer and where the specific surface area is determined. The shade area in the middle corresponds in the pressure range where the pores are filled-up by the adsorbed species. A *single* imaginary pore is shown in horizontal fashion filled with spheres of diameter equal to the pore radius r . The scaling/measuring of pore length in this way leads to b . The dimensionality of the space according to the principles of fractal geometry is $D \approx \log b / \log r$

6. SOME SIMILARITIES BETWEEN THE ANISOTROPIC DEVELOPMENT OF MICELLES AND PORES OF MCM AND SBA-TYPE MATERIALS AND THE MECHANISM OF ANISOTROPIC DEVELOPMENT OF PLANT CELLS

A point of interest is that the fundamental geometrical and physicochemical principles controlling the development of anisotropy in plant cells on one hand and the generation of surfactant micelles, and eventually the ordered mesoporous solids, on the other bear remarkable similarities as seen in Figure 7. This is another example of perhaps unintended biogenesis in the development of ordered mesoporous materials.

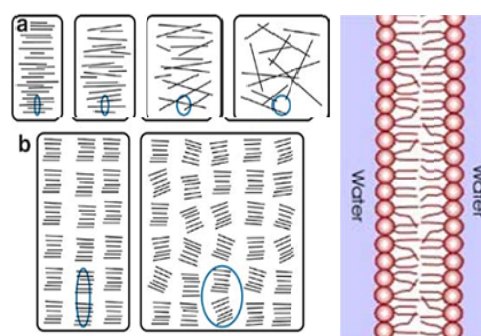


Figure 7: *Left:* For appreciating the role of cellulose microfibrils in the development of cell anisotropy in plants. The degree of anisotropy, shown by the blue ellipses, is controlled by the extend of microfibril alignment, consisted of strands of cellulose which are made up of a 500-15000 units of glucose with every other oriented 180° relative to its neighbor. The direction of anisotropy development is normal to the direction of the microfibril alignment [Baskin, T. I., 2005] *Right:* Mechanism for micelles formation serving as templates to create internal porosity in MCM-type solids.

The structural elements are surfactant species $C_nH_{2n+1}N^+(CH_3)_3$. Their orientation is always vertical to the long axis of micelles and the resulting pore channels.

Acknowledgements: This research has been co-financed by the European Union (European Social Fund – ESF) and Greek national funds through the Operational Program "Education and Lifelong Learning" of the National Strategic Reference Framework (NSRF) - Research Funding Program: THALIS- Investing in Knowledge Society Through the European Social Fund.

REFERENCES

Pomonis, P. J., Armatas, G. S., 2004. "A Method for the Estimation of Pore Anisotropy in Porous Solids", *Langmuir*, 20, 6719.

- Pomonis, P. J., Armatas, G. S., 2012. Chapter 3, "The Pore Anisotropy in Porous Solids" in "Anisotropy Research" Editor H. Lemu, Nova Science Publishers, New York, p.45.
- Pomonis, P. J., Tsaousi, E. T., 2009. "Frenkel-Halse -Hill Equation, Dimensionality of Adsorption and Pore Anisotropy", *Langmuir*, 25, 9986.
- Katsoulidis, A.P., Petrakis, D.E., Armatas, G.S., Pomonis, P.J., 2007. "Microporosity, Pore Anisotropy and Surface Properties of Organized Mesoporous Silicates Containing Cobalt and Cerium, *J. Mater. Chem.*, 17, 1518.
- Katsoulidis, A.P., Tsaousi, E.T., Armatas, G.S., Petrakis, D.E., 2009. "Organized mesoporous silico-nickelates and silico-lanthano-nickelates: Crystallogenes vs. morphogenesis and microporosity vs. pore anisotropy" *Microporous and Mesoporous Materials* 122, 175.
- Baskin, T. I., 2005, "Anisotropic expansion of the plant cell wall" *Ann. Rev. Cell Dev. Biol.*, 21, 203.

GRAIN SIZE ASSESSMENT IN SUPERCOARSE HARDMETALS WITH COBALT AND NICKEL BASED MATRICES

Janusz Richter^{1,a}, Katarzyna Harabas^{1,b}

1. Silesian University of Technology, Faculty of Materials Engineering and Metallurgy,
Department of Materials Science, ul. Krasińskiego 8, 40-019 Katowice, Poland
a. Corresponding author (janusz.richter@polsl.pl)

ABSTRACT: Set of the supercoarse sintered carbides with nonconventional, nickel based binder has been manufactured. The new chemical composition of a metal matrix might contribute to changes in the sintering process involving occurrence of the eutectic liquid phase. Therefore measurements of WC grain size chord lengths using both classical and automatic methods have been performed. The employed Kolmogorov-Smirnov and Mann-Whitney statistical tests made it possible to compare the investigated sintered carbides with the commercial coarse grained grade and classify the former as supercoarse sinters. The statistical assessment of chord length distributions obtained with both measuring methods showed that the classical and automatic methods are not consistent, which may be attributed to the smallest possible length being measured in each case.

1. INTRODUCTION

Hardmetals (also called sintered carbides) are composites of tungsten carbides and metal, most often cobalt. The supercoarse grades of hardmetals has been developed to provide materials with simultaneously high toughness and wear resistance. The unique properties combination of these materials is perfectly appropriate for coal mining and similar applications. Substitution of cobalt metal matrix with nickel based binders is aimed at improving corrosion resistance while retaining not worse mechanical properties and material cost [Fernandes, 2009]. The changed chemical composition of metal matrix affects sintering process, especially formation of liquid eutectic. Due to different features of this phase (composition and temperature range of occurrence), the objective assessment of the resulting grain size is of importance. Tungsten carbide grain size in conventional and experimental sinters have been measured using both classical and automatic methods. This approach, together with statistical testing, should enable assessment of the grain size and the measuring methods.

2. MATERIAL

Four grades of supercoarse sintered carbides with nickel based matrix and reduced or eliminated cobalt content have been designed and manufactured. Fraction of WC carbide particles was the same in all samples (90.5 wt.%). The differentiated metal matrices are characterised in Table 1.

Table 1: Description of the investigated sinters.

Sinter symbol	Components of metal matrix (M –metal other than Co, Ni)
NiM	Ni, M (no cobalt)
NiCoM1	Co<9.5 wt.%, Ni, M – less than NiM
NiCoM2	Co-as NiCoM1 Ni-less than NiCoM1 M-more than NiCoM1
NiCoM3	Co–more than NiCoM1/2 Ni-less thanNiCoM1/2 M-as NiCoM1
Co-super-coarse	Co-9.5 wt.%
Co-coarse	Co-9.5 wt.%

Example microstructures of the cobalt and nickel containing sinters are shown in Figure 1. In case of the samples with cobalt matrix traditional etchant was applied, the remaining samples required modification of the etchant composition and etching parameters.

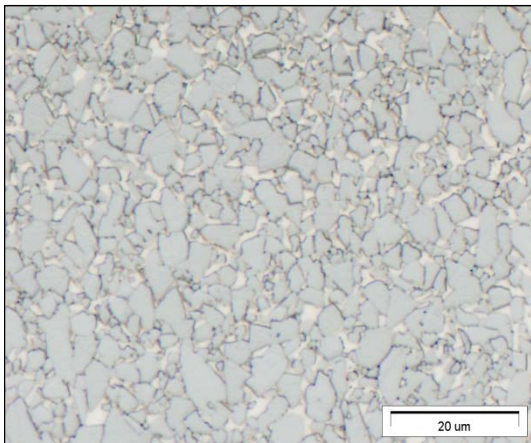
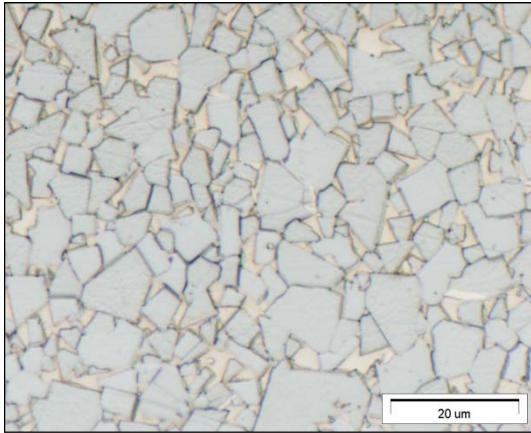


Figure 1: Microstructure of Co (top), NiCoM2 (bottom) sinters, light microscope, x1500.

3. EXPERIMENTAL

First stage of the WC grain size assessment consisted in grain chord lengths measurements on light microscopy images at x1500 magnification, according to ISO 4499-1 standard. Then the same samples have been evaluated using automatic image analysis method. The results obtained with both methods are presented in Table 2.

Table 2: Results of tungsten carbide particles chord length measurements using classical and automatic methods.

Sinter symbol	Average WC particles chord length [μm] (standard deviation)	
	Classical method	Automatic method
NiM	2.83 (1.09)	1.81 (1.50)
NiCoM1	2.72 (1.09)	1.96 (1.52)
NiCoM2	2.86 (1.08)	1.91 (1.45)
NiCoM3	2.84 (1.23)	1.97 (1.59)
Co-super-coarse	3.91 (2.63)	2.99 (2.41)
Co-coarse	1.91 (1.41)	1.59 (1.41)

For quantitative metallography needs perfect preparation of a metallographic specimen is of importance. Proper etching and correctly performed image acquisition allowed to reconstruct and reveal the grain boundaries. Metllo software was used in the quantitative materialographic investigations of the experimental sinters [Szala, 2001]. The initial grey images were subjected to several additional morphology transformations to remove image defects which had occurred during the preparation and to eliminate shadow from the microstructure images recorded by light microscope. An example of the initial grey image and detected (binarised) final image of WC particles to be measured are shown in Figure 2.

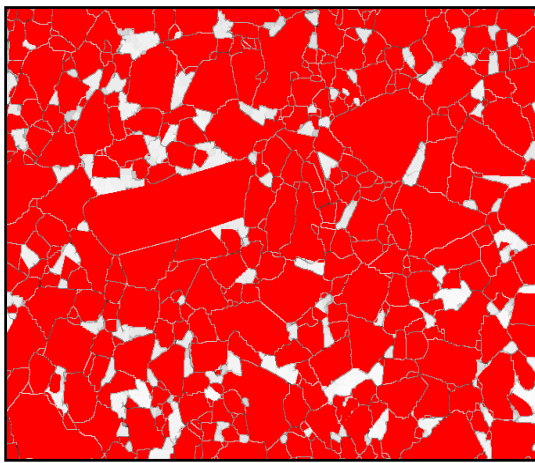
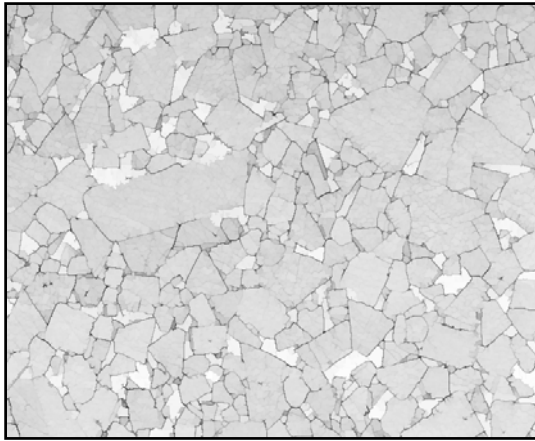


Figure 2: Grey image of Co-supercoarse sinters (top), final binary image of WC grains areas (bottom).

The λ Kolmogorov test of goodness of fit revealed deviation of all chord length distributions from the normal distribution and therefore nonparametric Kolmogorov-Smirnov test has been performed [Maliński, 2010]. Its results shown that all distributions of the experimental supercoarse grades significantly differ from that of the reference coarse sinter ($\lambda > \lambda_{0.05}$). To prove that this difference means longer grain chords the Mann-Whitney test with one-sided alternative hypothesis has been employed. The results of the test proved that the chord lengths of the nominally supercoarse sinters are actually longer than in the reference coarse sample (in case of both classical and automatic measurements). The chord length distributions obtained through the classical and automatic

method have been compared using the same tests. It was found that both methods yield significantly different results, the chord lengths being longer when measured conventionally.

4. SUMMARY AND CONCLUSIONS

Five experimental WC particles-metal matrix sinters have been manufactured using identical WC supercoarse powder, fraction of tungsten carbide being equal (90.5 wt.%) in all samples. Beside the typical cobalt matrix, four versions of matrices containing nickel have been investigated. To evaluate possible differences in the resulting WC grain size, the chord lengths were measured using both classical and automatic methods. For the automatic image analysis purposes the required high quality of the light microscopy images was obtained through optimisation of the metallographic microsection specimens, including the etching methodology. It is to be seen (Figure 2) that the grains visible on the final binary image perfectly correspond to these on the grey image. The chord lengths ranged from 2.72 μm to 3.91 μm when measured classically and from 1.81 μm to 2.99 μm in automatic method, in the reference commercial coarse grade 1.81 μm to 1.59 μm respectively. Distributions of the obtained values have been tested using the nonparametric Kolmogorov-Smirnov and Mann-Whitney statistical tests. It was found that all experimental, nominally supercoarse samples, actually belongs to supercoarse group of sintered carbides, this result being corroborated by the values of the chord lengths measured with both classical and automatic method. With the aid of the same statistical tests the employed measuring methods have been compared. This evaluation revealed statistically significant difference between the results yielded by this two methods. Automatic method, due to easiness of quick measuring large number

of chords and ability of measuring one pixel sized chord lengths, is more accurate and less time consuming in comparison to the conventional one.

Based on the results obtained the following conclusions may be formulated:

- replacing cobalt with nickel based alloys in the metal binder influences the tungsten carbide grain size but it is significantly larger than in the commercial coarse grade (hence the experimental sinters may be classified as supercoarse grades),
- the automatic image analysis and measurements of chord lengths in the supercoarse WC-metal matrix sinters is more accurate than the conventional method; it is less time consuming in case of properly etched samples,
- the statistical tests (Kolmogorov-Smirnov and Mann-Whitney) are effective method for evaluating grain size distributions and methods of their measurement.

Acknowledgements: The article is based on the research project financed by NCN, project number N N507 222240.

The valuable discussions with dr. Marian Maliński (Silesian University of Technology) and dr. Jan Krajzel (Sintered Carbides "BAILDONIT" Katowice, Poland) are gratefully acknowledged.

REFERENCES

- Fernandes, C.M., 2009. Carbide phases formed in WC-M (M = Fe/Ni/Cr) systems, *Ceramics International*, Vol.35, p.369.
- Maliński, M., 2010. Wybrane zagadnienia statystyki matematycznej w Excelu i pakiecie Statistica, Wydawnictwo Politechniki Śląskiej, Gliwice Poland.
- Szala, J., 2001. Zastosowanie metod komputerowej analizy obrazu do ilościowej oceny mikrostruktury, Wydawnictwo Politechniki Śląskiej, Gliwice Poland.

APPLICATION OF NANO-SIZED UP-CONVERSION PHOSPHORS DOPED WITH RARE-EARTH ELEMENTS IN POLYMER PHOTONICS

Alexander G. Savelyev^{1, a}, Evgeny V. Khaydukov¹, Andrey V. Nechaev², Vladislav Ya. Panchenko¹, Vladimir A. Semchishen¹, Victor I. Sokolov¹, and Andrey V. Zviagin¹

1. Institute on Laser and Information Technologies of the Russian Academy of Sciences, Department of advanced laser technologies, Moscow, Russia

2. Lomonosov Moscow State University of Fine Chemical Technologies, Moscow, Russia
a. A.G.Savelyev@gmail.com

ABSTRACT: We have synthesized 20-100 nm up-conversion anti-Stokes crystals of β - NaYF₄:Yb³⁺Er³⁺, β - NaYF₄:Yb³⁺Tm³⁺, and NaYF₄:Yb³⁺Tm³⁺Er³⁺ phosphors with conversion coefficient 2-3% at 100 W/cm² pump intensity. A special method for embedding the nano-phosphors into photocurable liquid compositions on the basis of new fluorinated acrylic monomers is employed. These monomers have the fluorination degree above 80% and the absorption coefficient 0.26 dB/cm in the 1500 nm telecom range. The method of deep UV contact lithography is employed to fabricate polymer waveguides with embedded nano-phosphors.

The technique for measuring the IR propagation loss in the polymer waveguides is proposed. It is based on embedding nano-phosphors at concentration 0.005% into polymer waveguide core. The technique can be used for analyzing the waveguides with extremely low scattering losses as well as waveguide splitters and directional couplers.

1. INTRODUCTION

Up-conversion nano-phosphors (NAF) possess a high conversion coefficient (CC), photostability, and multiwavelength photoluminescence spectrum. The cheap infrared diode lasers can be used for optical pump. The most promising up-conversion nano-crystals are NaYF₄, doped with ions Yb³⁺, Er³⁺, Tm³⁺. Matrix NaYF₄ is effective for anti-Stokes emission.

Er³⁺ (or Yb³⁺ and Tm³⁺) in the corresponding molar ratio 18% and 2%.

The synthesis is based on the coordinate stabilization of sol precursors in the solution of oleic acid. Sodium, yttrium, ytterbium, erbium, and thulium were used as precursors. The process proceeds at high temperature in oxygen free environment.

2. RESULTS AND DISCUSSIONS

2.1. Structure and Synthesis

The recently developed techniques were utilized to synthesize anti-Stokes NAF [Mai, *et al.*, 2006]. We optimized the chemical reaction in order to produce particles with an enhanced CC and appropriate dimensions. Our aim was to synthesize 10-100 nm nano-crystals NaYF₄ doped with trivalent lanthanides Yb³⁺ and

The resulting powder consists of cubic nano-crystals, so called α -phase with low CC of pump to luminescence. It needs for further processing in the narrow temperature range around 310°C. The final β -phase of crystals has a hexagonal lattice and possesses a high CC [Wang *et al.*, 2006]. The obtained conversion coefficient has a value 2%, which is comparable with world counterparts,

described in the literature [Wu, *et al.*, 2009].

The TEM photo and the schematic diagram of produced NAF are presented in Fig. 1. The crystal lattice NaYF₄ was doped with ytterbium (Yb³⁺) and erbium (Er³⁺) or thulium (Tm³⁺) ions depending on further applications. Ytterbium (Yb³⁺) and (Tm³⁺/Er³⁺) have functions of sensibilizers and activators correspondingly during the luminescence process in NAF.

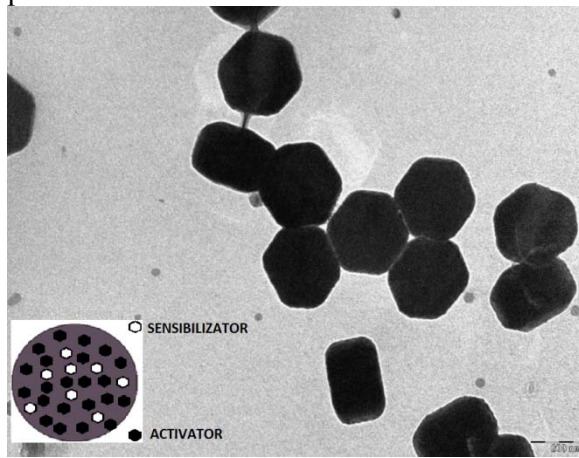


Figure 1: TEM photography of anti-Stokes NAF NaYF₄:Yb³⁺:Tm³⁺. The inset illustrates a schematic diagram of NAF.

In the present work we investigated NAF doped with Yb³⁺ and Tm³⁺ (NaYF₄:Yb³⁺:Tm³⁺), doped with Yb³⁺ and Er³⁺ (NaYF₄:Yb³⁺:Er³⁺), and doped simultaneously with Yb³⁺, Er³⁺ and Tm³⁺ (NaYF₄:Yb³⁺:Tm³⁺:Er³⁺).

2.2. Luminescent Properties of Nano-Phosphors

The luminescence in NAF occurs due to complicated multistage processes. Ion Yb³⁺ effectively absorbs the optical pump at 975 nm wavelength and transmits neighbor ions Er³⁺ (or Tm³⁺) in the excited metastable state. Two excited ions Er³⁺ can effectively redistribute the total energy by exciting one of ions to the higher energy level, due to de-excitation another one to the ground level – this process is called up-conversion [Page *et*

al., 1998]. The energy-level diagram explaining the up-conversion mechanism is represented in Fig. 2. The excited ion Er³⁺ can radiate photons of higher energy than the infrared pump photons. Therefore, we can observe luminescence in the visible green and red range of wavelengths. The photoluminescence spectra of nano-phosphors are presented in Fig. 3. The luminescence spectrum can be varied by doping NAF with Yb³⁺ and Er³⁺ or Yb³⁺ and Tm³⁺. One can manage the spectrum of photoluminescence in NaYF₄:Yb³⁺:Tm³⁺:Er³⁺ by adjusting the concentrations of Er³⁺ and Tm³⁺.

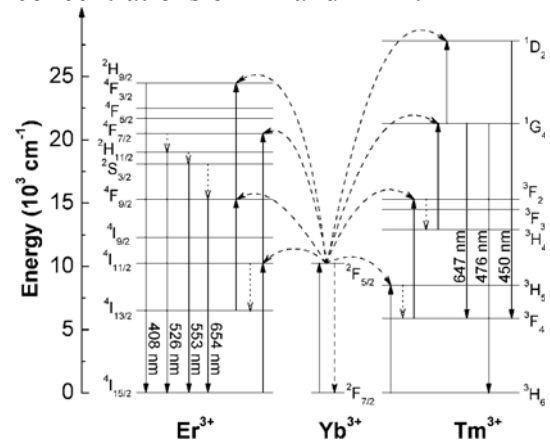


Figure 2: Energy level diagram, of the up-conversion mechanism for Yb³⁺, Er³⁺, and Yb³⁺, Tm³⁺ in the crystal matrix. The pump photon gets absorbed by the ion Yb³⁺, and transmits it to the excited state ²F_{5/2}. The energy level ⁴I_{13/2} (Er³⁺) or ³H₅ (Tm³⁺) gets populated due to the non-radiating resonance energy transmission.

Obviously, the excitation of NAF photoluminescence is a nonlinear process. This process is described by a system of kinetic equations of energy level populations in the ion Er³⁺. Levels 1 (ground), 2, 3 represented in Fig. 2 specify energy states ⁴I_{15/2}, ⁴I_{11/2}, ⁴F_{5/2}, correspondingly. We consider the simplest case – the three level quantum system with luminescence yield at 650 nm wavelength.

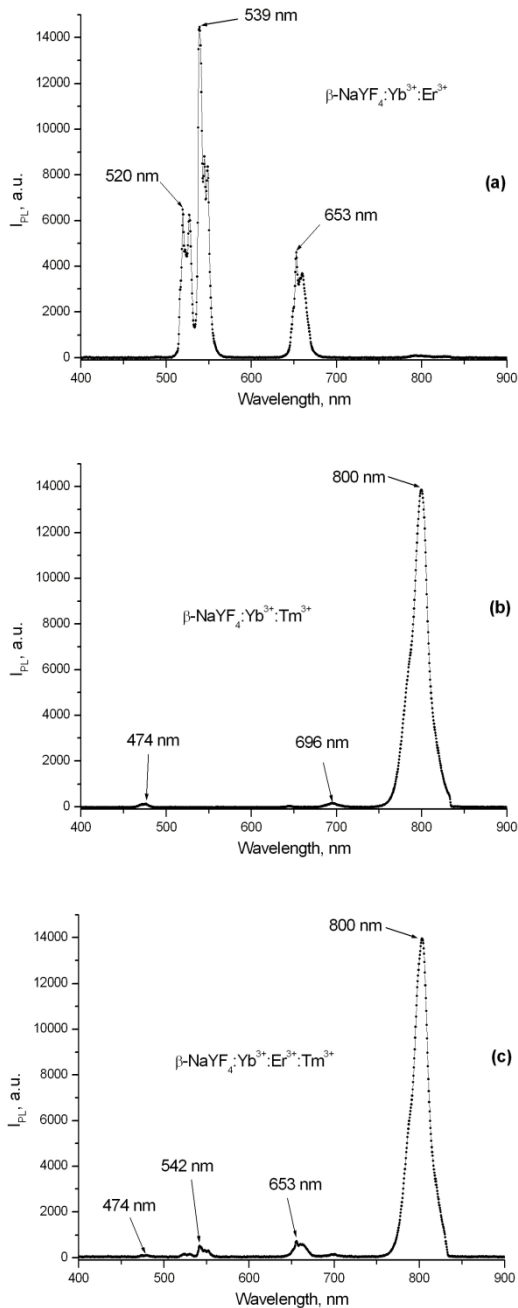


Figure 3: Photoluminescence spectra of nano-phosphors β - $\text{NaYF}_4:\text{Yb}^{3+}\text{Er}^{3+}$ (a), β - $\text{NaYF}_4:\text{Yb}^{3+}\text{Tm}^{3+}$ (b), and β - $\text{NaYF}_4:\text{Yb}^{3+}\text{Tm}^{3+}\text{Er}^{3+}$ (c) with optical pump at 975 nm wavelength.

$$dN_3/dt = W_i N_2^2 - (W_{31} + W_{32}) N_3,$$

$$dN_2/dt = -2W_i N_2^2 - W_2 N_2 + W_{32} N_3,$$

$$dN_1/dt = W_i N_2^2 + W_2 N_2 + W_{31} N_3,$$

where N_1 , N_2 , N_3 – populations at levels 1, 2, 3; W_{31} , W_{32} – probabilities of transitions $3 \rightarrow 1$ and $3 \rightarrow 2$; W_i –

probability of up-conversion, when one ion populates the level 3, and another one – the ground level 1. Analyzing kinetic equations, one can conclude that at low pump intensities the luminescence signal is proportional to P^2 due to N_2^2 . Thus, CC of NAF depends on the pump intensity linearly. Measuring intensity dependence of CC is the key control parameter to define optimal parameters of an optical probe system and a chemical synthesis.

2.3. Producing Stable Colloids on the Basis of Nano-Phosphors

The water colloids with NAF can be produced by employing different fabrication techniques. Nevertheless, the most effective technique to obtain a stable water colloid is based on covering NAF by amphiphilic polymers. The amphiphilic polymers consist of molecules with hydrophobic and hydrophilic terminals. The hydrophobic terminals of amphiphilic polymers can connect to the surface of NAF covered with hydrophobic oleic groups. The hydrophilic terminal remains obverse of the particle. Thus, NAF becomes to be a hydrophilic particle, stable in water colloids.

We utilized the surface modification technique to produce monomer-soluble stable complexes of NAF. These complexes can be used to produce liquid compositions based on fluorinated acrylic monomers and suitable for deep UV photo polymerization.

2.4. Propagation Loss Measurement in the Polymer Waveguides

We propose a new method of the propagation loss measurement in the polymer waveguides based on embedding nanophosphors. The up-conversion nanophosphors were embedded in the waveguide cores of s-shaped and circular waveguides. The refractive index of

nano-phosphores was close to the refractive index of the polymer. Nevertheless, in order to avoid any scattering losses the concentration of nano-particles in the waveguide core composition was approximately 0.01%. However, even this small amount of nano-crystals was enough to observe a photoluminescence. The light at 975 nm wavelength, launched into the waveguide, is visualized as a bright shining in the waveguide cores (see Fig. 4 and Fig. 5). We can estimate the propagation loss by measuring the photoluminescence intensity along the track. The presented technique is non-destructive in comparison with a standard cutback method and takes into account both absorption and scattering losses.



Figure 4: The photograph of 975 nm light in the s-shape planar waveguide with embedded nano-phosphors.



Figure 5: The photograph of 975 nm light propagation in the circular planar waveguide with embedded nano-phosphors.

2.5. Bragg Grating Inscription in the Polymer Matrix with Embedded Nano-Particles

The interferometric technique was employed at the wavelength of He-Cd laser (325 nm) to fabricate 1D and 2D Bragg gratings in the photocurable polymer with embedded NAF. The photography made by luminescent microscope illustrates the grating (see Fig. 6). The period of fabricated Bragg gratings is in the range from 500 nm up to 10 μm .

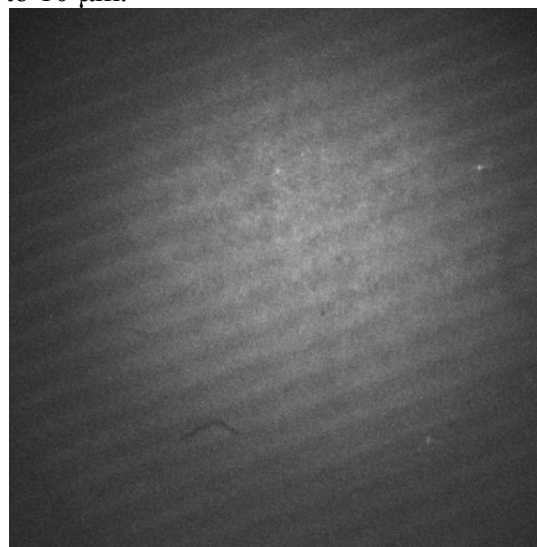


Figure 6: Luminescent microscopy of inscribed 1D Bragg grating with embedded nano-phosphors.

3. CONCLUSIONS

We developed a synthesis and optimized a chemical reaction of producing up-conversion anti-Stokes NAF. The luminescence spectra were measured: β - $\text{NaYF}_4:\text{Yb}^{3+}\text{Er}^{3+}$, had spikes at 520, 539, and 653 nm; β - $\text{NaYF}_4:\text{Yb}^{3+}\text{Tm}^{3+}$ at 474, 696, and 800 nm, and β - $\text{NaYF}_4:\text{Yb}^{3+}\text{Tm}^{3+}\text{Er}^{3+}$ had a strong spike at 800 nm and three small spikes at 474, 542, and 653 nm.

The stable colloids with NAF were produced. The monomer colloids can be used to fabricate the optoelectronic components, such as: waveguides, couplers and Bragg gratings.

The synthesized nanoparticles can find an application as markers, in order to visualize the light propagation in the planar optoelectronic systems. The analysis of the photoluminescence intensity decay along the waveguide allows estimating the propagation loss.

Acknowledgements: The reported study was partially supported by RFBR, research projects No. 12-07-31223 МОЛ_a, 12-02-31845 МОЛ_a, 13-07-00976_A, grant of the President of Russian Federation for the state support of young Russian scientists MK-6798.2013.9, and NSCH-6141.2012.2.

REFERENCES

- Mai, H. X., Zhang, Y. W., Si, R., Yan, Z. G., Sun, L. D., You, L. P., & Yan, C. H. (2006) *Journal of the American Chemical Society* **128**, 6426-6436.
- Page, R. H., Schaffers, K. I., Waide, P. A., Tassano, J. B., Payne, S. A., Krupke, W. F., & Bischel, W. K. (1998) *Journal of the Optical Society of America B-Optical Physics* **15**, 996-1008.
- Wang, F., Chatterjee, D. K., Li, Z. Q., Zhang, Y., Fan, X. P., & Wang, M. Q. (2006) *Nanotechnology* **17**, 5786-5791.
- Wu, S. W., Han, G., Milliron, D. J., Aloni, S., Altoe, V., Talapin, D. V., Cohen, B. E., & Schuck, P. J. (2009) *Proceedings of the National Academy of Sciences of the United States of America* **106**, 10917-10921.

TENSILE PROPERTIES OF GROUND COLEMANITE FILLED POLYPROPYLENE HOMOPOLYMER

Şenol Şahin and Tülin Şahin^a

Kocaeli University, Department of Mechanical Engineering, Kocaeli, Turkey
a. Corresponding author (tulsah@kocaeli.edu.tr)

ABSTRACT: In this study the effect of the ground colemanite (GC) substance, to the tensile properties of the polypropylene homopolymer (PPH) material, was studied. The average particle size ($d_{0.5}$) of the GC substance was 20.6 μm . The PPH raw material was filled with GC at different percentage rates (5, 7.5, 10, 12.5, 15, 17.5, 20, 22.5, 25, 27.5 and 30%) by weight with a twin-screw extrusion machine by constant extrusion parameters. Firstly, the melt flow rates (MFR) of the filled (PPH/GC composite) and unfilled (pure PPH) raw materials were determined. Secondly, the pure and the composite raw materials were pressed into standard tensile specimens with an injection-moulding machine by constant injection parameters. The test experiments were performed with samples at constant experiment conditions. The results were given according to the increasing amount of GC filler content in PPH base material. It was detected that, GC substance increases the MFR, Young's modulus and tensile strength at break, while it decreases the tensile strength at yield, the tensile strain at yield and at break of the material.

Keywords: Polypropylene homopolymer, Ground colemanite, Composite, Tensile Properties, Melt flow rate

1. INTRODUCTION

For small or big, kitchen or bathroom, electrical or electronic household appliances and in computer technology, polypropylene (PP) is a frequently used material [Bentham, 1999]. During the production of goods with PP raw material by using several methods, before only in order to reduce the cost of the product [Osman, 2004] however nowadays to improve the mechanical, thermal and electrical properties, some kind of filling materials are added while forming operation is done [Kwon, 2002]. Within this scope, especially PPH materials, with micro particle filling substance such as talc, calcium carbonate and as a reinforcement substance glass fiber, are preferred because of their high rigidity and good thermal performances. Another reason of their preferability is the high price-volume-performance relation of this material, compared to commonly used other materials [Pukánszky, 1995]. The

semi-crystalline thermoplastics and the applications that filled with various micro particles of these have been subjected to numerous studies. Many researches accomplished to understand the deformation characteristics of these thermoplastic materials [Zhou and Mallick, 2002]. It is a common opinion that, in composites with micro particles, particle size, adhesion between surfaces [Wulin *et al.*, 2000] and surface characteristics influence the performance of filled system substantially. Besides, it is known that particle shape, particle distribution and filler amount rate have a significant influence on system performance [Wah *et al.*, 2000].

However there isn't observed any kind of scientific studies for the tensile properties of GC filled PPH materials. Because of that reason the purpose of this study is to determine the change on rigidity and toughness values of GC filled PPH

composite materials depending on their filler amount ratio.

2. EXPERIMENTAL

2.1 Materials

In this study, the PPH has been used, which commercial name is MOPLEN HP500N (Basell Service Company B.V.) and values with 900 kg/m^3 density and 12 g/10 min ($230^\circ\text{C}/2.16 \text{ kg}$) MFR. The other values of PPH from the manufacturer is 1450 MPa modulus of flexural, 33 MPa, tensile strength at yield and 10% tensile elongation at yield about some mechanical properties for injection molding applications, according to ASTM D standard.

As the additive and/or filling substance, the mineral with the commercial name GC (Eti Mine Works General Management) was used. Some of the main properties of GC substance, which is obtained from mine site in Turkey-Bigadiç, given in Table 1, 2 and 3.

Table 1: Chemical specification.

Component	Unit	Content
B ₂ O ₃	%	40.00±0.50
CaO	%	27.00±1.00
SiO ₂	%	6.50 Max

Table 2: Sieve specification.

Particle Size	Unit	Content
+ 600 μm	%	0.02 Max.
+ 250 μm	%	0.50 Max.
- 75 μm	%	87.00±5.00
- 45 μm	%	75.00±5.00
Moisture	%	1.00 Max.
Bulk Density	g/cm^3	0.80-1.00

In the Table 4, features of the K5 PEW (is product name) - Empolim PE Wax (is brand name) (Zirve Polimer San. Tic. Ltd. Şti.) which is used as lubricant, are given. This lubricant substance is added

0.5% by weight rate to pure PPH material, during the production with different weight amount rates of GC filling materials.

Table 3: Particle size analysis results.

Specification	Unit	Typical
Average diameter (d0.5)	μm	20.596
TopCut (d0.9)	μm	66.559
Specific Surface Area	m^2/g	1.04

Table 4: Technical properties.

Specification	Unit	Typical Value
Structure		Less molecular polymer. ($n_{av.}=700$)
Appearance		White color flake or dust
Melting point	$^\circ\text{C}$	95± 10
Bulk density	kg/m^3	500 ± 20
Acid Index		0
Soap Index		0
Purity	%	95 ± 5

2.2. Composite Preparation

For the PPH/GC composite raw materials production, twin-screw extruder (Coperion Werner and Pleiderer ZSK 25 P8.2 E WLE) has been used that has (L/D) 45 mm screw length and (L) 1125 mm helix length. Firstly, the lubricant substance PEWAX is added 0.5% by weight to pure PPH raw material in plastic raw material mixer. Later, the GC filled PPH composite raw materials were produced in different weight amount rates (5, 7.5, 10, 12.5, 15, 17.5, 20, 22.5, 25, 27.5 and 30 %) with the physical modification method. The production has been performed in extrusion of fixed parameters under the conditions of 900 rpm rotation speed, 30 kg/h production capacity, between 220°C and 245°C zone temperatures and 30°C cooling water bath

temperature. Each composite raw material has been performed dried at 50°C for 4 hours.

2.3. Sample Preparation

Pure PPH and PPH/GC composite raw materials was injection molded according to ISO 527-2 Type-1A tensile test samples which have dimensions as 216 mm x 10 mm x 4 mm by an injection machine (Haitian Plastics Machinery HTF 90W) with 46 mm screw diameter (D) and 20 screw length (L/D). In molding process done by considering ISO 294-1 standard, injection parameters which are fixed 235°C as nozzle temperature, 230°C/225°C/220°C as zone temperature, 1400 bars as injection pressure, 700 bars as holding pressure, 60 seconds as waiting time and 30°C as die cooling water temperature used. Test samples were conditioned before tests according to ISO 291.

2.4. Melt Flow Rate Test

Melt flow rate (MFR) experiments are done according to ISO 1133 standard, with the 4106 E Model of the Zwick-Roell brand test device. Experiments are done on granule of pure PPH and PPH/GC composite raw materials. For MFR tests to calculate the sample weight, 4.4 times of density was calculated and precisely weighed before tests. The experiments were performed at 230°C test temperature with 2.16 kg test load. The values taken from the device with g/10 min unit are taken as MFR results.

2.5. Tensile Test

The tensile tests were done by considering ISO 527-1 with a tensile test machine (INSTRON 4411 H 4240) which has a capacity of 5 kN with Bluehill-2 software (ver. 2.6) and Clip - on static extensometer (INSTRON 2630-111) on it. According to ISO 527-2 standard, 216 mm x 10 mm x 4 mm sized Type-1A tensile samples were placed in the tensile

test machine, so that injection entrance is on the fixed grip of the tensile test machine.

The tests were done under 22°C±1°C temperature and 50%±10% humidity. For each value at least 5 test specimens were used. Obtained values were statistically considered according to Chauvenet Criteria [Holman, 1994].

3. RESULT AND DISCUSSION

It is important to mention that pure PPH raw material is used without the exposition of twin-screw extruder parameters as it is in PPH/GC composite raw materials. Also during the study pure PPH raw material was used without addition of PEW.

In Figure 1 change on MFR of pure PPH material according to increasing addition of GC filling material amount is shown. In the graphic, it is seen that addition of 5 wt% GC increases 35% MFR value of pure PPH material. On the other hand, it is determined that addition of more than 5wt% GC, decreased the MFR value of PPH/GC composite materials. Even though it is discovered also that 30 wt% GC filled PPH/GC composite materials, had 10% higher MFR value, compared to pure PPH material.

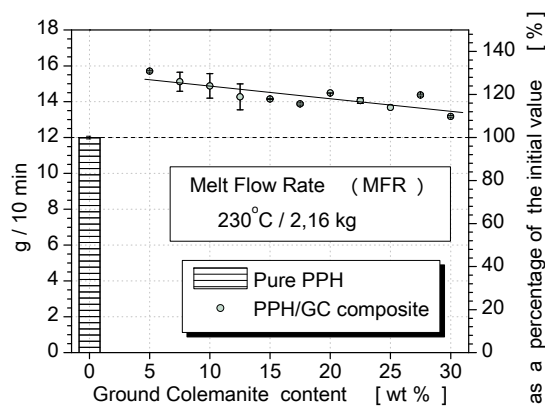


Figure 1: The change of the melt flow rate of PPH material.

Figure 2 shows the affect on Young's Modulus (E) with increasing amount of GC in pure PPH materials. From the figure it is possible to see that 5 wt% of GC increases Young's Modulus around 3%. Addition of GC material more than 5wt% to PPH/GC composite material, increased E value much more. At the end it is found that 30wt% of GC filling material have approximately 45% increases E value than pure PPH material.

In Figure 3, change on the maximum tensile stress (σ_M) depending on increasing amount of GC filling material is shown. It is seen that 5 wt% GC decreased the maximum tensile stress of pure PPH material around 9%. On the other hand, increase of GC amount more than 5 wt%, decreases the maximum tensile stress of PPH/GC composite much more. It is seen that 30wt% GC filled PPH/GC composite materials have around 32% lower maximum tensile stress than pure PPH materials.

In Figure 4, change on maximum tensile strain (ϵ_M) value of pure PPH material with the increase of GC filling material is given. By the figure it can be seen that 5wt% GC decreases the maximum tensile strain of pure PPH material around 14%. Addition of GC amount higher than 5wt% causes much more wane on the maximum tensile strain of PPH/GC composite materials. It is too seen that 30wt% GC filled PPH/GC composite material have around 50% lower maximum tensile strain value than pure PPH materials.

Figure 5 shows us change on tensile break stress (σ_B) value of pure PPH material with the addition of GC filling material. It is determined that 5wt% GC in pure PPH material increase the tensile break stress about 23%. PPH/GC composite materials containing GC substance amount higher than 5wt% had

lower tensile break stresses. However, tensile break stress of PPH/GC composites including 25 wt% GC had almost the same value with pure PPH material. In addition to this PPH-GC composite materials filled with 30wt% of GC had tensile break Stress only 4% lower than the pure material.

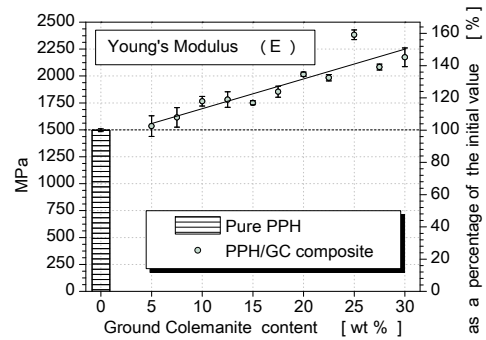


Figure 2: The change of the Young's modulus of PPH material.

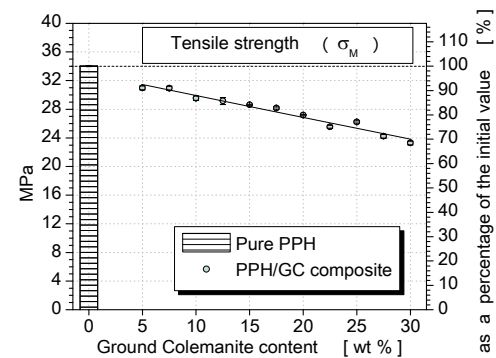


Figure 3: The change of the stress at yield of PPH material.

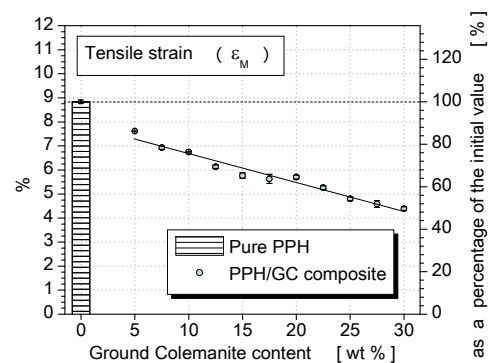


Figure 4: The change of the strain at yield of PPH material.

In Figure 6, changes on tensile break strain (ϵ_B) value with addition of GC filling material into pure PPH material is given. From the figure it is seen that amount of 5 wt% GC in pure PPH material reduces suddenly the Tensile Break Strain around 94%. Addition of more than 5 wt% GC filling material also lowered much more the tensile break strain.

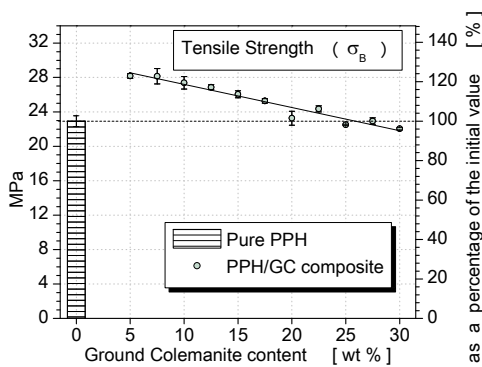


Figure 5: The change of the stress at break of PPH material.

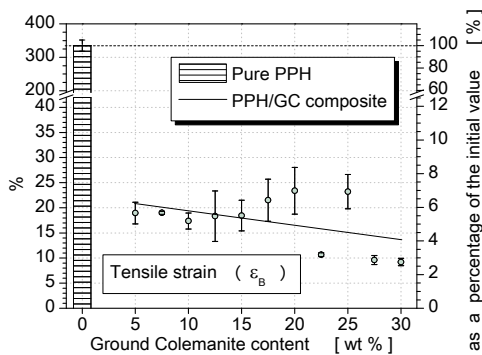


Figure 6: The change of the strain at break of PPH material.

4. CONCLUSIONS

It is discovered that each tensile characteristics of pure PPH material is influenced by the addition of 5wt% GC filling material. In experiments, increase on the values of Young's Modulus with 3% and tensile break stress with 23% is seen. However decrease on maximum tensile stress with 9%, maximum tensile strain with 14% and tensile break strain with 94% is determined. It is also seen

that tensile characteristics of PPH-GC composite materials are affected from increasing amount of GC filling material. Increasing GC filling material amount rose Young's Modulus of PPH/GC composites but decreased Maximum tensile stress, tensile break Stress, Maximum tensile Strain and Tensile Break Strain. But even if the increasing GC filling material amount caused decrease on tensile break stress, it is also seen that PPH/GC composite material with 25wt% GC filling material had approximately the same value with pure PPH material.

REFERENCES

- Bentham, J., 1999. Appliances, In: J.Karger-Kocsis, editor. Polypropylene: An A-Z reference, Kluwer Publishers, Dordrecht, P. 29. ISBN 0412802007.
- Osman, M. A., Atallah, A. and Suter, U. W., 2004. Influence of excessive filler coating on the tensile properties of LDPE – calcium carbonate composites, *Polymer*, 45, 1177.
- Kwon, S., Kim, K. J., Kim, H., Kundu, P. P., Kim, T. J., Lee, Y. K., Lee, B. H. and Choe, S., 2002. Tensile property and interfacial dewetting in the calcite filled HDPE, LDPE, and LLDPE composites, *Polymer*, 43, 6901.
- Pukánskyz, B., 1995. Particulate filled polypropylene: structure and properties, In: J. Karger - Kocsis, editor. Polypropylene: Structure, blends and composites, Chapman & Hall, London, P. 1. ISBN 0412584301.
- Zhou, Y. and Mallick, P. K., 2002. Effects of Temperature and Strain Rate on the Tensile Behavior of Unfilled and Talc-Filled Polypropylene. Part I: Experiments, *Polymer Engineering and Science*, 42, 12, 2449.
- Wulin, Q., Mai, K. And Zeng, H., 2000. Effect of Silane-Grafted Polypropylene on the Mechanical Properties and Crystallization Behavior of Talc/Polypropylene Composites, *Journal of Applied Polymer Science*, 77, 2974.
- Wah, C. A., Choong, L. Y. and Neon, G. S., 2000. Effects of titanate coupling agent on rheological behaviour, dispersion characteristics and mechanical properties of talc filled polypropylene, *European Polymer Journal*, 36, 789.
- Holman, J. P., 1994. Experimental Methods for Engineers, 6th ed., McGraw-Hill, New York.

THE EFFECT OF THERMAL CYCLES ON FRACTURE BEHAVIOUR OF FILLED CALCIUM CARBONATE POLYPROPYLENE RANDOM COPOLYMER

Tülin Şahin^{1,a}, Zümeer Köksal Altıntaş², Şenol Şahin¹

1. Kocaeli University, Machine Engineering Department, İzmit, Turkey

2. Kocaeli University, Machine Engineering Department, İzmit, Turkey

a. Corresponding author (tulsah@kocaeli.com.tr)

ABSTRACT: Thermal fatigue might be damaging in structures internally constrained, which cannot expand or contract freely as in composite materials. During thermal cycling, both matrix and fiber expand or contract according to their coefficients of thermal expansion. This, in turn, influences the structural integrity of the composite and can limit the life of a composite material. In this article, in deference to environment conditions and working temperatures, thermal cycling applications on Polypropylene containing CaCO₃ at the different temperatures were realized. In this artical, in deference to environment conditions and working temperatures thermal cycling applications of PPrC (Polypropylene random copolymer) containing CaCO₃ at the different temperatures were realized. For different (25, 50, 100, 200) thermal cycling, according to ISO180 standard, charpy impact test was done. Properties of physical and mechanical features are explained as for that filling material and thermal cycle outputs. In this study, the crack propagation characteristic of the material exposed to thermal cycling and the absorbed energy amount during the crack initiation and propagation were analyzed.

Keywords: Thermal Cycling, Polypropylene Random Copolymer, Mechanical Properties

1. INTRODUCTION

Thermal exposure combined with mechanical loading can produce significant damage accumulation in polymer composites which can alter their mechanical and permeability properties [Bechel 2003, Ahborn and Knaak 1988, Nettles and . Biss 1996]. All materials expand or contract during temperature changes. Thermal fatigue might be damaging for structures internally constrained, which cannot expand or contract freely as in composite materials. The composite consists of two distinct components, each with different mechanical properties and coefficients of thermal expansion. During thermal cycling, both matrix and fibre expand or contract according to their coefficients of thermal expansion. As they are internally constrained, temperature fluctuations cause stress build-up at the interface

[Biernacki 1999]. Constraint of thermal expansion causes thermal stresses, which may also initiate and propagate fatigue cracks [Spera 1975]. This, in turn, influences the structural integrity of the composite and can limit the life of a composite material [Morris 1989].

Plastic materials indicate different mechanic features at every temperatures. mechanic properties of the materials will be change, which working long time at the high temperatures. For this reason, the physical life of the materials being exposed to thermal aging must be established [Şahin 2002].

In this article, in deference to environment conditions and working temperatures thermal cycling applications

of PPrC (Polypropylene random copolymer) containing CaCO₃ at the different temperatures were realized. For different (25, 50, 100, 200) thermal cycling, according to ISO180 standard, Charpy impact test was done. Properties of physical and mechanical features are explained as for that filling material and thermal cycle outputs. In this study, the crack propagation characteristic of the material exposed to thermal cycling and the absorbed energy amount during the crack initiation and propagation were analyzed.

2. EMPIRICAL STUDY

2.1. Materials

PP-R as a basic polymer used in this study in natural color and granule form was supplied from Borealis Company under the trade name of RA130E (polypropylene random copolymer).

Table 1: Manufacturer's data for physical and mechanical properties of PP-R pipe material

	Test Method	Test conditions	RA130E Natural
Tensile yield strength	ISO 527-2	50 mm/min	25 MPa
Tensile yield elongation	ISO 527-2	50 mm/min	%13.5
Tensile elasticity module	ISO 527	1 mm/min	900 MPa
Charpy impact (with notch)	ISO 179	+23°C	20 kJ/m ²
Charpy impact (with notch)	ISO 179	-20°C	2 kJ/m ²
Hardness	ISO 868	Shore D	60
Vicat softening temperature	ISO 306	B (50 N)	65 °C
Density	ISO1183	gr/cm ³	0.900

2.2. Preparing Test Samples

Test samples were prepared in two groups in this study. For the first group, calcium carbonate (CaCO₃) mineral filler was added into the natural material during injection at the ratios of 5%, 15%, and 30% by volume. The test sample of natural material (unfilled) were prepared

by injection for the second group. The first and second group test samples were manufactured by employing Erat FE130/95 Model Injection Machinery.

Table 1 shows some significant physical and mechanical properties provided by the manufacturer taken through the standard test samples manufactured by injection molding method [Leong et al. 2004, Sahin ve Yayla 2005]. Table 2 shows some basic properties of CaCO₃ manufactured in granule form and used for the entire polyolefin group.

Table 2: Some data about calcium carbonate (CaCO₃) used in the study

	Test Method	Mineral Material
CaCO ₃ ratio	-	%98
Average particle diameter (D%50)	-	µm 2
The highest particle diameter (D%98) [TopCut]	-	µm 10
Density	ISO787/10	g/ml 2.17
Brightness	DIN 53163	%85(Ry, C/2)

2.3. Material Testing

2.3.1. Thermal cycle

After shaping %5, %15 and %30 PPrC filled materials into Charpy test's standard sample dimensions, the sample parts are hold 1 min in a water filled receptacle which is set at 5 C°. After that they are again hold 1 min in another receptacle at stable 100 C°. This is determined as one cycle. That procedure is repeated 25 times, 50 times, 100 times and 200 times. The samples are dried in a room temperature without using any tools or methods. After that, all materials, which are filled and non-filled, are gathered and Charpy tests are done to these parts in a room conditioned to 20 C° and the results of the experiments are analyzed and graphics are drawn with their mechanical outputs.

2.3.2. Charpy impact test

Instrumented impact testing provides valuable information on energies involved in the fracture process, giving individual evaluation of the energy for crack initiation and also the energy required to propagate the crack through the material, which is not possible with the conventional Charpy impact test. In many materials, the formation of the crack at the notch root occurs just prior to or at the peak load. Therefore, it is a reasonable approximation to define the energy up to the peak load as the ‘crack initiation resistance’ [Sahin And Yayla 2005, Manahan et al. 2000].

Charpy tests were applied on the Charpy samples for determining the effect of calcium carbonate (CaCO_3) on the behaviors of PP-R materials against impacts at the temperature of $22^\circ\text{C} \pm 1^\circ\text{C}$ and $50\% \pm 10$ humidity ratios according to ISO 179 standard. These tests were carried out through instrumented Charpy impact test device with strike rate of 2.53 m/s under the trademark of CEAST. The values for the materials such as maximum force (F_{Max}) [N], maximum energy W [J] and the energy at maximum force ($W_{F_{\text{max}}}$) [J] were determined by using force (F)-time (t)- and force (F)-distance (x) diagrams derived from Charpy tests. Two types of energy were obtained from the tests. One is the energy until maximum force and this can be considered as Charpy crack initiation energy [$E_{F_{\text{max}}}$]. The other one is the total energy spent across the impact known as conventionally Charpy maximum impact energy. Consequently, the difference between these two energies may be considered as Charpy crack propagation energy [E_{pro}]. This energy comes after the maximum force.

The values derived from Charpy test samples used for each value were statistically evaluated according to

Chouvenant criterion and variations were shown on graphics as % based on natural (unfilled) Charpy sample [Holman 1994].

3. RESULTS

Besides applied thermal cycle, amount of CaCO_3 in PPRc material causes great changes on materials’ mechanical features and that may give us significant outputs in order to compare endurance against brittle fracture.

Mechanical effects occurred by CaCO_3 in PPRc material, according to thermal cycle, are shown as it is seen at graphics below in Figure 1 to 4. Ratio of filling material, number of cycle cause changes on, maximum energy, crack initiation energy and propagate crack energy of the material.

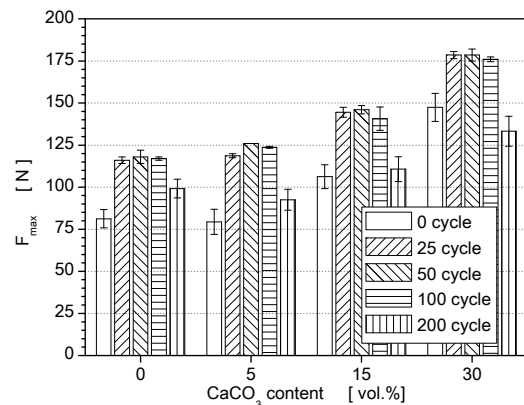


Figure 1: Maximum Force

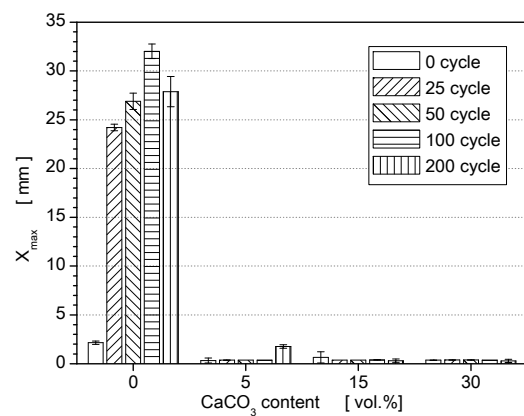


Figure 2: The crack propagation energy

Maximum breaking force rises with ratio of filling material and thermal cycle round.

Thermal cycle applied on pure material boosts the value of crack propagate energy; hence that causes increase on maximum energy. In addition to this, to reinforce the material decreases the energy of crack propagates.

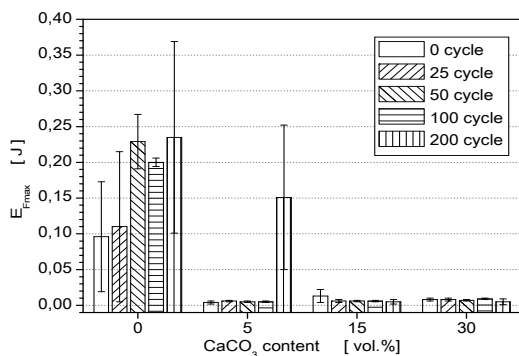


Figure 3: Crack initiation energy

Adding filling material caused high decline on crack initiation energy of material. And that rises tendency of damage formation. The effect of thermal cycle actually cannot be observed because of this decline on crack initiation energy.

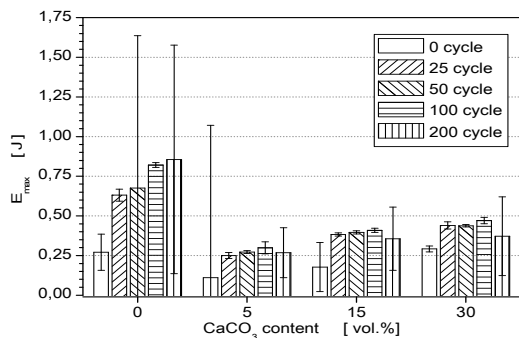


Figure 4: Maximum energy

Proper to the literature reinforcing with CaCO_3 lessens total crack energy. But, it is observed that %30 filled material has higher crack energy than the %5 filled material. Thermal cycle round is directly proportionate to total crack energy of non-filled material. But in 200 cycles,

filled material's crack energy decreases in figure 4.

In the experiments four different values are criticized and it is observed that filling procedure is not important after a defined limit. Thermal cycle's relatively positive results are signals that inner structure of plastic changes into a regular state (it is formed to crystalline structure). When PPRc material's usage areas are considered, differentiation on material's cracking behaviors, which may change the material's state model, caused by continuous temperature changes is important for working productivity.

REFERENCES

- Bechel, V.T., Fredin M. B., Donaldson S.L., Kim R. Y. and Camping J.D., 2003. Composites: Part A 3, 663..
- Ahborn K. and Knaak S ., 1988. *Cryogenics* 28, 273.
- T. Nettles and E.S . Biss, 1996. Low Temperature Mechanical Testing of Carbon-Fiber/Epoxy Resin Composite Materials. NASA Technical Memorandum, NASA Center for Aerospace Information, pp3663.
- Biernacki K., Szyszkowski W. and Yannacopoulos S .1999., *Composites: Part A* 30, 1027.
- Spera, D. A., 1975. What is Thermal Fatigue in Thermal Fatigue of Materials and Components, Philadelphia, PA., American Society for Testing and Materials, vol. 3.
- Morris W.L., James M.R. and Inman R.V., 1989. *J. Engng.Mat. Tech.* 331.
- Şahin, Ş. 2002. Polipropilen Random Kopolimer (PPRC) Boruların Mekanik Özelliklerine Etki Eden Parametrelerin İncelenmesi. Doktora Tezi, Kocaeli Üniversitesi Fen Bilimleri Enstitüsü.
- Tamer SINMAZÇELİK and A.Armağan ARICI, 2006. *J MATER SCI* 41, 1233–1241.
- Leong, Y.W., Mohd.Ishak, Z.A., Ariffin, A., 2004. *Journal Of Applied Polymer Science*, 91, 3327-3336.
- Sahin S. And Yayla P., 2005. *Polymer Testing* 24, 613–619.
- Manahan Sr., M.P, Cruz Jr., C.A., Yohn, H.E., In: Peraro, J.S (Ed.) ,2000. *Astm Stp 1390*, American Society For Testing And Materials, West Conshohocken, Pa.
- Holman, J. P., 1994. *Experimental Methods For Engineers*, Sixth Edition, Mcgraw-Hill, Inc., ISBN 0-07-029666-9, Singapore

SYNTHESIS AND CHARACTERIZATION OF ZSM-5 ZEOLITE FROM WHEAT HULL ASH

Pınar Terzioğlu^{1,a}, Sevil Yücel², and Mehmet Öztürk¹

1. Muğla Sıtkı Koçman University, Faculty of Sciences, Department of Chemistry, Muğla, Turkey

2. Yildiz Technical University, Faculty of Chemistry and Metallurgy, Department of Bioengineering, Istanbul, Turkey

a. Corresponding author (pinarterzioglu@mu.edu.tr)

ABSTRACT: Wheat hull is an abundantly available residue from wheat milling industry which has an important value due to its silica content. The husks are generally burned in open air, thus bring serious pollution problems. It is necessary then, to utilize the silica of this agrowaste. The extraction of silica from natural sources such as rice hull, sugarcane bagasse and wheat hull is very simple and rapid. The extracted silica can be evaluated in many fields for production of silica based materials. Silica is one of the main raw material for zeolite production. Zeolites are micro-porous crystals that can be used in many fields ranging from adsorption to construction.

In the present study, wheat hull ash silica was used to synthesize ZSM-5 zeolite. Extraction of amorphous silica with approximately 88% purity was performed from acid leached wheat hull ash by an alkali solution. The extracted silica was used as a natural source to synthesize ZSM-5 zeolite under hydrothermal condition. Characterization of silica and ZSM-5 zeolite were investigated by X-ray diffraction, Fourier transform infrared spectroscopy, and scanning electron microscope analyses. Results revealed that wheat hull ash is a suitable material for production of SiO₂ which is the main constituent of zeolite.

Keywords: Ash; wheat hull; silica; zeolite.

1. INTRODUCTION

Wheat hull is a lignocellulosic residue of wheat milling industry which is disposed of and left to decay but is generally burned in open air fires and causes serious environmental problems including land and air pollution [Kaya *et al.* 2008]. However, it can be evaluated as a good precursor for silica and silica based product's synthesizes such as ceramic, silicon carbide, silicon nitride, silicon tetrachloride, silica gel and zeolite [Motojima *et al.* 1995; Kalapathy *et al.* 2000; Sun and Gong 2001]. In the

literature very little information was found that addressed the recovery of wheat hull ash as a source of active silica.

Terzioğlu and Yücel found that the wheat hull ash obtained by burning at 600°C for

5 hour has 43.2% silica content and was used to produce magnesium silicate.

Zeolites are natural or synthetic nano- and micro-porous crystalline compounds which have been used in a range of industrial application as separation agents, catalysts and ion exchangers [Wittayakun *et al.*, 2008]. ZSM-5 is an important zeolite with high silica and low aluminium content was reported first by Mobil Co. in 1972 [Argauer *et al.*, 1972]. It is often used as a catalyst in organic reactions due to its unique pore structure and high acidity. ZSM-5 zeolite has been synthesized hydrothermally by use of

pure chemicals as silica and aluminium source in the presence of organic templates. Various types of zeolites have been synthesized by use of rice husk ash as an active silica source [Nur, 2001; Prasetyoko et al., 2006; Ghasemi and Younesi, 2011].

The present study aimed to synthesize and characterize zeolite ZSM-5 from wheat hull ash which is a cheap byproduct of agricultural industry and a practical silica source for the first time.

2. MATERIALS AND METHODS

2.1. Materials

The chemicals used in production of zeolite ZSM-5, which were analytical reagent grade, NaOH, H₂SO₄, HCl, tetrapropylammonium bromide (TPABr), n-propyl amine (n-PA), and aluminum sulfate (Al₂(SO₄)₃.16H₂O), were supplied by Sigma-Aldrich. The wheat hull samples were collected from Marmara region-Turkey.

2.2. Methods

2.2.1. Preparation of sodium silicate solution

The silicate solution from the acid leached wheat hull was prepared adapting the method of Kalapathy and Proctor [Kalapathy and Proctor, 2000]. The wheat hulls were washed with distilled water to eliminate the major impurities such as clay particles. After washing step, the hulls were immersed in 1M HCl solution for 6 h with stirring under reflux to eliminate the metallic ingredients and then washed with distilled water until the pH of the filtrate dropped to 6, dried at 105°C for 12 h. The acid leached wheat husk was burned in an incineration furnace (Nüve, Turkey) at 750°C for 6 hours.

20 grams of ash were placed into a 2 L flask, 250 milliliters of 1 M sodium

hydroxide solution was added, and the flask was capped with a watch glass. The mixture was boiled for two hour with constant stirring using a magnetic stirring bar (IKA, Germany). Then the mixture was filtered under vacuum, the upper carbon residues were washed with 60 mL of hot water to separate clear sodium silicate solution from carbon residues [Ozgul-Yucel *et al.*, 2004]. The silicate solution was preserved in a polyethylene bottle until used.

2.2.2. Preparation of silica

The silicate solution was titrated with 1N HCl solution with constant stirring to a pH of 8. The soft gel was aged for 20 hours. The obtained gel was gently broken and the slurry was centrifuged for 15 minutes at 2500 rpm. The clear supernatants were poured. The slurry was washed with deionized water several times and the centrifugation was repeated. The gel was dried in an oven at 80°C for 12 hours and then washing and drying steps were repeated. The obtained silica powder was preserved in a polyethylene bottle until used.

2.2.3. Preparation of ZSM-5 zeolite

The synthesis of ZSM-5 zeolite was carried out by hydrothermal crystallization with the molar composition of 0.25 Na₂O: 0.02 Al₂O₃ : 1SiO₂ : 0.02 TPABr: 75 H₂O according to that of Panpa and Jinawath [Panpa and Jinawath, 2009]. A stoichiometric quantity of wheat hull silica (2.5 g) and NaOH (0.68 g) was completely dissolved in distilled water at 80°C with constant stirring. An TPABr solution was prepared by mixing 0.5 g of TPABr with 10 mL distilled water at 50°C for 20 minute, and then added to the predispersed silica solution. Also, 1 mL n-Propyl amine solution was added and the mixture was stirred for 15 minute. On the other hand, the aluminum sulfate (0.457 g) and 0.05 mL concentrated H₂SO₄ was dissolved in

10 mL distilled water completely, and then added to the sodium silicate- TPABr solution. The pH of the mixture was set to about 11 by using 0.1 M H₂SO₄ solution. The solution was subjected to crystallization at 150°C for 8 days in Teflon-lined stainless steel autoclaves. Finally, the solid product was separated by filtration, washed with distilled water and dried at 110°C for 18 h. The zeolite was calcined at 550°C for 5 h in an incineration furnace.

2.2.4. Characterization of starting materials and zeolite

The obtained wheat hull ash was characterized by X-ray fluorescence (XRF).

The morphologies of the wheat hull ash silica and zeolite were studied by SEM after carbon coating using a JEOL JSM 5410 LV (Japan) instrument. The Fourier transform infrared spectra of ZSM-5 zeolite was measured with Thermo Scientific Nicolet iS10;USA in the range of 500–2000 cm⁻¹. The crystalline structure of the produced silica and zeolite were examined by an X'Pert XRD (Philips Panalytical X'Pert Pro, The Netherlands) with CuK α radiation using an acceleration voltage of 45 kV and a current of 40 mA.

3. RESULTS AND DISCUSSION

3.1. Characterization of Wheat Husk Ash

The chemical composition of wheat hull ash as analyzed by X-ray fluorescence is presented in Table 1.

Table 1: The chemical composition of wheat hull ash

Composition	Wheat hull ash (wt%)
SiO ₂	99,3
K ₂ O	0.14
CaO	0.29
MnO	0.044

Fe ₂ O ₃	0.021
CuO	0.045

3.2. Morphology of Silica and ZSM-5 Zeolite

Figure 1 illustrates the SEM image of the silica extracted from wheat hull ash. The silica particles were irregular in shape with a size that was generally in micron order.

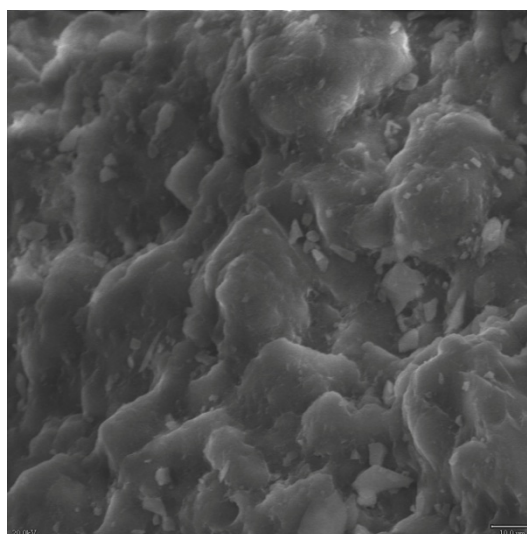


Figure 1: SEM image of wheat hull ash silica (1000x)

As can be seen from Figure 2 the particle size distribution of ZSM-5 zeolite is not uniform. The spherical structures were observed. The crystals with average size of 15 -70 μ m were obtained.

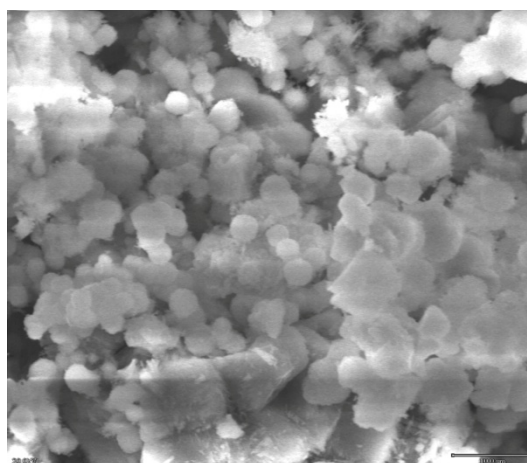


Figure 2: SEM image of ZSM-5 zeolite (2000x)

3.3. FT-IR Analysis of ZSM-5 Zeolite

The infrared spectrum of ZSM-5 zeolite in the region of 2000-500 cm^{-1} is shown in Figure 3. The vibration modes of 1046 and 793 cm^{-1} are corresponding to internal vibration of SiO_4 and AlO_4 tetrahedra. The small peak near 1235 cm^{-1} is assigned to the asymmetric stretching vibration of SiO_4 and AlO_4 tetrahedra in the ZSM-5 zeolite framework. The sharp peak at 545 cm^{-1} is characteristic of double ring tetrahedral vibration and also ZSM-5 zeolite crystalline structure [Panpa and Jinawath, 2009; Shirazi et al., 2008]. The peak at 1625 cm^{-1} is due to the H-OH bending vibrations of the adsorbed water molecules.

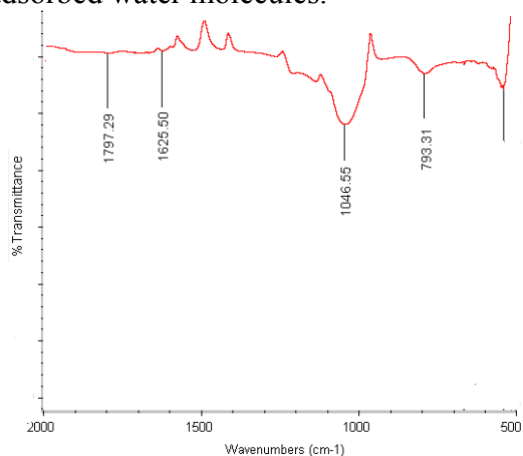


Figure 3: FT-IR spectra of prepared ZSM-5 zeolite

3.4. XRD Analysis of Silica and ZSM-5 Zeolite

The XRD pattern of silica and ZSM-5 zeolite are presented in Figure 4. The XRD pattern of wheat hull ash silica shows it to be amorphous, which is approved by the absence of any well-defined sharp peaks. The XRD pattern of ZSM-5 zeolite clearly displays that it has crystalline structure recognized by the presence of sharp peaks.

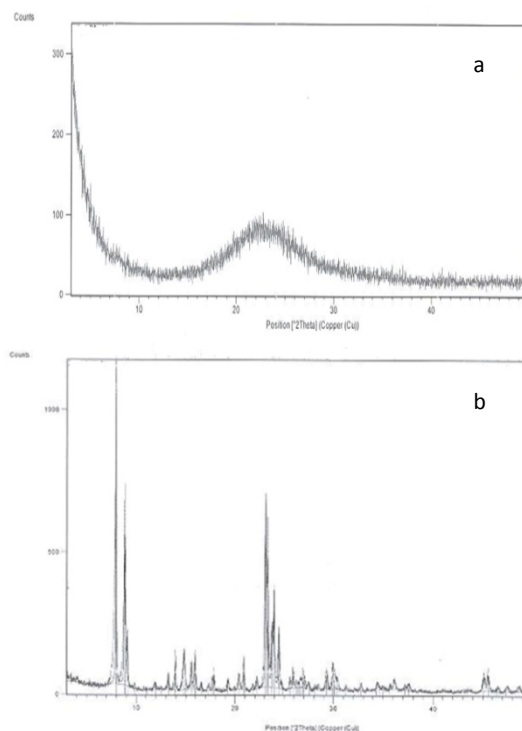


Figure 4: XRD patterns of (a) wheat hull ash silica (b) prepared ZSM-5 zeolite

4. CONCLUSION

The proper evaluation of wheat hull may bring economic benefits in the future as well as contributing to efforts of waste management by reducing environmental pollution.

Acknowledgements: This study was funded by Mugla Sıtkı Kocman University, Coordination of Scientific Research Projects (BAP) with project number 12/135.

REFERENCES

- Argauer, R.J., Kensington, M.D., Landolt, G.R., and Audubon, N. J., Crystalline Zeolite ZSM-5 and Method of Preparing the Same US Patent 3702886, Mobil Co., 1972.
- Ghasemi, Z., and Younesi, H., 2011. Preparation and Characterization of Nanozeolite NaA from Rice Husk at Room Temperature without Organic Additives, Journal of Nanomaterials, doi:10.1155/2011/858961.
- Kalpathy, U., Proctor, A., and Shultz, J., 2000. A simple method for production of pure silica from rice hull ash, Bioresource Technol., 73, 257-262.
- Kaya, D., Çanka Kılıç, F., Baban, A., and Dikeç, S., 2008. Administrative, institutional and

- legislative issues on agricultural waste exploitation in Turkey, *Renew. and Sustainable Energy Rev.*, 12, 417-436.
- Motojima, S., Hori, Y., Gakei, S. and Iwanaga, H., 1995. Preparation of Si_3N_4 whiskers by reaction of wheat husks with NH_3 , *J. Mat. Sci.*, 30, 3888-3892.
- Nur, H., 2001. Direct synthesis of NaA zeolite from rice husk and carbonaceous rice husk ash, *Indonesian Journal of Agricultural Sciences*, 1, 40–45.
- Ozgul-Yucel, S., Tolay, M., Erdag, S. and Turkay, S., 2004. Magnesium silicate synthesis from rice hull ash, *J. Am. Oil Chem. Soc.*, 81, 619-620.
- Panpa, W. and Jinawath, S., 2009. Synthesis of ZSM-5 zeolite and silicalite from rice husk, *Applied Catalysis B: Environmental*, 90, 389-394.
- Prasetyoko, D. , Ramli, Z., Endud, S., Hamdan, H. and Sulikowski, B., 2006. Conversion of rice husk ash to zeolite beta, *Waste Management*, 26(10), 1173–1179.
- Shirazi, L., Jamshidi, E. and Ghasemi, M. R. 2008. The effect of Si/Al ratio of ZSM-5 zeolite on its morphology, acidity and crystal size, *Cryst. Res. Technol.* 43,12, 1300 -1306.
- Sun, L. and Gong, K., 2001. Silicon-based materials from rice husks and their applications, *Ind. Eng. Chem. Res.* ,40, 5861-5877.
- Terzioglu, P. and Yucel, S., 2012. Synthesis of magnesium silicate from wheat husk ash: Effects of parameters on structural and surface properties, *BioResources*, 7(4), 5435-5447.
- Wittayakun, J., Khemthong, P. and Prayoonpokarach S., Synthesis and characterization of zeolite NaY from rice husk silica, *Korean J. Chem. Eng.*, 25(4), 861-864.

ZEOLITE FILLED POLYVINYLALCOHOL MEMBRANE PREPERATION AND ALCOHOL DEHYDRATION BY PERVAPORATION

Filiz Ugur Nigiz^{1,a}, Nilufer Durmaz Hilmioglu¹

1. Kocaeli University, Chemical Engineering Department, Kocaeli, Turkey
a. filiz.ugur@kocaeli.edu.tr

ABSTRACT: Pervaporation (PV) is a membrane process which separates azeotropic and thermal sensitive compounds efficiently. Compared to the other membrane processes, a phase change occurs during the transition in PV. The selected material dissolved onto the membrane surface, diffuses through the membrane and desorbed as vapor phase.

The performance and productivity of the system are directly related to the membrane selection. In PV; polymeric, inorganic and composite membranes are used. Generally, inorganic membranes are suitable for commercial scaled plants since they are durable and can be operated at high temperature. On the other hand inorganic materials are expensive and it is hard to form them as membrane since they are brittle. Polymeric materials are able to form as membrane module but polymers are organic structured material and it is not possible to use them at high temperature. Therefore the inorganic filled polymeric membranes which are called as “Mixed Matrix” or “composite” membranes have become more suitable.

In this study pristine and 3A zeolite loaded polyvinylalcohol membranes have been prepared and operated in PV process to dehydrate isopropanol-water mixture. The performance of PV has been determined by flux and selectivity. Effects of zeolite loading, feed composition and temperature on performance have been evaluated.

1. INTRODUCTION

Isopropanol (IPA) is a chemical raw material which is mostly used for agricultural, pharmaceutical and electronics industry. In these processes, IPA and water should be highly pure. In order to purify the IPA and water, a series of complicated separation steps are required. After physical and thermal treatment steps, an azeotrope form occurs between water and IPA at 12 wt. % of water and it is not possible to separate this form by conventional methods. Azeotropic distillation and liquid-liquid extraction methods are suitable to separate azeotropic solutions, however this process is high costly and consume more energy [Yu *et al.*, 2011, Mosleh *et al.*, 2012, Urtiga *et al.*, 2012]. Pervaporation is cost effective and environmental friendly membrane process which separates azeotropic, thermal sensitivity compounds. During the

operation, the vacuum pressure which is applied from the downstream side of the membrane, causes a phase change. The selected liquid compounds pass through the membrane as vapor phase. Therefore, separation is achieved without a thermal stage or an additional azeotrope breaker solvent [Feng *et al.*, 1997, Slater, 1989, Roza *et al.*, 2006, Lipnizki *et al.*, 1999, Hoof *et al.*, 2003, Vallieres *et al.*, 2004].

In literature, hydrophilic polymers such as poly(vinylalcohol), chitosan, alginate and polyimide or hydrophobic polymers such as poly(dimethylsiloxane) have been used as membrane material. Due to the thermal and chemical durability of the zeolites, in most commercial facilities NaA based zeolite membranes are used [Li *et al.*, 2010, Edit *et al.*, 2009, Bhat *et al.*, 2006, Lu *et al.*, 2000].

In this study, pristine and 5, 10 wt. % of 3A loaded membranes were prepared by solution casting and evaporation method. They were employed at PV system to separate IPA/water mixtures at different concentrations.

2. MATERIALS AND METHODS

2.1. Membrane Preparation

For the preparation of pristine membrane; a desired amount of PVA was dissolved in water at 90 C° for three hours and then it was poured on to glass petri dish. Composite membranes were prepared almost same way; 5, 10 wt. % of 3A (with respect to the dry polymer weight) was added to the polymer-water solution and mixed at 90 C° for three hours and then it was poured onto glass petri dish. Membranes were cross-linked with gluteraldehyde and post cured in vacuum oven at 50 C°.

2.2. Swelling Experiment

Swelling experiments were carried out to determine affinity of the membranes to the water. Pristine and zeolite loaded membranes were immersed about 24 hours in 5, 10 and 15 wt. % of water-alcohol solutions at room temperature. The swelling degrees of all membranes were determined by the measurements of initial and final weight of dry and swollen membranes. This process was repeated until a steady state swelling degree was obtained.

$$S_d = (W_s - W_d / W_d) * 100 \quad (1)$$

S_d , is the swelling degree (%), W_s is the weight of swollen membrane, W_d is the weight of dry membrane [Nunes *et al.*, 2006].

2.3. Pervaporation Experiments

Membranes were performed in pervaporation experiments to separate isopropanol-water mixtures. Experiments were carried out in different water

concentration (5, 10, 15 wt. % of water in water/alcohol solution) at room temperature. The volume capacity of the membrane cell was 500 ml and the active membrane area was 28,26 cm². Experiments were operated about five hours. Pervaporation performance was calculated as a function of flux and selectivity.

$$J = m / A.t \quad (2)$$

$$\alpha = (P_w / P_i) / (F_w / F_i) \quad (3)$$

J is water flux (kg/m².h), m is the weight of water (kg), t is time (h), α is water selectivity, F_w and P_w are the water mass fractions in feed and permeate respectively, F_i and P_i are the isopropanol mass fractions in feed and permeate respectively [Nunes *et al.*, 2006]. Experimental PV set up has been shown in figure 1.

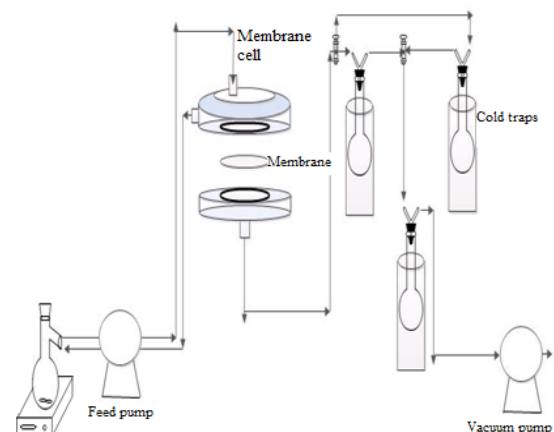


Figure 1: Experimental PV unit

3. RESULTS AND DISCUSSION

3.1. Swelling Experiment

As seen in figure 2, zeolite loading causes an increase at degree of swelling value. Zeolite 3A is well known hydrophilic inorganic particles so it is expected that the zeolite loading enhances the degree of swelling.

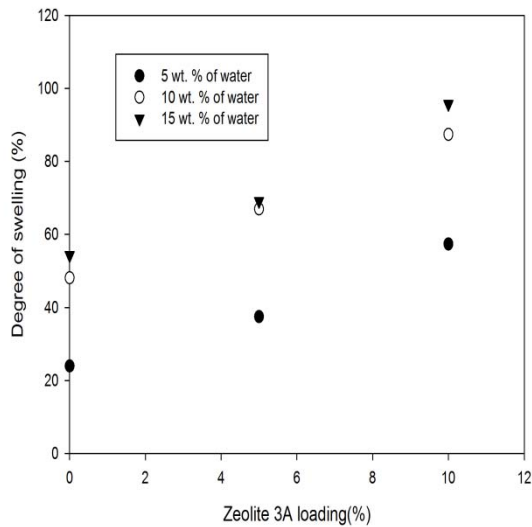


Figure 2: Effect of zeolite loading and water concentration on swelling degree

Degree of swelling also increases with the water concentration at feed mixtures. These lines prove the membrane and zeolite affinity to water.

Swelling degree is important factor which affect the flux and selectivity parameters. It is possible to predict that how the flux and selectivity will change with feed composition or zeolite loading.

3.2. Effect of Zeolite Loading and Water Concentration on Flux

As seen in figure 3, flux is positively affected from both water concentration in feed mixture and and zeolite loading in membrane. Flux lines verified the swelling values.

As the water concentraion in feed mixture increases, the driving force between the two sides of membrane increases. Also the water causes to swell and expand the polymer chains so enhancing of the flux values are expected.

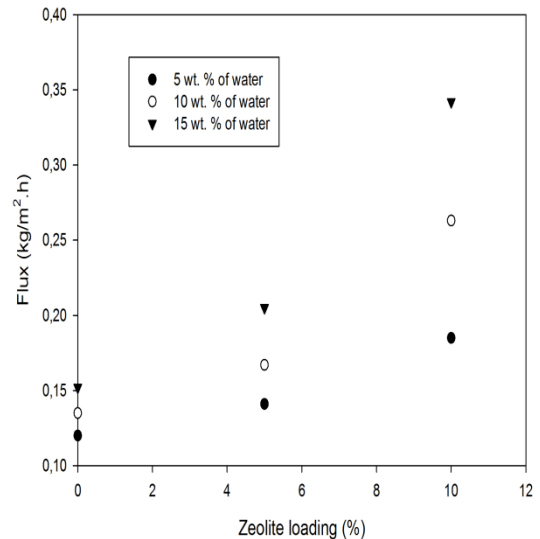


Figure 3: Effect of zeolite loading and water concentration on flux

3.2. Effect of Zeolite Loading and Water Concentration on Selectivity

Figure 4 shows the selectivity changes. Increasing water concentrations causes a decrease in selectivity values of pristine and loaded membranes.

Because of the expanded voids of polymer, non selective transport of isopropanol would be occurred and it would be decreased the selectivity values.

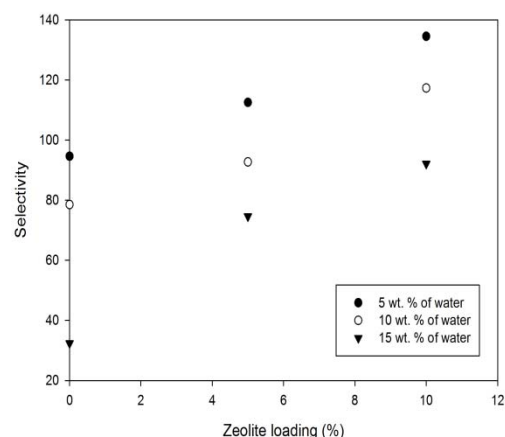


Figure 3: Effect of zeolite loading and water concentration on selectivity

On the other hand, adding of 3A to the membrane increases the selectivity values due to the selective sorption ability of the zeolites.

4. CONCLUSION

In this study, pervaporative separation ability of pristine and 5 and 10 wt % of 3A loaded PVA membranes in IPA/water mixtures have been investigated. Pervaporation performance was evaluated according to the effect of zeolite loading and water concentration on flux and selectivity. As the water content was increased in feed mixture, flux values increased. However selectivity adversely affected. On the other hand, addition of zeolite into the PVA matrix, both flux and selectivity were enhanced.

Flux and selectivity are two important factors for commercially available membranes. It is desired the selectivity should be 10 at least. In this study, highest flux and selectivity values were observed with 10 wt. % of zeolite loaded membrane. With respect to this result, it is possible to conclude that the 3A zeolite loaded PVA membranes are suitable to separate IPA from water/IPA solution.

REFERENCES

- S. Mosleh, T. Khosravi, O. Bakhtiari, T. Mohammadi, 2012, Zeolite filled polyimide membranes for dehydration of isopropanol through pervaporation process, *chemical engineering research and design* 90, 433–441.
- C. Yu, Y. Liu, G. Chen, X. Gu, W. Xing, 2011, Pretreatment of Isopropanol Solution from Pharmaceutical Industry and Pervaporation Dehydration by NaA Zeolite Membranes, *Chinese Journal of Chemical Engineering*, 19, 904-910
- X. Feng and R.Y.M Huang, 1997, Liquid Separation by Membrane Pervaporation: A Review, *Ind. Eng. Chem. Res.*, 36 1048-1066.
- K.V. Ramana, K. Ganesan, L. Singh, 2006, Pervaporation performance of a composite bacterial cellulose membrane: dehydration of binary aqueous–organic mixtures, *World Journal of Microbiology & Biotechnology*, 22, 547–552.
- C.S. Slater, 1989, Membrane Technology For Energy Conservation in Traditional and Emerging Engineering Fields, *IEEE*, 1731-1736.
- M. Roza, E. Maus, 2006, Industrial Experience with Hybrid Distillation –Pervaporation or Vapor Permeation Applications, *ICHEME*, 619-627.
- F. Lipnizki, R.W. Field, P.K. Ten, 1999, Pervaporation-based hybrid process: a review of process design, applications and economics, *Journal of Membrane Science*, 153, 183-193.
- V.H. Hoof, L.V. Abeele, A. Boukenhoudt, C. Dotremont, R. Leysen, 2003, Economic Corparation Between Azeotropic Distillation and Different Hybrid Systems Combining Distillation with Pervaporation fort he Dehydration of Isopropanol, *Seperation and Purfication Technology* 37, 33-49.
- Q. Li, P. Yu, T. Zhu, L. Zhang, L. Qian, Y. Luo, 2010, Pervaporation performance of crosslinked PVA and chitosan membranes for dehydration of caprolactam solution, *Desalination and Water Treatment*, 16, 304-312
- A.M. Urtiaga, E.D. Gorri, I. Ortiz, 2006, Pervaporative recovery of isopropanol from industrial effluents, *Separation and Purification Technology*, 49, 245–252.
- S.D Bhat, B.V.K Naidu, G.V. Shanbhag, S.B. Halligudi, M. Sairamand, T.M. Aminabhavi, 2006, Mesoporous molecular sieve (MCM-41)-filled sodium alginate hybrid nanocomposite membranes for pervaporation separation of water–isopropanol mixtures, *Sep. Purif. Technol.*, 49, 56–63.
- S.P. Nunes and K.V. Peinemann, *Membrane Technology in the Chemical Industry*, 2006, P:2
- C. Vallieres, E. Favre, 2004, Vacuum versus sweeping gas operation for binary mixtures separation by dense membrane processes, *Journal of Membrane Science*, 244:17–23.
- S.Y. Lu, C.P. Chiu, H.Y. Huang, 2000, Pervaporation of acetic acid/water mixtures through silicalite filled polydimethylsiloxane membranes, *Journal of Membrane Science*, 176, 159–167.

SURFACE ROUGHENING OF STAINLESS STEEL PLATES BY ELECTROCHEMICAL ETCHING TECHNIQUES USED FOR POROUS P/M APPLICATIONS

Onur Günel¹, Yusuf Usta^{2,a}

1. Başkent University, Fac. of Engineering, Mechanical Eng. Dept., Ankara, Turkey

2. Gazi University, Fac. of Engineering, Mechanical Eng. Dept., Ankara, Turkey,

a. Yusuf Usta (yusta@gazi.edu.tr)

ABSTRACT: Stainless steel porous structures are a solution for increasing the surface area in order to improve the heat transfer capacity specially used in fuel cell's heat exchangers. Powder metallurgy is one of the production types of such porous surfaces. Due to leakage of cooling fluids, powders must be stacked on a solid substrate from same material of the powders. Higher toughness of stainless steel materials causes a difficulty for bonding of those powders and the substrate. Surface roughening of the substrates are one of the methods to improve the bonding capability. In this study, an electrochemical method which is applied under $\text{FeCl}_3 \cdot 6\text{H}_2\text{O}$ acidic media has been used to have corrosions on the surfaces of the substrates. A substrate which is 0.6 mm in thickness and AISI 316L material is selected for roughening tests. Taguchi method has been used to employ numeric values of the experimental parameters such as temperature, electrical current, stirring, concentration and the time. The effects of these parameters on the surface roughness are investigated and a max. of 23 μm surface roughness is measured whereas 30 μm are noted on some areas. The larger pitting corrosions are observed with the increasing concentration, temperature and the time.

1. INTRODUCTION

The resistance of austenitic stainless steels to pitting corrosion in the presence of chloride is enhanced by higher chromium (Cr), molybdenum (Mo), and nitrogen (N) content. A relative measure of pitting resistance is given by The PREN (Pitting Resistance Equivalent Number). PREN of Type 316L is between 28.38 and 22.6, calculated from the equation $\text{PREN} = \% \text{Cr} + 3.3 \times \% \text{Mo} + 16 \times \% \text{N}$ [Baboian, 1995].

A sharp rise in pitting corrosion rate can occur with only a slight change of the corrosion conditions, such as chemical media, corroding concentration, or temperature [Szkłarska-Smiałowska, 1986,].

The aim of this work is to increase roughness of the surface for a bonding between powders and the substrate. For this purpose, electrochemical method was

applied under $\text{FeCl}_3 \cdot 6\text{H}_2\text{O}$ acidic media to have pitting corrosion on the surface of stainless steel substrate. Experimental parameters and even their numerical values were assumed such as temperature (25, 40, 70 °C), electrical current (1.5, 2.5, 4 A), stirring (none, medium fast), concentration of acidic media (5%, 10%, %15 $\text{FeCl}_3 \cdot 6\text{H}_2\text{O}$ solution) and the reaction time (20, 40, 60 min.). The effects of these parameters on the surface roughness are investigated by Taguchi experiment design method. This method is one of the useful methods to determine the optimum combination through different parameters and different levels [Güral, 2003].

2. EXPERIMENTAL

The AISI 316L austenitic stainless steel was used as the test material. The

chemical composition is shown in Table 1 [Klar and Samal, 2007].

Table 1: Chemical composition of the AISI 316L stainless steel

Content of elements [w,%]	Cr	Ni	Mn	Si	S	C	P	Mo	N	Fe
	16.0	10.0	2.0	1.0	0.03	0.03	0.04	2.0	0.0	balance
	-	-						-	-	
	18.0	14.0						3.0	0.03	

AISI 316L stainless steel is commonly used for the production of tanks for transportation of aggressive substances, especially in chemical and petrochemical industry, also due to high resistance of corrosion they can be used in fuel cell.

The rectangular stainless steel sheet metal substrates were mechanically cut into a test specimen. Dimensions of specimens were 90×55 mm with the thickness of 0.6 mm.

The specimens were manually roughened with silicon carbide abrasive paper of 150 grits. They were then cleaned with acetone and dried.

Before employing the electrochemical tests, Taguchi experiment design was used to reduce the number of tests. Taguchi orthogonal array design was used because of electrochemical experiments have 5 different parameters. Experimental scheme is shown in Table 2. It should be noted that none, medium and high levels of the stirring parameter are relative values. The effects of the chosen parameters on the surface roughness were investigated by statistical software.

Table 2: Experimental Scheme

Sol. (%w)	Current (A)	Temp (°C)	Time (min)	Stirring
5	1,5	21	20	None
5	1,5	25	20	Medium
5	1,5	25	20	Fast
5	2,5	40	40	None
5	2,5	40	40	Medium
5	2,5	40	40	Fast
5	4	70	60	None
5	4	70	60	Medium
5	4	70	60	Fast
10	1,5	40	60	None
10	1,5	40	60	Medium
10	1,5	40	60	Fast
10	2,5	70	20	None
10	2,5	70	20	Medium
10	2,5	70	20	Fast
10	4	25	40	None
10	4	25	40	Medium
10	4	25	40	Fast
15	1,5	70	40	None
15	1,5	70	40	Medium
15	1,5	70	40	Fast
15	2,5	25	60	None
15	2,5	25	60	Medium
15	2,5	25	60	Fast
15	4	40	20	None
15	4	40	20	Medium
15	4	40	20	Fast

3. ELECTROCHEMICAL TESTS

The electrochemical tests were carried out in the different concentration of acidic media, electrical current and temperature, time and stirring of the chemical bath as well. The corrosive medium was prepared having 3.5 % NaCl, 3.5 % HCl, and varied concentrations of 5%, 10%, %15 FeCl₃.6H₂O.

After applying electrochemical pitting corrosion process, specimens were cleaned to rout out the residual corrosion. Cleaning steps are explained below. Concentrations of cleaning chemicals are shown in Table 3.

- Specimens were brushed in acetone then dried.
- Immersed in NH₄OH solution between 5 and 10 min. and scoured away.
- Immersed in CrO₃ and AgNO₃ solution at boiling temperature.

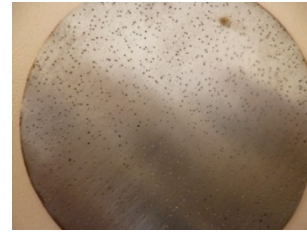
Table 3: Cleaning Solutions

Sol.	NH ₄ OH	AgNO ₃	CrO ₃	H ₂ O
1	135 gr	-	-	1 lt.
2	-	10 gr.	50 gr.	1 lt.

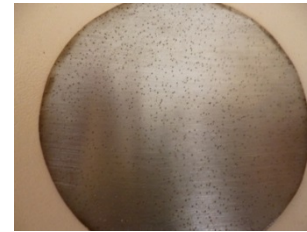
Each specimen was tested for surface roughness using surface roughness measurement equipment, Taylor Hubson Surtronic 3+. Average surface roughness (Ra) were obtained and recorded.

4. RESULTS AND DISCUSSION

The specimens were attacked by pitting corrosion during the electrochemical etching. The density of pitting with the stirring level is depicted in Figure 1 and the change in the appearance of pitting surfaces was clearly observed comparing none-stirred and fast-stirred acidic medium. Moreover, on the none-stirred medium, the pits are bigger than the pits on the fast-stirred medium (Figure 2).

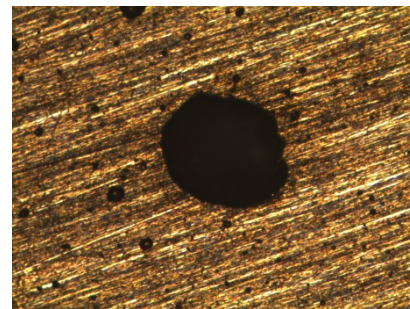


a. Pit density with none-stirred bath

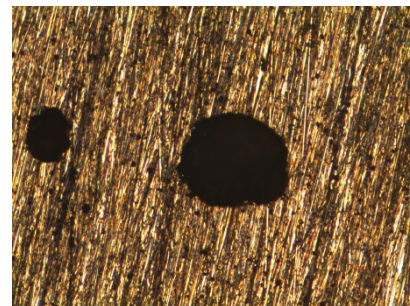


b. Pit density with fast-stirred bath

Figure 1: The pitting corrosions on the surfaces after electrochemical corrosion test in 5% FeCl₃ at 25°C.



a. None-stirred specimen



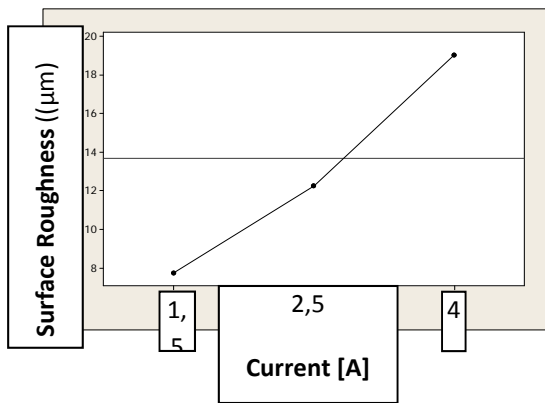
b. Fast-stirred specimen

Figure 2: Microscopically observed pit size and shape on a surface.

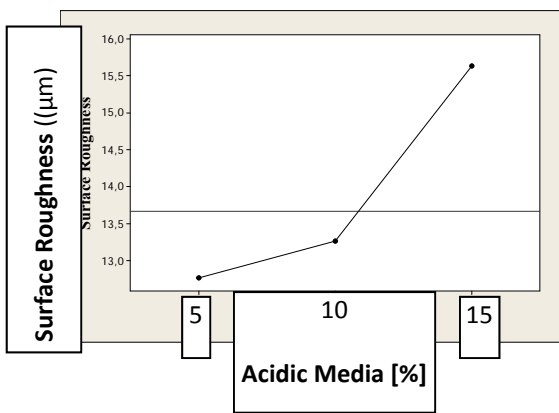
It is figured out that the average surface roughness (Ra) is significantly effected by electrical current, concentration of acidic media and time (Figure 3). Surface roughness increases with increasing electrical current (Fig. 3a), whereas the

concentration of the acidic medium shows the same affect (Fig. 3b).

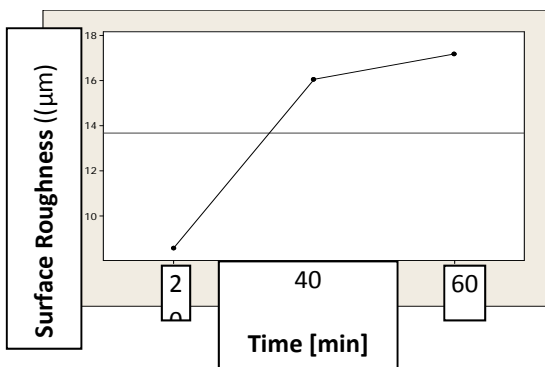
Etching time shows higher effect on the surface roughness with the smaller durations then becomes less effective (Fig. 3c). It can be concluded that both higher current and concentration of acidic media should be preferred to achieve enough roughness on the surfaces.



a. Effect of electrical current



b. Effect of the concentration of acidic media



c. Effect of the time

Figure 3: Average surface roughness vs. electrical current, concentration of acidic media and time.

It is seen that the shape of pits is seems like a water drop (Fig. 4) and in general, the size of pits is a function of electrical current and time (Figure 5). Increased size of pits with higher electrical current and the time was observed. As similar to the surface roughness, density of electrical current has high effect on the pit size.

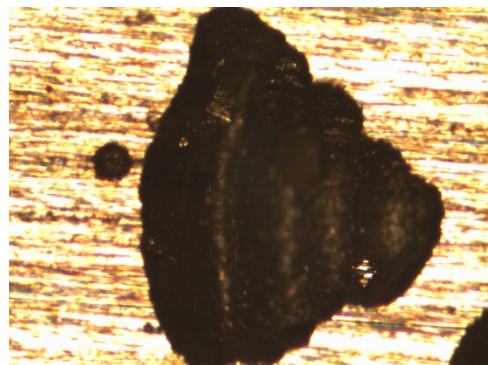
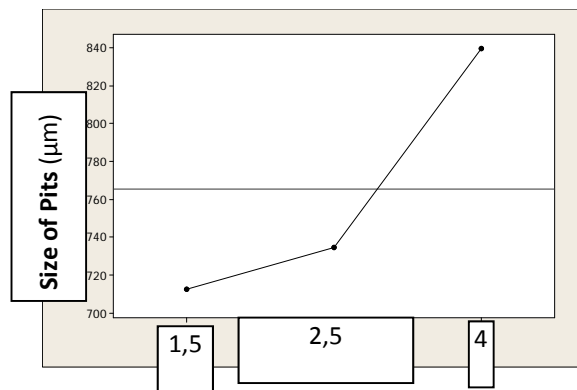
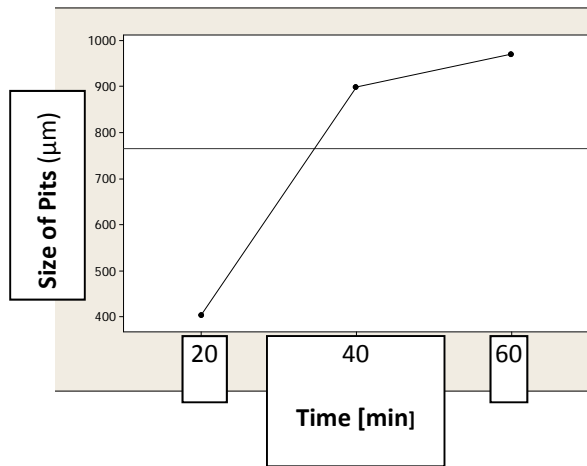


Figure 4: Shape and size of the pits.



a. Effect of electrical current on the pit size



b. Effect of time on the pit size

Figure 5: Average size of pits vs. electrical current and time.

On the other hand, stirring of the medium showed a reducing effect on the size of pits (Figure 6). It is advisable to stir the medium to have smaller but dense pits on the substrate surfaces as possible.

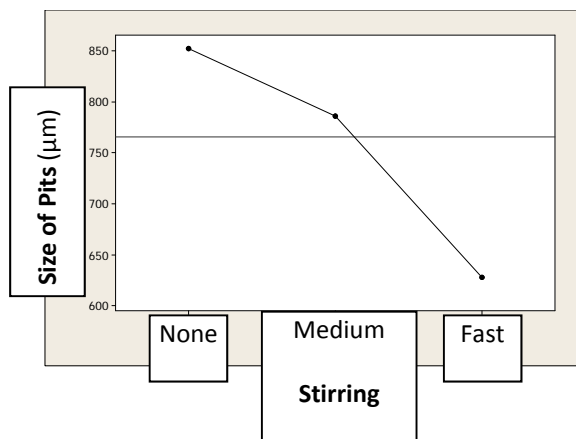


Figure 6: Effect of stirring on the size of pits

Surface roughness tests showed that acidic medium temperature did not show a comparable effect. A very slight increase with the increasing temperature was observed. Therefore effect of the temperature on the surface roughness was not discussed in this study.

5. CONCLUSION

- Density of pitting increases with the increasing temperature and stirring

level, but pit size decreases with the increasing stir level (Figure 6). The variation is seen in Figure 1.

- Surface roughness increases with the increasing concentration of acidic media (Figure 3). Nevertheless, higher etching time also increases both surface roughness and the pit size (Fig 3c, 5b).
- It is advisable to select higher electrical current and concentration of media as well as higher etching time to have proper roughness on the substrates. It is also very important that acidic medium must be stirred in order to have dense and regularly distributed pits.

Further studies will be compacting of roughened substrates with the powders using hot pressing. The minimum surface roughness will be defined under varied compaction pressures therefore numeric values of the parameters for the etching processes will be assigned.

Acknowledgement: This study has been supported by the Scientific Research Projects, Gazi University, Turkey. Project no is 06/2012-40.

REFERENCES

- Baboian, R., 1995, Corrosion Test and Standards: Application and Interpretation, ASTM Manual Series, Philadelphia and USA.
- Güral, G., 2003, Gazaltı Kaynağında Proses Parametrelerinin Optimizasyonu, Dokuz Eylül Üniversitesi Fen Bilimleri Enstitüsü Yüksek Lisans Tezi, İzmir.
- Klar, Erhard, Samal Prasan, 2007, Austenitic Grades, Powder Metallurgy Stainless Steel, 1st Ed., ASM International, United States of America, 16.
- Szklarska-Smialowska, Z, 1986, Pitting Corrosion of Metals, NACE, Houston, TX.

SYNTHESIS AND CHARACTERIZATION OF HYDROXYAPATITE

Sevim HAMAMCI ALIŞIR¹, A.Elif ÇİÇEKLİ^{2,a}

1. Department of Materials Science and Engineering, Ondokuz Mayıs University, Faculty of Engineering
55139 Kurupelit / SAMSUN/TURKEY

2. Department of Materials Science and Engineering, Ondokuz Mayıs University, Faculty of Engineering
55139 Kurupelit / SAMSUN/TURKEY

a. Corresponding author (aelif1559@gmail.com)

ABSTRACT: Biomaterials are used to replace or support the human organs or tissues. There are four different groups of biomaterials such as metallics, ceramics, polymers and composites. Biocompatibility is considered as the most important feature in biomaterials, allowing the surrounding tissue to differentiate normally and preventing undesired reactions. Hydroxyapatite is one of the forms of calcium phosphate which is designated as $\text{Ca}_{10}(\text{PO}_4)_6(\text{OH})_2$. Hydroxyapatite has a high biocompatibility and slow degradation. The chemical structure of hydroxyapatite and bone mineral is very similar. There may be very strong bonds between the surface of hydroxyapatite bone-implant bone and accelerates the growth of this surface. Space consisting of hydroxyapatite in bone tumor surgery, as the filler material, as a bridge to grab the bone defect repair of a broken bone, supply and implant dentistry tooth root used in coatings. Hydroxyapatite ocular implant is used in practice Hydroxyapatite, in plastic surgery, cheek, upper and lower jaw, nose, forehead, face such as are used in the reconstruction of the parts. The aim of this study was to sintering of hydroxyapatite powders were synthesized and characterized by different degrees of sintering is.

1. INTRODUCTION

Today, one of the biggest advances in biomaterials science disciplines saved, interacts with biological systems, intensive efforts have been made to adapt to the development of new materials. Biomaterials in the human body to perform the functions of living tissue, or natural or synthetic materials that are used to support. Therefore, a certain period of time or permanently biomaterials in contact with body fluids in [1]. The most important feature for Biomaterials bio-compatibility. Two types of bio-compliance may be mentioned, these structural and surface biocompatibility. Congruency, the body tissues in a biomaterial physical, chemical, and is biocompatible. Structural compatibility, the mechanical behavior of the material under optimum harmony of body tissues. [2].

This study, which is widely used in biomedical applications of artificial bone

applications and provides information about the excellent characteristics HA synthesized and characterized.

2. HYDROXYAPATITE

The term describes the apatite crystallographic structure similar to a family of compounds. Therefore it does not specify a particular composition.. Hydroxyapatite [$\text{Ca}_{10}(\text{PO}_4)_6(\text{OH})_2$] the best-known and important member of this family.

Ca and P elements in the chemical structure of HA are available. They are located on the bone and tooth mineral elements. This material contains the same elements in the composition of the body against foreign materials, the response is much less and the young bone cells will adhere to the surface of HA and multiply. Even the bone material at the interface of HA with high bioactivity is composed of a very strong bonds. It sometimes becomes very high strength bonds.

Orthopedic implants made of metal coating on bone cells in young HA is very strong adhesion to the metal surface of HA coating is removable and can create the danger of causing infections. In addition to coatings, which was used directly in terms of the mechanical properties of HA remains weak. Also synthetic HA, according to natural bone, the mechanically weak, and there are differences in bioactivity. Natural bone on HA, HA synthetic, they are biologically more active. [3].

Synthetic HA weaknesses in the last 20 years many studies have been conducted to strengthen. [4-5]. To provide both mechanical and biological aspects of development, studies have focused on the production of nano-crystalline HA. Natural bone structure of nano hydroxyapatite ($\text{HA}, \text{Ca}_{10}(\text{PO}_4)_6(\text{OH})_2$) and the collagen fibers is a composite of the inorganic / organic nanocomposite synthesis, high bioactivity, and excellent affinity for vital properties.

3. PRODUCTION METHODS

In recent years many different approaches have been obtained in different sizes, the nano-crystalline HA. Luo and Nieh calcium nitrate and ammonium phosphate by using (1995) the solution by spray drying method HA Near particle size of 20 nm was obtained. [6]. Then using the method of nano-HA to synthesize radio frequency plasma spray in size from 10 to 100 nm have generated HA powder. [7]. stoichiometric using the sol-gel method HA (Ca / P = 1,67) are easier to produce. Also at lower temperatures than the other methods is performed. HA synthesized by this method, but always in the second phase comprise a calcium phosphate. Therefore, the amounts of chemicals used to produce HA stoichiometric determined very accurately. Many different substances can be used as a solvent in this method: ethanol, gels, and alkoxides phosphors used solvents. Kuriakose et al.

HA sizes of 8-10 nm in ethanol was obtained by this method using the solvent [8]. Han et al. citric acid combustion by using the sol-gel method can achieve HA sizes ranging from 80 to 150 nm. [9]. Kalita et al. ethanol and water-based sol-gel nano-crystalline HA powder produced using techniques of 10-50 nm in diameter. [3]. Nano-HA was obtained using the hydrolysis method. Shih et al. stoichiometric and 20 nm in diameter with this method produced nano-HA. [10]. Sarig et al. PH 7.4 at room temperature and dilute solutions of calcium chloride and sodium phosphate in the form of direct precipitation of the plate with nano-crystalline HA found similar results. [11]. It can be used in medical applications to ensure that the reason for the production of pH. We also provide direct solutions in settling the microwave irradiation was used immediately after mixing. Another method used in the mechanochemical method. This method Manually et al. used to produce nano-HA in the solid state by a method that is quite challenging. [12].

In this method for synthesizing nano-HA and TCP calcium oxide (CaO) and calcium hydrogen phosphate ($\text{CaHPO}_4 \cdot 2\text{H}_2\text{O}$) was used. Finally the particulate HA is possible to produce nano-precipitation method [13-14, 15]. First, Professor. Robert H. With this method, developed by Doremus and students with stoichiometric HA and nano-grain size is made possible. [16].

4. SINTERING CHARACTERIZATION

HA with micron-sized particles, nano-particle sintering at the same temperature as a result more easily decomposed by HA. HA micron particle size may not have a homogeneous structure. HA sintering micron particle size is difficult, to get a more dense material to very high temperatures (eg. 1200 ° C and higher) is

required. Decayed faster than sintering at high temperatures create undesirable secondary phases and is composed of particles having non-uniform grain sizes. HA sintered at high temperatures, CaO, TCP tends to decay. This secondary phase formation and the formation of coarse-grained structure, biocompatibility and mechanical properties involve weakening. [16-18].

In order to obtain a homogeneous structure of HA nano-scale investigations are ongoing. [17, 19, 20]. HA nano lower temperatures (below 1100 ° C) and at elevated temperatures becomes sintering can be prevented problems that might occur. [17,19].

The stability of the material, sintering conditions and determine the main factors affecting the mechanical properties and chemical composition of the material, particle size and surface chemistry. HA synthesized nano-particulate medium at a pH also quite important parameter. Proper stoichiometry (Ca / P = 1,67), homogeneous, with crystal structure similar HA nano-grained powders more easily seen that the sintering. In general, with micron-size particles suitable for HA sintering temperature 1100 C. [4, 16, 17].

Figure 1 X-ray diffraction (XRD) of the values obtained with HA observed. Figure 1-b, very small grain size in the dried HA (≈ 20 nm) that are. XRD spectra of HA dried height is low, and a very large hill. This suggests that the very small particle size of the material. In Figure 1-c 1100 °C sintered HA s have a crystalline structure appears to be very high. Figure 1-c, mounds appear quite narrow because of XRD and high.

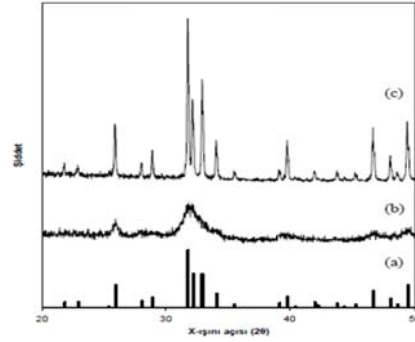
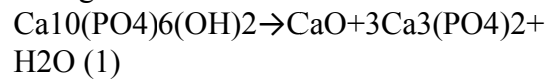


Figure 1: X-ray diffraction pattern of HA: a) Standard HA (JCPDS # 9-432), b) HA dried at 90 ° C, c) 1100 C sintered HA [14].

HA ceramics, such as the measurement of particle size is generally a scanning electron microscope (SEM). Also with the use of the XRD spectra of hillocks, particle sizes can be calculated with the formula of Scherrer. As a result of sintering at temperatures above 1100 C. The reaction is generally conventional Ha reaction 1 shows the secondary phase (calcium oxide and TCP) begin to diverge.



Homogeneity, achieved an identical crystal structure and stoichiometry of nano-grained HA s as a result of sintering at temperatures up to 1300°C, the decomposition remains stable. [20]. Density close to the theoretical density of material can be obtained thereby.

5. RESULT

Which is an important step in the synthesis of hydroxyapatite sintered hydroxyapatite on the structure of degrees and periods of very active.

REFERENCES

- [1] Kejanlı H.*, Taskın M.*, Çalığılı U., “ The Effect on the Connecting Characteristic of Welding Temperature And Period on The Joining With the Diffusion Bonding Using Ni and Cu Interlayer of Ti45.0Ni49.6Cu5.4 Composites” *Electronic Journal of BioTechnology*, 2010 (1) 41-51

- [2] Wintermantel, E., Mayer, J., Blum, J., Eckert, K.L., Luscher, P. and Mathey, M., 1996. Tissue engineering scaffolds using superstructures, *Biomaterials*, 17, 83-91, 1996.
- [3] Kalita, S.J., Bhardwaj, A. ve Bhatt, H.A. (2007). Nanocrystalline calcium phosphate ceramics in biomedical engineering. *Materials Science Engineering C* 27, 441-449.
- [4] Fang, Y., Agrawal, D.K., Roy, D.M. ve Roy, R. (1995). Fabrication of transparent hydroxyapatite ceramics by ambient-pressure sintering. *Materials Letters* 23, 147-151.
- [5] With, G.D., Dijk, H.J.A.V., Hattu, N. ve Prijs, K. (1981). Preparation, microstructure and mechanical properties of dense polycrystalline hydroxyapatite. *Journal of Materials Science* 16, 1592-1598.
- [6] Luo, P. ve Nieh, T.G. (1995). Synthesis of ultrafine hydroxyapatite particles by a spray dry method, *Materials Science and Engineering C* 3, 75-78.
- [7] Xu, J.L., Khor, K.A., Dong, Z.L., Gu, Y.W., Kumar, R. ve Cheang, P. (2004). Preparation and characterization of nano-sized hydroxyapatite powders produced in a radio frequency (rf) thermal plasma, *Materials Science and Engineering A* 374, 101-108.
- [8] Kuriakose, T.A., Kalkura, S.N., Palanichamy, M., Arivuoli, D., Dierks, K., Bocelli, G. ve Betzel, C. (2004). Synthesis of stoichiometric nano crystalline hydroxyapatite by ethanol-based sol-gel technique at low temperature, *Journal of Crystal Growth* 263, 517-523.
- [9] Han, Y., Li, S., Wang, X. ve Chen, X. (2004). Synthesis and sintering of nanocrystalline hydroxyapatite powders by citric acid sol-gel combustion method, *Materials Research Bulletin* 39, 25-32.
- [10] Shih, W.J., Chen, Y.F., Wang, M.C. ve Hon, M.H. (2004). Crystal growth and morphology of the nano-sized hydroxyapatite powders synthesized from $\text{CaHPO}_4 \cdot 2\text{H}_2\text{O}$ and CaCO_3 by hydrolysis method, *Journal of Crystal Growth* 270, 211-218.
- [11] Sarig, S. ve Kahana, F. (2002). Rapid formation of nanocrystalline apatite, *Journal of Crystal Growth* 237, 55-59.
- [12] Manuell, C.M., Ferraz, M.P. ve Monteiro, F.J., (2003). Synthesis of hydroxyapatite and tri calcium phosphate nanoparticles-preliminary studies, *Bioceramics*, 15, 240-242.
- [13] Evis, Z. (2006). Al³⁺ doped nano hydroxyapatites and their sintering characteristics, *Journal of the Ceramic Society of Japan* 114, 1001-1004,
- [14] Evis, Z. ve Doremus, R.H. (2007). Hot-pressed hydroxylapatite/monoclinic zirconia composites with improved mechanical properties, *Journal of Materials Science* 42, 2426-2431
- [15] Evis, Z. ve Doremus, R.H. (2008). Effect of AlF_3 , CaF_2 and MgF_2 on hotpressed hydroxyapatite-nanophase alpha-alumina composites, *Materials Research Bulletin* 43, 2643-2651.
- [16] Jarcho, M., Bolen, C.H, Thomas, M.B., Bobick, J., Kay, J.F. ve Doremus, R.H. (1976). Hydroxylapatite synthesis and characterization in dense polycrystalline form, *Journal of Materials Science* 11, 2027-2035.
- [17] Akao, M., Aoki, H. ve Kato, K. (1981). Mechanical properties of sintered hydroxyapatite for prosthetic applications, *Journal of Materials Science* 16, 809-812.
- [18] Santos, J.D., Knowles, J.C., Reis, R.L., Monteiro, F.J. ve Hastings, G.W. (1994). Microstructural characterization of glass-reinforced hydroxyapatite composites, *Biomaterials* 15, 5-10.
- [19] Ruys, A.J., Wei, M., Sorrell, C.C., Dickson, M.R., Brandwood, A., ve Milthorpe, B.K. (1995). Sintering effects on the strength of hydroxyapatite, *Biomaterials* 16, 409-415.
- [20] Ahn, E.S., Gleason, N.J., Nakahira, A. ve Ying, J.Y. (2001). Nanostructure processing of hydroxyapatite-based bioceramics, *Nano Letters* 1, 149-153.

SYNTHESIS AND CHARACTERIZATION OF Pr³⁺ DOPED YTTRIUM ALUMINUM GARNET (YAG) NANOPHOSPHORS

Ceren Yılmaz¹ and Uğur Ünal^{1,2,3,a}

1. Graduate School of Materials Science and Engineering, Koc University, Istanbul, Turkey

2. Department of Chemistry, Koc University, Istanbul, Turkey

3. Koc University Surface Science and Technology Center (KUYTAM), Koc University, Istanbul, Turkey

a. Corresponding author (ugunal.ku.edu.tr)

ABSTRACT: We have synthesized Pr:YAG nanopowders via modified sol-gel processes. First technique is citrate-nitrate method which involves nitrate salts of the metals and citric acid as chelating agent. Second process is Pechini method that requires introduction of ethylene glycol different than citrate-nitrate system. The formation process and structure of the phosphor powders were investigated by means of MS coupled TG-DTA, XRD and SEM. Thermal analysis revealed that both precursors contain nitrates, carbonates and unburnt carbon that were released before crystallization. Both methods yielded phase-pure YAG crystallites upon calcination at temperatures between 850-1200°C directly from the amorphous structure without any phase-transformations. However, YAG nanocrystals were obtained at lower calcination temperatures and with lower crystallite sizes by using Pechini system. The average primary particle size calculated was 16 nm for Pr(1%):YAG calcined at 850°C for 3 hours. In addition, photoluminescence characteristics of Pr:YAG powders were characterized. Production of transparent ceramics from these powders is under process. Transparent, polycrystalline Pr:YAG materials will be tested for lasing activity.

1. INTRODUCTION

Since the first solid state laser ruby devised by Mainmann in 1960, solid state lasers became everyday products that are widely used in high speed metal machining, red-green-blue (RGB) light sources in laser printers and projectors, high resolution medical imaging systems such as Optical Coherence Tomography and multi-photon Imaging [Ikesue and Aung, 2008]. Glass or single crystals are the conventional gain media for solid state lasers but single crystals are far more preferred in many industrial applications. Both challenges of the Czochralski method to grow single crystals and the demand for construction of high power lasers fueled research for alternative laser gain media. Since Ikesue reported polycrystalline, transparent Nd:YAG ceramics synthesized by reactive sintering that could operate with a performance comparable to single-crystal laser [Ikesue *et al.*, 1995],

producing ceramic laser gain medium, especially YAG systems, has attracted considerable interest. In this solid-state reaction route that Ikesue introduced, corresponding oxides of constituent elements of the laser medium are ball milled to obtain a homogenous mixture and then the mixture is pressed into a pellet isostatically. Finally, the pellet is sintered at high temperatures under vacuum. Second widely used method for the synthesis of ceramic lasers is coprecipitation, which is based on precipitation of ceramic material from aqueous solution of its constituent elements [Lu *et al.*, 2000]. The precipitate is slip-casted and sintered under vacuum to obtain the desired material. Moreover, conventional ceramic preparation techniques such as citrate-nitrate and Pechini have also been used to produce YAG and rare earth-doped YAG ceramics [Veith, *et al.*, 1999; Li *et al.*,

2007]. These methods allow better control on the stoichiometry, synthesis of pure compounds, and defect-free crystal structure. They also enable heavy and homogeneous doping. Furthermore, it is possible to obtain desired structures at lower synthesis temperatures. Although there is extensive work on Nd:YAG, fewer reports exist on Pr:YAG ceramics. In addition, in majority of these studies solid-state reactions were used to obtain the polycrystalline material [Ikesue and Sato, 2001; Zhang *et al.* 2011]. In this present study, we report two different, modified sol-gel processes to grow polycrystalline, nano-sized Pr:YAG.

2. EXPERIMENTAL

$\text{Al}(\text{NO}_3)_3 \cdot 9\text{H}_2\text{O}$ (Alfa Aesar, %99.999), $\text{Y}(\text{NO}_3)_3 \cdot 6\text{H}_2\text{O}$ (Alfa Aesar, %99.9); and Pr_2O_3 (Alfa Aesar, %99.9) dissolved in nitric acid were used as metal precursors. Metal precursors were mixed in aqueous solution to obtain $\text{Y}_{2.97}\text{Pr}_{0.03}\text{Al}_5\text{O}_{12}$ (1 % Pr^{3+} doped YAG). Anhydrous citric acid (Sigma) was used as chelating agent so that [metal cation]/[citric acid] ratio was 3. Moreover, in Pechini process, ethylene glycol (Sigma) was added into the mixture to increase rate of the polyesterification reactions. The mixtures were heated at 90°C overnight and the obtained gel was carbonized at 200°C or 300°C firstly for 2 hours, then it was sintered at different temperatures from 850°C to 1200°C for 3 hours to yield polycrystalline ceramic powders.

The Nd:YAG powders were mixed with tetraethoxysilane (TEOS, Alfa Aesar), deflocculant Dolapix CE64 (Zschimmer & Schwarz GmbH Co., 2wt%) and binder polyethylene glycol (PEG, Sigma-Aldrich, 0.5wt%) to yield 1 % Pr^{3+} doped YAG. The mixture was ball milled for 24 hours before viscosity measurements (at 25°C , Kinexus) or vacuum sintering at 1750°C , 10^{-5} mbar for 12-30 hours.

Thermo-gravimetric analysis (TGA) of the precursors was carried out in air at a heating rate of $10^\circ\text{C}/\text{min}$ from room temperature to 1100°C by Seiko Exstar TG/DTA 6300). Field-emission scanning electron microscope (FE-SEM; ZEISS Ultra Plus) was used to observe morphology of the samples. The crystal structure and phase purity of the samples were analyzed by X- diffraction (XRD) analysis using Bruker/D2 phaser with Cu $\text{K}\alpha$ radiation. Fluorescence spectrum was measured at room temperature with a fluorescence spectrometer (Horiba Jobin Yvon-Fluoromax 3) using xenon lamp as light source.

3. RESULTS and DISCUSSION

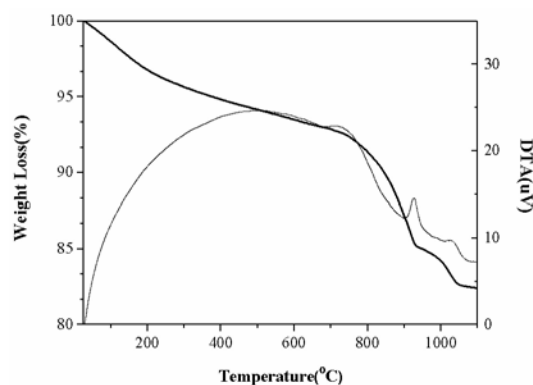


Figure 10: TG/DTA curve of Pr:YAG powder prepared by Pechini process.

The TG and DTA profiles of the brown ash produced by Pechini method are shown in Figure 1. Between 25°C and 750°C there is no significant DTA peak and weight loss is around 8%. This indicates that combustion reactions of the citrate network and of nitrate groups were almost complete at 300°C . Between 750°C and 1040°C , 10% weight loss was observed and corresponding DTA curve shows 3 exothermic peaks at 724 , 820 and 1030°C . This mass loss was detected to be due to CO_2 evolution by mass spectroscopy (data not shown). The exothermic peaks in this temperature range were reported to stem from oxidation of unburnt carbon and

crystallization of YAG [Veith, *et al.*, 1999].

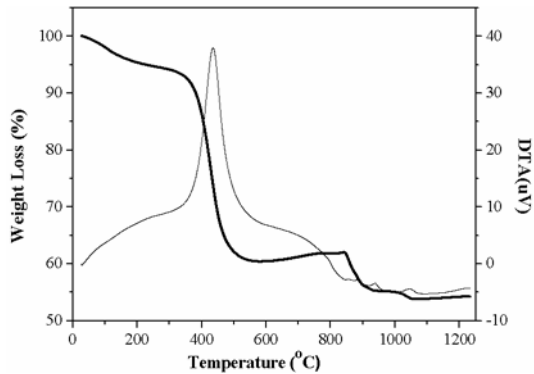


Figure 11: TG/DTA curve of Pr:YAG powder prepared by citrate-nitrate method.

Figure 2 displays TG\DTA curves of the ash prepared by citrate-nitrate process and carbonized at 200°C. A total weight loss of 49% indicates that thermal treatment at 200°C was not sufficient for complete combustion of the organic precursors used. The sharp weight loss and accompanying exothermic DTA peak observed between 300°C and 500°C corresponds to decomposition of nitrate and hydroxycarbonate groups [Li *et al.*, 2007]. Four, rather small exothermic peaks are observed at higher temperatures 817, 866, 937, 1047°C. In a similar study where citric acid was used as catalyst, crystallization temperature of YAG was specified as 942°C [Lu *et al.*, 2002]. To compare the effect of these synthetic processes on the physical properties of the powders, samples were calcined at 850, 950, 1100 and 1200°C and characterized. When XRD diagrams of the products were analyzed, crystallization below 900°C was not detected for the powders obtained by citrate-nitrate method in-line both with literature and thermal analysis (Figure 3). However, complete crystallization of the polycrystalline, phase-pure, cubic $Y_3Al_5O_{12}$ structure was observed at 900°C. Analysis of the diffraction diagram confirms that amorphous powder

crystallizes directly into YAG form without any phase transformation. Increasing calcination temperature does not effect crystal structure of the end product but crystal sizes of the samples increase. Crsytal sizes, calculated by Debye-Scherrer equation, change between 24.5nm (900°C) and 35.8nm (1200°C).

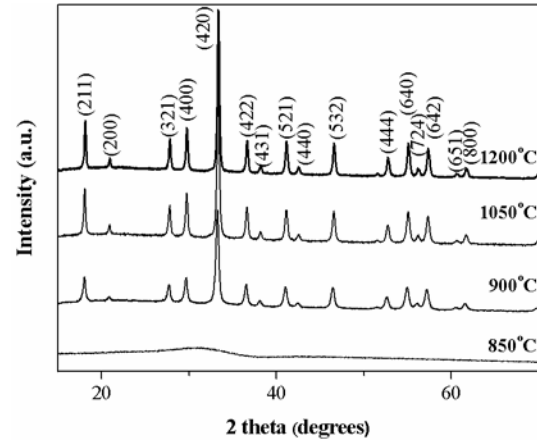


Figure 12: XRD patterns of 1% Pr: YAG samples prepared by citrate-nitrate method.

XRD diagrams of the powders prepared by Pechini process are given in Figure 4. All characteristic reflections of cubic YAG with no signs of secondary phases were observed for the sample calcined at 850°C. Similarly, increase in calcination temperature results in increase in crystal size. Still, crystals obtained by Pechini process are smaller than the particles synthesized by citrate-nitrate technique 16.9nm (850°C) and 21.8nm (900°C). Furthermore, phase-pure YAG crystals can be produced at lower annealing temperatures by using Pechini method. Moreover, extending calcination time to 6 hours (850°C) also resulted in larger crystals (22nm).

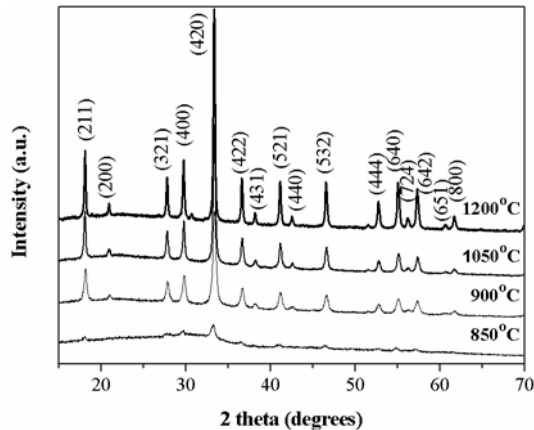


Figure 13: XRD patterns of 1% Pr: YAG samples prepared by Pechini process.

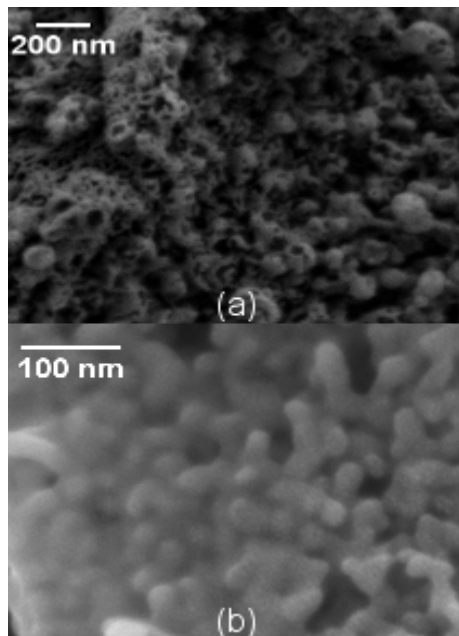


Figure 5: FE-SEM images of Pr: YAG samples prepared by (a)Pechini process and (b) citrate-nitrate method.

FE-SEM images of the powders annealed at 900°C are shown in Figure 5. Grains with sizes ranging between 30-90nm were observed to form agglomerations in both cases. Similar to crystal size, grain size also increases with calcination temperature. When the powders were calcined at 1200°C, agglomerations larger than 100nm appeared (data not shown). However, shapes of the particles vary according to the production technique. Powders obtained by citrate-nitrate method are in the form of hemispheres whereas particles produced by

Pechini process are completely spherical in shape.

Emission spectrum of Pr:YAG dispersed in ethanol is given in Figure 6. Upon excitation with 350nm light, photoluminescence spectrum is dominated by 5d-4f transitions of Pr⁺³ around 380nm and 4f-4f transitions at around 490 and 610nm.

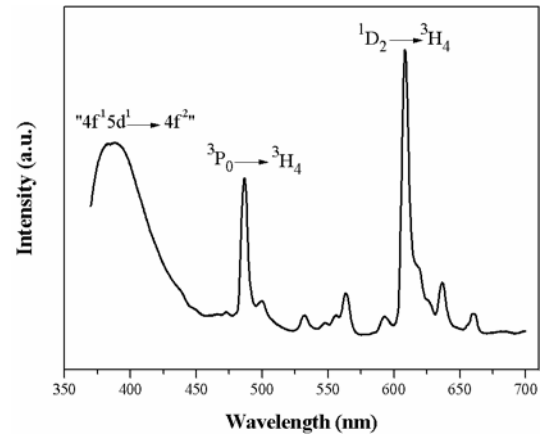


Figure 6: Photoluminescence spectrum of 1% Pr: YAG powder.

To prepare transparent Pr:YAG ceramics, the powder should be sintered at 1700°C under high vacuum. Slip casting was chosen as green body preparation technique. To be able to produce pore-free, high density, transparent material homogenous slip slurry with high solid content and low viscosity is required. Since Pr:YAG powders prepared are in nanometer-size regime, slurry properties of the samples are quite different from clay suspensions. Therefore, rheological properties of the powders were studied before vacuum sintering. The rheological behavior of Pr:YAG slip was studied by measuring the viscosity at varying shear rates while maintaining different dispersant (Dolapix CE 64 0.5, 1, 2 wt%) amounts at constant solid content (30 wt%) with 0.5 wt% binder and TEOS (0.28% SiO₂) as a sintering aid as shown in Figure 7. High initial viscosity decreases gradually with increasing shear rate which suggests typical shear-thinning behavior for all suspensions. Most

probably there are still aggregates in the slurries and flocculated structures are broken down releasing entrapped liquid with applied stress. Both initial viscosity of the suspensions decrease and the slurries flow easier as Dolapix concentration is increased. The viscosity value (2 wt% Dolapix) is 3.6 mPa.s at the maximum shear rate ($\dot{\gamma}=600 \text{ s}^{-1}$). From the above results, suspensions based on a solid content of 30 wt% including 2 wt% Dolapix was chosen to form the green body. Production of transparent ceramics from this green body is under process. Transparent, polycrystalline Pr:YAG materials will be tested for lasing activity.

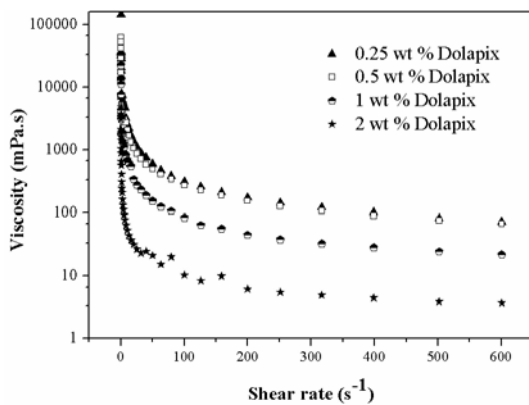


Figure 7: Rheological behavior of Pr:YAG suspensions including 30 wt% YAG, 0.5 wt% PEG, 0.28% SiO₂ and different amounts of Dolapix.

4. CONCLUSIONS

We have synthesized Pr:YAG nanopowders both with citrate-nitrate and Pechini techniques. Pure, polycrystalline Pr:YAG could be obtained by both processes; however, Pechini synthesis yielded smaller Pr:YAG crystals and at lower calcination temperatures. After calcination, aggregates formed and to be able to prepare flowing, homogenous slip slurry, a dispersing agent (Dolapix) was used. Amount of optimum deflocculant was determined by viscosity measurements. The formed green body

will be vacuum sintered and tested for lasing activity.

Acknowledgements: Authors thank to the Scientific and Technological Research Council of Turkey (TUBITAK) for financial support. We also thank to Turkish Ministry of Development for the financial support provided for the establishment of Koc University Surface Science and Technology Center (KUYTAM).

REFERENCES

- Ikesue, A., Kinoshita, T., Kamata, K. and Yoshida, K. 1995. Fabrication and optical properties of high-performance polycrystalline Nd:YAG ceramics for solid-state lasers. *J. Am. Ceram. Soc.*, Volume (78), 1033.
- Ikesue, A. and Sato, Y. 2001. Synthesis of Pr Heavily-Doped, Transparent YAG Ceramics *Journal of the Ceramic Society of Japan*, Volume (109), 640.
- Ikesue, A. and Aung Y.L. 2008. Ceramic laser materials, *Nature Photonics*, Volume (2), 721.
- Li, J., Pan, Y., Qiu, F., Wu, Y., Liu, W. and Guo J. 2007. Synthesis of nanosized Nd:YAG powders via gel combustion. *Ceramics International*, Volume (33), 1047.
- Lu, J., Prabhu, M., Xu, J., Ueda, K., Yagi, H., Yanagitani, T. and Kaminski, A. 2000. High-power Nd:YAG ceramic laser. *Jpn J. Appl. Phys.*, Volume (39), L1048.
- Lu, Q., Dong, W., Wang, H. And Wang, X. 2002. A Novel Way to Synthesize Yttrium Aluminum Garnet from Metal – Inorganic Precursors. *Journal of American Ceramics Society*, Volume (85), 490.
- Veith, M., Mathur, S., Kareiva, A., Jilavi, M., Zimmera M. And Huch, V. 1999. Low temperature synthesis of nanocrystalline Y₃Al₅O₁₂(YAG) and Ce-doped Y₃Al₅O₁₂ via different sol-gel methods. *Journal of Materials Chemistry*, Volume (12), 3069.
- Zhang, S., Li, C., Pang, R., Jiang, L., Shi, L. and Su, Q. Energy transfer and excitation wavelength dependent long-lasting phosphorescence in Pr³⁺ activated Y₃Al₅O₁₂. *Journal of Luminescence*, Volume (131), 273

ELECTRODEPOSITION OF LAYERED MANGANESE OXIDES UNDER HYDROTHERMAL CONDITIONS

F.Eylül Saraç¹, Uğur Ünal^{1,2,3,a}

1. Koç University, Graduate School of Science and Engineering, Istanbul, Turkey
2. Koç University, Department of Chemistry, Istanbul, Turkey
3. Koç University Surface Science and Technology Center, Istanbul, Turkey
a. Corresponding author (ugunal@ku.edu.tr)

ABSTRACT: Efficient and low-cost energy storage has become the leading problem today. Electrochemical capacitors (EC) are the promising materials with combining high energy and high power density. Among various materials, manganese oxides are one of the most researched ones as ECs because of their abundance, low-cost, and environmentally friendliness. We have synthesized manganese oxides with or without surfactants onto different substrates by electrodeposition under hydrothermal conditions to achieve enhanced pseudocapacitance. This possible electrodes for electrochemical capacitors showed excellent pseudocapacitive behavior in cyclic voltammetry measurements. They reached up-to 620F/g in the potential range of 0.9V and scan rate of 20mV/s.

1. INTRODUCTION

Renewable energy production and storage has become one of the most important issues in today's world. To store energy, there are two main types of devices known as batteries and capacitors [Chuang & Hu, 2005]. Batteries have higher energy density with respect to capacitors; however, they suffer from limited cycle life because of storing energy by irreversible Faradaic reactions [Prasad & Miura, 2004].

In recent years, electrochemical capacitors (EC) have gained much attention due to their longer cycle life and higher power density than batteries [Arbizzani *et al.*, 2001]. They are the intermediate devices between conventional capacitors and batteries in terms of energy density [Song *et al.*, 2012]. Since they have high rate of charge-discharge, they can be used in systems where peak power is needed like mass rapid transit, hybrid vehicles, elevators, memory back-up devices, etc [Hu *et al.*, 2011]. There are mainly two

types of EC as electric double-layer capacitors (EDLC) which utilizes charge separation at the interface between electrode and electrolyte, and pseudocapacitors which utilize reversible redox reactions within the active material of the electrode for energy storage [Hu *et al.*, 2011]. It is known that pseudocapacitors have higher energy densities than EDLCs [M. Wu *et al.*, 2004].

As pseudocapacitors, there are mainly three types of electrode materials used up-to-date: high-surface area carbon, conducting polymers, and transition metal oxides or hydroxides [Xia *et al.*, 2010]. Among these, transition metal oxides, for instance oxides of Cr, Ru, Mn, Ir, Co, Mo, W, Ni, V, etc., are the most promising materials since they have several oxidation states and have high specific capacitance and power [Q. Li *et al.*, 2007]. RuO found to have perfect capacitive behavior but it is not practical to use since it has high toxicity and cost along with its rarity in nature

[Wohlfahrt-Mehrens *et al.*, 2002]. Thus, researchers tried to focus on enhancing charge storage properties of low cost transition metal oxides like Ni, Co, or Mn [Hu & Tsou, 2003].

Manganese oxides attracted great interest since it is an abundant, environmentally friendly material [D. Liu *et al.*, 2008]. However, it has low electrical conductivity and formation of thicker active materials make its specific capacitance go to lower values [J. Li *et al.*, 2008]. To overcome this problem, 3-D, porous, and large surface area electrodes must be produced. In order to synthesize efficient electrodes with high performance active materials which are manganese oxides, different techniques are used such as sol-gel synthesis, chemical precipitation, hydrothermal synthesis [Staiti & Lufrano, 2009], physical vapour deposition, and electrodeposition [Fan *et al.*, 2011]. Among these, electrodeposition is the most promising technique since properties of active materials like thickness, porosity, morphology can be controlled simply by changing the delivered charge during deposition or deposition bath conditions like temperature, pH, duration, or pressure [Nakayama *et al.*, 2005].

In order produce thin films of manganese oxides, we have used cathodic electrodeposition. Cathodic electrodeposition, unlike anodic one, does not cause to dissolve or oxidize the substrate material thus leading to usage of many metals. Also, when the solution is aqueous and potential is enough to let electrolysis of water, deposition occurs along with generation of hydrogen gas which provides to obtain porous structures without using a template [Xia *et al.*, 2011].

Substrate choice for active material is also an important issue for effective

electrode production. We have used nickel mesh in our research since it has a 3-D, porous, high-surface area material. Also, since nickel is a metal, it has high electronic conductivity and due to its light weight web, it has high structural strength. This porosity and high-surface area leads for electrons and protons move easily between electrode and electrolyte across the active material, and thus, higher specific capacitances.

2. EXPERIMENTAL

In order synthesize manganese oxides onto nickel mesh substrate, 3-three electrode cell was used. Electrochemical deposition setup is a hydrothermal reactor which allows temperature control during synthesis up to 200°C. Prior to deposition, nickel mesh was degreased with acetone and etched with hydrochloric acid solution. The reference electrode was Ag/AgCl electrode, the counter electrode was platinum wire, and the working electrode was pretreated nickel mesh. The solution of deposition contained 0.05M MnCl₂·4H₂O and 0.05M K₂SO₄. During deposition, a constant cathodic potential was applied varying from -1.4V and -1.1V. In order to see the effect of mass load of active material on electrochemical properties, deposition duration was varied from 1 to 5 minutes. Also, in order to see the hydrothermal condition effect, a room temperature synthesis at the same duration and applied potential was conducted.

In order investigate the effect of temperature, deposition duration and applied potential on morphology, Scanning Electron Microscopy (SEM, ZEISS EVO LS15) was used. In order to identify the crystal structure of the active material, X-Ray Diffraction (XRD, BRUKER D2 PHASER) was used.

To analyze the electrochemical performance of the produced manganese

oxides, Cyclic Voltammetry (CV) technique was utilized. The measurements were done simply in a three-electrode cell containing same electrodes with the deposition setup where working electrode was the nickel mesh deposited with manganese oxide. The electrolyte solution contained 0.5M K_2SO_4 . The films were scanned between 0.0V and 0.9V with a scan rate of 20mV/s.

3. RESULTS AND DISCUSSION

During deposition at room temperature, when negative potential was applied to the system, there was gas evolution at the counter and working electrodes indicating electrolysis of water. This is actually the crucial point of the formation mechanism of manganese oxides during cathodic deposition. When reduction of water occurs at cathode, working electrode, hydrogen gas evolution starts along with hydroxyl ion formation. This hydroxyl ions cause a local pH increase at the cathode and results precipitation of manganese hydroxide since Mn^{2+} ions are already attracted to the negative cathode. Upon drying, these hydroxides transforms into corresponding oxides. This gas evolution obviously cannot be observed in hydrothermal conditions since the system is closed but XRD patterns showed that similar crystalline structures are obtained.

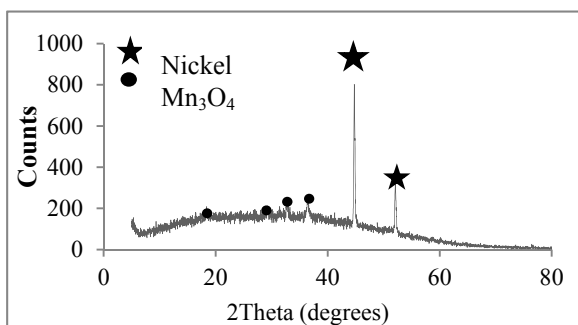


Figure 1: XRD pattern of manganese oxide synthesized at 130°C at -1.1V for 15 minutes.

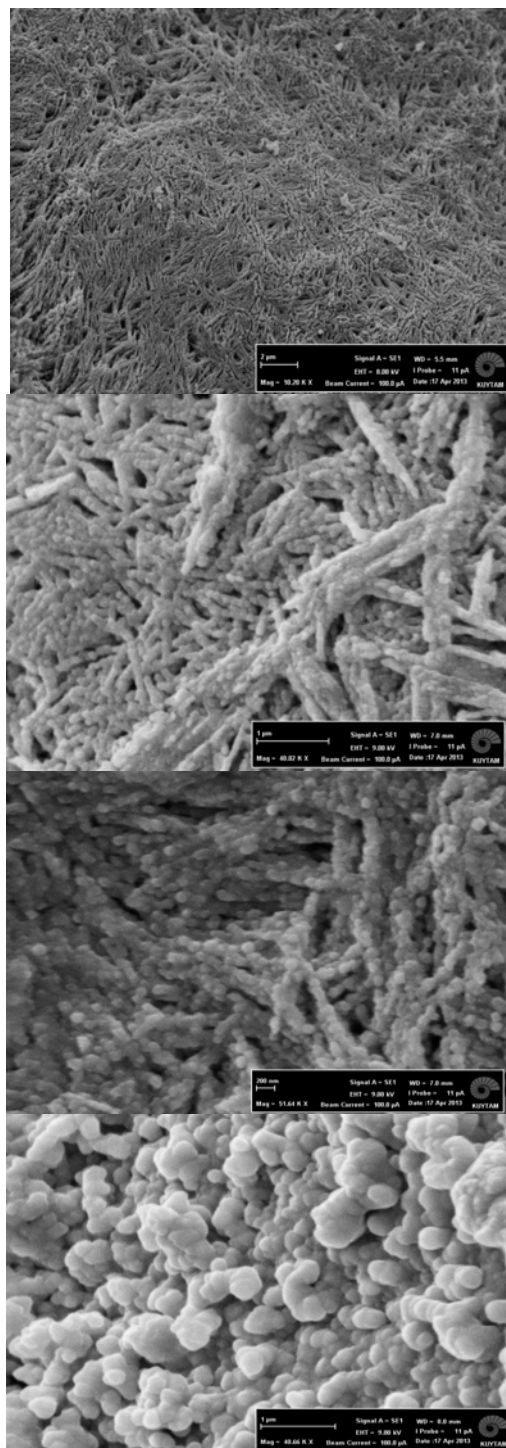


Figure 2: SEM images of MnO synthesized at 130°C for 15min at a) -1.4V b) -1.3V c) -1.2V and d) -1.1V.

It was found that the structure in Figure 1 belongs to Mn_3O_4 (hausmannite).

As it can be seen from Figure 2, SEM images reveal the morphology difference

between synthesized manganese oxides at different potentials. It should be mentioned that at room temperature, there was no deposition observed below -1.4V. However, in hydrothermal conditions, manganese oxides can successfully synthesized up-to -1.1V. Below is a table of comparison of electrochemical performance between films deposited at different potentials in hydrothermal conditions. As it can be seen from Table 1, as the potential applied during deposition decreases, specific capacitance of the material actually increases. This may due to the formation of distinguishable nano-sized structures formed at -1.1V which will increase the surface area of the active material leading the higher specific capacitance.

Table 1: Specific capacitances of films deposited at 100°C for 15min at different potentials.

Potential (V)	SC (F/g)
-1.4V	10.2
-1.3V	18.9
-1.2V	33.4
-1.1V	82.2

This is a useful result because we could synthesize the material, actually an enhanced one, with lower potentials applied to the system by just changing the deposition temperature. After we saw that we can decrease the potential up-to -1.1V, we tried to optimize the deposition parameters like temperature and duration in order to enhance the specific capacitance of manganese oxides.

Table 2: Specific capacitances of films produced in different conditions.

Duration /Temperature	5min	15min
100°C	225.0F/g	82.2F/g
130°C	315.6F/g	286.2F/g

As it is evident from Table 2, when the deposition temperature increases and

duration decreases, specific capacitance increases. The temperature effect is under investigation, but duration effect is clear. When the deposition time increases, the film thickness (or mass load) also increases and this will decrease the specific capacitance since it is harder for electrons for protons to diffuse into the electrolyte from the electrode. This is why formation of porous active material is also a crucial point as it was mentioned before.

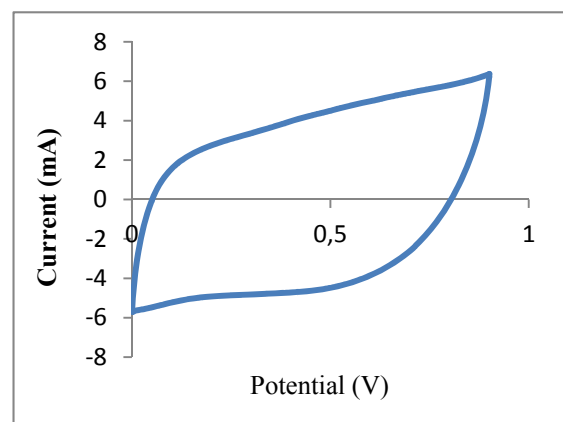


Figure 3: Cyclic Voltammogram of film synthesized at 130°C for 15min at potential of -1.1V.

As it can be seen from Figure 3, the films synthesized at hydrothermal conditions showed excellent capacitive behavior with their high reversibility and rectangular-like shape.

The problem in literature is, however, the decrease of specific capacitance with cycle number. Generally 30-40% of capacitance values retained after several cycles. In contrast, our films showed excellent retainment of capacitive behavior. Interestingly, with increasing cycle number, our films' specific capacitances increase and showed almost 11000% increase just in the 35.cycle with respect to the first cycle as it is shown in Figure 4.

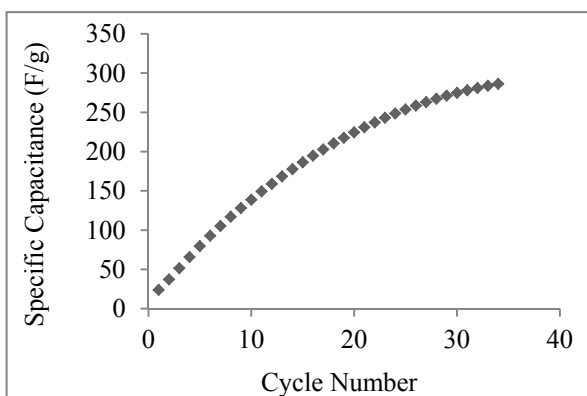


Figure 4: Specific capacitance vs cycle number of film synthesized at 130°C for 15min at potential of -1.1V.

4. CONCLUSIONS

Manganese oxides onto nickel mesh substrate were successfully synthesized by cathodic electrodeposition in hydrothermal conditions. The films synthesized showed excellent pseudocapacitive behavior and could reach specific capacitances up-to 315F/g which is a high value among literature. This enhanced pseudocapacitance is attributed to the porous structure of active material obtained by cathodic deposition and high-surface area of nickel as the current collector.

Acknowledgements: The authors are grateful to Koç University for financial support to this project and KUYTAM for infrastructure.

REFERENCES

Arbizzani, C., Mastragostino, M. and Soavi, F., 2001. New trends in electrochemical supercapacitors, *Journal of Power Sources*, 100, 164.

Chuang, P.-Y. and Hu, C.-C., 2005. The electrochemical characteristics of binary manganese–cobalt oxides prepared by anodic deposition, *Materials Chemistry and Physics*, 92(1), 138.

Fan, Z. et al., 2011. Characteristics and electrochemical performances of supercapacitors using double-walled carbon nanotube/ δ -MnO₂ hybrid material electrodes, *Journal of Electroanalytical Chemistry*, 659(2), 191.

Hu, C.-C. et al., 2011. A hierarchical nanostructure consisting of amorphous

MnO₂, Mn₃O₄ nanocrystallites, and single-crystalline MnOOH nanowires for supercapacitors, *Journal of Power Sources*, 196(2), 847.

Hu, C.-C. and Tsou, T.-W., 2003. The optimization of specific capacitance of amorphous manganese oxide for electrochemical supercapacitors using experimental strategies, *Journal of Power Sources*, 115(1), 179.

Li, J., Yang, Q.M. and Zhitomirsky, Igor, 2008. Nickel foam-based manganese dioxide–carbon nanotube composite electrodes for electrochemical supercapacitors, *Journal of Power Sources*, 185(2), 1569.

Li, Q. et al., 2007. An investigation of Cu²⁺ and Fe²⁺ ions as active materials for electrochemical redox supercapacitors, *Journal of Electroanalytical Chemistry*, 611(1-2), 43.

Liu, D. et al., 2008. Hydrous Manganese Dioxide Nanowall Arrays Growth and Their Li + Ions Intercalation Electrochemical Properties, *Chemistry of Materials*, 20(4), 1376.

Nakayama, M. et al., 2005. Electrodeposition of manganese and molybdenum mixed oxide thin films and their charge storage properties, *Langmuir: the ACS journal of surfaces and colloids*, 21(13), 5907.

Prasad, K.R. and Miura, N., 2004. Potentiodynamically deposited nanostructured manganese dioxide as electrode material for electrochemical redox supercapacitors, *Journal of Power Sources*, 135(1-2), 354.

Song, M.-K. et al., 2012. Anomalous pseudocapacitive behavior of a nanostructured, mixed-valent manganese oxide film for electrical energy storage, *Nano letters*, 12(7), 3483.

Wohlfahrt-Mehrens, M. et al., 2002. New materials for supercapacitors, *Journal of Power Sources*, 105(2), 182.

Wu, M. et al., 2004. Redox deposition of manganese oxide on graphite for supercapacitors, *Electrochemistry Communications*, 6(5), 499.

Xia, H. et al., 2010. MnO₂ nanotube and nanowire arrays by electrochemical deposition for supercapacitors, *Journal of Power Sources*, 195(13), 4410.

Xia, H., Lai, M.O. & Lu, L., 2011. Nanoporous MnO_x thin-film electrodes synthesized by electrochemical lithiation/delithiation for supercapacitors, *Journal of Power Sources*, 196(4), 2398.

MESOPOROUS MATERIALS FROM A NOVEL SILICA SOURCE

Sujitra Wongkasemjit^{1,a}, and Rujirat Longloilert¹

1. Chulalongkorn University, Petroleum and Petrochemical College, and Center of Excellence for Petrochemical and Materials Technology, Bangkok 10330, Thailand

a. Corresponding author: dsujitra@chula.ac.th

ABSTRACT: Generally, mesoporous silicas are synthesized via sol-gel process using structure directing agent, catalysts (acid or base), solvent, and commercially available silica source (mainly TEOS). The commercially available silica sources are mostly found to be easily hydrolyzed, resulting in amorphous silica rather than forming mesoporous silica. A novel silica source with a moisture stable, known as silatrane, was employed to the synthetic process. Since the mesoporous silicas themselves are deficiently employed as a catalyst, the incorporation of hetero atoms to their structures can solve this drawback. The extraordinary mesoporous silicas as well as the metal loaded mesoporous silicas using moisture-stable silatrane, the properties, and their applications will be discussed.

1. INTRODUCTION

The M41S and SBA families have attracted remarkable attentions due to their high surface area, ordered pore structure array, and narrow pore size distribution [Shao *et al.*, 2005]. However, the SBA family has thicker walls, providing a better hydrothermal stability and larger pore size than M41S [Tunglumlert *et al.*, 2007]. The mesoporous silicas are typically achieved by using surfactant or amphiphilic triblock copolymer as a structure-directing agent in basic or acidic media.

In general, the sources of silica for both families are sodium silicate, tetraethylorthosilicate (TEOS) [Giraldo *et al.*, 2007]. Wongkasemjit's group introduces home-made silatranes (Figure 1), as silica source. These novel precursors are not only easily prepared from silicon dioxide and trialkanolamine (TEA) in ethylene glycol (EG) solvent, but are also moisture stable. With the latter remarkable property, the silatrane precursors have proved to be a good candidate for synthesis of not only mesoporous [Thanabodeekij *et al.*, 2006; Tunglumlert *et al.*, 2007; Samran *et al.*,

2011], but also microporous materials [Sathupanya *et al.*, 2003; Phiriyawirut *et al.*, 2003; Phonthammachai *et al.*, 2003]. In addition, the applications of these materials, including heterogeneous catalysts, are mentioned accordingly.

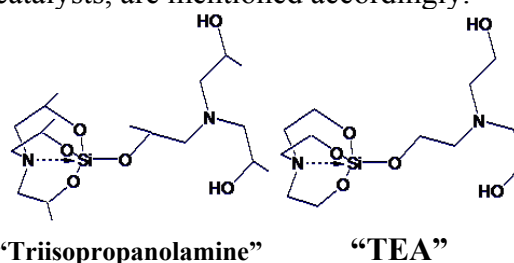
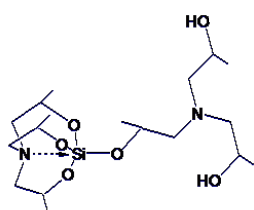
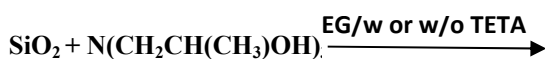


Figure 1: Home-made silatranes

2. SILATRANE AND ITS APPLICATION

Silatranes, a class of chelate compounds of pentacoordinated silicon, have been known and investigated since 1963, with initial studies by M. G. Voronkov and co-workers [Voronkov *et al.*, 1982]. The structural properties of silatranes have also been widely considered [Nasim *et al.*, 1991; Hencsei *et al.*, 1991]. Typically silatranes are synthesized via the reaction of halo-, hydro-, and alkoxy silanes with triethanolamine or its derivatives. In

1991, Laine and coworkers developed a method for synthesizing organosilicon compounds directly from silica and EG in only one step, so called the Oxide One-Pot Synthesis or “OOPS” process, in the presence of tetraethylenediamine (TETA) catalyst. Moreover, Piboonchaisit *et al.* in 1999 successfully synthesized silatrane complexes from silica and TIS (triisopropanolamine) via OOPS process with and without TETA (eq. 1), and the obtained products exhibited similar properties. However, the reaction time is two times faster in the presence of TETA, meaning that TETA could be used as an accelerator for this reaction.



(eq.1)

Owing to the hydrolytic stability in air for periods up to several weeks, silatranes are good candidates for being used as precursors in ceramic processing via sol-gel technique, as studied by Charoenpinijkarn *et al.* (2001) who mechanistically investigated the sol-gel processing of silatranes. In 2006, the extremely high surface area MCM-41 was successfully synthesized directly from silatrane precursor by Thanabodeekij and coworkers. They found that the MCM-41 structure could be formed in a narrow range of ion concentration at a wide range of temperature. However, the larger pore size was obtained at a higher temperature. In this case, 100 °C provided a high-quality MCM-41. BET surface area was affected by the surfactant concentration. Interestingly, a surface area as high as 2,400 m²g⁻¹ was achieved with the surfactant-to-silatrane ratio of 0.6 at 60

°C, while 1.72 cm³g⁻¹ of pore volume was obtained at the similar surfactant ratio and 100 °C.

In 2007, Tunglumlert *et al.* synthesized a cubic SBA-1 at room temperature using cationic surfactant, and found that the shape of SBA-1 crystals relied on the alkyl chain length of the surfactant. Three-dimensionally ordered mesopores were obtained at a high surfactant concentration and elevated synthesis temperature (50 °C). The morphology of the obtained materials indicated an octahedron, consistent with six square {100} and 12 hexagonal {110} planes with a cubic symmetry. The surface area was as high as 1000–1500 m²/g with an adsorption volume of 0.6–1.0 cm³/g.

Samran and coworkers in 2011 successfully synthesized a well-ordered and stable dimensional mesoporous SBA-15 silica at room temperature using a nonionic triblock copolymer (P123) as a structure-directing agent via two different routes. One experiment was conducted at room temperature while the other via the microwave-assisted hydrothermal method. The products of the two methods were found to be comparable and provided large surface areas (486–613 m²/g), pore diameter (45–67 Å), and channel volumes (0.6–0.8 cm³/g). The first route of the SBA-15 synthesis provides the advantage, of using room temperatures for an economical, energy-saving process in the large scale production of thermally stable SBA-15.

Recently, MCM-48 with *Ia3d* symmetry and three-dimensional pore structure was also synthesized using silatrane precursor [Longloilert *et al.*, 2011]. The results revealed that all synthesis parameters affected the MCM-48 synthesis. Various techniques used for characterizing MCM-48 showed a long-range ordered structure with a truncated octahedral shape and a

surface area as high as 1300 m²/g with a pore size of 2.86 nm.

Mechanistically, the reaction generated TEA molecules which were the by-product from the hydrolysis of silatrane. TEA can also act as a structure-directing agent for the system, resulting in a lower requirement of the CTAB concentration. Moreover, TEA could also improve the surfactant-packing parameter which drives the MCM-48 formation.

3. SYNTHESIS OF METAL-LOADED MESOPOROUS SILICA

Wongkasemjit's research group have expanded their work by incorporating heteroatoms into the silica framework and have also studied their activity towards the oxidation of organic molecules. Tunglumlert *et al.* (2008) were interested in the room temperature synthesis of Fe-SBA-1 using FeCl₃ via sol-gel process. The results illustrated that up to 6 wt% Fe could be contained in SBA-1 framework without destroying the mesopore order. The BET surface area was 1062 m²/g with the pore diameter around 2.1 nm.

Other colleagues (Thitsartarn *et al.*, 2008) in Wongkasemjit's research group synthesized Fe-MCM-41 by both sol-gel and impregnation methods to compare their catalytic activity on the epoxidation of styrene as a catalyst. The results revealed that the optimal condition to obtain hexagonal Fe-MCM-41 was at 60 °C reaction temperature for 7 h and 550 °C of calcinations temperature with 1 °C/min. The maximum Fe loading while maintaining the MCM-41 structure was at 2.5%. However, at higher 2.1% of Fe, the iron species were found within both the framework and extra-framework. The in-framework iron was active for the conversion of styrene with H₂O₂. Moreover, the catalyst prepared from sol-gel technique had greater performance for

the epoxidation of styrene than the impregnated catalyst. The content of 1% Fe loading via sol-gel process reached 65% selectivity of styrene oxide and 22% of styrene conversion.

To overcome the loss of hydrothermal stability, two different heteroatoms were loaded in supports known as bimetallic catalysts. These catalysts usually improve their stability and also provide catalytic activity and selectivity. Thus, in 2013, Maneesuwan and coworkers prepared Fe-Ce-MCM-48 from silatrane via sol-gel technique using cerium glycolate and FeCl₃ as metal precursors. The results showed that a high dispersion of Fe and Ce in silica framework was obtained with 0.01 Fe/Si and 0.01-0.07 Ce/Si ratios. All samples possessed a high surface area (approximately 1,200 m²/g) and narrow pore-size distribution. A similar study by Longloilert *et al.* (2012) incorporated only Ce or Cr to the mesoporous MCM-48 synthesized from silatrane and studied the MCM-48's properties influenced by the introduction of Ce as well as Cr. The results showed that materials still retained the structure of MCM-48, with a long range-ordered structure and high surface area (up to 1500 m²/g) even loading metals (Ce or Cr) to the structure. The hydrothermal stability test of Ce- or Cr-MCM-48 was better than the pure MCM-48. Interestingly, according to the SEM results, the MCM-48 structure morphologically changed when loaded with different metal species.

Thanabodeekij *et al.* in 2007 were interested in the production of Mo-MCM-41, producing a high dispersion of Mo onto MCM-41 support through incipient wetness impregnation using silatrane and molybdenum glycolate precursors. The structure of hexagonal arrays was maintained even when 10% mol of Mo (or 0.265g MoO₃/g SiO₂) was loaded. The surface area reached 1600 m²/g with

3 nm pore size. The photocatalytic activity of the synthesized Mo-MCM-41 catalyst was tested toward the peroxidative bromination, and the results showed that Mo loading onto uncalcined MCM-41 exhibited a high activity, as compared to Mo loading onto calcined MCM-41. Additionally, in 2009, Wongkasemjit *et al.* synthesized Mo-SBA-1 via sol-gel process at room temperature while Che *et al.* (2001) prepared at low temperature (0 °C). The obtained materials in this work preserved a well-ordered mesostructure and a surface area greater than 1000 m²/g. The maximum loading of tetrahedral-coordinated Mo was around 5 mol% without any extra-framework. This material was studied its activity on the epoxidation reaction of styrene monomers. The optimum condition for this reaction was found at 70 °C reaction temperature, for 3 h reaction time using 0.1g of catalyst containing 7.2 mol% Mo content. The maximum conversion of styrene reached 60%.

Thanabodeekij *et al.* In 2005 prepared Ti-MCM-41 using silatrane and titanium glycolate precursors via sol-gel method. The obtained materials had a very high surface area (up to 2300 m²/g) even loading 1-5% titanium. The MCM-41 structure was maintained as the Ti content increased. They also tested these catalysts through the peroxidative bromination, and the activity was found to be impressive. Then, in 2008, Tunglumlert *et al.* synthesized Ti-SBA-1 at room temperature using the same precursors. The results demonstrated that Ti was accommodated on SBA-1 support up to 10 wt%. The surface area was around 1000 m²/g with 2nm average pore diameter.

Apart from the oxidation of organic molecules, the catalytic pyrolysis of waste tires to light olefins using meta-

containing mesoporous material was also performed. Generally, the production of light olefins has been derived mostly from steam crackers and refinery fluid catalytic cracking units. Moreover, their demand has been continuously increasing, and the waste tire material has caused environmental problems. Therefore, the pyrolysis of waste tires to gain the light olefins, such as ethylene and propylene, has been viewed as a promising solution to both issues. Dũng *et al.* (2009) and Witpathomwong *et al.* (2011) prepared Ru/MCM-41 and Ru/MCM-48, respectively, via the conventional wetness impregnation, and used as a catalyst in waste tire pyrolysis. They found that a considerably high yield of light olefins (four and two times higher than non-catalytic pyrolysis) was achieved over 2% Ru/MCM-41 and 0.7% Ru/MCM-48, respectively. Furthermore, these catalysts also provided the lightest oil with the highest concentration of single ring aromatics and low contents of polycyclic aromatics. Additionally, it could reduce the poly- and polar-aromatic compounds, as well as the sulfur content in the derived oil.

4. CONCLUSIONS

There were many types of mesoporous silicas synthesized from the moisture stable silica source known as silatrane. These materials possessed extraordinary properties, making them valuable in a wide range of applications. Until now, the potentials for biological applications have attracted much attention. However, the activities described in this paper have focused mainly on the organic reaction.

Acknowledgements: The authors acknowledge the Thailand Research Fund (TRF), the Ratchadapisake Sompote Fund, Chulalongkorn University for financial support.

REFERENCES

- Bickmore, C. and Laine, R. 1996. Synthesis of Oxynitride Powders via Fluidized-Bed Ammonolysis, Part I: Large, Porous, Silica Particles. *J. Am. Ceram. Soc.* 79:2865-77.
- Charoenpinijkarn, W., Suwankruhasn, M., Kesapabutr, B., Wongkasemjit, S., and Jamieson A.M. 2001. Sol-gel processing of silatranes. *Eur. Polym. J.* 37:1441-1448.
- Düng, N. A., Klaewkla, R., Wongkasemjit, S., and Jitkarnka, S. 2009. Light olefins and light oil production from catalytic pyrolysis of waste tire. *J. Anal. Appl. Pyrolysis* 86(2):281-286.
- Giraldo, L. F., López, B. L., Pérez, L., Urrego, S., Sierra, L., and Mesa, M. 2007. Mesoporous Silica Applications. *Macromol. Sym.* 258(1):129-141.
- Halachev, T., Nava, R., and Dimitrov, L. 1998. Catalytic activity of (P)NiMo/Ti-HMS and (P)NiW/Ti-HMS catalysts in the hydrogenation of naphthalene. *Appl. Catal. A Gen.* 169(1):111-117.
- Hartmann, M. 2005. Ordered Mesoporous Materials for Bioadsorption and Biocatalysis. *Chem. Mater.* 17(18):4577-4593.
- Hencsei, P. 1991. Mass-spectrometric Study of Ring Substituted Silatranes. *Struct. Chem.* 2:21.
- Laine, R., Blohowiak, K., Robinson, T., Hoppe, M., Nardi, P., Kampf, J., and Uhm, J. 1991. Synthesis of Pentacoordinate Silicon Complexes from SiO₂. *Nature.* 353:642-4.
- Longloilert, R., Chaisuwan, T., Luengnaruemitchai, A., and Wongkasemjit, S. 2011. Synthesis of MCM-48 from silatrane via sol-gel process. *J. Sol-Gel Sci. Technol.* 58(2):427-435.
- Longloilert, R., Chaisuwan, T., Luengnaruemitchai, A., and Wongkasemjit, S. 2012. Synthesis and characterization of M-MCM-48 (M = Cr, Ce) from silatrane via sol-gel process. *J. Sol-Gel Sci. Technol.* 61(1):133-143.
- Maneesuwan, H., Longloilert, R., Chaisuwan, T., and Wongkasemjit, S. 2013. Synthesis and characterization of Fe-Ce-MCM-48 from silatrane precursor via sol-gel process. *Mater. Lett.* 94(0):65-68.
- Piboonchaisit, P., Wongkasemjit, S., and Laine, R. 1999. A Novel Route to Tris(silatranyloxy-i-propyl) amine Directly from Silica and Triisopropanolamine, Part I. *Sci. Asia.* 25:113-119.
- Samran, B., Aungkutrannont, S., White, T., and Wongkasemjit, S. 2011. Room temperature synthesis of Ti-SBA-15 from silatrane and titanium-glycolate and its catalytic performance towards styrene epoxidation. *J. Sol-Gel Sci. Technol.* 57(2): 221-228.
- Tanglumlert, W., Imae, T., White, T. J., and Wongkasemjit, S. 2007. Structural Aspects of SBA-1 Cubic Mesoporous Silica Synthesized via a Sol-Gel Process Using a Silatrane Precursor. *J. Am. Ceram. Soc.* 90(12):3992-3997.
- Tanglumlert, W., Imae, T., White, T. J., and Wongkasemjit, S. 2008. Preparation of highly ordered Fe-SBA-1 and Ti-SBA-1 cubic mesoporous silica via sol-gel processing of silatrane. *Mater. Lett.* 62(30):4545-4548.
- Tanglumlert, W., Imae, T., White, T. J., and Wongkasemjit, S. 2007. Structural Aspects of SBA-1 Cubic Mesoporous Silica Synthesized via a Sol-Gel Process Using a Silatrane Precursor. *J. Am. Ceram. Soc.* 90(12):3992-3997.
- Thanabodeekij, N., Gulari, E., and Wongkasemjit, S. 2007. Highly dispersed Mo-MCM-41 produced from silatrane and molybdenum glycolate precursors and its peroxidation activity. *Powder Technol.* 173(3):211-216.
- Thanabodeekij, N., Sadthayanon, S., Gulari, E., and Wongkasemjit, S. 2006. Extremely high surface area of ordered mesoporous MCM-41 by atrane route. *Mater. Chem. Phys.* 9:131-137.
- Thanabodeekij, N., Tanglumlert, W., Gulari, E., and Wongkasemjit, S. 2005. Synthesis of Ti-MCM-41 directly from silatrane and titanium glycolate and its catalytic activity. *Appl. Organomet. Chem.* 19(9):1047-1054.
- Thitsartarn, W., Gulari, E., and Wongkasemjit, S. 2008. Synthesis of Fe-MCM-41 from silatrane and FeCl₃ via sol-gel process and its epoxidation activity. *Appl. Organomet. Chem.* 22(2):97-103.
- Voronkov, M.G., Dyakov, V.M., and Kirpichenko, S.V. 1982. Silatranes, *J. Organomet. Chem.* 233:1-147.
- Witpathomwong, C., Longloilert, R., Wongkasemjit, S., and Jitkarnka, S. 2011. Improving Light Olefins and Light Oil Production Using Ru/MCM-48 in Catalytic Pyrolysis of Waste Tire. *Energy Procedia* 9(0):245-251.
- Wongkasemjit, S., Tamuang, S., Tanglumlert, W., and Imae, T. 2009. Synthesis of Mo-SBA-1 catalyst via sol-gel process and its activity. *Mater. Chem. Phys.* 117(1):301-306.

SUPERACIDIC MESOPOROUS SULFATED TITANIA-SILICATES FOR DEHYDRATION OF FRUCTOSE

Emre Kılıç¹, Selahattin Yılmaz^{2,a}

1. Izmir Institute of Technology, Department of Chemical Engineering, Izmir, Turkey

2. Izmir Institute of Technology, Department of Chemical Engineering, Izmir, Turkey

a. Corresponding author (selahattinyilmaz@iyte.edu.tr)

ABSTRACT: Mesoporous titania-silicates are known as superacidic and thermally stable materials. In the present study, sulfated titania-silicate catalysts were prepared via sol-gel and hydrothermal method. They were tested for fructose dehydration. Reaction tests were carried out in dimethylsulfoxide (DMSO) at 110 °C under atmospheric pressure. Fructose initial concentration was 6 wt % and catalyst amount was 0.5 g. Different sulfated catalysts were also used for comparison. Maximum HMF selectivity (93 %) was obtained by sol-gel prepared sulfated titania silicate. It was attributed to the mesoporous structure, presence of strong superacid sites, especially Bronsted sites and highly active chelating bidentate bonds formed during sulfation.

1. INTRODUCTION

5-hydroxymethylfurfural (HMF) is known as the key intermediate in order to convert the biomass to valuable chemicals such as polymers, bio-fuels, bulk chemicals [Guo et al., 2012]. The most effective way of producing the HMF is sugar conversion, especially dehydration of fructose [Yang et al., 2011; Zhang et al., 2012].

Fructose dehydration reaction occurs on the acid sites of the catalyst. Strength and density of the acid sites on catalyst affect the product distribution significantly. It was also reported that Lewis sites are responsible for fructose conversion where Bronsted sites are responsible from HMF formation [Weingarten et al., 2011].

Wide range of heterogeneous catalysts (e.g. resins, metal sulfates, metal phosphates, heteropolyacids and zeolites) has been investigated in literature. Some of heterogeneous catalysts have low stabilities due to leaching, some of them are not selective and promote side product formation; such as formic acid and levulinic acid [Guo et al., 2012; Qi et al., 2009]. Thus, researchers are trying to

find a stable, active and selective catalyst for fructose dehydration.

Sulfur ions and sulfate groups create Bronsted and strong acid sites when loaded on support, thus they are very active for fructose dehydration. They can also be used without leaching problem in polar aprotic solvents, such as DMSO, acetone, dimethylamide. On the other hand, no one solve the leaching problem when sulfates are used in alcohols or in water [Yadav et al., 2004; Juan et al., 2007]. Sulfates were loaded on many different supports in literature; such as iron oxide, alumina, titania and zirconia. Zirconia is known as the good support for sulfates. It strongly interacts with sulfur ions and creates strong and Bronsted acid sites. However, it has low surface area which may be enhanced by loading them on to a support. Carbon based supports also give satisfactory HMF yields since carbon atoms play an important role (on protonation) on reaction mechanism. For that reason, sulfates are loaded onto a carbon based support.

In recent years, mixed oxides, especially titania-silicates became important as

acidic catalysts. They are prepared by several methods such as sol-gel, precipitation and impregnation where the most stable one is sol-gel [Sharma et al., 2012]. Sol-gel synthesized titania-silicates have very stable structure, super acidic centers and regular mesopores. However, they have merely Lewis acid sites. Bronsted sites can be created by sulfation of these titania silicates. It was observed by many investigators that Ti in these mixed oxides prevent the leaching of sulfur, also in alcohol or water [Li et al., 2013; Sharma et al., 2012].

In this study, sulfated catalysts, SO_4/ZrO_2 , SO_4/SiO_2 , SO_4/AC , $\text{SO}_4/\text{ZrO}_2/\text{SiO}_2$, $\text{SO}_4/\text{ZrO}_2/\text{AC}$, $\text{SO}_4/\text{TiO}_2\text{-SiO}_2$, $\text{SO}_4/\text{Ti-SBA-15}$ were prepared by different methods for fructose dehydration.

2. EXPERIMENTAL

2.1. Materials

D-Fructose (>99 %), Titanium isopropoxide (>99 %), acetonitrile (>98%), sulfuric acid (>98 %), hydrochloric acid (98 %), orthophosphoric acid (85 %), zirconium chloride (98 %), dimethylsulfoxide, methylisobutylketone, ammonium sulfate (98 %) and tetraethylorthosilicate (98 %) were supplied from Sigma Aldrich Chemie.

2.2. Catalyst Preparation

2.2.1. Preparation of sulfated zirconia catalyst

3 % S loaded sulfated zirconia was prepared according to the procedure by Yadav et al. (2004). Precipitated $\text{Zr}(\text{OH})_4$ was treated with H_2SO_4 . This catalyst was referred as SO_4/ZrO_2 .

2.2.2 Preparation of sulfated activated carbon and silica

3 % S loaded sulfated activated carbon and silica were prepared according to the procedure by Khayoon et al (2011). AC& SiO_2 was sulfated by sulfuric acid. These catalysts were referred as SO_4/AC and SO_4/SiO_2 .

2.2.3 Preparation of sulfated zirconia loaded silica and activated carbon catalysts

3 wt. % S and 10 wt. % SO_4/ZrO_2 loaded silica and activated carbon supported catalysts were prepared following the procedure by Juan et al. (2007). $\text{Zr}(\text{SO}_4)_2$ dissolved in water at room temperature was loaded by impregnation. These catalysts were referred as $\text{SO}_4/\text{ZrO}_2/\text{AC}$ and $\text{SO}_4/\text{ZrO}_2/\text{SiO}_2$.

2.2.4 Preparation of titania-silicate and sulfated titania silicate

A mixture of 10 ml tetraethylorthosilicate (TEOS), 8 ml H_2O and 35 ml ethanol were prepared and 0.2 ml HCl was added to this solution. This mixture was allowed to stir for 2 h. After 2 h, 10 wt % of titanium isopropoxide (TISOP) dissolved in ethanol (TISOP/ethanol=1:10) was added. Then, solution temperature was increased to 80 °C. Gel formed was dried at 80 °C for 24 h. After drying, it was calcined at 550 °C for 6 h. Calcined $\text{TiO}_2\text{-SiO}_2$ powders were then sulfated using 5 ml/g catalyst of 1 M $(\text{NH}_4)_2\text{SO}_4$ solution. Sulfated powder was calcined at 450 °C for 6 h to obtain $\text{SO}_4/\text{TiO}_2\text{-SiO}_2$.

2.2.5 Preparation of sulfated ti-sba-15

Pluoronic P-123 (6 g) was dissolved 150 ml water and stirred for 3 h at 50 °C. Then, 5 g of HCl was added to this solution. 3.5 g of titanium isopropoxide and 20 g TEOS were added to the solution and stirred for 24 h at 50 °C. The resulting gel was transferred to the autoclave and kept at 100 °C for 24 h to form Ti-SBA-15. This material was then

dried at 100 °C for 24 h and calcined at 550 °C for 6 h. Calcined Ti-SBA-15 was sulfated by treating with 0.5 M chlorosulfonic acid in dichloromethane. The resultant material was calcined at 450 °C for 6 h to obtain SO₄/Ti-SBA-15.

2.3. Catalyst Characterization

The Philips X'Pert Pro diffractometer with CuK α radiation was used to determine crystalline structures of the samples. BET Micromeritics-Gemini V was used to determine the surface area of catalyst by nitrogen physisorption. Micromeritics AutoChem II instrument was used to determine acidity of the samples by using Temperature-Programmed Desorption of Ammonia (NH₃-TPD) method. Liquid phase titration method (using 0.5 M NaOH) was also used to determine the acidity.

2.4. Catalytic Activity Tests

All the activity tests were performed in a 200 ml stirred multiple reaction station under atmospheric pressure. Activity tests were performed as follows. Initially, 40 ml solvent and 0.5 g catalyst was stirred in the reactor until reaction temperature (110 °C) was reached. Then, 6 wt % of fructose dissolved in 10 ml DMSO was added. After that samples were taken from the reactor at different time intervals up to 180 min.

3. RESULTS AND DISCUSSIONS

3.1. Characterization Results

XRD analysis showed that most of the crystal phases in pure zirconia were monoclinic (XRD results are not given). Small anatase crystals were observed for SO₄/TiO₂-SiO₂. No crystal peaks were observed for other catalysts.

Textural properties and acidity results of the sulfated catalysts are shown in Table 1. Catalysts other than activated carbon had mesopores ranging between 2.5-7.0

nm. Sulfated titania-silicates had the largest pores. AC, SiO₂ and SBA-15 supported catalysts were found to have very high surface areas.

NH₃-TPD results of TiO₂-SiO₂ are shown in Figure 1. It was found that pure TiO₂-SiO₂ has high amount of weak acid sites. After sulfation, these acid sites were removed by formation of chelating bidentate bonds which provided superacidic and Bronsted acid sites.

AC, SiO₂ and SBA-15 supported catalysts had high acidities (Table 1) which may be attributed to the well dispersion of the sulfates on to these supports [Juan et al., 2007]. On the other hand, acid site densities of these catalysts were lower, which was described as the amount of acid sites per unit surface area of the catalyst. In literature, most of the researchers reported the presence of direct relation between HMF yield and acid site density instead of acid site amount [Weingarten, et al., 2011].

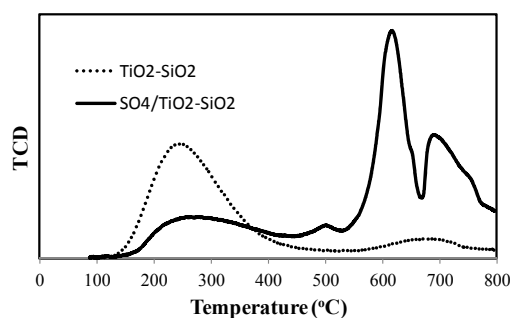


Figure 1: NH₃-TPD results of TiO₂-SiO₂ and SO₄/TiO₂-SiO₂

3.2. Reaction Results

Fructose conversions obtained over different sulfated catalysts are given in Figure 2. All catalysts were very active. This was related to strong acidity and higher acid site density of the catalysts [Weingarten et al., 2009]. Catalysts other than silica supported ones and SO₄/Ti-SBA-15 converted fructose completely in 1 h.

The best selectivity of HMF, around 90 %; was achieved by SO₄/TiO₂-SiO₂ catalyst (Figure 3). Selectivity obtained by SO₄/Ti-SBA-15 was also high (80 %). High selectivity obtained over SO₄/TiO₂-SiO₂ was attributed to the presence of chelating bidentate bonds, highest acid site density and larger mesopores in this catalyst. Chelating bidentate bonds are known as superacidic strong Bronsted sites and directly related to the HMF formation. Larger mesopores increase the rate of fructose adsorption to acid site. They also prevented the collision of fructose molecules, thus side product formation was minimized [Qi et al., 2009]. Silica supported catalysts, SO₄/SiO₂ and SO₄/Zr/SiO₂ gave the lowest selectivity. This result was related to the hydrophilic surface of silica, which might cause rehydration of HMF [Juan et al., 2007]. Also low acid site densities of these catalysts could contribute low yields obtained [Qi et al., 2009].

Figure 4 shows a relation between acid site density, fructose decomposition and HMF yield. Conversion raised with the acid site density up to 2 μmol/m² and then it reached to 100 %. A slight decrease in conversion at acid site density about 2.61 was observed over SO₄/Ti-SBA-15 catalyst. This was attributed to the lower Lewis site content of this catalyst [Sharma et al., 2013]. Increase in acid site density enhanced the catalytic activity and promoted the HMF yield.

To explain the detailed relation between HMF formation and acidity, turnover frequency (TOF) of the different catalysts was calculated by the following expression,

$$TOF = \frac{(\text{moles of HMF})}{(\text{time}) \times (\text{moles of acid sites})}$$

and are given in Table 1. No relation between acid density and TOF was obtained. This indicated that not only the

acid site density was important also the strength and type of acid sites were also important. Maximum TOF was obtained with SO₄/TiO₂-SiO₂ which had the highest acid site density.

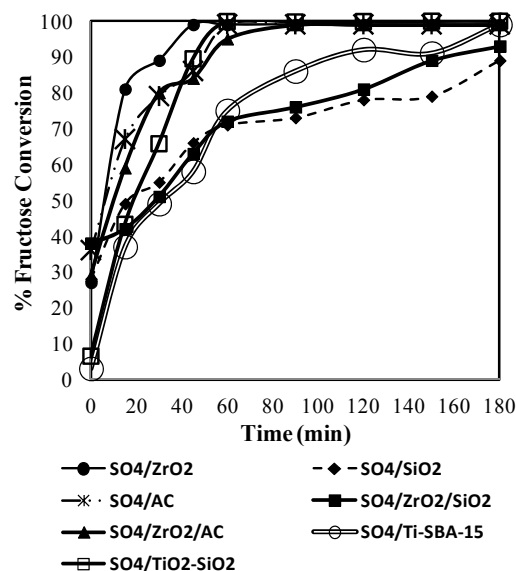


Figure 2: Effect of different sulfated catalysts on fructose conversion.

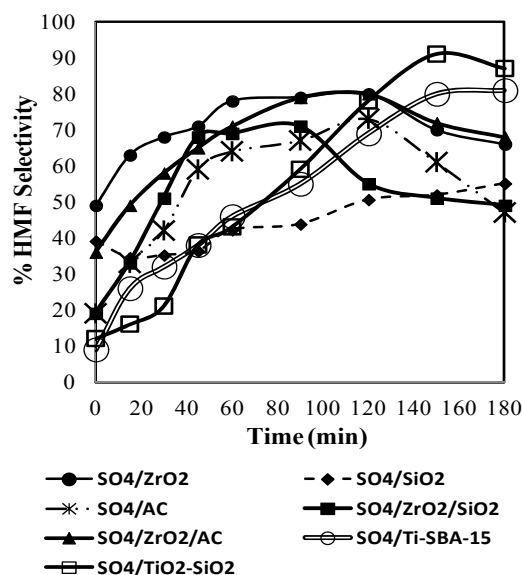


Figure 3: Effect of different sulfated catalysts on HMF selectivity.

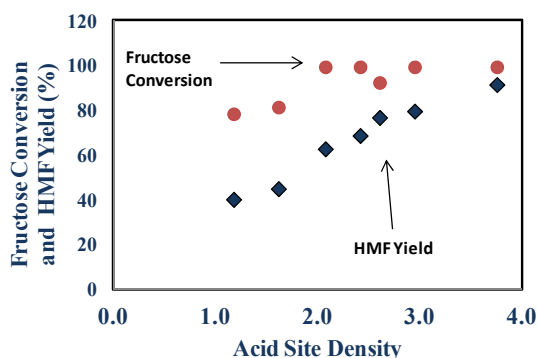


Figure 4: Effect of acid site density on HMF yield

Table 1: Textural and acidity properties and activity results of sulfated catalysts

Catalyst	BET Surface Area (m ² /g)	Pore Size (Å)	Acidity (μmol/gcat)	Acid site density (μmol/m ²)	TOF (mol HMF/mol acid sites*h)	HMF Yield (%)
SO ₄ /ZrO ₂	192	52	567	2.95	20	79
SO ₄ /SiO ₂	578	35	683	1.18	17	40
SO ₄ /AC	683	8.2	1420	2.08	13	62
SO ₄ /ZrO ₂ /SiO ₂	416	25	674	1.62	19	45
SO ₄ /ZrO ₂ /AC	543	5.4	1314	2.42	15	68
SO ₄ /TiO ₂ -SiO ₂	289	69	1086	3.76	24	91
SO ₄ /Ti-SBA-15	636	60	1660	2.61	13	76

3. CONCLUSIONS

Catalysts activity and selectivity were affected by the type and method of catalyst preparation. Mesopore structure provided high catalyst activity, as expected. Selectivity to HMF was controlled by type and strength of acid sites. SO₄/TiO₂-SiO₂ catalyst which had chelating bidentate bonds providing acidity gave the highest HMF yield (91%). Also SO₄/Ti-SBA-15 catalyst provided good yield (76%).

REFERENCES

Guo, F., Fang, Z., Zhou, T., 2012. Conversion of Fructose and Glucose into 5-hydroxymethylfurfural with Lignin-derived Carbonaceous Catalyst under Microwave Irradiation in Dimethyl Sulfoxide-ionic

Liquid Mixtures, *Bioresource Technology*, 112, 313.

Juan, J.C., Zhang, J., Jiang, Y., Cao, W., Yarmob, M.A., 2007. Zirconium Sulfate Supported on Activated Carbon as Catalyst for Esterification

of Oleic Acid by n-Butanol under Solvent-free Conditions, *Catalysis Letters*, 117, 153.

Khayoon, M.S., Hameed, B.H., 2011. Acetylation of glycerol to biofuel additives over sulfated activated carbon catalyst *Bioresource Technology*, 102, 9229.

Li L., Liu S., Xu J., Yu S., Liu F., Xie C., Ge X., Ren J., 2013. Esterification of itaconic acid using Ln-SO₄^{2-/-}/TiO₂-SiO₂ (Ln = La³⁺, Ce⁴⁺, Sm³⁺) as catalysts, *Journal of Molecular Catalysis. A: Chem*, 368, 24.

Qi, X., Watanabe M., Aida T. M., Smith Jr. R., 2009. Sulfated Zirconia as a Solid Acid Catalyst for the Dehydration of Fructose to 5-

- Hydroxymethylfurfural. Catalysis Communications 10, 1771.
- Sharma R. V., Soni K. K., Dalai A. K., 2012. Preparation, characterization and application of sulfated Ti-SBA-15 catalyst for oxidation of benzyl alcohol to benzaldehyde, Catalysis Communications, 29, 87.
- Weingarten, R., Tompsett, G.A., Conner, W.C., Huber, G.W., 2011. Design of solid acid catalysts for aqueous-phase dehydration of carbohydrates: The role of Lewis and Bronsted acid sites, Journal of Catalysis, 279, 174.
- Yadav, G. D., Murkute, A. D., 2004. Preparation of a Novel Catalyst UDCaT-5: Enhancement in Activity of Acid-Treated Zirconia Effect of Treatment with Chlorosulfonic Acid vis-à-vis sulfuric acid, Journal of Catalysis, 224, 218.
- Yang, F., Liu, Q., Bai, X., Du, Y., 2011. Conversion of Biomass into 5-hydroxymethylfurfural Using Solid Acid Catalyst, Bioresource Technology, 102, 3424.
- Zhang, Z., Liua, B., Zhao, K., 2012. Conversion of Fructose into 5-HMF Catalyzed by GeCl_4 in DMSO and [Bmim]Cl System at Room Temperature, Carbohydrate Polymers, 88(3), 891.

MECHANICAL PROPERTIES OF A COMPOSITE PRODUCED BY USING ELECTROLESS Ni PLATED Fe-Co-Cr POWDERS

Eyüp Donat¹, Ayhan EROL¹, Ahmet YONETKEN^{2,a},

¹ Faculty of Technology, Afyon Kocatepe University, 03200, Afyonkarahisar, Turkey
aerol@aku.edu.tr, eyupdonat_03_88@hotmail.com

² Faculty of Engineering, Afyon Kocatepe University, 03200, Afyonkarahisar, Turkey
a. Corresponding Author (yonetken@aku.edu.tr)

ABSTRACT: The microstructure, mechanical properties and corrosion characteristics of Ni plated %30Fe -%30Co and %10Cr powders were investigated using specimens produced by tube furnace sintering at 800-1200°C temperature. A uniform nickel layer on Fe-Co and Cr powders was deposited prior to sintering using electroless plating technique. A composite consisting of quintet additions, a metallic phases, Fe, Cr and Co, within a matrix of Ni has been prepared under Ar shroud and then tube furnace sintered. XRD, SEM (Scanning Electron Microscope), corrosion behavior in acidic media were investigated to characterize the properties of the specimens. Experimental results carried out for composition (%30Fe-%30Co-%10Cr)30Ni at 1200°C suggest that the best properties as 186.54 HV were obtained at 1200°C

Keywords: Sintering, intermetallic, Electroless nickel plating

1. INTRODUCTION

The use of protective coatings for Improved mechanical and physical-chemical properties of metals and alloys is now an urgent task of materials science. [1-3] Cobalt, nickel and chromium is one of the most important constituents of functional materials for excellent corrosion and wear-resistant alloys. Ti-Co-Cr alloys are widely used for medical prosthetic implant devices, such as knee implants, metal-to-metal hip joints and dental prosthetics [4]. Non-precious metals and alloys (Co-Cr, Ni-Cr) are recent trend replacing precious or noble alloy in dentistry. Almost 90% of all removable partial dentures are now cast from non-precious alloys containing Co, Cr, Ni [5]. These alloys possess better mechanical properties, therefore can be easily cast into desired thinner shapes in oral cavity, the salinity of saliva approaches that of seawater and tends to be highly corrosive to most non-noble metals [6]. In designing non-precious alloys, Cr is added in the range of 10-

30% to obtain an optimum value of corrosion resistance and mechanical strength. The corrosion resistance in addition to other consideration such as affordability, biocompatibility and mechanical properties of alloys plays an important role [7-9]. Electroless nickel platings have found wide uses in many fields, because the technique of electroless plating was invented and the high performance product with high hardness, wear resistance and corrosion resistance were produced. Several advantages like low cost, easy formation of a continuous and uniform coating on the surface of substrate with complex shape, and capability of depositing on either conductive or nonconductive parts have attracted a lot of interests from the academy and the industry [10].

In this study, the Metal-metal composites were obtained by using electroless nickel (Ni) plating with Fe-Co-Cr powders.

2. MATERIAL-METHOD AND PREPARATION OF SAMPLE

In this study, Iron (Fe), Chromium (Cr), Cobalt (Co) and Nickel (Ni) powder were used as metal powder. Fe, Co and Cr powders with 20 μ m grain size and 99.5% purity and Ni powders with 3 μ m size and 99.5% purity, which were both provided from Johnson Matthey Materials Technology Company, were used. The aim of this study was to deposited Iron (Fe), Chromium (Cr), Cobalt (Co) powders with Ni. It was thought that Ni powders can either be added in the mixture directly or obtained through plating with nickel chloride (NiCl₂.6H₂O) used in electroless nickel plating bath [7].

Table 1: Chemicals of nickel plating bath and their ratios

Chemicals	Conditons
Iron (Fe)	9g
Chromium (Cr)	3g
Cobalt (Co)	9g
Nickel Chloride (NiCl ₂ .6H ₂ O)	36g
Hydrazine Hydrate (N ₂ H ₄ .H ₂ O)	20%
Distile Water	80%
Temperature(°C)	90-95°C
pH Value	9-10

2.1 Method and Preparation of Sample

In the experimental study the samples were prepared through two different methods. In the first method, homogeneous mixture obtained through mixing 30%Fe-10%Cr-30%Co-Ni powders for a day was shaped in hydraulic press coolly under 200 bar and made ready for sintering. In the second method, silicon carbide powders were plated using electroless nickel plating technique and then shaped in hydraulic press again coolly under 300 bar pressure. The shaped samples were sintered for an hour within the temperature range 800-1200°C under argon gas atmosphere in tube furnace. The sintered samples were made ready

for mechanical and metallographic analyses. In electroless Ni plating bath, 30%Co-10%Cr-30%Fe powders, Nickel chloride, Ammoniac, Hydrazine hydrate and pure water by weight were used. The contents of the plating bath are given in Table 1.

3. EMPIRICAL RESULTS

In the study, the samples prepared and shaped (pressed) through two different methods were sintered at temperatures ranging from 800°C to 1200°C in tube furnace and made ready for physical, mechanical and metallographic analyses.

3.1. Density

The pre-sintering and post-sintering densities of the samples prepared using two different methods were determined. In Figure 1, the density change graphic for plated and non-plated samples depending on the temperature is shown. The densities of the samples obtained after sintering were calculated by using ($d=m/V$) calculation formula (Figure 1). Here m is the mass of sintered sample; v is the volume of sintered sample, calculated geometrically. When Figure 1 is examined highest density is at 1200°C composites as 5.85 gr/cm³ and the lowest density has 5.43 gr/cm³ values at 800°C.

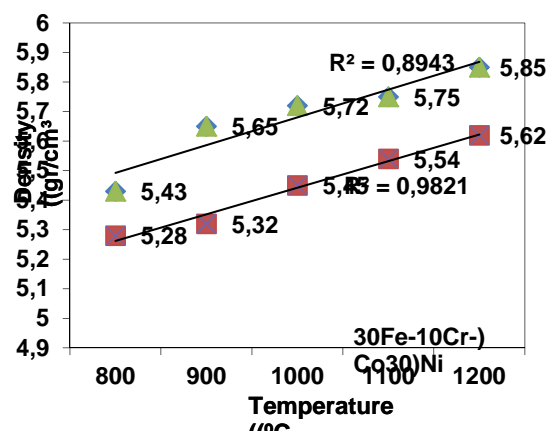


Figure 1: Density graphic of Fe-Cr-Co-Ni composite materials

3.2. Micro hardness

The micro hardness-temperature change diagram is shown in Fig. 2. The micro hardness values of the composite samples produced using tube furnaces sintering technique within the temperature range 1200°C from powders obtained as a result of plating Fe-Co-Cr powders through electroless Ni plating method in tube furnace were given. According to this, the highest micro hardness value in the composite samples produced using electroless plating method was observed to be 186,54HV at 1200°C

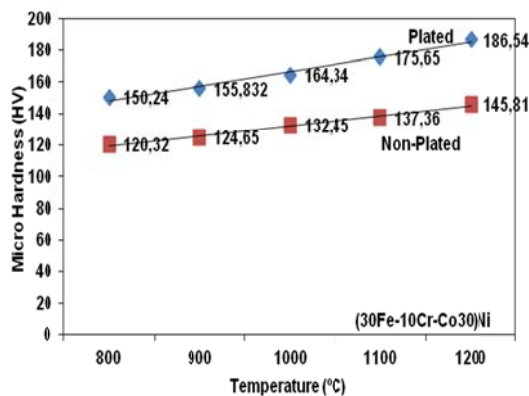


Figure 2: Micro hardness graphic of Fe-Cr-Co-Ni composite materials

3.3. Compression Strength

In this study, compression strength from mechanical tests applied on the specimens after sintering was examined. In Figure 3, compression test was applied on the plated specimens and specimens fabricated without plating. As can be understood from the graphic, the highest strength was achieved as 105,17MPa at 1200°C in the plated specimen. The highest compression strength in the non-plated specimen was 93MPa at 1200°C.

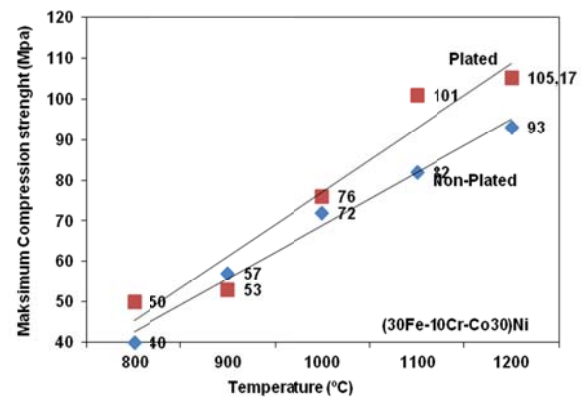
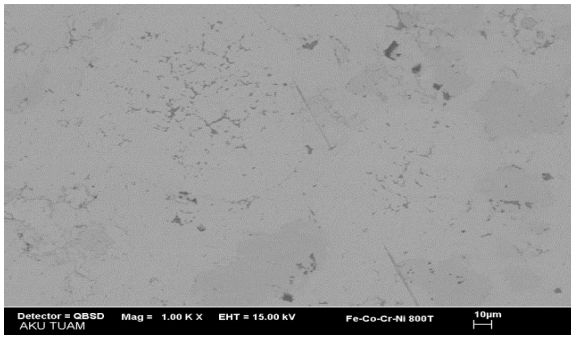


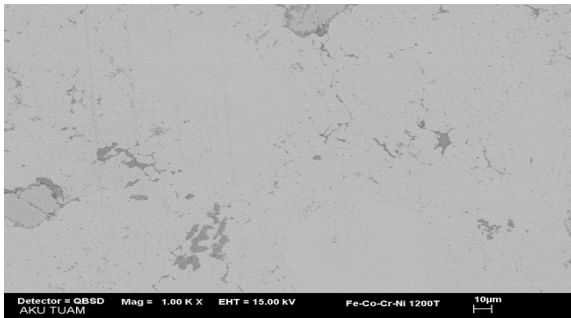
Figure 3: Compression strength graphic of Fe-Cr-Co-Ni composite materials

3.4. SEM Analysis

After the specimens sintered at different sintering temperatures were secured within resin and surface polishing processes were completed, their photographs were taken and EDX analyses were carried out by SEM (LEO 1430 VP equipped with RONTEC EDX) with magnifications of 1kX. The SEM photograph of Ni plated Co-Cr-Fe powders, which yielded the best result in terms of mechanical strength in the sintered specimens (plated with Ni and prepared by normal mixture method) during the study, after sintering at 800°C and 1200°C is shown in Figures 4a and 4b. SEM photographs of non-plated Co-Cr-Fe-Ni powders taken after sintering at 800°C and 1200°C are also given. The SEM analysis result of the metal matrix composite specimen obtained from Ni plated (Co-Cr-Fe) powders sintered at 1200°C is shown in Figures 5a and 5b. The pores do show a homogenous distribution.

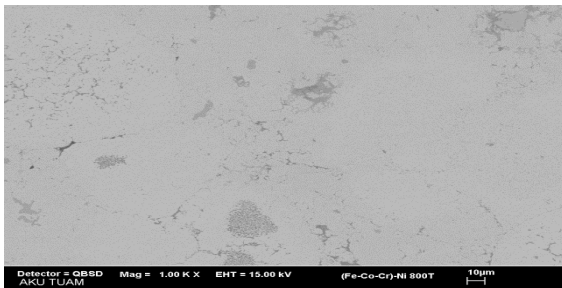


a)800°C

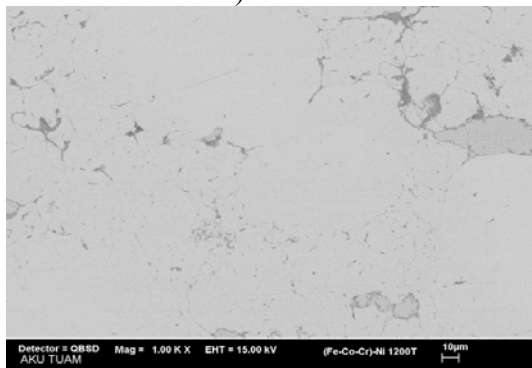


b)1200°C

Figure 4: SEM view of Co-Cr-Fe-Ni composite



a)800°C



b)1200°C

Figure 5: SEM view of Ni Plated (Co-Cr-Fe) composite

3.5 XRD Analysis

After sintered, plated and non-plated specimens were characterized by XRD analysis. See in Fig.6-7. As can be understood from the analysis results, the existence of FeNi, CrCo, FeTi, Fe₂Ti and Ni peak in the graphs shows that Fe-Co-Cr powders were plated with Ni. The XRD analysis of Fe-Co-Cr composite fabricated at 1200 °C from powders Ni plated through the same way is shown in Figure 7. As can be seen, FeNi, CrCo, FeTi, Fe₂Ti and Ni phases occurred in the fabricated metal-metal composite.

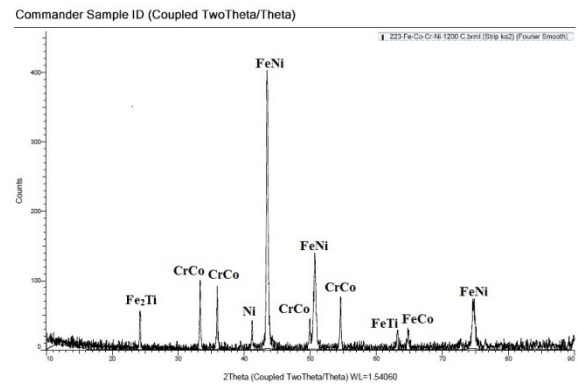


Figure 6: X-ray diffraction patterns of the Fe-Co-Cr-Ni sintered at 1200°C

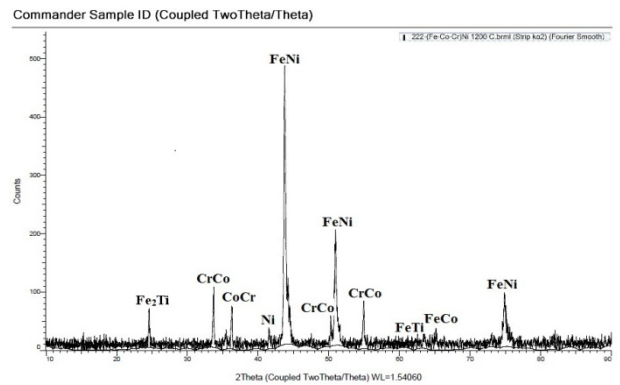


Figure 7: X-ray diffraction patterns of the Ni Plated Fe-Co-Cr sintered at 1200°C

4. CONCLUSION

The following results were concluded from the experimental findings

- he highest compression strength was obtained as 105,17MPa at 1200°C. The highest non-plated sample post-sintering comprehension was achieved at 1200°C as 94MPa.
- The highest density in composite made from Ni-plated Fe-Co-Cr powders sintered at different temperatures was obtained as 1200°C The highest density plated sample was found as 5,85gr/cm³ at 1200°C. The density in the non-plated sample was estimated to be 5,62 gr/cm³.
- The highest microhardness in composite samples fabricated using electroless Ni-plating method was found as 186,54HV at 1200°C. The highest microhardness value in the samples fabricated with non-plated powders was tested to be 145,81HV at 1200°C.
- It was also found out that the mechanical properties of the plated samples are higher than those of the non-plated samples. It was concluded that Co-Cr-Fe powders give positive results to Ni-plating.

REFERENCES

- [1] Misaelides P, Hatzidimitriou A., Noli F., Pogrebnjak A.D., Tyurin Yu.N., Kosionidis S., Preparation, characterization, and corrosion behavior of protective coatings on stainless steel deposited by plasma detonation, Surf. And Coat. Tech., 180-181 (2004), 290-296
- [2] Misaelides P., Noli F., Tyurin Y.N., Pogrebnjak A.D., Perdikakis G., Application of ion beam analysis to the characterization of protective coatings prepared by plasma detonation techniques on steel samples, Nucl. Instr. and Meth. in Phys. Res., Section B, 240 (2005), No 1-2, 371-375
- [3] Pogrebnjak A.D., Lebed A.G., Ivanov Yu.F., Modification of single crystal stainless steel structure (Fe-Cr-Ni- Mn) by high-power ion beam, Vacuum, 63 (2001), No.4, 483- 486
- [4] <http://www.astm.org/> ASTM F75 Co-Cr alloy.
- [5] J.C. Wataha, J. Prosthet. Dent. 87 (2002) 351.
- [6] G. Saravanan, S. Mohan, , " Structure, composition and corrosion resistance studies of Co-Cr alloy electrodeposited from deep eutectic solvent (DES)", Journal of Alloys and Compounds 522 (2012) 162– 166
- [7] J.C. Wataha, C.T. Hanks, Z. Sun, Dent. Mater. 11 (4) (1995) 239.
- [8] G. Schmalz, H. Langer, H. Schweikl, J. Dent. Res. 77 (10) (1998) 1772.
- [9] L. Reclaru, J.M. Meyer, Biomaterials 19 (1) (1998) 85.
- [10] Zhang Q., Wu1, M., and Z. Wen 'Electroless nickel plating on hollow glass microspheres' 'Surface & Coatings Technology' 192 (2005) 213– 219

CONTROLLED CRYSTALLIZATION OF 0.25Li₂O.0.2SiO₂-0.75BaO.2SiO₂ GLASS

Burcu Ertuğ^{1a}, Burcu Nilgün Çetiner², Hasan Gökçe¹, Z. Engin Erkmen²,
M. Lütfi Öveçoğlu¹

1. Istanbul Technical University, Department Of Metallurgical and Materials Engineering, 34469 Maslak,
Istanbul, Turkey.

2. Marmara University, Department of Metallurgical and Materials Engineering, 34722 Göztepe, Istanbul,
Turkey.

a. Corresponding author (burcuertug@gmail.com)

ABSTRACT: In the present study, the crystallization behaviour of 0.25Li₂O.0.2SiO₂-0.75BaO.2SiO₂ glass was investigated. DTA curves of 0.25Li₂O.0.2SiO₂-0.75BaO.2SiO₂ glass exhibited a small endothermic peak, which shows the glass transition temperature, T_g and a broad exothermic peak, which shows the crystallization of both lithium disilicate and barium disilicate phases together. The optimum nucleation temperature and time were determined by Marotta method. After the nucleation heat treatment, the glass showed amorphous phase separation as shown by optical images. The glass was heat treated at 675, 720 and 765°C for 1h. The glass-ceramic's microstructures were examined by SEM. It was concluded that the crystallization temperature has a great effect on the morphology of the glass-ceramic phases formed.

Keywords: Lithium disilicate, barium disilicate, glass-ceramic, microstructure.

1. INTRODUCTION

Crystal growth in glasses has been an area of extensive experimental study. Crystal growth rates in stoichiometric systems are described in terms of 2D nucleated growth [Burgner et al., 2001]. Glass-ceramics are fine-grained polycrystalline materials formed when glasses of suitable compositions are heat treated and thus undergo controlled crystallisation to the lower energy, crystalline state [Rawlings et al., 2006]. The glass-ceramics exhibit better wear, oxidation and chemical resistance, higher hardness and dimensional stability in comparison to glasses [Buchner et al., 2011].

Controlled crystallization process is realized by the nucleation and crystallite growth corresponding to two different temperatures, latter being the higher temperature [Küchler et al., 2007]. In the controlled crystallization process, all the

crystalline phases are precipitated from the parent glass. The parent glass can be in the form of bulk or glass powder, which exhibit volume and surface crystallization, respectively [Zhang et al., 2008]. For practical applications, lithium disilicate glass-ceramics have been widely used in the areas of ceramic-metal sealing and dental restoration [Wen et al., 2007].

In the present study, the production of the lithium disilicate glass-ceramics and the examination of the microstructures were carried out.

2. EXPERIMENTAL PROCEDURE

The glass-ceramic studied was prepared to give lithium disilicate (Li₂O.2SiO₂) and barium disilicate (BaO.2SiO₂) phases together; 0.25Li₂O.0.2SiO₂-0.75BaO.2SiO₂. It contains barium disilicate as the major constituent. Glass transition and

crystallization temperatures of the glass composition were determined by differential thermal analysis (DTA) with a heating rate of 10°C/min. under static atmosphere using a simultaneous thermal analyser (Netzch). The nucleation and crystallization heat treatments were planned according to the DTA results. In order to carry out the microstructural studies, bulk glass and glass-ceramic samples were polished and then etched with diluted HF solution for 20-30s., coated with carbon and crystallized microstructures were compared with each other using scanning electron microscope (JEOL JSM-330).

3. RESULTS AND DISCUSSION

DTA curves of 0.25Li₂O.0.2SiO₂-0.75BaO.2SiO₂ composition studied exhibited a small endothermic peak, which shows the glass transition temperature, T_g and a broad exothermic peak, which shows the crystallization of both lithium disilicate and barium disilicate phases together as shown in Fig.1.

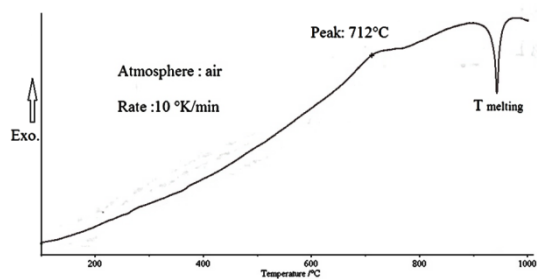


Figure 1: DTA curve of lithium disilicate glass

The optimum nucleation parameters were determined by Marotta method. DTA curve of as-cast glass was taken as the reference graph. The nucleation treatments were carried out between 490-550°C by 10°C steps. Each time the crystallization peak temperature was detected precisely. The particular nucleation temperature which exhibits the lowest crystallization temperature was

defined to be the optimum nucleation temperature. The optimum nucleation time was determined by the similar method. The optimum nucleation temperature for 0.25Li₂O.0.2SiO₂-0.75BaO.2SiO₂ was determined to be 540°C for 0.5h.

Even after heat treatment at low nucleation temperatures, i.e 510°C as shown in Fig.2, 0.25Li₂O.0.2SiO₂-0.75BaO.2SiO₂ glass indicated amorphous phase separation, which shows that phase separation occurred during cooling from the melt. Each of the dual phase, Li₂O.2SiO₂-BaO.2SiO₂, included 33.3mol% of Li₂O and BaO, respectively and do not show phase separation when prepared as single phase [Goharian et al., 2010].

However, when these phases were found together in the same microstructure, phase separation occurred even in the as-cast state.

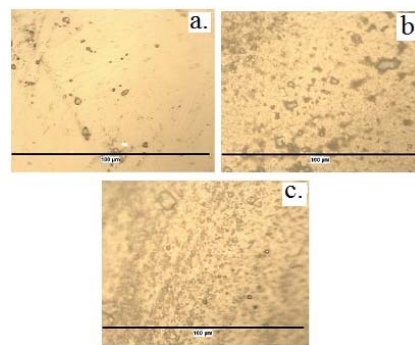


Figure 2: The optical images of the nucleated samples, (a) 510°C/ 1h. x1000 (b) 530°C/1h. x1000 and (c) 540°C/3h. x1000

The heat treatments of bulk specimens were carried out by two steps. In the first step, the specimens were subjected to nucleation heat treatments at 540°C for 0.5h. In the final step, the nucleated specimens were subjected to crystallization heat treatments at 675, 720 and 765°C for 1h.

SEM images of the crystallized samples were given in Fig.2. According to DTA curves in Fig.1., 3 different crystallization temperatures were chosen. First the onset of the broad exothermic effect was taken as the heat treatment temperature, which is 675°C. A standard heat treatment duration was chosen as 1h.

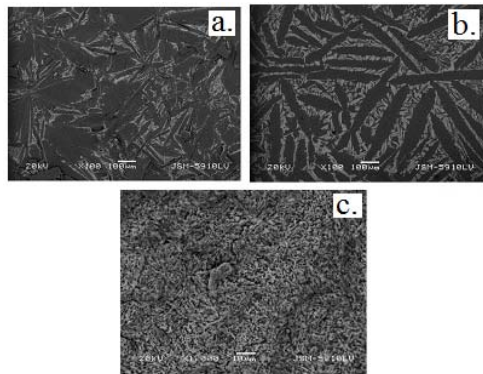


Figure 3: SEM images of the specimens crystallized at a. 675, b. 720 and c. 765°C.

In Fig.3.a, the radial crystals were observed in the microstructure. The spherulites are isolated in a glass matrix and retain their overall spherical shape, resulting from uniform radial fibrillar growth as suggested by [Lewis and Smith,1976]. The diameters of the spherulites which grow in the amorphous matrix phase were determined to be approximately 200µm after two-stage heat treatment at 540°C for 0.5h. and at 675°C for 1h. Fig.3.b shows that both phases were distinct after heat treatment at 720°C for 1h. because the amount of barium disilicate phase increased due to increased heat treatment temperature. When the heat treatment temperature was increased beyond the broad exothermic effect in DTA curve,i.e 765°C lithium disilicate and barium disilicate phases started to disperse in each other and a fine microstructure formed as can be seen from Fig.3.c.

4.CONCLUSION

A novel composition of $0.25\text{Li}_2\text{O}\cdot 0.2\text{SiO}_2\cdot 0.75\text{BaO}\cdot 2\text{SiO}_2$ was prepared and suggested for the dental applications. The crystallization process of $0.25\text{Li}_2\text{O}\cdot 0.2\text{SiO}_2\cdot 0.75\text{BaO}\cdot 2\text{SiO}_2$ glass was investigated in detail using thermal analysis, optical microscope and SEM techniques. The optimum nucleation parameters were determined using DTA by Marotta method. After the crystallization heat treatments at 675, 720 and 765°C, spherulitic, elongated and fine dispersed morphologies were observed.

REFERENCES

- Buchner, S., Lepienski, C. M., Soares Jr, P. C., Balzaretto, N.M., 2011. Effect of High Pressure on the Mechanical Properties of Lithium Disilicate Glass Ceramic, *Materials Science and Engineering A*, Volume (528), 3921-3924.
- Burgner, L.L., Weinberg, M.C., 2001. Assessment of crystal growth behavior in lithium disilicate glass, *Journal of Non-Crystalline Solids*, Volume (279), 28-43.
- Goharian, P., Nemat, A., Shabani, M., Afshar, A., 2010. Properties, crystallization mechanism and microstructure of lithium disilicate glass-ceramic, *Journal of Non-Crystalline Solids*, Volume (356), 208-214.
- Küchler, R., Kanert, O., Vereget, T., Jain, H., 2007. Effect of devitrification on ion motion in lithium disilicate glass, *Journal of Non-Crystalline Solids*, Volume (353), 3940-3946.
- Lewis, M.H., Smith, G., 1976. Spherulitic growth and recrystallization in barium silicate glasses, *Journal of Materials Science*, Volume (11), 2015-2026.
- Rawlings, R. D., Wu, J. P., Boccaccini, A. R. J., 2006. Glass-ceramics: their production from wastes. A review, *Mater. Sci.*, Volume (41), 733-761.
- Wen, G., Zheng, X., Song, L., 2007. Effects of P_2O_5 and sintering temperature on microstructure and mechanical properties of lithium disilicate glass-ceramics, *Acta Materialia*, Volume (55), 3583-3591.
- Zhang, W., Gao, H., 2008. Preparation of Machinable Fluoramphibole Glass-Ceramics from Soda-Lime Glass and Fluormica, *International Journal of Applied Ceramic Technology*, Volume (5), 412-418.

VICKERS MICROHARDNESS (HV) AND INDENTATION FRACTURE TOUGHNESS (K_{IC}) OF 0.25Li₂O.2SiO₂-0.75BaO.2SiO₂ GLASS AND GLASS-CERAMIC

Burcu Ertuğ^{1a}, Burcu Nilgün Çetiner², Hasan Gökçe¹, Z. Engin Erkmen²,
M. Lütfi Öveçoğlu¹

1. Istanbul Technical University, Department Of Metallurgical and Materials Engineering, 34469 Maslak, Istanbul, Turkey.

2. Marmara University, Department of Metallurgical and Materials Engineering, 34722 Göztepe, Istanbul, Turkey.

a. Corresponding author (burcuertug@gmail.com)

ABSTRACT: In the present study, the mechanical properties of 0.25Li₂O.2SiO₂-0.75BaO.2SiO₂ glass and glass-ceramic were investigated. The glass samples were nucleated in the temperature range of 490-550°C for 1h. After the optimum nucleation temperature was determined by DTA analysis, the glass samples were heat treated at a nucleation duration range of 0.5-3h. By the peak temperatures derived from DTA curves, the nucleated samples were crystallized at 675, 720 and 765°C. After as-cast, nucleated and crystallized samples were surface finished, Vickers indentation test was carried out using 200gr. load and indentation fracture toughness was calculated by measuring the crack length, c using 500gr. load. The effect of nucleation temperature on Vickers microhardness and indentation fracture toughness was minor. The crystallization temperature affected the mechanical properties dramatically.

Keywords: Lithium disilicate, barium disilicate, Vickers microhardness, Indentation Fracture Toughness.

1. INTRODUCTION

The hardness, brittleness, and fracture toughness of the brittle materials such as glasses and glass-ceramics are generally determined by the crack indentation methods, i.e Vickers indentation[Lawn and Marshall, 1979]. Vickers indentation are used to carry out the quality control tests of small sized specimens[Evans and Charles, 1976].

Although, Vickers indentation method is regarded as an unreliable method to determine the fracture toughness of the brittle materials, it is still a very popular method to determine the mechanical properties of the ceramics materials. One reason for this popularity is the usage of empirical constants in the calculation of the indentation fracture toughness,

depending on the material[Quinn and Bradt, 2007; Morrell, 2006].

For the calculation of indentation fracture toughness, K_{IC} the following equation is utilized.

$$K_{IC} = 0.016 \cdot (E/H)^{1/2} \cdot (P/c^{3/2}) \quad [\text{Scholz, 2004}].$$

Where κ is 0.016, is an empirical constant that depends on the geometry of the indenter. The elasticity modulus, E of barium titanate was taken as 70GPa. Vickers microhardness, H was measured by the previous indentations. P is the applied load to create indentation and c is the crack half-length[Scholz, 2004].

2. EXPERIMENTAL PROCEDURE

The glass-ceramic studied was prepared to give lithium disilicate ($\text{Li}_2\text{O} \cdot 2\text{SiO}_2$) and barium disilicate ($\text{BaO} \cdot 2\text{SiO}_2$) phases together; $0.25\text{Li}_2\text{O} \cdot 0.2\text{SiO}_2 - 0.75\text{BaO} \cdot 0.2\text{SiO}_2$. It contains barium disilicate as the major constituent. Glass transition and crystallization temperatures of the glass composition were determined by differential thermal analysis (DTA) using a thermal analyser (Netzch). The nucleation and crystallization heat treatments were planned according to the DTA results. In order to carry out the microstructural studies, bulk glass and glass-ceramic samples were polished and then etched with diluted HF solution for 20-30s., coated with carbon and crystallized microstructures were compared with each other using scanning electron microscope (JEOL JSM-330). Vickers microhardness and fracture toughness were obtained using Shimadzu tester using 200 and 500gr. loads, respectively.

3. RESULTS AND DISCUSSION

The optimum nucleation temperature of lithium disilicate ceramic was determined by Marotta method as shown in Fig.1.

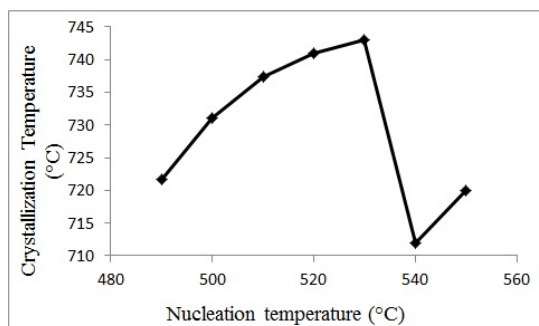


Figure 1 The crystallization temperature variation vs. nucleation temperature graph derived by DTA scan.

The granulated glass powders were subjected to nucleation heat treatments in a range of 490-550°C. The crystallization peak temperature increased with the nucleation temperature up to 540°C.

After the nucleation heat treatment at 540°C for 1h., the crystallization peak temperature derived from DTA scan, decreased dramatically to 712°C. After this nucleation temperature, crystallization occurs further at 720°C.

The samples were exposed to nucleation heat treatment with optimum parameters, i.e at 540°C for half an hour. After the nucleation, the samples were subjected to crystallization at 675, 720 and 765°C for 1h. The radial crystals were present in SEM images of the sample heat treated at 675°C for 1h. as shown in Fig.2.a. It was deduced from DTA scan that at this temperature, most of the microstructure was composed of lithium disilicate phase. Thus early crystallized lithium disilicate phase could exhibit a spherulitic morphology. However after 720°C, two distinct lithium disilicate and barium disilicate phases were present. After the

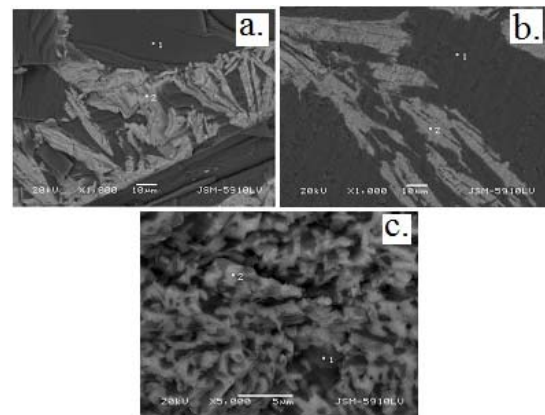


Figure 2 SEM images of the samples heat treated at a. 675, b. 720 and c.765°C.

final crystallization temperature of 765°C, a fine microstructure was observed including dispersion of both phases in the microstructure.

The mechanical properties of lithium disilicate glass-ceramics were also determined after the crystallization heat treatments done at 3 different temperatures.

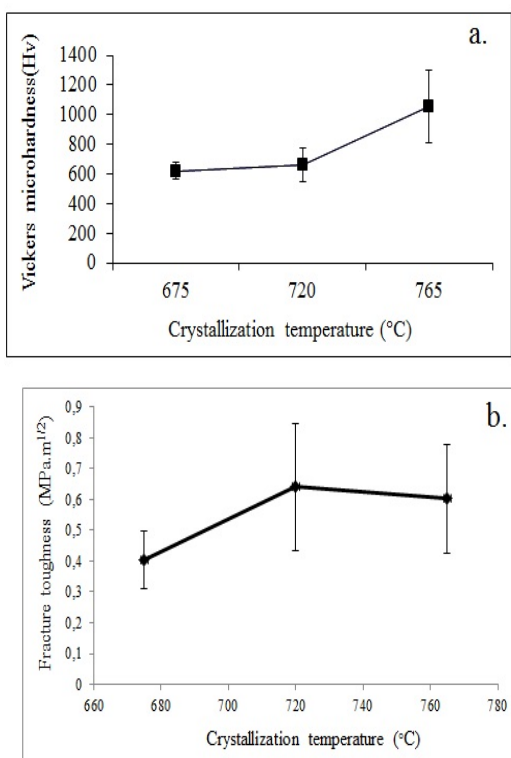


Figure 3 a. Vickers microhardness vs. crystallization temperature. and fracture toughness vs. crystallization temperature.

Vickers microhardness results of lithium disilicate ceramics increased with the crystallization temperature. When the crystallization temperature was raised from 675 to 765°C, Vickers microhardness increased from 618 Hv to 1053.8 Hv. Especially after the final crystallization heat treatment, Vickers microhardness increased dramatically. However, the tendency of indentation fracture toughness was not similar to that of Vickers microhardness. As the crystallization temperature was raised from 675 to 720°C, the K_{IC} increased but after the heat treatment at 765°C for 1h., K_{IC} somewhat decreased. However, the standard deviation of K_{IC} should be considered while evaluating the fracture toughness results.

4. CONCLUSION

Using Marotta method, lithium disilicate based glass-ceramics was successfully produced. In the first stage, the optimum

nucleation parameters were determined to be 540°C for 0.5h. After the nucleation 3 different crystallization heat treatments were done. The peak temperatures were derived from DTA scans to be 675, 720 and 765°C. SEM images indicated two distinct phases of lithium disilicate and barium disilicate after 675 and 720°C. However, after 765°C fine microstructures which were composed of dispersion of both phases were present. The highest Vickers microhardness obtained in this study was 1053.8Hv after the crystallization at 765°C. The highest indentation fracture toughness, K_{IC} was measured in the sample crystallized at 720°C and the value was 0.64MPa.m^{1/2}.

REFERENCES

- Evans, A.G., Charles, E.A., 1976. Fracture toughness determinations by indentation. *Journal of the American Ceramic Society*, Volume (59), 371–2.
- Lawn, B.R., Marshall, D.B., 1979. Hardness, toughness, and brittleness—indentation analysis. *Journal of the American Ceramic Society*, Volume (62), 347-50.
- Morrell, R., 2006. Fracture toughness testing for advanced technical ceramics: internationally agreed good practice. *Advances in Applied Ceramics*, Volume (105), 88-98.
- Quinn, G.D., Bradt, R.C., 2007. On the Vickers indentation fracture toughness test. *Journal of the American Ceramic Society*, Volume (90), 673-80.
- Scholz, T., Schneider, G.A., Munoz-Saldana, J., Swain, M. V., 2004. Fracture toughness from submicron derived indentation cracks. *Applied physics letters*, Volume (84), 1-3.

SYNTHESIS AND SURFACE PROPERTIES OF Ga-Te co-doped ZnO NANORODS

Seçkin Akin^{1,a} and Savaş Sönmezoğlu²

1. Department of Physics, Faculty of Kamil Özdağ Science, Karamanoğlu Mehmetbey University, Karaman, Turkey

2. Department of Materials Science and Engineering, Faculty of Engineering, Karamanoğlu Mehmetbey University, Karaman, Turkey

a. Corresponding author (seckinakin@kmu.edu.tr)

ABSTRACT: In this study, undoped ZnO and Ga-Teco-doped ZnO semiconductor thin films were grown on fluorine tin oxide (FTO) glass substrates by using sol-gel spin coating technique. The effects of Ga-Te dopants on the structural, optical and morphological properties of produced thin films were analyzed. Both thin films exhibit a high ZnO (002) diffraction peak indicating a strong c-axis orientation. Additionally, high-quality growth in the crystal structure of the films was seen in the surface images. SEM images also help us to draw a conclusion that the Ga-Te codoping has a strong effect on the ZnO morphology to obtain a nanorod based structures. The nanorods have diameters in the range of 50 - 80 nm and lengths of ~1 µm.

1. INTRODUCTION

The nanocrystalline oxide film that is used as a working electrode plays a significant role in the operation of DSSCs. Among the nanocrystalline oxide alternatives to TiO₂, ZnO has recently emerged as the most promising alternative with marked performance improvements [Zhang *et al.*, 2009; Saito M and Fujihara, 2008]. The potential advantages of ZnO in DSSCs include its desirable photochemical properties, good electron transport collection, fast charge transfer due to electron mobility, and its resistance to photocorrosion.

A promising strategy reported in the literature for improving the electron transport in DSSCs is to replace the nanoparticle-based photoelectrode with a single-crystalline nanorod (or nanowire or nanotube) photoelectrode because less light is scattered [Lai *et al.*, 2011]. The large surface area of rod-shaped structures facilitates good absorption of incident light, and the length of the rod enables an effective separation and

transfer of the photo-generated charges [Sönmezoğlu *et al.*, 2012].

In this study, undoped ZnO and Ga_{0.5}Te_{0.5}ZnO photoanodes were obtained by using a spin-coating method and their physical properties were investigated.

2. EXPERIMENTAL

The sol was prepared by dissolving 2.35 g zinc acetate dehydrate [Zn(CH₃COO)₂·2H₂O] in 150 mL of methanol [CH₃OH] at 60 °C. The solution was stirred thoroughly using a magnetic stirrer for 2 h. At the same time, 1 ml triethylamine [C₂H₅)₃N] and 0.2 ml ethylene glycol [HOCH₂CH₂OH] were added drop by drop to the solution as a stabilizer until the solution became transparent, and then mixing was continued for an additional hour. Gallium (III) nitrate hydrate (GaN) and telluric acid [Te(OH)₆] were used as sources of gallium and tellurium to obtain Ga_{0.5}Te_{0.5}ZnO thin films. After sol formation, a spin-coating process (3000 rpm for 30 s) was used to cover the front

surface of the ultrasonically cleaned FTO-conducting glass with ZnO and Ga_{0.5}Te_{0.5}ZnO nanoparticles. This process was repeated ten times and obtained undoped ZnO and Ga_{0.5}Te_{0.5}ZnO thin films were subjected to pre-heating at 400 °C for 5 min in a hot air oven after each spinning process. Finally, the films were subjected to an annealing process at 550 °C for 1 h in a pre-heated oven.

3. RESULTS AND DISCUSSION

3.1. X-Ray Diffraction Analysis

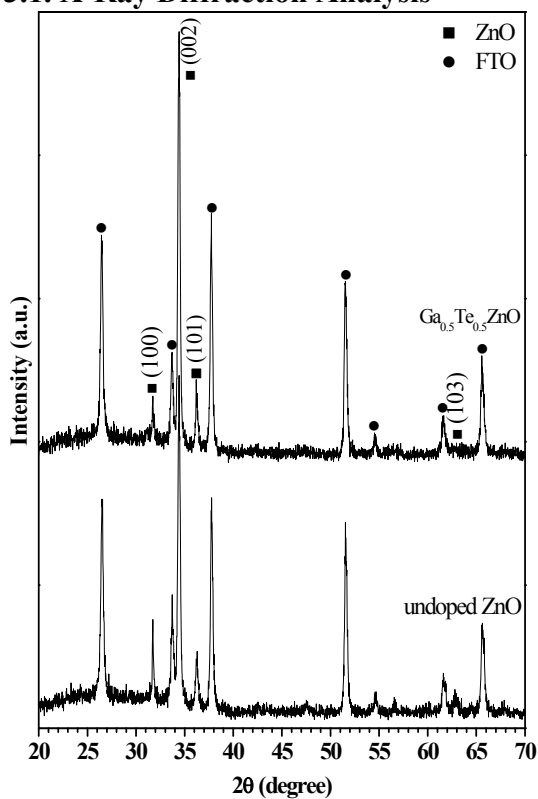


Figure 1: X-ray diffraction patterns.

The diffraction patterns of the samples are depicted in Figure 1. The solid square crystal peaks of ZnO match with the (100), (002), (101), and (103) crystal planes of ZnO (JCPDS card no: 36-1451; a=3.249 Å and c=5.206 Å). As clearly seen in Figure 1, the samples had a high ZnO (002) diffraction peak, which indicated that the samples were strongly c-axis oriented.

The crystallite size was estimated using the Scherrer equation[Cullity, 1978]. The crystallite size was found as 32.29 and 37.20 nm for undoped ZnO and Ga_{0.5}Te_{0.5}ZnO thin films, respectively. As shown, the crystallinity of the ZnO thin films increased by Ga-Te codoping.

3.2. SEM Analysis of Nanostructured Thin Films

The SEM photographs for surface morphologies of undoped and Ga-Te codoped ZnO thin films are presented in Figure 2.

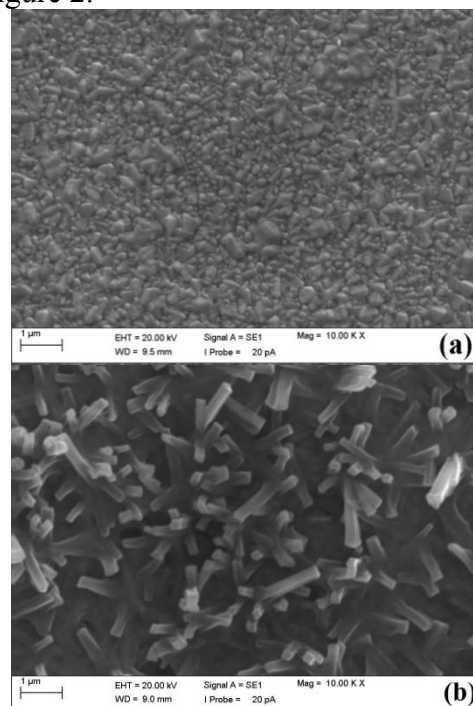


Figure 2: SEM images of (a) undoped ZnO, (b) Ga_{0.5}Te_{0.5}ZnO thin films.

The high-quality growth in the crystal structure of the films can be seen in the surface images, similar to that observed in Figure 1. The substrate surfaces of undoped ZnO thin film (Figure 2-a) is well covered with grains that are almost uniformly distributed over the surface. In addition, as a result of the contribution of Ga-Te co-doping (Figure 2-b), the formation of nanorods oriented perpendicular to the sample surface was observed. The nanorods had diameters in

the range of 60 - 80 nm and lengths of ~1-2 μm .

3.3. Spectral Characterizations

The observed UV-vis spectra of the thin films are shown in Figure 3.

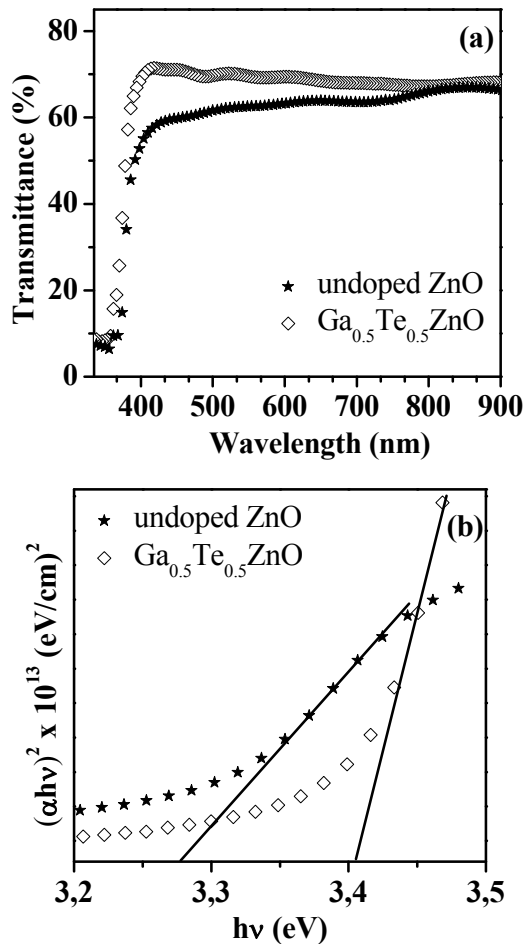


Figure 3: (a) Transmittance spectra and (b) Tauc plot of Ga_{0.5}Te_{0.5}ZnO thin films.

Figure 3-a indicates that the Ga_{0.5}Te_{0.5}ZnO nanorod thin film is highly transparent in the visible range of the electromagnetic spectrum with a transmission reaching values of 70%. Furthermore, Figure 3-b shows a $(\alpha h\nu)^2$ versus $h\nu$ plot for the samples. Following the conventional method of extrapolating the linear range of the Tauc plot, the optical band gap energy (E_g) for the thin films was obtained. The undoped ZnO thin film exhibited an optical absorption

edge below 3.28 eV, which shifted toward higher energies (3.40 eV) with Ga-Te codoping.

4. CONCLUSIONS

Based on the physical measurements of the undoped ZnO and Ga_{0.5}Te_{0.5}ZnO thin films, the following main points emerge: i) the intensities of the dominant diffraction peaks at (002) plane for hexagonal ZnO increased as Ga-Te codoping was incorporated into the ZnO structure, ii) the SEM images suggest that the Ga-Te co-doping has a strong effect on the ZnO morphology and the ability to obtain nanorod-based structures, iii) the obtained results show that nanorod shaped structures facilitate good absorption of the incident light.

Acknowledgements: This study is supported by the Scientific Research Commission of Karamanoğlu Mehmetbey University (Project No: 30-M-12).

REFERENCES

- Cullity, B.D., 1978. Elements of X-Ray Diffraction, Addison-Wesley Publishing Company, London..
- Lai, M.H., Lee, M.W., Wang, G.J. and Tai, M.F., 2011. Photovoltaic Performance of New-Structure ZnO-Nanorod Dye-Sensitized Solar Cells, International Journal of Electrochemical Science, 6, 2122.
- Saito, M. and Fujihara, S., 2008. Large Photocurrent Generation in Dye-Sensitized ZnO Solar Cells, Energy and Environmental Science, 1, 280.
- Sönmezoğlu, S., Taş, R., Akın, S. and Can, M., 2012. Polyaniline Micro-Rods Based Heterojunction Solar Cell: Structural and Photovoltaic Properties, Applied Physics Letters, 101, 253301.
- Zhang, Q., Dandeneau, C.S., Zhou, X. and Cao, G., 2009. ZnO Nanostructures for Dye-Sensitized Solar Cells, Advanced Materials, 21, 4087.

STATISTICAL ANALYSIS OF INDENTATION FRACTURE TOUGHNESS (K_{IC}) OF 0.25Li₂O.2SiO₂-0.75BaO.2SiO₂ GLASS AND GLASS-CERAMIC

Burcu Ertuğ^{1 a}, Burcu Nilgün Çetiner², Hasan Gökçe¹, Z. Engin Erkmen²,
M. Lütfi Öveçoğlu¹

1. Istanbul Technical University, Department Of Metallurgical and Materials Engineering, 34469 Maslak, Istanbul, Turkey.

2. Marmara University, Department of Metallurgical and Materials Engineering, 34722 Göztepe, Istanbul, Turkey.

a. Corresponding author (burcuertug@gmail.com)

ABSTRACT: In the present study, in order to determine the indentation fracture toughness (K_{IC}) data for 0.25Li₂O.2SiO₂-0.75BaO.2SiO₂ glass and glass-ceramic, Vickers microhardness test was carried out on the samples. To calculate K_{IC} , Young's modulus, E and the hardness, H_v values were used. The mean crack half-length, \bar{c} and the mean fracture toughness, \bar{K}_{IC} were measured and calculated, respectively along with the coefficient of variations. The cumulative probability, P_i was expressed versus normalized crack length, c / \bar{c} . Using K_{IC} and P_i values, $\ln[1/(1-P)] - \ln K_{IC}$ graph was drawn according to well-known two parameter Weibull distribution equation. By this graph, Weibull modulus, m and scale parameter, K_0 were determined and compared with each other.

Keywords: Glass-ceramic, Indentation Fracture Toughness, Statistical Analysis, Weibull modulus.

1. INTRODUCTION

Fracture of brittle materials (e.g. ceramics) usually initiates from flaws, which are distributed in the material. The probability of failure increases with load amplitude and with size of the specimens. A failure criterion connects the size of the flaw with a critical load. The Griffith/Irwin criterion predicts that crack-like flaws get critical, if their stress intensity factor $K = \sigma \cdot Y \sqrt{\pi \cdot a}$ exceeds the fracture toughness K_{IC} [Danzer et al., 2007]. Commonly used statistical parameters to describe one aspect of structural reliability is the Weibull modulus (m). Higher values of Weibull modulus correspond to materials with greater structural reliability [Bona et al., 2003]. The Weibull modulus is sometimes called the shape parameter, has a value

between 5 and 20 for technical ceramics [Saghafi et al., 2009].

The probability of failure depends on the distribution the weak spots or regions or planes where cracks start and propagate. Since it is closely related to the material toughness, the Weibull statistics may provide some supplementary data to the analysis of material resistance to fracture [Glysiak, 2007]. Despite having much better hardness compared to conventional metallic materials, the major limitations of ceramics for structural and specific non-structural applications are the poor toughness and low strength reliability. More clearly, a low m value indicates non-uniform distribution of highly variable crack length (broad strength distribution), while a high m value implicates uniform

distribution of highly homogeneous flaws with narrower strength distribution[Basu et al., 2009].

2. EXPERIMENTAL PROCEDURE

The details of the preparation of 0.25Li₂O.2SiO₂-0.75BaO.2SiO₂ glasses were given elsewhere[Ertug et al., 2011]. Glasses were nucleated at 490-550°C for 1h. were selected as the test specimens. After surface finishing, Shimadzu Vickers indenter was used to make indentations on the specimens at loads of 200-500gr. for 30s. After applying each load, symmetrical indentations and cracks were formed. Following the indentations, the crack lengths were measured by the optical system which is equipped in Vickers tester. For the calculation of indentation fracture toughness, K_{IC} the following equation is utilized.

$$K_{IC} = 0.016 \cdot (E/H)^{1/2} \cdot (P/c^{3/2}) \quad [\text{Gong et al., 2001}].$$

Where κ is 0.016, is an empirical constant that depends on the geometry of the indenter. The elasticity modulus, E of barium titanate was taken as 99GPa. Vickers microhardness, H was measured by the previous indentations. P is the applied load to create indentation and c is the crack half-length.

3. RESULTS AND DISCUSSION

The mean crack half-length, \bar{c} and the coefficient of variation for 15 indentation crack half-lengths, σ_c were calculated by the following formulas.

$$\bar{c} = \frac{\sum_{i=1}^N c_i}{N}$$

$$\sigma_c = \frac{1}{\bar{c}} \sqrt{\frac{\sum_{i=1}^N (c_i - \bar{c})^2}{N}}$$

Where c_i is the *i*th measured crack half-length and N=15 is the total number of

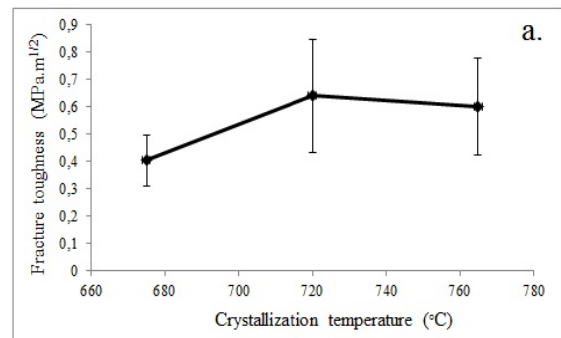
indentations. Vickers indentation and crack half-length data were given in Table 1.

Table 1: A. Vickers indentation data B. Crack half-length data for crystallization temperature.

T _C (°C)	H _v (kg/mm ²)	Standard deviation	σ _{H_v} a.
675	618	57,82559987	0.09
720	659,8	111,766274	0.17
765	1053,8	242,21829	0.23

T _C (°C)	Crack half-length, c (μm) b.		
	Mean (μm)	Standard deviation (μm)	σ _c
675	35.91	5.5	0.15
720	26.24	4.84	0.18
765	23.5	4.75	0.2

The mean indentation fracture toughness, \bar{K}_{IC} and the coefficient of variation, σ_K were calculated by the similar formulas to crack half-length as in Fig.1. The resultant indentation fracture toughness, \bar{K}_{IC} values were in good agreement with the literature results. Gong et. al found that indentation fracture toughness, \bar{K}_{IC} of soda-lime glass to be 0.75-0.85 MPa.m^{1/2} [Gong et al., 2001].



T _C (°C)	Indentation fracture toughness, K _{IC} (MPa.m ^{1/2}) b.		
	Mean	Standard deviation	Coefficient of variation
675	0,4045	0,120208153	0.3
720	0,64	0,235442845	0.36
765	0,6022	0,268700577	0.45

Figure 1: a. Indentation fracture toughness, K_{IC} versus nucleation temperature and b. the distribution of K_{IC} values.

The indentation toughness values were used by least-square method to determine Weibull parameters. The indentation fracture toughness data was ordered from minimum to maximum and each value was given a cumulative probability of occurrence, P_i by the following formula.

$$P_i = i-0.5/15$$

Where $N=15$ is the number of indentations. P_i and K_{IC} were related to each other by two parameter Weibull distribution equation as follows(8).

$$\ln \ln (1-P) = m \cdot \ln K_{IC} - m \cdot \ln K_0$$

where m and K_0 are Weibull parameters namely, Weibull modulus and scale parameter, respectively.

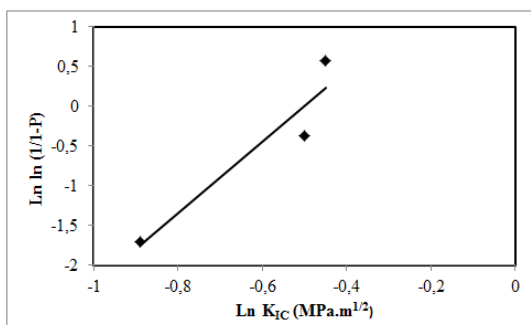


Figure 2: A. Weibull plot for indentation fracture toughness data.

Fig.2 shows Weibull plots for the indentation fracture toughness data at each load. $\ln \ln (1-P)$ - $\ln K_{IC}$ plots indicated a linear relationship.

By using the linear equation of Weibull plot, Weibull modulus and scale parameter were determined to be m , 4.52 and K_0 , 1.34 $\text{MPa.m}^{1/2}$, respectively.

4.CONCLUSION

Indentation fracture toughness, K_{IC} increased first dramatically and then remained slightly constant after 720°C. Weibull plots for K_{IC} data were drawn, which were shown to be linear, in order to determine shape parameter, m and scale parameter, K_0 .

Since the fracture toughness shows high variation, the calculated Weibull modulus was low, the flaws were clustered inconsistently in the crystallized ceramics. The glass-ceramics made from components of low Weibull modulus is expected to exhibit low reliability.

REFERENCES

- Danzer, R., Supancic, P., Pascual, J., Lube T., 2007. Fracture Statistics of Ceramics - Weibull Statistics and Deviations from Weibull Statistics, Engineering Fracture Mechanics, Volume (74), 2919-2932.
- Bona, A.D., Anusavice, K.J., DeHoff, P.H., 2003. Weibull analysis and flexural strength of hot-pressed core and veneered ceramic structures, Dental Materials, Volume (19), 662-669. 12.
- Saghafi, A., Mirhabibi, A.R., Yari G.H., 2009. Improved linear regression method for estimating Weibull parameters, Theoretical and Applied Fracture Mechanics, Volume (52), 180-182.
- Lysiak, G., 2007. Fracture toughness of pea: Weibull analysis, Journal of Food Engineering, Volume (83), 436-443.
- Basu, B., Tiwari, D., Kundu, D., Prasad, R., 2009. Is Weibull Distribution the Most Appropriate Statistical Strength Distribution for Brittle Materials?, Ceramics International, Volume (35), 237-246 .
- Ertug, B. and Demirkesen, E., 2012. The Controlled Crystallization of and Spherulitic Morphology in $\text{Li}_2\text{O} \cdot 2\text{SiO}_2$ - $\text{BaO} \cdot 2\text{SiO}_2$ Glasses, Transactions of the Indian Ceramic Society, Volume (71), 1-6.
- Gong, J., Chen, Y., Li, C., 2001. Statistical analysis of fracture toughness of soda-lime glass determined by indentation, Journal of Non-Crystalline Solids, Volume (279), 219-223.

EFFECTS OF MODIFIED ZnO NANO POWDER ON THE MECHANICAL AND ANTICORROSION PROPERTIES OF POLYESTER POWDER COATINGS

B. Shirkavand Hadavand^{1*}, M. Ataefard², H. Fakharizadeh Bafghi^{1,3}

¹Institute for Color Science and Technology, Department of Resin and Additives, Tehran, Iran

²Institute for Color Science and Technology Department of Printing Science and Theology, Tehran, Iran

³Peka Chemie Industrial Company, Research and Development Center, Tehran, Iran

a. Corresponding author: shirkavand@icrc.ac.ir

ABSTRACT: In this study, the effects of modified Nano ZnO on thermal and anticrossion properties of polyester powder coating were studied. For achieving this, by twin screw extruder, polyester powder coating were prepared using Zinc Oxide (1, 3 and 5% w/w) Nano particles which modified by vinyl trimetoxy silane (VTMS) and triethoxy methyl silane (TEMS). Functionalized Nano particles were characterized by FT-IR and TGA. Thermal properties of polyester/nano ZnO powder coating were characterized by DSC and Gel time. Mechanical properties of polyester/nano ZnO powder coating were characterized by pendulum hardness, Impact and mandrel tests. Anticrossion properties were evaluated by salt spray methods. Morphology and dispersion state of particles in samples were studied by field emission scanning electron microscopy (FE-SEM). The results shown that the surface of Nano ZnO was modified in a acceptable form with good dispersion of nano particles in polymeric matrix. The mechanical and anticrossion properties of polyester/nano ZnO powder coating increased whit additional nano particles up 3 % w/w.

1. INTRODUCTION

Powder coating is a technology for coating products with dry powder. The main material in this process is a mixture of polymeric resin and fillers [1]. The powder can be sprayed electro statically onto the substrate surface, or the substrate (product) can be dipped into a fluidized bed of suspended powder. During post heat curing, the particles flow and fuse into a strong adhering coating. The result is a high quality coating with excellent durability [2]. The final properties of the powder coatings depended on the basic materials and recently nono inorganic particles are widely used in row materials [3].

Inorganic particles with micro and nano sizes are increasingly used as fillers in polymeric matrix to improve different properties [4, 5]. Inorganic particles are

not easily dispersed in polymeric matrix, unless a dispersing agent is used. Also silane coupling agents are often used to form stable chemical bonds with both inorganic and polymer [6, 7].

The aim of this research is study on mechanical and anti corrosion resistance of nano ZnO with and without modification in polyester powder coating.

2. EXPERIMENTAL

2.1. Materials

Polyester resin (TC-3004) supplied by Alymer (Korea), triglycidyl isocyanurate (TGIC) as a hardener supplied by ChangzhouNiutang (China), PLP100 leveling agent supplied by KSCNT Co (Korea), benzoin from AnadoluKimya, and Nano ZnO (10-30 nm) supplied by

US Research Nanomaterials Inc (USA), vinyl trimethoxy silan (VTMS), triethoxy methyl silan (TEMS), ethanol and isopropyl alcohol supplied by Merck Company (Germany). Metallic substrates (aluminium and iron) were used in the form of panels with dimensions of 5mm × 50mm × 50mm.

2.2. Surface Functionalization of Nano-ZnO with Silane Coupling Agents

The dried nano ZnO was ultrasonicated in isopropyl alcohol and then silan coupling agents and some drops of hydrochloric acid were added to the mixture and mixed for 24 h at ambient temperature. Finally, the suspension was filtrated and washed with ethanol to remove unreacted materials. The solid was dried at 60 for more than 24 h.

2.3. Preparation of Polyester/ZnO Nanocomposite

The polyester resin with different amounts of modified and non modified nano zinc (1, 3, and 5% W/W) were mixed in an internal mixer for 10 min. This procedure was performed in order to achieve a homogeneous dispersion of nanoparticles.

2.4. Preparation of Powder Coating

Polyester resins with different nano ZnO, TGIC hardener and other additives were extruded in the twin screw extruder. The extruder has thread diameter of 20mm, manufactured by YantaiDonghui Powder Processing Equipment Co. The chips obtained after the processing were ground in a bench top knife-mill (OMC), and sieved (200 mesh), to obtain an averaged particle size of 55 μm. The coatings were applied on prepared plates by electrostatic spray gun manufactured by Gema Company. The Curing process was carried out in an air circulation oven at 200°C for 10 min.

3. RESULT AND DISCUSSION

3.1. Nano ZnO Characterization

FT-IR spectra of pure nano-ZnO particle and modified nano-ZnO particle are shown in Figure 1. FT-IR spectra of pure and modified nano ZnO particle indicated the structure of the compound and modification with coupling agents.

3.2. Morphology and the Dispersion

Morphology of nanoparticles in polyester matrix was studied using field emission scanning electron microscopy (FE-SEM). Fig. 2 shows the FE-SEM graph of the surface morphology of pure polyester powder coating (Fig. 2-a) and nano-ZnO modified with VTMS (Fig. 2-b). Both of the Fig. 2-b indicated the uniform dispersion of the ZnO particles in the polyester matrix.

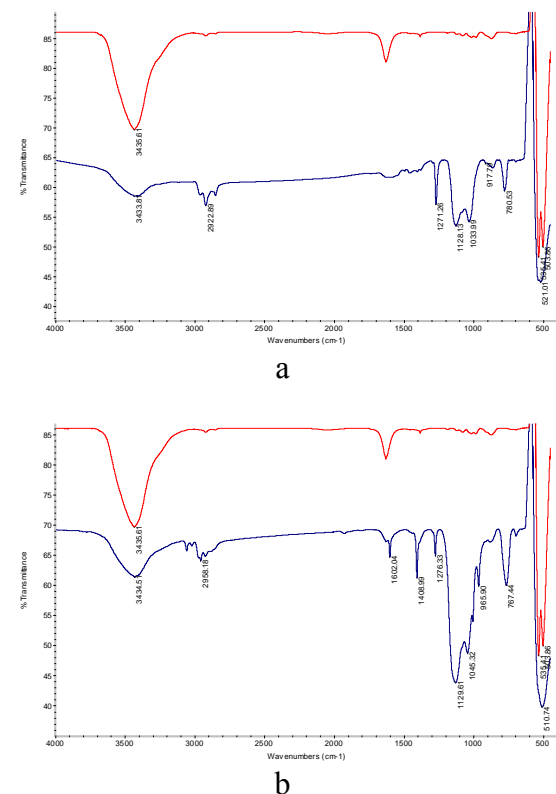


Figure 1: FTIR spectra of nano ZnO modified with TEMS (a) and VTMS (b).

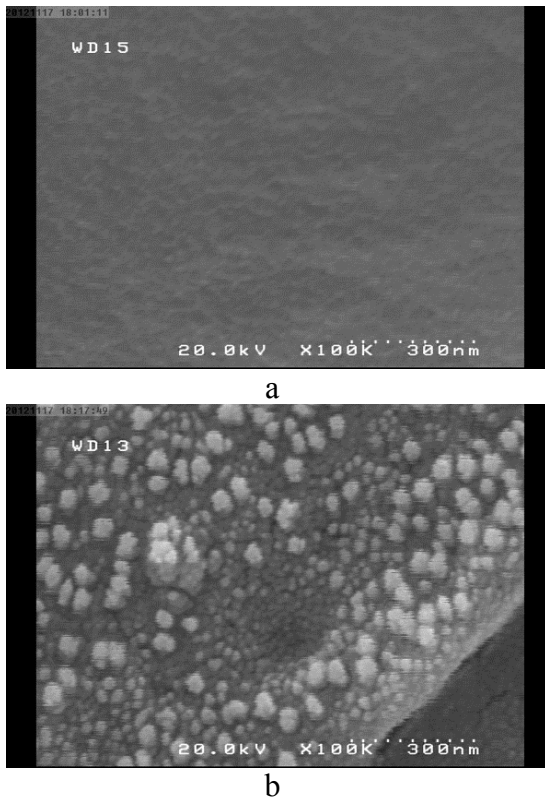


Figure 2: FE-SEM graph of pure polyester powder coating (a) and nano-ZnO modified with VTMS (b).

3.3. Thermal behaviors

In Table 1 the results of DSC for cured nanocomposite were demonstrated. The results shown that the T_g and melting point for all the samples are without any significant changes.

Table 1: DSC results of cured film.

Samples	T_g °C	T_m °C
Neat Polyester	46.2	64.3
1 % TEMS-Nano ZnO/ Polyester	46.3	64.1
3 % TEMS-Nano ZnO/ Polyester	46.2	64.5
5 % TEMS-Nano ZnO/ Polyester	46.4	64.2
1 % VTMS-Nano ZnO/ Polyester	46.3	64.1
3 % VTMS-Nano ZnO/ Polyester	46.2	64.5
5 % VTMS-Nano ZnO/ Polyester	46.4	64.2

3.4. Mechanical Properties

Mechanical properties such as gel time (DIN 55990), flexibility (ASTM D 522) and impact resistance (D2794 ASTM) are shown in Table 2. All the results indicated no changes or improvement for the coatings.

Table 2: Mechanical properties of cured film.

sample	Gel time (Sec)	flexibility (mandrel mm)	Impact resistance (kg.cm)
Neat Polyester	460	5	100
1 % Nano ZnO/ Polyester	423	4.5	100
3 % Nano ZnO/ Polyester	402	4	102
5 % Nano ZnO/ Polyester	395	6	90
1 % TEMS-Nano ZnO/ Polyester	418	4.5	102
5 % TEMS-Nano ZnO/ Polyester	400	4	105
5 % TEMS-Nano ZnO/ Polyester	392	5	92
1 % VTMS-Nano ZnO/ Polyester	416	4.5	103
3 % VTMS-Nano ZnO/ Polyester	400	3.5	110
5 % VTMS-Nano ZnO/ Polyester	390	5	95

3.5. Corrosion Resistance

The corrosion resistance of coatings was carried out by salt spray test according to ASTM B-117 method. The results show that the adhesion and corrosion performances of coatings are obviously improved after the chemical modification of nano particles. Also results show that

the use of silane coupling agent enhances the adhesion of the coating (scored 5B in the adhesion test) to the metal substrate. Corrosion resistance of coatings for modified nano ZnO compared with unmodified were remarkably improved. It can be concluded that the improvement of corrosion resistance of coatings for modified nano ZnO compared with unmodified is for good dispersion of nanoparticles in the resultant films and effects on the properties of coatings.

4. CONCLUSION

In this research nano zinc oxide were modified with coupling agents and used in polyester powder coating formulation. The characterization of nano particle by FTIR indicated the chemical modification. Results were shown that chemical modifications of nano ZnO improve mechanical properties and corrosion resistance of coatings.

REFERENCES

- Kittle, K.J. and Rushman, P. F., 1997, Powder coating compositions and their use, U.S. Patent No. 5,635,548.
- Misev, T.A., 1991. Powder Coatings, Chemistry and Technology, Wiley, Chichester.
- 2012, Polyester-based powder coatings with nano particles, Focus on Powder Coatings, 2012, 2.
- Yap, Y.L., You A.H., Teo, L.L. and Hanapei, H., 2013. Inorganic Filler Sizes Effect on Ionic Conductivity in Polyethylene Oxide (PEO) Composite Polymer Electrolyte, Int. J. Electrochem. Sci., 8, 2154.
- Plesa, I., Ciuprina, F. and Notingher, P. V., 2010. Dielectric Spectroscopy of Epoxy Resin with and without Inorganic Nanofillers, J. Advanc. Res. in Phys. 1, 1.
- Posthumus, W., Magusin, P.C.M.M., Brokken-Zijp, J.C.M., Tinnemans A.H.A. and Linde, R. van der, 2004. Surface modification of oxidic nanoparticles using 3-methacryloxypropyltrimethoxysilane, J. Colloid and Inter. Sci., 269, 109.
- Aly, A.A., Zeidan, El-Sh. B., Alshennawy, A. A., El-Masry A. A. and Wasel, W. A., 2012. Friction and Wear of Polymer Composites Filled by Nano-Particles: A Review, World J. of Nano Sci. Eng., 2, 32.

SYNTHESIS OF METALLIC COPPER NANOWIRES AT LOW TEMPERATURE

Cansu Noberi^{1,a}, Figen Kaya¹ and Cengiz Kaya¹

1. Department of Metallurgical and Materials Engineering, Yildiz Technical University, Davutpasa Campus, Esenler, Istanbul, Turkey

a. Cansu Noberi (cnoberi87@gmail.com)

ABSTRACT: In this study, metallic Cu nanowires were synthesized using simple aqueous reduction method at low temperature. Copper (II) Nitrate, sodium hydroxide, ethylenediamine (EDA) and hydrazine were used as precursors. $\text{Cu}(\text{NO}_3)_2$ used as a Cu source where both EDA and hydrazine used as a reduction agents. Obtained solution was heated till 60°C and held that temperature for an hour while the solution was mixed continuously using a magnetic stirrer. The pH value was very high nearing 13, which was lowered by using distilled water before separation of precipitations. As the precipitated nanofibres were in pure metallic state, after filtering they were stored inside the ethanol in order to prevent oxidation. Scanning electron microscopy (SEM) was used for identification of the morphology and size measurement of synthesized nanowires. Finally, X-ray (XRD) analysis was performed for the phase determination and confirmation of pure metallic copper structure.

1. INTRODUCTION

In recent years, nanotubes and nanowires structures have been gained considerable attraction due to their optical, electrochemical and electronical properties and have been studied for wide range of application areas, such as antibacterial, catalysis and energy production. Using materials in nano-scale have advantages like good conductivity, small size and low cost. In this study, copper nano particles were used in order to have optimum values with a low cost. Copper nano particles were synthesized using hydrothermal method.

2. EXPERIMENTAL

Copper (II) nitrate ($\text{Cu}(\text{NO}_3)_2$), sodium hydroxide (NaOH), ethylenediamine (EDA) and hydrazine (N_2H_4) were precursors. $\text{Cu}(\text{NO}_3)_2$ were used as a Cu source. In order to synthesize metallic Cu nanowires 15M NaOH solution were prepared as a first step (Figure 1(a)). Separately $\text{Cu}(\text{NO}_3)_2$ solution was also prepared and those two were mixed during the magnetic stirring till have a

dark blue color at the end (Figure 1(b)). As a final step EDA and hydrazine were added to the solution (Figure 1(c)) and kept at 60°C for an hour (Figure 1(d)).

The final color was reddish brown and the pH was around 13. It was lowered using deionized water during washing process and fixed at 7. Final product was kept in ethanol in order to prevent oxidation of pure metallic Cu nanowires. The purity of the nanowires was proved using XRD analysis. SEM analysis was performed to assess the morphology and the length of Cu nanowires.

3. RESULTS AND DISCUSSION

Figure 1 represents the synthesis steps of pure metallic Cu nanowires. Although the first obtained color was dark blue during the synthesis, final color of the product was reddish brown.

Figure 2 shows the XRD analysis of the Cu nanowires. When it compared with the standard of Cu nanowires (JCPDS card no: 85-1326) it could be said that

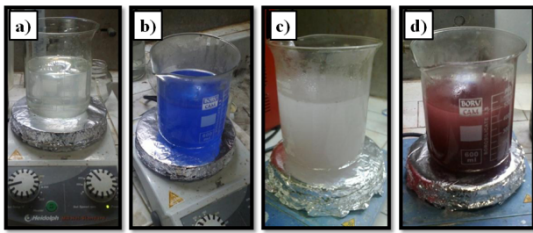


Figure 1: NaOH solution (a), dark blue color after $\text{Cu}(\text{NO}_3)_2$ addition (b), heating until 60°C (c) and the final product with reddish brown color after an hour (d).

there is no any peaks represent contamination. That proves the final product consist of pure metallic Cu only.

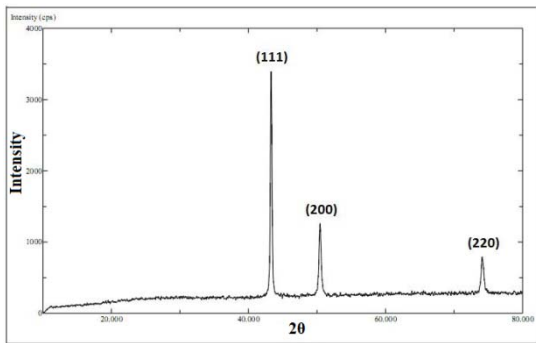


Figure 2: XRD analysis of metallic Cu nanowires

Figure 3 indicates SEM analysis pictures of synthesized nanowires. According to those images it can be said that the distribution of nanowires are homogeneous. Their lengths are app. 1-10 μm whereas their diameters are between 150-200nm.

4. CONCLUSION

In this study pure metallic Cu nanowires were synthesized via low temperature method. Obtained solution was kept for an hour at 60°C . After washing and separation process nanowires held into

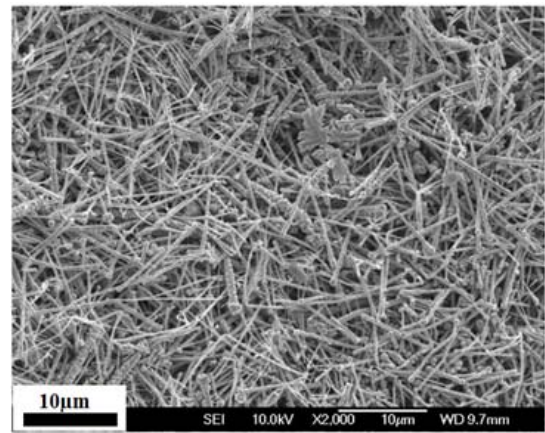


Figure 3: SEM micrographs of Cu nanowires

the ethanol in order to prevent oxidation. The crystallinity, phase and the purity of the sample was determined using XRD analysis. SEM micrographs were used to investigate morphology and the size distribution.

Acknowledgements: This work was funded by TUBITAK (The Scientific and Technological Research Council of Turkey) under the contract number 109R007. Financial support from The Office of Scientific Research Fund of Yildiz Technical University is also acknowledged.

EXPERIMENTAL INVESTIGATION OF THE EFFECT OF THERMAL CONDUCTIVITY OF DENSITY IN EPS

İbrahim UZUN¹, Murat Kadir YEŞİLYURT²

1. Kırıkkale University, Faculty of Engineering, Department of Mechanical Engineering, Kırıkkale, Turkey

2. Bozok University, Faculty of Engineering–Architecture, Department of Biosystem Engineering, Yozgat, Turkey

a. Corresponding author: kadir.yesilyurt@bozok.edu.tr

ABSTRACT: The need for energy is increasing every day, the need for this requirement would be decreased by the use of insulation materials in the world. EPS, which is synthetic thermal insulation material, has micro and macro structure of the porosity, which emerge during the production stage, to reduce heat transfer thus increasing the resistance of the thermal conductivity of building elements, depending on the point of application. Insulation material of EPS thermal conductivity values are determined according to the density change that can be used in practice is to find the appropriate density value. Thermal conductivity is a physical property of material which depends on temperature, material composition, moisture content, geometry and porosity. In this study investigated the temperature dependence of thermal conductivity of insulating materials of EPS. Different density values of samples (14 kg/m³ – 32 kg/m³) are determined Lasercomp Fox 314 for the thermal conductivity changing with temperature. Carbon reinforced EPS samples were also experimentally measured and compared with the white EPS. As a result, carbon reinforced EPS insulating material has a lower thermal conductivity values than other EPS.

Keywords: *EPS, thermal conductivity, density*

1. INTRODUCTION

Energy requirements of countries have been continuously increasing as a result of population growth, industrialization and more energy consuming devices. Efficient use of energy is required for limited level of resources as well as the energy consumed quickly. Energy crisis has experienced from 1999 to the present in our country. The ratio of energy consumption from domestic production by 30% and is estimated to fall to 25% in 2020. According to the 1999 data; the distribution of energy consumption was 37% industry, 32% housing, 23% transport, 5% agriculture and 3% in other sectors [Anonymous, 1999]. On the other hand according to the 2009 data, the distribution of energy consumption, average of 41% of the heating of homes and buildings, 33% in industry, 20% in transport, 5% agriculture and 1% used in other areas hence residential savings is

very important [Anonymous, 2009]. Given that the annual data on the rate of increase in residential energy consumption should be examined carefully. 80% of residential energy consumption is used for heating as well as living quarters in the industry, given the heated social facilities and administrative buildings for heating, thermal insulation becomes even more important. Due to increasingly deteriorate ecological balance as a result of environmental pollution and increasing energy requirements as a result of technological developments, methods and measures to minimize the use of energy in all areas of renewable energy sources used in conjunction with an orientation to come to the fore the need to save energy and the maximum benefit.

Thermal energy conservation in buildings, thermal systems, power transmission lines and the use of a topical

issue in many areas, but not a new invention [Kaya *et al.*, 2006]. Insulation is very important for comprising a portion of total energy consumption buildings. This is important not only in terms of energy economy but also limited

the energy resources and consumption carefully [Pehlivanlı, 2009]. In Figure 1 have shown that the thermal conductivity of different insulating material.

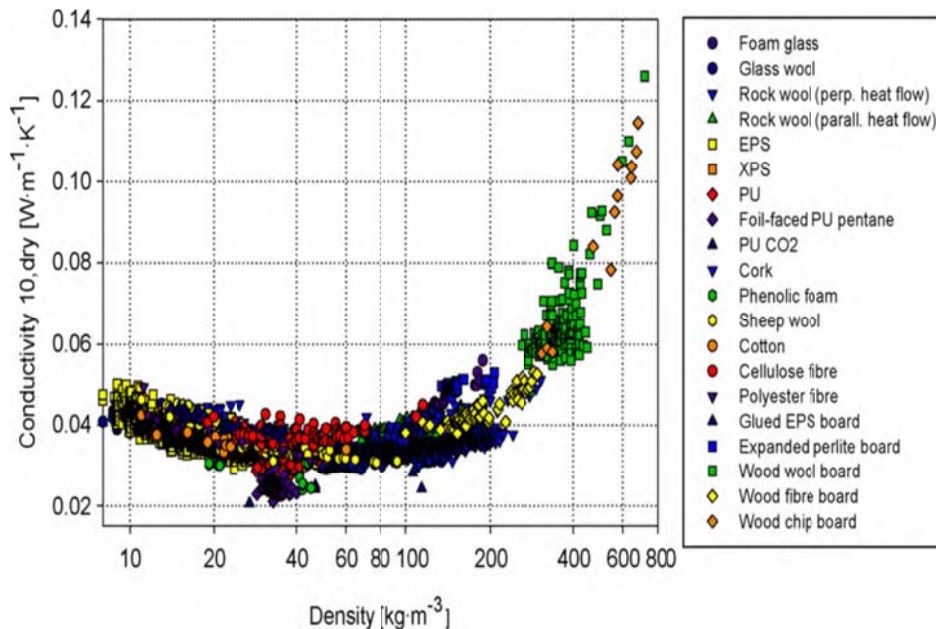


Figure 1: Thermal conductivity of insulating materials at 10 °C [Munoz *et al.*,2010]

The importance of the use of a lightweight thermal insulation properties of building materials is increasing with each passing day for reducing energy loss in buildings. The basic functions of lightweight construction materials ensure thermal insulation in buildings and using environments. These are porous materials which are generally poor load-bearing properties [Pehlivanlı, 2009]. Polymeric foams are most commonly used as thermal insulating, comfort cushioning and packaging materials [Jacobs *et al.*, 2007]. One of this kind of insulation materials is Expanded Polystyrene Styrofoam (EPS). EPS contained billions of porosity so that this insulation materials have low thermal conductivity. In present day, producers have done a good insulating materials with reflecting

reinforcement. This is used for insulating which reflects sun's rays so that this materials have lower thermal conductivity than white EPS [Uzun *et al.*; 2012].

2. MATERIAL AND METHOD

EPS insulation panels, which is one of porous building materials are the most important feature to be light and thermal conductivity values are lower than the other wall elements. Because the amount of dry air contained in the porous structure is the most important parameter for low thermal conductivity which is the primary property of an insulation material. As is known increase the porosity of material, generally decrease the density of material, thermal conductivity and strength. The

relationship between the value of thermal conductivity – density, experimental measurements were performed to see the change in the structure element of EPS. Thermal conductivity of EPS thermal insulation boards investigated experimentally the effect of production parameters and shows the density on thermal conductivity is approximately 90% effective [Mihlayanlar *et al.*, 2000]. Another studies show that the thermal conductivity of EPS changed reversely with density [Mihlayanlar *et al.*, 2000; Munoz *et al.*, 2000; Schellenberg *et al.*, 2010; Chudzik, 2012; Gnip *et al.*, 2012]. EPS insulation panels that are required for these measurements was obtained from local market and test specimens were prepared 30x30x5 cm dimensions. The most accurate way to determine its value for a specific sample is to measure it accordingly to a standard method. The guarded hot plate and the heat flow meter hot plate [Anonymous,1991; Anonymous,1991; Anonymous, 2001]. This specimens was measured the Fox 314 heat flow meter which is measured the low thermal conductivity of the materials. According to TS EN 13163 standard, test specimen in the form of sheet or test specimen, which is nearly identical to each other, these are placed between the heating and cooling units of the heat flow meter for instance Fox 314 which is shown schematic diagram of working principle in Figure 1.

The average temperature of both the surface of the test specimens and the temperature difference between the two surfaces is provided with a constant steady state conditions.

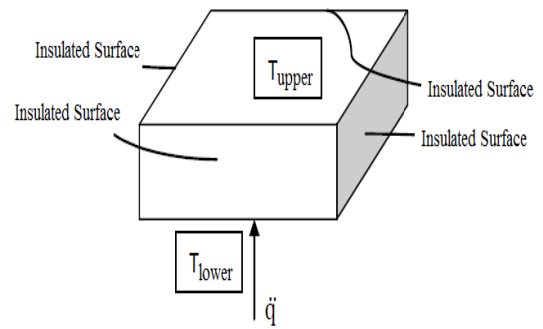


Figure 2: Schematic Diagram of Working Principle of FOX 314

Heat flow meter measuring the area of the test specimens simultaneously in the central region and the center of the device, provides a one-way flow velocity and constant density. Temperature difference with steady state condition, thermal conductivity is found that using thickness of material and heat flux. This determination is calculated by taking the form of one-dimensional heat conduction problem.

Table 1: Average and projected thermal conductivity of EPS [Anonymous, 2013].

EPS Density (kg/ m ³)	Thermal Conductivity k (W/mK) Average	Thermal Conductivity k (W/mK) Projected
14	0,0384	0,040
16	0,0370	0,039
16 (Carbon reinforced)		0,031
18	0,0359	0,038
20	0,0350	0,037
22	0,0343	0,036
24	0,0338	0,036
26	0,0333	0,035
28	0,0330	0,035
30	0,0327	0,035
32	0,0324	0,034

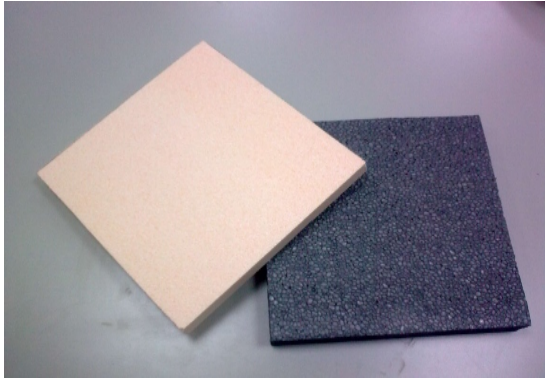


Figure 3: White and Carbon Reinforced EPS

Lasercomp Fox 314 heat flow meter is used for thermal conductivity measurement. Thermal conductivity values are determined at various temperatures for white EPS and carbon reinforced EPS which is developed in recent years to reduce the transfer of heat by reflecting the sun's rays reflecting feature.

Specimens which is prepared for the experiment is measured the thermal conductivity other than the standart average temperature of 10 °C and these temperatures are 5, 15, 20, 25, 30 °C. Also this situation is repeated at different density levels. Temperature dependence of thermal conductivity values are given in the form of graphs. Also these values are compared with average and projected values of EPS which is found in the literature. In this graphs shows that the thermal conductivity of EPS is decreasing reversely density and also increasing the temperature.

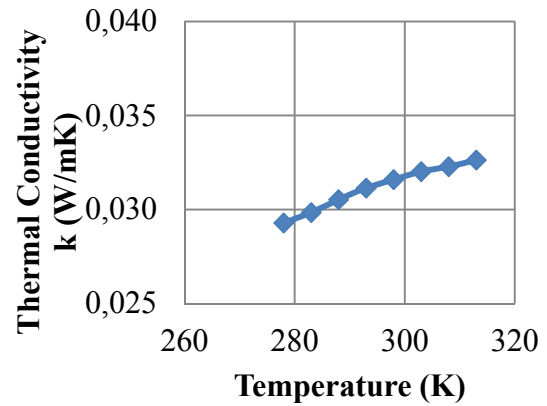


Figure 4: Thermal conductivity of 14 kg/m³ carbon reinforced EPS

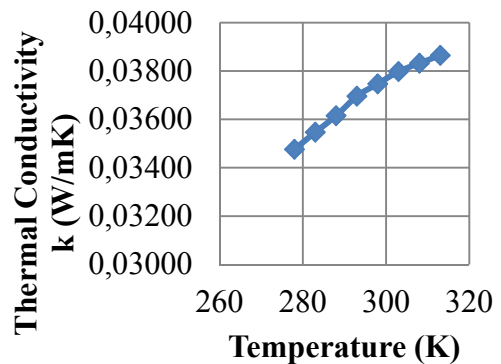


Figure 5: Thermal conductivity of of 18 kg/m³ EPS

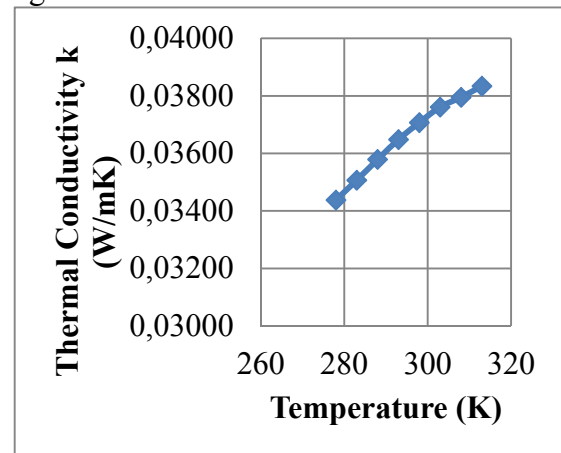


Figure 6: Thermal conductivity of 22 kg/m³ EPS

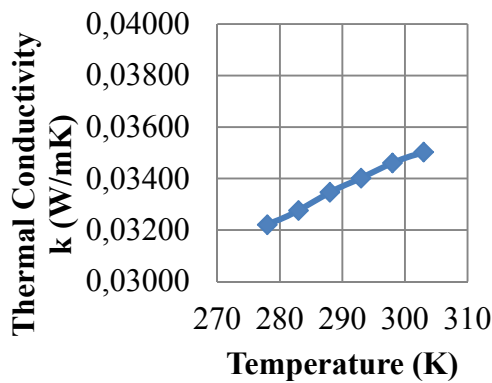


Figure 7: Thermal conductivity of 28 kg/m³ EPS

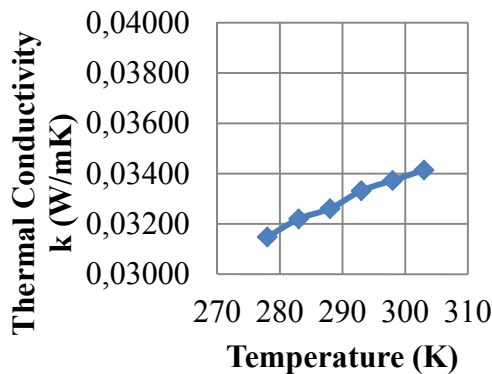


Figure 8: Thermal conductivity of 32 kg/m³ EPS

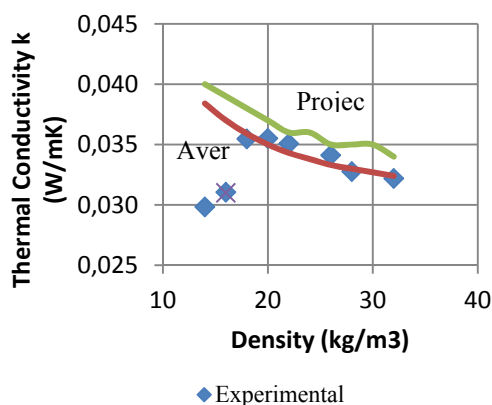


Figure 9: Thermal conductivity of EPS

CONCLUSION

Experimental results show that with the increase in density, decrease in the value of thermal conductivity for white EPS. Considering in the plane EPS which is high density has small size of porosity.

But this may not be true for insulating materials. Because of decreasing thermal conductivity with increasing density. This situation may be related to pore size, shell structure of the material or density of polistren which is the raw material of EPS. Also when looing at the values of thermal conductivity of carbon-reinforced EPS insulation boards thermal conductivity is about 20% lower than white EPS. This is due to the structure of said reflective feature. Generally when density of materials increase thermal conductivity increase. But thermal conductivity of EPS insulating board decrease with increasing density. This situation is related to the structure of the pore. The most important parameter is also the relationship between convection and radiation to the size of the pores that explain better the thermal conductivity and density correlation.

REFERENCES

- Anonymous, 1991. ISO 8301, Thermal Insulation – Determination of Steady-state Thermal Resistance and Related Properties – Heat Flow Meter Apparatus, International Organization for Standardisation, Geneva.
- Anonymous, 1991. ISO 8302, Thermal Insulation – Determination of Steady-state Thermal Resistance and Related Properties – Guarded Hot Plate Apparatus, International Organization for Standardisation, Geneva.
- Anonymous, 1999, 2009. Turkey Statistical Agency www.tuik.gov.tr
- Anonymous, 2001. EN 12664, Thermal Performance of Building Materials and Products – Determination of Thermal Resistance by Means of Guarded Hot Plate and Heat Flow Meter Methods – Dry and Moist Products of Medium and Low Thermal Resistance, European Committee for Standardisation, Brussels.
- Anonymous, 2013. Society of Polystyrene Manufacturers, www.pud.org.tr
- Uzun, İ., Ünal, P., 2012. Isıl İletkenliğin Farklı Yoğunluktaki EPS ürünler İçin Değişimi, EPS haber.
- Munoz, F. D., Anderson, B., Cejudo-Lopez, J. M., Andres, A. C., 2010. Uncertainty in the Thermal of Insulation Matrials, Energy and Buildings, Vol. 42, 2159 – 2168.

- Jacobs, L.J.M., Danen, K.C.H., Kemmere, M.F., Keurentjes, J.T.F., 2007. A Parametric Study Into The Morphology of Polystyrene – Co – Methyl Methacrylate Foams Using Supercritical Carbon Dioxide As A Blowing Agent, *Polymer*, 3771 – 3780.
- Pehlivanlı, Z., 2009. Gazbeton Malzemesinin Isıl İletkenliğinin Nem ve Sıcaklıkla Değişiminin İncelenmesi, *Int. J. Eng.. Research and Development*, Vol 1, No 2.
- Mıhlayanlar, E., Dilmaç, Ş., Güner, A., 2008. Analysis of the Effect of Production Process Parameters and Density of Expanded Polystyrene Insulation Boards on Mechanical Properties and Thermal Conductivity, *Materials and Design*, Vol. 29, 344 – 352.
- Schellenberg, J., Wallis, M., 2010. Dependence of Thermal Properties of Expandable Polystyrene Particle Foam on Cell Size and Density, *Journal of Cellular Plastics*, Vol. 46, No. 209.
- Chudzik, S., 2012. Measurement of Thermal Parameters of a Heat Insulating Material Using Infrared Thermography, *Infrared Physics and Technology*, 55, 73 – 83.
- Gnip, I., Vejelis, S., Vaitkus, S., 2012. Thermal Conductivity of Expanded Polystyrene (EPS) at 10 oC and its Conversion to Temperatures within Interval from 0 to 50 oC, *Energy and Buildings*, Vol. 52, 107 – 111.
- Kaya, M., Aydın, H., 2006. Isı Yalıtım Malzemesi Poliüretan Köpüğün Üretim Yöntemleri ve Özellikleri, *Celal Bayar University, Journal of Technical Sciences*, Vol 6, No 2.

SECTION B
Catalytic Aspects

MESOPOROUS MATERIALS WITH ORDERED PORE STRUCTURES CATALYTIC APPLICATIONS

Timur Doğu

Middle East Technical University, Department of Chemical Engineering, Ankara, Turkey
a. Corresponding author (tdogu@metu.edu.tr)

ABSTRACT: Silicate, alumina and zirconia/ceria based high surface area mesoporous materials with ordered pore structures have highly attractive properties as catalyst supports. Catalytic performances of such materials can be enhanced by the incorporation of metals, metal oxides, organics and/or acid sites into their structure by direct synthesis or post-synthesis methods. Effects of synthesis conditions on the structure of such mesoporous materials and some of the recent catalytic applications on dry and steam reforming reactions to produce hydrogen, selective oxidation, production of non-petroleum transportation fuel alternatives and chemicals from alcohols, and on environmental catalysis are reviewed in this presentation.

1. INTRODUCTION

Discovery of mesoporous materials with regular array of uniform pores and high surface areas opened new opportunities in catalysis research. M41S family [Kresge, *et al.*, 1992], and SBA-type silicate structured mesoporous materials [Zhao *et al.*, 1998] are two of the most popular examples of such high surface area materials with ordered pore structures. Such mesoporous materials are considered as attractive catalyst supports due to their low pore diffusion resistance for the transport of reactants to the active sites and less susceptibility to coke formation as compared to microporous catalytic materials. MCM-41 and SBA-15 are two of the silicate structured mesoporous materials, which were extensively used as catalyst supports in recent decades. MCM-41 has uniform pores in the range of 2-4 nm and has surface area values over 1000 m²/g. SBA-15, with larger pore diameters and thicker pore walls, has higher hydrothermal stability than MCM-41 [Ooi and Bhatia, 2007; Jaroniec and Solovyov, 2006; Aktas *et al.*, 2011].

Synthesis of a wide variety of SBA-type materials, like SBA-1, SBA-11 (cubic), SBA-12 (3D hexagonal), SBA-16 (cubic-cage) and SBA-15 (2D hexagonal) are reported in the literature. SBA-15 has a bimodal pore structure, which contains some micropores within the corona region around the ordered mesopores. Such micropores are created by the penetration of the poly ethylene oxide chains of the surfactant (Pluronic) used during the synthesis of this material. Synthesis conditions, such as the pH of the synthesis solution, temperature and duration of hydrothermal synthesis, calcination conditions etc., were reported to have strong influence on the structural properties of the final product [Aktas *et al.*, 2011; Brodie *et al.*, 2008; Gao *et al.*, 2008]. Mesocellulose silica foam (MCF) is another mesoporous material which is composed of large uniform spherical cells interconnected by uniformly sized windows [Lettow *et al.*, 2000]. More recently, mesoporous alumina with higher hydrothermal stability than silicate structured materials [Morris *et al.*, 2008; Yuan *et al.*, 2008] and zirconia/ceria based materials with ordered pore

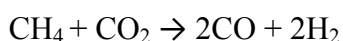
structures attracted the attention of catalysis researchers.

Catalytic performances of such mesoporous materials were generally enhanced through incorporation of metals, metal oxides, organic components and/or acid sites into their structure by direct synthesis or post synthesis methods [Sener *et al.*, 2006; Gucbilmez *et al.*, 2006]. A review of some of the catalytic applications of such mesoporous materials carried out in our research group is given in this presentation.

2. CATALYTIC APPLICATIONS

2.1. Reforming Reactions

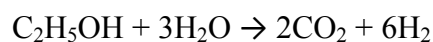
Hydrogen production by steam reforming reactions and production of synthesis gas by dry reforming of methane are two of the examples of applications of mesoporous catalytic materials with ordered pore structures. Dry reforming of methane is expected to yield a syngas with a H₂/CO ratio being close to one, from two of the most abundant greenhouse gases, namely CH₄ and CO₂. This gas may then be used for the synthesis of chemicals and fuels through Fischer-Tropsch reactions and/or through dimethyl ether production.



Ni based materials are among the most active catalysts for this reaction. Coke formation and occurrence of reverse water gas shift reaction are two of the important problems causing catalyst deactivation and decrease of hydrogen yield, respectively. Our studies performed with bimetallic Pd-Ni impregnated MCM-41 [Damyanova *et al.*, 2009] and with Ru or Rh incorporated Ni-MCM-41 type catalytic materials prepared by the one-pot route proved the advantages of using such mesoporous catalysts in dry reforming. Improved catalyst stability and improvements on coke formation due

to the contributions of Ru and Rh are some of the positive results obtained in these studies [Yasyerli *et al.*, 2011; Arbag *et al.*, 2010]. More recently, dry reforming studies performed with Ni incorporated mesoporous alumina based catalysts showed that almost zero coke formation could be obtained over the material prepared by the hydrothermal route and modification of the material with tungsten oxide had also positive effect on minimization of coke formation [Arbag *et al.*, 2013].

Due to the storage and transportation problems of hydrogen, its on-board production from liquid fuels attracted the attention of researchers in recent decades. Ethanol, with a high hydrogen content, is one of the promising feedstocks to produce hydrogen through steam reforming [Ozdogan *et al.*, 2007]. In principle, upto six moles of hydrogen can be produced per mole of ethanol through this reaction.



However, thermodynamic limitations and the occurrence of side reactions limit the approach to the maximum value of hydrogen yield. Sorption enhanced reforming of ethanol over Ni and Co incorporated MCM-41 type catalysts and using CaO as the CO₂ adsorbent, gave hydrogen yields close to the maximum value of six per mole of ethanol [Gunduz and Dogu, 2012]. Our more recent studies proved that mesoporous alumina (MA) was more stable than MCM-41 for this reaction and Co-Mg incorporated MA prepared by the one-pot route gave very high hydrogen yields even in the absence of a CO₂ adsorbent.

2.2. Alternative Fuels and Chemicals from Syngas and by Dehydration of Alcohols

Methanol, ethanol and their derivatives are considered as potential alternatives to petroleum as transportation fuels and also for the production of petrochemicals. Dehydration of methanol yields dimethyl ether, which is one of the most promising non-petroleum diesel fuel alternative.



Similarly, dehydration of ethanol yields diethyl ether and also ethylene, depending upon the type of catalyst used and the reaction conditions. Such dehydration reactions require solid acid catalysts with high Bronsted acidity. As it was shown in our recent studies, silicotungstic acid and tungstophosphoric acid incorporated silicate and alumino silicate type catalytic materials were highly active and stable in dehydration of alcohols to produce DME, DEE and ethylene [Varisli *et al.*, 2008; Varisli *et al.*, 2010; Ciftci *et al.*, 2010; Ciftci *et al.*, 2012]. Novel mesoporous nanocomposite WO_x -Silicate structured acidic catalysts prepared by the one-pot route also showed excellent performance in ethanol and methanol dehydration. It was shown that these solid acid catalysts had a unique structure composed of WO_x nanorods and W nanoballs within the amorphous mesoporous silicate lattice [Varisli *et al.*, 2009]. Nafion-incorporated silicate structured mesoporous catalysts by the one-pot route were also found to have surface area values in the range of 595-792 m^2/g and these materials also showed good performance in DME synthesis from methanol [Ciftci *et al.*, 2010]. More recently [Celik *et al.*, 2013], it was shown that DME can also be produced directly from synthesis gas using bi-functional catalysts mixtures composed of methanol synthesis and silicotungstic acid incorporated silicate

structured mesoporous catalyst pairs. Experiments performed at 50 bar and in a temperature range of 200-300°C indicated the positive effect of CO_2 in the feed stream on DME selectivity.

2.3 Selective Oxidation Applications

Oxidative dehydrogenation of ethane and propane to produce ethylene and propylene have major thermodynamic advantages over the non-oxidative dehydrogenation processes. However, product selectivity problems limit the wide use of such processes. In a series of experiments performed with V and Ce incorporated SBA-15, promising results were obtained in oxidative dehydrogenation of propane [Aktas *et al.*, 2010; Aktas *et al.*, 2011]. It was shown that synthesis conditions of the mesoporous catalysts had important effects on the incorporation of the active species (V and Ce) into the structure of the catalyst, hence on its catalytic performance.

V and Cu incorporated MCM-41 like catalytic materials were also shown to give good performance in selective oxidation reactions [Nalbant *et al.*, 2008; Gucbilmez *et al.*, 2006]. Gucbilmez and co-workers showed that high ethylene selectivity values could be obtained by selective oxidation of ethanol over V-MCM-41, which might allow production of petrochemicals from a non-petroleum feedstock.

2.4. Some Environmental Catalysis Applications

Catalytic degradation of waste plastics is a promising route for the conversion of these materials to valuable chemicals and fuels. Performances of MCM-like alumino silicate and alumina loaded SBA-15 on catalytic degradation of polypropylene were tested and results proved the importance of Al/Si ratio and

the synthesis procedure on their catalytic performance [Obali *et al.*, 2009, 2011].

Another environmental application of MCM-41 like mesoporous materials was high temperature removal of H₂S from fuel and process gases, by incorporation of Cu into such materials. Comparison of the performances of the materials prepared by the one-pot and impregnation routes showed higher sulfur retention capacity in the case of impregnated materials [Ozaydin *et al.*, 2008].

3. CONCLUDING REMARKS

Silicate, alumina and zirconia based mesoporous materials with ordered pore structures have highly attractive properties as catalyst supports. Pore size distributions of such materials can be adjusted by use of different surfactants. Synthesis conditions of these materials have very strong influence on their structure and also on the incorporation of active metals/metal oxides into their structure. Literature studies showed number of applications of these materials on different catalytic applications. Some of these applications on steam/dry reforming reactions, dehydration/selective oxidation reactions etc. proved potential use of such catalysts in industry.

Acknowledgements: Financial support of TUBITAK (Project Numbers 111M338, 108M571, 111M449), Middle East Technical University and Gazi University Research Funds are gratefully acknowledged.

REFERENCES

- Aktas, O., Yasyerli, S., Dogu, G. and Dogu, T., 2011. Structural variations of MCF and SBA-15-like mesoporous materials as a result of differences in synthesis solution pH, *Materials Chem. Physics*, 131, 151.
- Aktas, O., Yasyerli, S., Dogu, G. and Dogu, T., 2010. Effect of synthesis conditions on the structure and catalytic performance of V- and Ce incorporated SBA-15 like materials in propane selective oxidation, *Ind. Eng. Chem. Res.*, 49, 6790.
- Arbag, H., Yasyerli, S., Yasyerli, N. and Dogu, G., 2010. Activity and stability enhancement of Ni-MCM-41 catalysts by Rh incorporation for hydrogen from dry reforming of methane, *Int. J. Hydrogen Energy*, 35, 2296.
- Arbag, H., Yasyerli, S., Yasyerli, N., Dogu, G. and Dogu, T., 2013. Coke minimization in dry reforming of methane by Ni incorporated mesoporous alumina catalysts synthesized following different routes: Effects of W and Mg, *Topics on Catal.*, (in pres).
- Brodie-Linder, N., Dosseh, G., Alba, S.C., Audonnet F. and Imperor-Clerc, M., 2008. *Mater. Chem. Physics*, 108, 73.
- Celik, G., Arinan, A., Bayat, A., Ozbekelge, H.O., Dogu, T. and Varisli, D., 2013. Performance of silicotungstic acid incorporated mesoporous catalyst in direct synthesis of dimethyl ether from syngas in the presence and absence of CO₂, *Topics in Catalysis*, (in pres).
- Ciftci, A., Varisli, D. and Dogu, T., 2010. Dimethyl ether synthesis over novel silicotungstic acid incorporated nanostructured catalysts, *Int. J. Chem. Reactor Eng.*, 8, A45.
- Ciftci, A., Sezgi, N.A. and Dogu, T., 2010. Nafion-incorporated silicate structured nanocomposite mesoporous catalysts for dimethyl ether synthesis, *Ind. Eng. Chem. Res.*, 49, 6753.
- Ciftci, A., Varisli, D., Tokay, K.C., Sezgi, N.A. and Dogu, T., 2012. Dimethyl ether, diethyl ether and ethylene from alcohols over tungstophosphoric acid based mesoporous catalysts, *Chem. Eng. J.*, 207-208, 85.
- Damyanova, S., Pawalec, B., Arishtirova, K., Fierro, J.L.G., Sener, C. and Dogu, T., 2009. MCM-41 supported PdNi catalysts for dry reforming of methane, *Appl. Catal. B.*, 92, 250.
- Gao, F., Zhang, Y., Wan, H., Kong, Y., Wu, X., Dong, L. and Li, B., 2008. Microporous Mesoporous Mater., 110, 508.
- Gunduz, S. and Dogu, T., 2012. Sorption enhances reforming of ethanol over Ni- and Co- incorporated MCM-41 type catalysts, *Ind. Eng. Chem. Res.*, 51, 8796.
- Gucbilmez, Y., Dogu, T. and Balci, S., 2006. Ethylene and acetaldehyde production by selective oxidation of ethanol using mesoporous V-MCM-41 catalysts, *Ind. Eng. Chem. Res.*, 45, 3496.
- Jaroniec, M. and Solovoy, L.A., 2006. Assessment of ordered and complementary pore volumes in polymer templated

- mesoporous silicas and organosilicas, *Chem. Commun.*, 2242-2244.
- Kresge, C.T., Leonowicz, M.E., Roth, W.J., Vartuli, J.C. and Beck, J.S., 1992. A new family of mesoporous molecular sieves prepared with liquid crystal templates, *Nature*, 359, 710.
- Lettow, J.S., Han, Y.J., Schmidt-Winkel, P., Yang, P., Zhao, D., Stucky, G.D. and Ying, J.Y., 2000. *Langmuir*, 16, 8291.
- Morris, S.M., Fulvio, P.F. and Jaroniec, M., 2008. Ordered mesoporous alumina-supported metal oxides. *J. Am. Chem. Soc.*, 130, 15210.
- Nalbant, A., Dogu, T. and Balci, S., 2008. Ni and Cu incorporated mesoporous nanocomposite catalytic materials, *J. Nanoscience Nanotechnol.*, 8, 549.
- Obali, Z., Sezgi, N.A. and Dogu, T., 2011. The synthesis and characterization of aluminum loaded SBA-type materials for polypropylene degradation, *Chem. Eng. J.*, 176-177, 202.
- Obali, Z., Sezgi, N.A. and Dogu, T., 2012. Catalytic degradation of polypropylene over alumina loaded mesoporous catalysts, *Chem. Eng. J.*, 207-208, 421.
- Ooi, Y.S., and Bhatia S., 2007. Aluminum containing SBA-15 as cracking catalyst for the production of biofuel from waste used palm oil, *Microporous Mesoporous Mater.*, 102, 310.
- Ozaydin, Z., Yasyerli, S. and Dogu, G., 2008. Synthesis and activity comparison of copper-incorporated MCM-41-type sorbents prepared by one-pot and impregnation procedures for H₂S removal, *Ind. Eng. Chem. Res.*, 47, 1035.
- Ozdogan, E., Dogu, T. and Dogu, G., 2007. Ni-MCM-41 type mesoporous catalysts synthesized by one-pot hydrothermal procedure for steam reforming of ethanol, *Int. J. Chem. Reactor Eng.*, 5, A111.
- Sener, C., Dogu, T. and Dogu, G., 2006. Effects of synthesis conditions on the structure of Pd incorporated MCM-41 type mesoporous nanocomposite catalytic materials with high Pd/Si ratios, *Microporous Mesoporous Mater.*, 94, 89.
- Varisli, D., Dogu, T. and Dogu, G., 2008. Silicotungstic acid impregnated MCM-41-like mesoporous solid acid catalysts for dehydration of ethanol, *Ind. Eng. Chem. Res.*, 47, 4071.
- Varisli, D., Dogu, T. and Dogu, G., 2009. Novel mesoporous nanocomposite WO_x-silicate acidic catalysts: Ethylene and diethyl ether from ethanol, 48, 9394.
- Varisli, D., Dogu, T. and Dogu, G., 2010. Petrochemicals from ethanol over a W-Si-based nanocomposite bidisperse solid acid catalyst, *Chem. Eng. Sci.*, 65, 153.
- Yasyerli, S., Filizgok, S., Arbag, H., Yasyerli, N. and Dogu, G., 2011. Ru incorporated Ni-MCM-41 mesoporous catalysts for dry reforming of methane..., *Int. J. Hydrogen Energy*, 36, 4863.
- Yuan, Q., Yin, A.X., Luo, C., Sun, L.D., Zhang, Y.W., Duan, W.T., Liu, H.C. and Yan, C.H., 2008. Facile synthesis for ordered mesoporous γ -aluminas with high thermal stability, *J. Am. Chem. Soc.*, 130, 3465.
- Zhao, D., Feng, J., Huo, Q., Melosh, N., Fredrickson, G.H., Chmelka, B.F. and Stucky, G.D., 1998. Triblock copolymer synthesis of mesoporous silica with periodic 50 to 300 angstrom pores, *Science*, 279, 548.

PHOTOCATALYTIC ACTIVITY OF FILM STRUCTURES COMPRISING TITANIA XEROGEL IN POROUS ANODIC ALUMINA

Oksana Linnik¹, Makxym Zhukovskiy¹, Nataliia Smirnova¹, Eugeny Krutko²,
Anatoly Kulak², Nikolai Gaponenko^{3,a}, Ahmed Asharif³, Liudmila Khoroshko³,
Marina Meledina³, Taisia Orekhovskaya³, Viktor Borisenko³

1. O. Chuiko Institute of Surface Chemistry National Academy of Sciences of Ukraine, General Naumov St. 17, 03164 Kyiv, Ukraine
2. Institute of General and Inorganic Chemistry, Surganova 9/1, 220072 Minsk, Belarus
3. Belarusian State University of Informatics and Radioelectronics, P. Browka 6, 220013 Minsk, Belarus
a. Corresponding author (nik@nano.bsuir.edu.by)

ABSTRACT: A honey-comb structure of porous anodic alumina with a tailor-made size of meso- or macropores is considered as a template for photocatalytic coating. Sol-gel derived titania in porous anodic alumina film has been demonstrated as an efficient photocatalytic coating. Its photocatalytic performance in an aqueous solution after calcination at 400 °C correlates with the size of the pores and the thickness of the porous alumina film. Strong photocatalytic activity for the porous alumina films of 1.5 µm thickness with a size of the pores of 60-70 nm after deposition of the titania xerogel is reported.

1. INTRODUCTION

Titanium dioxide (TiO₂, titania) is a promising material exhibiting photocatalytic property perspective for different redox processes including the photocatalytic purification of water [Gnatyuk *et al.*, 2005; Shankar *et al.*, 2009; Smirnova *et al.*, 2009]. Photocatalytic methods of deep purification of water have attracted considerable attention due to the possibility of complete destruction of chloro-, nitro-, and polycyclic aromatic compounds through their mineralization in the absence of consumable reagents. Titanium dioxide is most commonly being used for that in the form of photocatalytically active dispersed particles of pure anatase or its mixture with rutile. The porous film of titanium dioxide may also be synthesized electrochemically [Shankar *et al.*, 2009]. Film structures titania xerogel/porous anodic alumina (PAA) also reveal photocatalytic activity [Gaponenko *et al.*, 2010; Gaponenko *et al.*, 2012; Linnik *et al.*, 2013]. In this paper we report on

the use of porous anodic alumina film as a template for sol-gel synthesis of titania and the photocatalytic activity of such structures.

2. EXPERIMENTAL

Two groups of the samples were fabricated comprising porous anodic alumina coated with sol-gel derived titania. The first group was prepared from Al (99.99 purity), for the second group of the samples a low-cost Al (99.5 purity) was used.

The PAA films of the first group were fabricated via a two-step anodization of the aluminium foil (99.99% purity) 25×76 mm in size in 0.5 M oxalic acid solution or 0.04 M and 1 M orthophosphoric acid solution. After the first step the anodic alumina formed was removed in a mixture of orthophosphoric acid and chromium (IV) oxide at 60 °C, leaving nanotextured aluminum surface. The second anodization was used to grow porous alumina films with a thickness of 1-40 µm. Then the remaining aluminum substrate was

dissolved in a solution of hydrochloric acid (15%) and copper chloride (0.5%) in order to get a free-standing porous alumina membrane. The pores were subsequently enlarged by etching in a phosphoric acid solution (50%) at 20 °C. Titania was synthesized on the first group of samples by the sol-gel method using titanium tetraisopropoxide as a precursor and a three-block copolymer of polyethyleneoxide and polypropyleneoxide (Pluronic P123) as a template in an alcoholic medium. One-layered films were deposited on PAA membranes by a dip-coating technique with the withdrawal rate of 1.5 mm/s. The samples were heated to 400 °C in air with the rate of 1 °C/min [Smirnova *et al.*, 2009].

Photocatalytic degradation of the organic dye Rhodamine B ($C=1 \times 10^{-5}$ mol/L, pH=6-7 and at 20 °C) and tetracycline hydrochloride ($C=2 \cdot 10^{-5}$ mol/L, pH=7 and at 25 °C) of the first group of samples was performed under permanent mixing for 220 min and 90 min, respectively. The titania/substrate structures were put inside the quartz reactor containing the pollutant solution and illuminated with a 1000 W middle-pressure mercury lamp. The Rhodamine B or tetracycline hydrochloride concentrations before and after irradiation were monitored at 550 nm and 357 nm, respectively by Lambda 35 UV-vis spectrophotometer (Perkin Elmer). The probes were withdrawn every 20 min.

For fabrication of the second group of the samples PAA was fabricated by a two-step anodization of the aluminum foil (99.5%) 2.9×4 cm in size in 1 M H₃PO₄ aqueous electrolyte at the voltage of 90 V. Finally the samples were kept for 10 min in 1 M H₃PO₄ solution to increase the pore size. Then they were dried at 100 °C for 30 min. TiO₂ was synthesized over porous anodic alumina by the sol-gel method using titanium tetraisopropoxide

Ti(OC₃H₇)₄ as a titania precursor in ethylene glycol monomethyl ether. pH of the sol was adjusted with concentrated nitric acid to be 1. Titania was spin-on deposited at 2700 rpm for 30 s followed by drying at 200 °C for 10 min, and a final heat treatment in air at 400 °C for 30 min. From 1 to 5 layers of the xerogel were deposited.

Photocatalytic degradation of the organic dye Rhodamine C with the initial concentration of 40 micromole/l was performed with the use of the second group of samples in a 8 ml double-walled glass reactor transmitting radiation at wavelength above 320 nm. The samples with PAA/titania xerogel were located in the reactor containing the dye solution and illuminated there with the light of 120 W Hg quartz lamp for 2 h. The concentration of the dye was *in situ* monitored by recording absorption spectra of the dye solution at $\lambda = 551-554$ nm.

3. RESULTS AND DISCUSSION

SEM examination reveals that the thickness of titania in the pores depends on the thickness of porous anodic alumina. The thinnest titania layer of 10-30 nm was formed in the porous layer of 40 μ m thickness. Titania is homogeneously distributed over the surface of the pores when the thickness of the porous layer ranges from 1.5 μ m to 40 μ m. No blocking of the pores is observed. After titania deposition the widest pores in the range of 60-70 nm were obtained for the porous anodic alumina film of 1.5 μ m thickness (Figure 1), whereas the pores with predominant size of 50-60 nm and 30-35 nm were obtained for the porous anodic alumina of 40 and 3 μ m thickness respectively.

Crystallization of titania to anatase phase at 400 °C was confirmed by the appearance of well-resolved Raman peaks at 142 and

637 cm^{-1} attributed to the main anatase vibration modes [Linnik *et al.*, 2013].

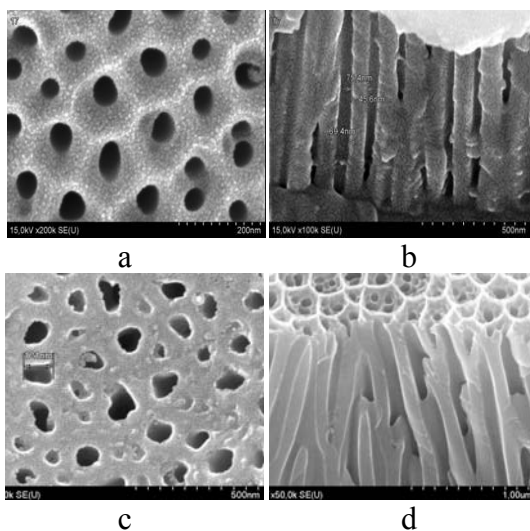


Figure 1: SEM top view (a,c) and cleaved edge (b,d) of the structure porous anodic alumina/titania xerogel fabricated from Al 99.99% (a, b) and Al 99.5 (c, d) by dipping (a,b) and spinning (c,d).

The photodegradation results obtained (Figure 2) clearly show that the dye destruction rates correlate with the thickness of porous anodic alumina that determinates in turn by the thickness of titania layer interacting with light during photocatalysis.

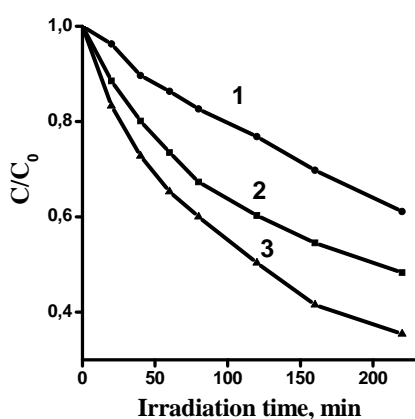


Figure 2: Photodegradation of Rhodamine B in the presence of the first group of the samples with porous anodic alumina as thick as 40 μm (1), 3 μm (2) and 1.5 μm (3).

The thinner the porous alumina layer is, the more dye degrades in the presence of titania/porous alumina structure.

The influence of substrates nature on the photocatalytic performance of titania was also examined in the degradation reaction of tetracycline hydrochloride (TC) (Figure 3).

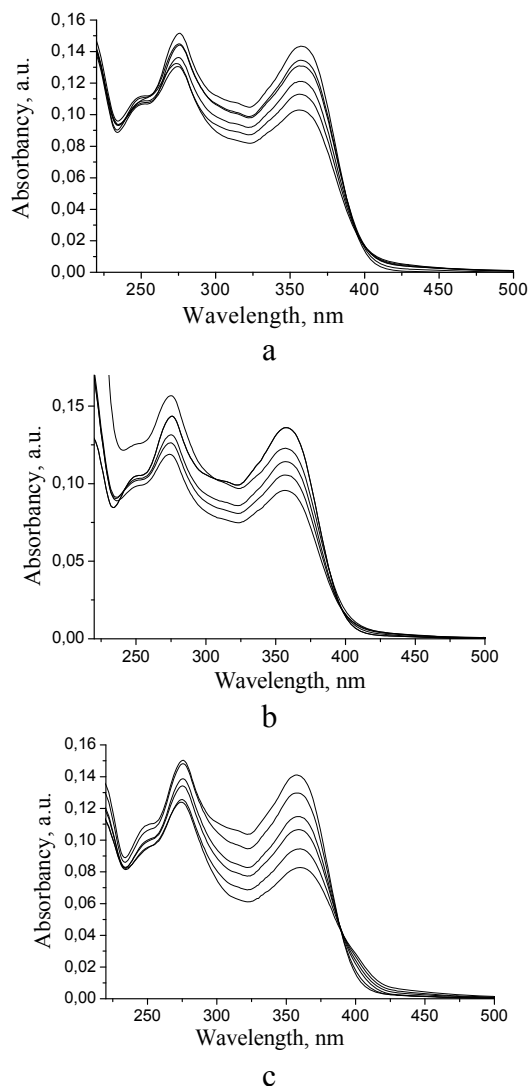


Figure 3: Absorption spectra evolution of aqueous TC solution during photocatalytic degradation over mesoporous TiO_2 films covered on textured Al (a), Al (b), and PAA (3 μm).

Reaction rate constants are drastically increased in the presence of titania on

the substrates in the order: PAA (3 μm) > Al > textural Al (Table 1).

Table 1. Reaction rate constants of photocatalytic degradation of TC over TiO_2 covered on the different substrates.

Film	Substrate	$k_d \cdot 10^5 \text{ s}^{-1}$
blank	Al	2.0
TiO_2	textured Al	4.7
TiO_2	Al	6.7
TiO_2	PAA (3 μm)	8.5

Concurrent decrease in the intensity of two absorption bands at 275 nm and 357 nm assumed the degradation reaction of TC rather than the oxidation process [Linnik *et al.*, 2009; Eremenko *et al.*, 2011]

The rate constant of the dye photodegradation determined from the slope of the initial part of kinetic curve (Figure 4) increases with increasing the number of TiO_2 layers from 1 to 5. However, under exposure above 0.5 h, lowering of the rate constant is observed due to the limitation of the photocatalytic process by delayed diffusion of oxygen into the pores of PAA.

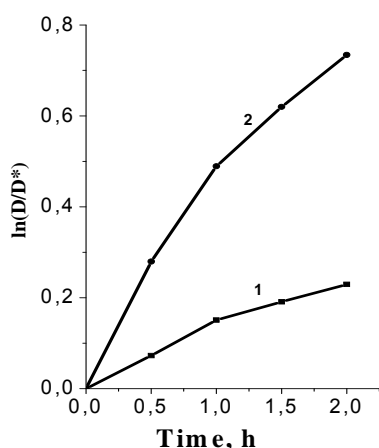


Figure 4: Time dependences of the relative decrease in Rhodamine C concentration (D/D^*) on PAA films fabricated from Al 99,5 coated with one (1) and five (2) titania xerogel layers.

In conclusion, titania xerogel deposited into porous anodic alumina is crystallized into anatase phase during annealing at 400 °C. The morphology of the porous alumina affects photocatalytic activity of titanium dioxide formed therein. Thus the highest activity was obtained for the porous anodic alumina film of 1.5 μm thickness with the pores of 60-70 nm after titania deposition in the process of photodegradation of Rhodamine B. Photocatalytic activity of TiO_2 covered PAA of 3 μm is shown to reach maximum in the degradation of TC solution over the references samples. Photocatalytic activity of titanium dioxide/PAA structures formed on the aluminum of technical purity has been shown in the model reaction of Rhodamine C photodegradation in its aqueous solution under UV illumination.

Acknowledgements: This work was partially supported by Belarusian Foundation for Basic Researches, grant T12MC-025.

REFERENCES

- Gnatyuk, Yuriy; Smirnova, Nataliia; Eremenko, Anna *et al.*, 2005. Photoelectrochemical characterization and photocatalytic properties of mesoporous $\text{TiO}_2/\text{ZrO}_2$ films, *Adsorption Science & Technology*, Vol. 23 (6), P. 497
- Shankar, K., Basham, J.I., Allam, N.K. *et al.*, 2009. A Review of Recent Advances in the Use of TiO_2 Nanotube and Nanowire arrays for Oxidative Photoelectrochemistry, *J. Physical Chemistry*, Vol. 113, P. 6327
- Gaponenko, N.V.; Orekhovskaya, T.I; Nikolaenko, I.A., 2010. Titanium oxide xerogel films in porous aluminum oxide for photocatalytic application, *Journal of Applied Spectroscopy*, Vol. 77 (3), P. 432
- Gaponenko, N.V., Kortov, V.S., Smirnova, N.P., 2012. Sol-gel derived structures for optical design and photocatalytic application, *Microelectronic Engineering*, Vol. 90, P. 131
- Smirnova, N.P, Manuilov, E.V., Korduban, A.M. *et al.*, 2009. Design of TiO_2 -based films modified with Ag nanoparticles with controlled optical and photocatalytic properties, *Nanomaterials and Supramolecular Structures*, Springer Science+Business Media B.V., P. 131

- Linnik, O., Manuilov, E., Snegir, S. et al., 2009. Photocatalytic degradation of tetracycline hydrochloride in aqueous solution at ambient conditions stimulated by the gold containing zinc-titanium oxide films, Journal of Advanced Oxidation Technologies, Vol. 11, No. 3, Vol. 12, No. 2, P. 551
- Eremenko, A., Smirnova, N., Gnatiuk, Iu. et al., 2011. Silver and Gold Nanoparticles on Sol-Gel TiO₂, ZrO₂, SiO₂ Surfaces; Optical Spectra, Photocatalytic Activity, Bactericide Properties Book 3: Composite Materials, INTECH, P. 2,
- Linnik, O.; Smirnova, N.; Zhukovskiy, M. et al., 2013. Influence of Support Nature on Photocatalytic Activity of TiO₂ Film, Advanced Science, Engineering and Medicine, Vol. 5, No 4, P. 281

DEVELOPMENT OF THREE WAY CATALYTIC CONVERTERS FOR ELIMINATION OF HYDROCARBONS, CARBON MONOXIDE AND NITRIC OXIDE IN AUTOMOTIVE EXHAUST

Aylin Civan^{1,a}, Duygu Gerçeker¹, Işık Önal¹

1. Middle East Technical University, Chemical Engineering Department, Ankara, Turkey
a. Corresponding author (civan.aylin@metu.edu.tr)

ABSTRACT: Pd-Rh containing and Pd-only three-way catalysts were synthesized by impregnation of metals on ceria-zirconia mixed oxide. The catalytic activity tests were carried out using a dynamic test system constructed to simulate the automotive exhaust conditions. The activities of the fresh and thermally aged monolithic catalysts were compared in terms of light-off temperatures. All catalysts showed resistance against thermal aging and did not lose activity. The light-off temperatures of the Pd-Rh containing catalyst C1 and Pd-only catalyst C2 appeared to be very close to each other, indicating that the absence of Rh in the catalyst composition did not make a dramatic change on the activity. Also, the other Pd-only catalyst C3 showed a remarkable catalytic activity despite its very low amount of metal.

1. INTRODUCTION

Air pollution arising from automobiles is a global concern. As the numbers of vehicles are dramatically increasing all over the world, emission limits are pushed down rapidly by the legislations. Automobile manufacturers are seeking solutions to improve the performance of their catalysts in order to meet the limits demanding as low as 99% conversion of the exhaust gases [Matsumoto, 2004].

The main pollutants in automobile exhaust are partially burned hydrocarbons (HC), carbon monoxide (CO) and nitrogen oxides (NO_x), mostly NO. The development of Three Way Catalytic Converters was dictated by the need to simultaneously convert these compounds into relatively harmless ones; CO₂, NO₂ and H₂O.

In general, emissions depend on air-to-fuel (A/F) ratio. Lean burn engines (A/F>14.7) are advantageous due to their significant fuel economy, however the performance is maximized in gas

conditions close to the stoichiometric feed ratio (A/F=14.7). Because,

appropriate amounts of oxidizing and reducing agents are needed at stoichiometric ratio to be able to perform catalytic reactions listed in Table 1 [Kaspar *et al.*, 2003]. A/F ratio in the engine is controlled by an O₂ sensor and oscillated around the stoichiometric value at a frequency of 0.5 or 1 Hz [Farrauto *et al.*, 1999]. The performance of a TWC is interpreted by its 'Light-off Temperature' which is defined as the temperature at which the conversion of a specific reactant is 50% [Noh *et al.*, 1999]. Most of the emissions are released during the cold start period of the engine, thus catalysts with low light-off temperatures are needed to be developed.

Table 1: Reactions occurring in the automotive exhaust catalysts

<i>Oxidation</i>	$2\text{CO} + \text{O}_2 \rightarrow 2\text{CO}_2$ $\text{HC} + \text{O}_2 \rightarrow \text{CO}_2 + \text{H}_2\text{O}^{\text{a}}$
<i>Reduction</i>	$2\text{CO} + 2\text{NO} \rightarrow 2\text{CO}_2 + \text{N}_2$ $\text{HC} + \text{NO} \rightarrow \text{CO}_2 + \text{H}_2\text{O} + \text{N}_2^{\text{a}}$ $2\text{H}_2 + 2\text{NO} \rightarrow 2\text{H}_2\text{O} + \text{N}_2$
<i>Water Gas Shift</i>	$\text{CO} + \text{H}_2\text{O} \rightarrow \text{CO}_2 + \text{H}_2$
<i>Steam reforming</i>	$\text{HC} + \text{H}_2\text{O} \rightarrow \text{CO}_2 + \text{H}_2^{\text{a}}$
^a Unbalanced reaction	

The state of art of a TWC consists of some common components. Noble metals such as Pt, Pd and Rh are used as active phases and they are dispersed CeO₂-ZrO₂ mixed oxide support for its oxygen storage ability [Shinjoh, 2006]. Pd and Pt are used for CO/HC conversions, Rh exhibits a lower activity for olefins, yet it is chosen for NO_x elimination [Gandhi *et al.*, 2003]. Pd is significantly less expensive than both Pt and Rh, but it is less resistant to sulfur poisoning. Research is generally focused on Pd/Rh containing catalysts. However, improved fuel quality (lower amounts of sulfur in the fuel), better engine control of the air to fuel perturbations and improved catalyst formulations make Pd a good candidate for meeting tighter future emission regulations [Farrauto *et al.*, 1999].

2. EXPERIMENTAL

In this study, three TWC catalysts with different compositions were prepared as shown on Table 2.

Table 2: Compositions of the catalysts

Catalyst	Composition
C1	0.65 wt% Pd and 0.1 wt % Rh separately impregnated on CZO support
C2	0.65 wt% Pd and 0.1 wt % Pd separately impregnated on CZO support
C3	0.1 wt% Pd impregnated on CZO support

2.1. Preparation of Ceria – Zirconia Mixed Oxide

The composition of the ceria-zirconia mixed oxide (CZO) was defined as Ce_{0.8}Zr_{0.2}O₂ and co-precipitation method was used. A solution with Ce/Zr ratio of 4 was prepared from cerium (III) nitrate hexahydrate (CeN₃O₉.6H₂O) and zirconyl nitrate hydrate (N₂O₇Zr.aq). H₂O₂ was added to the solution for complete oxidation. Then, NH₄OH was added for precipitation and the product was washed and filtered with 2-propanol. The product was dried at 150 °C for 12 h and the powder sample was grounded and calcined in an oven under dry air at 550 °C for 1 h.

2.2. Impregnation of Metals

Palladium (II) chloride solution and rhodium (III) nitrate solution were used as metal sources. For catalyst C1, Pd/Rh ratio was chosen as 6.5 and the metal percentages in total catalyst are 0.65 wt% and 0.1 wt% for Pd and Rh, respectively. For Pd-only catalyst C2, the ratio was kept the same as in C1 and Pd was used instead of Rh. Metal solutions were separately mixed in rotary evaporator with 1.2 times of water that can dissolve 1 g of support material. Then, the support sample was added to the mixture and the flask was immersed in the water bath at 80 °C while rotating under vacuum. When all the liquid evaporated, the flask was placed in an oven and the sample was dried at 150 °C for 12 h. The powder

sample was grounded and calcined in an oven under dry air at 550 °C for 1 h.

2.3. Preparation of Washcoating Slurry

Metal impregnated support material and gamma phase aluminum oxide ($\gamma\text{-Al}_2\text{O}_3$) were mixed in deionized water so as the total solid content of the slurry is 40 wt%. Also, pseudoboehmite was added to mixture as binder and after ball milling at 275 rpm for 30 min for homogenization, the washcoat was obtained.

2.4. Monolith Coating

Laboratory scale monoliths made of cordierites which are 22 mm in diameter and 13 mm in height and having 600 cells/in² were dipped into the washcoat and the excess slurry was blown out from the pores with dry air. The monolithic catalysts were obtained after drying at 150 °C for 12 h and calcination at 550 °C for 1 h.

2.5. Catalytic Activity Measurements

A dynamic test system constructed for simulating the operating conditions in automobiles was used for activity tests. Simulated exhaust gas composition (see Table 3) was passed through the monolithic catalyst placed inside the reactor.

During the test, Gas Hourly Space Velocity (GHSV) was 50000 h⁻¹ and O₂ was oscillated at 1 Hz frequency. The reactor was heated up to 600 °C with a rate of 5 °C/min and cooled by free convection. Analyses were performed by Mass Spectrometer and CO Analyzer.

Table 3: Concentration distribution of the simulated gas mixture

Gases	Concentration (ppm)
CO	1.00E+04
H ₂	2.30E+03
N ₂	5.76E+05
NO	1.50E+03
O ₂	7.67E+03
C ₃ H ₆	3.72E+02
C ₃ H ₈	1.24E+02
CO ₂	1.00E+05
SO ₂	2.00E+01

3. RESULTS AND DISCUSSION

Initially, fresh tests of the catalysts were performed. Since fresh tests may be misleading in terms of performance, the catalysts were aged at 900 °C and 1000 °C with dry air in order to simulate the long time exposure to high temperatures in the automobile exhaust.

The activities of the catalysts are compared in terms of their light-off (T50) temperatures. The light-off behaviors for conversions of CO, C₃H₆, H₂ and O₂ have typical “S” curve shapes (an example can be seen on Figure 1). However, the conversions of NO and C₃H₈ increase slowly as the temperature increases. T50 values of these components could not be read for some tests, but it does not mean poor catalytic activity.

For reporting, the T50 data of the cooling is step is chosen since the system becomes more stabilized after the heating step, therefore giving healthier data. The light-off temperatures for all tests are tabulated in Table 4 and comparative graphs for T50 values are given in Figure 2. For comparison, conversions of CO, NO, C₃H₆ and C₃H₈ are taken into account; other components such as H₂ and O₂ are not considered.

Table 4: Catalytic activity data of the catalysts C1, C2 and C3 after fresh and aged tests

	Species	T50 (°C)			Maximum Conversion (%)		
		C1	C2	C3	C1	C2	C3
<i>Fresh test</i>	CO	265	305	375	84.7	91.6	90.9
	NO	305	-	-	100	100	100
	C ₃ H ₆	267	295	356	100	100	99.5
	C ₃ H ₈	327	332	411	89	100	100
<i>Test after aging at 900 °C</i>	CO	244	221	396	97.7	95.7	97.9
	NO	299	348	-	94.4	100	89.3
	C ₃ H ₆	286	285	334	100	99.6	99.2
	C ₃ H ₈	306	340	400	90.7	100	99.8
<i>Test after aging at 1000 °C</i>	CO	304	236	382	97.5	99.7	98.6
	NO	251	-	-	100	88.4	100
	C ₃ H ₆	243	236	327	99.4	99.2	100
	C ₃ H ₈	324	363	-	92.9	100	91.6

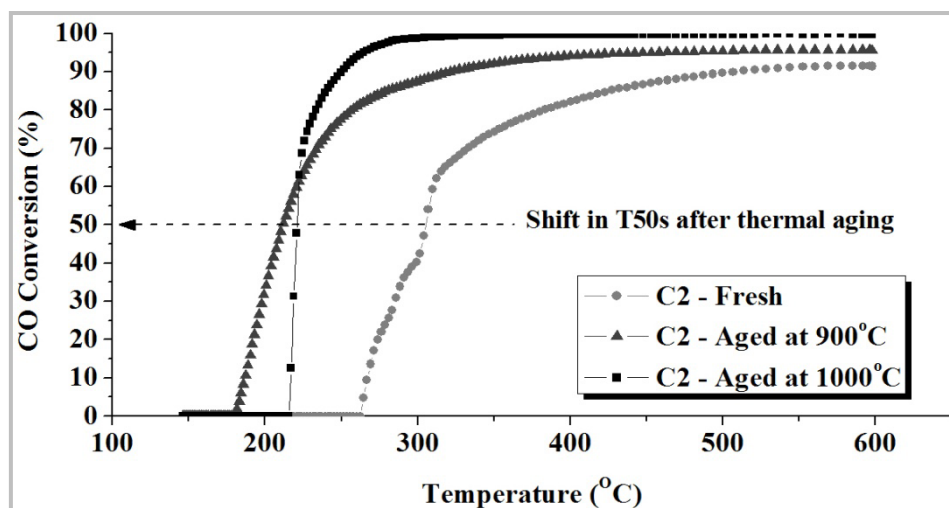


Figure 1: Conversion curves of CO in fresh and aged tests of the catalyst C2

Thermal deactivation is the major deactivation pathway for a TWC. Exposure to high temperatures results in sintering of the oxygen storage component and loss of its redox property [Fornasiero *et al.*, 2000]. Also, sintering and alloying of noble metals, metal-losses and metal-support interactions are other deactivation mechanisms caused by thermal aging [Granados *et al.*, 2006].

After aging the monolithic catalysts at 900°C and 1000°C, light-off temperatures merely changed for all catalysts, indicating that the activity was not lost. This result can be attributed to the

synthesis method in which the metals are separately impregnated on the support for catalysts C1 and C2. In this way, the chance of agglomeration and/or alloying of the metal particles are prevented up to a certain extent. Deactivation due to particle growth was not observed for catalyst C3 since the metal content is very low.

The activity of the catalyst C1 improved after aging at 900 °C for CO and C₃H₈ components, but their T50 values slightly increased after aging at 1000 °C. Since Rh is reduced at high temperatures, NO

conversion of C1 was enhanced after thermal treatment. The activity of the catalyst C2 for CO conversion improved after aging at 900 °C, but decreased slightly after 1000 °C (See Figure 1 for the shifts in T50s). C₃H₆ conversion of C2 was positively affected by thermal aging, and a similar profile was observed for C3. Comparisons for NO could not be made for the catalyst C2 and C3 since the T50 values could not be observed as their conversions proceeded over 50%, indicating a good activity. T50 values of the catalyst C3 are higher than the others'

as expected, yet its performance was not bad, considering its very low metal loading. C1 was expected to show a better activity profile than C2, since it has Rh in its composition which is similar to conventionally used TWC catalysts. However, the light-off temperatures of C1 and C2 are very close to each other in overall. Therefore, it is suggested that the replacement of Rh with Pd is possible, and even a catalyst with a very low Pd metal content can give sufficient catalytic activity

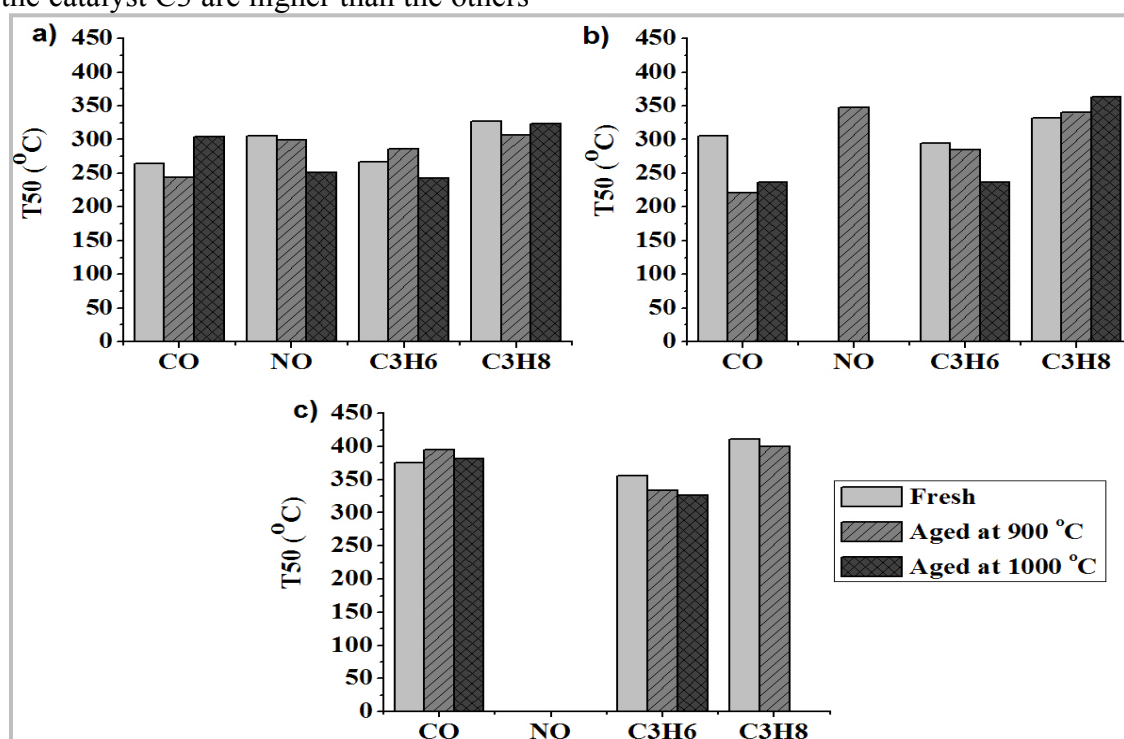


Figure 2: Light-off temperatures of CO, NO, C₃H₆ and C₃H₈ conversions by a) Catalyst C1 b) Catalyst C2 and c) Catalyst C3

4. CONCLUSION

In this study, effect of thermal aging and the role of metals on the catalytic activity were investigated. Catalyst C1 (0.65 wt% Pd + 0.1 wt % Rh on CZO) having a composition similar to the conventional catalysts was compared with Pd-only catalysts C2 (0.65 wt% Pd + 0.1 wt % Pd on CZO) and C3 (0.1 wt % Pd on CZO). Almost no activity loss was observed for

all catalysts after thermal aging. Light-off temperatures of C1 and C2 are virtually the same for all components which shows that the absence of Rh did not have a negative impact on the catalytic activity. In fact, using only Pd other than using Pd with Rh might be decreasing the chance of deactivation by alloying of these two metals. Furthermore, Pd-only catalyst C3 gave intriguing results. Despite its very low metal loading, C3 yielded

considerably good catalytic activity. Therefore, further research can be

performed on developing and optimizing the compositions of Pd-only catalysts.

Acknowledgements: The authors acknowledge the grant (Project No: 111M777) provided by TUBITAK (The Scientific and Technological Research Council of Turkey).

REFERENCES

- Farrauto, R. J., Heck, and R. M., 1999. Catalytic Converters: state of the art and perspectives *Catalysis Today*, Volume 51, 351.
- Fornasiero, P., Monte, R. D., Montini, T., Kaspar, J., and Graziani M., 2000. Thermal Stability and Oxygen Storage Capacity of Noble Metal/Ceria-Zirconia Catalysts for the Automotive Converters with the On-Board-Diagnostics (OBD), *Studies in Surface Science and Catalysis*, Volume 130, 1355.
- Gandhi, H. S., Graham, G. W., and McCabe, R. W., 2003. Automotive Exhaust Catalysis, *Journal of Catalysis*, Volume 216, 433
- Granados, M. L., Galisteo, F. C., Mariscal, R., Alifanti, M., Gurbani, A., Fierro, J. L. G., and Fernandez-Ruiz, R., 2005. Modification of a three-way catalyst washcoat by aging: A study along the longitudinal axis, *Applied Surface Science*, Volume 252, 8442
- Kaspar, J., Fornasiero, P., and Hickey, N., 2003. Automotive catalytic converters: current status and some perspectives, *Catalysis Today*, Volume 77, 419
- Matsumoto, S., Recent advances in automobile exhaust catalysts, 2004. *Catalysis Today*, Volume 90, 183
- Noh, J., Yang, O., Kim, D. H., and Woo, S. I., 1999. Characteristics of the Pd-only three-way catalysts prepared by sol-gel method, *Catalysis Today*, Volume 53, 575
- Shinjoh, H., 2006. Rare earth metals for automotive exhaust catalysts, *Journal of Alloys and Compounds*, Volume 408, 106

PHOTOCATALYTIC ACTIVITIES OF ZnO AND Pd-ZnO DOPED BY BOROHYDRIDE REDUCTION METHOD

Nuray Güy^{1,a}, Mahmut Özacar¹

1. Department of Chemistry, Art and Science Faculty, Sakarya University, 54187, Sakarya, Turkey

a. Corresponding author (nurayg@sakarya.edu.tr)

ABSTRACT: In the present study, ZnO was synthesized by a simple and fast microwave assisted method. The Pd-doped on ZnO nano photocatalyst was carried out by borohydride reduction method. The Pd-doped and undoped ZnO nano photocatalysts were characterized by X-ray diffraction (XRD), scanning electron microscope (SEM) and energy dispersive spectroscopy (EDS). Afterwards, the photocatalytic activities of the produced ZnO and Pd-ZnO were investigated using Basic Blue 17 (Toluidine Blue) photodegradation with UV lamp irradiation.

1. INTRODUCTION

The dye pollution caused by textile wastewaters is one of the most important sources of environmental contamination. The removal of dyes from aqueous effluents is of significant environmental, technical, and commercial importance [Özacar and Sengil, 2005a and b]. These dyes, which many of them are azo compounds that can be effectively removed by photocatalysis. Photocatalysis has received intensive attention because of its potential ability for eliminating the dyes in water and wastewater without causing secondary pollution. Semiconductor materials as photocatalysts have been extensively used for the photocatalytic degradation of dyes [Chen *et al.*, 2008]. Zinc oxide is a wide band gap (3.37 eV at room temperature) semiconductor with large exciton binding energy of 60 meV [Phuruangrat *et al.*, 2009]. ZnO-based photocatalysts have attracted much attention because of its excellent properties, such as high chemical stabilizations, nontoxicity, and abundance in nature [Zhong *et al.*, 2012]. Different ZnO nanostructure materials have been prepared by many methods such as microwave heating, chemical-precipitation, sol-gel process, gas condensation, hydrothermal process and

hydrolysis in polyol medium [Krishnakumar *et al.*, 2009]. Among all of synthesis methods, microwave microwave-assisted synthesis has attracted much attention because it has advantages of being faster, simpler and more energy efficient. The photocatalytic performance of ZnO can be improved by various techniques. Doped of ZnO by noble metals is an effective method to promote the photocatalytic performance [Zhong *et al.*, 2012].

The aim of this study is to investigate the effect of Pd-doped on the photocatalytic activity of nano ZnO prepared by borohydride reduction method using Basic Blue 17 (Toluidine Blue, BB17) photodegradation with UV light irradiation.

2. EXPERIMENTAL

2.1. Materials

Zinc chloride (ZnCl₂, Merck), sodium hydroxide (NaOH, Merck), palladium chloride (PdCl₂, Alfa-Aesar), sodium borohydride (NaBH₄, Merck), Basic Blue 17 (BB17) (commercial grade), and ethanol (Merck) were purchased and used without further purification. All compounds except BB17 were reagent

grade. Deionized water was used throughout the entire experiments.

2.2 Preparation of Photocatalyst

The ZnO powder was prepared by microwave-assisted heating process. The preparation method of undoped ZnO powders is as follows: 0.50 g of ZnCl₂ was dissolved in 10 mL of distilled water then 10 mL 0.80 g of NaOH solution was slowly added dropwise into the solution and stirred for 1 h to obtain a well-dissolved solution. The mixture was heated to 100 °C in a microwave oven with a controlled power of 700 W for 5 min and then cooled at room temperature naturally. The precipitate was centrifuged, washed with distilled water and absolute ethanol several times, and then dried in an oven at 60 °C for 24 hours.

For the preparation of doped ZnO powders is follows: 100 mg of ZnO prepared by microwave method was dispersed in 40 mL of distilled water. Desired PdCl₂ solution was added into the above solution to obtain weight ratio of Pd/ZnO is %5. Then 0.0175 M 10 mL sodium borohydride solution as a reducing agent was added dropwise to the mixture and stirred for 1 h at room temperature. The dark grey precipitate was separated by centrifugation and washed distilled water and absolute ethanol several times, and then dried in an oven at 60 °C for 24 hours.

2.3. Characterization of Photocatalysts

The obtained samples were confirmed by powder X-ray diffraction (XRD, RIGAKU D max 2200 X-ray diffractometer with Cu KR (λ) 0.154 nm radiation) in the 2θ angles ranging from 10 to 90. The morphologies of Pd-doped and undoped ZnO nano photocatalysts were characterized by using a scanning electron microscope (SEM, JEOL JSM-6060 LV operated at 20 kV). The surface

composition of the samples were identified with energy dispersive spectroscopy (EDS). Shimadzu UV-2401PC spectrophotometer was used to measure the absorbance of BB17 solution.

2.4. Photocatalytic Testing

Photocatalytic activities of the synthesized photocatalysts were investigated by measuring the degradation of Basic Blue 17 (BB17) in aqueous solution under UV light irradiation. The molecular structure of the BB17 is given in Fig. 1. For each experiment, 50 mg of photocatalyst was dispersed in 100 mL of 16 mg/L of the BB17 aqueous solution. Prior to UV irradiation, the suspensions were magnetically stirred in the dark for 30 min to ensure establishment of adsorption/desorption equilibrium of BB17 on surfaces of the photocatalysts in the aqueous solutions. 5 mL of the aliquots were sampled at predetermined time intervals, centrifuged and analyzed by recording variations in the absorption band (664 nm) in the UV-Vis spectra of BB17.

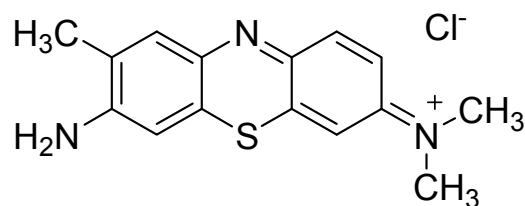


Figure 1: The chemical structure of BB17.

3. RESULTS AND DISCUSSION

3.1. Characterization of Photocatalysts

Figure 2 illustrates the XRD patterns of ZnO and Pd-doped ZnO powders. As shown in Fig. 2, all strong peaks can be indexed as the pure hexagonal phase of

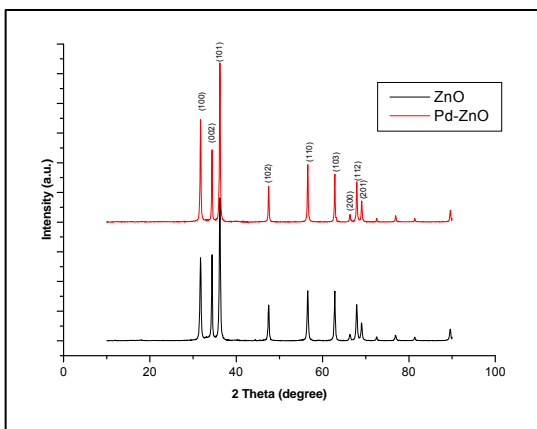


Figure 2: XRD patterns of Pd-doped and undoped ZnO nano photocatalysts.

wurtzite-type ZnO, which agrees well with the reported data (JCPDS No. 79-0206). Comparing with the diffraction peaks of pure ZnO and Pd-doped ZnO samples, no characteristic peaks of dopant Pd metal impurities and other phases such as $Zn(OH)_2$ and PdO are observed. The absence of diffraction lines of Pd phases on the ZnO photocatalyst suggests that the doped Pd did not form large particles but were highly dispersed in the micropores of the ZnO structure or the size of Pd crystallites were too small to be detected [Zhong *et al.*, 2012].

The morphology of the samples was characterized by SEM. Figure 3(a)–(b) shows the SEM images of undoped ZnO and Pd-doped ZnO. As can be seen from Figure 3(a) and 3(b), the morphologies of undoped ZnO and Pd-doped ZnO are irregular nanoplates. The images also suggest that Pd doping in ZnO does not change the plate morphology evidently. To determine the surface composition of the Pd-doped ZnO was used to EDS analysis technique and the result is given in Figure 4. EDS measurements show that Pd content in the nanoplates is about 5.1 %. The EDS results are semiquantitative because the EDS spectra were acquired from rough-surfaced, as-grown aggregates.

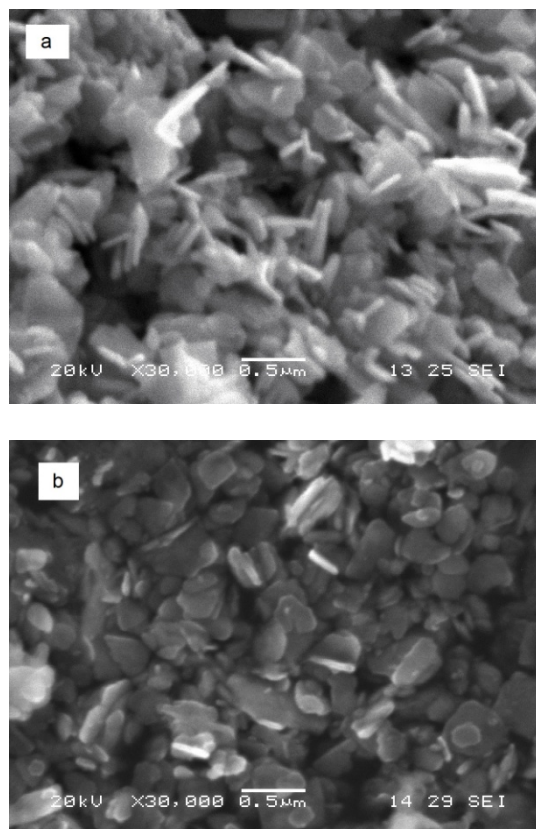


Figure 3: SEM images of: (a)Undoped ZnO, (b)Pd-doped ZnO.

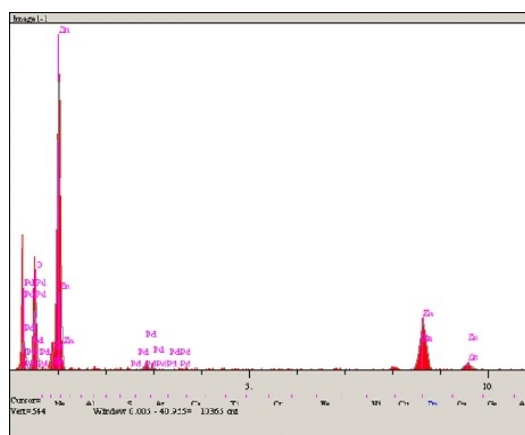


Figure 4: EDS image of Pd-doped ZnO.

3.2. Photocatalytic Activity

The photocatalytic activities of the undoped ZnO and Pd-doped ZnO photocatalysts were evaluated by the degradation of BB17 under UV irradiation. Figure 5 shows the results of photocatalytic degradation of BB17 using undoped ZnO and Pd-doped ZnO

photocatalysts, C_0 and C represent the initial concentration after the adsorption-desorption equilibrium for 30 minute and at the reaction time t concentration of BB17, respectively. As can be seen, Pd-doped ZnO photocatalyst exhibit better photocatalytic activity than undoped ZnO. Upon irradiation of ZnO by UV light energy of higher or equal than its band gap energy, the electron is excited from the valence band (VB) to the conduction band (CB), generating an electron/hole (e^-/h^+) pair. The (e^-/h^+) pair leads formation hydroxyl radicals ($\cdot\text{OH}$), superoxide radical anions ($\cdot\text{O}_2^-$) and hydroperoxyl radicals ($\text{HOO}\cdot$), these radicals are the oxidizing species in the photocatalytic oxidation processes. The hydroxyl radical is one of the most powerful oxidizing species and then attack organic compounds present at or near the surface of the photocatalysts.

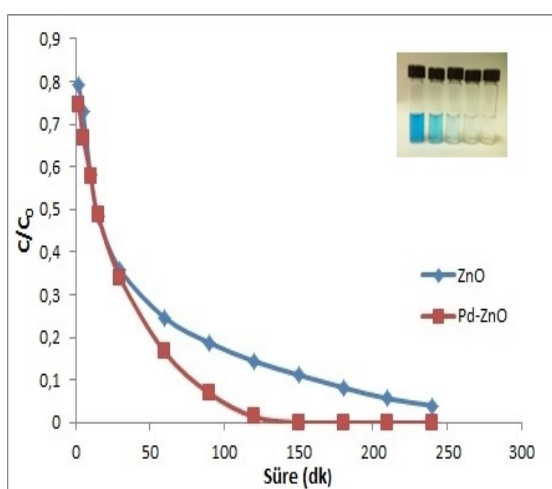


Figure 5: The photodegradation of BB 17 by the undoped ZnO and Pd-doped ZnO.

The positive effect of Pd deposits is commonly due to the fact that Pd nanoparticles on the semiconductor surface behave like electron sinks, which provide sites for the accumulation of photogenerated electrons, and then improve the separation of photogenerated electrons and holes. The photoexcited electrons on the CB under UV

irradiations can transfer from ZnO to Pd nanoparticles. Therefore, Pd nanoparticle reduces the recombination of photoinduced electrons and holes and prolongs the lifetime of the electron-hole pairs. Subsequently, the electrons can be captured by the adsorbed O_2 , and the holes can be trapped by the surface hydroxyl radical species ($\cdot\text{OH}$). It is accepted that hydroxyl radical species show little selectivity for attacking dye molecules and are able to oxidize the pollutants due to their high oxidative capacity. Therefore Pd-doped ZnO shows better photocatalytic activity for BB17 degradation due to increasing the lifetime of the electron-hole pairs [Chang *et al.*, 2009, Lu *et al.*, 2008].

4. CONCLUSIONS

In summary, ZnO nanoplates were successfully synthesized via a simple microwave-assisted hydrothermal method. The Pd-doped on ZnO nano photocatalyst was carried out by borohydride reduction method. The obtained samples were characterized by XRD, SEM and EDS. The photocatalytic activity investigation was carried out by performing the degradation of BB17 dye under UV light over as-synthesized undoped ZnO and Pd-doped ZnO photocatalysts. Pd-doped ZnO photocatalyst exhibits better dye degradation efficiency than undoped ZnO. Pd-doped ZnO completely degrades the BB17 dye at 120 min, while ZnO degrades 95% of BB17 at 240 min. The presence of palladium increases the surface hydroxyl contents of ZnO and promotes the separation of photoinduced electron-hole pairs to form more active hydroxyl radicals, and then enhances the photocatalytic activity of ZnO.

Acknowledgements: The authors acknowledge the support of the TUBA and OYP.

REFERENCES

- Chang, Y., Xu, J., Zhang, Y., Ma, S., Xin, L., Zhu, L., and Xu, C., 2009. Optical Properties and Photocatalytic Performances of Pd Modified ZnO Samples, *J. Phys. Chem.*, 113, 18761.
- Chen, C., Wang, Z., Ruan, S., Zou, B., Zhao, M., Wu, F., 2008. Photocatalytic degradation of C.I. acid orange 52 in the presence of Zn-doped TiO₂ prepared by a stearic acid gel method. *Dyes Pigments* 77, 204.
- Krishnakumar, T., Jayaprakash, R., Pinna, N., Singh, V.N., Mehta, B.R., and Phani, A.R., 2009. Microwave-assisted synthesis and characterization of flower shaped zinc oxide nanostructures, *Materials Letters* 63, 242–245.
- Lu, W. Gao, S. and Wang, J., 2008. One-Pot Synthesis of Ag/ZnO Self-Assembled 3D Hollow Microspheres with Enhanced Photocatalytic Performance, *J. Phys. Chem. C*, 112, 16792.
- Ozacar, M., Sengil, I.A., 2005a. A kinetic study of metal complex dye sorption onto pine sawdust, *Process Biochemistry* 40, 565.
- Ozacar, M., Sengil, I.A., 2005b. Adsorption of metal complex dye from aqueous solutions by pine sawdust, *Bioresource Technology* 96, 791.
- Phuruangrat A., Thongtem T., and Thongtem, S., 2009. Microwave-assisted synthesis of ZnO nanostructure flowers, *Materials Letters* 63, 1224.
- Zhong, J.B., Li, J.Z., He, X.Y., Zeng, J., Lu, Y., Hu, W., and Lin, K., 2012. Improved photocatalytic performance of Pd-doped ZnO, *Current Applied Physics*, 12, 998.

USE OF METAL DOPED ZSM-5 ZEOLITE CATALYSTS IN METHYLATION OF 2-METHYLNAPHTHALENE

ÜmitSerdar Erol¹, Mustafa Güllü²and Ali Karaduman^{1,a}

1. Ankara University, Faculty of Engineering, Chemical Engineering, Ankara, Turkey

2. Ankara University, Faculty of Science, Chemistry, Ankara, Turkey

a. Corresponding author (karaduman@ankara.edu.tr)

ABSTRACT:2,6-Dimethylnaphthalene (2,6-DMN) is produced with methylation of 2-methylnaphthalene (2-MN). 2,6-Dimethylnaphthalene (2,6-DMN) is a significant compound for polyethylene naphthalate (PEN) which is new polyester. When compared with polyethylene terephthalate (PET), PEN has better qualities. For production of 2,6-Dimethylnaphthalene various medium and large-pore zeolite catalysts can be used in the fixed-bed flow reactors. The main question of 2,6-DMN production is to develop a catalyst with high selectivity to 2,6-DMN at acceptable conversion of 2-MN. One of these zeolites which is commonly used as catalyst catalysts is ZSM-5. In this work, the methylation of 2-MN over Ni, Fe and Pd doped ZSM-5 zeolite catalysts were investigated. 2-MN, methanol and 1,3,5-trimethylbenzene mixture (1:5:5 molar ratio) were fed into a fixed-bed flow reactor in all experiments. Effects of temperature and weight hourly space velocity (WHSV) on 2-MN conversion were examined. The experiments were carried out at a temperature ranging from 200 to 450 °C and WHSV ranging from 1 to 3 h⁻¹. The liquid products were analyzed using the GC-MS in MSD (Mass Selective Detector) with Rxt-5 MS Column.

1. INTRODUCTION

2,6-Dimethylnaphthalene (2,6-DMN) is an important chemical as a precursor of 2,6-naphthalenedicarboxylic acid which is a monomer for polyethylene naphthalate (PEN). PEN is a new and a very significant material for polymer industry [Liang *et al.*, 2010]. PEN has superior qualities than polyethylene terephthalate (PET) such as lower oxygen permeability, thermal shrinkage, oligomer extraction and higher resistance to radiation, hydrolytic resistance and glass transition temperature [Park *et al.*, 2002].

In the preceding studies made by different researchers they also used zeolites which were modified with different transition metals such as Fe and Pt. By this way conversion of 2-MN and selectivity of 2,6-DMN were increased [Song, 2007].

As seen in Figure 1 polyethylene naphthalate is produced with condensation polymerization of ethylene glycol and 2,6-naphthalene dicarboxylic acid (2,6-NDCA) [Liang and Schobert, 2010]. 2,6-NDCA can be synthesized by oxidation of 2,6-DMN. 2,6-DMN has been produced via methylation of 2-MN over zeolites which have different pore sizes and surface areas such as ZSM-5, ZSM-11, ZSM-12, Y, mordenite, MCM-22 and Beta in a fixed-bed flow reactor [Song, 1998]. In these studies there are two main difficulties. First is reaching an acceptable conversion of 2-MN and second is high selectivity of 2,6-DMN. Because of the formation of other unaccepted DMNs such as 2,7-DMN, 2,3-DMN and 1,8-DMN selectivity of 2,6-DMN is low [Song *et al.*, 2007].

There are lots of works in the literature related to production of 2,6-DMN [Lin *et*

al., 2010]. These works concentrate on different production methods such as methylation, transalkylation and disproportionation [Zhang *et al.*, 2010]. In

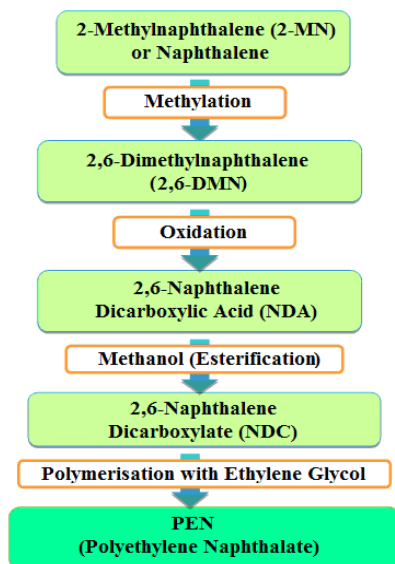


Figure 1: The manufacture steps of PEN

this work, production of 2,6-DMN via methylation of 2-MN with methanol over metal doped ZSM-5 zeolite in a fixed-bed flow reactor was studied.

2. EXPERIMENTAL

2.1. Samples of Catalyst

ZSM-5 zeolite pellets (Surface area=400 m²/g and SiO₂/Al₂O₃=280) were supplied from Zeolyst. First the pellets were cation exchanged, calcined and metal atoms were doped over them. Metal atoms were doped through impregnation method [Guo *et al.*, 2004]. According to this method in the first step 0.202 g of Fe(NO₃)₃.9H₂O were dissolved in pure water and added into 1.821 g of pellets. This mixture was kept in atmospheric conditions for 24 hour, dried in 200 °C and calcined. All metal containing pellets were prepared same way and labeled as seen in Table 1.

Table 1: Descriptions and codes of the catalysts prepared with impregnation method

Catalyst Description	Catalyst Code
ZSM5 Zeolite pellets	Z5
ZSM5 Zeolite pellets containing 10 % Fe by weight	10FEZ5
ZSM5 Zeolite pellets containing 10 % Ni by weight	10NIZ5
ZSM5 Zeolite pellets containing 0.1 % Pd by weight	01PDZ5

2.2. Characterization

Characterization of metal modified catalysts was carried out by using ZEISS EVO 40 scanning electron microscope which has four different (SE, BSE, EDX and VPSE) detectors and wolfram filament electron source. Besides images of the pellets mapping analyze was performed.

2.3. Catalytic Reaction

Catalytic tests were carried out in an experimental set-up which basically consisted of a high pressure liquid pump, nitrogen tube, flowmeter, specially designed a fixed-bed flow reactor surrounded by a furnace with a temperature controller, a condenser, phase separator.

The reactant mixture of 2-MN, methanol and 1,3,5-trimethyl benzene (TMB) (Sigma Aldrich) was injected by a high pressure liquid pump into the tubular reactor, in the middle of which 2 ml of catalyst in the form of pellets were charged. Before the experiments, for activation the catalyst samples were heated in the reactor under N₂ atmosphere (1.5 ml/min) to 500 °C and kept at this

temperature for 30 minutes. Then the temperature was decreased to the value for which the experiment was performed. The reaction products were condensed by ethylene glycol which circulated in the jacket at -10 °C . For all experiments four samples were taken with one hour intervals. Liquid products were analyzed by using ThermoFinnigan GC-MS which has MS detector and Zebtron (ZB-1MS) column (60 m x 0.25 mm). The injector, MS transfer line and ion source were kept at 280 °C, 300 °C and 230 °C, respectively. Under 0.7 ml/min He flow, the oven initial temperature was 95 °C then increased to 125 °C with 1 °C/min rate, from 125 °C to 200 °C with a rate of 5 °C/min and from 200 °C to 230 °C with a rate of 20 °C/min. Split ratio was 70. The conversion of 2-MN was calculated as follows:

$$\% \text{ Conversion of 2-MN} = \frac{(m_0 - m)}{m_0} \times 100$$

where m_0 is 2-MN mass in the feed and m is 2-MN mass in the liquid product.

3. RESULTS AND DISCUSSION

3.1. Characterization of the Metal Impregnated ZSM-5Zeolite Pellets

Fig. 2, 3 and 4 represent the SEM images of Fe, Ni and Pd modified ZSM-5 zeolite catalysts, respectively. From these images content of the catalyst and elemental dispersion of metal atoms inside the catalyst can be seen. In these images Si, Al and O come from the zeolite itself. Fe, Ni and Pd images shows that metal atoms are homogeneously impregnated to the zeolite catalyst.

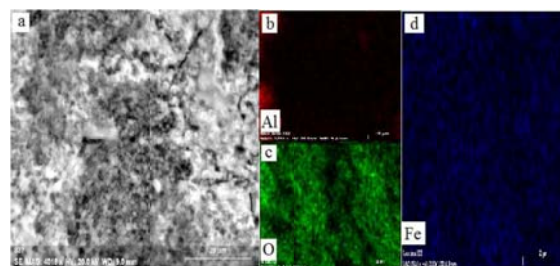


Figure 2: SEM images of 10FEZ5 and mapping results of elemental dispersion.

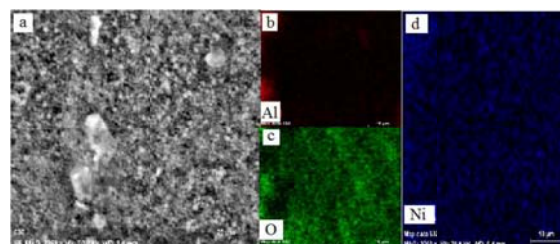


Figure 3: SEM images of 10NIZ5 and mapping results of elemental dispersion.

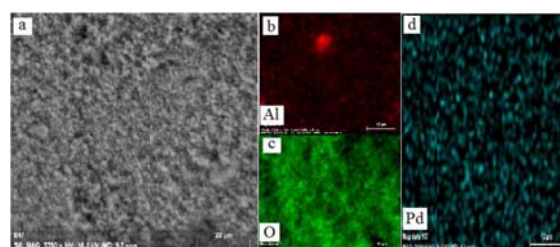


Figure 4: SEM images of 01PDZ5 and mapping results of elemental dispersion.

3.2. 2,6-DMN Synthesis over Modified ZSM-5Zeolite

Results that are given in Table 2-5 were obtained by GC-MS analysis of the liquid products. According to these results as seen in Fig. 5 2-MN conversion always changed from catalyst to catalyst for the same temperature and WHSV.

Table 2: Mass percentages of the MNs and DMNs synthesized with Z5

Compound	WHSV=1 h ⁻¹
	450 °C
2-MN	12.04
1-MN	4.68
2,6-DMN	2.18
2,7-DMN	1.24
1,4-DMN	-
1,6-DMN	4.55
1,2-DMN	0.99
2,3-DMN	1.86
1,8-DMN	1.46
unknown	-

Table 3: Mass percentages of the MNs and DMNs synthesized with 10FEZ5

Compound	WHSV=1 h ⁻¹
	450 °C
2-MN	7.00
1-MN	0.29
2,6-DMN	0.83
2,7-DMN	0.11
1,4-DMN	0.88
1,6-DMN	0.58
1,2-DMN	0.29
2,3-DMN	0.25
1,8-DMN	0.44
unknown	6.81

Table 4: Mass percentages of the MNs and DMNs synthesized with 10NIZ5

Compound	WHSV=1 h ⁻¹
	450 °C
2-MN	30.59
1-MN	0.85
2,6-DMN	0.56
2,7-DMN	0.47
1,4-DMN	0.66
1,6-DMN	0.26
1,2-DMN	0.25
2,3-DMN	0.31
1,8-DMN	0.02
unknown	-

On the other hand it is understood from Figure 6 that it is not possible to give a specific temperature and a catalyst in which 2,6-DMN/2,7-DMN value was the highest level. As seen in Fig. 7 2,6-DMN and other DMNs concentration increased with temperature whereas product composition did not change importantly with WHSV. For the catalyst which was modified with Fe, for 450 °C temperature and WHSV = 1 h⁻¹, 2,6-DMN concentration was at the highest level.

Table 5: Mass percentages of the MNs and DMNs synthesized with 01PDZ5

Compound	WHSV=1 h ⁻¹
	450 °C
2-MN	10.80
1-MN	2.23
2,6-DMN	1.57
2,7-DMN	1.58
1,4-DMN	1.15
1,6-DMN	1.79
1,2-DMN	0.64
2,3-DMN	1.03
1,8-DMN	0.46
unknown	2.83

and DMNs synthesized with 01PDZ5

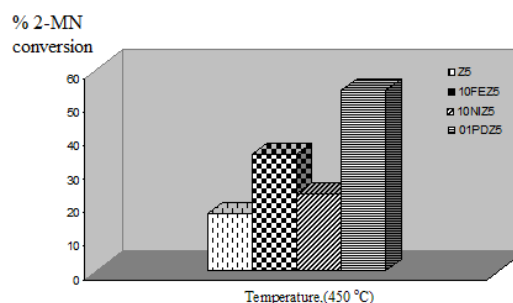


Figure 5: % mass conversion of 2-MN with temperature for WHSV = 1 h⁻¹

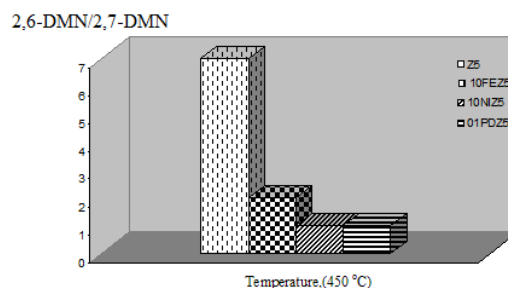


Figure 6: Change of 2,6-DMN / 2,7-DMN values with temperature for WHSV = 1 h⁻¹

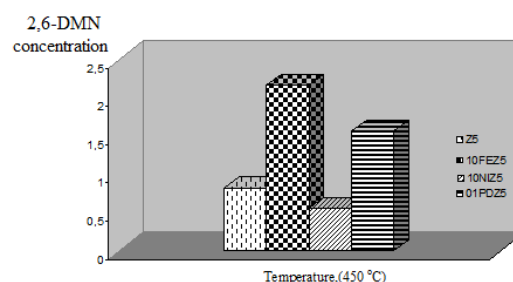


Figure 7: Mass percentage of 2,6-DMN in the liquid products for WHSV = 1 h⁻¹.

4. CONCLUSIONS

Synthesis of 2,6-DMN with methylation of 2-MN over metal doped ZSM-5 zeolite catalyst was carried out in this work. First metal containing catalyst pellets were prepared by impregnation method. SEM images reveals how the metal atoms homogeneously dispersed over catalyst pellets. With these catalysts, synthesis of 2,6-DMN from 2-MN and methanol was achieved. While analyzing liquid product first 2,6-DMN and 2,7-DMN were successfully separated from each other. For this purpose a longer GC-MS column was used. Analyze results revealed that besides 2,6-DMN other DMNs were synthesized. And synthesis of them increased with temperature. Analyze results showed that at 200 °C some of the DMNs were not synthesized. At the end of the study it is understood that from all aspects Fe modified ZSM-5 zeolite is the most suitable catalyst among the catalyst which were tested in this work.

Acknowledgement

This work is supported by The Scientific and Technological Research Council of Turkey (TÜBİTAK). We are thankful and gratefully appreciate TÜBİTAK for this support (Project Number: 112M297).

REFERENCES

- Guo, X., Shen, J., Sun, L., Song, C., Wang, X., 2004, Effects of SiO₂/Al₂O₃, MgO Modification and Hydrothermal Treatment on the Catalytic activity of HZSM-5 Zeolites in the methylation of 4-Methylbiphenyl with Methanol, *Applied Catalysis A: General*, 261(11), 183
- Inui, T., Pu, S.B., Kugai, J.I., 1996, Selective neutralization of acid sites on the external surface of H-ZSM-5 crystallites by a mechanochemical method for methylation of methylnaphthalene, *Appl. Catal. A Gen.*, 146(2), 285.
- Liang, Z., Xinmen, G., Min, L., Xiangsheng, W., Chunshan, S., 2010, Methylation of 2-Methylnaphthalene with Methanol over NH₄F and Pt Modified HZSM-5 Catalysts, *Chinese Journal of Chemical Engineering*, 18(5), 742.
- Lin, L., Fang, Y., Hu, H., 2006, Selective Synthesis of 2,6-Dimethylnaphthalene by Methylation of 2-Methylnaphthalene with Methanol on Zr/(Al)ZSM-5, *Catalysis Communications*, 7(11), 255.
- Park, J., Wang, J., Lee, C., Park, S., 2002, Methylation of Naphthalene with Methanol over Beta, Mordenite, ZSM-12 and MCM-22 Zeolite Catalysts, *Bull. Korean Chemical Society*, 23(7), 1011.
- Song, C.S., 2000, Shape-selective isopropylation of naphthalene over H-mordenite catalysts for environmentally friendly synthesis of 2,6-dialkylnaphthalene, *C. R. Acad. Sci. Paris IIcChimie*, 3(8), 477.
- Song, C.S., Schobert, H.H., 1996, Non-fuel uses of coals and synthesis of chemicals and materials, *Fuel*, 75(6), 724.
- Song, C.S., 1998, Recent advance in shape-selective catalysis over zeolites for synthesis of specialty chemicals, *Stud. Surf. Sci. Catal.*, 113(7), 163.
- Song, C.S., Shen, J.P., Reddy, K.M., Sun, L., Lillwitz, L.D., 2007, Shape selective Fe-MFI catalyst for synthesis of 2,6-dimethylnaphthalene by methylation with methanol, *Stud. Surf. Sci. Catal.*, 170(13), 1275.
- Zhang, C., Guo, X., Song, C., Zhao, S., Wang, X., 2010, Effects of Steam and TEOS Modification on HZSM-5 Zeolite for 2,6-Dimethylnaphthalene Synthesis by Methylation of 2-Methylnaphthalene with Methanol, *Catalysis Today*, 149(7), 196.

SODIUM BOROHYDRIDE HYDROLYSIS FOR HYDROGEN PRODUCTION OVER A HIGHLY EFFICIENT Co-B/PANI CATALYST

Ferhat Baydaroglu¹, Aydin Hasimoğlu¹, Ercan Özdemir^{2,a}

1. Gebze Institute of Technology, Department of Chemistry, 41400, Kocaeli, Turkey

2. Gebze Institute of Technology, Clean Energy & Nanotechnology Research Center
41400, Kocaeli, Turkey

a. Corresponding author (e.ozdemir@gyte.edu.tr)

ABSTRACT: The objective of the present study was to develop an efficient catalyst for hydrolysis of NaBH₄. In this research, unsupported and polyaniline supported cobalt boride catalysts were synthesized using reduction-precipitation method for hydrogen generation from sodium borohydride stabilized in 10% (w/w) of NaOH solution. According to experimental results, polyaniline supported cobalt boride catalyst showed better performance than that of unsupported one. The influences of NaOH concentration (1-20 wt%), NaBH₄ concentration (1-20 wt%) and reaction temperature (20-50 °C) on the performance of the catalysts were examined. Structural and morphological properties of the catalysts were investigated. The results show that PANI supported cobalt catalysts can be used in a hydrogen generator for mobile applications due to their high catalytic activity.

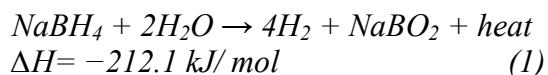
1. INTRODUCTION

Proton exchange fuel cells (PEM-FCs) are promising systems for the efficient utilization of hydrogen as fuel. Furthermore, hydrogen and PEM-FCs seem to be ideal to replace the petroleum and internal combustion engine to decrease the negative effects of fossil fuels such as decreasing CO₂ which is the basic greenhouse effect gas [Muir and Yao, 2011]. However, hydrogen storage is still an important challenge that must be overcome for effective use of hydrogen and development of hydrogen economy.

Hydrogen can be kept as pressurized gas, cryogenic liquid and solid fuel such as hydrides, carbon materials. Each of them has different advantages and disadvantages [Billur *et al.*, 2007]. Storage of hydrogen as cryogenic liquid (below -252.87 °C) is good for high energy densities but huge amount of energy is needed for both liquefaction and storage processes. What's more, a

refrigeration unit is required to keep hydrogen at cryogenic state thus adding cost and weight [Trudeau, 1999]. High-pressure storage of hydrogen gas is limited by the weight of the keeping tanks, possible leakage and safety issues. Another option is to use the chemical hydrides as a pure hydrogen source upon decomposition for PEM-FCs [Zhou, 2005]. Especially, sodium borohydride (NaBH₄) is the most remarkable one due to its high hydrogen storage capacity (10.8 wt%), long stability in basic media, non-flammability of NaBH₄ solutions, easy control of H₂ generation in the presence of heterogeneous catalysts, hydrogen generation even at low temperatures, and environmentally friendly and recyclable by-product, borax [Amendola *et al.*, 2000; Patel *et al.*, 2008].

The exothermic hydrolysis reaction occurs according to the Eq.(1) to give 4 moles hydrogen using catalyst [Baydaroglu *et al.*, 2013].



Many researchers investigated the hydrolysis of sodium borohydride using the homogeneous (organic or inorganic acids) and heterogeneous catalysts. However, utilization of acids is limited due to the difficulty in reaction control. Nowadays, noble and transition metal catalysts are widely studied. Among them, cobalt boride catalyst is a promising candidate because of its relatively higher activity and lower cost [Jeong *et al.*, 2007, Delmas *et al.*, 2011]. It is a well-known fact that supported catalysts show much higher catalytic activities compared to unsupported powdered ones due to preventing the agglomeration which results in lower active surface area and catalytic activity (10). High surface area, porous structures such as metal oxides (SiO₂, Al₂O₃, etc), carbon structures (carbon black, carbon nanotubes) or polymeric materials with functional groups (especially amine group due to its anchoring effect) (Yan *et al.*, 2010) can be used as supporting material.

In this work, polyaniline was selected as a support material because of its cheap starting material (aniline), high environmental stability, non-solubility in most of the solvents and good thermal stability. In addition, the amino group in the main chain of PANI can provide a strong interaction between active material and PANI, which make it attractive material as support [Hangjun *et al.*, 2009]. In the present study, we focused on the preparation of Co-B/PANI catalysts and determination of hydrogen generation performance from alkali sodium borohydride solution under different working conditions.

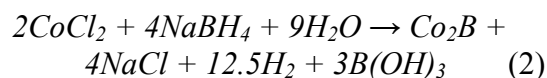
2. EXPERIMENTAL

2.1. Materials

All chemicals were analytical grade and used without further purification. Polyanniline was purchased from Alfa Aesar. Isopropanol (%99.5) and sodium borohydride (NaBH₄, %98) were supplied from Merck. Cobalt (II) chloride hexahydrate (CoCl₂.6H₂O, %99.9) was purchased from Alfa Aesar. Methanol (CH₃OH, min %99.9) was purchased from Sigma-Aldrich. Ultrapure water from a Sartorius Arium UV ultra-purification system having resistivity 18.2 MW-cm was used in catalyst preparation.

2.2. Preparation of the Co-B Catalysts

Unsupported cobalt boride catalyst was synthesized by reduction of CoCl₂ with 1 M NaBH₄ according to the following reaction;



In the preparation of supported catalysts, a required amount of PANI was suspended in solvent mixture of methanol, ultrapure water and isopropanol under stirring, and treated with ultrasonic probe for 5 minutes. The mixture was cooled. Afterwards, excess amount of NaBH₄ was added to cooled mixture and stirred mightily for a minute. Meanwhile, a required volume of CoCl₂ solution was diluted with ultrapure water. Subsequently, the suspension was poured at once into the diluted CoCl₂ solution while it was stirring vigorously. Finally, the resulting catalysts were separated by centrifugation, washed with ultra-pure water and dried at 70 °C for 5 h in a vacuum oven.

2.3. Catalytic Activity Testing

A definite amount of catalyst was placed in to the reactor. Then, aqueous solution of NaBH₄ was fed into the reactor

immediately. Hydrogen generation was started in a temperature controlled reactor equipped with magnetic stirrer at 700 rpm for all experiments. During the experiments hydrogen volume was measured as a function of time using gas burette.

3. RESULTS AND DISCUSSION

The hydrolysis of NaBH_4 was carried out at various temperatures ranging from 20 to 50 °C using 125 mg of PANI supported Co-B catalyst containing 4 wt.% Co under standard conditions: 10 mL of 10 wt.% NaBH_4 stabilized with 5 wt.% NaOH. It can be seen from Fig. 1a, hydrogen production volume increased sharply as the temperature increased gradually from 20 to 50 °C. All synthesized catalysts had favorable catalytic stability during the long-term hydrolysis reaction and the visual examination of HG plots show that data points fall approximately along a straight line, indicating no certain deactivation of the catalysts and also suggesting the zero order of the reaction kinetics.

The effect of the NaBH_4 concentration, varying from 1 to 20 wt.%, on the HG was investigated, while reaction temperature and NaOH concentration remained 40 °C and 5 wt.%, respectively. From Fig. 1.b one can see that the hydrogen generation rate increased as the NaBH_4 concentration was increased, though this enhancement was limited to NaBH_4 concentration of 10 wt.%. As NaBH_4 concentration was increased from 10 to 20 wt.% the rate of hydrogen generation decreased probably due to solubility limitation of both sodium borohydride and metaborate. High concentration of NaBH_4 also leads to increase in the viscosity and alkalinity of the reaction solution.

The influence of the NaOH concentration (1-20 wt.%) on the hydrogen generation

was investigated, while reaction temperature and NaBH_4 concentration remained 40 °C and 10 wt.%, respectively. The hydrogen generation volume on Co-B/PANI catalyst is shown in Fig. 1c. As the concentration of NaOH was increased from 1 to 5 wt.% the hydrogen generation volume was accelerated significantly, beyond 5 wt.%, however, it decreased gradually with increase of NaOH concentration. Although high NaOH concentration promotes the production of active cobalt boride components, it prevents the hydrolysis reaction of sodium borohydride. Furthermore, high NaOH concentration may result in more production of larger size Co-B particles, which cause low catalytic reactivity of the catalysts.

4. CONCLUSIONS

Hydrogen generation from catalytic hydrolysis of alkaline NaBH_4 over polyaniline-supported cobalt boride catalyst has been investigated. According to experimental results it can be concluded that a low cost PANI-supported cobalt catalyst has comparable hydrogen generation performance with noble metal catalysts and is a promising catalyst in NaBH_4 hydrolysis.

Acknowledgements:

This study was financially supported the Kale Group & Republic of Turkey Ministry of Science, Industry and Technology according to the project STZ-00891-1.

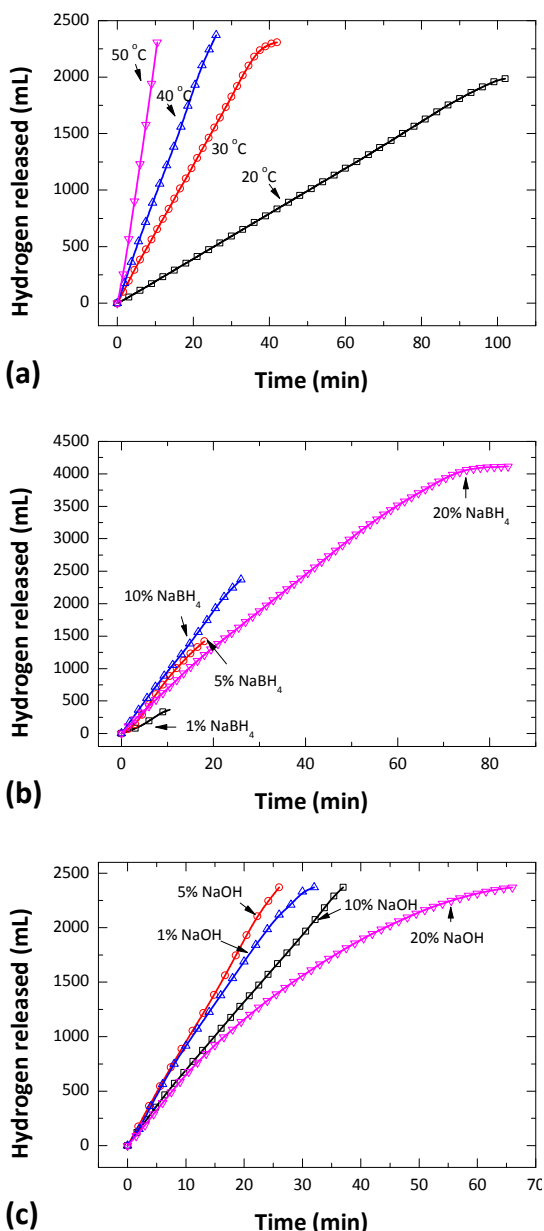


Figure 1: Effect of (a) Temperature; (b) NaBH₄ concentration and (c) NaOH concentration on hydrogen generation volume using 125 mg PANI-supported catalyst with 4.0 wt.% Co loading.

REFERENCES

Amendola, S.C, Sharp-Goldman, S.L., Janjua, M.S., Spencer, N.C., Kelly, M.T., Petillo, P.J., Binder, M., 2000. A safe, portable, hydrogen gas generator using aqueous borohydride solution and Ru catalyst, *International Journal of Hydrogen Energy*, (25), 969-975.

Baydaroglu F., Ozdemir E., Hasimoglu A., 2013. An effective synthesis route for improving the catalytic activity of carbon-supported

Co-B catalyst for hydrogen generation through hydrolysis of NaBH₄. *International Journal of Hydrogen Energy* (In press).

Billur S., Farida L., Michael H., 2007. Metal hydride materials for solid hydrogen storage: A review. *International Journal of Hydrogen Energy*, (32), 1121 – 1140.

Delmas J., Laversenne L., Rougeaux I., Capron P., Garron A., Bennici S., et al. 2011. Improved hydrogen storage capacity through hydrolysis of solid NaBH₄ catalyzed with cobalt boride. *International Journal of Hydrogen Energy*, (36), 2145-2153.

Hangjun D., Ge W., Mu Y., Yi L., Yingnan W., Xingxiong Y., 2009. Novel sea urchin-like polyaniline microspheres-supported molybdenum catalyst: Preparation, characteristic and functionality. *Journal of Molecular Catalysis A: Chemical*, (308), 25–31.

Jeong S., Cho E., Nam S., Oh I., Jung U., Kim S., 2007. Effect of preparation method on CoB catalytic activity for hydrogen generation from alkali NaBH₄ solution. *International Journal of Hydrogen Energy*, (32), 1749-1754.

Muir, S.S. Yao, X. 2011. Progress in sodium borohydride as a hydrogen storage material: Development of hydrolysis catalysts and reaction systems. *International Journal of Hydrogen Energy*, (36), 5983-5997.

Patel N., Patton B., Zanchetta C., Fernandes R., Guella G., Kale A., Miotello A., 2008. Pd-C powder and thin film catalysts for hydrogen production by hydrolysis of sodium borohydride. *International Journal of Hydrogen Energy*, (33), 287 – 29.

Trudeau ML. 1999. Advanced materials for energy storage. *MRS Bull*, (24), 23–26.

Yan L., Hong-Bin D., Lai-Peng M., Ping W., Hui-Ming C., 2010. Hydrogen generation from sodium borohydride solution using a ruthenium supported on graphite catalyst. *International Journal of Hydrogen Energy*, (35), 3023–3028.

Zhou, L. 2005. Progress and problems in hydrogen storage methods. *Renewable and Sustainable Energy Reviews*, (9), 395–408.

SYNTHESIS OF SOL-GEL DERIVED TiO₂ XEROGEL SUPPORTED METAL BORIDE CATALYSTS FOR HYDROGEN GENERATION BY HYDROLYSIS OF ALKALI SODIUM BOROHYDRIDE

Zümray V. Yiğit¹, Ferhat Baydaroğlu², Ercan Özdemir^{1,a}, Ali Ata¹

1. Gebze Institute of Technology, Clean Energy & Nanotechnology Research Center
41400, Kocaeli, Turkey
2. Gebze Institute of Technology, Department of Chemistry, 41400, Kocaeli, Turkey
a. Corresponding author (e.ozdemir@gyte.edu.tr)

ABSTRACT: Co-B and Ni-Co-B nanoparticles supported on sol-gel derived mesoporous anatase and rutile TiO₂ xerogel were synthesized as the catalyst of sodium borohydride hydrolysis for portable fuel cell applications. The effects of process parameters namely NaOH and NaBH₄ concentrations, reaction temperature and catalyst loadings on hydrogen production rate were investigated. The catalytic activity results showed that TiO₂ supported Co-B and Ni-Co-B catalysts exhibited higher activity than unsupported boride catalysts. Different calcination temperatures and calcination methods were also performed to observe the heat treatment effects on structural and morphological property of catalysts. All catalysts were characterized by XRD, TEM and SEM techniques.

1. INTRODUCTION

Environmental pollution has become a critical problem, hence alternative clean energy technologies are gaining current global attention in recent years [Charline *et. al.*, 2012; Krishnan *et. al.*, 2007]. The polymer electrolyte membrane (PEM) fuel cell technology is one of them which depends on the production of high purity hydrogen. Recent studies proved that NaBH₄ based pure and stable hydrogen generation systems are developing rapidly due to the high theoretical storage content of hydrogen, non-flammability, stability, controllable hydrolysis reaction, non-toxicity and renewability [Tian, *et.al.*, 2010; Ingersoll *et.al.*, 2007; Xu *et.al.*, 2008; Ye *et.al.*, 2007].

Sol-gel process has been one of the most popular catalyst preparation methods due to many advantages, including the possibility to control many parameters such as homogeneity, purity, porosity, surface area and sintering temperature of the final product. Furthermore, the final product could be shaped into several structural forms such as fibers, monoliths,

thin and thick film coatings, and powders by controlling the gelation conditions and the viscosity of the gelling solution. This process generally based on the precursor hydrolysis and polycondensation and the gel formation, which results in a crystalline network structure [Crişan *et.al.*, 2011; Charline *et.al.*, 2012; Vives and Meunier, 2008; Keshmiri *et.al.*, 2004.].

TiO₂ represents one of the most important sol-gel materials [Nakata and, Fujishima, 2012]. Nano- or micro-structures of TiO₂ have high ratio surface/volume and quantum yield [Crişan *et. al.*, 2011]. Hence, these particles have potential applications in several system and products in the environmental and energy fields such as self-cleaning surfaces, air and water purification systems, sterilization, hydrogen evolution, and photo-electrochemical conversion.

Titanium dioxide (TiO₂) is a crystalline material [1]. Of the seven polymorphs of

TiO₂, only rutile and anatase form have a commercial importance. Crystal phase transition of TiO₂ is mostly influenced by thermodynamics which is shown in this study [Yiğit]

In the present work, sol-gel derived titanium oxide used as support material and we successfully prepared Co-B/PANI catalysts and determined their catalytic activity under different working conditions.

2. EXPERIMENTAL

2.1. Materials

All chemicals were analytical grade and used without further purification.

2.2. Preparation of TiO₂ by Sol-gel Process

Titania nanoparticles were synthesized by a sol-gel process using titanium (IV) tetraisopropoxide as a starting precursor. Ethanol was used as an alcoholic solvent, and the reaction catalyzed by hydrochloric acid. The reaction was performed at room temperature. The as-synthesized titania was dried at 100 °C and calcined at 500 and 850 °C.

2.3. Preparation of the Co-B Catalysts

The catalysts were prepared by conventional impregnation method using aqueous precursor solutions of cobalt chloride as a metal source. The sol-gel derived TiO₂ was utilized as catalyst supports and total amount of active metal loading to catalysts was selected as 10 wt.%. A required amount of TiO₂ was suspended in ethanol under stirring and treated with ultrasonic probe. Then CoCl₂·6H₂O in ethanol was added dropwise while stirring vigorously. The impregnation onto titania supports was then carried out by stirring continuously for 12 h at room temperature. After evaporating excess ethanol the catalyst was dried in vacuum oven.

Cobalt impregnated titania catalyst was then reduced by adding 1.0 M sodium borohydride solution drop-wise. The resulting catalysts were separated by centrifugation, washed with water and dried in a vacuum oven.

2.4. Catalytic Activity Testing

A definite amount of catalyst was placed in to the reactor. Then, aqueous solution of NaBH₄ was fed into the reactor immediately. Hydrogen generation was started in a temperature controlled reactor equipped with magnetic stirrer at 700 rpm. During the experiments hydrogen volume was measured as a function of time using gas burette.

2.5. Catalysts Characterization

Powder X-ray diffraction patterns of the catalyst were obtained on Rigaku D/Max-2200/PC diffractometer using Cu-K α radiation. The 2 θ scan range was 10-90 with a step of 0.02. Morphology of catalysts was examined by a scanning electron microscopy (Philips XL30 SFEG) at an accelerating voltage of 15 kV. Elemental compositions of the catalysts were determined by scanning electronmicroscopy coupled with energy-dispersive X-ray spectroscopy (EDX).

3. RESULTS AND DISCUSSION

3.1. Preliminary Studies

The hydrogen production performances of Ni-Co-B and Co-B catalysts supported on titania, calcinated at 100, 500, and 850 °C, were evaluated in 10 mL of 10 wt.% NaBH₄ 5 wt.% NaOH solution at 40 °C. Fig. 1 shows the hydrogen generation volume of cobalt catalysts. As shown in the figure data points of hydrogen volume roughly follow a straight line with the reaction time, indicating the stable catalytic activity of the catalysts.

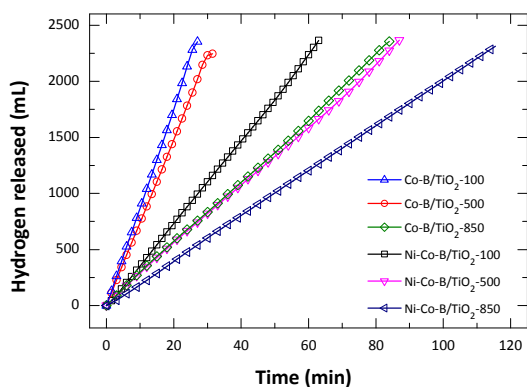


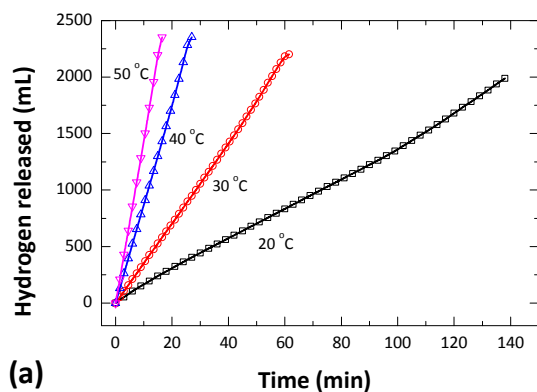
Figure 1: Hydrogen generation performance of nickel-cobalt (5wt%-5wt%) and cobalt (10 wt%) borides supported on titania at 40 °C.

It is well known that the supporting materials improve the dispersion of the loading metals, which creates more active sites contact with the reactant. It was observed that all supported cobalt boride catalyst exhibited higher catalytic activity than nickel-cobalt boride catalysts despite containing the same metal loading (10 wt%).

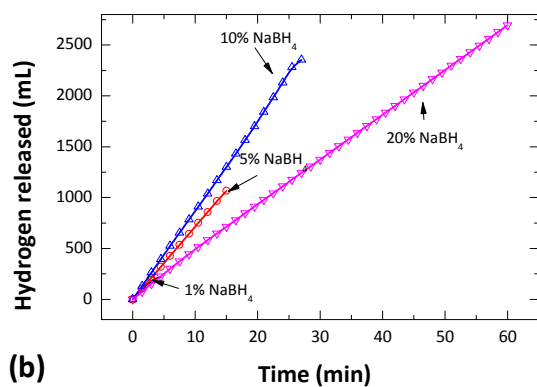
3.2. Effect of Process Parameter on Hydrogen Generation

The effects of sodium hydroxide concentration, reaction temperature and sodium borohydride concentration on the performance of the most active catalyst Co-B/TiO₂-100 were investigated in detail. It can be seen from Fig. 2a, hydrogen production volume increased with increasing reaction temperature. All synthesized catalysts showed no certain deactivation since HG curves lie approximately on a straight line. The effect of the NaBH₄ concentration, varying from 1 to 20 wt.%, on the HG was investigated, while reaction temperature and NaOH concentration remained 40 °C and 5 wt.%, respectively. Fig. 2b indicates that the hydrogen generation rate increased as the NaBH₄ concentration was increased up to 10 wt.%. As NaBH₄ concentration was increased from 10 to 20 wt.% the rate of hydrogen generation decreased probably

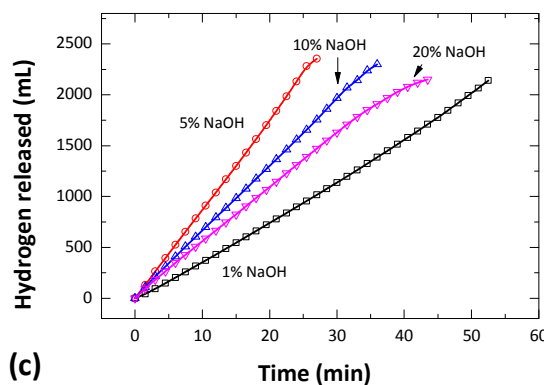
due to solubility limitation. High concentration of NaBH₄ also leads to increase in the viscosity and alkalinity of the reaction solution. The influence of the NaOH concentration on the hydrogen generation was investigated, while reaction temperature and NaBH₄ concentration remained 40 °C and 10 wt.%, respectively.



(a)



(b)



(c)

Figure 2: Effect of (a) temperature; (b) NaBH₄ concentration and (c) NaOH concentration on hydrogen generation volume using Co-B/TiO₂ catalysts with 10 wt.% Co loading.

The hydrogen generation volume on Co-B/TiO₂ catalyst is shown in Fig. 2c. As the concentration of NaOH was increased from 1 to 5 wt.% the hydrogen generation volume was accelerated significantly, Beyond 5 wt.% it decreased gradually with increase of NaOH concentration. Although high NaOH concentration promotes the production of active cobalt boride components, it prevents the hydrolysis reaction of sodium borohydride. Furthermore, high NaOH concentration may result in more production of larger size Co-B particles, which cause low catalytic reactivity

3.3. Characterization of Support and Catalysts

Fig.3 indicates the XRD pattern for as-prepared titania synthesized (TiO₂-100). As prepared nanosize particles showed anatase structure. XRD patterns of TiO₂ samples annealed at 500 °C (TiO₂-500)

also indicated the typical peaks associated with anatase. Annealing at 850 °C (TiO₂-850) resulted in diffraction peaks related only to the rutile structure. From SEM and TEM images of catalysts (Fig. 4), it was observed that the cobalt boride nanoparticles were distributed bulky on the support surface.

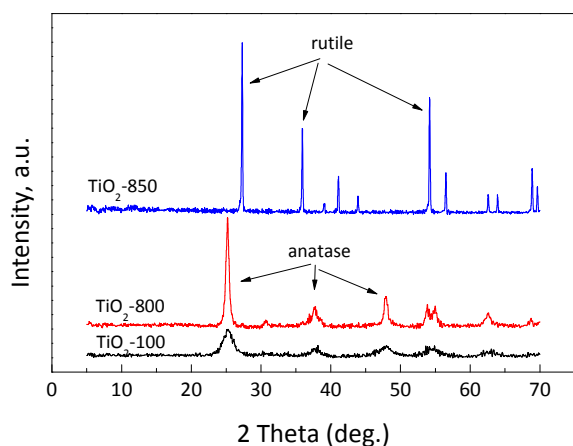


Figure 3: XRD patterns of as-synthesized and annealed titania supports.

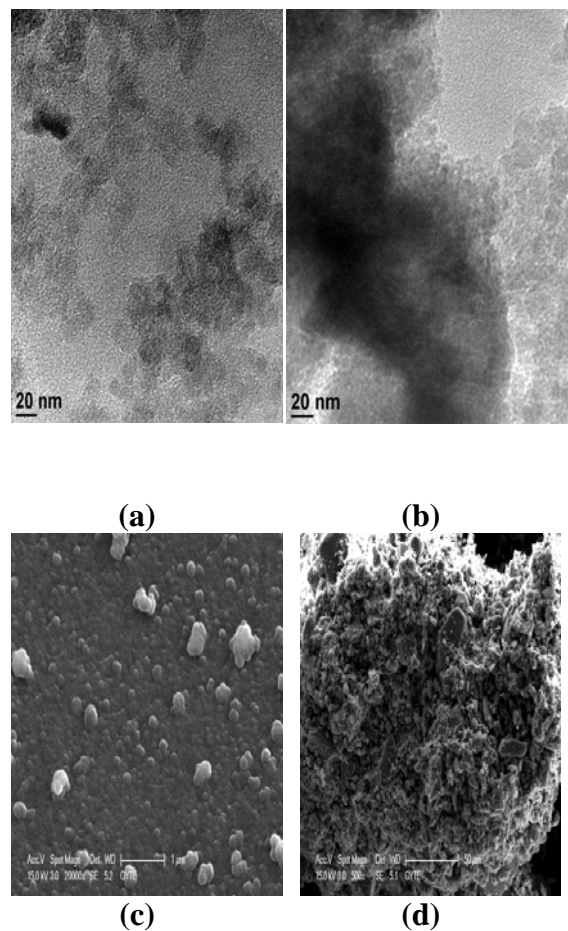


Figure 4: TEM image of (a) TiO₂ (b) Co-B/TiO₂, SEM image of (c) TiO₂ (d) Co-B/TiO₂, and EDX spectrum of (e) TiO₂ (f) Co-B/TiO₂

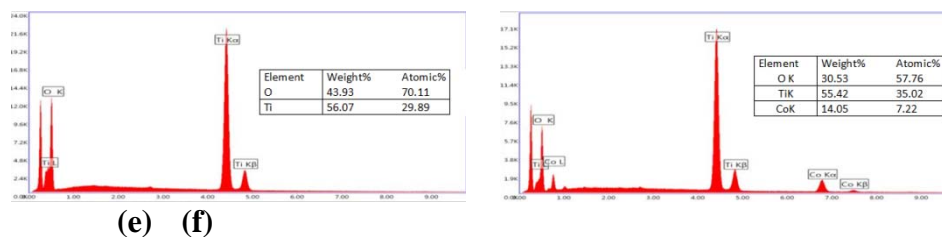


Figure 4: Cont., (e) TiO₂ (f) Co-B/TiO₂

REFERENCES

- Charline M. Malengreaux, Adrien Timmermans, Sophie L. Pirarda, Stéphanie D. Lamberta, Jean-Paul Pirarda, Dirk Poelman, Benoît Heinrichs, 2012. Optimized deposition of TiO₂ thin films produced by a non-aqueous sol-gel method and quantification of their photocatalytic activity, *Chemical Engineering Journal*, (195), 347–358
- Crișan, D., Drăgan, N., Răileanu, M., Crișan, M., Ianculescu, A., Luca, D., Năstută, A., Mardare, D., 2011. Structural study of sol-gel Au/TiO₂ films from nanopowders, *Applied Surface Science*, (257), 4227–4231
- Ingersoll, J.C., Mania, N., Thenmozhiyal, J.C., Muthaiah, A., 2007. Catalytic hydrolysis of sodium borohydride by a novel nickel-cobalt-boride catalyst, *Journal of Power Sources*, (173), 450–457
- Keshmiri, M., Mohseni, M., Troczynski, T., 2004. Development of novel TiO₂ sol-gel-derived composite and its photocatalytic activities for trichloroethylene oxidation, *Applied Catalysis B: Environmental*, (53), 209–219
- Krishnan, P., Hsueh, K-L., Yima, S-D., 2007. Catalysts for the hydrolysis of aqueous borohydride solutions to produce hydrogen for PEM fuel cells, *Applied Catalysis B: Environmental*, (77), 206–214
- Nakata, K., Fujishima, A., 2012. TiO₂ photocatalysis: Design and applications, *Journal of Photochemistry and Photobiology C: Photochemistry Reviews*, (13), 169–189
- Šegota, S., Čurković, L., Ljubas, D., Svetličić, V., Houra, I.F., Tomašić, N., 2011. Synthesis, characterization and photo-catalytic properties of sol-gel TiO₂ films, *Ceramics International*, (37), 1153–1160
- Tian, H., Guo, Q., Xu, D., 2010. Hydrogen generation from catalytic hydrolysis of alkaline sodium borohydride solution using attapulgite clay-supported Co-B catalyst, *Journal of Power Sources*, (195), 2136–2142
- Vives, S., Meunier, C., 2008. Influence of the synthesis route on sol-gel SiO₂-TiO₂ (1:1) xerogels and powders, *Ceramics International*, (34), 37–44
- Xu, D., Dai, P., Liu, X., Cao, C., Guo, Q., 2008. Carbon-supported cobalt catalyst for hydrogen generation from alkaline sodium borohydride solution, *Journal of Power Sources*, (182), 616–620
- Ye, W., Zhang, H., Xua, D., Maa, L., Yi, B., 2007. Hydrogen generation utilizing alkaline sodium borohydride solution and supported cobalt catalyst, *Journal of Power Sources*, (164), 544–548
- Yiğit, Z.V., Synthesis of Au@TiO₂ and Ag@TiO₂ core-shell structured nano particles by ultrasonic spray pyrolysis, Bachelor thesis:

SECTION C

Environmental and Hygienic Aspects

CHARACTERIZING THE ADSORPTION PROPERTIES OF NANOPOROUS MATERIALS FOR GAS STORAGE AND SEPARATION TECHNOLOGY

Darren P. Broom^{1,a}

1. Hiden Isochema Ltd, Warrington, UK
a. Corresponding author (dbroom@hidenisochema.com)

ABSTRACT: Nanoporous adsorbents are widely used for gas separation and purification. Activated carbons, activated aluminas, silica gels and zeolites are commonly used in industrial applications, but the number of available adsorbents has increased significantly in recent years due to the development of new types of nanoporous material, such as metal-organic frameworks, covalent organic frameworks and amorphous microporous organic polymers. In addition, the interest in the use of these materials for the storage of energy gases, such as hydrogen and methane, has grown dramatically. In each case, the assessment of the adsorption properties of new materials under practical conditions of temperature and pressure is crucial. In this article, we provide an overview of this aspect of research into the use of nanoporous materials for gas storage and separation technology, and include an introduction to the materials, their applications and the gas adsorption measurement techniques commonly used for application-oriented materials performance characterization.

1. INTRODUCTION

Nanoporous materials are of interest in a wide range of application areas [Lu and Zhao, 2004]. Gas separation and purification [Ruthven, 1984, Yang, 1997] using, for example, Pressure Swing Adsorption (PSA) or Temperature Swing Adsorption (TSA) is one of the major industrial uses. Typical adsorbents for this application include zeolites, silica gels and porous carbons [Yang, 2003]; however, these materials have also been investigated for emerging adsorption applications such as the storage of hydrogen [Broom, 2011] and methane or natural gas [Menon and Komarneni, 1998].

Adsorption has long been of interest to chemical engineers and the field continues to grow as new processes are developed. However, in parallel, there have been exciting developments and discoveries in the field of porous solids. New materials include metal-organic frameworks, covalent organic

frameworks and amorphous microporous organic polymers [Broom and Thomas, 2013]. Some of the new materials exhibit unique properties and, particularly in the case of metal-organic frameworks, unprecedented opportunities for the design of materials with different pore sizes and geometries, from the microporous (< 2 nm) to the mesoporous (2 – 50 nm) regime [Fang *et al.*, 2010, Song *et al.*, 2012], as well as features such as structural flexibility [Fletcher *et al.*, 2005]; thus offering the promise of new gas adsorption applications.

In order to assess the suitability of materials for industrial applications, it is necessary to assess their adsorption properties under practical conditions of temperature and pressure. For gas storage, this requires single component adsorption measurement at elevated pressures. For separation and purification, multicomponent measurement is required because of the importance of competitive adsorption [Broom and Thomas, 2013].

In this article, we will consider this characterization process.

2. NANOPOROUS MATERIALS

Activated carbons are amorphous carbonaceous materials, with highly developed porosity and large internal surface areas [Bansal and Goyal, 2005]. They can, in principle, be produced from any carbonaceous precursor using a physical activation method, but organic precursors can also be chemically activated [Wang and Kaskel, 2012]. Carbon Molecular Sieves (CMS) are related materials that can be produced, for example, by the deposition of carbon in the pore mouths of a porous carbonaceous precursor to introduce narrow pore constrictions [Chagger *et al.*, 1995, Reid and Thomas, 1999]. Different kinds of nanoporous silica are available. Commercial silica “gels” are usually xerogels, which are produced by evaporative drying of wet silica gels. Aerogels are produced in a similar manner, but the wet gel is instead dried under supercritical conditions [Pierre and Pajonk, 2002]. These materials have a disordered pore structure, but silicas with ordered pore networks can be produced using surfactant-templating [Barton *et al.*, 1999, Edler, 2011]. Zeolites are microporous crystalline aluminosilicates constructed from SiO_4 and AlO_4 tetrahedra. Numerous other zeolitic materials can be synthesised from other elements [Wright, 2008], however, and new zeolites continue to be discovered [Bellussi *et al.*, 2013].

New material classes include Metal-Organic Frameworks (MOFs) and Covalent Organic Frameworks (COFs). MOFs are constructed from metal ions or clusters, known as Secondary Building Units (SBUs), joined by organic linkers [Férey, 2008, MacGillivray, 2010, Kepert, 2011]. The selection of different linkers and SBUs allows the tailoring of

the pore size and surface area of these materials. COFs, meanwhile, are organic analogues of MOFs constructed from light elements, such as H, B, O, C and Si [Feng *et al.*, 2012, Ding and Wang, 2013].

3. ADSORPTION APPLICATIONS

Nanoporous materials are of interest for practical gas storage and separation applications due to their adsorption properties. Gas adsorption can be defined as the enrichment in the concentration of a gas species at the gas-solid interface. The narrow pores and large internal surface areas of nanoporous materials can lead to significant enhancement of the density of the adsorbed species in their pore networks compared to the bulk gas phase. For storage applications this can result in the adsorption of relatively large quantities of certain species, such as H_2 and CH_4 , at significantly lower pressures than those required for compressed gas storage or at higher temperatures than those required for liquid storage [Broom and Thomas, 2013].

For separation and purification, selective adsorption of certain gases and vapours can be used to separate one species from another or to remove contaminants from mixed gas streams. This typically uses fixed bed adsorption. In this case, the mixture is passed through an adsorbent column in which one or more of the components is more strongly adsorbed. The adsorbent column is then regenerated by reducing the pressure, as in PSA, or by heating, as in TSA [Ruthven, 1984, Yang, 1997, Sircar and Myers, 2003, Sircar, 2006]. These processes can be used for many gas phase applications, including H_2 purification, N_2 and O_2 production from air, He production from natural gas, natural gas treating and CO_2 capture [Yang, 2003, Häring, 2008, Tagliabue *et al.*, 2009, Broom and Thomas, 2013]. An alternative is the use

of nanoporous materials in membrane gas separation [Baker, 2004, Tanh Jeazet *et al.*, 2012, Shah *et al.*, 2012].

4. GAS ADSORPTION MEASUREMENT

In order to assess the suitability of a material for a particular adsorption application, it is necessary to determine its gas adsorption properties [Broom and Thomas, 2013]. For gas separation, data are also required by chemical engineers for process design [Sircar, 2007, Tagliabue *et al.*, 2009]. Storage applications require single component gas adsorption measurements at elevated pressures and practical operational temperatures, which are dependent to a certain extent on the species. Separation and purification require multicomponent measurements, also under practical conditions [Talu, 1998, 2011, Sircar, 2007].

The most common measurement types are the volumetric (or manometric) and gravimetric techniques, which can both be used to determine single component gas adsorption isotherms. The former is an indirect measurement, which uses the pressure in a system of a known, fixed volume to determine the amount of adsorption. Gas is dosed from a calibrated volume into the sample cell. The drop in pressure in the absence of adsorption can be calculated from the ratio of the dosing volume to the total (dead) volume of the measurement system; any further pressure reduction is then attributed to adsorption and used to determine the adsorbed quantity [Broom, 2011, Broom and Thomas, 2013]. The gravimetric technique, on the other hand, uses a microbalance to determine the amount of gas adsorbed from the weight change of the sample.

Both methods require corrections for the presence of the sample in the chamber. In the volumetric (or manometric) case,

these are the so-called dead volume or dead space corrections [Rouquerol *et al.*, 1999], which account for the difference between the volume of the empty and loaded sample cell. In the gravimetric case, the equivalent is the buoyancy correction, which accounts for the effect of weighing the sample in a gas of differing density through the course of adsorption isotherm determination.

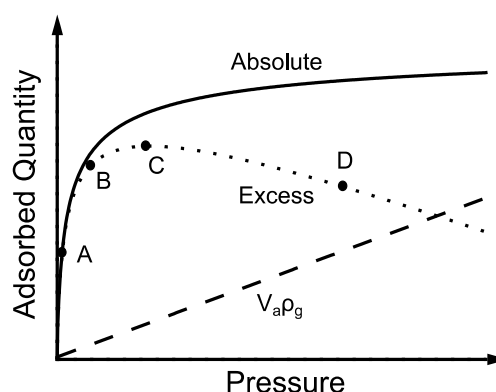


Figure 1: Illustration of the difference between the (experimentally-determined) excess and the absolute adsorption [Broom and Thomas, 2013]. At low pressures (A), the excess and absolute adsorption can be assumed to be approximately equal, which is generally the case, for example, for N_2 and Ar adsorption measurements performed at low temperatures for surface area and pore size characterization [Rouquerol *et al.*, 1999]. As the pressure increases, however, the two values begin to diverge (see point B). At a particular pressure, the excess reaches a peak (C), before decreasing further as the bulk gas phase density (ρ_g) becomes increasingly significant (D).

Both measurement methods determine the excess, rather than the absolute, adsorption. The latter is defined as the total amount of adsorbate present in the adsorbed phase. It is not possible to determine this directly using the measurement methods described above

because these techniques only determine the difference between a reference state, typically defined using helium, which is assumed to be non-adsorbing, and the state of the system in the event of adsorption.

The difference, in terms of the shape of the isotherms, between the excess and absolute adsorbed quantities is illustrated schematically in Figure 1. The conversion between the two quantities can be made by adding (to the excess adsorption) the term, $V_a\rho_g$, which is dependent upon the adsorbed phase volume, V_a , and the bulk gas phase density, ρ_g , at the measurement temperature and pressure. As shown in Figure 1, the $V_a\rho_g$ term becomes increasingly significant at elevated pressures.

In addition to adsorption isotherms, the kinetics of adsorption can, in principle, be measured using either technique. However, the gravimetric method allows the determination of adsorption under isobaric conditions, which simplifies the modelling of the adsorption or diffusion process [Chagger *et al.*, 1995, Broom and Thomas, 2013].

Single component adsorption measurements, particularly at elevated pressure, can be affected by a number of error sources [Broom, 2007, 2011, Thomas, 2009, van Hemert *et al.*, 2009, Broom and Thomas, 2013] and so care is required to ensure that uncertainties are minimised. Interlaboratory test exercises have demonstrated the susceptibility of elevated pressure gas sorption isotherm measurements to uncertainties [Gensterblum *et al.*, 2009, Zlotea *et al.*, 2009]. The validation of adsorption data is therefore important, although this has been performed only for a few adsorbate-adsorbent systems. This point was, for example, noted by Férey [Férey, 2008] with respect to H₂ adsorption by MOFs

[Thomas, 2009]. The interlaboratory study by Zlotea and co-workers [Zlotea *et al.*, 2009] on H₂ adsorption by a commercial porous carbon (Takeda CMS 4A), meanwhile, revealed a disturbing disparity [Harris, 2012] between data measured in different laboratories. It is not inconceivable that similar differences might be observed for other adsorbate-adsorbent systems if further studies were performed. In accordance with this view, Sircar and co-workers [Rynders *et al.*, 1997] noted that “adsorption equilibrium and kinetic data for the same gas-solid systems from different laboratories around the world often do not match with one another.” The problems that can arise are particularly well exemplified by the investigation and subsequent discussion of the hydrogen storage properties of carbon nanostructures, such as nanotubes and nanofibres [Hirscher *et al.*, 2002, Broom, 2007, 2011, Liu *et al.*, 2010, Tedds *et al.*, 2011]. A wide variety of storage capacities were reported for these materials; sample purity was an issue, but measurement accuracy undoubtedly played a significant role in the discrepancies and the resulting controversy.

The experimental determination of multicomponent (binary or higher) gas adsorption, however, is even more challenging than single component measurement [Talu, 1998, 2011]. Volumetric methods can be used by determining the composition of a gas mixture in equilibrium with a solid, but the accuracy of this approach is limited by the sample size and the need to ensure that the measurement is made under equilibrium conditions [Broom and Thomas, 2013]. Even if large samples are used and equilibrium is achieved, there is no way of controlling the equilibrium pressure of each component, and so in this respect the measured data are random [Rynders *et al.*, 1997, Sircar, 2007].

Furthermore, for newly synthesised materials, large samples are often unavailable.

Flowing gravimetric systems can be used to measure total uptakes and subsequent desorption of the adsorbed phase used to establish the amount of each component adsorbed, but there are still limitations to this approach, in terms of the sample size and the amount of adsorption exhibited by the material [Fletcher *et al.*, 2002, Broom and Thomas, 2013]. The study by Thomas and co-workers [Fletcher *et al.*, 2002], for example, used vapour sorption to demonstrate this method. In this case, the relatively strong interaction of the vapour phase species aided the feasibility of this approach.

The measurement of breakthrough curves, which are plots of the downstream composition of a gas mixture in response to a step change in the upstream composition across a packed adsorbent bed, provide an alternative, although this technique does not explicitly provide adsorption isotherms, adsorption kinetics or enthalpy values. It does, however, allow the qualitative and quantitative comparison of the performance of different materials for separation applications [Keskin *et al.*, 2010, Broom and Thomas, 2013].

5. APPLICATION-ORIENTED DATA

The characterization of the adsorption performance of nanoporous materials for practical applications involves the determination of equilibrium adsorption and desorption isotherms, adsorption and desorption kinetics and the enthalpies of adsorption for the relevant adsorbates. Each of these can be determined using the measurement techniques mentioned above.

The determination of adsorption and desorption isotherms, which are plots of

uptake versus pressure, as shown in Figure 1, allow the determination of the usable or working capacity of a material [Tedds *et al.*, 2011]. This parameter is important for both gas storage and gas separation [Tagliabue *et al.*, 2009, Krishna and Long, 2011, Broom and Thomas, 2013]. It can be defined as the difference between the uptake at the adsorption and desorption pressures for the particular process. For example, if A and D in Figure 1 were to indicate the uptake of the adsorbent at the lower and upper operating pressure of the process under consideration, the difference between the absolute uptakes at these two points would define the usable or working capacity of the adsorbent.

For separations, the selectivity, as well as the working capacity, is an important parameter. The definition of the selectivity of a material depends on the mechanism of separation. Most existing applications rely on equilibrium separation [Sircar and Myers, 2003, Yang, 2003, Ruthven, 2011], which exploits differences in the uptakes of different species under equilibrium conditions. In this case, the selectivity can be calculated by comparing the uptakes of different species from adsorption isotherms. Some processes, however, exploit differences in the kinetics of adsorption or diffusion [Sircar and Myers, 2003, Yang, 2003, Ruthven, 2011]. In this case, the ratio of the linear driving force rate constants for different species can be compared. This applies, for example, to air separation using carbon molecular sieves, which exploits differences in the diffusion rates of O₂ and N₂ through these materials [Chagger *et al.*, 1995, Reid and Thomas, 1999]. Kinetic data are therefore required for the assessment of the kinetic selectivity of a material.

The enthalpy of adsorption provides a measure of the strength of the interaction

between the adsorbate and the adsorbent, but it can be modified at higher uptakes by adsorbate-adsorbate interactions. The isosteric enthalpy of adsorption is determined at constant surface coverage or loading and can be calculated as a function of uptake from (absolute) adsorption isotherms determined at two or more closely spaced temperatures. The enthalpy of adsorption at zero surface coverage, meanwhile, provides a more fundamental measure of the adsorbate-adsorbent interaction, under conditions at which the adsorbate-adsorbate interactions should not play a significant role. For storage applications, the enthalpy of adsorption will determine the temperature at which a material can store significant amounts of a particular adsorbate. Optimum enthalpies of adsorption for hydrogen and methane storage at ambient temperature have, for example, been estimated [Bhatia and Myers, 2006]. Values of $15.1 \text{ kJ mol}^{-1} \text{ H}_2$ and $18.8 \text{ kJ mol}^{-1} \text{ CH}_4$ were determined. Care must be taken, however, when comparing the isosteric enthalpies determined using different data analysis methods because the choice of approach can significantly affect the result, even when using the same experimental data [Tedds *et al.*, 2011].

For separation applications, the enthalpy of adsorption for different species can determine the equilibrium separation capability of a given adsorbent. It is also one of the thermodynamic quantities required for process design [Sircar, 2007], because it provides a measure of the energy required for the regeneration of the adsorbent [Tagliabue *et al.*, 2009]. For separations, it should not be too high because otherwise the regeneration process will be too energetically costly.

In addition to the determination of single component adsorption isotherms and kinetics, and enthalpies of adsorption,

multicomponent adsorption is also required for gas separation applications, to ensure that competitive adsorption is taken into account. However, given the practical difficulties involved with multicomponent adsorption measurement, including their time-consuming nature, single component measurements provide an important starting point, particularly for material screening purposes.

6. CONCLUDING REMARKS

In this article, a brief overview of nanoporous materials and their characterization for gas storage and separation technology has been presented. The important properties include adsorption and desorption isotherms, adsorption and desorption kinetics, and the enthalpy of adsorption for different adsorbates and materials. The determination of these properties using, for example, the volumetric (or manometric) and gravimetric techniques has become relatively common and commercial instruments are now widely available. However, interlaboratory test exercises have recently shown that considerable discrepancies between data measured in different laboratories using the same material is possible. Future work should seek to clarify the reasons behind these discrepancies to help ensure better data reproducibility and validate the adsorption behaviour of different materials, including many of the new adsorbents that have recently been reported.

The development of new types of nanoporous materials, in recent years, offers the promise of new adsorption applications in gas separation technology [Li *et al.*, 2009, 2012, Broom and Thomas, 2013]. Features that may be exploited in this area include framework flexibility in the case of MOFs and the unprecedented ability to tailor the pore

size, geometry and surface chemistry of these materials from the microporous to the mesoporous regimes. Assessment of the suitability of new materials for these applications requires accurate and thorough characterization of their adsorption properties under practical conditions. Separation applications, in particular, require multicomponent adsorption measurements, which remain a technical challenge. Further developments in adsorption measurement methodology in this area would therefore be particularly valuable.

REFERENCES

- Baker, R.W., 2004. Membrane Technology and Applications, Wiley, Chichester, UK.
- Bansal, R.C. and Goyal, M., 2005. Activated Carbon Adsorption, CRC Press, Boca Raton, USA.
- Barton, T.J., Bull, L.M., Klemperer, W.G., Loy, D.A., McEnaney, B., Misono, M., Monson, P.A., Pez, G., Scherer, G.W., Vartuli, J.C. and Yaghi, O.M., 1999. Tailored Porous Materials, Chemistry of Materials, 11, 2633.
- Bhatia, S.K. and Myers, A.L., 2006. Optimum Conditions for Adsorptive Storage, Langmuir, 22, 1688.
- Bellussi, G., Carati, A., Rizzo, C. and Millini, R., 2013. New Trends in the Synthesis of Crystalline Microporous Materials, Catalysis Science and Technology, 3, 833.
- Broom, D.P., 2007. The Accuracy of Hydrogen Sorption Measurements on Potential Storage Materials, International Journal of Hydrogen Energy, 32, 4871.
- Broom, D.P., 2011. Hydrogen Storage Materials: The Characterisation of Their Storage Properties, Springer, London, UK.
- Broom, D.P. and Thomas, K.M., 2013. Gas Adsorption by Nanoporous Materials: Future Applications and Experimental Challenges, MRS Bulletin, 38, 412.
- Chagger, H.K., Ndaji, F.E., Sykes, M.L. and Thomas, K.M., 1995. Kinetics of Adsorption and Diffusional Characteristics of Carbon Molecular Sieves, Carbon, 33(10), 1405.
- Ding, S.-Y. and Wang, W., 2013. Covalent Organic Frameworks (COFs): From Design to Applications, Chemical Society Reviews, 42, 548.
- Edler, K.J., 2011. Mesoporous Silicates, Porous Materials, Wiley, Chichester, UK, 69.
- Fang, Q.-R., Makal, T.A., Young, M.D. and Zhou H.C., 2010. Recent Advances in the Study of Mesoporous Metal-Organic Frameworks, Comments on Inorganic Chemistry, 31, 165.
- Feng, X., Ding, X. and Jiang, D., 2012. Covalent Organic Frameworks, Chemical Society Reviews, 41, 6010.
- Férey, G., 2008. Hybrid Porous Solids: Past, Present, Future, Chemical Society Reviews, 37, 191.
- Fletcher, A.J., Benham, M.J. and Thomas, K.M., 2002. Multicomponent Vapor Sorption on Active Carbon by Combined Microgravimetry and Dynamic Sampling Mass Spectrometry, Journal of Physical Chemistry B, 106, 7474.
- Fletcher, A.J., Thomas, K.M. and Rosseinsky, M.J., 2005. Flexibility in Metal-Organic Framework Materials: Impact on Sorption Properties, Journal of Solid State Chemistry, 178, 2491.
- Gensterblum, Y., van Hermert, P., Billefont, P., Busch, A., Charrière, D., Li, D., Krooss, B.M., de Weireld, G., Prinz, D. and Wolf, K.-H.A.A., 2009. European Inter-laboratory Comparison of High Pressure CO₂ Sorption Isotherms. I: Activated Carbon, Carbon, 47(13), 2958.
- Häring, H.-W., 2008. Industrial Gases Processing, Wiley-VCH, Weinheim, Germany.
- Harris, R., 2012. Book Review: Hydrogen Storage Materials: The Characterisation of Their Storage Properties, International Journal of Hydrogen Energy, 37(9), 7950.
- Hirscher, M., Becher, M., Haluska, M., Quintel, A., Skakalova, V., Choi, Y.-M., Dettlaff-Weglikowska, U., Roth, S., Stepanek, I., Bernier, P., Leonhardt, A. and Fink, J., 2002. Hydrogen Storage in Carbon Nanostructures, Journal of Alloys and Compounds, 330-332, 654.
- Kepert, C.J., 2011. Metal-Organic Framework Materials, Porous Materials, Wiley, Chichester, UK, 1.
- Keskin, S., van Heest, T.M. and Sholl, D.S., 2010. Can Metal-Organic Framework Materials Play a Useful Role in Large-Scale Carbon Dioxide Separations?, ChemSusChem, 3, 879.
- Krishna, R. and Long, J.R., 2011. Screening Metal-Organic Frameworks by Analysis of Transient Breakthrough of Gas Mixtures in a Fixed Bed Adsorber, Journal of Physical Chemistry C, 115, 12941.
- Li, J.-R., Kuppler, R.J. and Zhou, H.-C., 2009. Selective Gas Adsorption and Separation in Metal-Organic Frameworks, Chemical Society Reviews, 38, 1477.
- Li, J.-R., Sculley, J. and Zhou, H.-C., 2012. Metal-Organic Frameworks for Separations, Chemical Reviews, 112, 869.

- Liu, C., Chen, Y., Wu, C.-Z., Xu, S.-T. and Cheng, H.-M., 2010. Hydrogen Storage in Carbon Nanotubes Revisited, *Carbon*, 48, 452.
- Lu, G.Q. and Zhao X.S., 2004. *Nanoporous Materials: Science and Engineering*, Imperial College Press, London, UK.
- MacGillivray, L.R., 2010. *Metal-Organic Frameworks: Design and Application*, Wiley, New Jersey, USA.
- Menon, V.C. and Komarneni S., 1998. Porous Adsorbents for Vehicular Natural Gas Storage: A Review, *Journal of Porous Materials*, 5(1), 43.
- Pierre, A.C. and Pajonk, G.M., 2002. Chemistry of Aerogels and Their Applications, *Chemical Reviews*, 102, 4243.
- Reid, C.R. and Thomas, K.M., 1999. Adsorption of Gases on a Carbon Molecular Sieve Used for Air Separation: Linear Adsorptives as Probes for Kinetic Selectivity, *Langmuir*, 15, 3206.
- Rouquerol, F., Rouquerol, J. and Sing, K., 1999. *Adsorption by Powders and Porous Solids: Principles, Methodology and Applications*, Academic Press, London, UK.
- Ruthven, D.M., 1984. *Principles of Adsorption and Adsorption Processes*, Wiley, New York, USA.
- Ruthven, D.M., 2011. Molecular Sieve Separations, *Chemie Ingenieur Technik*, 83(1-2), 44.
- Rynders, R.M., Rao, M.B. and Sircar, S., 1997. Isotope Exchange Technique for Measurement of Gas Adsorption Equilibria and Kinetics, *AIChE Journal*, 43(10), 2456.
- Shah, M., McCarthy, M.C., Sachdeva, S., Lee, A.K. and Jeong, H.-K., 2012. Current Status of Metal-Organic Framework Membranes for Gas Separations: Promises and Challenges, *Industrial and Engineering Chemistry Research*, 51, 2179.
- Sircar, S., 2006. Basic Research Needs for Design of Adsorptive Gas Separation Processes, *Industrial and Engineering Chemistry Research*, 45(16), 5435.
- Sircar, S., 2007. Recent Developments in Macroscopic Measurement of Multicomponent Gas Adsorption Equilibria, Kinetics, and Heats, *Industrial and Engineering Chemistry Research*, 46(10), 2917.
- Sircar, S. and Myers, A.L., 2003. Gas Separation by Zeolites, *Handbook of Zeolite Science and Technology*, Marcel Dekker, New York, USA, 1063.
- Song, L., Zhang, J., Sun, L., Xu, F., Li, F., Zhang, H., Si, X., Jiao, C., Li, Z., Liu, S., Liu, Y., Zhou, H., Sun, D., Du, Y., Cao, Z. and Gabelica, Z., 2012. Mesoporous Metal-Organic Frameworks: Design and Applications, *Energy & Environmental Science*, 5, 7508.
- Tagliabue, M., Farrusseng, D., Valencia, S., Aguado, S., Ravon, U., Rizzo, C., Corma, A. and Mirodatos, C., 2009. Natural Gas Treating by Selective Adsorption: Material Science and Chemical Engineering Interplay, *Chemical Engineering Journal*, 155, 553.
- Talu, O., 1998. Needs, Status, Techniques and Problems with Binary Gas Adsorption Experiments, *Advances in Colloid and Interface Science*, 76-77, 227.
- Talu, O., 2011. Measurement and Analysis of Mixture Adsorption Equilibrium in Porous Solids, *Chemie Ingenieur Technik*, 83(1-2), 67.
- Tanh Jeazet, H.B., Staudt, C. and Janiak, C., 2012. Metal-Organic Frameworks in Mixed-Matrix Membranes for Gas Separation, *Dalton Transactions*, 41, 14003.
- Tedds, S., Walton, A., Broom, D.P. and Book, D., 2011. Characterisation of Porous Hydrogen Storage Materials: Carbons, Zeolites, MOFs and PIMs, *Faraday Discussions*, 151, 75.
- Thomas, K.M., 2009. Adsorption and Desorption of Hydrogen on Metal-Organic Framework Materials for Storage Applications: Comparison with other Nanoporous Materials, *Dalton Transactions*, 1487.
- van Hemert, P., Bruining, H., Rudolph, E.S.J., Wolf, K.-H.A.A. and Maas, J.G., 2009. Improved Manometric Setup for the Accurate Determination of Supercritical Carbon Dioxide Sorption, *Review of Scientific Instruments*, 80, 035103.
- Wang, J. and Kaskel, S., 2012. KOH Activation of Carbon-based Materials for Energy Storage, *Journal of Materials Chemistry*, 22, 23710.
- Wright, P.A., 2008. *Microporous Framework Solids*, RSC Publishing, Cambridge, UK.
- Yang, R.T., 1997. *Gas Separation by Adsorption Processes*, Imperial College Press, London, UK.
- Yang, R.T., 2003. *Adsorbents: Fundamentals and Applications*, Wiley, New Jersey, USA.
- Zlotea, C., Moretto, P. and Steriotis, T., 2009. A Round Robin Characterisation of the Hydrogen Sorption Properties of a Carbon Based Material, *International Journal of Hydrogen Energy*, 34(7), 3044.

PHOTOVOLTAICS BASED ON SEMICONDUCTOR POWDERS

Dieter Meissner^a

Tallinn University of Technology, Dpt. of Material Science,
Ehitajate tee 5, 19086 Tallinn, Estonia
a. Corresponding author (dieter.meissner@ttu.ee)

ABSTRACT: The chapter will review the history of and current technologies based on semiconductor powders or spheres such as those of Texas Instruments / ATS, CV 21, Sphelar Power, FujiPream, Kyocera, Kyosemi, and Ball Semiconductor, before focusing on our own activities and those of crystalsol GmbH.

1. FRAME AND AIM

After nearly 60 years of development photovoltaics reached visibility in primary power diagrams at least in some countries. Exponential growth of solar panel production, steady improvements in efficiencies and thereby a pronounced decrease of module costs by meanwhile more than a factor of 1000 (from more than 1000 to less than 1 \$/W_p) today lead already to grid parity in some countries, including Germany. Leading scientists analyzing the possibilities to save the planet's climate and the potential for sustainable power use on a global level therefore see solar electricity and wind power as the main options [Lewis 2007; Lewis 2010; Meissner, 2010]. According to these calculations 10 - 30 TW of renewable power will be needed. Assuming that half of it would have to be provided by photovoltaics this accounts to 30 - 100 TW_p installed modules assuming an average capacity factor of 15 %. With a lifetime of 30 years this requires an annual production rate of 1 - 3 TW_p/a or 1-3 km²/hour for an assumed future plant efficiency of 20 %. In other words: 250 - 830 production lines would have to produce photovoltaic modules with an output of 1 m²/s. For comparison: the 2012 world's largest producer, Yingli, produced about 2.2 GW_p that year [CleanTechnica, 2013]. Therefore, in order for a substantial contribution of

photovoltaics to a global power supply very fast, large scale and low-cost production methods need to be developed. Here powder technologies may be the ideal solution to combine this requirement with high module efficiencies, as will be shown below.

2. THE ROOTS

The idea to produce solar cells from powder materials is nearly as old as the modern silicon-based solar cells. Already three years after AT&T Bell Lab's Chapin, Fuller and Pearson published their first commercially interesting silicon solar cell [Pearson *et al.*, 1954; Chapin *et al.*, 1954], their licensee and cell and module producing company Hoffmann Electronics patented a method to produce solar modules from silicon powders obtained obviously from grinding their precious crystals [Paradise, 1957]. Maurice Elliott Paradise, the inventor, thereby not only became the grandfather of powder-based solar cells, of which monograin membrane solar cells are modern variants, he also paved the way for spherical and spherular solar cells (see below).

Hoffmann Electronics at this time was the leading supplier of commercial solar modules, having started to sell 2% efficient cells already in 1955 for \$25/cell or \$1,785/Watt. In 1957 they had already

8 % efficient solar cells, in 1958 9% [Wikipedia, 2013]. In 1959 they filed modifications of this new type of cell. Matlow embedded “a plurality of semiconductor pieces in a transparent conductive supporting material” [Matlow, 1959], Ralph claimed a “large area solar cell panel” produced by depositing semiconductor particles (here still silicon) onto a metal film (e.g. Au/Sb), which upon heating forms an Ohmic contact, then sealing this with a plastic film between the particles before preparing a surface junction (e.g. an Al₂O₃ Schottky-junction) and a transparent front contact with a metal grid [Ralph, 1959]. How far these developments really went is unknown to the author. Unfortunately in 1977, after 36 years in business, the Board of Directors at Hoffmann Electronics decided to sell off the main division to Gould Electronics [Hoffmann, 2013].

In 1962 Elmer G. Fridrich of General Electric Company claimed an “electric component comprising a solid electrically insulating sheet interlocking a plurality of dispersed single crystals” of a photosensitive material “having major intermediate portions embedded in and irregular end portions protruding from and exposed at both sides of said sheet” with contacts on both sides [Fridrich, 1962]. In this patent also for the first time other materials than silicon are mentioned such as PbS and the sulfides, selenides and sulfo-selenides of cadmium. In their examples CdS is used. With this patent the single crystalline heterojunction monograin solar cell was born.

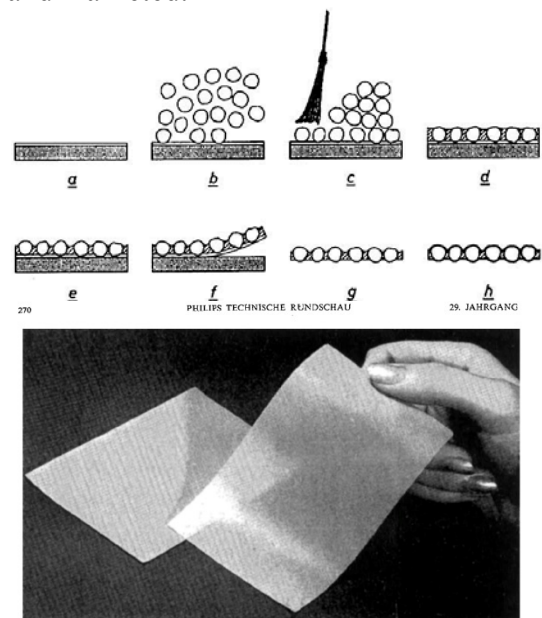
3. FIRST PRODUCTS

3.1. Valvo's monograin membranes

Based on several of above patents Philips Company in Eindhoven started to work on monograin membranes. Ties Siebold te Velde had filed a first patent in 1964

on LEDs based on ZnS or CdS films (NL6404898), using already a p/n junction [te Velde, 1964]. During the next year he filed a first Philips patent on monograin membrane devices [te Velde, 1965]. Here a monograin membrane device was patented with “a transparent contact containing areas of higher conductivity between the grains and lower conductivity above the grains”. 18 further patents were filed until 1973 specifying methods of membrane production as well as new applications such as the production of printed circuits.

Philips also developed different variants of p/n-type photovoltaic monograin membranes with similar and relatively complicated ways to produce p/n-grains [te Velde, 1968]. “Radiation-sensitive” devices were later specially protected in [te Velde, 1971]. However, probably due to the in that time not existing mass market, solar cells were never produced and marketed.



Einzelkornsichten

T. S. te Velde und G. W. M. T. van Helden

Figure 1: Philips production technology for CdS monograin membranes as produced in Valvo, Hamburg, until the 1990's [te Velde and van Helden, 1968b]. However, Valvo, Philips' production-

company in Germany, was producing monograin membrane based photoconductive elements containing 35 to 45 μm Cu-doped CdS particles in Hamburg until mid of the 1990s. It was a very small production line operated by one lady one day per week to produce about 100 monograin membranes of $10 \times 15 \text{ cm}^2$, which were processed during the rest of the week, i.e. overlapping In/Au contacts ($5 \times 5 \text{ mm}^2$) were evaporated on the two opposite sides, the membranes cut to the final pieces of 25 mm^2 , metal wires glued to the contacts and the membranes dipped into a transparent glue to seal and protect the device, followed by a quality control measurement of the photoconductivity.

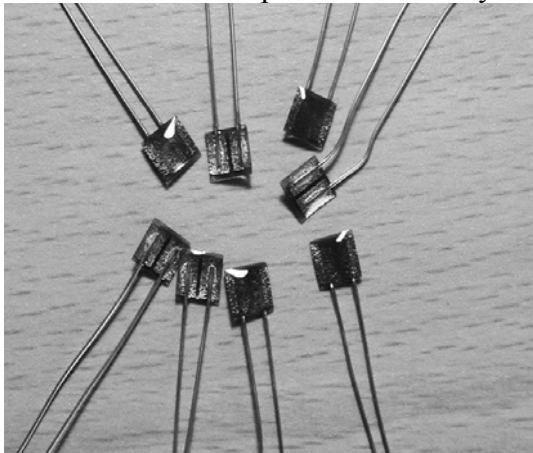


Figure 2: Volvo's monograin devices: $5 \times 5 \text{ mm}^2$ photoresistors.

This extremely easy and low-cost production method was taken over by the author and became the basis of Crystalsol's production process (see below). After finishing the photoconductor production at Valvo the monograin membrane production was stopped in Hamburg.

3.2 Spherical Solar

Another already historical production process is that of spherical solar cells, which was still in 2004 called "a revolutionary solar electricity technology breakthrough that provides an extremely

versatile and cost-effective method of generating solar electricity".

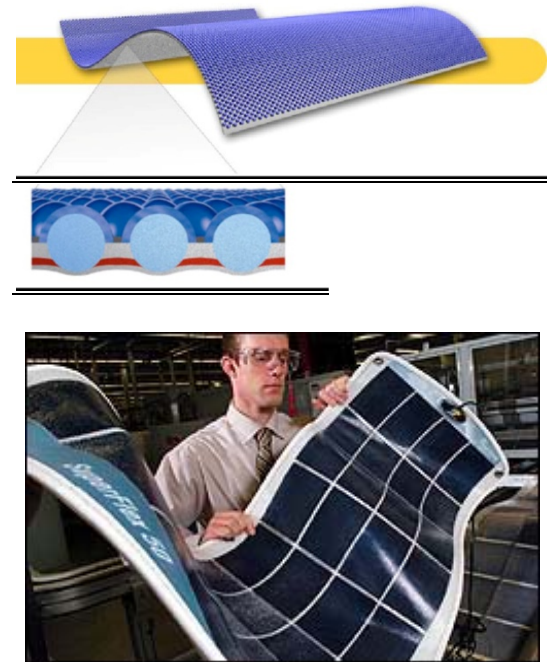


Figure 3: Schematic drawing and photograph of Sphelar Solar Cells [ATS, 2007].

Sphelar Solar™ spheres are bonded between two sheets of aluminum foil. The front foil determines the spacing of the spheres and acts as the electrically negative contact to the n layer. The back foil acts as the electrically positive contact to the p-type core of the spheres. Those design characteristics allow cells to be manufactured in different sizes for different uses.

The technology to use a monolayer of n- and p-type semiconductor spheres parallel and series connected (depending on the type) for direct conversion of solar energy into chemical energy by electrolysis of hydrogen bromide (HBr) had been developed and patented by Jack Kilby, Jay W. Lathrop and Wilbur A. Porter [Kilby *et al.*, 1975]. Here all spheres were covered with a metal film acting as electrodes in a HBr solution. Such arrangements were then combined with an appropriate fuel cell to regenerate HBr and use the stored energy in an

electric circuit. Besides for military and space applications TISES, the Texas Instruments Solar Energy System, was also developed for residential applications [Johnson, 1983].

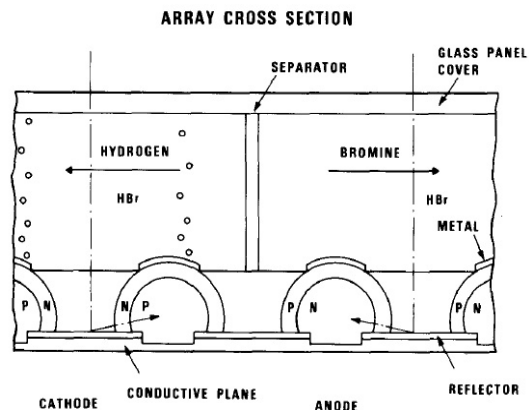


Figure 4: Schematic cross section of TISES solar chemical converter (left) and Block diagram of TISES [Johnson 1981].

The silicon spheres were inserted into pre-perforated aluminum foils (as used in shadow masks in the at that time common cathode ray TV screens). Here every semiconductor particle is only partly coated with a p/n-junction forming contact material contacting the aluminum foil. The uncoated inner part of the particle is here contacting a back contact separated from the aluminum foil be an insulating layer. About 30 x 30 cm² large cells contained about 17.000 silicon spheres built into an aluminum foil connected to a second Al-foil, producing a maximum of 100 W. The tiny Si-spheres grown by fast cooling of a melt are pressed into a perforated Al-foil and covered by a second Al-foil.

The series production should have started in 1993, to allow for an electricity kWh-price of only 0,23 \$. However, as part of a corporate restructuring, the company divested itself in 1995 of its solar technology project, which was sold to Ontario Hydro. Probably due a lack of support by the Canadian government the project was sold in 1997 to ATS, a former part of the team at Texas

Instruments in the early 1990s as a supplier of automated equipment. Here Hammerbacher, who joined ATS the same year, continued research and development. In 2002 ATS newly created a subsidiary, Spheral Solar Power Inc. (SSP), to begin commercial manufacture of the "next generation solar cells" at a 120,000-squarefoot-facility [Jalsevac, 2002]. In 2006 ATS decided to spin off it's solar activities under the name of Photowatt Technologies but delayed it "because of production troubles" [Hamilton, 2006]. In 2007 finally ATS announced that its subsidiary, Photowatt Technologies Inc., has signed a non-binding letter of intent to enter into a business relationship with Clean Venture 21 Corporation ("CV21") of Kyoto, Japan and Fujipream Corporation ("Fujipream") of Hyogo, Japan, in order to advance the development of its Spheral Solar™ Technology. ATS then treated Spheral for years as „a halted development project that has been wound down” [ATS, 2008]. After in 2011 ATS's PV producer Photowatt had started bankruptcy procedures all assets were finally sold in 2012 to Électricité de France SA (EdF) [ATS, 2012].

3.3 Kyosemi's Sphelar Solar Cell

Kyosemi Corporation, Japan, was founded in 1980 in Joyo City, Kyoto, Japan, as a research and development-oriented company. Today, it conducts business in the fields of “opto semiconductor devices” and solar power generation, and commercializes and markets original products including optical communication devices, optical sensing and control devices, and the spherical photovoltaic solar cell Sphelar® [Kyosemi, 2013]. Sphelar® is the trademark given in 2004 to a proprietary spherical solar cell product Kyosemi Corporation has developed on its own.

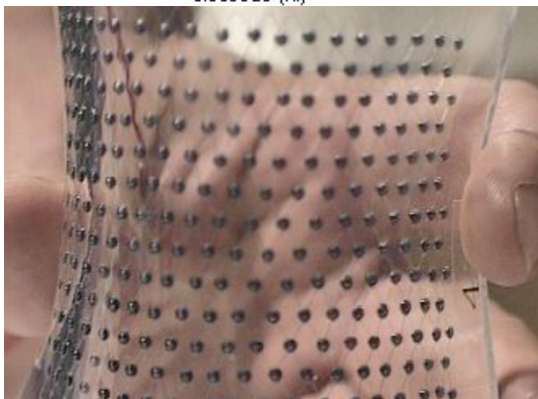
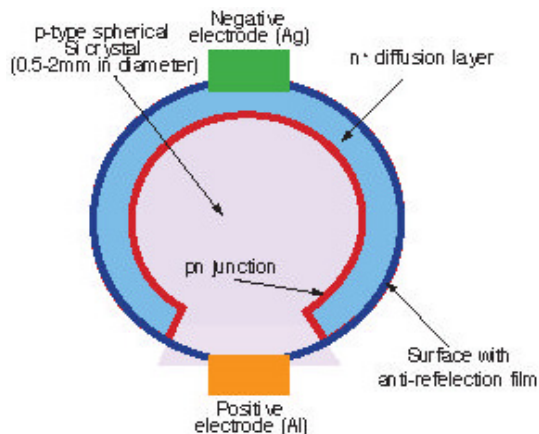


Figure 5: Scheme of a Kyosemi Sphelar® silicon particle, contacted (left) and Sphelar® Solar Module [Kyosemi, 2013].

In May 2012 Sphelar Power Corp. was established. Their products are aiming at highly transparent windows (Sphelar® BIPV) and consumer products (Sphelar® EIPV) such as Sphelar Lanterns, Garden Lights or even textiles [Kyosemi, 2013].

3.4 Kyocera Corp.

Kyocera Corporation was founded in 1959 to manufacture advanced ceramics and became a major supplier of solar cells, semiconductor packages, cameras, laser printers, electronic components and telecommunications equipment. Kyocera today is one of the world's largest vertically integrated producers and suppliers of solar energy panels. The company started in 2000 to file patents on particle-based photovoltaic devices very similar to the original Hoffman-devices [Sugawara *et al.*, 2000] as described above. The devices are based on p-type

crystalline silicon particles contacted on top by an amorphous n-type silicon film. Also the fabrication silicon spheres by using a dropping methods or a plate-based method were protected. Of special interested is the use of reflectors between the particles increasing the active area of the device, compare also the CV 21-modules below.

Kyocera continued research at on the manufacturing of silicon particles at least until 2008 [Sugawara *et al.*, 2008], commercial products are not known to the author.

3.5 Clean Venture 21

Clean Venture 21 Corporation was founded in 2001 in Kyoto by the former director of Matsushita's R&D center for PV Mikio Murozono, and installed its first molten silicon-dropping furnace at the University of Tokyo [CV21, 2013]. In a first patent of November 2000 Yoshihiro Hamakawa and coworkers already outline the final version of their silicon spheres-based device as well as their production process [Hamakawa *et al.*, 2000]. The silicon spheres are produced in a dropping process from a melt including a second heating process of the falling drop by a laser beam. In contrast to the above-mentioned processes the cooling happens in a few stories high falling tower, so that nicely spherical particles with diameters of about 1 mm are formed. After doping the outside they are picked up one by one, polished on one side and inserted into a substrate made from an array of small reflector cups, compare fig. 6.

In 2005 they displayed a first module at PVSEC Shanghai and signed a partnership for research, development, volume production and commercialization of photovoltaic Si solar cells with Fujipream Corp. of Hyogo, Japan [TechOn, 2005]. At that

time they claimed a conversion efficiency of 11.7 % and flexible cells. In 2007 they shipped the first $5 \times 15 \text{ cm}^2$ cells with micro reflector cups. Modules are then assembled from these cells. In July 2008 they installed the first 15 MW line and in August opened a new plant at Kisshoin, Minami Ward, Kyoto. Meanwhile several installations have been made in Japan and modules up to 130 W_p are offered on their website. CV21's rich patent portfolio deals with particle preparation as well as placing spheres at defined places and interconnecting them.

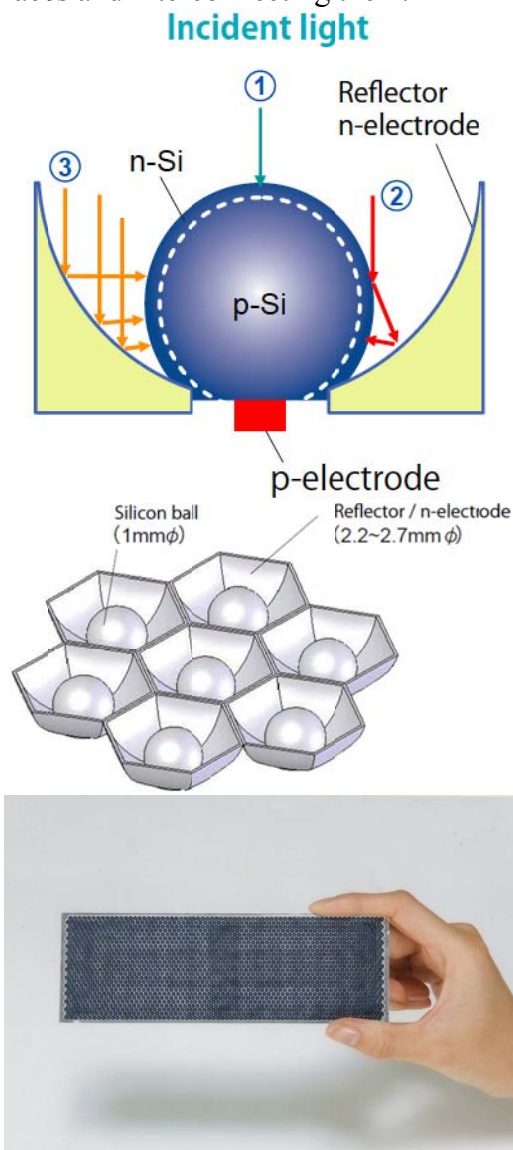


Figure 6: Scheme of a CV 21 silicon sphere / reflector assembly and a cell [CV21, 2013].

3.6. Other activities

In 1996 Ball Semiconductor Inc. [Ball Semiconductor Inc., 2009] was founded in Texas to commercialize applications based on silicon balls of about 1 mm in diameter demonstrating besides different electrical sensors and circuits in 2000 also a solar cell made from an assembly of these balls. The company also worked with different Japanese Universities through their Japanese office. Main application had been MEMS and three-dimensional acceleration sensors [Yoshida, 2001]. Their company website unfortunately is not accessible anymore.

In 1999 Mitsui High Tec (formerly Mitsui Mfg.), calling itself "the world's foremost supplier of lead frames for integrated circuits" [Mitsui High Tec, 2013], filed a patent describing a PV device resembling closely the appearance of a powder-based device, however, actually being based on a "a board with a surface with a plurality of spherical segments projecting from the board surface" [Fukui and Kimoto, 1999]. Onto this board thin film solar cells are deposited. So this type of device is actually not a powder-based solar cell. It is unknown to the author if Misui High tec continued their development.

Other companies active in spherical silicon solar cell developments include Fuji Machine Manufacture [Liu *et al.*, 2007a and b; Nagai *et al.*, 2007] and ZT Solar, Texas [Wang, 2001].

4. NEW MONOGRAIN MEMBRANE DEVELOPMENTS

4.1. TUT monograin membranes

Using Philips' Monograin Membranes the author worked on photoelectrochemical solar energy utilization already since 1980 under the supervision of Rüdiger Memming and Bertel Kastening at Hamburg University [Meissner *et al.*,

1982 and 1983]. When Valvo stopped their production line 15 years later the technology was transferred to his group at that time in Hannover, later Jülich. Even before this Enn Mellikov and his colleagues at Tallinn's Polytechnical Institute in Estonia developed powder improvement and growth techniques under the supervision of Jaan Hiie [Mellikov and Hiie, 1976 and 1977] to produce very high quality single-crystalline II/VI, mainly CdS-powders, well aware of the use of such powders in monograin membrane devices by Philips as described above. Soon later they had also developed their own monograin layer technology to produce microwave, light and x-ray sensors [Hiie *et al.*, 1980 a and b, Altosaar *et al.*, 1980]. Since this was still the Soviet time unfortunately most of their research was classified and even their patents kept secret, so that not much became really known to west until Estonia's independence in 1991 [Krustock *et al.*, 1990a and b].

Immediately after the author met the Tallinn group in a conference a very close collaboration started focusing on monograin membrane solar cells, first still based on chalcogenides such as CdSe, CdTe and their solid solutions [Mellikov *et al.*, 1993; Wirts, C. *et al.*, 1994; Hiie *et al.*, 1997], then on CIS and CIGS [Altosaar and Mellikov, 2000; Altosaar *et al.*, 2003a; Altosaar *et al.*, 2005; Timmo *et al.*, 2007; Dennler *et al.*, 2007], and finally on CZTS [Altosaar *et al.*, 2006 and 2008; Mellikov *et al.*, 2009 and 2011; Klavina *et al.*, 2011].

A basic patent on the molten salt growth of complex semiconductor powders was filed in 1998 [Meissner *et al.*, 1998] and became the basis of a first commercialization attempt together with the glass company Scheuten.

4.2. Scheuten's "Sunrise" approach

In 2000 the glass-coating company Scheuten from Venlo, The Netherlands, started collaborating with the research group at Tallinn University of Technology on glass-based CIGS monograin solar cells.

However, in 2003 they filed their own (extremely narrow) patent [Scheuten *et al.*, 2003] claiming CIGS coated glass balls as a base material. This finally led to a new concept called "Sunrise" based on sputtering layers of molybdenum, Cu, In, Ga and converting the latter in a sulfur/selenium atmosphere, followed by inserting the today about 200 μm -spheres into metal coated polymer film [Geyer *et al.*, 2006; Geyer, 2007]. Scheuten also applied for two patents with members of Enn Mellikov group at TUT [Altosaar *et al.*, 2003b and c] on details of the Cu(InGa)Se₂ production process, which again are extremely narrow strictly limiting them to this material and in the first case a first step of forming a CuIn- and/or CuGa-alloy and in the second case treating powders of this composition in a sulfur atmosphere. The collaboration stopped in 2007 and was finally terminated in 2008.

In 2007 Scheuten opened a pilot production facility in Venlo, The Netherlands. A 250 MW factory, planned already for 2009, has not been realized. In October 2008 Scheuten signed an agreement with RITEK, a leading optical disc and OLED group world-wide, to start a Joint Venture Company to manufacture CIGS thin film solar cell with issued capital of NT\$ 600 million at first stage, where each party takes 50% share holding. The JV Company is located at Hsin-Chu in Taiwan. "Production facilities for the manufacture of 30MW of solar cells will be in place towards the end of 2008. Capacity will be doubled each year from 2009 to 2010,

reaching 120MW by 2010. Production can be increased still further in the light of the future growth of market demand“ [Scheuten, 2007].

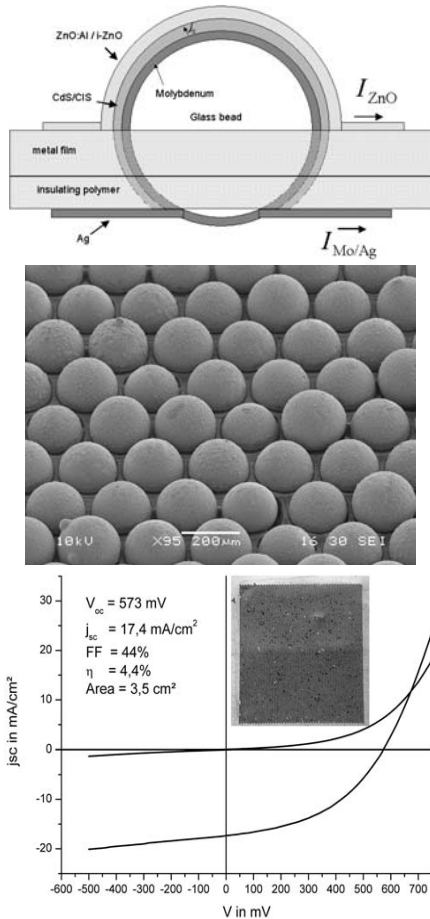


Figure 7: Scheme of a coated sunrise glass bead embedded into a metal film (left), CIS covered glass beads in metal film, and I/V-curve of a Efficiency of a 3.5 cm² glass bead solar cell including a picture of the module exhibiting a large number of missing beads [Geyer 2007].

A key problem of all technologies based on perforated foils seems to be the filling of all holes with spheres. As can be seen in a picture of an Scheuten Sunrise cell (fig. 11 right) a large number of defects seem result of an automated production process [Geyer 2006 and 2007]. As can be seen already from the patents of the different “spherical” companies (from Texas Instruments to ATS) an amazing effort was put into automating the

placement of silicon spheres into all holes of the perforated Al-foil.

4.3. *crystalsol's* Monograin Membrane Solar Modules

Based on the above-described Philips/Valvo monograin membrane technology the author further developed the technology to produce a powder-based monograin module production process [crystalsol, 2013]. By using this approach the semiconductor formation is separated from cell / module manufacturing, leading to substantial advantages during processing / manufacturing of such solar cells. A pilot production line was set up in its R&D facility already in 2007. In 2007 the author and his TUT colleagues decided to start the TUT spinout company *crystalsol OÜ* together with two colleagues from Austria willing to manage such a startup venture. A year later Crystalsol GmbH was founded by these 3 with Crystalsol OÜ later becoming its daughter.

Crystalsol is currently upscaling its proprietary powder production process [Meissner *et al.*, 1998] in Tallinn, Estonia, and developing a roll-to-roll module production in Vienna, Austria. The semiconductor crystal powders are produced in a molten salt, followed by surface treatment and annealing steps. A buffer layer is deposited on the surface in a classical chemical bath deposition (CBD) process forming the active interface and protecting the particles against ageing. Small solar cells are produced from this powder for quality control before it is supplied for module production.

Fig. 8 shows an early stage module production scheme [Meissner, 2008]. The production starts with the deposition of a polymer binder onto a temporary substrate foil 1. Conductive lines are introduced enabling the series connection of cells for monolithic integration followed by inserting a single layer of

powder particles (4). A transparent front contact (TCO) is deposited (6) in stripes for series connection, and a transparent encapsulation foil 9 seals the front side. The temporary substrate foil is removed from the back-side (19), which in a next stage is opened in an abrasion process 11. A carbon-based back contact is printed (12) and contact stripes are deposited, finalizing the series connection. A final encapsulation foil is applied and the modules cut off in desired lengths.

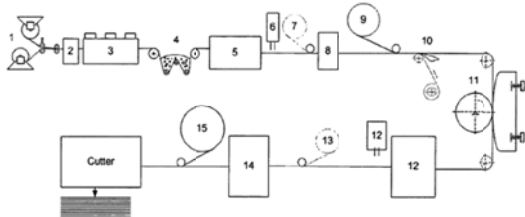


Figure 8: Crystalsol's patented production process as described in WO 2010 000581 [Meissner, 2008]

This process allows a roll-to-roll (R2R) module production started by a printing process of a polymer layer and directly ending with a sealed ready-to-use module. The solar cell material itself is prepared before in a bulk process allowing for any temperature and very high process control in the form of an about 50 μm single crystal powder of highest quality and homogeneity. Thereby all area upscaling problems - as crucial for all thin-film technologies - are avoided and the advantage of Silicon's wafer technology, to separate materials and module production and thereby being able to optimize both independently, is preserved, while on the other hand replacing the tedious cell handling, stringing and encapsulation by an ultra-fast R2R process.

Due to the crystalline structure of the semiconductor particles exhibiting different crystal planes and approaching a pyramidal structure packing densities of above 90 % are achieved. Spherical particles allow for only 85 % in dense packing as shown in Fig. 13 together with

a 20 x 20 cm^2 module. The shiny spots seen on this module are reflections from some of the crystals, which give the module a very special precious appearance. Monolithic series connection is achieved by use of metal wires embedded into the module allowing for a very cost effective production.

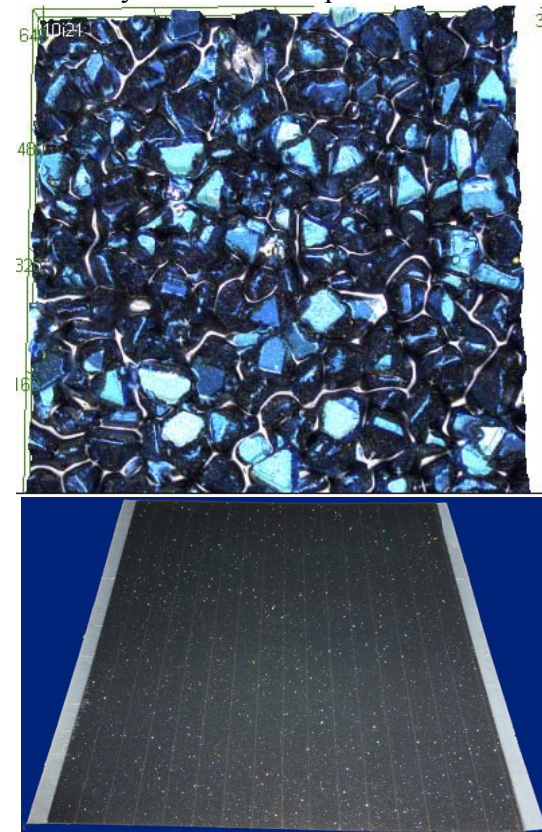


Figure 9: CZTS Monograin Membrane, Powder size 50-60 μm (top) and crystalsol monograin module of 20 x 20 cm^2

Crystalsol currently develops a production process based on the Kesterites $\text{Cu}_2\text{ZnSn}(\text{S}_x\text{Se}_{1-x})_4$ (CZTS) of different compositions, compounds very similar to the chalcopyrite CIGS but replacing the resource-limited and very expensive Indium by the abundant elements Zink and Tin. However, basically all compound semiconductors can be used in this process including also CIS, CIGS or CdTe (which also have been used already in TUT).

Copper-zinc-tin-chalcogenides (CZTS), especially $\text{Cu}_2\text{ZnSnS}_4$, $\text{Cu}_2\text{ZnSnSe}_4$ and

their solid solutions, often called also Kesterites due to their crystal structure, is considered as one of today's most promising new materials for photovoltaics [Unold and Schock, 2011; Siebentritt, 2013]. Efficiencies of up to 8.4 % as certified by Fraunhofer ISE (fig. 10) have been achieved as of today and will be further optimized in the future [crystalsol, 2013].

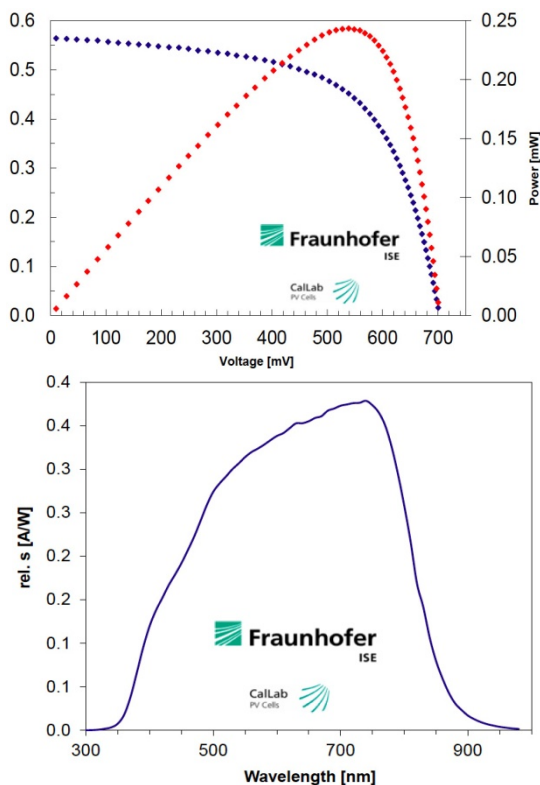


Figure 10: I/V curve and Quantum Yield spectrum of a crystalsol solar cell as certified by ISE Freiburg (Eff. \square = 8.4 %, U_{oc} = 703 mV, I_{sc} = 19,4 mA/cm², FF = 61,34 %)

5. SUMMARY

Although the idea to produce large-scale solar cells or modules of very high quality based on crystalline grains has been around since more than 50 years and several companies developed technologies to utilize this idea only recently first modules became commercially available. However, of the three companies currently active in commercializing this type of solar cells

only crystalsol aims at an ultra-cheap production process. Kyocera ns CV 21 both handle their spherical particles one by one in order to form Ohmic contacts to the inside and a p/n-junction on the rest of the surface, and place them in preformed structures. This does not allow for a fast large scale production process as needed for the high production rates required for a TW production in the near future to replace fossil fuel utilization and to save the world's climate.

ACKNOWLEDGEMENTS

Financial support by the Estonian Research Council is gratefully acknowledged. We also thank all our current and previous coworkers in Estonia, Germany, and Austria, of whom Academician Prof. Dr. Enn Mellikov, Dr. Jaan Hiie and Dr. Mare Altsaar should especially be mentioned.

REFERENCES

- Altsaar M. *et al.*, 1980, *Proc. 9th Int. Symp. Technical Committee on Photon-Detectors* 1980, 175.
- Altsaar M. and Mellikov E., 2000, CuInSe₂ Monograin Growth in CuSe-Se Liquid Phase, *Jpn. J. Appl. Phys.* 39, 65
- Altsaar M. *et al.*, 2003a, Monograin layer solar cells, *Thin Solid Films* 431, 466
- Altsaar, M. *et al.*, 2003b, V, *EP1548845*, priority date December 22, 2003;
- Altsaar, M. *et al.*, 2003c, Process to produce a Cu(In,Ga)Se₂ single crystal powder and monograin membrane solar cell comprising this powder *EP1548159*, priority date Dec. 3, 2003.
- Altsaar M. *et al.*, 2005, Further developments in CIS monograin layer solar cells technology, *Solar Energy Mat. Solar Cells* 87, 25
- Altsaar M. *et al.*, 2006, Cu₂ZnSnSe₄ Monograin Powders for Solar Cell Application, in: *4th World Conf. Photovoltaic Energy Conversion*, Waikoloa, HI, USA, 2006, IEEE 2006, p. 468.
- Altsaar M. *et al.*, 2008, Cu₂Zn_{1-x}Cd_xSn(Se_{1-y}S_y)₄ solid solutions as absorber materials for solar cells, *Physica Status Solidi (a)* 205, 167.
- ATS, 2007, ATS's Photowatt Technologies signs Letter of Intent to Jointly Develop Spherical Solar(TM) Technology, posted January 11, 2007, on ATS website, no longer online.

- ATS, 2008, A phrase used (at least until 2011) in several ATS statements including the Management's Discussion and Analysis, August 13, 2008, online at http://www.atsautomation.com/en/investor_relations/~media/Media/Documents/12_Investor_Relations/Financial_Reports/2009/Q1_09_MDA_FINAL.pdf, last accessed April 29, 2013.
- ATS, 2012, ATS reports first quarter fiscal 2013 results, August 14, 2012, online at http://www.atsautomation.com/~media/Media/Documents/12_Investor_Relations/Financial_Reports/2013/ATS_Q1_13_Press_Release_FINAL_CNW.ashx, last accessed April 29, 2013.
- Ball Semiconductor Inc., 2009, Website, online: <http://www.ballsemi.com/tech/energy.html>, is not available at least since April 2013, last accessed Jan. 24, 2009 and June 11, 2013.
- Chapin D.M. *et al.*, A New Silicon p-n Junction Photocell for Converting Solar Radiation into Electrical Power, *J. Appl. Phys.* 25, 676 - 677.
- CleanTechnica, 2013, Top 10 solar PV module suppliers in 2012, online <http://cleantechnica.com/2013/02/05/top-10-solar-pv-module-suppliers-in-2012/>, last accessed April 30, 2013.
- crystalsol, 2013, company website, online at www.crystalsol.com, last accessed April 30, 2013.
- CV21, 2013, CV21 Corporate Information, <http://www.cv21.co.jp/en/profile/index.php>, last accessed April 30, 2013.
- Dennler, *et al.*, 2007, A Self-Rechargeable and Flexible Polymer Solar Battery, *Solar Energy* 81, 947.
- Fridrich E.G., 1962, Photoconductive electrical component, *US3247477*, priority date October 3, 1962.
- Fukui A, and Kimoto K, 1999, Solar battery and method of treating a board for a solar battery, *US6420644 B1*, priority date Nov. 26, 1999.
- Geyer V. *et al.*, 2006, A Novel Approach to the Manufacture of Chalcogenide Thin Film Solar Cell, *Conf. Record 4th World Conf. Photovoltaic Energy Conv.*, Waikoloa, HI, USA, 2006, pp. 333
- Geyer, V., 2007, The sunrise concept: an alternative manufacturing method for thin film solar cells, *Glas Performance Days 2007*, p. 402.
- Hamakawa Y. *et al.*, 2000, Photovoltaic apparatus and mass-producing apparatus for mass-producing spherical semiconductor particles, *US2002096206 (A1)*, priority date Nov. 24, 2000.
- Hamilton T., 2006, ATS plunges on Spherical Solar delays, write down, Clean Break »Blog Archive», posted May 25, 2006, online at <http://www.cleanbreak.ca/2006/05/25/ats-plunges-on-spherical-solar-delays-writedown/>, last accessed April 29, 2013.
- Hiie J. *et al.*, 1980a, Photoconductive cadmium sulfide and cadmium sulfide selenide (CdSxSe1-x) layers for microwave range, *Proc. 9th Int. Symp. Technical Committee on Photon-Detectors*, 167
- Hiie J. *et al.*, 1980b, Cadmium sulfide monograin layers as detectors of visible and x rays, *Proc. 9th Int. Symp. Technical Committee on Photon-Detectors* 1980, 172.
- Hiie J. *et al.*, 1997, Growth of CdTe monograin powders, *Physica Scripta*, T69, 155
- Hoffman, 2013, Hoffman Video website: <http://www.hoffmanvideo.com/aboutus.asp>, last accessed April 26, 2013.
- Jalsevac P., 2002, Solar plant will bring ATS into 'new era,' employ 175, July 18, 2002, online at: http://www.therecord.com/links/generic_020718165850.html, last accessed May 17, 2009.
- Johnson E.L., 1981, The TI solar energy system development, *Tech. Dig. - Int. Electron Devices Meeting* 27, 2.
- Kilby J. *et al.*, 1975, Solar energy conversion, *US4021323*, priority date 28, 1975.
- Klavina I. *et al.*, 2011, Study of Cu₂ZnSnSe₄ monograin formation in molten KI starting from binary chalcogenides, *Thin Solid Films* 519, 7399.
- Krustok J. *et al.*, 1990a, The nature of recombination centres in silver and chlorine doped CdS phosphors, *J. Phys. Chem. Solids* 51, 1013
- Krustok J. *et al.*, 1990b, Nature of the 0.8 eV photoluminescence band of doped CdTe, *Sov. Phys. Semicond.* 24, 1176.
- Kyosemi, 2013, Kyosemi Sphelar Power Website <http://sphelarpower.com>, last accessed April 29, 2013.
- Lewis, N.S., 2007, Powering the Planet, *Engin. & Sci.* 2 (2007). 13
- Lewis, N.S., 2010, Global Energy Perspective, online at <http://nsl.caltech.edu/energy>, last accessed April 30, 2013.
- Liu Z, *et al.* 2007a, A concentrator module of spherical Si solar cell, *Sol. Energy Mat. Sol. Cells* 91, 1805.
- Liu Z., 2007b, Seeding method with silicon powder for the formation of silicon spheres in the drop method, *J. Appl. Phys.* 101, 093505.
- Matlow SL, Method of making a large area solar cell panel, *US3040416*, priority date May 13, 1959.
- Meissner D. *et al.*, 1982, Light Induced Hydrogen Formation at CdS Monograin Membranes, in: Rabani J., (Ed.): *4th International Conference on Photochemical Conversion and Storage of*

- Solar Energy*, Book of Abstracts, The Hebrew University of Jerusalem, Israel, 1982, p. 267.
- Meissner D. et al., 1983, Light Induced Generation of Hydrogen at CdS-Monograin Membranes, *Chem. Phys. Lett.* 96, 34.
- Meissner D., 1998, Monocrystalline powder and monograin membrane production, *WO9967449*, priority date June 25, 1998.
- Meissner D., 2008, Method for the production of a monograin membrane for a solar cell, monograin membrane, and solar cell, *WO201000581 (A2)*, priority date July 3, 2008.
- Meissner D., 2010, Energie für das Jahr 2050, Praxis der Naturwissenschaften - Chemie in der Schule 59 (2010), 6 - 10.
- Mellikov E. and Hiie J., 1976, Effect of flux nature on the morphology of a recrystallized powder, *Trudy Tallinskogo Politehnicheskogo Instituta* 404, 119
- Mellikov E. and Hiie J., 1977, Mechanism and kinetics of growth and morphology of cadmium sulfide crystals, *Tezisy Dokl. Vses. Soveshch. Rostu Krist.*, 5th 1, 146.
- Mellikov E. et al., 1993, Monograin A2B6 powders, *Surf. Coatings Technol.* 62, 688
- Mellikov E. et al., 2009, Monograin materials for solar cells, *Sol. Energy Mat. Sol. Cells* 93, 65
- Mellikov E. et al., CZTS monograin powders and thin films, *Adv. Mat. Res.* 222 (2011), 8.
- Mitsui High Tec, 2013, company website, online at <http://www.mitsuihightec.com>, last accessed April 30, 2013.
- Nagai T. et al., 2007, Characterization of spherical Si by photoluminescence measurement, *J. Appl. Phys.* 101, 103530
- Paradise M.E., 1957, Large Area Solar Energy Converter and Method for Making the Same", *US 2,904,613*, priority date August 26, 1957.
- Pearson G.L. et al., 1954, Solar Energy Converting Apparatus, *US 2,780,765*, filed March 5., 1954.
- Ralph EL, Method of making a solar cell panel, *US3038952*, priority date May 20, 1959.
- Scheuten J., 2003, Spherical or grain-shaped semiconductor element for use in solar cells and method for producing the same, *WO2005034149 A*, priority date October 2, 2003.
- Scheuten, 2007, company website: Research & Development: www.scheuten.nl/203, last accessed Dec. 10, 2012; Scheuten Solar Press Release, June 21, 2007.
- Siebentritt S., 2013, Why are kesterite solar cells not 20% efficient?, *Thin Solid Films* 535, 1.
- Sugawara S. et al., 2000, Photoelectric conversion device, *US2002023674*, priority patent priority date May 29, 2000.
- Sugawara M. et al., 2008, Crystalline silicon particle, production method thereof, and photoelectric conversion element using the same, *JP2010126393 (A)*, priority date Nov. 27, 2008.
- te Velde T.S., 1964, Semiconducting injection recombination radiation source, *NL6404898 A*, priority date Mai 1, 1964.
- te Velde T.S., 1965, Electrical monograin layers having a radiation permeable electrode , *NL6510095*, filed August 4, 1965.
- te Velde T.S., 1968a, Verfahren zum Herstellen elektronischer Bauelemente, *NL6813918*, priority date Sept. 27, 1968.
- te Velde T.S., 1971, Method of manufacturing a radiation-sensitive electronic device and device manufactured by using this method, *CA887890*, priority date December 7, 1971.
- te Velde T.S., and van Helden G..W.M.T., 1968b, Einzelkornschichten, *Philips Technische Rundschau* 29 (1968), 270
- TechOn, 2005, Newsletter, Dec. 9, 2005, http://techon.nikkeibp.co.jp/english/NEWS_EN/20051209/111508/ last accessed April 30, 2013.
- Timmo K. et al., 2007, CuInSe₂ monograin growth in the liquid phase of potassium iodide, *Thin Solid Films* 15, 5884
- Unold T. and Schock H.-W., 2011, Nonconventional (Non-Silicon-Based) Photovoltaic Materials, *Annu. Rev. Mater. Res.* 41, 297
- Wang, Y. et al., 2009, Spherical antireflection coatings by large-area convective assembly of monolayer silica microspheres, *Sol. Energy Mat. Sol. Cells* 93, 85.
- Wikipedia, 2013, Timeline of Solar Cells, online: http://en.wikipedia.org/wiki/Timeline_of_solar_cells, last accessed April 26, 2013.
- Wirts C. et al., 1994, Tailoring II/VI semiconductor materials properties to photoelectrochemical requirements, In: *10th Int. Conf. Photoelectrochem. Conversion Storage of Solar Energy*, Interlaken, Switzerland, p. 387
- Yoshida M., 2001, Ball semiconductor process and material, Proceedings EcoDesign 2001, Tokyo, Dec 11 -15, 2001, p. 1044

PRODUCTION OF ACTIVATED CARBON FROM BIOCHAR BY CHEMICAL ACTIVATION USING POTASSIUM HYDROXIDE

Dilek Angin^{1,a}, Hanife Kürkan¹ and Esra Altıntığ²

1. Sakarya University, Department of Food Engineering, Sakarya, Turkey

2. Sakarya University, Department of Chemical, Sakarya, Turkey

a. Corresponding author (angin@sakarya.edu.tr)

ABSTRACT: In this study, activated carbons were prepared by chemical activation with potassium hydroxide (KOH) of the biochar obtained through pyrolysis of safflower seed press cake. The influence of activation temperature on the yield, surface and chemical properties of the activated carbons were investigated. This purpose, the biochar were activated at temperatures ranging from 600 °C to 900 °C, heating rate of 10 °C/min and a KOH:biochar impregnation ratio of 1:1 under nitrogen atmosphere. The highest BET surface area was achieved as 1277 m²/g. The surface morphologies of the activated carbons were examined by scanning electron microscopy (SEM). As a result, it can be said that the biochar can be effectively used as a raw material for the preparation of activated carbon with KOH as activating agents. Also, the activated carbon obtained in this study can be used as a very promising adsorbent for pollution control and other applications.

1. INTRODUCTION

Activated carbons with high surface area and pore volume are carbonaceous materials that can be produced by physical and chemical activation processes [Ahmadpour and Do, 1997; Bagheri and Abedi, 2009]. Activated carbons have several important uses including solution purification (as in the clean-up of cane, beet and corn-sugar solutions), removal of tastes and odours from domestic and industrial water supplies, vegetable and animal fats and oils, alcoholic beverages, chemicals and pharmaceuticals and in the waste water treatment. It also finds use in purification of gases, liquid phase recovery, separation processes and as catalyst or catalyst support [Sahu et al., 2010].

Physical activation consists of reaction of a carbonized product with suitable oxidizing gases (i.e. air, steam or carbon dioxide) at temperatures in the 350-1100 °C [Olivares-Marín et al., 2006].

In chemical activation, raw material is impregnated with a dehydrating reagent

and heated in an inert atmosphere. The carbonization step and the activation step proceed simultaneously [Chandra et al., 2009]. The advantages of chemical activation are: its low energy and operating cost, higher carbon yields and large surface areas when compared with physical activation process [Gratuito et al., 2008]. Chemical activation has been successfully applied to the production of activated carbon using various chemical reagents i.e., ZnCl₂, H₂SO₄, H₃PO₄. Recently, alkali hydroxides such as KOH and NaOH have increasingly been used as activation reagents turning out high specific surface areas of the prepared activated carbons [Tay et al., 2009]. Chemical activation using KOH has been reported by many researchers. Several materials such as cherry stones [Olivares-Marín et al., 2006], date palm [Jibril et al., 2008], hazelnut bagasse [Demiral et al., 2008], cassava peel [Sudaryanto et al., 2006], biochar [Azargohar and Dalai, 2006] and olive seed waste [Stavropoulos and Zabaniotou, 2005] and have been used in the preparation of activated carbons by KOH activation.

In this study, activated carbons were prepared by chemical activation with potassium hydroxide (KOH) of the biochar obtained through pyrolysis of safflower seed press cake. The influence of activation temperature on the yield, surface areas and chemical properties of the activated carbons were investigated. This purpose, the biochar were activated at temperatures ranging from 600 to 900 °C, heating rate of 10 °C/min and a KOH:biochar impregnation ratio of 1:1 under nitrogen atmosphere. The surface morphologies of the activated carbons were examined by scanning electron microscopy (SEM).

2. MATERIALS AND METHODS

2.1. Material

Safflower seeds were supplied from Eskisehir Anatolia Agricultural Research Institute (ATAEM). Safflower seed press cake (SPC) was obtained from a mixture of Dincer and Yenice varieties by the cold-press extraction method [Şensöz et al., 2001].

2.2. Pyrolysis

For the production of the biochar, pyrolysis of the safflower seed press cake was carried out at 500 °C pyrolysis temperature and 50 °C/min heating rate in inert atmosphere (100 cm³/min). The proximate and elemental analyses of the biochar were performed [Angın et al., 2013].

2.3. Chemical activation

In this study, chemical activation of biochar was performed using potassium hydroxide. The impregnation ratio was calculated as the ratio of the weight of the used biochar to the weight of KOH in solution. The biochar was mixed with KOH, in a ratio KOH:biochar mass ratio of 1:1. Carbonization of the impregnated sample was carried out in tubular reactor (Protherm PTF 12) under nitrogen flow.

About 10 g of the impregnated sample was placed on a ceramic crucible in the reactor and heated up to the final carbonization temperature under the nitrogen flow (100 cm³/min) at heating rate of 10 °C/min and held for 1 h at this final temperature. The final carbonization temperature was varied from 600 °C to 900 °C. The resulting solids after carbonization were boiled at about 90 °C with 100 mL of 1 N HCl solution for 30 min to leach out the activating agent, filtered and rinsed by warm distilled water several times until the pH value was 6-7. Finally, they were then dried at 105±3 °C for 24 h, and weighed to calculate the yield.

2.4. Characterization

The yields of activated carbons were defined as the ratio of the sample weight after activation to the weight of the used biochar. The contents of C, H and N of the activated carbons were measured using a CARLO ERBA model EA 1108 Elemental Analyser. The oxygen contents of activated carbons were calculated by difference. The determination of the porosity of biochar and activated carbon sample were performed using physical adsorption of N₂ at 77 K (Quantachrome, Autosorb-1C). The surface areas were determined from nitrogen adsorption data by using Quantachrome software. Adsorption data were obtained over the relative pressure, P/P₀, range from 10⁻⁵ to 1. The sample was degassed at 300 °C under vacuum for 3 h. The N₂ apparent surface area was calculated by using the BET (Brunauer, Emmett and Teller) equation within the 0.01–0.2 relative pressure range [Yorgun et al., 2009].

Surface morphologies were studied by scanning electron microscopy (SEM). SEM images were performed using JEOL-JSM-6060LV Scanning Electron Microscope.

3. RESULTS AND DISCUSSION

The results of proximate and elemental analyses of the safflower seed press cake (SPC) and biochar are given in Table 1.

Table 1: Main characteristics of the bio-char.

Characteristics	Biochar
Moisture content (%)	1.36
<i>Proximate analysis</i> (%)	
Volatile Matter	16.30
Ash	10.50
Fixed carbon*	71.84
<i>Ultimate analysis</i> (%)	
Carbon	62.45
Hydrogen	1.85
Nitrogen	4.07
Oxygen*	31.63
H/C molar ratio	0.36
O/C molar ratio	0.51
Empirical formula	$\text{CH}_{0.36}\text{N}_{0.06}\text{O}_{0.38}$
HHV (MJ/kg)	31.81
BET surface area (m^2/g)	14.14

*By difference.

As can be seen from the table, biochar is a carbon-rich and having $\text{CH}_{0.36}\text{N}_{0.06}\text{O}_{0.38}$ empirical formula. The higher calorific value of the biochar is low but could be used directly as fuel. Also, the surface area of biochar was determined as $14.14 \text{ m}^2 \text{ g}^{-1}$ that it was considered as a raw material for production of activated carbon.

The yield is an important measure of the feasibility of preparing activated carbon from a given precursor. Activation temperature plays an important role on the yield of activated carbon. The effects of the carbonization temperature on the yields of activated carbon are shown in Figure 1.

It was found out that with increasing activation temperature, the activated carbon yields decreased for impregnation ratio (KOH:biochar) of 1:1 (wt%). When the activation temperature increased from

600 to 900 °C, the activated carbon yield decreased from 25.13% to 10.36%. As the temperature increases, there is a transition from the primary carbonization stage to the secondary stage. Accordingly, the chemical structure disintegrates even more as a result of which more tar is released and the activated carbon yield decreases [Sütcü and Demiral, 2009].

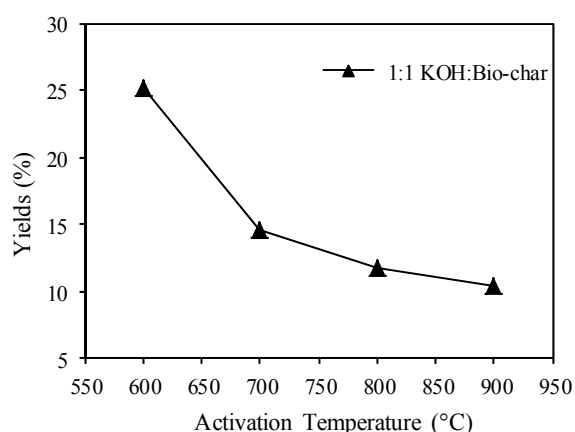


Figure 1: Effect of activation temperature on the yield of activated carbons.

The results of the elemental analysis of activated carbons obtained at different activation temperatures are shown in Table 2.

Table 2: Elemental analyses of activated carbons.

Activation Temperature (°C)	C	H	N	O*
600	68.11	2.77	3.38	25.47
700	70.44	2.38	2.97	24.21
800	72.09	2.68	2.77	22.46
900	73.80	2.66	2.48	21.06

*By difference.

With an increase in the activation temperature from 600 to 900 °C, the carbon content of the activated carbons increased from 68.11 to 73.80 wt.%; however, the oxygen and nitrogen

contents decreased from 25.47 to 21.06 wt.% and from 3.38 to 2.48 wt.%, respectively. Also, hydrogen and nitrogen content changed in the range of 2.38-2.77 wt.%. The carbon contents of activated carbons increased when compared to biochar (62.45 wt.%). This trend in the elemental analysis was found similar in activated carbons produced from other precursors such as waste tea and nutshells [Yagmur et al., 2009; Aygün et al., 2003].

In the chemical activation, the final activation temperature is important process parameters in determining the surface area of the activated carbon. The effects of activation temperature on the BET (Brunauer–Emmett–Teller) surface areas of the activated carbons are shown in Table 3.

Table 3: Effect of activation temperature on the surface area of activated carbons.

Activation Temperature (°C)	Surface Area (m ² g ⁻¹)
600	490.3
700	972.5
800	1277.0
900	1017.0

When the activation temperature was increased from 600 to 800 °C, the BET surface area increased significantly and reached maxima (1277 m² g⁻¹). However, at 900 °C, the trend was reversed. Above 900 °C, structural ordering, pore widening and/or the coalescence of neighboring pores seem to predominate, leading to a decrease in the surface area.

Figure 2 illustrates the SEM images of the activated carbons obtained at different activation temperatures with 1000x magnification. The SEM images of activated carbons obtained at 600-800 °C many orderly pores over the surface, forming a system of developed pore

structures. At 900 °C, the activated carbon had lower BET surface area due to shrinkage of carbons at post-softening and swelling temperatures, resulting in narrowing or closing pores. SEM images show the absence of any kind of porosity, as supported by the BET results.

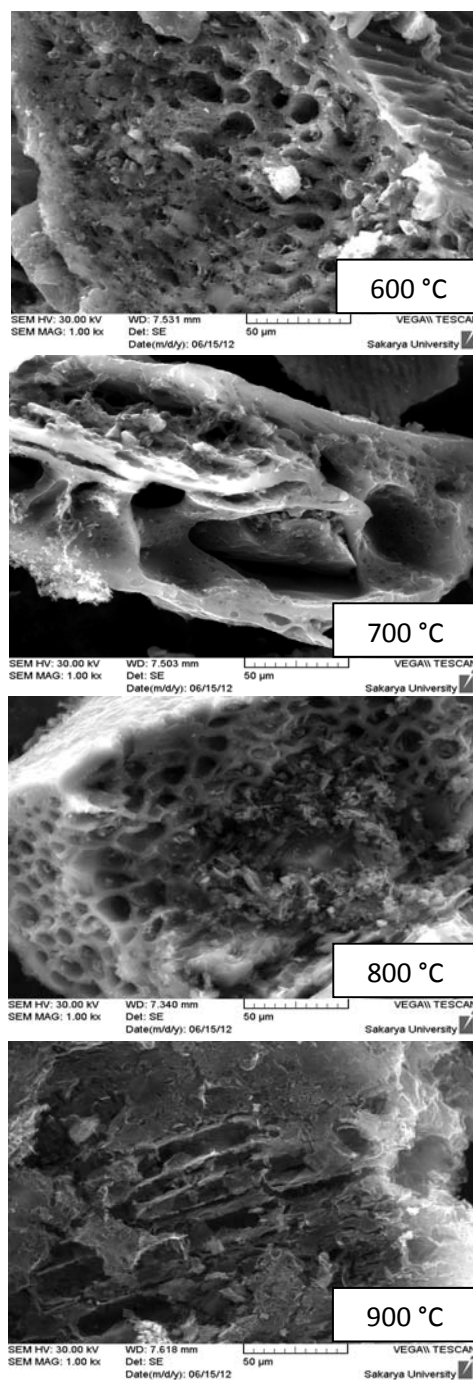


Figure 2: SEM images of activated carbons.

4. CONCLUSION

According to the results of this study, it is found that the effect of activation temperature on the yield, surface area and elemental composition of activated carbon were quite high. As a result, the safflower seed press cake biochar can be effectively used as a raw material for the preparation of activated carbon using chemical activation procedure. In addition, the activated carbon product with high surface area obtained in this study can be used as a very promising adsorbent for pollution control and other applications.

Acknowledgements: This work was supported by Sakarya University Scientific Research Foundation (Project number: 2010-01-16-003).

REFERENCES

- Ahmadpour, A. and Do, D.D., 1997. The preparation of activated carbon from Macademia Nutshell by chemical activation. *Carbon*, 35(12), 1723.
- Angin, D., Köse, T.E. and Selengil, U., 2013. Production and characterization of activated carbon prepared from safflower seed cake biochar and its ability to absorb reactive dyestuff, *Applied Surface Science*, In press.
- Aygün, A., Yenisoay-Karakaş, S. and Duman, I., 2003. Production of granular activated carbon from fruit stones and nutshells and evaluation of their physical, chemical and adsorption properties, *Microporous and Mesoporous Materials*, 66 (2-3), 189.
- Azargohar, R. and Dalai, A.K., 2008. Steam and KOH activation of biochar: experimental and modeling studies, *Microporous and Mesoporous Materials*, 110 (2-3), 413.
- Bagheri, N. and Abedi, J., 2009. Preparation of high surface area activated carbon from corn by chemical activation using potassium hydroxide, *Chemical Engineering Research and Design*, 87 (8), 1059.
- Chandra, T.C., Mirna, M.M., Sunarso, J., Sudaryanto, Y. and Ismadji, S., 2009. Activated carbon from durian shell: Preparation and characterization, *Journal of Taiwan Institute of chemical Engineers*. 40 (4), 457.
- Demiral, H., Demiral, I., Tümsek, F. and Karabacakoğlu, B., 2008. Pore structure of activated carbon prepared from hazelnut bagasse by chemical activation, *Surface and Interface Analysis*, 40 (3-4), 616.
- Gratuito, M.K.B., Panyathanmaporn, T., Chumnanklang, R.A., Sirinuntawittaya, N. and Dutta, A., 2008. Production of activated carbon from coconut shell: Optimization using response surface methodology, *Bioresource Technology*, 99(11), 4887.
- Jibril, B., Houache, O., Al-Maamari, R. and Al-Rashidi, B., 2008. Effects of H₃PO₄ and KOH in carbonization of lignocellulosic material, *Journal of Analytical Applied Pyrolysis*, 83 (2), 151.
- Olivares-Marín, M., Fernández-González, C., Macías-García, A. and Gómez-Serrano, V., 2006. Preparation of activated carbons from cherry stones by activation with potassium hydroxide, *Applied Surface Science*, 252 (17), 5967.
- Sahu, J.N., Acharya, J. and Meikap, B.C., 2010. Optimization of production conditions for activated carbons from tamarind wood by zinc chloride using response surface methodology, *Bioresource Technology*, 101 (6), 1974.
- Şensöz, S., Yorgun, S., Angin, D., Çulcuoğlu, E., Özçimen, D. and Karaosmanoğlu, F., 2001. Fixed-bed pyrolysis of rapeseed cake, *Energy Sources*, 23 (10), 873.
- Stavropoulos, G.G. and Zabaniotou, A.A., 2005. Production and characterization of activated carbons from olive-seed waste residue, *Microporous and Mesoporous Material*, 82 (1-2), 79.
- Sudaryanto, Y., Hartono, S.B., Irawaty, W., Hindarso, H. and Ismadji, S., 2006. High surface area activated carbon prepared from cassava peel by chemical activation, *Bioresource Technology*, 97 (5), 734.
- Sütçü, H. and Demiral, H., 2009. Production of granular activated carbons from loquat stones by chemical activation, *Journal of Analytical Applied Pyrolysis*, 84 (1), 47.
- Tay, T., Ucar, S. and Karagöz, S., 2009. Preparation and characterization of activated carbon from waste biomass, *Journal of Hazardous Materials*, 165 (1-3), 481.
- Yagmur, E., Ozmak, M. and Aktas Z., 2008. A novel method for production of activated carbon from waste tea by chemical activation with microwave energy, *Fuel*, 87 (15-16), 3278.
- Yorgun, S., Vural, N. and Demiral, H., 2009. Preparation of high-surface area activated carbon from Paulownia by ZnCl₂ activation, *Microporous and Mesoporous Materials*, 122 (1-3), 189.

STUDY OF ADSORPTION CAPACITY RECOVERY IN DIFFERENT ADSORBENTS FOR NITROGEN REMOVAL FROM DIESEL

Souza, W. C. ^a; Baia, L. V. ^a; Figueiredo, M. A. G. ^b; Chiaro, S.S.X. ^c.

^a Engineering and Technology of Petroleum and Petrochemicals Laboratory– Institute of Chemistry – State University of Rio de Janeiro,

^b Operation and Industrial Process Department, Chemical Institute – State University of Rio de Janeiro, Maracanã – CEP: 20550-900 – Rio de Janeiro – RJ – Brasil.

mgaya@uerj.br

^c PETROBRAS/ CENPES/ HPE, Cidade Universitária - CEP: 21941-915, Rio de Janeiro – RJ –Brasil

a. Corresponding author (mgaya@uerj.br)

ABSTRACT: The adsorption technique is a promising alternative to be employed in the removal of nitrogenous contaminants existing in diesel fuel in order to reduce the severity of Hydrotreating. However, the regeneration step of the adsorbent employed is very important for enabling industrially, the adsorption process. It was studied the following steps: adsorption and desorption [1] (by displacement with gas, by washing with solvent, by burning, by burning and a washing with solvent). It was tested clays and commercial activated carbon. It was found that the family of clays showed, in general, better performance in removing nitrogen compounds. In the desorption process by displacement with inert gas, carried out at two different temperatures, it was found that at a temperature of 200°C, the efficiency of clays showed a recovery efficiency greater than that obtained at 400°C. Desorption, by washing at room temperature, gave evidence that the methyl tert-butyl ether (MTBE), among the solvents tested, was what allowed greater recovery. The desorption process by burning at 450°C, without washing the adsorbent, showed a slight improvement compared to the burning eluted using the adsorbent. In tests for reuse, it was concluded that the clay presented good results showing a sharp decrease in adsorption capacity after the third series of washing, however recovering partially adsorption capacity after a controlled burning. Thus, desorption by displacement with gas and by burning obtained the best results, but they consume much energy and release harmful compounds. Therefore, it's necessary to invest in other recovery methods.

Keywords: adsorption; nitrogenous contaminants; desorption; recovery; reuse; clay.

1. INTRODUCTION

In recent years, the technique of adsorption has been studied as a promising alternative to be employed in removing nitrogen compounds existing in the diesel fuel in order to reduce the severity of removal of sulfur compounds during Hydrotreating (step catalytic reduction of contaminant species, in the presence of H₂ gas). Thus, to become milder levels of pressure and temperature in this process, it allows a reduction in production costs.

However, the step of regeneration of the spent adsorbent is of paramount importance to enable, economically, the adsorption process on an industrial scale, as well as the time of use. The recovery of the adsorbent is worn by the process known as desorption.

Desorption is a phenomenon that occurs when the chemical interactions that holds molecules of a substance (adsorbate) on the surface of a solid phase (adsorbent) are disrupted by some external factor.

Thus, the adsorbate is released amid a fluid phase (adsorptive). This process occurs as opposed to physical adsorption phenomenon in which the adsorbate molecules are attracted to the interfacial zone of the adsorbent due to the existence of uncompensated attractive forces in the surface. The interactions, involved in adsorption and desorption are ruptured, include the van der Waals forces (dispersion and repulsion) and electrostatic interactions (RUTHVEN, 1984).

Currently there are several techniques desorption being studied and employed, among the different justifications for carrying out them, in common, the search for cost reduction associated with the adsorption process and maximizing the efficiency of the regeneration process[1,2,3].

The desorption by washing with solvent is a widely studied because of their low cost associated. A 1:1 mixture of methanol: toluene was used for regeneration of the adsorbent based on activated carbon at 70 °C [1]. Aromatic solvents have been used by Sano et al. [2] to regenerate an adsorbent based on fiber of activated carbon for 2 hours at 70 °C under ultrasonic irradiation. Farag [3] used toluene to regenerate an adsorbent-based CoMo supported on carbon subsequently underwent ultrasound waves. Mustafa et al. [4] used washing with n-heptane to regenerate a zeolite tuff and then dried at 100°C. Ethanol was used for regenerating bed with typical zeolites at 25 °C and 65°C [5]. Tran et al. [6] used isooctane to regenerate gold ions supported on silica at room temperature. All these studies showed satisfactory results for regeneration of the adsorbent.

Desorption by oxidation is a method studied due to its very high performance, it was used a mixture of 20:80 He/O₂

during ramp from 90 °C to 600°C to regenerate zeolites [7]. He led to recover the initial capacity of the adsorbent. While Velu et al. [1] regenerated adsorbent worn by air flow through the bed at 300°C.

The thermal desorption is a technique widely used because it is simple [8]. Farag [3] recovery adsorbent based on activated carbon by heating at 600°C using a thermo-analyzer from Shimadzu TGA-50H. Chen et al. [8] regenerated an adsorbent AgNO₃/MCM-41 by heating at 200°C for 24 hours with an air flow of 50 ml / min. While Samokhvalov et al. [9] used, for heating, x-ray photoemission spectroscopy (XPS) with temperature-programmed and electron spin resonance in the range of 25 °C to 525 °C under vacuum and in the presence of air to regenerate sulfur selective adsorbent with Ag supported in Titanium.

In this study, the focus was desorption of used adsorbents to minimize costs for the adsorption, enabling economically an industrial adsorption plant. Different adsorbents were studied and those, that showed the highest performance in tests of adsorption, were subjected to different desorption techniques. From the adsorbents with best answers in desorption tests, it was carried out a study of reuse of them.

2. EXPERIMENTAL METHODS

Traditional adsorbents were tested, with acidic characteristics, such as commercial clays. Thus, we used seven commercial clays: C1, C2 and C3 from A Family and F2, F3, F3 and F4 from B family. Exploratory analyzes were also conducted with activated charcoals.

The characterization of the studied adsorbents involved the determination of the BET specific area, the area of micropores, the volume and pore

diameter. The textural properties were determined by nitrogen adsorption at liquid N₂ temperature (-193 ° C), in equipment ASAP 2400 from Micromeritics. The samples were subjected to degassing under vacuum (50 mTorr), temperature of 300 ° C for 1h. The pore volume distribution is presented based on data desorption. The analyzes were performed on pore equipment AUTOPORE III 9420 from Micromeritics.

In obtaining the kinetic curves of adsorption, we used a stirred tank provided with a heating system, where it is put in contact, at a given temperature, 60 g of the adsorbent and 300 ml of diesel (adsorptive) with a known concentration of compounds nitrogen (adsorbate). An aliquot of solution was withdrawn at certain periods of time starting from the introduction of the adsorbent in the fuel, since the set temperature of 40 °C. The concentration of these samples was determined by the total nitrogen analyzer (Antek).

The adsorption isotherms were obtained at 40 °C and 70 °C. The experiments were performed in stirred tank with temperature control and each sample was

taken after 1 h (sufficient time for equilibrium has been reached) counted from the contact of the adsorbent with diesel.

In these studies we used two loads with different properties: a petroleum fraction with low content of nitrogen (250 ppm) and other with a high content of nitrogen (1360 ppm) in order to check whether different compositions of nitrogen compounds significantly interfere with the adsorptive efficiency of traditional adsorbents.

The experiments aimed at obtaining the rupture curves (breakthrough) were made in a bench scale using a column of 5.1 cm internal diameter by 16 cm long. The bed was constructed using in all tests, 170 g of adsorbent selected. The region not occupied by the adsorbent column was filled with glass beads of 1mm diameter.

The adsorbents, that showed better performance in the kinetic tests, were subjected to different desorption tests. In the desorption experiment by displacement, nitrogen gas was used at temperatures of 250 ° C and 400 ° C for percolating the saturated bed.

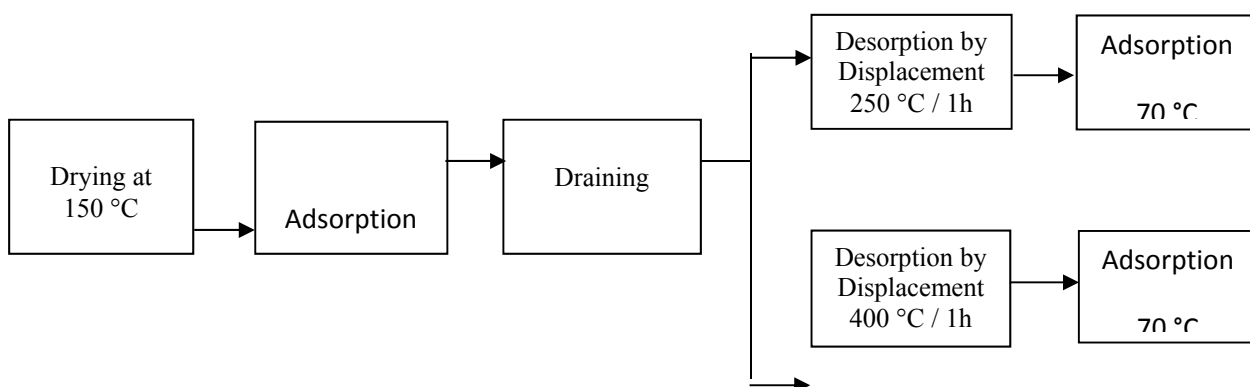


Fig. 1: Desorption by Displacement

In desorption tests by solvent extraction, two solvents were used at 70 °

C: methyl tert-butyl ether (MTBE) and n-hexane.

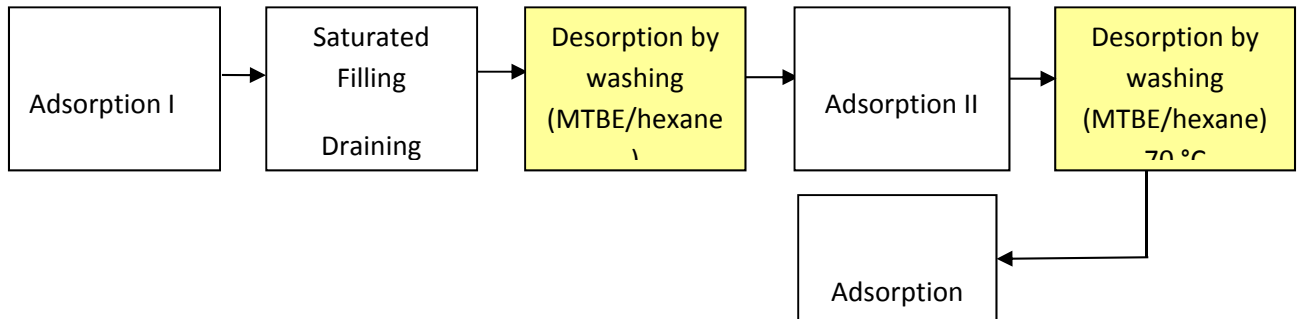


Fig. 2: Desorption by Washing

In the desorption test by oxidation, firing was performed in a controlled manner, effecting a slow increase of the oxygen content initially 0.5% in the air / nitrogen mixture, with

the column heated to 400 ° C (passage pure nitrogen). Once the temperature stabilized, we started feeding air at a predetermined flow rate as a function of the oxygen established content.

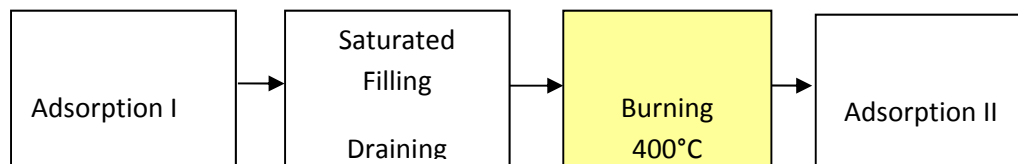


Fig. 3: Desorption by Burning

In desorption experiment by washing and burning, we analyzed the influence of the association between washing and burning at 400 °C in the regeneration process. In a first stage, burning was carried out after washing of the saturated clay with MTBE. In the second phase, was evaluated three successive washes with MTBE followed by a burning at 400 °C. In addition to the tests performed with MTBE, a washing / burning association was also employed with commercial ethanol.

In cycle washing tests, it was scheduled races performing the association between adsorption and washing. These tests were initiated starting from a fresh adsorbent pre-treated at 150 °C for 1 hour with nitrogen gas. After the first adsorption, it was made up the passage of MTBE trough the column. At the end of the process, the column was subjected to a drying process at 150 ° C for 1 hour. After first washing with MTBE, the adsorbent has undergone a further step of saturation in fuel with a high content of nitrogen, and then undergo second

washing step, with MTBE. After this last washing, the adsorbent was saturated

again, in order to evaluate its new adsorption efficiency.

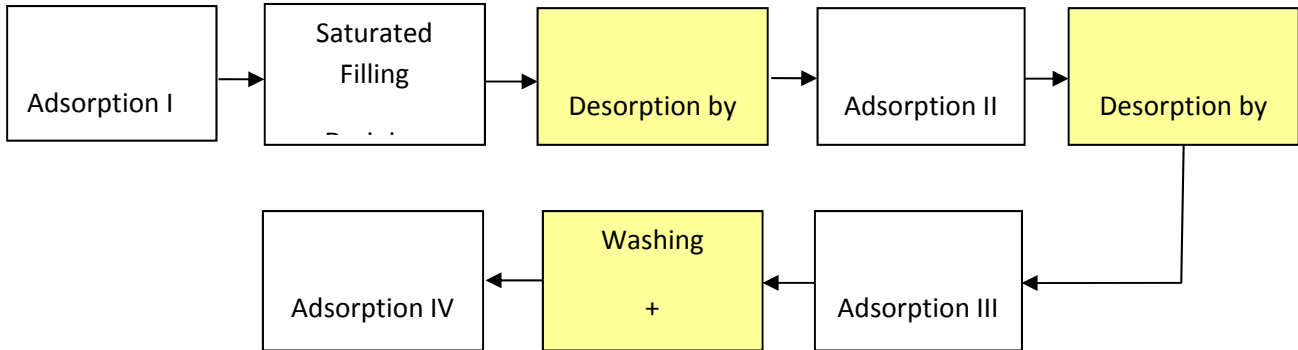


Fig. 4: Desorption by Washing+ Burning

3. RESULT AND DISCUSSION

Table 1: Physical Characterization of Adsorbers

Adsorber	Name	BET Area (m ² /g)	Micropore Area (m ² /g)	Micropore Volume (cm ³ /g)	Average Pore Diameter (Å)	Pore Volumes (cm ³ /g)	Average Pore Diameter (Å)
Activity Carbon	Carbon A	428	-	0.02	40	0.01	40
Activity Carbon	Carbon B	719	-	0.08	51	0.08	52
Clay	C	96	-	0.06	68	0.08	55
Clay	F1	280	-	0.29	56	0.32	49
Clay	F2	211	-	0.29	74	0.40	65
Clay	F3	239	-	0.35	74	0.38	64
Clay	F4	193	-	0.27	75	0.30	67
Clay	C1	202	-	0.32	100	0.37	100
Clay	C2	156	-	0.22	89	0.26	85
Clay	C3	270	-	0.21	55	0.26	50

^amicropore volume, mesopore volum from order of 0,05 cm³/g.

3.1. Adsorbent Characterization

Table 1 presents the results of BET solids, volume and pore diameter. About textural aspect, the clays with higher specific area were those of the F1 and C3. These values correspond to less than half of the values found for the B activated carbon, but in clays the pore volume is much higher and pore structure is different.

Although structurally similar to clays of A and B families, evaluated C clay, although with a considerable specific area, appears to be fresh, i.e. not having

been subjected to severe acid treatments (relative to the acid amount and time of exposure) due to its low pore volume.

The carbons presented exceptional areas, but, approximately, without pores in the region of mesopore.

3.2. Adsorption Tests

The Figure 1.1 (fuel with low nitrogen content) and Figure 1.2 (fuel with high nitrogen content) present the results of kinetic curves obtained at 40° C using, fuel with low and high contents of nitrogen respectively.

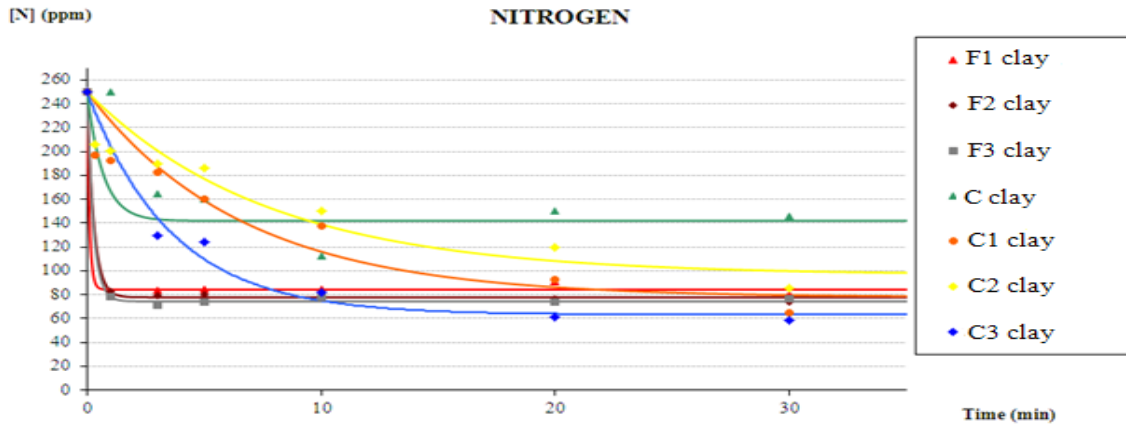


Fig.1.1: Kinect Curves obtained for commercial clays using fuel with low contents of nitrogen.

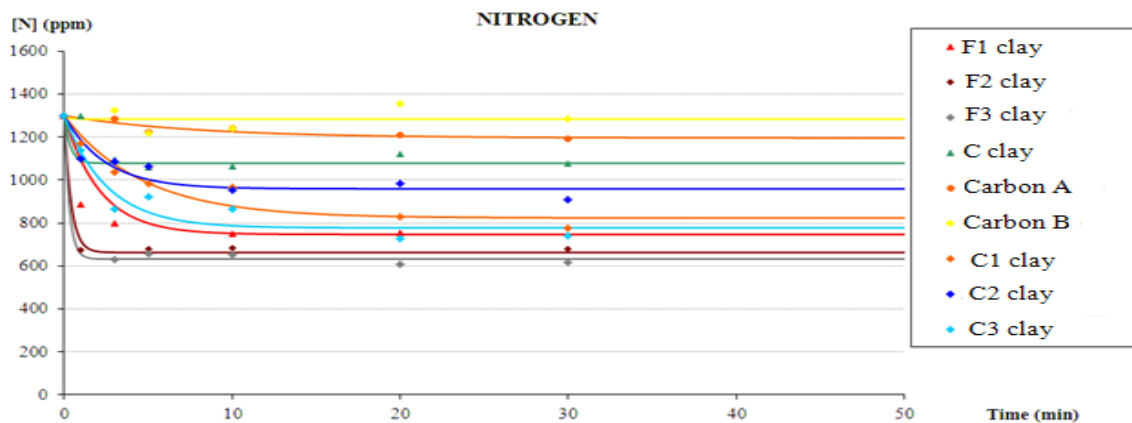


Fig.1.2: Kinect Curves obtained for commercial clays and for activities coals using fuel with high contents of nitrogen.

Considering an average error of +/- 10% of the total nitrogen concentration obtained using Antek, B commercial clays, highlighting the C1 clay, were the most promising adsorbents in the removal of nitrogen when analyzing the low-grade fuel. The A clays also presented good performance with a faster kinetics, but reached a purity level a little lower.

In the case of experiments with diesel with high content of nitrogen, B clays were better, mainly C1, and the A family. On the other hand, the carbons had the worst performance.

One possible explanation for the observed differences between the kinetic

curves of the different lots of fuel is related to different nitrogen compounds in each. Therefore it is extremely important to identify the types and concentrations of nitrogen compounds in order to permit inferences about the characteristics of adsorbents and their performance in the removal of these compounds.

Figure 2.1 shows the obtained adsorption isotherms at 40 ° C and 70 ° C to most promising adsorbents in kinetic tests (clays family A and B) using the fuel with high content of nitrogen.

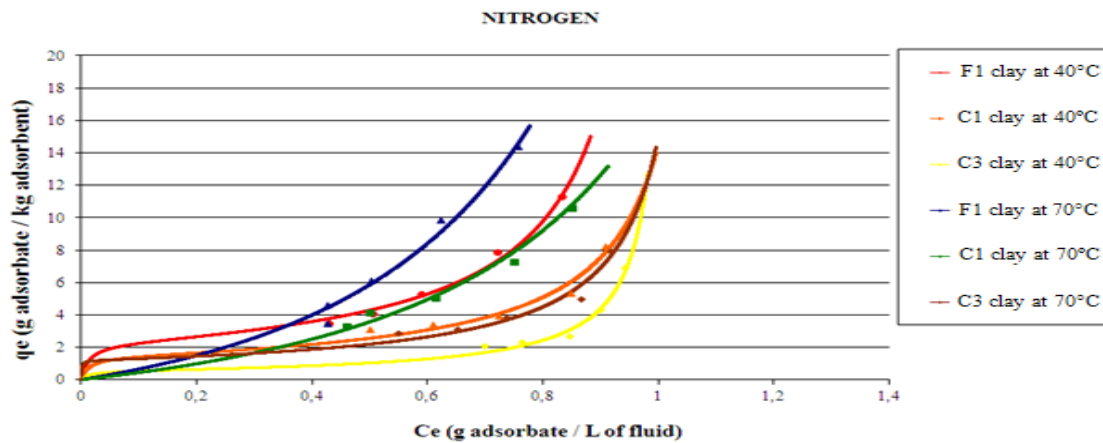


Fig. 2.1: Adsorption Isotherms for commercial clays at 40 °C and 70°C.

Isotherms with a concave shape and with a long plateau before its rise are usually unfavorable, because they present an effective behaving only for high concentrations of solute. Observing Figure 2.1, the most favorable isotherm as at 70 ° C such as at 40 ° C is F1 clay. On the other hand, from the three

analyzed ones, C3 clay at 40°C, showed the worst performance.

Figure 3 shows the breakthrough curves obtained with the C1 clay and B carbon, which were selected to compare two adsorbents with adsorption capacities for nitrogen quite different.

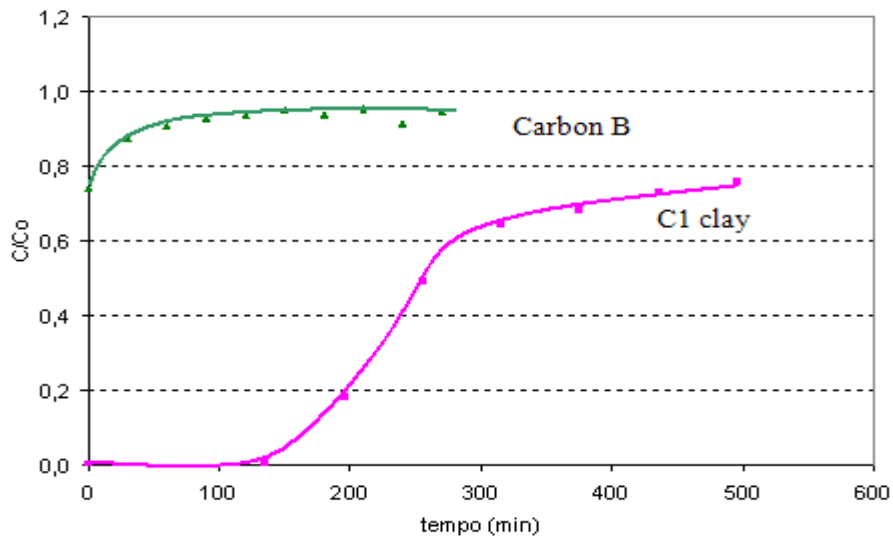


Fig.3: Elution Curves obtained with C1 clay and B activity carbon at 70°C.

It was observed a higher adsorption efficiency of C1 clay relative to B carbon. After 2h eluting, the bed with C1 clay was yet removing nitrogen while the carbon bed had already been practically exhausted.

3.3. Desorption Tests

In Figure 4, we show the calculated adsorption capacity for a new one filling made with C1 clay and an adsorption filling regenerated with the same desorption tests by displacement with N₂ gas at 250 °C and 400 °C. The mean

capacities are expressed in grams of adsorbed nitrogen / kg of used adsorbent in the fixed bed.

The capacities calculation results showed that desorption by displacement with an inert gas at 400 ° C promoted a decrease of only 9% in the clay original efficiency, differently from the desorption held at 250 ° C, which was a decrease of approximately 20%.

In Figure 5, it is showed the calculated adsorption capacity for a filling made with fresh C1 adsorbent clay and the capacity for the same adsorbent regenerated by washing with MTBE and hexane solvents.

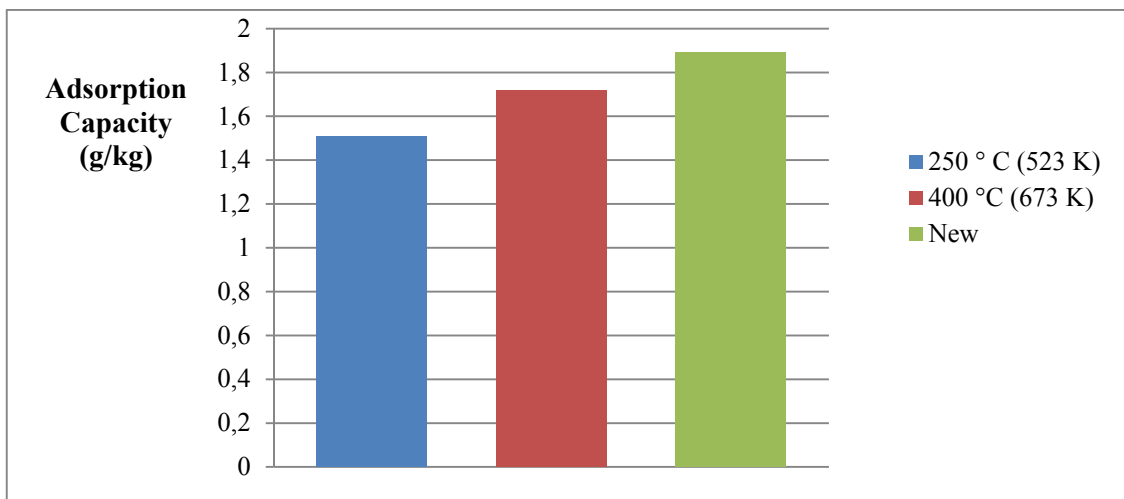


Fig.4: Adsorption capacity regenerated by desorption tests with displacement for C1 clay.

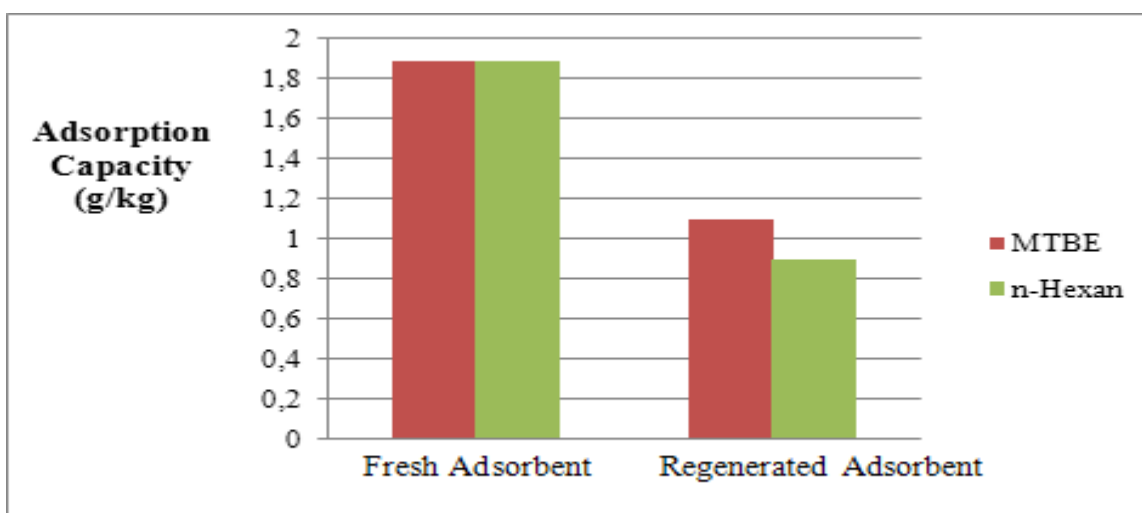


Fig.5: Regenerated adsorption capacity by desorption tests with solvent washing for C1.

The adsorption capacity calculations result for to regenerated clay, by washing with solvent, was greater for the solvent MTBE, with a reduction of 42% in the initial capacity of the adsorbent, compared to a reduction of 53% for regeneration with n-hexane.

In tests of successive washing, after first wash, there was obtained a capacity of 1.20 g of nitrogen per kg of C1 clay. Whereas, after the second wash, there was obtained a capacity of 0.725 g of nitrogen per kg of C1 clay. A reduction of approximately 40% between the two

washes. Considering which the initial capacity of this clay was 1.89 g / kg. This resulted in a reduction of 37% for the first wash and a reduction of 62% for the second one when compared to the initial capacity.

In the study of regeneration by controlled burning of the C1 clay was obtained, as a result, an adsorption capacity of 1.67 grams of nitrogen adsorbed / kilogram of regenerated adsorbent to the clay against an initial capacity of 1.89 g / kg of the same adsorbent. What represented a reduction of approximately 12%.

Aiming to expand the studies involving regeneration of C1 clay, we analyzed the influence of the combination of washing with burns at 400 ° C in the desorption process of fillings.

In a first step, firing was performed after washing saturated clay with MTBE. In a

second step, were tested three successive washes with MTBE followed by burning at 400 ° C. In addition to the tests performed with MTBE, the combination washing / firing was also used, as solvent, the commercial ethanol. The results from capacities calculating of the regenerated adsorbent comparing them with the initial capacity are shown in Figures 6.

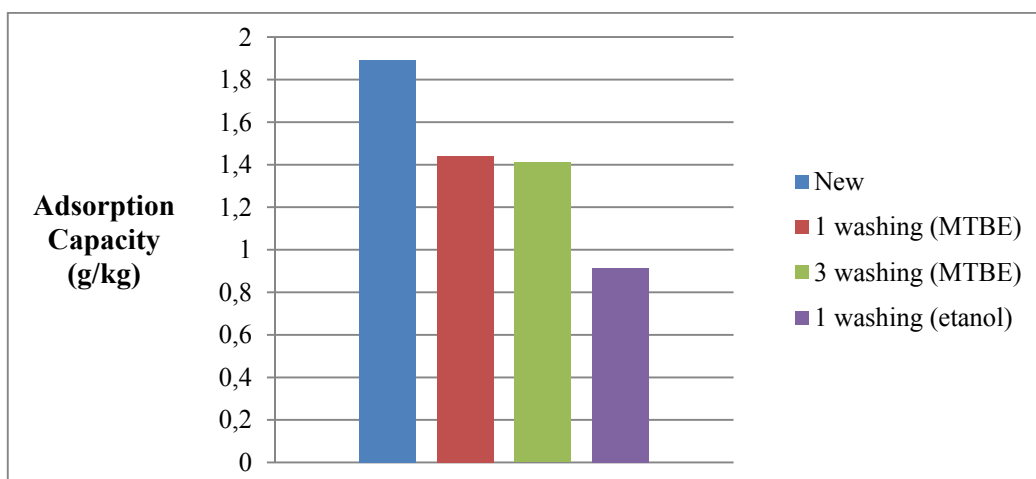


Fig.6: Adsorption capacity of regenerated clay from desorption test by washing associated to burning at 400 ° C for the C1 clay.

The results demonstrated that the combination of three successive washes with MTBE followed by a step of burning at 400 ° C, nearly reduces the efficiency of removal of clays in the same percentage that observed when using only one washing followed by firing, in other words, a reduction of about 25%.

The use of ethanol in the washing step, before firing, was not the best choice, because the removal efficiency of clays was reduced by over 50%.

4. CONCLUSION

From the results of tests performed on bench unit, it could be concluded that the clays showed removal efficiency to nitrogen higher than activated carbon for a diesel with high contaminant content . Among the clay adsorbents, the C1 clay

was superior to the others for removing nitrogenous contaminants.

Regarding the test results of regeneration by desorption with inert gas shift was more efficient in the recovery efficiency of C1 clays when held at 400 ° C. The desorption by washing with organic solvents showed that while MTBE has reduced the efficiency of removal of clays, about 42%, relative to n-hexane is what provides less reduction in efficiency. Until the first washing MTBE allowed a recovery of reasonable removal efficiency of the nitrogen clays. However, after the second washing efficiency was reduced by over 50%.

The desorption by washing with organic solvents showed that while MTBE has reduced the removal efficiency of clays, about 42%, it is what provides less

reduction in efficiency. Until the first washing, MTBE allowed a recovery of reasonable removal efficiency of nitrogen for the clays. However, after the second washing efficiency was reduced by over 50%.

The burning at 400 ° C, among the alternatives studied, was the process less reduced the efficiency of the clays. The association of washing with firing at 400 ° C provided better results when MTBE was used as solvent instead of ethanol.

A single washing with MTBE followed by burning at 400 ° C gave approximately the same recovery rate for the clay when it employed three successive washes with MTBE and burning at 400 ° C.

Thus, it is clear that among desorption methods tested, desorption by displacement and burning had higher incomes for regeneration clays. However, because they are methods associated with high energy expenditure and with emissions of compounds harmful to the environment, it is interesting to deepen in alternative regeneration methods, for example, regeneration by washing with solvent in order to make the latter as efficient as the first and obviously make it economically viable.

REFERENCES

- [1] Ruthven, D.M. Principles of Adsorption and Adsorption Processes. John Wiley & Sons, Inc.1984.
- [2] S. Velu, Watanabe S., Ma X., Song C. Regenerable Adsorbents for the Adsorptive Desulfurization of Transportation Fuels for Fuel Cell Applications. Prepr. Pap.-Am. Chem. Soc., Div. Fuel Chem. 2003; 48(2):526-528.
- [3] Sano Y., Sugahara K., Choi K., Korai Y., Mochida I. Two-step adsorption process for deep desulfurization of diesel oil. Fuel 2005; 84:903-910.
- [4] Chica A., Strohmaier K., Iglesia E. Adsorption, Desorption, and Conversion of Thiophene on H-ZSM5. Langmuir 2004; 20:10982-10991.
- [5] Farag H., Selective adsorption of refractory sulfur species on active carbons and carbon based

CoMo catalyst. Journal of Colloid and Interface Science 2007; 307: 1-8.

[6] Chen H., Wang Y., Yang F. H., Yang R. T. Desulfurization of high-sulfur jet fuel by mesoporous π -complexation adsorbents. Chemical Engineering Science 2009; 64: 5240-5246.

[7] Koriakin A., Ponvel K.M., Lee C. Denitrogenation of raw diesel fuel by lithium-modified mesoporous silica. Chemical Engineering Journal 2010; 162:649-655.

[8] Mustafa F., Al-Ghouti M. A., Khalili F. I., Al-Degs Y.S. Characteristics of organosulphur compounds adsorption onto Jordanian zeolitic tuff from diesel fuel.

Journal of Hazardous Materials 2010; 182:97-107.

[9] Samokhvalov A., Duin E. C., Nair S., Tatarchuk B. J. Adsorption and desorption of dibenzothiophene on Agtitania studied by the complementary temperature programmed XPS and ESR. Applied Surface Science 2011; 257: 3226-3232.

[10] Lin L., Zhang Y., Zhang H., Lu F. Adsorption and solvent desorption behavior of ion-exchanged modified Y zeolites for sulfur removal and for fuel cell applications. Journal of Colloid and Interface Science 2011; 360: 753-759.

[11] Tran D. T., Dunbar Z. W., Chu D. Regenerable sulfur adsorbent for liquid phase JP-8 fuel using gold/silica based materials. International Journal of Hydrogen Energy 2012; 37:10430-10434.

Cu-BTC /GRAPHITE OXIDE AND Cu-BTC/AMINATED GRAPHITE OXIDE COMPOSITES AS SUPERIOR ADSORBENTS OF CO₂ AT AMBIENT CONDITIONS

Mykola Seredych¹, Yunxia Zhao^{1,2}, Qin Zhong², and Teresa J. Bandosz¹

¹Department of Chemistry, The City College of New York 160 Convent Avenue, New York, NY 10031, USA

²School of Chemical Engineering, Nanjing University of Science and Technology, Nanjing, 210094 PR China
a. Corresponding author (tbandosz@ccny.cuny.edu)

ABSTRACT: Cu-BTC (MOF) and its composites with 10 wt. % graphite oxide (GO) and aminated graphite oxide (GO-U) were tested as adsorbents of CO₂ at ambient conditions. The dynamic adsorption test was performed at room temperatures. The composites show much higher CO₂ adsorption than the parent MOF. To understand the mechanism of adsorption the materials were extensively characterized using adsorption of nitrogen, SEM/EDX and XRD. The results indicate that the incorporation of GO and GO-U into the MOF crystals affects their structure and introduces imperfections, which result in more open copper sites. These sites are the centers for specific interactions with CO₂. The addition of aminated GO results in the more pronounced effects of heterogeneity owing to the presence of nitrogen. Both oxygen and nitrogen groups of GO seem to be involved in the bonds with copper centers. Amines are also able to interact with carboxylic groups of the BTC linkages. Formation of composites results in a significant increase in the volume of micropores and a decrease in their size. Those are the favorable features increasing the amount of CO₂ adsorbed.

1. INTRODUCTION

CO₂ adsorption on solid adsorbents is an environmentally friendly and simple process [D'Alessandro *et al.*, 2010]. It requires efficient adsorbents with the high adsorption capacity and easiness of regeneration. A group of materials used for CO₂ adsorption are metal organic frameworks (MOFs) [Hirscher, 2011]. They have become the attractive media for hydrogen storage [Tranchemontagne *et al.*, 2012], separation, catalysis, CO₂ capture [Millward and Yaghi, 2005; Stock and Biswas, 2011] and other industrial applications [Stock and Biswas, 2011]. As physical adsorbents, MOFs exhibit high CO₂ capacity and thus bring broad prospects, which have attracted attention of researchers [Millward and Yaghi, 2005]. Férey and coworkers created porous chromium terephthalate, MIL-101, which showed a very high CO₂

capacity reaching 390 cm³_{STP}/cm³ at 5 MPa [Llewellyn *et al.*, 2008].

In order to increase the dispersive forces in MOF, other materials, microporous [Gorka *et al.*, 2010] or layered [Petit and Bandosz, 2011; Xiang *et al.*, 2011] can be incorporated to their structure forming composite solids. These materials showed an improved porosity and adsorptive performance [Petit and Bandosz, 2009; Petit and Bandosz, 2011; Xiang *et al.*, 2011]. Jasra and coworkers [Prasanth *et al.*, 2011] synthesized a new MIL-101 composite with single wall carbon nanotubes (SWNT) tuning the pore size and pore volume of the material towards hydrogen sorption. More importantly, synergistic effects on porosity and chemistry of such composites result in a significant improvement in the adsorption of various gases. The composites of MOF-5 [Petit and Bandosz, 2011] or

HKUST-1 with graphite oxide has been synthesized and used as gas adsorbents [Petit *et al.*, 2010; Petit *et al.*, 2011]. On their surface much more toxic gases was adsorbed than on that of parent MOF. This was explained by the formation of new pores on the interface between two phases and active chemistry participating in reactive adsorption.

Recently, we have introduced new composites of MOF Cu-BTC and aminated graphite oxide and analyzed them as CO₂ adsorbents [Zhao *et al.*, 2013; Zhao *et al.*, 2013]. The objective of this work is the detailed comparison of the CO₂ adsorption on the composites of Cu-BTC with graphite oxide and with aminated GO. The differences in the performance are linked to different degree of surface heterogeneity caused by different chemistry of graphite oxide embedded within the composite.

2. EXPERIMENTAL

2.1. Materials

The preparation of Cu-BTC [Chui *et al.*, 1999] and GO and GO-U composites was done as described in details by Petit *et al.* [Petit *et al.*, 2011] and Zhao *et al.* [Zhao *et al.*, 2013]. GO-U and the MOF components were simultaneously dispersed/dissolved in the solvent by sonication thus the MOF units were allowed to grow in the presence of GO-U or GO in the reaction vessel. The content of the modified graphene phase was 10 wt. % of the parent Cu-BTC weight. The composites are referred to as MOF/GO and MOF/GO-U.

2.2. Methods

CO₂ dynamic adsorption: Assessment of the CO₂ adsorption capacity on the samples at atmospheric pressure was carried out using a TA instrument. About 20 mg of the adsorbent MOF/GO-U was placed in a small pan, heated up to 110 °C at a heating rate of 10 °C/min

under pure N₂ flow (100 ml/min) and held isothermally for 2 hours. The temperature was then decreased to 30 °C. At this stage, the sample was saturated by N₂. Then the gas was switched to pure CO₂ 50 mL/min and the sample was held isothermally at 30 °C for 2 hours. The weight increase (with high accuracy to three decimal places) during this stage was considered as the amount of CO₂ adsorbed.

Nitrogen adsorption: Nitrogen adsorption isotherms were measured using an ASAP 2020 analyzer (Micromeritics, Norcross, GA, USA) at -196 °C. Prior to the experiment, the samples were degassed at 120 °C overnight. The surface area S_{BET}, the total pore volume V_t, the micropore volume V_{mic} (Dubinin-Radushkevich method), and the mesopore volume V_{mes} were obtained from the isotherms. The pore size distributions were calculated using the DFT method [Lastoskie *et al.*, 1993]. Even though the exact surface model for our composite are not developed, using the existing model for the series of samples can bring some valuable information and the trend of the changes in the samples' porosity.

SEM/EDX: Electron-dispersive X-ray spectroscopy (EDX) analysis was done at magnification 10 KX with an accelerating voltage of 15.00 kV. A Cu atomic concentration is the average data calculated from four different spots of adsorbent surface analyzed by EDX

3. RESULTS AND DISCUSSION

The CO₂ adsorption profiles are collected in Figure 1. On MOF, MOF/GO and MOF/GO-U 2.00, 2.92 and 4.25 mmolCO₂/g are adsorbed at dynamic conditions at 30 °C, respectively. Thus formation of the composites increases the performance between 50 % to over 100 % in comparison with the parent MOF. To explain these differences, the porosity, texture and surface chemistry of the

samples tested have to be analyzed in details.

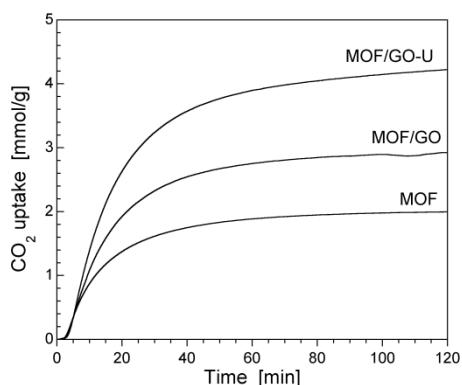


Figure 1: CO₂ adsorption profiles at 30°C.

The comparison of the X-Ray diffraction patterns showed that the MOF structure is preserved in the composites. Nevertheless a decrease in peaks intensity and small split of the most intense peak suggest some degree of disruption of the MOF crystals [Petit *et al.*, 2011; Zhao *et al.*, 2013].

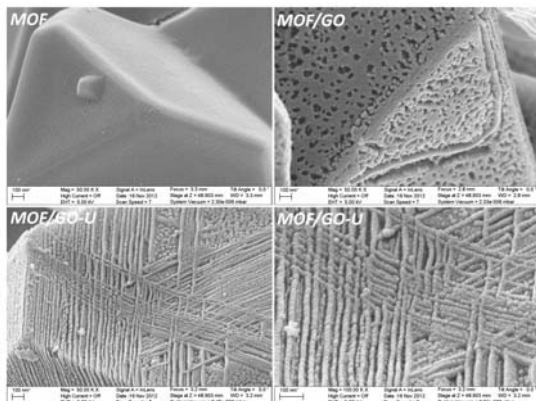


Figure 2: SEM images of the materials studied.

The comparison of SEM images for the samples studied is presented in Figure 2. As seen, the introduction of GO or GO-U to the composites causes visible defects in the MOF structures. The “lace-like” pattern is visible on the surface of the crystals, especially for the composites with aminated GO. This morphology must be the result of the interactions of

MOF with GO units. The latter are apparently embedded in the MOF crystals and the new porosity must emerge at the interface between two phases of the composites [Petit and Bandoz, 2009; Petit *et al.*, 2011; Zhao *et al.*, 2013]. This might also affect the surface chemistry of the composites.

Table 1: Parameters of the porous structure.

Sample	S _{BET} (m ² /g)	V _t (cm ³ /g)	V _{mic} (cm ³ /g)
MOF	892	0.428	0.379
MOF/GO	1010	0.491	0.436
MOF/GO-U	1367	0.663	0.572

The parameters of the porous structure calculated from the nitrogen adsorption isotherms are collected in Table 1. While for MOF/GO 13 % increase in the surface area is found, that enhancement for MOF/GO-U is 53 %. For both materials the synergistic effect is visible in comparison with the parameters of the porous structure evaluated assuming the hypothetical physical mixture of the composite components. The effect of the composite formation is seen in the volume of micropores which increases 15 % for MOF/GO and 51 % for MOF/GO-U. As suggested above, these pores are those formed on the interface between MOF and the modified graphene phase. The pore size distribution presented in Figure 3 shows that in MOF/GO-U 6 Å pores are present. In these pores the adsorption of CO₂ is expected to be enhanced owing to their size proximity to the diameter of the adsorbate molecule.

Assuming that the volume of small pores is a critical parameter, the dependence of the amount of CO₂ adsorbed on the volume of these pores was analyzed (Figure 4). Even though only three points are present, the excellent linear fit clearly indicates the physical adsorption mechanism.

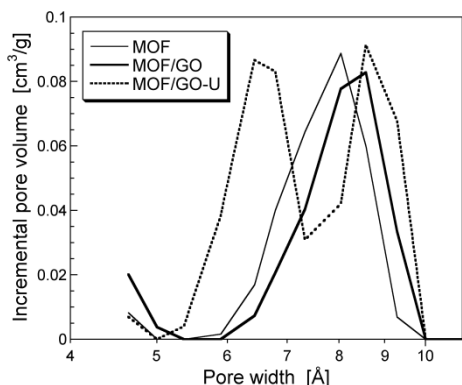


Figure 3: Pore size distributions.

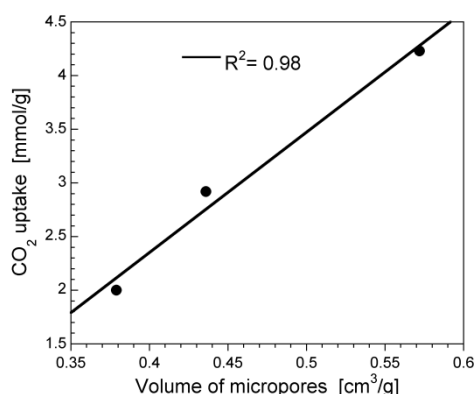


Figure 4: Dependence of the amount of CO₂ adsorbed on the volume of micropores.

Table 2: The content of elements on the surface in atomic %.

Sample	C	O	Cu
MOF	66.0	25.7	8.3±0.5
MOF/GO	61.8	26.6	11.6±0.9
MOF/GO-U	62.7	23.6	13.7±1.2

Since the formation of the composites is also expected to affect surface chemistry and CO₂ was indicated as interacting strongly/specifically with the open copper sites [Zhou *et al.*, 2011], the surface chemistry of the MOF and the composites was compared based on EDX analyses of the surfaces. As seen from Table 2, the ratio of copper to oxygen significantly increases in the composites. This suggests that the “chemical” defects beneficial for CO₂ adsorption are open copper sites. These new sites are in fact expected to be located in those new “interface” pores.

More defects on the surface of MOF/GO-U than those on that of MOF/GO are linked to the differences in the chemistry of the graphene based phase used to build these two composites [Zhao *et al.*, 2013; Seredych and Bandosz, 2007]. In the case of GO, epoxy groups are located on the basal planes and carboxylic groups on the edges of the graphene layers [Seredych and Bandosz, 2007]. On the other hand, the edges of the graphene layers of GO-U are decorated with amine groups originated from urea [Zhao *et al.*, 2013]. Some of urea can also be attached to basal planes via amide bonds. These leads to more chemically diverse sites on the GO-U than those on GO for reactions with MOF units. While in the latter case mainly epoxy and, to some degree, carboxylic groups can be involved in the reactions with the copper sites [Petit *et al.*, 2011], in the former samples copper can also form complexes with amine groups. The amine groups can also interact with carboxylic acid linkages. This causes that more open copper sites is detected in the surface of MOF/GO-U than those on MOF/GO. As a result, the materials tested exhibit an excellent adsorption capacity, higher than that measured on other promising materials addressed in the literature [Qian *et al.*, 2012].

4. CONCLUSIONS

The results presented in the paper show a significant enhancement in the CO₂ adsorption capacity of Cu-BTC (MOF) caused by its involvement in the formation of the composite with GO and aminated graphite oxide. Introducing a higher degree of chemical heterogeneity to GO results in more binding sites, which are involved in the composite formation. This leads to more defects in the MOF structures and formation of pores similar in sizes to CO₂ molecules. The defects, open copper sites and an

increase in the volume of micropores were found responsible for the over 100 % enhancement in CO₂ adsorption compared to the amount adsorbed on MOF.

Acknowledgements: This work was supported by ARO Grant W911NF-10-1-0039 and NSF collaborative grant CBET 1133112. The Scholarship from CSC (China Scholarship Council) for Yunxia Zhao is highly appreciated.

REFERENCES

- Chui, S. S.-Y., Lo, S. M.-F., Charmant, J. P. H., Orpen, G. and Williams, I. D., 1999. A Chemically Functionalizable Nanoporous Material [Cu₃(TMA)₂(H₂O)₃]_n, *Science*, 283, 1148.
- D'Alessandro, M., Smit, B. and Long, J.R., 2010. Carbon Dioxide Capture: Prospects for New Materials, *Angew. Chem. Int. Ed.*, 49, 6058.
- Gorka, J., Fulvio, P.F., Pikus, S. and Jaroniec, M., 2010. Mesoporous Metal Organic Framework-Boehmite and Silica Composites, *Chem. Commun.*, 46, 6798.
- Hirscher, M., 2011. Hydrogen Storage by Cryoadsorption in Ultrahigh-Porosity Metal-Organic Frameworks, *Angew. Chem. Int. Ed.*, 50, 581.
- Lastoskie, C., Gubbins, K.E. and Quirke, N., 1993. Pore Size Heterogeneity and the Carbon Slit Pore: A Density Functional Theory Model, *Langmuir*, 9, 2693.
- Llewellyn, P.L., Bourrelly, S., Serre, C., Vimont, A., Daturi, M., Hamon, L., Weireld, G.D., Chang, J.-S., Hong, D.-Y., Hwang, Y.K., Jung, S.H. and Férey, G., 2008. High Uptakes of CO₂ and CH₄ in Mesoporous Metal-Organic Frameworks MIL-100 and MIL-101, *Langmuir*, 24, 7245.
- Millward, A.R. and Yaghi, O.M., 2005. Metal-Organic Frameworks with Exceptionally High Capacity for Storage of Carbon Dioxide at Room Temperature, *J. Am. Chem. Soc.*, 127, 17998.
- Petit, C. and Bandoz, T.J., 2009. MOF-Graphite Oxide Composites: Combining the Uniqueness of Graphene Layers and Metal-Organic Frameworks, *Adv. Mater.*, 21, 4753.
- Petit, C., Mendoza, B. and Bandoz, T.J., 2010. Reactive Adsorption of Ammonia on Cu-Based MOF/Graphene Composites, *Langmuir*, 26, 15302.
- Petit, C. and Bandoz, T.J., 2011. Synthesis, Characterization, and Ammonia Adsorption Properties of Mesoporous Metal-Organic Framework (MIL(Fe))-Graphite Oxide Composites: Exploring the Limits of Materials Fabrication, *Adv. Funct. Mater.*, 21, 2108.
- Petit, C., Burrell, J. and Bandoz, T.J., 2011. The Synthesis and Characterization of Copper-Based Metal-Organic Framework/Graphite Oxide Composites, *Carbon*, 49, 563.
- Prasanth, K.P., Rallapalli, P., Raj, M.C., Bajaj, H.C. and Jasra, R.V., 2011. Enhanced Hydrogen Sorption in Single Walled Carbon Nanotube Incorporated MIL-101 Composite Metal-Organic Framework, *Int. J. Hydrogen Energy*, 36, 7594.
- Qian, D., Lei, C., Hao, G.-P., Li, W.-C. and Lu, A.-H., 2012. Synthesis of Hierarchical Porous Carbon Monoliths with Incorporated Metal-Organic Frameworks for Enhancing Volumetric Based CO₂ Capture Capability, *ACS Appl. Mater. Interfaces*, 4, 6125.
- Seredych, M. and Bandoz, T.J., 2007. Mechanism of Ammonia Retention on Graphite Oxides: Role of Surface Chemistry and Structure, *J. Phys. Chem. C*, 111, 15596.
- Stock, N. and Biswas, S., 2011. Synthesis of Metal-Organic Frameworks (MOFs): Routes to Various MOF Topologies, Morphologies, and Composites, *Chem. Rev.*, 112, 933.
- Tranchemontagne, D.J., Park, K.S., Furukawa, H., Eckert, J., Knobler, C.B. and Yaghi, O.M., 2012. Hydrogen Storage in New Metal-Organic Frameworks, *J. Phys. Chem. C*, 116, 13143.
- Xiang, Z., Hu, Z., Cao, D., Yang, W., Lu, J., Han, B. and Wang, W., 2011. Metal-Organic Frameworks with Incorporated Carbon Nanotubes: Improving Carbon Dioxide and Methane Storage Capacities by Lithium Doping, *Angew. Chem. Int. Ed.*, 50, 491.
- Zhao, Y., Seredych, M., Zhong, Q. and Bandoz, T.J., 2013. Aminated Graphite Oxides and their Composites with Copper-Based Metal-Organic Framework: In Search for Efficient Media for CO₂ Sequestration, *RSC Adv.*, 3, 9932.
- Zhao, Y., Seredych, M., Zhong, Q. and Bandoz, T.J., 2013. Superior Performance of Copper Based MOF and Aminated Graphite Oxide Composites as CO₂ Adsorbents at Room Temperature, *ACS Appl. Mater. Interfaces*, DOI: 10.1021/am4006989.
- Zhou, C., Cao, L., Wei, S., Zhang, Q. and Chen, L., 2011. A First Principles Study of Gas Adsorption on Charged Cu-BTC, *Comput. Theor. Chem.*, 976, 153.

NICKEL REMOVAL BY USING IMMOBILIZED MACRO FUNGUS: BATCH BIOSORPTION STUDIES

Tamer Akar¹, Sema Celik², Asli Gorgulu Ari³, Sibel Tunalı Akar¹

¹Department of Chemistry, Faculty of Arts and Science, Eskisehir Osmangazi University, 26480 Eskisehir, Turkey

² Department of Chemistry, Graduate School of Natural and Applied Sciences, Eskisehir Osmangazi University, 26480 Eskisehir, Turkey

³ Department of Elementary Education, Faculty of Education, Yildiz Technical University, 34210 Istanbul, Turkey

a. Corresponding author (sema.celik.87@hotmail.com)

ABSTRACT Heavy metal contaminated waters serious damage in the environment and living organisms. In recent years, biosorption is a considerable alternative process for the treatment of the heavy metal bearing effluents. Biosorption can be defined as the removal of different pollutants from aqueous media by biological materials. It is an attractive technology with the advantages of low cost, high yield and easily available of biomasses. In the present study, macro fungi *Lactarius salmonicolor* was immobilized in the silica gel matrix and successfully used for the removal of nickel ions from aqueous media. Operating conditions were optimized as functions of initial pH, agitation time, sorbent amount. Biosorption performance of the biomass continuously increased in the pH range 2.0–8.0. The coverage of the biosorbent surface by silica gel resulted in a significant increase in biosorption yield of nickel ions. The highest nickel loading capacity was obtained as 114.44 mg g⁻¹ using a relatively small amount of immobilized biosorbent. Biosorption equilibrium time was recorded as 5 min. As a result, Silica gel immobilized biomass of *L. salmonicolor* is suggested as a low cost and potential biosorbent with high biosorption capacity for the removal of nickel ions from contaminated solutions.

1. INTRODUCTION

Heavy metal contamination of industrial effluents is one of serious environmental problems, because they accumulate in living organisms and cause serious damages [Akar and Tunalı, 2005]. Nickel is used large number of industry from electroplating to long life battery. Untreated wastes of these industries can be damaging to the aquatic environment. Excessive intake of nickel by humans cause carcinogenic effects [Denkhaus and Salnikov, 2002]. Thus, removal of nickel from contaminated waters is a significant issue that requirements to be research. Different conventional treatment methods (precipitation, membrane separation, ion exchange, reverse osmosis and electrolysis etc.) are used for metal

containing wastewaters. However, their use is not applicable because of high treatment cost, the need for continuous input of chemicals, and the production of toxic sludge [Tunalı and Akar, 2006 and Han et al., 2006]. The treatment of metal contaminated waters with ecofriendly technologies is one of the popular research topic in recent years. The biosorption is considered as a potential alternative to existing traditional water treatment technologies, especially if suggested biomaterial is low-cost, readily available and has a good removal performance. Free and immobilized biosorbent materials can be utilized in the biosorption process but immobilized form is ideal especially in conventional unit operations. They have some important advantages such as improved

mechanical strength, online matrix isolation in flow analysis, low resistance to fluid flow and easy regeneration of biosorbent material [Akar et al., 2009]. As a biomass source, macro fungi have some important characteristics for sorption studies such as chemical stability, good mechanical properties in acidic and alkaline conditions and texture structure in dried form. It is easily and economically available anywhere and also possesses a tough texture in dried form [Maurya et al., 2006]. *Lactarius salmonicolor* (*L. salmonicolor*) was chosen as a model macro fungus in this study because meager information is available regarding biosorption capability and it is a natural and readily available biomaterial.

The purpose of this study was to develop a new low cost and ecofriendly biosorbent for the biosorption of Ni^{2+} . Our study describes the application of silica gel coated *L. salmonicolor* cells for the biosorptive removal of nickel ions from aqueous solutions. Biosorption conditions were optimized by varying experimental design parameters.

2. MATERIAL AND METHODS

Biosorbent and immobilization procedure Fresh biomass of *L. salmonicolor* was collected from its natural habitat in Gemlik, Turkey. The fruiting bodies of fungus were washed repeatedly with deionized water, dried at 60°C, ground using a laboratory mill (IKA A-11) and sieved to obtain uniform particle size (150 μm) of biosorbent. The sieved biomass was immobilized by applying the procedure previously suggested by Lopez and co-workers, except for the beads formation (Lopez et al., 1997). Briefly, 10 g of silica gel was dissolved by heating in 100 mL of 7% (w/v) aqueous solution of KOH. 5 g dry weight of biomass was added into solution with vigorous stirring. A measured amount of

phosphoric acid solution (20%) was added to provide gel formation. Immobilized biosorbent was dried and sieved using the same procedure described above.

2.1. Ni^{2+} Solutions and Analysis

A stock solution of Ni^{2+} (1000 mg L^{-1}) was prepared by dissolving a weighed quantity of $\text{Ni}(\text{NO}_3)_2 \cdot 6\text{H}_2\text{O}$ (analytical grade, Merck) in 1000 mL deionized water. It was used by diluting to prepare solutions in the concentration range 50 to 600 mg L^{-1} . The pH levels of the test solutions were adjusted to the required values by adding 0.1 N HNO_3 or 0.1 N NaOH and pH of the solutions was measured using a digital pH meter (HI 221 Hanna). The residual metal concentration in the aqueous phase was analyzed by atomic absorption spectrophotometer (AAS) (Unicam 929). Data presented are the mean values obtained from three independent experiments.

2.2. Biosorption Studies

The optimum pH for biosorption was determined by agitating the biosorption mixture containing 0.1 g of biomass and 50 mL of Ni^{2+} solutions (100 mg L^{-1}) at different pH values. The contact time was varied from 5 to 90 min using the same biosorption mixture described above. Nickel solutions with varying concentrations were used to evaluate the effect of initial metal ion concentration on the biosorption process. At the end of each test, biosorbent samples were separated from the biosorption medium by centrifugation at 4500 rpm for 5 min and supernatant was analyzed for the residual Ni^{2+} concentration.

3. RESULTS AND DISCUSSION

3.1. Effect of pH on the Biosorption Process

The pH of the aqueous solution has been identified as the most important parameter governing metal biosorption process.

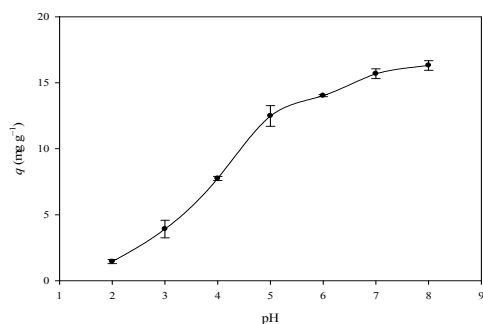


Figure 1: Effect of initial pH on the biosorption of Ni²⁺ ions on *L. salmonicolor* biomass

The results presented in Fig. 1 emphasize that no nickel biosorption was observed at highly acidic conditions. A notable increase in the biosorption capacity of biomass from 1.45 mg g⁻¹ to 14.03 mg g⁻¹ was recorded in the pH range 2.0 to 6.0 ($P < 0.05$). When the initial pH of the medium was adjusted to higher values up to 8.0 biosorption capacity did not significantly change ($P > 0.05$). Hence, further biosorption studies were carried out at pH 6.5 (original pH value of Ni²⁺ solution). The lower biosorption capacity observed at highly acidic conditions could be largely related to repulsive forces between metal cations and positively charged binding sites on the fungal cell wall. The negative charge density on the fungal cell surface increased with increase in pH as a result of the deprotonation of possible binding sites.

3.2 Effect of Biosorbent Amount on the Biosorption Process

The variation in biosorption yields of the biosorbent materials as a function of biomass dosage is depicted in Fig. 2. As

can be seen in this figure, the biosorption yield increased from 15.23 to 26.71% as the biosorbent dosage of the natural biomass was increased from 1.0 to 2.0 g ($P < 0.05$). Further increase in biosorbent dosage up to 3.0 g did not significantly change the uptake yield of the biosorbent ($P > 0.05$). This may be due to saturation of the metal binding sites on the biosorbent surface by nickel ions. A similar biosorption pattern was obtained for the silica gel coated *L. salmonicolor*. Ni²⁺ loading yield of the immobilized *L. salmonicolor* reached 83.56% with 1.8 g biosorbent dosage. At the same biosorbent amount, the biosorption yield of natural *L. salmonicolor* was only 19.40%. This behavior may be attributed to an increase in the negative charge density on the biosorbent surface after the immobilization process.

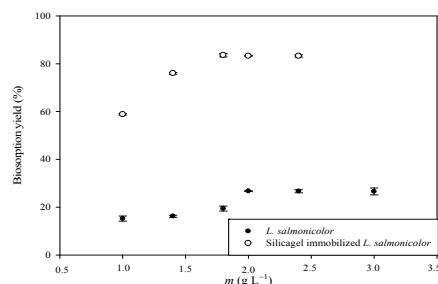


Figure 2: Effect of biosorbent dosage on the biosorption of Ni²⁺ ions on natural and immobilized *L. salmonicolor* biomass (initial pH:6.5, temperature: 25°C, Ni²⁺ concentration: 100 mg L⁻¹ V:50 mL).

3.3. Agitation Time of Biosorption Process

The agitation time of natural and immobilized biomasses for the biosorption of nickel ions are depicted in Fig. 3. Rapid biosorption rates were observed at the beginning of the process, then an equilibrium period was attained at 10 and 5 min for natural and immobilized *L. salmonicolor*, respectively. Figure. 3 also indicates that the equilibrium nickel biosorption capacities of natural and immobilized biomasses were 13.10 mg

g^{-1} and 44.74 mg g^{-1} , respectively. This rapid biosorption rate is an important characteristic for development and application of biosorbent material in water treatment technology.

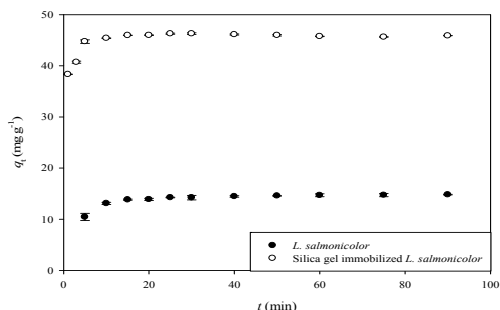


Figure 3: Effect of contact time on the biosorption of Ni^{2+} ions on natural and immobilized *L. salmonicolor* biomass.

3.4. Isotherm Modelling of the Biosorption Process

The Ni^{2+} biosorption capacity of natural and immobilized forms of *L. salmonicolor* biomass at different Ni^{2+} ion concentrations was evaluated using Freundlich (Equation (1)) and Langmuir (Equation (2)) isotherm models. The Freundlich model (Freundlich, 1906) assumes that the sorption surface is heterogeneous and binding sites have different sorption energies. The Langmuir model (Langmuir, 1918) assumes monolayer type of biosorption within the specific homogeneous sites of biosorbent.

The model equations are:

$$\text{Freundlich model } q_e = K_F C_e^{1/n} \quad (1)$$

Langmuir model

$$q_e = \frac{q_{\max} K_L C_e}{1 + q_{\max} K_L} \quad (2)$$

where K_F ($\text{L mg}^{\square 1}$) and n (dimensionless) are Freundlich constants, q_e ($\text{mmol g}^{\square 1}$) and C_e ($\text{mmol L}^{\square 1}$) are the amount of nickel ions biosorbed per specified amount of biosorbent and equilibrium metal ion concentration in solution, respectively. q_{\max} is the maximum monolayer biosorption capacity of biosorbent and K_L is a

constant related to the energy of biosorption ($\text{L mg}^{\square 1}$).

The general biosorption isotherm and predicted curves for the Freundlich and Langmuir models are shown in Fig. 6. The model parameters of the three isotherms along with r^2 values are presented in Table 1.

According to r^2 values in this table, nickel biosorption follows the two isotherm models in the order Freundlich > Langmuir for natural and Langmuir > Freundlich for immobilized *L. salmonicolor* at the experimental circumstances investigated. These findings indicate that the heterogeneous surface of the natural biosorbent was covered by a monolayer of nickel ions. On the other hand after the immobilization process the surface of the biomass became more homogeneous. The maximum monolayer biosorption capacities (q_{\max}) of the natural and immobilized biosorbents in batch mode are 1.16 mmol g^{-1} (68.08 mg g^{-1}) and 1.95 mmol g^{-1} (114.44 mg g^{-1}), respectively.

Table 1: Isotherm parameters for the biosorption of Ni^{2+} on natural and immobilized *L. salmonicolor* biomass

Biosorbent	Langmuir			Freundlich		
	q_{\max} (mmol g^{-1})	K_L (L mmol^{-1})	r_L^2	n	K_F (L mg^{-1})	r_F^2
<i>L. salmonicolor</i> <i>r</i>	1.16	2.83	0.97 2	1.5 5	0.26	0.99 1
Silica gel immobilized <i>L. salmonicolor</i> <i>r</i>	1.95	2.46	0.93 5	3.6 0	1.20	0.92 8

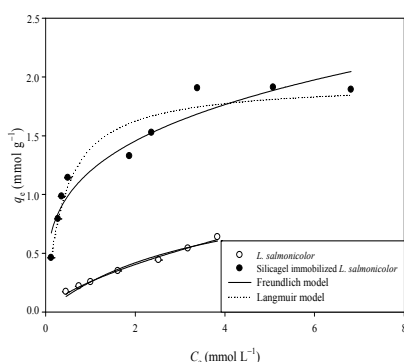


Figure 4: Experimental data and predicted curves for the biosorption of Ni^{2+} ions on natural and immobilized *L. salmonicolor* biomass.

4. CONCLUSION

This study reports the Ni^{2+} biosorption potentials of the natural and immobilized biomass of a macro fungi *L. salmonicolor*. The immobilized biomass was prepared by a simple immobilization technique and exhibited high biosorption capacity for Ni^{2+} ions (114.44 mg g^{-1}). The fast biosorption equilibrium was observed for natural and immobilized *L. salmonicolor*.

Acknowledgements

This work was supported by the Commission of Scientific Research Projects of Eskişehir Osmangazi University (ESOGU) with Project number 200819007. The authors gratefully acknowledge financial support by ESOGU.

REFERENCES

- Akar, T., Kaynak, Z., Ulusoy, S., Yuvaci, D., Ozsari, G. and Tunali Akar, S., 2009, Enhanced biosorption of nickel(II) ions by silica-gel-immobilized waste biomass: Biosorption characteristics in batch and dynamic flow mode, *Journal of Hazardous Materials*, 163, 1134-1141.
- Akar, T. and Tunali, S., 2005, Biosorption of performance *Botrytis cinerea* fungal by-products for removal of Cd(II) and Cu(II) ions from aqueous solutions, *Minerals Engineering*, 18, 199-1019.

Denkhaus, E. and Salnikow, K., Nickel essentiality, toxicity, and carcinogenicity, 2002, *Critical Reviews in Oncology Hematology*, 42, 35-56.

Freundlich, H.M.F., 1906, Über die adsorption in lösungen, *Zeitschrift für Physikalische Chemie*, 57, 385-470.

Han, R.P., Zhang, J.H., Zou, W.H., Xiao, H.J., Shi, J. and Liu, H.M., 2006, Biosorption of copper(II) and lead(II) from aqueous solution by chaff in a fixed-bed column, *Journal of Hazardous Materials*, 133, 262-268.

Langmuir, I., 1918, The adsorption of gases on plane surfaces of glass, mica and platinum, *Journal of American Chemical Society*, 40, 1361-1403.

Lopez, A., Lazaro, N. and Marques, A.M., 1997 The interphase technique: a simple method of cell immobilization in gel-beads, *Journal of Microbial Methods*, 30, 231-234.

Maurya, R.S., Mittal, A.K., Cornel, P. and Rother, E., 2006, Biosorption of dyes using dead macrofungi : Effect of dye structure, ionic strength and pH, *Bioresource Technology*, 97, 512-521.

Tunali, S. and Akar, T., 2006, Zn(II) biosorption properties of *Botrytis cinerea* biomass, *Journal of Hazardous Materials*, 131, 137-145.

APPLICATION OF OXIDIZED AND REDUCED ACTIVATED CARBON FOR PARA-NITROPHENOL REMOVAL

Mohammad Hassan Mahaninia¹, Tahereh Kaghazchi^{1,a} and Mansooreh Soleimani¹

1. Amirkabir University of Technology, Department of Chemical Engineering, Tehran, Iran

a. Corresponding author (kaghazch@aut.ac.ir)

ABSTRACT: Due to toxic properties of para-nitrophenol, it is necessary to remove this component from wastewater. In this work, introduction of oxygen functional groups on the surface of activated carbon have been investigated in order to enhance its adsorption properties toward para-nitrophenol. Functional groups on activated carbon produced from oxidation by NO_x-containing gaseous by-product and reduction by heat treatment at 700°C in H₂ flow. The modified activated carbons were characterized by several analysis methods, including N₂ adsorption/desorption, elemental analysis, FTIR spectroscopy, thermo-gravimetry analysis (TGA), scanning electron microscopy (SEM), pH of zero point charge, and Boehm titration. It was found that oxidation of activated carbon produces carboxylic acid, lactone, quinone, phenol, and nitro groups and reduction of activated carbon produces alcohol and amine groups. Also, the influences of these treatment methods on adsorption of para-nitrophenol on activated carbon were studied. Experimental results indicated that oxidized carbon had the higher adsorption rate and capacity toward Para-nitrophenol.

1 INTRODUCTION

Activated carbon is a carbon-based porous material with a relatively high surface area and porosity. This adsorbent contains various heteroatoms (e.g., O, N, P, and S) which affect the physicochemical properties of its. All of these properties make activated carbon an ideal adsorbent which have been developed for wide range of application for removal of inorganic and organic pollutants [Biniak et al., 1997, Kaghazchi and ShamsiJazeyi, 2010, Soleimani and Kaghazchi, 2008, Rodriguez-Reinoso and Molina-Sabio, 1998]

The adsorption of phenol and substituted phenols from aqueous solution on activated carbons has been intensively investigated for decades [Carlos, 2004, Paprowicz, 1990, Daifullah and Girgis, 1998]. The nature of the adsorption sites for substituted phenols was debated in many studies [Radovic *et al.*, 2000]. Many authors considered electron-rich regions located in graphene layers

interacting with the π electrons of the aromatic ring of phenols (π - π argument [Radovic *et al.*, 2000]), while numerous other authors supported the conclusion that some basic carbonyl surface groups form a bond with the aromatic ring of phenol (donor-acceptor argument [Radovic *et al.*, 2000]).

Undoubtedly, the experimental discrimination between these adsorption models is not easy because the modification of activated carbon may unintentionally modify most of its textural and chemical properties. For example, oxidation of activated carbon with nitric acid not only introduces both acidic and basic oxygen groups at the surface of carbon, but also may modify the nature of oxygen groups that were existed on activated carbon.

This study presents a study of para-nitrophenol (PNP) adsorption from aqueous solutions on oxidized and reduced activated carbon. The aim of this

work was investigation of additional information on the influence of oxygen species on the adsorption of substituted phenols. Oxygen functional groups have been introduced to commercial activated carbon (ROX) by NO_x-containing gaseous by-product (ACOX) and then these oxygen functional groups have been reduced by a gaseous reduction method (ACRED) to see if these groups have impact on para-nitrophenol adsorption.

2.RESULTS AND DISCUSSION

The data of determination of porous structure properties of all samples can be seen in Table 1. The surface area of modified AC was gradually decreased after oxidation, reduction, and grafting steps, as compared to the original activated carbon (ROX).

The decrease in surface area of activated carbon may occur because severe oxidation may weaken the graphitic ring structure of the micropores, decompose the binders of activated carbon, and cause blockage on the cavities.

The results of Boehm titrations and determination of pH of zero point were

listed in Table 2. As it is clear from this data, the pH of zero point charge of ACRED sample are higher than 7 (in the basic range); while ROX and ACOX was acidic due to carboxylic groups and other acidic oxygen functionalities. Reduction of activated carbon causes to formation of amine and alcohol that are naturally basic. This leads to produce basic adsorbents with the pH_{zpc} greater than 7.

Oxidation on the activated carbon surface was produced carboxylic acid groups rather than hydroxyl groups or basic functional group on ACOX sample; whereas the amount of hydroxyl group and total basic groups were increased in ACRED sample.

The total surface coverage was calculated based on a consideration of weight losses of desorbed molecules from the surface of activated carbon (Figure 1). Below 100°C, adsorbed water was desorbed from the surface (macropores) of activated carbon. Carboxylic acids and carbonyl groups may undergo decarbonylation reactions forming CO₂ and CO of C=O and C-O functional.,

Table1: Result of the porous structure properties of original and modified activated carbons.

	Surface Area (m ² /g)	Microporous volume (cm ³ /g)	Mesoporous volume (cm ³ /g)
ROX	916	0.36	0.33
ACOX	743	0.33	0.32
ACRED	696	0.31	0.31

Table 2: Boehm titration and point of zero charge results.

	ROX	ACOX	ACRED
Hydroxyl group (mmol/g)	1.4	0.3	1.64
Carboxyl group (mmol/g)	0.61	1.34	0.14
Carbonyl group (mmol/g)	0.04	1.86	0.08
Total acidic Sites (mmol/g)	0.184	2.16	0.12
Total Basic sites(mmol/g)	0.70	0.25	1.15
pH _{zpc}	6.87	4.13	8.12

Table 3: Thermogravimetry results for surface modified and virgin activated carbons.

	H ₂ O	CO ₂ CO (%)	Total surface coverage (%)
ROX	3.8	1.8	5.4
ACOX	6.1	24.9	31.7
ACRED	11.4	47.8	59.6

groups including hydroxyl groups as similarly concluded [Figueiredo *et al.*, 2000]. The surface coverage of samples is shown in Table 3.

The evolution temperature of CO₂ varies by chemical functional groups in accordance with decarboxylation reactions which may occur from 100°C to 400°C; (carboxylic acid groups), 200°C to 600°C (lactone groups), and >600°C (anhydride groups which includes CO) [Figueiredo *et al.*, 2000]. ACOX from HNO₃ treatment evolves CO₂ in the range of 130–827°C with maximum temperature of decomposition of 252°C [Otake and Jenkins, 2003].

The results of FTIR analysis are illustrated in Figure 2. The vibrational band at 1852 cm⁻¹ from ACOXID may be attributed to acid anhydride and overlapping with a lactone vibrational band. The strong vibrational band at 1760 cm⁻¹ indicates that AC was severely oxidized with HNO₃. The signal at 1,604 cm⁻¹ from ACOXID was assigned to an aromatic C=C or C=O for a highly conjugated system with an aromatic ring, such as quinine [Zhuang *et al.*, 1994].

Figure 3 shows SEM images for different samples. ACOX possess larger size pores than ROX and the surface appears to have been damaged by oxidation with nitric acid.

In Table 4, the results of elemental analysis of all samples have been listed. Clearly oxygen percentage in ACOX is

higher than other samples (28.1%) and the presence of 1.2% nitrogen in ACOX

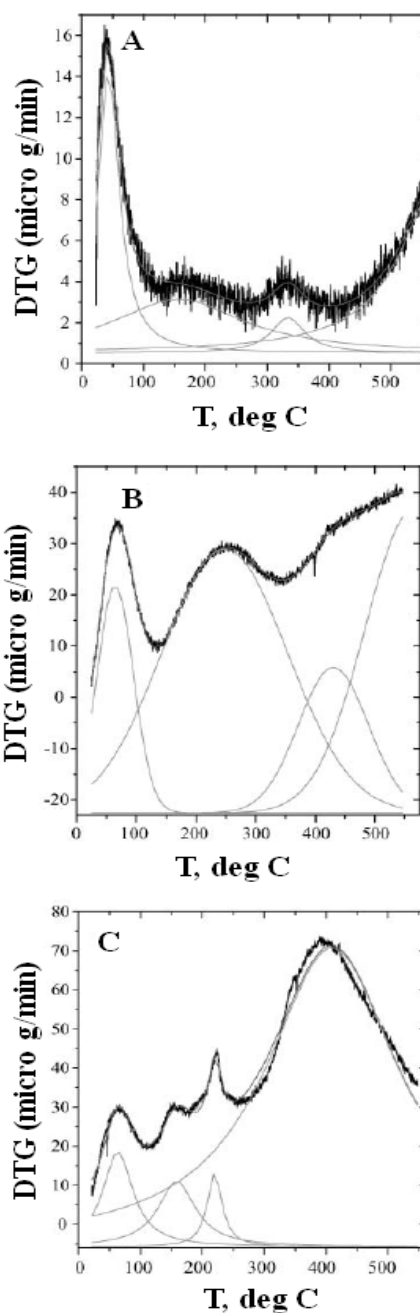


Figure 1: TGA results. [A = ROX, B =ACOX, C = ACRED].

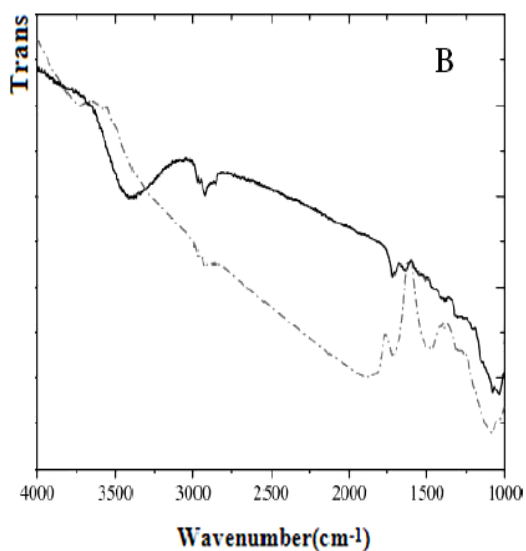
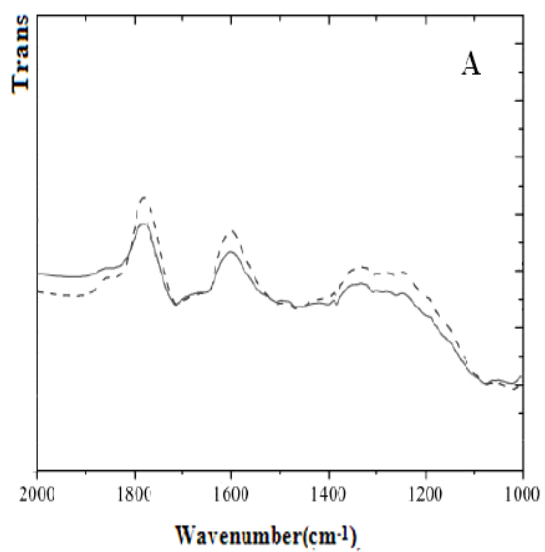


Figure 2: The FTIR spectra for ACOX (A: solid line = ROX, dash line= ACOX), ACRED (dash dot line= ACRED)

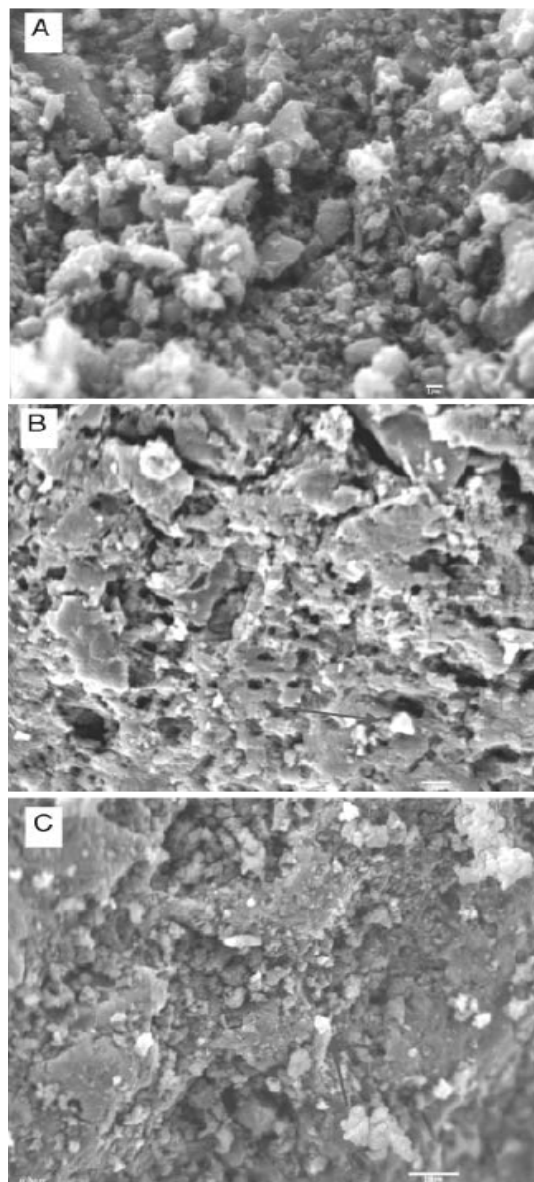


Figure 3: SEM images; A = ROX, B = ACOX, C = ACRED

provides strong support that an N-containing (NO₂) group was formed by oxidation.

Table 4: Elemental analysis of the activated carbons.

	Ultimate analysis (wt.%, daf)			
	C%	H%	N%	O%
ROX	85.1	0.4	0.4	14.1
ACOX	71.0	0.7	1.2	17.8
ACRED	60.3	1.2	1.6	36.9

The percentage of PNP removal from aqueous phase as a function of time has been shown in Figure 4.a. Based on this figure; the initial adsorption rate of ACRED is more than the ACOX. It can be seen that during the first hour of the process, a 40–50% of removal capacity was achieved, and the adsorption then gradually reached a steady state. The kinetically rapid adsorption by ACRED implied the generation of strong PNP-binding sites of the ACRED surface compare with ACOX sample.

In order to determine the PNP sorption capacity of the activated carbons, some equilibrium adsorption tests were carried out. Results of this experiment are shown by plotting the equilibrium adsorption capacity of adsorbents (q_e) versus C_e:

$$q_e = [V(C_0 - C_e)/M] \quad (1)$$

where C₀ and C_e are the initial and equilibrium concentrations of PNP in the solution, V is the volume of solution and M is the weight of the adsorbent in Figure 4.b. It can be seen that the amount of PNP adsorbed by ACRED sample at equilibrium conditions is much higher than ACOX sample. The decrease in adsorption capacity of ACOX can be seen. However, after reduction of ACOX to ACRED adsorption capacity was restored to the initial condition. This behavior supports the concept of π-π

interaction. Therefore, treatment of activated carbon by nitric acid strongly increases the number of carboxylic groups and carbonyl groups on activated carbon that withdraw electrons from the graphene layers and as a result it decreases the number of adsorption sites for PNP. This result rejects the concept of donor–acceptor.

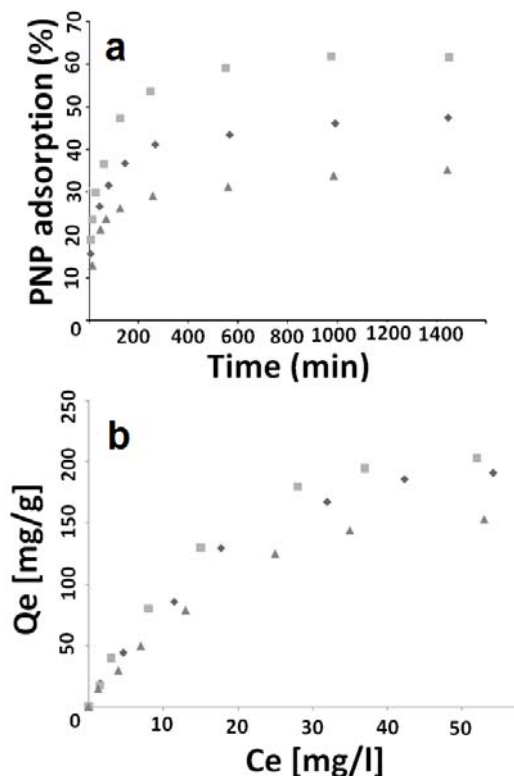


Figure 4:a: PNP adsorption as a function of contact time, b: Equilibrium isotherms ROX (■), ACOX (▲), and ACRED (◆). Operating conditions: t = 24 h; pH=6.0; T=25°C.

3. CONCLUSIONS

The presence of different functional groups on activated carbon surface was characterized by different methods. It was indicated that most of carboxylic and carbonyl groups were eliminated due to reduction of ACOX. The determination of adsorption isotherm led us to accept the donor–acceptor argument for ACOX. Logical relationship between the amounts of carboxylic and carbonyl groups on activated carbon with the PNP adsorption

capacity is observed for oxidized carbon. Consequently, oxidized carbon had the higher adsorption rate and capacity toward Para-nitrophenol., in agreement with donor–acceptor argument.

REFERENCES

- Biniak, S., Szymanski G., Siedlewski J., Swiatkowski A., 1997. The characterization of activated carbons with oxygen and nitrogen surface groups. *Carbon*, 35, 1799.
- Boehm, H.P., 1966. Chemical Identification of Surface Groups, *Advances in catalysis*, Academic Press, New York, 179.
- Carlos M-C., 2004. Adsorption of Organic Molecules from Aqueous Solutions on Carbon Materials. *Carbon*, 42, 83.
- Daifullah, A.A.M., Girgis B.S., 1998. Removal of some substituted phenols by activated carbon obtained from agricultural waste. *Water Res.*, 32(4), 1169.
- Figueiredo, J. L., Pereira, M.F.R., Freitas, M.M.A., Orfao, J.J.M., 1999 . Modification of the surface chemistry of activated carbons. *Carbon*, 37(9), 1379.
- Kaghazchi, T., ShamsiJazeyi, H., 2010. Modification of activated carbon using a NOx-containing gaseous by-product for enhanced Hg(II) removal from aqueous phase, *J. Ind. Eng. Chem.*, 17, 608.
- Otake, Y., Jenkins, R.G., 1993. Characterization of oxygen containing surface complexes created on a microporous carbon by air and nitric acid treatment. *Carbon*, 31(1), 109.
- Paprowicz, J.T., 1990. Activated carbons for phenols removal from wastewater. *Environ. Technol.*, 11, 71.
- Radovic, L.R., Moreno-Castilla C., Rivera-Utrilla J., 2000. Carbon materials as adsorbents in aqueous solutions, *Chemistry and physics of carbon*, Marcel Dekker, New York, 227.
- Rodriguez-Reinoso F., Molina-Sabio M., 1998. Textural and chemical characterization of microporous carbons. *Adv. Colloid Interface Sci.*, 76-77, 271.
- Soleimani, M., Kaghazchi, T., 2008. Activated Hard Shell of Apricot Stones: A Promising Adsorbent in Gold Recovery. *Chin. J. Chem. Eng.*, 16 (1), 112.
- Zhuang, Q.L., Kyotani, T., Tomita, A., 1994. Drift and TK/TPD analyses of surface oxygen complexes formed during carbon gasification. *Energy Fuels*, 8(3), 714.

REMOVAL OF THE AMPICILLIN ANTIBIOTIC IN AQUEOUS SOLUTION BY PHOTO-FENTON/ULTRASONIC-FENTON PROCESSES

Gamze KOYUNCU^{1,a}, Halil KUMBUR², Habibe Elif GÜLŞEN³

1. Mersin University, Department of Environmental Engineering, Mersin, Turkey

2. Mersin University, Department of Environmental Engineering, Mersin, Turkey

3. Mersin University, Department of Environmental Engineering, Mersin, Turkey

a. Corresponding author (gamzekoyuncu.33@gmail.com)

ABSTRACT: For many years, antibiotics, are an important group of pharmaceuticals, have been used to prevent human and animal diseases. However, as a result of this intensive usage, they are flowed into the soil, sediments, ground water, surface water and drinking water by urine, feces, both metabolized and non-metabolized forms as fertilizer. As they have complex organic compounds on their structures which are hard biodegradable, can create a pollution without decomposition for months. High concentrations of antibiotics cause a deterioration of the ecological balance due to their toxic effects onto the microorganisms. Also, low concentrations of antibiotics cause to win an antibiotic resistance in pathogenic and non-pathogenic bacteria and genotoxicity. Therefore, it is significant that antibiotic pollution control. In recent years, the new chemical and biological processes have been searched by researchers about antibiotic degradation. One of these methods is advanced oxidation processes. In this study; the reduction of ampicillin in aqueous solution was investigated by photo-fenton (UV/Fe²⁺/H₂O₂)/ultrasonic-fenton (US/Fe²⁺/H₂O₂) processes, a drug belonging to the class of β -lactam antibiotics. It was determined physical-chemical conditions (pH, Fe²⁺, antibiotic-H₂O₂ concentrations and reaction time) for the effects of reduction and treatment on ampicillin.

Keywords: Ampicillin, antibiotic, pharmaceutical, photofenton oxidation, ultrasonic fenton oxidation

1. INTRODUCTION

Pharmaceutical industry has shown the rapid development of the last 40 years as an industry segment [Saygı *et al.*, 2012]. Antibiotics are pharmaceutical agents which are commonly used in human and veterinary medicine to prevent several diseases. Recently, a variety of antibiotics have been detected in environment including surface water, groundwater, seawater, soils and treatment plant effluents due to their property of bioresistant [Fatta-Kassinos *et al.*, 2010]. So, antibiotic pollution has been a source of concern in terms of health and environment. Especially in developing countries, drug-induced wastes have been

granted the attention that they deserve in waste management. Since antibiotics are hardly decomposed, they must be removed from waters, soils and sediments. Ampicillin (AMP) is a semi-synthetic β -lactam antibiotic and has been excessively detected (20-80 $\mu\text{g/L}$) among the other types of antibiotics in waste water [Kümmerer, 2001]. Advanced Oxidation Processes (AOPs) are one of the treatment methods used for drug impurities. In this study, the reduction of ampicillin in aqueous solution was investigated by photo-fenton and ultrasonic-fenton processes.

2. MATERIALS AND METHODS

Antibiotics used in this study have been obtained from a pharmaceutical company in Mersin and were prepared as synthetic solutions. Hydrogen peroxide (H_2O_2 , 30%), ferrous sulfate ($\text{FeSO}_4 \cdot 7\text{H}_2\text{O}$ > 99.5%), sulfuric acid (H_2SO_4 , 98%) and sodium hydroxide (NaOH , 97%) were purchased from Merck. UV-A (black light bulb) lamp (6 W, 315-400 nm) as light source and a batch reactor have 2 L capacity were used for photo-fenton process. In ultrasonic-fenton experiments, an ultrasonic bath was used at 50 Hz.

Antibiotic stock solution of ampicillin was prepared using distilled water (500 mg/L). The maximum absorbance and concentrations of ampicillin were determined by UV - Visible Spectrophotometer (T90 + UV / Visible, PG Instruments) for oxidation experiments. These experiments were realized at the different pH (2-7), the different concentrations of Fe^{2+} (0.5-2.5 mM), H_2O_2 (5-30 mM), ampicillin (10-50 mg/L) for 20 minute reaction time and at 25 °C temperature.

3. RESULTS AND DISCUSSION

Two different oxidation processes were studied at removal of the antibiotic ampicillin experiments. The results of the two methods were compared according to the reduction efficiencies. Effect of pH onto the antibiotic is given in Figure 1.

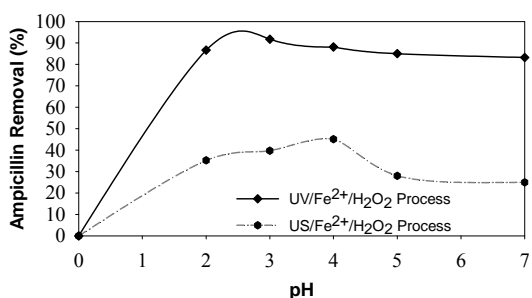


Figure 1. Effect of pH

The best removal of the antibiotic ampicillin was determined 91.78% at pH 3 by photo-fenton process and 45.13% at

pH 4 by ultrasonic-fenton process, respectively in Fig.1.

After optimum pH had been identified, the effect of concentration of Fe^{2+} was investigated at the conditions of 40 mg/L ampicillin, 20 mM H_2O_2 and optimum pHs for processes. The results are given in Figure 2.

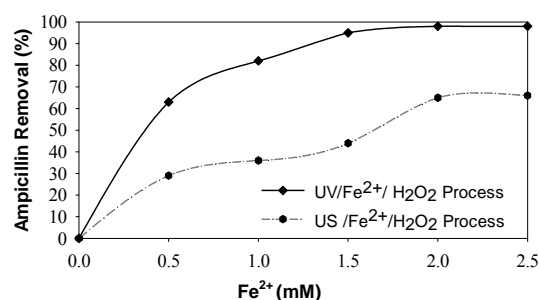


Figure 2. Effect of Fe^{2+} concentration

In this part, the optimum Fe^{2+} concentration was determined 95.12% at 1.5 mM for UV/ Fe^{2+} / H_2O_2 process and 65.43% at 2 mM for US/ Fe^{2+} / H_2O_2 process.

H_2O_2 experiments were performed at 40 mg/L antibiotic sample, pH 3, 1.5 mM Fe^{2+} for photofenton oxidation and pH 4, 2 mM Fe^{2+} for ultrasonik-fenton oxidation. The results are shown in Figure 3.

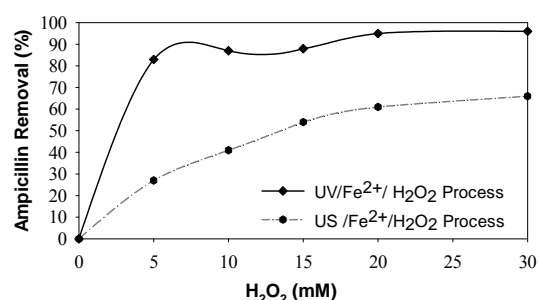


Figure 3. Effect of H_2O_2 concentration

The effect of H_2O_2 to the mineralization of antibiotic was optimized 95.49% at 20 mM H_2O_2 concentration for UV/ Fe^{2+} / H_2O_2 process and 66.31% at 30 mM H_2O_2 concentration for US/ Fe^{2+} / H_2O_2 process.

Antibiotic concentration onto the effect of the oxidation was investigated as the step of fourth treatment of ampicillin that is given in Figure 4 at the conditions of pH 3, 1.5 mM Fe²⁺, 20 mM H₂O₂ by UV/Fe²⁺/H₂O₂ oxidation process and pH 4, 2 mM Fe²⁺, 30 mM H₂O₂ by US/Fe²⁺/H₂O₂ oxidation process.

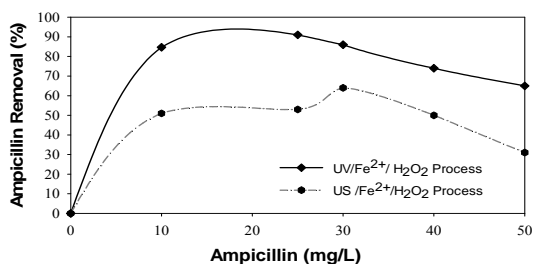


Figure 4. Effect of antibiotic concentration

The removal of ampicillin for both processes was decreased with increasing concentrations. 84.68%, 91%, 86.32%, 74.9%, 65.45% by photo-fenton and 51.28%, 53.61%, 64.11%, 50.76%, 31.28% by ultrasonic-fenton was found for 10, 25, 30, 40, 50 mg/L concentrations. Eventually, 25 mg/L ampicillin for UV/Fe²⁺/H₂O₂ and 30 mg/L ampicillin for US/Fe²⁺/H₂O₂ were optimized.

The influence of reaction time was analyzed for 60 minutes period of time at the last step of oxidation and analysis was conducted for 10 minutes that is given in Figure 5.

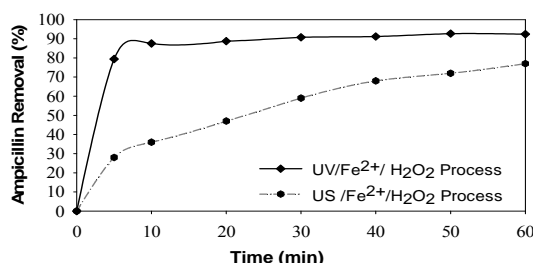


Figure 5. Effect of reaction time

According to the results, the removal of ampicillin at first 5 minutes was determined as 79.43% by photo-fenton and as 28.44% by ultrasonic-fenton. After

10 minutes the reduction was risen as 87.57% by photo-fenton and after 40 minutes as 68.90% by ultrasonic-fenton. 92.42% for UV/Fe²⁺/H₂O₂ and 77% for US/Fe²⁺/H₂O₂ were assayed as the maximum values at 60th minutes.

4. CONCLUSIONS

In conclusion, the optimum conditions of antibiotic ampicillin were found as pH 3, 20 mM H₂O₂, 1.5 mM Fe (2+), 25 mg/L of antibiotic concentration, 10 minutes reaction time by photo-fenton process and pH 4, 30 mM H₂O₂, 2 mM Fe (2+), 30 mg/L of antibiotic concentration, 60 minutes reaction time by ultrasonic-fenton process. Under these conditions, the removal of ampicillin and the molar ratio of Fe²⁺/H₂O₂ were determined as 87.57% and 1/13 by UV/Fe²⁺/H₂O₂ and as 77% and 1/15 by US/Fe²⁺/H₂O₂. As a result of this study, it has been observed that UV-supported fenton oxidation method was more effective than US-supported fenton oxidation. Mineralization was increased by raising the production of OH[•] radicals because of the fact that the complexes of Fe (III) to the reduction of Fe (II) under UV irradiation. Also, it has been thought that ultrasonic sound waves used in fenton oxidation is required a long reaction time to produce sufficient hydroxyl radicals.

REFERENCES

- Fatta-Kasinos, D., Bester, K., Kümmerer, K., 2010. Xenobiotics in the urban water cycle : mass flows, environmental processes, mitigation and treatment strategies. Environmental Pollution. Vol, 16. Springer.
- Kümmerer, K., 2001. Drugs in Environment: Emission of drugs, diagnostic aids and disinfectants into wastewater by hospitals in relation to other sources-a review. Chemosphere. 45:957-969.
- Saygı, Ş., Battal, D., Şahin, N., 2012. Çevre ve insan sağlığı yönünden ilaç atıklarının önemi-a review, Marmara Pharmaceutical Journal 16: 82-90.

ADSORPTION OF METHYLENE BLUE ONTO ACTIVATED CARBON PRODUCED BY MICROWAVE ASSISTED CHEMICAL ACTIVATION OF FILTER COFFEE WASTE

Gamzenur ÖZSİN^{*1}, Ersan PÜTÜN², Murat KILIÇ¹, Ayşe Eren PÜTÜN¹

¹Chemical Engineering Department, Anadolu University, TURKEY

²Materials Science and Engineering Department, Anadolu University, TURKEY

a. Corresponding author: (aeputun@anadolu.edu.tr)

ABSTRACT: Discharging of dyes to wastewaters in high concentration causes serious environmental and health problems because they are chemically stable and decompose difficultly. Therefore, several methods developed for the removal of dyestuffs from aqueous medium but feasible applications of most of the methods are limited. Adsorption process with efficient adsorbents is one of the most suitable methods because of low cost, simplicity of design, ease of operation, insensitivity to toxic pollutants and smaller amounts of harmful substances. In adsorption, activated carbon is one of the most preferred sorbent because of its unique porous structure. The present work was undertaken to investigate the potential of filter coffee waste as a precursor for preparation of activated carbon by microwave induced K_2CO_3 activation and to evaluate the produced activated carbon for methylene blue removal from the aqueous solutions.

1. INTRODUCTION

The discharge of synthetic dyes from several industries such as textile, leather, paper, and plastics into the environment has severe problems. Dyes in wastewaters decrease the sunlight penetration and so, hinder photosynthetic processes considerably. Besides, dyes by reducing oxygen levels in water lead to suffocation of aquatic flora and fauna [Ghaedi *et al.*, 2012]. The persisting color and the non-biodegradable nature of the spent dye baths therefore remain an aesthetic concern among the environmentalists for years [Foo and Hameed, 2011].

Methylene blue (MB) is one of the most commonly used organic substance for dyeing cotton, wood, and silk. Though MB is not strongly hazardous, it can also cause some harmful effects like other dyestuffs [Theydan and Ahmed, 2012].

Many physical, chemical and biological methods have been developed and applied for the removal of dyestuffs from

aqueous medium such as adsorption, biosorption, coagulation/flocculation, advanced oxidation, ozonation, membrane filtration and liquid-liquid extraction. But application of most of these methods is limited due to the feasibility point of view.

Adsorption process with efficient adsorbents is one of the most suitable methods due to low cost, simplicity of design, ease of operation, insensitivity to toxic pollutants and smaller amounts of harmful substances [Li *et al.*, 2013]. Activated carbons (ACs) are the most popular carbonaceous adsorbent materials with very high surface area which have been used in wastewater treatment process for removal of dyes. But ACs are highly cost effective and therefore production costs of ACs are required to be decreased by using both cheap raw materials and diminishing the energy requirements.

Producing AC by chemical activation method is extensively used because of some advantages as higher yields and well-developed porous structures. But long impregnation periods of precursor with chemical agent increase production costs of chemically AC from both practical and economical point of view. That's why, microwave induced chemical activation process has paid attention in recent years. In microwave field, the raw materials receive energy at a molecular level through dipole rotation and ionic conduction, and the energy is dissipated in the form of heat. Thus, microwave heating provides the advantages of uniform temperature distribution, rapid temperature rise and saving of energy [Liu *et al.*, 2010].

The main objective of this study was to evaluate the possibility of using filter coffee waste to develop a activated carbon by microwave assisted chemical activation and study its application to remove methylene blue from aqueous solutions. Filter coffee waste is selected as a starting material to produce AC since coffee is one of the popular beverages of the world and second largest traded commodity which cultivated in about 80 countries across the globe [Murthy and Naidu, 2012] After batch adsorption studies, equilibrium isotherms, kinetics and thermodynamic studies were also investigated to evaluate experimental data in this scope.

2. EXPERIMENTAL

2.1. Preperation and Characterization of Activated Carbon

Filter coffee wastes were obtained from a franchise store of Kahve Dünyası in Eskişehir. Wastes were washed with distilled water to eliminate the impurities and water solubles and dried at room temperature for 3 days prior to AC production.

The dried filter coffee wastes were impregnated with a weighted amount of K_2CO_3 and mixed with deionized water to form slurries. Then the impregnated samples were microwave treated for 6 min using 900 W microwave power. The pre-carbonized samples were then carbonized and activated in a stainless steel fixed bed Heinze reactor. Nitrogen with a flow rate of $100\text{ m}^3/\text{min}$ was continuously supplied to maintain the inert atmosphere of reactor and temperature was raised from room temperature to $700\text{ }^\circ\text{C}$ with a heating rate of $10\text{ }^\circ\text{C}/\text{min}$ and held there for 1 h.

After cooling the reactor, resulting activated carbons were then washed by hot distilled water and dried overnight at $105\text{ }^\circ\text{C}$. The dried products were then kept in tightly closed bottles for subsequent characterization and adsorption experiments.

N_2 adsorption isotherms of produces were measured using a surface area analyzer (Quantachrome-Autosorb) at 77 K. Prior to each measurement, samples were outgassed at $200\text{ }^\circ\text{C}$ for approximately 6 h to remove any moisture or volatiles within the existing pores of the material. The specific surface area of the samples were then determined from the adsorption isotherm using the multipoint BET (Brunauer, Emmett, and Teller) theory.

SEM analysis was used to visualize sample morphology before and after activation. Therefore, secondary electron images were obtained by a scanning electron microscope (Carl Zeiss EVO 50) for the sake of comparing the differences of raw material and the resultant activated carbon. Before imaging, samples were coated with a thin layer of Au-Pd under a vacuum.

2.2. Batch Adsorption Studies

The cationic dye, MB or Basic Blue, was used as an adsorbate in batch adsorption studies (Figure 1). A stock solution of 1.0 g/L was prepared by dissolving the appropriate amount of MB with deionized water. Batch adsorption studies were then performed in a set of 250 mL flasks containing MB solutions with various initial concentrations (300–700 mg/L). The amount of 3 g/L AC was added to each flask and kept at temperatures of 30, 40 and 50 °C on a shaker. Samples were taken at preset time intervals, centrifuged and the residual concentrations of methylene blue in the filtrate were found by detecting the absorbance by a double-beam UV–visible spectrophotometer.

The concentrations of MB solutions were determined by comparing absorbance to a calibration curve previously obtained. All experiments were duplicated and only the mean values were reported

The adsorbed MB per unit mass of AC, q_t (mg/g), and % removal of MB were calculated according to:

$$q_t = \frac{(C_i - C_t)}{W} \quad (1)$$

$$\text{Adsorption}(\%) = \frac{(C_i - C_e)}{C_i} \quad (2)$$

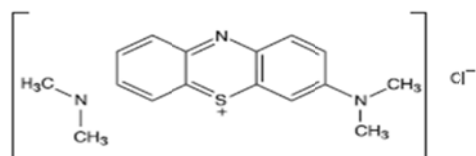


Figure 1: Chemical structure of methylene blue

Four reputable isotherm equations, namely the Langmuir, Freundlich, D-R and Temkin together with four kinetic models as pseudo-first order, pseudo-

second order, intraparticle diffusion and Elovich were applied to fit the experimental isotherm data of MB adsorption on AC. Besides, a thermodynamic analysis was carried out to clarify the temperature dependency of the adsorption process.

3. RESULTS & DISCUSSION

From the experimental results it is observed that the amounts of MB adsorbed onto the AC was increased rapidly at the early stages of adsorption (Figure 2). With prolonging the contact time they continued to increase but process slowed down with time and finally reached a plateau when the equilibrium was established between MB molecules and surface of the AC.

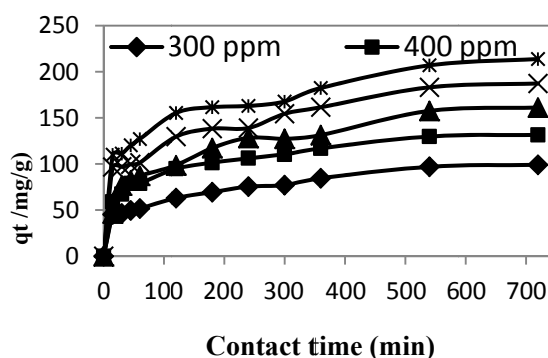


Figure 2: Effects of contact time and initial MB concentration on MB uptake

Increasing initial MB concentration caused increase in the driving force for the mass transfer, amount of methylene blue are adsorbed is increased. Experiments conducted with 700 mg/l MB solutions resulted with the highest uptake as 213,9 mg/g. When the temperature effect on MB adsorption was examined in a temperature range between 30 and 50 °C, it is observed that temperature has a slight increasing effect on adsorption of methylene blue.

According to Figure 2, adsorbent and MB system reached equilibrium for 3 h. Kinetic studies are important to understand the dynamic of the reaction in terms of order of the rate constant. Applying the pseudo-first order, pseudo-second order, intraparticle diffusion and Elovich kinetic models to adsorption data and comparing the correlation coefficients (R^2) values showed that the adsorption process follows the pseudo-second order model since the model yielded the best fit with the highest R^2 values (Figure 3). The R^2 for all initial MB concentrations were greater than 0.970 which indicates the suitability of the model. The rate constant of pseudo-second order adsorption, k_2 , values were found as 0.00106, 0.00061, 0.00047, 0.00052 and 0.00040 g/mg.min for 300, 400, 500, 600 and 700 mg /L initial MB concentrations, respectively.

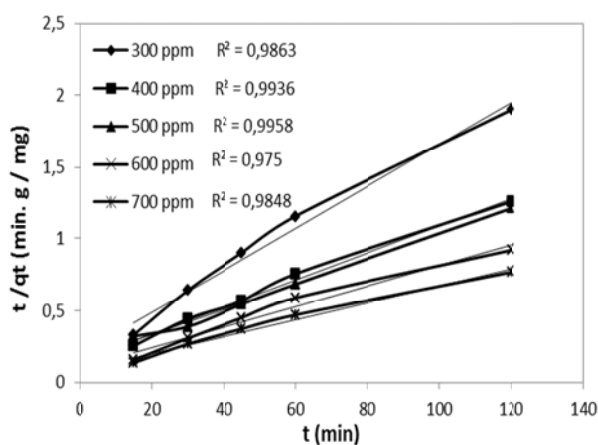


Figure 3: Plots of Pseudo-second order kinetic model

Adsorption isotherms are important for the description of how adsorbate will interact with an adsorbent and are critical in optimizing the use of adsorbent. Thus, the correlation of experimental equilibrium data using either a theoretical or empirical equation is essential for adsorption data interpretation and prediction [Ahmed and Dhedan, 2012]. According to the equilibrium models

applied to adsorption data, best fitting was obtained with Langmuir isotherm. This model assumes that adsorption takes place on a homogenous adsorbent surface of identical sites that are equally available and energetically equivalent with each site carry equal numbers of molecules and no interaction between adsorbate molecules.

To evaluate and make certain about the effect of temperature on adsorption process of MB onto AC, the thermodynamic parameters such as Gibbs free energy (ΔG^0), enthalpy (ΔH^0) and entropy (ΔS^0) are calculated and given in Table 1. The negative value of ΔG^0 shows the feasibility and the spontaneous nature of the adsorption. The positive value of ΔH^0 indicates that the adsorption is endothermic. On the other hand, the positive value of ΔS^0 demonstrates the increased randomness at the solid-solute interface and the affinity of the AC for the MB. In thermodynamic analysis, R^2 obtained from the fitting was found as 0.991 which is good enough to describe the temperature dependency of the system.

Table 1: Thermodynamic parameters for MB adsorbed onto AC.

T (°C)	ΔG^0 (kJ/mol)	ΔH^0 (kJ/mol)	ΔS^0 (j/mol K)
30	-23.170	3.689	198.338
40	-25.337		
50	-27.129		

REFERENCES

- Ahmed, M. J., Dhedan, S. K., 2012, Equilibrium isotherms and kinetics modeling of methylene blue adsorption on agricultural wastes-based activated carbons, Fluid Phase Equilibria, Volume 317, 9.
- Foo, K.Y., Hameed, B.H., 2011, Microwave assisted preparation of activated carbon from pomelo skin for the removal of anionic and cationic dyes, Chemical Engineering Journal, Volume 173, 385.

- Ghaedi, M., Heidarpour, S., Kokhdan, S. N., Sahraie, R., Daneshfar, A., Brazesh, B., 2012, Comparison of silver and palladium nanoparticles loaded on activated carbon for efficient removal of Methylene blue: Kinetic and isotherm study of removal process, *Powder Technology*, Volume 228, 18.
- Li, Y., Du, Q., Liu, T., Peng, X., Wang, J., Sun, J., Wang, Y., Wu, S., Wang, Z., Xia, Y., Xia, L., 2013, Comparative study of methylene blue dye adsorption onto activated carbon, graphene oxide, and carbon nanotubes, *Chemical Engineering Research and Design*, Volume 91, 361.
- Liu, Q. S., Zheng, T., Wang, P., Guo, L. 2010, Preparation and characterization of activated carbon from bamboo by microwave-induced phosphoric acid activation, *Industrial Crops and Products* Volume 31, 233.
- Murthy, P. S., Naidu, M. M., 2012, Sustainable management of coffee industry by-products and value addition—A review, *Resources, Conservation and Recycling*, Volume 66, 45.
- Theydan, S.K., Ahmed, M.J., 2012, Adsorption of methylene blue onto biomass-based activated carbon by FeCl_3 activation: Equilibrium, kinetics, and thermodynamic studies, *Journal of Analytical and Applied Pyrolysis*, Volume 97, 116.

ADAPTING NANOPOROUS SILICA MATERIALS FOR MOLECULAR FILTRATION AND THERMAL INSULATION

Ebenezer Twumasi^{1,a}, Christer Sjöström^{1,2}, Dr. Peter Norberg^{2,3}

1. KTH/Royal Institute of Technology, Building Science, Stockholm, Sweden

2. Svenska Aerogel AB, Gävle, Sweden

3. University of Gävle, Gävle, Sweden

a. Corresponding author (twumasi@kth.se)

ABSTRACT: This article presents investigations on the physical and adsorption properties of a new class of nanoporous materials for use as molecular filter media. The set out aim was to tailor the adsorption performance, through modification of the nanoporosity and via incorporation of trapping chemicals or co-adsorbents. An additional aim was to contribute a better understanding of filtration performance in relation to the physical and adsorption properties that are essential for the selection of nanoporous materials (as better adsorbents) to meet the needs of commercial filter media application. Secondly is presented R&D to explore and develop the new class of nanoporous materials with regard to its physical and porosity properties that are essential for the applicability as a thermal insulation material. The paper concludes by a brief address on some of the technology and commercial areas presently being focused, and the technology challenges emanating.

1. INTRODUCTION

The emergent mechanization and industrialization of society has resulted in most people spending by far more than 90 per cent of their lives indoors [Consumer product safety commission 1994; Leech et al. 2002]. Much of our time spent indoors is either at work or home and the rest being in the leisure centres, shopping centres and even a small amount inside vehicles. To ensure occupant's health and comfort in the built environment, the indoor air quality and thermal comfort must be at acceptable targets. The effect of chemical pollutants on the perceived indoor air quality and its health effects on the occupants as well as irreversible damage to vulnerable artefacts have been investigated in numerous studies. [Consumer product safety commission 1994]. The abatement of indoor air contaminants at low ppm level could be achieved by adsorption onto a solid porous material [John et al. 2000]. Molecular filtration is the term used to describe

filtration of chemical air pollutants having sizes at the molecular scale. This filter generally contains porous adsorbents and therefore its performance depends on the quality of adsorbent. Today activated carbons are the most prevalent alternative materials due to their high internal surface area and greater affinity for VOC's [Schweitzer 1979; Wang et al. 2005]. Despite these properties, its application is limited by flammability hazard and the tendency of pore clogging [Zhao et al. 1998]. Ordered mesoporous silicas have been synthesized using surfactant as templates. These mesoporous silicas exhibits high surface area and narrow pore size distribution in the meso range. These properties have led to their study for applications in fields such as molecular sieving, catalysis, selective adsorption of pollutant gases and so on [Zheng et al. 2007]. However, industrial applications of the mesoporous materials have been inhibited by surfactants toxicity and high cost [Lu 2004], low hydrothermal stability such as

in boiling water and mechanical stability during the attempt to pelletize with compression [Ryoo et al. 1996; Bonneviot et al.1998].These drawbacks provoke a doubt about its durability in practical application.

Human health in the indoor environment is not only affected by airborne pollutants, but also by conditions of thermal comfort. Creating thermal comfort for people is a prime purpose for heating and air conditioning indoor environment. Heating indoor space is an energy driven process and many studies have shown that a major portion of supplied space heating energy is lost through poorly insulated building fabric [IEA/ECBCS Annex 39 2005]. Increasing evidence of the inadequate nature of our major energy resources and large cost associated with environmental concerns, mandate utilization of advanced thermal insulation. One such insulation is vacuum insulation panels (VIP) [Wang et al. 2005; Zhao et al. 1998] which are made of an evacuated open porous material such as aerogel, fumed or precipitated silica and also glass fibres, placed inside a multilayer envelope and makes use of vacuum to suppress the gaseous heat transfer to zero. It has been shown that, VIPs made with nanoporous core material have superior performance over those made of microporous materials [Wang et al. 2005; Zhao et al. 1998]. However, the high cost of nanoporous materials is one of the major reasons behind the high cost of VIPs and its limited utilization in building industry. In order to overcome this cost barrier for the mass application of VIPs in the building industry, alternative low-cost nanoporous core material needs to be developed. The nanoporous material must achieve not only the thermal performance which provides value to the customer but also can be obtained by a simplified

production route that is cost effective and environmental friendly. Herein we focus on physical and chemisorption properties of new bimodal nanoporous silica modified with either impregnate chemical or co-adsorbent and employed as molecular filter. Further the thermal insulation of newly developed low density mesoporous silica is highlighted.

2. EXPERIMENTAL

The materials used in this study were synthesised according to method described elsewhere [Afriyie et al. 2013; Twumasi et al. 2012].

2.1 Materials Characterization

Textural properties of the materials were studied by nitrogen adsorption at 77 K using a Micromeritics TriStar 3. The materials were degassed under nitrogen condition for 3 hours at 250°C before measurement. The specific surface area and pore size were evaluated by Brunauer-Emmet-Teller (BET) and density functional theory (DFT) methods, respectively.

Dynamic adsorption: A setup similar to the ASHRAE 145.1 but with four parallel columns was used to test the adsorption capacities of the chemisorbents and composites. A detail description of the procedure has been provided in [Afriyie et al. 2013]. The adsorbents prepared or obtained were used without degassing to reflect a real life scenario.

The Thermal conductivity: of the mesoporous silica powders was measured with Transient Plane Source (TPS2500)

3. RESULTS AND DISCUSSION

3.1 Pore Properties of Modified MgCa-Silica

A nanoporous MgCa-silica recently developed by our group [Afriyie et al.

2013] has been modified with either potassium permanganate (KMnO₄) or coconut activated carbon (CAC). Physicochemical parameters of the starting substrate and the resultant modified materials are summarized in Table 1. Their sorption isotherms and the NLDFT pore-size distributions are shown in Figure 1. Overall, the composites and chemisorbent materials obtained exhibit a completely reversible type II isotherm similar to the parent MgCa-silica structure. Moreover, it follows that composite materials displays higher nitrogen uptake especially in lower relative pressure range 0.003-0.3 typical of microporous material. The results further (Table 1) shows that the composite materials show increase in specific surface area and total pore volume and the increase was relative to carbon content. On the contrary, chemisorbents display a decrease in nitrogen uptake as well as specific surface area and total pore volume. The decrease deepens as the amount of potassium permanganate increases.

As in parent MgCa-silica, similar pore distributions in the range of (1-32 nm) were observed for the composites as well as for chemisorbent materials. However with the chemisorbents, a decrease in pore volume in these pores was displayed. Nevertheless a micropore centred at 1.4 nm and mesopore at 5.4 nm as in parent MgCa-silica were observed. From these results, it will be reasonable to speculate that the pore entrances of chemisorbents were neither blocked nor shifted by the amount of KMnO₄ used in this work but rather disperse uniformly on the pore walls surfaces thereby reducing the surface area and pore volume available. In contrast to chemisorbents, composite materials exhibit an increase in pore volume in the pore diameter which ranges from 1-32 nm.

Upon increasing the carbon content to 45 wt% a micropore centred at 1.14 nm was introduced which was unique when compared to micropore diameter of parent CAC (1.22 nm) and MgCa-silica (1.4 nm).

3.2 Carbon-silica Composite for Dynamic Adsorption of Toluene

An air stream (50% RH at 23°C) containing ~ 80 ppm toluene was forced through the bed of carbon-silica composites PSC, with carbon content 32 wt% and 45 wt% as well as commercial sorbent carbon-alumina composite (Al-C). The toluene removal efficiency [%] as opposed to adsorbed

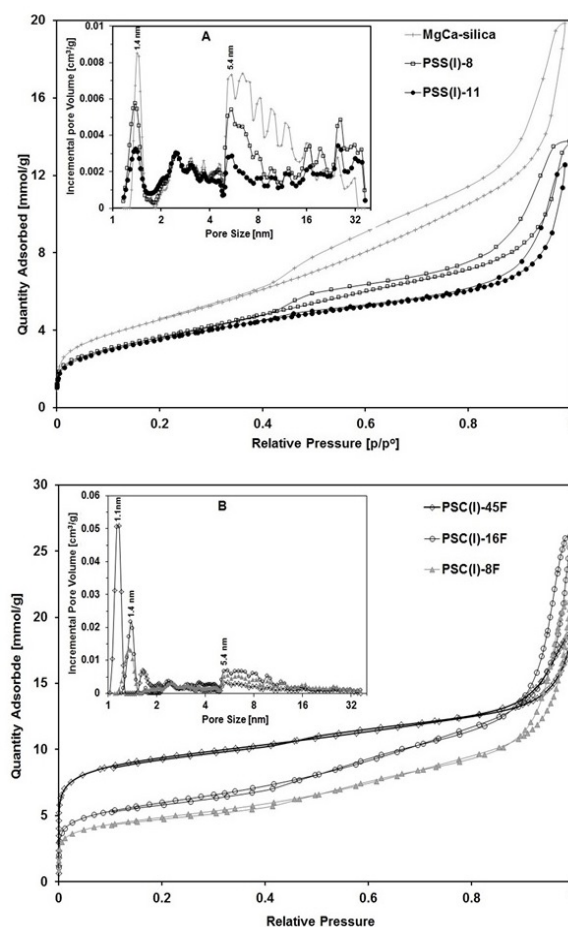


Figure 1: N₂ sorption isotherms of (A) MgCa-silica and its chemisorbents and

(B) carbon-silica composites with different carbon wt%. Their corresponding pore-size distribution are inserted.

Amount in wt% (grams toluene/grams sorbents) is shown in Figure 2. The uptake capacity of the carbon-silica composites shows a dependent on the amount of carbon. The composite PSC(I)-45F with 45 wt% carbon exhibits a better uptake performance over that of composites with 32 wt% carbon. From our previous studies the maximum uptake by MgCa-silica was 0.08 wt % at 0% efficiency. It is therefore obvious that the uptake by the composites were mainly contributed by the carbon composition. With this in mind, uptake capacity based solely on carbon content of the composite sorbent was estimated.

Comparison of adsorbed amount [wt%] of toluene at 0% efficiency based on the grams of carbon content point to uptake capacity of 28 wt% for PSC(I)-45F and 26 wt% for PSC(I)-32F after 22h. Interestingly, these capacity values of

Table 1: Pore parameters of chemisorbents and carbon-silica composites

Samples	S_{BET} (m^2/g)	S_{mic} (m^2/g)	V_{tot} (cm^3/g)	V_{mic} (cm^3/g)
MgCa-Sil	372	44.5	0.63	0.014
PSS(I)-8	320	10.3	0.49	0.003
PSS(I)-11	284	9.2	0.47	0.003
PSC(I)-8F	388	137	0.65	0.040
PSC(I)-16F	431	150	0.74	0.065
PSC(I)-32F	596	357	0.68	0.153
PSC(I)-45F	769	480	0.65	0.198

SBET - BET specific surface area, Vtot – total pore volume, Smic-micropore surface area and Vmic – micropores volume obtained from t-plot

carbon-silica composites are competitive when compared with results obtained for commercial coconut activated carbon (31.1 wt %) and significantly better than the alumina-carbon composite, (9.5 wt %).

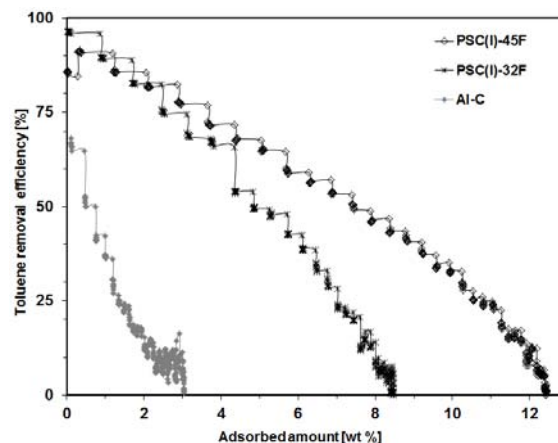


Figure 2: Comparative performance of carbon-silica composites with 32 or 45 wt% carbon vs. commercial alumina-carbon composite (Al-C).

3.3. Desulphurisation by chemisorbents

The MgCa-silica chemisorbents [PSS (I)-8 and PSS (I)-11] containing $KMnO_4$ were challenged with ~12 ppm. It is clearly seen that the uptake capacity was dependent on $KMnO_4$ content in the chemisorbent. As shown in Figure 3, when $KMnO_4$ wt% increased from ~8 to ~11 wt%, the PSS(I)-11 exhibits superior H_2S uptake performance over PSS(I)-8. The uptake capacities of PSS(I)-8 and PSS(I)-11 were 0.1 wt% and 3.2 wt% at 50% efficiency respectively.

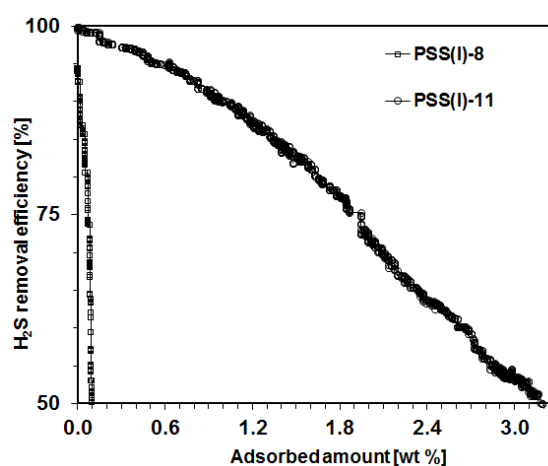
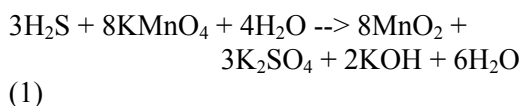


Figure 3: Comparative performance of chemisorbents with 8 wt% versus 11 wt% $KMnO_4$.



Theoretically when the uptake capacity of PSS(I)-8 (8.4 wt% KMnO_4) is calculated from the stoichiometric reaction (1) then 4.83 wt% uptake capacity is obtained. If the uptake of H_2S has followed a stoichiometric reaction directly related to the KMnO_4 amount, then we could have expected PSS(I)-8 to exhibit an uptake similar to that of the theoretical uptake and PSS(I)-11 value larger than obtained. This suggests that even though high levels of KMnO_4 may be present in the chemisorbent, it may not be available for reaction due to restrictions imposed by the method of preparation. From these observations we proposed that in the case where 8 wt% KMnO_4 is impregnated in PSS(I)-8, most ended up in pore walls with few on the internal pore surfaces available for reaction. As KMnO_4 increased to 11 wt% then the amount available on the pore wall surface for H_2S reaction is increased, hence the high uptake capacity in PSS(I)-11. Increasing KMnO_4 content above 11 wt%, however, was detrimental to the H_2S removal performance.

3.4 Effect of Pore Properties on Dynamic Adsorption

Results of the uptake capacities show a direct correlation between the composites toluene uptake capacities and their specific surface area and micropore volume. However no connection was observed in the case of chemisorbent uptake capacities and their pore properties. Even though no direct correlation was observed in this work, the cooperative effect of broad pore distribution and abundance of pores in the mesopore region for dynamic adsorption could not be ignored. This bimodal pore system is vital for effective molecular filtration as micropores are essential for

the trapping of molecules of diameter less than 1 nm [Hernandez et al. 2005] and at the same time have mesopore diameters large enough to allow for bulk diffusion and sufficiently energetic molecular collisions between the contaminant gas and the modified chemical or co-adsorbent to achieve meaningful reactivity. Furthermore, the mesopore volumes function as a storage place for the reaction products e.g. from oxidation of H_2S .

3.5 Thermal Conductivity of Mesopore Silica

Our on-going research focuses on the development of low density nanoporous material for thermal insulation application. A simple synthesis route has been developed to design low density mesoporous silica materials. So far, large surface area mesopore silica with density 70 kg/m^3 and porosity of $\sim 97\%$ have been achieved. Thermal conductivity values of 0.028 to $0.030 \text{ W (m. K)}^{-1}$ measured by transient plane sensor have been so far achieved. Significant steps in the control of the pore parameters and the particle morphology in relation to tapped density, as well as thermal conductivity has been taken.

4. CONCLUSIONS

Surface modification of MgCa-silica to chemisorbent and composites has successfully been achieved by the use of potassium permanganate and coconut activated carbon. The chemisorbents and composites obtained were effectively employed for dynamic adsorption of H_2S and toluene. Low density mesoporous silica material for thermal insulation has also been presented.

Acknowledgements: Svenska Aerogel AB is acknowledged for providing materials and contribution to synthesis technologies.

REFERENCES

- Afriyie E. T., Norberg P., Sjöström C. Forslund M., 2013. Preparation and Characterization of Double Metal-Silica Sorbent for Gas Filtration, *Adsorption* 19, 46-61.
- Bonneviot L., Beland F., Danumah C., Giasson S., Kaliaguine S., 1998. Mesoporous Molecular Sieves 1998: proceedings of the first international symposium: Studies in surface science and catalysis: 117, p.143-154.
- Consumer Product Safety Commission, American Medical Association, 1994. Environmental Protection Agency and the American Lung Association, Indoor Air Pollution. An Introduction for Health Professionals, CPSC Document #455, p.1
- Hernandez M. A., Corona L., Gonzales A.I., Rojas F., V. H. Lara, Silva F., 2005. Quantitative study of the adsorption of aromatic hydrocarbons (benzene, toluene, and *p*-Xylene) on dealuminated clinoptilolites, *Ind. Eng. Chem. Res.* 44, 2908-2916.
- IEA/ECBCS Annex 39, 2005. VIP-Study on VIP-components and panels for service life prediction of VIP in building applications, and vacuum insulation in the building sector-systems and applications, Subtask A/B reports /www.vip-bau.chS;
- John M. D., John F. S., Jonathan M. 2000. Indoor Air Quality Handbook, McGraw-Hill, New York, 271.
- Marsh H., 2001. Activated Carbon Compendium, A collection of papers from the journal Carbon 1996-2000, Elsevier Science Ltd.
- Schweitzer P.A., 1979. Handbook of separation techniques for chemical engineers, James Peter Associates Inc., McGraw-Hill, New York, 238.
- Twumasi E. Forslund M., Norberg P., Sjöström C., 2012. Carbon-Silica Composites Prepared by the Precipitation Method. Effect of the Synthesis Parameters on Textural Characteristics and Toluene Dynamic Adsorption, *J. Porous Mater.* 19, 333-343
- Wang C.M., Chung T.W, Huang C. M, Wu H., 2005. Adsorption Equilibria of Acetate Compounds on Activated Carbon, Silica Gel, and 13X Zeolite, *J. Chem. Eng. Data*, 50, 811
- Zhao X. S., Ma Q., Lu G. Q., 1998. VOC Removal: Comparison of MCM-41 with Hydrophobic Zeolites and Activated Carbon, *Energy & Fuels*, 12, 1051-1054

OPTIMIZATION OF PROCESS PARAMETERS FOR ARSENIC REMOVAL BY IRON CONTAINING ADSORBENTS USING BOX-BEHNKEN DESIGN

Aslı Özge Avcı Tuna^{1,a}, Esra Bilgin Simsek² and Ulker Beker³

1. Yildiz Technical University, Chemical Engineering Department, Istanbul, Turkey
 2. Yalova University, Chemical and Process Engineering Department, Yalova, Turkey
 3. Yildiz Technical University, Chemical Engineering Department, Istanbul, Turkey
- a. Aslı Özge Avcı tuna (asliozge85@gmail.com)*

ABSTRACT: In this study, arsenate removal by activated carbon based-iron containing adsorbents was carried out. Adsorption processes have been frequently applied to statistical analysis for maximization of removal efficiency and optimization all of the operating conditions, such as solution pH, initial concentration and temperature. A three-level, three-factor Box-Behnken Experimental Design was employed to find the optimum combination of process parameters for maximizing As(V) adsorption capacity of activated carbon-based iron containing adsorbents. The iron containing hybrid adsorbents were prepared by precipitation of iron oxide salts on activated carbon. The results showed that the adsorption capacities were ranged between 0.100 and 6.121 mg g⁻¹. The statistical significance of variables was determined using the analysis of variance (ANOVA). The validity of the constructed model was evaluated by lack of fit, coefficient of determination (R²), adjusted coefficient of determination (adjusted R²) and F-values. The high values of F indicate that the model can be explained by the regression equation.

1. INTRODUCTION

In recent years, chemometric tools have been applied to the optimization of analytical methods, considering their advantages such as a reduction in the number of experiments that need be executed resulting considerably less empirical work. These methods allow the development of mathematical models that permit assessment of the relevance as well as statistical significance of the factor effects being studied as well as evaluate the interaction effects between the factors. Response Surface Methodology is one of the approaches to evaluate the effective factors and select optimum conditions in limited number of experiment. Adsorption processes have been frequently applied to this statistical analysis for maximization of removal efficiency and optimization all of the operating conditions, such as solution pH, initial concentration and temperature.

The aims of present study were (i) synthesis of iron containing hybrid adsorbents based on activated carbon, (ii) characterization of the adsorbents, and (iii) investigation the effects of process parameters such as pH of the solution, temperature and initial adsorbate concentration on the adsorption of As(V) onto hybrid adsorbents using Box-Behnken methodology by STATISTICA version 8.0 (Statsoft, Tulsa).

2. EXPERIMENTAL

2.1. Materials

All the chemicals/reagents used in the study were of analytical grade and used without further purification.

2.2 Synthesis of Iron Containing Adsorbents

The iron containing hybrid adsorbents were prepared by precipitation of iron

oxide salts on activated carbon. Two series of adsorbents were synthesized by solutions containing FeCl₂ or FeCl₃, and were designated as AC-F2 and AC-F3, respectively.

2.3. Characterization of Adsorbents

The Fourier transform infrared (FTIR) spectra of adsorbents were recorded on a FTIR spectrometer (Perkin Elmer Spectrum One FT-IR Spectrometer) using attenuated total reflectance (ATR) method. Investigations of morphology and microstructure of the adsorbents were performed by a transmission electron microscopy (TEM) (FEI Tecnai G2 F20 X-Twin) at 200 kV accelerating voltage.

2.4. Adsorption of As(V) on AC-F2 and AC-F3

Adsorption studies were investigated by using batch equilibration techniques. Adsorption experiments were conducted to evaluate the effects of the independent variables on As(V) removal. For the adsorption process, three important operation parameters such as initial pH of solution (3.0-7.0), temperature (25-65°C), and initial As(V) concentration (0.5-8.5 mg L⁻¹) were selected as the independent variables (factors) while As(V) adsorption capacity of the hybrid adsorbents was the dependent variable (response).

The As(V) concentration in the aqueous solution was determined by atomic absorption spectrophotometer (Analytik Jena ContrAA 700 TR). The adsorption capacities of the adsorbents were calculated according to the mass balance on As (V) ions expressed as:

$$q_e = \frac{(C_0 - C_e) \cdot V}{M}$$

Here, q_e is the amount of As (V) adsorbed onto unit mass of the adsorbents (mg g⁻¹); C_0 and C_e are the initial and final

concentrations (mg L⁻¹) of As (V) ion in the aqueous solution, respectively; V is the volume of the aqueous phase (L) and m is the weight of adsorbent (g).

3. RESULTS AND DISCUSSIONS

3.1 Characterization of Adsorbents

FTIR analysis of AC-F2 indicated that the bands were assigned to ferroxide (δ-FeO(OH)), magnetite (Fe₃O₄), maghemite (γ-Fe₂O₃) and hematite (α-Fe₂O₃) forms while iron oxyhydroxide (FeO(OH)) forms were existed in the spectrum of AC-F3.

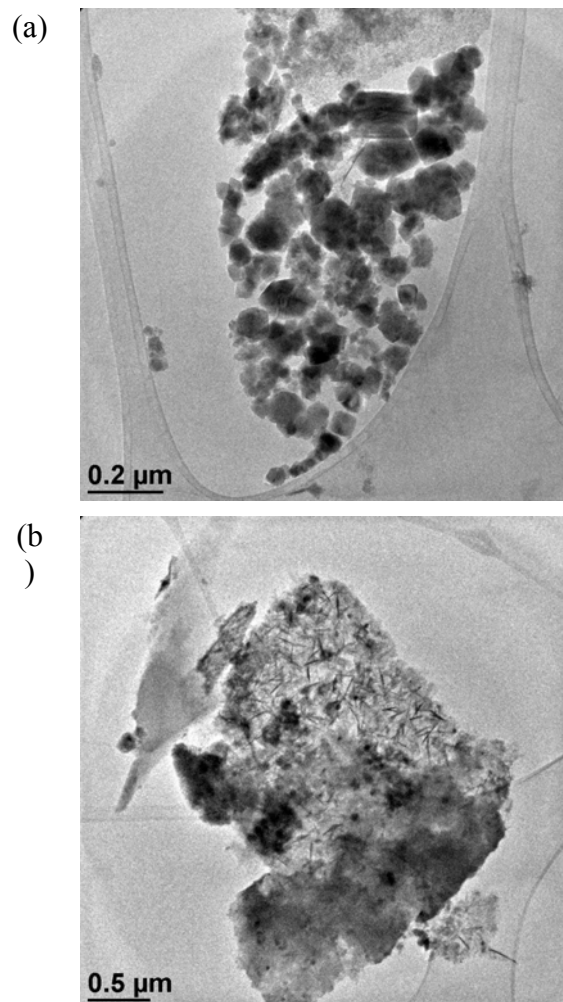


Figure 1: TEM images of (a) AC-F2 and (b) AC-F3

TEM images revealed that the formation of large hexagonal crystals indicate

feroxyhyte formed on the AC-F2 surface (Figure 1a). On the other hand, goethite is formed on AC-F3 surface since the shape of crystals are usually acicular and elongated along the crystallographic α direction [Cornell and Schwertmann, 2003].

3.2. As(V) Adsorption

The results showed that the adsorption capacities were ranged between 0.127 and 6.121 mg g⁻¹ for AC-F2, while the capacities of AC-F3 were found between 0.100 and 5.461 mg g⁻¹ for AC-F3. When the whole 17 runs examined together that AC-F3 has a greater As(V) adsorption capacity than AC-F2.

The statistical significance of variables was determined using the analysis of variance (ANOVA). The validity of the constructed model was evaluated by lack of fit, coefficient of determination (R²), adjusted coefficient of determination (adjusted R²) and F-values. The high values of F indicate that the model can be explained by the regression equation for both adsorbents.

The normal probability plot of the residuals is one of the most important diagnostic tools to determine the systematic departures from the assumption that errors have a normal distribution [Yetilmezsoy *et al.*, 2009]. The statistical significance of variables was evaluated using Student's t-test and data was presented in Figure 2. Analysis revealed that compared with other factors linear of pH and linear of concentration imposed the greatest effect on the sorption capacity of AC-F2 and AC-F3 in the studied range, respectively. The positive coefficients for the model indicate a synergistic or favorable effect on the As(V) adsorption capacity, although the negative coefficients denote an antagonistic or unfavorable effect on the adsorption of As(V).

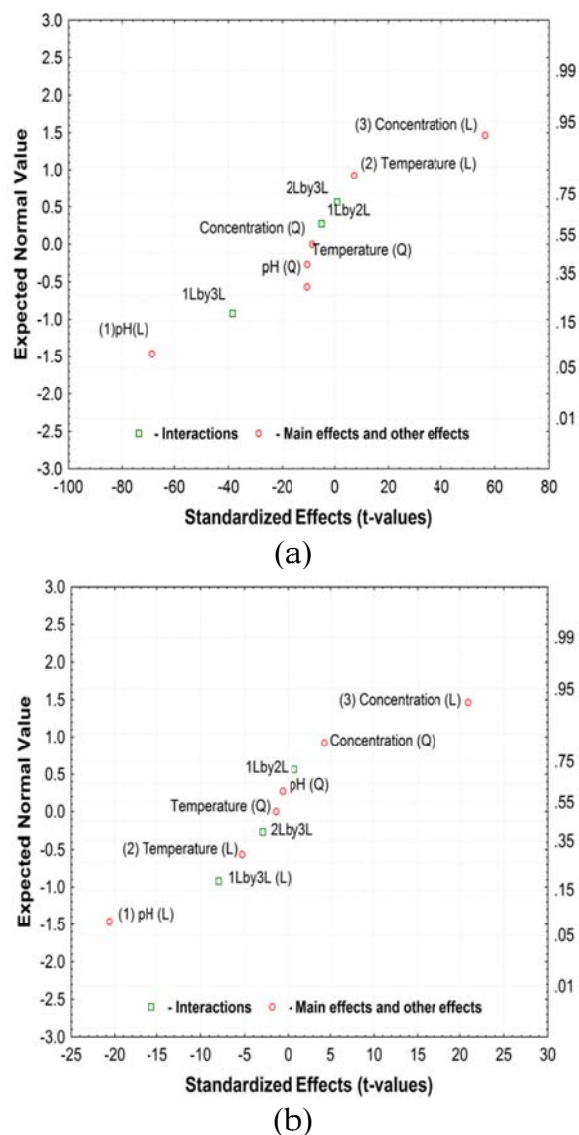


Figure 2: Normal probability plots of standardized effects of the studied factors and their interactions: (a) AC-F2 and (b) AC-F3

3. CONCLUSIONS

The results of the present study showed that the activated carbon based-iron containing adsorbents have been potential adsorbents for removal of As(V) with high adsorption performance from aqueous solutions.

Acknowledgements: This study was supported by Yildiz Technical University Scientific Research Projects Coordinating

Department under the Project No. 2011–01–04–DOP01.

REFERENCES

- Cornell, R. M., & Schwertmann, U. (2003). *The Iron Oxides: Structure, Properties, Reactions, Occurrence and Uses*. 2nd Edition, Germany: Wiley.
- Yetilmezsoy, K., Demirel, S., Vanderbei, R.J. (2009). Response surface modelling of Pb(II) removal from aqueous solution by *Pistacia vera* L.: Box-Behnken experimental design. *Journal of Hazardous Materials*, 171, 551-562.

BIOSORPTION OF REACTIVE RED 2 BY CTAB-MODIFIED POWDERED BIOMASS: ISOTHERM STUDIES

Tamer Akar¹, Melike Divriklioğlu^{2,a}

1. Department of Chemistry, Faculty of Arts and Science, Eskisehir Osmangazi University, 26480 Eskisehir, Turkey

2. Department of Chemistry, Graduate School of Natural and Applied Sciences, Eskisehir Osmangazi University, 26480 Eskisehir, Turkey

a. Corresponding Author (melikedivriklioglu@hotmail.com)

ABSTRACT: Recently researchers have studied on the improvement of the biosorption performance of different porous and powder biomaterials. The main objective of this work was to investigate the biosorption performance of CTAB-modified biomass of *Agaricus bisporus* at different concentrations of Reactive Red 2 (RR2) dye. Because isotherm studies are important applications for the understanding of the biosorption mechanism. The effect of initial dye concentration on the dye biosorption capacity of CTAB-modified biosorbents was explored between 100-400 mg L⁻¹ dye concentration. Langmuir and Freundlich isotherm models were tested to evaluate the equilibrium biosorption data. The monolayer biosorption capacity of modified biosorbent was found to be 141.53 mg g⁻¹. The results revealed that this new biosorbent was a promising alternative for eliminating RR2 from contaminated aquatic environment.

1. INTRODUCTION

In recent years, contamination of water sources with synthetic dyes as a consequence of various industrial activities has become a serious problem. Discharge of dye contaminated wastewaters into aquatic environment without adequate treatment can lead to adverse effects on the aesthetic quality of water bodies and impact the ecosystem by reducing the sunlight penetration and gas solubility in water. Also, some synthetic dyes may be carcinogenic or mutagenic in nature and can produce toxic amine compounds under degradative conditions (Pearce et al., 2003; Shin et al., 2002). Therefore, the treatment of dye contaminated aquatic systems and improvement of water quality are important topics in the field of environmental technologies.

Biosorption is an alternative low cost and ecofriendly technology to existing costly water treatment technologies and based on the biomaterial-pollutant interaction.

Current researches in this field demonstrated that different kinds of biomaterials interact with dye molecules, heavy metals and other organic substances and they successfully remove these contaminants from aqueous media (Akar et al., 2008; Herrero et al., 2008; Ju et al., 2008; Melgar et al., 2007; Park et al., 2007; Quintelas et al., 2006; Tunali et al., 2007; Volesky et al., 1999). The efficiency of the biosorption process depends on various factors including the type of biomass solution pH, temperature and the type of pollutant.

Currently a considerable interest focused on the improvement of the biosorption performance of biomaterials towards heavy metals or synthetic dyes. For this aim, surface modification procedures by different chemical agents have been suggested, including treatment of the biomass with sodium hydroxide (Ofomaja et al., 2009), sodium carbonate, disodium hydrogen phosphate (Janoš et

al., 2009), ethylenediaminetetraacetic dianhydride (Yu et al., 2008) and formaldehyde (Chen and Yang, 2006). Although in some recent studies, good biosorption performances were reported for the removal of metals by surfactant modified biomass (Bingol et al., 2009; Loukidou et al., 2003) a limited number of studies have so far been focused on the use of this type of biosorbents for decolorization of dye contaminated solutions (Oei et al., 2009).

The goal of the present study was to investigate the dye biosorption potential of cetyl trimethyl ammonium bromide (CTAB) modified *Agaricus bisporus* (*A. bisporus*) biomass for Reactive Red 2 dye (RR2) removal. This dye is highly water soluble and can be used for dyeing process for cellulose, nylon, silk and wool (So et al., 2002). *A. bisporus* macro fungus was chosen as a target biosorbent material because of its known biosorption ability towards dye molecules (Akar et al., 2009). Also macro fungi have some important characteristics for sorption studies such as chemical stability and good mechanical properties in acidic and alkaline conditions and texture structure in dried form (Matheickal and Yu, 1997).

2. METHODS

2.1. Preparation of the Modified Biosorbent and Dye Solutions

A. bisporus was purchased from a local market. Fruiting bodies of fungi were extensively washed with deionized water and dried at 80°C for 24 h. Dried biomass was crushed and sieved through an 212 µm ASTM Standard sieve to obtain uniform particle size. Powdered biomass was stored in glass bottles. 1.25 g of powdered biomass sample was suspended in 25 mL of CTAB solutions with concentration of 0.5% (w/v). The suspended mixture was stirred at 200 rpm and room temperature for 24 h. The

modified biosorbent sample was separated from the surfactant solution by filtration and washed with deionized water several times until free from bromide ions and the resulted biomass was dried as mentioned above. RR2 dye, obtained from Sigma–Aldrich Corporation, St. Louis, MO, USA, was used without further purification. A stock solution (1.0 g L⁻¹) was prepared by dissolving appropriate amount of dye in deionized water and the other concentrations were obtained by diluting this stock dye solution. Fresh dilutions were used in each experiment.

2.2. Apparatus

pH value of the solutions were monitored using a pH meter (HI 221 Hanna). The residual dye concentration in the supernatant was analyzed using a UV/vis spectrophotometer (Shimadzu UV-2550) at maximum wavelength of 538 nm.

Data presented are the mean values from three independent experiments. Experimental errors were estimated and are depicted with error bars. Statistical treatment of the results was done using SPSS 10.0 for Windows where it is possible to evaluate whether the effect and the interaction among the investigated factors are significant with respect to the experimental error.

2.3. Dye Biosorption Studies in Batch Mode

The batch mode biosorption tests were carried out by contacting an accurate weight amount of biosorbent with 25 mL of dye solutions. The dye–biomass mixture in 50 mL beakers was stirred on a multipoint digital magnetic stirrer at 200 rpm. In order to determine the effect of dye concentration on the biosorption process, RR2 concentrations were changed between 100 and 400 mg L⁻¹ within 25, 35 and 45°C.

Experiments were studied with 0.1 g L⁻¹ modified biosorbent within 40 min⁻¹ at pH 2. These values were explored at our previous work (Akar and Divriklioglu, 2010).

2.5. Biosorption Isotherm Studies

Batch biosorption applications were analyzed using Freundlich and Langmuir isotherm models. Freundlich model assumes that the uptake of sorbate occurs on a heterogeneous surface of the sorbent. Langmuir model describes the monolayer sorption process onto sorbent surface with specific binding sites. The linearized forms of the model equations are given as:

Freundlich model (Freundlich, 1906)

$$q_e = K_F C_e^{1/n} \quad (1)$$

Langmuir model (Langmuir, 1918)

$$q_e = \frac{q_{\max} K_L C_e}{1 + q_{\max} K_L} \quad (2)$$

In Eq. (1) K_F (L g⁻¹) and n (dimensionless) are Freundlich isotherm constants, being indicative of the extent of the biosorption and the degree of nonlinearity between solution concentration and biosorbent, respectively. The plot of $\ln q_e$ versus $\ln C_e$ for the biosorption was employed to generate K_F and n from the intercept and the slope values, respectively.

In Eq. (2) q_{\max} is the monolayer biosorption capacity of the biosorbent (mol g⁻¹); and K_L is the Langmuir constant (L mol⁻¹), and is related to the free energy of biosorption. A plot of $1/q_e$ versus $1/C_e$ for the biosorption of RR2 onto modified biomass shows a straight line of slope, $1/q_{\max} K_L$, and intercept, $1/q_{\max}$. In order to determine the favorability of biosorption, a dimensionless constant called as

separation parameter ' R_L ' was used and defined as in the Eq. (3).

$$R_L = \frac{1}{1 + K_L C_o} \quad (3)$$

where C_o is the highest initial RR2 concentration (mol L⁻¹). The value of separation parameter indicates the shape of isotherm to be either favorable ($0 < R_L < 1$), unfavorable ($R_L > 1$), linear ($R_L = 1$) or irreversible ($R_L = 0$) (Hall et al., 1966; Weber and Chakravorti, 1974).

3. RESULTS AND DISCUSSION

3.1. Evaluation of Biosorption with Different Isotherm Models

Isotherm studies are important applications for the understanding of the biosorption mechanism. Freundlich and Langmuir isotherm models were used for modelling the batch mode biosorption of RR2 on modified biosorbent.

The general biosorption isotherm plots for batch mode of operations are given in Figs. 1.

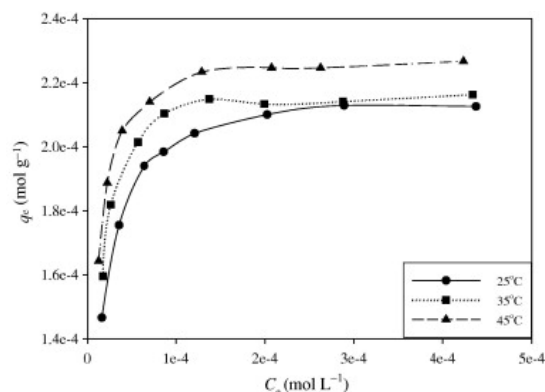


Figure 1: General isotherm plots for the batch mode biosorption of RR2 by modified biosorbent.

All of the isotherm model parameters for the biosorption are presented in Table 1 and Table 2. It is evident from the r^2 values that Langmuir model is suitable for describing both the batch mode biosorption of RR2 onto modified biomass surface. The values of R_L for batch studies found between 7.44×10^{-3}

and 3.90×10^{-1} indicated that the RR2 biosorption behavior of modified biomass can be considered as favorable ($0 < R_L < 1$). The maximum monolayer biosorption capacities (q_{\max}) of the modified biosorbent in batch mode are $2.17 \times 10^{-4} \text{ mol g}^{-1}$ (133.53 mg g^{-1}), $2.22 \times 10^{-4} \text{ mol g}^{-1}$ (135.37 mg g^{-1}) and $2.30 \times 10^{-4} \text{ mol g}^{-1}$ (141.53 mg g^{-1}) at 25, 35 and 45 °C, respectively. The increasing q_{\max} values of biosorption with the increasing temperature indicated that the process is endothermic in nature.

Table 1: Langmuir constants for the batch mode biosorption of RR2 onto modified biomass

	$q_{\max}(\text{mol g}^{-1})$	$K_L(\text{L mol}^{-1})$	r_L^2	R_L
25° C	2.17×10^{-4}	1.29×10^{-5}	0.99 7	1.17×10^{-2}
35° C	2.22×10^{-4}	1.57×10^{-5}	0.98 3	9.71×10^{-3}
45° C	2.30×10^{-4}	2.05×10^{-5}	0.99 9	7.44×10^{-3}

Table 2: Freundlich constants for the batch mode biosorption of RR2 onto modified biomass

	n	K_F	
25°C	9.33	5.18×10^{-4}	0.856
35°C	11.84	4.38×10^{-4}	0.788
45°C	12.05	4.53×10^{-4}	0.842

4. CONCLUSION

Dye biosorption process followed by pseudo-second-order kinetic model while the equilibrium data were found to follow with Langmuir isotherm model. CTAB modified biosorbent material was found to be simple, fast and efficient.

REFERENCES

Akar, T., Ozcan, A.S., Tunali, S., Ozcan, A., 2008. Biosorption of a textile dye (Acid Blue 40) by cone biomass of *Thuja orientalis*: estimation of equilibrium, thermodynamic and kinetic parameters. *Bioresour. Technol.* 99, 3057–3065.

Akar, T., Tosun, I., Kaynak, Z., Kavas, E., Incirkus, G., Tunali Akar, S., 2009. Assessment of the biosorption characteristics of a macro-fungus for the decolorization of

Acid Red 44 (AR44) dye. *J. Hazard. Mater.* 171, 865–871.

Akar, T. and Divriklioglu, M., 2010, Biosorption applications of modified fungal biomass for decolorization of Reactive Red 2 contaminated solutions: Batch and dynamic flow mode studies, *Bioresource Technology*, 101, 7271-7277.

Aksu, Z., Dönmez, G., 2003. A comparative study on the biosorption characteristics of some yeasts for Remazol Blue reactive dye. *Chemosphere* 50, 1075–1083.

Aksu, Z., Sen Cagatay, S., Gonen, F., 2007. Continuous fixed bed biosorption of reactive dyes by dried *Rhizopus arrhizus*: determination of column capacity. *J. Hazard. Mater.* 143, 362–371.

Bingol, A., Arslan, A., Cakici, A., 2009. Biosorption of chromate anions from aqueous solution by a cationic surfactant-modified lichen (*Cladonia rangiformis* L.). *J. Hazard. Mater.* 161, 747–752.

Chen, J.P., Yang, L., 2006. Study of a heavy metal biosorption onto raw and chemically modified *Sargassum* sp. via spectroscopic and modeling analysis. *Langmuir* 22, 8906–8914.

Freundlich, H.M.F., 1906. Über die adsorption in lösungen. *Z. Phys. Chem.* 57, 385–470.

Guo, W.Q., Ren, N.Q., Chen, Z.B., Liu, B.F., Wang, X.J., Xiang, W.S., Ding, J., 2008. Simultaneous biohydrogen production and starch wastewater treatment in an acidogenic expanded granular sludge bed reactor by mixed culture for longterm operation. *Int. J. Hydrogen Energy* 33, 7397–7404.

Hall, K.R., Eagleton, L.C., Acrivos, A., Vermeulen, T., 1966. Pore- and solid-diffusion kinetics in fixed-bed adsorption under constant-pattern conditions. *Ind. Eng. Chem. Fundam.* 5, 212–223.

Herrero, R., Lodeiro, P., Rojo, R., Ciorba, A., Rodríguez, P., Sastre de Vicente, M.E., 2008. The efficiency of the red alga *Mastocarpus stellatus* for remediation of cadmium pollution. *Bioresour. Technol.* 99, 4138–4146.

Hu, C., Yu, J.C., Hao, Z., Wong, P.K., 2003. Photocatalytic degradation of triazinecontaining azo dyes in aqueous TiO₂ suspensions. *Appl. Catal. B – Environ.* 42, 47–55.

Janoš, P., Coskun, S., Pilarová, V., Rejnek, J., 2009. Removal of basic (methylene blue) and acid (Egacid Orange) dyes from waters by sorption on chemically treated wood shavings. *Bioresour. Technol.* 100, 1450–1453.

Ju, D.J., Byun, I.G., Park, J.J., Lee, C.H., Ahn, G.H., Park, T.J., 2008. Biosorption of a reactive dye (Rhodamine-B) from an aqueous

- solution using dried biomass of activated sludge. *Bioresour. Technol.* 99, 7971–7975.
- Kannan, N., Sundaram, M.M., 2001. Kinetics and mechanism of removal of methylene blue by adsorption on various carbons – a comparative study. *Dyes Pigm.* 51, 25–40.
- Langmuir, I., 1918. The adsorption of gases on plane surfaces of glass, mica and platinum. *J. Am. Chem. Soc.* 40, 1361–1403.
- Loukidou, M.X., Matis, K.A., Zouboulis, A.I., Kyriakidou, M.L., 2003. Removal of As (V) from wastewaters by chemically modified fungal biomass. *Water Res.* 37, 4544–4552.
- Matheickal, J.T., Yu, Q., 1997. Biosorption of lead (II) from aqueous solutions by *Phellinus badius*. *Miner. Eng.* 10, 947–957.
- Melgar, M.J., Alonso, J., García, M.A., 2007. Removal of toxic metals from aqueous solutions by fungal biomass of *Agaricus macrosporus*. *Sci. Total Environ.* 385, 12–19.
- Mohan, S.V., Rao, N.C., Karthikeyan, J., 2002. Adsorptive removal of direct azo dye from aqueous phase onto coal based sorbents: a kinetic and mechanistic study. *J. Hazard. Mater.* 90, 189–204.
- Oei, B.C., Ibrahim, S., Wang, S., Ang, H.M., 2009. Surfactant modified barley straw for removal of acid and reactive dyes from aqueous solution. *Bioresour. Technol.* 100, 4292–4295.
- Ofomaja, A.E., Nadioo, E.B., Modise, S.J., 2009. Removal of copper(II) from aqueous solution by pine and base modified pine cone powder as biosorbent. *J. Hazard. Mater.* 168, 909–917.
- Pacchade, K., Sandhya, S., Swaminathan, K., 2009. Ozonation of reactive dye, Procion red MX-5B catalyzed by metal ions. *J. Hazard. Mater.* 167, 313–318.
- Padmesh, T.V.N., Vijayaraghavan, K., Sekaran, G., Velan, M., 2006. Biosorption of Acid Blue 15 using fresh water macroalga *Azolla filiculoides*: batch and column studies. *Dyes Pigm.* 71, 77–82.
- Park, H.G., Kim, T.W., Chae, M.Y., Yoo, I.K., 2007. Activated carbon-containing alginate adsorbent for the simultaneous removal of heavy metals and toxic organics. *Process Biochem.* 42, 1371–1377.
- Pearce, C.I., Lloyd, J.R., Guthrie, J.T., 2003. The removal of colour from textile wastewater using whole bacterial cells: a review. *Dyes Pigm.* 58, 179–196.
- Quintelas, C., Sousa, E., Silva, F., Neto, S., Tavares, T., 2006. Competitive biosorption of ortho-cresol, phenol, chlorophenol and chromium (VI) from aqueous solution by a bacterial biofilm supported on granular activated carbon. *Process Biochem.* 41, 2087–2091.
- Shin, M., Nguyen, T., Ramsay, J., 2002. Evaluation of support materials for the surface immobilization and decolorization of amaranth by *Trametes versicolor*. *Appl. Microbiol. Biotechnol.* 60, 218–223.
- So, C.M., Cheng, M.Y., Yu, J.C., Wong, P.K., 2002. Degradation of azo dye Procion Red MX-5B by photocatalytic oxidation. *Chemosphere* 46, 905–912.
- Tunali, S., Ozcan, A., Kaynak, Z., Ozcan, A.S., Akar, T., 2007. Utilization of the *Phaseolus vulgaris* L. waste biomass for decolorization of the textile dye Acid Red 57: determination of equilibrium, kinetic and thermodynamic parameters. *J. Environ. Sci. Health A* 42, 591–600.
- Volesky, B., Weber, J., Vieria, R., 1999. Biosorption of Cd and Cu by different types of *Sargassum* biomass. *Process Metall.* 9, 473–482.
- Weber, T.W., Chakravorti, R.K., 1974. Pore and solid diffusion models for fixed-bed adsorbents. *J. Am. Inst. Chem. Eng.* 20, 228–238.
- Yu, J., Tong, M., Sun, X., Li, B., 2008. Enhanced and selective adsorption of Pb²⁺ and Cu²⁺ by EDTAD-modified biomass of baker's yeast. *Bioresour. Technol.* 99, 2588–2593.

PURIFICATION OF ALCOHOL CONTAINING MESH WITH POWDER FILTERING MATERIALS

A.F. Ilyushchenko¹, V.M. Kaptsevich², N.N. Yakimovich³, R.A. Kusin², I.N. Chernyak^{1,a},
N.S. Ruchay⁴, A.I. Lembovich⁴

1. State scientific institution "Powder metallurgy Institute", Platonov st., 41, 220005, Minsk, Republic of Belarus

2. Education Establishment "Belarussian State Agriculture Technical University", Nezavisimosti av., 99, Minsk, Republic of Belarus

3. State scientific institution "Physical and Organic Chemistry Institute", Minsk, Surganova st. 13, 220072, Republic of Belarus

4. Education Establishment "Belarussian State Technology University", Sverdlova st., 13a, 220050, Minsk, Republic of Belarus

a. Corresponding author I.N. Chernyak (nil23niipm@tut.by)

ABSTRACT: The findings of investigations dealing with the appropriate effectiveness in separating yeast cells from fermented mesh with the help of powder filtering materials (PFM), set up in microfiltering module, are presented in the report. The aim of paper is the confirmation of possible use with respect to tangential filtration for implementation of mesh fermentation in continuous process mode. Bioreactor was simulated by the capacity with alcohol mesh (suspension of yeasts *Saccharomyces cerevisiae* with concentration 20 g/l). Compressed nitrogen suspension was supplied to filtering element where it was divided into two flows – concentrate and filtrate.

PFM out of titanium powders (with sizes of average pores 6.1; 8.5; 40 mkm) and corrosion resistant steel PKH18N15 (sizes of average pores 15 mkm) were tested. It has been established that PFM out of titanium powder with the average size of pores 40 mkm (retains 10% yeast cells) possesses lower effectiveness. Somewhat higher effectiveness is noted in filtering material out of corrosion resistant steel powder with average size of pores 15-30 %. Filter elements out of powders of grade titanium with average sizes of pores 10.3 and 6.1 mkm provided one hundred percent separation. It has been proved that PFM provide the capturing of yeast cells.

1. INTRODUCTION

Periodic process for mesh fermentation more spread in alcohol industry in ethanol production has a number of drawbacks: low productivity for fermentive devices, great time and heat energy costs as regards intercycle operations for device preparation for work, unstable life activity conditions and physiological state of population of yeasts which change in fermentation process from primary substract excess period to its full exhaustion time, sophisticated fight with infection particularly during primary fermentation period when excess substract is noted and

concentration of yeasts is not high, automatization process complexity. Mesh fermentation on a continuous-cyclic mode in an enormous battery of eight fermentive devices does not allow to get rid of the above-mentioned drawbacks [1, 2].

The promising way for challenge solution is the equipping of fermentive device with circulation microfiltration module contour operating on tangential mode and providing the return of yeast cells – ethanol producents into fermentive device with simultaneous selection of water and

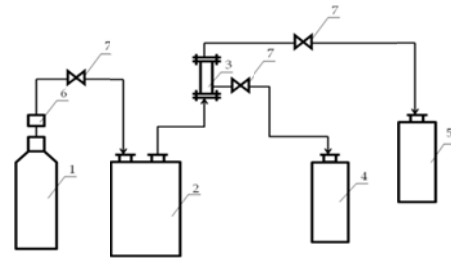
alcohol solution. It will allow to maintain high concentration of yeasts in the device at continuous mesh duct and it will provide a considerable increase in its productivity. Reliably high concentration of yeasts must provide full fermentation of mesh sugars and limit infection development in fermentive device. Absence or inconsiderable yeast biomass content in water and alcohol solution rejected from module will allow to decrease vapour consumption in further ethanol release and costs for purification of rectification columns. That is why development for filtering metal powders based material, different by essential advantages in comparison with other materials [3, 4], for continuous mesh fermentation in ethanol production is acute and has an important public and economic meaning. Filtering metal powders based materials (PFM) have essential advantages in comparison with other types of materials [3].

Aim of paper – efficiency investigation on separation of yeast cells from fermentive mesh with the help of powder filtering materials.

2. INVESTIGATION METHODS

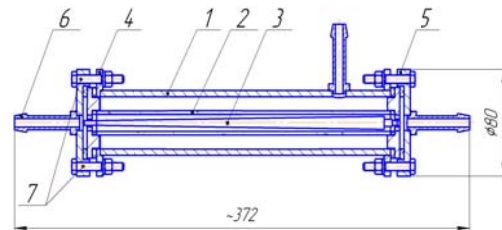
Investigation on efficiency in separating yeast cells by powder filtering materials was carried out on laboratory stand presented in figure 1. Bioreactor was modeled by capacity 2 with alcohol mesh (suspension of yeasts *Saccharomyces cerevisiae* with concentration 20 g/l (by 75 % humidity biomass), microfiltration module 3 was represented by body with inside installed cone rod to equal mesh flow rate along filter element axis (figure 2). Compressed air balloon was used as pressure source. Suspension of yeasts from capacity 2 by distortion bending and by compressed nitrogen was supplied to filtering element where it was divided into two flows – concentrate and filtrate. Concentrate was supplied to receiver5

and then it returned to capacity 2. Efficiency in separating yeast cells by filtering element was controlled by microscopy of filtrate samples in the preparation “crushed drop”. Filtering element input pressure was regulated by reducing gear within 0.1-0.3 MPa.



1 – pressure source, 2 – capacity with mesh, 3 – pilot microfiltration module, 4- filtrate receiver, 5 – concentrate receiver, 6 - reducing gear, 7 – valves for regulation of filtrate, concentrate and mesh consumptions.

Figure 1: Laboratory stand for investigating function efficiency for filtering elements.



1 – body, 2 filtering element, 3- cod, 4- body flange, 5 connective flange, 6- connecting branch, 7- fastening products

Figure 2: Pilot microfiltration module.

To conduct investigations with TPP-5, TPP-8, PTM titanium powders and corrosion stable PH18N15 grade steel powders by dry isostatic pressing method, four lengthy tubular filter elements with outer diameter 18, internal diameter 12.8 and length 240 mm were made. Characteristics of filter elements were determined by standard methods: sizes of pores were determined by GOST 26849-86, permeability coefficient

by GOST 25283-93, porosity by GOST 18898-98.

3. RESULTS AND DISCUSSIONS

Results of investigations for properties of filtering elements as well as ones of tests on laboratory stand are summarized in table 1.

Table 1: Properties and efficiency in capturing yeast cells for powder filtering materials.

Filtering element material	Permeability coefficient, $k, m^2 \times 10^{13}$	Average size of pores, d, mkm	Porosity	Specific Performance, $m^3/m^2 \times h$	Efficiency in separating yeast suspension, %
1	2	3	5	6	7
TPP-5	30.2	40	0.46	1.65	10.0
PKH18N15	18.1	15	0.38	1.30	30.0
TPP-8	8.9	8.2	0.35	0.95	100.0
PTM	6.8	6.1	0.32	0.90	100.0

Analysis for investigation results provided in table shows that PFM out of TPP-5 titanium powder with average size of pores 40 mkm and porosity 0.46 which retains only 10 % yeast cells possesses lower efficiency. Filtering material out of corrosion stable PH18N15 grade steel powder with average size of pores 15 and porosity 0.38 possesses somewhat higher efficiency in capturing yeast cells and possesses 30 %. Visually bad dividing capability in these materials is evidenced by high filtrate turbidity degree. One hundred separation of yeast cells was provided by filter elements out of TPP-8 titanium powders and PTM with average size of pores 10.3 and 6.1 mkm and porosity 0.35 and 0.32, correspondingly. At the same time, filter elements have relatively high calculating specific performance from one square meter (about 1 m³ per hour) in comparison with ceramic microfilters in proportionate sizes of pores [4]. Preliminary investigation results have also shown that in spite of relatively not high life span up to regeneration: 0.15-0.20 m³/m², washing of filter elements in reverse direction by water

with washing water consumption 0.08-0.1 m³ per one square meter of filtering surface restores their performance completely. In general principal conformity between permeability coefficients of materials and their specific performance, certain nonobservance of proportion between their values is noted what is explained mainly by measurement errors: specific performance was determined by way of measuring time segments with the help of stopwatch, time segments were required for filling definite volumes of concentrate and filtrate receivers.

Thus, investigation results have established that powder filtering materials provide required efficiency in capturing yeast cells out of alcohol containing mesh and can be used in microfiltration module construction to realize continuous fermentation process.

REFERENCES

1. Maltsev, P.M. 1980 Technology of fermentive factories. 2 edition, reviewed and added. - M.: Food industry, 560 p.
2. Kretov I.T. 1997. Technology equipment of fermentive industry enterprises. Voronezh: State University, 621 p.
3. Tumulovich M.Y, Mazyuk V.V., Pilinevich L.P. and Savich V.V. 2008. Purification of liquids by tangential filtration in porous powder materials. Powder metallurgy: republican interagency collection of proceedings, Minsk, Issue 31, P.239-245.
4. Kardashina L.F. and Gorlov E.A. 1996. Investigation on using ceramic microfilters for water preparation, Chemistry and water technology, Vol.18, №3, P.269-274.

RESEARCH AND DEVELOPMENT OF SURFACE-ACTIVE POWDER COMPOSITE MATERIAL BASED ON VISCOUS-FLOW WASTE

Komila Negmatova¹, Sayibjon Negmatov¹, Akrom Rajabov¹, Gappor Rahmonberdiyev¹, Jahongir Negmatov¹, Gulom Sharifov¹, Shodil Isakov¹

1. State Unitary Enterprise "Fan va Taraqqiyot", Tashkent State Technical University, Uzbekistan
a. Corresponding author: (polycomft2005@rambler.ru)

ABSTRACT: First time it was developed and scientifically proved the possibility of creating an effective surface-powder formulations of composite gossypol resin to stabilize the drilling fluids and their production technology, using local raw materials, wastes of oil and fat production, gossypol resins, non-ferrous metals - alyumak.

We developed the optimum compositions of modified powder composite gossypol resin type PCGR to stabilize drilling fluids and found that they have surface-active properties.

Shown the closeness of their surface activity at concentrations in drilling fluids more than 0.05% to the activity sulphanol, as compared to OP-10 is much higher, which suggests the possibility of their use as surfactants instead of expensive sulphanol and OP-10. Studies show that emulsifying properties of developed modified powder composite formulations of gossypol resin indicate that, due to their high surface activity, they are adsorbed on the alyumak surface, which is consistent with the theory of mono-molecular adsorption of American scientists Langmuir.

1. OBJECT AND THE RESEARCH TECHNIQUE

Objects of study are: *Na-karboksimetiltsejuloza* – *Na*- CMC, a polyacrylamide (PAA) and ferrolhlorlignosulfanat-1 (FHL -1), received on the basis of alcohol production wastes – lignin, and cotton oil (gossypol gum), caustic and soda ash, nedopal - a waste product of hydrogen nitrate of enterprise "Ferganaazot", gossypol gum - waste metal oil and fat productions, alumina – waste metal of the Tashkent factory on preparation and waste-handling of a breakage of a wastage of non-ferrous metals and nefteabad red clay.

Physical and chemical properties of ingredients instituted methods chemical, X-ray diffraction and the differential thermal

analysis. Operational characteristics (gravity, g/sm³; viscosity, with; dynamic

fluid loss, sm³/30 of mines; rate of strain of shear – CHC10, mg/sm²; hydrogen ion exponent - pH) elaborated composite compositions of chemical reactants and drill fluids have been instituted by methods, instruments and arrays according to requirements corresponding taken over in the CIS.

2. RESULTS OF STUDIES AND THEIR ANALYSIS

The way [Fathullaev *et al.*, 1988], updates gossypol gums with chemical combinations at which one are obtained with high stabilizing properties and applicable for pelletizing or caking is known.

Lack received modified gossypol the gum received on the introduced way is that it cannot be the water-soluble owing to physical and chemical properties and consequently cannot be used in the oil and gas industry for drilling wells. The way of reception of a lubricating additive to flush fluids [Bull. Inventions №12. Page 74 1974] in which one gossypol gum is exposed to treating by the alcohol, containing 1-20 atoms of carbon in the presence of sulfuric acid at temperature 65-120 °C is known.

Lack of the produced way is necessity of use of expensive sulfuric acid and its heating to temperature to 120 °C, and also that significant ecological harm to environment is done.

Wide application in the industry, especially in the boring equipment, [Fathullaev *et al.*, 1988] is found омыленная gossypol by gum, as an additive for lubrication of bearings of a rock-destruction tool that allows to raise durability of their operation on 20-23 %. However the existing technology of saponification gossypol gum owing to particular properties of the received product does not allow to receive the water-soluble powdery gossypol gum for cooking of drill fluids.

The closest prototype to the declared way is the way described in the literature [Fathullaev *et al.*, 1988] on which one gossypol gum saponification caustic itself – 4 %-s' aqueous solution and in a liquid state the handled gum as the reductant, goes for a fluid processing.

Technological lacks of an existing way are:

1. Necessity of conducting of process of saponification gossypol gums on the place of operation of boring holes that complicates and increases the cost of performance of drillings.

2. Delivery liquid saponification gossypol gum from a place of its cooking for a place of performance of drillings

demands significant transport expenditures and is economically unprofitable.

In the declared way the problem of meliorating of qualitative performances of composite powdery materials of different function, for example, in the chemical, oil and gas industry and in mechanical engineering by the introducing in the certain proportional relation powdery gossypol gums of various update dares: the water-soluble for drill fluids and in the chemical industry, and in the form of a melt – for corrosion prevention and stability increase on stream the boring equipment.

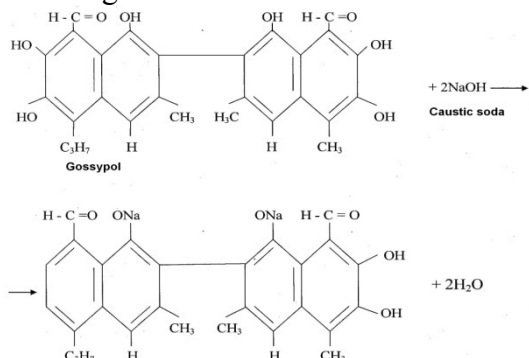
The task in view is reached by that for the purpose of reception of the water-soluble modified powdery gossypol gums as modifying agents are applied caustic, soda ash and alumna, being waste metal of waste-handling of the non-ferrous metals, playing a role of the catalyst and promoting transferring viscous-flow gossypol gums in a granular water-soluble state.

Therefore, for the purpose of reception of the water-soluble powdery gossypol gums by its physical and chemical update as modifying agents us have been chosen caustic and soda ash and alumna.

Update held by mixing heated to 90-950C is viscous-fluid gossypol gums with an aqueous saponification mud of caustic at involvement alumna as the catalyzed. Saponification mud within 3-5 minutes, blended with gossypol gum then within 15-20 minutes blended with soda ash. Mixing held in the mixer of type CM-3. Before mixing alumna micronized dismembrator pulpier type and had distribution of sizes within 10-100 microns.

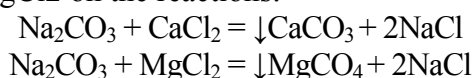
The dodge of transformation is viscous-fluid gossypol gums in a powdery state proceeds as follows.

At interplay gossypol gums with a saponification mud proceed polycondensation processes between carboxyl groups of synthetic fatty acids and hydro strong group of caustic under the following schema:



In the polycondensation process, simultaneously with the carboxyl groups of the resin is reacted gossypol resin alumina - Al_2O_4 . Formed at the same time water is evaporated, after drying the product.

Soda ash is introduced in the saponification of Na_2CO_3 gossypol resin to reduce its moisture content and transfer it to a more solid state. Soda ash absorbs a certain amount of water to form crystalline hydrates ($n Na_2CO_3 \cdot 2H_2O$), then goes into the crystalline state. When using highly mineralized formation water Na_2CO_3 reacts with the salts $CaCl_2$ and $MgCl_2$ on the reactions:



In this case, $CaCO_3$ and $MgSO_4$ deposited in the sediment, and salt water is released from these minerals.

As a result of processes occurring during the interaction gossypol resin saponified resin solution of $NaOH$, and with the participation of Al_2O_3 , molecules and oligomers corresponding gossypol resin converted into granular solid. The latter is obtained by grinding the composite resin powder gossypol.

Specifications obtained resin composition powder gossypol resin (CPGR) are presented in Table 1.

Table 1: Technical specifications of the modified composite powder gossypol resin – CPGR

Name index	Characteristic
Color	from light brown to brown
The consistency	solid powder
Mass fraction of total body fat mass to CPGR,%, not less than	5.5
Mass fraction of neutral fat to CPGR,%, not less than	1.5
Mass fraction of free alkali to CPGR,%, not less than	1.5
Moisture content,%, not more than	4.2
Hydrogen ion concentration (1% aqueous extract), pH	8,0-13,5
The stability of the emulsion, not less than an hour	2

To determine the optimal ratio of the components in CPGR changed the amount of caustic soda, which mainly affects the water solubility of the resin gossypol.

Example 1. In accordance with the process to determine the optimal ratio of the components took 100 grams gossypol resin is heated to a temperature of 90-95 0 C and stirred with 50 ml of saponification mixture consisting of 10% $NOOH$ (variable), and 20% Na_2CO_3 , 1% of the catalyst - alumina (constant).

Example 2. All other conditions being equal, as in Example 1, the concentration of the alkali solution was 15% $NaOH$.

Example 3. Other conditions being equal, as in Example 1, the concentration of the alkali solution was 20% NaOH.

The results of physical and chemical properties of the water-soluble powder gossypol resin modified resin are shown in Table 2.

Table 2: Physic-chemical properties of aqueous solution of powdered resin gossypol

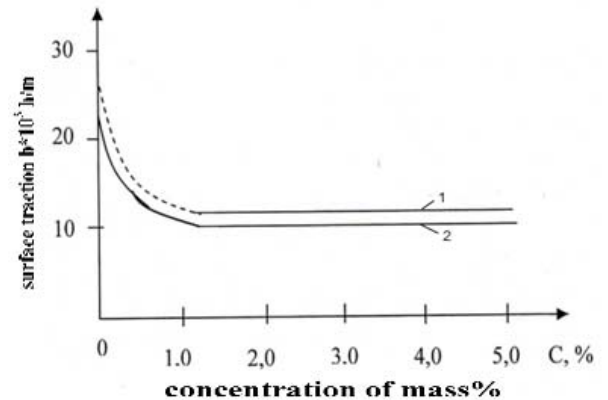
Number of samples	Aqueous solutions prepared using reagents					The parameters of the solution	
	Na OH, %	Na ₂ CO ₃ , %	aluma, %	γ , r/c M ³	T ₅₀₀ , cek	B ₃ , cm ³	pH
1	10	20	1	0,78	18,1	11	8
2	15	20	1	0,76	18,6	12	9,5
3	20	20	1	0,64	20,6	9	10

In accordance with the results presented in Table 2 best optimal performance on the physicochemical properties of a powdered soluble gossypol modified resin obtained in the 3rd example: it has a high water loss, lower specific gravity and low acidity. Table 1 and 2 show the compositions and properties of optimal composite developed vices shaped gossypol CPGR type resins. Further studies were designed performance vices shaped gossypol modified composite resins in particular, an anionic surface activity compared to known agents CPGR Sulphanol and OP-10. Found that CPGR at a concentration of 0.1% lowers the surface tension of water in two times. You can specify that in their ability to reduce surface tension CPGR superior reagent OP-10, but is close to Sulfanol (Table 3) [Negmatova, 2009; Negmatova et al., 2009].

Table 3: Surface tension of surfactant concentration SAS

Concentration, %	Surface tension N / m		
	CPGR-3	Sulfanol	OP-10
0,01	60,7	61,2	50,9
0,05	42,1	42,6	41,6
0,10	38,0	38,6	41,0
0,25	36,2	36,9	36,1
0,5	35,9	36,2	35,6
1,0	34,8	35,1	35,5

To assess the ability of emulsifying solution CPGR-3 were taken of the surface tension isotherms, which are shown in Fig.1.



1 on clay; 2-loam.

Figure 1: Dependence of interfacial tension on concentration CPGR in benzol.

Results of studies allow to conclude that 1 %-s' additive CPGR-3 suffices for supply of reliable emulsification in benzol. Thus interfacial tension of a mud is sharply slashed. At the big concentration (1,2 % and more) are observed an interfacial tension constancy that testifies to adsorption layer saturation.

Adsorption learning on variation of interfacial tension of mud CPGR-3 on clay and an adobe has demonstrated that with growth of concentration CPGR-3 interfacial tension is slashed evenly. CPGR-3 it is adsorbed more on clay, than on an adobe that is linked to mineralogical composition of adsorbent and it will well be matched the theory of monolayer adsorption of Lengmjura, i.e. permeate is adsorbed not on

all surface of adsorbent, and only on its active sites.

On the basis of the received experimental data it is possible to draw a conclusion that the drilling mud surfactants of serial CPGR-3 intended for reception of forward emulsions of type oil in water are reactants of semi colloidal type. Differently, CPGR-3 can form true (molecular) muds at low concentration and at high concentration - colloidal (thermodynamically steady micelles) muds and are non-Newtonian liquids.

For learning of effect of a synergism comparative studies of variation of interfacial tension from concentration of aqueous solutions CPGR-3 and sulphanole, both without additives, and with a polyelectrolyte additive were conducted. It is erected that the polyelectrolyte additive promotes more to falloff of interfacial tension of sulphanole; advantage of drug CPGR-3 synthesized by us thereby is experimentally affirmed.

On the basis of the held studies it is erected that development of effective technology of reception of the modified powdery composite compositions gossypol gums on the basis of domestic raw and wastage of productions is rather perspective direction. In this connection we elaborate scientifically-methodical principles which one have allowed to elaborate the effective production technology of the modified powdered composite compositions gossypol gums on the basis of an organic and inorganic domestic source of raw materials and a wastage of the productions, providing creation of composite multiphase compositions of chemical reactants with high physical and chemical and the operational characteristics, used for stabilizing of drill fluids.

3. CONCLUSIONS

1. For the first time it is elaborated and scientifically-is substantiated possibility of creation of effective surface active powdery composite compositions gossypol gums for stabilizing of drill fluids and technology of their production with use of a domestic source of raw materials, waste metal масложировых productions- gossypol gums, non-ferrous metals – alumna.

2. The basic laws of influencing of ingredients of composite compositions of chemical reactants on the physical and chemical processes proceeding between them, leading to increase technological and operating characteristics of drill fluids, and allowing conducting of drillings in the complicated geotechnical specifications are erected.

3. Modified powdered composite gossypol gums of type CPGR optimum compositions are elaborated for stabilizing of drill fluids and is erected that they exhibit surface-active properties. The affinity of their superficial activity is demonstrated at concentration in drill fluids more than 0,05 % to activity of sulphanole, and in comparison with OII-10 is appreciable above that testifies to possibility of their use as PEAHENS instead of expensive sulphanole and OII-10.

4. Studies of emulsifying properties of the elaborated modified powdery composite compositions gossypol gums point that, thanking their enhanced superficial activity, they are adsorbed on surfaces alumna and according to red clay with formation aggregation stable emulsion and slurries that will well be matched the theory of mono-molecular adsorption American Scientists Lengmjura.

REFERENCES

- The copyright certificate of the USSR № 512218 «the Stabilizing mixture» Bull. Inventions №16. With 81 1976.
- The copyright certificate of the USSR № 266988 «the Way of reception of a

- lubricating additive to flush fluids»
Bull. Inventions №12. Page 74 1974.
- E.Fathullaev, A.T.Dzhalilov, K.S.Minsker,
A.P.Maryin «Complex use of by-
products of waste-handling of a cotton
at reception of polymeric materials»
1988. Page 104 Tashkent. From-in
"Fan" the Uzbek Soviet Socialist
Republic.
- E.Fathullaev, A.T.Dzhalilov, K.S.Minsker,
A.P.Maryin «Complex use of by-
products of waste-handling of a cotton
at reception of polymeric materials»
1988. Page 86 Tashkent. From-in
"Fan" the Uzbek Soviet Socialist
Republic.
- Negmatova K.S.composite reactant for drill
fluids on the basis of a waste product
of chemical fertilizers//Composites. -
Tashkent, 2009. - № 3. – Pages 51-
53.
- Negmatova K.S., Salimsakov J.A.,
Rahimov H.J., Sharifov G. N,
Kobilov N.S. recover oil and fat
productions and reception of effective
composite oil-in-water emulsion drill
fluids// - Samarkand, 2009. - Pages
65-66.

PRODUCTION CHEMICALLY ACTIVATED CARBON FROM INDUSTRIAL WASTE MATERIAL AND ITS ADSORPTION BEHAVIOR IN THE DYE REMOVAL

E. Önal¹, N. Özbay¹, R. Z. Yarbay Şahin^{a1}, , and A. Ş. Yargıç¹

1 Chemical and Process Engineering Department, Bilecik Seyh Edebali University, TURKEY.
a. Corresponding author: (eylem.onal@bilecik.edu.tr)

ABSTRACT: In the present work producing activated carbon by chemical activation from peach stone used as a biomass and characterization of product was studied. Within this purpose, K_2CO_3 was used as chemical activation agent and impregnation ratio (50%) by mass was applied on biomass. Impregnation biomass samples were carbonized in a tubular furnace at 823 K and heating rate of 15 Kmin^{-1} under sweeping gas (N_2). Ultimate analysis, FT-IR, SEM, EDX, XRF and zeta potential analysis were applied to peach stone and activated carbon for characterization. The activated carbon obtained through carbonization of peach stone were used as an adsorbent for the removal of direct pink 3B.

1. INTRODUCTION

The textile industry plays an important role in the economies of numerous countries around the world. The industry emits dyes and pigments, which are the most obvious indicator of water pollution, into wastewater. Many dyes are harmful to human beings and have considerable resistance to biodegradation. Processes such as ion exchange, membrane separation and electrochemistry are effectively used for the removal of color from dye wastewaters, but the cost of these processes is the most important problem on application of these techniques. Also, different physicochemical and biological treatment methods such as coagulation/flotation, oxidation and filtration have been used for dye removal from wastewaters. But these methods are not effective for the dye removal without concurrent chemical treatment. Adsorption method can be used both effectively and economically on dye removal. The selected adsorbent should be environment- friendly, economical and demonstrates high removal efficiency. Activated carbon has been successfully used as an adsorbent for removal of dyes

from wastewater. Although activated carbon is the most used adsorbent, it is expensive. Furthermore, a regeneration step is needed after either exhausting the adsorbent capacity or the adsorption efficiency decreases below process requirements. Therefore, researchers seek the cheaper and largely available materials as an inexpensive and disposable adsorbent like low-cost plant and wood-based materials for activated carbon production [Ates and Un, 2013].

In the present study, peach stone has been used as an adsorbent source for the preparation of activated carbon by K_2CO_3 chemical activation. The adsorption ability of prepared activated carbon was tested towards to direct pink 3B.

2. EXPERIMENTAL

2.1. Activation Method

Peach stone was used in this study a source of activated carbon, obtained from a juice plant in Bursa/Turkey. It was then dried at room temperature and stored in a cool and dark room for 5 weeks and ground in a high-speed rotary cutting mill, and then screened to six fractions

from 0.224 mm to 1.8 mm. Average particle size of 0.59 mm was used for preparation of activated carbon. Production of activated carbon has involved by the carbonization of peach stone. K_2CO_3 as a chemical reagent added during the chemical activation process help produce more effective adsorbent. During the activation procedure, peach stone was impregnated with 50% K_2CO_3 for 24 h and then filtered and the resulting chemical loaded peach stone was placed in a tubular furnace and heated (15 Kmin^{-1}) to the final carbonization temperature of 823K for 30 min in the inert atmosphere (N_2). In all experiments, the heating rate was kept constant. After the cooling, the activated carbon was repeatedly washed with deionized water and dried at $105\text{ }^\circ\text{C}$. The carbonized material was used for adsorption experiments.

A commercial textile direct pink 3B. (C.I. Direct red 31) was obtained from a dye chemical industry around Bursa, located in Marmara region of Turkey of Turkey. A stock solution of dye (direct pink 3B) was prepared by dissolving an accurate quantity of dye in deionized water. Other concentrations prepared from stock solution by dilution varied between 100 and 400 mg dm^{-3} and the pH of the working solutions was adjusted to desired values with 0.1 M HCl or 0.1 M NaOH.

2.2. Characterization Activated Carbons

Surface areas of each activated carbon were calculated from N_2 adsorption isotherms by using BET (Brunauer–Emmett–Teller) method with Micrometrics Asap 2020 analyzer. The adsorption data of the total pore volume (V_{total}) were determined from the amount of nitrogen adsorbed at a relative pressure of 0.995 and calculated with the manufacturer's software. The same adsorption data were also used for

calculation of the micro pore volume by the t-plot method.

The mesopore volume (V_{meso}) was calculated by subtracting V_{micro} from V_{total} ($V_{\text{meso}} = V_{\text{total}} - V_{\text{micro}}$). The activated carbons were analyzed for carbon, nitrogen, hydrogen and oxygen (by difference) contents using LECO CHN628 elemental analyzer. A qualitative analysis of activated carbons was conducted by FT-IR transmission spectra using Perkin Elmer Spectrum 100 analyzer in wave number range of $4000\text{--}400\text{ cm}^{-1}$. The samples were well mixed with potassium bromide at a ratio of 1:99 and the mixture was pressed into pellets to be used in the analysis. SEM images and EDX analysis were recorded by using Zeiss Supra 40VP Scanning Electron Microscope. Samples were placed on carbon bands and coated with a thin layer of platinum in an nitrogen atmosphere using Qorum Q150RESDC Sputter Coater. The zeta potentials of samples were measured by a Zetasizer (MALVERN) equipped with a microprocessor unit. The unit automatically calculates the electrophoretic mobility of the particles and converts it to the zeta potential using the Smoluchowski equation.

2.3. Adsorption Studies

Batch experiments were carried out using 50 mL of dye solution with a known initial concentration ($50\text{--}400\text{ mg L}^{-1}$), adsorbent dose (2 g L^{-1}) and a pH (1) in glass containers (250 ml) at a constant agitation speed rate of 150 rpm for a certain contact time (10–240 min) by shaking in a thermostatic mechanical shaker. During the adsorption experiments, the dye absorbance after equilibrium was determined by centrifuging and analyzing the supernatant spectrophotometrically using a UV spectrophotometer (V-530 Jasco UV/VIS) at a wavelength that

corresponded to the maximum absorbance of the sample (520 nm)

3. RESULTS AND DISCUSSION

Table 1 shows the proximate ,component analysis, ultimate and XRF analysis results of peach stone. Low ash content of raw material indicates that the precursor is suitable for activated carbon production.

BET surface area of activated carbon is important because, like other physical and chemical characteristics, it may strongly affect the reactivity and combustion behavior. The higher surface areas are probably due to the opening of the restricted pores [Ioannidou and Zabaniotou, 2007]. The characteristics of the activated carbon are presented in Table 2. As can be observed, the carbon, hydrogen content and higher heating value are higher in the activated carbon when compared with the original biomass.

Table 1: Main characteristics of peach stone

Proximate analysis (wt.%) as received)	
Moisture	11.52
Volatiles	69.71
Fixed C	17.93
Ash	0.85
Bulk Density (kgm ⁻³)	560
Component analysis (wt.% as received)	
Extractives	0.66
Hemicellulose	2.48
Lignin	47.35
Cellulose	49.50
Holocellulose	52.03
Elemental analysis (wt.% daf basis)	
Carbon	33.97
Hydrogen	3.87
Nitrogen	0.39
Oxygen (by difference)	61.45
Empirical formula	CH _{1.36} N _{0.009} O _{1.35}

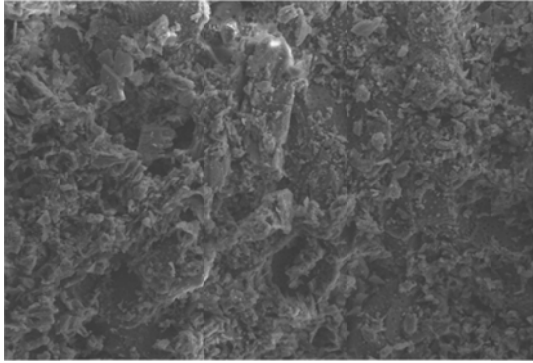
H/C molar ratio	1.36
O/C molar ratio	1,35
Calorific value (MJ/kg)	5.99
XRF analysis (wt.% as received)	
Mg	0,150
Si	0,249
P	0,303
K	0,442
Ca	1,843
Fe	0,109

Table 2: Characteristics of the activated carbon

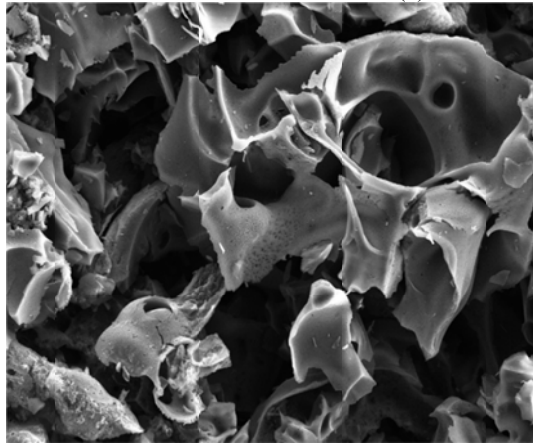
Ultimate analysis (wt.%)	
C	73.16
H	3.34
N	0.69
O	22.79
HHV (Mj/kg)	25.5
Typical properties	
S _{BET} (m ² /g)	76.77
V _T (cm ³ /g)	0.04594
V _{micro} (cm ³ /g)	0.027
V _{meso} (cm ³ /g)	0.01894
S _{micro} (m ² /g)	50.36
S _{ext} (m ² /g)	25.75
APD (A°)	30.71

Scanning electron microscopy (SEM) technique was used to observe the surface physical morphology of the samples. SEM micrographs of raw material and obtained activated carbon are given in Fig. 1. It is seen that structure of peach stone exists along with a little porosity.

SEM images of produced activated carbons is obvious that a wider porosity is created, thus the external surface areas of the chemically activated carbons are full of cavities. K_2CO_3 impregnated to sample formed sponge-like morphology after carbonization.



(a)



(b)

Fig.1: SEM images of raw material (a) and activated carbon(b)

The EDX analysis and zeta potential of activated carbon are given in Fig.2 and Fig.3 respectively.

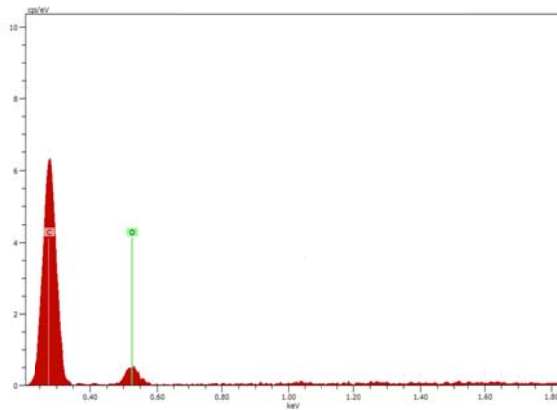


Fig. 2: EDX analysis for activated carbon

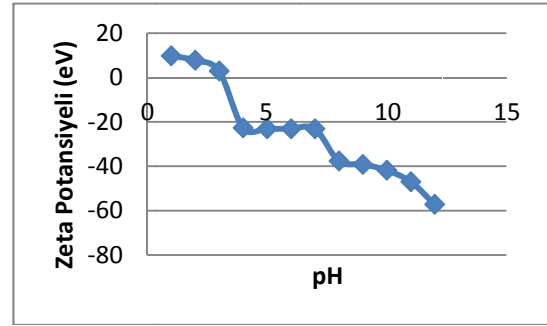
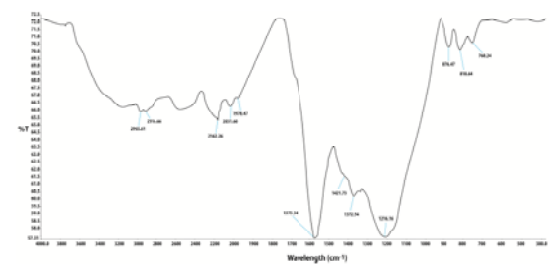


Fig.3: Zeta potential of activated carbon

EDX analysis of activated carbon were found to be compatible with its ultimate and XRF analysis results. The isoelectric point value obtained is 3.11.



(a)



(b)

Fig.4: FT-IR spectra of (a)raw material and (b)produced activated carbon

FT-IR spectra of raw material and activated carbon is given in Fig. 4. Functional groups are very important characteristics of the activated carbons, because they determine the surface properties of the carbons and their quality. FT-IR spectroscopy in its various forms is an important and forceful technique which can give useful information about structures. It can provide basic spectra of activated carbons, especially for determination of types and intensities their surface functional groups [Naseer and Hendawy,

2006]. The broad and flat band at about 3300–3400 cm^{-1} shows the presence of OH stretching vibration of alcohol, phenol or carboxylic acid. The strong band at 2950–2800 cm^{-1} represents C-H stretching vibration in methyl group. Another strong band at 1750 cm^{-1} is ascribed to C=O vibrations probably from esters, ketones or aliphatic acids. The band at 1620 cm^{-1} can be ascribed to C=C aromatic ring stretching vibration. The very strong band at 1070 cm^{-1} represents C=O stretching vibrations. The weaker bands between 765 and 530 cm^{-1} are ascribed to aromatic structures. It can be said that the chemical structure of peach stone, being a lignocellulosic material, is made up of different atomic groupings and a large number of functional groups. FT-IR spectrum of activated carbon differ from peach stone, which is a result of the chemical and thermal treatment. The OH stretching vibration band at about 3300–3400 cm^{-1} and C=O vibrations at 1750 cm^{-1} are disappeared for all activated carbons after carbonization. The band at 1470–1430 cm^{-1} is ascribed to C-H bending vibrations in CH_3 groups for activated carbon. The band at 1592–1530 cm^{-1} is the unsaturated stretching of C=C bonds.

The adsorption capacity of direct pink 3B removed by activated carbon from peach stone versus contact time for different initial dye concentration is illustrated in Fig. 5. The removal of direct pink 3B onto activated carbon was rapid initially and then slows down gradually until it attained an equilibrium beyond which there was no significant increase in the removal at all dye concentrations. It can be seen that the adsorbed amount of direct pink 3B increased. Large amounts of direct pink 3B was removed in the first 90 min and equilibrium was reached in 120 min. An increase in the initial dye concentration from 50 to 400 mg/L lead to an increase in the amount of dye from

24,08 to 108,9779 mg g^{-1} adsorbed onto activated carbon.

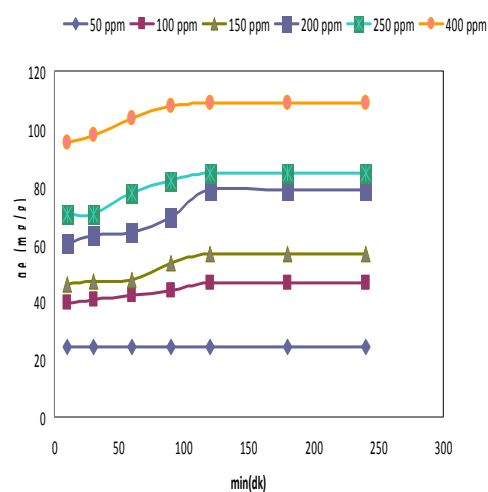


Fig.5: Effect of contact time for the adsorption of direct pink 3B onto activated carbon at 20°C and various initial dye concentration.

4. CONCLUSIONS

Preparation, characterization and adsorption properties of activated carbon from peach stone are described in this study. Effect of K_2CO_3 chemical activation agent on surface chemistry of activated carbons were investigated. Activated carbon from peach stone in this study has special characteristics and can be recommended as environmentally friendly activated carbon

REFERENCES

- Ateş, F. and Tezcan-Un, U., 2013. Production of char from hornbeam sawdust and its performance evaluation in the dye removal, *Journal of Analytical and Applied Pyrolysis*, Inpress..
- Ioannidou, O. and Zabaniotou, A., 2007. Agricultural residues as precursors for activated carbon production—A review, *Renewable and Sustainable Energy Reviews*, 11, 1966.
- Naseer, A. and Hendawy, E., 2006. Variation in the FTIR spectra of a biomass under impregnation, carbonization and oxidation conditions, *Journal of Analytical and Applied Pyrolysis*, 75, 159.

CO₂ ADSORPTION ON ZEOLITE X

Özgül Dere Özdemir^{1,a}, Müge Sarı Yılmaz¹, Nevin Karamahmut¹, Prof. Dr. Sabriye Pişkin¹

1. Yildiz Technical University, Department of Chemical Engineering, Istanbul, Turkey

a. Corresponding author (odere@yildiz.edu.tr)

ABSTRACT: Zeolites are crystalline aluminum-silicates, with group I or II elements as counterions. Their structure is made up of a framework of $[\text{SiO}_4]^{4-}$ and $[\text{AlO}_4]^{5-}$ tetrahedra linked to each other at the corners by sharing their oxygens (Querol *et al.*, 2002). Zeolites represent one of the most innovative adsorbents for a wide range of applications including air separation, air drying, CO removal from reforming gas, and CO₂ removal from natural gas [1]. World CO₂ emissions are expected to increase by 1.9 percent annually between 2001 and 2025. Developing countries' emissions are expected to grow above the world average at 2.7 percent annually between 2001 and 2025; and surpass emissions of industrialized countries near 2018. Accumulation of CO₂ concentration has caused global warming. So it is a major problem all over the world (Mulgundmath *et al.* 2012). The aim of this study is to evaluate the CO₂ adsorption behavior of Zeolite 13X. A volumetric-type apparatus was used to measure the CO₂ adsorption at 19.8 °C. It was found that CO₂ adsorption amounts of Zeolite 13X at 19.8 °C 103.55 kPa was 4.72 mmol/g.

Keywords: Zeolite 13X, CO₂, Global warming, Adsorption, BET

1. INTRODUCTION

CO₂ is the primary greenhouse gas, which is the largest contributor to global warming, emitted through human activities. CO₂ is naturally present in the atmosphere as part of the Earth's carbon cycle (the natural circulation of carbon among the atmosphere, oceans, soil, plants, and animals). Human activities are altering the carbon cycle both by adding more CO₂ to the atmosphere [2].

Main human activities are the combustion of fossil fuels such as coal, natural gas or petroleum, and industrial processes such as power plants, oil refining and the production of cement, iron and steel (Songolzadeh *et al.*, 2012).

Global emissions of CO₂, the main cause of global warming, increased by 3% in 2011, reaching an all-time high of 34 billion tonnes in 2011 (Olivier *et al.*, 2012). CO₂ emissions per country from

fossil fuel use and cement production were given in Figure 1.

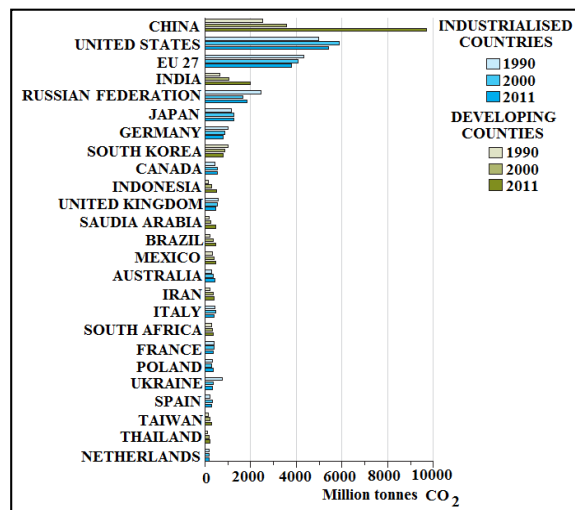


Figure 1: CO₂ emissions per country from fossil fuel use and cement production (Olivier *et al.*, 2012)

Wet flue gas desulfurization, and carbon capture technology are the a few technology options for the cleaning of

flue gas. However, they are often multi-step, complex, and costly. It is highly desirable to have a suitable single-step process for the simultaneous removal of CO₂ from the flue gas. Adsorption process may offer a promising way for the removal of CO₂ in flue gas because of the minimum energy requirements, relatively simple design and minimum waste disposal problems.

The correct selection of adsorbents is a very important procedure for adsorption system design. Zeolites are microporous crystalline materials with uniform-shaped pores of molecular dimensions, which are commonly used for gas separation and catalysis (Yi *et al.*, 2012).

CO₂ adsorption on zeolites is investigated by different researchers (Wang and Le Van, 2009; Xu *et al.*, 2009; Liu *et al.*, 2011; Zukal *et al.*, 2011; Hudson *et al.*, 2012)

In the present work, adsorption of CO₂ on zeolite was studied. Adsorption equilibrium measurement of pure gas was performed by automatic volumetric adsorption analyzer.

2. MATERIALS AND METHODS

Zeolite 13 X was obtained from CECA Co. The specific surface area of Zeolite 13X was determined by Micromeritics (ASAP 2020) automatic volumetric adsorption analyzer (BET) using nitrogen adsorption. On the other hand, CO₂ adsorption equilibrium data on Zeolite 13X experiments were performed by BET at 19.8 °C and 103.55 kPa. Before the adsorption experiments Zeolite 13X was degassed at 350 °C for 12 hours. CO₂ was pure.

3. RESULTS AND DISCUSSION

Specific surface area of Zeolite 13X was determined as 482.97 m²/g. The

adsorption isotherms of CO₂ on Zeolite 13X is shown in Figure 1.

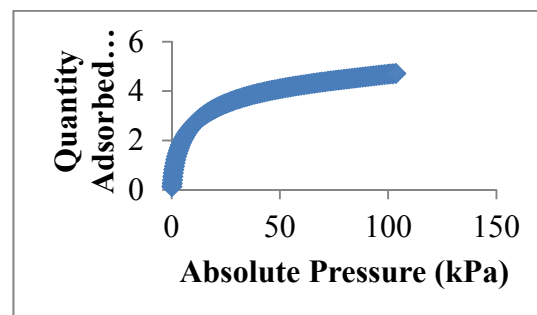


Figure 1: CO₂ adsorption isotherm of Zeolite 13zeoliX

CO₂ adsorption capacity of Zeolite 13X obtained in this study was comparison with the results in literature in Table 1.

Table 1: Comparison of Zeolite 13X CO₂ adsorption results with other studies.

Zeolite	Adsorbed Amount (mmol/g)	Pressure (kPa)/ Temperature (°C)	Reference
Zeolite 13X	4.72	103.55/19.8	Present Study
Zeolite 13X	4-4.5	150/35	Caveati <i>et al.</i> 2005
Zeolite 13X	≈4	150/40	Mulgundmath <i>et al.</i> , 2012
Zeolite 13X	≈3.5	300/100	Mulgundmath <i>et al.</i> , 2012

The adsorption amount of CO₂ on Zeolite 13 X was ≈3.5 mmol/g at 100 °C, 300 kPa while ≈4 mmol/g at 40 °C, 150 kPa presented in the work of Mulgundmath *et al.* The temperature was 35 °C in the study of Caveati *et al.* and they determined 4-4.5 mmol/g adsorped amount of CO₂. In this study, higher adsorption capacity of CO₂ (4.72 mmol/g) was determined. It is clear that the absorbed amount of CO₂ was decreased with increasing temperature due to exothermic adsorption process.

CO₂ has high quadrupole moment meaning that it is strongly absorbed by polar adsorbents due to strong interactions of CO₂ with zeolite 13X adsorbent surface (Mulgundmath *et al.*, 2012).

4. CONCLUSIONS

In this work, the adsorption equilibrium of CO₂ on Zeolite 13X was measured at 19.8 °C and in a pressure range from 0 to 103.55 kPa.

Adsorption capacity of CO₂ was determined 4.72 mmol/g with the experiment conditions. It is concluded that the absorbed amount of CO₂ was decreased with increasing temperature due to exothermic adsorption process.

REFERENCES

Cavenati, S., Grande, C., A. and Rodrigues, A., E., 2005, Layered Pressure Swing Adsorption for Methane Recovery from CH₄/CO₂/N₂ Streams, Springer Science and Business Media Adsorption, 11:549-554.

Hudson, M.R., Queen, W.L., Mason, J.A., Fickel, D.W., Lobo, R.F., and Brown, C.M., 2012, Unconventional, Highly Selective CO₂ Adsorption in Zeolite SSZ-13, Journal of American Chemical Society, 134, 1970-1973.

Liu, Z., Grande, C.A., Li, P., Yu, J., and Rodrigues, A.E., 2011, Adsorption and Desorption of Carbon Dioxide and Nitrogen on Zeolite 5A, Separation Science and Technology, 46: 434-451.

Mulgundmath, V.P., Tezel, F.H., Saatcioglu, T., and Golden, T.C., 2012, Adsorption and Separation of CO₂/N₂ and CO₂/CH₄ by 13X Zeolite, The Canadian Journal of Chemical Engineering, 90, 730-738.

Olivier, J. G.J., Janssens-Maenhout, G., and Peters, J.A.H.W., 2012, Trends in global CO₂ Emissions 2012 Report, PBL Netherlands Environmental Assessment Agency.

Querol, X., Moreno, N., Uman˜a, J.C., Alastuey, A., Hern´andez, E., Lo´pez-Soler, and Plana, A.F., 2002, Synthesis of Zeolites From Coal Fly Ash: an Overview, International Journal of Coal Geology, 50, 413-423.

Songolzadeh, M., Ravanchi, M.T., and Soleimani, M., 2012, Carbon Dioxide Capture and Storage: A General Review on Adsorbents,

World Academy of Science, Engineering and Technology 70, 225-232.

Wang, Y. and Le Van, M.D., 2009, Adsorption Equilibrium of Carbon Dioxide and Water Vapor on Zeolites 5A and 13X and Silica Gel: Pure Components, Journal of Chemical Engineering Data, 54, 2839-2844.

Xu, X., Zhao, X., Sun, L., and Liu, X., 2009, Adsorption Separation of Carbon Dioxide, Methane and Nitrogen on Monoethanol Amine Modified β-zeolite, Journal of Natural Gas Chemistry, 18, 167-172.

Yi, H., Deng, H., Tang, X., Yu, Q., Zhou, X., and Liu, H., 2012, Adsorption Equilibrium and Kinetics for SO₂, NO, CO₂ on Zeolites FAU and LTA, Journal of Hazardous Materials, 203-204, 111-117.

Zukal, A., Areal, C.O., Delgado M.R., Nachtigall P., Pulido, A., Mayerová J., and Cˆejka, J., 2011, Combined Volumetric, Infrared Spectroscopic and Theoretical Investigation of CO₂ Adsorption on Na-A Zeolite, Microporous and Mesoporous Materials, 146, 97-105.

- [1] <http://www.eia.gov/oiaf/1605/ggccebro/chapter1.html>
- [2] <http://www.epa.gov/climatechange/ghgemissions/gases/co2.html>

CRYSTALLIZATION OF SODIUM ORGANIC SALTS PRODUCED IN PARTIAL WET OXIDATION OF BLACK LIQUOR

Karhan Özdenkci^{1,a}, Jukka Koskinen¹, Kristian Melin¹, Kuppa Venkata Sarada¹,

1. Aalto University, Research Group of Plant Design, Espoo, Finland
a. Corresponding author (karhan.ozdenkci@aalto.fi)

ABSTRACT: Due to environmental issues and sustainable development aspects, it has recently become favorable to integrate biorefineries to process industry to produce biofuel, energy and chemicals. For instance, in pulp industry, black liquor (waste stream) has a significant biorefinery potential. One alternative treatment involves partial wet oxidation of black liquor to produce organic acids or the sodium salts of these acids. The purpose of this study is to investigate salt and acid recovery from partially wet oxidized black liquor. The paper illustrates crystallization of sodium formate and sodium acetate (two of major salts) in aqueous solution with respect to temperature and pH.

1. INTRODUCTION

Renewable energy has become an urgent need due to the increasing energy demand and environmental issues of fossil fuels. Moreover, even though biomass is potentially the greatest renewable energy supply, 1st generation bioprocesses consumes food source and requires additional water and land. Therefore, it has become favorable to integrate biorefineries with process industry.

Pulp and paper industry has a significant biorefinery potential: black liquor (waste of pulping process) is an important fuel source. However, the commercial treatment includes complete combustion of the organic content: not utilizing the biofuel potential and not feasible for non-wood mills. Moreover, the most investigated alternative (gasification followed by Fischer-Tropsch synthesis) has issues of economic feasibility and synthesis selectivity.

An alternative treatment suggested by Mudassar, et al., (2012) involves partial wet oxidation to produce organic acids (mainly acetic, formic, lactic and glycolic

acids) and their sodium salts by neutralizing sodium carbonate. Then, the

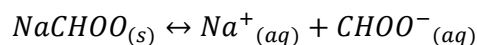
salts can be separated from other components by crystallization.

This paper investigates crystallization of sodium formate and sodium acetate in aqueous solution with respect to temperature and pH. The results are analysed to suggest a recovery process.

2. SALT AND ACID DISSOCIATION

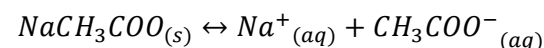
The aqueous sodium formate-acetate system has four reactions: dissolution of salts and dissociation of acids.

The dissolution of sodium formate:



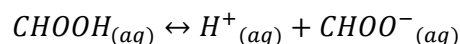
$$K_{sp1} = [Na^+][CHOO^-]$$

The dissolution of sodium acetate:



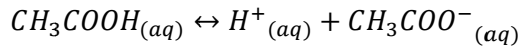
$$K_{sp2} = [Na^+][CH_3COO^-]$$

The dissociation of formic acid:



$$K_{a1} = \frac{[H^+][CHOO^-]}{[CHOOH]}$$

The dissociation of acetic acid:



$$K_{a2} = \frac{[H^+][CH_3COO^-]}{[CH_3COOH]}$$

It should be noted that the dissolution/dissociation products above assumes thermodynamically ideal mixture. For real solutions, the excess chemical potential should be included as well by activity coefficients. On the other hand, typical activity coefficient models, e.g. Debye-Hückel and Davies models, are valid in low concentrations, thus being inaccurate in the concentration ranges of salt crystallization in this study.

The solubility/dissociation products are determined by fitting experimental data to the empirical equation involving the temperature dependence:

$$\ln K = A + \frac{B}{T} + C \ln T + DT$$

The dissolution/dissociation products of sodium acetate and acetic acid were given at various temperatures by Fournier, et al. (1998). The dissolution product of sodium formate is fitted to the solubility data given by Yaws (2012). The data is in molal concentration and it is calculated in molar concentration by assuming 1000 g of water would have a volume of 1 L. This assumption is expected to have minor impact but more precise calculation can be performed by inserting sodium formate density. Figure 1 shows measured and calculated solubility product of sodium acetate vs. temperature as an example. The fitted parameters are given in Table 1.

The temperature dependence of formic acid dissociation constant was determined by Kim et al., 1996 as:

$$pK_{a1} = -57.528 + \frac{2773.9}{T} + 9.1232 \ln T$$

The partially wet oxidized black liquor can be characterized to determine total acetate and total formate content (i.e. the sum of ion and acid). Therefore, the solubility products are modified assuming that acid dissociation reactions are in equilibrium:

$$[Formate] = [CHOO^-] + [HCHOO]$$

$$[CHOO^-] = \frac{[Formate]}{1 + \frac{[H^+]}{K_{a1}}}$$

$$K_{sp1} = [Na^+] \frac{[Formate]}{1 + \frac{[H^+]}{K_{a1}}}$$

$$\beta_1 = K_{sp1} \left(1 + \frac{[H^+]}{K_{a1}} \right) = [Na^+][Formate]$$

and similarly,

$$[Acetate] = [CH_3COO^-] + [CH_3COOH]$$

$$\beta_2 = K_{sp2} \left(1 + \frac{[H^+]}{K_{a1}} \right) = [Na^+][Acetate]$$

where β_1 and β_2 are the modified solubility products of the salts in terms of total acetate/formate content (i.e., the sum of acidic and ionic forms).

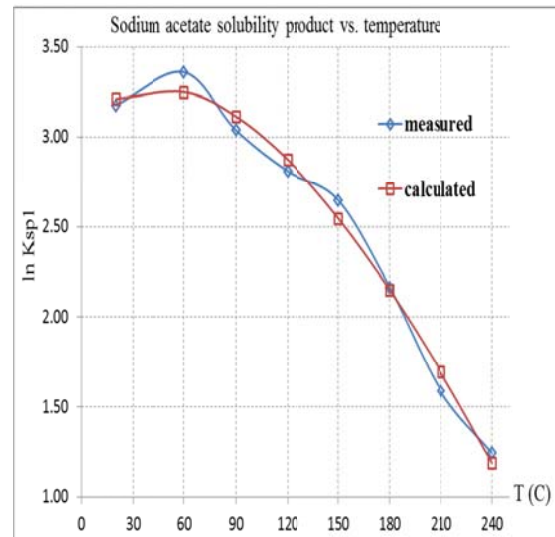


Figure 1. Sodium acetate solubility product versus temperature

Table 1. The parameters of empirical temperature dependence equations

	A	B	C	D
K_{sp1}	59.62	-13610	5.35	-0.132
K_{sp2}	-1.45	-2131	3.8	-0.033
K_{a2}	-1.504	-2608	1.62	-0.033

3. SALT AND ACID RECOVERY

The feed concentrations are selected based on the partially wet oxidized wheat straw black liquor in Mudassar, et al., 2012. The concentrations are:

$$\begin{aligned} \text{Sodium feed} &= 1.26 \text{ M} \\ \text{Formate feed} &= 0.42 \text{ M} \\ \text{Acetate feed} &= 0.84 \text{ M} \end{aligned}$$

The partial wet oxidation downstream is a liquid at high temperature, pressure and pH (e.g. 60 bars, 200 °C and pH 9). Thus, the stream can be concentrated by water evaporation. The concentrations after water evaporation are:

$$[\text{Component}_i] = \frac{\text{Component}_i \text{ feed}}{1 - \text{evaporation rate}}$$

Then, the species distribution is calculated by analytical solution of:

$$\begin{aligned} Q_1 &= [\text{Sodium}][\text{Formate}] \\ Q_2 &= [\text{Sodium}][\text{Acetate}] \end{aligned}$$

If $Q_1 > \beta_1$ and $Q_2 \leq \beta_2$: sodium formate

$$([\text{Sodium}] - a)([\text{Formate}] - a) = \beta_1$$

If $Q_2 > \beta_2$ and $Q_1 \leq \beta_1$: sodium acetate

$$([\text{Sodium}] - b)([\text{Acetate}] - b) = \beta_2$$

If $Q_1 > \beta_1$ and $Q_2 > \beta_2$: both salts

$$([\text{Sodium}] - a - b)([\text{Formate}] - a) = \beta_1$$

$$([\text{Sodium}] - a - b)([\text{Acetate}] - b) = \beta_2$$

where a and b represent crystallized sodium formate and sodium acetate.

Figure 2 and Figure 3 show the salt and acid recovery with respect to water evaporation, temperature and pH.

3.1 The effect of Water Evaporation

The feed concentrations are too low to recover salts. Nevertheless, the product stream of partial wet oxidation can be

concentrated by water evaporation and the steam can be utilized in pulping process or a CHP plant. Since the downstream of partial wet oxidation is at high temperature and pressure, the prior water evaporation rate can be controlled through a multistage flash operation. 70 % of water evaporation is still insufficient for salt crystallization. Therefore, Figure 2 shows only acid concentrations after 70 % water evaporation. Figure 3 shows the results for 90 % water evaporation. In this case, sodium acetate is recovered depending mainly on pH and slightly on temperature. However, the sodium acetate recovery is less than 65 % and sodium formate cannot be recovered yet.

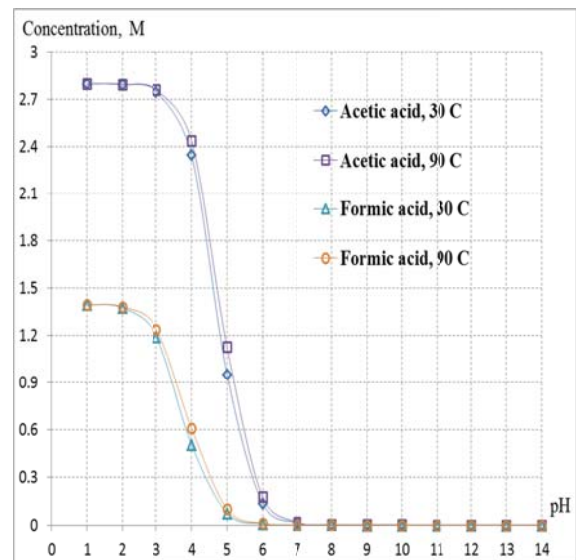


Figure 2. Acid recovery after 70 % water evaporation: $[\text{Formate}] = 1.40 \text{ M}$ and $[\text{Acetate}] = 2.80 \text{ M}$.

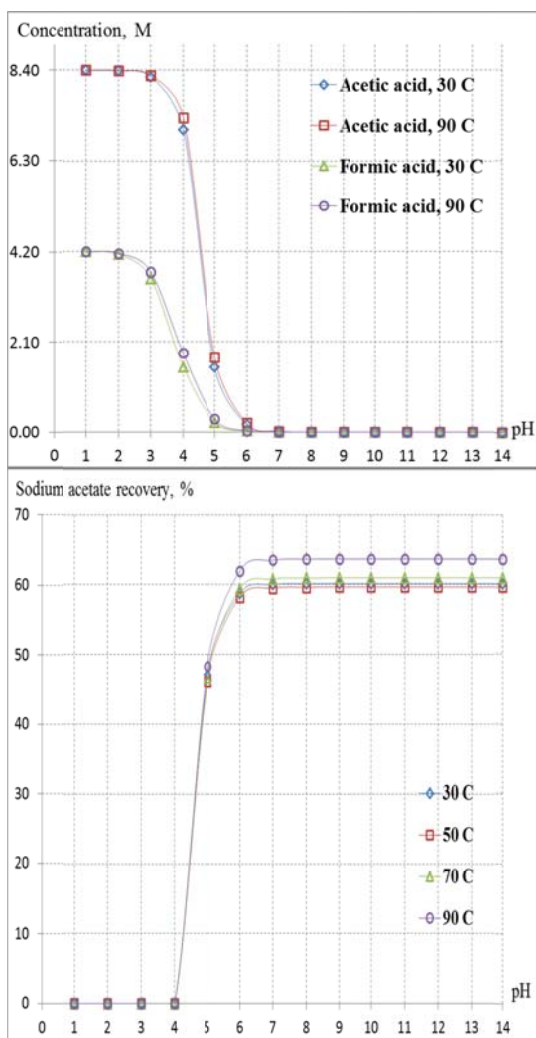


Figure 3. Acid and salt recovery after 90 % water evaporation: [Formate] = 4.20 M and [Acetate] = 8.40 M.

3.2 The Effect of pH

pH influences the distribution of the dissolved formate and acetate to the ionic form and acidic form. At low pH values, the dissolved acetate and formate content are in acidic form; therefore, ion concentrations are so low that the system does not reach supersaturation with respect to the salts. This fact is reflected to the calculation method as high values of modified dissociation products β_1 and β_2 , thus no solid recovery. Acid concentrations start to decrease after pH 2 and reaches to zero at pH 8. The sodium acetate recovery can be observed after pH 4. The sodium acetate recovery increases with pH and reaches the maximum values

at pH 8 while the acid concentrations reaches zero.

To sum up, salt recovery requires high pH (6 or above). In contrast, recovering acids in the free form requires low pH (3 for acetic acid and 2 for formic acid, or below). At higher pH (e.g. 4 or 5), the acetate/formate content consists of both ionic and acidic forms; therefore, extracting free form acids can require additional unit operation, such as reactive extraction.

3.3 The Effect of Temperature

As it can be observed from Figure 2 and Figure 3, temperature has minor impact on acid concentration and just noticeable impact on sodium acetate recovery. The trends with respect to pH are unaffected by temperature and the concentration or sodium acetate recovery values are close. The acid concentrations decrease with increasing pH and higher temperature causes slightly sharper decrease. In addition, sodium acetate recovery is higher at 90 °C. The recovery values are very close to each other in the other presented temperatures. Among those other temperature values, 30 °C provides slightly higher recovery. This can be expected from Figure 1 as well: the solubility of sodium acetate very slightly increase with temperature and decreases after around 60 °C. At 90 °C, the solubility is already lower than that at 30 °C. Furthermore, the sodium acetate is recovered in anhydrous form in higher temperatures that 40 °C but in trihydrate form at low temperatures (Dorn and Steiger, 2007). This fact was not included in this study but it is important to note that it is more favorable to recover the salts in anhydrous form.

As a result, 90 °C is more beneficial temperature: more salt recovery, salt in anhydrous form, and slightly more acid recovery.

4. CONCEPTUAL PROCESS DESIGN

Based on the results of this study, a preliminary process concept can be suggested for material recovery and energy integration. One option can be a single draft-tube crystallizer unit, which operates at 90 °C and pH can be adjusted depending on the desired products (acids or salts). On the other hand, under low pH, the vapour phase would contain significant amount of acids besides steam. This would rise a need for additional condensation or distillation unit to separate acids and evaporated water. In addition, the efficiency of steam utilization can be lower in this case.

More comprehensive alternative can be as shown in Figure 4, water evaporation followed by crystallization unit at high pH to recover the salt(s) and then another process unit where pH is reduced by adding acid (such as HI) to recover acids. The downstream of partial wet oxidation is at high pH, which is favorable for the recovery process. This stream can be concentrated by water evaporation in a flash (or multistage flash) and can go to the crystallizer. The crystallizer can recover sodium salts and high pH prevent acid in vapour form. Then, acids can be recovered by lowering pH. For the current, sodium acetate/formate system, the crystallizer can recover sodium acetate at high pH (8-9) and 90 °C (in anhydrous form). Then, lowering pH in another unit would provide the recovery of formic acid. In addition, the outlet steam of flash and crystallizer can be utilized in the parts of pulping process which require energy or in a CHP plant to produce electricity.

5. CONCLUSION

Integrated biorefinery concepts are getting more important to produce biofuels, energy and chemicals.

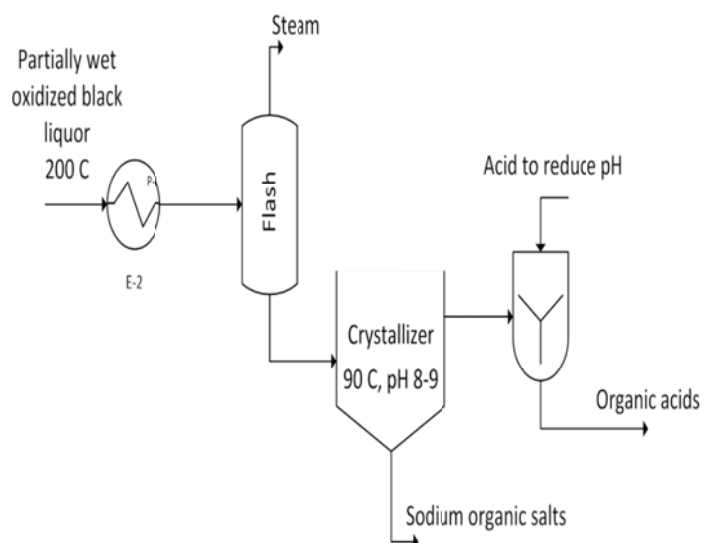


Figure 4. A preliminary process block diagram

Investigating alternative utilization of black liquor is crucial part of this field due to its lignocellulosic content. Partial wet oxidation is able to produce organic acids or salts. Therefore, this study investigates the crystallization of two of the major salts with respect to pH, temperature and the prior water evaporation rate.

This study presents relatively simple model for species distribution and it can be improved easily. In contrast, the software simulations (such as Aspen Plus) uses very complex models for activity coefficients and physical properties. Therefore, it can be challenge to provide necessary input data for those simulations.

This study can be extended by adding other major organic salts (sodium lactate and glycolate) and carbonate system the feed composition, and investigating suitable activity coefficient model.

It can be observed that pH has the major influence and temperature has minor

effects. In addition, water evaporation is required to enable the salt recovery. Temperature can be selected based on energy integration situation in the whole process. However, different pH values are required for salt recovery and acid recovery.

These results lead to a recovery process which involves first separation of salts at high pH and forming acids by lowering pH. In addition, preventing acid in vapour form is important for more efficient utilization of outlet steam.

REFERENCES

- Dorn, J., Steiger, 2007. Measurement and calculation of solubilities in the ternary system $\text{NaCH}_3\text{COO}+\text{NaCl}+\text{H}_2\text{O}$ from 278 K to 323 K. *J. Chem. Eng. Data*, 52(5), 1784
- Fournier, P., Oelkers, E. H., Gout, R., Pokrovski, G., 1998. Experimental determination of aqueous sodium-acetate dissociation constants at temperature from 20 to 240°C. *Chemical Geology*, 151(1-4), 69
- Kim, M. H., Kim, C. S., Lee, H. W., Kim, K., 1996. Temperature dependence of dissociation constants for formic acid and 2,6-dinitrophenol in aqueous solutions up to 175°C. *Journal of the Chemical Society, Faraday Transactions*, 92, 4951
- Mudassar, R., Melin, K., Sarada, K., Koskinen, J., Hurme, M., Kallas, J., 2012. Novel treatment method for black liquor and biomass hydrolysate by partial wet oxidation. *Proceedings of the 4th International Symposium on Energy from Biomass and Waste, Venice, November 12-15.2012.*
- Yaws, C. L., 2012. *Yaws' Handbook of Properties for Aqueous Systems*. Knovel

DISINTEGRATION&STABILIZATION OF MECHANICALLY DEWATERED INDUSTRIAL SLUDGE THROUGH SEMICONDUCTOR BASED HETEROGENEOUS & THIN FILM METHODS

Can Burak Özkal^{1,a}, Yayla Sezgin², -Tolga Tunçal¹ and Orhan Uslu³

1. Namık Kemal University, Environmental Engineering Department, Tekirdağ, Turkey
2. Namık Kemal University, Institute of Natural and Applied Sciences, Tekirdag, Turkey
3. Yeditepe University, Engineering Faculty, Civil Engineering Department, Istanbul, Turkey
a. Corresponding author (cbozkal@nku.edu.tr)

ABSTRACT: Photocatalytic sludge disposal experiments carried out with constant individual photon flux values of varying UV irradiation spectrums (UV-A, UV-B, UV-C, UV-Vis) through thin film and heterogenous photocatalysis methods (TFPC and HPC respectively). Thin film coated quartz substrates (TFCQS) prepared with sol-gel derived dip coating method using Titanium (IV) n-butoxide precursor. Photocatalysis applied through exposure of mechanically dewatered industrial treatment sludge samples (MDITS) to UV irradiation between two TFCQS. Photocatalytic effects on disintegration and stabilization efficiencies of the sludge samples were determined based on variations of sludge drying rate, unit power requirement (UPR) and reduction of the volatile suspended solids (VSS). Structure, size, band gap, film thickness and phase content by XRD, AFM, TEM and spectrophotometric analysis. Obtained results reveal that, simultaneous sludge drying and stabilization could be achieved through photocatalysis by disintegration of MDITS via nano-particles thus UPR is reduced consequently. Our initial results proposed that photocatalysis may become a promising and novel technology for sludge treatment sector.

1. INTRODUCTION

Since residual treatment sludge consists large amount of organic and inorganic pollutants it is generally classified as hazardous wastes. Primary components of sludge management are stabilization (reduction of organic matter (OM) and pollutants) and volume reduction. Many of the conventional methods would not be sufficient to reduce sludge moisture content of %98 in raw sludge (RS) to %10 based on current legislations. [Tunçal, 2011b]. Sludge treatment starts with mechanical dewatering (MD) in which most of the free water fraction is removed. The remaining %70 moisture content of sludge after MD is not only important for sludge conveying but also important for decreasing investment and operational costs of following sludge handling units. [USEPA, 1987; Metcalf

and Eddy, 2003]. Sludge disposal units of full scale wastewater treatment plants produce sludge with persistent organic pollutant (POP) content caused by transportation of highly non biodegradable pollutants(micro pollutants-Mp) up to sludge disposal units through several treatment steps in the system [Tunçal et al., 2011].

Effects of disintegration methods on mechanical dewatering and anaerobic digestion processes have been investigated by several researchers. A literature survey highlightes that all the labour intensified on raw sludge treatment so far [USEPA, 1987].

Photocatalysis (PC) is a combination of both photochemistry and catalysis and

requires a catalyst and photon flux of light to speed up a reaction. [Serpone, vd. 1989]. In an n-type semiconductor excited with a proper light source, electrons promotes to conduction band from valence band forming (+) charged holes behind [Schiavello, 1997].

High recombination rate of photo generated $e_{cb}^- - h_{vb}^+$ pairs have an adverse effect on photocatalytic activity of TiO_2 . Reduction/oxidation processes may occur on or around the surface of photon irradiated semiconductors. The photo generated holes may have potential ability to oxidize varying substrates through electron transfer but the oxidation of water to form OH radicals being the dominant mechanism in aqueous solutions, it causes contradiction for efficient oxidative species. [Fujishima eta al., 2000]

Frequent usage of TiO_2 from variety options of semiconductors arises from it's high stability, relatively lower cost and possibility of excitation by near UV-wavelength and UV fraction of the sunlight spectra. TiO_2 mainly consists of 3 crystal phases, rutile, brookite and the anatase phase with most photocatalytic activity, resulting from lower recombination rate of electron pairs. Arised from difficulties encountered in seperating TiO_2 particles from treated aqueous solution, stabilizing TiO_2 films on a surface just became a reasonable solution. Controlling optical and physicochemical properties of the prepared films are readily obtained with applying sol gel methodology.

Main scientific approach behind this study is based on reduction of sludge bound water content using photo-catalytic processes and generating a fast drying sludge with simultaneous stabilization through organic matter removal. In this study, it's aimed to provide simultaneous

sludge drying and stabilization (reducing organic content and POPs level) by means of applying UV photocatalysis on sludge samples with TiO_2 in both powder and thin film (TF) forms.

2. MATERIALS AND METHODS

2.1. Materials

Etanol (Merck), Glacial Acetic Acid (Merck), Nitric Acid (Merck) and Titanium (IV) n-butoxide (Fluka) were of analytical grade and used as received. Other chemicals used were also of analytical or laboratory grade. Deionized water was used for all synthesis and treatment processes. KSV Nima Medium Dip Coater Unit was used to thin film fabrication. The height the substrate was withdrawn to is 5 mm above the liquid surface, the speeds of withdrawal and immersion are 100 mm min^{-1} , the time to be kept there before the program stops is 20 seconds and the stirring speed were 0% from the maximum speed during the waiting time. The vertical angel between substrate and liquid surfaces were adjusted to 8° . Luzchem ICH 2 photoreactor was used for illumination source in the photocatalytic oxidation experiments. The photoreactor equipped with sixteen 8Watt fluorescent UV A lamps providing an illuminated area of about 0.092 m^2 , of which an active area of about 0.061 m^2 have fluctuations of under 8% in the incident power. UV A and UV B power density was measured with a Luzchem power meter. $0.002 \text{ M H}_2\text{O}_2$ was used as electron acceptor.

2.2. Sol-Gel Preparation and Dip-coating Procedure

TiO_2 thin films were deposited by means of sol-gel technique. The solution was prepared as follows. Titanium (IV) n-butoxide (Fluka) was used as precursor and ethanol (Merck) as solvent. The ethanol was slowly added to titanium (IV) n-butoxide together with stirring

(S₁). A secondary solution was prepared mixing glacial acetic acid with deionized water (S₂). S₂ solution was gradually added to S₁ solution drop wise. The final solution (sol-gel) was stirred for 1 h. The molar ratios of titanium (IV) n-butoxide, glacial acetic acid, deionized water and ethanol were 1:6:9:37 respectively. The deposition process was performed in a clean room.

The temperature of the room was 20±2 °C and the relative humidity 25%. The films were grown by single stage dip-coating on quartz glass substrates. The dimensions of quartz carriers (substrates) were 50 mm in length and width dimensions. It should be also denoted that only one side of a carrier was coated by TiO₂ thin films, allowing UV light penetration onto the TF. As-prepared wet films were first annealed at 300 °C for 10 minutes. Finally, the films were calcinated at 450 °C for 3 h. The slow two step annealing sequence was applied in order to ensure adequate removal of hydrocarbons from the fairly thick wet films.

Following the sol-gel routine (after condensation and gelation steps) the gel form is exposed to a drying procedure (ends up with) xerogel sequenced by a grinding process to obtain powder material. [Brinker et al., 1989; Pierre et al., 2002]

2.3. Structural Characterization

Appearance and structure of thin film surfaces were studied with scanning electron microscopy (SEM). The SEM work was carried out with SEM, JEOL JSM 6060. Before SEM analysis samples were coated with gold to increase the conductivity. Electron micrographs from the surface were taken utilizing low voltage (5 kV) charge balance. The surface morphology of the thin films was studied using a Nanosurf Easy Scan

Atomic Force Microscope (AFM). Crystallinity, crystallite size and phase relations of the TiO₂ TF's were characterized by X-ray diffraction (XRD). Diffraction data was collected with a Rigaku D/MAX-2200/PC diffractometer utilizing Bragg–Brentano geometry and Cu-K α radiation source with monochromator in front of the X-ray detector. Based on Sherrer equation particle size values related to peak width values are calculated.

Ultraviolet–visible (UV–vis.) absorbance spectra were obtained using a SHIMADZU UV-1800 instrument. Based on absorbance-reflectance results, film thickness values are determined through Lorentz-Lorenz equations, and 0,167 and 0,192 nm for pure thin film and Ag respectively. X-ray photoelectron spectroscopy (XPS) measurements were performed on a Thermo Scientific K-ALPHA with Al-k α source operating at 12.0 kV and 3 mA. The system was calibrated at 4f7/2 binding energy. Spot size and pass energy were 400 μ m and 30 eV respectively.

2.4. Preparing Samples and Photocatalysis Mechanism Setup

For the heterogenic PC studies, amount of TiO₂ powder (%, w/w) to be dosed into sludge samples estimated on the basis of DS content (%, w/w) of the sludge sample analyzed by Presica XM60 Moisture analyzer. In order to provide homogeneity, samplings from different points of sludge are mixed mechanically in teflon watch glasses. As prepared homogenous sludge samples are dosed with % 0,1 – 1 – 5 – 10 (on the w/w basis) proportions of TiO₂ powders and a total 1,5 gr of sample spreaded&layed uniformly amongst two 50mm x 50mm x 1mm quartz substrates (QS) covering approximately the whole surface. Analogously TF *photo-catalysis* (TFPC) performed via the same procedure. Then

TF coated and uncoated QS are exposed to UV-A, UV-B, UV-C, UV-vis spectrums respectively within context of the planned studies. Laying the sample amongst two sealed QS is mainly applied to retain moisture within. For TFPC, only one side of the substrates coated with TiO₂ film and sludge sample layed among the substrates in contact with the coated surfaces. In all studies sample loaded QS instantly placed upright in the photoreactor with both sides exposed to direct UV irradiation (See Figure 1).

Based on the observations through heterogenous and thin film studies with varying UV spectrums, studies focused and fixed on UV-A wavelength and fixed interval of TiO₂ dosage in heterogenous studies. TF studies rather intensified on effects of exterior electron acceptor (EA) addition with UV irradiation. Thus %1-5-10 w/w ratio kept constant for heterogenous PC studies while pure TiO₂ film and were used for deriving effects of electron acceptor (EA) addition on drying kinetics also with VSS reduction [Tunçal, 2011].

2.5. Drying Rate & Energy Estimation

Variation in sludge drying rates and energy required to remove unit volume of water from sludge samples, determined through analysis conducted with constant amount of samples obtained from varying experimental runs. Treated sludge samples scraped along the surface of the substrates and obtained sludge layed on aluminium plates covering a specific area with a specific thickness for making drying rate & energy calculations more susceptible. Energy required to remove unit volume of water (UPR) from sludge sample is estimated through Stefan Boltzman's Law & Equation.

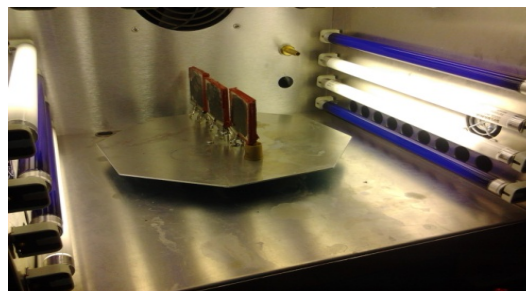


Figure 1: A view from inside the photoreactor.

3. RESULTS AND DISCUSSION

3.1. Material Analysis

Pure TiO₂ film shows absorbance values above 0.2 at 380 nm (UV A Region) that's indicative of induction of TiO₂ state and charge separation reactions on anatase TiO₂ surface (Fig. 2). It can also be stated that TF provides some UV-vis absorbance properties.

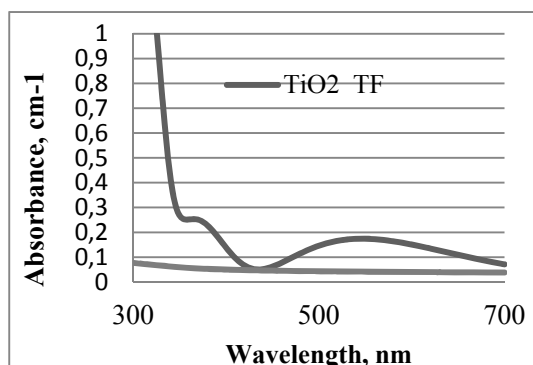


Figure 2: UV Absorbance Spectrum of uncoated QS and TF coated QS

SEM observation shows that the film surface morphologies are very smooth, homogeneous, dense and having no cracks (Figure 3). AFM was used to characterize the uniformity and particle size of films. The TiO₂ crystals exhibits spherical shape. In the present study, XPS analysis revealed that the actual binding energy positions corresponding to Ti 2p_{3/2} and Ti 2p_{1/2} lines for pure TiO₂ films were indicative of Ti³⁺ presence as the dominating Ti state, while some Ti⁴⁺ also exist in TiO₂ film.

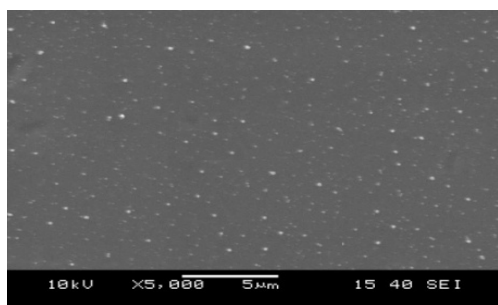


Figure 3: SEM image of TiO₂ thin film

3.2. Comparison Among Drying Kinetics and VSS Removal

As can be seen in the Figure 4, drying rate of UV-A irradiated samples are slightly lower. This phenomena may be explained by photon absorption (<400 nm) of TiO₂ nanoparticles therefore inducing the surface reactions via separated surface charges $e_{cb}^- - h_{vb}^+$. Thus smaller proportion of the UV-A energy is used for direct heating effect. TFPC in case of < 400 nm wavelengths of light exposure, led to enhances in sludge dewatering properties. TFPC reduced the UPR value of 1433 Joule/gr H₂O for raw sludge to 1120 and 1374 after treating via UV-A and UV-C PC respectively. Energy efficiency results also demonstrated that UV-A is more feasible source of UV irradiation in accordance with providing faster PC with semiconductor TiO₂. Following the UV-A absorbing properties observed from the heterogenic studies, consequent studies focused on sludge samples amongst the TFCQS's exposed to UV-A irradiation only.

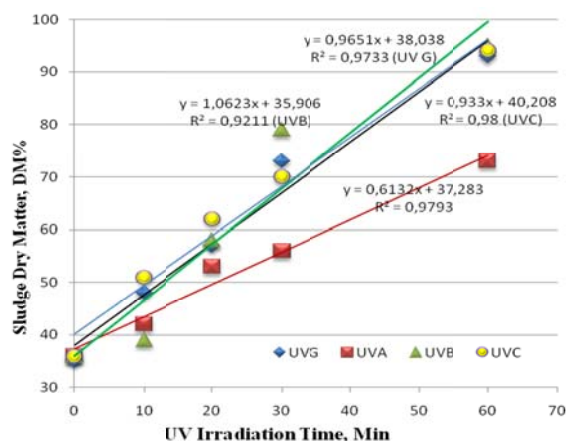


Figure 4: Effects of varying UV spectrum and duration on drying kinetics after TFPC

Varying volatile suspended solids (VSS) reductions has been observed for all wavelengths based on TiO₂ dosages. And VSS removal rate shown to be in accordance with 1st order reaction profiles. UV-C irradiation shown to provide higher VSS removal with its excessive photon energy inducing TiO₂ particles surface reaction. But its missing ability of penetrating deep into objects, solutions, slurries is a limiting factor for a possible excitation of semiconductor surface in a photon energy driven catalytic system. Taken into consideration the individual VSS removal effects of UV-B itself, UV-A found to be the most efficient wavelength for semiconductor TiO₂ based PC.

UV-A driven studies indicated that, drying time just got longer in both heterogenous and TF studies due to removal of free water while the final solids content remained constant following the non-ended mineralization of organic solids. (See Figures 5-6 respectively)

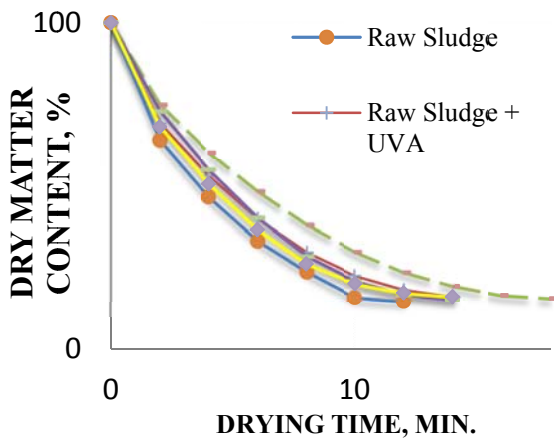


Figure 5: Effects of UV-A driven heterogenic PC studies on drying behavior of the samples.

Advances in dry matter content (DMC) arised from the conversion of organic matter to final mineralization products like $H_2O + CO_2$ that are partially removed by evaporation through TF layers during experimental runs. (Figure 6)

After H_2O_2 addition sludge dry matter raised from 10-12 % interval to upper 20 % band for TiO_2 TF studies with EA addition as can be seen from the (Figure 6). These results are in accordance with the VSS removal ratios of %40-50 as can be seen in Figure 7. Loss through VSS content of total solids gave rise to a sludge with better drying potential thus leading to an increased DMC %. Exothermic energy generated through VSS removal provided significant amount of additional drying.

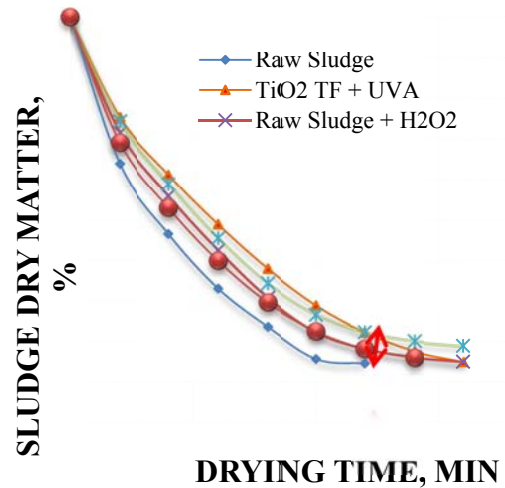


Figure 6: Effect of TFPC with EA addition on sludge drying potential in UV-A driven studies. $H_2O_2 = 0.002$ M

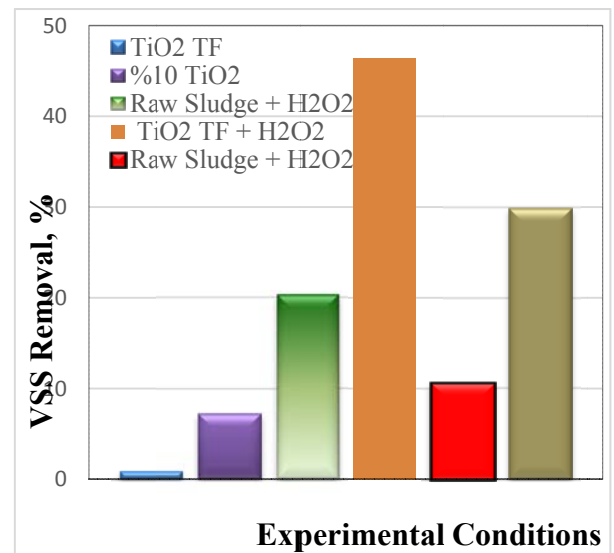


Figure 7: Effect of UV-A driven TFPC with EA addition on VSS reduction.

4. CONCLUSIONS

In this study, possibility of simultaneous drying and stabilization of industrial sludges through heterogenic and thin film photocatalysis investigated experimentally. Obtained results are indicative of possibility to achieve advanced sludge drying rates and final dry matter content with increased VSS removal with TF photocatalysis method. TF photocatalysis also outclasses

heterogenic methods with not being involved in the sludge matrix thereby causing almost no toxicity.

Minimizing the energy required for increasing the dry matter content up to 90% is another advantageous output of the method. Within context of TF methodology, shifting the absorbing properties of photocatalytic material to visible light interval should be a priority to make TF suitable for solar driven photocatalysis.

Acknowledgements: This work is founded by THE SCIENTIFIC AND TECHNOLOGICAL RESEARCH COUNCIL OF TURKEY TÜBİTAK (Project 111Y209)

REFERENCES

- Bransfield, S.J., Cwiertny, D.M., Roberts, A.L., & Fairbrother, D.H. (2006). Influence of copper loading and surface coverage on the reactivity of granular iron toward 1,1,1-trichloroethane. *Environmental Science Technology*, 40 (5), 1485-1490.
- Brezova, V., Dvoranova, D., & Stasko, A. (2007). Characterization of titanium dioxide photoactivity following the formation of radicals by EPR spectroscopy. *Research on Chemical Intermediates*, 33 (35), 251-268.
- Brinker, C. J. and Scherer, G. W., 1989, *Sol-gel Science*, Academic Press, New York.
- Centi, G., Ciambelli, P., Perathorner, S., Russo, P., *Catal. Today* 75 3–15. (2002)
- Chang, S.M., & Doong, R.A. (2006). Characterization of Zr-doped TiO₂ nanocrystals prepared by a nonhydrolytic sol-gel method at high temperatures. *Journal of Physical Chemistry B*, 110 (42), 20808-20814.
- Matos, J., Laine, J., & Hermann, J-M. (1998). Synergy effect in the photocatalytic degradation of phenol on a suspended mixture of titania and activated carbon. *Applied Catalysis B:Environmental*, 18, 281–91.
- Pierre, A.C., 2002, *Introduction to Sol-gel Processing*, Kluwer Academic Publisher, Boston.
- Robert, D., Malato, S., *Solar photocatalysis: a clean process for water detoxification*, *The Science of the Total Environment* 291 85–97, (2002)
- Schiavello, M., *Heterogenous photocatalysis*, Wiley, New York USA, (1997)
- Serpone, N., Pelizzetti, E., *Photocatalysis: Fundamentals and applications*, Wiley Canada, (1989)
- Tunçal T (b), *Improving Thermal Dewatering Characteristics of Mechanically Dewatered Sludge: Response Surface Analysis of Combined Lime-Heat Treatment*. *Water Environment Research*. 83(5), 405-410, (2011)
- Tunçal T; Jangam, S.V; Güneş, E (d). *Abatement of organic pollutant concentrations in residual treatment sludges: A review of selected treatment technologies including drying*, *Drying Technology*, DOI: 10.1080/07373937.2011.602307.
- Tunçal T., *Comparing alkaline and thermal disintegration characteristics for mechanically dewatered sludge*, *Environmental Technology*, 32:14, 1581-1588, (2011)
- US EPA, *Design manual dewatering wastewater municipal wastewater sludges*, Office of research and development, Washington DC 20460, EPA/625/1-87-014, (1987)
- Yamashita, H., Ichihashi, Y., Takeuchi, M., Kishiguchi, S., & Anpo, M. (1999). Characterization of metal ion-implanted titanium oxide photocatalysts operating under visible light irradiation. *Journal of Synchrotron Radiation*, 6, 451-452.

CAPTURE OF LOW MOLECULAR WEIGHT ORGANIC CONTAMINANT WITHIN MICELLE STRUCTURES IN MEUF

Gaye Kanaltı¹, Zeynep Traş¹, Aybike N. Olcay², Mehmet Polat¹ and Hurriyet Polat^{3,a}

1. Izmir Institute of Technology, Department of Chemical Engineering, Izmir, Turkey

2. Izmir Institute of Technology, Environmental Engineering program, Izmir, Turkey

3. Izmir Institute of Technology, Department of Chemistry, Izmir, Turkey

a. Corresponding author (hurriyetpolat.iyte.edu.tr)

ABSTRACT: Various anionic, cationic and nonionic surfactants were employed to remove Methylene Blue (MB) from water using Micellar Enhanced Ultra-Filtration (MEUF). This study demonstrates that MB can be removed from solution with efficiencies as high as 100%. However, the mechanism of capture was significantly different than that proposed in the literature. It seems that simple surfactants such as Sodium Dodecyl Sulfate (SDS) and Dodecyl Amine (DA) can only attach to MB in their molecular forms. No MB was removed from solution when these surfactant reached their Critical Micelle Concentration (CMC). The behavior was quite different for the non-ionic surfactants of higher molecular weight. It was observed that Ethoxylated Octyl Phenol (Triton X-100) and Polyethylene-Polypropylene-Polyethylene Oxide Block Copolymer (Pluronic 123) was able to remove MB from solution below and above the CMC. These findings are important in the sense that the correct mechanism of capture must be elucidated in order to custom-design surfactant for low molecular weight organic contaminants.

1. INTRODUCTION

Low Molecular Weight Contaminants (LMWCs) are an environmental concern because of their wide discharge by various industries and their difficulty in removal. Proper removal of these contaminants to the levels required by regulation for water use are either technologically troublesome or very expensive [Zeng and Li, 2011; Khosa, and Shah, 2011].

Methylene blue is a widely encountered LMWC (MW of less than 800 Dalton), whose removal is extremely problematic, especially at dilute concentrations required for water use. Water usage regulation requires that MB concentration must be lower than 1.5 ppm even for use for industrial purposes (Table 1).

Micellar Enhanced Ultra-Filtration (MEUF) has been reported as a new and novel technique to remove LMWCs from

polluted waters with success. The method is based on encapsulating organic species within larger micellar structures which were then separated from solution using ultra filtration membranes of larger pore sizes [Ghezzi and Robinson, 2008].

Table 1: Water qualities with respect to MB concentration (Ministry of Env. And Forestry).

Use of water	MB Conc. (ppm)
Drinking	0.05
Household	0.2
Industrial	1
Contaminated	>1.5

This study investigated the use of MEUF to remove MB from contaminated solutions down to drinking water levels. The study also aimed at understanding mechanism of MEUF; i.e. How the organic contaminants are removed from solution by surface active agents.

2. MATERIALS AND METHOD

2.1. Materials

The properties of the surfactants and the organic contaminant employed (Methylene Blue) are given in Table 2 and the structure of Methylene Blue is given in Figure 1.

Table 2: Selected properties of the surfactants and organic contaminant employed.

Compound	MW (D)	
Sodium Dodecyl Sulfate SDS	288	Anionic Surfactant
Dodecyl Amine DA	185	Cationic Surfactant
Ethoxylated Octyl Phenol TX-100	647	Non-ionic Surfactant
Methylene Blue MB	320	Organic contaminant

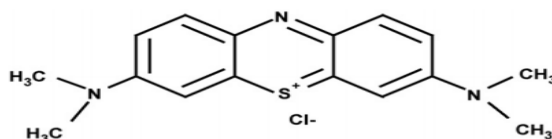


Figure 1: The structure of methylene Blue (MB) molecule.

2.2. Experimental Methods

The methods for characterization and analysis used in the study are summarized in Table 3 and the methodology employed in carrying out the experiment is shown in Figure 2.

Table 3: Analysis and characterization methods used.

Analysis	Method	Device
Surface Tension	Dü Noüy Ring	Krüss Tensiometer
Micelle Size	Laser Velocimetry	Malvern Master sizer
MB Concentration	UV Spectrophotometer	Perkin Elmer

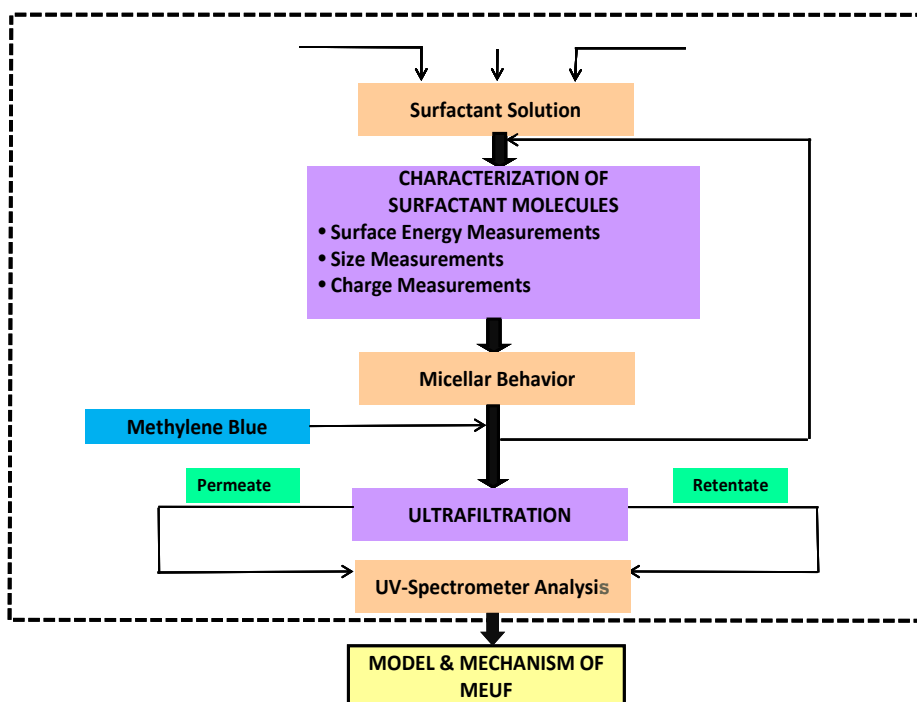


Figure 2: The methodology employed in this study.

3. RESULTS AND DISCUSSION

3.1. Surface Tension Measurements

To determine the forms of surfactant molecules as a function of surfactant concentration, the surface tension measurements were conducted and the results are presented in Figure 3 for SDS only and Figure 4 for all surfactants DA, TX-100 and P-123 together.

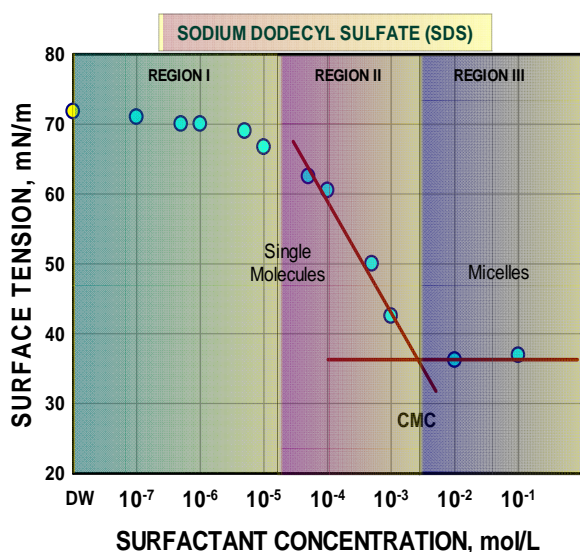


Figure 3: Surface tension results of SDS.

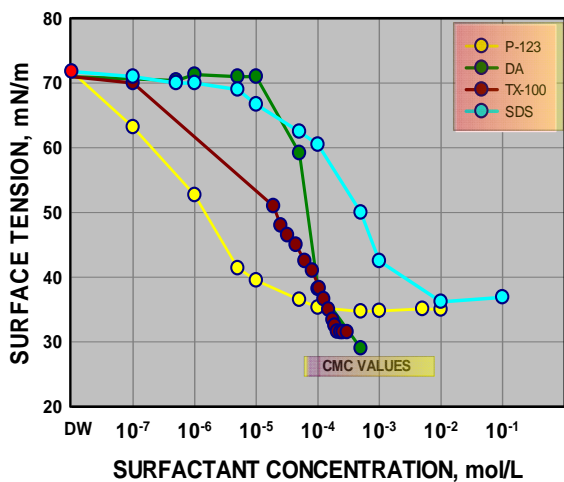


Figure 4: Surface tension results of different surfactants.

It was observed from these results that the changes in both the surface tension

values and the critical micelle concentrations (CMC) were significant. However, the lowest surface tension values obtained did not change very much.

Based on the results given above (Figure 3 and 4), the surface tension behavior for simple and polymeric surfactants could be divided into three concentration regions marked as Regions I, II and III. In the case of simple surfactants Region I and II are believed to consist principally of monomers (surface active) whereas Region III involves fully developed micelles. In the case of polymeric surfactant, P-123, however, Region II is a transition region between the two where dimers and trimers form.

3.2. Micelle Size Measurements

Micelle sizes of surfactants measured by Laser Velocimetry and presented in Figure 5 as a function of surfactant concentration and Figure 6 in the presence of contaminant (MB). These results agree perfectly with the theoretical micelle sizes in the literature which is also shown in the same figure. As it is seen the size of micelles decrease with an increase in concentration. It was found to be around 20 nm for P-123 and 10 nm for TX-100.

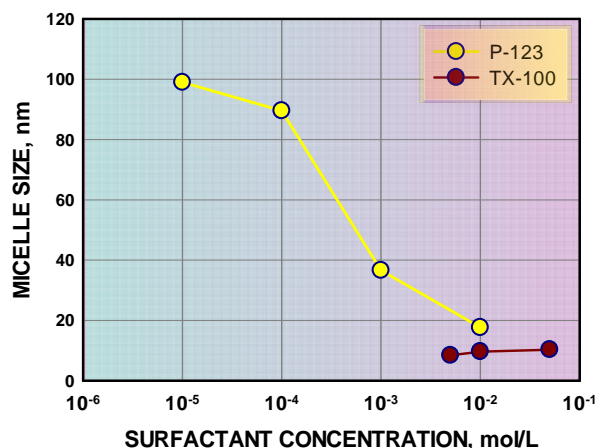


Figure 5: Micelle size of P-123 and TX-100.

However, no changes in the size of micelles were observed in the presence of the organic contaminants. These results were presented in Figure 6 for nonionic surfactants, p-123 and TX-100.

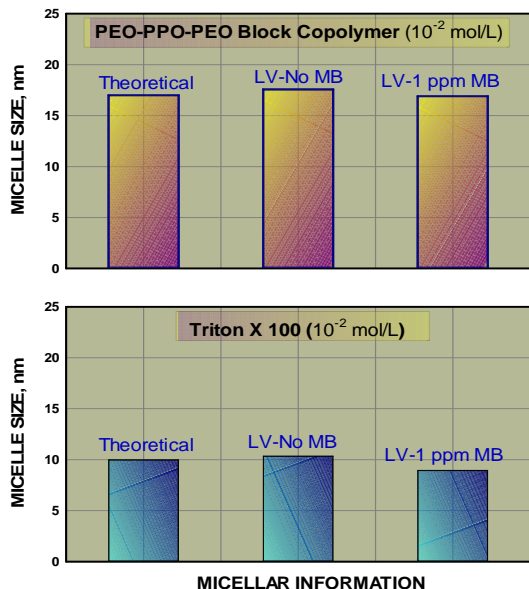


Figure 6: Micelle size of P-123 and TX-100 in the presence of MB.

3.3. MB Removal

The MB removal as a function of surfactant concentration results are presented in Figure 7. As it is seen the removal was very good with simple anionic (SDS) and cationic (DA) surfactants only below micelle concentration. It was also very high for polymeric surfactants, but both above and below CMC.

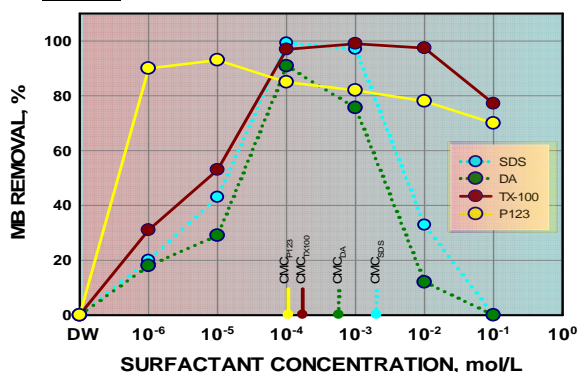


Figure 7. MB removal as a function of SDS, DA, TX-100 and P-123 concentrations.

This suggests a capture by hydrophobic parts of the surfactant molecules. However, the size measurement results shows no change in the size of the micelles in the presence of the organic contaminant (see Figure 6), therefore this work suggests that the assumption in the literature that organic contaminants are to be encapsulated within micelle structures for MEUF to work is questionable. Some other mechanism must also be responsible for removal; probably by dimers/trimers or by ionic heads of the surfactants. The exact form of capture mechanism must be further detailed at a more comprehensive study.

4. CONCLUSIONS

MEUF was very successful in the removal of the low molecular weight organic contaminant (MB) with as high as 100% removal efficiency in some cases. The removal was very good with simple anionic (SDS) and cationic (DA) surfactants only below micelle concentration. It was also very high for polymeric surfactants, but both above and below the CMC.

REFERENCES

- Zeng, G. M. And LI, X. Micellar-enhanced ultrafiltration of cadmium and methylene blue in synthetic wastewater using SDS, J.Hazard.Mater.185(2011)1304-1310.
- Khosa, S. Şah, Application of micellar-enhanced ultrafiltration for the removal of methylene blue from aqueous solution, J. Disper. Sci. Technol., 32(2011)260-264.
- Ghezzi, L., and Robinson, B. Removal and recovery of palladium(II) ions from water using micellar-enhanced ultrafiltration with a cationic surfactant.,J. Colloid Interface Sci., 329 (2008)12-17.

IDENTIFICATION AND TREATMENT OF HEAVY METALS FROM SOIL

Monica Saplonțai^{1,a}, Viorica Saplonțai¹, Roxana Trușcă² and Nicolae Bâlc¹

1. Technical University of Cluj-Napoca, Muncii Boulevard, 103-105, Cluj-Napoca, Romania

2. S.C.Metav-Research Development S.A., Bucharest, Romania

a. Corresponding author: monica_saplontai@yahoo.com

ABSTRACT: Due to the heterogeneous nature of the soil, several studies have focused on the interactions of heavy metals, presents in the soil, and the others constituents. Remediation of contaminated soils and removing the metals from contaminated soils are very costly and arduous tasks. As an alternative, in situ chemical immobilization is less costly than evacuating and filling the land, and provides a long-term solution to fix it, through the formation of stable and/or precipitated metallic minerals. The aim of this study is to identify the heavy metals from the soil (Baia Mare area, Romania) and to test the effects of treating the soil with hydroxyapatite. Determination of heavy metals from soil, it was done according to SR ISO 11047: 1998, ISO SR 11466: 1999, with Atomic Absorption Spectrophotometer and scanning electronic microscopy (Quanta Inspect F with EDAX). It has been identified Pb, Cd, Cu and Zn. Exchange capacity of metals has been reported for Cd^{2+} , Zn^{2+} and Cu^{2+} . HA has a greater affinity for Pb^{2+} . Apatites reactivity for Pb, Cd, Cu and Zn, has the following order: synthetic>biological>mineral. It is therefore necessary to examine the status of soil contamination with heavy metals and to assess their impact on the environment.

1. INTRODUCTION

It is well known that heavy metal contamination not only directly affects the physical and chemical properties of the soil, but reduces soil biological activity and decreases the availability of nutrients. Also represents a serious threat to human health by entering the food chain through water and soil.

Soil contamination with heavy metals is quite serious in some areas of Romania. Therefore, it is necessary to study the degree of heavy metal contamination in soil and assess their impact on the environment. Most studies on heavy metal contamination and environmental impact assessment of heavy metal begins with determining its spatial distribution [Cattle *et al.*, 2002].

In general, concentrations of pollutants can show complex spatial patterns, with high value and a high variation

coefficients. Therefore, it is difficult to detect polluted areas than a critical level, even if the data were collected from a large number of observation points. [Hendficks Franssen *et al.*, 1997]. This demonstrated that most soil properties may affect the spatial distribution of heavy metals [Lu *et al.*, 2003], [Banat *et al.*, 2005].

It can be said that soil properties, in general, seem to be correlated each other level [Goovaerts and Webster, 1994], [Webster *et al.*, 1994], [Dobermann *et al.*, 1995], [Dobermann *et al.*, 1997], [Castrignano *et al.*, 1998], [Castrignano *et al.*, 2000]. Some authors found that soil particle size plays an important role in the accumulation of heavy metals and fine grained soil often show high concentrations of heavy metals. [Williams *et al.*, 1994], [Rae *et al.*, 1997].

Remediation of contaminated soil and removal of metals from contaminated soil is very expensive and difficult. As an alternative, in situ chemical immobilization is less expensive than evacuation and filling of land and offers a long-term solution to address the formation of stable metallic minerals and/or precipitates [Vangronsveld and Cunningham, 1998]. Decrease in metal solubility and therefore their mobility reduces the risk of transport of heavy metals from contaminated soils in groundwater and surface water.

Environmental pollution in Baia Mare has left its mark on the health of the population. Thus, studies on the risk groups on pollution with lead, cadmium, arsenic indicated values for the concentration of pollutants in the human body that have exceeded the indicator reference levels especially lead (blood lead analysis is the main parameter to indicate the concentration of lead in the human body). The aim of this study is to identify the heavy metals from the soil (Baia Mare area, Romania) and to test the effects of treating the soil with hydroxyapatite.

2. MATERIALS AND METHODS

To analyze the current situation of soil quality in Baia Mare, 6 samples were taken from the soil from the affected area, of which 2 are taken outside the area affected by the operation (5, 6 control samples). Soil treatment was done with hydroxylapatite (HAP) that was obtained by wet chemical methods (precipitation) from CaCl_2 (Sigma-Aldrich) and Na_2HPO_4 (Sigma-Aldrich) as raw materials. [Saplontai *et al.*, 2012].

For determination of the pH, soil samples were prepared according to ISO 10390/2005- glass electrode in 1:5 (volume fraction) by Multiparameter Analyzer 255 HI laboratory.

Determination of heavy metals from soil, it was done according to SR ISO 11047:1998, ISO SR 11466:1999, with flame Atomic Absorption Spectrometer (GBC 932 AB PLUS) and scanning electronic microscopy (Quanta Inspect F with EDAX). External surface, morphology and structure of soil before and after treatment HA, were visualized by Scanning Electron Microscopy (SEM) and the chemical compositions were determined by the EDAX (Energy Dispersive Analysis of X-Rays) method using a QUANTA 133 Electron Microscope (FEI Company).

To determine the load soil contaminants in Baia Mare Depression is a long-term monitoring and analyzing heavy metals (Pb, Cd, Cu, Zn, Ni) in full form.

3. RESULTS AND DISCUSSION

The behavior of the chemical elements in soil is dictated mainly by its composition, of physico-chemical properties (such as pH and redox conditions), and the reaction of process such as absorption and precipitation / co-precipitation.

These characteristics determine the chemical bonds between elements and their distribution in the soil phases and components (fractions) system. With regard to all these considerations it is evident that the process of synthesis of HA plays a role. We have studied apatite powder with a specific surface and crystallinity appropriate [Saplontai *et al.*, 2012] by simple and inexpensive procedures without heat treatment, giving the minimum solubility of exposure to the natural elements.

In terms of pH, the samples analyzed (Fig 1), except the two control samples of soil (5 and 6) are characterized by a very acid pH.

Control soil samples have a neutral character. In this area, the pH values are between 4.5 and 6.3. (Fig. 1)

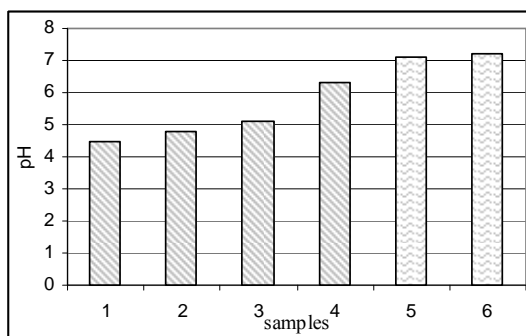


Figure 1. Values pH for samples

Soil quality in some points investigated, exceeds the normal values of heavy metals, but are below the alert and intervention threshold defined by Order 756/97, as shown in Table 2.

High concentrations of heavy metals in soils, with a low pH, are likely to increase the uptake of heavy metals by plants and humans, which presents a high risk to the health of people who consume contaminated agricultural products. In Table 1 are presented the concentrations of heavy metals in soil samples, taken before treatment with HAP.

Table 1. Values metal concentrations in samples

Samples	Concentration mg/l				
	Pb	Zn	Cu	Cd	Fe
1	50.35	35.52	25.62	0.8	8760
2	31.66	22.73	16.36	0.50	10953
3	60.66	29.4	23.43	0.67	19020
4	53.33	32.5	25.4	0.46	3280
6	-	25	8.66	0.80	6270
7	-	22	6.23	0.70	2467

Control soil samples (9 and 10), taken from a distance of 100 cm and 150 cm from the mining area, has a very low content of heavy metals, compared with samples of soil from perimeter of the two

points studied. This suggests that there is no obvious contamination of soils with heavy metals in the vicinity of the two companies.

Statistical data on the content of heavy metals from soil samples shows a very large variation in concentration, depending from the pedogeochemical ground place of collection. The main source of heavy metal pollution in the studied area, is the useful substance, brought to the surface by the mining process. Forms and amounts of soil where was found heavy metals, depend predominantly for natural or anthropogenic processes from sampling area. Individual soils with heavy metals were classified into three groups were classified into three groups according to the source and genesis, which were defined based on morphology, mineralogy and/or chemical composition. Each of these groups is characterized by a special combination of soil bearing heavy metals. The first group is characterized by existing minerals in the soil, the second group of ground-bearing heavy metals that would not be recognized as minerals and the third group, consisting of the common mineral rock. Figure 2 shows the SEM images of soil samples taken and identifying the composition of these samples by EDX .

Although this method of identification of heavy metals in soil is not a classical and usually method, the main problem arises in the identification and quantification of light elements due to absorption of X-rays from heavy metals. It is noted that the estimation of pollutants in soil can be identified by several methods of analysis. Traces of heavy metals from soil, such as Pb, Cu, Fe, Zn, Cd, also show a slightly larger value in almost all locations compared to the control samples. Pb, toxic element is present in almost all

locations. In the control sample are absent.

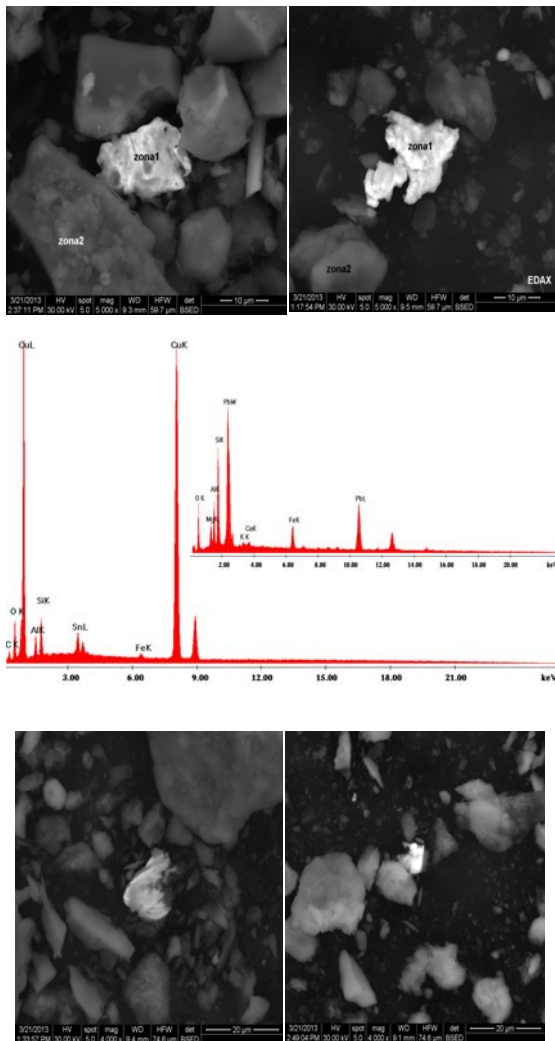


Figure 2. SEM and EDX images a) samples untreated with HAP; b) samples treated with HAP, dried at room temperature.

4. CONCLUSIONS

We studied the soil pH and heavy metals were identified by atomic absorption spectroscopy and scanning electron microscopy by EDX. It has been identified Pb, Cd, Cu and Zn. Exchange capacity of metals has been reported for Cd^{2+} , Zn^{2+} and Cu^{2+} . HA has a greater affinity for Pb^{2+} . Apatites reactivity for Pb, Cd, Cu and Zn, has the following order: synthetic>biological> mineral. It is therefore necessary to

examine the status of soil contamination with heavy metals and to assess their impact on the environment.

Acknowledgements: Project cofinance from Sectoral Operational Programme Human Resources Development 2007–2013; POSDRU/107/1.5/S/78534

REFERENCES

- Banat KM, Howari FM, Al-Hamad AA., 2005, Heavy metals in urban soils of central Jordan: should we worry about their environmental risks? *Environmental Research*, 97, 258
- Castrignanò A, Mazzoncini M, Giugliarini L., 1998, Spatial characterization of soil properties. *Advances in Geocology*, 31, 105
- Castrignanò A, Giugliarini L, Risaliti R, Martinelli N., 2000, Study of spatial relationships among some soil physico-chemical properties of a field in central Italy using multivariate geostatistics, *Geoder.*, 97, 39
- Cattle JA, McBratney AB, Minasny B., 2002, Kriging method evaluation for assessing the spatial distribution of urban soil lead contamination, *Journal of Environmental Quality*, 31,1576
- Dobermann, A., Goovaerts, P., George, T., 1995. Sources of soil variation in an acid Ultisol of the Philippines. *Geoderma* 68, 173
- Dobermann A, Goovaerts P, Neue HN, 1997,Scale-dependent correlations among soil properties in two tropical lowland rice fields. *Soil Science Society of America Journal*, 61, 1483
- Goovaerts P, Webster R, 1994, Scale dependent correlation between topsoil copper and cobalt concentrations in Scotland, *European Journal of Soil Science*, 45, 79
- Hendficks Franssen HJWM, van Eijnsbergen AC, Stein A, 1997, Use of spatial prediction techniques and fuzzy classification for mapping soil pollutants. *Geoderma*, 77, 243
- Lu Y, Gong ZT, Zhang GL, Burghardt W., 2003, Concentrations and chemical speciation of Cu, Zn, Pb and Cr of urban soils in Nanjing, China. *Geoderma*, 115, 101
- Rae JE. Trace metals in deposited intertidal sediments. In: Jickells TD, Rae JE (Eds.), 1997*Biogeochemistry of Intertidal Sediments*. Cambridge Univ. Press, Cambridge, 16
- Saplontai, M. Balc N., Saplontai V., Cojocaru I., Toth R., Moldovan M., 2012, Synthesis and characterization of nano hydroxyapatite used for immobilizing heavy metals *Review of Chemistry*, 63(12), 1228

- Vangronsveld, J.C.H.M. and Cunningham, S.D., Lepp, N.W and Mench, M. 1998. Physico-chemical aspects and efficiency of trace elements immobilization by soil amendments. In: Vangronsveld, J., Cunningham, S. D. (Eds), Metal-contaminated soils: In situ Inactivation and phytoremediation. R.G.Landes Co., Georgetown, TX, 151-182.
- Webster R, Atteia O, Dubois JP, 1994, Coregionalization of trace metals in the soil in the Swiss Jura. *European Journal of Soil Science*, 45, 205
- Williams TP, Bubb JM, Lester JN., 1994, Metal accumulation within salt marsh environments: a review. *Marine Pollution Bulletin*. 28, 277-29

PURIFICATION OF SLIME PHOSPHORIC ACID FROM Fe^{2+} CATIONS BY NATURAL ZEOLITE

G.Sh. Sultanbayeva, R.M.Chernyakova, U.Zh.Jussipbekov

Inst. of Chem. Sciences named after A.B.Becturov, Almaty, Kazakhstan,
a. Corresponding author(gitakz@rambler.ru)

The results of studies of slime phosphoric acid purification process are presented in this work. It was shown that the process of adsorption of phosphate ions as well as the iron cations by natural zeolite can be described by the Langmuir equation. The optimal conditions for sorption purification of slime phosphoric acid from iron cations are found.

1. INTRODUCTION

Phosphoric acid is used to produce phosphoric salts, it is often contaminated with cationic impurities. Furthermore, to reduce production losses slurry was added to it phosphoric acid, which are present in significant amounts of iron and aluminum. As a result, the quality of the products, in particular the sodium tripolyphosphate (STPP) is decreased. For quality products from a slurry of phosphoric acid, it must be pre-cleaning of metal impurities. First of all the iron cations that are prone to form complexes with phosphates and phosphoric acid.

Numerous methods for purifying phosphoric acid from iron cations by organic compounds. Application of the extraction method for purification of phosphoric acid is promising due to the high kinetic characteristics of the process, the ease of separation of two liquid phases, high selectivity and the possibility of a relatively complete regeneration of the extractant \square i, \square . However, at high levels of cleaning performance, the above methods for some items may not be optimal, since it does not solve the issue of utilization of organic waste, toxic chemicals, fire hazards, multiple stages.

Thus, most of the methods of purification of phosphoric acid from iron are not

effective because they based on the use of special equipment, expensive materials, reagents, and other means, leading to an increase in the cost oftreated acid, and do not meet current environmental requirements. The most appropriate way is the sorption using technologically and environmentally safe natural zeolites that have high sorption properties. The unique combination of properties - resistance to high temperatures and corrosive environments, the selectivity with respect to the large cations of alkaline earth and heavy metals, high absorptive capacity, and molecular sieve effect cause wide range of application in industry and agriculture.

2. MATERIALS AND METHODS

2.1 Materials

The objects of investigation are slime phosphoric acid (SPA) with concentration of 53,9% P_2O_5 and the concentration of (0,008%) Fe^{2+} and zeolite from Shankanaj deposit (Almaty oblast, Kazakhstan) of the following composition (wt %): K_2O : 1.38; Na_2O : 0.95; Fe_2O_3 : 0.16; Al_2O_3 : 10.81; SiO_2 : 65.28; CaO : 2.32; MgO : 0.93; losses on ignition: 18.5 is used.

2.2. Methods

General Procedure for research involves identifying the chemical composition includes a determination of the chemical composition of the zeolite samples, identifying sorption capacity of zeolite, the determination of absorbed iron zeolite and phosphate ions, the identification of the components adsorbed by physical and chemical methods of analysis.

Purification of H₃PO₄ by minimizing its metal impurities was conducted using treated zeolite in pellet.

Determination of metal cations is carried out by photolorimetric method using the Thermo Electron Corporation Spectronic Educator. The content of iron (II) in phosphoric acid solution, which was obtained after purification process, is determined with o-phenanthroline (Chempo, z.A.) [].

IR spectra of the sorbents were obtained with a double-beam infrared spectrometer Nicolet 5700 FT-IR in the range 400-4000 cm⁻¹ with samples as KBr-pellets

3. RESULTS AND DISCUSSION

The results of studies of slime phosphoric acid purification process depending on the ratio of zeolite: SPA showed that the minimum contents of iron cations in acid observed at low consumption of zeolite (S:L=5-10:100). Degree of removal reaches 85,5-86,0% and remains practically constant over the all time interval (Fig. 1, curve 1). During the time of contact phosphoric acid with zeolite the degree of purification drops to 81.46%.

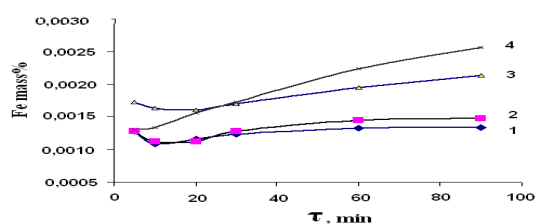


Fig.1: Removal of iron (II) depending on time of the process:

1- S:L=5:100; 2- S:L=10:100; 3- S:L=20:100; 4- S:L=30:100

At S:L = 20:100 after 20 minutes of sorbent acid mixing the degree of removal is reduced to 73.29%. In the case of using maximum quantity of zeolite there is a uniform increase of iron content in the acid with the process duration (Fig 1, curve 3), and the degree of purification, respectively, decreased to 67.98%.

The resulting sorption isotherm of iron (II) is satisfactorily described by the Langmuir equation. Sorption isotherm of iron (II) in the coordinates of the Langmuir equation is a straight linear, cotangent of the angle which corresponds to the am- limiting value of the specific adsorption of iron cations in SPA which is 0.980 mmol/g.

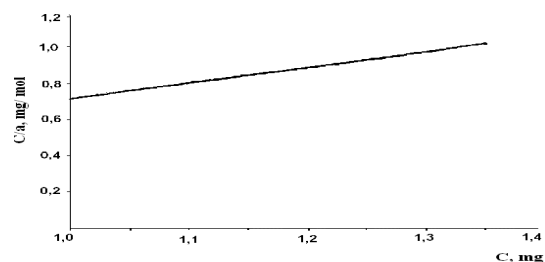


Fig. 2: Sorption isotherms of Fe by zeolite

The process of adsorption of phosphate ions as well as the iron cations are described by the Langmuir equation and has its adsorption isotherm obtained from the limiting value of the specific adsorption, which is 0.499 mmol/g (Fig.3). The value of phosphate ions sorption is less 2 times than specific adsorption of iron cations (0.980 mmol/g). This indicates that the zeolite has a preferred sorption capacity for iron, thereby creating conditions of minimum absorption of phosphate ions from the acid.

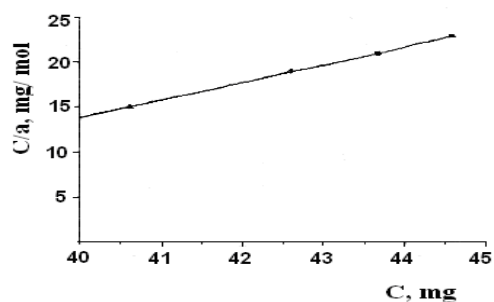


Fig. 3: Sorption isotherms of phosphate ions by zeolite

Thereby, the optimal conditions for sorption purification of slime phosphoric acid from iron cations, in which the quality of SPA on P₂O₅ not reduced, and the residual content of Fe²⁺ in it is 0.00112%, which corresponds to the phosphoric acid type A according to GOST 10678-76.

REFERENCES

- Patent USA #2202526. Phosphoric acid purification method from iron, lead and aluminum.
- Patent USA # 1642244. Phosphoric acid purification method from iron and aluminum.
- Standard 10678-76, Orthophosphoric acid thermal, Moscow, 1988
- Standard 10678-76, Orthophosphoric acid thermal, Moscow, 1988

REMOVAL OF COPPER FROM DILUTE SOLUTIONS USING SDS AIDED ACTIVE CARBON ADSORPTION

Karhan Özdenkci¹, Cagri Siretli¹, Hurriyet Polat² and Mehmet Polat^{1,a}

1. Izmir Institute of Technology, Department of Chemical Engineering, Izmir, Turkey

2. Izmir Institute of Technology, Department of Chemistry, Izmir, Turkey

a. Corresponding author (mehmetpolat@iyte.edu.tr)

ABSTRACT: This study investigates a novel technique for heavy metal removal from dilute waters. The basis is using a complexing surfactant to initially tie the heavy metal and then adsorption of the surfactant-metal complex onto a suitable substrate by hydrophobic attraction. The experiments investigated dilute levels of Cu (16 to 256 ppm). Active Carbon (AC) and Sodium Dodecyl Sulphate (SDS) were selected as the substrate and the surfactant. Copper removal was investigated at natural and various adjusted pH values, and in the presence and absence of SDS. Even though dilute wastewater typically causes capacity and efficiency issues, the proposed technique is more efficient in dilute solutions and has fast kinetics.

1. INTRODUCTION

Efficient and economic removal of heavy metals has become an important avenue due to progressively larger amounts heavy metals released into waters. The critical aspect in treatment for water reuse is that such treatment requires the capability to treat very dilute contaminant levels, i.e., treating large volumes to remove a unit mass of the contaminant.

Several commercial methods include reverse osmosis, precipitation, membrane processes and adsorption. However, these methods are unfeasible for large volumes of dilute waters: reverse osmosis requires very large units, precipitation has solid/liquid separation issue due to low amount of precipitate, and membrane processes become expensive due to the extensive electricity need and periodic replacement of the membrane.

Adsorption is an industrially accepted process: cheap, efficient and widely applicable method which creates less sludge. Active Carbon is a widely used adsorbent in large scales. However, the adsorption with Active Carbon becomes inefficient under low contaminant levels per unit volume.

This study investigates a novel adsorption based technique for the removal of trace amounts of heavy metals from dilute solutions. The work is based on using a complexing surfactant to initially tie the heavy metal from very dilute solutions, and then achieving adsorption of the surfactant-metal complex onto a substrate by means of hydrophobic attraction.

2. MATERIALS AND METHODS

2.1. Materials

Sodium Dodecyl Sulphate (SDS) from Sigma with 99% purity was used as the surfactant: Critical Micelle Concentration (CMC) of 8.25×10^{-3} M at 20 °C. AC from Merck was the adsorbent: Table 1 shows relevant properties. Ultra-pure water (18.2 MΩcm) was used in the solutions. Copper nitrate from Sigma was used for the copper solutions. 0.1 M and 0.01 M, nitric acid and sodium hydroxide were used for pH-adjusted experiments.

Table 1. Properties of the used AC

Parameter	Value
Loss on drying	≤ 10%
Particle size (≤100 μ)	90%
BET Surface Area	859 m ² /g
BJH Adsorption Cumulative Surface area (17 - 3000 Å)	284 m ² /g
Average pore diameter (Å)	29.94

2.2. Methods

2.2.1. Surface tension

Surface tension was measured for SDS solutions between 10⁻⁷ and 10⁻¹ M. Ring type surface tension method is used with the device Krüss K10 ST model.

2.2.2. SDS-AC adsorption

1 gr AC was placed into the bottles which include 90 ml water. The bottles were then shaken at 400 rpm for 1 hour. Next, 10 ml of SDS solutions with various concentrations were added into the bottles. These mixtures were shaken for 24 hours and filtered with 0.20 μ filters. Residual concentrations were analysed through surface tension measurements.

2.2.3. Metal removal experiments without pH adjustment

100 ml of solutions were prepared, containing 10⁻³ M SDS and 16, 32, 64, 128 and 256 ppm Cu. While the solutions were shaken at 400 rpm for 24 hours, AC was dried at 107°C. After this period, 1gr of the dried AC was added into each solution. Afterwards, the AC-SDS-metal solutions were shaken at 400 rpm. The samples from these solutions were filtered through 0.45 μ syringe filters after 1, 3, 6 and 24 hours, and pH of these filtered samples were also recorded. The residual solutions were acidified with HNO₃ (65% by volume) for the Atomic Absorption Spectrometry (AAS) analyses to determine the copper contents. Metal adsorption on AC in the absence of SDS was analysed with the same procedure.

2.2.4. pH-adjusted metal removal

1 gr of dried AC was added into the solutions containing 64 ppm copper and 10⁻³ M SDS. The pH values of the solutions were kept at 4, 5, 6, 7 and 8 by adding 0.1 M and 0.01 M nitric acid and sodium hydroxide for 3 hours of shaking. Afterwards, the samples were filtered by using the same method in metal removal experiments without pH adjustment. Furthermore, adsorption of copper on AC in the absence of SDS at pH 4, where precipitation was not an issue, was also determined through the same procedure. In addition, in order to compare the wet and dried AC, wet AC was tested as well with 64 ppm copper solution.

3. RESULTS AND DISCUSSION

3.1. Surface Tension

Figure 1 shows the SDS concentration dependence of the surface tension. CMC is observed as about 8x10⁻³ M.

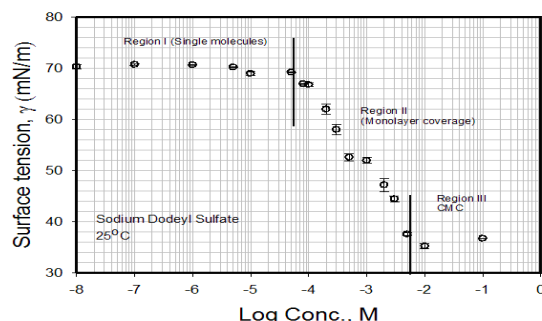


Figure 1. The surface tension at 25°C

The molecule per area at the surface is calculated by Gibbs adsorption equation;

$$\Gamma = -\frac{1}{RT} \frac{d\gamma}{d \ln C}$$

where R is gas constant, T is temperature, Γ is the surface excess concentration (mol/m²), and $d\gamma/d \ln C$ is the slope of the Region II (-6.96 mN/m). The surface excess concentration is calculated as 2.809x10⁻⁶ mol/m². Applying this value, the area at the surface was calculated as 59 Å² per SDS molecule. It was reported that the cross-section of the sulphate head group is 25 Å² [Retter et al., 2003].

Considering the electrostatic repulsion between the head groups, the parking area of SDS at the interface is higher than cross-section of the sulphate head group.

3.2. Surfactant Adsorption on AC

The surfactant adsorption is achieved by the hydrophobic attraction between alkyl chain of the surfactant and the surface of the adsorbent. However, some charges on the adsorbent surface may oppose or enhance the surfactant adsorption by electrostatic interaction.

In order to utilize the surfactant charge to singularly tie Cu species and also to use the alkyl group for attachment to AC surface, SDS molecules were treated with the dissolved Cu metal in advance in the metal removal experiments. In addition, since the surfactant molecule is tied to AC from its free alkyl chain, micelle formation can be detrimental.

The magnitude of the SDS adsorption on AC is determined by surface tension of the solutions. Figure 2 indicates that the adsorption percentage decreases with increasing initial SDS concentration.

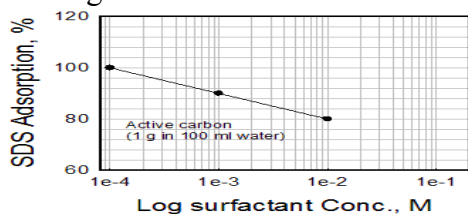


Figure 2. SDS adsorption on AC

At 10^{-1} M SDS, the surface tension of the residual solution is equal to that of region III: SDS adsorption percentage cannot be certainly defined. Similarly, adsorption percentage at 10^{-4} M of initial SDS is hypothetically assumed to be 100 %, considering the adsorption percentages at 10^{-2} and 10^{-3} M SDS.

As a result, the initial SDS concentration for metal removal experiments is chosen as 10^{-3} M. This choice is based on the highest SDS concentration with the aim of providing high surfactant-metal ratio to promise high adsorption percentage

while being below CMC. In addition, calculations regarding the surface area of AC favour 10^{-3} M SDS. Considering the adsorption of SDS onto the pores on the active carbon, the required area for 10^{-3} M SDS is calculated from the area per SDS molecule which is equal to 59 \AA^2 . For this concentration, with 90% adsorption, the parking area of the SDS molecules in 100 ml solution is 32 m^2 . As it is reported, the total length of an SDS molecule is 21.68 \AA so the pores on the active carbon having larger diameter than this value are accessible for adsorption. The surface area of the pores having diameter greater than 17 \AA is given as $284 \text{ m}^2/\text{g}$ in Table 1. Thus, it can be assumed that the suitable area of AC is sufficient for the adsorption of 10^{-3} M SDS. The adsorption capacity of AC is $9.3 \times 10^{-4} \text{ mmol}/\text{total surface area} (\text{m}^2)$. On the other hand, if the similar calculations are applied for 10^{-2} M SDS, the parking area reaches 284 m^2 for only 80% adsorption. Similarly, by using the adsorption capacity, the adsorption percentage at 10^{-1} M of initial SDS can be calculated as only 8% as maximum.

3.3. Copper Removal

Copper removal experiments are carried out both with and without pH adjustment at various initial copper concentrations. The chosen initial concentrations are based on the surfactant-metal ratio. The surfactant-metal ratios are 4:1, 2:1, 1:1, 1:2 and 1:4 corresponding to initial copper concentrations of 16, 32, 64, 128 and 256 ppm for 10^{-3} M SDS, respectively.

3.3.1. Kinetics of Copper Removal

Kinetic study of copper removal was applied at the time interval of 1-24 h without pH adjustment. The transient period of the process could not be observed: the observed data were nearly the same, thus reflecting the equilibrium. This is an indication of fast kinetics.

3.3.2. Effect of SDS-Metal ratio

The copper removal decreases with initial Cu concentration, i.e., increasing removal with increasing surfactant-metal ratio. Figure 4 shows the removal results without pH adjustment. The complete removal was achieved at 16 and 32 ppm, corresponding to surfactant-metal ratios of 4:1 and 2:1. Furthermore, at even 64 ppm, such high removal percentage was obtained as 82 %. Due to the low surfactant-metal ratio for 128 and 256 ppm, the removal remains at low values, which are 47 and 32 %, respectively.

It can be seen from Figure 4 that the solutions are progressively acidified as the initial Cu concentration increases, due to Lewis acid behaviour of Cu. Considering high pH of the filtered samples, precipitation definitely occurs in addition to the adsorption. In order to investigate the effect of pH, the experiments with pH adjustment were applied and discussed in Section 3.3.4.

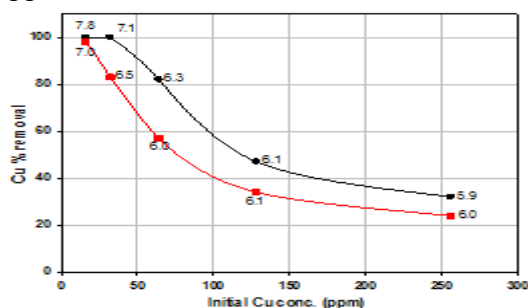


Figure 4. Copper removal with 10^{-3} M SDS (●) and without SDS (■): no pH adjustment, pH of filtered samples near the data points

3.3.3. Effect of SDS

Figure 4 indicates the effect of the presence and absence of SDS on metal removal. At high surfactant-metal ratio such as 4:1, there is no significant difference between the absence and presence of SDS. The reason of this is the fact that removal percentage even in the absence of SDS is very high due to precipitation. As the initial concentration

increases, the significant contribution of SDS to the copper removal can be observed clearly. Although the benefits of SDS on metal removal percentage decreases with the initial copper concentration, the difference in copper amounts removed from the solution with and without SDS is nearly the same for varying initial Cu concentration and lies between 16 and 20 ppm.

3.3.4. Effect of pH

The pH-adjusted experiments are implemented from the pH values which eliminate precipitation such as 4 or 5 to those leads to precipitation such as 8, considering the species distribution of copper in aqueous solution at various pH.

Due to the Lewis acid behaviour of transition metals, they form coordination complexes in aqueous solutions. This interaction of metal ions and water molecules leads to the hydrolysis reactions where coordinated water molecules are replaced by hydroxyl ions in sequencing steps due to increasing activity of the OH^- ions in solution. The proposed hydrolysis reactions of copper and their equilibrium constants are given in Table 5.

Table 5. The hydrolysis reactions and their equilibrium constants [Stumm and Morgan, 1995]

Hydrolysis reactions	K_{sp}
$\text{Cu}(\text{OH})_{2(s)} + \text{H}^+ \leftrightarrow \text{Cu}^{2+} + 2\text{H}_2\text{O}$	$10^{7.6}$
$\text{Cu}(\text{OH})_{2(s)} + \text{H}^+ \leftrightarrow \text{Cu}(\text{OH})^+ + \text{H}_2\text{O}$	$10^{-0.1}$
$\text{Cu}(\text{OH})_{2(s)} \leftrightarrow \text{Cu}(\text{OH})_{2(aq)}$	$10^{-8.6}$
$\text{Cu}(\text{OH})_{2(s)} + \text{H}^+ \leftrightarrow \text{Cu}(\text{OH})_3^- + \text{H}^+$	$10^{-19.2}$
$\text{Cu}(\text{OH})_{2(s)} + \text{H}^+ \leftrightarrow \text{Cu}(\text{OH})_4^{2-} + 2\text{H}^+$	10^{-32}

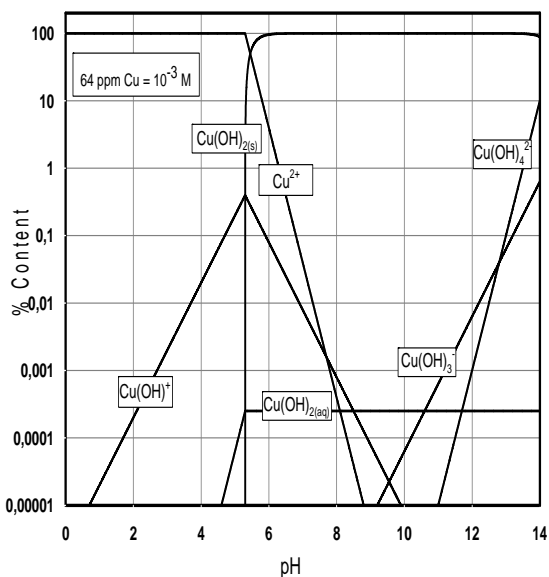


Figure 5. Copper species distribution at various pH. 64 ppm solution at 25 °C.

As shown in Table 5, Cu(OH)_2 can be present both as precipitated solid and dissolved aqueous phase. Figure 5 shows the calculated distributions for various copper species for total copper concentrations of 64 ppm at 25 °C. As shown in Figure 5, the dominant species below pH 5 is Cu^{2+} while the precipitation starts to occur after pH 5.

The results of pH adjusted experiments are shown in Figure 6. The results indicate that 39 % copper removal can be achieved by the adsorption, in the absence of precipitation and nearly all copper exist in Cu^{+2} , at pH 4. Increase in pH leads to sharp increase in the copper removal and complete removal is achieved at pH 7 and 8. This results from precipitation under high pH.

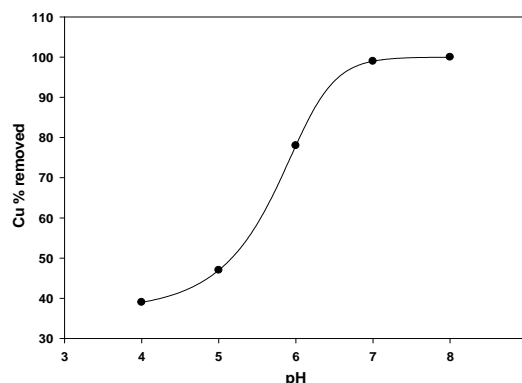


Figure 6. Copper removal at adjusted pH values from 100 ml solutions containing 64 ppm Cu, 10^{-3} M SDS and 1 g AC

Table 6. The pH-adjusted Cu adsorption:

Materials (pH 4, 64 ppm Cu, 3 hours)	Final Cu conc.	% Cu removed
10^{-3} M SDS, 1 gr AC	38.8	39
1 gr "wet" AC, no SDS	50.8	21
1 gr AC, no SDS	50.6	21

Table 6 determines the copper removal at pH 4 in the presence and absence of SDS. Similar to the results without pH adjustment, the presence of SDS enhances the adsorption capacity. In the case of SDS usage, 39 % removal is achieved whereas AC adsorbs only 21 %. The reason of 21 % adsorption in the absence of SDS is the surface functional groups on AC. Furthermore, wet AC gives no difference: it removes same amount of copper with dry AC.

4. CONCLUSION

This study investigated SDS aided copper removal from waters on hydrophobic AC substrate.

The SDS concentration for metal removal tests was selected by analysing the SDS-AC adsorption results and parking area aspect. It was concluded that 10^{-3} M SDS is suitable for 1 g AC in 100 ml solution: 90 % adsorption and sufficient surface.

The kinetics of the removal process could not been observed through time interval from 1 hour: the process has fast kinetics reaching equilibrium in shorter time.

SDS contributes to the removal due to the electrostatic attractions: copper removal increases with increasing SDS-copper ratio. Thus, higher removal is achieved under low initial copper concentrations. This is important in the sense that the proposed method performs better in more dilute solutions where the other methods have capacity and efficiency problems.

As an important parameter, the effect of pH was also investigated in order to analyse the precipitation influence. 39 % removal was observed at pH 4 excluding precipitation. The removal increases with increasing pH due to the important role of precipitation. Complete removal was achieved at high pH (7 and 8). Moreover, in the absence of SDS, AC removes 21 %

of copper at pH 4 due to the critical role of surface functional groups on AC.

REFERENCES

- Ahn, C. K., Park, D., Woo, S. H., Park, J. M., 2008. Removal of cationic heavy metal from aqueous solution by activated carbon impregnated with anionic surfactants. *Journal of Hazardous Materials*, 164 (2-3), 1130–1136
- Amarasinghe, B. M. W. P. K., Williams, R. A., 2007. Tea waste as a low cost adsorbent for the removal of Cu and Pb from wastewater. *Chemical Engineering Journal*, 132, 299–309
- Erdoğan, D., 2005. Removal of heavy metals from wastewaters by ion flotation. Thesis (MSc) İzmir Institute of Technology
- Retter, U., Tchachnikova, M., 2003. On the formation of surface micelles at the metal/electrolyte interface. *Journal of Electroanalytical Chemistry*, 550-551, 201-208
- Stumm, W., Morgan, J. J., 1995. *Aquatic Chemistry*, (Wiley-Interscience Publication)

MODIFICATION OF NATURAL ZEOLITE TO ENHANCE ITS NEUTRALIZING CAPACITY IN LACTIC ACID MEDIUM

İlker Polatoglu^{1*} and Fehime Cakıcıoğlu-Ozkan²

1. Celal Bayar University, Bioengineering Department, 45040-Muradiye Manisa

2. Izmir Institute of Technology, Chemical Engineering Department, Gulbahce Koyu, 35430-Urla Izmir

a. Corresponding author: İlker Polatoglu

ABSTRACT: The aim of this study is to investigate the enhancement of neutralizing capacity of natural zeolite by modification in lactic acid medium. For this aim zeolitic tuff from Gördes (Manisa) deposit and its modified form with Na₂CO₃ were interact with dilute C₃H₆O₃ (pH_i=4). The natural zeolite is named as low-silica clinoptilolite depending both on Si/Al ratio, cation content determined by ICP-AES and also characteristic peaks determined by X-Ray diffraction method. The characterization results also show that the total exchange capacity (TEC) increases with modification. The pH evolution results depicted that, the zeolites used in this study increased the medium pH by the possible mechanism of ion exchange and sorption. Final pH was higher when modified zeolite was used. This is because the modification made the surface rich in sodium and also with carbonate which is soluble in weak acid solution.

1. INTRODUCTION

A measure of the amount of hydrogen ions (H⁺) in a solution (pH) is one of the most important parameter in aqueous media. Its concentration affects the solubility of many substances and the activity of most systems which requires optimum proton concentration for higher efficiency [Ersoy and Çelik, 2002]. Proton concentration is very significant parameter for most processes such as water purification, waste treatment, cosmetics, electro coating, agricultural applications, pharmaceutical applications and food processing such as lactic acid fermentation. During the lactic acid fermentation processes, the pH decreases due to acid production and it is necessary to increase the medium pH between 5 and 6 for the lactic acid bacteria [Hetényi et al., 2011]. Various chemical substances such as adsorbents and ion exchangers have been used in order to adjust pH in solutions. The factors such as ion exchanger types added to adjust solution pH, their particle size, ion

concentration, cation type, hydrodynamics of the reaction system, solvent type and heat of solution can change the pH in a liquid system [Mirela et al., 2002].

In contrast to other adsorbents and ion exchangers, natural zeolites (CL) can adsorb molecules, depending on the size of the openings, thus functioning as molecular sieves [Gomonaj et al., 2000]. In addition to this tetrahedral aluminum content in the framework are responsible for the catalytic, sorptive and ion-exchange properties. CL could make a significant contribution to most process. Since many chemical processes are closely related to ion exchange, adsorption and catalysis [Kurama et al., 2002; Castellar et al., 1998]. CL can be modified according to particular interest while retaining the topology and crystallinity of the framework structure. Enrichment of CL with cations such as Na⁺, Ca²⁺ increases the ion exchange capacities of them. This type of modification can enhance its functions and increases the utility of it for various processes [Ackley et al., 2003].

Based on all of these considerations the aim of this study is to investigate the enhancement of neutralizing capacity of CL by modification in lactic acid medium. The kinetic study of pH was performed in order to yield some information about the mineral–water interactions and its buffering capacity. Characterization of solid and liquid phases was performed to explain the possible mechanism that could take place and how CL structure is affected by these interactions.

2. MATERIALS AND METHODS

In this study, sedimentary zeolitic tuff from Gördes Manisa) deposit and its modified form was used to analyze their neutralizing capacity in lactic acid medium. CL were ground and dry sieved to obtain the fraction between 38-106 μm . CL was modified by using 0.5 M Na_2CO_3 solution with a solid liquid ratio of 1:2 for 1h. 5 g of the obtaining materials CL* and CL were interacted with dilute $\text{C}_3\text{H}_6\text{O}_3$ ($\text{pH}_i=4$) in order to investigate their neutralizing capacity. These experiments were carried out in a shaker (GLF 1092) with a shaking rate of 200 rpm by using 744 Metrohm pH meter. CL, CL* and acid treated zeolites were characterized with various techniques, including ICP-AES (Varian ICP 96), XRD (Philips X-Pert Pro), (FTIR FTS3000MX), TGA (Shimadzu 51/51H), and Zeta sizer (3000 HAS).

3. RESULTS AND DISCUSSIONS

The characterization results show that the total exchange capacity (TEC) of CL and CL* represents the amount of exchangeable cations (Na^+ , K^+ , Ca^{2+} , and Mg^{2+}) was found as 2.77 and 3.79 meq/g respectively, determined by ICP-AES. TEC was very high for CL* due to the rich Na^+ content of zeolitic material. The amount of Na^+ ions increased while the

other cations decreased after the modification as shown in the Figure 1.

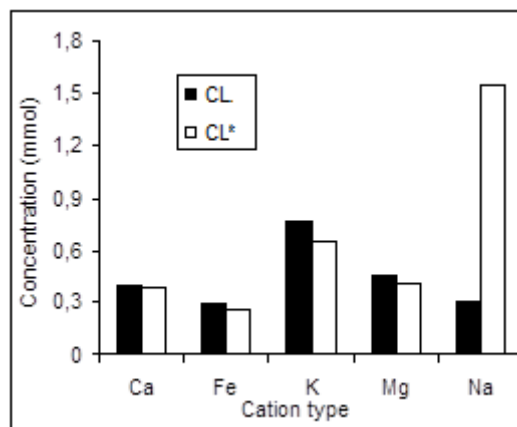


Figure 1: The concentration of cations in CL and CL*

However there was no balance between the increased and the decreased amount the cations. This shows not only ion exchange but also outer-sphere complexation of Na^+ with surface functional groups occurs as a result of modification. The Si/Al ratio of CL and CL* was found as 3.83 and 3.82 respectively. Modification of CL is not effective on Si/Al ratio but on TEC. Depending both on Si/Al ratio and cation content [Tsitsishvili et al. 1992] CL is named as low-silica clinoptilolite.

X-Ray diffraction of CL and CL* also shows the characteristic peak of clinoptilolite at 9.8° and 22.3° (marked as CL in Figure 2). Besides this some new peak corresponding to the albite high ($\text{Na}[\text{AlSi}_3\text{O}_8]$) (at 27.57° , 28.56° , 28.83° , 2θ) and sodium aluminum oxide ($\text{Na}_7\text{Al}_3\text{O}_8$) (the peak at 36.03° 2θ) was observed on the pattern of CL*.

The other methods FTIR and TGA were used in order to understand the changes in CL structure resulting from modification.

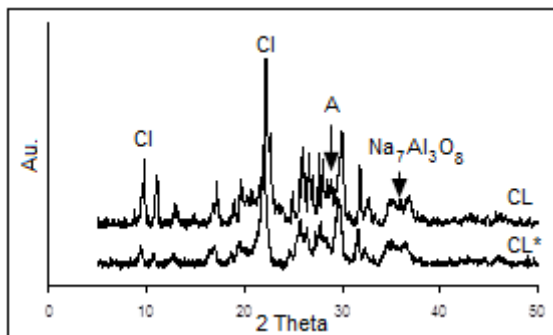


Figure 2: Crystal structure of CL and CL*.

In FTIR analysis shown in Figure 3 the main band observed at 1498 cm^{-1} for Na_2CO_3 detected as small vibration on CL*.

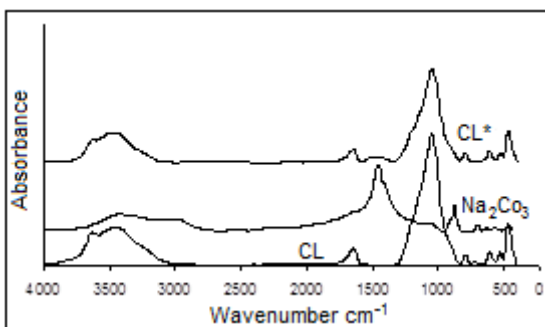


Figure 3: IR spectra of Na_2CO_3 , CL and CL*.

Decomposition of carbonate can be observed from the peak in the thermal gravimetric analysis between $600\text{--}710\text{ }^\circ\text{C}$ as shown in Figure 4.

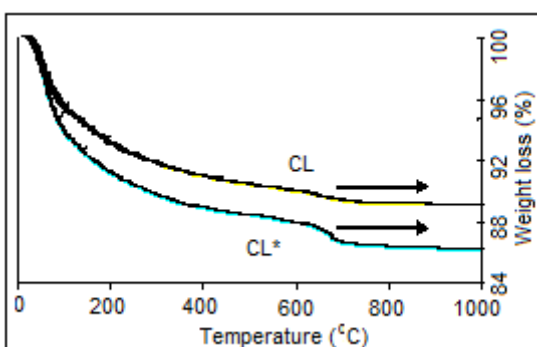


Figure 4: TGA curves of CL and CL*.

The pH evolution results showed that (Figure 5), the pH of 100 ml dilute $\text{C}_3\text{H}_6\text{O}_3$ ($\text{pH}_i=4$) reach the equilibrium in

very short time depicted in the inset of Figure 5 (9 min.) after the interaction between 5 g of zeolitic tuff (CL or CL*_s). The final pH (pH_f) was recorded as 7 and 10 respectively shows all the protons in solution were consumed by CL and CL*_s.

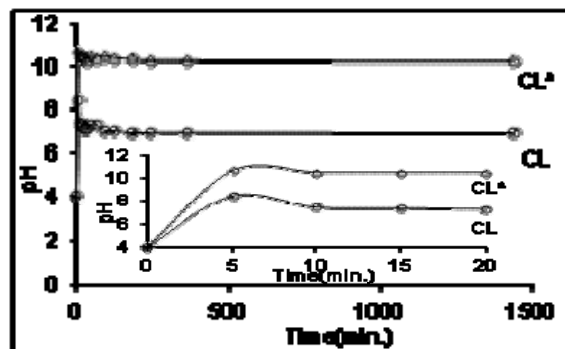
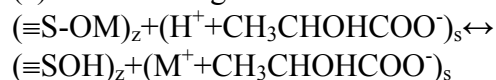


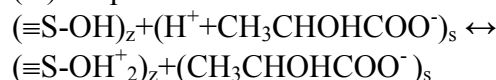
Figure 5: pH evolution of lactic acid solution in the presence of CL and CL* ($\text{pH}_i=4$).

Possible mechanisms between lactic acid and CL are given below:

(a) Ion exchange:



(b) Sorption:



In the mechanism (a) exchanged cation amount increases and not effective significantly on pH increase. In the second mechanism, the formation of protonated surface by sorption causes considerable decrease in proton concentration. By means of sorption the inner and/or outer surface complexation, precipitation (as sodium or calcium acetate) can occur. Final pH is higher for CL*. This is because the modification made the surface rich in sodium. Therefore exchanged sodium was high for modified zeolite as shown in Table 1. After lactic acid treatment CL and CL* were coded as CA and CA* respectively.

Table 1: Composition of exchangeable cations in starting (CL, CL*) and acid treated (CA and CA*) zeolites (mmol/g).

Codes	Na	K	Ca	Mg	Fe
CL	0.30	0.77	0.39	0.46	0.29
CA	0.29	0.76	0.38	0.45	0.28
CL*	1.55	0.65	0.38	0.41	0.26
CA*	1.22	0.64	0.37	0.37	0.25

The surface was rich also with carbonate which is soluble in weak acid solution CL* was analyzed after lactic acid interaction. The crystal structure did not change after the treatment as shown in the Figure 6.

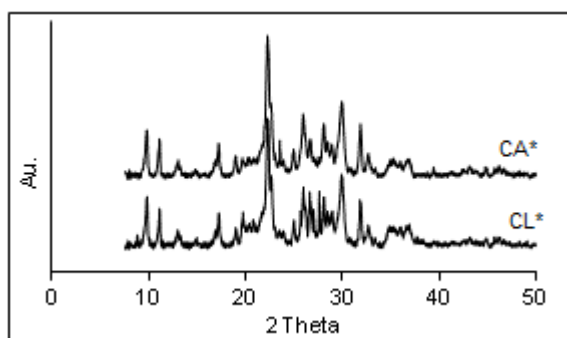


Figure 6: X-ray diffraction patterns of CL* and CA*.

4. CONCLUSIONS

Modification of CL enhances its neutralizing capacity (pH_f increases from 7 to 10) without changing its structure. However these pH values are not acceptable for lactic acid fermentation

media. The solid/liquid content should be optimized for this aim.

REFERENCES

- Ackley, M.W., Rege, S.U., Saxena, H., 2003. "Application of Natural Zeolites in The Purification and Separation of Gases", *Microporous and Mesoporous Materials*, 61, 25.
- Castellar, R.M., Aires-Barros, M.R., Cabral, M.S.J., Iborra, J.L., 1998. "Effect of Zeolite Addition on Ethanol Production from Glucose by *Saccharomyces Bayanus*", *J. Chem. Technol. Biotechnol.*, 73, 377.
- Ersoy, B., and Çelik, M.S., 2002. "Electrokinetic Properties of Clinoptilolite with Mono-and Multivalent Electrolytes", *Microporous and Mesoporous Materials*, 55, 305.
- Gomonaj, V., Gomonaj, P., Golub, N., Szekeresh, K., Charmas, B., Leboda, R., 2000. "Compatible Adsorption of Strontium and Zinc Ions as well as Vitamins on Zeolites", *Adsorption Science & Technology*, 18, 295.
- Hetényi, K., Németh, A., Sevelia, B., 2011. Role of pH-regulation in lactic acid fermentation: Second steps in a process improvement, *Chemical Engineering and Processing: Process Intensification*, 50: 293
- Kurama, H., Zimmer, A., Reschetilowski, W., 2002. "Chemical Modification Effect on The Sorption Capacities of Natural Clinoptilolite", *Chemical Engineering Technology*, 25, 301.
- Mirela, R., Stefanovic, S.C., Curkovic, L., 2002. "Evaluation of Croatian Clinoptilolite- and Montmorillonite-Rich Tuffs for Ammonium Removal", *Croatica Chemica Acta*, 75, 255.
- Tsitsishvili, G.V., Andronikashvili, T.G., Kirov, T.G., Filizova, L.D., 1992. "Natural Zeolites", Ellis Horwood, New York.

SECTION D
Biological and Medical Aspects

IMPORTANCE OF POROUS AND COLLOIDAL STRUCTURES IN BIOMEDICAL APPLICATIONS

Emir Baki Denkbaş^{1,a}, Cem Bayram², Doğa Kavaz¹, Tamer Çırak²,
Murat Demirbilek³

¹Hacettepe University, Chemistry Dept., Biochemistry Div., Ankara, Turkey

²Hacettepe University, Nanotechnology and Nanomedicine Div., Ankara, Turkey

³Bayındır Hospital, Microbiology Labs., Ankara, Turkey

a. Corresponding author (denkbas@hacettepe.edu.tr)

ABSTRACT: Biomaterials are artificially constructed materials and devices which used for assistancy or replacement of any function of living system using biomimicking approaches. We can use the biomaterials for different type of biomedical applications such as tissue engineering, drug delivery, prosthetic devices etc. In all cases, we have to simulate the natural tissues and organs based on their structure and functions. At this point, when we look at the morphology of the tissues, we can see that there is a porous matrix (i.e., extracellular matrix, ECM) for the cellular activities. On the other hand, we can transport the nutrients and metabolites by using some globular structures i.e., some macromolecules or nano scale materials. Therefore, briefly we can summarize that the porous and the colloidal shape of the biomaterials are dominant structures for the living systems. In this presentation, some of the biomedical applications such as wound dressing materials, tissue engineering scaffolds, surface treatments of biomedical devices, different applications for drug and/or any other active agent transport will be discussed based on the importance of porous and colloidal structures of the applied biomaterials.

1. INTRODUCTION

During the production of any biomaterials we have to be inspired by nature. At this point, especially biological infrastucture was constructed as an extended network of very small units and these networks are typically porous and the porous structure of the living organisms make possible to breath and to circulate the natural fluids in their body. This structure also gives an opportunity for heat insulation in living organisms. Additionally porous structure provides two critical functions: one of them related with migration abiltiy of the cells through the pores and second one is specific interactions of the cells with biomaterials. Here the porosity can be in the form of micro-, meso- or macropores. On the other hand another special morphology of the biological components is colloidal shape or geometry especially for the transportation of the biomolecules and other molecules in living system. We can simulate these kind of carriers

especially for the drug delivery and/or any other component transportation in living system as an artificial carrier. In this presentation some of the examples of porous and colloidal biomaterials will be presented. Those examples covers wound dressing materials, tissue engineering scaffolds, surface treatments of biomedical devices, different applications for drug and/or any other active agent transport etc. and they can be summarized as following subsections.

1.1. Wound Dressing Materials

Wound healing process is a dynamic one which can be divided into three phases as inflammatory phase, proliferation phase and maturation phase. Those phases are realized at different time periods, for example the inflammatory phase takes around ten days after traumatic events. Cell proliferation and matrix deposition phase or period begins after first day and takes almost a month. Inflammation and cell

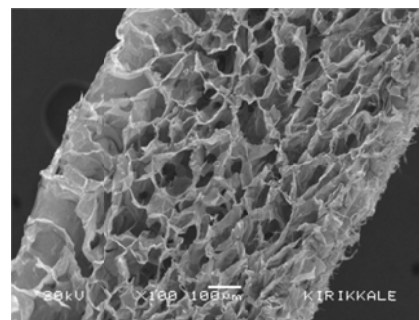
proliferation/matrix depositions occur parallelly between the first and ten days. Finally, maturation phase or matrix remodelling period begins at the time of maximum response of cell proliferation/matrix deposition phase and sometimes it takes around a year [Harding *et.al.*, 2002].

In the inflammatory phase, the blood flow allow essential cells, antibodies, white blood cells, growth factors, enzymes and nutrients to reach the wounded area. Afterwards, during the proliferation, new granulation tissue which is comprised of collagen and ECM, the angiogenesis is developed. Healthy granulation is dependent upon the fibroblast sufficient levels of oxygen and other nutrients supplied by the blood vessels. Maturation as the final phase involves remodelling of collagen type III to type I [David 2009].

Briefly in all phases the healing tissues need some cell migration and material transport to complete the healing mechanisms. Here the critical thing is that wound healing is not linear and often wounds can progress both forwards and back through the phases depending upon intrinsic and extrinsic forces at work within the patient [Wayne *et.al.*, 1998].

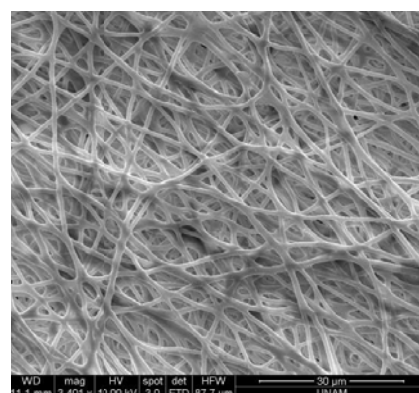
The biomaterials which can be used in the treatment of wound healing called as wound dressing materials. Generally these materials are included the porous and hydrogel structures. Additionally in last decades due to the developments of drug/active agent (i.e., cytokines or growth factors etc) delivery systems those dressing materials have some ingredients to facilitate the wound healing mechanisms. On the other hand these kind of ingredients have very short half-life, therefore the researchers are tried to encapsulate/load these agents into the micro or nanoparticles within the dressing materials to keep their bioactivities during the treatment periods. Some examples were given in Figure 1 and 2 for the representation of micro and

nanostructures for wound healing scaffolds [Keçeci, 2007; Karahaliloğlu, 2009].



A

Figure 1: SEM picture of alginate/ chitosan scaffolds



B

Figure 2: SEM picture of PHB nanofibers

Another very important subject is related with the infection risks during the wound healing treatments. It is possible to overcome this problem by using some molecules against to infections such as antibiotics, silver nanoparticles, nitric oxide etc. Controlled release of these agents would decrease the number of doses required to achieve the desired clinical effect, potentially reducing the risk of development of antibiotic resistance [Schaffer *et.al.*, 1997; Barraud *et.al.*, 2009; Moghmi *et.al.*, 2001; Jain *et.al.*, 2009; Widgerow, 2010].

In last decades, the researchers focussed on the engineered networks for wound dressing materials to get good cell adhesion, proliferation and differentiation mimicking the fibrous architecture of the extracellular matrix. The favorable technique is electrospinning for this

purpose and the large surface area and porosity of electrospun nanofibers enables good permeability for oxygen and water and the adsorption of liquids, and concomitantly protects the wound from bacterial penetration and dehydration. This feature shows electrospun nanofibers to be a suitable material for wound dressing materials [Trana *et.al.*, 2009; Khil *et.al.*, 2003; Wang *et.al.*, 2008].

1.2. Tissue Engineering Applications

The main goal of tissue engineering is to repair damaged or malfunctioned tissues by biocompatible materials alone or incubating with relevant cell types. Material selection for extracellular matrix preparation for tissue engineering application and fabrication technique of scaffold has critical importance on biological adaptation and functionality. Safety and biocompatibility tests are crucial to identify biological response obtained by material nature. In addition to biocompatibility and cytotoxic properties, biological effects of degradation products of materials are very important for in vivo applications. 3-dimensional scaffold will perform as a host for cells to form target tissue and in general this core materials are used temporarily during healing process. To prevent the foreign body reactions biodegradable materials are favored as scaffold backbones, which will be transformed into non-cytotoxic degradation sub-units.

Moreover, mechanical properties, porosity, orientation of prepared 3 dimensional porous shape of polymeric matrix have importance regarding to application type and target tissue. Biodegradable polymers like PDLLA have broad application fields because of their excellent and controllable mechanical strength, biocompatibility and safety properties.

Surface chemistry and topography of scaffolds have big importance for cellular adherence and growth. To increase biocompatibility and activity of tissue

engineered scaffolds; there is a high demand on modification or coating of surfaces of prepared polymeric structures or loading of particular systems onto surface. Feng *et al.*, indicated that magnetic nanoparticles trapped within cell-encapsulating gelatin hydrogels to create novel nanobiomaterials for three dimensional cell culture. Release of magnetic nanoparticles from hydrogels was investigated and no cytotoxic effect observed on released magnetic nanoparticles [Xu *et.al.*, 2012].

Especially, active agents can be loaded into particles to control the release kinetics of drugs or hormones and these particles bind chemically or physically to scaffolds during scaffold preparation process or post-process. Surface modifications or coatings are intended for increasing cell-scaffold compatibility and cellular interactions and also decrease the cytotoxicity. In our recent study, EDA (ethylene diamine) plasma modification of PDLLA scaffolds caused to decrease the oxidative stress on L929 fibroblast cells in contradiction to non-modified PDLLA scaffolds [Demirbilek, 2011].

Nowadays, popularity of nanofibers is increasing due to their ease of fabrication and controllable orientation. With electrospinning technique by using nanofibers, very oriented, 3 dimensional porous scaffolds are prepared, which are ideal materials to be used as scaffolds for tissue engineering, because of their nanoscale infrastructure which is very similar to target tissue and high surface-area volume ratio, which provide free surface for cells for binding of protein and membrane receptors [Karahaliloğlu *et.al.*, 2013].

1.3. Surface Treatments of Biomedical Devices

Material properties for an implant device can be briefly divided into two main titles as “bulk” and “surface”. Since the biocompatibility phenomena is mainly

related with the outer surface, the latter one – surface properties – become much more important for implant devices. Biological interactions with body fluids occur at the interface and the consequences of these interactions are the deterministic factors of the implant fate.

Porosity and pore size of implant surface is a critical point in bone formation. Implant surfaces should mimic the bone structure in scale and morphology for a better match and integration [Liu and Webster, 2007]. Bone structure is composed of two major constituent as hydroxyapatite and collagen. In cancellous bone porosity ratio changes in between 50 - 90%, whereas this ration does not exceed 30% in cortical bone.

In the very first seconds after the implantation the device is surrounded by body fluid and protein adsorption begins. Protein adsorption is a key feature for the *in vivo* tissue compatibility and healing since the adhered proteins have the mediating and regulating roles for cell attachment [de Jonge *et.al.*, 2008]. It is known that the surface roughness (increased surface area) and porosity is important in surface wettability [Papenburg *et.al.*, 2010]. Nanotube-like structures obtained by anodic oxidation also have more surface area and more reactive sites for initial protein interactions.

Metallic implants have been exposed to a vast of surface modifications such as etching, sandblasting and plasma spray in order to alter surface porosity. The obtained microporosity (<10 µm) was found as an enhancer for initial cell adhesion, proliferation, alkaline phosphatase activity and calcium containing mineral deposition [Anselme *et.al.*, 2002; Boyan *et.al.*, 2001]. Additionally, it is reported that the microporous titanium shows an osteoconductive nature, whereas smooth surfaces does not. Surface chemistry and material type changes may generate

undefined results but different topography of same material and chemistry is approved universally to have certain effects on cell response. In this context, many of the treatments above have been applied on metallic orthopaedic devices in the market.

Peri-implantitis is one of the major complications in the post-op period for orthopaedic and cardiovascular surgeries. Although sterile and aseptic conditions take place in the orthopaedic implantation procedure, infection risk changes in between 0.5% and 5%, whereas this ratio elevates to 14% after revision surgeries [Zilberman and Elsner, 2008]. Estimated cost for a single patient is foreseen as 50000 USD and the mortality ratio is 2.5% [Lentino, 2003]. Implant based infections are typically occurred by biofilm forming microorganisms especially Gram positive *Staphylococcus aureus* and *Staphylococcus epidermis* [Trampuz *et.al.*, 2003]. High dose antibiotic therapy is applied to the patient to overcome this problem. However, bacteria get much more resistance 10 to 1000 fold–against antibiotic penetration in biofilm structure [Campoccia *et.al.*, 2006].

Conventional, - oral and intervenous - routes both have the well-known disadvantages such as systemic toxicity, hepatic degradation and low effectivty of the targeted area. Because of these problems a rapid and site effective drug activity must be established at the relevant area. Drug releasing from the implant device without any coating material is a new topic for the local release of active agent and the porosity of the metal surface plays a key role in this subject [Yao and Webster, 2009]. Polymer or ceramic coating free drug loading can be possible if adequate space take place on implant surfaces.

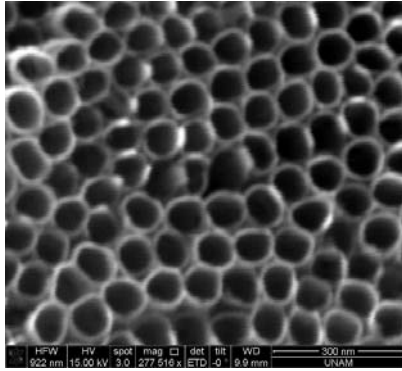


Figure 3: Nanotube shaped titania surface layer (aerial view)

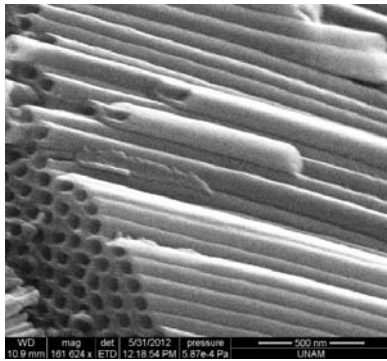


Figure 4: Nanotube shaped titania surface layer (side view)

In the last five years, biomolecule loading on anodized titanium surfaces have been reported in many studies [Peng *et.al.*, 2009; Ma *et.al.*, 2012; Gulati *et.al.*, 2012]. A porous layer consisting of nanotube shaped cavities can be generated on titanium surface with anodic oxidation procedure and the aspect ratio of this structural entities can be tuned with process parameters (Figure 3, 4) [Bayram, 2013]. Drug release ratio and time are directly related with the nanotube length and diameter and the pioneer work conducted by Peng and colleagues shows the paclitaxel drug – a common antiproliferative agent for the prevention of restenosis – can be released from titanium surfaces in several weeks without any barrier layer [Peng *et.al.*, 2009]. *In vitro* tests also showed that the bacterial adhesion decreases with loaded drug loading. Popat *et al.* showed that gentamicin loaded titania surfaces via

simple pipetting reduces *S. epidermis* by 40% [Popat *et.al.*, 2007].

1.4. Drug Delivery Systems

The aim of a delivery system is to transport the required amount of drug towards targeted region and to achieve the desired drug concentration [Wang *et.al.*, 2006].

Dose dumping and drug stability are the major disadvantages of conventional drug delivery systems. Hence, to address these problems, there is a need for smart materials in drug delivery applications, and nature offers an excellent solution.

Various drug delivery carriers can be used in this field such as liposomes, micelles, emulsions, hydrogels and polymeric micro or nanoparticles [Torchilin, 2005; Azarmi *et.al.*, 2008; Zhang *et.al.*, 2007].

Beside these materials, porous structures are frequently preferred. Especially the use of porous materials to encapsulate drug compounds in order to obtain steady drug release profiles has attracted much attention. Porous materials are classified based on their pore sizes as micro porous material, meso porous materials, macro porous materials and giga porous materials [Zdravkov *et.al.*, 2007].

Pore size is preferable according to the application. Thus, variable pore size is an obstacle that must be overcome. Moreover, these easily synthesized or designed materials are much attractive in various application fields [Li and Zhang, 2007].

Porosity occupies an important place in drug delivery systems. It can be affected by changing the size, shape and surface structure or other mechanical properties of material [Crofts and Park, 1995]. Porous materials contain external pores and internal pores which are interconnected to each other.

Most drugs can be dissolved or dispersed inside the core or can be attached to the material surface. Drug release kinetics are

controlled by surface phenomenon while sustained release depends on the penetration depth which is determined by the porosity [Colilla *et.al.*, 2007]. Thus, the kinetics of drug release are related to the pore size and pore size distribution of the material used. According to the surface based phenomenon, organized porous carriers contain large inner surface area, which allow the adsorption of large amounts of drugs or biomolecules. This idea also facilitates the solubility of poorly soluble drugs [Wu *et.al.*, 2011].

Many materials are utilized for the synthesis of porous carriers. Polymers such as poly lactic acid, poly (lactic-co-glycolic acid) (PLGA), chitosan, have been used as carriers for diagnostic and therapeutic agents.[Mora-Huertas *et.al.*, 2010]. Drug encapsulating polymer system is one of the most widely examined technologies to eliminate unnecessary drug dosing by altering parameters like polymer/drug ratio. Consequently, pore size can be varied with these parameters. In the past decade, biocompatible and biodegradable polymers have been reported in many studies. Moreover, they provide a desirable therapeutic environment with optimal response, minimum side effects and prolonged efficacy.

Bayram et al. prepared triamcinolone acetonide-loaded PHBHx microspheres, size varying between 50- 200 μm (Figure 5). They optimized the size and the size distribution of microspheres by changing stirring rate of the dispersion medium, emulsifier concentration and polymer/solvent ratio. Triamcinolone acetonide was dispersed into the polymer solution before the microspheres preparation and was encapsulated within the microspheres. The release studies indicated that, system had a slower release rate that 90 % of drug was released within 24 h [Bayram *et.al.*, 2008].

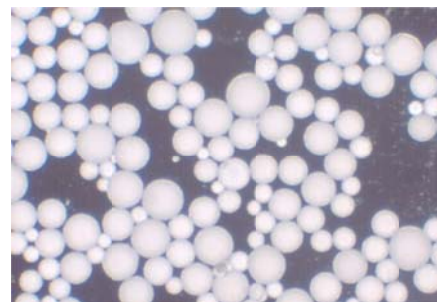


Figure 5: Optical micrograph of PHBHx microspheres.

Also, surface modifications of the carriers like micro or nanoparticles can be derivatized which would allow specific biochemical interaction with the proteins and receptors [Patrick Vlieghe and Michel, 2013; Zhao and Goldman, 2013]. Kılıçay et al., reported that they immobilized vitamin folic acid which has high affinity through the folate receptor that overexpresses on many human epithelial cancer cell surfaces such as uterus, colon, lung and ovary cancer, on the poly (3- hydroxybutyrate-co-3-hydroxyhexanoate nanoparticles to achieve active targeting of drug [Kılıçay *et.al.*, 2011]. Additionally, Kavaz et al. prepared iron oxide nanoparticles to be used to prepare antineoplastic agent loaded lectin attached biocompatible nanoparticles for targeted drug delivery systems [Kavaz *et.al.*, 2010] (Figure 6).

In other words, both covalent and noncovalent surface modification of polymer based micro or nanocarrier systems are capable in use of various applications such as imaging of *in vitro* and *in vivo* systems, cell-specific uptake studies, high capacity loading and delivery of both hydrophilic and hydrophobic drugs to the targeted region [Kim *et.al.*, 2006].

Instead of polymers, inorganic materials such as silica, hydroxyapatite or starch based components can be used [Peng *et.al.*, 2010; Li *et.al.*, 2008; Zhang *et.al.*, 2010; Yunpeng *et.al.*, 2013].

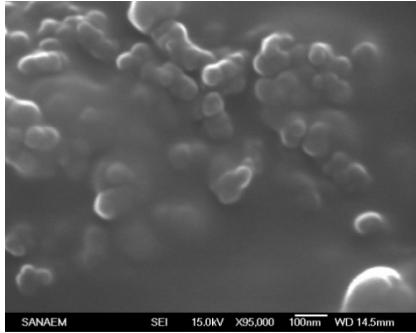


Figure 6: SEM micrograph of iron oxide, Fe₃O₄ nanoparticles.

Porous inorganic materials show high chemical and mechanical stability. Hydrophilic character and porous structure can be tailored to control the diffusion rate of an adsorbed or encapsulated drug, gene, or protein.

Hydroxyapatite is biocompatible, non-toxic, and have osteoconductive ability which is often used in orthopedic applications [Cheng *et.al.*, 2009]. Paul and Sharma reported that they mixed hydroxyapatite with a chitosan solution, and in order to stabilize the surface and the shape of the microspheres, glutaraldehyde was used as surfactant. Porous microspheres were obtained with pores consisting of chitosan in the hydroxyapatite structure [Paul *et.al.*, 1999].

Jain et al., compared floating carriers to non- floating microspheres *in vitro*. The derived calcium silicate based microspheres which have organized porous structures demonstrated *in vitro* floating character and had an effective release behavior. Release profiles showed that carrier systems easily compressed in to tablets or filled into capsules as an alternative drug delivery systems [Jain *et.al.*, 2006].

Acknowledgements: The authors acknowledge the grants provided by Hacettepe University, Scientific Researches Unit and TUBITAK.

REFERENCES

- Anselme K., Bigerelle M., Noel B., Iost A., Hardouin P., 2002, Effect of grooved titanium substratum on human osteoblastic cell growth. *J. Biomed. Mater. Res.* 60: 529-540.
- Azarmi S., Roa W.H., Lo benberg R., 2008. Targeted delivery of nanoparticles for the treatment of lung diseases. *Adv Drug Deliv Rev.* 60:863–875.
- Barraud, N., Schleheck, D., Klebensberger, J., Webb, J.S., Hassett, D.J., Rice, S.A. and Kjelleberg, S., 2009. Nitric Oxide Signaling in *Pseudomonas aeruginosa* Biofilms Mediates Phosphodiesterase Activity, Decreased Cyclic Di-GMP Levels, and Enhanced Dispersal. *Journal of Bacteriology*, 7333–7342.
- Bayram, C., 2013. Functionalization of metallic orthopedic implants, PhD. Thesis, Hacettepe University, Ankara, Turkey.
- Bayram C., Denkbaş, E.B., Kiliçay, E., Hazer, B., Çakmak, H.B., Noda, I., 2008. Preparation and Characterization of Triamcinolone Acetonide-loaded Poly(3-hydroxybutyrate-co-3-hydroxyhexanoate) (PHBHx) Microspheres, *Journal of Bioactive & Compatible Polymers*, 23: 334.
- Boyan B.D., Lohmann CH., Sisk M., Liu Y., Sylvia V.L., Cochran D.L., Dean D.D., Schwartz Z., 2001, Both cyclooxygenase-1 and cyclooxygenase-2 mediate osteoblast response to titanium surface roughness. *J. Biomed. Mater. Res.* 55: 350-359.
- Cai Y., Chen, Y., Hong, X., Liu Z., Yuan, Z., 2013. Porous microsphere and its applications, *International Journal of Nanomedicine*, 8, 1111-1120.
- Campoccia D., Montanaro L., Arciola C.R., 2006, The significance of infection related to orthopedic devices and issues of antibiotic resistance. *Biomaterials*, 27, 2331–2339.
- Cheng X.K., He Q.J., Li J.Q., Huang Z., Chi R., 2009. Control of pore size of the bubble-template porous carbonated hydroxyapatite microsphere by adjustable pressure. *Cryst Growth Des.*, 9(6):2770–2775.
- Colilla M., Balas F., Manzano M., Vallet-Regí M., 2007. Novel method to enlarge the surface area of SBA-15. *Chem Mater.*, 19:3099–3101.
- Crotts G., Park T.G., 1995. Preparation of porous and nonporous biodegradable polymeric hollow microspheres. *J Control Release.*, 35(2–3):91–105.
- de Jonge L.T., Leeuwenburgh S.C.G., Wolke J.G.C., Jansen J.A., 2008, Organic-Inorganic Surface Modifications for Titanium Implant Surfaces. *Pharmaceutical Research* 25: 2357-2369.
- Demirbilek, M.E., Demirbilek, M., Karahaliloglu, Z. Erdal, E., Vural, T. Yalçın, E., Sağlam, N. Denkbaş, E.B., 2011. Oxidative Stress

- Parameters of L929 Cells Cultured on Plasma-Modified PDLLA Scaffolds. *Appl Biochem Biotechnol.*, 164: 780-792
- Gulati K., Ramakrishnan S., Aw M.S., Atkins G.J., Findlay D.M., Losic D., 2012, Biocompatible polymer coating of titania nanotube arrays for improved drug elution and osteoblast adhesion, *Acta Biomaterialia*, 8, 449-456.
- Harding, K.G., Morris, H.L., Patel, G.K., 2002. Healing chronic wounds. *BMJ*, 324:160–163.
- Jain J., Arora S., Rajwade J.M., Omray P., Khandelwal S., Paknikar K.M., 2009. Silver nanoparticles in therapeutics: development of an antimicrobial gel formulation for topical use. *Mol Pharm.* 6 (5), 1388-401.
- Jain, S.K., Agrawal, G.P., Jain, N.K., 2006. A novel calcium silicate based microspheres of repaglinide: In vivo investigations, *Journal of Controlled Release*, 113, 111–116.
- Karahaliloğlu Z., 2009. Preparation and characterization of biopolymeric scaffolds in nanofibrillar structure, MSc Thesis, Hacettepe University, Ankara, Turkey.
- Karahaliloglu, Z. Demirbilek, M., Şam, M., Demirbilek, M.E., Sağlam, N., Plasma Denkbaş, E.B., 2013. Polymerization-Modified Bacterial Polyhydroxybutyrate Nanofibrillar Scaffolds. *J. Appl. Polym. Sci.* DOI: 10.1002/APP. 38370.
- Kavaz D., Odabaş S., Güven E., Demirbilek M., Denkbaş E.B., 2010. Bleomycin Loaded Magnetic Chitosan Nanoparticles as Multifunctional Nanocarriers, *J Bioact Comp Pol*, 25:3, 305-18.
- Keçeci, K., 2007. Preparation and characterization of cell-biopolymeric matrix composites to use in the treatment of bladder diseases, MSc Thesis, Hacettepe University, Ankara, Turkey.
- Khil, M.S., Cha, D., Kim, H.Y., Kim, I.S., Bhattarai, N., 2003. Electrospun Nano-fibrous Polyurethane Membrane as Wound Dressing. *J Biomed Mater Res Part B:Appl Biomater*, 67B: 675– 679.
- Kim H.K., Chung H.J., Park T.G.. 2006. Biodegradable polymeric microspheres with “open/closed” pores for sustained release of human growth hormone. *J Control Release*, 112(2):167–174/)
- Kılıçay, E., Demirbilek, M., Türk, M., Güven, E., Hazer, B., Denkbaş, E.B., 2011. Preparation and characterization of poly(3-hydroxybutyrate-co-3-hydroxyhexanoate) (PHBHHX) based nano- particles for targeted cancer therapy, *European Journal of Pharmaceutical Sciences*, 44, 310–320.
- Lentino J.R., 2003, Prosthetic joint infections: Bane of orthopedists, challenge for infectious disease specialists. *Clin Infect Dis*, 36, 1157–1161.
- Li J., Zhang Y., 2007. Porous polymer films with size-tunable surface pores. *Chem Mater.*, 19(10):2581–2584.
- Li Z.H., Jia Z., Luan Y.X., Mu T.C., 2008. Ionic liquids for synthesis of inorganic nanomaterials. *Curr Opin Solid State Mater Sci.*, 12(1):1-8.
- Liu H. and Webster T.J., 2007, *Bioinspired Nanocomposites for Orthopedic Applications*. In: *Nanotechnology for the Regeneration of Hard and Soft Tissues*, Webster TJ (ed.) World Scientific Publishing Co. Pte. Ltd., Singapore, pp 8.
- Ma M., Kazemzadeh-Narbat M., Hui Y., Lu S., Ding C., Chen D.D.Y., Hancock R.E.W., Wang R., 2012, Local delivery of antimicrobial peptides using self-organized TiO₂ nanotube arrays for peri-implant infections, *J Biomed Mater Res Part A: 100A: 278–285*.
- Moghimi, S.M., Hunter, A.C. and Murray, J.C., 2001. Long-Circulating and Target-Specific Nanoparticles: Theory to Practice. *Pharmacol Rev.*, 53 (2), 283-318.
- Mora-Huertas, C.E., Fessi, H., Elaissari, A., 2010. Polymer based nanocapsules for drug delivery. *Int. J. Pharm.* 385, 113–142.
- Papenburg B.J., Rodrigues E.D., Wessling M. Stamatialis D., 2010, Insights into the role of material surface topography and wettability on cell-material interactions. *Soft. Matter.* 6, 4377.
- Paul W. and Sharma C.P., 1999. Development of porous spherical hydroxyapatite granules: application towards protein delivery. *J Mater Sci Mater Med.*, 10(7):383–388.
- Peng C.Y., Zhao Q.H., Gao C.Y., 2010. Sustained delivery of doxorubicin by porous CaCO and chitosan/alginate multilayers-coated CaCO microparticles. *Colloids Surf A Physicochem Eng Asp.*, 353(2–3):132–139.
- Peng L., Mendelsohn A.D., LaTempa T.J., Yoriya S., Grimes C.A., Desai T.A., 2009, Long-Term Small Molecule and Protein Elution from TiO₂ Nanotubes, *Nano Letters*, 9, 1932-1936.
- Popat K.C., Eltgroth M., LaTempa T.J., Grimes C.A., Desai T.A., 2007, Decreased Staphylococcus epidermis adhesion and increased osteoblast functionality on antibiotic-loaded titania nanotubes, *Biomaterials*, 28, 4880-4888.
- Schaffer, M.R., Efron, P.A., Thornton, F.J., Klingel, K., Gross, S.S. and Barbul, A., 1997. Nitric oxide, an autocrine regulator of wound fibroblast synthetic function. *The Journal of Immunology*, 158: 2375-2381.
- Simpson, D.M. and Ross, R., 1972. The neutrophilic leukocyte in wound repair: A study with antineutrophil serum. *Journal of Clinical Investigation*, vol. 51, no. 8, pp. 2009–2023.
- Singer, A.J. and Clark, R.A.F., 1999. Cutaneous wound healing. *New England Journal of Medicine*, 341:738-746.

- Stadelmann, W.K., Digenis, A.G., Tobin, G.R., 1998. Physiology and Healing Dynamics of Chronic Cutaneous Wounds. *Am J Surg.*, 176 (Suppl 2A), 26S–38S.
- Torchilin V.P., 2005. Recent advances with liposomes as pharmaceutical carriers. *Nat Rev Drug Discov.*, 4:145–60.
- Trampuz A., Osmon D.R., Hanssen A.D., Steckelberg J.M., Patel R., 2003, Molecular and antibiofilm approaches to prosthetic joint infection, *Clin Orthop Relat Res*, 69–88.
- Trana, P.A., Zhang, L., Webster, T.J., 2009. Carbon nanofibers and carbon nanotubes in regenerative medicine. *Advanced Drug Delivery Reviews*, 61, 1097–1114
- Vlieghe, P. and Khrestchatsky, M., 2013. Medicinal Chemistry Based Approaches and Nanotechnology-Based Systems to Improve CNS Drug Targeting and Delivery, *Medicinal Research Reviews*, 33, No. 3, 457–516.
- Wang C., He C., Tong Z., Liu X., Ren B., Zeng F., 2006. Combination of adsorption by porous CaCO₃ microparticles and encapsulation by poly electrolyte multilayer films for sustained drug delivery. *Int J Pharm.*, 308:160–7.
- Wang, C.C., Su, C.H., Chen, C.C., 2008. Water absorbing and antibacterial properties of N-isopropyl acrylamide grafted and collagen/chitosan immobilized polypropylene nonwoven fabric and its application on wound healing enhancement. *J Biomed Mater Res*, 84A: 1006–1017.
- Widgerow A.D., 2010. Nanocrystalline silver, gelatinases and the clinical implications. *Burns*. 36 (7), 965-74.
- Wu C., Wang Z., Zhi Z., Jiang T., Zhang J., Wang S., 2011. Development of biodegradable porous starch foam for improving oral delivery of poorly water soluble drugs. *Int J Pharm.*, 403(1–2):162–169.
- Xu, F., Inci, F., Mullick, O., Gurkan, U. A., Sung, Y., Kavaz, D., Li, B., Denkbaş, E.B., Demirci, U., 2012. Release of Magnetic Nanoparticles from Cell-Encapsulating Biodegradable Nanobiomaterials. *ACS Nano*, Vol. 6 , No:8, 6640-6649
- Yao Ci and Webster T.J., 2009, Prolonged Antibiotic Delivery From Anodized Nanotubular Titanium Using a Co-precipitation Drug Loading Method, *J Biomed Mater Res Part B: Appl Biomater* 91B: 587–595.
- Zdravkov B., Čermák J.J., Janků J., Kučerová V., Šefara M., 2007. Pore classification in the characterization of porous materials. *Central European Journal of Chemistry*, 5(2):385–395.
- Zhang L., Gu F.X., Chan J.M., Wang A.Z., Langer R.S., Farokhzad O.C., 2007. Nanoparticles in medicine: therapeutic applications and developments. *Clin Pharmacol Ther.*, 83:761–769.
- Zhang Y., Zhi Z., Jiang T., Zhang J., Wang Z., Wang S., 2010. Spherical mesoporous silica nanoparticles for loading and release of the poorly water-soluble drug telmisartan. *J Control Release*, 145(3):257–263.
- Zhao, R., and Goldman, I.D., 2013. Folate and thiamine transporters mediated by facilitative carriers (SLC19A1-3 and SLC46A1) and folate receptors, *molecular aspects of medicine* 34, 373-385.
- Zilberman M., Elsner J.J., 2008, Antibiotic-eluting medical devices for various applications. *J Control Release*, 130, 202–215.

NANOSTRUCTURING OF BIOIMPLANTS THROUGH CHEMICAL MECHANICAL POLISHING

Zeynep Ozdemir¹, G. Bahar Basim^{1,a}

1. Özyeğin University, Mechanical Engineering, Istanbul, Turkey
a. Corresponding author (Bahar.Basim@ozyegin.edu.tr)

ABSTRACT: Implant surface composition and structure are critical design factors affecting the rate of osseointegration that is accepted as an indication of biocompatibility. The goal of this study is to induce Chemical Mechanical Polishing (CMP) based nano-scale random surface modification of titanium substrates to improve their biocompatibility. CMP is a novel way for processing the surface of biomaterials to manipulate the nature of the surface at an atomic scale. The CMP process involves both chemical and mechanical actions to lead material removal from the surface layer while inducing nano-scale surface structure simultaneously. In this study pure titanium plate surfaces are modified with various CMP pads composed of different structures including the standard microelectronic pads to much rougher abrasive papers with different particle sizes by using slurries with varying oxidizer concentrations. After the CMP applications the titanium surfaces were characterized through surface wettability by measuring contact angles with body serum and surface roughness evaluation by Atomic Force Microscopy (AFM). Bacteria growth tests were applied to evaluate the preliminary biocompatibility on the processed Ti samples.

1. INTRODUCTION

Biomaterials are widely used for dental prostheses, orthopedic devices, cardiac pacemakers and catheters [Shirkhanzadeh *et al.*, 1995]. Particularly titanium and its alloys are favored as bio implants due to their excellent surface characteristics which promote biocompatibility [Shibata *et al.*, 1998]. However, the surface of titanium maybe contaminated during casting due to its highly reactive nature which in turn lessens the biocompatibility and the mechanical properties at the tissue/bio implant interface [Akhter *et al.*, 2000]. Patients with bioimplants face on the average of 4% infection that maybe caused by the contamination and this ratio goes up to 40% for ventular support implants. In the case of infection, both medical treatment and the time spent in a medical institution would result in considerably high expenses. Therefore, it is very critical to produce implant materials without the contaminated surface layers and with a protective oxide

film formed on the surface to limit any further contamination to minimize risk of infection at the interface where they are exposed to the live tissue.

Metals tend to form native oxides when they are exposed to oxidizing environments which maybe a self-protective layer in some cases. One of the main processes where the protective metal oxide films are closely investigated is the Chemical Mechanical Planarization for metals (CMP) is used to planarize the interlayer metal connectors in microelectronics manufacturing. In CMP process, the top film surface of the metal is exposed to the chemicals in the slurry which is made of submicron size particles and corrosives. This interaction forms a chemically altered top film that is removed by the mechanical action of the slurry abrasive particles. The chemically altered top films have to be a protective oxide to enable planarization by stopping chemical corrosion on the recessed metal

surfaces while the elevated structures are polished [Kaufman *et al.*, 1991]. It has been shown by an earlier study that the application of CMP on Ti films has been very successful in terms of creating a titanium oxide film on the surface that has promoted biocompatibility in addition to helping removal of the reacted and contaminated surface layers [Chathapuram *et al.*, 2003]. The effect of oxidation of Ti films on cell activity improvement [Variola *et al.*, 2008] as well as hydroxyapatite formation [Jouanny *et al.*, 2010] has been shown in the literature. Hence, CMP application on Ti plates to remove the potentially contaminated surface layers and simultaneous formation of self-protective titanium oxide layers are believed to help improve the biocompatibility.

In this study, CMP technique is used to induce nano-smoothness and controlled nano-roughness on the titanium surfaces. It has been demonstrated earlier through inducing nano and micro patterns on various biomaterials that these structures help increase the cell growth capability of the bio implants [Kurella *et al.*, 2005]. However, for applications like artificial cardiac valves surfaces demoting cell growth may be needed for continuous functionality. Biocompatibilities of the titanium surfaces treated by CMP can be controlled by altering them to a very smooth or nano-structured surface structure and bring the advantage of applying the same process for many different applications. Our aim is to create engineered Ti based bio implants with self-protective surfaces to minimize chemical and bacterial reactivity, while promoting their biocompatibility through surface patterning.

2. EXPERIMENTAL

CMP and bacteria growth analyses were conducted on titanium foils with 1 mm thickness and 99.6% purity (TI000430)

obtained from Goodfellow Cambridge Limited. The original foil which was 300 x 300 mm in size was cut to 46 x 28 mm pieces to fit to the holder of the CMP tool. The original sample surface considered as baseline for the experimentation was annealed. In order to compare to the properties of the original surface against the surfaces prepared through CMP, polishing was conducted by using a desktop Tegrapol-31 polisher and 5% weight alumina (Al₂O₃) slurry with 50nm particle size. Slurries were prepared at pH 4 using nitric acid through ultrasonically long enough by repeated pH adjustment until the slurry was fully stabilized. CMP tests were conducted at 70 N downforce which is equivalent to a 7.88 psi pressure on the used sample size. Figure 1 illustrates the CMP set up used for the experiments. Initial samples were polished using a Suba IV subpad stacked under a polytex buff pad to obtain a very smooth surface. In addition, two sizes of sand paper (silicon carbide 150C and P320) were used in place of the polishing pad to create the micro structures through CMP. All CMP testing except for the first sample were conducted by using H₂O₂ as oxidizer. Samples ran with the polymeric CMP pads were polished for 5 minutes with ~3% oxidizer addition and samples ran by using the abrasive papers were polished by using 5%wt H₂O₂ for 2 minutes with P320 and 15%wt H₂O₂ for 1 minute with 150C to promote chemical activity in presence of very aggressive mechanical abrasion. Material removal rates were calculated through weighing the samples pre and post polish by a sensitive balance to the fourth digit after zero. All samples were cleaned in ultrasonic bath with pH 4 water for 5 minutes and dried with nitrogen gas before they were characterized.

All samples were characterized for wettability through contact angle measurements with simulated body fluid

(SBF) with a KSV ATTENSION Theta Lite Optic Contact Angle Goniometer using the sessile drop method. Five drops were measured on each sample. The drop image was stored by a camera and an image analysis system calculated the contact angle (Θ) from the shape of the drop. The microstructures of specimens were examined using a Nanomagnetics Atomic Force Microscope (AFM) with tapping mode and the surface roughness values were recorded on 10 x10 μm scan area. The biocompatibility analyses were conducted through bacteria growth analyses. Titanium plates were sterilized with autoclave (120°C, 20min.) before the microbiological analysis. Cronobacter Sakazakii (Gram-) was used as bacteria a species and 100 μl microorganisms from the nutrient broth microbial stock were spread on nutrient agar plates in sterile conditions. After the cultivation of bacteria, sterilized Ti plates were placed into each plate and incubated at 37 °C. The bacteria density was observed over 1, 3 and 7 days.

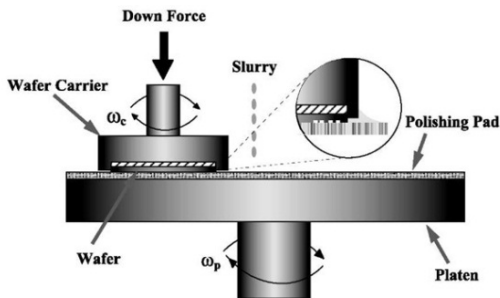


Figure 1: General representation of CMP.

3.RESULTS AND DISCUSSION

Results of the CMP tests for the selected polishing conditions on the titanium plates are summarized in Table 1. It can be seen that the material removal rates on the samples polished on the polymeric pads were low and particularly the CMP test without oxidizer resulted in negligible material removal. On the other hand, using the abrasive papers resulted in much higher removal rates although

the chemical component of the process was elevated by increased oxidizer (H_2O_2) concentration and the mechanical abrasion was limited by reduced polish times on the samples.

Contact angle values reflecting on the wettability of the surface were initially high on the anodized titanium surface with no treatment done. On the samples

Table 1: CMP conditions, removal rates and contact angles of the studied titanium surfaces.

Sample	Remove Rate ($\mu\text{m}/\text{min}$)	Roughness (nm)	CA
No treatment	N/A	118.77	83.89 \pm 2.79
CMP without H_2O_2	~0	117.11	44.74 \pm 3.18
CMP with 3% H_2O_2	0.11	78.05	32.43 \pm 5.25
CMP with 3% H_2O_2 + Ab P. (45 μm)	29.85	101.40*	54.34 \pm 7.19
CMP with 3% H_2O_2 + Ab P. (90 μm)	35.99	107.56*	65.53 \pm 6.37

*Since AFM tip cannot reach the grooves on the surface completely reported values lower than the real values.

prepared by CMP, the contact angles were higher as the surface roughness was increased through induced micro level roughness as seen from figure 2. The very high contact angle on the untreated sample can be explained through the different nature of the surface since the original sample was anodized creating a very thick oxide layer with a porous structure. Once the surface polish has started, the anodized oxide film started to be removed. Without the oxidizer in the slurry, the material removal rate was negligible yet the exposed titanium metal resulted in a change in the contact angle measurements. This is due to the fact that the surface energy of the fresh exposed titanium is higher and this leads to increased wettability response on the surface. Once the fresh surface of

titanium is exposed, the effect of roughness on the contact angle response starts to dominate. As can be seen in Figure 2, surfaces with an expected smoother finish, such as in the case of CMP application in the presence of oxidizer resulted in more wettability and hence a lower contact angle and the surfaces with the induced micro-roughness (such as the samples polished with abrasive papers) resulted in a higher contact angle.

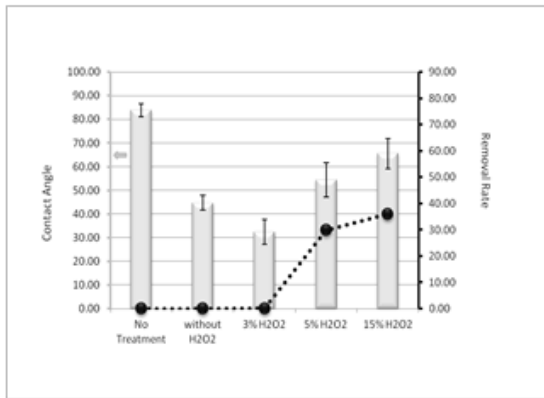


Figure 2: Remove rate and Contact angle measurement graph for each samples

In order to quantify the surface roughness of the polished surfaces, AFM analyses were conducted using tapping mode scanning on micrographs. Figure 3-a shows the AFM micrographs of the original untreated titanium plate and 3-b shows the micrograph of the surface after CMP conducted with the polymeric pad in the presence of 3% H₂O₂. As it can be seen the surface roughness reduced significantly after CMP from 118.77 nm rms value on the original sample to 78.05 nm rms value post CMP. The sample that has been buffed with the slurry without the oxidizer, however, remained the similar roughness as the original samples (117.11 nm) as consistent with the negligible material removal rates obtained in the absence of the oxidizer. It is clear that the original sample has a very porous surface that can be attributed to the anodization on the surface. When the

surface is buffed with CMP without the chemical component provided with the H₂O₂ addition, the porous surface oxide was removed partially. CMP process with the oxidizer present at 3%wt exposed the titanium surface and finally polishing with the abrasive papers induced major surface scratching while exposing the titanium. The corresponding sessile drop images are also shown in Figure 2. It can be seen that the increased roughness through porosity or induced scratching results in higher contact angle and hence less wettability.

In order to analyze the biocompatibility of the prepared surfaces, controlled bacteria growth analyses were conducted. Figure 4 illustrates the growth of bacteria for day 1, 3 and 7 after the samples were plated. It is clearly seen that the surfaces intentionally scratched tend to accumulate more bacteria colonies as compared to the smoother surfaces. Particularly the sample processes through proper CMP process allowed the least amount of bacteria growth around the titanium plate.

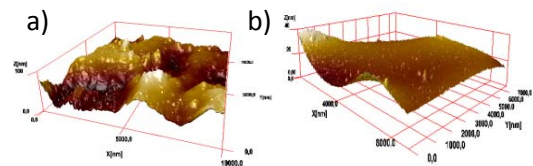


Figure 3: AFM micrograph of the titanium samples (a) as received sample without any treatment (z-scale 100nm) and (b) post CMP with oxidizer (z-scale 40nm).

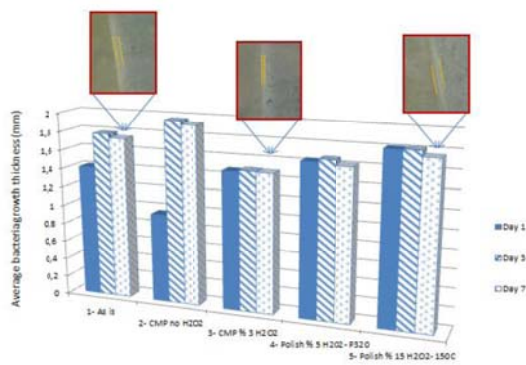


Figure 4: Bacteria growth analyses on titanium plates quantified by thickness of the bacteria layer surrounding the titanium plates.

4. CONCLUSION

It is known that the increased surface microstructure and surface oxidation can promote the biocompatibility of the implant surfaces. In this study, CMP is proposed as an alternative technique to induce microstructure to the titanium surfaces to enable more biocompatible surfaces. CMP technique can also demote the biocompatibility through creating very smooth surfaces and hence enables a systematic way to control the cell growth on the bio-implants depending on the selected application. Wettability analyses through contact angle measurements are also shown to be a valid and easy approach to detect the surface roughness.

Acknowledgements: The authors acknowledge the support from the Marie Curie International Reintegration Grants (IRG) Call: FP7-PEOPLE-RG-2009.

REFERENCES

- Akhter R, Okawa S, Nakano S, Kobayashi M, Miyakawa, 2000. Surface Composition and Structure of Titanium Polished with Aqueous Slurry of Ferric Oxide, *Dent Mater J* 19, 10.
- Chathapuram V.S., Du, T., Sundaram, K.B., Desai, V., 2003. Role of the oxidizer in the chemical mechanical planarization of Ti/TiN barrier layer, *Microelectronic Engineering* 65 478.
- Jouanny, I., Labdi, S., Aubert, P., Buscema, C., Aciejak, O., Berger, M-H., Guipont, V.,

Jeandin, M., 2010. *Thin Solid Films*, 518, 3212.

Kaufman, F.B., Thomson, D.B. Broadie R.E., Jaso, M.A., Guthrie, W.L., Pearson, M.B., Small, M.B., 1991. Chemical-Mechanical Polishing for Fabricating Patterned W Metal Features as Chip Interconnects *Journal of the Electrochemical Society*, 138, 3460.

Kurella, A., Dahotre, N.B., 2005. Surface Modification for Bioimplants: The Role of Laser Surface Engineering *Journal of Biomaterials Applications*, 20, 4.

Shibata K, Kamegai A., 1988. Titanium in dentistry: Biocompatibility of titanium. Quintessence, Tokyo, 35.

Shirkhanzadeh, M., Azadegan, M., Liu, G. Q., 1995. Bioactive delivery systems for the slow-release of antibiotics--incorporation of Ag⁺ ions into micro-porous hydroxyapatite coatings. *Mater Lett* 24, 7.

Variola, F. Yi, J-H, Richert, L., Wuest, J.D., Rosei, F. Nanci, A., 2008. Tailoring the surface properties of Ti6Al4V by controlled chemical oxidation, *Biomaterials*, 29, 1285.

FABRICATION OF HOLLOW HYDROXYAPATITE MICROSPHERES BY SPRAY DRYING

Fatih Erdem BAŞTAN, Gencer AĞTAŞ, Yıldız YARALI ÖZBEK, Fatih ÜSTEL

Sakarya University, Engineering Faculty, Department of Metallurgy and Materials Engineering, 54187, Esentepe-Sakarya-Turkey

ABSTRACT: Hydroxyapatite (HAp) is the main mineral of bone and teeth. It has excellent biocompatibility, bioactivity and osteoconductivity. Different hydroxyapatite powder shapes can be produced by spray drying method. The aim of this study was fabrication of hollow hydroxyapatite particles. In this study, hydroxyapatite was produced with chemical precipitation. 5 wt. % PVA (polyvinyl alcohol) was used to obtain hollow hydroxyapatite microspheres in slurry. Different parameters were used at spray dryer because of understanding the effect of parameters. X-Ray Diffraction and Scanning Electron Microscopy were used to investigate the phase and morphology structure.

Keywords: Hydroxyapatite, spray drying, hollow microspheres

1. INTRODUCTION

Hydroxyapatite is used to repair and reconstruct damaged and deformed parts of the human skeleton because of its high biocompatibility, bioactivity and osteoconductivity [1]. Hydroxyapatite has chemical similarities with human bone mineral [2]. Hence, hydroxyapatite forms a real bond with the surrounding bone tissue when implanted, it is used in many applications in dentistry and orthopedics [3]. Bone consists of 69 % calcium phosphate (especially hydroxyapatite), 21 % collagen, 9 % water and 1 % other constituents [4].

Hydroxyapatite can be synthesized with chemical precipitation, sol-gel, hydrothermal synthesis, mechanochemical synthesis methods. Hydroxyapatite is primarily synthesized by Hayek et al. with precipitation method [5]. In addition to low cost and easy operation, precipitated hydroxyapatite has small size, low crystallinity and high surface activation [6].

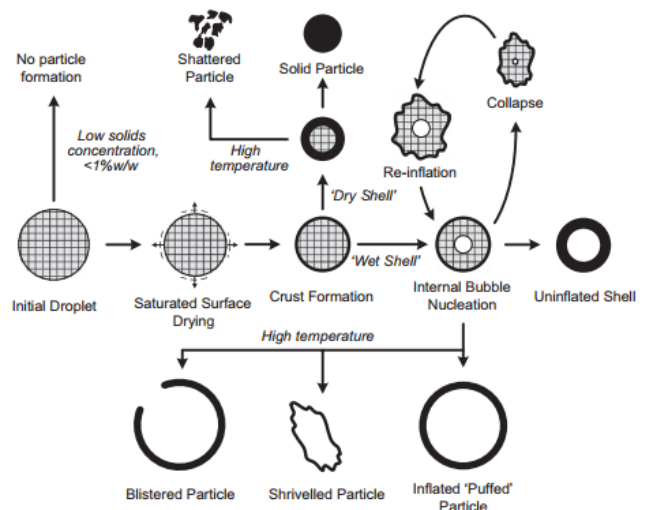


Figure 1: Schematic particle morphologies that drying droplets containing dissolved or suspended solids [7]

Spray drying method is used to fabricate powders with various morphologies like a hollow, spherical or donut shape [8]. Hollow structures are used to carry sensitive materials such as drugs, cosmetics and DNA [9]. Spray drying is the most effective method for good flowability and organizing the particle size distribution without any decomposition of structure. Due to ease

of operation, spray drying is attractive to use [10]. Different particle morphologies that droplets containing dissolved or suspended solids was shown at Fig. 1. Due to the fact that shell is impermeable, drying gas can break or shrink when the pressure forces inside the droplet exceed the mechanical strength of the shell [11]. During the diffusion process of moisture, PVA carried by the moisture would aggregate on the surface droplet. Aggregation of PVA could hamper further diffusion of the moisture that was still kept in the droplet, which resulted in the increases of the pressure inside the droplet [12].

2. EXPERIMENTAL PROCEDURE

HAp was produced with chemical precipitation method [13]. $\text{Ca}(\text{NO}_3)_2 \cdot 4\text{H}_2\text{O}$ (Merck, 98%), H_3PO_4 (Merck, 85%), were used for HAp synthesis and NH_4OH were used for pH adjustment. $\text{Ca}(\text{NO}_3)_2 \cdot 4\text{H}_2\text{O}$, H_3PO_4 , were dissolved in deionized water separately and NH_4OH was added to all of the solutions to increase the pH level to 10-11. After a while later, finally, orthophosphoric acid solution was added

slowly. Final pH level was measured about 10. After the solution was stirred for 24 hours at room temperature, hydroxyapatite particles were precipitated for 24 hours. Then the solution was filtered (Whatmann filter paper, Grade 3) with adding deionized water to remove remaining residuals.

As distinct from direct producing powder, hydroxyapatite gelatinous was not dried at a furnace. Hydroxyapatite gelatinous was used for spray drying slurry. 5 wt. % PVA (ZAG) was added to slurry heated up to 65 °C for dissolution of PVA and stirred with magnetic stirrer for 1 hour. The parameters for spray drying is given at Table 1. For characterization, SEM (TESCAN VEGA II) was performed to investigate the microstructure of powders, XRD (RIGAKU D/MAX/2200/PC) was performed to identify phases in the structure. Viscosity was measured with Brookfield DV-II. The product was calcinated at 900 °C with 10 °C/min heating regime. Particle size analyze was measured with Microtrac S3500.

Table 1: Spray Drying Parameters

Wt. % PVA	Viscosity (cp)	Air Pressure (bar)	Feed Rate (rpm)	Inlet Temp. (°C)	Outlet Temp. (°C)
5	210	1,5	10	200	105
	210	1,5	20	200	91
	210	1,5	30	200	85

3. RESULTS AND DISCUSSIONS

Hollow hydroxyapatite particles were produced successfully with spray drying both 5 wt. % PVA. It can be seen hollow hydroxyapatite particles at Fig 2. There were hollow and also damaged hollow

particles. The damage was created by the PVA that increased the pressure inside the droplet. Increasing the amount of PVA tends to the droplets to be donut-shape [12].

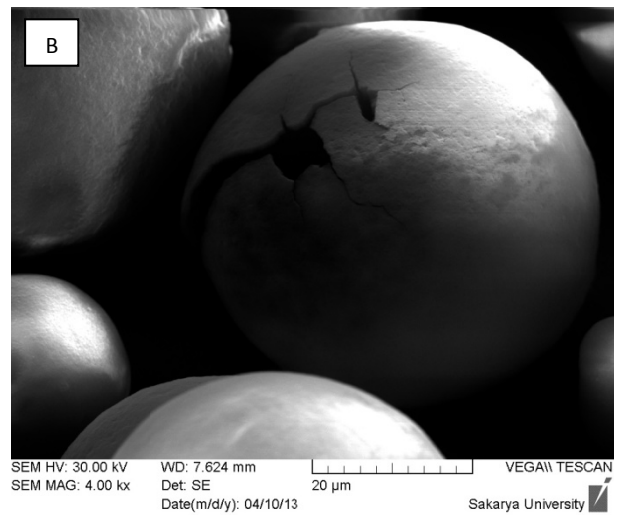
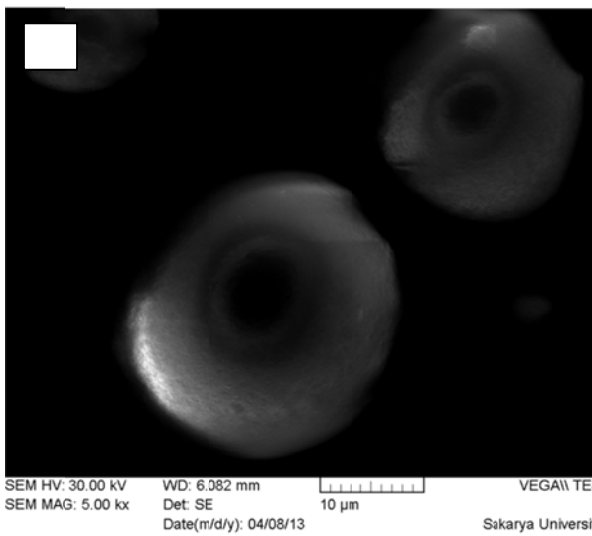
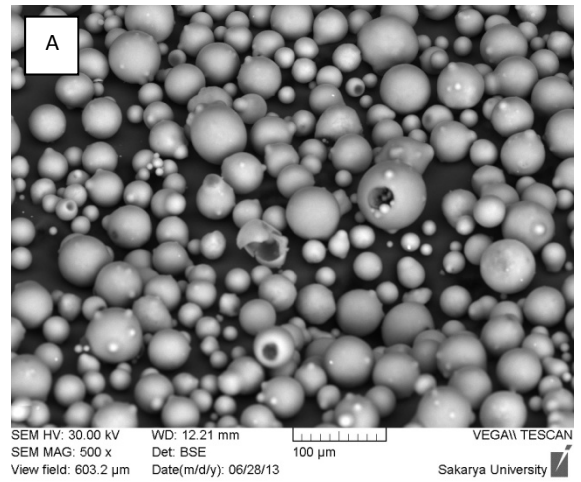
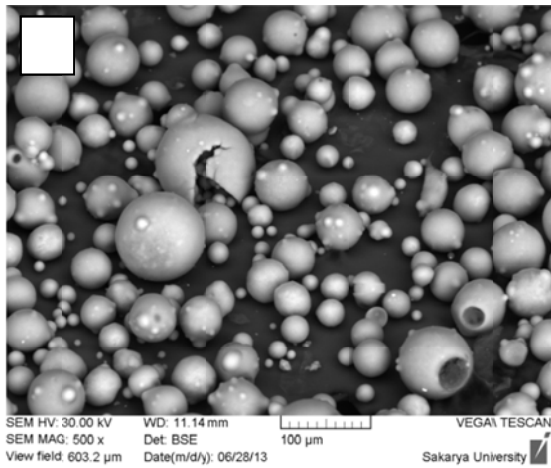


Figure 2: Hollow hydroxyapatite particles with 5 wt. %PVA, 1,5 bar air pressure and 10 rpm feed rate A) General view B) Detail view

Figure 3: Hollow hydroxyapatite particles with 5 wt. %PVA, 1,5 bar air pressure and 20 rpm feed rate A) General view B) Detail view

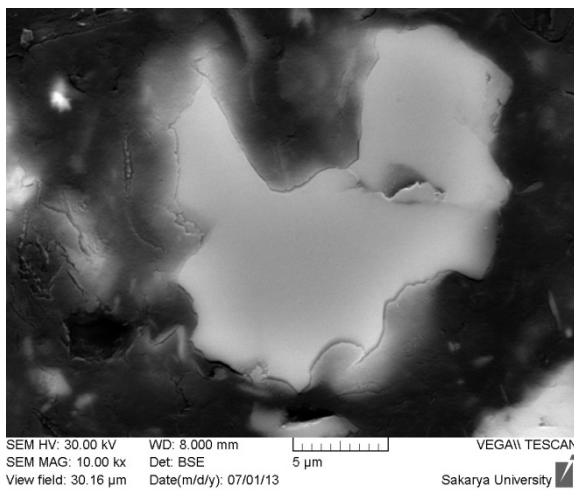
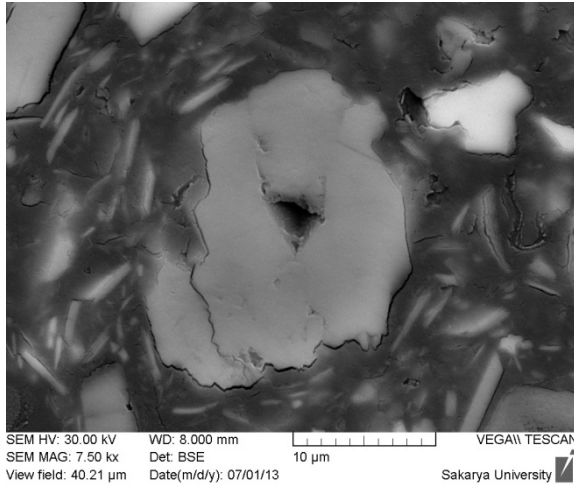


Fig 4: Polished hollow hydroxyapatite particles with 1,5 bar air pressure and 10 rpm feed rate

It was seen at Fig 3. that hollow particles were fabricated. Usually spray dried particles shape is spherical by nature. There were joint particles which was probably formed before drying. Two droplet might be crashed on the fly and dried together. Polished surface was seen at Fig 4. There were also cracks on the particles. I might be created when spray drying or polishing. On the other hand deficient particles was seen.

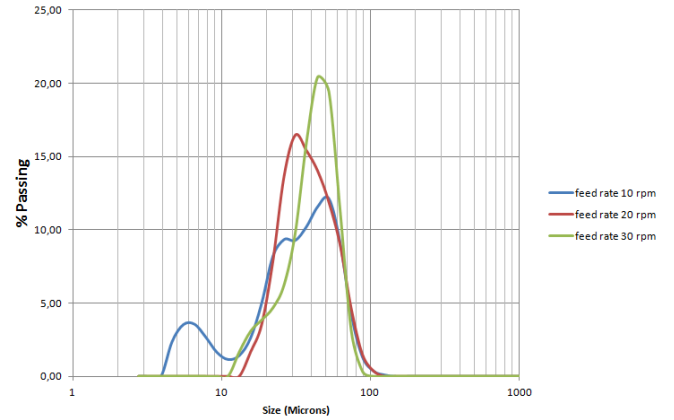


Fig 5: Particle Size Distribution Diagram

Feed rate effects on particle size distribution at constant air pressure. Particle size distribution was given at Fig 5. It was seen at figure that increasing the feed rate conducted to increase particle size. Particle size distribution is larger when the feed rate was 10 rpm. According to Table 2, average particle size was increased with increasing feed rate. 10% of particles was smaller than 6,73 µm when feed rate was 10 rpm, whereas 20,84 µm when feed rate was 20 rpm. This situation was about the total energy. Due to the constant atomization energy, slurry was splitted bigger particles with increasing feed rate.

Table 2: Size Percentiles of hollow Hydroxyapatite particles

	D10	D50	D90
Feed Rate 10 rpm	6,73 µm	30,62 µm	57,11 µm
Feed Rate 20 rpm	20,84 µm	33,53 µm	57,62 µm
Feed Rate 30 rpm	19,58 µm	38,59 µm	55,51 µm

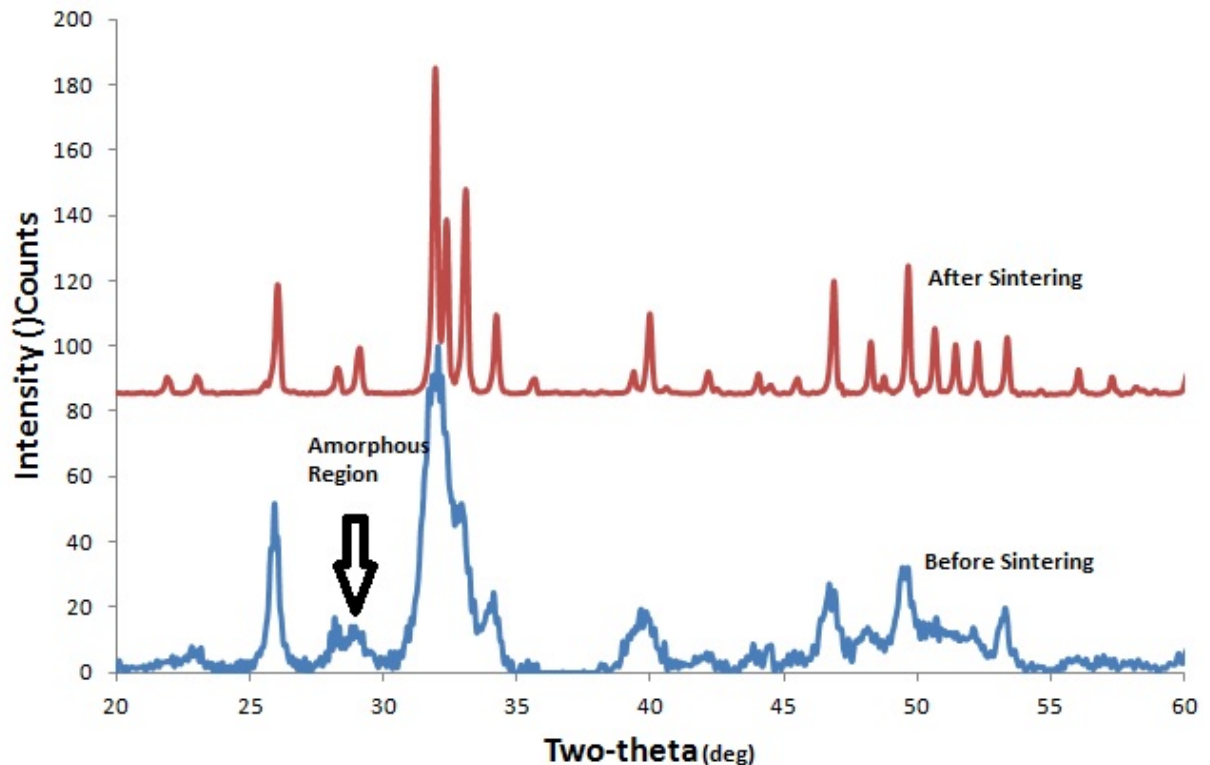


Fig 6: XRD patterns hydroxyapatite before and after sintering

X-Ray diffraction patterns were shown at Fig 6. Before sintering there was amorphous region that was become crystalline after sintering at 900 °C for one hour.

4. CONCLUSION

Hollow hydroxyapatite particles were fabricated with spray drying. PVA brought along to increase pressure inside the droplet. XRD results showed that there was amorphous region before sintering. After sintering, the structure became crystalline and, peaks were matched with reference peaks. Increasing feed rate got bigger particles, but much increasing would cause adhering the particles to chamber wall without drying.

REFERENCES

- [1] E. Meurice, A. Leriche, J.-C. Hornez, F. Bouchart, E. Rguiti, L. Boilet, M. Descamps, and F. Cambier, "Functionalisation of porous hydroxyapatite for bone substitutes," *Journal of the European Ceramic Society*, vol. 32, no. 11, pp. 2673–2678, Aug. 2012.
- [2] L. Cheng, F. Ye, R. Yang, X. Lu, Y. Shi, L. Li, H. Fan, and H. Bu, "Osteoinduction of hydroxyapatite/ β -tricalcium phosphate bioceramics in mice with a fractured fibula," *Acta Biomaterialia*, vol. 6, no. 4, pp. 1569–1574, Apr. 2010.
- [3] C. P. Yoganand, V. Selvarajan, J. Wu, and D. Xue, "Processing of bovine hydroxyapatite (HA) powders and synthesis of calcium phosphate silicate glass ceramics using DC thermal plasma torch," *Vacuum*, vol. 83, no. 2, pp. 319–325, Sep. 2008.
- [4] L. Pighinelli and M. Kucharska, "Chitosan–hydroxyapatite composites," *Carbohydrate Polymers*, vol. 93, no. 1, pp. 256–262, Mar. 2013.
- [5] Hayek E., Newesely H., Pentacalcium Hydroxyorthophosphate, *Inorganic Syntheses, Volume VII*, 1963
- [6] C. Liu, Y. Huang, W. Shen, and J. Cui, "Kinetics of hydroxyapatite precipitation at pH 10 to 11," *Biomaterials*, vol. 22, no. 4, pp. 301–306, Feb. 2001.
- [7] C. S. Handscomb, M. Kraft, and A. E. Bayly, "A new model for the drying of droplets containing suspended solids," *Chemical Engineering Science*, vol. 64, no. 4, pp. 628–637, Feb. 2009.
- [8] P. Roy, G. Bertrand, and C. Coddet, "Spray drying and sintering of zirconia based hollow powders," *Powder Technology*, vol. 157, no. 1–3, pp. 20–26, Sep. 2005.
- [9] Lou X. W., Archer L. A., Yang Z., *Hollow Micro-/Nanostructures: Synthesis and Applications*, Adv. Mater., pp. 3987–4019,

- 2008.
- [10] R. Sun, Y. Lu, and K. Chen, "Preparation and characterization of hollow hydroxyapatite microspheres by spray drying method," *Materials Science and Engineering: C*, vol. 29, no. 4, pp. 1088–1092, May 2009.
 - [11] Seydel P., Blömer J., Bertling J., Modeling Particle Formation at Spray Drying Using, *Drying Technology*, 24 137-146, 2006
 - [12] Yu B., Feng J. Y., Wahn L. S., Huang C., Li Y. F., Jia Z., Spray drying of Alumina Powder for APS: Effect of Slurry Properties and Drying Conditions Upon Particle Size and Morphology of Feedstock, *Bull. Mater. Sci.*, Vol. 34, 2011
 - [13] Bastan F. E., Ozbek Y. Y., Producing Anti-bacterial Silver Doped Hydroxyapatite Powders with Chemical Precipitation and Reshaping at Spray Dryer, *Materiali in Tehnologije*, 2013

EVALUATION OF MAGNESIUM-ALUMINUM METASILICATE AND SILICA CARRIERS FOR IMPROVING ORAL BIOAVAILABILITY OF POORLY SOLUBLE DRUG

Branko Vukosavljević, Marko Krstić, Jelena Đuriš, Zorica Đurić, Svetlana Ibrić^a

Department of Pharmaceutical Technology, Faculty of Pharmacy,
Vojvode Stepe 450, 11221, Belgrade, Serbia
a. Corresponding author (svetlana.ibric@pharmacy.bg.ac.rs)

ABSTRACT: Novel porous powder materials which are characterised by large adsorption capacity and high specific surface area could be potentially used as carriers for improving dissolution characteristics and oral bioavailability of poorly water soluble drugs. The aim was examination of solid dispersions with porous carriers, as potential solubility and dissolution rate enhancing delivery systems of low soluble model substance, Carbamazepine (CBZ). Four different porous adsorbents were used: Neusilin® UFL2 and FL2-both magnesium-aluminum metasilicate, Sylysia® 320(SYL)-synthetic porous silica and Diatomite(DIAT)-natural porous silica, in three drug/carrier weight ratios, using ethanol as a drug solvent. DSC, TGA, HSM, PXRD and FTIR analyses were performed in order to characterize physical state of CBZ and to identify potential interaction between CBZ and adsorbent. Drug release testing of dispersions was performed. DSC and PXRD curves have shown increasing of amorphous form of CBZ with increasing the ratio of the porous powder carrier. FTIR analyses have shown significant drug/carrier interaction. Dissolution rate of CBZ increased by enlarging the ratio of the carrier using NFL, SYL and NUFL, respectively. While using different ratios of DIAT, drug dissolution rate stays almost constant. Formulation of drug/carrier solid dispersions can be an effective method for improving drug dissolution rate and oral bioavailability.

1. INTRODUCTION

Carbamazepine (CBZ), is a widely used antiepileptic drug having narrow therapeutic index and relatively high plasma concentration variability [Martindale, 2007]. CBZ is a white or off-white crystalline powder exhibiting polymorphism. The form III is the polymorph used in commercial pharmaceutical formulations [Kobayashi, 2000] According to the Biopharmaceutics Classification System CBZ, as poorly soluble drug with high permeability, is classified as class II and water solubility varies in a range 0.11-0.26 mg/ml. Since the absorption of CBZ is limited by its solubility, improving the dissolution characteristics of CBZ may increase the rate of absorption and enhance its oral bioavailability [Leuner, 2000].

Solid dispersions possess the great potential in improving the dissolution characteristics of poorly soluble drugs. [Graig et al.,2002]. Due to increased wettability, improved dispersibility of drug particles, potential existence of the drug in amorphous form which mostly show improved solubility rate in comparison to crystal form, solid dispersions were investigated as fast and immediate solid dosage forms.

In recent years, various silica-based structures have been synthesized and analyzed as potential drug carriers for water insoluble drugs in order to address problems of limited drug solubility, e.g. synthetic ordered porous silica materials. These carriers, due to their biocompatibility, high surface area,

chemical inertness and diffusion controlled drug release mechanism, have been widely investigated for development of new drug-delivery systems.

Sylsilia is an amorphous SiO₂, with high specific surface area and porosity, is primarily used as a tablet excipient to improve the ease of powder flow through the tableting process [Ukmar, 2011]. *Neusilin* is a synthetic, amorphous form of Magnesium-Aluminum Metasilicate. It is a multifunctional excipient that can be used in direct compression, wet granulation, and also as a carrier for solid dispersions and self-micro emulsifying drug systems. Natural silica microcapsules from diatoms, as a new carrier for delivery of therapeutics, have been introduced and evaluated [Aw, 2012]. Diatoms, as a new potential drug carrier, have several advantages in comparison to usual synthetic silicas: natural origin, cheapness, complex 3-dimensional (3-d) architecture of silica walls called frustules, with highly ordered porous structures, high specific surface area, thermal stability and chemical inertness, potential diffusion and controlled drug release mechanism.

The aim of this study was to formulate solid dispersions of low soluble model substance-CBZ, with porous carriers, in order to enhance its solubility and dissolution rate and to examine formulations using thermal and non-thermal technics.

2. MATERIALS AND METHODS

2.1. Materials

Neusilin® UFL2 (NUFL) and Neusilin® FL2 (NFL) were obtained from Fuji Chemical Industry Co., Japan. Sylsilia 320 (SYL) was obtained from Fuji Sylsilia Chemical LTD, Japan. Diatomites (DIAT) were purified and classified from row diatomite mineral

supplied from MountSylvia, Pty. Ltd/Australia. CBZ was obtained from Galenika, Serbia. All other reagents were of reagent grade.

2.2. Methods

2.2.1. Preparation of solid dispersions

Solid dispersions were prepared using two methods.

Method A – CBZ was dissolved in Ethanol, 96% (v/v) and then incorporated on carriers: NUFL, NFL, SYL and DIAT in three weight ratios drug/carrier: 1:1, 1:2, 1:6. The resultant solid dispersions were kept for 3 days at room temperature and then collected. The dispersions were then pulverized using a mortar and a pestle, and stored in a desiccator at room temperature until use.

Method B - To prepare solid dispersion particles using evaporation, all carriers were suspended in CBZ solution in Ethanol, 96% in three weight ratios drug/carrier: 1:1, 1:2, 1:6. The suspensions obtained were evaporated in a vacuum evaporator (IKA RV 05, Staufen, Germany) at a rotation speed of 70 rpm at 70°C for about 30 min.

2.3. Characterization of Solid Dispersions

2.3.1. Differential scanning calorimetry (DSC)

DSC analysis were carried out on a computer-interfaced differential scanning calorimeter (DSC Q2000, TA Instruments). The samples were accurately weighed (1 – 2 mg) and heated from 20 to 200°C at a rate of 10°C/min, under a nitrogen purge gas flow of 50 ml/min.

2.3.2. Thermo-gravimetric analysis (TGA)

TGA analysis were carried out on a thermo-gravimetric analyzer (TGA Q5000, TA Instruments). The samples were accurately weighed (3 – 5 mg) and heated from 20 to 250°C at a rate of 10°C/min, under a nitrogen purge gas flow of 25 ml/min.

2.3.3. Hot stage microscopy (HSM)

HSM was undertaken using a Metler Toledo Hot Stage microscope (Hot- Stage FP82HT, Controller/processor FP 90, Microscope DME Model 13595, Camera PL-A622 firewire camera) and application software Studio Capture 3.1, in temperature range 20-250°C.

2.3.4. Powder X-ray diffraction (PXRD)

Measurements were performed using a Bruker AXS D8 Advance powder diffractometer, equipped with copper cathode ($\lambda = 0.15418$ nm, 40 kV, 40 mA). Patterns were obtained with step width of 0.02° and a detector in 2 θ between 4° and 40° at ambient temperature.

2.3.5. Fourier transform infrared spectroscopy (FT-IR)

FT-IR spectra in the region of 600–4000 cm⁻¹ for both starting materials and solid formulations were obtained using a Shimadzu IR-Prestige-21 FT-IR spectrometer coupled with a horizontal Golden Gate MKII single-reflection ATR system (Specac, 214 Kent, UK) equipped with a Zn Se lens, after appropriate background subtraction. Sixteen scans over the selected wave number range at a resolution of 4 cm⁻¹ were averaged for each sample.

2.4. Dissolution Studies

The USP II dissolution test apparatus (Erweka DT70, Germany) was used. The dissolution medium was water, volume 900 mL, temperature 37°C and the

rotating paddle speed was 50 rpm. Sampling was carried out at 5, 10, 15, 20, 30, 60, 90, 120, 150 and 180 minutes and the absorbance of carbamazepine was measured at 287 nm using the UV/VIS spectrophotometer Evolution 300 (Thermo Fisher Scientific, Cambridge, UK).

3. RESULTS AND DISCUSSION

3.1. Characterization of Solid Dispersions

DSC and PXRD analysis of CBZ, four different drug-carriers (NUFL, NFL, SYL and DIAT) and twenty four solid dispersions, formulated by using two methods (incorporation of CBZ on carriers after dilution in Ethanol, 96%- Method A and conventional solvent evaporation- Method B), in three weight ratios drug/carrier (1:1, 1:2, 1:6), were performed in order to characterize physical state of CBZ and FT-IR analysis mostly to identify potential drug/excipient interaction.

Thermal analysis of the pure drug substance demonstrated a characteristic CBZ form III thermogram with three events, as reported previously [Kobayashi, 2000]. The endothermic peak observed at 176.25 °C is attributed to the melting of the drug and involves a 37.78 J/g enthalpy change. This event is followed by an exothermic peak at 178.12 °C due to crystallization into form I, and the ΔH value calculated as the sum of these two events (21.85 J/g) represents the whole form III to form I transition. The third event observed at 192.34 °C ($\Delta H = 104.4$ J/g) is due to melting of form I. Non-thermal technique- PXRD confirmed above mentioned. Clearly visible peaks at values 2 θ – 13.1, 15.32, 19.52, 23.82 i 24.97 are characteristic for CBZ form III [Grzesiak et al., 2003].

DIAT thermogram shows one endothermic event (melting of the crystalline polymer) with its peak at 178.07 °C, with the enthalpy change of 1.804 J/g. Similarly, NFL has shown one endothermic event with its peak at 153.15 °C, with the enthalpy change of 3.964 J/g. NUFL and SYL have shown more amorphous nature, we can see potential glass transition on related thermograms. Absence of the melting peak in DSC curves of solid dispersions (CBZ/NUFL; CBZ/NFL; CBZ/SYL; CBZ/DIAT) suggests the transition of CBZ from form III to amorphous form. Deformation of characteristic bands for CBZ form III at 1605 and 1593 cm^{-1} (-C=O vibration and -NH deformation) in FT-IR spectra of solid dispersions may suggest that hydrogen bond between carbonyl group of CBZ and silanol group of adsorbent take part in formation of amorphous state of CBZ. Deformation of characteristic bands is weaker for Neusilin® FL2. It could be assumed that due to smaller specific surface area of NFL2 (150 m^2/g), in comparison to other three adsorbents (specific surface area of NUFL2 and SYL320 is $\approx 300 \text{ m}^2/\text{g}$), intensity of the interaction is lower as well. Drug amorphization was accompanied by improvement in the drug release rate. Adsorption in/on mesoporous materials (pore size 2-50nm) can lead to stabilisation of the amorphous drug (crystallization is greatly hindered and essentially suppressed). In order to verify the observations obtained by the DSC methodology, samples were heated on the hot-stage and observed under the polarized light microscope.

FTIR spectra of the physical mixtures all have CBZ form III peaks in the studied spectral range; with the peaks being more pronounced with the increase in CBZ content in the mixture. Therefore, results indicate the absence of solid-solid interactions between the drug and

polymer that could lead to a polymorphic transition.

3.6. In vitro release of Carbamazepine

Dissolution testing of CBZ in solid dispersions, with different carriers, is shown in Figure 1(a-d). When applying NUFL, NFL, SYL in formulations of solid dispersions, weight ratio drug/carrier 1:1 has shown slower drug release in comparison to pure CBZ. Possible explanation for this is the fact that CBZ have changed polymorphic form during the formulation process. It is documented [Kobajashy et al., 2000] that form I and Dihydrate form of CBZ have lower intrinsic dissolution rate and solubility in comparison to form III. Other formulations with weight ratio drug/carrier 1:2 and 1:6 have shown the increasing of drug release in comparison to pure CBZ. In all cases, weight ratio drug/carrier 1:6 has shown the highest dissolution rate. The explanation for this we can find in DSC and PXRD curves, which have shown increasing of amorphous form of the CBZ. Like above mentioned, drug amorphization is accompanied by improvement in the drug release rate. Other explanation for this can be greater contact surface area with medium and higher interaction CBZ/carrier which allows greater dissolution rate of a drug.

Drug release was increased using NFL, SYL, NUFL, respectively. This can be due to high specific surface area of adsorbents as well as CBZ/adsorbent interaction found by DSC and FT-IR analysis. In comparison to solid dispersions of CBZ with NUFL and SYL which have shown around 95% CBZ release in the first 15 min, solid dispersion of CBZ and NFL has shown slightly slower release, about 55% in 15 min (Fig.1b). This is probably due to smaller specific surface area of NFL in comparison to other three adsorbents and

consequently, solubility and release rate of CBZ was lower.

It is clear that while using different ratios of Diatomite, drug release stays almost constant. Solid dispersion of CBZ with Diatomite in weight ratio drug/carrier 1:6 (formulation DIAT(1:6)-A) has shown the highest dissolution rate. In weight ratio drug/carrier 1:1, there is a decreasing of dissolution rate of CBZ. Using Diatomite, during first 60min, 40% of CBZ was released (zero order kinetic), and then, in next 150 min, 20% more was released, which indicates that Diatomites can be potentially used as a carrier for sustained release.

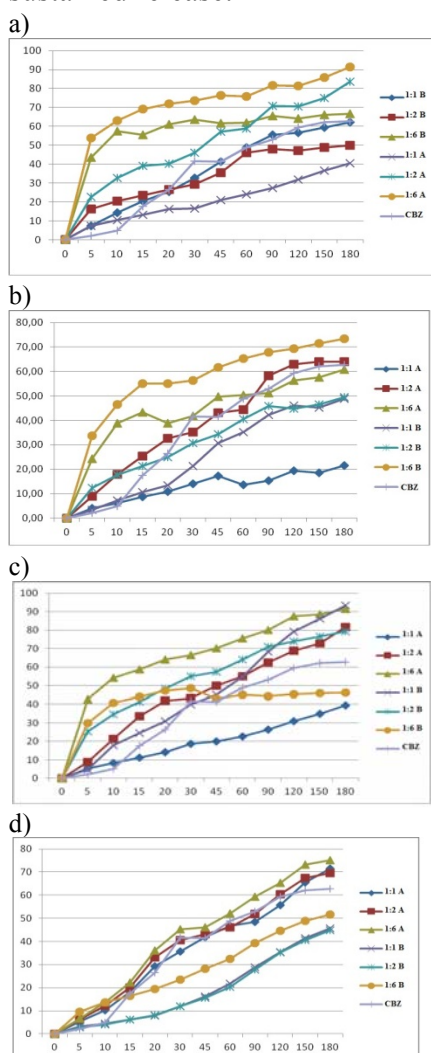


Figure 1: Carbamazepine dissolution profiles from prepared formulations in different ratios (1:1, 1:2 and 1:6) using two methods (A and B) with: a) Neusilin UFL2, b) Neusilin FL2, c) Sylisa, d) Diatomites

4. CONCLUSION

We demonstrated a significantly higher dissolution rate of solid dispersions of Carbamazepine with Magnesium-Aluminum Metasilicate and Silicon Dioxide carriers in comparison to pure Carbamazepine. Also, it is demonstrated that weight ratio drug/carrier have to be carefully chosen, because a dissolution rates can be lower than expected. These carriers can be used for increasing dissolution rate of API, but also for achieving sustained drug release.

REFERENCES

Martindale: The Complete Drug Reference. 34th ed. London: Pharmaceutical Press, 2005.

Kobayashi Y, Ito S, Itai S, Yamamoto K. . 2000. Physicochemical properties and bioavailability of carbamazepine polymorphs and dihydrate. *International Journal of Pharmaceutics*; 193: 137.

Grbic S, PhD dissertation, University of Belgrade, 2012

Leuner C, Dressman J. 2000. Improving drug solubility for oral delivery using solid dispersions. *European Journal of Pharmaceutics and Biopharmaceutics* 50, 47.

Craig D, 2002. The mechanism of drug release from solid dispersions in water-soluble polymer, *International Journal of Pharmaceutics* 231, 131.

Ukmar T, Maver U, Planinsek V, Kaucuc M, Gaberscek A, 2011. Understanding controlled drug release from mesoporous silicates: theory and experiment, *Journal of Controlled Release*, 155 (3), 409.

Aw M.S., Simovic S, Yu Y, Addai-Mensah J, Losic D, 2012. Porous silica microshells from diatoms as biocarrier for drug delivery applications, *Powder Technology*, 223, 52.

Smith, H., Brown, T.W. and Haven, M., 1999. Article Name, *Journal Name*, Volume (Number), Starting Page.

Kobayashi Y, Ito S, Itai S, Yamamoto K. 2000. Physicochemical properties and bioavailability of carbamazepine polymorphs and dihydrate. *International Journal of Pharmaceutics*, 193: 137.

Grzesiak, A.L.; Lang, M.; Kim, K.; Matzger, A.J. 2003. Comparison of the Four Anhydrous Polymorphs of Carbamazepine and the Crystal Structure of Form I. *Journal of Pharmaceutical Sciences*, 92, 2260.

ALGINATE NANOPARTICLES FOR CANCER THERAPY: EFFECT OF CROSSLINKER TYPE ON DRUG ACTIVITY

Umran Aydemir Sezer^{1,2}, Yasemin G. Isgor¹, Belgin S. Isgor^{1,a}

1 Department of Chemical Engineering and Applied Chemistry, Faculty of Engineering, Atilim University, Ankara, Turkey

2 Department of Biomedical Engineering, Middle East Technical University, Ankara, Turkey

a. Corresponding author (bisgor@atilim.edu.tr)

ABSTRACT: Nanoparticles as drug carriers can provide sustained release of encapsulated drug to the target cells. For this purpose, biocompatible polymers appear to be advantageous, and of these, alginate is usually produced via ionic cross-linking with calcium ion. For stable alginate nanoparticles, ANP, a new method has been proposed with use of Aerosol OTTM (AOT) as surfactant in addition to cross-linker ions. Using this new approach, doxorubicin (Dox) loaded manganese (Mndox) and zinc (Zndox) cross-linked ANPs were prepared for the first time, in addition to previously described calcium cross-linked ANPs (Cadox), in the present study. The controls were zinc, manganese and calcium cross-linked ANPs without Doxorubicin. Morphological characteristics, particle size distribution and zeta potential of these particles were investigated together with their drug release behavior. ANPs were found with a size range of 200-400 nm and negative values of zeta potential in the range of 34-65. The drug carriers demonstrated sustained release of Dox under in vitro conditions. These ANPs are still under evaluation via acellular and cellular in vitro assays to reveal the effect of cross-linker metal ions on drug uptake and effectiveness, considering that Mn and Zn are the essential cofactors of enzymes in drug metabolism and cellular functioning.

1. INTRODUCTION

Cancer is the main cause of death worldwide. Despite the serious drawbacks of using anticancer drugs, chemotherapy is one of the main treatments for cancer [Johnson *et al.*, 2010]. Doxorubicin (DOX) has been one of the most commonly used chemotherapeutic agents in the treatment of cancer, but like all anticancer drugs, its clinical application is often limited due to its side effects, in particular cardiotoxicity [Working *et al.*, 1999]. Various drug delivery systems have been developed in order to decrease these side effects by encapsulation of the drug within the drug vehicles [Liang *et al.*, 2010]. Alginate is one of the natural polymers used for many biomedical applications like wound dressing and tissue engineering scaffolds. Most recently, researchers have focused on the use of

alginate as drug delivery vehicles [Li *et al.*, 2008]. Alginate can be crosslinked with a variety of organic and divalent metal ions. Due to the toxicity of organic crosslinkers, metallic crosslinkers are preferred. The most used metallic crosslinker for alginate designed as drug delivery vehicles is calcium. Barium, strontium, iron and zinc crosslinked alginate microparticles and beads were investigated as drug and protein delivery vehicles [Morch *et al.*, 2006]. Alginate nanoparticles are attractive drug vehicles for cancer treatment [Khdair *et al.*, 2008; Chavanpatil *et al.*, 2007]. A novel system based on Aerosol complexation has an ability of release of drug in sustained duration. These systems indicated effective controlled release behavior and cellular activity. However, there is no report with the alginate nanoparticles

crosslinked with manganese and zinc. Manganese and zinc are essential metals as cofactors for driving cellular activities. The lower toxicity together with the essential roles in cellular activities can be attractive for drug activity when these metals are used as crosslinker in alginate nanoparticles loaded with anticancer drug.

In this study, an attempt was made to prepare novel nanoparticles for cancer therapy that can accumulate at the tumor site. For this purpose, alginate nanoparticles were prepared with a variable crosslinker types, and characterized. Different compositions of alginate nanoparticles (ANP) were prepared with different crosslinkers and model drug was doxorubicin (DOX). Their role on drug effectiveness as well as drug resistance at target tissue was evaluated by acellular in vitro enzymatic assays.

2. EXPERIMENTAL

2.1. Materials

Aerosol OTTM (AOT), Alginate, Dichloromethane (DCM, C₂H₂Cl₂), Calcium Chloride (CaCl₂), Manganese Chloride (MnCl₂) and Zinc Chloride (ZnCl₂) was purchased from Sigma (USA), Doxorubicin was obtained from local pharmacy (Saba Pharmaceuticals, Turkey). Other chemicals were purchased from Gerbu (Germany) at analytical grade.

2.2. Preparation of Alginate Nanoparticles

Nanoparticles were formulated by emulsification-crosslinking technology according to previously reported methods (Chavanpatil *et al.*, 2007). Sodium alginate solution in water was emulsified into AOT solution in methylene chloride by vortexing for 1 min over ice bath. The primary emulsion was further emulsified

into 15 mL of aqueous PVA solution by sonication for 1 min over ice bath to form a secondary water-in-oil-in-water emulsion. The emulsion was stirred using a magnetic stirrer, and 5 mL of aqueous calcium chloride solution was added gradually to the above emulsion. The emulsion was stirred further at room temperature for 24 h to evaporate methylene chloride. For preparing drug-loaded nanoparticles, drug was dissolved in the aqueous alginate solution, which was then processed as above. Nanoparticles formed were recovered by ultracentrifugation (Beckman, Palo Alto, CA) at 145000 g, washed two times with distilled water to remove excess PVA and untrapped drug, resuspended in water, and lyophilized. Table 1 summarizes the composition of alginate nanoparticles.

Table 1. Composition of Nanoparticles.

Composition	
Ca	Calcium crosslinked ANPs
Zn	Zinc crosslinked ANPs
Mn	Manganese crosslinked
CaDOX	Doxorubicin loaded Ca
ZnDOX	Doxorubicin loaded Zn
MnDOX	Doxorubicin loaded Mn

2.3. Material Characterization

Particle size of nanoparticles was determined by transmission electron microscopy (TEM). A drop of nanoparticle suspension in alcohol was placed on Formvar-coated copper grids (Ted Pella, Inc., Redding, CA) and allowed to equilibrate. Excess liquid was removed in oven. After drying, the nanoparticles were visualized using a transmission electron microscope (TEM; Philips/FEI, Inc., Briarcliff Manor, NY).

2.4. Doxorubicin Release from Alginate Nanoparticles (ANPs)

Doxorubicin release experiments from alginate nanoparticles were carried out in PBS, (0.01 M, pH 7.4) at 37°C. For this

purpose, doxorubicin loaded alginate nanoparticles were placed in a vial and immersed in 15 mL PBS solution. The samples were placed in shaker bath at 100 rpm at 37°C. Release solution was collected at predetermined time intervals and replaced with fresh PBS. Release studies were carried out as triplicate for each set of sample. The amount of gentamicin was determined with UV-VIS spectrometer from the absorbance at 480 nm and by using the calibration curve prepared with known concentrations of doxorubicin solutions.

2.5. Enzymatic Assays

The effect of complexes on enzymes, namely, GST and GPX were evaluated by employing methods which were miniaturized and optimized by our biochemistry research group (Isgor and Isgor, 2012). The change in total GST activity was measured against the substrate, 1-chloro-2,4-dinitro-benzene (CDNB), by monitoring the thioether (GSH-CDNB conjugate) formation at 340 nm. The measurements were performed in a 100 mM potassium phosphate buffer at pH 6.5 with 2.4 mM CDNB and 3.2 mM GSH, using optimized microplate application protocol.

The GPX activity was measured against the substrate, cumyl hydroperoxides (CumOOH), and the decrease in nicotinamide adenine dinucleotide phosphate (NADPH) was monitored at 340 nm. The GPX activity changes were measured by using purified GPX (37.5×10^{-3} unit/ml), 2 mM GSH, 0.25 mM NADPH, GSH-reductase (GR, 0.5 unit/ml) and 0.3 mM CumOOH, in 0.2 ml of 50 mM Tris HCl (pH 8.0). The enzyme calibration and the dose response curves were constructed using 3-4 independent experiments in 96 well microplates, each in triplicates, using Spectramax M2e, Multi-Mode Microplate

Reader (Molecular Devices Corporation, Sunnyvale, CA, USA).

3. RESULTS AND DISCUSSION

Figure 1 represents the TEM images of alginate nanoparticles prepared with use of different crosslinkers. As seen from TEM images, the nanoparticles are properly spherical in shape and well distributed. There is no significant difference in morphology between the nanoparticles crosslinked with different metal ions. The detected particle size of all nanoparticles were between 201-274 nm, whereas slight increase in size was observed for Doxorubicin loaded particles than corresponding drug free forms.

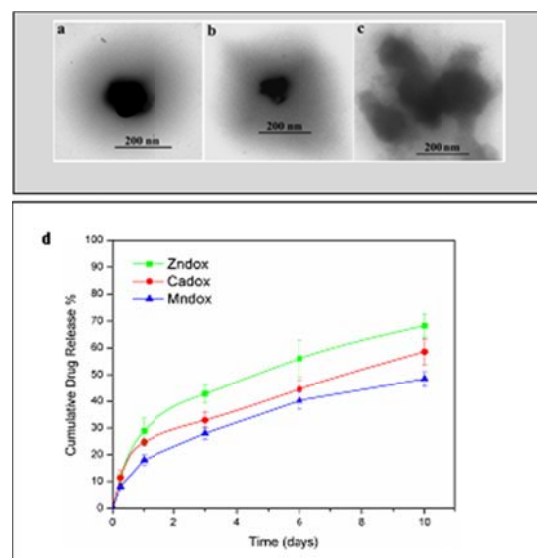
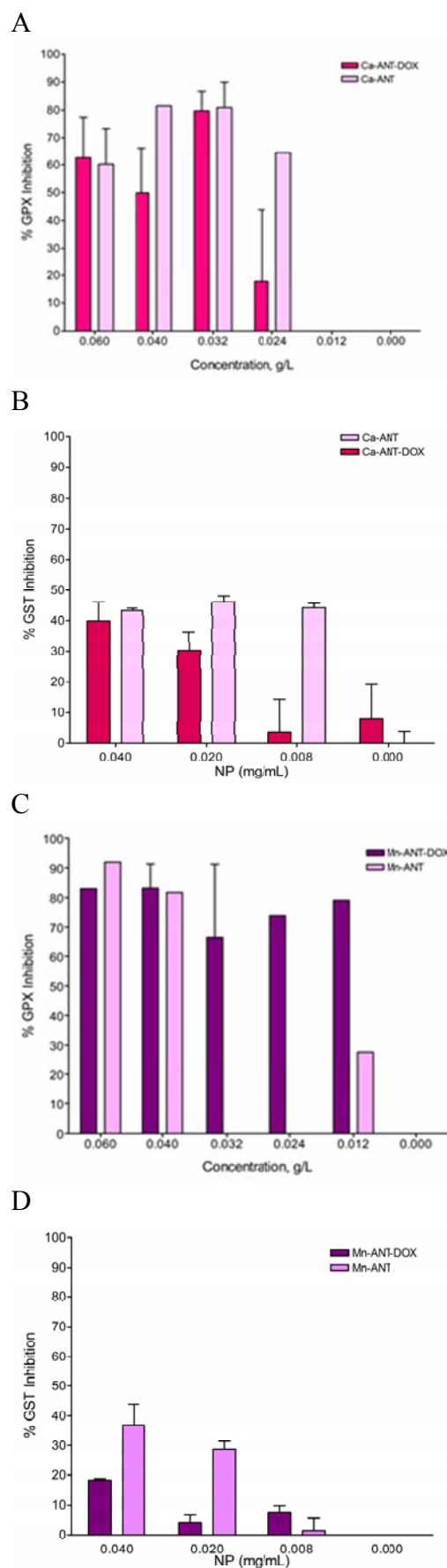


Figure 1: Transmission electron microscope images of ANPs: ZnDOX (a), MnDOX (b), CaDOX (c) and their drug release behaviours (d).

Doxorubicin release profiles of alginate nanoparticles were investigated in PBS (0.01 M, pH 7.4) at 37°C. Among all ANPs analyzed (Figure 1d), ZnDOX showed the fastest doxorubicin release profile, from which more than 68% of the loaded drug was released in 10 days. CaDOX and MnDOX nanoparticles showed 48% and 58% release of their drug load within the same period,

respectively. The rate and the amount of initial release of doxorubicin from nanoparticles showed the variation with types of crosslinkers with indication of biphasic behavior. The initial release from all particles leading to the burst of the doxorubicin could be related to the drugs closer to the surface. The slow release of the diffused doxorubicin from nanoparticles represent the second phase for release which can be explained by good swelling characteristics of alginate that lead to swell efficiently and release drug within the crosslinked polymer matrix in a sustained duration.

The effect of DOX free and DOX encapsulated nanoparticles were analyzed according to their effect on GST and GPX enzyme activities. Considering that GPX inhibition may prevent the drug resistance by facilitating the p53 mediated apoptosis upon DOX exposure, the GPX inhibition by biodegrading DOX free nanoparticle appears to be advantageous to increase drug effectiveness. As seen in Figure 2, in comparing DOX encapsulated and drug free ANPs, it was clear that the release profile of DOX from ANPs was not related with the GPX inhibition tendency of ANPs. However such affinity may be related with the stability of ANPs with and without drug encapsulation. Therefore ZnDOX was identified as the more consistent inhibitor of GPX, whereas CaDOX and MnDOX caused variable responses by interacting with GPX. GST is another enzyme target that is both responsible for increased drug resistance and decreased drug effectiveness, especially for chemotherapeutics needs to be transported from cell cytosol to nuclear region. The analysis of drug free ANPs showed that type of crosslinker do not have any significant effect on GST inhibition profile of ANPs where the maximum inhibition was not more than



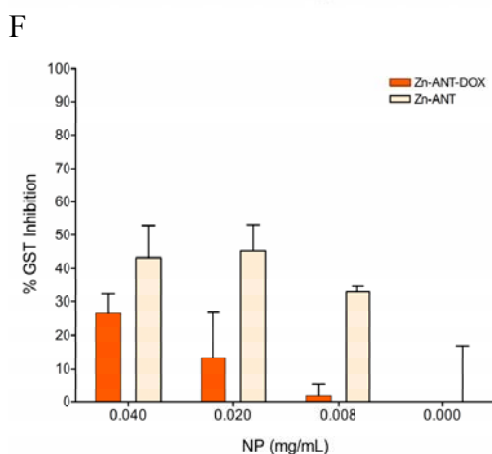
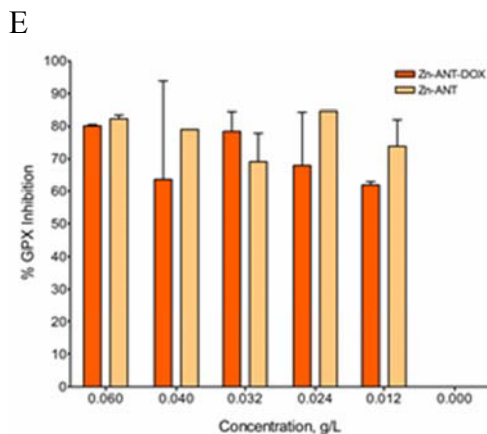


Figure 2: The bar graphs showing the effects of ANPs on GPX and GST enzymes (Dark Bars: doxorubicin encapsulated ANPs; Light Bars: drug free ANPs).

38%. On the other hand, as known with free DOX studies, the DOX encapsulated ANPs showed the dose dependent inhibition profile. Considering that maximum two day release profiles of the particles were used during the enzyme assays, the GST inhibition tendencies of DOX-ANPs appears to be consistent with drug release profiles of ANPs used, whereas the best candidate for GST inhibition was determined as ZnDOX, followed by MnDOX and CaDOX.

4. CONCLUSION

Doxorubicin loaded ANPs with different crosslinker type were prepared by oil-in

water emulsion technique, to be use as drug carrier for cancer treatments. Doxorubicin was released in a sustained period. The findings of the current study show that biodegradable, Zn-Alginate nanoparticles (Zn-ANT) can be potential drug carrier due to promising stability, consistent GST and GPX inhibitory tendency, and better drug release profile as compared to other ANPs prepared.

Acknowledgements: The authors gratefully acknowledge ATILIM BAP-1112-02 for funding and supporting the research.

REFERENCES

- Chavanpatil M. D., Khdair A., Panyam J. 2007. Polymer-Surfactant Nanoparticles for Sustained Release of Water-Soluble Drugs, *J Pharmaceutical Research*. 96(12), 3379.
- Johnson K.A. and Brown P.H. 2010. Drug development for cancer chemoprevention: Focus on molecular targets *Semin Oncol*. 37, 345.
- Isgor B. S. and Isgor Y. G. 2012. Effect of alpha-1-adrenoceptor blocker on cytosolic enzyme targets for potential use in cancer chemotherapy, *Int J Pharmacol*. 8, 333.
- Khdair A., Gerard B., Handa H., Mao G., Shekhar M. P. V. and Panyam J. 2008. Surfactant - Polymer nanoparticles enhance the effectiveness of anticancer photodynamic therapy, *J Molecular Pharmaceutics*. 5, 795.
- Li P., Dai Y.N., Zhang J.P., Wang A.Q. and Wei Q. 2008. Chitosan-alginate nanoparticles as a novel drug delivery system for nifedipine. *Int J Biomed Sci*. 4,221.
- Liang X.J., Chen C., Zhao Y., Wang P.C. 2010. Circumventing tumor resistance to chemotherapy by nanotechnology. *Methods Mol Biol*, 596,467.
- Mørch Y. A., Donati I., Strand B. L. and Skjåk-Bræk G. 2006. Effect of Ca²⁺, Ba²⁺, and Sr²⁺ on alginate microbeads. *Biomacromolecules*, 7,1471.
- Working P.K., Newman M.S., Sullivan T. and Yarrington J. 1999. Reduction of the cardiotoxicity of doxorubicin in rabbits and dogs by encapsulation in long-circulating, pegylated liposomes. *J Pharmacol Exp Ther*. 289,1128.

FABRICATION OF SCAFFOLD FOR CARTILAGE WITH SUBCHONDRAL BONE REGENERATION BY LAMINATION OF HYDROXYAPATITE/COLLAGEN NANOCOMPOSITE AND COLLAGEN

S.Oshima^{1,2}, K.Ozeki² and M.Kikuchi^{1,a}

1. Biomaterials Unit, Nano-Life Field, International Center for Materials Nanoarchitectonics, National Institute for Materials Science, Japan
2. Department of Mechanical Engineering, Ibaraki University, Japan
a. KIKUCHI.Masanori@nims.go.jp

ABSTRACT: A laminated scaffold with chondral and subchondral parts was fabricated with type-I collagen sponge and hydroxyapatite/collagen bone-like nanocomposite (HAp/Col) sponge. The HAp/Col sponge was prepared by gelation, freezing and lyophilization of the HAp/Col sol, a mixture of the HAp/Col fibers, phosphate buffered saline and collagen sol. A laminated scaffold was prepared by placing the HAp/Col sponge (sponge-sol method) or the HAp/Col sol (sol-sol method) on collagen sol followed by the same procedure for preparing the HAp/Col sponge. The scaffold was then dehydrothermally cross-linked. The microstructures of scaffolds were observed with a scanning electron microscope (SEM). Mean pore diameter of the scaffold was measured by the line-intercept method using SEM photos. The ultimate tensile strength (UTS) of the scaffold in PBS-wet condition was measured with a texture analyzer. The bonding part of the scaffolds seemed to be well unified. Mean pore diameters of the HAp/Col and collagen parts were 75 ± 3 and 85 ± 4 μm for the sponge-sol method, and 114 ± 10 and 76 ± 9 μm for the sol-sol method. The UTS of the scaffolds were 8.3 ± 1.5 kPa for the sponge-sol method and 6.6 ± 2.2 kPa for the sol-sol method. These results suggested that the laminated scaffold materials are expected to be good osteochondral regeneration scaffold.

1. INTRODUCTION

In general, seriously damaged articular cartilages require transplantation of autologous cartilage, or engineered chondrogenic cells or tissue. These transplantations faced the problem of bonding failure between transplanted and host tissues. The mosaicplasty, transplantation of osteochondral tissues from non sliding-surface of an articular cartilage, showed good results due to good bonding between transplanted and host cartilages by fixation at the subchondral region. However, one big problem is a remaining of defects at the donor site. Thus, a laminated scaffold mimic transplant tissue in mosaicplasty having both chondral and subchondral parts would be a good candidate for cartilage regeneration to improve bonding

between engineered and host tissues as well as ignoring extraction of healthy donor tissues. Type-I collagen sponge has been proven as a good scaffold for articular cartilage regeneration and used by many researchers and companies. For subchondral regeneration, hydroxyapatite ceramics is one of the candidates due to its high performance in enhancement of osteogenic activity of cells but not good at biodegradability. A hydroxyapatite/collagen bone-like nanocomposite (HAp/Col) [Kikuchi *et al.*, 2001] sponge [Kikuchi *et al.*, 2004a] is a strong candidate for subchondral region, because it has sponge-like viscoelasticity, promotes osteogenic function of cells to secrete calcium phosphate on extracellular matrices [Yoshida *et al.*, 2010], and is

incorporated into bone remodeling process [Kikuchi *et al.*, 2001, 2004b] to be substituted with newly formed bone.

In this study, the laminate scaffold was prepared by two methods using the HAp/Col and collagen. Mean pore diameters and ultimate tensile strengths of the scaffolds were measured to evaluate the scaffold availability for practical use.

2. MATERIALS AND METHODS

2.1. Preparation of Laminate Scaffold

Type-I atelocollagen sol extracted from porcine dermis was purchased from Nitta Gelatin Inc., Osaka, Japan. Hydroxyapatite/collagen bone-like nanocomposite (HAp/Col) was synthesized according to the method described in [Kikuchi *et al.*, 2001 and 2003]. Briefly, 199.1 cm³ of 400 mM Ca(OH)₂ suspension (prepared by burning and hydration from alkaline analysis grade CaCO₃, Wako Pure Chemicals, Japan) and 398.2 cm³ of 120 mM H₃PO₄ aqueous solution with 2.01 g of type-I atelocollagen were simultaneously titrated into a reaction vessel, in which 199.1 cm³ pure water was previously added via auto-titration units at 30 cm³/min under maintaining pH and temperature of the solution in the reaction vessel at 9 and 40 °C, respectively. The HAp/Col obtained was lyophilized and stored in 4 °C refrigerator. The HAp/Col sol and sponge were prepared by the method in [Kikuchi *et al.*, 2004a]. Briefly, the HAp/Col sol was prepared by mixing of the HAp/Col with 10x phosphate buffered saline (PBS) containing type-I atelocollagen at 0.85 mass% to the HAp/Col. The HAp/Col sponge was prepared from the HAp/Col sol by gelation at 37 °C for 2 h followed by freezing at -20 °C and lyophilization. Collagen sol was prepared by the conventional process, i.e., pH and ion concentration were adjusted to those of

body fluid by addition of 1N NaOH and 10x PBS.

A laminated scaffold for cartilage regeneration together with subchondral bone was prepared by the following two methods; one was a “sponge-sol” method that the HAp/Col sponge was placed on the collagen sol. Another was a “sol-sol” method that the collagen sol was placed on the HAp/Col sol. The sponge-sol or sol-sol construct obtained was incubated at 37 °C for 2 h for gelation of sols, frozen at -20 °C to form pores and lyophilized followed by dehydrothermal cross-linking at 140 °C for 12 h. Amounts of used of the HAp/Col and atelocollagen were calculated from expected size of a scaffold, 11 mm in diameter and 10 mm (5+5 mm) in height.

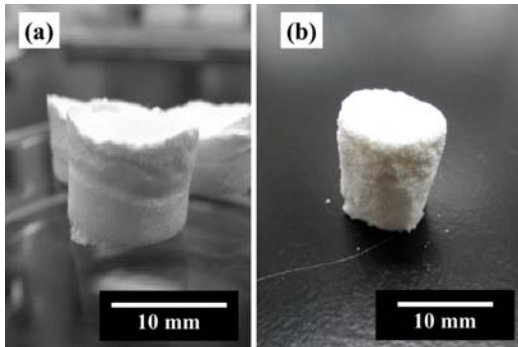
2.2. Microstructure Observation

Cross-sections of the two types of scaffolds were observed with a scanning electron microscope (SEM, JEOL Ltd.) at accelerating voltage of 20 kV. Mean pore diameters for both scaffolds in the HAp/Col and collagen regions were measured and calculated by the line-intercept method using each 3 images from both regions at 50x magnification.

2.3. Ultimate Tensile Strength Test

Bonding strength between the HAp/Col and collagen sponges in the scaffold under a PBS wet condition was evaluated by an ultimate tensile strength (UTS) measured with a texture analyzer (Stable Micro Systems Ltd.) at a crosshead speed of 500 μm/min. The scaffold was fixed to aluminum SEM stage with cyanoacrylate adhesive (Aron Alpha Extra, Toagosei Co., Ltd., Japan) as chucking parts. A diameter of the scaffold was 10 mm. Heights of each region for the sponge-sol scaffold were 3 mm for the HAp/Col and 5 mm for the collagen regions, and heights for the sol-sol scaffold were 5 mm for both regions.

3. RESULTS AND DISCUSSION



The laminated scaffolds prepared by the Figure 1: Photographs of the laminate scaffolds prepared by (a) sponge-sol method and, (b) sol-sol method. Upper is the HAp/Col and bottom is collagen.

sponge-sol and sol-sol methods were shown in Figure 1 (a) and (b).

The HAp/Col sponge sank 2 mm into the collagen sol during the preparation, thus collagen intrusion was observed with SEM photo at the bonding region between the HAp/Col and collagen (Figure 2 (a).) For the mimicry of the osteochondral region, this graded interface seemed “mineralized cartilage” region. However, as a result, height of the sponge-sol scaffold became 8 mm in total with 3 mm for the HAp/Col, 2 mm for the graded and 3 mm for the collagen parts. In the sol-sol method, no obvious intrusion was observed; thus, heights of

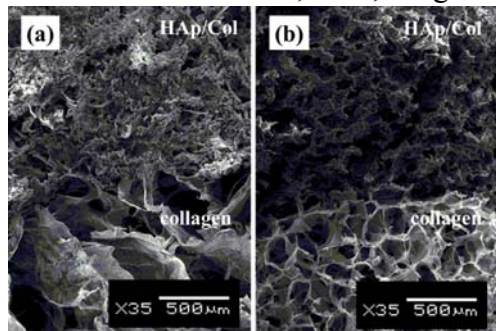


Figure 2: Scanning electron micrographs of surface cross-section at boundary between the HAp/Col and collagen of the scaffolds prepared by (a) sponge-sol and (b) sol-sol methods. Upper is the HAp/col region, and bottom is collagen region.

the HAp/Col and collagen regions were 5 mm each. However, flatness bonding interface between the HAp/Col and collagen regions seemed worse than that of the sponge-sol scaffold. Diameters of both scaffolds decreased to 10 mm by the shrinkage during dehydrothermal cross-linking. These results suggested that the sponge-sol method requires controlling sinking depth of the HAp/Col sponge into the collagen sol by time and viscosity of the collagen sol, but they are easily controlled. Contrarily, flatness of bonding interface will be required for the sol-sol scaffold.

The laminated scaffolds retained water in their pore and walls in a wet condition, and revealed sponge-like viscoelasticity mainly at the HAp/Col part.

Mean pore diameters for the HAp/Col and collagen parts of laminated scaffolds were respectively 75 ± 3 and 85 ± 4 μm for the sponge-sol, and respectively 114 ± 10 and 76 ± 9 μm for the sol-sol. These pore sizes could be sufficient for cell intrusion as bioresorbable materials.

Figure 3 shows the UTS of the scaffolds. The UTS of the sponge-sol and sol-sol scaffolds were 8.3 ± 1.5 kPa and 6.6 ± 2.2 kPa, respectively.

For the sponge-sol scaffold, 4 were

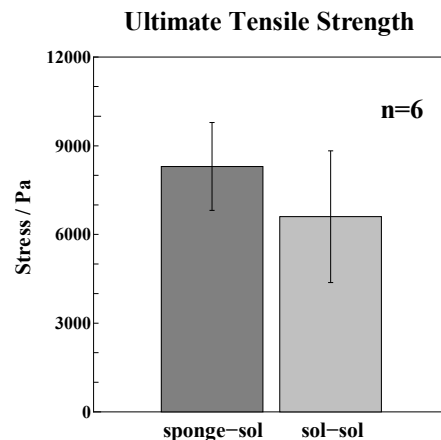


Figure 3: Ultimate tensile strength of the sponge-sol and the sol-sol scaffolds.

broken at the HAp/Col region, and 2 were broken at collagen region. For the sol-sol scaffold, 4 were broken at the HAp/Col region, one sample was broken at the HAp/Col region, one sample was broken at the HAp/Col-collagen boundary, and one was broken at the collagen region. Minimum UTS was measured for the scaffold broken at the collagen region; thus, the scaffold at least had a sufficient UTS for handling in cell culture and surgical operation.

The UTS of the sponge-sol scaffold was stronger than that of the sol-sol sponge in trend. In addition, HAp/Col-collagen boundary seemed stronger in the sponge-sol scaffold than the sol-sol one, because bonding region of the sponge-sol scaffold was enhanced by covering the HAp/Col sponge by collagen sponge intruded during the preparation.

4. CONCLUSION

The laminated scaffolds prepared by the sponge-sol and sol-sol methods had sufficient pore diameter and strength for handling as tissue engineering scaffolds. The scaffold prepared by the sponge-sol method had a graded bonding region that mimicked a chondral-subchondral interface, mineralized cartilage. Both laminated scaffolds considered as good candidates for scaffolds for osteochondral regeneration.

REFERENCES

- Kikuchi, M., Itoh, S., Ichinose, S., Shinomiya, K., and Tanaka, J., 2001. Self-organization Mechanism in a Bone-like Hydroxyapatite/collagen Nanocomposite Synthesized in vitro and its Biological Reaction in vivo, *Biomaterials*, (22), 1705.
- Yoshida, T., Kikuchi, M., Koyama, Y., and Takakuda, K., 2010. Osteogenic Activity of MG63 Cells on Bone-like Hydroxyapatite/collagen Nanocomposite Sponges, *Journal of Materials Science: Materials in Medicine*, (21), 1263.
- Kikuchi, M., Ikoma, T., Syoji, D., Matsumoto, H.N., Koyama, Y., Itoh, S., Takakuda, K., Shinomiya, K. and Tanaka, J., 2004 a.

- Porous Body Preparation of Hydroxyapatite/collagen Nanocomposites for Bone Tissue Regeneration, *Key Engineering Materials*, (561), 254
- Kikuchi, M., Ikoma, T., Itoh, S., Matsumoto, H. N., Koyama, Y., Takakuda, K., Shinomiya, K., and Tanaka, J., 2004 b. Biomimetic Synthesis of Bone-like Nanocomposites Using the Self-organization Mechanism of Hydroxyapatite and Collagen, *Composites Science and Technology*, (64), 819.
- Kikuchi, M., Itoh, S., Matsumoto, H.N., Koyama, Y., Takakuda, K., Shinomiya, K. and Tanaka, J., 2003. Fibrillogenesis of Hydroxyapatite/Collagen Self-Organized Composites, *Key Engineering Materials*, (567), 240

MORPHOLOGY OF MICELLAR STRUCTURES IN SIMULATED BODY FLUID FOR DRUG DELIVERY PURPOSES

Fatoş Nacar¹, Ahmet Erkin Ermiş¹, Mehmet Polat¹ and Hurriyet Polat^{2,a}

1. Department of Chemical Engineering, Izmir Institute of Technology, Urla, Izmir, Turkey
2. Department of Chemistry, Izmir Institute of Technology, Urla, Izmir, Turkey
a. Corresponding author (hurriyetpolat@iizte.edu.tr)

ABSTRACT: Micellar structures are becoming increasingly important in drug delivery applications. Morphology of these structures is a factor determining the form and the amount of the drug to be enveloped as well as how the release mechanisms will function. Though there are numerous works on micelles in the literature in aqueous media, understanding is lacking with respect to the specifics of the micelle formation and the exact morphology of the micelles produced within simulated body fluids.

The work focuses on the conditions to create well-defined micellar structures in simulated body fluids using some selected polymeric surface active agents (PEO-PPO-PEO triblock copolymers). The form of surfactant on the liquid-gas interface, micelle size distributions and electrokinetic potentials were the parameters studied. It was found that the micellar formation behaviour was quite different in simulated body fluids than that observed in simple aqueous media. The size and shape of the micelles were higher in simulated body fluid. The electrolytes in the simulated body fluid affect the micelle size and charge.

1. INTRODUCTION

The delivery of therapeutic compounds can be hindered by their poor water solubility. Therefore, use of micellar structures for solubilizing these compounds has become extremely important. Micelles of triblock copolymers is one promising example due to their unique composition; characterized by a hydrophobic core, which solubilizes the drug, and a hydrophilic corona which acts as a stabilizer [Gaucher, *et al.*, 2005; Sachs-Barrable *et al.*, 2007; Plapied, 2011; Hunter *et al.*, 2012; Ensign, *et al.*, 2012].

Most data with respect to the use of polymeric surfactants in drug delivery is based on the work carried out in distilled water. However, presence of electrolytes in solution should affect both the size and the shape of the surfactant molecules due to the screening effect of the ionic species.

Simulated body fluid is an electrolyte solution. Therefore, a detailed morphological study of polymeric surfactant molecules in electrolytic body fluids is important for effective encapsulation of drug molecules within micellar structures.

The purpose of this study was a) to study in detail the concept of micelle and the process of micellization b) to investigate and compare the micellar structures in simulated body fluid (SBF) c) to explore the concept of micelle as a tool in drug delivery system. Therefore, a comprehensive study was carried out to determine the changes that may take place in the surface energies, sizes and charges of the micellar structures when they are prepared in simulated body fluids as opposed to distilled water.

2. MATERIALS AND METHODS

2.1. Materials

Some selected PEO/PPO/PEO type tree block co-polymers were employed. The properties of these polymeric surfactants are given in Table 1.

Table 1: Selected properties of the PEO/PPO/PEO type block co-polymers employed.

	Chemical Structure	M.W.
P-123	$(\text{HO}(\text{CH}_2\text{CH}_2\text{O})_{20}(\text{CH}_2\text{CH}(\text{CH}_3)\text{O})_{70}(\text{CH}_2\text{CH}_2\text{O})_{20}\text{H}$	5800
L-64	$(\text{HO}(\text{C}_2\text{H}_4\text{O})_{13}(\text{C}_3\text{H}_6\text{O})_{30}(\text{C}_2\text{H}_4\text{O})_{13}\text{H}$	2900
P-104	$(\text{HO}(\text{CH}_2\text{CH}_2\text{O})_{27}(\text{CH}_2\text{CH}(\text{CH}_3)\text{O})_{61}(\text{CH}_2\text{CH}_2\text{O})_{27}\text{H}$	5900
F-127	$(\text{HO}(\text{CH}_2\text{CH}_2\text{O})_{100}(\text{CH}_2\text{CH}(\text{CH}_3)\text{O})_{65}(\text{CH}_2\text{CH}_2\text{O})_{100}\text{H}$	12500

2.2. Methods

2.2.1. Preparation of simulated body fluids

Simulated body fluid is an electrolyte solution which has ion concentrations nearly equal to those of human blood plasma and is buffered at pH 7.40 with 50 mM trishydroxy methylaminomethane and 45 mM hydrochloric acid at 37°C [Oyane, *et al.*, 2003]. The formula of the prepared body fluids is presented in Table 2.

Table 2: Composition of the body fluids prepared.

Order	Reagents	Amounts
1	NaCl	7.996 g
2	NaHCO ₃	0.350 g
3	KCl	0.224 g
4	K ₂ HPO ₄ ·3H ₂ O	0.228 g
5	MgCl ₂ ·6H ₂ O	0.305 g
6	1M-HCl	40 ml
7	CaCl ₂	0.278 g
8	Na ₂ SO ₄	0.071 g
9	(CH ₂ OH) ₃ CNH ₂	6.57 g

2.2.2. Characterization methods employed

The methods for characterization and analysis used in the study are summarized in Table 3.

Table 3: Analysis and characterization methods used.

Analysis	Method	Device
Surface Tension	Dü Nouÿ Ring	Krüß Tensiometer
Micelle Size	Laser Velocimetry	Malvern Mastersizer
Micelle Charge	Laser Velocimetry	Malvern Mastersizer

3. RESULTS AND DISCUSSION

3.1. Surface Tension Studies: Association of Surfactant Molecules

Surface tension studies are conducted in both distilled water and SBF to determine the association behaviour of these molecules. The results are given in Figure 1. As it is seen from the figure that the surface tension values did not change significantly. This is expected due to the nonionic character of these surfactant, P-123.

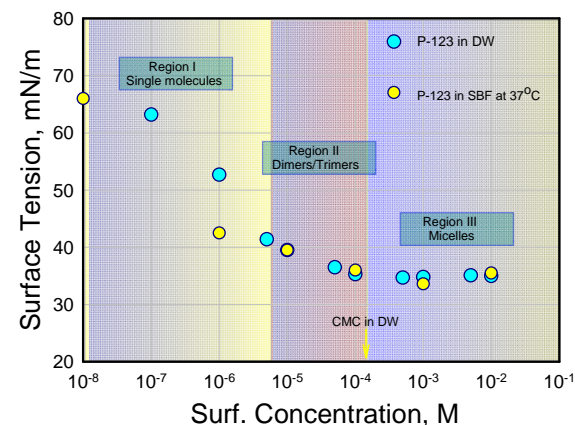


Figure 1: Surface tension of P-123 in Distilled water and Simulated Body Fluid.

The surface tension values of other surfactants employed were also given in

Figure 2 for water and in Figure 3 for SBF to observe the differences in their association behaviour in water-SBF and their adsorption behaviour at water-SBF/air interface.

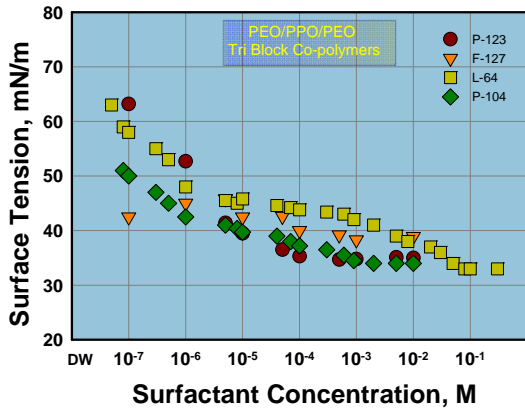


Figure 2: Surface tension of P-123, F-127, L-64 and P-104 in Distilled water.

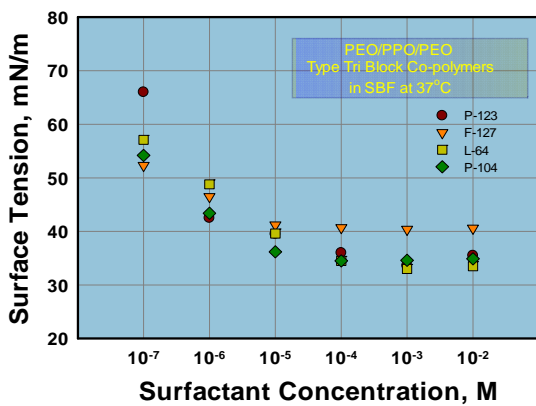


Figure 3: Surface tension of P-123, F-127, L-64 and P-104 in SBF at 37°C.

3.2. Micelle Size Measurements

Micelle size of polymeric surfactants both in water and SBF were measured and presented in Figure 4. As it is seen the micelle size of polymeric surfactants in some cases were almost an order of magnitude larger in SBF than in DW.

2.1. Micelle Charge Measurements

Micelle charge of polymeric surfactants in both distilled water and SBF were measured and presented in Figure 5. It was observed that the micelle charge of

some polymeric surfactants 2-4 folds increased in SBF when compared to those observed in DW.

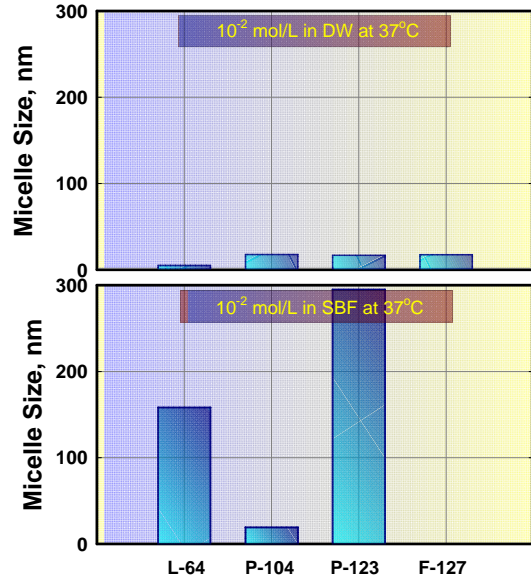


Figure 4: Micelle size of surfactants in distilled water and simulated body fluid.

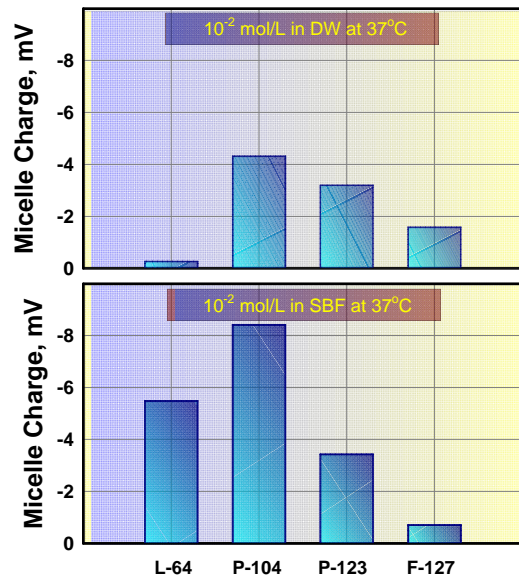


Figure 5: Micelle charge of surfactants in distilled water and simulated body fluid.

4. CONCLUSIONS

Behavior of micellar structures both with respect to micelle size and charge was observed to be quite different in

simulated body fluids compared to that observed in distilled water.

This conclusion has important implications in drug delivery using micelles since previous knowledge is based on studies which were carried out in distilled water.

Specifics:

- i. Surface tension of the surfactant solutions did not show a significant difference between DW and SBF.
- ii. Micelle size of polymeric surfactants in some cases were almost an order of magnitude was larger in SBF than in DW.
- iii. Micelle charge of some polymeric surfactants 2-4 folds increased SBF when compared to those observed in DW.

REFERENCES

- Ensign, L. M., Cone, R., Hanes, J., 2012, Oral drug delivery with polymeric nanoparticles: the gastrointestinal mucus barriers, *Advanced Drug Delivery Reviews*, <http://dx.doi.org/10.1016/j.addr.2011.12.009>.
- Hunter, A. C., Elsom, J., Wibroe, P. P., and Moghimi, S. M., 2012, Polymeric particulate technologies for oral drug delivery and targeting: a pathophysiological perspective, *Nanomedicine: Nanotechnology, Biology, and Medicine*, 5-20.
- Gaucher, G. et.al., 2005, Block copolymer micelles: preparation, characterization and application in drug delivery, *Journal of Controlled Release* 109 169–188
- Oyane, A. et.al., 2003 Preparation and assessment of revised simulated body fluids, *Journal of Biomedical Materials Research* 65 188-195
- Plapied, L., Duhem, N., des Rieux, A., Preat, V., 2011, Fate of polymeric nanocarriers for oral drug delivery, *Current Opinian in colloid and Interface Science*, (16), 228-237.
- Sachs-Barrable K, Lee, S. D., Wasan E. K., Thomton, S. J., Wasan K. M., 2007, *Advanced Drug Delivery Reviews*, (60), 692-701.

IN-VITRO RELEASE OF THEOPHYLLINE THROUGH CELLULOSE ACETATE MEMBRANES MODIFIED BY n-SiO₂

Gülşen Asman^{1,a}, Mürvet Taşkın¹

1. Gazi University, Faculty of Science, Department of Chemistry, Ankara, TURKEY
a. Corresponding author (gulsena@gazi.edu.tr)

ABSTRACT: Release characteristics of theophylline from n-SiO₂ modified cellulose acetate membranes (n-SiO₂-CA) were investigated at in-vitro conditions. The effect of the thickness of the membrane, pH of donor and receiver solutions, concentration of theophylline and temperature on the release performances of theophylline from membranes was studied. As the thickness of the membrane increased the transfer of theophylline decreased in accordance with Fick's first law. It was concluded that the permeation of theophylline through the membranes is high for the pH's at which theophylline has high solubility. Increase in theophylline concentration and temperature increased the amount of theophylline transferred from the membranes. The activation energy for the transfer of theophylline from n-SiO₂-CA membranes was found as 12.17 J/mol.

1. INTRODUCTION

Theophylline (1,3-dimethyl xanthine) is a commonly used drug in the treatment of asthma and chronic obstructive pulmonary disease and its dosages require careful management by taking in care of serious side-effects since its pharmacokinetic properties are mainly affected with age, diet, smoking habits and other medications [Lee, 1985; Sweetman, 2002]. However theophylline had a low therapeutic index and small changes in plasma levels might result in therapeutic failure or adverse effects therefore the clinical use of theophylline was limited (Stavric 1988; Paloucek and Rodvold 1988; Minton and Henry 1996). There is a great interest for the controlled release studies of theophylline by using polymeric membrane systems in pharmaceutical studies (Heard et al. 2006; Grassi et al. 2001; Siepmann et al. 2007; Zhao et al. 2006; Prabakaran et al. 2004; Liu et al. 2005; Bayraktar et al. 2005; Makhija and Vavia 2003; Bi et al. 2007; Bi et al. 2008). CA is an attractive polymer in the preparation of transdermal delivery membranes (Wang et al. 2002; Rao and Diwan 1997; Meier et al. 2004; Chen et al. 2010; Makhija and Vavia

2003). But, CA as a rate controlling membrane material for transdermal drug delivery system generally requires plasticizers and some modifications to improve its permeation performances (Reverchon and Cardea 2004; Wang et al. 2002; Valente et al. 2005; Rao and Diwan 1997, Makhija and Vavia 2003). In this study n-SiO₂ was used to modify cellulose acetate (CA) membranes.

1.1. Preparation of n-SiO₂-CA Membranes and Permeation Studies

n-SiO₂-CA membranes were prepared by dry casting method. For this aim 6% CA (m/v) solution that contains 10% n-SiO₂ with respect to the dry mass of polymer, was prepared in acetone as casting solution and predetermined amount of casting solution was used to cast the membranes by using glass petri dishes. Membranes were immersed in 6M HCl solution, that was determined as a solvent for n-SiO₂ particles and then they were applied to sonication at a frequency of 50 kHz (Elmasonic X-tra 50Hmodel) for definite time intervals to prepare n-SiO₂-CA membranes.

Permeation studies were carried out at $32\pm 1^\circ\text{C}$ by using Franz type diffusion cell. The donor compartment holds theophylline solution (5 mg/mL) and acceptor compartment was filled with buffer at different pH values (pH 2.10-7.4). Phosphate (pH 7.4) or acetate (pH 2.1- 5.0) buffer solutions were used depending on the desired pH. Membranes were equilibrated with buffer solution before the permeation studies. The receiver solution was sampled periodically and samples were replaced with equal volume of fresh buffer solution. The concentrations of theophylline solution were determined spectrophotometrically at 272 nm by using Unicam 4802 UV/VIS double beam spectrometry.

2. RESULTS AND DISCUSSION

2.1. Effect of Membrane Thickness on the Permeation of Theophylline through n-SiO₂-CAMembranes

n-SiO₂-CA membranes were prepared at a thickness of 40 μm , 70 μm , 100 μm and 130 μm , and permeation studies were carried out as explained above. The results of the permeations were given in Figure 1.

As it is stated in the figure, transfer of theophylline decreased with the increase in the membrane thickness in accord to Fick's first law. Although the greater permeation was obtained in case of the membrane with a thickness of 40 μm , the rest of the study was carried out by using the membranes at a thickness of 70 μm because of its most comfortable preparation conditions.

2.2. Effect of pH on the Permeation of Theophylline through n-SiO₂-CAMembranes

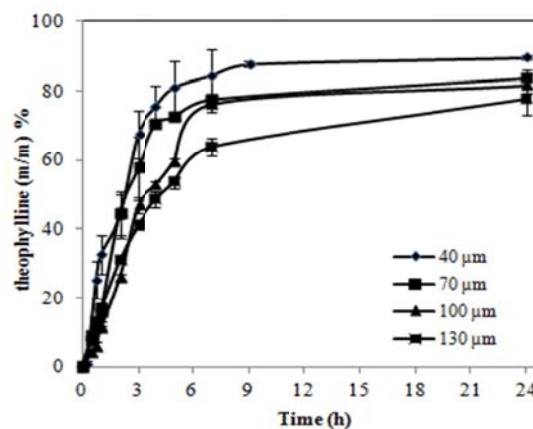


Figure 1: Effect of membrane thickness on the permeation of theophylline through n-SiO₂-CA membranes (pH: 7.40, $t = 32\pm 1^\circ\text{C}$).

The effect of pH on the permeation performance of the n-SiO₂-CA membranes was studied at two steps: in the first step the pH of receiver solution was changed as long as the donor compartment was kept at constant pH of 7.4. In the second part the study, the pH of receiver solution was kept constant at pH of 7.4 while donor compartment solution pH was changed.

As a first part, pH of the donor solution (theophylline solution at a concentration of 5 mg/mL) was kept constant at pH of 7.40 and the pH of the receiver solution was adjusted as pH: 7.40, 5.50, 4.30, 3.50 and 2.10; the results of the permeation was stated in Figure 2.

As it is seen from the figure, the greater permeation for theophylline was obtained at pH of 2.10 while the smaller was obtained at pH of 3.5. The permeation percentages obtained at the other studied pH values were ranged between these two pH values and they are so close to each other.

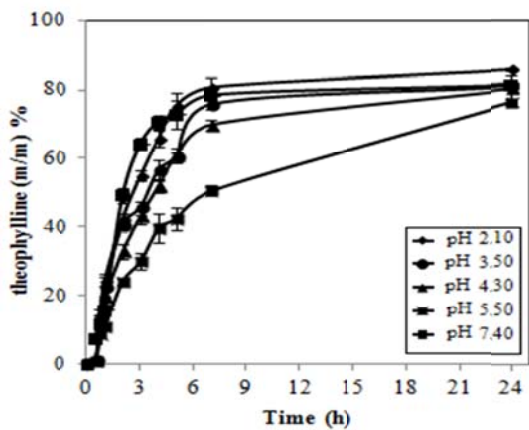


Figure 2: Effect of the pH of receiver solution on the permeation of theophylline through n-SiO₂-CA membranes (pH of donor solution is 7.4, t = 32±1 °C)

At the second stage, the pH of the receiver solution was kept constant at pH of 7.4 while donor compartment solution pH was changed as pH of 7.40, 5.50, 4.30, 3.50 and 2.10. The results of the permeation was stated in Figure 3.

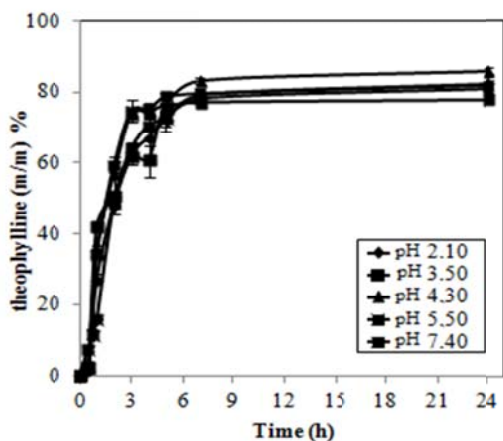


Figure 3: Effect of the pH of donor solution on the permeation of theophylline through n-SiO₂-CA membranes (pH (donor)= 7.4, t = 32±1 °C)

As it clearly understood from the figure, almost the same transfer percentages were obtained for all pH values studied, at pH 5.5 lower permeation was obtained. Bi et al. (Bi et al. 2007), studied the effect

of pH on the solubilities of theophylline and proposed the following equation.

$$C_s = 0.0209k^4 - 0.5864k^3 + 6.0873k^2 - 27.791k + 54.183$$

(1)

$$(3 \leq k \leq 12, r = 0.9881)$$

C_s= Solubility of theophylline (mg/mL)

k = pH value

The solubilities of theophylline at the studied pH values were calculated by using Eq.1 and given in Table 1.

Table 1: Solubilities of theophylline at different pH values

pH	Solubility (mg/mL)
7.40	6.92
5.50	7.03
4.30	7.76
3.50	9.48

Swelling ratio, S_w, of the membranes were computed by using Eq.2

$$S_w = \frac{W - W_0}{W_0} \quad (2)$$

Where, W and W₀ are the wet and dry mass of the membranes respectively. Swelling ratio values of the membranes in theophylline and buffer solutions at different pH values were calculated by using Eq.2 and stated in Table 2 and Table 3 respectively.

Table 2: Effect of pH of theophylline solution on the swelling ratio of n-SiO₂-CA membranes

pH (Theophylline solution, 5 mg/mL)	Swelling Ratio
2.10	2.70
3.50	2.48
4.30	2.13
5.50	1.29
7.40	1.88

Table 3: Effect of pH of buffer solution on the swelling ratio of n-SiO₂-CA membranes

pH	Swelling Ratio
2.10	1.83
3.50	1.79
4.30	1.48
7.40	1.36
5.50	1.15

As it is seen from the tables, decrease in pH increased the solubility of theophylline (Table 1) and the swelling ratio of n-SiO₂-CA membranes also increased at low pH values (Table 2 and 3). From the comparison of Table 2 with Table 3 it can be concluded that greater interaction between the membrane and theophylline since S_w values corresponding to theophylline solutions are greater than that obtained with buffer solutions. This might be the reason of getting lower permeation percentage at pH 3.5 at which theophylline have great solubility. Since at pH 5.5 membranes have low S_w , it acts as a barrier surface in case of constant acceptor pH and almost the same permeation percentages were obtained for all the pH values studied, as stated in Figure 3.

2.3. Effect of Theophylline Concentration on the Permeation of Theophylline through N-SiO₂-CA Membranes

In order to determine the effect of theophylline concentration on the permeation performance of n-SiO₂-CA membranes, theophylline solution was prepared at a saturated concentration, and pH was kept constant at 7.4. The results of the permeation were reflected in Figure 4. As it is seen from the figure increase in concentration increased the permeated amount of theophylline through the n-SiO₂-CA membranes.

2.4. Effect of Temperature on the Permeation of Theophylline through N-SiO₂-CA Membranes

To determine the effect of temperature on the permeation of theophylline through n-SiO₂-CA membranes the study were conducted at 32±1°C, 37±1°C and 39±1°C, which are the skin surface temperature, body temperature and fever

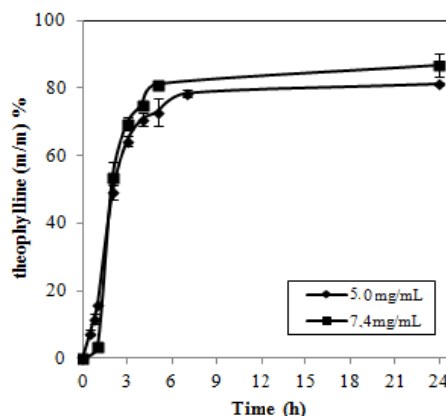


Figure 4: Effect of concentration on the permeation of theophylline through n-SiO₂-CA membranes (pH=7.4, t = 32±1 °C)

body temperature respectively. The results were reflected in Figure 5.

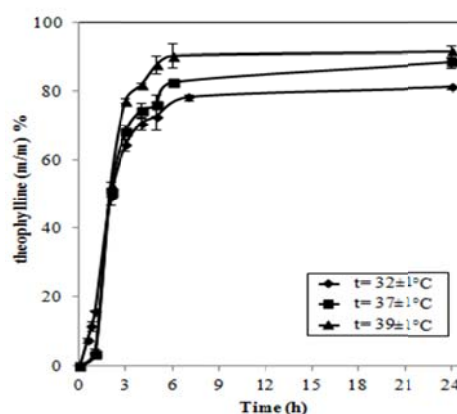


Figure 5: Effect of temperature on the permeation of theophylline through n-SiO₂-CA Membranes (pH=7.4)

As it is seen from the figure, increase in temperature increased the permeated amount of theophylline through the n-SiO₂-CA membranes. The transfer of the molecules through a polymeric

membrane follows an Arrhenius type of relation and given by Eq. 3 (Lai et al. 1993; Ruckenstein and Liang 1996; Rhim et al. 1997; Asman et al. 2008),

$$J = A \cdot e^{-E_a/RT} \quad (3)$$

where J is the mass transferred per unit area in unit time (kg/m²h), A is the preexponential factor and E_a is the overall activation energy in J/mol. E_a for the permeation of theophylline through n-SiO₂-CA membranes was determined from the slope of linear regression line of logarithmic permeation rate versus the reciprocal of the absolute temperature and was found as 12.17 J/mol.

ACKNOWLEDGEMENTS:

This study was supplied by Gazi University Research Fund.

REFERENCES

- Asman G., Sanli O., Tuncel D., 2008. pH and Temperature Sensitive In-vitro Release of Salicylic Acid through Poly(vinyl alcohol-g-acrylamide) Membranes. *J Appl Polym Sci* 107, 3005.
- Bayraktar O., Malay Ö., Özgarip Y., Batgün A., 2005. Silk fibroin as a novel coating material for controlled release of theophylline. *Eur J Pharm Biopharm* 60, 373.
- Bi Y., Mao S., Gan L., Li Y., Wang C., Xu N., Zheng Y., Cheng Q., Hou S., 2007. A controlled porosity osmotic pump system with biphasic release of theophylline. *Chem. Pharm. Bull.* 55(11), 1574.
- Bi Y., Zhang Y., Zhao J., Mao S., Hou S., 2008. A controlled porosity osmotic pump system with biphasic release theophylline: Influence of weight gain on its in vivo pharmacokinetics. *Chem. Pharm. Bull.* 56(6), 792.
- Chen W., Su Y., Zhang L., Shi Q., Peng J., Jiang Z., 2010. In situ generated silica nanoparticles as pore forming agent for enhanced permeability of cellulose acetate membranes. *J. Membr. Sci.* 348, 75.
- Grassi M., Colombo I., Lapasin R., 2001. Experimental determination of the theophylline diffusion coefficient in swollen sodium alginate membranes. *J. Cont. Rel.* 76, 93.
- Heard C.M., Johnson S., Moss G., Thomas C.P., 2006. In vitro transdermal delivery of caffeine, theobromine, theophylline and catechin from extract of guarana, paullinia cupana. *Int. J. Pharm.* 317, 26.
- Lai J.Y., Chen R.Y., Lee K.R., 1993. Polyvinyl alcohol γ -ray grafted nylon 4 membrane for pervaporation and evapomeation. *Sep. Sci. Tech.* 28 (7), 1437.
- Lee, P.I., 1985. Kinetics of drug release from hydrogel matrices. *J. Cont. Rel.* 2, 277.
- Liu J., Lin S., Li L., Liu E., 2005. Release of theophylline from blend hydrogels. *Int. J. Pharm.* 298, 117.
- Makhija S.N. and Vavia R.P., 2003. Controlled porosity osmotic pump based controlled release systems of pseudoephedrine I. Cellulose acetate as a semipermeable membrane. *J.Cont.Rel.* 89, 5.
- Meier M.M., Kanis L.A., Lima J.C., Pires A.T.N., Soldi V., 2004. Poly(caprolactone triol) as plasticizer agent for cellulose acetate films: influence of the preparation procedure and plasticizer content on the physic-chemical properties. *Polym. Adv. Technol.*, 15, 593.
- Minton N.A. and Henry J.A., 1996. Acute and chronic human toxicity of theophylline. *Hum. Exp. Toxicol.*, 15, 471.
- Paloucek F.P., Rodvold K.A., 1988. Evaluation of theophylline overdoses and toxicities. *Ann. Emerg. Med.*, 17(2), 135.
- Prabakaran D. Singh P., Kanaujia P., Jaganathan K.S., Rawat A., Vyas S.P., 2004. Modified push-pull osmotic system for simultaneous delivery of theophylline and salbutamol: development and in vitro characterization. *Int. J. Pharm.* 284, 95.
- Rao P.R. and Diwan P.V., 1997. Permeability studies of cellulose acetate free films for transdermal use: influence of plasticizers. *Pharm. Acta. Helv.* 72, 47.
- Reverchon E. and Cardea S., 2004. Formation of cellulose acetate membranes using supercritical fluid assisted process. *J. Membr. Sci.* 240, 187.
- Rhim J.W., Yoon S.W., Kim S.W., Lee K.H., 1997. Pervaporation separation and swelling measurement of acetic acid-water mixtures using crosslinked PVA membranes. *J. Appl. Polym. Sci.* 63, 521.
- Ruckenstein E. and Liang L., 1996. Poly(acrylic acid)/ poly(vinyl alcohol) semi and interpenetrating polymer network pervaporation membranes. *J. Appl. Polym. Sci.* 62, 973.
- Siepmann F., Hoffmann A., Leclercq B., Carlin B., Siepmann J., 2007. How to adjust drug release patterns from ethylcellulose coated dosage forms. *J. Cont. Rel.* 119, 182.

- Stavric B.,1988. Methylxanthines: toxicity to humans. I. Theophylline. Food. Chem. Toxicol. 26, 541.
- Sweetman, S. C., 2002. Martindale the Complete Drug Reference', Pharmaceutical Press., London, 777-785.
- Valente A.J.M., Polishchuk A.Y., Burrows H.D., Lobo V.M.M., 2005. Permeation of water as a tool for characterizing the effect of solvent, film thickness and water solubility in cellulose acetate membranes. Eur. Polym. J. 41, 275.
- Wang F.J., Yang Y.Y., Zhang X.Z., Zhu X., Chung T., Mochhala S., 2002. Cellulose acetate membranes for transdermal delivery of scopolamine base. Mater. Sci. Eng. 20, 93.
- Zhao X., Liu J.P., Zhang X., Li Y., 2006. Enhancement of transdermal delivery of theophylline using microemulsion vehicle. Int. J. Pharm. 327, 58.

NON-DEGRADABLE POROUS POLY(VINYL ALCOHOL) HYDROGELS FOR CARTILAGE TISSUE ENGINEERING

Bodugoz-Senturk H^{1,2,a}; Bichara DA¹; Ling D¹; Gupta C¹; Randolph MA^{2,3}; and Muratoglu OK^{1,3}

1. Harris Orthopaedic Laboratory, Massachusetts General Hospital, Boston, MA, USA

2. Harvard Medical School, Orthopaedics, Boston, MA, USA

3. Plastic Surgery Research Laboratory Massachusetts General Hospital, Boston, MA

a. Corresponding Author (hsenturk@partners.org)

ABSTRACT: Degradable polymeric scaffolds currently applied in tissue engineering to deliver cells in situ for cartilage repair suffer from weak constructs and incomplete matrix production. Non-degradable porous PVA hydrogel with open pores and channels showed similar EWC and mechanical strength to swine articular cartilage. Such a device in cartilage repair would delay further continued degeneration, and in turn, more invasive surgical treatments.

1. INTRODUCTION

Defective cartilage tissue is a major clinical problem. To date, there have been no successful strategies to repair or regenerate cartilaginous tissues with successful long-term outcomes. Current strategies employ degradable polymeric scaffolds to deliver chondrocytes which often suffer from lack of strength of the construct, as well as incomplete matrix production. We propose to use a non-degradable porous hydrogel scaffold that can provide necessary and tailored mechanical strength to cartilage repair constructs seeded with chondrogenic cells. This will allow natural dynamic load transfer to the cells, which has been shown to be a major part of their developmental pathway to produce the correct composition of cartilage. Using theta gelation method [Bodugoz, 2008; Ruberti, 2004] in the presence of two competing gelling agents; a high molecular weight polymer such as polyacrylamide (PAAm) and a low molecular weight polymer such as Polyethylene glycol (PEG), we developed a porous polyvinyl alcohol (PVA) hydrogel with interconnected pores and continuous channels (Fig 1-2) large enough to allow chondrocyte infiltration and extracellular matrix

(ECM) deposition [Bodugoz, 2008]. The effect of molecular weight (MW) and concentration of gelling agent on physical properties of the hydrogel is reported in this study. These hydrogels enhanced the neo-cartilage formation in a subcutaneous nude mouse model using swine articular chondrocytes [Bichara, 2011].

2. MATERIALS AND METHODS

Porous PVA hydrogels were prepared by dissolving PVA (MW=115,000g/mol) in the presence of (1) Polyacrylamide-co-Acrylic acid (PAAm-co-AAc, PVA-A) and (2) PAAm in DI water at 90°C. Solutions (1) and (2) were separately mixed with the gelling agent consisting of two different molecular weight PEG (MW=400g/mol and PEG600g/mol) to make gels PVA-A and PVA-B, respectively. A third gel was made with PVA and PAAm and mixed with PEG400/PEG200 mixture (PVA-C). Each solution was molded and cooled to room temperature for gelation for 24h [Bodugoz-Senturk]. Gels were rehydrated in DI water at room temperature until equilibrium.

The equilibrium water content (EWC) was measured using a Thermogravimetric analyzer. Total creep strain (TCS) was determined by applying a

100N load for 10 hours followed by a relaxation period under a 10N load for 10 hours on cylindrical samples in DI water at 40°C. A phenomenological model was developed to quantify the viscoelastic response of hydrogels and cartilage to stresses. The model used here was an extension of Kelvin-Voigt model [Ward, 2004]. To estimate the parameters we fitted our model to experimental results and minimized the mean squared error.

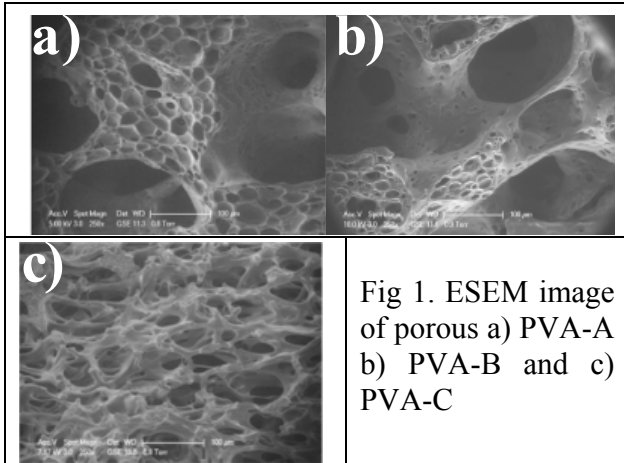


Fig 1. ESEM image of porous a) PVA-A b) PVA-B and c) PVA-C

Porosity of the hydrogels was measured with solvent extraction method using ethanol. Pore size was determined by using the Image Analysis Software [nih.org]. PVA-A hydrogel was seeded with swine articular chondrocytes (PVA-H) and implanted in nude mice for 6 weeks. Upon retrieval the construct was tested for EWC and creep.

3. RESULTS

Both PVA-PAAm-co-AAc and PVA-PAAm formulations had open pores (20-200µm) and interconnecting channels (Fig 1). Changing the high molecular weight gelling agent from PAAm-co-AAc to PAAm did not change the overall porous structure of the hydrogel significantly (Fig 1a, 1b, Table 1).

Replacing lower molecular weight gelling agent mixture PEG400/PEG600, with PEG400/PEG200 resulted in smaller pores; average pores size of PVA-C (100µm) was smaller than PVA-A and PVA-B (180 and 160µm) (Fig 1, Table 1). EWC of all three hydrogels, PVA-A, PVA-B, and PVA-C (90%), and the implanted hybrid construct (91%) was higher than EWC of swine cartilage (77%). All three hydrogel types showed similar unconfined creep resistance (~80%) to that measured with swine cartilage (81%). Ex vivo the hydrogel/cell construct (PVA-H) exhibited better creep resistance than the acellular hydrogels and swine cartilage. Elastic modulus of the acellular hydrogels was higher than those of swine cartilage and PVA-H. Time dependent response to creep deformation (T) of all acellular hydrogels, PVA-H, and swine cartilage were similar (Table 1). After the *in vivo* period the PVA-H stained positive for the presence of proteoglycans. There was no fibrous tissue at the interface between the hydrogel matrix and the cartilage tissue (Fig 2).

Table 1: EWC, TCS, elastic modulus (EM), time constant (τ), porosity(Φ), and average pore size (APS) of the PVA hydrogels.

Sample	EWC (%)	TCS (%)	EM (MPa)	τ (h)	Φ (%)	APS (mm)
PVA-A	90±0.3	83±4	4±2	1±0.6	82±5	180
PVA-B	91±0.4	81±1	4±0.1	2±0.3	85±5	160
PVA-C	90±0.4	80±1	4±0.2	2±0.1	84±5	100
PVA-H	91±1	74±2	2±0.1	2±0.02	-	-
Swine Cartilage	77±0.3	81±4	2±0.1	2±0.3	-	-

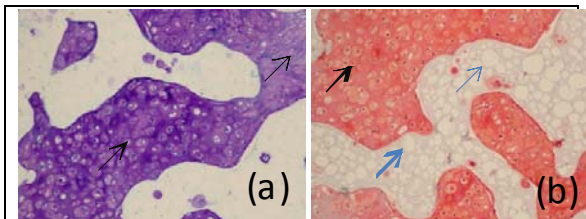


Fig 2. Hydrogel/Cell construct and cartilaginous matrix after 6 weeks in nude mice stained with toluidine blue (a) and Safranin-O (b).

4. DISCUSSION

Pore size and the morphology of the hydrogels are not only important to host the chondrocytes, but they also play a key role to maintain nutrient flow. When prepared by theta-gelation method, PVA hydrogels exhibit semi-crystalline gel networks with 10-20 μ m closed pores (1, 3).

In theta-gel method, addition of a low molecular weight gelling agent PEG into aqueous PVA solution reduces the quality of the solvent with decreasing temperature, forcing the PVA to phase separate and crystallize. One can alter the pore morphology of the gel network by changing the molecular weight and concentration of PVA and the gelling agent. We modified the theta gelation method by using high molecular weight gelling agent (a non-ionic (PAAm) or an ionic (PAAm-co-AAc)) along with PEG in PVA solution which resulted in larger pores (50-200 μ m). We also found that the pores were interconnected and open to the surface which is desirable to grow cartilage. The porous PVA hydrogels in their acellular form and after cell seeding and 6 weeks in vivo were similar to swine articular cartilage in terms of their viscoelastic properties.

5. CONCLUSIONS

Degradable polymeric scaffolds currently applied in tissue engineering to deliver cells in situ for cartilage repair suffer from weak constructs and incomplete matrix production.

Non-degradable porous PVA hydrogel with open pores and channels showed similar EWC and mechanical strength to swine articular cartilage. Such a device in cartilage repair would delay further continued degeneration, and in turn, more invasive surgical treatments. We have shown that theta gelation can be used to synthesis and alter the pore morphology of the gel network by to for interconnected pores which is desirable to grow cartilage. We were able to grow cartilage in these porous PVA hydrogels which were similar to swine articular cartilage in their mechanical properties and water content.

REFERENCES

- Bichara DA, et al. *Tissue Eng Part A*. 2011, (3-4):301-9.
- Bodugoz-Senturk, H et al. *Biomaterials*, 2008, 29(2): 141-9.
- Ruberti J et al. US Pub. No. 200040092653, 2004 May 13, 2004.
- Ward I, et al. *An Introduction to Mechanical Properties of Solid Polymers*.2004, (4):64. <http://rsbweb.nih.gov/nih-image/>.

CHARACTERIZATION AND DETERMINATION OF BIOFILM FORMING POTENTIAL OF A WASTE SERICIN-RICH PROTEIN MIXTURE

Goksen Capar^{1,2,a}, S.Saniye Aygun¹, M. Ruşen Geçit¹ and Kang Li³

1. Middle East Technical University, Engineering Sciences Department, Cankaya, Ankara, Turkey

2. Ankara University, Water Management Institute, , Ankara, Turkey

3. Imperial College, London, Department of Chemical Engineering, South Kensington Campus, London, UK
a. gcapar@ankara.edu.tr

ABSTRACT: A sericin-rich silk protein mixture (S_R) recovered from silk wastewaters was obtained in powder form and characterized in terms of molecular weight, elemental composition, pH, moisture and ash contents. The biofilm forming potential of the protein powder for making packaging materials was determined. Films made of protein mixture were quite fragile, hence protein mixture was blended with polyvinyl alcohol (PVA) at 5/100 ratio. Films were cast on glass sheets where glycerol was used as a plasticizer. These films were characterized in terms of oxygen permeability and mechanical properties. Although PVA films were found to be impermeable to oxygen, addition of sericin-rich protein powder resulted in higher oxygen permeability of films. The mechanical properties were found suitable for packaging purposes. These results revealed that sericin-rich protein powder can be used as an additive in making biofilms for packaging purposes where oxygen transmission is not a problem.

1. INTRODUCTION

Sericin is a valuable silk protein, which is currently discarded as a waste in textile industry in Turkey. Sericin has a variety of end-uses in industries such as cosmetics and pharmaceuticals, as well as production of biomaterials and membranes [Mori and Tsukada, 2000; Zhang, 2002]. In recent years, interest has grown for sericin recovery from silk wastewaters in view of promising research findings related to its useful properties such as antioxidation, UV resistance, moisture absorption and biocompatibility [Mondal *et al.*, 2007]. The aim of this study is to determine the characteristics and biofilm forming potential of a sericin-rich protein mixture recovered from silk wastewaters in an attempt to contribute to the value-added utilization of waste sericin.

2. RESULTS AND DISCUSSION

2.1. Characterization of Recovered Powder Material

Sericin was recovered from wastewater by a two-stage process; nanofiltration plus ethanol-induced precipitation, where the precipitate was converted to powder form by freeze-drying [Capar *et al.*, 2008; Capar, 2012]. The pictures of pure sericin standard obtained commercially (S_C) and sericin-rich mixture (S_R) recovered from wastewater are depicted in Figure 1. The LC-MS analysis of recovered protein mixture revealed that the powder contains 92.9% sericin and 7.1% actin cytoplasmic A3 protein, where the iso-electric point (pI) of sericin is 5.9 [Capar, 2012].

Sericin is a family of proteins with a wide range of molecular weights (MW), i.e., 6-467 kDa. This is due to the fact that MW of sericin is affected by factors such as pH, temperature and processing time. In this work, the MW of commercial and

recovered sericin samples were determined as 138 kDa and 90 kDa, respectively. Recovered sericin can be classified as high-MW sericin (>20 kDa), which is suitable for making biomaterials [Zhang, 2002]. As seen from Table 1, elemental compositions of commercial and recovered samples are similar, although C, H and N contents of S_R are slightly lower. The differences were attributed to the fact that commercial powder is pure sericin, whereas recovered powder contains 7% impurity.



Figure 1: Powder sericin; (a) commercial (b) recovered from wastewater.

Table 1: The elemental composition of sericin-rich powder (dry basis)

	S _C	S _R
C%	42.5	37.9
H%	6.4	5.8
N%	13.9	10.2
S%	0.3	0.4
Total (%)	64.9	54.3

As seen from Table 2, pH of S_C was acidic whereas pH of S_R was near neutral, which is attributed to the possible differences in methods of recovery. Recovery method of S_R is unknown, but it seems to be applied at acidic conditions. On the other hand, sericin was recovered under neutral pH in this work. Moisture content of S_C was higher than that of S_R. On the other hand, ash content of S_C was lower than that of S_R, which means that the organic content of recovered sericin was lower. This was attributed to the likely presence of some inorganic matter such as salts in the

recovered sample as well as the presence of another protein in the mixture.

Table 2: pH, moisture and ash contents

	S _C	S _R
pH	3.9	7.7
Moisture, %	7.4	3.1
Ash, %	2.7	14.4

2.2. Biofilm Forming Potential of Recovered Material

The biofilm forming potential of recovered sericin-rich protein mixture was determined in order to evaluate its compatibility as a packaging material. Films made of pure sericin are known to be too fragile, therefore it is generally blended with other materials. In this work, sericin-rich mixture was blended with polyvinyl alcohol (PVA) (hot water soluble, average molecular weight 70 kDa, viscosity 11-14 cP). It has been reported that a hydrogel obtained by the mixture of sericin and PVA shows perfect elasticity and moisture absorption-desorption properties [Yoshii *et al.*, 2000]. Glycerol was used as plasticizer.

PVA solutions of 10% (w/w) were prepared by stirring and heating at 80 °C for 3 h. Sericin solutions of 5% (w/w) were prepared in a similar way by stirring and heating at 60 °C for about 3 h. The pH of the sericin solutions was adjusted to 10 by NaOH (0.5 M) to enhance its solubility. The glycerol solution was prepared by mixing glycerol with water and stirring (40% v/v). Sericin/PVA blend ratio of 5/100 was used. The blend solutions were stirred and heated at 80 °C for at least 1 h and then degassed for 1 h. After adjusting the blade thickness to 250 µm, and setting up the casting machine, 5-10 mL of solution was poured into the reservoir of the blade, which was then cast on glass. Then, the films were left overnight for drying at 30° C, followed by heat treatment at 75 °C for 30 min to improve cross-linking. After the films

were removed from glass, they were labeled and stored at room conditions (Figure 2). The specifications of films are given in Table 3. Films were characterized by oxygen permeation, SEM and mechanical properties.



Figure 2: Biofilm made of PVA and recovered sericin-rich protein powder.

Table 3: Specifications of films

Film type	Sericin/PVA	Glycerol (%)
PVA	0/100	0
PVA+Gly	0/100	1
PVA+Gly+S _C	5/100	1
PVA+Gly+S _R	5/100	1

As seen from Table 4, the permeances of pure PVA films with and without glycerol are almost the same and very low, which indicate that PVA films are impermeable to oxygen. On the other hand, preliminary studies had shown that films including sericin have good oxygen permeabilities (data not shown). Therefore, films including sericin were subjected to permeability tests (Table 5).

Table 4. Permeances of pure PVA films

Film type	Test duration (min)*	Permeance* (mol m ⁻² s ⁻¹ Pa ⁻¹)
PVA	1268	5.9 x 10 ⁻¹⁷
PVA+Gly	1265	6.0 x 10 ⁻¹⁷

*average of two samples from the same film

Table 5. Permeability of sericin films

Film type	Permeability (Barrer) (cm ³ .cm)/(s.cm ² .cmHg) x10 ⁻¹⁰
PVA+Gly+S _C	3258 ± 93
PVA+Gly+S _R	1371 ± 88

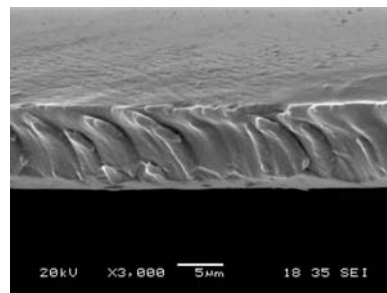


Figure 3: SEM analysis of pure PVA film

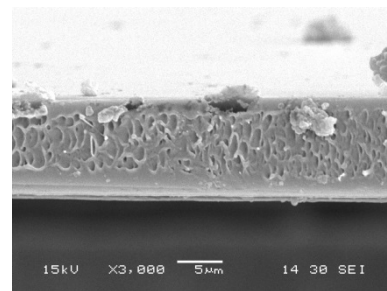


Figure 4: SEM analysis of sericin film (PVA+Gly+S_R)

As seen from Figure 3, films made of pure PVA are dense, symmetric and nonporous, which supports the results of very low oxygen permeance. However, when sericin is added into the films, a porous structure is observed, which is not uniform throughout the cross-section. (Figure 4). These results show that addition of sericin increases the oxygen permeability of films significantly, due to the formation of porous structure.

The mechanical properties of films were also determined. Tensile strength of a material is the maximum stress it can withstand while being stretched or pulled before failing or breaking. Hence, it is a measure of film integrity. Tensile strength of films (1) PVA, (2) PVA + Gly, (3) PVA + Gly + S_C and (4) PVA + Gly + S_R were determined as 12.1 MPa, 12.7 MPa, 12.6 MPa and 20.5 MPa, respectively (Figure 5). These results show that addition glycerol and commercial sericin did not improve tensile strength, whereas addition of sericin-rich protein powder significantly increased tensile strength. This may be due to differences in recovery methods of

sericin samples. The recovery method of commercial sericin is unknown, but its pH is 3.9, which implies that it was recovered at acidic conditions. On the other hand, sericin-rich protein powder was recovered via membrane processes plus ethanol precipitation and has a pH of 7.7. Furthermore, S_R contains another protein, actin cytoplasmic A3. The ash contents were also different, where S_R has much higher inorganic content as compared to S_C . All these factors might have contributed to the improved tensile strength of the film containing S_R . However, more research is needed to verify these results.

For comparison, it is useful to note that tensile strengths of some materials such as human skin, high-density polyethylene and steel are 20 MPa, 37 MPa and 400 MPa, respectively [Wikipedia, 2013]. The tensile strength of a biodegradable film made of wheat gluten (protein) was reported as 8 MPa, where addition of xylan (polysaccharide) reduced the tensile strength down to 2 MPa depending on its type and ratio of addition. These films were found acceptable [Kayserilioglu *et al.*, 2003]. It can be inferred from these information that recovered sericin-rich powder is mechanically compatible as a biofilm additive.

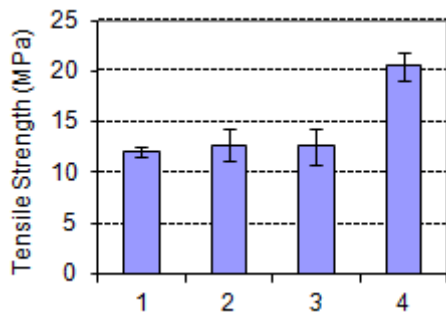


Figure 5: Tensile strength (1) PVA (2) PVA + Gly (3) PVA + Gly + S_C (5/100) (4) PVA + Gly + S_R (5/100) (average of 2 duplicate films, where 5 samples from each film were measured)

Young's modulus is a measure of film stiffness and measures the resistance to elastic deformation under load. Young's Modulus for films (1) PVA, (2) PVA + Gly, (3) PVA + Gly + S_C and (4) PVA + Gly + S_R were determined as 352 MPa, 182 MPa, 234 MPa and 392 MPa, respectively (Figure 6). It is clear that addition of glycerol as a plasticizer resulted in decreased Young's modulus, i.e., decreased stiffness. This is expected as the addition of plasticizer aimed to increase flexibility of films. However, addition of recovered sericin increased stiffness of films. For comparison, some examples of Young's modulus are given: 800 MPa for high density polyethylene, 200.000 MPa for steel, 10-100 MPa for rubber and 500 MPa for teflon.

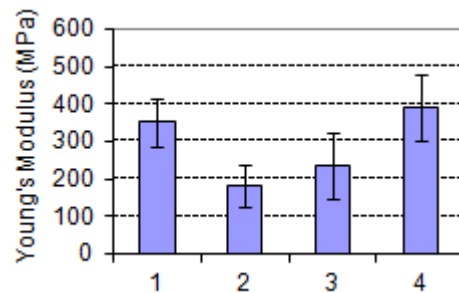


Figure 6: Young's modulus (Conditions are same as in Figure 5)

Elongation at break, which is a measure of film stretching was determined as 82%, 138%, 115% and 108% for (1) PVA, (2) PVA + Gly, (3) PVA + Gly + S_C and (4) PVA + Gly + S_R , respectively (Figure 7). As expected, addition of plasticizer resulted in a significant increase of film stretching. On the other hand, presence of sericin caused some reduction in stretching property, but it was still higher than that of pure PVA films.

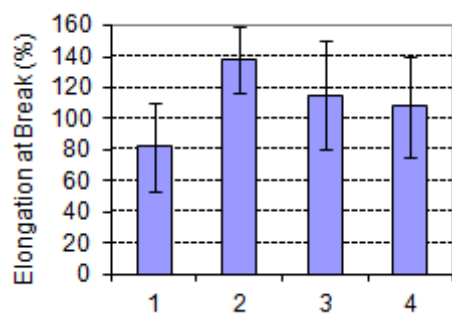


Figure 7: Elongation at break (Conditions are same as in Figure 5)

3. CONCLUSIONS

A biofilm was prepared using sericin-rich protein powder recovered from silk wastewaters by membrane processes.

The recovered sericin-rich powder had a molecular weight of 90 kDa, which is classified as high-molecular weight.

The pH, moisture and ash contents of recovered sericin differed from those of commercial sericin, which was attributed to possible variations of recovery methods. The C, H and N contents of recovered sericin was slightly lower than that of commercial sericin. This was attributed to the fact that recovered powder was a mixture of two proteins rather than pure sericin.

PVA films were dense, nonporous and impermeable to oxygen whereas sericin films were porous and permeable to oxygen.

The mechanical properties of films were satisfactory; it was revealed that sericin can be used as an additive of packaging materials for those applications where oxygen transmission is not a problem.

Acknowledgements:

The authors acknowledge the grant provided by the Scientific and Technological Research Council of Turkey (TUBITAK) via Project No 106 M 062 and British Council for the grant

provided under Science Partnership Programme.

REFERENCES

- Capar, G., Aygun, S. S., and Gecit, M. R., 2008. Treatment of Silk Production Wastewaters by Membrane Processes for Sericin Recovery, *J. Membr. Sci.*, (32), 920–931.
- Capar, G., 2012. Separation of Silkworm Proteins in Cocoon Cooking Wastewaters via Nanofiltration: Effect of Solution pH on Enrichment of Sericin, *J. Membr. Sci.*, (389), 509.
- Kayserioglu B., Bakir U., Yilmaz L., and Akkas N., 2003. Use of Xylan, an Agricultural by-product, in Wheat Gluten Based Biodegradable Films: Mechanical, Solubility and Water Vapor Transfer Rate Properties, *Bioresource Technology*, (87), 239.
- Mondal, M., Trivedy, K., and Kumar, S. N., 2007. The Silk Proteins, Sericin and Fibroin in Silkworm, *Bombyx mori* Linn., - a Review, *Caspian J. Env. Sci.*, (5), 63.
- Mori, H., and Tsukada, M., 2000. New Silk Protein: Modification of Silk Protein by Gene Engineering for Production of Biomaterials, *Rev. Mol. Biotechnol.*, (74), 95.
- Zhang, Y., 2002. Applications of Natural Silk Protein Sericin in Biomaterials, *Biotechnol. Adv.*, (20), 91.
- Wikipedia, 2013, http://en.wikipedia.org/wiki/Ultimate_tensile_strength.

TITANIUM-BASED COMPOSITE FOR BIOMEDICAL APPLICATIONS

Jan Ryszard Dabrowski^{1,a}, Piotr Deptula², Marcin Klekotka³

1,2,3. Bialystok University of Technology, Department of Materials and Biomedical Engineering,
Bialystok, Poland

a. Corresponding author (j.dabrowski@pb.edu.pl)

ABSTRACT: Titanium and its alloys (Ti-Al-V) comprise one of the most promising groups of biomaterials used in bone surgery, owing to the fact that they possess a great number of valuable bio-functional features. On the other hand, however, the alloys also have certain disadvantages as they contain toxic additives in the form of aluminum and vanadium, and show poor tribological properties. This paper presents the results of a research study on new titanium composite materials with a graphite filler (5-20%), obtained using the methods of powder metallurgy. Structural, mechanical, tribological and biological tests of the composites were performed in the course of the research. It was found out that composite materials with a 10% graphite content manifested the best bio-functional properties, especially with respect to their mechanical and tribological characteristics.

The produced sinters were used as a construction material of a frictional contact in a dynamic stabilizer of hip fractures, whose sensitive parts are particularly exposed to tribological wear. Operational tests of the modified/improved device showed a significant increase of its durability/resilience, as compared to the commercial product.

1. INTRODUCTION

The alloys most commonly used in medicine are austenitic steels, cobalt alloys, and titanium alloys, as well as pure titanium [Long and Rack, 1989]. Among these materials, those based on titanium are the most promising. The commercial titanium alloy most frequently applied in alloplastics is the two-phase titanium alloy containing aluminum and vanadium (Ti-6Al-4V). The use of titanium alloys as bearing surfaces in total replacements for people is limited by their very poor tribological properties and wear resistance. This is a serious drawback of this type of implant alloys, significantly limiting their application in biotribological systems (e.g. joints, dental system) [Anokhin et al., 1998].

There have been numerous research studies of these materials, concentrated on modifying their mechanical and tribological properties [Hagiwara et al., 1998]. These properties make plastic forming and machining of titanium alloys difficult and for this reason new technologies are sought that will offer new possibilities to obtain more competitive titanium-based alloys and composites for biomedical applications [Henriques et al., 2001]. Modern technologies in the production of biomaterials, e.g. powder metallurgy, are finding an increasingly wide area of applications. Furthermore, new technologies allow to create composite materials with different types of fillers, improving the tribological or mechanical properties of the materials [Seagle et al., 1999].

This paper presents the results of tests of a composite material based on titanium intended for biomedical applications.

2. MATERIALS AND METHODS

The composite samples were obtained by means of powder metallurgy. Tested were titanium powder-based composite materials with a 10% volume fraction of graphite (Ti +10%C). The commercially pure titanium powder by Atlantic Equipment Engineers, with a purity of 99.7% and a particle size below 150 μ m; and graphite powders, with a particle size below 40 μ m, were dry-mixed for 15 minutes in a Pulverisette 6 ball mill and cold-pressed under a pressure of 600MPa and then sintered for 3 hours in a pipe furnace, in a protective atmosphere, at a temperature of 1230 °C. During the sintering, a vacuum of about 10⁻⁵ mbar was applied. The samples were pressed in a Marciniak envelope press and then subjected to heat treatment at 1000°C for one hour.

The observations of metallurgic samples of porous implant materials and the analysis of their chemical composition were carried out using an optical microscope and a HITACHI S-3000N scanning microscope. Their hardness was determined using the Brinell method. Microhardness of the obtained alloys was analyzed using the Vickers method, by means of the Hanemann head mounted on NEOPHOT 21.

The tribological tests of the obtained sinters were carried out by means of the pin-on-disc tribometer. The coefficient of friction was calculated from the maximum values of friction force, describing extreme resistances to motion. The counter-sample, in the form of a ring, was made from Ti-6Al-4V alloy.

The tribological tests were carried out in a distilled water environment, at room

temperature. Due to the nature of the samples, porous implant materials were compressed using the INSTRON 8502 hardness testing machine, and then the compression curves were analyzed.

The potentiodynamic corrosion tests were performed using the Atlas-Sollich 9933 elektrochemical interface kit for electrochemical testing. The impedance corrosion tests were performed using the AutoLab PGSTAT100. The samples were tested in 0.5 M NaCl. The reference electrode was the saturated calomel electrode.

Interaction of the biomaterial with primary human osteoblast cultures was also analyzed. A wide range of research methods were used to determine the following: culture cells adhesion, cytotoxicity, cell viability, secretory and proinflammatory activity of cells, and morphology, for the samples of sintered biomaterials on the 3rd and the 7th day of tests.

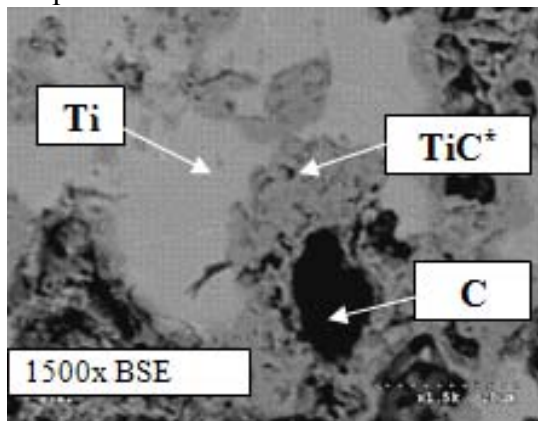
3. RESULTS AND DISCUSSION

The composites based on titanium with a graphite content were characterized by a high relative density. At the optimum sintering temperature and sintering time, determined on the basis of preliminary tests, a compactibility of over 90% was obtained. This is due to the beneficial lubrication properties of graphite during the compaction process. Envelope compaction increased this value to 99%. Structural tests revealed a multi-material composite structure. Three phases were obtained, i.e. a soft titanium matrix, a 2.6% residual graphite, and a new phase that was the result of interaction between the matrix and the filler – secondary carbides (Fig. 1). The nature of the material, i.e. a hard carbide phase in a soft matrix and residual graphite with good lubricating properties, suggests

good tribological properties of the obtained sinters.

The hardness of the composites largely depended on sintering temperature. The optimum temperature of 1230°C allowed to obtain materials with a hardness of about 220 HB, the hardness of pure titanium being about 84 HB. Microhardness of the matrix composites averaged 350 HV_{0,1}. The results of strength tests are presented in a table (Fig. 1). It can be seen that the materials have sufficient compressive strength, while the coefficients of elasticity are relatively low, which is of considerable importance in the case of materials for biomedical applications

Figure 1: Microstructure of the obtained composite Ti-C.



The table summarizes the values of corrosion potentials and corrosion currents calculated by extrapolating anodic sections and cathodic curves using the POL-99. In the case of porous sinters, it is difficult to estimate the actual surface of the sinter, which makes it impossible to compare current densities for the sintered materials and the solid alloy.

Table 1: Corrosion characteristics of the tested materials.

Material	E _{kor} [mV]	I [μA]
Ti-6Al-4V	-267	0.0497
Ti+10C	-157	1.28

Therefore, the table 1 shows the values of current.

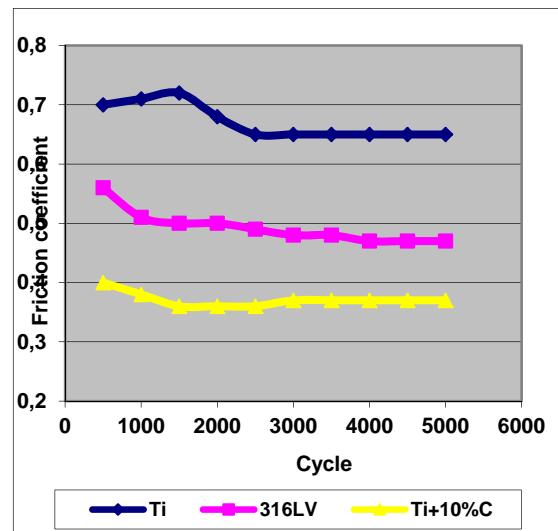


Figure 2: Tribological properties of the tested materials.

The results indicate appropriate corrosion properties of the new materials, obtained by means of PM. The value of current for the composite is at an acceptable level. The results indicate good tribological properties of the obtained composites from the point of view of biomedical applications. The composites were characterized by lower coefficients of friction and higher wear resistance than the commercial materials. The coefficient of friction for the composite was almost twice lower than for pure titanium and considerably lower than for the commercial alloy (Fig. 2). This is an important advantage of these materials, as it makes it possible to use them as a friction pair in constructions for biomedical research.

The results of biological tests (in vitro) of the obtained materials display very beneficial qualities. The tests show a lower adhesion of cells to the composite than in the case of the commercial material, Ti-6Al-4V alloy. The cytotoxicity test showed no differences between the commercial materials and

the obtained composite. The cell viability test, performed using NHOst Vialight on the 3rd and the 7th day of culturing, showed that viability rates on TCPS control surfaces and on the composite surfaces were almost twice lower than the corresponding rate for commercial titanium (Tab. 2).

Table 2: Results of biological tests (after 7 days).

Material	Cell adhesion, CV [OD]	Cytotoxicity [CPS]
Ti-C	0,1	4200
Ti-6Al-4V	0,15	4200

Due to the promising properties, the developed material was used as bushing in a dynamic hip stabilizer (Fig.3).

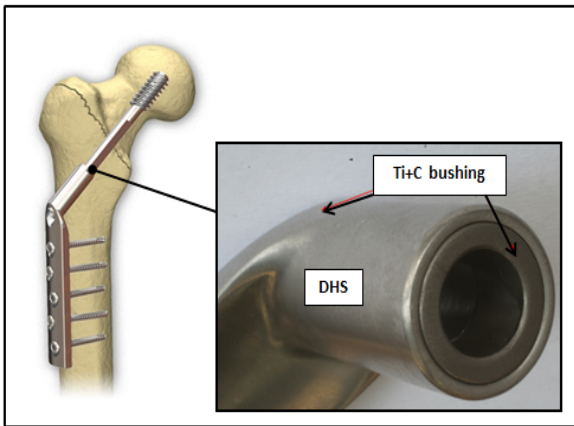


Figure 3: The dynamic hip stabilizer employing the titanium composite.

The fatigue strength and wear resistance of the element were also examined. The results of these studies, however, will be the subject of further publications.

4. CONCLUSIONS

On the basis of the obtained test results, it can be concluded that the new material, developed in the Department of Materials Science and Biomedical Engineering, intended for use in biomedical

applications, is characterized by beneficial bio-functional features. In many aspects, a titanium-based composite with a graphite content has better properties than the commercial materials widely used in medicine. The composites are also characterized by good tribiological properties.

Acknowledgements: This paper was financed by grantPR/WM/1/2010/NCBR

REFERENCES

- Anokhin V.M., Ivasishin O.M., Petrunko A.N., 1998. Structure and properties of sintered titanium alloyed with aluminum, molybdenum and oxygen, *Materials Science and Engineering*, A243, 269.
- Hagiwara M., Kim S. J., Emura S.: Blended elemental P/M synthesis of Ti-6Al-1.7Fe-0.1Si alloy with improved high cycle fatigue strength, 1998. *Scripta Materialia*, 39, 1185.
- Henriques V.A.R., Bellinati C.E., da Silva C.R.M., 2001. Production of Ti-6%Al-7%Nb alloy by powder metallurgy (P/M), *Journal of Materials Processing Technology*, 118, 212.
- Long M., Rack H.J, 1998. Titanium alloys in total joint replacement – a materials science perspective, *Biomaterials*, 19, 1621.
- Seagle S.R., Yu K.O., Giangiordano S., 1999. Consideration in processing titanium, *Materials Science and Engineering A243*, 237.

DESIGN OF NANOSTRUCTURED SURFACES OF THE DNA-ACTIVE FILM-LIKE ACRYLAMIDE/N-(2-DIBENZYLAMINO-ETHYL)-ACRYLAMIDE

Olga Sinitsyna¹, Nadejda Davydova^{1,a}, Vladimir Sergeev¹, Elena Laukhina², Alexei Khokhlov¹

1. A.N. Nesmeyanov Institute of Organoelement Compounds Russian Academy of Sciences, Moscow, Russian Federation

2. The Biomedical Research Networking center in Bioengineering, Biomaterials and Nanomedicine, Barcelona, Spain

a. Corresponding Author (davydova@ineos.ac.ru)

ABSTRACT: Synthesis of multifunctional macromolecules has become an important topic as advances are made in biological sensing technology. Various templates that may be quantified with presentation of bioactive molecules and control over their density and orientation are required. The paper shows that a dewetting process may be successfully utilized for engineering nanostructured surfaces of the thin films based on the DNA-active copolymer acrylamide/N-(2-dibenzylamino-ethyl)-acrylamide (**1**). The morphology of the film surfaces was studied using Atomic Force Microscopy (AFM). By a variation of the concentration of **1** in its water solutions, two types of surface morphology were installed. The optimum concentration of **1** in water, which allows regular porosity patterning of the surface of the nanostructured **1**-based films, was found. Therefore, the films of **1** offer promise for applications where structural nanometer scale bio-sensing is required.

1. INTRODUCTION

Bio-sensitive nanostructured polymer surfaces are of strong interest with respect to basic research as well as for future biomedical applications. With the increasing demand on miniaturization of sensing devices the evolved polymer structures have to be decreased in their spatial dimensions as well. In this context, the development of thin films based on multifunctional macromolecules that are able to recognize different biomacromolecules has become an important topic. Recently, we described the synthesis of the copolymer acrylamide/N-(2-dibenzyl-amino-ethyl)-acrylamide (**1**, Figure 1) and showed that the copolymer **1** was able to form complexes with double-stranded DNA: filamentous structures from 0.5 to 2.3 nm in thickness were observed using AFM technique [Davydova N.K., Sinitsyna O.V., Yaminsky I.V. et al., 2012;

Davydova N.K., Sinitsyna O.V., and Zinoviev K.E., 2012].

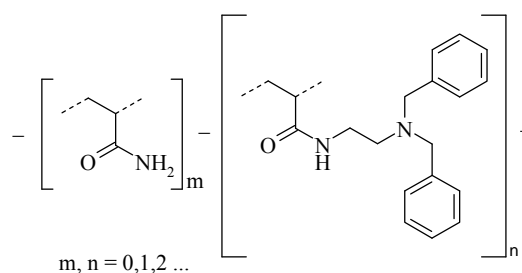


Figure 1: Structure of the copolymer **1**.

It should be noted that this DNA-active copolymer **1** is functionalized with the tertiary amino groups being able to interact with DNA.

To extend the capability of **1** to be used as an active component in bio-sensing nanotechnology we have to develop the preparation of thin **1**-based films with

controlled nanostructured surfaces. Taking into account that controlled dewetting of polymeric films may be successfully used for engineering nanostructured polymer surfaces [Müller-Buschbaum P., 2003], we suggested to use this process for building-up nanostructured **1**-based films. In the present paper, AFM was applied to prepare nano-scale studies of the surfaces of the **1**-based films.

Here we present the preparation of nano-patterns of the thin **1**-based films using the dewetting process. The effect of the concentration of **1** in its water solution on the nanopattern of the film surfaces will be discussed.

2. MATERIALS AND METHODS

The reagents and solvents were obtained commercially and purified using crystallization and distillation, respectively.

Copolymer **1** was prepared by free-radical polymerization in aqueous medium using red-ox system of ammonium persulfate – tetramethylethylenediamine [Davydova N.K., Sinitsyna O.V., Yaminsky I.V. et al., 2012].

Clean crystals of natural mica were utilized as the film supports.

Film preparation:

Two water solutions of different concentrations of **1** (3 mg/ml and 0.03 mg/ml) were prepared using bidistilled water. Films were cast from water solutions of **1** over mica-based support (2.5 μ l) and dried under ambient conditions.

The AFM experiments were performed using multifunctional scanning probe microscope “FemtoScan”, produced by Advanced Technologies Center. Scanning

was performed in contact and tapping modes of AFM. fpC11 cantilevers, produced by Institute of Physical Problems named after F. V. Lukin, were used in the contact mode and Mikromasch cantilevers of the 15 series were used in the tapping mode.

The experimental AFM data were processed and analyzed by the “FemtoScan Online” software (Advanced Technologies Center).

3. RESULTS AND DISCUSSION

To generate the patterned surfaces at the nanometric level, we used a controlled dewetting process. Taking into account that viscosity (concentration) of casting solutions is one of the key parameters, which control the dewetting process, the surface properties of the resulting **1**-based films were tailored by controlling the concentration of the copolymer in the water solutions used for film casting. In line with research aim we prepared two **1**-based films from solutions that significantly differ in concentration. Film A was prepared by drop casting of concentrated water solution of **1** (3 mg/ml) over a mica crystal whereas film B was formed on a mica surface using a much diluted water solution (0.03 mg/ml). The surface topography was characterized by the AFM, revealing different morphologies for films A and B illustrating the possibility to tune a structural surface relief of **1**-based films by concentration control.

3.1. Surface Morphology of Film A

It is evident from the AFM image (Figure 2), that there exist not numerous pore-like structures on the smooth surface of film A: 10 pores per 100 μ m². The average pore diameter is 218 \pm 71 nm. The average pore depth is 1.9 \pm 1.2 nm.

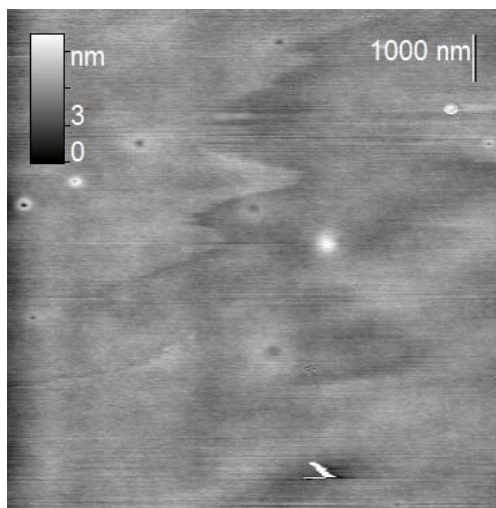


Figure 2: The typical AFM image of the surface of film A. The frame size is $10.3 \times 10.3 \mu\text{m}^2$.

It should be noted that concentrated solution of **1** allowed us to prepare a thin film of low surface roughness. The maximum height difference was found as 30 nm in defect-free areas with the square of $4 \mu\text{m}^2$, the root-mean-square roughness being 0.8 nm.

3.2. Texture of Film B

In contrast to film A, the surface of film B has a regular submicro porous structure (Figures 3 and 4). The average pore diameter is 300 nm (the standard deviation of 230 nm). The average pore depth is 9.4 nm (the standard deviation of 3.7 nm). The data were calculated for 60 pores. Some large pores, which have the diameters from 1000 nm to 2500 nm and the depth of 11.8-11.9 nm, may be also observed. It seems that the depth of the large pores is the same order as the thickness of the copolymer film. The comparative analysis of the AFM images of films A and B clearly shows that the concentration of **1** in casting solutions may be used for texture surface control.

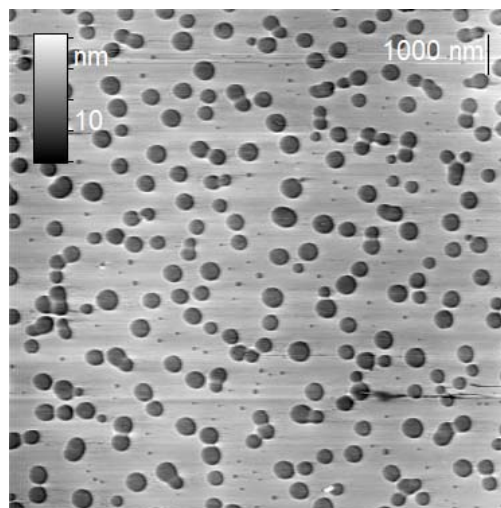


Figure 3: The typical AFM image of the surface of film B. The frame size is $11.2 \times 11.2 \mu\text{m}^2$.

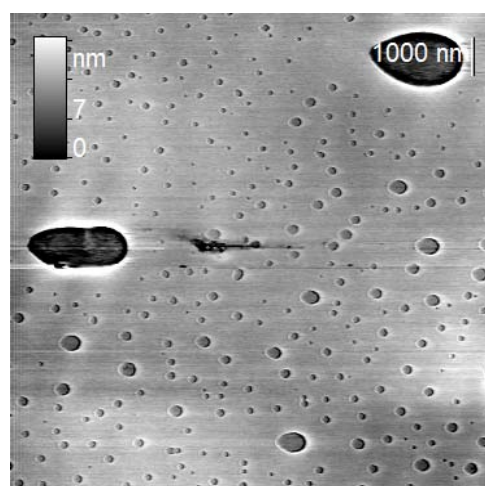


Figure 4: AFM image of the surface of film B. The frame size is $11.2 \times 11.2 \mu\text{m}^2$. There are two large pores in the frame.

The above presented AFM data show that a special attention should be given to control the wettability process during a sensing layers preparation. Below we will focus on the wettability process of the **1**-based films.

Copolymer **1** contains hydrophobic moieties, which leads to the increase of the interface potential between the copolymer film and the hydrophilic mica

surface. As a result, the copolymer film becomes unstable during the solvent evaporation and pores nucleation occurs. The pores are shown in Figure 5 with higher resolution. A filter of “highlight” was applied to the image to demonstrate the structure of the surface inside and outside the pore (Figure 6).

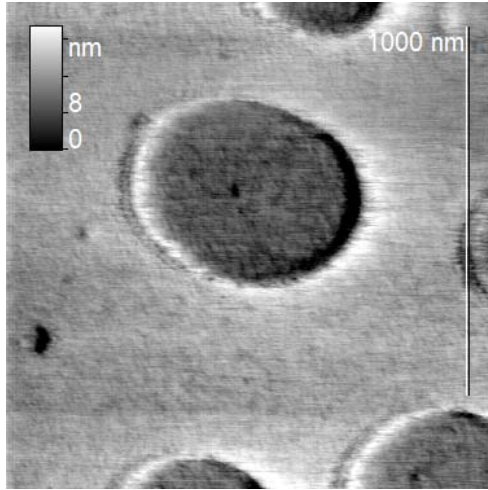


Figure 5: AFM image of the pore-like structure formed on the surface of film B. The frame size is $1.24 \times 1.24 \mu\text{m}^2$.

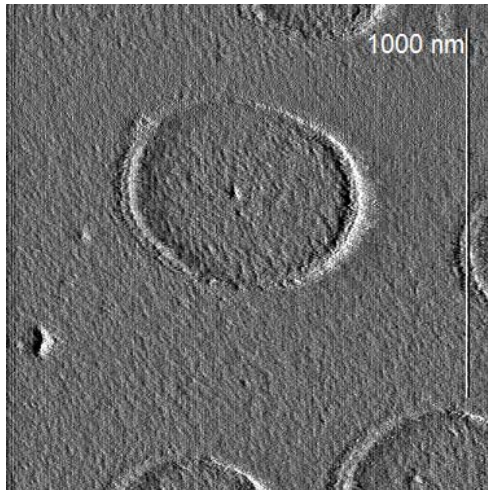


Figure 6: An AFM image of the submicro pore-like structure at the surface of film B. The frame size is $1.24 \times 1.24 \mu\text{m}^2$. The filter "highlight" was applied to the image.

It should be noted that any difference between the surface structure inside and

outside the pore didn't found by visual observation. But the root-mean-square roughness was slightly higher for the inner region. The roughness was calculated for the regions with the area of $0.11 \mu\text{m}^2$. The roughness parameters are listed in Table 1. Since the mica surface is atomically smooth, its roughness is determined mainly by the noise of the microscope. The noise level doesn't exceed 0.1 nm. The surface roughness inside the pore is an order of magnitude larger than the roughness of pure mica, therefore a thin layer of the copolymer remains on the mica surface.

Table 1: Roughness parameters for surfaces inside and outside the pore.

R_{max} is the maximum height difference, R_q and R_a are the root-mean-square and arithmetic average roughness, R_{sk} is skewness, and R_{ku} is kurtosis.

Parameter	R_{max} , nm	R_q , nm	R_a , nm	R_{sk}	R_{ku}
Inside	23.24	1.662	1.239	-1.207	9.364
Outside	11.48	1.28	1.015	-0.229	3.215

The lateral forces distribution (Figure 7) shows that the areas inside the pores are characterized by a higher value of the lateral forces.

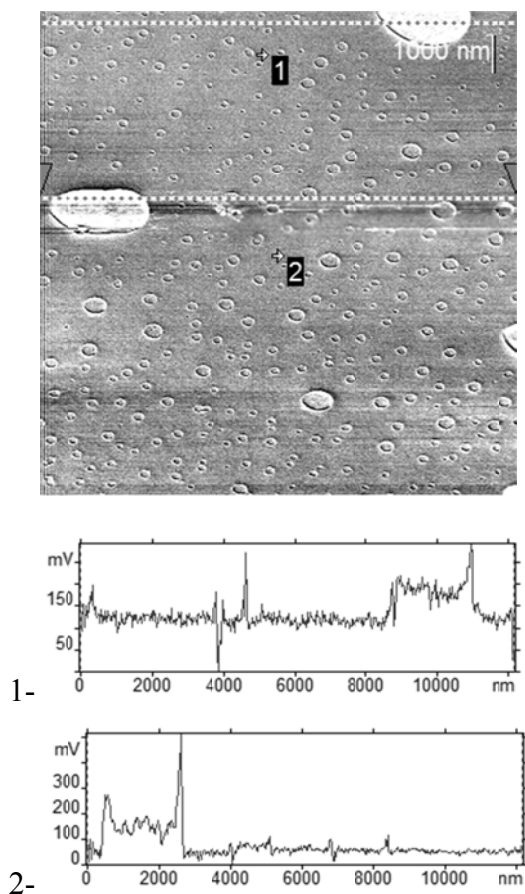


Figure 7: Image of lateral force distribution on film B; the frame size is $11.2 \times 11.2 \mu\text{m}^2$. Two surface cuts (1-, 2-) are shown.

One of the possible reasons of the high lateral forces can be the increase of the surface roughness inside the pores. Moreover, mica becomes negatively charged in water solutions. The smaller the thickness of the copolymer film, the weaker it screens the charged. The additional electrostatic interaction between the AFM probe and the surface also can lead to the stronger lateral forces.

4. CONCLUSIONS

- Copolymer **1** was synthesized.
- The thin films based on the DNA sensitive copolymer **1** with different surface morphologies were prepared.

- The dewetting process was successfully utilized for engineering different nanostructured surfaces of the developed thin films.

- The effect of the concentration of **1** in its water solution on the nanopattern of the film surfaces was studied and the optimum concentration, which allows regular porosity patterning of the film surfaces, was found.

Acknowledgements:

1. The work was supported by the Agreement 8650 with Ministry of Education and Science of Russian Federation.

2. E.L. thanks CIBER-BBN, an initiative funded by the VI National R&D&i Plan 2008-2011, Iniciativa Ingenio 2010, Consolider Program, CIBER Actions and financed by the Instituto de Salud Carlos III with assistance from the European Regional Development Fund.

REFERENCES

Davydova N.K., Sinitsyna O.V., Yaminsky I.V., Kalinina E.V., and Zinoviev K.E., 2012. Synthesis and Study of New Copolymers Capable of Forming Molecular Complexes with DNA, *Macromolecular Symposia*, December, Vol. 321-322, Issue 1, p. 84.

Davydova N.K., Sinitsyna O.V., and Zinoviev K.E., 2012. Preparation of synthetic copolymers potentially capable to interact with biomacromolecules, *AIP Conf. Proc.*, 1459, p. 220.

Müller-Buschbaum P., 2003. Dewetting and pattern formation in thin polymer films as investigated in real and reciprocal space (invited review); *J.Phys.: Condens.Matter* **15**, R1549.

Reiter G., 1992. Dewetting of thin polymer films, *Phys. Rev. Lett.* Vol.68, p. 75.

Chang S.S., Tsoi W.C., Higgins A.M., Kim J.-S., Winfield J.M., and James D.T., 2010. Self-assembled, molecularly aligned conjugated polymer nanowires via dewetting, *Adv. Funct. Mater.* Vol. 20, Issue 18, p. 3045.

ANTI-INFLAMMATORY AND CHEMICAL COMPOSITION OF TWO PLANTS FAMILY ASTERACEAE GROWING IN SAUDI ARABIA

Eman Elsharkawy^{1,a}, Mona Alshathly² and Mohamed Helal³

1. Northern Border University, Chemistry Department, Arar, Saudi Arabia
Desert Research center, Eco-Physiology Department, Egypt

2. Northern Border University, Zoology Department, Arar, Saudi Arabia

3. Northern Border University Chemistry Department, Rafha, Saudi Arabia

a. Corresponding author (elsharqawyeman@yahoo.com)

ABSTRACT: The study was designed to investigate the anti-inflammatory and composition of essential oil of two plant family Asteraceae, *Acheliafragmentissima* and *lactucaserriola* growing under dry desert condition. The Anti-inflammatory effect of volatile oil extracted by hydrodistillation of plants was studied using carrageenan induced paw edema. Essential oil (100 mg/kg) and (200 mg/kg) were tested the two plant show high inhibition after four hour, concentration (200 mg/kg) show high inhibition than (100 mg/kg) after 4 hours. Sesquibinene hydrate, Azuline and alpha-Bisabolol are the main constituents of the volatile oil were investigated by capillary GC and GC-MS. The discussion shows the role of chemical compound azuline in inflammatory inhibition.

1. INTRODUCTION

The diversity of medicinal and aromatic plant species and varieties is important from both scientific and practical points of view. In the 21st century, attention is focused on the cultivation and preservation of medicinal and aromatic plants and on the evaluation of their quality.

From the earliest times, herbs have been prized for their pain-relieving and healing abilities and today we still rely largely on the curative properties of plants. According to World Health Organization, 80 % of the people living in rural areas depend on medicinal herb as primary healthcare system, the herbal formulations can be designed to attack the cancerous cells without harming normal cells of the body (Larkin, 1983; Saxe, 1987).

Inflammation is a part of the complex biological response of vascular tissues to

harmful stimuli, such as pathogens, damaged cells or irritants. It is characterized by redness, swollen joint that is warm to touch, joint pain, its stiffness and loss of joint function. Inflammation is either acute or chronic. Under specific circumstance, it could turn into a chronic state and subsequently become a causative factor in the pathogenesis. Inflammation is a self-defense reaction in its first phase, hence regarded as the main therapeutic target and often, the best choice to treat the disease and alleviate the symptoms (Dubois *et al.*, 1998).

Anti-inflammatory drug, a drug which inhibits or suppresses most inflammatory responses of an allergic, bacterial, traumatic or anaphylactic origin as well as being immunosuppressant. They include the corticosteroids (e.g. betamethasone, fluorometholone, hydrocortisone acetate, loteprednololone, prednisolone,

rimexolone, riamcinolone). They are sometimes combined with an antibiotic drug (e.g. betamethasone combined with neomycin or sulfacetamide, dexamethasone combined with neomycin or polymyxin B). Corticosteroids have side effects, such as enhancing the activity of herpes simplex virus, fungal overgrowth, raising intraocular pressure or cataract formation. There are other anti-inflammatory drugs that are non-steroidal (NSAID) and have little toxicity. They act mainly by blocking prostaglandin synthesis. These include diclofenac sodium, flurbiprofen sodium, indomethacin, ketorolac, nepafenac and oxyphenbutazone.

Medicinal herbs are known as sources of phytochemicals, or active compounds that are widely sought after worldwide for their natural properties. They are useful source of essential oil and have been used for a long time in the perfumery, cosmetic, food and pharmaceutical industry. Essential oils are volatile, lipophilic mixtures of secondary plant compounds, mostly consisting of monoterpenes, sesquiterpenes and phenyl propanoids. The qualitative and quantitative improvement of essential oil production presents an area of high commercial interest (Copetta *et al.*, 2006; Khaosaad *et al.*, 2006).

At present and in the future, we use medicinal plants as a good source of food and drugs, we used *acheliafragments* as herbal tea and we eat *lactucaserriola* which grow in our habitats.

Achilleafragrantissima, Asteraceae family is a common plant in the Mediterranean region, Africa, Asia, and easily found growing in fields and on roadsides. It contains high percentage of flavonoids, tannins, volatile oils, sterols and triterpenes. Also it contains unsaturated amides, and

sesquiterpene lactones. *Achilleafragrantissima* was highly valued as a medicinal plant for its antiseptic properties. It was used to cover cuts and sores and hasten scar tissue formation, but till now no clinical uses for *Achilleafragrantissima* is described (Hamzah, *et al.*, 2006). *Achilleafragrantissima*, it grows in dry areas, steppe and desert. Bedouins collect it in the badia, where it is common. It is the last species of *Achillea* to flourish, it has a strong smell and a bitter taste for this reason it is usually mixed with sugar, but the flowers are eaten alone, for diabetes, stomach (alone, or mixed with *Teucrium polium*), muscular rheumatism (fumigation), cough (to drink in the morning with sugar) (Kharma and Hassawi, 2006; Mustafa, *et al.*, 1992).

Where *lactucaseriolla* an annual or biennial weed with prickly leaves that emit a milky sap when cut prickly lettuce is most commonly a weed of nurseries orchards, roadsides, and agronomic crops and is found throughout the Saudi Arabia, North region. The whole plant is rich in a milky sap that flows freely from any wounds. This hardens and dries when in contact with the air. The sap contains lactucarium, which is used in medicine for its anodyne, antispasmodic, digestive, diuretic, hypnotic, narcotic and sedative properties. Lactucarium has the effects of feeble opium, but without its tendency to cause digestive upsets, nor is it addictive. It is taken internally in the treatment of insomnia, anxiety, neuroses, hyperactivity in children, dry coughs, whooping cough, rheumatic pain etc. Concentrations of lactucarium are low in young plants and most concentrated when the plant comes into flower it is collected commercially by cutting the heads of the plants and scraping the juice into china vessels several times

aday until the plant is exhausted (Leila joudi, *et al.*, 2011).

The genus *Lactuca* are chosen because it have very important properties, The plant *L. serriola* contains flavonoids, sesquiterpen lactone which have strong anticancer effects on breast cancer (Elsharkawy and Elshathely, 2013).

In this study, we extend the phytochemical and comparison of volatile oils between two genus family asteraceae and discuss the role of azulene in these plant as anti-inflammatory agent.

2. MATERIALS AND METHODS

2.1. Plant Material

Flowering aerial parts of two plants of family asteraceae, *Achillea fragrantissima* and *Lactuca serriola* samples. were collected from wild population growing in Northern Region (Arar) in Saudi Arabia in April 2012, The identity of the plants have been kindly verified by Prof. Dr. A. Kamal, Faculty of Science, Northern Border University. Voucher specimens were deposited in the Herbarium of Faculty of Science, Northern Border University. (girl's department).

2.2. Sample Preparation

The fresh aerial parts of *plants* (500 gm plant powder) were extracted by percolation with a mixture of n-hexane-ether (1:1, v/v) and the solvents were removed subsequently under reduced pressure. The yield was 1.2% and 0.9% for crude oil respectively.

2.3. Analysis

The constituents of the volatile oils obtained from the n-hexane-ether extracts were analyzed by GLC and GC-MS as reported (El-Shazly, *et al.*, 2002a). Compounds were identified by comparison

of their retention indices (RI), (C9 to C24 n-alkane mixture) and mass spectra with those reported in the literature, (El-Shazly, *et al.*, 2002a; 2002b; Adams, 1995; Engel, *et al.*, 1998; Goad and Akihisa 1997).

2.4. Anti Inflammatory Method

The method developed by (Winter, *et al.*, 1962) was employed. Albino wistar rats of either sex (120- 130 g) were divided into various groups of six animals each. Animals were deprived of food for 12 h prior to experiment and only water was given ad-libitum. First group was used as a control group and received 1 ml of distilled water (10ml/kg); the second group received indomethacin orally (10 mg/kg) suspended in distilled water. Other groups received test compounds at a dose of 100 and 200 mg/kg orally dissolved in distilled water.

One hour after the administration of the compounds, carrageenan suspension (0.1 ml of 1% w/v suspension in 0.9% saline solution) was injected into the sub planter region of left hind paw of animals. Immediately, the paw volume was measured initial paw volume using plethysmometer UGO Basile 21025 Comerio, Italy) before carrageenan injection. Thereafter, the paw volume was measured after 1, 2, 3 and 4 h after carrageenan administration. The difference between initial and subsequent readings gave the change in edema volume for the corresponding time. Edema volume of control (V_c) and volume of treated (V_t) were used to calculate percentage (%) inhibition and (%) edema volume by using following formula:

$$\% \text{ Inhibition} = [1 - (V_t/V_c)] \times 100$$

2.5. Statistical Analysis

Values were expressed as means \pm S.E. Comparisons between means were carried out using one way ANOVA followed by

least significant difference (LSD) and Tukey multiple comparisons test. The $P < 0.05$ was accepted as being significant in all types of statistical tests. SPSS software (version 17) was used to carry out all.

3. RESULT AND DISCUSSION

The oil extracted has a pale yellow color and fragrant pleasant odor. Most of their components could be identified unambiguously by GC-MS. through direct comparison (mass fragmentation, retention index) with published data as well as computer library search. The unidentified components mainly consisted of a mixture of oxygenated monoterpenes and sesquiterpenes. The most component of *L. serriola* are sesquisabinene hydrate, limonine oxide, Thunbergol, and Globulol while β -caryophyllene and thujol found in minor amount but *A. fragmentissima* oil are rich with bisbolone epoxide, caryophyllene oxide, also limonine, menthol, azulolin, santolinaalchole, lanceol, cedern and thujone are found in moderate amount (Table 1).

Essential oils isolated from Aromatic plants have wide applications in perfumery, flavor, cosmetic and pharmaceutical industries. They have been used by human being since ancient times, and despite many of them being substituted by synthetic ones, the demand for essential oils obtained from natural sources is increasing (Guilten, *et al.*, 1996).

While Northern region found that it is subject to high temperatures in summer and very cold in winter this diversity make the plant which subject to this condition accumulate some natural compound and other compound to live and survive in these habitats, this compound which formed under stress are important and have many medicinal uses as azuline, many

paper report for the important of azulin as anti-inflammatory and Bedouin People used the plant, *Acheliafor* many uses for skin diseases so we take the plant and screened in vivo for anti-inflammatory activity by inhibition of carragenan induced rat paw edema method at the dose of 100 and 200 mg/kg orally. Results are presented in Table (2) as percent edema increase at the right hind paw and percent inhibition.

Significant anti inflammatory activity was observed with inhibition in edema of 71.9% for (100 mg/Kg) and 79.4.5% for 200 mg/kg after 4 h of *A. fragmentissima* extract, while *L serriolla* show inhibition in edema of 73.4% for (100 mg/Kg) and 78.3% for 200 mg/kg after 4 h. with comparable to standard drug indomethacin (89.5%) against paw edema induced by carrageenin (Figure 1).

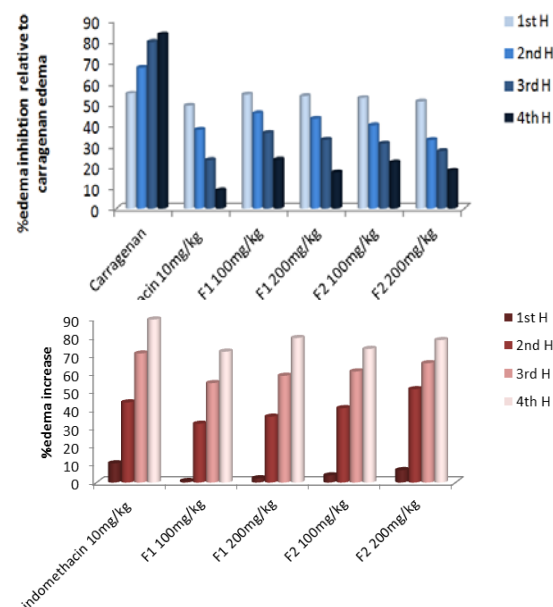


Figure 1: Anti-inflammatory of oil extracts at different concentration.

Table 1: Chemical compositions of plants oil (*A. fragrantissima* and *L. serriolla*) by GC-Maas

	Chemical Compound	Af	Ls
1	Eucalyptol	-	0.28
2	SantolinaAlcohol	0.03	-
3	Camphor	-	4.8
4	Viridiflorol	-	2.95
5	Oxazolidine	-	0.93
6	Sesquisabinene hydrate	-	15.09
7	limonene oxide	-	2.93
8	limonene	1.52	2.9
9	limonene dioxide	1.52	-
10	B-Caryophyllene	0.87	2.0
11	Caryophyllene oxide	1.54	-
12	Globulol	-	6.51
13	Thunbergol	-	8.95
14	alpha.-selinene	-	1.2
15	α-humulene (Caryophyllene)	0.67	0.28
16	Flacarinol	-	1.35
17	alpha.-Phellandrene	0.38	-
18	Thujol	-	0.39
19	Thujone	0.30	-
20	Lanceol	0.86	-
21	Bergamotol	0.86	-

22	Cederne	0.36	-
23	α-Cubebene	0.36	-
24	alpha.-Bisabolol	1.95	-
25	Bisbolen epoxide hydrate	1.45	-
26	Azulene	0.67	-
27	Gernygerinol	0.12	-
28	α-Tocopherol	0.08	-
29	γ-Tocopherol	0.08	-
30	Bisboloneep oxide	1.54	-
31	Menthol	1.36	-

Table 2: Anti-inflammatory of oil extracts at different concentration

Time(H)	% EDEMA			%INHIBITION				
	1 st	2 nd	3 rd	4 th	1 st	2 nd	3 rd	4 th
Control	54.8 ± 2.9	67.1 ± 4.4	79.5 ± 4.1	83 ± 4.7	-	-	-	-
Indomethacin	49 ± 4.2	37 ± 4.1*	23 ± 3.0*	8.6 ± 0.9*	10.5	44	70	89
F1 100mg/kg	54 ± 2.7	45.5 ± 2.3*	36 ± 3.8*	23. ± 2.3 ^{*a}	0.78	32	54.6	71.9
F1 200mg/kg	53 ± 2.3	42.8 ± 1.9*	32 ± 2.4*	17 ± 1.7*	2.3	36	58.6	79.4
F2 100mg/kg	52.7 ± 2	39.7 ± 1.1*	31 ± 3.1*	22 ± 1.7 ^{*a}	3.9	40.8	61	73.4
F2 200mg/kg	51 ± 4.9	32.7 ± 2.6*	27 ± 2.2*	18 ± 1.6*	6.8	51.3	65.5	78.3

3.1. Discussions

Herbal drugs are currently used all over the world because of their safe and effective properties. *A. fragmentissima* and *L. serriola* are useful plants which have lots of therapeutic function. The characteristic of two plant as anti-inflammatory agent is due to antioxidants of essential oil on the wound sites, where two plant contain azulene and Oxazolidinone. *A. fragmentissima* and *L. serriola* respectively, many reviews proved the anti-inflammatory effect of azulene this agree with our study which proved the anti-inflammatory effect of two plants.

Azulene oil is a beauty product derived from flowers in the Asteraceae family, and most commonly distilled from German chamomile flowers. It is used to moisturize and soothe irritated skin and remove sticky residue, particularly after hair removal procedures such as waxing and shaving. The oil is noted for its sweet smell and blue color, the name azulene comes from the Spanish word azul, which means blue. Many azulene oils also contain other natural ingredients that help to soothe the skin, such as vitamin E (Hamzah, *et al.*, 2006), *A. fragmentissima* in addition to azulene it contains (α -tocopherol, γ -tocopherol) and vitamin E.

It is often quite difficult to compare the results obtained from different studies, because the compositions of the essential oils can vary greatly depending upon the geographical region, the variety, age of the plant, the method of drying and the method of extraction of the oil (Al-Reza *et al.*, 2009). The hydrodistillation of the plant extracts gave pale yellow oil with major components of the oil having phenolic compounds, oxygenated mono- and sesquiterpenes, and their respective hydrocarbons (In recent years, several

researchers have reported that mono- and sesquiterpene hydrocarbons and their oxygenated derivatives as the major components of essential oils of plant origin, which have potent anti-inflammatory effect, and such findings were also confirmed in the present investigation (Peana, *et al.*, 2002; Fernandes, *et al.*, 2007; Ko, *et al.*, 2008).

4. CONCLUSIONS

The results presented in this report suggest possible applications of essential oil from two plants *A. fragmentissima* and *L. serriola* family asteraceae as a useful anti-inflammatory agent.

REFERENCES

- Adams, R.P., 1995. Identification of essential oil components by gas chromatography/mass spectrometry, 4th edition, Allured Pub. Corp, Illinois USA.
- Al-Reza, S.M., Bajpai, V.K. and Kang, S.C., 2009. Antioxidant and antilisterial effect of essential oil and organic extracts from *Zizyphus jujube*, Food Chem Toxicol, 47:2374-2380.
- Copetta, A., Lingua, G. and Berta G., 2006. Effects of three AM fungi on growth, distribution of glandular hairs, and essential oil production in *Ocimum basilicum* L. var. Genovese, Mycorrhiza, 16:485-494.
- Dubois, R.N., Abramson S.B., Crofford L., Gupta R., Simon L.S., van de putte, L.A. and Lipsky, P.E., 1998. Cyclooxygenase in biology and disease, FASEB J, 12:1063-73.
- Elsharkawy, E. and Alshathely, M., 2013. Anticancer activity of *Lactuca serriola* growing under dry desert condition of northern region in Saudi Arabia, J Nat Sci Res, 3(2):2224-3186.
- El-Shazly, A., Dorai, G. and Wink M., 2002a. Composition and antimicrobial activity of essential oil and hexane-ether extract of *Tanacetum santolinoides* (DC.) Feinbr. and Fertig., Z Naturforsch, 57c:620:623.
- El-Shazly, A., Dorai, G. and Wink M., 2002b. Chemical composition and biological activity of the essential oils of *Senecioaegyptius* var. discoideus Boiss, Z Naturforsch, 57c:434-439.

- Engel, R., Gutmann M., Hartisch, C., Kolodziej, H. and Nahrstedt, A., 1998. Study of the composition of the volatile fraction of *Hamamelisvirginiana*, *Planta Med* 64:251-258.
- Fernandes, E.S., Passos, G.F., Medeiros, R., Cunha, F.M., Ferreira, J., Campos, M.M., Pianowski, L.F. and Calixto, J.B., 2007. Anti-inflammatory effects of compounds alpha-humulene and (-)-trans-caryophyllene isolated from the essential oil of *Cordia verbenacea*, *Eur J Pharmacol*, 569:228-236.
- Goad, L.J. and Akihisa, T., 1997. Analysis of sterols, Blackie Academic and Professional, an imprint of Chapman and Hall, London.
- Hamzah, M., Mohammad H., Semreen, N. and Ahmad, R., 2006. Anti-inflammatory activity of achelia and *Ruscus* topical gel on Carageenan-induced Paw edema in rats, *Acta Polonae Pharma Drug Res*, 63(4):277-280.
- Ko, H.H., Hung, C.F., Wang, J.P. and Lin, C.N., 2008. Anti-inflammatory triterpenoids and steroids from *Ganoderma lucidum* and *G. tsugae*, *Phytochemistry*, 69:234-239.
- Khaosaad, T., Vierheilig, M., Nell, K., Zitterl-Eglseer and Novak, J., 2006. Arbuscular mycorrhiza alters the concentration essential oils in oregano (*Origanum* sp., Lamiaceae), *Mycorrhiza*, 16(6):443-446.
- Khurma, A., and Hassawi, D., 2006. The antimicrobial activity and the genetic relationship of *Achillea* species, *Biotechnology*, 5(4):501-507.
- Kupper, T.S. and Fuhlbrigge, R.C., 2004. Immune surveillance in the skin: mechanisms and clinical consequences, *Nat Rev Immunol*, 4:211-222.
- Leila, j., Ghassem, H.B. and Hamide, S., 2011. Introduction the medicinal species of *Asteraceae* family in Ilkhji and Sharafaldin regions of Esat Azarbaijan in Iran, *J Amer Sci*, 7(5):455-458.
- Larkin, T., 1983. Herbs are often more toxic than magical, *FDA Consum*, 17:4-11.
- Mustafa, E., Abdalla, M., Abu Zarga and Sabri, S., 1992. Constituents of *Achillea fragrantissima* and effects of 13-O-desacetyl ethoxyfraglaucolide on rat isolated smooth muscle, *Fitoterapia*, 63:526-533.
- Peana, A.T., Aquila, P.D., Panin, F., Serra, G., Pippia, P. and Moretti, M.D.L., 2002. Anti-inflammatory activity of linalool and linalyl acetate constituents of essential oils, *Phytomedicine*, 9:721-726.
- Saxe, T.G., 1987. Toxicity of medicinal herbal preparations, *Am Fam Physician*, 35:135-42.
- Winter, C.A., Risely, E.A. and Nuss, G.W., 1962. Carageenan induced edema hind paw of the rats as an assay for anti-inflammatory drugs, *Proc Soc Expt Bio Med*, 1:544-547.

AMINO ACIDS ADSORBED ONTO CELLULOSE AS A WAY TO INCREASES THE CELLULOSE'S OXIDATION BY SUPPORTED Y ZEOLITE TO COSTLY COMPOUNDS

Enrique Lima¹, Magali Hernández¹, Ariel Guzmán-Vargas^{2,a}

1. Instituto de Investigaciones en Materiales, Universidad Nacional Autónoma de México, Mexico

2. Instituto Politécnico Nacional – ESIQIE-LiMpCa-Qf, Zacatenco, Mexico

a. Corresponding author (aguzmanv@ipn.mx)

ABSTRACT: Phenylalanine was adsorbed onto the surface of microcrystalline cellulose, which caused changes in the morphology and texture at the cellulose surface. The amino acid grafting partially modified the hydrogen bonding network of the cellulose structure, leading to more reactive cellulose residues that were facily oxidised to gluconic acid by oxygen in the presence of gold zeolite supported catalysts.

1. INTRODUCTION

Cellulose is the largest organic raw material in the world, and many efforts have been made to convert cellulosic materials into valuable chemicals and renewable fuels [Kamm, 2007].

Cellulose forms an extensive network of intra- and intermolecular hydrogen bonds, which confers remarkable chemical stability and makes the direct utilisation of cellulose a challenge, being the heterogeneous catalysis the most promising via to convert cellulose. From cellulose and their model molecules, some appreciated products have been obtained by catalysis, for instance bioethanol, ethylene glycol, glycolic acid, among others [Van de Vyver, 2011].

Cellulose is often studied through the rough cellobiose model which is converted catalytically to obtain insights for the development of efficient routes of cellulose degradation.

Recently, the catalytic oxidation of cellobiose to gluconic acid in the presence of oxygen catalysed by gold nanoparticles loaded on several supports was reported [Tan et al., 2009]. The best results were obtained with a catalyst based on gold nanoparticles in an acidic

support. The works where cellulose was used instead cellobiose are scarce [An, et al., 2012]. This work intends to disturb the hydrogen bonds network of microcrystalline cellulose and then catalytically oxidise the material to gluconic acid in the presence of gold nanoparticles supported on the acid porous zeolite HY. To perturb the cellulose surface and increase its reactivity, amino acid phenylalanine was grafted onto the cellulose surface weakening the hydrogen-bond network.

2. EXPERIMENTAL PROCEDURES

2.1 Materials

Phenylalanine, microcrystalline cellulose and all reagents and solvents were acquired from Sigma Aldrich (USA).

Microcrystalline cellulose (MC) was hydrothermally treated with alanine. MC was suspended in 100 mL aqueous solution containing ¹³C-enriched amino acid. The suspension was stirred for 1 hour, the pH adjusted to 5 and then refluxed for 5 hours. Lastly, the solid was separated by centrifugation and washed repeatedly until the wash water pH became neutral. The MC functionalised was named PhA-MC. In order to

elucidate the effect of the amount of amino acid adsorbed on the cellulose surface, other samples were prepared varying the amount of phenylalanine, fundamentally a sample with a lower and two with a higher amount of phenylalanine than in PhA-MC were prepared. Sample with the lowest amount of amino acid was named PhA-MC-l and two with higher amount were labelled PhA-MC-h and PhA-MC-vh. The amount of phenylalanine is reported in Table 1.

Catalyst Au-HY was prepared from zeolite NH₄Y (Si/Al ratio of 5.1), which was heated at 400 °C for 6 h to obtain the corresponding protonated HY zeolite. The HY zeolite was suspended in a solution of colloidal Au (5 nm) purchased from Sigma Aldrich (USA). After 3 hours, the solid was separated by centrifugation, repeatedly washed, dried at 50 °C and reduced at 400 °C under hydrogen flow for 4 hours. The amount of gold in the catalyst was 0.8 wt%. This catalyst was named Au-HY. Another gold-faujasite catalyst was prepared in a similar way except that the compensating cation was changed using cesium to obtain Au-CsY. The gold loading was similar for both catalysts.

2.2. Characterisation

The chemical analysis was obtained using XPS. The analysis was carried out using a VG Microtech ESCA2000 Multilab UHV system, with a Mg K α X-ray source (1253.6 eV) and a CLAM4 MCD analyzer. The peak positions were referenced to the C 1s hydrocarbon groups in 284.50 eV central peak position.

The XRD patterns were acquired using a diffractometer (D8 Advance-Bruker) coupled to a copper anode X-ray tube.

A Kratky camera coupled to a copper anode tube was used to measure the

SAXS curves. The distance between the sample and the linear proportional counter was 25 cm, and a Ni filter selected for the Cu K α radiation. The SAXS data were processed with the ITP program [Glater, 1982], where the angular parameter (h) is defined as $h = 4\pi\sin \theta/\lambda$, where θ and λ are the X-ray scattering angle and wavelength, respectively. The fractal dimension of the scattering objects was evaluated from the slope of the curve $\log I(h)$ versus $\log(h)$ according to the Porod law [Ibarra et al., 2005].

¹³C CP MAS NMR spectra were obtained at a frequency of 100.58 MHz using a 4 mm cross-polarisation (CP) MAS probe spinning at a rate of 5 kHz. Typical ¹³C CP MAS NMR conditions for ¹H-¹³C polarisation experiment used a $\pi/2$ pulse of 4 μ s, contact time of 1 ms and delay time of 5 s. Chemical shifts were referenced to a solid shift at 38.2 ppm relative to TMS.

The morphology of the samples was studied with a SEM Jeol 7600 scanning electron microscope.

Gold catalysts were analysed by transmission electron microscopy, in a 120 kV LEO-912AB (ZIES). The TEM images were processed digitally from the negative films by using a film scanner. Size distribution measurements for Au particles were performed on digital images by using the image analysing software Image-Pro.

2.3. Catalytic Tests

The conversion of cellulose was carried out in a 100 mL Teflon-lined stainless-steel autoclave. Cellulose samples and the catalyst were added into the autoclave pre-charged with H₂O. Then, O₂ was introduced, and the temperature was increased to 110 °C to start the reaction. After three hours, the liquid products

were analysed by HPLC (Perkin Elmer) equipped with a TransgenomicTM CARBONSep CHO-620 column.

3. RESULTS AND DISCUSSION

3.1. Grafted Cellulose

The amount of amino acid adsorbed at the cellulose samples as determined by XPS is reported in Table 1. According with other grafting cellulose experiments [Trejo-O'Reily et al., 1997], the percentage of OH groups kinetically available are between 2 and 3 %. The XPS technique was used to evaluate the amino acid content because it is a surface technique and the amino acids were expected to remain adsorbed at cellulose surface. The XRD patterns of pure cellulose and amino acid-cellulose are displayed in Figure 1. Amino acid adsorption did not cause the collapse of the crystalline structure of the cellulose within the limits of the bulk XRD technique.

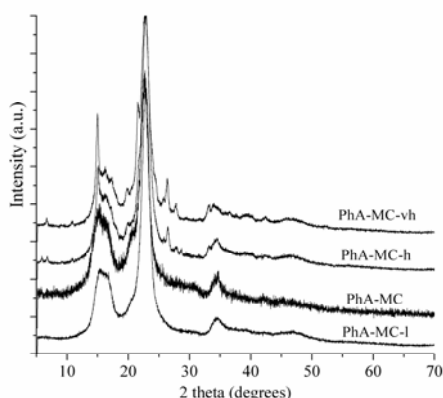


Figure 1: XRD patterns of the grafted and ungrafted celluloses.

The ¹³C CP/MAS NMR spectra displayed in Figure 2 and the peak assignments confirmed the presence of amino acids in the cellulose samples. The peak assignments were made according to the carbon atom numbering on the structures included on the right of the figure. In the MC spectrum, all peaks (C1-C6) of the

glucose units of cellulose were well resolved. Furthermore, the presence of two broad peaks, marked AC, revealed that a fraction of cellulose was amorphous [Hult et al., 2002].

The spectra of celluloses loaded with phenylalanine, clearly resolved the peaks due to phenylalanine were well resolved at 35, 56, 125, 129, 131, 136 and 174 ppm. The chemical shifts of the cellulose carbons C-2 and C-4 (63 and 81 ppm, respectively) were shifted upfield. The NMR peaks corresponding to carbons C-3 and C-5 become broader than the signals observed in pure cellulose. The main difference observed in the peaks of phenylalanine adsorbed on cellulose and pure phenylalanine was that the aromatic peaks between 120-140 ppm become broader as a consequence of adsorption suggesting that the aromatic ring of phenylalanine interacts with cellulose.

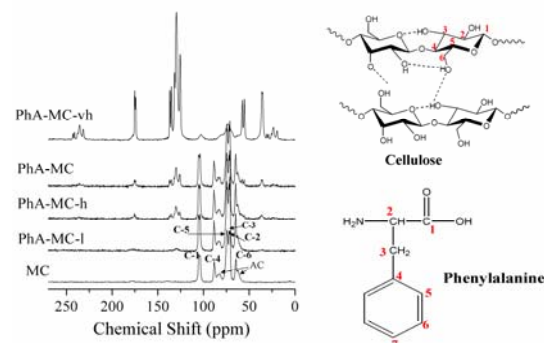


Figure 2: ¹³C CP MAS NMR spectra of the grafted and ungrafted celluloses.

Table 1: The composition and texture parameters of cellulose samples.

Code Sample	Amount (wt%) of amino acid	Fractal Dimension
MC	-	2.1
PhA-MC	3.7	2.7
PhA-MC-l	2.4	2.5
PhA-MC-h	5.6	2.7
PhA-MC-vh	8.2	2.8

The sample fractal dimension values of samples under study are reported in Table 1. Lower fractal dimension values correspond to smoother surfaces. MC exhibited the smoothest surface, and, as expected, PhAla-MC had significantly increased roughness measurements compared with MC. Actually, from XRD and NMR results phenylalanine could be interacting through the aromatic ring by adsorbing parallel to the (002) planes of cellulose. This orientation would break the hydrogen bonds in the cellulose network, causing a rougher surface.

Actually, morphology of cellulose is also modified by amino acid adsorption. Figure 3 compares the SEM images of PhA-MC-l and PhA-MC-vh revealing that increasing the amount of adsorbed phenylalanine the formation of a porous network is favoured instead planar smooth surfaces.

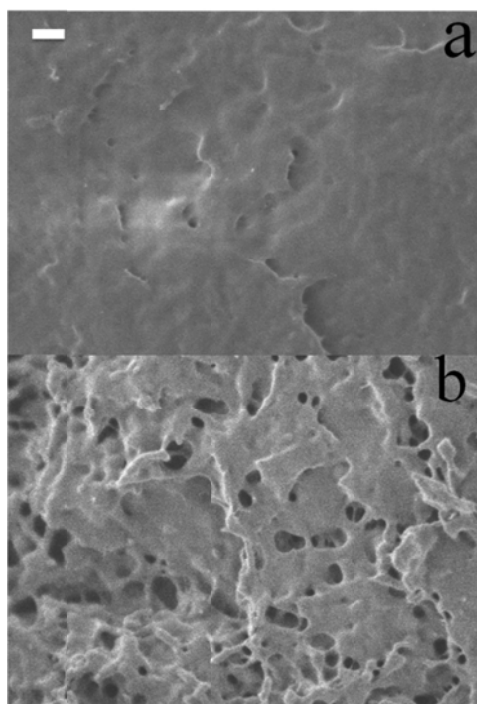


Figure 3: SEM images of PhA-MC-l (a) and PhA-MC-vh (b). Bar scale is equal to 100 nm and apply for both images.

3.2. Au-Y Catalysts

The XRD pattern and ^{27}Al and ^{29}Si MAS NMR spectra of the catalysts confirmed that the structure of the faujasite zeolite was maintained after gold loading. TEM showed that the maximal population density of Au particles over the surface was close to 40 Au particles per $1 \times 10^4 \text{ nm}^2$ surface area. The particle size distribution was relatively homogeneous in Au-HY, with a majority of the particles close to 5 nm. The Au particle size distribution was less homogeneous on CsY but the average size of the particles was also close to 5 nm.

3.3. Catalytic Oxidation of Grafted Cellulose

The overall catalytic results, Table 2, suggest that the modification of the cellulose surface significantly increased its reactivity, leading to an increase of the direct catalytic oxidation of cellulose. PhA-MC was selectively oxidised to gluconic acid using the Au-CsY catalyst, but this selectivity decreased significantly with Au-HY, which can be explained by the changes in basicity of the support. Earlier, it was found that catalysts using basic supports were more selective for gluconic acid than glucose [Tan et al., 2009].

Table 2: Oxidation of grafted cellulose by oxygen in the presence of Au-HY or Cs-HY catalyst.

Code Cellulose Sample	Cellulose conversion (%)	Selectivity (%)		
		Glucose	Gluconic acid	Other
PhA-MC-l	9	16	72	12
PhA-MC	14	17	61	22
PhA-MC-h	16	41	38	21
PhA-MC-vh	41	39	23	38

	PhA-MC-l	11	42	35	23
	PhA-MC	52	58	29	13
	PhA-MC-h	48	46	30	24
	PhA-MC-vh	39	47	27	26

Even when Au-CsY is a selective catalyst, overall, the best catalyst was Au-HY. An increase in the catalytic oxidation is not always obtained with an increase of phenylalanine.

The highest activity was found when amino acid is loaded at moderate concentration (samples PhA-MC and PhA-MC-h). Although the fractal dimension value of the grafted samples increases always with the amount of amino acid, the catalytic activity decays for the highest amount of amino acid which means that cellulose covered by an excess of amino acid cannot be depleted and oxidised.

4. CONCLUSION

The surface of cellulose was modified by grafting phenylalanine. Texture and morphology are significantly modified by amino acid adsorption. The catalytic oxidation of cellulosic materials was determined by both the gold-catalyst itself and the cellulose modification. Adsorbed cellulose was significantly more reactive than pure cellulose. Amount of amino acid is a key parameter to modify cellulose surface; moderate amounts (3-5 wt %) assures the highest reactivity. Au-HY was more efficient catalyst than Au-CsY.

Acknowledgements: The authors would like to acknowledge COFAA-SIP-IPN, CONACYT for Grant 128299, 101319 and PAPIIT-UNAM IN107110.

REFERENCES

- An, D., Ye, A., Deng, W., Zhang, Q., Wang, Y., 2012. Selective Conversion of Cellobiose and Cellulose into Gluconic Acid in Water in the Presence of Oxygen, Catalyzed by Polyoxometalate-Supported Gold Nanoparticles, *Chemistry - A European Journal*, 18 (10) 2938.
- Glatter, O. (1982). *Small-Angle X-ray Scattering*, edited by O. Glatter & O. Kratky, pp. 119-196. London: Academic Press.
- Hult, E.L., Liitiä, T., Maunu, S.L., Hortling, B., Iversen, T., 2002. Cellulose crystallinity and ordering of hemicelluloses in pine and birch pulps as revealed by solid-state NMR spectroscopic methods, *Carbohydr. Polym.*, 49 (4) 231.
- Ibarra, I.A., Loera, S., Laguna, H., Lima, E., Lara, V., 2005. Irreversible Adsorption of an Aztec Dye on Fractal Surfaces, *Chemistry of Materials* 17 (23) 5763.
- Kamm, B., 2007. Produktion von Plattformchemikalien und Synthesegas aus Biomasse, *Angewandte Chemie*, 119 (27), 5146.
- Tan, X., Deng, W., Liu, M., Zhang, Q., Wang, Y., 2009. Carbon nanotube-supported gold nanoparticles as efficient catalysts for selective oxidation of cellobiose into gluconic acid in aqueous medium, *Chemical Communications*, 46, 7179.
- Trejo-O'Reilly, J.A., Cavaille, J.Y., Gandini, A., 1997. The surface chemical modification of cellulosic fibers, *Cellulose*, 4 (4) 305.
- Van de Vyver, S., Geboers, J., Jacobs, P.A., Sels, B.F., 2011. Recent Advances in the Catalytic Conversion of Cellulose, *ChemCatChem* 3

POROUS POLYLACTIDE AS MEDICAL SCAFFOLD

Marek Kozłowski^{1a}, Joanna Macyszyn¹

1. Wrocław University of Technology, Faculty of Environmental Engineering, Wrocław, Poland
a. marek.a.kozlowski@pwr.wroc.pl

ABSTRACT: Cellular structure formation in polylactide (PLA) has been described. Different methods of foaming have been tested and the porous morphology has been evaluated by means of the optical and scanning electron microscopy. Polymer foaming parameters have been correlated with the morphology details. Pore size and pore density as well as the connectivity of cells have been evaluated. Polylactide was characterized in respect of its viscoelastic properties in a molten state, by thermomechanical characteristics and differential scanning calorimetry. Mechanical properties of the porous polylactide at compression and bending stress have been described.

1. INTRODUCTION

Polymer scaffolds are one of the most promising solutions to the problems associated with tissue engineering. Scaffolds used in tissue engineering should imitate biological functions of the extracellular matrix to maintain the structure and contribute to the growth, adhesion and cell differentiation [Chen *et al.*, 2002; Owen *et al.*, 2010; Dhandayuthapani *et al.*, 2011]. For the construction of the microporous structures, micro and nonwoven different materials have been used, including metals, ceramics, hydrogels, as well as the natural and synthetic polymers, and polymer composites. The most widely studied polymers for the repair of bone and cartilage are PGA [Freed *et al.*, 1994], PLA [Tschoeke *et al.*, 2009; Maquet *et al.*, 2009], and PLGA copolymers [Vozzi *et al.*, 2003], PCL [Oh *et al.*, 2007], PLA / PCL [Vaz *et al.*, 2005], PEO, PPF.

Ideal scaffolds for tissue regeneration should be biocompatible, bioresorbable, biodegradable, have a porous structure (open pores), and exhibit a suitable strength properties (Table 1). There are many methods for preparation of polymeric scaffolds, for example particulate leaching, thermally induced phase separation (TIPS), electrospinning,

gas foaming, methods based on solid freeform fabrication, rapid prototyping techniques (stereolithography, selective laser sintering - SLS, 3 dimensional printing or plotting).

Table 1: Mechanical properties of human tissue [Vaz *et al.*, 2006].

	Tensile Strength [MPa]	Compressive Strength [MPa]	Young Modulus [MPa]
Cancel- lous bone	8	4-12	50-100
Cortical bone	60-160	130-180	3-30·10 ³
Cartilage	3,7-10,5	-	0,7-15,3
Ligament	13-46	-	65-541
Tendon	24-112	-	143-2310

2. EXPERIMENTAL

2.1. Materials

In this study PLA 3052D supplied by NatureWorks was used. Polylactide was dried at 70°C for a minimum of 4 h before processing. A commercial grade blowing agent Hydrocerol PLC742 (Clariant) was used in an amount of 2,0 wt.%.

2.2. Crystallinity

Crystallinity of polylactide has been evaluated by means of the differential scanning calorimetry using an instrument

DSC Q20 (TA Instruments, USA). A thermal ramp running from -20°C up to 250°C at the rate of 10°C min⁻¹ under nitrogen allowed calculations of the percentage of crystallinity according to:

$$\text{Percentage of crystallinity [\%]} = \frac{[\Delta H_m - \Delta H_c]}{\Delta H_m^\circ} \times 100\%$$

where ΔH_m (J/g) is the melting enthalpy, ΔH_c (J/g) is the cold crystallization enthalpy and ΔH_m° is the melting enthalpy of a 100% crystalline PLA reported to be equal to 93 J/g.

2.3. Rheological Properties

The rheological measurements were carried out with Haake RheoStress 6000 rotational rheometer (Thermo Scientific) using a plate-plate measuring system and a gap between the plates of 1 mm. The test was performed in the oscillatory mode at temperature of 160°C.

2.4. Foaming Process

Cellular structure was obtained during the continuous foaming extrusion process using the single screw extruder Rheomex 252 (Haake, Germany) composed of 3 heated zones and the extrusion die. The temperature was set on: 150-160-165-145°C (low), 150-160-170-150°C (medium), 150-160-175-155°C (high) temperature. The screw rotation speed was 15 rpm.

Second method of the polymer foaming was a batch process. Samples thickness of 0.2 mm and diameter of 13 mm were prepared using by means of press moulding at temperature of 160°C and pressure of 5 MPa. The specimens were saturated with nitrogen in the pressure chamber at room temperature (23-25°C) under pressure of 5 MPa for 48 hours. Then the pressure was released and the sample was immediately immersed in the glycerine bath temperature of 145°C for 5 minutes.

2.5. Cellular Morphology

Scanning electron microscopy (SEM) was used to characterize the morphology of foamed samples. Sputtering with gold was performed prior to the observations which were carried out with VEGA microscope (Tescan). Morphology studies were also carried out using an optical microscope AXIO Image M1m (ZEISS).

2.6. Density

The foam density was evaluated by a buoyancy method with the density kit mounted on a balance (Mettler Toledo).

3. RESULTS AND DISCUSSION

3.1. Properties of PLA

The degree of crystallinity and thermal properties have a significant influence on the foaming process of polymers [Kozłowski, 2012]. Poly (lactic acid) 3052D is of a semicrystalline structure, the degree of crystallinity is about 33%. The glass transition temperature (T_g) was of 66°C and the melting temperature (T_m) of 158°C (Figure 1). The melting temperature determines the upper limit of foaming of the polymer.

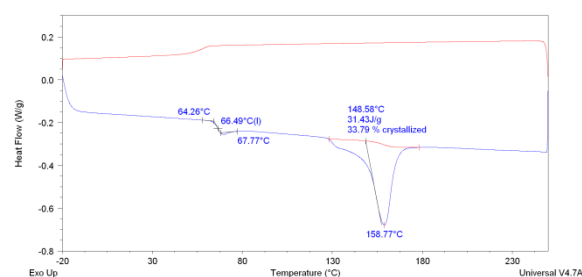


Figure 1: DSC results.

Materials in the molten state must have a viscosity low enough to permit dissolving the gas and cell nucleation. The melt strength should be high enough to maintain the foamed structure and avoid the cell coalescence. Rheological studies have shown that PLA 3052D has a high

melt viscosity (Figure 2) with the pseudoplastic character of flow.

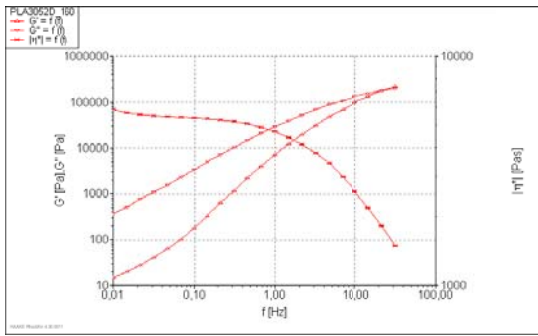


Figure 2: Rheological properties.

The high degree of crystallinity of PLA causes the formation of small pores (Figure 3). The cellular structure is dependent on the temperature during the foaming process.

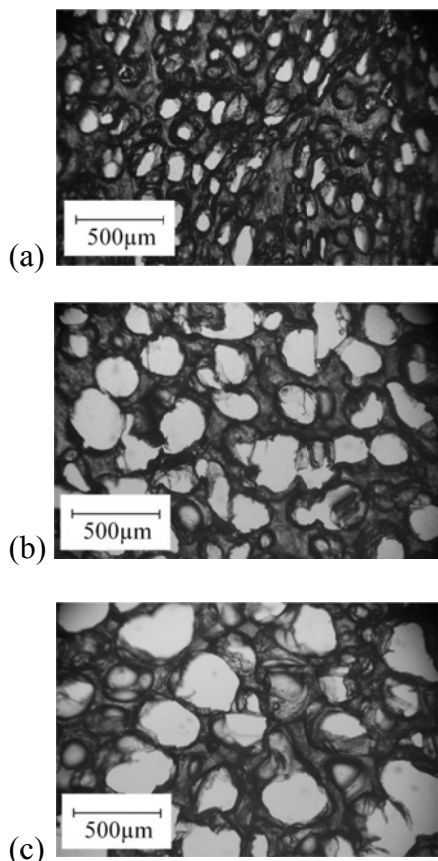


Figure 3: Cellular structure of poly(lactide) obtained at: a) low b) medium c) high temperature using foaming extrusion process.

Preparation of the porous structure at a low temperature (Figure 3, a) causes the formation of pores in the range of 100 μm using foaming extrusion process. High melt viscosity due to low temperature makes difficult the pores to grow. An increase in temperature results in its lower viscosity, which allows an unlimited growth of the pores (size of 300-400 μm) and the ability to connect the cells (Figure 3, c), which is beneficial in the production of scaffolds.

Batch foaming technology with gas saturation of polylactide samples resulted in obtaining a fine cellular structure (Figure 4). The high pressure caused that the gas was dissolved in PLA and cell nucleation and growth started in the polymer matrix after decompression. High temperature of the bath affected a growth of a large number of small pores (size of about 10-50 μm) The cell walls became thin, leading to their rupture and formation of the open cell structure.

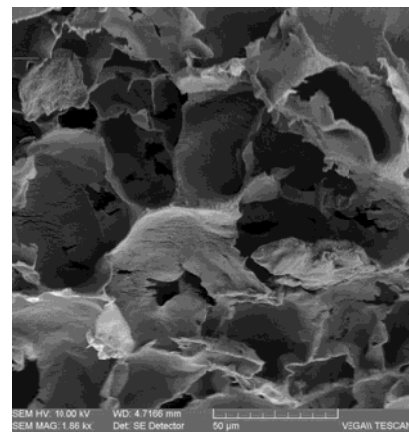


Figure 4: Cellular structure of poly(lactide) using batch foaming process.

Foaming process has enabled a reduction of polylactide density (Table 2). However, the mechanical properties of the foamed materials were inferior to that of the bulk matrix. Nevertheless, the mechanical properties of PLA with a cellular structure are suitable for use as polymeric scaffolds.

Table 2: Density and mechanical properties PLA and cellular PLA.

Material	Density [g/cm ³]	Young Modulus [MPa]	Bending Strength [MPa]
PLA	1,24	3736	112,63
Cellular PLA	0,68	994	21,74

4. CONCLUSION

The cellular structure in polylactide was generated using the foaming extrusion process and batch process. The resulting cells were in the range of 300-400 µm if using a chemical blowing agent and extrusion, and 10-50 µm while a direct method of gas saturation was used. Both materials exhibited the low density and good mechanical properties.

Acknowledgements: The work was supported by Wrocław Research Centre EIT+ within the project "The Application of Nanotechnology in Advanced Materials" - NanoMat (POIG.01.01.02-02-002/08) co-financed by the European Regional Development Fund (Operational Programme Innovative Economy, 1.1.2).

The Authors wish to thank Dr S. Frackowiak for his help in rheological measurements and Dr M. Gasior for microscopic images.

REFERENCES

- Chen G., Ushida T., and Tateishi T., 2002. Scaffold Design for Tissue Engineering, *Macromol. Biosci.*, (2), 67.
- Owen S. C., and Shoichet M. S., 2010. Design of Three-dimensional Biomimetic Scaffolds, *Journal of Biomedical Materials Research*, (94A), 1321.
- Dhandayuthapani B., Yoshida Y., Maekawa T., and Kumar D. S., 2011. Polymeric Scaffolds in Tissue Engineering Application: A Review, *International Journal of Polymer Science*, (1), 1.
- Freed L. E., Vunjak-Novakovic G., Biron R. J., Eagles D. B., Lesnoy D. C., Barlow S. K., and Langer R., 1994. Biodegradable Polymer Scaffolds for Tissue Engineering, *Nature Biotechnology*, (12), 689.

- Tschoeke B., Flanagan T. C., Koch S., Harwoko M. S., Deichmann T., Ellá V., Sachweh J. S., Kellomäki M., Gries T., Schmitz-Rode T., and Jockenhoevel S., 2009. Tissue-Engineered Small-Caliber Vascular Graft Based on a Novel Biodegradable Composite Fibrin-Polylactide Scaffold, *Tissue Engineering Part A*, (15), 1909.
- Maquet V., Martin D., Malgrange B., Franzen R., Schoenen J., Moonen G., and Jérôme R., 2009. Peripheral Nerve Regeneration Using Bioresorbable Macroporous Polylactide Scaffolds, *Journal of Biomedical Materials Research*, (52), 639.
- Vozzi G., Flaim C., Ahluwalia A., and Bhatia S., 2003. Fabrication of PLGA Scaffolds Using Soft Lithography and Microsyringe Deposition, *Biomaterials*, (24), 2533.
- Oh S. H., Park I. K., Kim J. M., and Lee J. H., 2007. In vitro and in vivo Characteristics of PCL Scaffolds with Pore Size Gradient Fabricated by a Centrifugation Method, *Biomaterials*, (28), 1664.
- Vaz C. M., Tuijl S., Bouten C. V. C., and Baaijens F. P. T., 2005. Design of Scaffolds for Blood Vessel Tissue Engineering Using a Multi-layering Electrospinning Technique, *Acta Biomaterialia*, (1), 575.
- Kozłowski M., 2012. Lightweight Plastic Materials *in* Thermoplastic Elastomers. El-Sonbati A. Z. (Ed.), *InTech*, Rijeka, 2012, 291.

FABRICATION AND CHARACTERIZATION OF POROUS BIOGLASS CERAMIC

Kerim Emre ÖKSÜZ^{1,a}, Hanlar BAĞIROV¹, Hasan YILMAZ¹,
Buket SİLAHŞOR¹, Vedat YILDIRIM¹

¹Cumhuriyet University, Metallurgical & Materials Engineering Department, 58140, Sivas, Turkey.
a. Corresponding author (kerimemreoksuz@gmail.com)

ABSTRACT : Many kind of bioactive materials including bioglasses, bioglass–ceramics, and calcium phosphate ceramics, have been developed and some of them are now applied to repair and reconstruct diseased or damaged bones or tissues. Much attention has recently been devoted to investigation of these materials since they expand the range of bioresorbability and mechanical properties of bioceramics. The aim of this study is to explain the manufacturing process of bioceramics with controlled porosity by a simple method. Al₂O₃ and ZrO₂ were added to the matrix in order to increase the hardness and strength. Sodium-free bioglass material is derived from reagent grade chemicals. Wood flour with a grain diameter of 100 µm is used as a filling material. Composites were sintered in a furnace at 850°C for 3h. The samples were characterized from a microstructural point of view, in order to evaluate the pore morphology, dimension and degree of interconnectivity.

1. INTRODUCTION

One of the latest lines in materials science concerns materials for replacing defective bone parts. They may be subdivided into bioinert ones and bioactive ones in accordance with their behavior in the body. Bioactive materials participate in metabolism and are resorbed and replaced by newly formed bone tissue. They include calcium phosphate glasses and glass ceramics, synthetic hydroxyapatite (SHAp), and biological hydroxyapatite (BHAp), as well as composite materials (CM) based on them [Kanazawa, 1999 ; Doremus, 1992 ; LeGeros et al., 1995 ; Dubok, 2000 ; Ostrovskii, 1999]. All bioactive materials form an interfacial bond with bones or tissue. However, the time dependence of bonding, the strength of bond, the mechanism of bonding and the thickness of the bonding zone differ for the various biomaterials. Bonding to bone was first demonstrated for a certain compositional range of bioactive glasses which contained SiO₂, Na₂O, CaO and P₂O₅ in specific proportions [Balamurugan et al., 2007]. Bioactive materials used for

implantation must meet various requirements: medical ones determined by the purposes of the reconstructive surgical operations, and by individual patient features; technological ones involved in making and processing the materials giving implants effective from the viewpoint of physicommechanical and constructional parameters; and economic ones, which are determined by the cost of the raw material and the energy consumed in making the implants. Pores of various sizes in the implant and even in the individual granules are required for the biomaterials to interact with the physiological medium in the organism [Doremus, 1992; LeGeros et al., 1995 ; Dubok, 2000]. The porous structure favors ion exchange and intergrowth with binding bone tissue, as well as the penetration of blood-bearing vessels and cells, which provide bone precursors in the implant [Gruntovskii and Malyshkina, 1999 ; Malyshkina et al., 1998]. Methods of making calcium phosphate biomaterials are very varied in technology and economics. The technological differences have a substantial effect on the characteristics of the product, so it is

important to know the advantages and shortcomings of each method of making the materials in order to provide properties needed for the best use [Ivanchenko et al., 2003]. In this experimental study, some of the bioglass compositions were prepared and the influence of the P₂O₅.CaO bioglass addition on the sinterability porosity and mechanical properties of ZrO₂-Al₂O₃ ceramics were investigated.

2. EXPERIMENTAL PROCEDURE

2.1. Processing

High-purity Zirconium(IV) oxide (1µm) , 99.5% (metals basis excluding Hf), Hf <100ppm and aluminum oxide (1µm), alpha-phase, 99.99% (metals basis) powders (*Alfa Aesar*) and bioactive P₂O₅.CaO bioglass powder (*Merck Chemicals*) were used as starting powders. Moist wood flour with a grain diameter of 200 µm is used as a filling material. The glass composition is based on % 75 mol of P₂O₅ and % 25 mol of CaO. The powders were mixed, pre-calcined and then melted at at 1100± 50°C in 100 ml alumina crucibles in air atmosphere [Majhi et al., 2011] for 2 h. The glass was obtained after quenching in cold distilled water and powered to a final maximum size of 45-50 µm. Initially, wt.%2 ZrO₂ and Al₂O₃ were added to bioglass powder separately and the mixture was allowed to mix for 60 min with T₂F Turbula for homogenized thoroughly. Bioceramic powders were compacted by cold uniaxial pressing at 400 MPa for 60s. These pressed specimens had dimensions of 10 mm in diameter and 5 mm height. The green compacts were sintered at 850°C, in a muffle furnace for 3h, with heating and cooling rates of 10°C/min. These samples were polished by 600-,1000-, and 1200-, of silicon carbide and aluminum oxide.

3. RESULTS OF BIOGLASS-CERAMIC SAMPLES

3.1 Bioglass Characterization

Fig. 1 shows the X-ray diffraction (XRD) patterns of the P₂O₅.CaO bioglass. It shows a diffractogram with amorphous characteristics, typical of the glassy material.

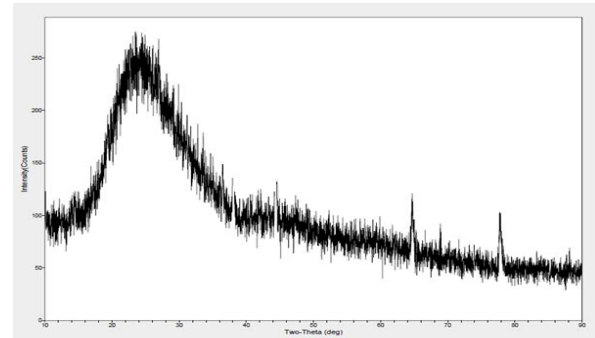


Fig 1: XRD pattern of the P₂O₅.CaO bioglass.

The relative density and porosity of the sintered materials were determined using Archimedes's water displacement method, as specified by European Standard EN 99 (ISO 10545-3, 1991). The compositions of the bioglass samples, theoretical density, sintered density and relative density results are shown in Table. 1. The vacuum method (ISO 10545-3) was used in the laboratory to determine water absorption with greater precision. Vacuum method allows all open pores to be filled and the vacuum process was conducted in a chamber in which the air pressure was lowered to a value of 10⁻³ mbar and held at that value for 30 minutes. Fig. 2 presents the relative porosity and water absorption in samples sintered at 850°C. Values were determined according to equation (1) The foregoing formulas contain the following magnitudes, all expressed in grams (g) :

$$E_v = \frac{m_2 v - m_1}{m_1} \times 100 \quad (\%) \quad (1)$$

m₁ : mass of the dry tile

m_{2v} : mass of the tile impregnated with water after the vacuum process and weighing, also under vacuum.

Table. 1: Theoretical density, sintered density and relative density sintered at

Samples	Theoretical density (g/cm ³)	Sintered density (g/cm ³)	Relative density (%)
a- %85 Bio-glass-%15 wood	2.3555	0.96	40.75
b- %83 Bio-glass-%15 wood-wt. %2 ZrO ₂	2.4207	1.655	68.36
c- %83 Bio-glass-%15 wood-wt. %2 Al ₂ O ₃	2.3822	1.739	73.0

850°C.

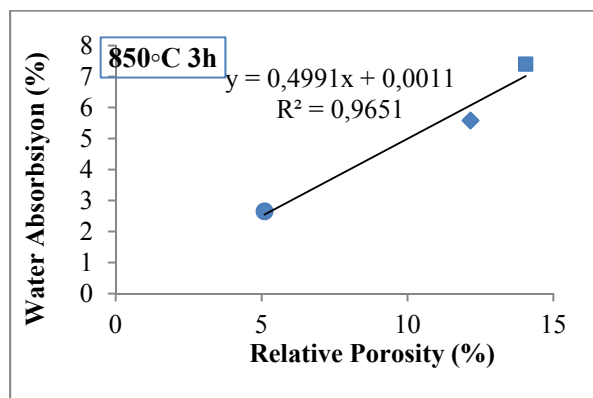


Fig 2. Relative porosity and water absorption in samples sintered at 850 °C.

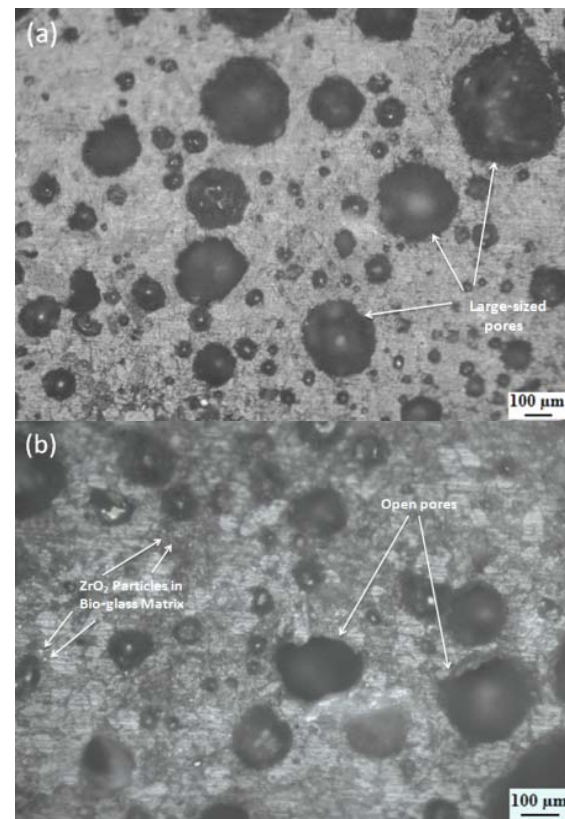
3.2 Hardness and Microstructural Analyses

Microhardness values was measured under a load of 0.2 kg-f for each sample. Microstructure of the bioceramics was examined using high magnification optical microscope. Bioglass samples sintered with 2 wt.% of ZrO₂ and Al₂O₃, presented high hardness and promoting the matrix design. Micro-Hardness's for the bio-glass ceramic composites are shown in Table 2.

Table 2: Micro-Hardness's for the bio-glass ceramic composites.

Samples	Micro-Hardness (0.2kg-f)	Temperature (°C)	Sintering Time (h)
a- %85 Bio-glass-%15 wood	541.8	850	3
b- %83 Bio-glass-%15 wood-wt. %2 ZrO ₂	725.8	850	3
c- %83 Bio-glass-%15 wood-wt. %2 Al ₂ O ₃	1246	850	3

Fig. 3 shows representative micrographs of sintered bioglass samples with 2% ZrO₂ and 2% Al₂O₃. In both cases the observed microstructures were quite similar, showing equiaxed pores of bio-glass ceramics with an average pore size of about 50-150 μm.



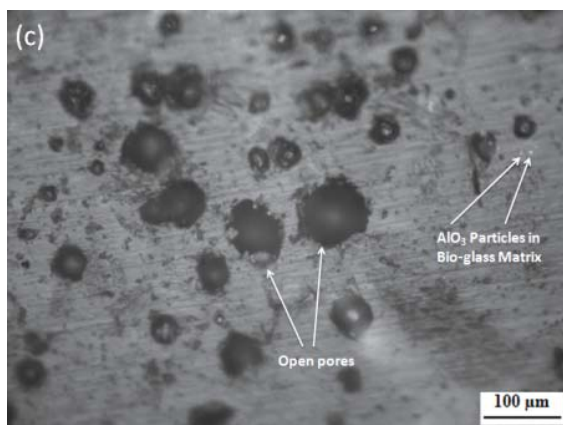


Fig. 3. The porous microstructures of bioglass samples. (a) %85 Bio-glass-%15 wood. (b) %83 Bio-glass-%15 wood-wt. %2 ZrO₂. (c) %83 Bio-glass-%15 wood-wt. %2 Al₂O₃.

4. CONCLUSIONS

The effects of reinforcement particles on the microstructure and mechanical properties of porous bioglass compositions fabricated by PM were investigated. Microstructure observation demonstrates a relative homogenous distribution in bioglass matrix of reinforcement particulates. The addition of 2 wt. % Al₂O₃ promoted an increase in hardness in the order of % 71.69 when compared to samples with 2 wt. % ZrO₂. Disperse Al₂O₃ particles addition also increased hardness in between the walls of the pores. When porous structure was examined, it is seen that every pore in the meshwork is connected to other pores. From this study it can be concluded that the average hardness value of 1246 HV, the average density of 1.73 g/cm³, relative porosity %5.10 and water absorbability value % 2.65 were achieved by sintering at 850 °C for 3h with the addition of 2 wt.% Al₂O₃ in bioglass ceramic.

REFERENCES

Anbalagan Balamurugan, Gerard Balossier, Sanjeevi Kannan, Jean Michel, Avito H.S. Rebelo, Jose M.F. Ferreira, Development and in vitro characterization of sol-gel derived CaO-P₂O₅-SiO₂-ZnO bioglass, *Acta Biomaterialia* 3 (2007) 255-262.

- A. Ostrovskii, "Osteoplastic materials in modern paraodontology and implantology," *Novoye v Stomatologii*, No. 6, 39-54 (1999)
- G. Kh. Gruntovskii and S. V. Malyskhina, "Hydroxyapatite ceramics: Features of reactions with bone tissue," *Tr. Krymskogo Meduniversiteta*, 135, 127-128 (1999).
- Liana A. Ivanchenko, Nataliya D. Pinchuk, "Making Calcium Phosphate Biomaterials", *Powder Metallurgy and Metal Ceramics*, July 2003, Volume 42, Issue 7-8, pp 357-371.
- M.R. Majhi, Ram Pyare and S.P. Singh, "Studies on Preparation and Characterization of Na₂O-CaO-P₂O₅-ZrO₂", *Bioglass-ceramics*, International Journal of Scientific & Engineering Research Volume 2, Issue 8, August-2011 1 ISSN 2229-5518.
- R. Z. LeGeros, J. P. LeGeros, G. Daculsi, and Kijkowska, "Calcium phosphate biomaterials: Preparation, properties, and biodegradation," *Encyclopaedic Handbook of Biomaterials and Bioengineering*, Marcel Dekker Inc., New York (1995), pp. 1429-1463.
- S. V. Malyskhina, N. V. Dedukh, G. Kh. Gruntovskii, et al., "Morphological features of bone tissue reconstruction in the plastic treatment of defects with hydroxyapatite ceramics", *Ortopediya, Travmatologiya i Protezirovanie*, No. 3, 110-114 (1998).
- T. Kanazawa, *Inorganic Phosphate Materials* [Russian trans.], Nauk. Dumka, Kiev (1998).
- R. H. Doremus, "Review bioceramics," *J. Mat. Science*, No. 27, 285-297 (1992).
- V. A. Dubok, "Bioceramics: Yesterday, today, and tomorrow," *Poroshk. Metall.*, Nos. 7-8, 69-87 (2000).
- http://www3.ipc.org.es/guia_colocacion/info_tec_colocacion/los_materiales/baldosas/caract_fis_qui/absorcion_agua.html

NANO-SIZED UPCONVERSION PHOSPHORS FOR DEEP OPTICAL IMAGING OF BIOLOGICAL TISSUES

Victor I. Sokolov^{1,a}, Evgenii V. Khaydukov¹, Andrei V. Nechaev², Vladislav Ya. Panchenko¹, Vladimir N. Seminogov¹, Vladimir A. Semchishen¹, Anna E. Guller³, Andrei V. Zvyagin¹

1. Institute on laser and information technologies of the Russian academy of sciences. Shatura, Russia

2. M.V. Lomonosov Moscow State University of Fine Chemical Technologies. Moscow, Russia

3. I.M. Sechenov First Moscow State Medical University. Moscow, Russia

a. Corresponding Author (visokol@rambler.ru)

ABSTRACT: The nano-sized upconversion phosphor powders on the basis of inorganic crystallite host β -NaYF₄ doped with the rare-earth ions Yb³⁺, Er³⁺, Tm³⁺ are synthesized. The particles have the size in the range from 10 to 100 nm and are stable in water solutions due to the special chemical modification of the surface. The upconversion efficiency coefficient of nanophosphors (i.e. power conversion of the pumping light to anti-Stokes luminescence) is 2 - 2.5%. The possibility of optical imaging of biological tissues labeled with upconversion nanophosphors by 975 nm laser light at diagnostically significant depth 10 mm is demonstrated experimentally. It is shown that by using the multi-fiber probe one can enhance the lateral resolution of strip markers by a factor of 2 in comparison with the resolution obtained with conventional CCD registration technique. The method can be used for deep high-resolution optical imaging of pathological bio-tissues in medicine.

1. INTRODUCTION

In recent years upconversion nanophosphors (UCNF) have received considerable attention as markers for optical diffusion tomography of biological tissues [1-11]. In particular, they have a number of advantages in comparison with dye or quantum dot markers. UCNF have high conversion coefficient (CC) in the range 2 – 3%, photoluminescence (PL) peaks in the region of optical transparency of biotissues (700 - 900 nm) and are nontoxic. In this paper we demonstrate that by using upconversion nanophosphors β -NaYF₄:Yb³⁺:Er³⁺:Tm³⁺ one can perform high-resolution deep optical imaging of biological tissues.

2. RESULTS AND DISCUSSIONS

2.1. Synthesis of Upconversion Nanophosphors

The synthesis of upconversion nanophosphors β -NaYF₄:Yb³⁺:Er³⁺ and

β -NaYF₄:Yb³⁺:Tm³⁺ is based on the coordinate stabilization of salts of metal precursors (Na, Y, Yb, Er, Tm) in the solution of oleic acid, which proceeds at high temperature in the oxygen-free environment. At this stage the powders have cubic crystal lattice (α -phase) and are characterized by relatively low conversion coefficient (CC) of pumping light into anti-Stokes PL signal.

To increase CC one needs to perform the additional thermal processing of UCNF at 310°C. The resulting powders have hexagonal crystal lattice (β -phase) and higher CC in the range 2 – 2.5 %. The SEM microphotograph of the β -NaYF₄:Yb³⁺:Tm³⁺ nanopowder and that of single hexagonal β -NaYF₄:Yb³⁺:Tm³⁺ nanocrystal are shown in Fig. 1.

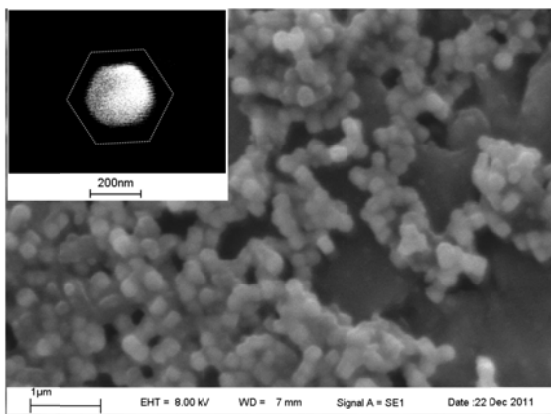
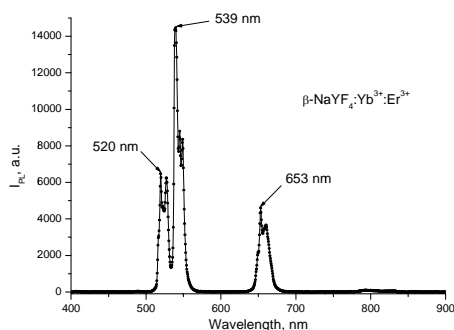
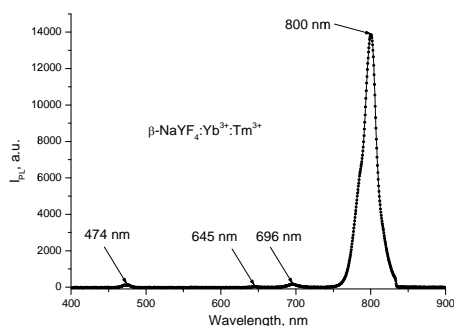


Figure1: SEM microphotograph of β - $\text{NaYF}_4:\text{Yb}^{3+}:\text{Tm}^{3+}$ nanopowder. Inset: microphotograph of the single nanocrystal with clearly visible hexagonal shape.

The PL spectra of β - $\text{NaYF}_4:\text{Yb}^{3+}:\text{Er}^{3+}$ and β - $\text{NaYF}_4:\text{Yb}^{3+}:\text{Tm}^{3+}$ nano-powders excited by 975 nm laser light are shown in Fig. 2. One can see that β - $\text{NaYF}_4:\text{Yb}^{3+}:\text{Tm}^{3+}$ has a strong PL peak around 800 nm, i.e. in the region of optical transparency of biological tissues.



a)



b)

Figure 2: Photoluminescence spectrum of β - $\text{NaYF}_4:\text{Yb}^{3+}:\text{Er}^{3+}$ (a) and β - $\text{NaYF}_4:\text{Yb}^{3+}:\text{Tm}^{3+}$ (b) nano-powders excited by 975 nm laser light.

2.2. Creation of Water-Soluble Complexes (Stable Colloids) on the Basis of Nanophosphors

To create stable water colloids we have modified the surface of UCNF with amphiphilic polymers. The molecules of the amphiphilic polymer have hydrophilic and hydrophobic end groups. Since nanophosphors are synthesized in the solution of oleic acid, their surface is covered by hydrophobic oleic groups. The hydrophobic end groups of the amphiphilic polymer are attached to the oleic groups, while the hydrophilic end groups of the polymer are facing outward. As a result, the UCNF particle becomes hydrophilic and stable in water solutions. This technique permits to stabilize the water colloids of nanophosphors within few weeks.

2.3. Registration of PL Signal From the UCNF Labeled Biological Tissue

The optical imaging of bio-tissues labeled with UCNF markers was performed with the optical tomographic setup assembled in our lab. The scheme of the setup is shown in Fig. 3. The photo-luminescent markers in the form of polymer strips with embedded β - $\text{NaYF}_4:\text{Yb}^{3+}:\text{Er}^{3+}$ powder were placed on the slide and covered with 4 mm thick phantom. The width of the strips was 1.5 mm, the distance between the strips was $\Delta x = 3 - 12$ mm. The phantom was made from polyvinyl chloride with embedded TiO_2 nanoparticles to simulate the scattering properties of real biological tissues.

The phantom – strip markers assembly was illuminated by collimated 975 nm laser light, the width of the illuminated region exceeded considerably the distance between the marker strips. The registration of the PL signal was performed with EMCCD camera focused on the upper surface of the phantom. The cut-off filter was used to remove the 975 nm pumping radiation.

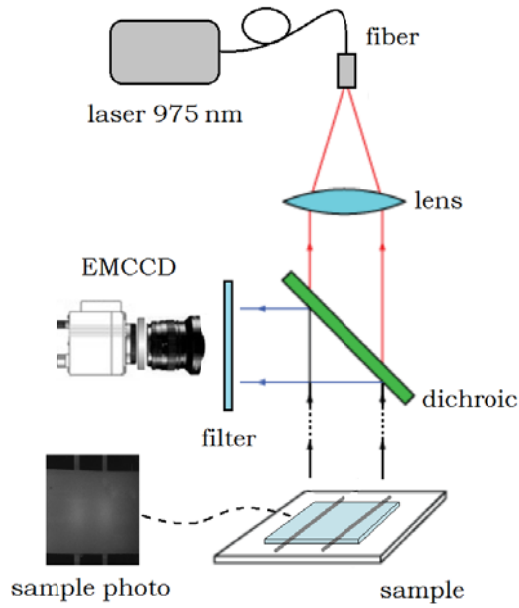


Figure 3: Scheme of the tomographic setup for measuring the intensity distribution from UCNF markers in biological tissues.

Figure 4 shows the experimentally measured distribution of the anti-Stokes PL signal from the single strip marker along the surface of the phantom. One can see that the distribution of optical signal transmitted through the absorbing and scattering medium (phantom) can be approximated by Lorentz curve

$$I(x) = \frac{1}{a^2 + b^2(x - x_0)^2} \quad (1)$$

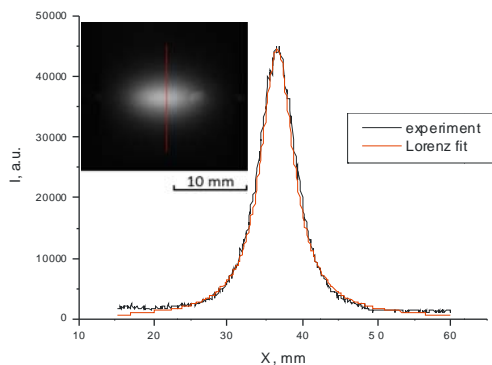


Figure 4: Distribution of the anti-Stokes PL signal $I(x)$ from the single strip marker along the surface of the phantom (along the vertical line, see Inset). The Lorentz fit is shown by the solid line.

If two marker strips are available, the resulting distribution of PL signal measured by EMCCD camera is the sum of the Lorentz curves

$$I(x) = \frac{1}{a^2 + b^2(x - \Delta x/2)^2} + \frac{1}{a^2 + b^2(x + \Delta x/2)^2} \quad (2)$$

where Δx is the distance between the strips, a and b are constants. The function $I(x)$ (2) has two maximums I_{\max} and a local minimum I_{\min} at $x = 0$.

In Fig. 5 one can see the experimentally measured distribution of PL signal $I(x)$ from two marker strips with $\Delta x = 3.5$ and 7.1 mm correspondingly, as well as theoretically calculated Lorentz curves (1) and (2). One can see that the theoretical and experimental curves fit well.

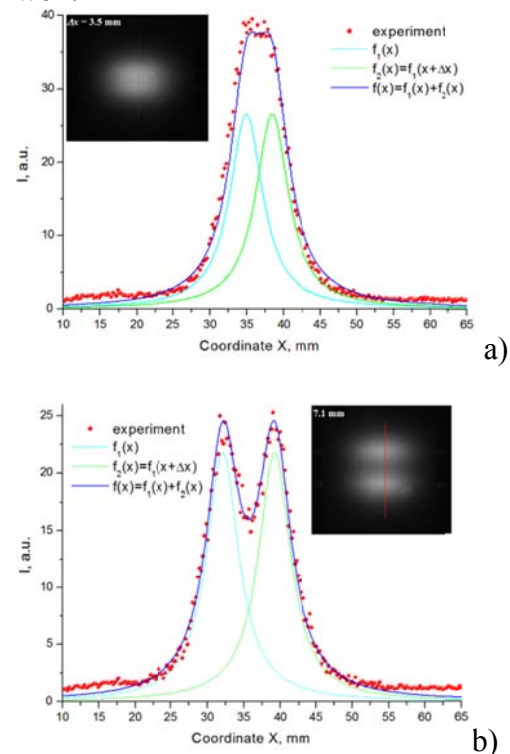


Figure 5: Distribution of the anti-Stokes PL signal from two marker strips along the vertical line (see Inset). The distance between the strips is $\Delta x = 3.5$ mm (a) and 7.1 mm (b).

Consider the resolution parameter

$$R = (I_{\max} - I_{\min}) / I_{\max} \times 100\% \quad (3)$$

which is the ratio of the minimal intensity I_{\min} of the signal between two peaks to the peak intensity I_{\max} of the signal, see Fig. 5. Figure 6 shows the experimentally measured and theoretically calculated R as a function of distance Δx between marker strips. Following the Rayleigh criteria $R = 20\%$ one can conclude that with EMCCD camera the resolution equals $\Delta x = 5.3$ mm.

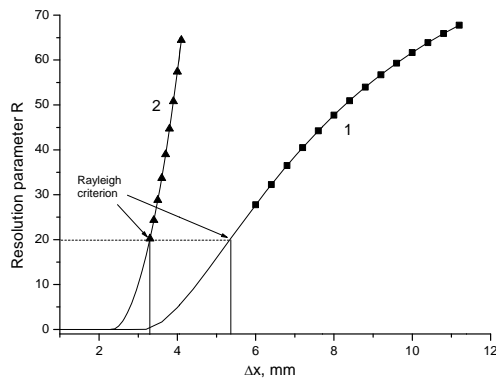


Figure 6: Experimentally measured (rectangles) and theoretically calculated (1) curve $R(\Delta x)$ when the distribution of PL signal is measured with EMCCD camera. For comparison, triangles and (2) correspond to the curve $R(\Delta x)$ measured with the moving multi-fiber probe (see below).

2.4. Increasing the Resolution of Deep Optical Imaging of Biological Tissues Using Multi-Fiber Probe

To increase the resolution of the optical imaging of UCNF markers in biological tissues we have proposed the new approach based on the fiber-optic tomographic setup, Fig. 7. The multi-fiber probe contains the central metalized fiber for launching the 975 nm pumping light surrounded by seven fibers for collecting the PL signal from nanophosphors. Optical imaging of strip markers is performed by moving the fiber

tip along the surface of the phantom, the gap between the tip and phantom being 0.5 mm.

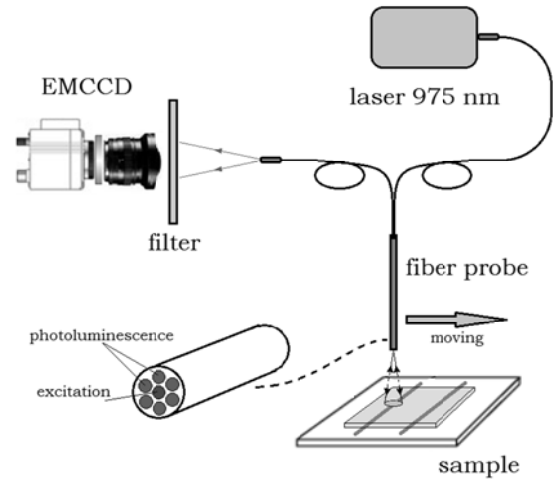


Figure 7: Scheme of the experimental setup for measuring the intensity distribution from $\beta\text{-NaYF}_4:\text{Yb}^{3+}:\text{Er}^{3+}$ markers through the phantom using multi-core fiber probe.

The experimentally measured and theoretically calculated resolution parameter R as a function of distance Δx between marker strips is shown in Fig. 6. It follows from Fig. 6 that with the multi-fiber probe one can resolve the marker strips separated by $\Delta x = 3.2$ mm. Thus by using the multi-fiber probe one can enhance the lateral resolution of optical imaging by a factor of 2 in comparison with the resolution obtained with CCD registration technique.

By using the multi-fiber probe we have successfully registered PL signal from $\beta\text{-NaYF}_4:\text{Yb}^{3+}:\text{Tm}^{3+}$ marker through 10 mm thick phantom, Fig. 8. The power of the 975 nm pumping laser radiation did not exceed 0.7 Wt/cm^2 .

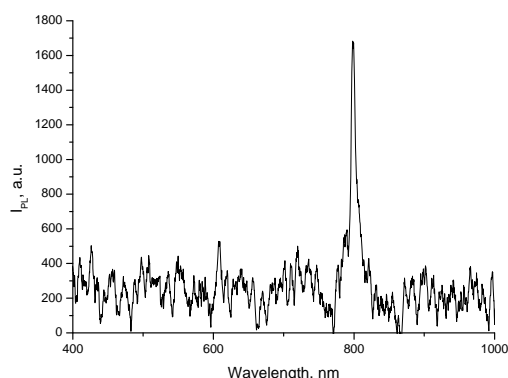


Figure 8: PL spectrum from β - $\text{NaYF}_4:\text{Yb}^{3+}:\text{Tm}^{3+}$ marker measured through 10 mm thick phantom using multi-fiber probe.

3. CONCLUSIONS

By using the multi-fiber probe one can enhance the lateral resolution of optical imaging by a factor of two in comparison with the registration technique based on EMCCD camera. The possibility of optical imaging of bio-tissues labeled with β - $\text{NaYF}_4:\text{Yb}^{3+}:\text{Tm}^{3+}$ nanophosphors at diagnostically significant depth 10 mm was demonstrated.

Acknowledgements

This study was partially supported by RFBR research projects 12-04-01258-a, 12-02-31845mol_a, 13-02-01138-a, and by president grant NSCH-6141.2012.2.

REFERENCES

1. Ntziachristos, V., 2010. Going Deeper than microscopy: the optical imaging frontier in biology, *Nat. Methods*, 7, 613.
2. Ntziachristos, V., Ripoll, J., Wang, L.H., and Weissleder, R., 2005. Looking and listening to light: the evolution of whole-body photonic imaging, *Nat. Biotechnol.*, 23, 313.
3. Huang, X.H., Neretina, S. and El-Sayed, M.A., 2009. Gold nano-rods: from synthesis and properties to biological and biomedical applications, *Adv. Mater.*, 21, 4880.
4. Welsher, K., Sherlock, S.P. and Dai, H.J., 2011. Deep-tissue anatomical imaging of mice using carbon nano-tube fluorophores in the second near-infrared window, *Proc. Natl. Acad. Sci. U.S.A.*, 108, 8943.

5. Haase, M. and Schafer, H., 2011. Upconverting nanoparticles, *Angew. Chem., Int. Ed.*, 50, 5808.
6. Bouzigues, C., Gacoin, T. and Alexandrou, A., 2011. Biological applications of rare-earth based nanoparticles, *ACS Nano*, 5, 8488.
7. Bunzli, J.C.G., 2010. Lanthanide luminescence for biomedical analyses and imaging, *Chem. Rev.*, 110, 2729.
8. Boyer, J.C. and van Veggel, F.C.J.M., 2012. Absolute quantum yield measurement of colloidal $\text{NaYF}_4:\text{Er}^{3+},\text{Yb}^{3+}$ upconverting nanoparticles, *Nanoscale*, 2, 1417.
9. Xu, C. T., Axelsson, J. and Andersson-Engels, S., 2009. Fluorescence diffuse optical tomography using upconverting nanoparticles, *Appl. Phys. Lett.*, 94, 251.
10. Svenmarker, P., Xu, C. T. and Andersson-Engels, S., 2010. Use of nonlinear upconverting nanoparticles provides increased spatial resolution in fluorescence diffuse imaging, *Opt. Letters*, 3516, 2789.
11. Xu, C. T., Svenmarker, P., Liu, H., Wu, X., Messing, M.E., Wallenberg, L.R. and Andersson-Engels, S. 2012. High-resolution fluorescence diffuse optical tomography developed with nonlinear upconverting nanoparticles, *ACS Nano*, 6, 4788.

SILVER AND ZINC OXIDE BASED NANO POWDERS AND THEIR POLYMER BASED NANOCOMPOSITES FOR ANTIBACTERIAL APPLICATION

Tuğçe ÖZMEN¹, Ezgi ABATAY¹, Alper ARSLANOĞLU², Berna NALBANT³ and Metin TANOĞLU^{4,a}

1. Department of Biotechnology and Bioengineering, Faculty of Engineering, Izmir Institute of Technology, Gulbahce Campus, 35430 Urla, Izmir, Turkey
 2. Department of Molecular Biology and Genetics, Faculty of Science, Izmir Institute of Technology, Gulbahce Campus, 35430 Urla, Izmir, Turkey
 3. AKG Yalıtım ve İnşaat Malzemeleri Sanayi ve Ticaret A.Ş., 35070 Işıkkent, Izmir, Turkey
 4. Department of Mechanical Engineering, Faculty of Engineering, Izmir Institute of Technology, Gulbahce Campus, 35430 Urla, Izmir, Turkey
- a. Corresponding author metintanoglu@iyte.edu.tr (M. Tanoglu)

ABSTRACT: There is a dramatic increase in exposure of humans to microorganisms which present in indoor and outdoor, with in environmental pollution. The technological development is increased to create steril areas by the improvement of antibacterial materials. The silver (Ag) and zinc oxide (ZnO) nanopowders are being used for the preparation of the polymer based antibacterial nanocomposite materials. In this study; the Ag and ZnO nanopowders obtained were characterized by means of dynamic light scattering (DLS), scanning electron microscopy (SEM) / EDX, thermogravimetric analysis (TGA), X-ray diffraction (XRD), and fourier transform infrared spectroscopy (FTIR). Nano-sized Ag/polyester and ZnO/polyester nanocomposites were prepared with different weight fractions. In addition, Ag coated ZnO particles were prepared using AgNO₃ solutions. Similarly, Ag/ZnO/polyester nanocomposites were prepared and tested. The antibacterial properties of Ag/polyester and ZnO/polyester nanocomposites are being analyzed against gram positive and gram negative bacteria.

Keywords: Silver-nano powder, Nanocomposites, Characterization, Antibacterial properties

1. INTRODUCTION

Microorganisms have caused great harm to human beings for a long time. The technological development is increased to create steril areas by the improvement of antibacterial materials [Xu *et al.*, 2008]. Polymer based antibacterial nanocomposite materials are of current research interest due to its strong toxicity toward a wide range of microorganisms, and concurrently a particularly low human toxicity [Konwar *et al.*, 2010]. In modern technology improvement of the antibacterial materials could be help to enhance the living standard of the people [Dallas *et al.*, 2011].

The objective of this paper is to investigate nano-sized Ag/polyester and ZnO/polyester nanocomposites were prepared and tested. In addition, Ag coated ZnO particles were prepared using AgNO₃ solutions and then similarly, ZnO/Ag/polyester nanocomposites were tested. The nanopowder of Ag, Zn, ZnO/Ag were characterized by SEM, XRD, FTIR. The antibacterial properties of Ag/polyester, ZnO/polyester and ZnO/Ag/polyester nanocomposites are being analyzed against gram positive and gram negative bacteria.

2. EXPERIMENTAL PROCEDURE

2.1. Materials

In order to produce nanocomposites, Ag, ZnO and Ag-ZnO were used as a filler, polyester was used as a matrix material.

2.2. Production of Nanocomposites

The polyester resin was prepared by using mechanical mixing method. In this technique polyester, cobalt octoate (CoNaP) 0.2 wt% (with respect to resin) methyl ethyl ketone peroxide (MEKP) 2 wt% (with respect to resin) were mixed together until the homogenous dispersion was obtained. After the curing of resin at 80 °C and obtained.

After completion of the resinification 3 wt% (with respect to resin) Ag nanopowder was added to the mixture and stirred continuously for half an hour. After the curing of sample at 80 °C and Ag-polyester nanocomposites were obtained.

Similarly, 3 wt% (with respect to resin) ZnO nanopowder was added to the mixture and stirred continuously for half an hour under the same condition. Finally ZnO polyester were obtained.

ZnO/Ag⁰ powder was prepared with reduction process. In this process, ZnO and ionized water was mixed for half an hour. After adding 1wt% AgNO₃, this mixture stirred continuously at pH 4.5 for four hour at 70 °C. Nitrate ions was filtered and washed with distilled water for purification. The remaining ZnO/Ag in filter paper was dried at 400 °C for three hour in the oven and obtained ZnO/Ag⁰ powder. These powder was added similarly to the polyester system.

2.3. Characterization

Zn-Ag doped polyesters was performed bacterial test using E.coli and antibacterial properties of polyester was determined. Overnight grown culture of E.

coli was diluted, and plated on LB agar. Sample were kept on the plates and incubated at 37 °C for 16 h. The plates were taken out, and the inhibition area was observed.

The silver nanoparticles (AgNPs), zinc oxide (ZnO) and zinc oxide/silver (ZnO/Ag) nanopowder and particle morphology was characterized by means of Scanning Electron Microscopy (SEM) using FEI Quanta 250 FEG equipment to approve the shape and size.

The crystallographic structures of materials were analyzed by using X-ray Diffraction (XRD) method on an Philips X'Pert Pro model to provide the zinc oxide/silver powder was completely and successfully produced.

FTIR analysis was used determining the structure of the functional groups of organic compounds by Shimadzu IRPrestige-21 FTIR-8400S.

Dynamic light scattering (DLS) was used to determine the grain size.

The Backscattered Electrons Detector (BSED) was used to reveal the amount of silver element onto the zinc oxide metal.

3. RESULTS AND DISCUSSIONS

3.1. Microstructural properties

SEM images were used to evaluate the surface morphology of the silver deposited on the surface.

The scanning electron micrographs of silver nanoparticles in Figure 1a-d. According to SEM image, the average size of Ag NPs are calculated as 110 nm. The SEM observation with higher magnification (50 000 x), (25 000 x), (10 000 x) on the silver powder is shown in Figure 1-b,1-c,1-d, respectively.

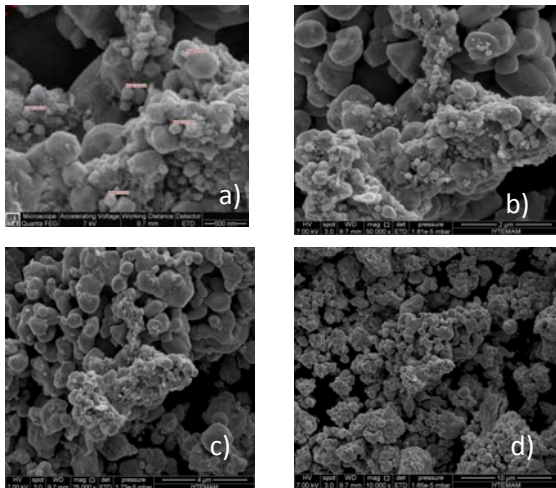


Figure 1: High magnification SEM image of Ag NPs.

The scanning electron micrographs of zinc oxide particles in Figure 2a-d. According to SEM image, the average size of zinc oxide nanoparticles are calculated as 165 nm. The SEM observation with higher magnification (50 000 x), (25 000 x), (10 000 x) on the zinc oxide powder is shown in Figure 2-b,2-c,2-d, respectively.

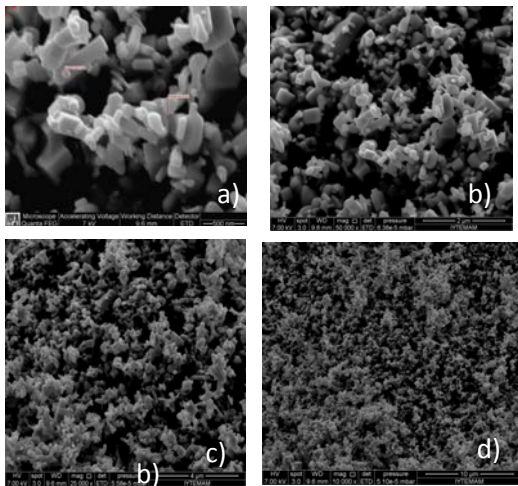


Figure 2: High magnification SEM image of zinc oxide particles.

The scanning electron micrographs of zinc oxide/silver (ZnO/Ag) powder in Figure 3a-e. ZnO/Ag powder were characterized by means of Electron

Transfer Dissociation, (ETD) in Figure 3b-c. The SEM observation with higher magnification (50 000 x) and (25 000 x) on the ZnO/Ag powder is shown in Figure 3b-c; respectively.

The Backscattered Electrons Detector (BSED) was used to reveal the amount of silver element onto the zinc oxide metal in Figure 3d-e. The difference of the atomic number of silver and zinc element showed that silver element whose atomic number is 47 is brighter than zinc element whose atomic number is 30 lower than silver.

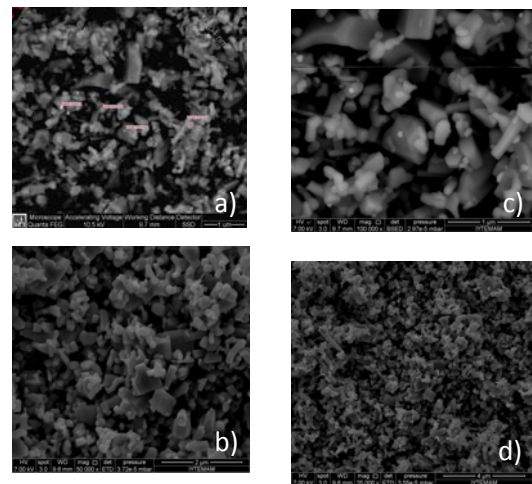


Figure 3: The SEM image of zinc oxide/silver (ZnO/Ag) particles.

In Figure 4, ZnO/Ag powder was characterized by the help of the SEM and EDS (Energy-dispersive X-ray spectroscopy) and the elemental analysis were performed. According to Table 1 results showed that O, Zn, Ag were separated 19.64 %,80.19 % and 0.17 % by weight; respectively.

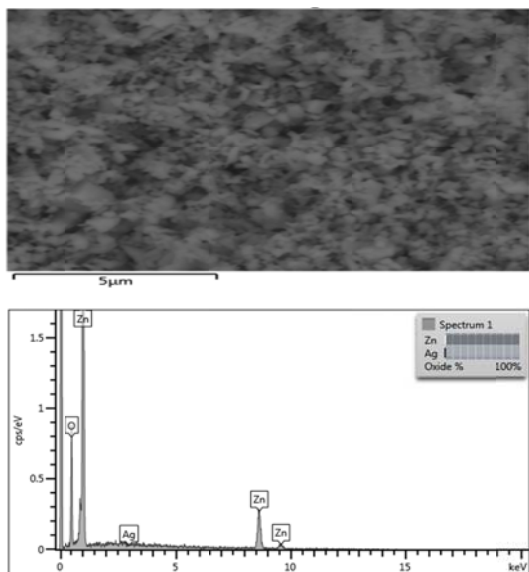


Figure 4: SEM images of ZnO/Ag powder and EDS spectrum.

Table 1: Elemental analysis of ZnO/Ag powder

Element	Wt%	Atomic %
O	19.64	49.98
Zn	80.19	49.95
Ag	0.17	0.07
Total:	100.00	100.00

According to Figure 5 the size of the silver nanoparticles were obtained 100 nm. While the measurement of the silver powder is in distilled water and the result showed that there is no agglomeration occurred because of using the sonicator instrument is used.

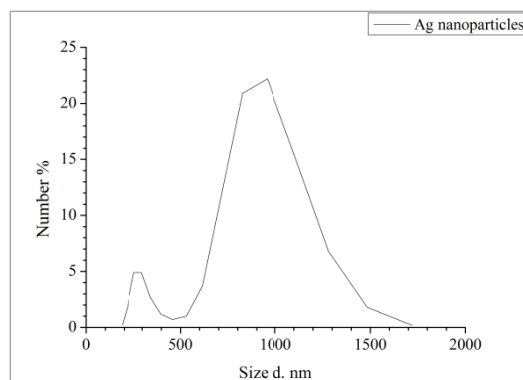


Figure 5: Size analyses of silver nanoparticles by Dynamic Light Scattering (DLS).

The XRD pattern of the Ag, ZnO nanoparticles is shown in Figure 6. As seen in the figure, these nanoparticles shows a narrow peak that indicates high fracture of crystalline phases with the these nanoparticles structure.

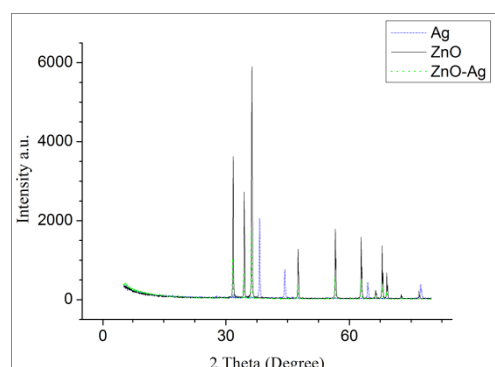


Figure 6: XRD pattern of Ag, ZnO and ZnO-Ag nanoparticles.

The region between 1500 and 400 cm^{-1} is frint print region, and peaks in this area are not considered. Infrared spectra of silver nanoparticles are shown in Fig. 6. 2346, corresponds C=O stretching peaks [Paulo *et al.*, 2011]. This peak occurs due to the device property. Device detects the CO_2 in the air and gives its characteristic peak. The aromatic CH stretch appears at 3100-3000 cm^{-1} There are aromatic CC stretch bands (for the carbon-carbon bonds in the aromatic ring) at about 1500 cm^{-1} [Paulo *et al.*, 2011]. Band

characteristic of nitrate ions is that at 1349 cm^{-1} but this band is absent our system so we can say that NO_3^- removes this system. Therefore, this spectrums confirmed the absent of the NO_3^- in the silver nanoparticles.

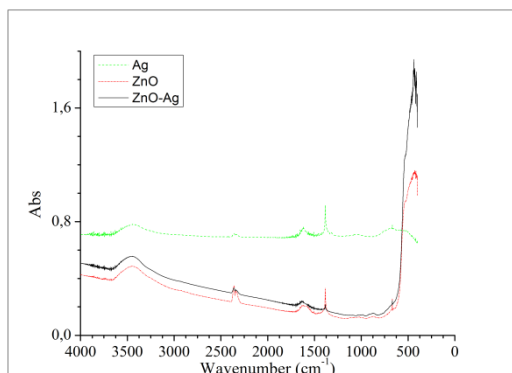
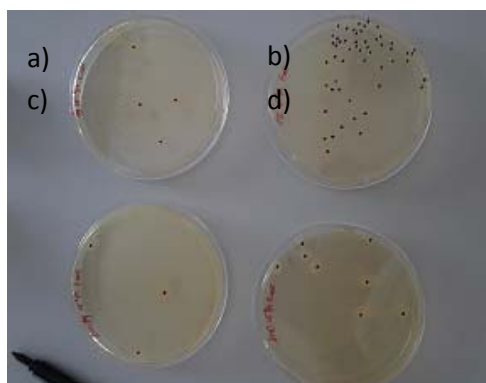


Figure 7: FTIR spectra of Ag-doped ZnO powder, Ag powder, ZnO powder.

4. ANTIBACTERIAL PROPERTIES

The antibacterial activity of the polyester based Ag, ZnO, ZnO-Ag nanocomposites against E.coli was tested based on zone of inhibition tests. The results show that the nanocomposites have good efficacy against these bacteria.

Fig. 8 shows the antibacterial activity of the Ag/ZnO/ZnO-Ag polyester



nanocomposites via a zone inhibition test.

Figure 8: Zone of inhibition test against E.coli bacteria for Ag/ZnO/ZnO-Ag polyester nanocomposites of (a) Ag PE, (b) neat PE, (c) ZnO-Ag PE, and (d) ZnO PE.

5. CONCLUSION

In conclusion, ZnO nanoparticles embedded polyester nanocomposites have been synthesized using a simple in situ reduction method using AgNO_3 as a reducing agent under ambient conditions. The ZnO-Ag nanocomposites have been evaluated as an antimicrobial agent and show the enhanced contact antimicrobial efficacy against Gram negative bacteria (E. coli). These results that the ZnO-Ag nanocomposites have the potential to be considered as effective and long-lasting bactericidal surface coating material in future antibacterial and biomedical applications.

Acknowledgements: This study is supported by AKG Yatırım ve İnşaat Malzemeleri Sanayi ve Ticaret A.Ş. and Ministry of Science and Technology of Industry, Republic of Turkey (SAN-TEZ, Project No. 1209-STZ.2012-1)

REFERENCES

- Allas, P., 2011. Silver polymeric nanocomposites as advanced antimicrobial agents: Classification, synthetic paths, applications, and perspectives, *Advances in Colloid and Interface Science* 166 119-135.
- Konwara U., Karaka N., Mandalb M., 2010. Vegetable oil based highly branched polyester/clay silver nanocomposites as antimicrobial surface coating materials *Progress in Organic Coatings* 68 265-273.
- Paula A. Zapata, Laura Tamayo, Maritza Páez, et al. 2011. Nanocomposites based on polyethylene and nanosilver particles produced by metallocenic “in situ” polymerization: synthesis, characterization, and antimicrobial behavior, *Macromolecular Nanotechnology*, 47, 1541-1549.
- Xu, Y., 2008. Study on the preparation and properties of silver-doped borosilicate antibacterial glass, *Journal of Non-Crystalline Solids* 354 1341-1345.

ANALYSIS OF THE GROWTH OF ALPHA-LACTALBUMIN PROTEIN NANOTUBES FUNCTIONAL FOR FOOD APPLICATIONS

Özgür Tarhan^{1,a} and Şebnem Harsa¹

1. İzmir Institute of Technology, Food Engineering Dept., Urla, İzmir, Turkey

a. ozgurtarhan@iyte.edu.tr

ABSTRACT: Alpha-lactalbumin (α -La), the second major protein in whey, produces nano tubular structures in the presence of calcium ions by self-assembly process after partial hydrolysis with *Bacillus licheniformis* protease. They promise functionality in some food applications with their gelation, viscosifying and encapsulation capabilities, besides some non-food applications eg. using as scaffolds for tissue engineering. The constructed α -La nanotubes (α -LaNTs) were regular hollow strands with uniform dimensions of about 20 nm in width and 1 micron in length, according to microscopy. Both intensity and apparent hydrodynamic radius increased along with nanotube growth. Calcium to protein concentration ratio affects critically nanotube formation and stability. As the protein concentration decreased, UV absorbance change was also decreased. The increased calcium concentration also increases absorbance values due to aggregation and turbidity. Stability increased with increasing protein concentration. The α -LaNTs enhanced the gel formation with increased stiffness and viscoelasticity. These gels can be used for the entrapment of some bioactive materials and coloring agents for various food applications.

1. INTRODUCTION

Protein and peptide nanotubes developed from food grade proteins are novel functional particles with potential industrial applications. The second major whey protein alpha-lactalbumin (α -La) is capable of forming nanotubes (α -LaNTs) by self-assembly after partial hydrolysis with *Bacillus licheniformis* protease [Ipsen *et al.*, 2001, Graveland-Bikker *et al.*, 2004]. Self-assembly is identified by the spontaneous and reversible aggregation due to polymerization of molecules by noncovalent intermolecular interactions such as hydrogen bonding, electrostatic, hydrophobic and Van der Waals interactions [Rajagapol and Schneider, 2004]. It is a 'bottom up' approach in which proteins and peptides are used as monomeric building blocks for the development of higher order structures. These nanotubes are reported as formed in three steps: conformational destabilization by hydrolysis of protein, nucleation by formation of peptide dimers, and nanotube elongation by binding of additional dimers to critical nucleus [Ipsen and Otte, 2007]. Calcium

plays critical role in nanotube growth by linking peptide dimers and leading nanotube elongation. Protein concentration is also important in nanotube growth. Below certain concentration formation of fibrillar and random aggregates are induced [Otte *et al.*, 2005]. The concentrations of calcium and protein are also effective in the stability of the gels triggered by these nanotubes. The presented study aims to investigate the effect of calcium and protein concentrations on the growth and stability of α -LaNTs and nanotubular gels.

2. RESULTS AND DISCUSSION

2.1. Microscopic Analysis of α -LaNTs

AFM and TEM images of α -LaNTs developed were shown in Figure 1. They were longer than 100 nm up to few micron with approximately 20 nm width. They appeared as regular hollow strands with uniform morphology. The dimensions and morphologies of the structures are consistent with the literature [Ipsen *et al.*, 2001, Graveland *et al.*, 2004].

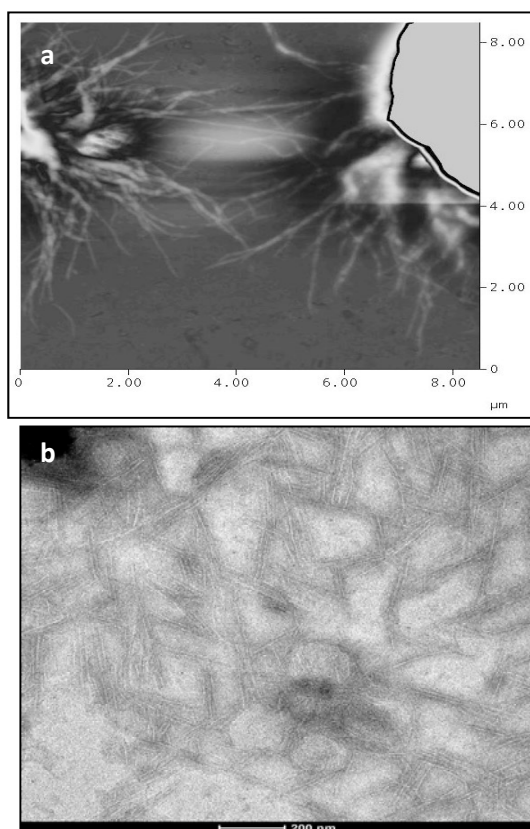


Figure 1: AFM (a) and TEM (b) images of α -LaNTs.

2.2. Analysis of Nanotube Growth

DLS and UV-spectrophotometry studies were carried out to investigate nanotube growth. Figure 2 represents intensity and particle size difference with time during nanotube (NT) growth. When the calcium concentration increased the lag period (representing hydrolysis) was decreased and intensity difference increased. The lag time for standard protein with the molar ratio of (calcium to α -la) 3 and 5 were about 45 min and 35 min, respectively. The apparent hydrodynamic radius was also increased along incubation period. The structures were linear rods, not spherical objects, so hydrodynamic radius can not be measured in fact, but estimated as increased apparently. Graveland-Bikker and coworkers studied nanotube growth at different molar ratio of Ca^{++}/α -La (R=0 to R=9) and reported that nanotube

formation favored at R=2 and R=5 [Graveland-Bikker *et al.*, 2004].

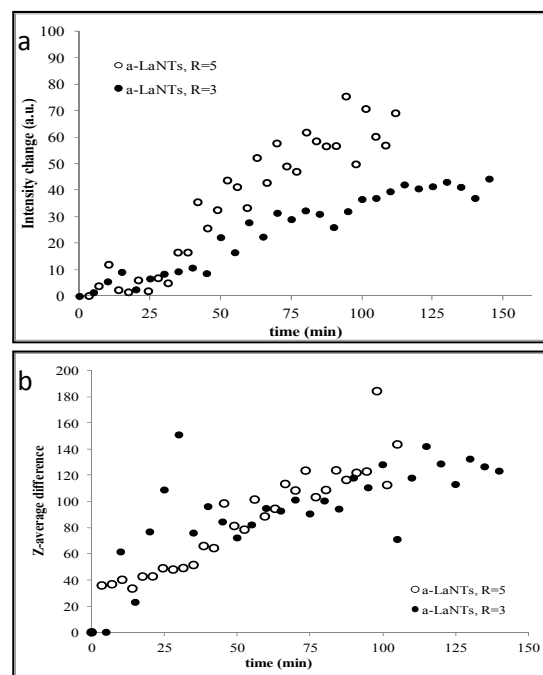


Figure 2: Scattering intensity (a) and particle size (b) distributions with time during NT growth.

Figure 3 presents UV spectra presenting nanotubular growth and gelation with protein concentrations of 0.5% (a), 1% (b), and 3% (c), respectively and molar ratio of Ca^{++}/α -La of 3, 5, 10. After first 18 hour-incubation at 50 °C, samples were stored at 4°C for 48 hour, and then re-incubated in order to detect absorbance changes as an indicator of stability of the formed protein nanotubules and gels. It is obvious that the increased calcium concentrations increase absorbance, but not provide good stability, if protein concentration is low. Surprisingly, absorbances were expected greater than R5 at R10, however they were lower. This may be due to filtration of reaction mixture (protein, calcium and enzyme) for removal of impurities prior to incubation. Filters with 1 micron pore size may hold some amount of calcium after a critical concentration due to fouling during filtration. Stability

increased with increasing protein concentration, but in fact, calcium and protein ratio was more critical than their individual effects.

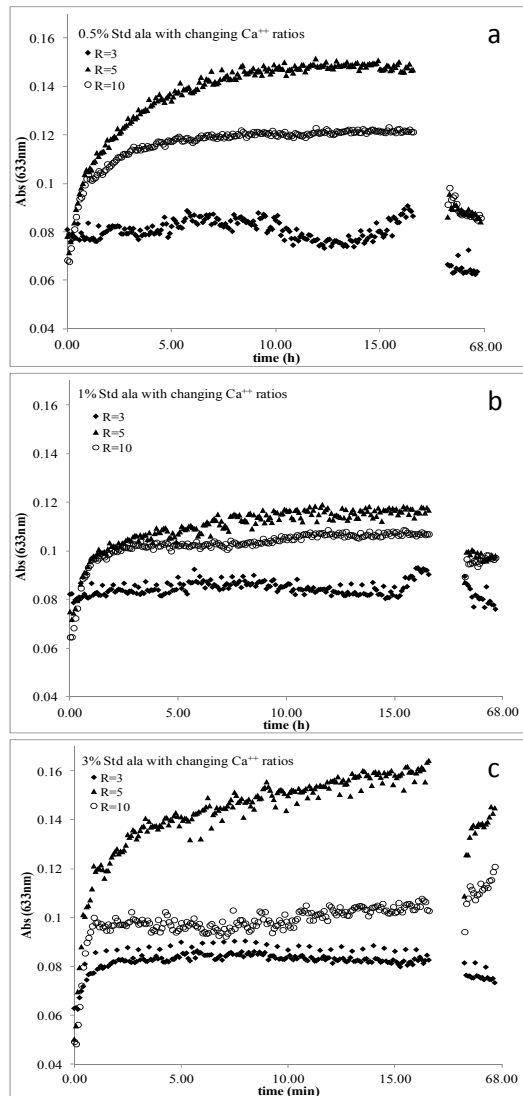


Figure 3: UV spectra taken during nanotube growth and gelation with the protein concentrations of a) 0.5%, b) 1% and c) 3%, and changing Ca^{++} amounts

2.3. Gelation analysis of α -LaNTs

Protein solutions containing enzyme and calcium were prepared, and incubated in rheometer for nanotubular growth and gelation. Samples were subjected to dynamic oscillation with a strain of 0.005 and a frequency of 0.5 Hz in plane geometry and time sweep mode. Gelation was defined at the point that $G' > 1$.

Storage and loss modulus nanotubular gels formed by changing protein and calcium concentrations were indicated in Figure 4.

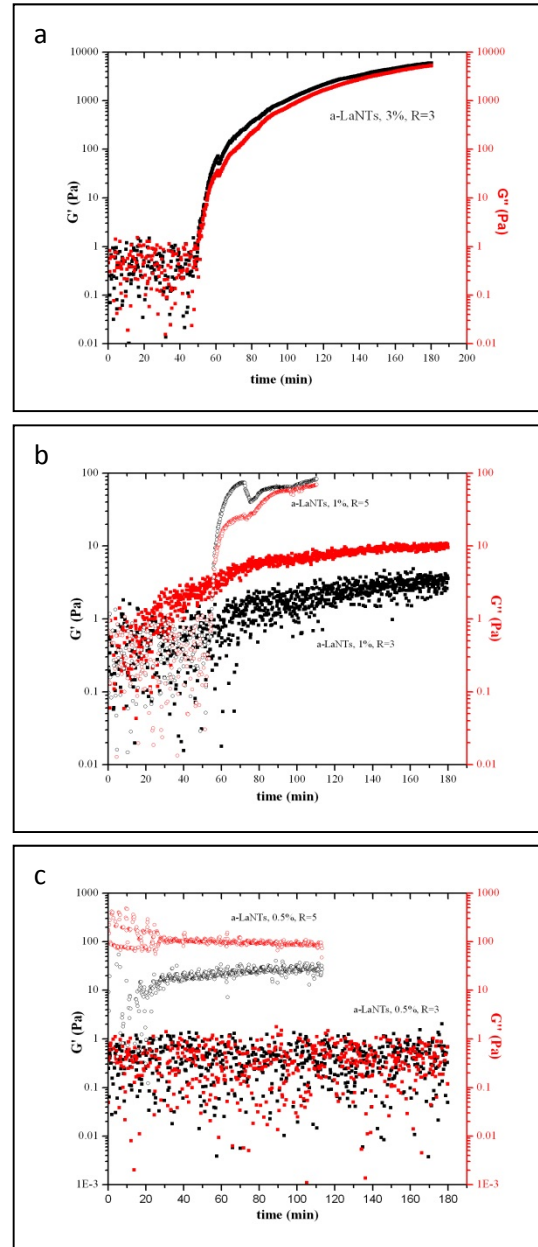


Figure 4: Young's modulus of α -La nanotubular gels with protein concentrations of a) 3%, b) 1% and c) 0.5%, and changing Ca^{++} amounts.

When the protein concentration was 3% with the molar ratio of calcium to protein at R=3, gelation started at around 50 min (Figure 4a). Gelation time for 1% protein with R=3 and R=5 were detected as about

55 and 60 min, respectively (Figure 4b). For 0.5 % protein concentration no gelation was detected at R=3, and very weak gelation was observed at R=5 (Figure 4c). Viscoelastic gel formation was triggered by nanotube growth at optimum protein (3%) and calcium (R=3) concentration. As the calcium concentration was increased gel formation was favored, however as the protein concentration was lowered gel formation was unfavored. At high calcium concentrations, more random aggregates were induced, and this gave rise to formation of turbid gels. The viscoelasticity of the gels were also decreased by decreasing protein concentrations. These results are in agreement with the ones obtained by the UV-spectrophotometry.

The nanotubular gels can be used for various applications in food processing. One of them is the use of these gels as the carriers of natural colorants. The results of dye-binding assay revealed that the gel matrix entraps coloring agents with transparent appearance (data not shown). Therefore, the α -La nanotubular gels can be enriched with the natural coloring agents and used for coating applications, in pastry and candy industries. In addition, the viscoelasticity and stiffness of these gels were modified by blending with some polysaccharides (data not shown). This enables the gels available for various other applications. Different active agents can also be entrapped within these hydrogels to improve their functionality. The α -LaNTs are hollow structures with the cavity of ~8 nm [Graveland-Bikker and Kruif, 2006]. Some bioactive agents may also be carried in the pores of these tubules for delivery purposes. The studies related to such applications are underway.

In conclusion, protein nanotubes and subsequently transparent gels were

formed by self-assembly in the presence of calcium, after partial hydrolysis of α -La. Both calcium and protein concentrations critically affected nanotube and gel formation. The resultant gels promise functionality in food applications with desired additional modifications.

Acknowledgements: The authors would like to thank Central Lab in METU for TEM, Center for Material Research in IzTech for AFM analyses, and IzTech Biotechnology Research Lab for UV-measurements. Special thanks to Res. Asst. Oylum Çolpankan and Sema Yıldız, and Prof. Dr. Metin Tanoğlu for rheological measurements, and Res. Asst. Özge Tunusoğlu and Assoc. Prof. Dr. Mustafa Demir for DLS measurements. This work was supported financially by the The Scientific and Technological Research Council of Turkey (109O866, 2010-2011) and İzmir Institute of Technology, Scientific Research Projects fund (İYTE03, 2009-2011).

REFERENCES

- Graveland-Bikker, J.F., Ipsen, R., Otte, J., and de Kruif, C.G., 2004. Influence of Calcium on the Self-assembly of Partially Hydrolyzed α -lactalbumin, *Langmuir* (20), 6841-6846.
- Graveland-Bikker, J.F., and de Kruif, C.G., 2006. Unique Milk Protein Based Nanotubes: Food and Nanotechnology Meet, *Trends in Food Sci. & Tech.* (17), 196-203.
- Ipsen, R., Otte, J., and Qvist, K.B., 2001. Molecular Self-assembly of Partially Hydrolysed α -lactalbumin Resulting in Strong Gels with a Novel Microstructure, *J. of Dairy Res.*, 68 277-286.
- Ipsen R., and Otte J., 2007. Self-assembly of Partially Hydrolysed α -lactalbumin, *Biotech. Advances* (25), 602-605.
- Otte, J., Ipsen, R., Bauer, R., Bjerrum, M. J., and Waninge, R., 2005. Formation of Amyloid-like Fibrils upon Limited Proteolysis of Bovine α -lactalbumin, *Int. Dairy Journal* (15), 219-229.
- Rajagapol, K., and Schneider, J.P., 2004. Self-assembling Peptides and Proteins for Nanotechnological Applications, *Current Opinion in Structural Biology*, (14): 480-486.

ELEMENTAL RELEASE COMPARISON OF SELECTIVE LASER SINTERING METHOD AND CONVENTIONAL DENTAL CASTING ALLOYS USING ICP-MS

Ayça Açıklan¹, Yurdanur Uçar^{1,a}, Aytaç Dönerci², Nur Deniz Kıcırcı³, Tunç Tüken³

¹: Cukurova University, School of Dentistry, Department of Prosthetic Dentistry, Adana-Turkey

²: Republic of Turkey, Ministry of Health, Adana HıfzıSıhhaInstitute, Adana-Turkey

³: Cukurova University, Science and Art Faculty, Chemistry Department, Adana-Turkey

a: YurdanurUçar (ysanli@cu.edu.tr)

ABSTRACT: Selective Laser Sintering Method (SLS) is a rapid production technique used for dental restorations. The aim of this study was to measure the ion release from dental alloys into artificial saliva. Disks (n=6/group) with 11mm diameter and 3mm thickness were prepared for cast NiCr and CoCr and laser sintered CoCr groups. The thermostat was set on 37±0.1 °C open atmosphere, and then the specimens were electrolyzed with 0.7 mV potential. The percent concentration and total amount of ions passing into the solution were assessed with ICP-MS in ppm. Two-way ANOVA followed by Tukey test was used to analyze differences between 3 groups and different elements (Cr, Fe, Ni, Co, Mo, Cs, V, Nb). V and Nb were not detectable by ICP-MS. The release of Fe, Co, Mo and Cs was not statistically significantly different. Release of nickel in cast CoCr (0.0027 ppm) alloy was higher than laser sintered (0.0008 ppm) alloy. Cast CoCr (0.369 ppm) has higher elemental release for cobalt than laser sintered CoCr (0.312 ppm). SLS procedure decreases the elemental release from CoCr alloy. Total ion release is statistically significantly lower for SLS compared to the other two groups. SLS procedure seems promising for dental framework construction.

1. INTRODUCTION

Contemporary clinical dental applications need rapid and sensitive production due to patients' expectations. Different dental production methods were used for more than a century, in the first instance Taggart's lost wax technique is used in dental laboratories [Schillingburg, 1981]. However the disadvantages of this procedure, such as castability, roughness, marginal adaptation failures, leveling and polishing difficulties, low corrosion resistance and low biocompatibility; necessitated a new manufacturing method to minimize biological problems and structural incompatibility that are encountered during casting of alloys [Annusavice, 2003]. There are many systems using CAD-CAM technology for

rapid production of fixed restorations like "Selective Laser Sintering Method, SLS".

It has been declared that the laser sintering technology has superior advantages compared to the conventional casting techniques. To fabricate a restoration with conventional technique includes many laboratory procedures and lots of processes that can disrupt the comfort of the patient in clinical practice. To have success in these practice all stages must be performed with precision [Ucar Y, 2009]. With the use of SLS technology, problems in all of these stages can be converted into an advantage.

SLS is a new technology and a new area for researchers for dental applications. Previous studies have compared the shear

bond strengths of cast NiCr and CoCr alloys and the laser-sintered CoCr alloy to a dental porcelain [Akova T, 2008], the fit of laser-sintered crowns prepared from a CoCr alloy with conventionally cast base metal alloys[Ucar Y, 2009],the marginal and internal fit of 3-unit laser sintered CoCrFDPs and cast FPDs[Anders Ö, 2011]. All authors concluded DMLS as a promising technology for dental applications. SLS technique increases the mechanical properties due to its different production method. When compared in the same content with two different alloys, SLS has higher values. For laser sintered Co Cr alloy the yield strength, the ultimate tensile strength and the hardness values were higher than the conventionally cast CoCr and NiCr alloys [Gürbüz GA, 2012]. Take home message of all of these studies is that SLS is a method that improves various properties of base metal alloys. Before the common clinical application of this new technology the biocompatibility of the laser sintered metal is a very important question to be answered.

The elements that are initially uncharged inside the alloy lose electrons and become positively charged ions as they are released into solution[Wataha JC, 2000].Corrosion is measured by release of the elements directly by spectroscopic methods. There are a lot of elemental release tests that can be used. ICP-MS is a sensitive method that measures the amount of released element according to the elemental atomic mass on the periodic table [Bergman M, 1975].

The aim of this study was to compare the elemental release from laser sintered CoCr dental alloy and conventionally cast metal alloys (CoCr and NiCr)using ICP-MS. The hypothesis of this work was laser sintered CoCr has lower ion release than

conventionally cast base metal dental alloys.

2. MATERIAL AND METHOD

The compositions of these alloys in wt.%, as given by the manufacturer, are shown in Table1. The test samples were discs with 11mm diameter and 3mm thickness and 1mm hole was placed in the middle of the disc for electrical contact (n=6).A copper wire (electrical contact) was soldered in the middle of the disc and the entire sample was embedded in epoxy resin.

Surface procedures were done according to ISO 10271. To polish the electrodes, initially a number of different metallographic abrasive papers (400, 800, 1000, 1200, 2000 grit)were used. Specimens were rinsed with distilled water and ultrasonically cleaned for 3min, before each test.

In this study, the artificial saliva was used as electrolyte. The test temperature for the open circuit potential was set at 37 °C in order to simulate the clinical conditions. Fusayama artificial saliva solution was used with the mixture of chemical salts (Merck & Co, New Jersey-ABD) in 1L distilled water (Ph: 4.9).

The CH Instrument was used to electrolyze the alloys with 50 ml fresh solution and new glass flasks for each measurement. The thermostat was set at 37±0.1 °Cto measure the open circuit potential and then the specimens were electrolyzed at 0.7 mV potential using CH Instrument 604 No 64721A as multi-potentiostat (CH Instruments Inc., Austin TX, ABD) considering the observed the gas output. The percent concentration of ions and total amount of ions passing to the artificial saliva solution were also used to estimate the concentration of the ions leached into the artificial saliva solutions using ICP-MS

(ThermoElemental X 7 ICP-MS, England) in ppm.

3. RESULTS

The two-way ANOVA and *post-hoc* Tukey tests were used for each element (Cr, Fe, Ni, Co, Mo, Cs, V, Nb). V and Nb were not detectable by ICP-MS. Fe, Co, Mo, Cs release were not statistically significantly different. The release of nickel (Ni) from cast CoCr (0.0027 ppm) dental alloy was higher than the laser sintered (0.0008 ppm) alloy. A similar result was found for cobalt (Co). Cast CoCr (0.369 ppm) alloy had higher elemental release compared to the laser sintered CoCr (0.312 ppm). Data regarding the elemental release values are given in the Table 2.

4. DISCUSSION

The results of this study confirmed that SLS is a promising technique for the dental applications [Akova T, 2008; Ucar Y, 2009; Abou T, 2011; Örtorp A, 2011; Anders Ö, 2011; Gürbüz GA, 2012].

For all of the base metals tested in the current study, Ni and Cr release were statistically different. However, releases of the other elements were not statistically significant. Ni release in cast CoCr (0.0027 ppm) dental alloy was higher than in laser sintered (0.0008 ppm) alloy. According to alloy composition Laser sintered CoCr alloy has less than 0.1wt.% Ni although conventionally cast CoCr alloy does not include Ni (Table 1). For Co cast CoCr group (0.369 ppm) has statistically higher elemental release than the laser sintered CoCr (0.312 ppm).

5. CONCLUSIONS

Based on the elemental release results of the current study the SLS procedure decreases the elemental release from CoCr alloy by increasing the corrosion resistance. The procedure seems promising.

For the clinical applications of SLS procedure, cell culture tests need to be conducted to further evaluate the biocompatibility of laser sintered alloy.

REFERENCES

- AbouTara, M., Eschbach, S., Bohlsen, F., Kern, M., 2011, Clinical outcome of metal-ceramic crowns fabricated with laser-sintering technology. *Int J Prosthodont.*, 24:46.
- Akova, T., Uçar, Y., Alper, T., 2008. Comparison of the bond strength of laser-sintered and cast metal dental alloys to porcelain, *Dental Materials*, 24:1400.
- Anders, Örtorp., David, Jönsson., Alaa, Mouhsen., Per Vult von Steyern, 2011, The fit of cobalt-chromium three-unit fixed dental prostheses fabricated with four different techniques: A comparative in vitro study, *Dental Materials* 27:356.
- Anusavice, KJ., 2003, Phillips' Science of Dental Materials. 11th ed. Saunders.
- Bergman, M., Ginstrup, O., 1975, Dissolution rate of cadmium from dental gold solder alloys. *Acta Odontol Scand*, 33:199.
- Gürbüz, GA., 2012, Phd dissertation, Cukurova University, Adana, Turkey, Selektiflazersinterizasyonu ile oluşturulan Co-Cr kronların porselen fırınlaması aşamalarında boyut stabilitesinin değerlendirilmesi ve alaşımın mekanik özelliklerinin incelenmesi,
- Örtorp, A., Jönsson, D., Mouhsen, A., Vult, von Steyern P., 2011, The fit of cobalt-chromium three-unit fixed dental prostheses fabricated with four different techniques: a comparative in vitro study. *Dent Mater.* 27:356.
- Shillinburg, H., Hobo, S., 1981, *Fundamentals of Fixed Prosthodontics*, 2nd edition, Quintessence Publishing Co., Chicago, Berlin, Tokyo.
- Ucar, Y., Akova, T., Akyil, MS., Brantley, WA., 2009. Internal fit evaluation of crowns prepared using a new dental crown fabricating technique laser sintered Co-Cr crowns. *J Prosthet Dent*, 102:253.
- Wataha, JC., 2000, Biocompatibility of dental casting alloys: A review, *J Prosthet Dent*; 83:223.

Table 1: The compositions of these alloys in wt.%

	Co	Cr	Ni	Mo	W	Si	Fe	C	Mn	Nb	Ce
EOS Co-Cr SP	63,8	24,7	-	0,1	5.4	1,0	0,5		0,1		
BegoWiron 99		22.5	65	9.5		1	0.5	0.02		1	0.5
BegoWirobond C	61	26		6	5	1	0.5	0.02			0.5

Table 2: Elemental release of different ions (ppm)

Groups	Cr	Fe	Ni	Co
NiCr	0,0059±0,005 2 A	0.0029±0.00 32A	0.0724±0.0 774B	0.0034±0.00 58A
CoCr	0,0082±0,005 8 A	0.0005±0.00 11A	0.0027±0.0 022A	0.0369±0.03 16B
Lazer	0,0045±0,003 6 A	0.0018±0.00 3A	0.0008±0.0 001A	0.0312±0.01 94AB
Groups	Mo	Cs	V	Nb
NiCr	0.0063±0.006 5A	0.0002±0.00 02A	.000±.000 A	.000±.000A
CoCr	0.0034±0.001 7A	0.0004±0.00 06A	.000±.000 A	.000±.000A
Lazer	0.0023±0.001 7A	.0000±0.000 1A	.000±.000 A	.000±.000A

DNA ADSORPTION ONTO SILICA AEROGEL

Senem Yetgin^{1,a}, Devrim Balköse²

1. Izmir Institute of Technology, Izmir, Turkey

2. Izmir Institute of Technology, Izmir, Turkey

a. Senem YETGIN (*senemyetgin@gmail.com*)

ABSTRACT: DNA is used for gene therapy, biological sensor preparation and the creation of nano-sized structures in recent years. Not only DNA purification but also DNA interactions with different surfaces are directly or indirectly based on the adsorption of DNA. Solid phase extraction (SPE) is the most useful technique for DNA purification. Increase of the adsorption capacity and reduction of the analysis time are the essential part of the new development. Silica is the most commonly used material for SPE and increasing its adsorption capacity is firstly required. This study focuses on producing silica alcogel by a sol gel process and drying the alcogel by supercritical ethanol drying to obtain silica aerogel with high DNA adsorption capacity. The DNA adsorption capacity of the silica aerogel was higher than that of a commercial silica gel. 22.52 % and 8.41% uptakes from 100 ng/ μ l DNA solution at pH 5 were determined for silica aerogel and commercial silicagel respectively. DNA adsorption in silica aerogel best fitted to Freundlich isotherm with K_f and n constants of 211 and 2.3 respectively.

1. INTRODUCTION

Silica aerogel have been used in a wide range of applications such as catalytic supports, thermal insulation in solar window systems (Pierre and Pajonk 2002; Estella et al., 2008). Nucleic acids are adsorbed on silica and glass surfaces under chaotropic solution conditions. DNA adsorption by silica was extensively investigated (Melzak et al 1996; Mao et al., 1994). DNA adsorption by silica was controlled by three effects (i) weak electrostatic repulsion forces, (ii) dehydration, and (iii) hydrogen bond formation. Calf thymus DNA's molecular weight (M_w) was measured as 8.3×10^6 (Tanigawa et al., 1996) and 6×10^6 g/mol as determined by multiangle laser light scattering (Sundaresan et al., 2008). It is a very long molecule in cylindrical shape having 100 nm diameter.

In the present study silica aerogel with high pore volume and surface area was aimed to be prepared diameter for higher adsorption capacity for calf thymus DNA.

2. MATERIALS AND METHODS

The materials listed in Table 1 were used in producing silica alcogels by sol-gel processing. Calf thymus DNA supplied by Sigma Aldrich (D1501) was used in adsorption experiments

Table 1: Materials and their specifications

Materials	Specifications
TEOS-	98% (Aldrich)
Ethyl alcohol	99.8% (Riedel)
Ammonium-hydroxide	28-30% (Aldrich)
Hydrochloric acid-	37% (Merck)

Silica alcogel was prepared by a two steps sol gel procedure. The details of the method developed by Brinker and co-workers have been described by Ru et al. (Ru et al. 2010). Hydrochloric acid was used as an acid catalyst of the hydrolysis of tetraethylorthosilicate (TEOS) in the first step. TEOS, ethanol (EtOH), distilled water and hydrochloric acid were mixed in a 250 cm³ glass bottle at a molar ratio of 1:6:4:10⁻³ and led to be stirred for 30 min, and a hydrolysis solution was obtained. In the second step,

ammonia, as a base catalyst, was added drop-wise into the solution resulting from the first step, at the molar ratio of TEOS: NH_4OH equals to $1:10^{-2}$. The alcogel formed by keeping the mixture for 940 hours at 25°C was washed several times with ethanol. The aim of this part is remove excess water present inside the alcogel structure. After preparation of the silica alcogel and the washing procedure, the alcogel having 84.3% ethanol, 1.1% water and 14.6% silica was dried by ethanol supercritical drying. The supercritical pressure of ethanol is 6.36 MPa). A super critical state was achieved by heating the system to 250°C and 72 bar. In a typical experiment, approximately 5.0 g of wet solid and 100 cm^3 ethanol was placed in the reactor in PARR 5500 Series Compact Reactor as shown in Figure 1.

SCD was carried out above the critical temperature of ethanol as shown in Figure 2. Prepared aerogel and a commercial silicagel (Sigma Aldrich) were characterized through nitrogen adsorption techniques using Micromeritics ASAP 2000. The adsorption isotherms of calf thymus DNA from aqueous solutions were determined by measuring the DNA concentrations in solutions in equilibrium with commercial silica gel and silica aerogel synthesized in the present study using NanoDrop ND-1000 UV-VIS spectrophotometer

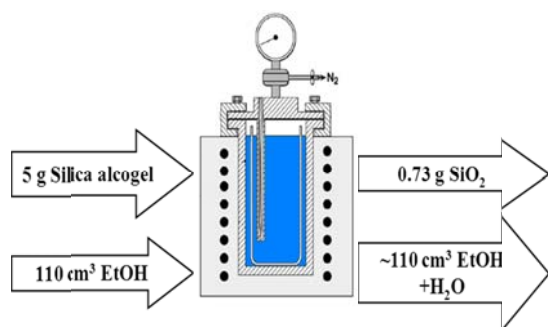


Figure 1: Schematic representation of supercritical ethanol drying system

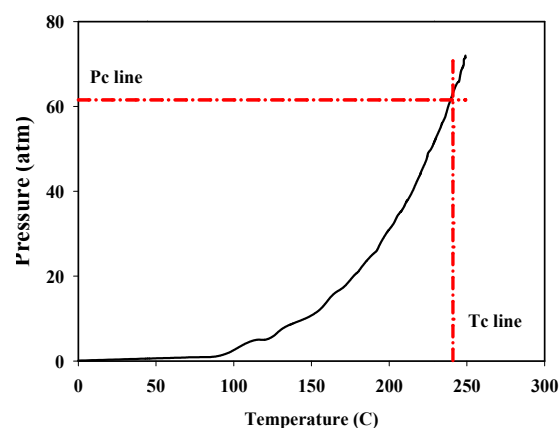


Figure 2: Pressure-Temperature relation of ethanol in closed reactor

3. RESULT AND DISCUSSION

The nitrogen adsorption isotherms of the aerogel and commercial silicagel are as shown in Figure 3. The aerogel obtained had $1107\text{ m}^2/\text{g}$ surface area and 4.2 nm pore diameter as determined by nitrogen gas adsorption at 77 K . Data for aerogel and the commercial silicagel were as listed in Table 2.

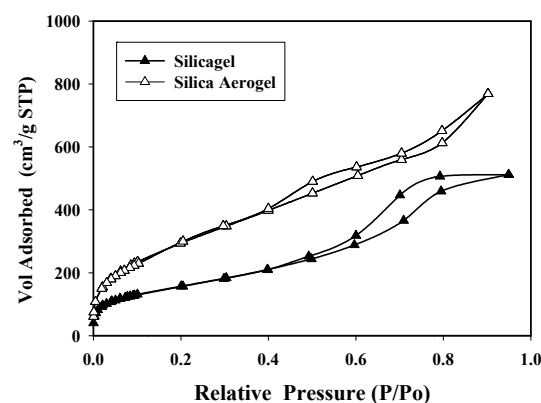


Figure 3: Nitrogen adsorption and desorption isotherms of Aerogel and Commercial silica gel

Table 2: Surface characteristics of the Aerogel and commercial silica

Properties	Sigma Aldrich-Silicagel	Aerogel
Single Point Surface Area (m ² /g)	556	1055
BET Surface Area (m ² /g)	571	1107
Langmuir Surface Area (m ² /g)	787	1549
Average Pore Diameter (nm) (4V/A by BET)	5.5	4.2
Single Point Total Pore Volume (cm ³ /g)	0.79	1.19
Max Micropore Volume (cm ³ /g)	0.20	0.36

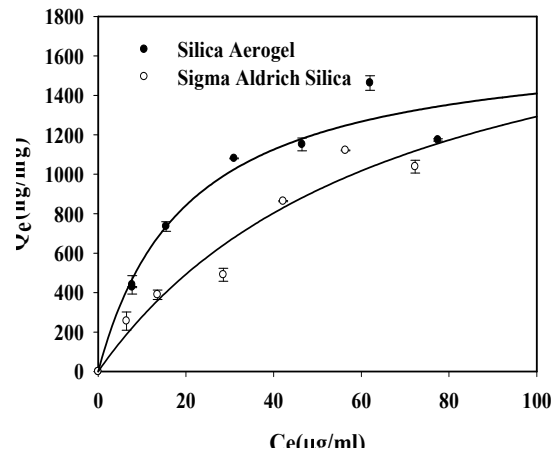


Figure 4: Adsorption isotherm of DNA on Silica Aerogel and Silica gel at pH 5

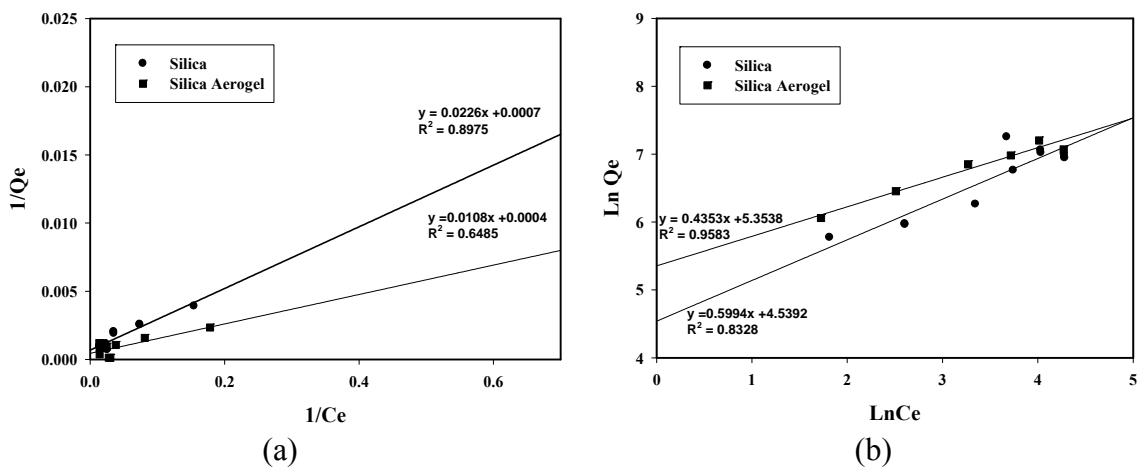


Figure 5: a. Langmuir and b. Freundlich Adsorption Models of DNA adsorption on Silica Aerogel and Silica gel

DNA adsorption isotherms are illustrated in Figure 4. 22.52 % and 8.41% uptakes from 100ng/ μ l DNA solution at pH 5 were determined for silica aerogel and commercial silica gel respectively. It was found that the DNA adsorption capacity was higher for silica aerogel than that of

commercial silica gel. Langmuir and Freundlich model graphs are shown in Figure 5.(a) and (b) respectively. DNA adsorption in silica aerogel best fitted to Freundlich isotherm with K_f and n constants of 211 and 2.3 respectively.

4. CONCLUSION

As a result before solid phase extraction method (SPE) was discovered, DNA was purified by time consuming methods using toxic hazardous materials. Research is still going on adjust the analysis time for DNA purification after cell lysis. Silica aerogel was found to be a very promising material. Aerogel has nearly two times great adsorption capacity than silicagel at 20-40 µg/ml DNA concentration. The large surface area of aerogel had a positive effect on DNA adsorption capacity.

REFERENCES

- Estella J., Echeverria J. C., Julian M.L., Garrido J., (2008). Effect of Supercritical Drying Conditions in Ethanol on The Structural and Textural Properties of Silica Aerogels. *J Porous Mater*, Volume (15), 705
- Melzak K. A., Sherwood, C. S., Turner, R. B. F., and Haynes, C. A. (1996). Driving Forces for DNA Adsorption to Silica in Perchlorate Solutions. *J. Colloid Interface Sci.*, Volume (181), 635
- Pierre A. C., Pajonk G. M. (2002). Chemistry of Aerogels and Their Applications. *Chem. Rev.*, Volume (102), 4243
- Ru Y., Guoqiang L., Min L. (2010). Analysis of The Effect of Drying Conditions on the Structural and Surface Heterogeneity of Silica Aerogels and Xerogel by Using Cryogenic Nitrogen Adsorption Characterization. *Microporous and Mesoporous Materials*, Volume (129), 1
- Sundaresan N., Suresh H. C., Thomas T., Thomas T. J., Pillai C. K. S, (2008). Liquid Crystalline Phase Behavior of High Molecular Weight DNA: A Comparative Study of the Influence of Metal Ions of Different Size, Charge and Binding Mode. *Biomacromolecules*, 9, 1860–1869
- Tanigawa M., Suzuto M., Fukudome K., Yamaoka K. (1996). Changes in Molecular Weights and Molecular Weight Distributions of Differently Stranded Nucleic Acids after Sonication: Gel Permeation Chromatography/Low Angle Laser Light Scattering Evaluation and Computer Simulation. *Macromolecules* 29, 7418-7425.
- Mao Y., Daniel L. Y., Whittaker N., Saffiottil U. (1994). DNA Binding to Crystalline Silica Characterized by Fourier-Transform Infrared Spectroscopy. *Environ Health Perspectives*, Volume (102), 165

SECTION E

Transport and Surface Chemistry

CHANGES IN MAGNETIC PROPERTIES FROM PARTICLES TO ATOMIC CLUSTERS

José Rivas^{1,2,a}, Enrique Carbó-Argibay¹ and M. Arturo López-Quintela²

1. INL – International Iberian Nanotechnology Laboratory, 4715-330 Braga, Portugal

2. Laboratory of Magnetism and Nanotechnology (NANOMAG). Research Technological Institute. University of Santiago de Compostela, 15782 Santiago de Compostela, Spain

a. Corresponding Author (jose.rivas@inl.int)

ABSTRACT: During last four decades, our concept of physicochemical properties has changed notably. Optical, magnetic, catalytic, mechanical... properties are not the same since nanoscience appearance. In particular, magnetic properties such as superparamagnetism, reported in the first half of 20th century, were investigated more exhaustively in magnetic nanoparticles/clusters since 90's. Moreover, the fascinating properties of magnetic nanoparticles allow to apply them in different fields, such as biosensing, magnetic storage, drug delivery, hyperthermia or MRI (Magnetic Resonance Imaging). Together with studies of magnetic properties, synthesis processes of magnetic nanoparticles/clusters are crucial to design nanoparticles/clusters with desired properties. For this reason, it's fundamental to understand mechanisms involved in particles formation to be modified in such a way that allow us a fine-tuning of the magnetic response. In this sense, microemulsion techniques constitute a potent method to obtain metal or metal oxide nanoparticles/cluster.

1. INTRODUCTION

Metal (0) clusters are nanoparticles having a small number of atoms (usually less than 100-200) or sizes below circa 1-2 nm. Below such size range the *free* electrons of the metal nanoparticles become *frozen* and the metals lose their metal behavior, which is clearly detected by the disappearance of the characteristic plasmon bands of the metals. In such range, a bandgap is opened at the Fermi level, increasing the magnitude of the gap as the cluster size is reduced. Due to this bandgap, which can be as high as 3 to 4 eV for the smallest clusters having only 2 to 3 atoms, and the extra-stabilization by electronic closing shells, clusters – contrary to the general belief- are very stable. Novel and fascinating properties, which strongly differ in many cases from the properties of bulk and nanoparticles of the same material, appear at this nanometer/sub-nanometer transition. For example, fluorescence [Zheng *et al.*,

2004], catalysis [Vilar-Vidal *et al.*, 2012], magnetism [Yamamoto *et al.*, 2004], and circular dichroism [Schaaff and Whetten, 2000] have been found in such clusters, which are not exhibited for the same material in larger sizes. However, all these studies are very limited because of the procedures used for the cluster synthesis. Only very small amounts of highly polydisperse samples can be obtained after difficult separation procedures [Petty *et al.*, 2004] [Negishi and Tsukuda, 2003]. In the last years we developed, among others, novel microemulsion-based methods for the synthesis of clusters, which allows their production with relatively good monodispersity [López-Quintela and Rivas, 2005] [Guillén-Villafuerte *et al.*, 2006] [Ledo-Suárez *et al.*, 2007] [Rodríguez-Vázquez *et al.*, 2008] [Vázquez-Vázquez *et al.*, 2009] [Selva *et al.*, 2010] [Vilar-Vidal *et al.*, 2010] [Santiago González *et al.*, 2010] [López-Quintela *et al.*, 2012].

2. RESULTS AND DISCUSSION

As we have commented previously, clusters are particles with less than 100-200 atoms and sizes below 1-2 nm. However, nanoparticle term refers to materials with sizes ranging from a few to 100 nm. In this range of sizes, magnetic properties (and other physicochemical properties) are different from those observed in bulk materials.

Besides, physicochemical properties of nanoparticles and clusters are different from each other due to the presence of discrete energy level. Quantization of energy levels in clusters is an evidence of quasi-molecular behavior (Figure 1). Therefore we have to analyze separately magnetic properties of bulk materials, nanoparticles and clusters (in decreasing order of material size).

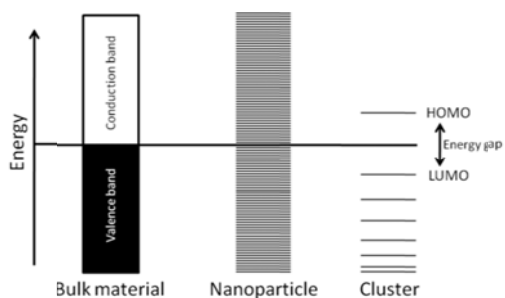


Figure 1: Density of states for bulk materials, nanoparticles and clusters, showing discretization of energy levels in clusters.

2.1. Magnetic Properties In Nanoparticles

The most important distinctive of magnetic nanoparticles is their superparamagnetic behavior [Neel, 1949]. In spite of superparamagnetism had been reported by Neel in 1949, it wasn't a key goal for scientific community until 90's [Wiedwald and Ziemann, 2010], when miniaturization of bits became a hot topic, trying to get the objective of a Tbit/inch².

Superparamagnetic nanoparticles in the presence of an external magnetic field become magnetized until their saturation magnetization. When magnetic field is removed, they don't show any residual magnetic interaction [Wahajuddin and Arora, 2012]. This remarkable property is size and temperature-dependent and normally appears (at room temperature) in nanoparticles around 10-20nm. In this range of sizes, particles don't present a multi-domain structure (as in ferromagnetic bulk materials), but rather a single magnetic domain that act as a "single super spin" with a high magnetic susceptibility (Figure 2).

When a magnetic field is applied to these particles, they provide a stronger and quicker magnetic response, compared to bulk magnetic materials, with negligible remanence (residual magnetization) and coercive force (necessary field to bring magnetism to zero after magnetization of the sample has been driven to saturation).

In the presence of an external magnetic field, superparamagnetic nanoparticles tend to align to it, but once the external magnetic field is removed, thermal agitation cancels residual magnetization.

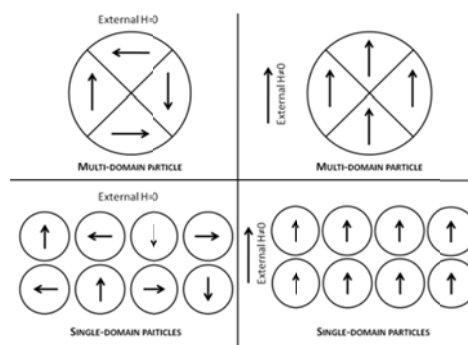


Figure 2: Magnetic behavior of a multi-domain magnetic particle (up) versus single-domain magnetic particles (bottom) in the presence (right) or the absence (left) of an external magnetic field.

Stoner-Wohlfarth model is an extensively used model for analyzing the magnetization of single-domain ferromagnets [Stoner and Wohlfarth, 1948]. Stoner-Wohlfarth model is very useful for simulating magnetic properties of small magnetic particles (non-interacting particles).

In 90's, numerous methods for synthesis of superparamagnetic nanoparticles were developed. The main objective was to apply this kind of magnetic nanoparticles in different fields, such as biosensing, magnetic storage, drug delivery, contrast agent in MRI (Magnetic Resonance Imaging), etc.

However, morphology control (shape and size) in synthesis of magnetic nanoparticles is a fundamental parameter due to magnetic properties are determined by it.

Keeping in mind this goal, different methods have been employed to synthesize magnetic nanoparticles such as microemulsions, sol-gel processes, hydrothermal method, hydrolysis and thermolysis of precursors, etc [Lauren *et al.*, 2008].

One of the most developed fields of application for magnetic nanoparticles is biomedicine. Particles designed for this application must have high magnetization values, must be monodispersed and their sizes should be smaller than 100 nm [Laurent *et al.*, 2008]. In addition, magnetic nanoparticles in biomedicine have to be coated for being biocompatible and also conjugated with drugs, antibodies, nucleotides or other biomolecules in order to form a targetable nanomaterial.

An important field that merges magnetic and plasmonic properties of nanoparticles is magnetoplasmonics. This kind of

particles is particularly attractive for their application in diagnosis, due to the complementarity of MRI (Magnetic Resonance Imaging) and plasmonics techniques. In addition, bifunctional magnetoplasmonics nanomaterials (core/shell or dimers) present very interesting magnetic, optical and even catalytic properties.

$\text{Fe}_3\text{O}_4@Au$ core shell or Fe_3O_4 -Au particles are the most common structures in magnetoplasmonics. $\text{Fe}_3\text{O}_4@Au$ core shell structures (superparamagnetic) have been employed as SERS substrates, for detection of molecules, with results notably better than those obtained for conventional gold nanoparticles under same conditions [Wheeler *et al.*, 2012]. On the other hand, Au- Fe_3O_4 nanoparticles have been used in electrochemical immunosensors for detection of biomolecules [Wei *et al.*, 2010]..., improving the sensitivity and detection limit of the immunosensor.

2.2. Atomic Quantum Clusters And Their Magnetic Properties

An atomic quantum cluster is a group of atoms (2-200 atoms) with a well-defined composition and one or several stable geometries. Their size is comparable to Fermi wavelength of an electron (approximately 0.5 nm for Au and Ag) and therefore their properties are different from nanoparticles. Due to their small size they present quantum effects that are responsible of new physicochemical properties such as photoluminescence, magnetism, catalytic activity...

At the same time, clusters can be divided in two types: big clusters (200 – 20 atoms) and small clusters (20 – 2 atoms). Big clusters are made of a metallic core protected by strong ligands (dendrimers, thiols or phosphines), while small clusters don't need any ligand to stabilize them.

Basically, synthesis methods of clusters can be divided in: top-down or bottom-up. Top-down approach uses nanoparticles or bulk materials as precursors of clusters, mainly through etching processes. Bottom-up approach employs atoms or ions as building blocks for cluster formation.

The production of monodisperse magnetic nanoparticles down to few atoms (clusters) is nowadays one of the most important challenges in Nanotechnology. The microemulsion technique is a powerful method to prepare simple metallic and oxide NPs, as well as, core-shell and “onion-like” NPs [López-Quintela and Rivas, 1993] [López-Quintela and Rivas, 1996] [López-Quintela *et al.*, 2003]. Although microemulsions cannot be considered as real templates, they constitute an elegant technique, which can provide a very good control of the final particle size. The reason for that is complex interplay mainly between three parameters, namely, surfactant film flexibility, reactant concentration and reactant exchange rate [López-Quintela, 2003]. By adequately choosing these three parameters one can get a homogeneous distribution of particle sizes down to few atoms.

During last decades, many efforts have been dedicated to characterize the physicochemical properties of clusters. Among these properties, magnetism takes a prominent place but also remain as a field where still we have questions to answer.

Magnetic properties in clusters not only depend on size, but also depend on symmetry of clusters and therefore on cluster shape. Cluster symmetry determines charges distribution and therefore magnetic moment depends on symmetry. Magnetic moment of clusters

depends on the symmetry and size of clusters. Clusters present permanent magnetic moments (in ferromagnetic and paramagnetic transition metal elements). Besides, averaged magnetic moment per atom is higher than in bulk materials.

As we have commented, there are several parameters involved in magnetic properties of clusters: geometry, coordination number, bond distances, symmetry and size [Duan and Zheng, 2001].

Some studies have shown that magnetic moment in clusters increases with symmetry. For example Fe_{13} clusters with I_h symmetry present larger magnetic moments than Fe_{13} with O_h or D_{3h} symmetry [Dunlap, 1990]. However, contrary to the previous case (Fe_{13}), magnetic moment of Fe_{55} cluster with I_h symmetry is lower than for Fe_{55} cluster with O_h symmetry [Duan and Zheng, 2001]. This behavior suggests that the dependence of the magnetic moment on cluster symmetry is also cluster's size dependent.

Even, nonmagnetic bulk materials, show magnetic properties as a cluster. Is the case of Rhodium, whose clusters Rh_{12} – Rh_{32} are magnetic, contrary to observed in Rhodium bulk [Cox *et al.*, 1993].

In the case of 3-atoms gold clusters (Au_3), they present paramagnetic behavior, very different from the Au bulk that displays diamagnetic properties [Santiago González *et al.*, 2010].

3. CONCLUSIONS

In summary, in this proceeding a brief summary of changes in magnetic properties from bulk materials to nanoparticles and clusters have been shown. Properties of different materials (bulk, nanoparticles or clusters) must be studied separately, assuming that

magnetic behavior shown by bulk materials could be very different from that displayed by same material in nanoscale or sub-nanoscale (clusters) range.

Development of facile synthesis methods for preparation of monodisperse samples constitutes one of most important challenges in nanomagnetism. In this sense, microemulsion technique is a promising route to achieve this goal.

Acknowledgements: This work was partially funded by Programa Operacional Regional do Norte (ON.2) (Project NORTE-070124-FEDER-40). E.C.-A. acknowledges the I2C Plan (Xunta de Galicia, Spain) for a postdoctoral fellowship.

REFERENCES

- Cox, A.J., Louderback, J.G. and Bloomfield, L.A., 1993. Experimental Observation of Magnetism in Rhodium Clusters, *Physical Review Letters*, 71 (6), 923.
- Duan, H.M. and Zheng, Q.Q., 2001. Symmetry and magnetic properties of transition metal clusters, *Physics Letters A*, 280 (5-6), 333.
- Dunlap, B.I., 1990. Symmetry and cluster magnetism, *Physical Review A*, 41 (10), 5691.
- Guillén-Villafuerte, O., García, G., Anula, B., Pastor, E., Blanco, M.C., López-Quintela, M.A., Hernández-Creus, A. and Planes, G.A., 2006. Assembly of Subnanometric 2D Pt Nanoislands in Parallel Rows onto Au(111) by Self-Organization of Pt Clusters, *Angewandte Chemie International Edition*, 45 (26), 4266.
- Laurent, S., Forge, D., Port, M., Roch, A., Robic, C., Vander Elst, L. and Muller, R.N., 2008. Magnetic Iron Oxide Nanoparticles: Synthesis, Stabilization, Vectorization, Physicochemical Characterizations, and Biological Applications, *Chemical Reviews*, 108 (6), 2064.
- Ledo-Suárez, A., Rivas, J., Rodríguez-Abreu, C.F., Rodríguez, M.J., Pastor, E., Hernández-Creus, A., Oseroff S.B., López-Quintela, M.A., 2007. Facile Synthesis of Stable, Sub-Nanosized Silver Atomic Clusters in Microemulsions, *Angewandte Chemie International Edition*, 46 (46), 8823.
- López-Quintela, M.A. and Rivas, J., 1993. Powerful Method to Obtain Ultrafine Particles, *Journal of Colloid and Interface Science*, 158 (2), 446.
- López-Quintela, M.A. and Rivas, J., 1996. Nanoscale magnetic particles: Synthesis, structure and dynamics, *Current Opinion in Colloid & Interface Science*, 1 (6), 806.
- López-Quintela, M.A., Rivas, J., Blanco, M.C. and Tojo, C., 2003. Chapter 6, *Nanoscale Materials*, Kluwer Academic Publishers, 135.
- López-Quintela, M.A., 2003. Synthesis of nanomaterials in microemulsions: formation mechanisms and growth control, *Current Opinion in Colloid & Interface Science*, 8 (2), 137.
- López-Quintela, M.A. and Rivas, J., 2005. Procedure for the synthesis of atomic quantum clusters. Spanish patent application No.P200502041.
- López-Quintela, M.A., Calvo, J. and Rivas, J., 2012. Synthesis of Subnanometric Nanoparticles, *Encyclopedia of Nanotechnology*, Bhushan, Bharat (Editor), Springer Verlag, 2639.
- Neel, L., 1949, *Annales Geophysicae (CNRS)*, 5, 99.
- Negishi, Y. and Tsukuda, T., 2003. One-Pot Preparation of Subnanometer-Sized Gold Clusters via Reduction and Stabilization by meso-2,3-Dimercaptosuccinic Acid, *Journal of the American Chemical Society*, 125 (14), 4046.
- Petty, J.T., Zheng, J., Hud, N.V. and Dickson, R.M., 2004. DNA-Templated Ag Nanocluster Formation, *Journal of the American Chemical Society*, 126 (16), 5207.
- Rodríguez-Vázquez, M.J., Blanco, M.C., Lourido, R., Vázquez-Vázquez, C., Pastor, E., Planes, G.A., Rivas, J. and López-Quintela, M.A., 2008. Synthesis of Atomic Gold Clusters with Strong Electrocatalytic Activities, *Langmuir*, 24 (21), 12690.
- Santiago González, B., Rodríguez, M.J., Blanco, C., Rivas, J., López-Quintela, M.A. and Gaspar-Martinho, J.M., 2010. One Step Synthesis of the Smallest Photoluminescent and Paramagnetic PVP-Protected Gold Atomic Clusters, *Nano Letters*, 10 (10), 4217.
- Schaaff, T.G. and Whetten, R.L., 2000. Giant Gold-Glutathione Cluster Compounds: Intense Optical Activity in Metal-Based Transitions, *The Journal of Physical Chemistry B*, 104 (12), 2630.
- Selva, J., Martinez, S.E., Buceta, D., Rodríguez-Vázquez, M.J., Blanco, M.C., López-Quintela, M.A. and Egea, G., 2010. Silver Sub-nanoclusters Electrocatalyze Ethanol Oxidation and Provide Protection against

- Ethanol Toxicity in Cultured Mammalian Cells, *Journal of the American Chemical Society*, 132 (20), 6947.
- Stoner, E.C. and Wohlfarth, E.P., 1948. A mechanism of magnetic hysteresis in heterogeneous alloys, *Philosophical Transactions of the Royal Society A: Physical, Mathematical and Engineering Sciences*, 240 (826), 599.
- Vázquez-Vázquez, C., Bañobre-López, M., Mitra, A., López-Quintela, M.A. and Rivas, J., 2009. Synthesis of Small Atomic Copper Clusters in Microemulsions, *Langmuir*, 25 (14), 8208.
- Vilar-Vidal, N., Blanco, M.C., López-Quintela, M.A., Rivas, J. and Serra, C., 2010. Electrochemical Synthesis of Very Stable Photoluminescent Copper Clusters, *The Journal of Physical Chemistry C*, 114 (38), 15924.
- Vilar-Vidal, N., Rivas, J. and López-Quintela, M.A., 2012. Size Dependent Catalytic Activity of Reusable Subnanometer Copper (0) Clusters, *ACS Catalysis*, 2 (8), 1693.
- Wahajuddin, Arora, S., 2012. Superparamagnetic iron oxide nanoparticles: magnetic nanoplatforms as drug carriers, *International Journal of Nanomedicine*, 7, 3445.
- Wei, Q., Xiang, Z., He, J., Wang, G., Li, H., Qian, Z. and Yang, M., 2010. Dumbbell-like Au-Fe₃O₄ nanoparticles as label for the preparation of electrochemical immunosensors, *Biosensors and Bioelectronics*, 26 (2), 627.
- Wheeler, D.A., Adams, S.A., López-Luke, T., Torres-Castro, A. and Zhang, J.Z., 2012. Magnetic Fe₃O₄-Au core-shell nanostructures for surface enhanced Raman scattering, *Annalen der Physik*, 524 (11), 670.
- Wiedwald, U. and Ziemann, P., 2010. Preparation, properties and applications of magnetic nanoparticles, *Beilstein Journal of Nanotechnology*, 1, 21.
- Yamamoto, Y., Miura, T., Suzuki, M., Kawamura, N., Miyagawa, H., Nakamura, T., Kobayashi, K., Teranishi, T. and Hori, H., 2004. Direct Observation of Ferromagnetic Spin Polarization in Gold Nanoparticles, *Physical Review Letters*, 93 (11), 116801.
- Zheng, J., Zhang, C. and Dickson, R.M., 2004. Highly Fluorescent, Water-Soluble, Size-Tunable Gold Quantum Dots, *Physical Review Letters*, 93 (7), 077402.

INVESTIGATION OF HYDROXYAPATITE (HA) COATINGS WEAR BEHAVIOUR CREATED ON THE SURFACE OF Ti6Al4V MATERIALS AFTER DIFFERENT ACTIVATION PROCEDURES

Ibrahim AYDIN^{1,a}, Hakan ÇETİNEL² and Ahmet PASİNLİ³

1. Celal Bayar University MOSB MYO, Machine, Manisa, Turkey

2. Celal Bayar University Engineering Faculty, Mechanical Engineering, Manisa, Turkey

3. Ege University EGE MYO, Machine, İzmir, Turkey

a. Corresponding author (Ibrahim.aydin@cbu.edu.tr)

ABSTRACT:In biomaterials technology, in order to increase the biocompatibility of the implant materials surfaces the surface is coated by hydroxyapatite (HA) which is a compound of calcium phosphate (CaP). Implant materials are generally made up of stainless steel, cobalt-chrome and titanium alloys. In this study the implant material was a titanium alloy: Ti6Al4V. The scope of the study is to investigate the HA coatings wear behavior adhered on the surface of Ti6Al4V materials by applying varying activation procedures. During the processes, NaOH and NaOH + H₂O₂ activation procedures were conducted. The HA coating processes were applied based on biomimetic methods. Wear tests were performed by applying 5N and 10N loads on the coated surfaces. Finally, it's found that, NaOH + H₂O₂ activation procedure applied on HA coatings had less amount in wear on HA coatings when compared that of NaOH activation procedure.

1. INTRODUCTION

Similar to bone plates and bone screws, titanium alloy (Ti6Al4V) hip prosthesis is a material used in orthopedic implant processes [Hench, 1991]. In order to increase the biocompatibility, HA coatings are widely preferred in titanium alloys in implant materials [Kokuba et al, 1999 and Ciobanu et al, 2009]. An instance, phosphate based HA that forms the inorganic structure of the human bone and teeth is being used in dentistry since 1970 [Li, 2002].

The favorable property of HA is its biological compatibility. HA forms a direct chemical bond with sclerenchyma. In placing the HA particles or posed blocks to bones; the new tissue forms in 4 to 8 weeks [Bajpai, 1990]. HA pored structure, as the cells grow into the pores, helps the tissues grow into the implants. Also, acting as a canal system, pores in the HA structure help blood and other important body fluids reach the bone structure. HA has an absorption rate of

5-10% a year. Studies show that HA implants are first covered with fibro vascular tissues, and the grown lamella in the tissue turns into bone [Yetkin, 2001]. Osteoconductive properties of HA helps in attaching to the bone tightly. Also HA is known to have powerful chemical bonding tendencies for bone proteins [Bajpai, 1985]. Body reactions are minimum because of the non-toxic properties of HA [Capello et al, 1997]. There are many methods for HA coating. Kokubo et al. were the first to be able to coat HA on different biomaterials in synthetic body fluids (SBF) [Kokuba et al, 1999]. Tas obtained calcium HA ceramic dust at the high chemical homogeneity and purity in pH 7.4 and 37 °C biomimetic conditions by changing the values that are prepared by SBF [Tas, 2004].

In this study the implant material was a titanium alloy: Ti6Al4V. The scope of this study is to investigate the HA coatings wear behavior adhered on the

surface of Ti6Al4V materials by applying varying activation procedures. During the processes, NaOH and NaOH + H₂O₂ activation procedures were conducted. The HA coating processes were applied based on biomimetic methods. Wear tests were performed by applying 5N and 10N loads on the coated surfaces.

2. MATERIALS AND METHODS

2.1. Preparation of Coatings

Chemical composition of the Ti implant alloy (Ti6Al4V) used in this study was given in Table 1.

Biocompatible hydroxyapatite coatings were deposited onto Ti6Al4V as substrate dimension is 10x 10 x 1.2 mm. Firstly, Ti6Al4V alloy substrates were abraded with SiC paper and then cleaned by detergent water, distilled water and lastly acetone. Both NaOH and NaOH+H₂O₂ solutions were used for the chemical etching process to compare their merits after the biomimetic coating. In activation process, purified materials were held in 100 mL 5M NaOH + 0.5 mL H₂O₂ (30%) solution and 100 mL 5 M NaOH solution in 60 °C for 24 hours, separately. Then they were washed with distilled water and dried in 40 °C for 24 hours. The etched substrates were finally heat-treated at 600°C in a microprocessor-controlled furnace with heating rates of 5°C/min, soaked at 600°C for 1 h and were then cooled slowly in the furnace down to room temperature. In hydroxyapatite coating process, implant materials pretreated in the solution that was prepared as pH 7.4 with lactic acid/lactate buffer according to SBF values as in Table 2. Meanwhile, fresh SBF fluid was emitted in with peristaltic pump 150 mg/day.

At the end of the process, materials were washed with distilled water and dried in 30 °C for 4 hours [Aydin at al, 2012].

Table 1: Chemical composition of Ti alloy substrate (Aydin at al, 2012).

Element	(wt %)
N	0.0030
C	0.0050
H	<0.0005
Fe	0.1000
O	0.0900
Al	6.2100
V	3.8700
Y	<0.0010
Others	<0.3000
Ti	Balance

Table 2: Preparation of 2.5 X Lac-SBF (total volume= 2.5 L) (Aydin at al, 2012).

Reagents	Amount (g)
CaCl ₂ ·2H ₂ O	2.2973
MgCl ₂ ·6H ₂ O	0.7625
KCl	0.9325
NaCl	12.0533
Na ₂ HPO ₄ ·2H ₂ O	1.1125
Na ₂ SO ₄	0.1775
NaHCO ₃	5.6708
Na-lactate (70-72%, d:1.375-1.385)	10.4573
Lactic acid (1 M)	40.0 (mL)

2.2. Mechanical Tests

In order to detect the behavior of the coatings wear, CSM(Instruments) Tribometer was used. The corresponding component was 6mm in diameter and called as 100Cr6 in this type tribometer. The process was applied with 5N and 10N loading with a velocity of 1cm/s and 20 m path.

3. RESULTS

In this study, 5N and 10N loading was applied on substrate of hydroxyapatite (HA) coatings. Two activation procedures were applied on HA coatings which are NaOH and NaOH + H₂O₂ and finally the wear rates and the average friction coefficients of the HA coatings

with respect to the loadings of 5N and 10N are plotted in Figures 1 and 2 respectively.

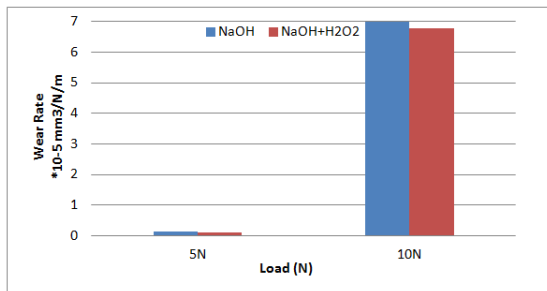


Figure 1: Wear rates of the hydroxyapatite coatings with respect to the loadings of 5N and 10N.

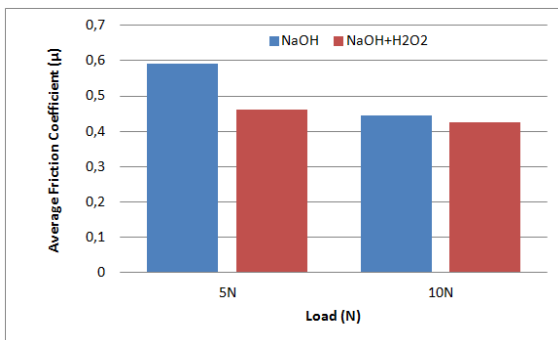


Figure 2: Average friction coefficients of the hydroxyapatite coatings with respect to the loadings of 5N and 10N.

Finally, it's found that, NaOH + H₂O₂ activation procedure applied HA coatings both had less amount in wear and less average friction coefficient when compared that of NaOH activation procedure.

REFERENCES

Hench L.L., 1991. Bioceramics from concept to clinic. *J. Am. Ceram. Soc.* 74 (7), 1487-1510.

Kokubo T., Kim H.M., Miyaji F., Takadama H., Miyazaki T., 1999. Ceramic-metal and ceramic-polymer composites prepared by a biomimetic process. *Composites Part A: App. Sci. and Man.* 30, 405-409.

Ciobanu, G., Carja, G., Ciobanu, O., Sandu, I., Sandu, A., 2009. SEM and EDX studies of bioactive hydroxyapatite coatings on titanium implants. *Micron.* 40, 143-146.

Li F., Feng Q.L., Cui F.Z., Li H.D., Schubert H., 2002. A Simple biomimetic method for Calcium phosphate coating. *Surface Coat. Tech.* 154, 88-93.

Bajpai, P.K., 1990. Ceramic Amino Acid Composites for Repairing Traumatized Hard Tissues. In: *Handbook of Bioactive Ceramics, vol.II: Ca-P and HA Ceramics.* Yamamuro, T., Hench, L.L., and Wilson-Hench, J., (Eds.), CRC Pres, Bato Raton, FL, pp. 255-270.

Yetkin, H., 2001. *Biomaterials in Orthopedy.* 8th Biomedical Science and Technology Symposium (BIOMED8), IL02, METU Ankara/TURKEY.

Bajpai, P.K., Fuchs, C.M., 1985. Development of a hydroxyapatite bone grout. In: *proceedings of the first annual scientific session of the academy of surgical research.* San Antonio, Texas, Hall, C.W. Ed., Pergamon Pres, New York, NY. pp. 50-54.

Capello, W.N., D'Antonio, J.A., Finberg, J.R., Manley, M.T., 1997. HA-coated total hip femoral components in patients less than fifty years old. *Jour. of Bone Joint Surg.* 79A, 1023-1029.

Tas A.C., Bhaduri S.B., 2004. Rapid coating of Ti6Al4V at room temperature with a calcium phosphate solution similar to 10×SBF. *Journal of Materials Research.* 19, 2742-2749.

Aydın, İ., Pasinli, A., Çetinel, H., 2012. "Determination of Fracture Toughness of Calcium Phosphate Coatings Deposited Onto Ti6Al4V Substrate by Using Indentation Technique", 2nd International Advances in Applied Physics & Materials Science Congress, 26-29 April., Antalya.

STUDY OF TRANSPORT OF LIQUIDS THROUGH GLASSY POLYMERS BY NEW EXPRESS DYNAMIC TECHNIQUE

Anton Belogorlov^{1,a}, Alexey Grekhov¹, Elena Pastukhova¹,
Yury Eremin¹, Alexey Yushkin², Alexey Volkov²

1. National Research Nuclear University MPhI, Molecular Physics Department, Moscow, Russian Federation

2. A.V.Topchiev Institute of Petrochemical Synthesis RAS, Moscow, Russian Federation
a. Anton Belogorlov (abelogorlov@mephi.ru)

ABSTRACT: In this work we investigated the transport of ethanol, propanol, ethylene glycol, glycerol and water through the high-permeability polymer poly[1-(trimethylsilyl)-1-propyne] (PTMSP). This membrane material can be used for organic solvent nanofiltration and membrane gas-liquid contactors. Membrane material was characterized by helium pycnometry and nitrogen adsorption. Measurement of liquid flow through the membrane was carried out by dynamic pressure decay method [Grekhov *at al.*, 2012] at temperatures of 20 to 90°C and pressure range of 10-200 bar. The results were interoperated in the frame of solution-diffusion model and quasi-hydrodynamic flow regime.

1. INTRODUCTION

The advances of membrane technology have led to development of new materials with unique properties for the separation of mixtures, such as glassy polymers. These materials have high mechanical and film-forming properties and used as membrane materials for gas and vapor separation, pervaporation, nanofiltration of organic mixtures and membrane gas-liquid contactor. This wide range of applications requires an understanding of material behavior during the operation, which is closely related not only with its original structure, but also with the interaction of the material and the separated mixture.

At present for the description of liquids transport [Geens, 2006], [Wijmans and Baker, 1995] through the material used as the control parameters the external conditions: pressure (P) и temperature (T); properties of liquids: surface tension (γ) and viscosity (η); structural characteristics of material: porosity (ϵ), tortuosity (τ) and surface area of pores

(S); parameters of liquid - material interaction: swelling (SD), sorption coefficient (K) and diffusion coefficient (D). In this paper study of transport of ethanol, propanol, ethylene glycol, glycerol and water through the high-permeability polymer poly[1-(trimethylsilyl)-1-propyne] (PTMSP) was carried out by dynamic pressure decay method [Grekhov *at al.*, 2012]. Liquids are different in both their physical and chemical properties and the type of the interaction with the polymer.

2. EXPERIMENTAL

The high free volume glassy polymer poly[1-(trimethylsilyl)-1-propyne] (PTMSP) was used as a membrane material. The PTMSP sample was synthesized and provided by Prof. V.S. Khotimsky (TIPS RAS) [Khotimsky *at al.*, 2003]. The dense PTMSP membranes were prepared also in TIPS RAS by method described in [Grekhov *at al.*, 2012]. Density, surface area and free volume was obtained by helium pycnometry and nitrogen sorption by

MICRO-ULTRAPYC 1200e and Nova 1200e (Any Gas) (Quantachrome Instruments, USA) presented in (Table1).

Table 1: PTMSP properties.

Density, g/cm ³	0.9634±0,0004
Surface area, m ² /g	855±26 (BET) 1309±40 (Langmuir)
Free volume, cm ³ /g	0.65±0.02

Surface tension and viscosity for ethanol, propanol, ethylene glycol, glycerol and water and temperature dependences was obtained from [Haynes, 2012].

Characteristics of experimental device presented in (Table 2)

Table 2: Characteristics of experimental setup.

Pressure range, bar	from 10 to 300
Volume range, cm ³	from 0.01 to 10
Pressure error, bar	< 1
Volume error, ml	< 0.04
Temperature, °C	from 30 to 90
Time, h	up to 10
Membrane sample diameter, cm	2
Membrane sample thickness, μ	from 10 to 100
Liquids	Any non-corrosive liquids
Sensitivity of fluid flux, ml/h or permeability, kg/(bar·h·m ²)	0.01 or 5·10 ⁻⁷

High sensitivity of experimental setup and wide range of pressure and temperature allow to carry out study of transport of liquids through glassy polymer.

3.RESULTS

Temperature dependences for permeability of investigated systems presented on Figure 1 – 4. In a permeation experiment, the permeability coefficient calculated as:

$$P = \frac{\Delta V \cdot \rho \cdot d}{S \cdot \Delta t \cdot \Delta p} \quad (1)$$

where ΔV is the volume of permeate [m³], ρ is the density of liquid [kg/m³], d is the membrane thickness [m], S is the membrane surface area [m²], Δt is the time interval [h], Δp is trans-membrane pressure [bar].

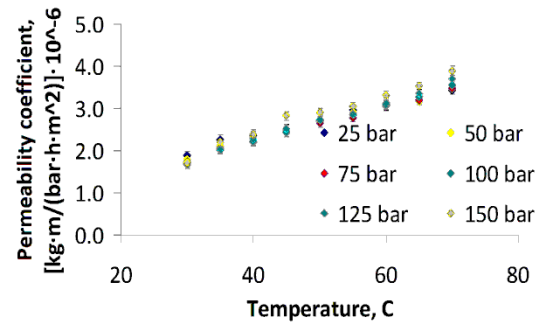


Figure 1: Temperature dependence of the permeability coefficient for PTMSP-EtOH system

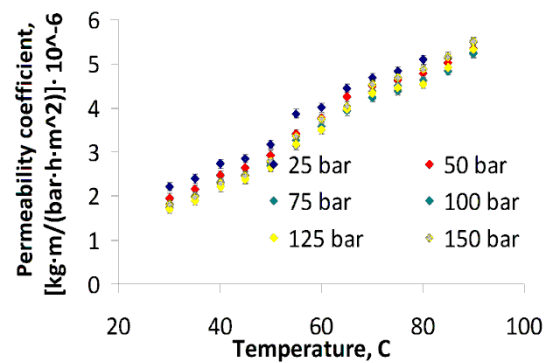


Figure 2: Temperature dependence of the permeability coefficient for PTMSP-PrOH system

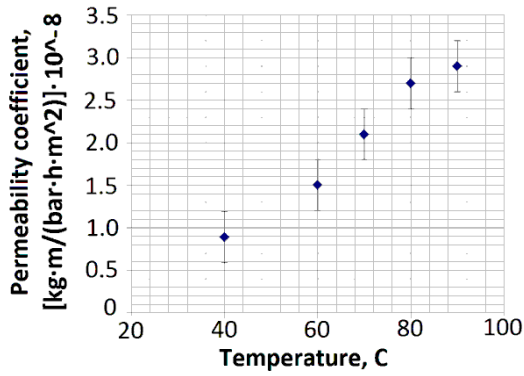


Figure 3: Temperature dependence of the permeability coefficient for PTMSP-ethylene glycol system

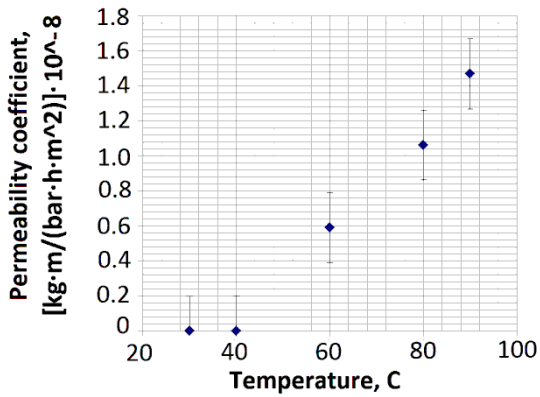


Figure 4: Temperature dependence of the permeability coefficient for PTMSP-water system

Transport of glycerol through the PTMSP under this study was not observed. Temperature increase leads to significant increase of permeability up to three times for ethylene glycol and threshold behavior of permeability for water.

4. DISCUSSION

For analysing results obtained for alcohols we used relation for permeability from [Geens, 2006]:

$$P(T) \sim \frac{1}{\eta(T) \cdot \gamma(T)} \quad (2)$$

For expression (2) the ratio of permeability, surface tension of liquid

and viscosity as a function of temperature was calculated as:

$$A(T) = \frac{P(T)}{P(30^0 C)}$$

$$B(T) = \frac{\gamma(30^0 C)}{\gamma(T)} \quad (3)$$

$$C(T) = \frac{\eta(30^0 C)}{\eta(T)}$$

The results presented on (Figure 5 and 6).

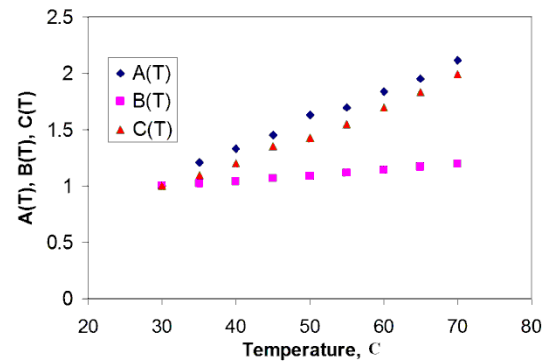


Figure 5: Temperature dependences for EtOH and PTMSP-EtOH system at 100 bar

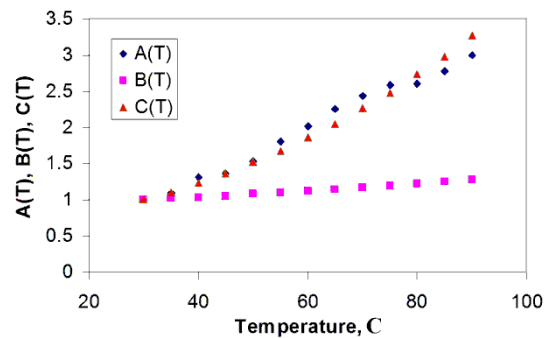


Figure 6: Temperature dependences for PrOH and PTMSP-PrOH system at 100 bar

A good agreement of dependences A(T) and C(T) for alcohols let us to conclude about quasi-hydrodynamic flow regime for such systems.

Diffusion transport was obtained for ethylene glycol – PTMSP system and water – PTMSP system. Temperature dependence for permeation data has a good agreement with solution - diffusion model [Wijmans and Baker, 1995]. The results of comparison presented on (Figure 7).

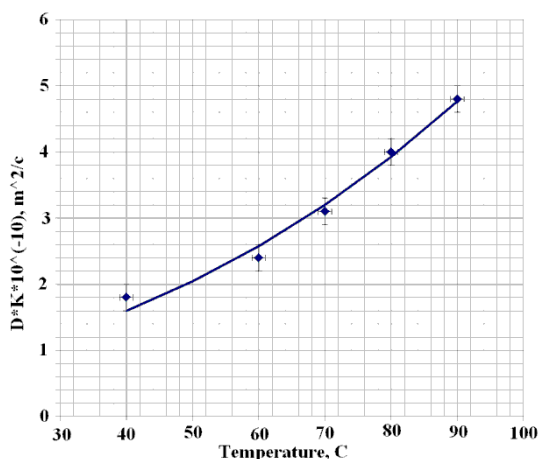


Figure 7: Temperature dependence of the permeability for PTMSP- ethylene glycol system (points – experiment, solid line - calculation)

Thus the experimental data and comparison with common models of liquids transport allow us to conclude about quasi-hydrodynamic regime for strongly interacting alcohol - PTMSP systems (sorption of liquids and swelling of polymer), for weakly interacting ethylene glycol - PTMSP system (sorption of liquid without swelling of polymer) and non-interacting water - PTMSP system (without sorption of liquid and swelling of polymer) as diffusion regime. For water - PTMSP system observed the effect of temperature threshold.

Acknowledgements: Authors express the gratitude to V.S. Khotimskii for providing of polymer samples.

REFERENCES

- Grekhov Alexey, Belogorlov Anton, Yushkin Alexey, Volkov Alexey, 2012. New express dynamic technique for liquid permeation measurements in a wide range of trans-membrane pressures *Journal of Membrane Science*, Volumes 390–391, 160.
- Geens J., Van der Bruggen B., Vandecasteele C., 2006. Transport model for solvent permeation through nanofiltration membranes, *Sep. and Pur. Tech.*, 48, 255.
- Wijmans J.G., Baker R.W., 1995. The solution–diffusion model: a review, *J. Membr. Sci.*, 107, 1.
- Khotimsky V.S., Tchirkova M.V., Litvinova E.G., Rebrov A.I., Bondarenko G.N., 2003. Poly[1-(trimethylgermyl)-1-propyne] and poly[1-(trimethylsilyl)-1-propyne] with various geometries: their synthesis and properties. *J. Polym. Sci., Part A: Polym. Chem.*, 41, 2133.
- Handbook of chemistry and physics: A ready reference book of chemical and physical data edited by William M. Haynes, David R. Lide, Thomas J. Bruno. 93. Boca Raton: CRC, 2012.

ADSORPTION KINETICS OF STEAM METHANE REFORMER (SMR) OFF GAS ON MIL-53(AL)

Alev Güneş Yerkesikli^{1,a} and Fehime ÇakıcıoğluÖzkan¹

1. Izmir Institute of Technology, Chemical Engineering, İzmir, TURKEY
a. Corresponding author (fehimeozkan@iyte.edu.tr)

ABSTRACT: Adsorption kinetics of steam methane reformer off-gas, H₂, CO₂, CH₄, CO in MIL 53 (Al) adsorbent was studied by using the Zero Length Column (ZLC) method. Analysis of the response curves obtained at 100 ml/min helium flow rate for the temperature range of 301 K-373 K was used to obtain diffusion coefficient and Henry's constant. The results show that the calculated diffusivity values are strongly dependent on temperature. The study reveals that transport of gases is controlled by intra and inter particle resistances.

1. INTRODUCTION

Hydrogen is an environmentally clean energy fuel. In the world, most of the hydrogen is produced by Steam Methane Reforming (SMR) processes because of its efficiency and lowest investment cost [Liu *et al.*, 2005]. SMR-off gas contains H₂ (86.5-52%), CO₂ (10-25%), CH₄ (1.3-8%), CO (0.25-10%). Hydrogen can be used as an energy source into a fuel cell. However its application needs high purity hydrogen: at least %99.99 for PEM fuel cells. As a result of that, it is critical to remove impurities from the off-gas to separate and optimize the hydrogen production. Adsorbent choosing is very important step for the rational design of the separation by adsorption process, where the diffusion coefficients in the crystals of adsorbents are also great importance. In the last decade, MOFs as a new family of nanoporous materials [Yaghi *et al.*, 1998] are assembled by directly bonding metal clusters with organic linkers. Zero length column (ZLC) method is relatively inexpensive method and can be used to measure the nature of the adsorption parameters: diffusion coefficient (D) and Henry constants (K) [Barcia *et al.*, 2005]. In literature there are limited numbers of kinetic studies on application of ZLC

technique. In this study the diffusion of SMR-off gas in a MIL-53(Al) adsorbent has been investigated by the

ZLC method. The effect of temperature on the diffusion character is investigated and the diffusion mechanism is also discussed. ZLC method validity was investigated and realistic diffusion coefficients in MIL 53 (Al) adsorbent were determined.

2. EXPERIMENTAL

ZLC system includes zero length column packed with adsorbent, oven (Binder ED 53), gas flow controllers (Aalborg, DFC 26) and mass spectrometer (Hiden HPR 20). Water vapour trap (Agilent) placed prior to the mass flow controllers reduces detriot effect of water vapor on gas adsorption. The ZLC cell consists of a small amount of adsorbent (≈ 2 mg) in powder form sandwiched between two sintered discs (35 μ m) (Alltech) in a 1/8-in. Swagelok fitting. Quartz wool was used to close remaining space of ZLC cell. The ZLC is located into an oven to regenerate and perform the adsorption experiments at desired temperature. Prior to adsorption ZLC was heated at 200 °C (1 Kmin⁻¹ heating ramp) to remove water

vapor and some impurities by flowing of helium at 10ml/min for 3 or 14 h. Adsorption were carried out at 303, 343 or 373 K by flowing adsorptive gas (3 % v/v) in the ZLC. When adsorbent reached equilibrium the desorption (response) curve was obtained by switching adsorptive to purge gas, He at 100 ml/min.

3. RESULTS AND DISCUSSION

ZLC is a macroscopic technique for measurement of diffusivity of pure and multicomponent gases in porous solids. It is well mixed cell minimizing the external heat and mass transfer resistance. In this study, CO₂, H₂, CO and CH₄ adsorbed ZLC packed with MIL53(Al) is purged at 303, 343 or 373 K and desorption (response) curves were obtained. The response curves were fitted with equation 1 and to obtain parameters D_c and L (Table 1) by using the crystal size (R_c=31.5x10⁻⁵ cm) volume (V_s =5.68x10⁻⁴ cm³) for 2.02 mg of MIL53(Al).

$$\frac{C}{C_o} = 2L \sum_{n=1}^{\infty} \frac{\exp(-\beta_n^2 D_c t / r^2)}{\beta_n^2 + L(L-1)} \quad (1)$$

The L value, at a given temperature, proportional to the flow rate (F) was used to calculate the equilibrium constant (K) (Eq. (2)).

$$L = \frac{1 \text{ purge flowrate } r^2}{3 \text{ crystals volume } K D_c} = \frac{\left(\frac{r^2}{D_c}\right)}{\left(\frac{3KV_s}{F}\right)} \quad (2)$$

The L value is an important parameter for determining whether the transport process is controlled by intraparticle resistance (equilibrium) or interparticle resistance) diffusion (Brandaniet al., 1996). If the L value is very low (<0.5), i.e., intraparticle transport is much faster than interparticle one and desorption process will be controlled by interparticle mass transfer

resistance. If L goes ∞, mass transfer in ZLC is controlled by intraparticle resistance (Brandi and Ruthven, 1996).

From the L values obtained (0<L<10) for CO₂, H₂, CO and CH₄ gases it can be concluded that both interparticle and intraparticle resistance contribute the mass transfer. The parameters obtained (Table 1) are affected by temperature in a consistent way; the diffusivity of CO₂, CH₄, H₂, CO in the pores increases with increasing temperature; equilibrium constant on the surface of the pores decreases with increasing temperature.

There is evidence for Knudsen is transport mechanism of these gases in the pores: the calculated lowest mean free path is 10³ times higher than average pore diameter of MIL 53(Al); temperature dependency is lower for transport diffusivity than molecular diffusivity.

As seen from Table 1 the Henry's law constant decreases with increasing temperature, as expected for physical adsorption. The Van't Hoff equation with neglecting the differences in heat capacities between the adsorptive and adsorbate, can be used to calculate heat of adsorption:

$$K = K_0 \exp(-\Delta H / RT) \quad (3)$$

Table 1: Transport parameters of SMR off-gas adsorption on MIL 53 (Al)

Gas	T °C	L	100*D/R ² (s ⁻¹)	D (m ² /s) (10 ⁻¹²)	K (10 ⁺³)
CO ₂	34	2.88	1.40	3.44	146
	70	2.95	3.27	8.07	61
	100	3.10	3.81	9.40	34
CH ₄	34	3.56	1.54	3.80	117
	70	3.82	3.29	8.10	47
	100	5.10	4.05	9.98	28
H ₂	34	2.3	1.38	3.40	203
	70	2.65	2.47	6.10	89
	100	2.72	2.60	6.40	83
CO	34	1.22	1.54	3.8	163
	70	3.82	2.79	6.9	55
	100	4.2	3.23	7.9	43
Gas	T °C	L	100*D/R ² (s ⁻¹)	D (m ² /s) (10 ⁻¹²)	K (10 ⁺³)
CO ₂	34	2.88	1.40	3.44	146
	70	2.95	3.27	8.07	61
	100	3.10	3.81	9.40	34
CH ₄	34	3.56	1.54	3.80	117
	70	3.82	3.29	8.10	47
	100	5.10	4.05	9.98	28
H ₂	34	2.3	1.38	3.40	203
	70	2.65	2.47	6.10	89
	100	2.72	2.60	6.40	83
CO	34	1.22	1.54	3.8	163
	70	3.82	2.79	6.9	55
	100	4.2	3.23	7.9	43

The heat of adsorption calculated is listed in Table 2. Negative heat of adsorption values indicates that the adsorption is exothermic; heat is evolved. Specific (Dipole moment and quadrupole moment) and Nonspecific (polarizability, dispersion and repulsion) interactions are affected to the heat of adsorption values.

The contribution of nonspecific interactions is pronounced on the order of heat of adsorption values:

$$\text{CO}_2(49,4\text{kJ/mol}) > \text{CH}_4(47,1 \text{ kJ/mol}) > \text{CO}(38,7 \text{ kJ/mol}) > \text{H}_2(34,1\text{kJ/mol})$$

As a result, the highest heat of adsorption values were obtained for CO₂. Polarizability is the decisive property for adsorption of these gases.

Table 2: Sorbate properties and heat of adsorption, activation energy values

Adsorptive	Temperature range(°C)	E (kJ/mol)	ΔH (kJ/mol)	Polarizability ×10 ²⁵ /cm ³	Kinetic diameter Å	Dipole moment×10 ¹⁸ esu cm	Quadrupole moment×10 ²⁶ esu cm ²
CH ₄	34-100	41.4	-47.1	25.93	3.8	0	0
CO		40.9	-38.7	19.5	3.6	0.1098	2.5
CO ₂		43.9	-49.4	29.11	3.3	0	4.30
H ₂		41.2	-34.1	8.04	2.8	0	0.662

The temperature dependence of the diffusivity, correlated by the Arrhenius equation was used to calculate the diffusive activation energy E;

$$E = -R \left(\frac{\partial \ln D}{\partial (1/T)} \right) \quad (4)$$

where T is the temperature (K) and R is the ideal gas constant. The activation energies derived from the diffusivity data as described above are listed in Table 2. Effect of pore size on transport diffusivity is not clear

4. CONCLUSIONS

The adsorption kinetics for SMR off-gas (CO₂, H₂, CO and CH₄) on MIL 53(Al) was measured in the 301-373 K temperature range by the ZLC method. The experimental data were well correlated with the model (R² > 0.98 and SSE > 10⁻⁷). Both the interparticle and intraparticle resistance contribute the mass transfer of CO₂, H₂, CO and CH₄. Heat of adsorption is the highest for CO₂ depending on its high polarizability. The diffusivity ration is about 1 for the binary gas. The diffusivity values are dependent on temperature.

REFERENCES

- Alev Güneş Yerkesikli, PhD thesis, Adsorption of Reformer Off-Gas on NaX Zeolite and Metal Organic Framework, (MIL53(Al)): Equilibria and Kinetics, Izmir Institute of Technology, İzmir, 2013
- Barcia, P. S., Silva, J. A. C., Rodrigues, A. E., 2005. Adsorption equilibrium and kinetics of branched hexane isomers in pellets of BETA zeolite. *Micropor Mesopor Mat*, 79 (1-3), 145.
- Brandani, S., Ruthven, D.M., 1996. Analysis of ZLC Desorption Curves for Gaseous Systems. *Adsorption*, 2, 133.
- Liu, X. W., Li, J. W., Zhou, L., Huang, D. S.; Zhou, Y. P., 2005. Adsorption of CO₂, CH₄ and N₂ on ordered mesoporous silica molecular sieve. *Chem Phys Lett.*, 415 (4-6), 198.
- Loos, J-B W.P., Verheijen, P.J.T., Moulijn, J.A., 2000. Improved Estimation of Zeolite Diffusion Coefficients from Zero-Length Column Experiments, *Chemical Engineering Science.*, 55, 51

EXPERIMENTAL AND THEORETICAL STUDY ON STYRAX OFFICINALIS ACTIVATED CARBON ADSORPTION OF LEAD AND ZINC FROM AQUEOUS SOLUTION

Tolga Depci^{1,a}, Ali Riza Kul², Keith A. Prisbrey¹, Yunus Onal³ and Jan D. Miller¹

1. University of Utah, Department of Metallurgical Engineering, Salt Lake City, UT, USA
 2. Yuzuncu Yil University, Department of Chemistry, Van, Turkey
 3. Inonu University, Department of Chemical Engineering, Malatya, Turkey
- a. Corresponding author (tdepcei@gmail.com)*

ABSTRACT: Activated carbon derived from *Styrax officinalis* seeds (Balıkesir, Turkey) was investigated as an alternative low-cost adsorbent for the removal of lead and zinc from aqueous solution. Activated carbon (AC) was produced chemically with a reasonable yield (38 %) and was found to have a remarkable surface area (1212 m²/g) with a well-developed pore structure. To determine the nature of the adsorption process, the effects of initial metal concentration (20 – 50 mg/L) was investigated using a batch adsorption technique. The adsorption isotherm data were best fitted by Langmuir model and the adsorption capacity for Pb (II) was found to be higher than adsorption capacity for Zn (II) at 298 K. Preliminary ab-initio simulations (using Gaussian 09) were also performed for both Pb and Zn adsorption. The reactivity calculations from molecular orbital theory reveal that lead has a higher reactivity towards the graphite surface in comparison to zinc. Independent Gibb's free energy calculations (using MOPAC) further reinforce the fact that lead has a higher tendency to adsorb at the graphite surface than zinc at 298K.

1. INTRODUCTION

Lead and zinc are the most utilized important heavy metals and used by many industries in large amounts. However, these heavy metals are not biodegradable and tend to accumulate in living organisms and cause several acute and chronic toxic effects on human health [Gaballah and Kilbertus, 1998; Veli and Alyuz, 2007].

A wide range of various treatment methods (namely, ion exchange, chemical precipitation, membrane system, coagulation and adsorption) have been reported to be used for removal of heavy metals [Fu and Wang, 2011]. Among the methods, adsorption has been universally accepted as one of the most effective pollutant removal processes. Adsorption for removal of Pb and Zn from industrial effluents is mostly confined to the use of granular/powdered activated carbon as

adsorbent. However, commercial activated carbon is expensive and to overcome this disadvantage, considerable attention has been given to the preparation of activated carbons derived from readily available and low cost materials and waste materials, like lignite and apple pulp etc. [Depci 2012; Depci *et al.*, 2012].

The current research focuses on finding a plausible explanation to understand the adsorption Pb and Zn by commercial activated carbon and activated carbon prepared from local biomass, as an alternative low-cost adsorbent. The emphasis of this research is to address the explanation by experimentation and with the aid of computational chemistry tools. In this regard, laboratory adsorption experiments for removal of Pb and Zn from aqueous solution were carried out

using activated carbon (AC) derived from *Styrax officinalis* seed. *Styrax officinalis* seed was selected as a carbon source, since it is a low-cost lignocellulosic material abundantly available in Balikesir (Turkey) and if effective for adsorption could represent an inexpensive source of activated carbon.

Molecular dynamics simulations (MDS) can be used for description of the dynamic behaviour of selected species in the aqueous phase [Allen, 2004].

2. MATERIALS AND METHODS

2.1. Preparation and Pore Size Distribution of AC

Crushed *Styrax officinalis* seeds (particle size less than 2 mm) were mixed with KOH (weight ratio of 1:1) and the required amount of distilled water was added to this mixture. Then, the mixture was dried at 105° C in a furnace to obtain an impregnated sample. The impregnated sample was heated to the activation temperature of 800° C for 1 hour under N₂ flow (100 ml/min) at the rate of 10° C.min⁻¹. The obtained activated carbon was filtered and washed with distilled water several times to remove residual chemicals.

Surface area, pore size distribution and pore volume of AC was measured from nitrogen adsorption isotherms at 77 K in the range of 10⁻⁶ to 1 relative pressures by a Tri Star 3000 (Micromeritics, USA) surface analyzer. Pore size distribution and the features of pore structure were determined using BJH methods and t-plot, respectively. Prior to the measurement, the sample was degassed at 400 °C for 2 h.

2.2. Adsorption experiments

Adsorption studies were conducted in routine manner by the batch technique due to its simplicity and reliability. 0.1 g

of AC was introduced into test tubes (50 ml) containing various concentrations with 25 ml aqueous solutions of Pb (II) or Zn (II) at pH 4.5 - 5. The mixtures were shaken in a thermally controlled automatic shaker at 110 rpm at different temperatures for a prescribed time to attain equilibrium. Adsorption isotherms using seven solutions with different metal ions concentrations (i.e., 20, 25, 30, 35, 40, 45, 50 mg/L) and their parameters were calculated by non-linear method which was determined using the solver add-in with Microsoft's spreadsheet, Microsoft Excel.

The amount of Pb (II) and Zn (II) adsorbed on AC, *q* (mg/g.) was calculated by the mass balance equation.

$$q = \frac{(C_0 - C) * V}{W}$$

where, *C*₀ (mg/l) is the initial metal ion concentrations and *C* (mg/l) is residual metal ion concentrations in solution at time *t*, *V* (L) and *W* (g) are the volume of the solution and the weight of the dry activated carbon.

2.3. Computational Chemistry

Computational chemistry has been used with a variety of activated carbon models [Allouche *et al* 2012; Ferro *et al* 2013]. Two computational strategies were used: Amber's steered molecular dynamics (SMD) capability, and Amber's Molecular Mechanics/Poisson Boltzmann Surface Area (MMPBSA) procedure. Avogadro [Hanwell, 2012] and VMD (Beckman Institute) were also used to build, optimize, and visualize the different atom-cluster models of activated carbon.

For density functional theory (DFT), calculations Gaussian 09 with SDD pseudopotentials and a B3LYP basis set were used. For the semi empirical calculations Mopac 12 [Stewart, 2012] and a PM6 basis set were used. For the

force field calculations, Amber 12 [Case et al 2012] with GAFF force fields for graphite and UFF force fields were applied for lead and zinc.

3. RESULTS AND DISCUSSION

3.1. Experimental Part

The BET surface area of AC was found to be 1212 m²/g and the micro-pore area constitutes of 76.30 % of the total BET surface area with a well-developed pore structure and an average pore diameter of 2.16 nm. It appeared that activated carbons were dominantly micropores. It is produced with a reasonable yield, 38 %.

The adsorption isotherm data were fitted using these well-known two-parameter, Langmuir [Langmuir, 1918] and Freundlich [Freundlich, 1906] isotherm models. The non-linear isotherm parameters were determined using the solver add-in with Microsoft's spreadsheet, Microsoft Excel. The adsorption isotherm for Pb (II) and Zn (II) in single element system can be identified using Langmuir models according to R² values. Therefore, only the Langmuir equation and plot (Figure 1) are given in the text.

$$\text{Langmuir Equation } q_e = \frac{Q_0 b C_e}{(1 + b C_e)}$$

where, C_e is the equilibrium metal ions concentrations in the aqueous phase (mg/L), q_e is the adsorption capacity (mg/g), b (L/mg) and Q₀ (mg/g) are Langmuir isotherm constants, where Q₀ signifies the theoretical monolayer capacity. The adsorption capacities of heavy metals decrease in the order of Pb(II) (Q₀, 17.26 mg/g) < Zn(II) (Q₀, 12.43 mg/g). McBride [1989] declared that the specific adsorption of heavy metals in an affinity sequence is related to ionic potential, electronegativity and softness parameters. The electronegativity of Pb(II), 2.33, is

greater than that of Zn(II), 1.65 [Zhang, 2011], so the adsorption capacity of Pb(II) is expected to be greater than that of Zn(II). Minceva et al. [Minceva et al., 2008] claimed that the enthalpy of ions is the factor to explain the adsorption order at adsorbent surfaces. Values of enthalpy of hydration decrease depending on atomic number and ionic size, so Pb (II) ions have greater accessibility at the activated carbon surface than Zn (II). The same order is followed in the present study.

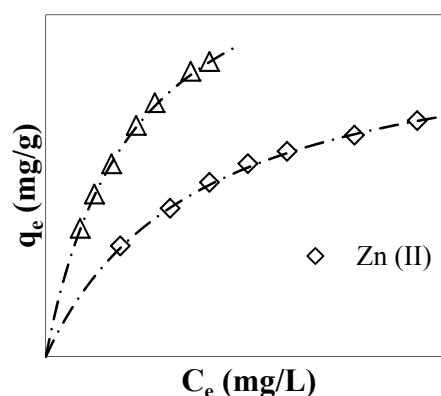


Figure 1: The plots of non-linear isotherm Langmuir model for the removal of Pb (II) and Zn (II) (contact time, 40 min; pH, 4.5 - 5.0; AC dose, 4g/L).

3.2. Computational Chemistry Analysis

Since the AC has been shown to have a graphitic structure, the first model consisted of two graphite unit cells (Figure 2). Total energy was calculated using semi empirical quantum mechanics, and upon bonding to the surface lead and zinc adsorption energies were compared using:

$$\text{Energy} = \text{complex} - \text{receptor} - \text{metal}$$

where 'complex' is the energy of graphite with the metal adsorbed, 'receptor' is the energy of graphite alone, and 'metal' is the energy of zinc or lead alone. Calculating total energy at the PM6 level in Mopac 12 for complex, receptor, and

metal gave an adsorption energy of -2.9 eV for zinc as compared to lead's -23.8 eV. The more negative energy of adsorption for lead is associated with its greater propensity to be adsorbed by AC.

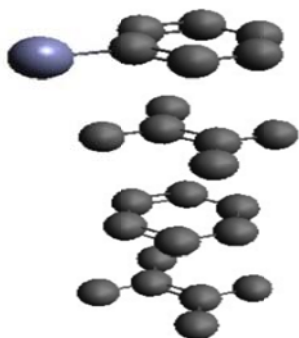


Figure 2: Two graphite unit cells with zinc adsorbed (ball and stick representation). Blue big ball represents zinc.

In the second model consisting of a larger graphite chunk embedded in water (Figure 3), lead and zinc adsorption energies were compared using force field calculations with Amber 12's steered molecular dynamics (SMD) and Poisson-Boltzmann surface analysis (MMPBSA). In the SMD simulation an artificial spring was created between a point on a graphite surface and a lead or zinc ion ~20 Angstroms out. Through use of this artificial spring the ions were aimed at an irregularity in the graphite surface where basal and edged planes met. As the simulation time progressed in 0.5 femto-second steps and the ion reached the surface, total energy increased and ended on a high point. The increase for lead was ~10 kcal/mol as compared to zinc's ~30 kcal/mol. These increases occurred despite the decrease in energy expected from relaxing a stretched spring. From these force field results the smaller increase in energy for lead ion to reach the surface was associated with a greater propensity for adsorption.

In the MMPBSA analysis the influence of water, including ion desolvation

through adsorption, was calculated using statistical mechanic's ensemble averages over time. The energetic for a hypothetical gas phase without water was calculated from van der Waals and electrostatic forces.

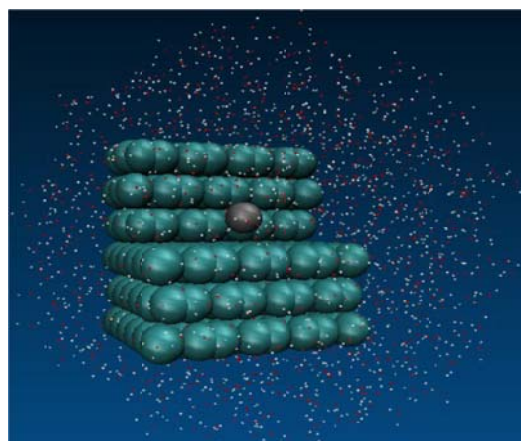


Figure 3: Graphite chunk and adsorbed zinc ion (van der Waals radii representation) embedded in water (shown as dots).

These were then combined with water values calculated from the Poisson Boltzmann equation and water cavity corrections. Finally, the change in Gibbs free energy of adsorption was calculated. Energy decreased by -12.8 kcal/mol for lead adsorption, and by only -3.1 kcal/mol for zinc adsorption. Understanding this force field result was straight forward. In this case the larger decrease in Gibbs free energy upon adsorption was also associated with lead's greater propensity to be adsorbed. Although the energetics of adsorption had different values depending on the DFT vs. semi empirical vs. force field calculations, all gave the same trend: the propensity for lead adsorption by graphite was higher than zinc. This was also confirmed by a frontier orbital analysis where the smaller difference between the graphite's highest occupied molecular orbital (HOMO) and the adsorbing ion's lowest unoccupied molecular orbital (LUMO) indicates a greater reactivity.

For example, lead's difference was 0.84 eV as compared to zinc the difference for 3.10 eV in a semi empirical quantum calculation. The energetic distance between empty receptive orbitals of lead ion and filled outer electron orbitals of graphite was smallest, indicating greater reactivity of lead. Thus all computational chemistry calculations indicate that graphite has a greater adsorption potential for lead.

4. CONCLUSION

Activated carbon was produced from *Styrax officinalis* Seed with a reasonable yield of 38 % and has remarkable surface area (1212 m²/g). The micro-pore area constitutes of 76.30 % of the BET surface area with a well-developed pore structure having an average pore diameter is 2.16 nm. The adsorption isotherms of Pb(II) and Zn(II) on AC is consistent with the Langmuir model. The adsorption capacities of heavy metals decrease in the order of Pb(II) (17.26 mg/g) < Zn(II) (12.43 mg/g). The adsorption energies of Pb and Zn were calculated as -23.8 eV -2.9 eV, respectively. The larger energy of adsorption for lead was associated with its greater propensity to adsorb. The Gibbs free energies of adsorption changes for Pb and Zn were calculated as -12.8 kcal/mol and -3.1 kcal/mol respectively. These calculations also indicate that lead's greater propensity to be adsorbed. Experimental results and computational chemistry analysis results compatible with each other, indicating greater reactivity for lead.

REFERENCES

- Allen, M.P., 2004. Computational Soft Matter: From synthetic Polymers to Proteins. John von Neumann Institute for Computing, Julich, Germany, 1.
- Allouche, A., and Krstic. P.S., 2012. Atomic hydrogen adsorption on lithium-doped graphite surfaces, *Carbon* (50), 510.
- Case, D.A., Darden, T.A., and Cheatham, T.E. , III et al 2012. AMBER 12, University of California, San Francisco.
- Depci, T., 2012. Comparison of activated carbon and iron impregnated activated carbon derived from Gölbaşı lignite to remove cyanide from water, *Chem. Eng. Journal* (181) 467.
- Depci, T., Kul, A.R., and Onal, Y., 2012. Competitive adsorption of lead and zinc from aqueous solution on activated carbon prepared from Van apple pulp: Study in single- and multi-solute systems, *Chem. Eng. Journal* (200-202), 224.
- Ferro, Y., Fernandez, N., Allouch, A., and Linsmeier, C., 2013. Adsorption of beryllium atoms and clusters both on graphene and in a bilayer of graphite investigated by DFT. *J. Phys.: Condens. Matter* (25) 015002.
- Fu, F., and Wang, Q., 2011. Removal of heavy metal ions from wastewaters: A review, *J. Environ. Man.* (92), 407.
- Freundlich, H., Adsorption in solution, *Phys. Chem. Soc.* (40), 1361.
- Gaballah, I., and Kilbertus, G., 2007. Recovery of heavy metal ions through decontamination of synthetic solutions and industrial effluents using modified barks, *J. Geochem. Explor.* (620), 241.
- Hanwell, M.D., Curtis, D.E., Lonie, D.C., Vandermeersch, T., Zurek, E., and Hutchison, G.R., 2012. Avogadro: An advanced semantic chemical editor, visualization, and analysis platform, *J. Cheminformatics*, 4.
- Langmuir, I., 1918. The adsorption of gases on plane surfaces of glass, mica and platinum, *J. Am. Chem. Soc.* (40), 1361.
- McBride, M.B., Reactions controlling heavy metal solubility in soils, *Adv. SoilSci.* (10), 1.
- Minceva, M., Fajgar, R., Markovska, L., and Meshko, V., 2008. Comparative study of Zn²⁺, Cd²⁺ and Pb²⁺ Removal from water solution using natural clinoptilolitic zeolite and commercial granulated activated carbon. Equilibrium of adsorption, *Sep. Sci. Technol.* (43), 2117.
- Stewart, J.J.P., 2012. Stewart Computational Chemistry, Colorado Springs, CO, USA, [HTTP://OpenMOPAC.net](http://OpenMOPAC.net).
- Veli, S., and Alyuz, B., 2007. Adsorption of copper and zinc from aqueous solutions by using natural clay, *J. Hazard. Mater.* (149), 226.
- Zhang, M., 2011. Adsorption study of Pb(II), Cu(II) and Zn(II) from simulated acid mine drainage using dairy manure compost, *Chem. Eng. J.* (172), 361.

HYDRAULIC CONDUCTIVITY AND SUCTION CHARACTERIZATION OF GÖRDES ZEOLITE BLOCKS

Seda Durukan^{1,a}, Arif Ş. Kayalar² and Ender Başarı³

1. Celal Bayar University MOSB MYO, Construction Technology, Manisa, Turkey

2. Dokuz Eylül University Engineering Faculty, Civil Engineering, İzmir, Turkey

3. Celal Bayar University Engineering Faculty, Civil Engineering, Manisa, Turkey

a. Corresponding Author (seda.durukan@cbu.edu.tr)

ABSTRACT: Zeolite is a favorable micro-porous material in many industrial applications as commercial adsorbents, e.g., agriculture, radioactive cleanup, water, air, gas and wastewater treatment, mining and landfilling applications, etc. Zeolites are usually defined by their porosities, pore size distributions and adsorption capacities. However, depending on the developing studies regarding zeolites, more characterization knowledge is needed. In instance, lately, zeolite bentonite mixtures are offered for use of liner materials. In this study, the hydraulic conductivity and suction characteristics of block zeolite (Clinoptilolite) samples from Gördes, Manisa, Türkiye is identified. When studying with a porous material, it's very critical to know the hydraulic conductivity and the suction characteristics of the porous grain itself. In this regard, block samples of 5 cm in diameter with varying heights were subjected to falling head type hydraulic conductivity tests after CO₂ permeation through the blocks in order to prevent trapped air formation. The suction characteristics were also determined on compacted zeolite samples of 4 cm in diameter for varying grain sizes in addition to zeolite blocks by using filter paper method with Whatman No.42 filter papers. The results are drawn and discussion is presented.

1. INTRODUCTION

Many studies had been conducted on preventing subsurface contamination such as leakage through liners under landfills. Landfills are usually lined with low permeability materials, such as geomembranes and/or mineral layers that can contain leachate produced by the waste [Klepppe & Olson, 1985; Othman et al., 1994; Lin & Benson, 2000; Abichou et al., 2002]. In general compacted bentonitic mixtures are used as layers for their low hydraulic conductivity and high adsorption capacity. Sand bentonite mixtures (SBMs) are widely used as a liner. Lately, zeolite bentonite mixtures (ZBMs) were proposed as an alternative to SBMs depending on the adsorption capacity of zeolite [Kayabali, 1997; Tuncan et al., 2002; Kaya & Durukan, 2004].

Compacted liners are naturally unsaturated. Nevertheless, soil suction is one of the most essential parameter describing soil moisture condition for unsaturated soils in landfill liners [Fredlund & Rahardjo, 1993; Fredlund et al., 1995; Agus et al. 2010]. Thus, the suction characteristics of liner materials are of primary interest for use of a liner. Soil suction has two components matric suction and osmotic suction. Matric suction corresponds to the capillary rise in voids and particle surface hydration and the osmotic suction arise from the presence of dissolved solutes in the pore fluid [Bulut et al., 2001].

Zeolite is a tecto-silicate and in contrast to other tecto-silicates such as feldspar, quartz the zeolite framework is remarkably open. It shows infinite, three-

dimensional systems of tunnels and cages where the exchangeable cations as well as water molecules are situated [Jacobs & Förstner, 1999]. These channels and cages are adequate for adsorbing molecules smaller than these channels and/or tunnels so, in this regard, zeolites are called as “molecular sieves”. Zeolite minerals as micro-porous materials would affect the hydraulic conductivity of the mixture. Thus, the hydraulic conductivity of zeolite itself is important as it will directly have an influence on the hydraulic conductivity of the mixture.

In this study, based on the limited discussion above, suction characteristics of zeolite grains having different grain sizes and zeolite blocks were investigated. In addition the saturated hydraulic conductivity of zeolite blocks was determined.

2. BRIEF BACKGROUND

Zeolite minerals have been searched for their adsorption characteristics, pore size distributions, porosities and etc. [Mondale et al., 1994; Özkırım & Yörükoğulları, 2005]. Lately, zeolite is also proposed for use of a landfill liner material. The most critical design parameter of a liner is the hydraulic conductivity. The hydraulic conductivity of a liner is desired to be equal or lower than 10^{-9} m/s.

ZBMs are found to have higher hydraulic conductivities when compared to that of SBMs. The reason for this situation was contributed to the porous structure of zeolite minerals [Ören et al., 2011].

Soil suction characteristics of ZBMs were investigated in the study of Durukan & Aksoy (2012). The authors revealed that the decrease in matric suction values while water content increases are found to be more significant than total suction values. They also concluded that, similar

to water content relation; increase in matric suction values while bentonite content increases are found to be more significant than total suction values.

3. MATERIALS AND METHODS

3.1. Materials

Commercial fine zeolite, granular zeolite and zeolite blocks are used to indicate their suction characteristics by using filter paper (FP) method. Natural zeolite was supplied from Gördes, Manisa, Türkiye.

The zeolite blocks were 5 cm in diameter. The sampling stage of the blocks can be seen in Figure 1. From Figure 1, it's seen that while determining the hydraulic conductivity of zeolite blocks, samples were collected from different directions in order to investigate the anisotropic conditions.



Figure 1: The sampling stage of zeolite blocks.

Besides hydraulic conductivities of zeolite blocks, zeolite grains and blocks were also investigated for their suction characteristics. Compacted powdered zeolite (-No.200), compacted granular zeolite (1.18-2 cm) and zeolite blocks (Ø 5 cm) were investigated for their suction parameters which are matric and total suction.

The compacted samples are prepared by standard effort having a diameter of 4 cm in plexiglass tubes. The water contents of the powdered, granular, and block samples were 30%. The tests for all samples were run by using distilled water.

3.2. Methods

The matric and total suction of the samples can easily be determined by filter method which is a common, inexpensive and easy technique. In this study, Whatman no.42 type filter papers are used. The system, which can be seen in Figure 2, is held closed at a constant temperature of 21 °C for 7 days to reach the equilibrium in the incubator (ASTM D5298-03).

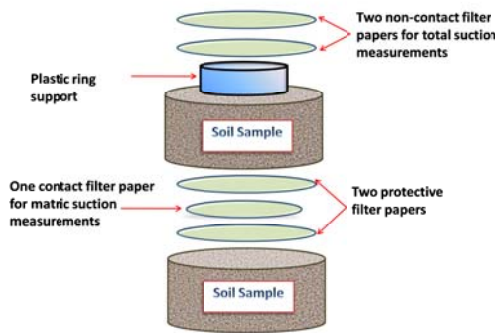


Figure 2: The suction measurement system.

The test procedure and calibration curves for filter papers are defined and given in ASTM D 5298-03. Some researchers proposed different calibration curves for matric and total suction calculation (Chao, 2007). However, in this study, ASTM procedure is followed which offers a single calibration curve for both matric and total suction calculation (Figure 3).

Agus et al. (2010) shows that measuring total suction by filter paper method is somewhat complicated. The authors revealed that the measurement of total suction needed longer time when compared to matric suction. They concluded that the closed system to measure the total suction characteristics

needed longer time in order to reach equilibrium of dissolved solutes.

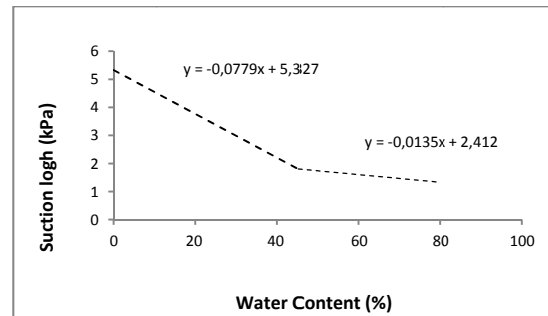


Figure 3: The calibration curve given in ASTM D5298-03.

The hydraulic conductivity was measured with a flexible wall cell and falling head procedure was applied. However, before permeation, to avoid trapped air formation and to fasten the permeation process, carbon dioxide (CO₂) percolation through the samples was recommended.

According to Lee & Black (1972), in order to reach full saturation quicker and easier, it's convenient to use a gas which can dissolve in water better. As Henry's Constant for CO₂ is much larger than that is for air, when compared to air it's easier to reach full saturation when CO₂ was percolated through the sample. In other words, by percolating CO₂, water permeation would be easier just because that CO₂ would dissolve in water easier when compared to air.

An instance, Mulilis et al. (1975) percolated CO₂ through a sand sample for approximately about 15 minutes. Afterwards, the samples were subjected to water permeation. In addition, the permeation measurements began till the sample was observed to have no bubbles which meant that there were no CO₂ left in the sample. Similarly, in order to avoid the trapped air bubbles in the block zeolite sample, the CO₂ percolation was applied as seen in Figure 4. The

permeation of CO₂ was controlled depending on the observed bubbles from the outflow line (Figure 5). After the CO₂ percolation process, each flexible wall cell was attached to the falling head permeation system.

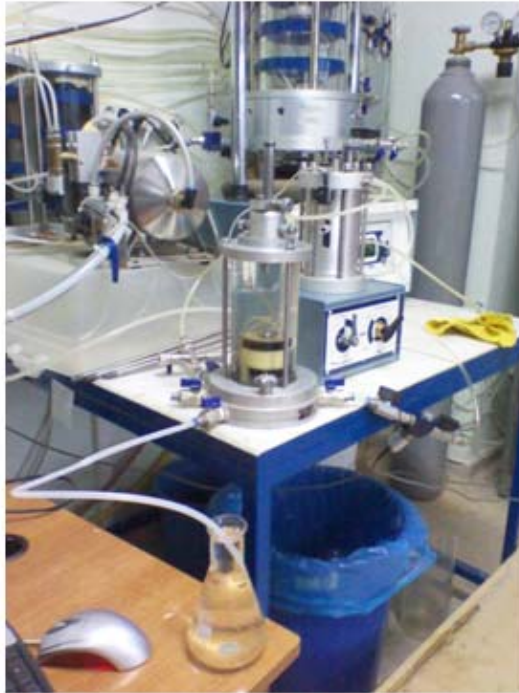


Figure 4: The CO₂ permeation through the block samples.



Figure 5: The control of the bubbles formed from the CO₂ permeation through the block samples.

4. RESULTS

The suction behavior of compacted powdered zeolite, compacted granular zeolite and zeolite blocks was investigated. The matric and total suction of samples are given in Figure 6. The total suction had a fluctuating trend. However, the matric suction increased with an increase in grain size. The total suction results support the findings of Agus et al. (2010) who suggested that the total suction measurement needed longer time to reach the equilibrium.

Both matric and total suction of the block sample are higher than both the powdered and granular zeolite samples. The reason of this situation may be due to the higher void ratio of the block sample which is known to have continued pores in its structure. Meaning that, the voids in a sample may be in contact to each other which resulting in higher matric suction. Matric suction might have increased due to an increase in continuity of the pores while the grain size increases.

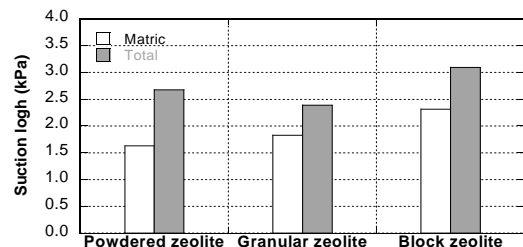


Figure 6: Suction characteristics of powdered, granular and block zeolite samples.

After the CO₂ percolation 3 samples from different directions were run for hydraulic conductivity tests. The average hydraulic conductivity of block zeolite samples was found to be 1.1×10^{-9} m/s. When compared to impervious sand grains, zeolite in a bentonitic mixture seems to increase the hydraulic conductivity of the mixture supporting the study of Ören et al. (2011).

5. CONCLUSIONS

1. Block zeolite samples were found to have more suction than granular and powdered zeolite samples have.

2. The higher matric suction for block samples is contributed to the presence of the tunnels and cages in zeolite structure. Moreover, it's concluded that these pores may be continuous which causes higher matric suction values.

3. The average hydraulic conductivity of zeolite blocks was found to be 1.1×10^{-9} m/s.

REFERENCES

- Abichou, T.H., Benson, C.H., Edil, T.B., 2002. Micro-structure and hydraulic conductivity of simulated sand-bentonite mixtures. *Clays and Clay Minerals* 50 (5), 537-545
- Agus, S.S., Schanz, T., & Fredlund, D.G., 2010. Measurements of Suction versus Water Content for Bentonite-Sand Mixtures. *Canadian Geotechnical Journal*, 47, 583-594
- American Society for Testing and Materials, 1999. Annual book of the ASTM standards, Vol. 04-08, West Conshohocken, PA
- Bulut, R., Lytton, R.L. & Wray, W.K., 2001. Suction measurements by filter paper. *Expansive Clay Soils and Vegetative Influence on Shallow Foundations*, ASCE Geotechnical Publication (eds. C. Vipulanandan, M.B. Adison, and M. Hasen), ASCE, Reston, Virginia, 115, 243-261
- Chao, K.C., 2007. Design principles for foundations on expansive soils. Dissertation, Colorado state University, Fort Collins, Colorado
- Durukan, S. & Aksoy, Y.Y., 2012. A study on the suction characteristics of compacted zeolite-bentonite mixtures. *Proceedings of 3rd International Conference on New Developments in Soil Mechanics and Geotechnical Engineering*,
- Fredlund, D.G. & Rahardjo, H., 1993. *Soil Mechanics for Unsaturated Soils*. John Wiley and Sons, Inc.
- Fredlund, D.G., Gan, J.K.M. & Gallen, P., 1995. Suction Measurements on Compacted Till Specimens and Indirect Filter Paper Calibration Technique. *Transportation Research Record*, 1481
- Jacobs, P.H., & Förstner, U., 1999. Concept of subaqueous capping of contaminated sediments with active barrier systems (ABS) using natural and modified zeolites. *Water Res.*, 33 (9), 2083-2087
- Kaya, A. & Durukan, S., 2004. Utilization of bentonite-embedded zeolite as clay liner. *Applied Clay Science* 25, 83-91
- Kayabali, K., 1997. Engineering aspects of a novel landfill material: bentonite amended natural zeolite. *Engineering Geology* 46, 105-114
- Kleppe, J. H. and Olson, R.E., 1985. Desiccation cracking of soil barriers. ASTM, Special technical Publication, 874, 263-275
- Lin, L.-C. & Benson, C.H., 2000. Effect of wet-dry cycling on swelling and hydraulic conductivity of GCLs. *Journal of Geotechnical and Geoenvironmental Engineering* 126, 40-49
- Mondale, K.D., Carland, R.M., & Aplan, F.F., 1994. The comparative ion exchange capacities of natural sedimentary and synthetic zeolites. *Minerals Engineering*, 8 (415), 535-548
- Mulilis J.P., 1975. The effects of method of sample preparation on the cyclic stress-strain behavior of sands. PhD Thesis, University of California, Berkeley.
- Othman, M., Benson, C., Chamberlain, E., & Zimmie, T., 1994. Laboratory testing to evaluate changes in hydraulic conductivity caused by freeze-thaw: state-of-the-art. *Hydraulic Conductivity and Waste Contaminant Transport in Soils*, ASTM, STP, 1142, 227-254
- Ören, A.H., Kaya, A., and Kayalar, A.Ş., 2011. Hydraulic conductivity of zeolite bentonite mixtures in comparison to sand bentonite mixtures. *Canadian Geotechnical Journal*, 48(9), 1343-1353
- Özkırım, İ. & Yörükoğulları, E., 2005. Characterisation of BET isotherm from Manisa-Gördes natural zeolite (clinoptilolite). *Dumlupınar Üniversitesi Fen Bilimleri Enstitüsü Dergisi*, 9, 65-70.
- Tuncan, A., Tuncan, M., Koyuncu, H. & Guney, Y., 2002. Use of natural zeolites as a landfill liner. *Waste Management and Research*, 21(1), 54-61

ENHANCED PHOTO- AND UNDER X-RAY LUMINESCENCE FROM XEROGELS EMBEDDED IN MESOPOROUS ANODIC ALUMINA

Nikolai Gaponenko ^{1,a}, Vsevolod Kortov ², Vladimir Pustovarov ²,
Liudmila Khoroshko ¹, Maria Rudenko ¹, Ahmed Asharif ¹, Igor Molchan ³,
George Thompson ³, Artur Podhorodecki ⁴, Jan Misiewicz ⁴, Sergey Prislopskii ⁵

1. Belarusian State University of Informatics and Radioelectronics, P.Browki St.6, 220013 Minsk, Belarus

2. Ural Federal University named after the first President of Russia B. N. Yeltsin, Mira St. 19,
620002 Yekaterinburg, Russia

3. Corrosion and Protection Centre, School of Materials, The University of Manchester,
Manchester M13 9PL, United Kingdom

4. Institute of Physics, Wrocław University of Technology, 50-370 Wrocław, Poland

5. Stepanov Institute of Physics, National Academy of Sciences of Belarus, 220072 Minsk, Belarus

a. Corresponding Author (nik@nano.bsuir.edu.by)

ABSTRACT: In our previous work we have shown that porous anodic alumina (PAA) films with pore and cell sizes ranging from 100 to 190 and 240 to 270 nm, respectively, have been generated on aluminum and monocrystalline silicon substrates followed by spin-on sol-gel derived coating with the subsequent thermal treatment producing microporous xerogel. The xerogel/PAA structures doped with lanthanides reveal strong luminescence of lanthanides under ultraviolet and X-ray excitation, with the strongest luminescence in the direction along the channels of the pores. In this paper Terbium-doped yttrium aluminum composite was synthesized onto porous anodic alumina by the co-precipitation method. The $YAlO_3$ phase was revealed after the heat treatment at 1000 °C. The terbium luminescence excited by X-rays was observed along with the intense photoluminescence. The synthesis procedure is of interest for the development of radiation-resistant luminescent film.

1. INTRODUCTION

A low-cost honey-comb matrix of porous anodic alumina possesses a tailor-made cellular porous structure [Thompson, G. *et al.*, 1981]. In our previous papers we reported on strong luminescence of xerogels doped with lanthanide ions (Er, Tb, Eu) embedded in porous anodic alumina with the channels of the pores about 100 – 190 nm [Gaponenko, N. *et al.*, 1997; Gaponenko, N. *et al.*, 2000; Gaponenko, N. *et al.*, 2001; Gaponenko, N. *et al.*, 2002; Molchan, I. *et al.*, 2005; Gaponenko, Kortov, Smirnova *et al.*, 2012; Gaponenko, Kortov, Rudenko *et al.*, 2012; Podhorodecki *et al.*, 2010]. The distribution of the xerogels corresponding to the chemical contents of silica, willemite, titania, alumina, doped with lanthanides in PAA was investigated confirming its presence

inside the pores near the pore bases and at the walls depending on xerogel content and annealing temperature.

In addition to photoluminescence (PL), terbium luminescence under X-rays from film structure xerogel/porous anodic alumina was reported [Gaponenko, Kortov, Smirnova *et al.*, 2012; Gaponenko, Kortov, Rudenko *et al.*, 2012]. Yttrium- alumina composites, $Y_3Al_5O_{12}$ and $YAlO_3$, doped with lanthanides receive considerable interest as radiative resistant scintillating material [Martin *et al.*, 2006; Potdevin *et al.*, 2009]. In this work, we report on synthesis of the porous anodic alumina/ $YAlO_3$:Tb structure and its strong terbium photo- and under X-ray luminescence.

2. EXPERIMENTAL

In the experiments, superpure aluminium (99.999 %) was deposited by magnetron-sputtering onto a planar side of a polished monocrystalline silicon wafer, which had been coated with 50 nm adhesion-promoting tantalum layer. Porous anodic alumina was generated by a two-step anodizing in 1 M phosphoric acid at a constant voltage of 120 V and temperature of 10-12°C or at 130 V in 1.2 M phosphoric acid at 17°C. After the first anodizing the anodic alumina layer was removed in a mixture of chromic and phosphoric acids at a temperature of 60-70 °C. The second anodizing was carried out under the same conditions, thus resulting in complete anodizing of the remaining aluminium film. The pore widening was undertaken for the selected samples by immersion in an aqueous 50 vol. % solution of phosphoric acid at room temperature for 25 minutes.

Yttrium-aluminacomposite doped with terbium were prepared using stage-by-stage dissolution of nitrate salts (Sigma Aldrich) $Y(NO_3)_3 \times 4H_2O$ (99.99% purity), $Al(NO_3)_3 \times 9H_2O$ (98 % purity) and $Tb(NO_3)_3 \times 5H_2O$ (99.9 % purity) in an aqueous-alcoholic solution, with the pH adjusted to 2 with dilute nitric acid. As a citric acid in the molar ratio [metal ions]/[citric acid] = 1/3 was used as stabilizer. The molar ratio of Y^{3+}/Al^{3+} for all the solutions was 1.76; the terbium concentration was varied from 0.4 to 9.6 mol.%. Terbium-containing solution was deposited on porous anodic alumina by sequential spinning from one to ten layers at a rate of 2700 rpm, followed by drying at 200°C and a final 30-min annealing at temperatures up to 1000°C.

The radioluminescence (RL), was excited by a laboratory X-ray source of type URS-55 with a BSV-2 X-ray tube (Cu anticathode, $U_a = 40$ kV, $I_a = 15$ mA). The RL spectra in the range of 300-700 nm

were measured using an MDR-23 monochromator and a FEU-106 photomultiplier.

3. RESULTS AND DISCUSSION

The $YAlO_3$ phase from the fabricated structure was detected with X-ray diffraction technique [Potdevin *et al.*, 2009]. Figure 1 shows scanning electron micrographs of the structure after generation of one $YAlO_3$ layer. Deposition of one layer results in incomplete filling of the pores remaining most channels of the pores opened. After deposition of ten coatings an $YAlO_3$ layer of approximately 1 μ m thickness is formed on the top of the porous layer, with fractures probably generated during annealing.

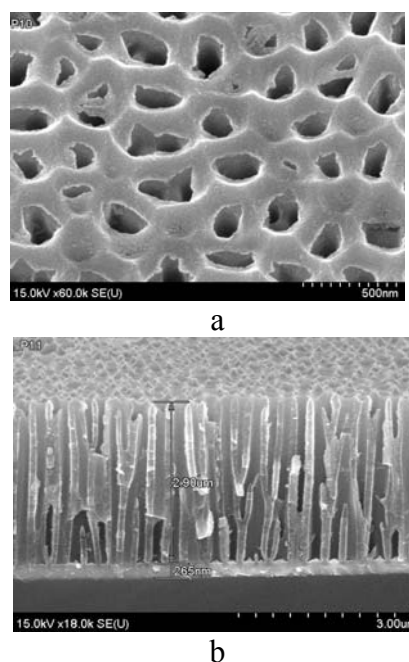


Figure 1: Scanning electron micrographs of the PAA formed in the 1M H_3PO_4 electrolyte (a) and etched in the orthophosphoric acid for 25 min (b) with the deposited one layer of the $YAlO_3:Tb$ composite after annealing at 1000 °C for 30 min.

The RL and PL spectra of the $YAlO_3$ composite doped with 2.9 mol. % of terbium are presented in Figure 2.

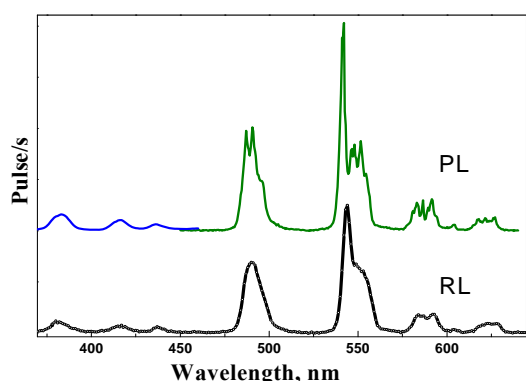


Figure 2. The RL and PL spectra of the YAlO_3 composite doped with 2.9 mol. % of terbium deposited on porous anodic alumina

The observed radioluminescence bands are associated with weaker $^5\text{D}_3 \rightarrow ^7\text{F}_j$ ($J=6, 5, 4$) and stronger $^5\text{D}_4 \rightarrow ^7\text{F}_j$, ($J=6, 5, 4, 3$) transitions of trivalent terbium ions embedded in the YAlO_3 host. The same bands were well resolved in photoluminescence spectra with the temperature range 10 – 300 K. [Podhorodecki, A et al, 2010]. It should be noted that the intensity of RL from this sample is much stronger than that of Tb-doped Al_2O_3 and TiO_2 xerogels embedded in porous anodic alumina reported previously [Gaponenko, Kortov, Smirnova *et al.*, 2012; Gaponenko, Kortov, Rudenko *et al.*, 2012].

In conclusion, terbium-doped YAlO_3 films were fabricated on porous anodic alumina layer grown on monocrystalline silicon wafer. Strong room-temperature terbium luminescence under X-rays excitation was observed. The synthesis procedure is of interest for the development of radiation-resistant luminescent film with low grain size of thin film scintillator.

Acknowledgements: This work has been supported by the Grant No. NN507321240 of the Polish National Science Centre and by the Grant

T12MC025 of Belarusian Foundation for Basic Research.

REFERENCES

- Thompson, G.E., Wood, G.C, 1981. Porous anodic film formation on aluminium, *Nature*, Vol. 290, № 5803. P. 230
- Gaponenko, N.V., Parkun, V.M., Katernoga O.S. et al., 1997. Erbium and terbium photoluminescence in silica sol-gel films on porous alumina, *Thin Solid Films*, Vol. 297, N 1–2. P. 202
- Gaponenko, N.V., Davidson, J.A, Hamilton B. et al., 2000. Strongly enhanced Tb luminescence from titania xerogel solids mesoscopically confined in porous anodic alumina, *Applied Physics Letters*, Vol. 76, N 8, P. 1006
- Gaponenko, N.V., Sergeev, O.V., Stepanova E.A. et al., 2001. Optical and structural characterisation of erbium-doped TiO_2 xerogel films processed on porous anodic alumina, *Journal of The Electrochemical Society*, Vol. 148, N 2, P. H13
- Gaponenko, N.V., Molchan, I.S., Thompson G.E. et al., 2002. Photoluminescence of Eu-doped titania xerogel spin-on deposited on porous anodic alumina, *Sensors and Actuators A*, Vol. 99, P. 71
- Molchan, I.S., Gaponenko, N.V., Thompson, G.E. et al., 2005. Optoelectronic applications of porous anodic alumina, *Transactions of the Institute of Metal Finishing*, Vol 83, P. 233
- Gaponenko, N.V., Kortov, V.S., Smirnova, N.P. et al., 2012. Sol-gel derived structures for optical design and photocatalytic application, *Microelectronic Engineering*, Vol. 90, P. 131
- Gaponenko, N.V., Kortov, V.S., Rudenko, M.V. et al., 2012. Inhomogeneous nanostructured honeycomb optical media for enhanced cathodo- and under-x-ray luminescence, *Journal of Applied Physics*, Vol. 111, P. 103101
- Podhorodecki, A., Bański, M., Misiewicz, J. et al., 2010. Influence of annealing on excitation of terbium luminescence in YAlO_3 films deposited onto porous anodic alumina, *Journal of the Electrochemical Society*, V. 157, No 6, P. H628
- Martin, T., Koch, A., 2006. Recent developments in X-ray imaging with micrometer spatial resolution, *Journal of Synchrotron Radiation*, No 13, P. 180
- Potdevin, A., Lechevallier, S., Chadeyron, G. et al., 2009. Waveguiding terbium-doped yttrium aluminum garnet coatings based on the sol-gel process, *Thin Solid Films*, No 517, P. 4610

INVESTIGATION OF SOLUBILITY AND TRANSPORT OF BORIC ACID IN ETHANOL AT SUBCRITICAL AND SUPERCRITICAL CONDITIONS

Ayşe BUDAK¹, Mehmet GÖNEN^{2,a}

1. Süleyman Demirel University, Engineering Faculty, Department of Environmental Engineering, Batı Yerleşkesi, Isparta, 32260, Turkey
2. Süleyman Demirel University, Engineering Faculty, Department of Chemical Engineering, Batı Yerleşkesi, Isparta, 32260, Turkey
 - a. Corresponding Author (gonen19@gmail.com)

ABSTRACT: In this study, the solubility of boric acid was investigated in ethanol at supercritical and subcritical conditions. Experiments were carried out in stainless steel reactor under mixing rate of 800rpm, in the temperature range of 150°C-250°C and corresponding pressures between 0.9-7.1MPa. A certain amount of the ethanol-boric acid mixture in the expansion vessel was dried at room temperature in petri dish. The powder obtained from ethanol phase was characterized by fourier transform infrared spectroscopy (FTIR), x-ray diffraction (XRD) and thermal gravimetric (TG) analyses. It was determined that there is neither interaction between ethanol and boric acid nor any change in the its structure during the extraction. Between 52%-82% of boric acid initially placed in the reactor was transported into the second vessel at subcritical and supercritical conditions. It was found that the transport of boric acid in supercritical ethanol was increased with temperature. The solubility of boric acid in ethanol was calculated using the transported amounts as 3.0-8.3g B(OH)₃ /100 mL ethanol under those conditions. The transportation of boric acid with ethanol at subcritical and supercritical conditions can be used in its extraction from boron minerals, such as ulexite and tincal.

1. INTRODUCTION

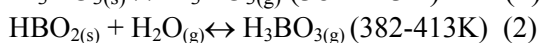
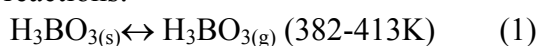
Boric acid is an important boron product which is widely used in the production of boron derivatives and in the formulation of many end products. There are various forms of boric acid which are orthoboric acid, (B(OH)₃), metaboric acid (HBO₂); and tetraboric acid (H₂B₄O₇). Among them the orthoboric acid is mostly known as just boric acid. It is found in nature as sassolite mineral. Although normal boiling point of boric acid is 170.9°C, when it is heated slowly it loses its water to form metaboric acid.

The solubility of boric acid in various solvents is an important parameter which determines progress of reaction or progress of other unit operations, such as extraction and crystallization. Aqueous solubility of boric acid varies between

2.52-27.53% with respect to temperature range of 0-100°C. In dilute solutions, boric acid forms borate anion (B(OH)₄⁻) and H⁺ which provides an acidic character in aqueous phase. Boric acid has solubility of 94.4 g/L in ethanol at 25°C [Othmer, 1994]. Another important issue for boric acid is its vapor pressure when it is mixed with water and subjected to heating.

The first study related to the vaporization of H₂O-B₂O₃ system was performed by Stackelberg and his coworkers. They determined the amount of boric acid which was carried by passing steam over the solid boric acid as function of temperature (382-453K) at steam pressure of 1 atm and as a function of steam pressure (1.33x10⁴-1.01x10⁵) at

various temperatures. They observed that boric acid converted into metaboric acid when heated to above 413K by steam flow at 1 atm. They also concluded that water vapor pressure (1.20×10^4 - 1.01×10^5 Pa) had no influence on the rate of sublimation of orthoboric acid, any increase beyond 1.01×10^5 Pa caused a nearly linear increase in boron volatility of the metaboric acid. They gave the boron species pressure-temperature relationship regarding to the following reactions:



The vapour pressure of boric acid was determined using transpiration apparatus utilized with thermogravimetric instrument the range of 326-375K by Pankajavalli and his coworkers. The sublimation enthalpy of boric acid was reported as $174,1 \pm 4,7$ kJ/mol at mean temperature of 345K. The temperature dependence of vapour pressure was expressed as following: $\log(P/\text{Pa}) = 26,83(\pm 0,09) - 9094(\pm 246)/T$ (K). As it can be inferred from their experimental data, the evaporation rate of boric acid was accelerated by increasing temperature and mass loss was found as 20.94 μg at 363K. This value is corresponding to about 59.83% of mass loss [Pankajavalli et al., 2007].

Recently, the investigation of the boric acid vaporization was studied by Balasubramanian and his coworkers (2008) using transpiration thermogravimetry and Knudsen effusion mass spectrometry (KEMS). They found the congruent vaporization of boric acid from the binary mixture of H_2O - B_2O_3 system and proposed a vapor pressure equation of $\log[P(\text{H}_3\text{BO}_3)/\text{Pa}] = -(5199 \pm 74)(T/\text{K}) + (15.65 \pm 0.23)$ which is valid in the temperature range of 295-413K [Balasubramanian et al., 2008].

The extraction of boric acid from alkaline metal borate treated by sulfuric acid was studied using a superheated steam by Shiloff in 1972. Metal borates (razorite and kernite) reacted with sulfuric acid (96%) in the range of 150°C-250°C. It was directly contacted with superheated steam for a period of 3.5 hours and enabled boric acid to volatilize into the gas phase. Subsequently, this stream was cooled and an aqueous solution of boric acid was obtained. The boric acid was crystallized from that solution [Shiloff, 1972].

Borate and gaseous polyborate anions were studied by Attina and her co-workers (1992). It was reported that emitted vapor from solid boric acid in the range of 20-100°C was a mixture of boric acid-water vapor. While the partial vapour pressure of boric acid was 10^{-7} Torr at temperature 20°C, it was measured as 3×10^{-5} Torr at 80°C. It was found that the remaining product after evaporation experiment was largely undecomposed $\text{B}(\text{OH})_3$, since its surface was coated by HBO_2 that prevented its further decomposition [Attina et al., 1992]. As summarized above, there were some articles regarding to the boric acid volatility in water.

In this study, the solubility and transport of boric acid was investigated in ethanol at supercritical and subcritical conditions.

2. EXPERIMENTAL

Commercial boric acid powder from Etimine Inc., Turkey with purity of 99.9% (wt) was used in solubility experiments. B_2O_3 content of this product was a 56.25% (wt). Ethanol ($\text{C}_2\text{H}_5\text{OH}$) was used with 99.8% (vol.) purity in solubility and extraction experiments.

The extraction system consists of a high temperature and pressure reactor (PARR 5513), a temperature controller (PARR

4848), a nitrogen cylinder, and a circulating cooling bath (Polyscience

9606). Before heating the reactor, nitrogen gas was passed through the

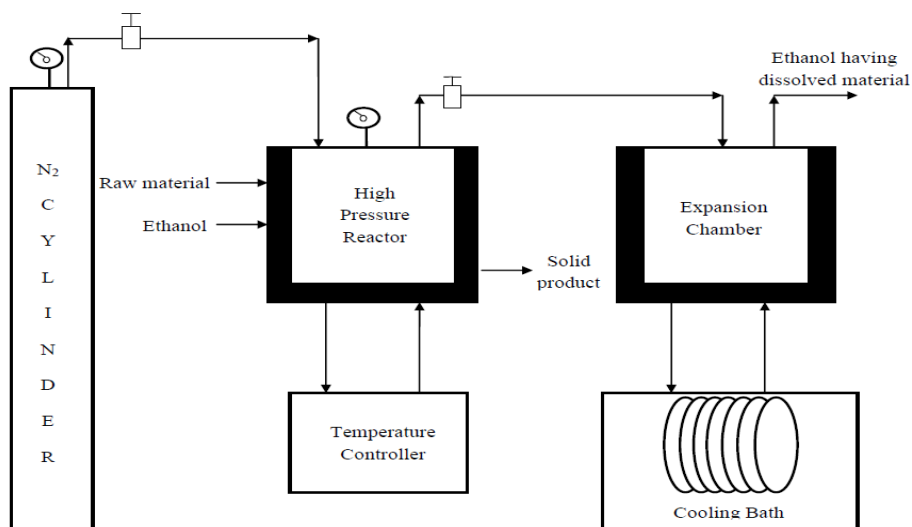


Figure 1: Experimental Setup

system to remove any remaining oxygen in the reactor and pipelines. The experimental setup used in solubility measurements is shown in Figure 1. Different solid/liquid (S/L) ratios were used in the experiments as shown in Table 1. In the experiments boric acid-ethanol mixture was subjected to temperature range of 150°C-250°C, and corresponding pressures under the mixing rate of 800 rpm for different time periods in the closed reactor. When the reactor reached to the desired conditions, mixing was stopped and the mixture was transferred into the expansion vessel by keeping the temperature constant for the runs, where supercritical conditions exist. When the pressure in the reactor decreased to the atmospheric pressure, the system was purged with N₂ gases. Then, the mixture in the expansion chamber was taken and its volume was measured. Aliquot amount of mixture was dried in petri dish and remaining solid was weighted and characterized by TG, FTIR and XRD. Boric acid transportation efficiency was calculated by dividing the extracted amount to initially placed boric acid amount.

The characterization of the powder obtained from the experiments were performed by using infrared spectrometer (Perkin Elmer Spectrum II), X-ray powder diffraction equipment (Philips X'Pert Pro), thermal gravimetric analyzer (Perkin Elmer Diamond TG/DTA). IR spectra were recorded in the range of 4000-400 cm⁻¹ wavenumber using KBr technique. X-ray powder diffraction measurements were obtained at CuK α ($\lambda=1,54 \text{ \AA}$, 40 mA, 45kV) radiation. In thermal gravimetric analyses, 10 mg of samples were loaded into an alumina pan and heated from 30°C to 1000°C at 10°C.min⁻¹ under N₂ flow of 10 ml min⁻¹.

3. RESULT AND DISCUSSION

Boric acid solubility in ethanol was investigated at different temperatures. In the experiments, certain amount of boric acid was mixed with different amounts of ethanol. Then, temperature was increased to the value which is above and below the critical temperature of ethanol (241°C). The most important result of boric acid-ethanol interaction is the transportation of boric acid when the ethanol was expanded into second vessel at the

Table 1: Boric Acid-Ethanol Interaction and its Results

Experiment No	Temperature, °C	Pressure, atm	Boric acid, g	S/L ratio, g/ml	Extraction time, min	C ₂ H ₅ OH outlet, ml	Recovery, %
E-1	250	69	3.76	0.075	0	49	67.24
E-2	250	71	2.51	0.050	5	48	58.68
E-3	250	62	3.75	0.075	10	49	73.50
E-4	250	70	5.00	0.100	5	50	82.24
E-5*	200	28	5.00	0.100	10	48	64.63
E-6*	200	28	3.75	0.075	5	49.5	74.70
E-7	200	29	2.50	0.050	0	47	75.49
E-8*	200	28	5.00	0.100	0	49	64.16
E-9	200	29	2.50	0.050	10	48	76.65
E-10*	150	10	5.00	0.100	5	49	52.33
E-11*	150	9	3.75	0.075	0	50	63.74

*There is remaining glassy material in the reactor

constant temperature. The amount of ethanol was determined by using the critical density of ethanol and volume of reactor (0.1dm³). Since boric acid has hydroxyl groups in its structure, it is easily dissolved in alcohols and aqueous solutions having hydroxyl groups. The results obtained from experiments were shown in Table 1. As seen from those results, when the temperature increased from 150°C to 250°C at 1/10 solid-liquid ratio, boric acid transportation has increased from 52% to 82%. At the same time, increasing of solid/liquid ratio from 0.05 to 0.1 at 250°C, has positively affected the boric acid transportation too. Extraction time effect has been investigated between 0-10 minutes of extraction. An increase in the extraction time did not bring a significant change in the extraction efficiency (just about 5%). In all experiments, it is clearly seen that not all of the boric acid initially placed in the reactor was transported into expansion vessel. This result may be caused by either of the following cases: remaining of the aliquot amount ethanol in the pipelines and vaporization of some boric acid during the separation of boric acid and ethanol mixture as reported by Pankajavalli and et al (2007). In the experiments carried out at below 241°C, a

little amount of boric acid remained as a glassy material which was anticipated as anhydrous boric acid (B₂O₃) in the reactor. There is another issue regarding to the boric acid loss, in which boric acid and ethanol may react to form borate esters. In order to detect the presence of triethyl borate, the liquid mixture at the end of experiment was analyzed by IR spectrometer. As shown in Figure 2. a., there is no specific peak of triethyl borate at 1340cm⁻¹ as pointed by [Colthup et al., 1990].

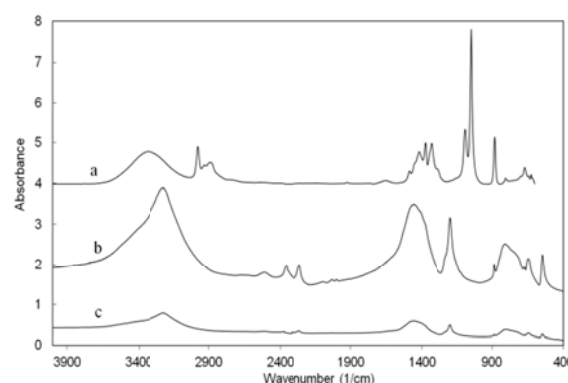


Figure 2: FTIR spectra of a)-boric acid-ethanol mixture, b)-pure boric acid and c)-powder obtained in the SCE system.

The functional groups of boric acid and obtained powder after ethanol extraction were investigated whether there is a change in their structure or not in the

range of 4000-400 cm^{-1} wavenumber. When FTIR spectra of pure boric acid (Fig. 2.b) and powder obtained at the end of extraction (Fig. 2.c) were compared it was determined that boric acid did not undergo any structural alteration during supercritical extraction.

The thermal analysis of the powder product was shown in Figure 3. Thermal decomposition of powder occurred in two steps. In the first step, which starts at 100°C and ends 148°C, the product lost 30% of its initial mass, which corresponds 2 moles of water. The water was formed by polymerization of hydroxyl groups in boric acid structure and metaboric acid was an intermediate product. In the second step, metaboric acid polymerized further to form water and turned into B_2O_3 . Total mass loss of powder was determined as 45.7%, which is consistent with the water content of boric acid (43.73%). According to the mass loss occurred in heating, the powder product was boric acid and it was not affected during extraction.

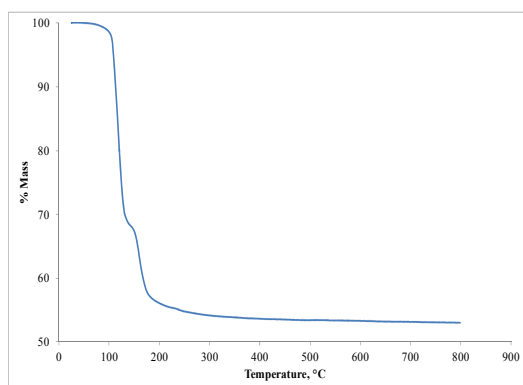


Figure 3: TG curve of powder obtained in SCE system (E-5).

When XRD pattern of the powder obtained at the end of ethanol extraction was compared with one in the literature (JCPDS-30-0199), it was concluded that there was neither change in boric acid structure nor any interaction with ethanol. The major peaks observed at 2θ value of 14.6°, 14.9°, 28.05° belong to boric acid.

4. CONCLUSION

When the temperature was increased from 150°C to 250°C at 1/10 solid-liquid ratio, boric acid transportation has been increased from 52% to 82%. The solubility of boric acid in ethanol was calculated as 3.0-8.3g $\text{B}(\text{OH})_3/100$ mL ethanol under those conditions. In the experiments carried out at below 241°C, a little amount of boric acid remained as glassy material which was anticipated as anhydrous boric acid in the reactor. The separation of boric acid from ethanol was performed by conventional evaporation. The transportation of boric acid with ethanol at subcritical and supercritical conditions can be used in its extraction from boron minerals, such as ulexite and tincal.

Acknowledgements: The authors acknowledge the financial support of The Scientific and Technical Research Council of Turkey (TÜBİTAK) (project num. 111M639).

REFERENCES

- Attinà, M., Cacace, F., Occhiucci, G., and Ricci, A., 1992. Gaseous borate and polyborate anions. *Inorganic Chemistry*, 31, 3115.
- Balasubramanian, R., Lakshmi Narasimhan, T.S., Viswanathan, R., Nalini S., 2008. Investigation of the vaporization of boric acid by transpiration thermogravimetry and Knudsen Effusion Mass Spectrometry. *J. Phys. Chem. B*, 112, 13873.
- Colthup, N. B.; Daly, L. H.; Wiberley, S. E., 1990. *Introduction to Infrared and Raman Spectroscopy*; Academic Press:San Diego, CA., 356.
- Kirk-Othmer, *Encyclopedia of Chemical Technology*, 4th ed.; John Wiley and Sons: New York, 1994; Vol. 4, 252.
- Pankajavalli, R., Anthonysamy, S., Ananthasivan, K., Vasudeva, Rao, P.R., 2007. Vapour Pressure and Standard enthalpy of sublimation of H_3BO_3 . *J. of Nuclear Materials* 362, 130.
- Shiloff, J.C., *Boric Acid Production* (1972) U.S. Patent, 3.650.690.
- Stackelberg, M. V., Quatram, F., Dressel, J. Z., 1937. *Elektrochem*, 43, 14.

ANALYSIS OF MULTIPHASE TRANSPORT PROCESSES AND FLUID DISPERSION IN SINTERED POROUS STRUCTURES

Nils Hornig^a, Udo Fritsching

University of Bremen, Particle and Process Engineering, Badgasteinerstr. 3, 28359 Bremen, Germany
a. Corresponding Author (hornig@iwt.uni-bremen.de)

ABSTRACT: This work focusses on the simulation and experimental study of multiphase transport processes and fluid dispersion in porous structures, as they occur for the generation of mono dispersed droplet sizes in membrane emulsification processes. The internal fluid dispersion of two non-miscible fluids in premix membrane emulsification processes is investigated to understand the connection between the internal fluid dispersion and the structural properties of the membrane. Therefore, CFD methods are implemented for a prediction of resulting droplet sizes and distributions under a certain energy input for fluid dispersion to occur. As models of sintered porous structures, randomly generated sphere packings under predetermined structural parameters are investigated as well as computer tomogram models of sintered glass particle structures of different porosity classes. The model validation has been achieved through single phase simulations of momentum transport related to experimental pressure drop measurements and analytical pressure drop correlations. In addition, ceramic membrane structures were fabricated, characterized and the generated product emulsion droplet sizes compared to such generated with sintered glass structures.

1. INTRODUCTION

Membrane emulsification processes using microstructured membranes reveal the possibility to produce emulsions with controlled droplet sizes in the μm -range with narrow droplet size distributions [Nazir *et al.*, 2010]. Such emulsions are commonly used in several industries, like food, cosmetics and health care. Compared to traditional emulsification techniques, like colloid mills, rotor-stator systems, high-pressure homogenizers and ultrasonic emulsification, membrane emulsification processes require an at least one order of magnitude lower energy input per unit volume of produced emulsion, while reducing shear and extensional stresses [Nazir *et al.*, 2010, Charcosset *et al.*, 2004, Karbstein *et al.*, 1995].

The relation between process parameters, such as the transmembrane pressure difference, and droplet detachment is well understood [Bibette *et al.*, 1995]. In addition, coalescence phenomena at the

membrane surface have been investigated experimentally as well as through multiphase simulations [Krause *et al.*, 2010, Lambrich *et al.*, 2004, Van der Graaf *et al.*, 2004].

Through the process variant of premix membrane emulsification, it is possible to gain higher product flux rates, caused by a decreased disperse phase viscosity. Here, a coarser premix is forced through the microstructured membrane via applying a transmembrane pressure difference, as schematically shown in Figure 1.

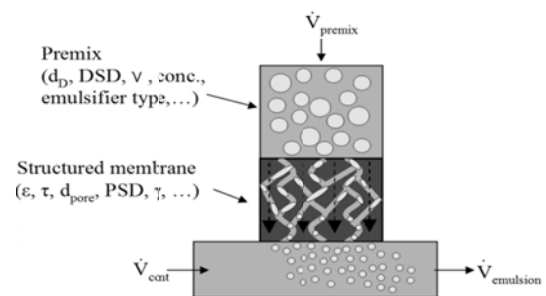


Figure 1: Schematic of premix membrane emulsification process

The resulting droplet size and distribution of the product emulsion is dependent on process parameters, such as the transmembrane pressure difference, as well as material properties, which are dependent on e.g. the emulsifier type. Furthermore, the premix emulsion properties, such as the initial droplet size and distribution (DSD), the viscosity ν and concentration affect the product emulsion properties. In comparison to direct membrane processes, the interior structure has a significant effect on the resulting droplet size [Krause *et al.*, 2009] as e.g. the pore sizes d_{pore} and their distribution (PSD) affect the droplet breakup through changes in Laplace pressure inside the pores [Nazir *et al.*, 2010], which is also dependent on the wetting behaviour, described by the contact angle γ . Beside the pore sizes and distributions, the porosity ε and the pore tortuosity τ affect the hydrodynamic behaviour of the membrane and are directly related to the resulting pressure loss and hence required energy input. Conclusively, the hydrodynamic behaviour and hence resulting droplet size for emulsification processes can precisely be tuned by tailoring the interior structure of the membrane.

2. STRUCTURES

To investigate the effect of interior membrane structure on the product emulsion properties, such as droplet size and distribution, two different structure materials were investigated. Sintered glass structures made of borosilicate glass 3.3 (81 wt% SiO_2 + 13 wt% B_2O_3) were used [Robu, 2013] with several structure types at different pore sizes and porosities. The values of pore volume as well as pore size range were given by the fabricator and were validated via Hg intrusion for this work. For declaration of these structures, the porosity ε as well as the median pore size $d_{\text{pore},0.5}$ is denoted (see Table 1).

To investigate the influence of primary sinter particle shape on the resulting emulsion properties, membrane structures were also fabricated via ionotropic gelation of ceramic slurry into CaCl solution. The procedure of structure fabrication and tailoring has been successfully approved for the filtration of bacteria in aqueous solutions [Klein *et al.*, 2012]. The spherules were yielded out of the gelation process, were dried and arranged in order to form the green body, which was sintered at a specific time and duration. The fabrication process reveals the possibility to tailor the primary particle size and distribution and hence the resulting interior membrane structure, like the pore size and distribution. Several structure shapes could be produced, as Figure 2 shows cylindrical (left) and disk-like samples (right) for membrane emulsification purposes.

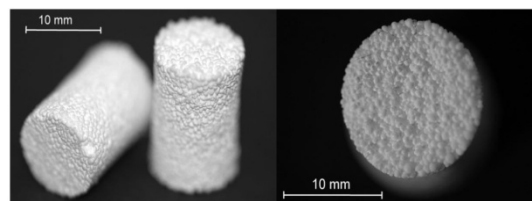


Figure 2: Tailored membrane structures fabricated via ionotropic gelation of ceramic slurry

As reported in literature, the contact angle for water + SDS emulsifier + oil on alumina membrane surfaces showed contact angles of $\gamma < 5^\circ$. This shows the hydrophilic character for alumina membrane surfaces and the suitability for the production of O/W emulsions [Schröder, 1999]. After a sample characterization, the ceramic structures were glued into supportive glass holders and implemented into the premix emulsification facility. The collection of membranes investigated in this work is shown in Table 1.

Table 1: Investigated structures for premix membrane emulsification

Porosity ϵ [-]	Pore diameter $d_{\text{pore},0.5}$ [μm]	Material
0.36	70	$\text{SiO}_2+\text{B}_2\text{O}_3$
0.41	28	$\text{SiO}_2+\text{B}_2\text{O}_3$
0.42	13	$\text{SiO}_2+\text{B}_2\text{O}_3$
0.34	186	$\text{Al}_2\text{O}_3+\text{SiO}_2$
0.41	288	$\text{Al}_2\text{O}_3+\text{SiO}_2$

3. EXPERIMENTAL PROCEDURE

To determine the fluid dispersion inside the investigated membrane structures, a procedure of generating reproducible coarse model premix emulsions was developed. Using a rotor-stator device (IKA® T18 basic UltraTurrax®) with varying stirring time and rotation speed (rpm), several initial premix droplet sizes could be produced. The coarse premix emulsions contained single distilled water, rapeseed oil and emulsifier. The dynamic phase boundary stabilization behaviour of the used emulsifier type is affecting the resulting droplet size in the coarse premix, whereas several emulsifiers were studied having different molar masses and diffusive behaviours. Regular emulsifiers commonly used in e.g. food industry are used in this work: Polysorbat 20 (Tween20®; fabricator: Sigma Aldrich Chemie GmbH, Steinheim, Germany), Polysorbat 80 (Tween80®; fabricator: Alfa Aesar GmbH & Co KG, Karlsruhe, Germany) as well as sodium dodecyl sulfate (SDS) (fabricator: Sigma Aldrich Chemie GmbH, Steinheim, Germany). For the production of each premix, the emulsifier was homogenized into single distilled water at a high rotation speed for a constant time, maintaining an emulsifier concentration of approx. twice the emulsifier's individual critical micelle concentration (CMC). Around 200 ml of coarse premix was emulsified into single distilled water each run. All emulsions in this work were characterized via laser diffraction measurement.

4. RESULTS

4.1. Premix Preparation

The initial coarse O/W emulsions were produced with several rpms and dispersion times. Figure 3 shows the reproducible premix Sauter droplet sizes $d_{3,2}$ in dependency on the dispersion time for two rotational speeds.

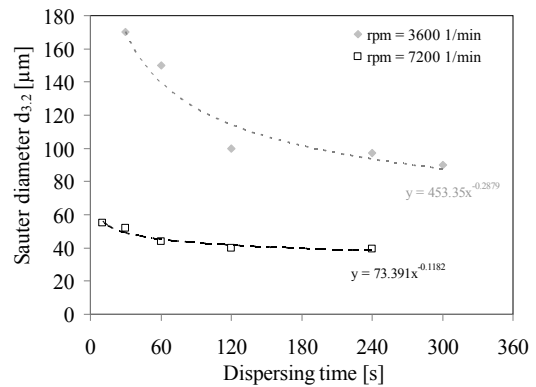


Figure 3: Sauter diameter in dependency on dispersing time and rpm of rotor-stator device for Polysorbat 20 emulsifier (O/W emulsion)

Droplets with Sauter diameters between 40 and 170 μm could be produced using Polysorbat 20 emulsifier in the investigated range of process parameters, as shown in Figure 3. The droplet sizes reach minimum values with increasing dispersion times, since the probability of every fluid element being dispersed in the rotor-stator device increases with increasing dispersion time, while decreasing its size magnitude with higher rpm. A premix droplet size of $d_{3,2} = 64 \mu\text{m}$ was used for emulsification runs with sintered glass structures as well as $d_{3,2} = 177 \mu\text{m}$ for sintered ceramic structures, because of the overall higher pore size magnitude. The ratio of initial Sauter droplet diameter $d_{3,2}$ to median pore diameter $d_{\text{pore},0.5}$ give the following results:

$$\text{SiO}_2+\text{B}_2\text{O}_3: \quad d_{3,2} / d_{\text{pore},0.5} = 0.9 \dots 4.9$$

Al₂O₃+SiO₂: $d_{3,2} / d_{\text{Pore},0.5} = 0.6 \dots 1.0$

4.2. Premix Membrane Emulsification

Regarding constant initial premix droplet sizes, Figure 4 shows the span values for premix membrane emulsification runs, which were obtained from the measured droplet size distributions of the product O/W emulsions.

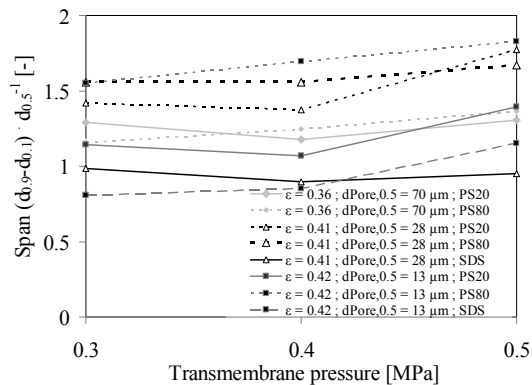


Figure 4: Span values of produced O/W emulsions in dependency on transmembrane pressure for different emulsifiers (SiO₂+B₂O₃ structures)

Figure 4 shows an increase of span values for increasing transmembrane pressures. The outlet pore velocity increases with increasing transmembrane flux, which correlates linearly with the applied transmembrane pressure. If the surface stabilization kinetics of the emulsifier is not sufficiently fast to stabilize the newly formed phase boundary, larger fluid elements are generated, broadening the droplet size distribution. Hence, the emulsifier type shows a strong dependency on the broadness of the product emulsion droplet size distribution, as SDS give smallest span values through its high dynamic phase boundary stabilization kinetics. Furthermore, Hg intrusion measurements have shown a broader pore size distribution for structure types with larger pore diameters. This leads to higher span values of the product emulsion droplets in dependency on the emulsifier type.

The product emulsions generated with sintered ceramic membranes were analyzed the same way, as Figure 5 shows the calculated span values according to Figure 4.

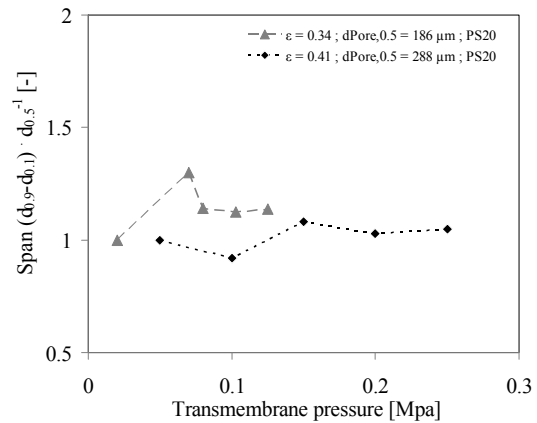


Figure 5: Span values of produced O/W emulsions in dependency on transmembrane pressure for Polysorbat 20 emulsifier (Al₂O₃+SiO₂ structures)

Figure 5 proves the fabrication route of ionotropic gelation process for the fabrication of tailored ceramic membrane structures to be valid for the generation of narrow distributed O/W emulsions with span values of around 1 for structures of $d_{\text{pore},0.5} = 288 \mu\text{m}$. In the investigated ranges of pressure, a minimum span values arises. Because of the overall higher magnitude of disperse phase flux rates using the sintered ceramic structures, the maximum transmembrane pressure was set to 0.15 and 0.25 MPa for process stability reasons. A further variation of structural and process parameters is to be conducted.

5. FLOW SIMULATIONS

To reveal transport processes in sintered porous structures, CFD simulations have shown good agreement to experimental data. In order to predict resulting droplet sizes of the emulsification process through multiphase simulations, the ceramic membrane structures needed to be modeled adequately. For the tailored

fabrication of ceramic membranes, the interior structural parameters (pore size, tortuosity, porosity) needed to be extracted from CFD simulations. Since the ceramic structures consist of spherical and statistically positioned primary particles, a random number algorithm for positioning spherules in a predefined container was used. The models porosity and particle sizes were defined initially. Several structures under varying porosities were generated and the single phase momentum transport was validated with Ergun correlation. Furthermore, a sintering representation was implemented as predefined threshold for overlapp between neighbouring spherules, in order to represent the membrane structures gained by ionotropic gelation process in a most realistic manner. To neglect wall effects, representative volume elements were defined and validated through single phase momentum transport simulations, as the modelling route shows Figure 6.

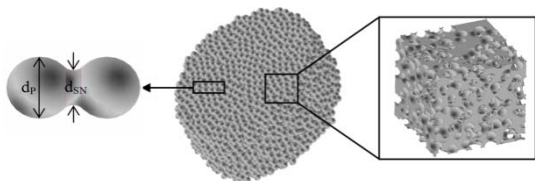


Figure 6: Modelling route to generate statistic sphere packing models

6. SUMMARY

A new method of generating membranes used for premix membrane emulsification processes was introduced with the aim to generate narrow distributed product emulsions. Sintered glass structures were investigated prior to extract a connection between pore size distribution and resulting broadness of emulsion droplet sizes. The experimental investigation combined with CFD flow simulations aims to extract fabrication parameters for tailored structures to produce predictive and narrow distributed emulsion droplets.

Acknowledgements: This work is supported by the German Research Foundation (DFG) within the graduate school 1375 PoreNet “Nonmetallic Porous Structures for Physical-Chemical Functions” at the University of Bremen.

REFERENCES

- Bibette, J., Calderon, F., Poulin, P., 1999. Emulsions: basic principles, Rep. Prog. Phys., 62, 969.
- Charcosset, C., Limayem, I., Fessi, H., 2004. The membrane emulsification processes - a review, J. Chem. Technol. Biotechnol., 79, 209.
- Karbstein, H., Schubert, H., 1995. Developments in the continuous mechanical production of oil-in-water macro-emulsions, Chem. Eng. Process., 34, 205.
- Klein, T.Y., Treccani, L., Rezwan, K., 2012. Ceramic Microbeads as Adsorbents for Purification Technologies with High Specific Surface Area, Adjustable Pore Size and Morphology Obtained by Ionotropic Gelation, J. of American Ceramic Soc., 95(3), 364.
- Krause, F., Fritsching, U., 2010. Modelling drop interactions with topological changes in liquid-liquid dispersions, 7th International Conference on Multiphase Flow ICMF 2010 Proceedings, University of Florida, USA.
- Krause, F., 2012. Einfluss der Mikrofluidik beim Membranemulgieren, Differentielle Betrachtung mittels numerischer Simulation und Experiment, Dissertation, Universität Bremen.
- Lambrich, U., Vladisavljevic, G.T., 2004. Emulgieren mit mikrostrukturierten Systemen, Chem. Ing. Tech., 76, 376.
- Nazir, A., Schroen, K., Boom, R., 2010. Premix emulsification: A review, J. Membr. Sci., 362, 1. Robu® Glasfilter-Geräte GmbH, 2013. www.robuglas.com.
- Schröder, V., 1999. Herstellen von Oel-in-Wasser-Emulsionen mit mikroporesen Membranen, Dissertation, University of Karlsruhe.
- Van der Graaf, S., Schroën, C.G.P.H., Van der Sman, R.G.M., Boom, R.M., 2004. Influence of dynamic interfacial tension on droplet formation during membrane emulsification, J. of Coll. and Int. Sci., 277, 456.

SYNTHESIS, CRYSTAL STRUCTURE, AND NITROGEN-GAS-ADSORPTION PROPERTY OF CHAIN COMPLEX OF DINUCLEAR RHODIUM(II) BENZOATE AND ETHYLENEDIAMINE

Masahiro Mikuriya^{1,a}, Kazuya Ouchi¹, Yasutaka Nakanishi¹, Daisuke Yoshioka¹, Hidekazu Tanaka², and Makoto Handa²

1. Kwansai Gakuin University, School of Science and Technology, Sanda 669-1337, Japan

2. Shimane University, Interdisciplinary Graduate School of Science and Engineering, Matsue 690-8540, Japan

a. Corresponding Author (junpei@kwansai.ac.jp)

ABSTRACT: The title compound, an adduct of rhodium(II) benzoate [Rh₂(O₂CC₆H₅)₄] ([Rh₂(bz)₄)] with ethylenediamine (en), [Rh₂(bz)₄(en)]_n·4nCH₃CN, was synthesized, and the crystal structure was determined by the single-crystal X-ray diffraction method at 90 K. It crystallizes in the triclinic space group *P*2₁/*c* with *a* = 10.149(3) Å, *b* = 20.250(5) Å, *c* = 19.180(5) Å, α = 103.602(5)°, *V* = 3831.3(17) Å³, *D*_x = 1.586 g/cm³, and *Z* = 4. The *R*1 [*I* > 2σ(*I*)] and *wR*2 (all data) values are 0.0704 and 0.1931, respectively, for all 7844 independent reflections. The crystal contains zig-zag chain molecules with an alternating arrangement of Rh₂(bz)₄ [Rh-Rh 2.4004(12) Å] and en, and acetonitrile molecules. The adsorption property was confirmed for N₂ with a specific surface area of 7.5 m²/g.

1. INTRODUCTION

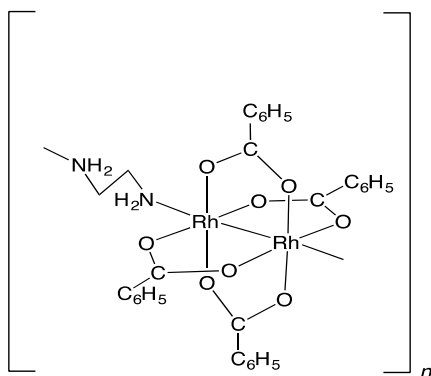
Dinuclear metal(II) carboxylates [M₂(O₂CR)₄] with a lantern-like core have attracted much attention because of their unique structures and properties [Mori *et al.*, 1999]. These molecules can be employed as a building unit to construct one-dimensional chain compounds by the use of linker ligands such as pyrazine for the open axial sites. We reported that a chain compound of copper(II) benzoate with pyrazine (pyz) has a gas-adsorption property for N₂ [Nukada *et al.*, 1999]. Therefore we have engaged in synthesis of this kind of chain compounds based on metal carboxylates. Rhodium(II) and molybdenum(II) carboxylates can be considered to be robust compared with those of copper(II) carboxylate because of the presence of metal-metal bonding, and both of the axial sites of the dinuclear core are available for the axial coordination of the bidentate linker ligands to give one-dimensional chain compounds. We reported that molybdenum(II) acetate forms one-dimensional polymer

compounds with some linker ligands (L) such as pyrazine, [Mo₂(O₂CCH₃)₄L]_n [Handa *et al.*, 1995]. Very recently, we found some of these compounds do not adsorb nitrogen gas [Mikuriya *et al.*, 2013d]. On the other hand, some chain compounds of rhodium(II) carboxylates with *N,N'*-bidentate ligands adsorb nitrogen gas [Mikuriya *et al.*, 2003; Mikuriya *et al.*, 2011; Mikuriya *et al.*, 2013a; Mikuriya *et al.*, 2013b; Mikuriya *et al.*, 2013c]. In order to understand the adsorption properties of these compounds, systematic investigations are needed for the chain compounds.

Ethylenediamine (en) is an interesting *N,N'*-bidentate ligand, which is similar to piperazine (pip) and 1,4-diazabicyclo[2.2.2]octane (dabco), but has a different orientation of the nitrogen donor atoms. In this study, we synthesized a new chain compound from a reaction of rhodium(II) benzoate and en, determined the crystal structure by the

X-ray crystallography, and measured the adsorption property for nitrogen gas, which is the first example of an ethylenediamine adduct of rhodium(II) carboxylate, as shown in Figure 1.

Figure 1: Chemical structure of $[\text{Rh}_2(\text{bz})_4(\text{en})]_n$.



2. EXPERIMENTAL

Rhodium(II) benzoate was prepared by a method described in the literature [Mikuriya *et al.*, 2003]. A 28 mg (0.47 mmol) portion of en was added to a solution of rhodium(II) benzoate (100 mg, 0.15 mmol) in 30 cm³ of ethanol, and the solution was stirred overnight. The precipitate was collected, washed by acetonitrile, and dried under vacuum. Yield, 64 mg (47%). Anal. Found: C, 48.09; H, 3.72; N, 3.65%. Calcd for C₃₀H₂₈N₂O₈Rh₂: C, 48.02; H, 3.76; N, 3.73%. IR (KBr, cm⁻¹): 3348 ($\nu_{\text{as}}\text{NH}_2$), 3291 ($\nu_{\text{s}}\text{NH}_2$), 2960 ($\nu_{\text{as}}\text{CH}_2$), 2880 ($\nu_{\text{s}}\text{CH}_2$), 1560 ($\nu_{\text{as}}\text{COO}$), 1397 ($\nu_{\text{s}}\text{COO}$). Diffuse reflectance spectra: λ_{max} 470sh ($\nu(\text{Rh}-\text{O}) \rightarrow \nu^*(\text{Rh}-\text{O})$), 536 ($\nu^*(\text{Rh}_2) \rightarrow \nu^*(\text{Rh}_2)$) nm. X-ray quality crystals were grown by the slow diffusion of en with rhodium(II) benzoate in ethylene glycol and acetonitrile.

X-ray diffraction data for these crystals were collected at 90 K on a Bruker CCD X-ray diffractometer (SMART APEX) using graphite-monochromated Mo-K α radiation. Crystal data and details concerning data collection are given in

Table 1. The structure was solved by direct methods, and refined by full-matrix least-squares methods. The hydrogen atoms were inserted at their calculated positions and fixed there. All of the calculations were carried out on a Pentium IV Windows 2000 computer utilizing the SHELXTL software package. Crystallographic data have been deposited with Cambridge

Table 1: Crystal and experimental data

Chemical formula: C ₃₈ H ₄₀ N ₆ O ₈ Rh ₂
Formula weight = 914.58
$T = 90$ K
Crystal system: triclinic
Space group: $P2_1/c$
$a = 10.149(3)$ Å
$b = 20.250(5)$ Å $\beta = 103.602(5)^\circ$
$c = 19.180(5)$ Å
$V = 3831.3(17)$ Å ³
$Z = 4$
$D_x = 1.586$ g/cm ³
Radiation: Mo K α ($\lambda = 0.71073$ Å)
$\mu(\text{Mo K}\alpha) = 0.921$ mm ⁻¹
$F(000) = 1856$
Crystal size = 0.23 x 0.15 x 0.01 mm ³
No. of reflections collected = 21789
No. of independent reflections = 7844
θ range for data collection: 1.48 to 26.38°
Data/Restraints/Parameters = 7844/0/439
Goodness-of-fit on $F^2 = 0.803$
R indices [$I > 2\sigma(I)$]: $R1 = 0.0704$, $wR2 = 0.1678$
R indices (all data): $R1 = 0.1674$, $wR2 = 0.1931$
$(\Delta/\sigma)_{\text{max}} = 0.001$
$(\Delta\rho)_{\text{max}} = 3.932$ eÅ ⁻³
$(\Delta\rho)_{\text{min}} = -1.724$ eÅ ⁻³
Measurement: Bruker Smart APEX CCD diffractometer
Program system: SHELXTL
Structure determination: Direct methods (SHELXS-97)
Refinement: full matrix least-squares (SHELXL-97)
CCDC deposition number: 942176

Crystallographic Data Centre: Deposit number CCDC-942176. Copies of the data can be obtained free of charge via <http://www.ccdc.cam.ac.uk/conts/retrieving.html> (or from the Cambridge Crystallographic Data Centre, 12, Union Road, Cambridge, CB2 1EZ, UK; Fax: +44 1223 336033; e-mail: deposit@ccdc.cam.ac.uk).

The adsorption isotherm of N₂ at 77K on [Rh₂(bz)₄(en)]_n was measured by a Quantachrome Autosorb-1-C. Prior to the adsorption, the sample was evacuated at 298K for 2 h.

3. RESULTS AND DISCUSSION

The molecular structure determined by X-ray crystal structure analysis is shown in Figure 2. Selected bond distances and angles are given in Table 2. The asymmetric unit contains one dinuclear Rh₂(bz)₄ unit and two halves of en molecules for a chain molecule, and four acetonitrile molecules. The dinuclear Rh₂(bz)₄ unit has a lantern-type dinuclear core bridged by four benzoate ions in a *syn-syn* fashion. The Rh1-Rh2 distance is 2.4004(12) Å, which is in the range of 2.35–2.45 Å, found in dinuclear rhodium(II) carboxylates [Mikuriya *et al.*, 2003; Mikuriya *et al.*, 2011a; Mikuriya *et*

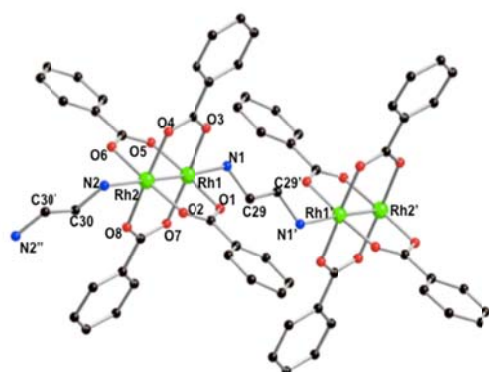


Figure 2: Molecular structure of [Rh₂(bz)₄(en)]_n · 4nCH₃CN. Hydrogen atoms and solvent molecules are omitted for clarity.

et al., 2011b; Mikuriya *et al.*, 2013a; Mikuriya *et al.*, 2013b; Mikuriya *et al.*, 2013c]. The coordination geometry around each rhodium atom is an elongated octahedron.

The bond distances of the Rh and basal O atoms are 2.013(8)–2.048(6) Å, which are comparable to those found in rhodium(II) carboxylates and their chain compounds [Mikuriya *et al.*, 2003; Mikuriya *et al.*, 2011a; Mikuriya *et al.*, 2011b; Mikuriya *et al.*, 2013a; Mikuriya *et al.*, 2013b; Mikuriya *et al.*, 2013c]. The apical Rh1-N1 and Rh2-N2 distances are 2.270(8) and 2.244(8) Å, respectively, which are also in the normal range as apical bonding for the rhodium(II) carboxylate adducts [Mikuriya *et al.*, 2003; Mikuriya *et al.*, 2011a; Mikuriya *et al.*, 2011b; Mikuriya *et al.*, 2013a; Mikuriya *et al.*, 2013b; Mikuriya *et al.*, 2013c]. It is to be noted that the ethylenediamine molecules links dinuclear Rh₂(bz)₄ units to form a zig-zag chain molecule with the Rh2-Rh1-N1 and Rh1-Rh2-N2, Rh1-N1-C29, and Rh2-N2-C30 angles of 176.5(2), 175.7(3), 111.7(6)°, and 114.0(6), respectively. This is in contrast with the case for the linear chain

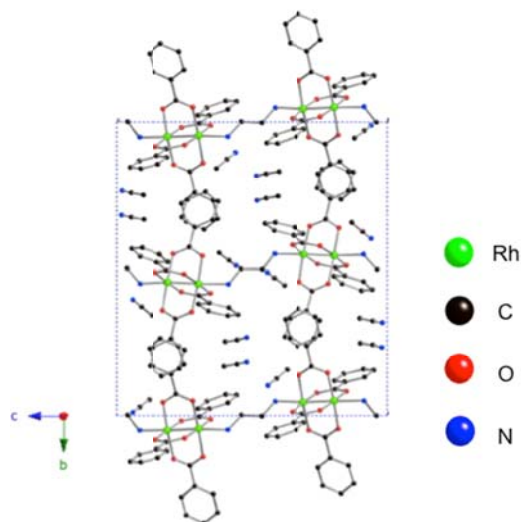


Figure 3: Packing diagram of [Rh₂(bz)₄(en)]_n · 4nCH₃CN.

Table 2: Selected bond distances (Å) and angles (°) of $[\text{Rh}_2(\text{bz})_4(\text{en})]_n \cdot 4n\text{CH}_3\text{CN}$.

Rh1-O1 2.025(8)	Rh2-O6 2.013(8)
Rh1-O7 2.038(7)	Rh2-O8 2.032(7)
Rh1-O3 2.041(7)	Rh2-O2 2.044(8)
Rh1-O5 2.046(8)	Rh2-O4 2.048(6)
Rh1-N1 2.270(8)	Rh2-N2 2.244(8)
Rh1-Rh2 2.4004(12)	
N1-Rh1-Rh2 176.5(2)	N2-Rh2-Rh1 175.7(3)
Rh1-N1-C29 111.7(6)	Rh2-N2-C30 114.0(6)

complex of rhodium(II) acetate with dabco [Mikuriya *et al.*, 2013a]. In the crystal, acetonitrile molecules are incorporated among these chain molecules (Figure 3).

The adsorption isotherm of N_2 (77 K) on this complex was measured. The adsorption isotherm belongs to Type II in IUPAC classification with a small specific surface area (S_{BET}), estimated from the BET equation, of $7.5 \text{ m}^2\text{g}^{-1}$, although the presence of a steep rise at low relative pressure (p/p_0) can be recognized (Figure 4). The amount of the adsorbed N_2 gas is dependent on the linker ligand in the order as follows, which is based on the S_{BET} value: $[\text{Rh}_2(\text{piv})_4(\text{pym})_2]$ (Hpiv = $\text{HCO}_2\text{C}(\text{CH}_3)_3$, pym = pyrimidine) ($1 \text{ m}^2/\text{g}$) < $[\text{Rh}_2(\text{bz})_4(\text{en})]_n$ ($7.5 \text{ m}^2/\text{g}$) < $[\text{Rh}_2(\text{piv})_4(\text{pym})]_n$ ($16.8 \text{ m}^2/\text{g}$) < $[\text{Rh}_2(\text{bz})_4(\text{pip})]_n$ ($52.7 \text{ m}^2/\text{g}$) < $[\text{Rh}_2(\text{O}_2\text{CCH}_3)_4(\text{bpe})]_n$ (bpe = 1,2-bis(4-pyridyl)ethane) ($65.6 \text{ m}^2/\text{g}$) < $[\text{Rh}_2(\text{piv})_4(\text{pyz})]_n$ ($70.7 \text{ m}^2/\text{g}$) < $[\text{Rh}_2(\text{piv})_4(4,4'\text{-bpy})]_n$ ($122.0 \text{ m}^2/\text{g}$) \sim $[\text{Rh}_2(\text{piv})_4(\text{bpe})]_n$ ($122.0 \text{ m}^2/\text{g}$) < $[\text{Rh}_2(\text{piv})_4(\text{bpe})]_n$ (bpe = *trans*-1,2-bis(4-pyridyl)ethylene) ($140.2 \text{ m}^2/\text{g}$) < $[\text{Rh}_2(\text{piv})_4(\text{dabco})]_n$ ($186.2 \text{ m}^2/\text{g}$) < $[\text{Rh}_2(\text{O}_2\text{CCH}_3)_4(\text{dabco})]_n$ ($190.1 \text{ m}^2/\text{g}$) [Mikuriya *et al.*, 2003; Mikuriya *et al.*, 2011a; Mikuriya *et al.*, 2013a; Mikuriya

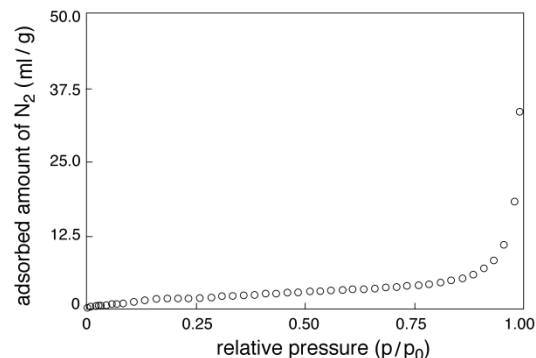


Figure 4: Nitrogen adsorption isotherm of $[\text{Rh}_2(\text{bz})_4(\text{en})]_n \cdot 4n\text{CH}_3\text{CN}$.

et al., 2013b; Mikuriya *et al.*, 2013c; Mikuriya *et al.*, 2013d]. It could be concluded that large and bulky linker ligands afford larger vacant spaces for the chain-assembled complexes, resulting in a higher adsorption property for these systems.

4. CONCLUSION

The present complex has a zig-zag chain structure and incorporated acetonitrile molecules in the crystal. The adsorption property was observed for N_2 gas. This is in contrast with the case for the molybdenum(II) acetate chain compounds.

Acknowledgements: The present work was partially supported by MEXT-Supported Program for the Strategic Research Foundation at Private Universities.

REFERENCES

- Handa, M., Mikuriya, M., Kotera, T., Yamada, K., Nakao, T., Matsumoto, H., Kasuga, K., 1995, Linear Chain Compounds of Molybdenum(II) Acetate Linked by Pyrazine, 4,4'-Bipyridine, and 1,4-Diazabicyclo[2.2.2]octane, *Bull. Chem. Soc. Jpn.*, 68, 2567.
- Mikuriya, M., Higashiguchi, M., Sakai, T., Yoshioka, D. and Handa, M., 2003, Chain Compounds of Rhodium(II) Benzoate Bridged by *N,N'*-Didentate Ligands, *Progress in Coordination and Bioinorganic Chemistry*, Slovak Technical University Press, Bratislava, Slovakia, 213.

- Mikuriya, M., Yoshioka, D. and Handa, M., 2006. Magnetic interactions in one-, two-, and three-dimensional assemblies of dinuclear ruthenium carboxylates, *Coord. Chem. Rev.*, 250, 2194.
- Mikuriya, M., 2008. Copper(II) Acetate as a Motif for Metal-Assembled Complexes, *Bull. Jpn. Soc. Coord. Chem.* 52, 17.
- Mikuriya, M., Yamamoto, J., Yoshioka, D., Tanaka, H. and Handa, M., 2011a, Synthesis, Crystal Structures, and Adsorption Properties of Chain Complexes of Rhodium(II) Pivalate with *N,N'*-Bidentate Ligands, *New Trends in Coordination, Bioinorganic and Applied Inorganic Chemistry*, Slovak University of Technology Press, Bratislava, Slovakia, 311.
- Mikuriya, M., Yamamoto, J., Yoshioka, D., Tanaka, H. and Handa, M., 2011b, Synthesis and Crystal Structure of Chain Complex of Rhodium(II) Pivalate and *trans*-1,2-Bis(4-pyridyl)ethylene with an N₂-Adsorption Property, *X-ray Struc. Anal. Online*, 27, 27.
- Mikuriya, M., Yamamoto, J., Ouchi, K., Yoshioka, D., Tanaka, H. and Handa, M., 2013a, Synthesis, Crystal Structure, and N₂-adsorption Property of a Chain Complex of Rhodium(II) Acetate and 1,4-Diazabicyclo[2.2.2]octane, *X-ray Struc. Anal. Online*, 29, 7.
- Mikuriya, M., Ouchi, K., Nakanishi, Y., Yoshioka, D., Tanaka, H. and Handa, M., 2013b, Synthesis, Crystal Structure, and N₂-adsorption Property of a Chain Complex of Rhodium(II) Benzoate and Piperazine, *X-ray Struc. Anal. Online*, 29, 21.
- Mikuriya, M., Yamamoto, J., Ouchi, K., Takada, S., Yoshioka, D., Tanaka, H. and Handa, M., 2013c, Synthesis and Crystal Structure of a Chain Complex of Rhodium(II) Acetate and 1,2-Bis(4-pyridyl)ethane Having an N₂-Adsorption Property, *X-ray Struc. Anal. Online*, 29, in press.
- Mikuriya, M., Kaihara, N., Yamamoto, J., Takada, S., Yoshioka, D., Tanaka, H. and Handa, M., 2013d, Synthesis and Crystal Structure of a Chain Complex of Molybdenum(II) Acetate and 1,2-Bis(4-pyridyl)ethane Aiming at N₂-Adsorption Property, *X-ray Struc. Anal. Online*, 29, in press.
- Mori, W., Hoshino, H., Nishimoto, Y., and Takamizawa, S., 1999, Synthesis and Gas Occlusion of New Micropore Substance Rhodium(II) Carboxylates Bridged by Pyrazine, *Chem. Lett.*, 331.
- Nukada, R., Mori, W., Takamizawa, S., Mikuriya, M., Handa, M., and Naono, H., 1999, Microporous Structure of a Chain Compound of Copper(II) Benzoate Bridged by Pyrazine, *Chem. Lett.*, 367.

PROCEDURE FOR CONTACT DETECTION BETWEEN PLATY COHESIVE PARTICLES

Hamed Bayesteh¹, Ali Asghar Mirghasemi^{2,a}

1. School of Civil Engineering, College of Engineering, University of Tehran, Iran

2. School of Civil Engineering, College of Engineering, University of Tehran, Iran

3. Author_3's Institution, Department, City, Country

a. Corresponding author (aghasemi@ut.ac.ir)

ABSTRACT: The discrete element method framework has been previously shown to accurately model cohesive soil behavior at the microscopic level. The most important step in the simulating cohesive particles process is contact detection. An applicable contact detection algorithm should be devised based on the micromechanical behaviour of the cohesive soils at the particle scale. This paper presents a new method for the detection of platy cohesive particles contact. The proposed method considers not only the mechanical contacts, but also the diffused double layer (DDL) repulsion between clayey minerals. The particles in mechanical contact and the particles in DDL repulsion are recognized by separate algorithms. The detection is designed by a sequential step-by-step process, bringing the focus onto the micromechanical interactions between clay minerals. Each interparticle force is individually calculated in the local system and transferred to the global system by a mathematical expression. Attempts are made to devise a clear algorithm to embed in discrete element method computational programming based on the clay's micromechanics. Based on the proposed algorithms, a new 2D DEM code has been programmed and a verification example is addressed. Also, one-dimensional compressibility behaviour of the clayey soils has been simulated and the results are compared with theoretical expectations.

1. INTRODUCTION

The representative elementary volume (REV) of the soil media usually consists of particles, micro-pores, macro pores and pore fluid as same as other porous media [Delage, 2007]. In spite of these discrete parts, soils have been traditionally assumed as continuum material both in theoretical and numerical analysis. According to the discontinuous nature of the soils, several studies have been indicated that the microstructural approach (numerical and experimental methods) is the best sight for monitoring soil behaviours [Pusch and Yong, 2006].

From numerical point of view, the common numerical method which can simulate material behaviours at particle-level (microscopic) has been known as discrete element method that was first

introduced by Cundall and Strack, 1979 [Cundall and Strack, 1979]. Usually in the DEM, a large number of discrete particles involved where each particle is interacting with neighboring elements based on the existing interparticle forces. Finding the particles which are in contact is the most important, time consuming and challenging step in DEM analysis which has been named "contact detection"[Munjiza, 1998].

A convenient method for contact detection depends not only on the shape of the particles but also on the type of interparticle forces. Several algorithms have been proposed to contact detection for non-cohesive granular material with various shape such as discs and spheres, ellipses, polygonal particles and irregular

shapes [Abedi and Mirghasemi, 2011]. In addition, several microstructure laboratory investigations have been indicated that the shape of the clays in 2D is as like as a very narrow rectangular at the particle scale and their cluster's shape are similar to disc or ellipse [Yong 2000]. In order to simulate cohesive soil behaviours by DEM, several studies have been performed in which the clayey particle's shapes are assumed to be a circle or ellipse [Ammeri *et al.*, 2009]. Anandarajah used DEM to study clay behaviour at the particle scale with real shape. The authors recently developed a DEM model for simulating clays behavior at particles scale by considering real shape of the particles [Bayesteh and Mirghasemi, 2013].

As can be seen in the literature, most contact detection algorithms are useful for simulating granular media but not for modeling clayey soil behaviours at the particle scale since clayey soils shapes in this scale are similar to a cube in 3D and very narrow rectangular in 2D. Also the existing contact detection methods can't detect the real electro-chemical interactions between clayey particles. In addition, a comprehensive contact detection method between platy cohesive particles hasn't been addressed yet. The aim of this paper is to describe a new algorithm for contact detection of two-dimensional clayey assembly.

2. THEORY

The purpose of contact detection is to find particles which have actual interaction and avoid processing contact interaction when particles are far from each other in order to reduce CPU running times.

Despite of granular soils, physico-chemical interaction between clay minerals is the effective interparticle force which includes double layer

repulsive force and Van Der Waal's attractive force [Yong, 2000] because the clay mineral's surface have negative electrical charge. According to this type of inter-particle forces, definition of a real contact law and contact detection algorithm are very complicated.

Double layer repulsive force and Born's repulsive force are the main forces between clay minerals according to their specific surface area (SSA), cation exchangeable capacity (CEC) and pore fluid chemistry [Mattar, 2005].

The charged clay surface and the cloud of ions next to it are together known as the diffuse double layer (DDL) that controls the interaction between clay particles [Mitchell and Soga, 2005]. Repulsion is accrued due to the overlapping two DDL which have been schematically depicted in Figure 1.

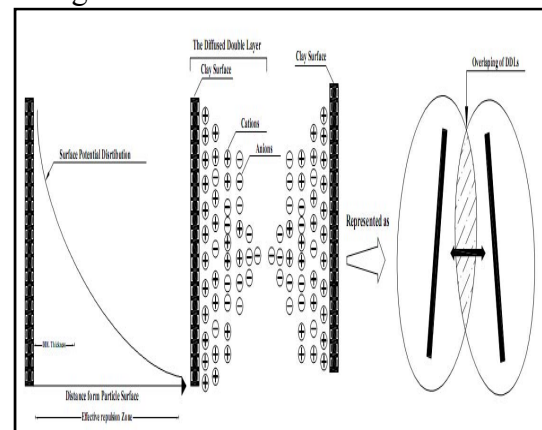


Figure 1: Schematic of diffuse double layer and mechanism of repulsion development

The Gouy-Chapman diffuse double layer theory is the famous theory that has been used to model the interaction between clay particles and pore fluid [Sridharan, 1982]. Bayesteh and Mirghasemi [2013] developed a method to calculate the repulsive force Based on previous studies.

In order to find the discrete particles

which are in contact in DEM simulation, an algorithm should be devised to calculate an effective repulsion zone based on the thickness of DDL, geometry of particles and effective distance between them. This effective area around the discrete particles named area of repulsion (AOR).

3. CONTACT DETECTION

In seeking simplification and effectiveness in programming, the contact detection procedure is proposed to take the following three steps:

- Step 1: Finding the particles may be in contact and setting the contact list
- Step 2: Finding particles which are in contact by double layer repulsion and calculating related forces.
- Step 3: Finding particles which have mechanical contact and calculating related forces.

The first task to detect particles in contact is to find particles that are close enough to have probability of mechanical or electro-chemical contact. The boxing method has been used for tracing particles. In this method, the physical problem space is divided into square boxes. Next, a discrete element is assumed to map onto cells and the corresponded box is found according to their position of the particle's center. As shown in Figure 2, the box which contains particle's center is hatched and denoted by number 5. Then the boxes near the location of the assumed particle are identified based on the mechanism of inter-particle forces.

In order to identify suitable boxes near an assumed discrete element, the mechanism of both mechanical and electro-chemical interaction should be considered. Therefore two types of boxes are assumed in this study (Figure 2). Type 1 is comprised of adjacent boxes which

their particles may be in mechanical contact. Type 2 includes boxes which are located in the effective repulsion area and recognized according to the thickness of DDL.

Based on thickness of DDL, farther boxes from a discrete element should be considered in order to detect particles in repulsive contact so that the boxes in type 2 are more than type 1. By result, an efficient method should be used to identify the type 2 of boxes based on clay microstructure behaviour.

In order to reach the above aim, the main task is to define the effective repulsion area around a discrete particle which is illustrated in Figure 2 by a rectangular. Based on the DDL theory, the length on this rectangular is as same as particle length and its wide is depends on thickness of DDL which is named "TOL". As mentioned before, this distance (TOL) usually is about three to five times the DDL thickness existing at the both sides of discrete element [23,30]. To be more conservative, the rectangular of effective repulsion area is approximated with a circle ($R = 2 \times \text{TOL}$) where R is the circle's radius.

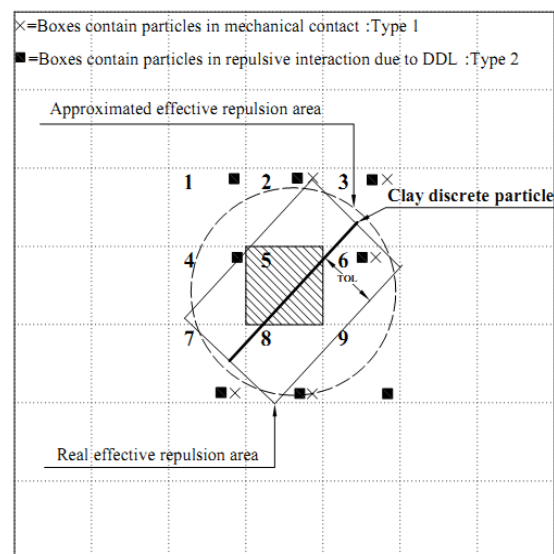


Figure 2: Schematic diagram of boxing area and effective repulsion area

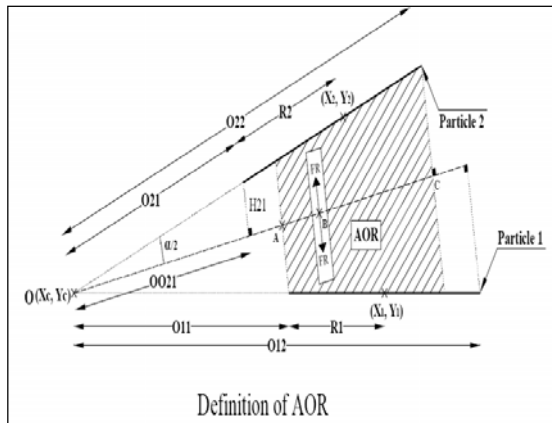


Figure 3: Definition the area of repulsion (AOR) between two particles

3.1. Repulsion Contact Detection And Calculation

By considering Figure 1, the first task to detect repulsion contact is finding the area of repulsion AOR between two particles by neglecting the particles between them which are named “middle particles”. The zone of interaction between two particles is estimated by finding the virtual intersection point "O" between them and finding the AOR that is the hatched trapezium area in Figure 3. Details of the method were addressed in the previous study [Bayesteh and Mirghasemi].

Based on the position and magnitude of the overlap between pair particles, the mechanical force will be developed. It means that if there is no overlap between particles, no mechanical contact is induced. The main scope of this section is to devise an algorithm to find two particles in contact and to calculate mechanical contact force using proper contact law.

In the proposed procedure, the overlap length is calculated based on position of the intersection point between two particles. Firstly, the equation line of each particle is determined based on its geometry. Then the virtual intersection point between two lines is determined by using “Kramer law”. Distance between

virtual cross point and center point of the particle is denoted by (d_i) and the half of the length of particle is denoted by (R_i). Therefore, an overlap exists if both d_1 and d_2 are less than related R .

When the distance between two particles is less than the defined mechanical cutoff, mechanical force will be developed. Also, the resultant mechanical force induces the moment.

4. VERIFICATION TEST SIMULATION

A (1400×1400 nm) box media is considered and confined by four straight lines denoted as walls. The walls are assumed to be rigid and only have transitional deformation. A Number of 350 clay particles with random location and orientation are automatically placed within this box area using a computer random-generator. The initially generated assembly (Figure 4) is similar to a loose dry clay where there aren't any physico-chemical and mechanical forces between particles. In this situation (in absent of the DDL repulsive forces), particles have irregular distances between each other. While some of them are very close, there are large distances between others. When the repulsive and mechanical force program modules are turned on, interparticle forces are induced. In this case, submerging clay minerals in the electrolyte media is simulated. Based on the new inserted inter-particle forces, particles move until equilibration between mechanical and physico-chemical forces and new arrangement forms so that distances between adjacent particles are changed. This stage is named relaxation. The assembly arrangement after relaxation is depicted in Figure 5. In this equilibrium condition, the spacing between particles becomes more uniform than what was seen in the initial assembly. Also, there isn't any overlap between discrete element which is

emphasizes the accuracy of simulation. A window from initial assembly (C) and relaxed assembly (C1) are selected and zoomed in Figure 6, respectively. The more uniform distance between particles in the relaxed assembly indicate that activating DDL repulsive forces between one discrete element and neighboring particles (which have distances less than TOL with the target particle) lead to change the position of this particle. These displacements and rotations depend not only on the magnitude of interparticle forces and moments, but also on their direction. When the particle's movement causes overlap with adjacent particles, mechanical forces are induced. As a result in the next step of simulation overlap between particles vanishes due to moving discrete elements.

For example assume particles 1, 2 and 3 at the "C" zoomed window in Figure 6. Before leaching electrolyte and activating DDL repulsive forces, they are close to each other and the distance between them are less than double layer thickness (which is about 10 nm in this model). But when the repulsion is activated, they move and rotate to reach equilibrium based on the AOR between them as depicted in "C1" window. The area of repulsion between particles 1 and 3 (AOR1) induces (FR_1) and (MR_1) on both particles 1 and 3 which their magnitudes depend on the particles geometry and distance between them. Although the magnitude of (FR_1) on both particles has same value, but its direction on the global system and its point of action on the each particle have different values.

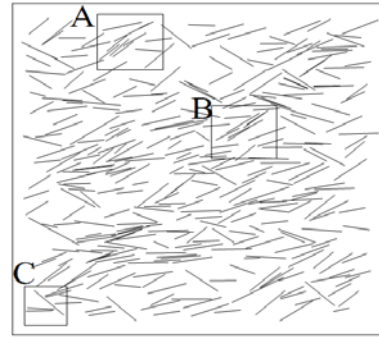


Figure 4: Initial assembly of clay particles

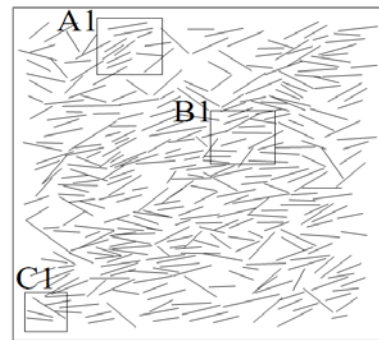


Figure 5: Particle's arrangement after relaxation

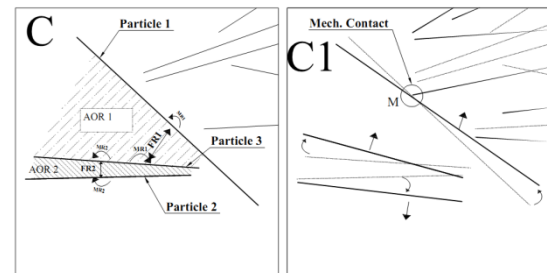


Figure 6: Schematically AOR between part of the particles and their movements due to inter-particle forces

Mechanical forces at contact point prevent moving particles when an overlapping is induced. For example, assume the mechanical contact point which is denoted by "M" in Figure 6. Due to repulsion between particle 1 and 3, particle 1 is moving to reach point "M". The mechanical force develops at this point and restricts its free movement. So, this particle rotates around this point to release its acceleration due to repulsion until equilibrium is achieved. This deformed shape satisfies the physical feasible of real particle rearrangements.

5. CONCLUSION

A procedure to contact detection for platy cohesive soils has been presented in order to apply in discrete element simulation. The proposed method takes in account not only the mechanical force, but also double layer repulsion mechanism to detect the contact between particles.

This procedure is based on a clear step-by-step process and the computational algorithm is easy to be implemented. In this method, the particles in contact are recognized from mechanical point of view and those are in DDL repulsion by applying boxing method. A validation with respect to qualitative assessment has been performed by modeling compressibility behaviour of clay particles and the details of deformation process have been addressed.

REFERENCES

- Abedi S., and Mirghasemi, A.A., 2011. "Particle shape consideration in numerical simulation of assemblies of irregularly shaped particles". *Particology*, Vol. 9, No. 4, 387,397.
- Ammeri A., Jamei M. and Bouassida M., 2009. "Numerical study of bending test on compacted clay by discrete element method: tensile strength determination", *Int. J. Computer Applications in Technology*, Vol.34, No.1, 13-22.
- Anandarajah, A. 1994. "Discrete Element Method for Simulating Behaviour of Cohesive Soil", *J. Geotech. Engrg., ASCE*, Vol. 120, No. 9, 1593-1613
- Bayesteh, H. and Mirghasemi, A.A., 2013. Procedure to detect the contact of platy cohesive particles in discrete element analysis. *Powder Technology*, Vol. 244, 75-84.
- Bayesteh, H. and Mirghasemi, A.A., 2013. Numerical simulation of pore fluid characteristic effect on the volume change behavior of montmorillonite clays. *Computers and Geotechnics*, No. 48, 146-155.
- Cundall, P.A. and Strack, O.D.L., 1979. "A discrete numerical model for granular assemblies", *Geotechnique*, Vol. 29, No. 1, 47-65.
- Delage, P. 2007. "Microstructure features in the behaviour of engineered barriers for nuclear waste disposal." *Proc., Experimental Unsaturated Soil Mechanics*, Springer, New York, 11–32.
- Mattar M.I., 2005. "Modeling of montmorillonite clay-water interaction with particle subdivision using three dimensional discrete element methods" PhD thesis, Fargo, North Dakota.
- Mitchell, J. K. and Soga, K., 2005. "Fundamentals of soil behaviour". John Wiley and Sons. Inc., 558.
- Munjiza, A., Andrews, K.R.F., 1998. NBS contact detection algorithm for bodies of similar size. *International Journal for Numerical Methods in Engineering*, 43:131–149.
- Pusch, R. and Yong, R., 2006. "Microstructure of Smectite Clays and Engineering Performance", Taylor and Francis, New York, 330.
- Sridharan, A., and Jayadava, M. S. 1982. Double layer theory and compressibility of clays. *J. Geotechnique*, 32, No. 2, , 94-99.
- Yong, R. N. 2000. *Geoenvironmental engineering: Contaminant soils, pollutant fate and mitigation*. By CRC Press LLC. , 307

MORPHOLOGY OF MICELLES AND MICELLAR AGGREGATES AS A FUNCTION OF ELECTROLYTE VALENCE AND CONCENTRATION

Aybike Nil Olcay¹, Mehmet Polat² and Hurriyet Polat^{3,a}

1. Izmir Institute of Technology, Department of Environmental Engineering, Izmir, Turkey

2. Izmir Institute of Technology, Department of Chemical Engineering, Izmir, Turkey

3. Izmir Institute of Technology, Department of Chemistry, Izmir, Turkey

a. Corresponding author (hurriyetpolat@iyte.edu.tr)

ABSTRACT: Micellar structures are becoming increasingly important in numerous applications from drug delivery to waste treatment. Morphology of these structures are extremely important in the applicability and the outcome of these applications. Despite this, the literature is still not very clear on how the micelle formation takes place and the aggregation behavior of the formed micelles with changing solution conditions. In this study, micelle development and micellar interactions in the presence of electrolytes of varying valence and at a wide electrolyte strength spectrum for model cationic, anionic and non-ionic surface active agents were studied. The surface tension, micelle size distribution and electrokinetic potentials were the main parameters studied. It was shown that the association behavior of surfactant molecules, size and charge of the micelles or the micellar aggregates is strongly affected by the valence and the strength of the electrolyte in solution for ionic surfactants.

1. INTRODUCTION

Surface tension is one of the most common techniques for investigating the adsorption and association behavior of surfactants at air/water interfaces. The micellization behavior of surfactants, however, is very important in many application areas such as drug, textile, environment, food, cosmetic and etc.. Micellization is also complex and depends on surfactant type, concentration and environmental conditions. The presence of electrolytes are expected to effect the association behavior of surfactants. There are some studies to elucidate this relation [Santos *et al.*, 2009]

According to the related studies in the past (Santos, *et al.*, 2009; Dong *et al.*, 2008; Miyagishi, 2001), the critical micelle concentration (CMC) of the ionic surfactants decrease by adding of an inert salt. This is explained by the presence

ions that compress the electric double layer surrounding the micelles, and consequently induce the screening of the electrostatic repulsion among the polar head groups.

It is also found that addition of salt also decreases the CMC's of nonionic surfactants and the reduction is always lower than CMC's of ionic surfactants [Miyagishi *et al.*, 2001].

According to Iyota *et al.*, [Iyota *et al.*, 2006], surface tension increases linearly with increasing molality of inorganic salt for the three salts and the slope of the surface tension vs. molality line increases in the order $\text{NaCl} < \text{CaCl}_2 < \text{LaCl}_3$.

Therefore, it can be seen that there is a need on the effect of electrolytes on how the micellar structures develop and behave in the literature. Hence, in this study, a systematic studies under well-defined solution conditions for the effect

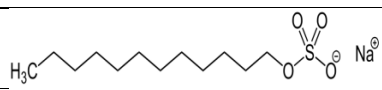
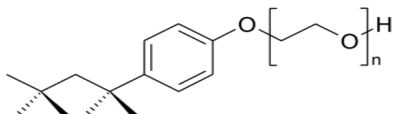
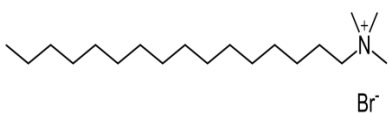
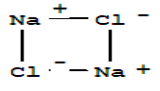
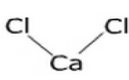
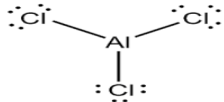
of electrolytes of various valence and concentration on micellar structure have carried out.

2. EXPERIMENTAL

2.1. Materials

The selected properties and the structures of the surfactants and the electrolytes employed are given in Table 1.

Table 1: Selected properties and chemical structures of surfactants and electrolytes

Compound name	MW (g/mol)	Chemical structure	Explanation
Sodium Dodecyl Sulfate (SDS)	288		Anionic Surfactant
Ethoxylated Octyl Phenol, (T-X100)	647		Nonionic Surfactant
Hexadecyl trimethyl-ammonium bromide, (CTAB)	364		Cationic Surfactant
Sodium Chloride, (NaCl)	58		Electrolyte with +1 charge
Calcium Chloride, (CaCl2)	110		Electrolyte with +2 charge
Aluminium Chloride, (AlCl3)	133		Electrolyte with +3 charge

2.2. Methods

2.2.1. Surface tension measurements

Measurements were performed with a Kruss Digital Tensiometer K10T using the Du-Nouy Ring method. The ring method is based on a force measurement similar to the plate method. The ring is usually made up of platinum or platinum-iridium alloy of a radius (R) of 2–3 cm. The measuring device is a vertically suspended ring with a precise geometry. When the ring is brought into contact with the liquid, the liquid “jumps” to the ring and pulls it into the liquid. The force caused by this wetting is measured by pulling the ring up to the level of the liquid surface (Kruss Tensiometer Users

Manual; Adamson, 1997). The surface tension of the liquid is determined from the measured force using the equation:

$$\gamma = \frac{F}{p \cos \theta} f$$

where γ is the surface tension, F is the the maximum force, p is the the perimeter of the three-phase contact line is equal to twice the circumference of the ring: $p = 4pR$. and f is a correction factor due to additional volume of liquid is lifted during the detachment of the ring from the interface and θ is contact angle measured for the liquid meniscus in contact with the ring surface [Drelich, 2002].

2.2.2. Size and charge measurements of micelles.

Size and zeta potential measurements were carried out in Malvern Zeta Sizer Nano ZS. The device employs a combination of laser Doppler velocimetry and phase analysis light scattering (PALS).

2.2.3. Determination of the association of surfactant molecules and critical micelle concentration

Surface tension values were plotted as a function of surfactant concentrations and the concentration regions where the slope of the curve is different were marked. These regions were evaluated and the effect of surfactant type and the environmental conditions on these regions were determined. A picture that gives a general behaviour of a surfactant is given in Figure 2. As it is seen there should be different concentration regions where surfactant molecules have different forms. These plots were also used to obtain the critical concentrations where micelles start to form.

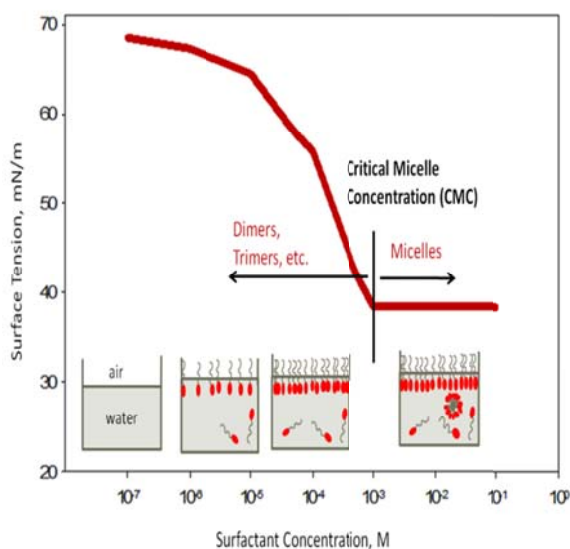


Figure 2: General behaviour of surfactants

3. RESULTS AND DISCUSSION

3.1. Surface Tension Measurements

3.1.1. Sodium Dodecyl Sulfate (SDS): an anionic surfactant

Surface tension versus SDS concentration data is given in Figure 3 for NaCl, CaCl₂ and AlCl₃ solutions at different concentrations (such as 10⁻⁴, 10⁻³, 10⁻² M) respectively. As it is seen the electrolyte effect is at intermediate surfactant concentrations (below CMC) where surfactant molecules are still in their single form.

CaCl₂ and AlCl₃ seem to have similar behaviour (decreased surface tension) compare to NaCl. NaCl, on the other hand, showed unexpected behaviour and increased surface tension in the concentration range between 10⁻⁴-10⁻² M. The decrease in surface tension and CMC as in the case of CaCl₂ and AlCl₃, could be explained by the presence ions that compress the electric double layer surrounding the micelles that will reduce the repulsion among the polar head groups.

The surface tension values after formation of micelles, however, was similar. The effect of electrolyte concentration looks complicated and should be studied in detail.

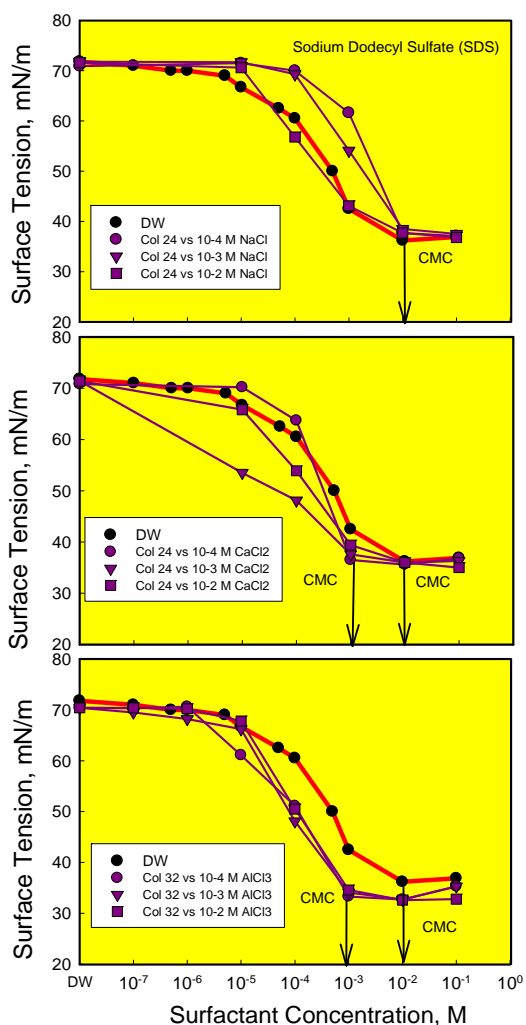
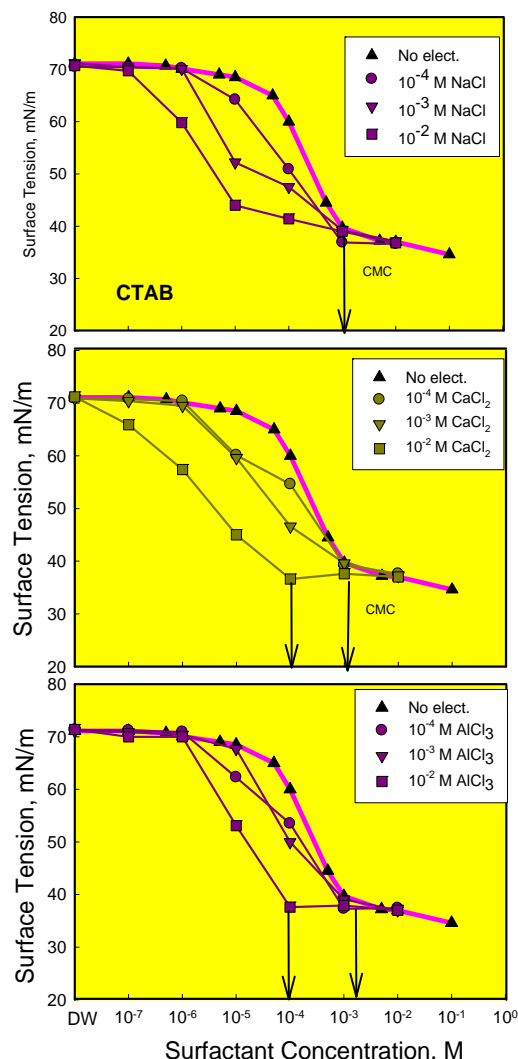


Figure 3: Surface tension vs SDS concentration in the presence of NaCl, CaCl₂, AlCl₃.

3.1.2. Hexadecyl Trimethyl-Ammonium Bromide,(CTAB): A Cationic Surfactant

Surface tension versus CTAB concentration data is given in Figure 4 for NaCl, CaCl₂ and AlCl₃ solutions at different concentrations (such as 10⁻⁴, 10⁻³, 10⁻² M) respectively. Similar to the other ionic surfactant, SDS, the effect of electrolyte is at intermediate and low surfactant concentrations (below CMC) where surfactant molecules are still in their single form.



FFigure 4: Surface tension vs CTAB concentration in the presence of NaCl, CaCl₂, AlCl₃.

3.1.3. Ethoxylated Octyl Phenol (TX-100): A Nonionic Surfactant

Surface tension versus TX-100 concentration data is given in Figure 5, for NaCl, CaCl₂ and AlCl₃ solutions at different concentrations (such as 10⁻⁴, 10⁻³, 10⁻² M) respectively. As it is seen the electrolyte effect is negligible.

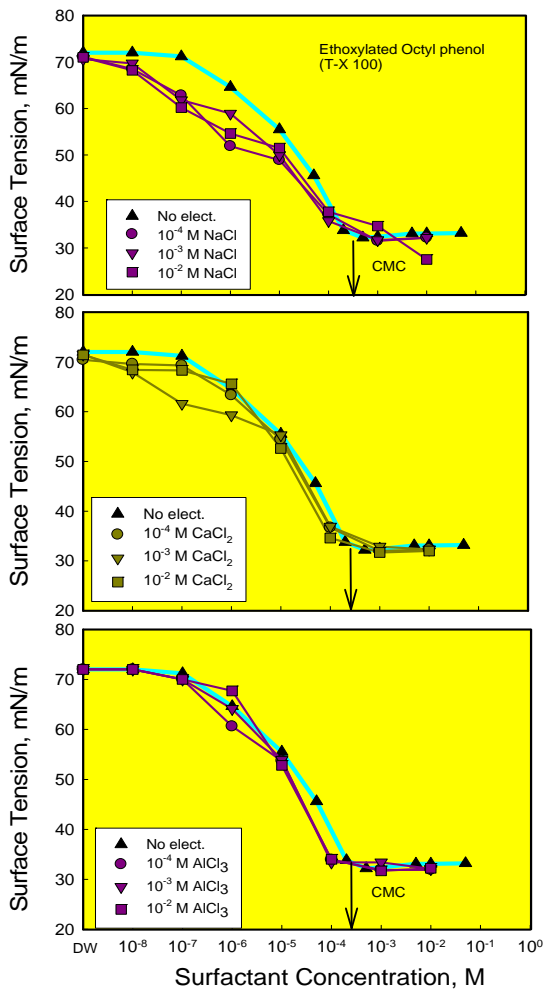


Figure 5: Surface tension vs CTAB concentration in the presence of NaCl, CaCl₂ and AlCl₃.

3.2. Micelle Size and Charge Measurements

The size and charge of micelles for these surfactants were measured. The results of the charge measurements are presented in Figure 6. The results of the size measurements, on the other hand, were not reproducible due to the creation of loose, large aggregates of micelles themselves. Therefore, using size measurements alone may be misleading and not be sufficient enough to determine the size of single micelles in these cases. In general the magnitude of electrostatic charges on micelles which is negative in the case of anionic surfactant and positive in the case of cationic surfactant, decreased with an increase in electrolyte

concentration (Figure 6). However, this effect looks complex and should be studied further.

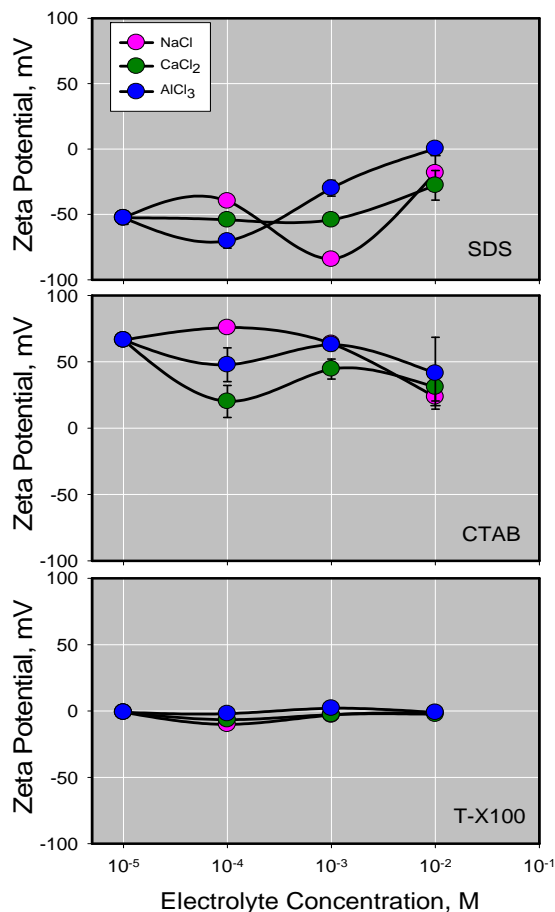


Figure 6: Zeta Potential vs Electrolyte Concentration.

4. CONCLUSIONS

In this study, micelle development and micellar interactions in the presence of electrolytes of varying valence and at a wide electrolyte strength spectrum for model cationic, anionic and non-ionic surface active agents have been studied. The surface tension, micelle size distribution and electrokinetic potentials were the main parameters studied.

It was seen that the micelles seems to be generating aggregates which lead to fluctuating size data in the Zeta Sizer. These results which may be misleading are not presented here and this effect will be studied further.

On the other hand, both the surface tension and the charge of the surfactant molecules and the micelles are strongly affected by the valence and the strength of the electrolyte in solution. However, this is true only for the ionic surfactants, both anionic and cationic. There was no appreciable effect on non-ionic surfactant.

The fact that the presence of electrolytes of different valence causes significant changes in the aggregation behavior and the surface charge of the surfactant aggregates should have important implications in the study of micelles. This effect should especially be considered in such areas as drug delivery and contaminant removal which employ micellar structures.

REFERENCES

- Santos, F. K. G., Neto, E.L.B., Moura, M.C.P.A., Dantas, T.N.C. and Neto, A.A.D., 2009. Molecular behavior of ionic and nonionic surfactants in saline medium, *Colloids and Surfaces A*, 333, 156
- Dong, B., Zhao X., Zheng L., Zhang J., Li N. and Inoue T., 2008. Aggregation behavior of long-chain imidazolium ionic liquids in aqueous solution: Micellization and characterization of micelle microenvironment, *Colloids and Surfaces A*, 317, 666
- Miyagishi, S., Okada, K. and Asakawa, T., 2001. Salt Effect on Critical Micelle Concentrations of Nonionic Surfactants, N-Acyl-N-methylglucamides (MEGA-n), *Journal of Colloid and Interface Science*, 238, 91
- Iyota, H., Tomimitsu T., Shimada, K., Ikeda, N., Motomura K. and Aratono, M., 2006. Charge number effect on the miscibility of inorganic salt and surfactant in adsorbed film and micelle: Inorganic salt–octyl methyl sulfoxide mixtures, *Journal of Colloid and Interface Science*, 299, 428
- Harkins, W.D, Jordan, H.F, 1930. A method for determination of surface and interfacial tension from the maximum pull on a ring. *J. Am. Chem. Soc.* 52, 1751.
- Drelich, J., Fang, C., White, C.L., 2002. *Encyclopedia of Surface and Colloid Science*, 3154

THE DISPERSION PROPERTIES OF MICRONIZED MARBLE SUSPENSIONS IN THE PRESENCE OF INORGANIC AND POLYMERIC DISPERSANTS

Selçuk Koltka¹, Sinem Güvercin², Tuba Ekelik², Orhan Özdemir³, Eyüp Sabah^{2a}

1. Ermas Marble Tourism Industry Trade Co., Ula-Muğla, Turkey

2. Afyon Kocatepe University, Mining Engineering Department, Afyonkarahisar, Turkey

3. Istanbul University, Mining Engineering Department, Avcılar, Istanbul, Turkey

a. Corresponding author (esabah@aku.edu.tr)

ABSTRACT: Calcium carbonate (CaCO_3) is the most widely used filler and/or extender material in paper, paint, plastic, sealant, adhesive and several other industries, each of which requires specific product characteristics in terms of chemical purity, particle size distribution, shape and surface area, whiteness, and rheological behavior etc. Ground and precipitated calcium carbonates (GCC and PCC) are the two main sources. GCC is extracted through mining in the form of limestone, marble, dolomite or chalk, and it is wet or dry ground depending on the final product requirements. Even though cheaper, dry grinding is often limited to a minimum particle size of 2-3 μm . More expensive wet grinding, which usually yields finer material, may be the required form of grinding when the final product must be in slurry form (i.e. in paper or paint applications). When GCC or PCC is in slurry form, solid concentration should be maximized to reduce transportation and drying costs without sacrificing the viscosity and stability of the slurry. Use of dispersants is the preferred method for achieving this. Electrokinetic studies in the literature showed that slurry stability is affected significantly by the zeta potential of calcium carbonate and its impurities.

1. INTRODUCTION

Calcium carbonate (CaCO_3) is the most widely used filler mineral in many industries such as paper industry (as filler and coating), paint industry (as filler and extender), plastic industry (as filler), and sealant and adhesive industry (as filler). Each application requires very specific product characteristics in terms of chemical purity, particle size distribution, particle shape and surface area, whiteness, and rheological behavior etc.

There are two sources of calcium carbonate, namely ground calcium carbonate (GCC) and precipitated calcium carbonate (PCC) in the world. GCC is extracted from the earth, and is present in varying quantities in the form of calcite, aragonite, vaterite (= pure calcium carbonate), limestone, chalk, marble or travertine (= industrially

important source rocks). Following its extraction, GCC is ground either under dry or wet conditions depending on the final product requirements. While dry grinding is a cheaper method, and often limited to a minimum particle size of 2-3 μm , wet grinding is more expensive, and used for production of fine and ultra fine material or when the final product must be a slurry (paper or paint application). During the wet grinding of calcium carbonate, it is important to establish the criteria to control rheological and electrochemical properties of suspensions so as to attain a high solid volume with adequate fluidity while maintaining sufficient stability against aggregation and settling of the particles. Use of dispersants is the preferred method for achieving this.

Electrochemical properties of calcium carbonate and rheological characteristics of their suspensions have been investigated in the literature for many years (Tobori and Amari, 2003; Abd El-Rahiem and Arafa, 2004; Garcia et al., 2004; He, 2005; Abd El-Rahiem et al., 2008). These studies mostly focused on electrokinetic behavior of different sources of calcium carbonates (limestone, chalk and other calcites) and its impurities, and showed that the dispersive behavior of the calcium carbonate in the suspension is significantly affected due to changes on the zeta potential of the calcium carbonate in the presence of these impurities.

In this matter, the aim of this study is to beneficiate the ultrafine marble particles by dispersion process. In this purpose, the zeta potential and dispersion properties of micronized marble suspensions in the presence of inorganic and polymeric dispersants containing carboxylate groups in aqueous medium were determined, and the influence of the dispersant type on the quality of the marble slurry dispersion was investigated in detail. In addition, the parameters affecting the dispersion process such as pH, density of the pulp, and electrokinetic potential of micronized marble particles in the presence and absence of inorganic and polymeric dispersants were also studied.

2. MATERIALS AND METHODS

2.1. Materials

The waste marble sample with high purity (98.93 wt. % CaCO_3) was provided by the Ermas Marble Tourism Industry Trade Co. in Turkey. The particle size distribution of the sample was obtained using Mastersizer 2000 by Malvern. And, the density of the micronized marble was determined using a pycnometer method. According to the

particle size distribution of micronized marble, the mean particle size or d_{50} is 5.76 μm . The specific surface area and specific gravity of the sample is about 2.11 m^2/g and 2.62 g/cm^3 , respectively.

Two different chemicals were used as possible dispersants for the dispersion of micronized marble suspensions. The aqueous concentrated suspensions of micronized marble particles were prepared by slowly adding to an aqueous solution of the dispersants employed under controlled stirring using a high shear homogenizer (IKA) at 2000 rpm for 60 min.

2.2. Methods

The indirect characterization of micronized marble suspensions by measuring zeta potential is feasible because the relationship between zeta potential and apparent viscosity is valid for a lot of solid/dispersant system. The zeta potentials of micronized marble without and with dispersants were determined by Zetasizer Nano Z (Malvern Instruments) which uses micro-electrophoresis/electrophoretic light scattering technology.

Anton Paar QC Rheometer was used for the rheological measurements. The viscosity measurement cell has equipment providing the water circulation. In this set-up, dispersions remained at a constant temperature during the measurements ($25 \pm 1^\circ\text{C}$). The viscosity measurements were carried out at between 0 and 1100 s^{-1} shear rates using CC 39 container and ST 22 spindle, the recording were done at 700 s^{-1} shear speeds.

3. RESULTS AND DISCUSSION

3.1. Characterization of the Sample

The mineral composition of the marble sample showed in Figure 1 was obtained

by FTIR spectroscopy, measured in the range of 0–4000 cm^{-1} using KBr pellet method.

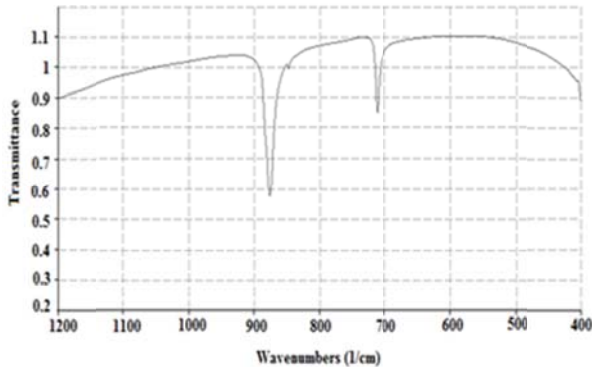


Figure 1: FTIR spectra of Marble limestone.

Calcium carbonate has two different crystal forms, calcite and aragonite, and that calcite shows strong absorption peaks at 1430, 875, and 712 cm^{-1} in its IR spectrum. These peaks are attributable to the vibration of carbon-oxygen double bond in the carbonate ion (White, 1974). The comparison of IR bands of the marble and six carbonate minerals (two synthetic and four natural) show that the IR spectrum of marble had also two main peaks at 876 and 712 cm^{-1} bands which are characteristic for calcite (Vdovic, 2001). The semi-quantitative X-ray diffraction method also revealed the presence of 98% calcite and 2% quartz. The chemical analysis by XRF method provided some more data on the composition of the marble. The results compiled in Table 1 showed a very low amount of Si, Al, Mg and Fe.

Table 1: Chemical composition of marble.

Components	Amount (%)
CaO	55.40
SiO ₂	0.18
MgO	0.24
Fe ₂ O ₃	0.02
Al ₂ O ₃	0.08
K ₂ O	0.23
SO ₃	0.01
SiO	0.01
BaO	0.11

3.2. Electrokinetic Potential Measurements

3.2.1 Effect of pH

Figure 2 illustrates the zeta potential profile of marble versus pH. Since the calcium carbonate dissolves at acidic pH values, the measurements were carried out at narrow pH range between 6.4 and 11. As seen from Figure 2, the zeta potential profile for the marble ranged from -12.6 mV at pH~6.4 to -28.3 mV at pH~11.0 at $25 \pm 1^\circ\text{C}$. The surface charge of marble particles scarcely changed by the change in pH under the conditions that the activity of CO_3^{2-} or Ca^{2+} was kept constant.

Although the sample used in this study is metamorphic origin and medium-grained and coarse-crystalline calcium carbonate (Uz and Özdamar, 1999; Çelik et al., 2011), sedimentary origin calcium carbonate presents the organic matter as a coating and/or incorporated in the structure, and shows a negative surface charge with increase in pH.

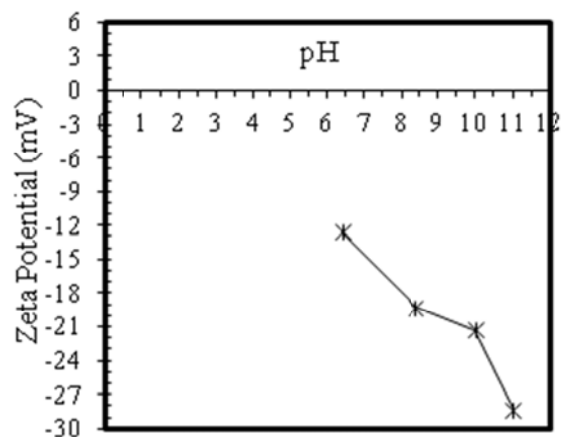


Figure 2: Zeta potential-pH profile of marble.

3.2.2. Effect of Dispersant

The zeta potential measurements of marble origin calcium carbonate in the

presence of inorganic and polymeric dispersants were carried out as a function of dosage from 0,1% to 0,6% (0.1%, 0.2%, 0.3%, 0.35%, 0.4%, 0.5%, 0.6%, 1.2%) and the results are presented in Figure 3.

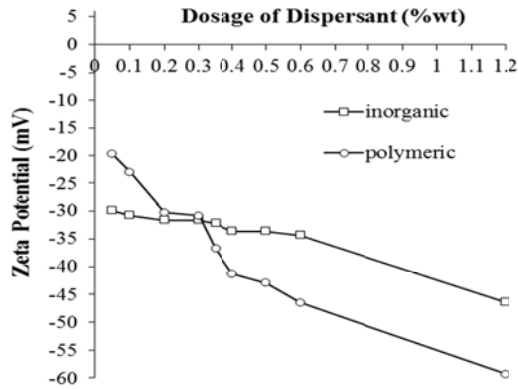


Figure 3: Zeta potential of marble as a function of type and amount of dispersant.

The results indicated that polymeric dispersants are more efficient compared to inorganic dispersants on the marble suspension which is agree with the literature [Toraman, 2012]. For example, while the zeta potential of marble origin calcium carbonate in the presence of inorganic dispersant at the higher dosage (1.2% wt/wt) is -46.4 mV, that is -59.3 mV in the presence of polymeric dispersant at the same dosage. However, since it won't be cost effective to obtain marble suspensions at higher dosages, there must be chosen lower dosages.

3.3. Slurry Rheology of Marble Limestone

3.3.1. Effect of solid concentration

Figure 4 presents the rheological properties of the marble limestone suspension at four different solid concentrations ($<52.4 \mu\text{m}$, d_{10} : 1.01; d_{50} : 5.46; d_{90} : 21.27) in the absence of dispersant at room temperature ($25 \pm 0.2 \text{ }^\circ\text{C}$).

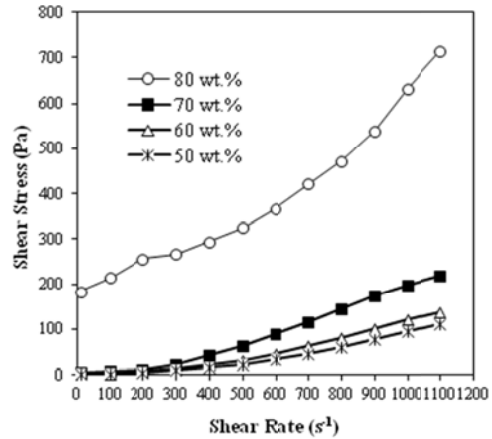


Figure 4: Shear speed vs. shear stress at different solid ratios.

Figure 5 shows the typical non-Newtonian behaviour with a yield stress value and remarkable shear thinning characterization both strongly dependent on the solid concentration [He *et al.*, 2004]. Clearly, the slurry rheological behaviour is transformed from a weakly dilatant characteristic (shear-thickening) to an evidently pseudoplastic (shear thinning) one with a yield stress when the solids concentration is increased from 70 wt.% to 80 wt.% [He, 2005]. However, as seen from Figure 6, most of the liquid is trapped in pores at 50%, 60% and 70% solid ratios and at high shear stress, and the particles show resistance the flow with the increasing shear stress, and it causes increase in the viscosity.

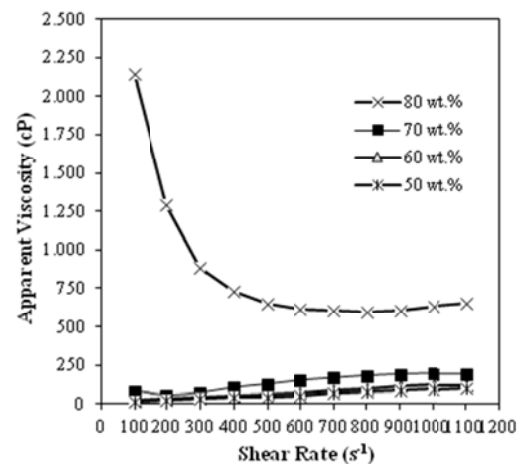


Figure 5: Apparent viscosity vs. share rate at different solid ratios.

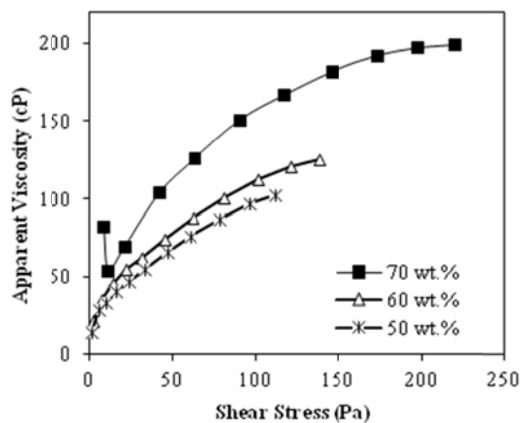


Figure 6: Apparent viscosity vs. shear stress at different solid ratios.

3.4. Effect of dispersant dosage

The effect of amount of inorganic dispersant (0.1%, 0.3%, 0.4%, 0.6% and 1.2%) on the viscosity at different pH values (6.4-11) is shown in Figure 7. The changes in the viscosities of Marble suspensions at pH 6.4 and at 50%, 60% and 70% solid ratios were marginal despite the increase in the dispersant dosage. The viscosity values of the marble suspensions at pH 8.4 and 10 are similar. Both literature [Greenwood et al., 2002] and the economics of the process and the sufficient conditions for stabilization, the optimum dispersant dosage was chosen as 0.4% at natural pH (8.4)

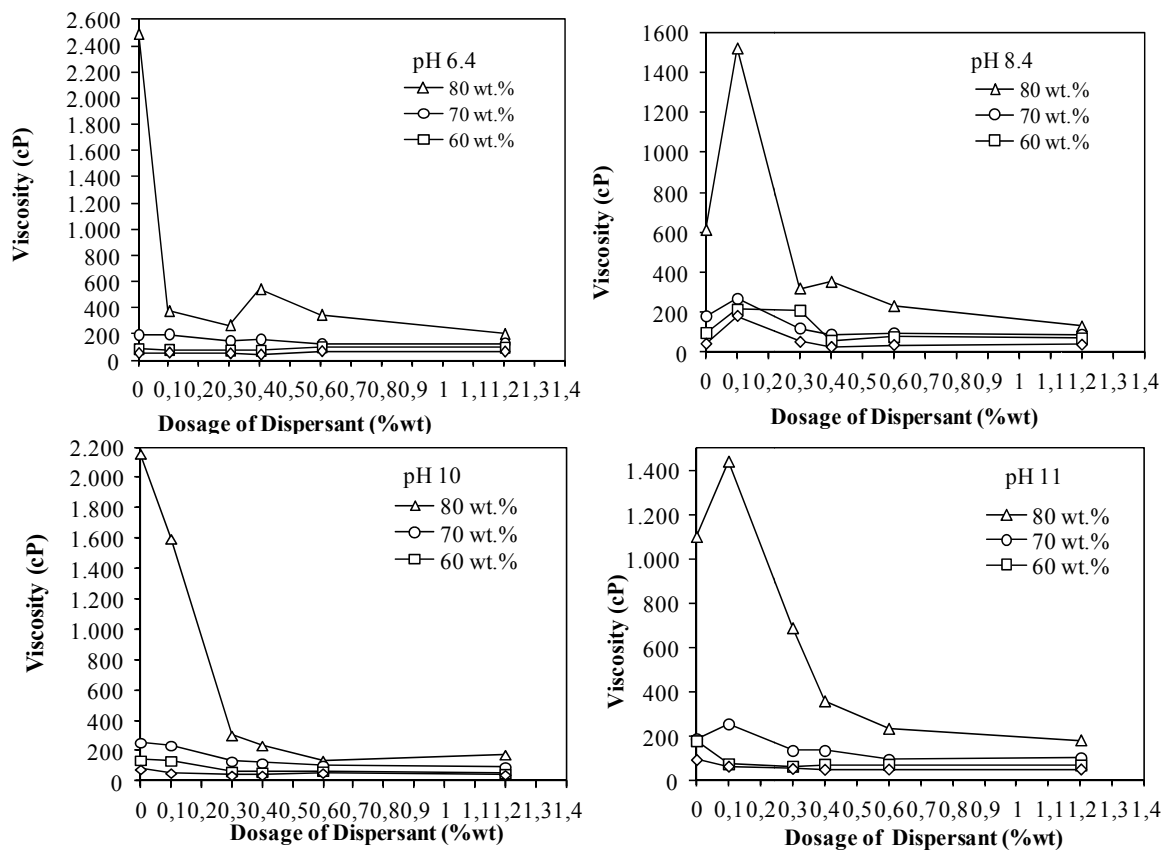


Figure 7: Effect of amount of inorganic dispersant on suspension viscosity at different pH.

The effect of amount of polymeric dispersant (0.1%, 0.3%, 0.4%, 0.6% and 1.2%) on the viscosity at different pH values (6.4-11) is shown in Figure 8. The changes in the viscosities of Marble

suspensions at pH 6.4 and at 50%, 60% and 70% solid ratios were marginal despite the increase in the dispersant dosage. The viscosity values of the marble suspensions at pH 8.4 and 10 are

similar. The effect of dispersant on the viscosity of the suspension is limited at low pH values and 50%, 60%, and 70% solid ratios. However, the addition of dispersant at the dosage of 0.1% showed a decrease at the viscosity at higher solid ratio (80%). Higher dispersant dosages showed no effect on the lowering the viscosity. At all solid ratios and polymer dosages, the lowest viscosity value of the suspension was obtained at natural pH (8.4). Particularly, the reason for obtaining higher viscosity at lower pH

value (pH 6.4) at all solid ratios and dispersant dosages compared to others is that marble particles at low pH values have low zeta potential due to compression of electrical double layer, hence marble particles settle down as flocs.

Finally, in order to obtain economic dispersed calcium carbonate suspension, the optimum dispersant dosage was determined as 0.1% (wt/wt).

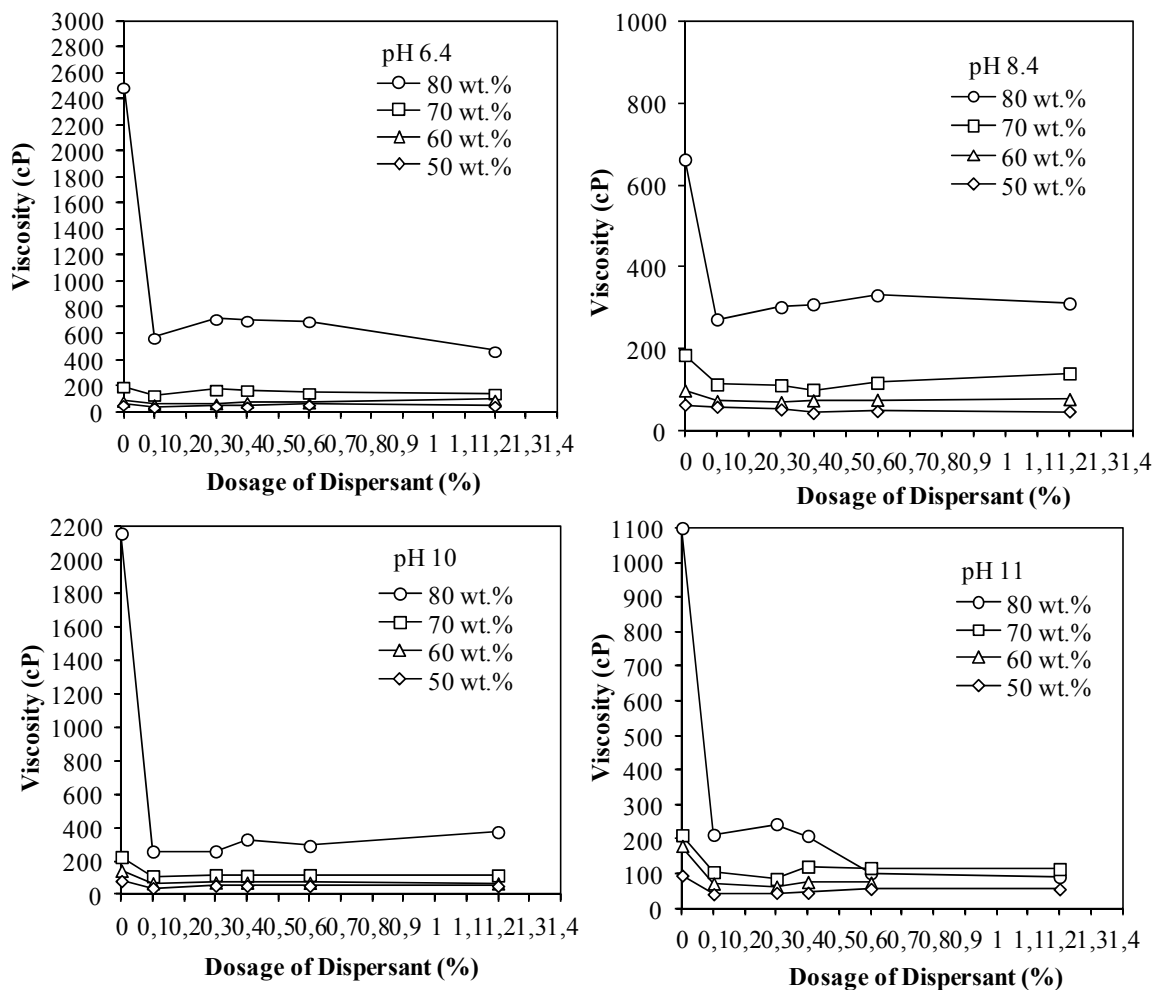


Figure 8: Effect of amount of polymeric dispersant on suspension viscosity at different pH.

4. CONCLUSIONS

The natural pH of marble origin calcium carbonate is found to be pH 8.4. The zeta potential of the sample showed higher negative surface charge. As Vodicek [Vodicek, 2001] showed that the negative

surface charge proves the presence of organic matters in the sample. While the zeta potential of marble origin calcium carbonate in the presence of inorganic dispersant at higher dosages (1.2 wt/wt) showed -46.4 mV of zeta potential, it

showed -59.3 mV in the presence of polymeric dispersant at the same dosage. The results also showed that the effect of polymeric dispersant on the change of the surface charge of marble origin calcium carbonate is significant.

The rheological behavior of marble suspensions at different solid ratios is non-Newtonian, and has weak dilatants characteristic at the weight percents of 50%, 60% and 70%. In the case of 80% solid ratio, the rheological behavior of the marble suspension changed to pseudoplastic behavior from weak dilatants. While the stable marble suspension at 70% solid ratio after the efficient grinding process gave the viscosity of 181 cP at natural pH (8.4), the viscosity of the suspension was decreased to 89.1 cP after the addition of inorganic dispersant at dosage of 0.4% with 50.7% decrease. In the case of polymeric dispersant, the viscosity of the suspension was decreased to 111 cP at dosage of 0.1% with 38.6% decrease.

Acknowledgements: This work was supported by The Scientific and Technological Research Council of Turkey (TUBITAK). Project number: Undergraduate scholarships 2241/A.

REFERENCES

- Abd El- Rahiem, F.H., Selim, K.A., Ibrahim, S.S. and Arafa, M.A., 2008. Preparation and Benefication of Egyptian Limestone To Be Suitable for Filler and Pharmaceutical Application, *The Journal of Ore Dressing*, 10(20), 1-8.
- Abd EL-Rahiem, F.H. and Arafa, M.A., 2004. Some Aspects on Selective Dispersion of Fine Particles with Special Emphasis on Egyptian Ground Calcium Carbonate, *The Journal of The South African Institute of Mining and Metallurgy*, 104(4), 223-228.
- Çelik, M.Y., Yeşilkaya, L., Ersoy, M. and Turgut, T., 2011. Investigation of the Relationship between Grain Size and Knoop Hardness on Carbonate Natural Stones, *Madencilik*, 50(2), 29-40 (Turkish).
- Garcia, F., Bolay, L.N., Trompette, J.L. and Frances, C., 2004. On Fragmentation and Agglomeration Phenomena in An Ultrafine Wet Grinding Process: The Role of Polyelectrolyte Additives, *International Journal of Mineral Processing*, 74, 43-54.
- Greenwood, R., Rowson, N., Kingman, S. and Brown, G., 2002. A New Method for Determining The Optimum Dispersant Concentration in Aqueous Grinding, *Powder Technology*, 123, 199-207.
- He, M., Wang, Y. and Forssberg, E., 2004. Slurry Rheology in Wet Ultrafine Grinding of Industrial Minerals: A Review, *Powder Technology*, 147, 94-112.
- He, M., 2005. Rheological Behaviour in Wet Ultra-Fine Grinding of Limestone, Licentiate Thesis, Division of Mineral Processing, Department of Chemical Engineering and Geosciences, Luleå University of Technology, Luleå -Sweden, 44 p.
- Tobori, N and Amari, T. 2003. Rheological Behavior of Highly Concentrated Aqueous Calcium Carbonate Suspensions in The Presence of Polyelectrolytes, *Colloids and Surfaces A: Physicochemical Engineering Aspects*, 215, 163-171.
- Toraman, Ö.Y. 2012. Öğütmeye Yardımcı Kimyasallar, *Türkchem Chemical Laboratory Technolohy*, 29, 24-25.
- Uz, B. and Özdamar, Ş, 1999. Geological-Petrographic-Chemical Evaluation of Muğla-Yatağan Marbles, *Türkiye’de Mermer Yapı ve Dekorasyon Dergisi*, 62-63, 42-52 (Turkish).
- Vdović, N., 2001. Electrokinetics Behaviour of Calcite – The Relationship with Other Calcite Properties, *Chemical Geology*, 177, 241-248.
- White, W.B, 1974. The Carbonate Minerals, In *The Infrared Spectra of Minerals*, Ed: VC Farmer, Mineralogical Society, London, pp. 227-284.

ADSORPTION OF LEAD (II) IONS FROM AQUEOUS SOLUTION ON POROUS AND CRYSTALLINE HAP

Arzu Yakar^{1,a}, Ismail Girgin²

1. Afyon Kocatepe University, Department of Chemical Engineering, 03200, Afyonkarahisar, Turkey

2. Hacettepe University, Department of Mining Engineering, 06800 Beytepe, Ankara, Turkey

a. Corresponding author: (ayakar@aku.edu.tr)

ABSTRACT: Adsorption tests were done to determine the Pb^{2+} removal capacities of synthesized products of p-HAP and c-HAP from aqueous solutions. In these tests, p-HAP was found to be more effective and Pb^{2+} removal capacity was found as 220.62 mg/g with corresponding value for c-HAP being only 75.95 mg/g. XRD and SEM analysis done on both samples collected after adsorption tests showed that Pb^{2+} removal was based on formation of hydroxypyromorphite ($Pb_5(PO_4)_3(OH)_2$). For p-HAP and c-HAP, L-type adsorption were observed in Giles's classification system. Langmuir, Freundlich and Dubinin-Radushkevich (D-R) isotherms were applied to determine the adsorption capacity of adsorbents. The mean energy of adsorption, E, was also calculated from the determined D-R isotherm parameters. The values E of p-HAP and c-HAP were found as 1.58 and 2.36 kJ/mol, respectively. Kinetic studies indicated that Pb^{2+} adsorption on p-HAP and c-HAP in a single component system followed second-order kinetics. Considering the available data, removal of Pb^{2+} ions was explained by dissolution-precipitation mechanism and it was concluded that especially p-HAP could be successively used for the removal of Pb^{2+} ions from aqueous solutions.

1. INTRODUCTION

Heavy metals which are found in soil and waste waters are very toxic to humans and most other forms of life. Lead is one the most toxic elements and the main causes for environmental pollution [Ewers and Schlipkötter, 1991; Watanabe M.E., 1997] are as the result of usage in batteries, cable coverings, explosives, paints, pesticides, analytical reagents and as an additive in gasoline. Lead causes a large variety of toxic effects, including gastrointestinal, muscular, reproductive, neurological and behavioral and genetic defectivenesses [Johnson, 1998; Davis *et al.*, 1992] and its toxicity is due to the ability of Pb^{2+} to amalgamate several enzymes [Ewers and Schlipkötter, 1991].

As the level of heavy metals in the environment continue to enlarge, it is becoming increasingly important to enhance methodologies for in-situ

remediation of contaminated sites. Besides active carbon [Davini, 2001, Malik *et al.*, 2002], clays and related minerals such as pyrophyllite, zeolite, bentonite etc. have been explored as sorbents not only for organic species [Lin and Puls, 2000; Juan and Pedersen, 2005] but also for heavy metal ions [Gier and Johns, 2000; Bradl, 2004]. Also, use of apatite for waste water treatment has been tested and a very high capacity for removing divalent heavy metal ions from contaminated soil and water [Wang and Ariyanto, 2007; Boisson *et al.*, 1999] was observed.

The main purpose of this study is to predict adsorption mechanism and to find out lead uptake efficiency of synthesized porous (p-HAP) and crystalline (c-HAP) hydroxyapatites.

2. EXPERIMENTAL

2.1. Lead Adsorption Experiments

Synthesized p-HAP and c-HAP hydroxyapatites with BET specific surface areas of 106.6 m²/g and 25.9 m²/g, respectively were used [Engin and Girgin, 2009] in the adsorption experiments conducted in PP beakers. A stock lead solution of 1000 mg/L was prepared from Pb(NO₃)₂ using deionized water and this stock solution was serially diluted to prepare solutions of varying initial Pb²⁺ concentrations between 1 to 500 mg/L for use in the adsorption tests. 0.1 g of p-HAP or c-HAP powder was added to the beaker containing 50 mL aqueous lead solution and magnetically stirred at room temperature for 2h. Adsorbents were filtered through milipore filter apparatus (0.45µm) and dried at room temperature. After determining the pH values, filtrates were analyzed for remaining lead using ICP Spectrometer (Thermo IRISH, ICP-OES). For kinetic data, 0.4 g p-HAP and c-HAP powders were stirred separately with 200 mL of 100 mg/L Pb(NO₃)₂ solution at room temperature for 2h and samples were taken at pre-determined time intervals from the solution for lead analysis. Morphology of the powders were investigated using Bruker scanning electron microscope (SEM) and the XRD patterns were taken by Rigaku D-MAX 200 X-ray diffractometer. The amount of metal ions sorbed per unit mass of apatite (mg metal ions/g apatite), q_e, were calculated by using Equation 1.

$$q_e = \frac{(C_0 - C_e) \times V}{m} \quad (1)$$

Where; V is volume of the aqueous solution (L), m is amount of the adsorbent (g), C₀ and C_e are the initial and equilibrium concentration of the metal ions in the aqueous solution (mg/L), respectively.

3. RESULTS AND DISCUSSION

3.1. Kinetics of the Adsorption

Figure 1 shows the changes in the amounts of the metal ions adsorbed over time calculated using Equation-4. As can be seen, Pb²⁺ removal from the solution using p-HAP and c-HAP powders show similar tendencies and the removal capacities are almost same. Adsorption of Pb²⁺ ions by both powders is fast for the first 5 minutes, slows down until 10th minute and the equilibrium is reached after 15 minutes. Therefore, optimum removal time for lead was determined to be 15 min.

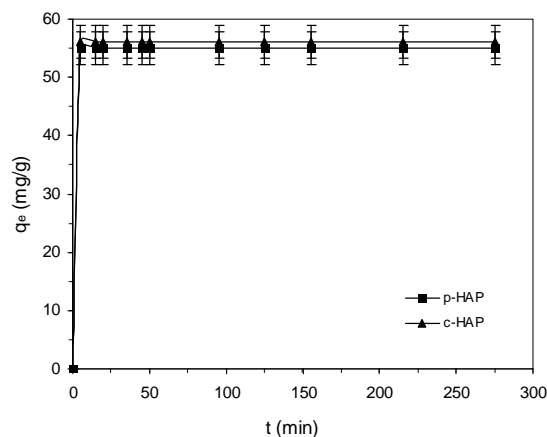


Figure 1: Adsorption kinetics of Pb²⁺ ions on p-HAP and c-HAP surfaces

Two kinetic models; the pseudo-first order and the pseudo-second order, were tested to explain the adsorption kinetics and the rate constants of Pb²⁺ on p-HAP and c-HAP powders were calculated (data not given). The second-order kinetics is in good agreement with both data and the second-order kinetics shows closer approximation to the experimental data for q_e (data not given).

3.2. Effects of Metal Ion Concentration

In order to evaluate the effect of initial metal ion concentration on adsorption characteristics of p-HAP and c-HAP, a series of experiments were conducted and the results are given in Table 1 which

shows that the amount of Pb^{2+} removed per unit mass of p-HAP increases with increasing initial Pb^{2+} concentration in the solution and reaches a value of 220.62 mg/g for an initial Pb^{2+} concentration of 450 mg/L. On the contrary, the amount of Pb^{2+} adsorbed on c-HAP increases with increasing initial Pb^{2+} concentration up to 285.90 mg/L initial Pb^{2+} concentration, reaches an equilibrium value of 75.95 mg/g and then shows a slight decrease to 74.35 mg/g at an initial Pb^{2+} concentration of 448.40 mg/L. For p-HAP and c-HAP, L-type adsorption were observed in Giles's classification system (Figure 1).

Table 1: Experimental results of p-HAP and c-HAP at different initial concentrations of Pb^{2+}

Initial Concentration of Pb^{2+} (mg/L)	p-HAP	c-HAP
	q_e (mg/g)	q_e (mg/g)
0.75	0.32	0.31
8.50	4.17	4.19
44.75	22.28	22.24
92.50	46.17	45.63
285.90	140.18	75.95
448.40	220.62	74.35

The adsorption of Pb^{2+} on p-HAP and c-HAP were also analyzed by using Langmuir [Langmuir, 1918], Freundlich [Freundlich, 1926] and Dubinin-Radushkevich [Dubinin and Radushkevich, 1947] isotherms (data not given). The experimental data for both adsorbents well fit with the Langmuir model (data not given). According to D-R isotherm, the adsorption energy values for the adsorption of Pb^{2+} on p-HAP and c-HAP are 1.58 kJ/mol and 2.36 kJ/mol, respectively (data not given). The evaluation of the experimental results show that physical adsorption is the predominant mechanism for both samples.

Hydroxypyromorphite ($Pb_{10}(PO_4)_6(OH)_2$) peaks were detected as a new phase (JCPDS card no: 2-0700) in the XRD patterns for both cases (47, 48, 49) (data not given). This alteration is also recognized in the SEM micrographs and EDS analyses (data not given).

4. CONCLUSIONS

In this study, experimental results show that synthesized HAP powders are effective in the removal of Pb^{2+} ions from aqueous solutions. XRD and SEM analysis performed on p-HAP and c-HAP collected after adsorption tests showed that Pb^{2+} removal was based on formation of hydroxypyromorphite ($Pb_5(PO_4)_3(OH)_2$). The mean energy of adsorption, E, of p-HAP and c-HAP were found as 1.58 and 2.36 kJ/mol, respectively. Kinetic studies indicated that Pb^{2+} adsorption on p-HAP and c-HAP in a single component system followed second-order kinetics. The batch experiments demonstrated that the p-HAP (220.62 mg/g) was more efficient than c-HAP (75.95 mg/g) for removing Pb^{2+} ions from solution and it has a potential to be used as an adsorbent.

REFERENCES

- Ewers V., Schlipkötter, H.W., 1991., Lead. In: Merian, E.(Ed.) Metals and their compounds in the environment. VCH, Weinheim.
- Watanabe M.E., 1997, Phytoremediation on the brink of commercialization, Environ. Sci. Technol. 31, 182.
- Johnson, F.M., 1998, The genetic effects of environmental lead, Mutation Research, 410, 123.
- Davis, A., Ruby, M.V. and Bergstrom, P.D., 1992, Minerologic controls on arsenic and lead bioavailability in soils from the Butte mining district, Montana, USA, Environ. Sci. and Technol., 26, 461.
- Davini, P., 2001, The effect of certain metallic derivatives on the adsorption of sulphur dioxide on the active carbon, Carbon. 39, 419.
- Malik, D.J., Strelko, V., Streat, M., Puziy, A.M., 2002, Characterization of novel modified active carbons and marine algal biomass for

- the selective adsorption of lead, *Water Res.* 36, 1527.
- Lin Z. and Puls, R.W., 2000, Adsorption, desorption and oxidation of arsenic affected by clay minerals and aging process, *Environmental Geology*, 39, 753.
- Juan G. and Pedersen J.A., 2005, Adsorption of Sulfonamide Antimicrobial Agents to Clay Minerals, *Environ. Sci. Technol.*, 39, 9509.
- Gier S. and Johns W.D., 2000, Heavy metal-adsorption on micas and clay minerals studied by X-ray photoelectron spectroscopy, *Applied Clay Science*, 16, 289.
- Bradl H.B., 2004, Adsorption of heavy metal ions on soils and soils constituents, *Journal of Colloid and Interface Science*, 277, 1.
- Wang, S., Ariyanto, E., 2007, Competitive adsorption of malachite green and Pb ions on natural zeolite, *J. Colloid Interface Sci.* 314, 25.
- Boisson, J., Ruttens, M., Mench, M., Vangronsveld, J., 1999, Evaluation of hydroxyapatite as a metal immobilizing soil additive for the remediation of polluted soils. Part 1. Influence of hydroxyapatite of metal exchangeability in soil, plant growth, and plant metal accumulation, *Environ. Pollut.*, 104, 225.
- Engin A., Girgin İ., 2009, Synthesis of Hydroxyapatite by Using Calcium Carbonate and Phosphoric Acid in Various Water-Ethanol Solvent Systems, *Central European Journal of Chemistry*, 7, 745.
- Langmuir, I., 1918, The adsorption of gases on plane surfaces of glass, mica and platinum, *J. Am. Chem Soc.*, 40, 1361.
- Freundlich, H., 1926, *Colloid and Capillary Chemistry*, Methuen, London, 39.
- Dubinin, M.M., Radushkevich, L.V., 1947, *Proc. Acad. Sci. U.S.S.R. Phys. Chem. Sect.* 55, 331.

EXPERIMENTAL INVESTIGATION OF THE SELECTIVE PERMEABILITY OF HOLLOW GLASS MICROSPHERES WITH NANOSTRUCTURED SHELL

Vitaly Zinovyev^{1,a}, Ivan Kazanin¹, Vadim Lebiga¹ and Alexey Pak¹

1. Khristianovich Institute of Theoretical and Applied Mechanics, Novosibirsk, Russia
a. Corresponding author (zinoviev@itam.nsc.ru)

ABSTRACT: In these experiments was shown the different types of sorbents under study are impermeable to methane and air but they are permeable to helium. The rate of the processes of absorption and desorption of helium are mainly depended on the difference of the partial pressures of helium inside and outside of the microparticles, if other parameters are fixed (temperature, size of the particles, et cetera). It has been established that the presence of associated gas in the volume phase has almost no effect on the sorption and desorption of helium. Modified cenospheres demonstrated a significant increase, more than an order of magnitude, in the rate of absorption of helium compared with microspheres. In turn, for the microspheres have been undergone joint granulation with aluminum hydroxide the permeability coefficient was increased by almost two orders of magnitude compared to the initial microspheres.

1. INTRODUCTION

Currently, the production of helium in the industry is mainly carried by the cryogenic distillation of natural gas. Since the helium content in the natural gas is small and usually no more than 0.05-0.5%, the liquefaction total hydrocarbons is required to highlight it. This makes the low-temperature technology of the gas component separation from the mixture is very energy efficient and economically viable. Therefore, the relevance is to create new non-cryogenic ways of helium obtaining, which are more advantageous in terms of cost reduction and efficiency of the production process.

There are two basic methods are non-cryogenic separation of gas mixtures: membrane and adsorption.

The driving force of the gas separation is the partial pressure difference on different sides of the membrane. The most suitable material for membranes for recovering helium from natural gas can

be quartz glass, which is permeable to helium and practically impermeable to other components of the natural gas.

There is an opportunity to significantly improve technological characteristics of facilities for extraction helium from natural gas, if as the gas separation membranes use hollow glass microparticles, the wall of which has selective permeability for helium.

The spherical shape of the microparticles can significantly increase the total surface area through which is happened the process of separating components of the gas mixture. Also, due to the spherical form, the particles have higher mechanical strength, that and as a result can significantly improve the performance for installations of helium from natural gas. Furthermore, the damage of some membrane elements does not lead to malfunction of the entire facility.

The aim of this study was to investigate the effect of selective permeability of

helium by means of different nanostructured micro-objects.

2. EXPERIMENTAL

BACKGROUNDS AND MATERIALS

As a substance to be able to adsorb the helium the various micro-objects with nanostructured porous membranes were used: hollow microspheres made of sodium borosilicate glass with a diameter of 40 - 100 μm and a wall thickness of about 1 μm (a); modified alumina and silica cenospheres with diameter of $130 \pm 10 \mu\text{m}$ and a wall thickness of 5-8 μm (b); and composite granulated sorbent based from microspheres (a) and aluminum hydroxide (c). Pictures of sorbents are shown in Figure 1.

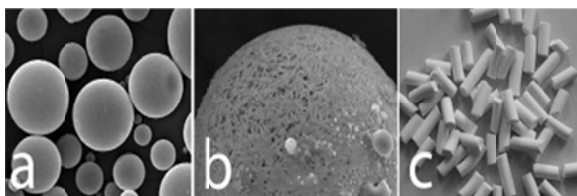


Figure 1: Pictures of different type of sorbents

Hollow microspheres: made of sodium borosilicate glass they are looking as hollow balls from 5 up to 250 μm in diameter with the wall depth from 2 up to 10 μm .

The chemical composition and physical properties of the microspheres can vary significantly. From the physical properties of the microspheres can be noted the spherical shape, the low density, the thermal stability, the chemical inactivity and specially the high hydrostatic strength.

In this paper were used hollow glass microspheres with monomodal particle size distribution with maximum in diameter around 55 μm and a wall thickness of about 1 μm .

Cenospheres: aluminosilicate hollow cenospheres are formed during

combustion of coal to the power station. On the properties of coal ash cenospheres are close to the hollow microspheres, hollow cenospheres, but the price is several times lower than that of the microspheres.

Cenospheres have a shape close to spherical and smooth outer surface. Particle size can vary between 5 - 400 microns and wall thickness of 2-30 microns. We used cenospheres from power station Reftinskaya, characterized by an average wall thickness of 5-8 μm . After aerodynamic separation and hydrostatic density separation through sieve (mesh size between 125 and 160 μm .) with simultaneously vacuuming, the size of microparticles was ranged from 125 to 160 μm . Then cenospheres were modified by etching the initial particles by fluorochemical reagent.

Composite sorbent: Application of sorbents in the form of free flowing fine powders in practice is very difficult and requires the installation of special filter elements. It is much more convenient and practical to work with some sorbents that are in the bound state and is used in the form of granules.

As a helium adsorber of the composite sorbent was used hollow glass microspheres mentioned above, and as binder was - aluminum hydroxide, granules photo is shown in Fig. 1c.

2.1. Experimental Stand

In order to study the permeability of the different sorbents were used following gases: air, methane, helium and their mixtures. A special stand was made for experiments, which was based on a stainless steel tank volume $0.55 \cdot 10^{-3} \text{ m}^3$, length 1.1 m and a diameter of 0.025 m. Stand was equipped with shut-off and control valves and instrumentation as shown in Figure 2. To avoid the

penetration of the sorbent particles in the lead-in track, valves and sensors, at the ends of the tank was installed special material filters.

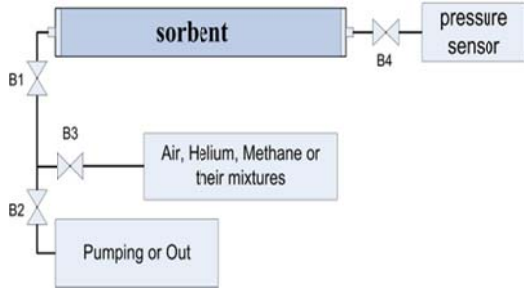


Figure 2: Scheme of the experimental stand

2.2. Experimental Technique

Experiments on sorption and desorption processes of helium sorbents were performed as follows. The tank filled with sorbent was previously evacuated and then it was pumped with a gas (helium, methane, air, or their mixture) up to a working pressure. Further, after closing all valves the pressure change inside the tank was recorded over time. After the process of sorption finishing the whole rest gas was removed by relief the pressure up to atmospheric one and by following evacuation. And then, after overlapping all valves, the pressure inside the tank was recorded again during the desorption process. Pressure sensor data were recorded on a computer hard drive with an interval from 1 second to 1 minute. All experiments were carried out at ambient temperature about 20 ± 3 °C.

2.3. Checking of Sorbents Permeability With Relation to Air and Methane

First, experiments were conducted with the air and methane as the working fluid at an initial pressure in the tank ~ 0.5 - 0.75 MPa. In Figure 3 is shown a graph of pressure versus time. It is seen that the pressure remains practically unchanged over time. Some pressure fluctuations are associated with change in ambient temperature during the tests.



Figure 3: Permeability checking of different sorbents

2.4. Sorption/Desorption Experiments

Next, there were done a few series of experiments on sorption and desorption of helium by different types of sorbents. The experiments were conducted for both pure helium and air-helium, methane-helium mixtures with a volume concentration of helium 25% and 2.25%, for different initial gas pressure in the tank: from 0.05 up to 0.95 MPa. In Figures 4-6 are shown the curves of pressure drops in the tank with different types of sorbents: for sorption (upper graphs) and desorption (lower graphs).

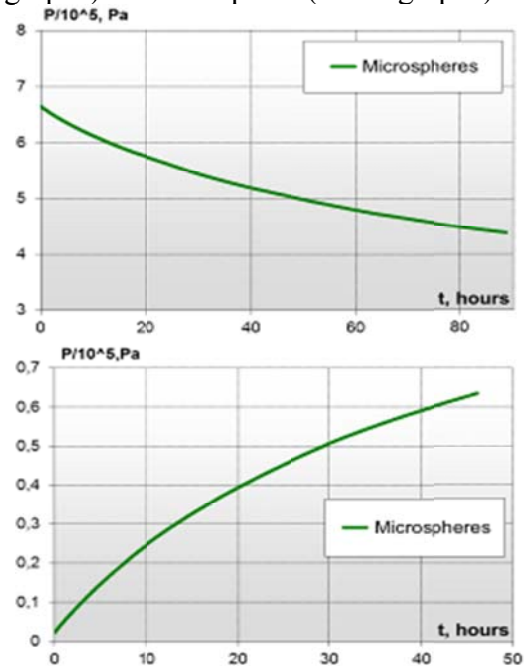


Figure 4: Pressure drop for microspheres due to sorption and desorption

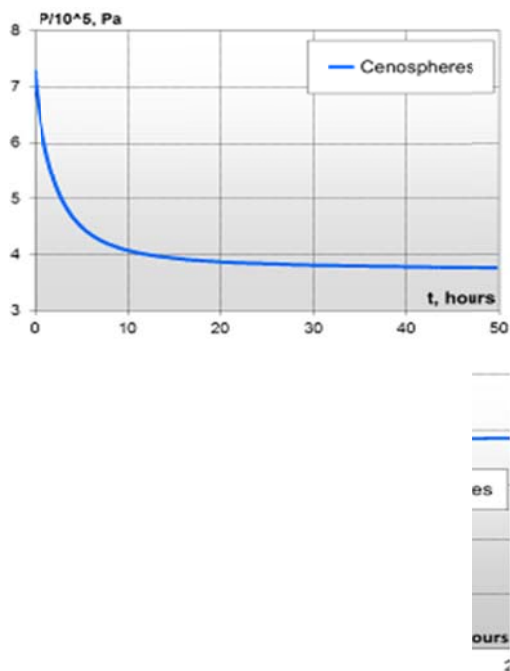


Figure 5: Pressure drop for cenospheres due to sorption/desorption

As can be seen from the graph of sorption, the pressure in the tank is varied significantly over time. Since the tank is almost sealed, the observed pressure drop is happened due to the penetration of helium into the hollow particles. In the process, the difference of the partial pressures of helium inside and outside the particles decreases, leading to lower rates of sorption process. At the end of the sorption lean mixture was removed from the tank through a pressure relief to atmosphere, followed by evacuation to a pressure of 0.01 MPa, in order to create a reverse differential partial pressure of helium inside and outside of the particle to provide conditions for the desorption process. Increasing the pressure in the tank over time indicates about the helium desorption from the micro objects.

It should be noted the different nature of the sorption and desorption dependencies for the composite sorbent, see Figure 6, with comparison Figs 4 and 5. Firstly, the rate of sorption is significantly increased,

and secondly, the shape of dependencies has two modes: the first one with a more rapid rate of the process, the second one, much decelerated rate of the process.

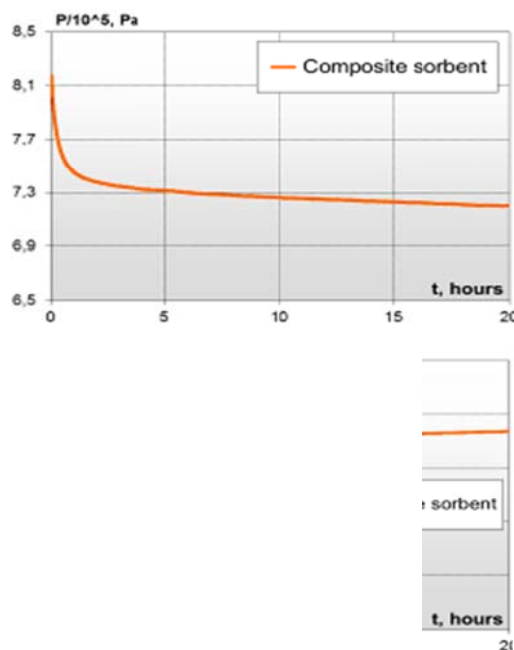


Figure 6: Pressure drop for composite sorbent due to sorption /desorption

For a correct comparison of the results of experiments carried out under different conditions the data could be conveniently presented in the normalized form:

$$P_{norm} = \frac{P_{current} - P_{equilibrium}}{P_{initial} - P_{equilibrium}},$$

where P is the pressure.

Applying this normalization to the results to the sorption of helium by cenospheres under different initial pressure of helium, to the sorption and desorption of helium by cenospheres from air-helium mixtures with helium volume concentration as 25% and 2.25% correspondingly we can finally reduce all data to similar dependencies. As it is seen from Figure 7, all dependencies are practically the same, what indicates about the similarity of the sorption and desorption processes.

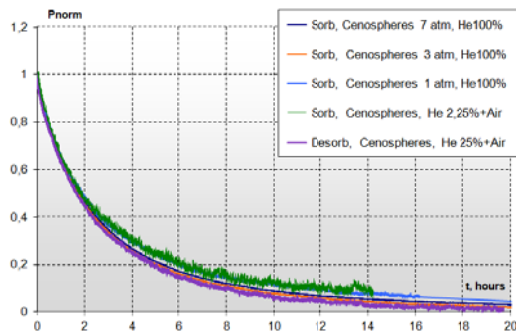


Figure 7: Pressure drops at sorption/desorption of helium by cenospheres after normalization

The same we have for helium, air-helium and methane-helium mixture in case of composite sorbent as it is seen from the Figure 8, where it is clear that a sorption and desorption processes for composite sorbent are also similar.



Figure 8: Sorption/desorption of helium by composite sorbent after normalization

In Figure 9 is shown a comparison of sorption rates for microspheres, modified cenospheres and composite sorbent in the normalized form. Modified cenospheres showed significant, more than an order, increase in the sorption rate of helium comparing with the microspheres, while the permeability of the microspheres used inside the composite sorbent after going through the preliminary granulation procedure is growing in almost two orders of with relation to initial microspheres themselves.

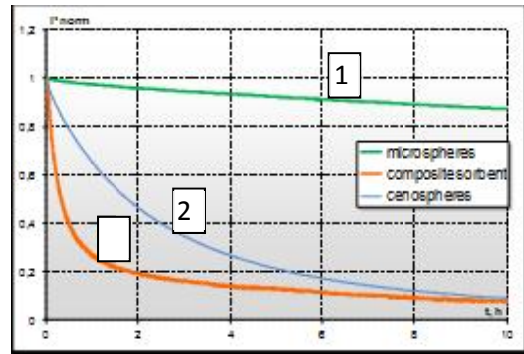


Figure 9: Sorption rate for different sorbents: 1–initial microspheres, 2 – modified cenospheres and 3-composite sorbent

3.CONCLUSIONS

There was shown by experiments that the different types of sorbents under study are impermeable to methane and air but they are permeable to helium. The rate of the processes of absorption and desorption of helium are mainly depended on the difference of the partial pressures of helium inside and outside of the microparticles, if other parameters are fixed (temperature, size of the particles, and so on). It has been established that the presence of associated gas in the volume phase has almost no effect on the sorption and desorption of helium.

Modified cenospheres demonstrated a significant increase, more than an order, in the rate of absorption of helium compared with microspheres. In turn, for the microspheres have been undergone joint granulation with aluminum hydroxide the permeability coefficient was increased by almost two orders of magnitude compared to the initial microspheres.

Acknowledgements: This work was supported financially by Siberian Branch of Russian Academy of Sciences (Interdisciplinary Integration Project No 91) and by grant of President of Russia for leading scientific school (SS-1541.2012.1).

SECTION F
Modeling and Simulation

COMPUTATIONAL STRUCTURE CHARACTERIZATION TOOLS FOR THE ERA OF MATERIAL INFORMATICS

Lev Sarkisov^{1,a}

1. Institute for Materials and Processes, School of Engineering, University of Edinburgh, Edinburgh, United Kingdom

a. Corresponding author (Lev.Sarkisov@ed.ac.uk)

ABSTRACT: Current advances in synthesis of new porous materials outpace our ability to test them in real adsorption applications. This situation is particularly evident in the area of metal-organics frameworks (MOFs), where hundreds of new MOFs are reported every year and the number of possible MOFs is virtually infinite. How to make sense out of this vast number of existing and possible structures?

In this article, I will review the application of computational structure characterization tools for systematic description and classification of porous materials and their adsorption properties. Using examples from recent research in my group and others, I will discuss how the information obtained from computational characterization can be used to identify the most promising materials for a specific application before any costly and time consuming experimental effort is committed. I will finally touch upon the need for the tools to systematically organize the information generated in computational studies. These tools combined with the recent impressive advances in synthesis of porous materials may fundamentally change the way we approach material discovery, starting the era of material informatics.

1. INTRODUCTION

Adsorption in porous materials has been considered as an energy efficient alternative to absorption and distillation processes for industrial scale separations, including carbon dioxide removal from power plant streams and air separation. Other applications where adsorption is important include catalysis, gas storage, sensing and drug delivery, to name a few. Development of these applications critically depends on whether a suitable porous material exists with affinity, selectivity and other characteristics meeting the requirements of the application in question. In the recent years progress in adsorption technologies has been stimulated by the unprecedented advances in the material science, where in addition to the conventional porous materials, such as activated carbons and zeolites, new families of porous

structures have emerged, including molecularly imprinted polymers (MIPs), metal-organic frameworks (MOFs) and polymers with intrinsic microporosity (PIMs).

Let us focus on just one new family of materials, metal-organic frameworks, or MOFs. Figure 1 shows a number of papers published since 1999, which mention MOFs and a substantial proportion of these articles actually report newly discovered MOFs. The large number of already reported MOFs and essentially infinite number of possible MOFs stems from the principle of their synthesis based on a self assembly from building blocks, provided by metal complexes and organic linkers. Naturally, organic chemistry can provide an

inexhaustible array of components for this approach.

It seems that this enormous variety of available and possible porous structures should substantially benefit the development of adsorption technologies, as for every specific application it should be possible to find or design a range of materials with properties perfectly matching the requirements. This however is not the case and at the moment there is no single industrial application based on MOFs. There are several reasons for this.

On one hand, to be used on industrial scale, MOFs must overcome several objective challenges associated with their stability, scalability of production and cost. On the other hand, the rate with which new MOFs are being discovered and reported clearly outpaces our ability to test them in any practical adsorption applications.

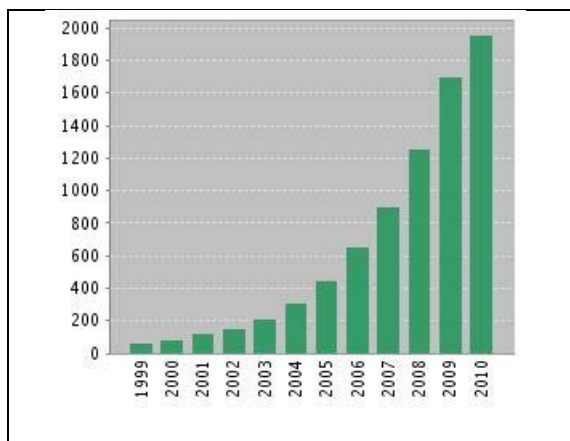


Figure 1. Number of articles published between 1999 and 2010, with “metal-organic framework” used as the key word. Source: Thomson Reuters (ISI) Web of Knowledge.

This is where computational structure characterization tools may become incredibly useful. To understand how they can help to streamline and accelerate the process between material discovery

and the actual application, it is instructive to briefly review the typical steps involved in this process, as shown in Figure 2. Once the structure of a new material is characterized via X-ray crystallography (if it is crystalline), the next steps involve structural characterization using physical adsorption of nitrogen or argon at cryogenic conditions, and helium porosimetry (or mercury porosimetry for macroporous structures). From these measurements the surface area, pore size distribution (PSD) and pore volume are obtained. In order to develop an actual adsorption application, in the next stage of the process, adsorption equilibrium data is acquired for single components and mixtures, as well as transport characteristics of the material. It is important to note here that experimental measurement of multi-component adsorption isotherms and transport diffusion coefficients remains extremely challenging and time consuming.

The idea of computational structural characterization tools is to replace as many of the experimental steps as possible with analogous computational procedures. Computational tools may provide a quick and efficient way to assess characteristics of porous materials, relate them to each other, provide reference values for various properties of the materials for future comparison with experiments, and in general, pre-screen large sets of candidate materials so that only a smaller group of most promising structures is indeed explored at the next experimental stage.

Starting with one of the first articles on modelling of adsorption in MOFs [Duren *et al.*, 2004], we have been developing and extending the arsenal of computational characterization tools and a range of possible ways to use them. The methodology behind these tools is

provided in our earlier publications [Sarkisov and Harrison, 2011; Sarkisov, 2012b; Sarkisov, 2012c]. The focus of this article is to review applications of these tools using examples from the research in my group as well from the research of other groups.

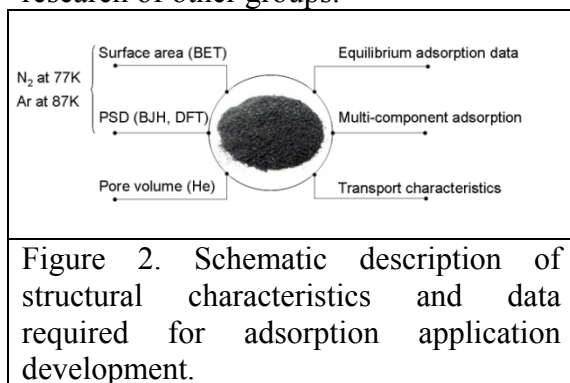


Figure 2. Schematic description of structural characteristics and data required for adsorption application development.

2. RESULTS

2.1 Structural Characterization of Porous Materials

Physical adsorption of nitrogen at 77K (or argon at 77K and 87K) is a standard experimental technique to obtain structural characteristics of a porous material, such as surface area, pore volume, and pore size distribution [Rouquerol *et al.*, 1998]. This is a two stage process, where in the first stage an adsorption isotherm is measured and in the second stage this isotherm is interpreted using a theory or a method, such as Langmuir or Brunauer-Emmett-Teller (BET) [Brunauer *et al.*, 1938] methods for the surface area and classical Barrett-Joyner-Halenda (BJH) method [Barrett *et al.*, 1951] or more modern NLDFT [Ravikovitch *et al.*, 2000] approach for pore size distribution (PSD). These methods involve a number of assumptions and sound understanding of these assumptions (and hence the limitations of the methods) is a prerequisite for accurate results. For example, both Langmuir and BET methods of obtaining the surface area are based on a notion that nitrogen molecules form a layer of well defined capacity on

the surface of the structure (multilayer formation is allowed in BET) and formation of this layer can be identified from the adsorption isotherm. Thus, knowing the size of a nitrogen molecule, the surface area of the structure can be defined. In both theories molecules do not interact with each other within the layer, and in BET molecules of one layer can serve as binding sites for the formation of the next layer. Even for the perfectly homogeneous surfaces, without any defects, this picture is oversimplified. To obtain PSD, BJH and NLDFT methods start by assuming the geometry of pores in the structure. Typically cylindrical pores, slit pores or spherical cavities are considered (in more advanced approaches some combinations of those geometries can be also tackled). Again, this is an oversimplified representation of the real materials, with complex disordered structures, such as porous glasses, carbons and polymers clearly containing pores of far more complex geometry, and even crystalline materials such as MOFs not quite conforming to the aforementioned pore shapes used in the PSD analysis.

Consider now molecular simulations, where the positions of atoms are provided explicitly (they can either correspond to the crystallographic data or to an approximate model of the material). Various geometric characteristics, such as surface area and distribution of voids, can be defined and calculated directly. Gelb and Gubbins explored the consistent way to define these characteristics and their correspondence to those obtained from the adsorption isotherm measurements [Gelb and Gubbins, 1998, 1999]. For this, they considered a realistic model of a disordered porous glass. To mimic the experiments, nitrogen adsorption isotherm was generated using grand canonical Monte Carlo, and the conventional methods of analysis (such

as BET and BJH) were applied to this isotherm. Indeed, they showed that the accessible surface area (one can envision it as the surface created by the centre of a probe spherical nitrogen molecule rolled over the atoms of the model structure) is reasonably consistent with BET and even the geometric pore size distribution (where a point belongs to a pore defined as the largest sphere that contains the point and does not overlap with the atoms of the structure) is in acceptable agreement with the PSD from BJH. In MOFs, these methods have been extended over a series of articles [Duren *et al.*, 2004; Duren *et al.*, 2007; Walton and Snurr, 2007; Sarkisov and Harrison, 2011]. In particular, Walton and Snurr showed that the accessible areas calculated for nitrogen as a probe molecule are in very good agreement with the experimental and simulated BET surface areas. This implied that, despite all the drastic assumptions involved in the BET theory, it is able to correctly capture the property of interest here, which is the extent of molecular surface of a porous structure as seen by a nitrogen molecule.

With this consistency established, there are now several modes in which accessible and experimental BET surface areas can be used. For disordered materials, accessible surface areas can be employed to drive the construction of the molecular models of these materials towards realistic representation, correctly reflecting the experimentally observed properties. For MOFs and other crystalline materials which do not have ambiguity about their molecular structure, calculated accessible surface areas provide the reference, ideal values. Deviation of the BET areas from these reference values may be indicative of either incorrect application of the BET method, or deviation of the structure of the sample from the ideal crystalline one

(due to incomplete evacuation, partial collapse or defects). Finally, analysis of the accessible surface areas can be used to understand the limiting theoretical values of the surface areas of various molecule building blocks and guide synthesis of materials with particularly high surface areas [Sarkisov, 2012a].

Calculation of the pore volume can be done in a manner consistent with the Helium porosimetry [Talu, Myers, 2001], by using the Widom insertion method [Widom, 1963]. Again, this calculation provides an ideal value that can be compared with the experimental one to assess the quality of the sample. On the other hand, this property is directly related to the capacity of the material and hence gas storage applications, and its calculation can guide the design of MOFs with optimized performance in this specific context. A closely related property to this is the maximum pore size, which in case of MOFs identifies the largest cage present in the structure. Pore limiting diameter on the other hand gives the size of the largest spherical probe with respect to which the porous structure is accessible. This property is important to assess whether a molecule of a particular size can fit in the pores of the structure. Sholl and co-workers used this property, for example, to screen for MOFs and zeolites with optimal properties for kinetic separations of gases, such as methane, carbon dioxide and hydrogen [Haldoupis *et al.*, 2010; Watanabe *et al.*, 2009; Haldoupis *et al.*, 2011].

Recently, we introduced a unified, simple to use simulation package, called Poreblazer (current version is 3.0.2) for computational characterization of ordered and disordered porous materials [Sarkisov and Harrison, 2011]. Both Linux and Windows versions are available from the group website,

including the source code written in Fortran 90. The details of the code implementation are provided in our original publication [Sarkisov and Harrison, 2011].

Poreblazer calculates pore volume, accessible surface area, largest pore diameter, pore limiting diameter and pore size distribution. As an example, here we consider three typical, well known MOFs, IRMOF-1 [Eddaoudi *et al.*, 2002], HKUST-1 [Chui *et al.*, 1999] and MIL-47 [Barthelet *et al.* 2001], with Table 1 summarizing their structural characteristics as obtained from Poreblazer, and Figure 3 showing PSDs in these materials.

Table 1: Calculated structural characteristics of selected MOFs. V_p is the pore volume (from the Helium porosimetry simulation), SA is the accessible surface area, D_{max} is the maximum cavity diameter and PLD is the pore limiting diameter.

MOF	V_p (cm^3/g)	SA (m^2/g)	D_{max} , Å	PLD, Å
IRMOF-1	1.353	3378.17	14.85	7.65
HKUST-1	0.853	1910.59	12.74	6.37
MIL-47	0.629	1324.04	7.56	7.07

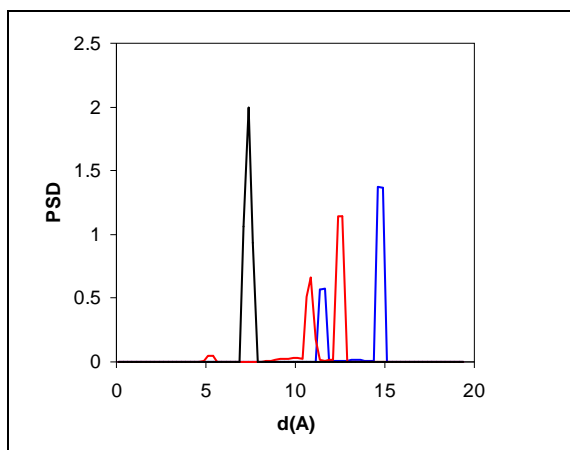


Figure 3. Pore size distribution in IRMOF-1 (blue), HKUST-1 (red) and MIL-47 (black).

2.2 Sensing Applications Using MOFs

In the next two sections I review several examples of using computational tools in the development of the actual adsorption applications. Grand canonical Monte Carlo is a standard simulation technique to generate equilibrium adsorption data [Frenkel and Smit, 2002]. In comparison to the experiments, it offers several advantages. Firstly, simulation of multi-component adsorption requires little additional effort, compared to single component isotherms. Simulations can be run at any temperature or pressure of interest, whereas in experiments extreme conditions (such as high pressure) require specialized equipment which is more expensive and more difficult to operate. Finally, simulations are quick in comparison to the experiments, where it is not unusual to have tens of hours of equilibration time per point on the adsorption isotherm. Current computational methods make it possible to acquire a full adsorption isotherm within hours (or even minutes depending on the system) and the effort can be substantially parallelized using modern cluster supercomputers, allowing one to simultaneously generate data for thousands of structures and adsorbate species under variety of conditions. One may wonder why computer simulations of adsorption have not replaced experiments to a wider extent. The key challenge for molecular simulation of adsorption is the availability of the accurate force fields to describe inter- and intramolecular interactions within the system. Without bespoke, validated force fields molecular simulations can not offer accurate predictions. None of the currently available force fields have been developed purposefully for the adsorption processes, and this has been widely recognized as the key bottle neck in the field.

Some applications do not require complete adsorption isotherms. Consider, for example, sensing of explosives, warfare agents, or volatile organic compounds in ambient air. The actual device may consist of a film of porous material. Detection event is associated with binding of target molecules to the porous material. This event must then be amplified and transduced using one of the conventional technologies such as quartz crystal microbalance (QCM), microcantilever sensor, or surface acoustic wave (SAW) device. Species we are interested in detecting are typically present in the atmosphere in very small amounts (ppb or even ppt concentrations). From the adsorption process perspective this corresponds to the very low pressure regime on the adsorption isotherm, where loading is a linear function of pressure and is described by the Henry's constant of adsorption. High value of the Henry's constant implies high affinity of the material towards the target adsorbate. Computational screening of materials for this application can then focus on the efficient calculation of Henry's constants for target adsorbates in candidate porous structures [Sarkisov, 2012c]. Additional information that can be extracted from this calculation is the intrinsic selectivity of the material in the zero loading regime which is simply a ratio of two Henry's constants for two adsorbates.

In the previous publication, I introduced calculation of Henry's constant of adsorption and other characteristics of porous materials in zero loading regime, using finely discretized lattice representation of porous space [Sarkisov, 2012c]. Calculation on the lattice offers several advantages. In addition to the overall Henry's constant of adsorption and selectivity for the whole material, it generates some data on the local properties and allows one to locate

regions of the porous space specifically responsible for high affinity and selectivity. Furthermore, as the Henry's constant is linked to the excess chemical potential (using the well known statistical mechanics relations), these constants calculated for individual lattice sites make it possible to explore the free energy landscape in the porous structure and detect free energy barriers, which would make the structure inaccessible to a molecule of a particular size or geometry [Sarkisov, 2012b]. For the details and parameters of these calculations I refer the reader to the original publications [Sarkisov, 2012c; Sarkisov, 2012b].

Here let me focus on the insights that can be gained from these calculations. Figure 4 shows Henry's constants of adsorption at 300K for several organic molecules and in two typical MOFs, IRMOF-1 and HKUST-1. In general, as the size of the molecule increases its interaction with the porous material also increases leading to higher Henry's coefficients. Smaller pores (HKUST-1) also lead to stronger interactions in the pore and higher affinities (as long as the molecules can fit inside the pores). Aside from these general, fundamental insights, data on Henry's coefficients can be directly used to evaluate suitability of a MOF in sensing applications. Using experimental data for detection sensitivity of QCM devices and the simulated Henry's coefficients of adsorption, it has been evaluated that a QCM sensing device based on IRMOF-1 should be able to detect presence of TNT in concentrations as low as 1 ppb [Sarkisov, 2012c]. For HKUST-1 this limit is even lower at about 0.45-0.145 ppb (as estimated for different conformations of TNT molecule) [Sarkisov, 2012b]. These are of course ideal figures, completely neglecting presence of water vapour in the air, competitive binding of similar

species and other factors. However, these calculations can be used to identify a group of promising structures, whose performance under realistic conditions should be evaluated in detailed experimental studies.

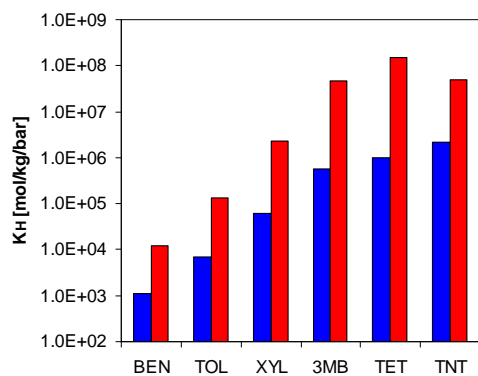


Figure 4. Henry's constants of adsorption in zero loading regime at 300K in IRMOF-1 (blue) and HKUST-1 (red). From left to right the data is for benzene (BEN), toluene (TOL), p-xylene (XYL), 1,2,4-trimethylbenzene (3MB), tetraline (TET) and trinitrotoluene (TNT).

Henry's constant of adsorption characterizes affinity of the material toward a particular adsorbate. To make screening strategies more efficient (in other words they identify smaller and more focused group of materials), other properties of the candidate structures should be taken into account. To illustrate this point, consider again adsorption of TNT in HKUST-1. On one hand, according to the analysis given above, this MOF seems to be very promising for TNT detection. On the other hand, structural characterization of HKUST-1 reveals pore limiting diameter of 6.37\AA between the cages of the structure and a question naturally arises whether molecules of TNT can actually penetrate into the structure. The lattice calculations allow us to answer this question using rigorous analysis of the free energy barriers [Sarkisov, 2012b]. Figure 5 shows the free energy barriers for various

organic molecules and TNT in HKUST-1. For most of the species, the free energy barrier is below 30 kJ/mol, however for TNT it is substantially higher at about 100 kJ/mol, making the structure effectively inaccessible to TNT under ambient conditions [Sarkisov 2012b].

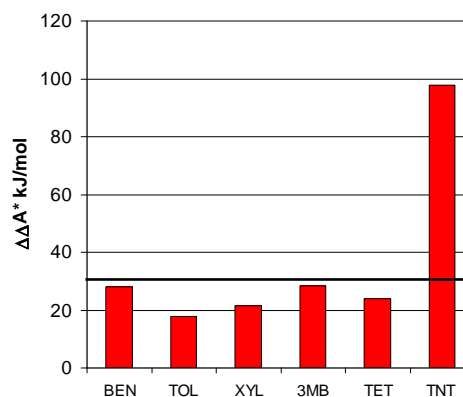


Figure 5. Free energy barriers $\Delta\Delta A^*$ (kJ/mol) in HKUST-1 with respect to benzene (BEN), toluene (TOL), p-xylene (XYL), 1,2,4-trimethylbenzene (3MB), tetraline (TET) and trinitrotoluene (TNT). Black line corresponds to 30 kJ/mol.

2.3 Breath Analysis Using MOFs

An application, closely related to sensing is breath analysis. Breath analysis is one of the most promising techniques for non-invasive diagnostics, particularly for lung cancer detection and disease progression [Buszewski *et al.*, 2007; Horvath *et al.*, 2009]. The key challenge is to accurately and consistently detect presence of biomarkers in ppb and ppt concentrations in exhaled human breath, which is a complex mixture, properties of which also depend on a number of factors, such as subject age and mode of sample collection. Porous materials can be used to capture these biomarker molecules and pre-concentrate them to improve the sensitivity of analysis. Development of new porous materials tailored for this application may substantially advance breath analysis technology. However, in order to be suitable for this application, the candidate

porous material must be stable with respect to water vapour (as exhaled air is almost saturated in water), be hydrophobic (to avoid condensation of water in the pores), have pores accessible to the biomarker molecules of interest and show high affinity towards these molecules.

A number of materials, such as activated carbons, zeolites and polymers have been investigated in the context of VOC capture applications [Woolfenden, 2010]. Several aspects of MOFs make them promising materials for this application: the size and the shape of MOF pores can be tuned to be compatible with target molecules of a particular size and shape; being made from organic components MOFs should exhibit hydrophobicity (at least in comparison with natural zeolites) and high affinity towards organic biomarker species. On the other hand stability of MOFs in the presence of water has been recognized as one of the most serious challenges for the application and further development of these materials [Low *et al.*, 2009; Kusgens *et al.*, 2009; Schoenecker *et al.*, 2012].

Here we attempt to assess suitability of MOFs in this application. As the first step we explore their affinity with respect to several species that have been identified as potential lung cancer biomarkers [Buszewski *et al.*, 2007; Horvath *et al.*, 2009]. IRMOF-1 is not stable under humid conditions. HKUST-1 is more stable under humid conditions, but the presence of open metal sites and uncertainty about their interaction with water molecules, complicates further analysis. Instead, we focus on MIL-47 [Barthelet *et al.* 2001], a material that has been shown to be reasonably stable under a number of conditions and features rhomboidal one-dimensional channels, with sizes compatible with various

organic species. Henry's constants of adsorption at 300K and isosteric heats of adsorption for several representative species in MIL-47 are shown in Figure 6. Experimental adsorption enthalpy on MIL-47 for normal alkanes up to heptane was measured by Finsy and co-workers [Finsy *et al.*, 2009]. Extrapolation of their data to higher alkanes (in a similar way as it is done in the work of Deroche *et al.* [Deroche *et al.*, 2011]), suggests adsorption enthalpy for n-decane to be around 82 kJ/mol which is in excellent agreement with the result here. Maes and co-workers measured zero coverage adsorption enthalpy of styrene in MIL-47, among other things [Maes, *et al.*, 2010]. Their result (57.0 kJ/mol) is again in excellent agreement with the simulated value (56.2 kJ/mol). It is also instructive to compare performance of MOFs with other materials, such as zeolites. It has been noted by several groups, that in many aspects adsorption of hydrocarbons in MOFs is similar to that in zeolites. For example, Finsy and co-workers showed that n-heptane enthalpy of adsorption in MIL-47 (58.1 kJ/mol from experiments and 62.9 kJ/mol from simulations) is higher than in NaY (Si/Al 2.7) zeolite (51.9 kJ/mol) but quite lower than in Mordenite (77.0 kJ/mol) [Finsy *et al.* 2009]. Adsorption enthalpy of n-decane in ZSM-5 was been measured to be about 110 kJ/mol [Stach *et al.*, 1986], whereas simulated Henry's constant was estimated at $7.56 \cdot 10^{11}$ mol/kg/bar [Smit and Siepmann, 1994]. These values substantially exceed those observed here for MIL-47, which is not surprising given smaller size of the pores in ZSM-5 (5.5-7Å).

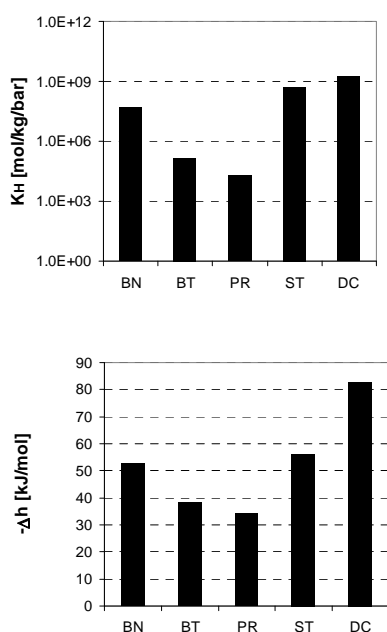


Figure 6. Henry's constants of adsorption at 300K (top) and isosteric heat of adsorption (bottom) for MIL-47. From left to right the data is for benzaldehyde (BZ), butanone (BT), propanol (PR), styrene (ST), and n-decane (DC).

These preliminary results indicate affinity of MOFs with respect to small molecules can be predicted with a reasonable level of accuracy using computational tools, and this affinity is comparable to that of zeolites. Given virtually infinite number of possible MOFs and Zeolitic Imidazolate Frameworks, or ZIFs (which tend to be very stable and hydrophobic materials) [Phan *et al.*, 2009], it is obvious that further studies into breath analysis using these materials as pre-concentrators is required and justified.

3. PERSPECTIVES

Recent discoveries in synthetic chemistry and material science suggest that virtually infinite number porous materials is possible and so far only a small fraction them has been realized experimentally. This may profoundly change the way adsorption applications are developed and

optimized, with emphasis shifted toward computational modelling.

Indeed, there are already several examples of high throughput computational screening and optimization of porous materials for adsorption applications. For example, in a recent study Wilmer *et al.* performed a computational screening of more than 130,000 virtual MOFs to identify the most promising candidates for methane storage [Wilmer *et al.*, 2011]. In another example, Haldoupis and co-workers explored various parameters, including the Henry's constant of adsorption and diffusion activation energy, of more than 250,000 zeolites in application to methane and hydrogen adsorption [Haldoupis *et al.*, 2011]. Lin *et al.* performed in silico screening of zeolites and ZIFs for carbon capture [Lin *et al.*, 2012].

In these screening protocols several key properties, directly related to the material performance in adsorption application, are calculated and correlated against various structural characteristics, such as surface area, pore volume and so on, in order to establish key structure-property relations. This motivated interest in computationally efficient ways to calculate these properties, and not surprisingly several alternative packages emerged, such as Zeo++ and MOFomics [Willems *et al.*, 2012; First *et al.*, 2011; First and Floudas, 2013].

Screening protocols performed on hundreds of thousands of structures generate vast amounts of data. Processing this data also requires development of new tools and algorithms that are quite different from the conventional molecular modelling and should be appropriately called material informatics tools. This is the area where substantial progress is yet to be made.

REFERENCES

- Barrett, E.P., Joyner, L.G., Halenda, P.P., 1951 *Journal of the American Chemical Society*, 73(1), 373.
- Barthelet, K., Marrot, J., Riou, D., Ferey, G., 2001. *Angewandte Chemie-International Edition*, 41(2), 281.
- Brunauer, S., Emmett, P.H., Teller, E., 1938. *Journal of the American Chemical Society*, 60, 309.
- Buszewski, B., Keszy, M., Ligor, T., Amann, A., 2007, *Biomedical Chromatography*, 21(6), 553.
- Chui, S.S.Y., Lo, S.M.F., Charmant, J.P.H., Orpen, A.G., Williams, I.D., 1999, *Science*, 283(5405), 1148.
- Deroche, I., Rives, S., Trung, T., Yang, Q., Ghoufi, A., Ramsahye, N.A., Trens, P., Fajula, F., Devic, T., Serre, C., Ferey, G., Jobic, H., Maurin, G., 2011. *The Journal of Physical Chemistry C* 115(28), 13868.
- Duren, T., Millange, F., Ferey, G., Walton, K.S., Snurr, R.Q., 2007. *Journal of Physical Chemistry C*, 111(42), 15350.
- Duren, T., Sarkisov, L., Yaghi, O.M., Snurr, R.Q., 2004. *Langmuir*, 20(7), 2683.
- Eddaoudi, M., Kim, J., Rosi, N., Vodak, D., Wachter, J., O'Keeffe, M., Yaghi, O.M., 2002. *Science*, 295(5554), 469.
- Finsky, V., Calero, S., Garcia-Perez, E., Merkling, P.J., Vedts, G., De Vos, D.E., Baron, G.V., Denayer, J.F.M., 2009. *Physical Chemistry Chemical Physics*, 11(18), 3515.
- First, E.L., Floudas, C.A., 2013. *Microporous and Mesoporous Materials*, 165, 32.
- First, E.L., Gounaris, C.E., Wei, J., Floudas, C.A., 2011. *Physical Chemistry Chemical Physics*, 13(38), 17339.
- Frenkel, D., Smit, B., 2002. *Understanding molecular simulation : from algorithms to applications*, 2nd ed. Academic Press, San Diego, London.
- Gelb, L.D., Gubbins, K.E., 1998, *Langmuir*, 14(8), 2097.
- Gelb, L.D., Gubbins, K.E., 1999. *Langmuir*, 15(2), 305.
- Haldoupis, E., Nair, S., Sholl, D.S., 2010. *Journal of the American Chemical Society*, 132(21), 7528.
- Haldoupis, E., Nair, S., Sholl, D.S., 2011. *Physical Chemistry Chemical Physics*, 13(11), 5053.
- Horvath, I., Lazar, Z., Gyulai, N., Kollai, M., Losonczy, G., 2009. *European Respiratory Journal*, 34(1), 261.
- Kusgens, P., Rose, M., Senkovska, I., Frode, H., Henschel, A., Siegle, S., Kaskel, S., 2009. *Microporous and Mesoporous Materials*, 120(3), 325.
- Lin, L.-C., Berger, A.H., Martin, R.L., Kim, J., Swisher, J.A., Jariwala, K., Rycroft, C.H., Bhowan, A.S., Deem, M.W., Haranczyk, M., Smit, B., 2012. *Nat. Mater.*, 11(7), 633.
- Low, J.J., Benin, A.I., Jakubczak, P., Abrahamian, J.F., Faheem, S.A., Willis, R.R., 2009. *Journal of the American Chemical Society*, 131(43), 15834.
- Maes, M., Vermoortele, F., Alaerts, L., Couck, S., Kirschhock, C.E.A., Denayer, J.F.M., De Vos, D.E., 2010. *Journal of the American Chemical Society*, 132(43), 15277.
- Phan, A., Doonan, C.J., Uribe-Romo, F.J., Knobler, C.B., O'Keeffe, M., Yaghi, O.M., 2009. *Accounts of Chemical Research*, 43(1), 58.
- Ravikovich, P.I., Vishnyakov, A., Russo, R., Neimark, A.V., 2000. *Langmuir*, 16(5), 2311.
- Rouquerol, J., Rouquerol, F., Sing, K.S.W., 1998. *Absorption by Powders and Porous Solids*, Academic Press, London.
- Sarkisov, L., 2012a. *Advanced Materials*, 24(23), 3130.
- Sarkisov, L., 2012b, *Physical Chemistry Chemical Physics*, 14(44), 15438
- Sarkisov, L., 2012c. *Journal of Physical Chemistry C*, 116(4), 3025.
- Sarkisov, L., Harrison, A., 2011. *Molecular Simulation*, 37(15), 1248.
- Schoenecker, P.M., Carson, C.G., Jasuja, H., Flemming, C.J.J., Walton, K.S., 2012. *Industrial & Engineering Chemistry Research*, 51(18), 6513.
- Smit, B., Siepmann, J.I., 1994. *Journal of Physical Chemistry*, 98(34), 8442.
- Stach, H., Lohse, U., Thamm, H., Schirmer, W., 1986. *Zeolites*, 6(2), 74.
- Talu, O., Myers, A.L., 2001, *Aiche Journal*, 47(5), 1160.
- Walton, K.S., Snurr, R.Q., 2007. *Journal of the American Chemical Society*, 129(27), 8552.
- Watanabe, T., Keskin, S., Nair, S., Sholl, D.S., 2009. *Physical Chemistry Chemical Physics*, 11(48), 11389.
- Widom, B., 1963. *Journal of Chemical Physics*, 39(11), 2808
- Willems, T.F., Rycroft, C., Kazi, M., Meza, J.C., Haranczyk, M., 2012. *Microporous and Mesoporous Materials*, 149(1), 134.
- Wilmer, C.E., Leaf, M., Lee, C.Y., Farha, O.K., Hauser, B.G., Hupp, J.T., Snurr, R.Q., 2011. *Nat. Chem.* 4(2), 83.
- Woollfenden, E., 2010. *Journal of Chromatography A*, 1217(16), 2685.

ANALYSIS OF SWELLING BEHAVIOUR OF CLAY MINERALS BY DISCRETE NUMERICAL SIMULATION

Hamed Bayesteh¹, Ali Asghar Mirghasemi^{2,a}

1. School of Civil Engineering, College of Engineering, University of Tehran, Iran

2. School of Civil Engineering, College of Engineering, University of Tehran, Iran

3. Author_3's Institution, Department, City, Country

a. Corresponding author (aghasemi@ut.ac.ir)

ABSTRACT: The development of physically meaningful mathematical models for describing the geotechnical engineering behavior of expansive soils requires an understanding at the particle level. The discrete element method (DEM) framework has been previously shown to accurately model clay behavior at the microscopic level. Based on micromechanical calculation, a discrete element model for expansive soils has been developed by considering the following inter-particle forces present in the clay-water-electrolyte system: electrical double-layer repulsive force and mechanical force. The analytical solution is used to calculate the repulsive force and the assembly is assumed to be two-dimensional. The results of numerical tests using this model have been described and discussed. Simulations include the effect of pore fluid chemistry on the swelling behaviour of the clays and their microfabric anisotropy. The results of these simulations show that by increasing electrolyte concentration, the swelling pressure reduces. Also, the fabric anisotropy increases by increasing swelling pressure. The proposed model appear to capture the microscopic response on expansive soils patterns consistent with theoretical considerations especially the Gouy-Chapman diffuse double layer theory, serve to verify the validity of physico-chemical theories employed and help interpret experimental data more fundamentally in terms of the system variables.

1. INTRODUCTION

Compacted active clays are currently used as barriers in geo-environmental projects because of their low permeability and high buffering capacity [1,2]. In spite of benefits of these sensitive active clays like Montmorillonite, they are known as a problematic soil because of their great specific surface areas (SSA) and high cation exchange capacities (CEC) due to the fact that more surface area is exposed to the water following the formation of the new microstructure [3]. Volume change behaviour of the sensitive clays is one of the challenging tasks in soil engineering. Changing in the environmental condition, water table, seepage and leaching action and stress level after loading on the soil are the important factors that cause compression in clayey soils [4]. In contrast to granular

materials, volume change behaviour of the clays is very complex and depends not only on the solid skeleton structure and pore size distribution, but also on the interaction between clay minerals and pore fluid chemistry [5,6], so an overlap of skills is essential to predict true behaviour of clays [7].

In addition, it has been shown that the clay's volume change are strongly depends on their micro fabric, therefore the microstructural methods are the best tools for monitoring their behaviour [8-10]. From microstructural point of view, in the past decades several experimental studied have been reported on the influence of mineral composition and pore fluid characteristics in compressibility behaviour of clays [11-16]. In these studies, laboratory

odeometer test commonly has been used to model one-dimensional compressibility behaviour of clays and verification tools like XRD analysis or SEM photos have been prepared to discover the microstructural changes during compression [17]. Studies have been indicated that pore fluid chemistry, cation exchangeable capacity, stress history, stress state, temperature and mineral type are the most important factors which are controls the volume change behaviour of clays [2,18,19].

Although the experimental methods lead to understanding the real clay behaviour, they have some limitations to control all parameters influencing the results. In addition, it is impossible to follow changing various interparticle forces during experimental tests [4]. Based on above limitations to control and monitor all parameters affecting on material behaviour in laboratory tests, in the past decade, researchers have been urged to use proper numerical methods instead of experimental method [21,22].

The common numerical method which can simulate material behaviours at particle-level (microscopic) has been known as discrete element method [23] which recently has been used as a computer virtual laboratory [22,24]. According to the discontinuous nature of the soils, many researchers have been interested in the use of DEM in the past decades for modeling cohesiveless soils behaviours [23, 25-30].

In order to simulate clay behaviors by DEM, some studies have been performed [31-35]. Anandarajah[36] assumed clay particles as straight lines and used electrical repulsive force based on Gouy-Chapman theory to model clay behaviour by DEM. Based on this study, complimentary researches have been done in the past decade [37,38]. The

authors developed a novel DEM model to simulate clay behavior from microstructural point of view [39, 40].

The main aim of this paper is to systematically examine numerically volume change behaviour of clays at different pore fluid compositions, as well as at different stress levels. For this purpose, the simulations have been performed on pure montmorillonite with different salt concentrations. Also, changing in the particles arrangements during volume change behaviour has been evaluated.

2 SIMULATION METHOD

The DEM assumes a representative elementary volume (REV) and discretize its particles to the rigid elements that are interacting with neighboring elements based on the existing interparticle forces. Evaluation of the internal forces, contact detection and integration of the Newton's second law by central difference method are three important computational steps in DEM. In a DEM analysis, from the known particle velocity (boundary loading), integrate to find the relative displacement between pair particles. Next, the interparticle forces are determined according to the suitable contact laws. Then, Newton's second law is applied to find acceleration of the particles. Finally, integrate two times from acceleration to find the new relative displacement on location of the particles. This cycle is repeated for all particles to reach the needed cycles [23].

Based on above algorithm, definition of the contact law is an important step which causes the interparticle forces. In spite of granular materials, there are not only mechanical forces between clay minerals, but also physico-chemical interaction between them. Double layer repulsive force and Van Der Waals attractive force are the main forces

between clay minerals according to their specific surface area (SSA), cation exchangeable capacity (CEC) and pore fluid chemistry [41,42].

The repulsive force between some clayey minerals is more important than attractive force [5,8,42] so that in this study, the attractive force has been neglected [6].

2.1 Double layer repulsive force

Electrically, clay minerals behave like plane capacitors. The planes, namely the clay crystal faces, are considered to be uniformly negatively charged over their surface. When they are located in a fluid, these charges are counterbalanced by positive ions and an electrical field is locally developed; as a result, the cations concentration decreases with distance to the clay particles [43]. The clay surface and the distributed charges adjacent it called the diffused double layer (DDL) [3,5,11,42]. The Gouy-Chapman diffuse double layer theory is the famous theory that has been used to model the interaction between clay particles and pore fluid [2,11,12,42,44]. Based on this theory, Langmuir's equation (1) has been used to calculate the double layer repulsive force between parallel infinite clay plates [42], where "u" is nondimensional potential between two parallel particles at any distance. "k" is Boltzmann's constant ($= 4.8 \times 10^{-10}$ esu).

$$P = 2nkT(\cosh u - 1) \quad (1)$$

The DDL repulsive force between two inclined platy particles was detailed addressed in the developed model by authors [40]. Briefly, the repulsion calculated by defining an area of repulsion which is called "AOR". The repulsive force and its location calculated based on the quality of the AOR.

2.2. Mechanical Force

When two particles approach each other very closely and their outer electron

clouds start to overlap, strong repulsive force occurs because electrons of one molecule are forbidden to enter. This phenomenon was called Born's repulsion [50]. So, the normal (F_N) and shear (F_s) forces are developed as a function of the penetration distance Δ illustrated in equation (2) where K is stiffness coefficient. The normal and shear penetration length between two particles are calculated based on their intersection point and magnitude of the overlap. In the pioneer studies, linear stiffness was used to model granular materials [23] and in the further researches, nonlinear stiffness has been used for DEM simulation [25,51]. Mirghasemi et al. [26] shown that nonlinear stiffness has less impact on the macroscopic behaviour of the assembly and for simplicity; suitable linear coefficient can be used instead of nonlinear one.

The used contact law is shown schematically in Figure 1 where the upper bound of the shear force demonstrated by Mohr-Colomb failure criteria. In this model, contacts cannot carry tensile force so that when the normal force is negative, contact will be deleted [23]. When two particles closed each other less than the defined mechanical cutoff, mechanical force will be developed. Also, the resultant mechanical repulsion induces the moment which is calculated according to the distance between center of the particle and intersection point (\vec{r}) as equation (3).

$$\begin{bmatrix} F_N \\ F_s \end{bmatrix} = \begin{bmatrix} K_N & 0 \\ 0 & K_s \end{bmatrix} \times \begin{bmatrix} \Delta_N \\ \Delta_s \end{bmatrix} \quad (2)$$

$$\vec{M} = \vec{r} \times \vec{F} = \vec{r} \times \vec{F}_N + \vec{r} \times \vec{F}_s \quad (3)$$

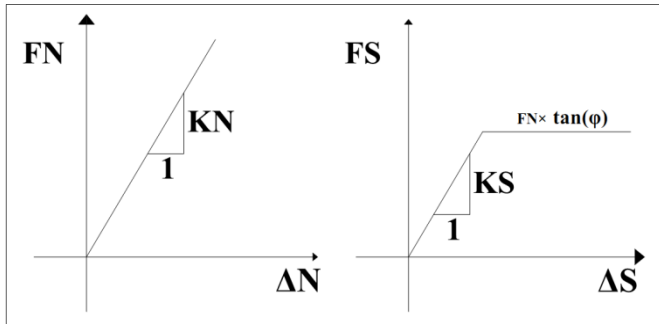


Figure 1: Inter-particle mechanical contact law.

3 ANALYSIS DETAILS

In order to simulate 2D one-dimensional compressibility behaviour of clays, a (1400 × 1400 nm) box media like classical oedometer test is selected which is confined by four straight lines denoted as walls. The walls are assumed to be rigid and only have transitional deformation. After that, 350 clay particles with random location and orientation are automatically placed within this box area by using a computer random-generator algorithm. According to the SEM photos, the montmorillonite particle's lengths are usually between 80 nm to 220 nm with 1 nm to 3 nm thickness [3,5]. The grain size distribution of simulated sample, natural montmorillonite and synthetic clay based on experimental investigations [52] are depicted in Figure 2. As seen the selected particle size distribution in this study is located within the existing particle size ranges. The specific surface area (SSA) and cation exchangeable capacity of montmorillonite are assumed to be 800 m²/g and 100 meq/100g respectively [42,48]. The initial assembly of clay particles is shown in Figure 3. In order to define interaction between walls and internal particles, these walls are assumed as a clay particle so there are mechanical and repulsive forces between walls and adjacent clay particles during compression.

Salt concentration is the most important

parameters of pore fluid chemistry which are control the volume change behaviour of montmorillonite [3]. In order to investigate the influences of this factor, a test program is devised. The salt types and concentrations are selected based on common pore fluid characteristics in the engineering projects in the range of 0.1M to 0.001M [41].

The initial assembly (Figure 3) is like a sample of dry clay so there aren't any physico-chemical and mechanical forces between particles. When the repulsive and mechanical force program modules are turned on, the repulsive and mechanical forces are activated and simulate the conditions when the clay minerals are submerged in electrolyte media. Based on the new interparticle forces, a new arrangement forms, distance between adjacent particles is changed and they move until equilibration between mechanical and physico-chemical forces [36]. This stage is named relaxation. The assembly arrangement after this relaxation is depicted in Figure 4. By comparison between Figure 3 and 4, it is found that the distribution of spacing between particles in Figure 4 is more uniform than that of initial assembly (Figure 3). In order to simulate one-dimensional compression, two horizontal walls are moved with prescribed velocity to reach to the needed strain. Based on selected time step, the number of computation cycles should be chosen in such a way to reach a static equilibrium state. In order to complete simulation with reasonable timescale, the particle density is scaled up to use a time step of ~ 1s [53].

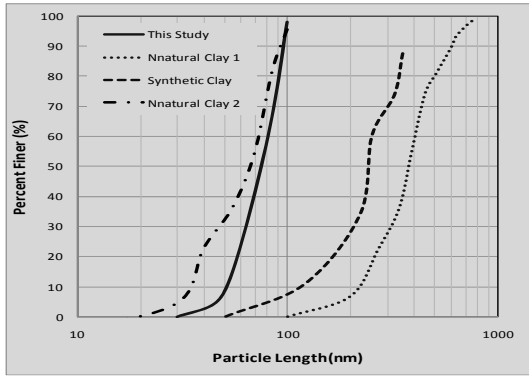


Figure 2: Particle size distribution curve

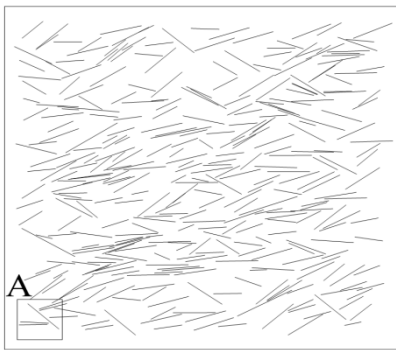


Figure 3: Initial assembly of clay particles

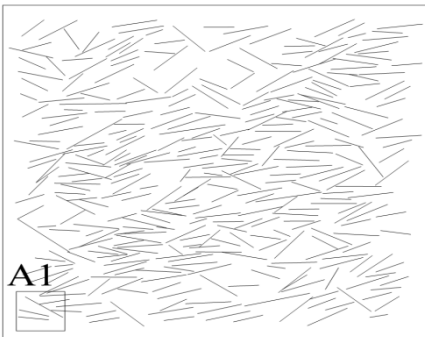


Figure 4: Particle's arrangement after relaxation

4. VERIFICATION

Validation with respect to experimental results and qualitative assessment establishes physical plausibility are two common methods which have been used to verify discontinuous numerical models in more than 100 published validation studies [54]. Therefore in this study, these two validation methods have been done and will be addressed in this

section. In qualitative assessment, visually simulation behaviour to establish physical viability is examined [54]. Verification by experimental results are presented in the next section.

In the initial assembly (absent of the DDL repulsive forces), particles have irregular distances related each other and some of them are very close in spite of large distance between others (Figure 3). When repulsive and mechanical interparticle forces are activated (Figure 4), particles move until equilibration between mechanical and physico-chemical forces is obtained. As a result distances between adjacent particles will be changed and new particle arrangement is formed. This stage is named relaxation. The spacing between particles in the new arrangement becomes more uniform than that of initial assembly. The uniformity in spacing is due to equilibration between DDL repulsive force and mechanical contacts. Also, there isn't any overlap between discrete elements which emphasizes the accuracy of the simulation.

5. RESULTS AND DISCUSSION

The influence of the pore fluid concentration on the compression curve on sodium-montmorillonite is shown in Figure 5. The initial void ratio for these types of electrolytes is different due to the initial interparticle forces. The less electrolyte concentration ($n = 0.001$ M) shows a higher void ratio value at a given applied vertical stress in comparison with the more electrolyte concentration ($n = 0.1$ M). A final pressure of 4000 Kpa was required to maintain constant volume in the ($n = 0.001$ M) electrolyte concentration and only 1600 Kpa for $n = 0.1$ M. The thickness of the diffuse double layer is directly depends on the electrolyte concentration. It is proportional to the inverse square root of the electrolyte concentration [3].

Therefore, increasing in the presence of the chemical in the pore fluid solution causes reduction of the DDL's thickness and consequently reduces the repulsive force between particles. So, at the same void ratio, the repulsive force decreases by increasing electrolyte concentration as shown in Figure 5.

To microfabric evolution during compression, the histograms of the particles orientation have been prepared at each loading step. This histogram is an angular distribution diagram can then be drawn as a rose diagram giving the number of particles as a function of their orientation. For example, the initial particle's histogram is illustrated in Figure 6. It can be observed that at the initial state, since the particles were randomly generated, there is not significant anisotropy for the particle's orientation. As a result the histogram is approximately alike a circle. Figures 6 and 7 show the particle's histograms after compression up to 1000 Kpa and 2000 Kpa respectively. In these situations assemblies of particles are compressed and their orientations are changed. By increasing the vertical load, particles rotate to have an orientation perpendicular to the loading direction. As a result the intensity of particles' orientation increases along horizontal axes.

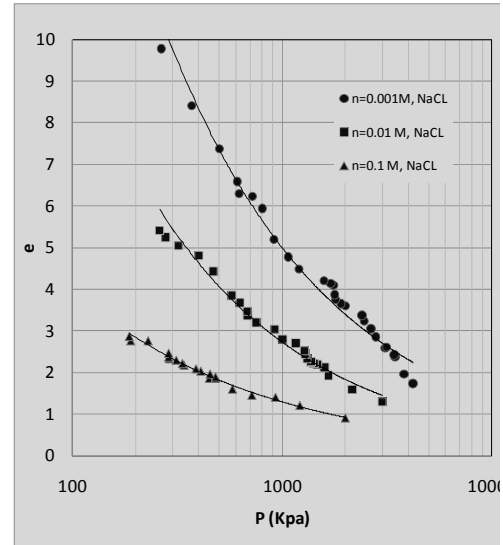


Figure 5: (e) plotted against (log p) for montmorillonite immersed in NaCl solution at various concentration

6 CONCLUSION

A series of DEM simulations are presented to model the impact of pore fluid characteristics on the volume change behaviour of the montmorillonite clays. For this aim, a DEM code has been prepared by considering both mechanical and DDL repulsive force as interparticle forces. The results show that volume change behaviour is directly depends on the thickness of diffused double layer. Increasing the electrolyte concentration, leads to reduction of both thickness of DDL and void ratio. But by considering the DDL theory, the temperature has a little effect on the void ratio.

The DEM results are verified with experimental and theoretical data as good agreement was achieved. It is concluded that DEM can be used as a virtual laboratory and powerful tools in order to simulate clay behaviour at the particle scale. Furthermore, microfabric evolution during compression is regularly traced which is a difficult and sensitive task in experimental methods. The results show that increasing vertical pressure causes

re-orientation of the particles perpendicular to the direction of loading. Also, intensity of the anisotropy increases during compression.

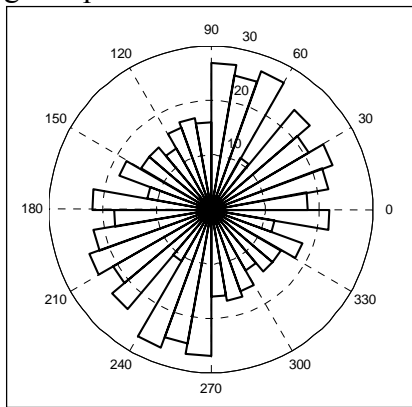


Figure 6: Microfabric's histogram in initial state

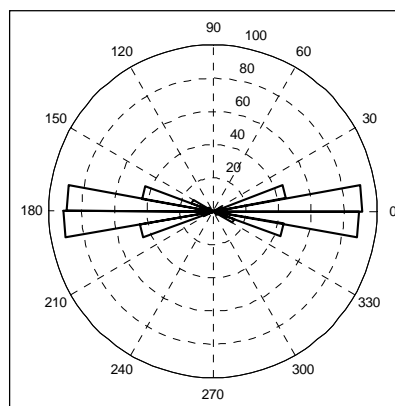


Figure 7: Microfabric's histogram after compression up to ($p = 2000 \text{ Kpa}$)

REFERENCES

- [1] Pusch, R. and Yong, R., 2006. "Microstructure of Smectite Clays and Engineering Performance", Taylor and Francis, New York, 330.
- [2] Komine, H. 2008. "Theoretical Equations on Hydraulic Conductivities of Bentonite-Based Buffer and Backfill for Underground Disposal of Radioactive Wastes", Journal of Geotechnical and Geoenvironmental Engineering, Vol. 134, No. 4, 497-508.
- [3] Mitchell, J. K. 1993. "Fundamentals of soil behaviour". John Wiley and Sons. Inc., 422.
- [4] Sridharan, A., and Rao, V. 1973. Mechanisms controlling volume change of saturated clays and the role of the effective stress concept, *Geotechnique*, 23, No. 3, 359-382.
- [5] Yong, R. N., and Warkentin, B. P. 1975. Introduction to soil behaviour. New York: Macmillan.
- [6] Mitchell, J. K. and Soga, K., 2005. "Fundamentals of soil behaviour". John Wiley and Sons. Inc., 558.
- [7] Soga, K. and Jefferies, S.A., 2008. "Contributions to Geotechnique 1948-2008: soil science and interdisciplinary aspects of geotechnical engineering", *Geotechnique*, 58, No. 5, 441-448.
- [8] Collins, K. and McGrown, A., 1974. "The form and function of microfabric features in a variety of natural soils", *Geotechnique* 24, No. 2, 223-254.
- [9] Koch, D. 2002. Bentonite as basic materials for technical base liners and site encapsulation cut-off walls. *Applied Clay Science*. No. 21, 1-11.
- [10] Ichikawa, Y., Kawamura, K., Fujii, N. and Kitayama, K. 2004. "Microstructure and micro/macro- diffusion behaviour of tritium in bentonite", *Applied clay science*, 26, 75-90.
- [11] Bolt, G. H. 1956. "Physico-chemical analysis of the compressibility of pure clays," *Geotechnique*, 6, 86-93.
- [12] Mesri, G., and Olson, R. E., 1971. Consolidation characteristic of montmorillonite. *Geotechnique* 21, 341-352.
- [13] Di Maio, C., Santoli, L., and Schiavon, P. 2004. Volume change behaviour of clays: the influence of mineral composition, pore fluid composition and stress state. *Mechanics of Materials*, 36, 435-451.
- [14] Monroy, R., Zdravkovic, L. and Ridley, A., 2010. "Evolution of microstructure in compacted London clay during wetting and loading", *Geotechnique*, 60, No. 2, 105-119.
- [15] Wahid, A. S., Gaji, A. and DI Maggio, R. (2011), Chemo-mechanical effects in kaolinite. Part 1: prepared samples, *Geotechnique* 61, No. 6, 439-447.
- [16] Siddiqua, S., Blatz, J., and Siemens, G. 2011. Evaluation of the impact of pore fluid chemistry on the hydromechanical behaviour of clay-based sealing materials. *Can. Geotech. J.*, No. 48, 199-213.
- [17] Baille, W., Tripathy, S. and Schanz, T., 2010. "Swelling pressures and one-dimensional compressibility behaviour of bentonite at large pressures", *Applied Clay Science*, Vol. 48, 324-333.
- [18] Gens, A. and Alonso, E.E., 1992. "A framework for the behaviour of unsaturated

- expansive clays", *Canadian Geotech J.*, 29, 1013–1032.
- [19] Delage, P. 2007. "Microstructure features in the behaviour of engineered barriers for nuclear waste disposal." *Proc., Experimental Unsaturated Soil Mechanics*, Springer, New York, 11–32.
- [20] Olsen, H. W., 1960. Hydraulic flow through saturated clays. 9th national conference on clays and clay minerals, 131-161.
- [21] Zdravkovic, L. and Carter, J., 2008. "Contributions to Geotechnique 1948-2008: constitutive and numerical modeling", *Geotechnique*, 58, No. 5, 405-412.
- [22] Simonsen, B. and Tatsuoka, F., 2008. "Geotechnics: The next 60 years", *Geotechnique*, 58, No. 5, 49-60.
- [23] Cundall, P.A. and Strack, O.D.L., 1979. "A discrete numerical model for granular assemblies", *Geotechnique*, Vol. 29, No. 1, 47-65.
- [24] Munjiza, A. 2004. *The combined finite-discrete element method*. John Wiley & Sons Ltd, 333.
- [25] Ng, T.T. and Dobry, R., 1992. "A non-linear numerical model for soil mechanics", *International Journal for Numerical and Analytical Methods in Geomechanics*, Vol. 16, , 247-263.
- [26] Mirghasemi, A.A., Rothenburg, L. and Matyas, E.L., 1997. "Numerical simulation of assemblies of two-dimensional polygon-shaped particles and effects of confining pressure on shear strength", *Soils and Foundation*, Vol.37, No.3, 43-52.
- [27] Kruyt, N.P. and Rothenburg, L. 1998. Statistical theories for the elastic moduli of two-dimensional assemblies of granular materials. *International Journal of Engineering Science*. Vol. 36, 1127–1142.
- [28] Seyed Hosseininia, E., Mirghasemi, A. A., 2006. "Numerical Simulation of Breakage of Two-Dimensional Polygon-Shaped particles using Discrete Element Method", *Powder Technology*, No. 166, 100-112.
- [29] Li, X. and Yu, H. S., 2009. Influence of loading direction on the behavior of anisotropic granular materials. *International Journal of Engineering Science*, No. 47, 1284–1296.
- [30] Scholtes, L., Chareyre, B., Nicot, F. and Darve, F., 2009. Micromechanics of granular materials with capillary effects. *International Journal of Engineering Science* 47, 64–75.
- [31] Iordanoff I., Fillot N. and Berthier Y., 2005. "Numerical study of a thin layer of cohesive particles under plane shearing", *Powder Technology* 159, 46 – 54.
- [32] Zhang R. and Li J., 2006. "Simulation on mechanical behaviour of cohesive soil by Distinct Element Method", *Journal of Terramechanics*, Vol.43, No. 3, 303–316.
- [33] Kock I. and Huhn K., 2007. "Influence of particle shape on the frictional strength of sediments: A numerical case study", *Sedimentary Geology*, 196, 217–233.
- [34] Vesga L.F., Vallejo L.E. and Lobo-Guerrero S., 2008. "DEM analysis of the crack propagation in brittle clays under uniaxial compression tests", *Int. J. Numer. Anal. Meth. Geomech*; 32:1405–1415.
- [35] Ammeri A., Jamei M. and Bouassida M., 2009. "Numerical study of bending test on compacted clay by discrete element method: tensile strength determination", *Int. J. Computer Applications in Technology*, Vol.34, No.1, 13-22.
- [36] Anandarajah, A. 1994. "Discrete Element Method for Simulating Behaviour of Cohesive Soil", *J. Geotech. Engrg., ASCE*, Vol. 120, No. 9, 1593-1613.
- [37] Anandarajah, A., 2003. "Discrete element modeling of leaching-induced apparent over-consolidation in Kaolinite", *Soils and Foundations*, Vol. 43, No. 6, 1-12.
- [38] Yao M., 2001. "Three-Dimensional Discrete Element Method Analysis of Cohesive Soil" PhD thesis, Johns Hopkins University.
- [39] Bayesteh, H. and Mirghasemi, A.A., 2013. Procedure to detect the contact of platy cohesive particles in discrete element analysis. *Powder Technology*, Vol. 244, 75-84.
- [40] Bayesteh, H. and Mirghasemi, A.A., 2013. Numerical simulation of pore fluid characteristic effect on the volume change behavior of montmorillonite clays. *Computers and Geotechnics*, No. 48, 146-155.
- [41] Yong, R. N. 2000. *Geoenvironmental engineering: Contaminant soils, pollutant fate and mitigation*. By CRC Press LLC. , 307.
- [42] Van Olphen, H., 1991. *An introduction to clay colloid Chemistry*, Wiley Interscience, New York, Second edition, 301.
- [43] Meunier, A. (2005). "Clays". Springer, Inc., 472.
- [44] Tripathy, S., Sridharan, A. and Schanz, T., 2004. "Swelling pressures of compacted bentonites from diffuse double layer theory", *Can. Geotech. J.* 41, 437–450.
- [45] Anandarajah, A. and Lu, N. 1991. "Numerical Study of the Electrical Double-Layer Repulsion between Non-Parallel Clay Particles of Finite Length", *International Journal for Numerical and Analytical*

- Methods in Geomechanics, Vol. 15, No. 10, 683-703
- [46] Lu, N. and Anandarajah, A. 1992. Empirical estimation of double layer repulsive force between two inclined clay particles of finite length. *Journal of Geotechnical and Geoenvironmental Engineering*, Vol. 118, No. 4, 628-634.
- [47] Sridharan, A., and Jayadeva, M. S. 1982. Double layer theory and compressibility of clays. *J. Geotechnique*, 32, No. 2, , 94-99.
- [48] Sridharan, A., and Choudhury, D. 2002. Swelling pressure of sodium montmorillonites. *Géotechnique*, 52, No. 6, 459-462.
- [49] Low, P. F. 1980. The swelling of clay. II. Montmorillonite. *J. Soil. Soc. Am.* 44, No. 4, 667-676.
- [50] Lu, N., Anderson, M.T., Likos, W.J. and Mustoe, G.W., 2008. "A discrete element model for kaolinite aggregate formation during sedimentation", *Int. J. Numer. Anal. Meth. Geomech.*; 32:965-980.
- [51] Bonilla, R.R.O., 2004. "Numerical simulation of undrained granular media", PhD thesis, University of Waterloo, Waterloo, Ontario, Canada.
- [52] Cadene, A., Durand-Vidal, S., Turq, P. and Brendle, J (2005). "Study of individual Namontmorillonite particles size, morphology, and apparent charge", *Journal of Colloid and Interface Science* 285, 719-730.
- [53] Thornton, C. 2000. Numerical simulations of deviatoric shear deformation of granular media. *Géotechnique*, 50, No.1, 43-53.
- [54] Maclaughlin, M. M., and Doolin, D. M., 2006. "Review of validation of the discontinuous deformation analysis (DDA) method". *International Journal for Numerical and Analytical Methods in Geomechanics*, 30:271-305.
- [55] Sherard, J. L., Dunnigan, L. P., and Decker, R. S. 1976. Identification and nature of dispersive soils. *J. Geotech. Eng., ASCE*, Vol. 102, No. GT 4, April, pp. 298-312.
- [56] Hattab, M. and Fleureau, J.M., 2011. Experimental analysis of kaolinite particle orientation during triaxial path. *Int. J. Numer. Anal. Meth. Geomech*, 35:947-968.
- [57] Quilgley, R. M. and Thompson, C. D., 1966. The fabric of anisotropically consolidated sensitive marine clay. *Canadian geotechnical journal*, Vol. 3, No. 2, 61-73.
- [58] Satake, M. 1982. Fundamental quantities in the graph approach to granular materials. *Proc., U.S./Japan Seminal on New Models and Constitutive Relations in the Mechanics of Granular Materials*, Itasca, N.Y., 9-19.

ARTIFICIAL NEURAL NETWORK APPROACH TO PREDICT OF EFFECT OF PROCESS CONTROL AGENT ON THE MICROHARDNESS OF AL-AL₂O₃ COMPOSITE POWDERS PRODUCED BY MECHANICAL ALLOYING

A. Canakci^{1,a}, T. Varol¹, S. Ozsahin²

¹Karadeniz Technical University, Metallurgical and Materials Eng. Dept., Trabzon, Turkey.

²Karadeniz Technical University, Woodworking Industrial Eng. Dept., Trabzon, Turkey.

a. Corresponding author (aykut@ktu.edu.tr)

ABSTRACT: In this study, an artificial neural network approach is generated to predict of effect of process control agent on microhardness of Al-10 wt.% Al₂O₃ composite powders fabricated by mechanical alloying. This composite powder was synthesized by utilizing planetary high energy ball mill for different milling times of 0.5, 1, 2, 4, 6, 8, 10h. Ball mill velocity was 400rpm and ball to powder weight ratio was 10:1. Methanol was used as process control agent (PCA). Different amounts of methanol (1, 2, 3 wt. %) were used to study the effect of the process control agent on microhardness of the Al-Al₂O₃ composite powders. The microhardness of composite powders was determined by a microhardness tester. As a result of the study neural network was found successful for the prediction of effect of process control agent on the microhardness of Al-Al₂O₃ composite powders produced by mechanical alloying.

Keywords: Artificial Neural Networks; Mechanical alloying; Powder metallurgy; Process control agent (PCA)

1. INTRODUCTION

Ceramic particle-reinforced metal matrix composites (MMCs) provide a good combination of strength attained from ceramic reinforcements and toughness due to the underlying metal matrix. Aluminum is a widely used matrix material in MMCs primarily because of its low weight, low cost and ease of fabrication. The preferred reinforcement in MMCs should have high modulus, low density, good wettability, proper shape with a certain aspect ratio to minimize stress concentration, and thermal expansion coefficient comparable to that of the metal matrix to minimize the development of internal stresses due to temperature changes [Gudlur et al. 2012; Mortensen and Llorca, 2010; Mishnaevsky, 2007].

Mechanical alloying (MA) is one of the potential processes to synthesize ceramic

particle strengthened metal matrix composite powders. One concern is that through MA process different types of nanostructured powders can be prepared [Luo et al. 2012]. PCA has to be added into the powder mixture prior to MA. The addition of PCA is to modify the surface condition of the deformed particles by impeding the clean metal to metal contact necessary for cold welding [Lu and Zhang 1999; Suryanarayana, 2001; Pilar et al. 2008; Long et al. 2010].

ANN models have been recently studied, with the objective of achieving human-like performance in many fields of knowledge engineering [Hayajneh et al. 2009; Dashtbayazi et al. 2007]. However,

an artificial neural network model has not been established yet for understanding the effect of amount of process control agent on microhardness of Al-Al₂O₃ MMCs. In this study, an attempt was made to use an ANN model to predict of microhardness of Al-Al₂O₃ composites to study the effect of amount of process control agent.

2. EXPERIMENTAL

2.1. Materials

The as-atomized Al alloy powders (Günder Exotherm Company, Turkey) with an average powder particle size of 127µm and Al₂O₃ particles (99.7 % purity, Wacker Ceramic Company, Germany) with an average particle size of

13 µm were used as raw materials. The chemical composition of the as-atomized Al alloy (in wt. %) is 1.230Fe, 1.000Si, 1.000Pb, 0.710Cu, 0.530Zn, 0.116Mn, 0.071Ti, 0.050Mg and Al (balance). Methanol was used as the process control agent in varying amounts of 1, 2 and 3 wt. % to study its effect of on the process. Table 1 lists all the process variables employed in this work. The microhardness values of the as-received and milled powders were measured using a microhardness tester (Struers microhardness tester) at a 10 g load. For each sample, five hardness tests were performed in order to eliminate the possible errors.

Process Code	Methanol (%wt.)	Milling Time (h)								Milling Speed (rpm)	Ball-to-powder weight ratio
		0	0.5	1	2	4	6	8	10		
P ₁	1%	0	0.5	1	2	4	6	8	10	400	10:1
P ₂	2%	0	0.5	1	2	4	6	8	10	400	10:1
P ₃	3%	0	0.5	1	2	4	6	8	10	400	10:1

2.2. Artificial Neural Network (ANN) Model

The sigmoid function (Eq.2) is the most common activation function in the ANN because it combines nearly linear behavior, curvilinear behavior, and nearly constant behavior. All of these components depend on the value of the input. In the cell model, a bias with +1 value may increase the net input or polarization threshold input (θ_j) by a value of, -1, thereby decreasing the net input according to:

$$\text{net}_j = \sum_{i=1}^n x_i w_{ij} - \theta_j \quad (1)$$

where x_i indicates the i . input, w_{ij} is the connection weight from j . element to i . element, θ_j is the polarization value (negative of the threshold value), and n indicates the sent input signal of the artificial neuron number in the previous layer.

The produced output is sent via network connections between different cells, as explained by:

$$y_j = f(\text{net}_j) = \frac{1}{1 + e^{-\text{net}_j}} \quad (2)$$

3. EXPERIMENTAL

3.1. Collecting the Experimental Data

From the well known and widespread identification tools, the root mean squared error (RMSE) and the mean absolute percentage error (MAPE) values are calculated from Eqs.3 and 4. Models that produce the best estimated values were selected as the forecasting models.

$$RMSE = \sqrt{\frac{1}{N} \sum_{i=1}^N (t_i - td_i)^2} \quad (3)$$

$$MAPE = \frac{1}{N} \left(\sum_{i=1}^N \left| \frac{t_i - td_i}{t_i} \right| \right) \times 100 \quad (4)$$

where t_i is the real value, td_i is the model prediction value and N is the number of testing data.

3.2. Neural Network Architecture

Figure 1 shows the ANN models containing one input layer, two hidden layers and one output layer. The methanol ratio and milling time were used as the input variables, while the microhardness was used as the output variables in the ANN models. The processing element numbers (neurons) of the hidden layers were 7 and 6 for the model in Fig. 1.

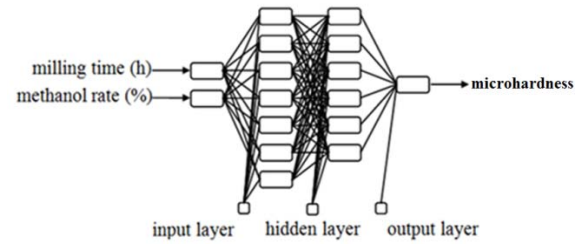


Fig. 1: The ANN architecture selected as the prediction model for the and microhardness.

3.3. Network Training And Testing

The normalization (scaling) operations were carried out using Eq. 5:

$$X_{\text{norm}} = 2 \times \frac{X - X_{\text{min}}}{X_{\text{max}} - X_{\text{min}}} - 1 \quad (5)$$

where X_{norm} is the normalized value, X is the true value of the variable, X_{min} is minimum value of the data set and X_{max} is the maximum value of the data set.

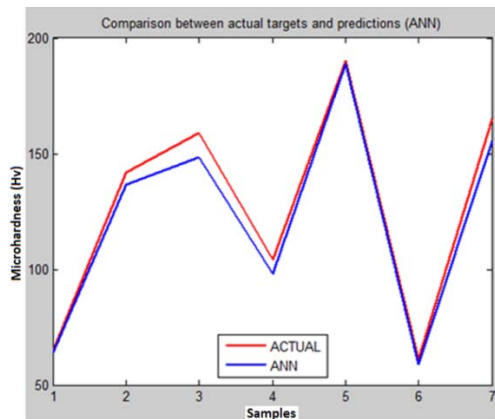
4. RESULTS AND DISCUSSION

The ANN was tested for accuracy using the test values (Table 2) selected from the experimental results that were not used during the learning processes. In most cases, the neural network prediction is very close to the actual value.

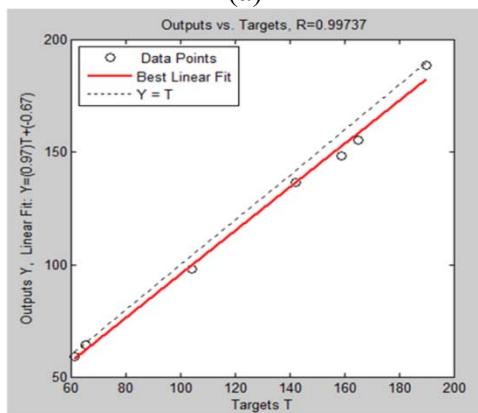
Table 2. Experiment data and predicted output from the ANN network for testing set

	No	Methanol rate (%)	Milling time (h)	Microhardness			
				Measured	Predicted	Deviation	% Error
Testing Datas	2	1.0	0.5	65.0	64.28	0.72	1.10
	5	1.0	4.0	142.0	136.83	5.17	3.64
	7	1.0	8.0	159.0	148.34	10.66	6.70
	12	2.0	2.0	104.0	97.99	6.01	5.78
	16	2.0	10.0	190.0	188.95	1.05	0.55
	19	3.0	1.0	61.0	58.82	2.18	3.58
	22	3.0	6.0	165.0	155.64	9.36	5.67
			MAPE	3.8606			
			RMSE	6.2151			

Figs.2a and 2b show the relationship between the real and calculated values obtained using the prediction models. The mean absolute percentage errors (MAPE) were 3.86% for microhardness. With respect to the results obtained from the plots of the ANN prediction, the highest MAPE value of 3.86% demonstrates that the network effectively generates sensitive results.



(a)



(b)

Fig. 2:(a)The comparison of measured values and ANN values for the microhardness, (b)Regression analysis for the neural network responses

Fig. 2b shows the regression analysis of the ANN model for the microhardness. The correlation coefficient was obtained to be 0.99, indicating good agreement between the experimental results and the model prediction ($R_{\text{microhardness}} = 0.99737$). The statistical results namely,

the root-mean squared error (RMSE) and the mean absolute percentage error (MAPE), are within an acceptable range and meet the integrity of the ANN learning and testing stages. Thus, reasonable agreement between the predicted and experimental data supports the accuracy of the model.

4. CONCLUSIONS

The mean absolute percentage error (MAPE) for predicted values does not exceed 3.86%. Therefore, using ANN values, satisfactory results can be estimated rather than measured which thereby reduces the testing time and cost. Moreover the amount of PCA has a large effect on the properties of the powder.

Acknowledgements

The authors are grateful to the Karadeniz Technical University Research Fund for financially supporting this research (No: 2007.112.10.2). The researchers would also like to thank the Gundogdu Exotherm Service for providing the Al powders.

REFERENCES

- Gudlur, P., Forness, A., Lentz, J., Radovic, M. and Muliana, A., 2012. Thermal and mechanical properties of Al/Al₂O₃ composites at elevated temperatures, *Materials Science and Engineering A* 531, 18.
- Mortensen, A., Llorca, J., 2010. Metal Matrix Composites, *Annual Review of Materials Research* 40, 243.
- Mishnaevsky, L., 2007. *Computational Mesomechanics of Composites: Numerical Analysis of the Effect of Microstructures of Composites on their Strength and Damage Resistance*, Wiley-Interscience.
- Luo, X.T., Yang, G.J. and Li, C.J., 2012. Preparation of cBNp/NiCrAl nanostructured composite powders by a step-fashion mechanical alloying process, *Powder Technology* 217, 591.
- Lu, L. and Zhang, Y.F., 1999. Influence of process control agent on interdiffusion between Al and Mg during mechanical alloying, *Journal of Alloys and Compounds* 290, 279.

- Suryanarayana, C., Mechanical alloying and Milling, *Prog. Mater. Sci.* 46 (2001) 1.
- Pilar, M., Escoda, L., Sunol, J.J. and Greneche, J.M., 2008. Magnetic study and thermal analysis of a metastable Fe-Zr-based alloy: Influence of process control agents, *Journal of Magnetism and Magnetic Materials*, 320, 823.
- Long, B.D., Zuhailawati, H., Umemoto, M., Todaka, Y. and Othman, R., 2010. Effect of ethanol on the formation and properties of a Cu-NbC composite, *Journal of Alloys and Compounds* 503, 228.
- Hayajneh MT, Hassan AM, Mayyas AT., 2009. Artificial neural network modeling of the drilling process of selflubricated aluminum/alumina/graphite hybrid composites synthesized by powder metallurgy technique. *Journal of Alloys and Compounds*, 478, 559.
- Dashtbayazi, M.R., Shokuhfar, A., Simchi, A., 2007. Artificial neural network modeling of mechanical alloying process for synthesizing of metal matrix nanocomposite powders. *Mater Sci Eng A*, 466, 274.

A STUDY FOR ANISOTROPY OF POROUS AND POWDER MATERIALS FROM A DIFFERENT PERSPECTIVE: 'USE OF ORTHONORMAL PARTS OF ELASTIC CONSTANT TENSOR'

Çiğdem Dinçkal^{1,a}

1. Çankaya University, Department of Civil Engineering, Ankara, Turkey
a. Corresponding ; Author. (cdinckal@cankaya.edu.tr)

ABSTRACT: Many porous and powder materials in engineering are anisotropic and inhomogeneous due to the varying composition of their constituents. For a deep understanding of physical properties of these materials, use of tensors is inevitable. In this paper, an innovational general form and more explicit physical property of elastic constant tensor in terms of its orthonormal parts are presented. As applications, numerical examples from various porous and powder materials are given.

Furthermore norm and norm ratio concepts are introduced to measure and compare the anisotropy degree for different porous and powder materials with the same or different anisotropic elastic symmetries. For these materials, norm and norm ratios are computed. It is suggested that norm may be used as a criterion for comparing overall effect of the properties of anisotropic materials and norm ratios can be used as a criterion to represent the anisotropy degree of materials.

To summarize, main contributions of this work are to investigate the elastic and mechanical properties of an anisotropic porous and powder material from a different perspective, determine anisotropy degree of that material and also anisotropic elastic symmetry type for a porous and powder material given from an unknown symmetry.

1. INTRODUCTION

A material is isotropic if its mechanical and elastic properties are the same in all directions. When this is not true, the material is anisotropic. In order to understand the physical properties of the anisotropic materials, use of tensors by decomposing them is important. Tensors are the most significant mathematical entities to describe direction dependent physical properties of solids and the tensor components characterizing physical properties which must be specified without reference to any coordinate system.

The constitutive relation for linear anisotropic elasticity, defined by using stress and strain tensors, is the generalized Hooke's law [Nye, 1964]

$$\sigma_{ij} = C_{ijkl} \varepsilon_{kl} \quad (1)$$

This formula demonstrates the well-known general linear relation between the stress tensor whose components are σ_{ij} and the strain tensor (symmetric second rank tensor) whose components are ε_{kl} . C_{ijkl} are the components of elastic constant tensor (elasticity tensor) C_{ijkl} satisfies three important symmetry restrictions. These are

$$C_{ijkl} = C_{jikl} \quad C_{ijkl} = C_{ijlk} \quad C_{ijkl} = C_{klij}, \quad (2)$$

which follow from the symmetry of the stress tensor, the symmetry of the strain tensor and the elastic strain energy. These restrictions reduce the number of independent elastic constants C_{ijkl} from 81 to 21. Consequently, for anisotropic materials (with triclinic symmetry) the elastic constant tensor has 21 independent components. The indices are

abbreviated according to the replacement rule given in the following Table[Nye, 1964]:

Table 1: Abbreviation of indices for four and double index notations.

four index notation	11	22	33	23, 32	13, 31	12, 21
double index notation	1	2	3	4	5	6

In literature, the works for orthonormal decomposition of any rank tensors can be summarized as; it was first proposed by [Gazis, et. al, 1963], developed by [Tu, 1968] who gave name as integrity basis treated the strain energy function as a polynomial in the strain components and lead to determination integrity basis for invariant functions of the strain components for each one of the 32 crystallographic point groups. Using the integrity basis, orthonormal tensor basis which spans the space of elastic constants was derived. Furthermore, Srinivasan and Nigam (1969) identified invariant elastic constants for each crystal class.

Here, the purpose of the work is to represent elastic constant tensor of porous and powder materials in terms of its orthonormal parts.

2. DECOMPOSITION PROCESS

In analyzing the elastic and mechanical properties of anisotropic linear materials, elastic constant tensor is introduced in specification of physical properties for many anisotropic materials. In this work, porous and powder materials possessing transversely isotropic and orthorhombic symmetry are selected for application.

2.1. Form Invariant

A physical property of tensor is resolved along the triads v_1, v_2, v_3 denoting the unit vectors along the material coordinate axis [Srinivasan and Nigam, 1969]. The symmetry properties of the material, due

to the geometric or crystallographic symmetry, can be defined by the group of orthonormal transformations which transform any of these triads v_a into its equivalent positions. For each of the symmetry classes selected, as reference system a rectangular Cartesian coordinate system $Oxyz$ is chosen, so related to the material directions v_1, v_2, v_3 in the material under consideration that the symmetry of the material may be described by one or more of the

transformations. Transformations in which the coefficients satisfy the orthogonality relations are called linear orthogonal transformations. In this formulation, the number of elastic constants and their values do not depend on the choice of the coordinate system. The form invariant expression for the components of elastic constant tensor, the elastic stiffness coefficients is,

$$C_{ijkl} = v_{ai} v_{bj} v_{ck} v_{dl} A_{abcd} \quad (3)$$

Where summation is implied by repeated indices, v_{ai} are the components of the unit vectors v_a ($a=1,2,3$) along the material direction axes. A_{abcd} is invariant in the sense that when the Cartesian system is rotated to a new orientation $Ox'y'z'$, then (3) takes the following form;

$$C'_{ijkl} = v'_{ai} v'_{bj} v'_{ck} v'_{dl} A_{abcd} \quad (4)$$

Where v_1, v_2, v_3 form a linearly independent basis in three dimensions but they are not necessarily always orthogonal (it is a general case). The orthogonality condition used in this work, is a particular case for elastic constant tensor so the corresponding reciprocal triads must satisfy the following relation

$$v_{ai} v_{aj} = \delta_{ij} \quad (5)$$

The expression given in (5) can be rewritten as

$$v v^T = \mathbf{I} \quad (6)$$

Where \mathbf{I} is identity matrix which is

$$\begin{bmatrix} \delta_{11} & \delta_{12} & \delta_{13} \\ \delta_{21} & \delta_{22} & \delta_{23} \\ \delta_{31} & \delta_{32} & \delta_{33} \end{bmatrix} = \begin{bmatrix} 1 & 0 & 0 \\ 0 & 1 & 0 \\ 0 & 0 & 1 \end{bmatrix}. \quad (7)$$

Since $\delta_{ij} = 1$ ($i = j$) or $\delta_{ij} = 0$ ($i \neq j$).

2.2. Orthonormalized Basis Elements

By appropriate use of δ_{ij} , elements of the orthonormal tensor basis can be constructed. Symmetry in crystal means simply invariance of the properties with respect to the transforms of some subgroup of the orthogonal group, whereas the properties of an isotropic medium are invariant with respect to all the transforms of the orthogonal group. In other words, it explains the form of C_{ijkl} tensor for any isotropic medium and it is invariant with respect to the all transforms of the orthogonal group. However there is a unique tensor that is not affected by all orthogonal transforms, it is a unique tensor, apart from a scalar factor, so C_{ijkl} can be expressed as combinations of the components δ_{ij} of that tensor with certain coefficients. There are only three different such combinations which contain four subscripts i, j, k, l namely $\delta_{ij}\delta_{kl}$, $\delta_{ik}\delta_{jl}$, $\delta_{il}\delta_{jk}$. Because of the symmetry of C_{ijkl} , i and j are permuted. So the elements takes the new form; $\delta_{ij}\delta_{kl}$ and $\delta_{ik}\delta_{jl} + \delta_{il}\delta_{jk}$. For other symmetry types, these elements are used in a suitable form, when constructing orthonormalized basis. Form-invariant expression of isotropic symmetry is formed by the following two basis elements:

$$\delta_{ij}\delta_{kl}, \quad \delta_{ik}\delta_{jl} + \delta_{il}\delta_{jk} \quad (8)$$

So, the decomposition of C_{ijkl} for triclinic system with no elastic symmetries is given in terms of its orthonormalized basis elements as

$$C_{ijkl} = \sum_K (C, A_{ijkl}^K) A_{ijkl}^K, \quad (K = I \dots XXI), \quad (9)$$

Where (C, A_{ijkl}^K) represents the inner product of C_{ijkl} and K^{th} elements, A_{ijkl}^K , the orthonormalized basis elements and given for each elastic symmetry types, besides, the inner products for triclinic symmetry are obtained as

$$\begin{aligned} (C, A_{ijkl}^I) &= \frac{1}{3}[(C_{11} + C_{22} + C_{33}) + 2(C_{12} + C_{13} + C_{23})], \\ (C, A_{ijkl}^{II}) &= \frac{1}{3\sqrt{5}}[2(C_{11} + C_{22} + C_{33}) + 6(C_{44} + C_{55} + C_{66}) - 2(C_{12} + C_{13} + C_{23})], \\ (C, A_{ijkl}^{III}) &= \frac{1}{\sqrt{6}}[3C_{33} - (C_{11} + C_{22} + C_{33})], \\ (C, A_{ijkl}^{IV}) &= \frac{1}{\sqrt{3}}[3C_{13} + 3C_{23} - 2(C_{12} + C_{13} + C_{23})], \\ (C, A_{ijkl}^V) &= \frac{1}{\sqrt{30}}[-2(C_{11} + C_{22} + C_{33}) + 4(C_{44} + C_{55} + C_{66}) + 2(C_{12} + C_{13} + C_{23})], \\ (C, A_{ijkl}^{VI}) &= \sqrt{\frac{2}{3}}[C_{44} + C_{55} - 2C_{66}], \quad (C, A_{ijkl}^{VII}) = \sqrt{\frac{1}{2}}[C_{11} - C_{22}], \\ (C, A_{ijkl}^{VIII}) &= [C_{13} - C_{23}], \quad (C, A_{ijkl}^{IX}) = \sqrt{2}[C_{44} - C_{55}], \\ (C, A_{ijkl}^{X}) &= 2\sqrt{2}C_{46}, \quad (C, A_{ijkl}^{XI}) = 2C_{35}, \\ (C, A_{ijkl}^{XII}) &= 2C_{15}, \quad (C, A_{ijkl}^{XIII}) = 2C_{25}, \\ (C, A_{ijkl}^{XIV}) &= 2\sqrt{2}C_{45}, \quad (C, A_{ijkl}^{XV}) = 2C_{16}, \\ (C, A_{ijkl}^{XVI}) &= 2C_{26}, \quad (C, A_{ijkl}^{XVII}) = 2C_{36}, \quad (C, A_{ijkl}^{XVIII}) = 2\sqrt{2}C_{56}, \\ (C, A_{ijkl}^{XIX}) &= 2C_{24}, \quad (C, A_{ijkl}^{XX}) = 2C_{34}, \quad (C, A_{ijkl}^{XXI}) = 2C_{14}. \quad (10) \end{aligned}$$

3. NUMERICAL ANALYSIS

The elastic coefficients in GPa for SiC_p/2124 Al Composite with SiC volume 10% are given [Jung, et al., 1999].

$$C_{ij} = \begin{bmatrix} 12938 & 6405 & 6434 & 0 & 0 & 0 \\ 6405 & 12938 & 6434 & 0 & 0 & 0 \\ 6434 & 6434 & 13295 & 0 & 0 & 0 \\ 0 & 0 & 0 & 3438 & 0 & 0 \\ 0 & 0 & 0 & 0 & 3438 & 0 \\ 0 & 0 & 0 & 0 & 0 & 3267 \end{bmatrix} \quad (11)$$

By employing the formula for transversely isotropic symmetry given in (10), inner products are calculated as

$$\begin{aligned} (C, A^I) &= 259.06, (C, A^{II}) = 150.04, (C, A^{III}) = 2.08, \\ (C, A^{IV}) &= 1.53, (C, A^V) = 3.43, \quad (12) \end{aligned}$$

The elastic constant tensor for the material can be represented in the form

$$C_{ijkl} = 259.06 A_{ijkl}^I + 150.04 A_{ijkl}^{II} + 2.08 A_{ijkl}^{III} + 1.53 A_{ijkl}^{IV} + 3.43 A_{ijkl}^V \quad (13)$$

From (13), isotropic and transversely isotropic of the material are constructed as

$$I = 259.06 A_{ijkl}^I + 150.04 A_{ijkl}^{II} \quad (14)$$

$$TI = 2.08 A_{ijkl}^{III} + 1.53 A_{ijkl}^{IV} + 3.43 A_{ijkl}^V \quad (15)$$

By adding (14) and (15) elastic constant tensor of the composite in matrix form can be denoted as

$$C_{ij} = \begin{bmatrix} 131.086 & 639853 & 639853 & 0 & 0 & 0 \\ 639853 & 131086 & 639853 & 0 & 0 & 0 \\ 639853 & 639853 & 131086 & 0 & 0 & 0 \\ 0 & 0 & 0 & 335503 & 0 & 0 \\ 0 & 0 & 0 & 0 & 335503 & 0 \\ 0 & 0 & 0 & 0 & 0 & 335503 \end{bmatrix} + \begin{bmatrix} -1.706 & 0.0647 & 0.3547 & 0 & 0 & 0 \\ 0.0647 & -1.706 & 0.3547 & 0 & 0 & 0 \\ 0.3547 & 0.3547 & 1.864 & 0 & 0 & 0 \\ 0 & 0 & 0 & 0.8297 & 0 & 0 \\ 0 & 0 & 0 & 0 & 0.8297 & 0 \\ 0 & 0 & 0 & 0 & 0 & -0.8853 \end{bmatrix} \quad (16)$$

4. NORM CONCEPT AND ANISOTROPY DEGREE

Norm is an invariant of the material. Euclidean norm is used for computations as a measure in this work. Comparison of magnitudes of the Euclidean norm gives valuable information about the origin of the physical property under examination. Euclidean norm of a Cartesian tensor is defined as

$$N = \|C\| = \{C_{ijkl} \dots C_{ijkl} \dots\}^{\frac{1}{2}} \quad (17)$$

Since the basis constructed here is orthonormal and $C_{ijkl} \dots$ is in the space spanned by that orthonormal basis $\{A^K\}$, it is straightforward to see that, now the norm

$$N = \|C\| = \{\sum_K (C_{ijkl} A_{ijkl}^K)^2\}^{\frac{1}{2}} \quad (18)$$

The norm of nearest isotropic tensor, denoted by C_{ijkl}^o , of C_{ijkl} is therefore

$$N_i = \|C^o\| = \{\sum_{K=I} (C_{ijkl}^K)^2\}^{\frac{1}{2}}, (K = I, II) \quad (19)$$

In similar way, with respect to the tensor C_{ijkl} , the nearest tensors of other symmetry classes within the class spanned by the basis $\{A^K\}$ can be read off from the representation and their norms may be computed according to (18).

By using the norms, the nearest isotropic tensors of lower symmetries can be found via the following formula

$$\varepsilon^o = \frac{\|C\| - \|C^o\|}{\|C\|} \quad (20)$$

Where ε^o is a scalar constant independent of the rotation of the axes. It is a measure of 'nearness' of the nearest isotropic tensor. It is obvious that the anisotropy of the material, for instance, the symmetry group of the material and the anisotropy of the measured property depicted in the same materials may be quite different. For instance, a property which is measured in a material can almost be isotropic but the material symmetry group itself may have very few symmetry elements. For lower symmetric materials, the elastic constant tensor has parts; isotropic and anisotropic. Norm ratios for these parts are demonstrated as N_i/N and N_a/N respectively. Although the norm ratios of different parts represent the anisotropy of that particular part, they can also be used to assess and compare the anisotropy degree of a material property as a whole.

Table 2: Elastic constant data of SiC_p/2124 Al Composites from transversely isotropic symmetry [Jung, et. al, 1999]

SiC Vol. %	Elastic-Stiffness Constants C _{ij} (GPa) for transversely isotropic symmetry				
	C ₁₁	C ₁₂	C ₂₃	C ₃₃	C ₄₄
20%	145.86	68.06	66.42	151.06	40.66
30%	169.30	71.52	69.09	175.42	51.29

Table 3: Elastic constant data of SiC_p/2124 Al Composites from orthorhombic symmetry [Jung, et. al, 1999]

SiC Vol %	Elastic-Stiffness Constants C _{ij} (GPa) for orthorhombic symmetry								
	C ₁₁	C ₁₂	C ₁₃	C ₂₂	C ₂₃	C ₃₃	C ₄₄	C ₅₅	C ₆₆
20 %	139.9	64.49	58.4	141.9	62.08	146.19	40.66	41.01	38.82
30 %	167.6	70.79	67.25	168.09	68.89	175.63	51.39	51.4	48.75

Table 4: The norm and norm ratios

SiC Vol. %	N _i	N _a	N	N _i /N	N _a /N	ε°
20% for O	297.69	7.68	297.95	0.999	0.026	0.0009
30% for O	351.09	7.54	351.30	0.999	0.021	0.0006
20% for T	311.46	4.89	311.61	0.999	0.016	0.0005
30% for T	353.50	6.07	353.66	0.999	0.017	0.0005

T: Transversely Isotropic, O: Orthorhombic

From Table 4, norm ratios for isotropic parts are the same. So it is useful to compare the norm ratios for the anisotropic parts. According to calculated results, the most anisotropic property exhibited by the SiC_p/2124 Al composites from orthorhombic symmetry with SiC Vol. 20%. Since the larger value of N_a/N is the one for this material. While same material from transversely isotropic symmetry with same SiC Vol. is the most isotropic with the lowest value of N_a/N.

5. RESULTS AND CONCLUSION

The decomposition method presented can also be carried out for porous and powder materials possessing other symmetry classes such as isotropic, cubic, tetragonal, trigonal and triclinic.

It also has more significant effects on many applications in following fields such as:

1) Calculation of norm and norm ratios for assessing and comparing the anisotropic properties of porous and powder materials.

2) Examining the material symmetry types in detail,

3) Observing a material which possesses a particular symmetry type can be explained in another anisotropic symmetry.

4) Determination of materials possessing same crystal symmetry type which are highly anisotropic or close to isotropy,

5) Understanding the mechanical and elastic behavior of porous and powder materials.

REFERENCES

- Nye, J. F., 1964. Physical Properties of Crystals, Their Representation by Tensors and Matrices, Oxford University Press, pp.131.
- Gazis, D. C., Tadjbakhsh and Toupin R.A., 1963. The elastic tensor of given symmetry nearest to an anisotropic elastic tensor, Acta Cryst., vol. 16, pp. 917-922.
- Yih-O Tu, 1968. The decomposition of an anisotropic elastic tensor, Acta Cryst., A24, pp. 273-282.
- Srinivasan, T. P., Nigam, S. D., 1969. Invariant elastic constants for crystals, Journal of Mathematics and Mechanics, vol. 19, pp. 411-420.
- Jung, H.K., Cheong, Y.M., Ryu, H.J. and Hong, S.H., 1999. Analysis of anisotropy in elastic constants of SiC_p/2124 Al metal matrix composites, Scripta Materialia, Vol. 41, No.12, pp.1261-1267.

DISCRETE ELEMENT MODELING OF SPHERICAL COPPER POWDER COMPACTION PROCESS

Faruk GÜNER^{1,a}, Ömer Necati CORA² and Hasan SOFUOĞLU²

1. Bayburt University, Department of Mechanical Engineering, Bayburt, Turkey

2. Karadeniz Technical University, Department of Mechanical Engineering, Trabzon, Turkey

a. *Corresponding author* (fguner@bayburt.edu.tr)

ABSTRACT: Three main approaches are available in literature to numerically analyze the powder compaction process. Those are 1) Continuum media approach, 2) Micromechanics approach, 3) Discrete element method (DEM). Current study aimed for understanding deformation and tribological behavior of spherical copper powder in cold compaction process by using DEM. Prior to finite element modeling, powders 200 micron in diameter were randomly distributed into a die cavity for resembling the actual process. Each powder was then modeled individually as deformable body with 3-D tetragonal elements. Different material models including von Mises, Cam-Clay, Shima-Oyane, and Mohr-Coulomb models were utilized for comparison purposes. The results showed that material models made important changes on the flow behavior of the copper powder.

1. INTRODUCTION

The flow behavior of powder in cold compression has been studied by many researchers. In recent decades three main approaches, namely; continuum media approach, micromechanics approach and discrete element method, have been developed to numerically analyze powder compaction process. In the first one, powders were considered as continuous isotropic medium disregarding the contact interactions between individual powders while the second approach offer a systematic and rigorous work to describe the behavior of porous materials, however; both of their predictive capability can be limited. A metal powder compaction process has been successfully analyzed to determine residual stresses by continuum approach. [Jonsén and Häggblad, 2005].

In the micromechanical approach in which granular materials modeled as an assembly of interacting particles, analysis focuses on one particular powder and it then incorporates the discrete nature of granular materials. Researchers developed both impressive problems and results on

induction from micro to macro scale. For example, coordination numbers of Young's and bulk moduli of powder needed to be determined to adapt the values obtained from micro to macroscale [Kruyt et al., 2009].

Discrete element method (DEM) uses finite element procedure to determine stress-strain relations of each particle and their mathematical relations were given in the literature [Chung and Oui, 2011]. Cylindrical tablet compaction process has been studied with commercial finite element analysis software, discovering DEM as an efficient method to simulate these types of processes [Frenning, 2008]. High density compaction can also be simulated by this approach [Jerier et al, 2010]. DEM was also applied to various kind of material as shown in the compaction behavior of aggregated ceramic powders [Martin and Bouvard, 2006]. In their study, the specific contact bond forces between primary particles were investigated using DEM. Friction, material and geometrical features were the other parameters to simulate

the process. The most of the above mentioned studies defined all particles as a solid continuum body by either gluing particles to each other or defining contact zones for particles which can become contact during compaction. The objective of this study was, therefore, to determine deformation and tribological characteristics of spherical powder compaction process that takes place at room temperature condition by using DEM. In DEM, each powder was modeled individually as deformable body with 3-D elements. After 3D modeling of the process was created, the model was then exported to the DEM to identify the effects of different material models including von Mises, Cam-Clay, and Shima-Oyane, Mohr-Coulomb model on the deformation and tribological characteristics of spherical powder compaction process.

2. MODEL DESCRIPTION

Simulating and analyzing the process in 3D makes it more complex and requires more sensitivity. In this study, the powders were filled into die randomly in order to have more realistic simulation for the actual powder compaction process so that powders can freely rotate or move to another position. In random filling, the powders were filled into the die with gravitational effect. The geometrical shape of model used in this study was taken from the experimental cold compaction study of spherical copper powders performed by [Cora et al., 2009] and shown in Figure 1. Copper powders of 200 micron in diameter were randomly distributed into a die cavity in order to accomplish 3D modeling of the powder compaction process. After creating 3-D solid model, the meshing procedure was performed by MSC Patran 2012 software.

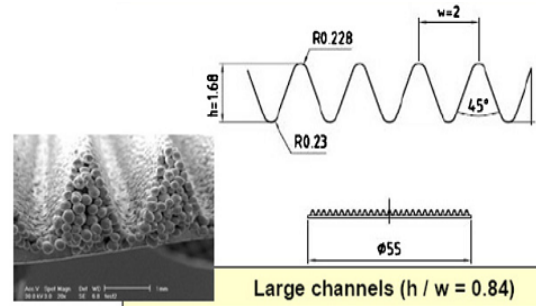


Figure 1: Geometrical shape of model [Cora et al., 2009]

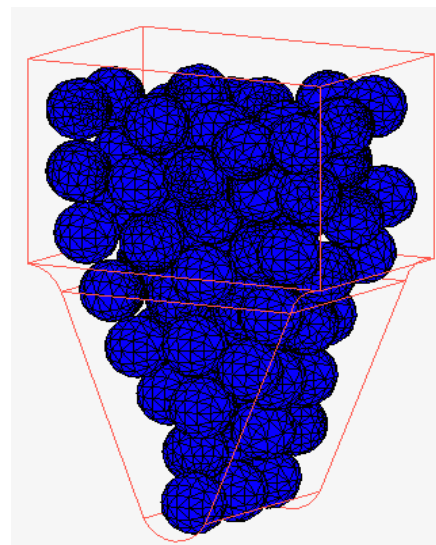


Figure 2: 3-D model of powder compaction process

The final model was contained 74 elastic-plastic isotropic discrete deformable bodies (powders) with 60076 3-D tetrahedral elements using 15255 nodes and illustrated in Figure 2. This meshed 3-D model was then exported to MSC Marc Mentat software to carry out the finite element analysis of the cold powder compaction process.

The convergence check was performed by the residual or displacement testing option. In the first option, the largest residual force divided by the maximum reaction force where the division has to be smaller than tolerance of 0.1. In the displacement testing method,

convergence is satisfied if the maximum displacement of the last iteration is small compared to the actual displacement change of the increment as described in Marc 2012 Volume A: Theory and User Information Guide. Full Newton-Raphson iterative procedure was used in this implicit analysis. Coulomb bilinear (displacement) friction model was assumed at the interfaces with a friction coefficient of 0.1. This coefficient of friction represents the friction at the interfaces of both the die wall-powder and powder-powder.

Material model was one of the main challenges of this study. Four different material models were used to determine the stresses on the powders. These are von Mises, Cam-Clay, Mohr-Coulomb and Shima Oyane material models. Power law was used to characterize the stress-strain behavior of the powder through von-Mises material model. Although Cam-clay model basically defined for soil materials, there are successful uses of this model for metal powders. It is very simple to define the yield locus of powder with Mohr-Coulomb model known also as Drucker-Prager model while Shima-Oyane model is especially constructed for copper powders. Table 1 shows the constitutive equations for these models and σ_y , is the yield stress, ε_o , initial yield strain, $\bar{\varepsilon}$, equivalent strain, $\dot{\bar{\varepsilon}}$, equivalent strain rate, p , hydrostatic stress, q , deviatoric stress, p_c , preconsolidation pressure, M slope of critical state line, $A, B, m, n, \alpha, \gamma, c$, and β are defined to be material constants.

Table 1: Constitutive Equations for each material model

Material Model	Constitutive Equation
Von-Mises	$\sigma_y = A(\varepsilon_o + \bar{\varepsilon})^m + B\dot{\bar{\varepsilon}}^n$
Modified Cam-Clay, [Callari,	$f(\sigma, p_c) = \left(\frac{q^2}{M^2} \right) + p(p - p_c) = 0$

1998]	
Mohr-Coulomb, [K hoi, 2010]	$q + p \tan(\beta) + c = 0$
Shima-Oyane, [Shima-Oyane, 1976]	$\Phi = \left(\frac{q}{\sigma_Y} \right)^2 + \alpha (1-D)^\gamma \left(\frac{p}{\sigma_Y} \right)^2 - D^m$

3. DEM ANALYSIS AND RESULTS

MSC Marc (v 2012.1.0), commercial finite element analysis software was used in this study. First DEM analysis has performed with von-Mises material model. Material parameters used in this analysis were taken as $E=110000 \text{ N/mm}^2$, $\nu=0.35$, $A=451.6 \text{ N/mm}^2$ and $m=0.328$. [Altan et al., 1983]

The analysis was taken 184760 seconds with Intel CPU I5 2.27 GHz CPU. After 30 powders were reached over % 25 strain changes, the model was then remeshed. Model was contained 60565 tetrahedral elements at the end of the analysis. The maximum equivalent von-Mises stress was 407 N/mm^2 and its distribution using von-Mises material model through the model was shown in Figure 3. Young's modulus was required to be calculated according to relative density in Cam-Clay material model. Equation 1, defines Young's modulus for porous materials. [Lewis et al., 2005]. The initial material constants for spherical copper powder was taken as $b=5.56$, $c=4.49$ and $\phi=0.6$. Young's modulus was calculated to be 1150 N/mm^2 utilizing the following equation.

$$E = E_0 \exp \left[- (b\phi + c\phi^2) \right] \quad (1)$$

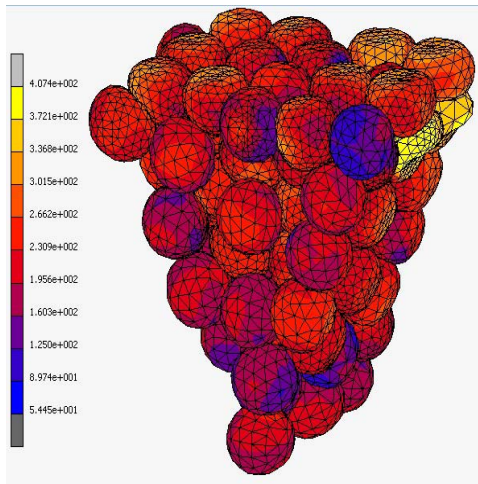


Figure 3: Equivalent von-Mises stress obtained utilizing von-Mises model.

In Cam-Clay material model, virgin compression ratio, $\lambda=0.166$ and recompression ratio, $k=0.022$, was taken from the experimental study of Martinet al. [Martin et al., 2004]. While the slope of critical state, M , has taken to be 1.1512 [Park, 2007]. Remeshing was carried out in the analysis and 13 bodies wereremeshed to cause 911 elements increasing in the model. In Cam-Clay material model, the maximum equivalent von-Mises stress was calculated to be 388 N/mm^2 and Figure 4 shows its distribution through the model.

The internal friction angle, β , that depends on relative density, needed for Mohr-Coulomb material model was taken as $\beta=25.6^\circ$ [Vyal and Laptev, 2002]. Another parameter that must be defined in Mohr-Coulomb material model is the yield stress value.

Although there were several values for copper given in the literature, 58.86 N/mm^2 given by Shima and Oyane [Shima and Oyane, 1976] in their model was selected. The maximum equivalent von-Mises stress was obtained as 196 N/mm^2 in Mohr-Coulomb material model and Figure 5 displays its distribution through the model.

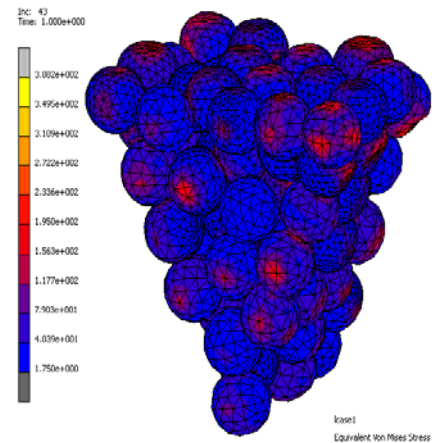


Figure 4: Equivalent von-Mises stress obtained utilizing Cam-Clay model.

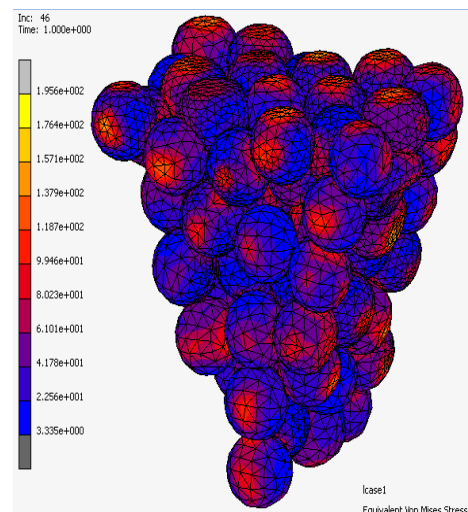


Figure 5: Equivalent von-Mises stress obtained utilizing Mohr-Coulomb model

Shima-Oyane material model used for the analysis is more complex than the others due to its empirical establishment. These material parameters, α, γ, m and the yield stress σ_y , were taken from the original study of Shima-Oyane [Shima and Oyane, 1976] as $\alpha=6.25, \gamma=1.028, m=2.5, \sigma_y=58.86 \text{ N/mm}^2$. Utilizing these parameters and definition of Marc Mentat software, viscosity, μ , was calculated to be 130.8 N.s/mm^2 . Also, Poisson ratio, ν , was determined as 0.13 depending on relative density [Alves et al., 2006]. The maximum equivalent von-Mises stress was 247 N/mm^2 and its distribution for

Shima-Oyane material model was illustrated in Figure 6.

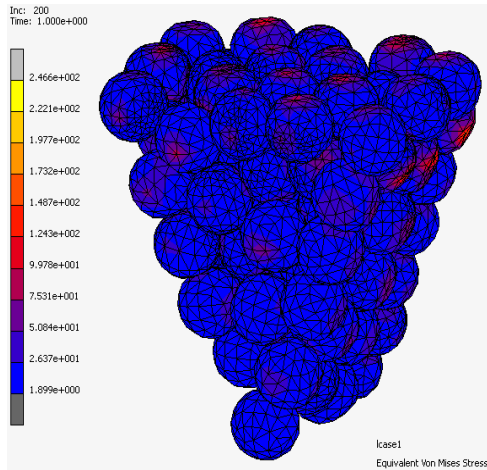


Figure 6: Equivalent von-Mises stress obtained utilizing Shima-Oyane model

4. CONCLUSION

In recent study, DEM used to analyze 3-D cold powder die compaction process. Stresses occurred on copper powders due to different types of material models were investigated. It was found out that three-dimensional discrete element analysis was more confident than two or three-dimensional continuum in simulating 3-D cold powder dies compaction process and flow behavior of powder. It was also determined that the stress values obtained in different material models were distinct.

REFERENCES

Altan, T., Oh, S. and Gegel, H., 1983, Metal Forming Fundamentals and App., ASM
 Alves, L.; Martins, P. and Rodrigues J., 2006, A New Yield Function For Porous Materials, J.ofMat. Pro. Tech., 179,36
 Callari, C., Auricchio, F. and Sacco, E., 1998, A Finite-Strain Cam-Clay Model in the Framework of Multiplicative Elasto-Plast., Int.J. of Plas., Vol.14 No.12, pp. 1155
 Chung, Y.C. and Ooi, J.Y.; 2011, Linking of Discrete Element Model with F.E.A. for Analysing Structures in Contact with Particulate Solids, Powder. Tech., 217,107
 Cora, O.N., Usta, Y. and Koc, M., 2009, Micro-Manufacturing of Micro-Scale Porous Surface Structures for Enhanced Heat Transfer Application: An Experimental

Process Optimization Study, J.ofMicromechanicsMicroeng., 19 045011
 Frenning, G., 2008, An Efficient Finite/Discrete Element Procedure for Simulating Compression of 3D Particle Assemblies, Comp. Meth. App. Mech. Eng. 197, 4266
 Jerier, J., Richefeu, V., Imbault, D. and Donze, F., 2010, Packing Spherical Discrete Element for Large Scale Simulation, Comp.Meth.App.Mech.Eng, 199,1668
 Jonsén, P. and Häggblad, H.-A., 2005, Modelling and Numerical Investigation of The Residual Stress Strain in a Green Metal Powder Body, Powder Tech., 155, 196
 Khoei, A., 2010, Computational Plasticity in Powder Forming Processes, Elsevier
 Kruyt, N., Agnolin, I., Luding, S. and Rothenburg, L., 2009, Micromechanical Study of Elastic Moduli of Loose Granular Materials, J. Mech. Physic of Sol., 58,1286
 Lewis, R., Gethin, D., Yang, S. and Rowe, R., 2005, A Combined Finite-Discrete Element Method Simulating Pharmaceutical Powder Tableting, Int.J.Num.Met.Eng., 62,853
 Martin, C. and Bouvard, D., 2006, Discrete Element Simulation of the Compression of Aggregated Ceramic Powders, The American Ceramic Society, 89,3379
 Martin, C.L., 2004, Elasticity, Fracture and Yielding of Cold Compression Metal Powder, J.Mech. and Phy.of Sol., 52,1691
 Park, J., 2007, A Yield Function for Copper Powders in Compression, J. of Mat. Pro. Tech., 187, 672
 Shima, S. and Oyane, M.; 1976, Plasticity Theory for Porous Met., Int. J. of Mec. Sc., 18, 285
 Vyal, E.Y. and Laptev, A.M., 2002, Strength of Unsintered Powder Compression with Axial and Radial Loading, Powder Metal & Powder Ceramic, 41, 5

KINETIC MONTECARLO SIMULATION OF SEMICONDUCTOR HETEROEPITAXY ON FEATURED SUBSTRATES

Hassan KASSEM^{1,a}

1. Lebanese University, Fac. of engineering, Al Hadat, Lebanon

a. Corresponding Author (*has_kas@hotmail.com*)

ABSTRACT: We investigate by a Kinetic Monte Carlo simulation the intermixing mechanisms during the growth of mismatched thin films on featured substrates. The Monte Carlo scheme is associated with an elastic energy term based on the valence force field approximation which is used to describe the strain effect on the lattice mismatched film. The stress is relaxed along “atomic chain” at each step of the simulation. It has been shown that using featured substrates enhance the interdiffusion due to the presence of the step boundaries. The effect of various experimental conditions: growth temperature, growth rate and the characteristics of deposited film: lattice mismatch, force constants, chemical binding energy on the intermixing are reported.

1. INTRODUCTION

Heteroepitaxial growth of lattice mismatched materials has been extensively studied for many years, both on theoretical and experimental grounds. Imperfect substrates can be the origin of the nucleation of defects^{1,2,28} and the enhancement of intermixing. Intermixing generally modifies electronic and optical properties of materials. It may reduce the quality of the devices by the introduction of impurity levels inside the band gap. But it can also contribute to improve the quality of the devices. Indeed, intermixing relaxes the deposited layers and prevents, in some cases, the formation of extended dislocations, which generate new sources of device degradation. Therefore controlling intermixing is very crucial for the proper design of the devices.

In the case of optical properties of heteroepitaxial films, intermixing smoothes the variations of the total misfit between the substrate and the

deposited layer, and changes the chemical composition of this layer. So modification of the optoelectronic characteristics of the devices can be observed by the variation of the band structure, bands offsets and the confinement potentials³.

Generally, interdiffusion is seen during high temperature annealing processes and is assisted by defects like vacancies and interstitials. At low temperature the interdiffusion is of course reduced, but still substantial intermixing can be observed as a result of surface segregation driven by surface energy and strain energy considerations^{4–6}.

It has been reported in the literature that surface kinetics may also play an important role in the intermixing mechanism⁴ which, in turn, may affect the kinetics. In particular, stress variations resulting from intermixing of materials during growth can produce morphological changes^{7,8} related, for example, to island sizes and their statistical distributions.

In the case of Ge/Si quantum dots,

the question of intermixing is important. Earlier experiments show an abrupt Ge/Si interface 6,10,12,13,16. Investigations on Ge island characteristics as a function of experimental conditions have shown that inhibiting stress relaxation due to intermixing may favour uniform size distribution 7–9,17 which is the primary factor for obtaining high performance devices.

In this paper, we propose to study the interdiffusion in the case of featured substrate presenting a mesa on the total substrate by using the Kinetic Monte Carlo technique. Section 2 is dedicated to the description of the model and the results are reported in section 3. The effect of different experimental conditions such as growth temperature, growth rate, and lattice mismatch, chemical binding energies, and bending force constants are investigated.

2. MODEL

The general simulation technique has been explained in detail previously¹. A Kinetic Monte Carlo (KMC) process has been associated to a Valence Force Field (VFF) energetic model to investigate the kinetics of the surface evolution and to describe strain effects, coming from the different nature of the deposited film and the substrate. The model is founded on a set of elementary atomic mechanisms. Their choice represents the key points for a KMC simulation to describe the correct behavior of the film growth. Briefly, our KMC simulation proceeds as follows. When an event has occurred, local strain and stress are changed, by minimizing the strain energy calculated using the VFF potential. Activation energy and hopping rate for each possible event on the surface are then determined. The activation energies are reduced, with respect to the

number of broken bonds, by the amount of strain energy relaxed during the corresponding event, accelerating atomic moves in the more strained regions. Next, a time is attributed to each possible event, using the Arrhenius law and the Poisson's probability distribution, to account for their random nature. The event having the lowest time is executed and a new cycle can begin.

The simulation is founded on a set of events classified in three main categories:

1. Classical events used in most MC simulations: deposition, evaporation and surface migration. Deposition of an atom is defined randomly on an empty site on the surface. Evaporation is defined by removing this atom from the surface. The migration of atoms on the surface is considered along atomic chains which correspond to site lines with high mobility.

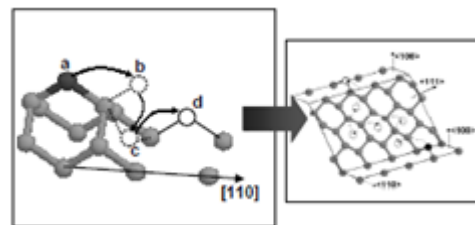


Figure 1: Interlayer migration through two steps: a; initial position, b; cristal side, c; interstitial position and d; final position of the atom. Interstitial-interstitial migration, temperature

2. Interlayer migrations via interstitial positions are the origin of surface roughening and defect creation¹⁸. In compound semiconductors, interlayer migrations are almost over two atomic steps in order to avoid antisite defects. In our simulation, we have decomposed the double step interlayer migrations by introducing an intermediate state where the atom sits in a lattice interstitial

position. Figure 1 presents this interlayer migration over two atomic steps. The mechanism is done by breaking only one bond along the diffusion way of atom in occupying interstitial position. Let us consider an atom in position (a) at the edge of a step. The classical migration is done from position (a) to position (b) by breaking one bond. But the atom can't be fixed because it has only one bond with the film. So the atom falls in position (c) which is an interstitial position where the atom establishes two bonds with its neighborhood atoms. This position is very stressed because the angles between the atomic bonds are very different from those of perfect crystal. So this atom moves quickly to position (d). The atoms can, of course, effectuate the reversed way. Moreover, we have previously shown that such atoms with high local strain can rapidly move around facets, from interstitial to interstitial positions, to stabilize quite far from their initial positions.

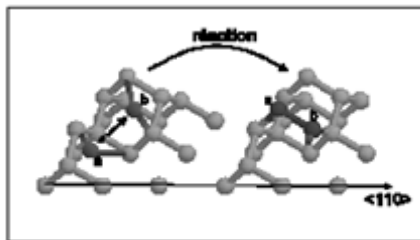


Figure 2: Interlayer migration through two steps: a; initial position, b; cristal side, c; interstitial position and d; final position of the atom. Interstitial-interstitial migration, temperature

3. The third concept concerns the interaction between atoms in interstitial positions. The interactions follow from the high mobility and the availability of single atoms in interstitial positions. Along its migration path (fig. 2), the interstitial atom may come close enough to another atom in the same situation. In this case, the two atoms may form one bond

between them and another bond with the atoms in the deposited layer. This reaction will bring both atoms in normal substitution positions. The result is the introduction of atoms in hanging positions with only one bond directed toward the surface and a second bond with the atom in an upper layer. The importance of this atomic position is the observation of defects like vacancies or dislocations.

When an event is produced, the structure needs to be relaxed by minimizing its total energy. This energy is based on the classical concept of chemical bond breaking to which we have added a strain energy¹⁹. The strain energy is evaluated using the empirical Valence Force Field (VFF) approximation²⁰ for the bond length variations and using a simplified Stillinger Weber type potential²¹ for the bond angle deformations.

$$E_{\text{strain}} = \sum \text{bonds } k_r (\tau - r_0)^2 + \sum \text{angles } k_\theta (\theta - \theta_0)^2$$

Where k_r and k_θ are respectively the stretching and bending force parameters related to the elastic constants of the materials. r_0 is the perfect crystal bond length, Δr is the bond length variation, and θ is the angle between two adjacent bonds. The important difference between k_r and k_θ values in semiconductor materials (k_r is usually 20-50 times larger than k_θ) and the greater difficulty to distort bonds than angles, lead us to the approximation that surface bond lengths are close to those of the substrate and film, while the bond angle variations may be large and, are defined by minimizing bending term¹. Developing the energy in a second order power series of atomic displacements is another approximation which allows the energy minimization to be achieved

in a single step, using a Newton-Raphson algorithm, saving computer time. The VFF approximation presents several advantages:

- (i) it is well adapted to non compact semiconductor structures,
- (ii) it is simple enough to allow the execution of multi-million minimization needed to simulate the growth,
- (iii) an activation energy depending on the local strain can be easily defined.

The above model have been successfully applied to the heteroepitaxial growth of semiconductors to show the roughening and faceting of the growing layer²², to propose a new mechanism of interface dislocation formation^{1,2} and to describe the tendency to island formation with increasing lattice mismatch²³.

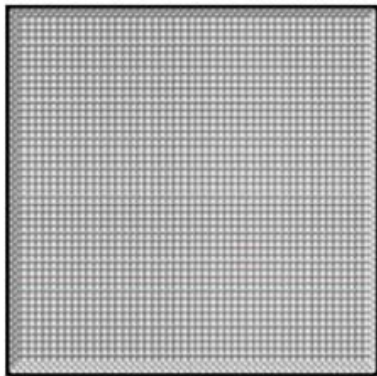


Figure 3: View of the featured sunstrate presenting complete rectangular four atomic layer mesa with steps boundaries having facets (some figure obtained if we present the view of he substrate atoms diffused into the deposited film at 600 K if deposited atoms are not presented in this picture.

3.RESULTS AND DISCUSSION

Simulations have been performed to deposit four atomic layers on a 50x50 atoms (001) oriented substrates. Zincblende structures are assumed for both the substrate and the deposited film and periodic boundary conditions

are applied on both lateral directions. Non perfect substrate is represented by a complete rectangular four atomic layer mesa with steps boundaries having $\{111\}$ facets (fig. 3). The following values of the parameters have been used to reproduce experimental conditions. The lattice mismatch is taken as 8%, which is the case in highly mismatched III-V heterostructures, like GaSb/GaAs ...

The growth temperature is set to 700K and the growth rate is 2 ML/s. In order to avoid statistical fluctuations, the results presented in the following are averaged over seven different simulations using different sets of random numbers. The parameters of the energy model correspond to that of GaAs and similar materials. In particular, the chemical bonding is assumed to result from first neighbor interactions with a magnitude of 1.6 eV/bond. An angular force parameter of 1.1 eV has also been used in the simulations. The same values of energy parameters have been used for the substrate and for the deposited film, to avoid parameter multiplication. Further, sequential variations of the individual parameters have been considered to illustrate their effect on the global intermixing.

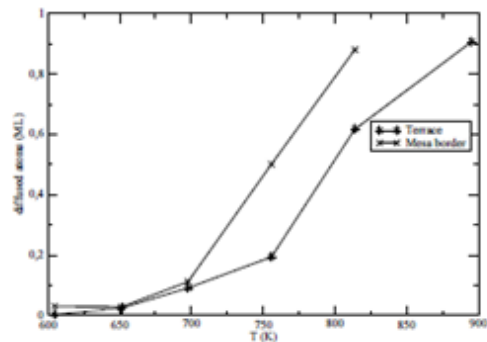


Figure 4: The number of substrate atoms, in monolayer, diffused in the film as a function of deposition temperature.

Figure 4 shows the number of substrate atoms, expressed as monolayer fraction, which have diffused from the substrate

into the deposited film, as a function of temperature. The two curves in figures 4 represent the number of diffusing atoms from the flat terrace region and from the border of the mesa with $\{111\}$ faceted steps. We observe that intermixing is largely increased by the temperature. Indeed, when the temperature increases, vacancies are created within the substrate with the film substrate becoming rough. As a result of the presence of vacancies, atoms from deep layers of the substrate migrate towards the deposited film. At 800K, three atomic layers in the middle of the substrate are involved while at 900K, more than four substrate layers participate to the intermixing. To note that at the border of the mesa, four layers from the mesa and four underneath layers from the base substrate participate to the interdiffusion.

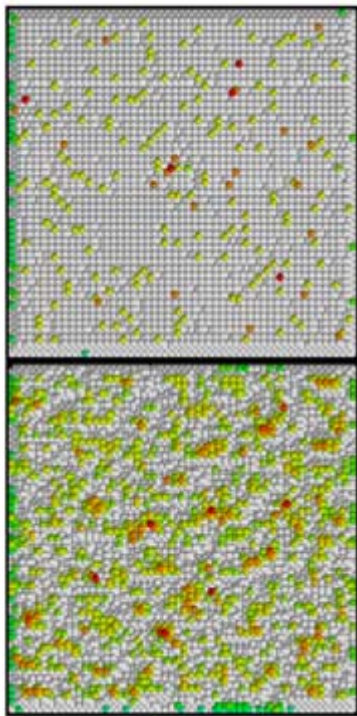


Figure 5: View of the substrate atoms diffused into the deposited film at 700K (first figure) and 900K (second figure). Deposited atoms are not represented in this picture.

We see clearly that in figures 3 and 5 in which we present the substrate atoms in the deposited film, at different temperatures. At 600K, no atom has diffused in the film and substrate atoms remains at their initial position (figure 3). We should mention that we have deposited four atomic layers on the substrate. These atoms are not visible in the figure since deposited atoms are not shown in the figure for sake of clarity. At 700K (first), few diffused substrate atoms are seen in the film. Deposited atoms which have diffused in the substrate (not shown in the figure) are the vacancies appearing in the substrate. At 900K (second figure 5), the interface becomes completely rough, containing a large amount of vacancies and also atoms coming from the deposited film. We see that interdiffusion on the featured substrate is increased with respect to perfect substrate (figure 4). This follows directly from the large strain present at the boundaries of mesa. This large strain has been previously shown to enhance the creation of dislocation in heteroepitaxial growth². Comparing the rate of interdiffusion on flat terraces to that at the mesa borders presenting steps with $\{111\}$ facets, an increase of more than 0.3 monolayer is observed at high temperature. At low temperatures, the enhancement is very small since the strain energy is difficult to overcome. We should mention that atoms on the $\{111\}$ facets do not participate to the interdiffusion (clearly seen in figures 5), as a result of the high stability of these facets. Due to the high mobility of atoms on these facets, they offer an efficient path for the intermixing of atoms between the substrate and the deposited film. We see clearly in figure 6 that the deposited film and diffused substrate atoms tend to fill the valley between these facets.

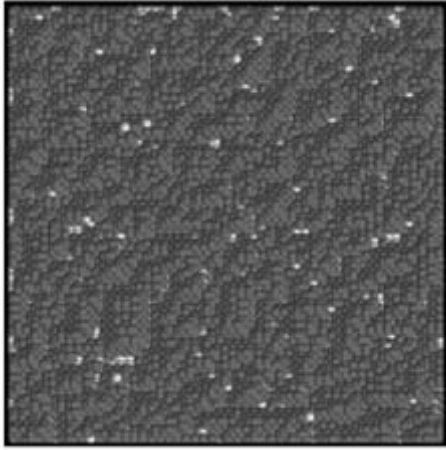


Figure 6: Morphologie of the film after four deposited layers at 700K

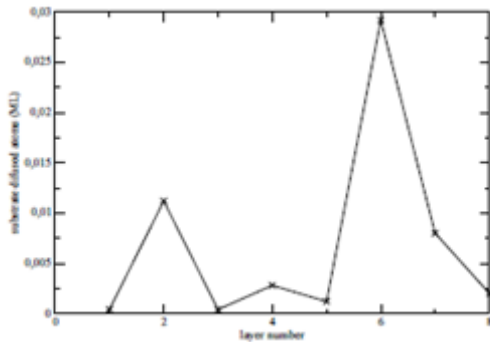


Figure 7: Spatial distribution of diffused substrate atoms; their number as a function of layer number

The curve in figure 7 presents the spatial distribution of substrate atoms diffused in the film. We find the majority of the diffused atoms comes from the last layer of the substrate. This atoms diffused first to the second preceding layer (layer number 6), then a part of them diffuses to layer 8 and to the layer 4 in the valleys between the facets of the mesa. These atoms entering to the valley continue their way to the bottom of the valley.

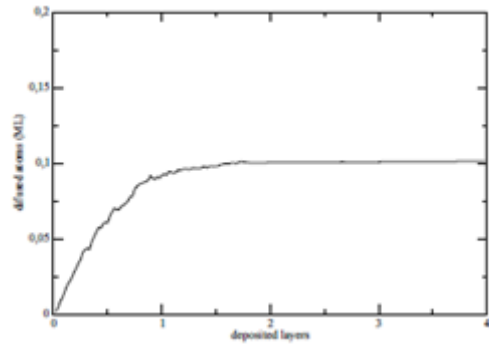


Figure 8: The number diffused substrate atoms, in monolayer, as a function deposited layers

Figure 8 shows the dependence of interdiffusion on time. It is clearly observed that interdiffusion is accelerated during the first stage of growth, as a result of strain relaxation. The number of vacancy creation decreases with further deposition and stabilizes, in all cases investigated here, before the deposition of four atomic layers is completed.

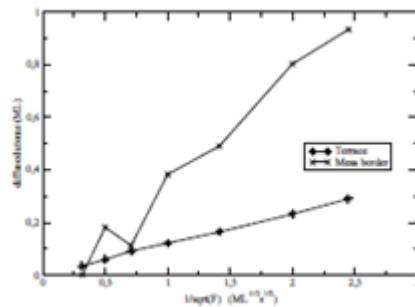


Figure 9: The number of diffused substrate atoms, in monolayer as a function of root square of 1/F, where F is the deposition rate.

The dependence of intermixing on the growth rate is shown in Figure 9. The increasing growth rate decreases the number of substrate atoms in the deposited film. We explain this result as a kinetic effect; the completion of layers in the deposited film prevents subsequent interdiffusion. Indeed, we can observe that the intermixing is inversely

proportional to the square root of growth rate, in agreement with conventional diffusion theory. Again, a large enhancement of interdiffusion at the border of the mesa is observed. A particular feature of these result is the statistical fluctuations which are observed, even after averaging results over several sets of independent random numbers. These fluctuations, at the border of the mesa are due to the much small number of atoms present at these boundaries, with respect to the total number of atoms on the substrate surface.

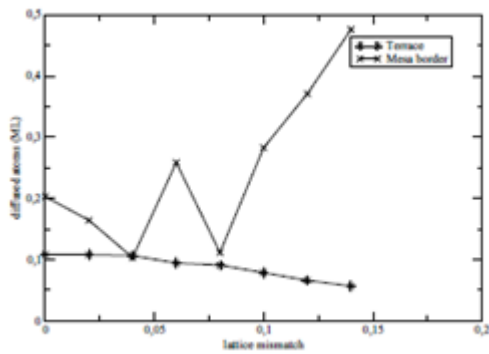


Figure 10: The number of diffused substrate atoms, in monolayer, as a function of lattice mismatch

Figure 10 shows the number of substrate atoms diffused in the film as a function of lattice mismatch. We show that intermixing is decreased with increasing lattice mismatch, in agreement with previous experimental observations where lattice mismatch has been employed to inhibit the intermixing²⁴. In fact, at high lattice mismatches, the deposited atom, which has diffused into the substrate, is located in an unstable position due to the high strain and tends to return into the deposited film. This leads to an increased number of vacancies in the substrate during the first stages of the film growth. In a later stage, most of these vacancies are repopulated by substrate atoms coming from the

deposited film, reducing therefore the intermixing. The interdiffusion is normally enhanced at the mesa boundaries, as previously and statistical fluctuations are seen in figure 10. But one can observe that the general trend of variation of interdiffusion changes near the mesa boundaries when the interdiffusion increases with the lattice mismatch. As mentioned above, the creation of vacancies in the substrate and in the deposited film play an important role in strain relaxation. At mesa boundaries, the strain relaxation has been shown to be preliminary due to misfit dislocation creation which are easily formed at step edges^{1,2}. Misfit dislocations offer migration channels to substrate which can massively diffuse into the deposited film. Increasing the lattice mismatch, thus the strain energy, favors the creation of misfit dislocations. The result is a large increase of substrate atoms migrating towards the deposited film via these dislocations (see fig. 10).

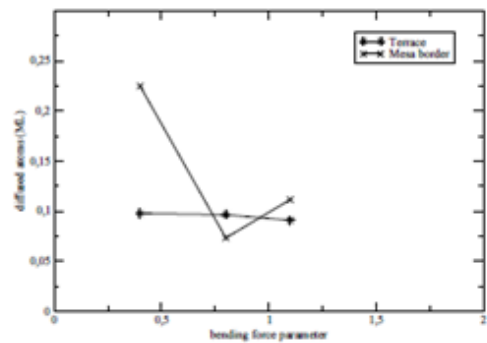


Figure 11: The number of diffused substrate atoms, in monolayer, as a function of parameter of deposited bending force atoms

If we consider that lattice mismatch effect is due to the strain energy, we should observe a similar behavior when depositing hard materials with large elastic constants. This assumption is clearly seen in figure 11 which shows the

interdiffusion as function of bending force parameters. We have used three values of force parameters: 1.1, 0.8 and 0.4 eV corresponding respectively to GaSb, InAs and ZnS cases. We find that larger bending constant, i.e. higher strain energies, lead to lower intermixing, in agreement with our assumption. Here, the interdiffusion trends are similar on flat terraces and at step edges. Indeed, an increase of the force parameters of the deposited atoms increases the strain energy in the substrate. This makes the diffused atom less stable, enhances its back motion to the deposited film and finally decreases the interdiffusion.

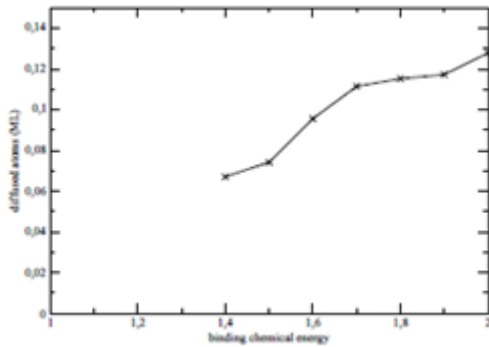


Figure 12: The number of diffused substrate atoms, in monolayer as a function of chemical binding energy

Finally, the dependence of the interdiffusion on chemical binding energies of deposited films on featured substrate is shown in figure 12. We observe that intermixing is increased with this binding energy. This results from the fact that substrate atoms are less attached to each other with respect to atoms in the film enhancing the motion of substrate atoms into the film.

4. CONCLUSION

In this paper, we have studied the effect of temperature of growth, deposition rate, lattice mismatch, bending force parameters, and chemical binding energy on the intermixing during heteroepitaxial growth by using the

Kinetic Monte Carlo technique. The effect of strain have been taken into account by allowing local relaxation of the substrate and the film after each single event, and by introducing the strain energy in the activation barriers to enhance the atomic motion in the stressed regions. We have proved that interdiffusion is increased with temperature due to atomic diffusion from deep layers of the substrate. We have also shown that featured substrate increases the interdiffusion compared to perfect substrates as a result of enhancement of the interdiffusion at step edges where the strain is important. Investigating the intermixing as a function of the lattice mismatch, two different behaviors are observed on flat terraces and step edges. This results from the different mechanisms of strain relaxation through vacancies on flat terraces and through misfit dislocation at step edges. Finally it is shown that the growth rate and force parameters inhibit the interdiffusion due respectively to kinetic effects and to deposited atom stability in the substrate. The results reported in this paper are in agreement with more recent experimental observations on the interdiffusion and alloying during deposition of germanium on silicon (001) substrates^{25–27}. A more thorough study for a quantitative analysis, as a function of experimental conditions and especially annealing cycles, is in progress.

This work is currently in development towards a detailed study of time evolution of diffusing atoms and vacancies in individual layers of the substrate and film. It could also be extended to study the spacial distribution of diffusing atoms and vacancies in the substrate and the film. This is interesting to investigate cluster formation. The correlation between

various parameters, studied in this paper, can be used for the engineering of enhancement or inhibition of intermixing in the design of devices.

REFERENCES

- 1 J. Dalla Torre, M. Djafari Rouhani, R. Malek, D. Esteve, G. Landa, *J. Appl. Phys.* 84 (1998) 5487.
- 2 M. Djafari Rouhani, H. Kassem, J. Dalla Torre, G. Landa , A. Rocher, D. Esteve, *J. Materials science and engeneering B88* (2002)181-185.
- 3 C. Van de Walle, R.M. Martin, *Phys. Rev.* 34 (1986) 5621.
- 4 P.C. Kelires, J. Tersoff, *Phys. Rev. Lett.* (63 (1989) 1164.
- 5 S. Jeong, K. Oshiyama, *Surf. Sci.* 436 (1999) L666.
- 6 J.H. Cho, M.H. Kang, *Phys. Rev. B*61 (2000) 1688.
- 7 S.A. Chaparro, J. Drucker, Y. Zhang, D. Chandrasekhar, M.R. McCartney, D.J. Smith, *Phys. Rev. Lett.* 83 (1999) 1199.
- 8 S.A. Chaparro, Y. Zhang, J. Drucker, D. Chandrasekhar, D.J. Smith, *J. Appl. Phys.* 87 (2000) 2245.
- 9 A.L. Barabasi, *Appl. Phys. Lett.* 70 (1997) 2565.
- 10 D.E. Jesson, S.J. Pennycook, J.M. Baribeau, *Phys. Rev. Lett.* 66 (1991) 750.
- 11 N. Ikarashi, K. Akimoto, T. Tatsumi, K. Ishida , *Phys. Rev. Lett.* 72 (1994) 3198.
- 12 M. Diani, D. Aubel, J.L. Bischoff, L. Kubler, D. Bolmont , *Surf. Sci.* 291 (1993) 110.
- 13 M. Sasaki, T. Abukawa, H.W. Yeom, M. Yamada, S. Suzuki, S. Sato, S. Kono , *Appl. Surf. Sci.* 82/83 (1994) 387.
- 14 L. Patthey, E.L. Bullock, T. Abukawa, S. Kono, L.S.O. Johansson , *Phys. Rev. Lett.* 75 (1995) 2538.
- 15 H.W. Yeom, M. Sasaki, S. Suzuki, S. Sato, S. Hotoi, M. Iwabuchi, K. Higashiyama, H. Fukutani, N. Nakamura, T. Abukawa, S. Kono , *Surf. Sci.* 381 (1997) L533.
- 16 A. Ikeda, K. Sumitomo, T. Nishioka, T. Yasue, T. Koshikawa, Y. Kido , *Surf. Sci.* 385 (1997) 200.
- 17 J.A. Floro, E. Chason, R.D. Twisten, R.Q. Hwang, L.B. Freund , *Phys. Rev. Lett.* 79 (1997) 3946.
- 18 M. Djafari Rouhani, M. Sahlaoui, A.M. Gu and D. Esteve, *J. Mat. Sci. Eng. B* 28 (1994) 200.
- 19 H. and M. Methfessel , *Phys. Rev. B* 52 (1995) 11059.
- 20 R.M. Martin , *Phys. Rev. B* 1 (1970) 4005.
- 21 F. Stillinger and T. Weber , *Phys. Rev. B* 31 (1985) 5262.
- 22 M. Djafari Rouhani, R. Malek, A.M. Gue, D. Esteve , *J. Mat. Sci. Eng. B*37 (1996) 25.
- 23 M. Djafari Rouhani, R. Malek, D. Esteve , *Thin Solid Films* 318 (1998) 61.
- 24 J. Jeon, E.H. Chen, V. Gopal, E.P. Kvam, J.M. Woodall , 1998 *Electronic Materials Conf.* , Charlottesville, Virginia, June 24 - 26, 1998.
- 25 N.E.B. Cowern, P.C. Zalm, P.Van der Sluis, D.J. Gravesteijn, W.B. De Boer, *Phys. Lett.* 72(1994)2585.
- 26 K. Shum, P.M. Mooney, J.O. Chu, *Appl. Phys. Lett.* 71(1997)1074.
- 27 F. Boscherini, G. Capellini, L. Di Gaspare, F. Rosei, N. Motta, S. Mobilio, *Appl. Phys. Lett.* 76(2000)682.
- 28 Hassan KASSEM, *Physics Procedia*, Volume 21, 2011, Pages 134-139.

SIMULATION OF FLOW THROUGH OPEN CELL COPPER FOAMS USING MICROTOMOGRAPHY STRUCTURE

Mohamad Zafari, Masoud Panjepour^a, Mahmoud Meratian
Isfahan university of technology, Department of materials engineering, Isfahan, Iran
a. Corresponding author (panjepour @cc.iut.ac.ir)

ABSTRACT: Due to the increasing metallic foams roll in industries, the need of simulating the fluid flow in metallic foams to understand the effect of parameters like porosity on the flow is increasing nowadays. Flow in porous media could be investigated from two approaches. In the first view the semi-empirical equations were used to obtain the mean value of variables. However, in the second one the equations were studied in macroscopic scale and the local value of the variables such as velocity and pressure were obtained. In this study, foams were simulated with 92 percent porosity. The geometry of these foams was obtained by using X-ray Computed Tomography (XCT). Impacting the fluid flow to the walls of media caused velocity to increase which had higher rate of increasing at the higher velocities. Finally the results were compared to the experimental data using Reynolds number. In this comparing there was high agreement (>99%) between the numerical calculations and experimental results. The equations showed that for Reynolds less than 1 the flow remains laminar.

1. INTRODUCTION

Open cell metal foams have unique properties such as high surface area to volume ratio, high strength to weight ratio (specific strength), sound adsorption and proper corrosion resistance [Moreira et al, 2004]. Therefore due to these properties, metal foams have been a great development in various industries. The industrial applications of these foams are in different industries such as automobile, aerospace, food industries, catalytic beds and heat exchangers [Banhart, 2001]. In these applications, particularly in catalytic beds and heat exchangers understanding of fluid flow behavior is really important [Fourie and Du Plessis, 2002]. For further studies of flow behavior, first should determine foams geometric structure and then solving flow equations.

1.1. Foams Geometric Structure

Finding foam geometry structure has a long history and it has been turned to a

fascinating subject of research in different fields including, engineering, materials science, biology, mathematics and many other fields, over more than a century. Metal foams do not have equilibrium state structures. Quenching or work hardening usually is taken place, before reaching to an equilibrium which causes a further accidental structure [Bock, 2011]. It should also be considered that foams structure type depends largely on the type of production method; hence introduction a general model seems difficult. X-ray tomography or computed tomography (CT) are widely used medical imaging such as tumor and crack detection in bones. This method is based on the absorptivities of different materials to the X-ray and in 1972 was introduced to construct 3 dimension images from 2 dimension basic images. X-ray CT method different resolutions depending on the ability and the sample size can be done. Therefore for high resolution, X-ray μ CT will be selected [Bodla, 2012].

1.2. Flow Equation

Due to extreme disordered structure of foams, most research are experimental and rendered models are experimental or semi empirical. Therefore in these models flow properties are achieved using average volumetric equations. Darcy model is one of the first models rendered in this field (macroscopic scale) [Edouarda and Lacroixa, 2008].

$$-\frac{dP}{dx} = \frac{\mu}{K}u \quad (1)$$

In this model $-\frac{dP}{dx}$ is pressure drop gradient in the flow direction, μ dynamic viscosity and K permeability tensor of the materials which for a homogeneous porous and isotropic media will be constant. And also apparent velocity is $v = \frac{Q}{A}$ which Q is volumetric flow rate and A is cross section, perpendicular to the flow direction.

After Darcy, many researchers showed that Darcy's law is valid just for low velocity that pressure drop and velocity have a linear relation. Thus Darcy's law is modified and the general equation of pressure drop through a porous media can be expressed by Dupoit-Forchheimer model [Weigang et al, 2008].

$$-\frac{dP}{dx} = \frac{\mu}{K}u + \frac{\rho C_f}{\sqrt{K}}u^2 \quad (2)$$

In this equation C_f is inertia coefficient of porous media. It shows that in low Re, pressure drop is caused by viscous energy dissipation and in high Re, is caused by kinetics energy dissipation [Despois and Mortensen, 2005].

In addition to the research on macroscopic models, several researches have been done on microscopic models such as computational fluid dynamics. Microscopic models are used to survey the validation of mechanism in macro scale and also achieving useful information in micro scale including local velocity. [Weigang et al, 2008] studying

3 dimensional fluid flow in a tetracaihedra and demonstrate different fluid regimes primarily depends on the type and the nature of the porous media. On the basis of micro tomography images Bodla et al. in 2012 came to this conclusion that permeability with uniform porous size has an inverse relationship with pore size [Bodla et al, 2012]. The aim of this research is to simulate the flow in micro scale using tomography images made by GeoDict (trial version) software. For discretization of momentum and continuity equations, finite volume method and structural grid method were used.

1.3. Solving Procedure

Because of limited memory size, a $10*10*10\text{mm}^3$ of the foam was simulated. After grinding, the written code was used to solve the equation. For an incompressible Newtonian flow, continuity and momentum equations expressed follows:

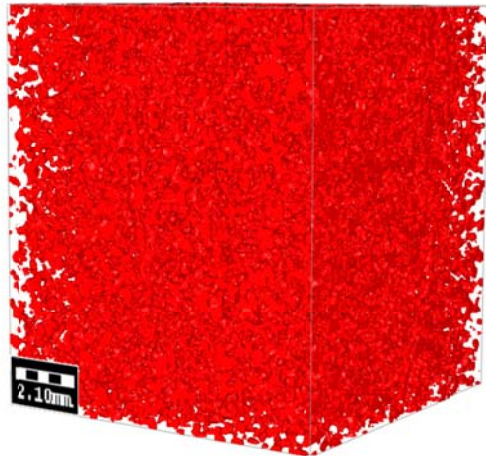
$$\nabla u = 0 \quad (3)$$

$$u \cdot \nabla u = -\nabla p + \mu \nabla^2 u \quad (4)$$

Here the fluid is air and in these equation constants including air viscosity $\mu = 1.789 * 10^{-5}$ Pa.s and air density $\rho = 1.225 \text{ kg/m}^3$.

In addition "p" and "u" are local pressure and velocity respectively. Simple algorithm is used to solve the velocity and pressure couple and the convergence criterion for solving the equations is 10^{-6} . In figure 1 microtomography of sample foam using GeoDict software (trial version) is shown. For input, boundary conditions are of velocity inlet type and for output are of pressure-outlet type.

It should be considered that for separating solid and fluid in the foam, no slip conditions lead to a stable flow within the foam and an output pressure as same as atmosphere.



→ Figure 1. Microtomography of sample foam with 92% porosity.

2. RESULT AND DISCUSSION

The static pressure at the inlet velocity of 1m/s for foam sample with 92% porosity is shown in figure 2.

In the graph by increasing in z value in flow direction, the value of pressure drop will be increased and therefore follows a linear relationship. Therefore 10 mm as an entry length can be adequate for a fully developed velocity.

2.1. Boundary Condition Effect

The graph of pressure drop vs inlet velocity for symmetric boundary conditions at the wall is shown in figure 3. It is observed that by increasing velocity, the pressure drop will be increased. In fact by increasing the resistance against flow, the pressure gradient will be increased which based on Darcy's law. Increasing in pressure drop in high velocities is higher.

By fitting these graphs with equation 2, permeability and inertia coefficient can be obtained. At the first the value of permeability was calculated by the use of first degree equation term and then by means of permeability and nonlinear

equation term, Orgun coefficient is calculated and these values are shown in table 1.

Table 1. Permeability and inertia coefficient predictions.

Boundary condition	$K_{air} (m^2)$	C_f
Symmetry	2.36×10^{-9}	0.071

2.2. Friction Factor

Friction factor based on Re in equation 4 is calculated as equation 5.

$$Re_K = \frac{\rho U \sqrt{K}}{\mu} \quad (4)$$

$$f = \frac{-\frac{\partial P}{\partial x_i} \sqrt{K}}{\rho u^2} \quad (5)$$

In this equation $\frac{\partial P}{\partial x_i}$ is pressure gradient calculated in the flow direction, k is permeability, ρ is density and v is velocity. Consider to permeability equation 2, a new equation for friction factor is obtained as follows:

$$f = \frac{1}{Re_K} + C_f \quad (6)$$

Friction factor information of the foam sample with 92% porosity by modification of Peak, Vafai and Bodla is shown (Figure 4). As it is seen in the figure 4, in low Re, there is a linear equation based on Re which is caused by overcoming of viscous forces and by increasing of Re number, nonlinear term due to overcome the inertia forces starts to increase and friction factor has no linear relationship with Re anymore.

This will be happened at proximate $Re > 1$. Modifications provided in references are often close to 92 porosity and in the graph there is a very good between the modifications and the work has been done.

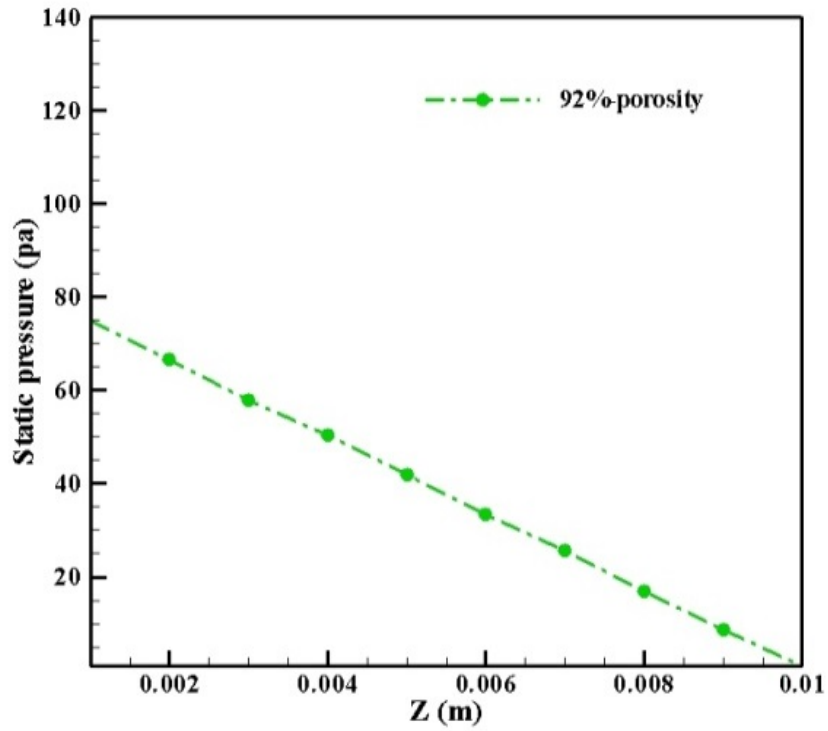


Figure 2. Pressure drop along the foam bed.

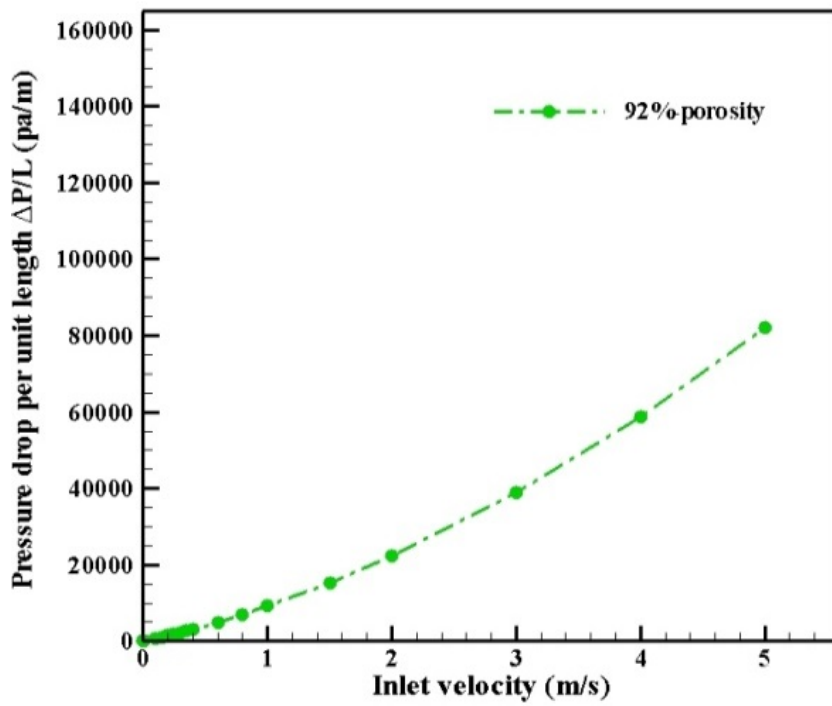


Figure 3. Pressure drop gradient $\Delta P/L$ vs apparent velocity u for symmetry boundary conditions at the walls.

3. CONCLUSION

3 dimensional simulating of fluid flow in foam sample with 92 porosity by means of microstomograph images in GeoDict (trial version) software has been rendered. The results verified selected dimension which can be mentioned as a proper length of beds in flow direction for reaching a fully developed velocity and also low difference in pressure drop

between symmetric boundary condition and non-slip boundary condition. The analysis of the fluid flow showed two linear and nonlinear region which for surveying transient Reynolds number, the graph of friction factor vs Reynolds number was drawn. The obtained graph from the simulation, showed very good agreement with experimental result.

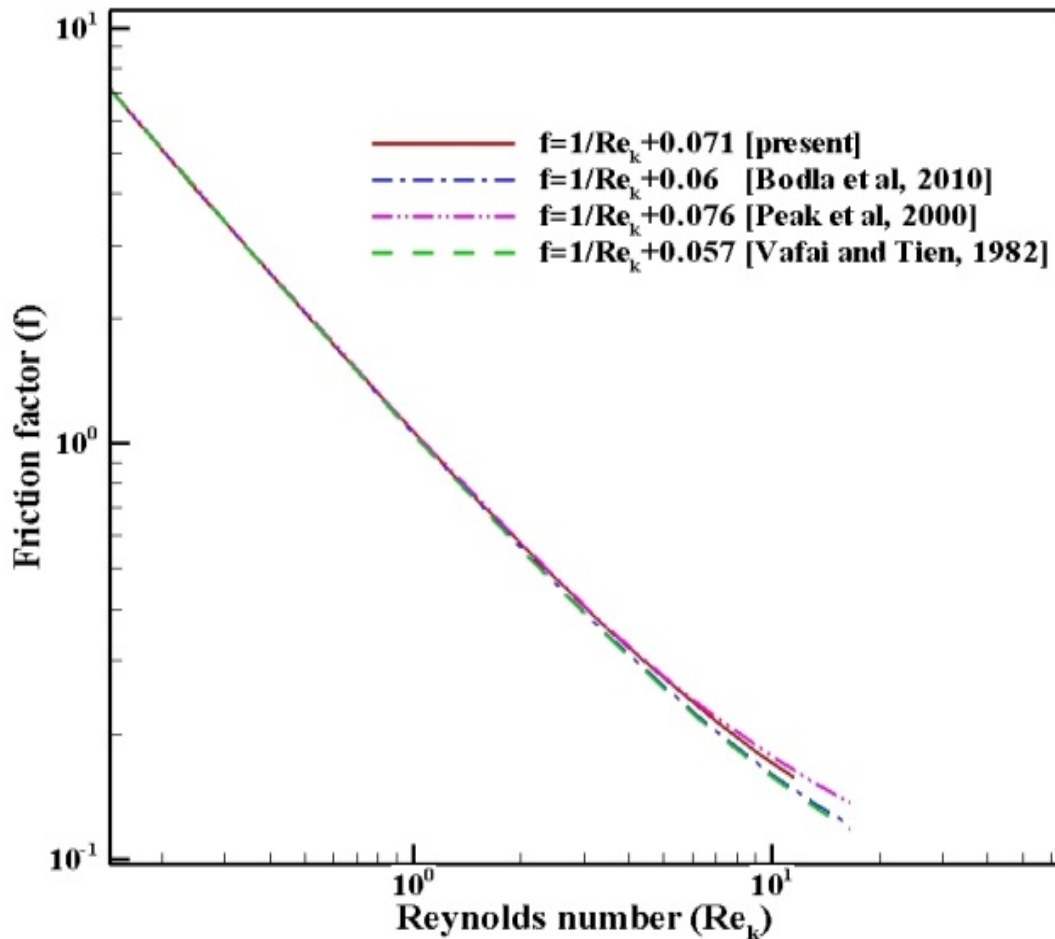


Figure 4. friction factor vs Refor foam sample with 92% porosity in comparison with other sample with about 90% porosity, from the references.

REFERENCES

- Banhart, J., 2001. Manufacture, characterization and application of cellular metals and metal foams, *Progress in Materials Science*, 46, 559.
- Bodla, K., Murthy, J., Garimella, S., 2010. Microtomography-based simulation transport through open cell metal foams, *Computation and Methodology*, 58, 527.
- Bock, J.J., 2011. A geometric study of liquid retention in open cell metal foams, University of Illinois at Urbana-Champaign
- Despois, J.F., Mortensen A., 2005. Permeability of open-pore microcellular materials, *Acta Material*, 53, 1381.
- Edouarda, D., Lacroixa M., Huua, C.P., Luckb F., 2008. Pressure drop modeling on solid foam : State of the art correlation, *Chemical Engineering*, 144, 299.
- Fourie, J.G.; Du Plessis, J.P., 2002. Pressure drop modeling in cellular metallic foams *Chemical Engineering Science*, 57, 2781.

- Moreira, E.A., Innocentini, M.D.M., Coury, J.R., 2004. Permeability of ceramic foams to compressible and incompressible flow, *European Ceramic Society*, 24, 3209.
- Paek, J.W., Kang, B.H., Kim, S.Y., Hyun, J.Y., 2001. Effective thermal conductivity and permeability of aluminum foam materials, *Thermophysics*, 21(2), 453.
- Vafai, K., Tien, C.L., 1982. Boundary and inertial effects on convective mass transfer in porous media, *Heat and Mass Transfer*, 25, 1183.
- Weigang, X., Hongtao, Z., Zhenming, Y., Jinsong, Z., 2008. Numerical investigation on the flow characteristics and permeability of three dimensional reticulated foam materials, *Chemical Engineering*, 140, 562.

CONTINUUM SIMULATION OF THE DISCHARGE OF POWDERS IN SILOS WITH AND WITHOUT INSERTS

Silvia Volpato¹, Riccardo Artoni², Andrea C. Santomaso^{1a}

1. APTLab – Advanced Particle Technology Laboratory, Dipartimento di Ingegneria Industriale, Università di Padova, Italy

2. L'UNAM / IFSTTAR, Route de Bouaye CS4 44344 Bouguenais, France
a. Corresponding author (andrea.santomaso@unipd.it)

ABSTRACT: In this work the results of several simulations of full-scale silo discharge were carried out using the hydrodynamic continuum model proposed by Artoni et al., Chem.Eng.Sci. 64 (2009), 4040-4050. These simulations have been compared with experimental literature data on the wall stresses and the flow patterns observed during discharge of the silo with and without inserts. The comparison has shown the ability of the model to capture quantitatively the main features of both the flow and the wall stress profiles even when flow corrective inserts are put in the hopper of the silo in order to convert the discharge regime from funnel flow to a mass flow regime.

1. INTRODUCTION

The discharge flow regime in silos can need to be improved in order to keep residence times of the material sufficiently uniform, to avoid the formation of stagnant zones or to reduce segregation. This corresponds working in the mass flow regime instead of the funnel or core flow regimes. One possibility for avoiding problems related to funnel flow is to promote mass flow by retrofitting the hopper with specific inserts. An insert, when correctly designed and positioned, can reduce stagnant zones in a silo with a relatively shallow hopper, leading to a flow pattern approaching mass flow.

The aim of this work was to validate numerical simulations using the valuable source of experimental data on the full-scale funnel flow silo published by the Tel-Tek Research Institute in Porsgrunn, Norway. Simulating silo flow with models capable to predict velocity and stress profiles at full-scale becomes important for design and operation since silo phenomena are known to be sensitive to scale effects [Härtl *et al.*, 2008].

2. THE MODEL

The numerical models describe the flow of granular materials like a fluid with non Newtonian viscosity characteristics.

2.1. Governing Equations

The flowing granular material has been modeled as a continuum pseudo-fluid through the conservation equations for mass, linear momentum (Navier-Stokes equation) and translational kinetic energy. The effect of the interstitial fluid has been neglected, the pseudo-fluid has been considered incompressible and the stress tensor assumed symmetric.

Under these assumptions, the continuity equation becomes:

$$\nabla \cdot \bar{v} = 0$$

and the Navier-Stokes equation:

$$\rho \frac{\partial \bar{v}}{\partial t} + \rho \bar{v} \cdot \nabla \bar{v} = -\nabla p - \nabla \cdot \mathbf{\Pi} + \rho \bar{g}$$

with:

$$\Pi_{ij} = -\rho d_p^2 \eta' \left(\frac{\partial v_i}{\partial x_j} + \frac{\partial v_j}{\partial x_i} \right)$$

where ρ is the bulk density, \bar{v} the velocity vector, p the isotropic part of the stress tensor, $\mathbf{\Pi}$ the deviatoric stress tensor, \bar{g} the gravity vector.

The conservation equation can be written as:

$$\frac{3}{2} \left(\rho \frac{\partial \theta}{\partial t} + \rho \bar{v} \cdot \nabla \theta \right) = -\Pi : \nabla \bar{v} - \nabla \cdot \mathbf{q}^T - z^T$$

where \mathbf{q}^T and z^T are the diffusive flux and the dissipation rate of fluctuating energy respectively.

The stress tensor Π can be related to the shear rate using a viscosity which depends on the granular temperature θ :

$$\eta' = \eta_0 \exp\left(\frac{\theta^*}{\theta}\right)$$

where θ depends on particles velocity fluctuations and is therefore a measure of the local mobility of the particles:

2.2. Numerical Implementation

A commercial CFD software has been used to solve the system of conservation equations with several customizations (Artoni et al., 2009a).

Momentum balance has been closed by Navier slip relation at the wall and by a tangential stress free upper boundary, while the outlet velocity was fixed (0.7 m/s). The model parameters were fitted to reproduce the behavior of stresses and velocity profiles in the shallow silo without internals, then the same parameters were used to test the predictions against data for granular flow in the silo with internals.

3. THE TEL-TEK EXPERIMENTS

The experiments (Härtl et al., 2008, Wójcik et al. 2012) were performed in a full-scale cylindrical silo 9.05 m high with an inner diameter of 2.52 m. The conical hopper was 1.25 m high, the inclination angle to the vertical was 44 ° and the outlet material was 0.1 m. The emptying rate was 17-25 m³/h.

The material used in the experiments was dry and cohesionless crushed quartz sand. The properties of the sand are resumed in Table 1.

Table 1: Material properties for the sand.

Bulk density (kg/m ³)	1370
Particle size (mm)	0.6-2
Angle of repose (°)	36
Wall friction angle (°)	17

The experiments were performed in the silo without inserts and in the silo with inserts. Various insert type and position have been investigated, but in this article only two cases have been reported: silo without inserts and with inverted double cone insert.

The inverted double cone insert (DC I) was 1.62 m high with a diameter of 0.6 m. The insert had a shorter upper cone of 30° to the vertical pointed upwards and a taller upper cone of 15° pointed downwards. The bottom of the insert coincided with the bottom of silo hopper.

4. NUMERICAL RESULTS AND DISCUSSION

4.1. Silo Without Inserts

Without inserts the silo discharged in funnel flow regime with a considerable dead zone at the hopper wall.

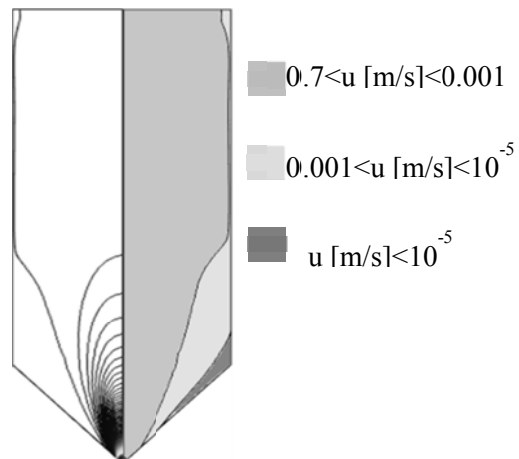


Figure 1: Flow profiles in silo without insert.

In the simulations, for sake of visualization, three different zones have been identified in the silo during

discharge (Fig.1): a central rapidly flowing channel which was surrounded by a slowly flowing zone and a stagnant zone near the silo wall.

The transition between the zones was smooth and the boundary values reported in Fig. 1 have been arbitrarily chosen. In any case the comparison of these maps in the different geometric configuration can give information on the effects of the inserts on the flow patterns as will be seen in the following. Also in the Tel-Tek experiments with the use of the tracer three different zones were identified as did for simulation. The outlet velocity was fixed at 0.7 m/s corresponding to the average value calculated from the flow rates in the experiments.

In Fig. 1 flow profile are given in terms of iso-velocity lines on the left side of each silo configuration. On the right side instead the three zone characterized by different velocity ranges are identified.

For the stress profiles the comparisons have been possible on a more quantitative ground. It was found a nice agreement between the simulated normal and tangential stresses at the wall and the experimental ones as shown in Fig. 2.

The wall normal stresses, obtained through the model implemented in CFD code, had the typical features expected from a discharging granular material. In the cylindrical upper section, the stress did not increase linearly with the depth but approached an asymptote. A local switch stress peak occurred at the transition from the vertical section to the hopper. Below the transition the stresses decreased again asymptotically towards zero at the hopper outlet. The stress peak was well predicted in position and magnitude by the model.

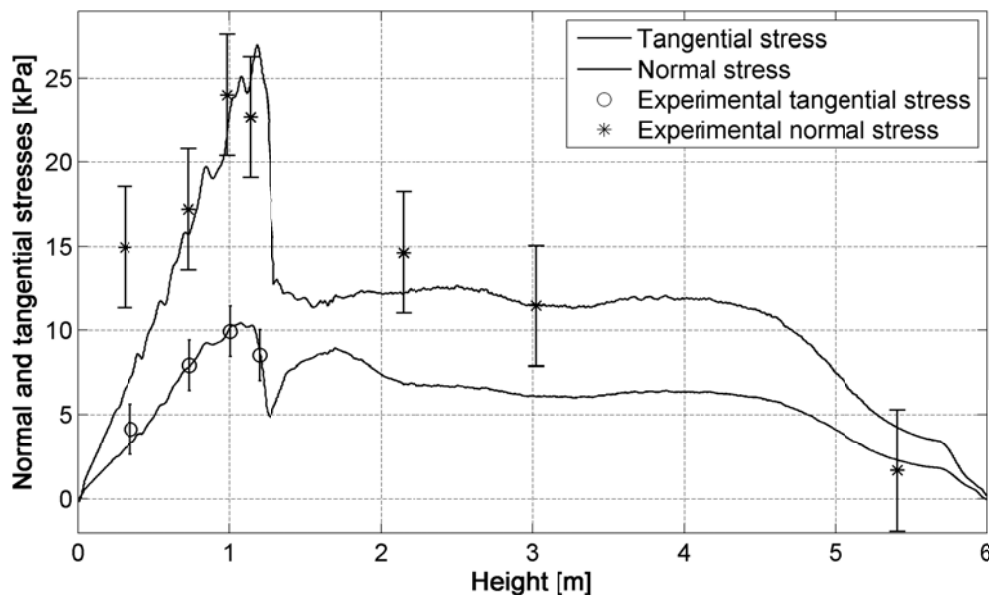


Figure 2: Comparison between simulations and experiments for the normal and tangential stresses at the wall in the silo without inserts.

4.2. Silo With Double Cone Insert

Simulations with inserts in the silo showed the expected modification of the flow channel. In particular, with double cone insert (Fig.3) the flow channel widened with respect to the case without

insert. The double cone insert improved the discharge flow in the vertical upper section of the silo. However from Fig. 3 it is possible to observe that the stagnant zone on the hopper wall, even if reduced with respect to the case without insert,

did not disappeared completely so that the mass flow was not achieved. Similar conclusions have been obtained also in the Tel-Tek experiments. The simulated results for the double cone gave very similar stress profiles to experimental results (Fig.4).

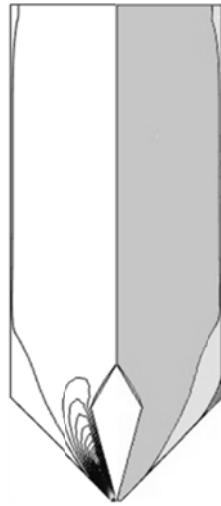


Figure 3: Flow profiles in silo with double cone insert. Explanation of the colors is given in legend of Fig.1.

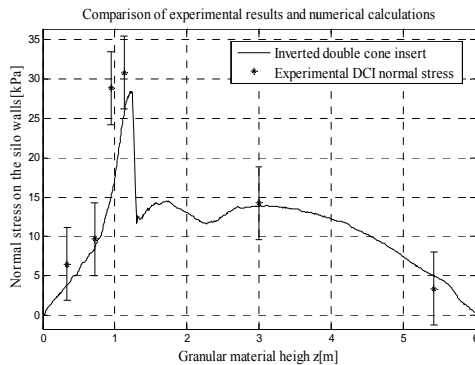


Figure 4: Comparison between simulations and experiments for the normal stress on silo wall with double cone insert.

In general there was agreement between the Tel-Tek experiments and the model predictions even though the simulated stress peaks tended to slightly underestimate the experimental ones.

4.3. Stresses on The Inserts

Information on the stresses exerted by the moving sand on the inserts was not available from the Tel-Tek experiments since pressure cells were placed only on the external walls. The simulations however allowed us to obtain wall stress information also on the inserts. In Fig. 5 a stress on double cone insert is reported.

At the top of the inserts where the sand starts to weight on the walls of the insert there is an abrupt increase of the normal stresses, then they stresses start to decrease from the maximum value.

4.4. Tangential Stresses

Tangential stresses at the wall can give information on the internal flow patterns. In Fig.2 the tangential stress in the silo without inserts was reported. Here in Fig. 6a and 6b a portion of the same profile around the hopper transition is compared to the granular temperature θ map.

A decrease of θ ('cooling') corresponds to a decrease of the shear inside the material. In Fig. 6a two peaks of the tangential stress can be observed: the first corresponds to the transition from the cylindrical section of the silo to the hopper, while the second (upper) can be associated to the transition of the granular material from the flowing to the stagnant zone.

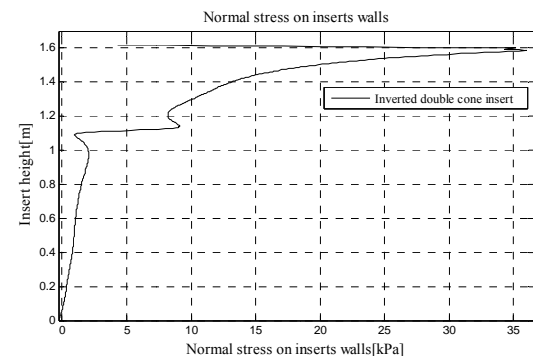


Figure 5: Normal stress on insert walls.

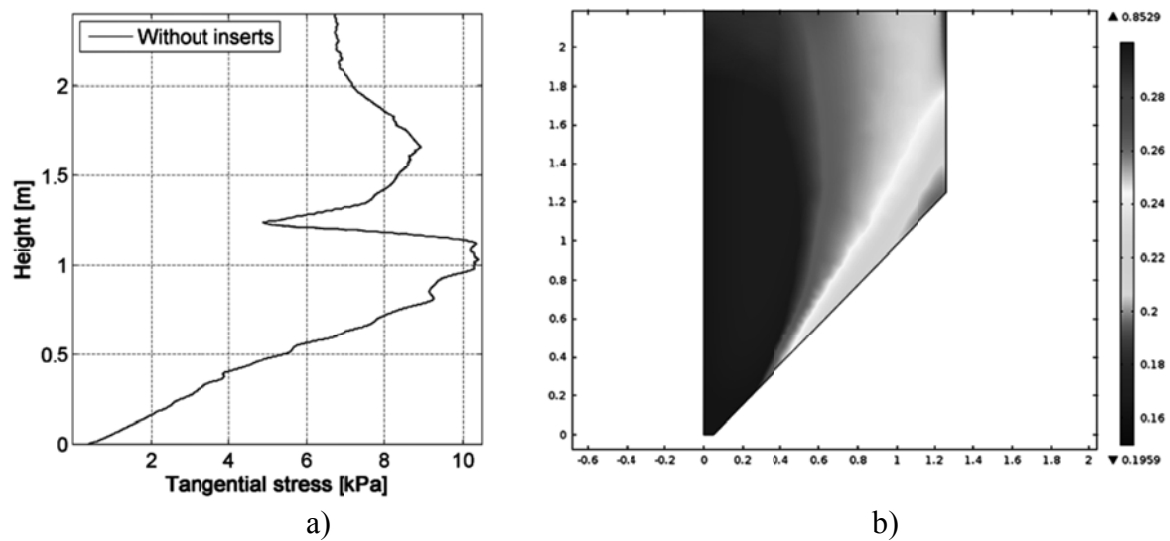


Figure 6: Tangential stresses (a) and granular temperature maps (b) for the silo without insert.

5. CONCLUSION

In this work a continuum model has been applied to simulate dense flow of dry sand in a full-scale silo with a shallow hopper operating in funnel flow. The effect of flow corrective inserts has been studied. The simulations have been compared with experimental data from literature. The model was first calibrated on data without inserts and then used to predict the flow and stress profiles for the case with inserts. The results presented in this work showed that model can be used a predictive tool.

In fact both stress and flow profiles with and without inserts compared well, both qualitatively and quantitatively with the Tel-Tek experiments. Furthermore the model allowed to obtain stress information on insert walls which are difficult to obtain by experiments and can be important for design purposes.

REFERENCES

- Artoni, R., Santomaso, A.C., Canu P., 2009, Simulation of dense granular flows: dynamics of wall stress in silos. *Chem. Eng. Sci.*, **64**, 4040.
- Artoni, R., Santomaso, A.C., Canu, P., 2009, Effective boundary conditions for dense granular flows. *Phys. Rev. E*, **79** (3), 031304.

- Artoni, R., Zugliano, A., Primavera, A., Canu, P., Santomaso, A.C., 2011, Simulation of dense granular flows: comparison with experiments. *Chem. Eng. Sci.*, **66**, 548.
- Härtl, J., Ooi, J.Y., Rotter, J.M., Wójcik, M., Ding, S., Enstad, G.G., 2008, The influence of a cone-in-cone insert on flow pattern and wall pressure in a full-scale silo. *Chem. Eng. Res. Des.*, **86**, 370.
- Schulze, D., 2007, *Powders and Bulk Solids - Behavior, Characterization, Storage and Flow*, Springer.
- Tuzun, U., Nedderman, R.M., 1985, Gravity flow of granular materials round obstacles. II. Investigation of the stress profiles at the wall of a silo with inserts. *Chem. Eng. Sci.*, **40**(3), 337.
- Wójcik, M., Tejchman, J., Enstad, G.G., 2012, Confined granular flow in silos with inserts - Full-scale experiments, *Powder Tech.*, **222**, 15.
- Yang, S.C., Hsiau, S.S., 2001, The simulation and experimental study of granular materials discharged from a silo with the placement of inserts, *Powder Tech.* **120** (3), 244.

MODELING THERMAL ENERGY STORAGE USING POROUS ADSORBENTS

Burcu Ugur¹, Shedia Stephens¹ and F. Handan Tezel^{1,a}

1. University of Ottawa, Department of Chemical and Biological Engineering, Ottawa, Canada

a. Corresponding author (handan.tezel@uottawa.ca)

ABSTRACT: Thermal energy storage system in adsorbent beds is a promising technology as it enables the storage of excess solar energy received from solar panels or the storage of excess thermal energy produced in power plants. This system stands out from other thermal energy storage systems as heat storage in adsorbent beds eliminates the heat loss with respect to storage time, and more than 50 cycles can be performed in one bed without any performance loss [Dicaire and Tezel, 2011]. In this study, water vapour adsorption from ambient air for the release of the thermal energy is modeled by using Wolfram Mathematica. This modeling is done by performing a mass balance in the column, water accumulation balance in the pellet, energy balance in the column, and energy balance around the column wall. Comparison between the modeled and experimental results show that the model estimates breakthrough time, and energy density with high accuracy.

1. INTRODUCTION

Fossil fuels, such as coal, petroleum and natural gas, form the world's primary energy source by having a share of more than 85% in total energy consumption. Fossil fuels are non-renewable energy sources as they take millions of year to form, and currently, reserves are being depleted much faster than the new ones are being formed. Therefore, it is expected that in the near future, world will approach a peak in fossil fuel production and consumption, causing a remarkable price increase and shortages in energy sources [Duncan, 2009].

Environmental effects of the fossil fuel combustion are also a big concern as the pollution of ambient air is primarily caused by it. Principal air pollutants resulting from fossil fuel combustion are carbon monoxide, sulphur oxides, nitrogen oxides and particulate matter as they effect lungs and respiratory track, and are poisonous. Moreover, burning fossil fuels produces around 5.5 gigatonnes of carbon dioxide (CO₂) per year, and forms 50% of the gases that are

thought to be responsible for the greenhouse effect [Kasting, 1998].

Existing systems need to be improved and new technologies need to be developed in order to increase the share of the renewable and sustainable energy sources in total energy consumption. Thermal energy storage is one of these emerging technologies. In this process, instead of obtaining thermal energy from conventional sources, like fossil fuels, it is collected from unconventional sources, like solar radiation and/or power plants that have excess thermal energy. This collected thermal energy is stored in adsorbent beds during regeneration run and can be released by performing exothermic adsorption of water vapour from air to heat the flowing process air. This heated air can then be used for space or water tank heating. The main advantage of this system is that it allows energy storage without any depletion during the storage period [Abedin and Rosen, 2011].

Adsorption process is summarized in three steps. Firstly, adsorbate molecules are transferred from the bulk fluid to the surface of the adsorbent. Then, they diffuse into the pores of the adsorbent, and finally, they are adsorbed on the surface of the pores. Adsorption can be explained by using mass and heat transfer phenomena, and the surface interaction between adsorbates and active sites of the adsorbent [Chou, 1987].

The main objective of this study is to model the exothermic adsorption of water vapour from air by Wolfram Mathematica and to compare this model with the experimental results for its verification. Modeling is done by using macro pore properties of the adsorbent, and physical properties of gas stream (air) with changing temperature and humidity. This model can be used to estimate breakthrough time and curve, energy density, and the temperature profile of any water vapor adsorption system at different column volumes and at different volumetric flow rates.

2. EXPERIMENTAL SETUP

Experimental procedure is composed of mainly two steps: adsorption and regeneration. During adsorption, air supply, which comes from the air compressor of the building, passes through the air filter in which solid particulates are removed. This filtered air then enters the bubbler to increase its relative humidity to around 97% by using an ultrasonic fog generator. In order to prevent water droplets from entering the adsorption column, humid air exiting the bubbler enters into a water trap. Then, humid air enters the column and exits as heated, and dry. Column outlet humidity increases gradually with respect to time, and air is heated up to around 80°C at the column exit.

During the regeneration process, air again passes through the air filter. Then, it enters to an in-line air heater and heated up to the regeneration temperature of 250°C. This heated air is passed through the saturated adsorption column in order to remove the adsorbed water molecules from the pores and regenerate the column.

3. MODEL DESCRIPTION

Before starting the modeling process, some simplifying assumptions are made such as:

- Gas stream has a constant volumetric flow rate and superficial velocity
- Gas behaves as an ideal gas,
- There is instantaneous adsorption at the pellet surface
- There is no radial concentration and temperature change in the column.

Firstly, a mass balance in the column is performed by considering the mass accumulation in the column, axial dispersion in the column, mass transfer due to convection, and mass transfer due to adsorption [Hashi et al., 2010].

In order to estimate the total amount of water adsorbed by the adsorbent pellets, an additional mass balance for water accumulation of water in the pellet is considered. Adsorbed water amount is calculated by using the mass transfer coefficient of the gas stream and the water concentration difference between the gas stream and the adsorbed phase at equilibrium (which is calculated by using Temperature Dependent Toth Isotherm). [Hashi et al., 2010; Wang and LeVan, 2009].

Temperature of the exiting air from the column and the energy density of the system are estimated through energy balances. Energy balance in the column is performed by considering the

accumulation, conduction, convection terms, as well as the heat released due to adsorption and heat loss from the walls. Heat loss from the column wall is modeled by doing an additional energy balance around the column walls by considering the convection from walls to the gas stream in the column, as well as the convection from walls to the ambient air [Hashi et al., 2010; Incropera et al., 2007].

Physical properties of the working gas stream such as density, heat capacity, axial dispersion coefficient, mass transfer coefficient, thermal capacity and heat transfer coefficient are estimated for varying temperature, humidity, pressure and volumetric flow rate of the stream [Churchill and Chu, 1975; Hashi et al., 2010; Incropera et al., 2007; Perry and Green, 2008; Wakao and Funazkri, 1978]

4. RESULTS AND DISCUSSION

The combined mass and energy balances are solved numerically by using method of lines technique in Mathematica to obtain breakthrough curve (Figure 1) and temperature versus time graph (Figure 2) which are compared with experimental results.

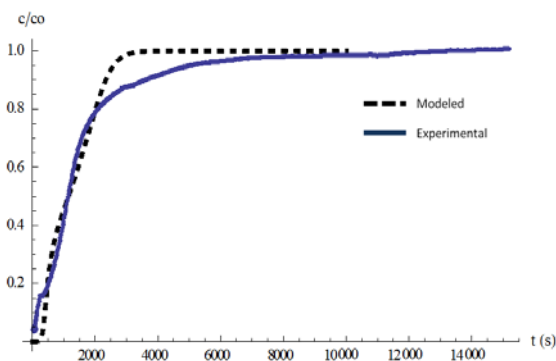


Figure 1: Breakthrough curve for 62.76 mL column at 20 L/min.

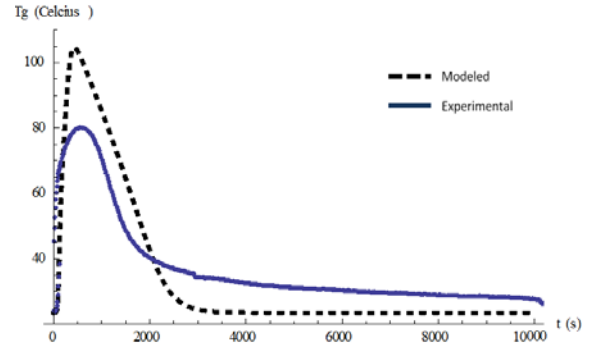


Figure 2: Temperature versus time graph for 62.76 mL column at 20 L/min.

As seen from Figure 1, model estimates the breakthrough time with high accuracy but there is a difference between the saturation times of the model and the experiment due to the instantaneous adsorption assumption at the pellet surface for the model. As the model neglects the required time of the water molecules to be adsorbed on the pellets, it estimates that adsorption occurs much faster. However, in the experimental case, adsorption is not instantaneous and therefore column reaches saturation slower as water molecules need some time to be adsorbed in the pellets.

In Figure 2, modeled and experimental temperature versus time graphs of the outlet air are shown. A difference between the model prediction and the experimental results occurs due to the same instant adsorption assumption for the model.

5. CONCLUSION

In this study, a mathematical model for water vapour adsorption from ambient air is obtained and compared with the experimental data for thermal energy storage applications. This comparison shows that modeled results are in a good agreement with the experiments as it estimates the breakthrough time and energy density with high accuracy. The only differences between the model and the experimental data are the difference between the saturation time, maximum

temperature reached, and the rate of the temperature decrease with respect to time. These differences are caused due to the assumption of instant adsorption at the pellet surface for the model. However, they can be eliminated by performing an additional mass balance around the particles considering the rate of water vapour diffusion in the pores.

Acknowledgements

Authors would like to thank NSERC and Ottawa Technology Transfer Network for funding.

REFERENCES

- Abedin, A. H., Rosen, M. A., 2011, A Critical Review of Thermochemical Energy Storage Systems, *The Open Renewable Energy Journal*, 4, 42-46.
- Chou, C. L., 1987, Dynamic Modelling Of Water Vapor Adsorption by Activated Alumina, *Chemical Engineering Communications*, 56,1-6, 211-227.
- Churchill, S.W., Chu, H. H. S., 1975, Correlating Equations for Laminar and Turbulent Free Convection from a Horizontal Cylinder, *Int. J. Heat Mass Trans.*, 18, 1049-1053.
- Dicaire, D. N., Tezel, H. F., 2011, Regeneration and efficiency characterization of hybrid adsorbent for thermal energy storage of excess and solar heat, *Renewable Energy*, 36, 3, 986-992.
- Duncan, R., 2009, The City of Austin Energy Depletion Risks Task Force Report, Austin Energy, Texas, U.S.
- Hashi, M., Thibault, J., Tezel, F.H., 2010, Recovery of ethanol from carbon dioxide stripped vapour mixture: adsorption predicting and modeling, *Ind. Eng. Chem. Res.* 49, 8733–8740.
- Incropera, F.P., Dewitt, D.P., Bergman, T.L., Lavine, A.S., 2007, *Introduction to Heat Transfer*, 6th Edition, Wiley, New Jersey.
- Kasting, J. F., 1998, The Carbon Cycle, Climate, and the Long-term Effects of Fossil Fuel Burning, *Consequences*, 4, 1.
- Perry, R. H., Green, D. W., 2008, *Perry's Chemical Engineers' Handbook*, 8th Edition, McGraw-Hill, New York.
- Wakao, N., Funazkri, T., 1978, Effect of fluid dispersion coefficients on particle-to-fluid mass transfer coefficients in packed beds: correlation of Sherwood numbers, *Chem. Eng.. Sci.*, 33, 1375-1384.
- Wang, Y., LeVan, M. D., 2009, Adsorption Equilibrium of Carbon Dioxide and Water Vapor on Zeolites 5A and 13X and Silica Gel: Pure Components, *J. Chem. Eng. Data*, 54, 2839-2844.

SECTION G
Industrial Applications

NANOPOROUS AEROGELS AND THEIR COMPOSITES FOR THERMAL INSULATION APPLICATIONS

Deniz Sanli¹ and Can Erkey^{1,2,a}

1. Department of Chemical and Biological Engineering, Koç University, 34450, Sariyer, Istanbul, Turkey

2. Koç University Tüpraş energy Center (KÜTEM), 34450, Sariyer, Istanbul, Turkey

a. Corresponding author (cerkey@ku.edu.tr)

ABSTRACT: An aerogel is a special form of a highly porous material with a very low density which is composed of individual nano-sized particles that are connected to form a three dimensional network. The unique properties of these materials with open pores and high surface areas are attributed to their irregular solid structure which can be tuned through the proper selection of the preparation conditions. The fascinating properties of various aerogels such as low thermal conductivity, low sound velocity, high optical transparency, high electrical conductivity and high surface areas can be exploited to develop new materials for energy related technologies. After an overview of different types of aerogels, the techniques used in their synthesis and for control over their nanoporous structure, various aerogel based products that are already in the market and that are under development for thermal insulation applications will be presented. The heat transfer mechanisms in insulating nanoporous composite materials will be highlighted and how tuning the pore structure of aerogels and their composites will lead to reductions in thermal conductivity will be discussed. Various chemistries under development for improvement of mechanical and chemical properties by surface modification of aerogels will be highlighted. Research needs for reduction of material costs will be discussed.

1. AEROGELS AND PROPERTIES

Aerogels are highly porous materials with nanometer size features that have been attracting considerable attention due to their unique properties. Aerogels were firstly synthesized in 1931 by Samuel Kistler who defined them as the materials keeping their pore and network structure intact upon exchanging their pore liquid with a gas [Kistler, 1931]. Kistler synthesized a variety of aerogels of different nature including silica, alumina, tungstic oxide, ferric oxide, stannic oxide and nickel tartrate aerogels [Kistler, 1931]. In addition to such inorganic aerogels, organic aerogels based on cellulose, nitrocellulose, gelatin, agar and egg albumin were also prepared by Kistler. Among these various kinds, silica aerogels have been one of the most widely synthesized and studied aerogels, so far.

Silica aerogels can be synthesized by a two-step sol-gel process. The various steps of this procedure are represented schematically in Figure 1. The most intriguing properties of silica aerogels are their low density, low sound velocity, high optical transparency, high electrical conductivity, high surface area, high porosity and low thermal conductivity [Fricke, 1992]. More importantly, their properties can be tailored for a specific application either by manipulation of the synthesis parameters during the sol-gel process or by post-treatment of the synthesized aerogels [Pierre, 2002]. Silica aerogels can be prepared to have bulk densities 3 to 500 kg/m³, porosities 80% to 99.8%, mean pore diameters 15 to 150 nm, surface areas 100 to 1200 m²/g, and thermal conductivities 0.015 to 0.030 W/mK. Owing to these flexible characteristics silica aerogels have been utilized in various applications such as thermal insulation, catalysis,

photocatalysis, adsorption and energy storage [Baetens, 2011]. Considerable research efforts are also underway to develop aerogels as supports for electrocatalysts for fuel cells, as adsorbents for CO₂ removal or H₂ storage and as components of electric double layer capacitors for energy storage.

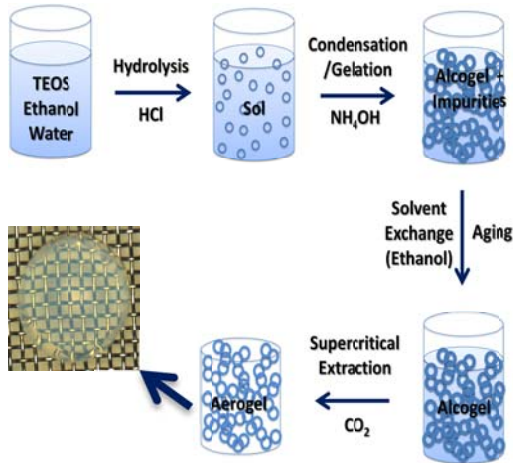


Figure 1: Two-step sol-gel process for the synthesis of silica aerogels.

The bulk properties of silica aerogels are governed by the surface properties owing to the substantial surface to volume ratio which is a result of the very high surface areas. Therefore surface chemistry and properties plays a crucial role for the bulk material properties as well as the extent of application areas. Silica aerogels are inherently hydrophilic materials, that is, they contain surface hydroxyl groups which dominate the chemical properties due to the high surface area. However, with surface modification the desired chemical groups can be obtained to alter the material properties. For instance, hydrophobic silica aerogels were obtained by reactive supercritical deposition of hexamethyldisilazane (HMDS) which resulted in the replacement of surface hydroxyl groups with the tri(methyl)silyl groups [Kartal, 2010]. Amine groups were also introduced to silica aerogel surface by using specific compounds such as bis(trimethoxysilylpropyl)amine

(BTMSPA) [Nguyen, 2010], and 3-aminopropyltriethoxysilane (APTES) [Meador, 2005].

2. HEAT TRANSFER IN AEROGELS

Being multi-scale materials having pore features at the nanometer range, aerogels are multi-component materials as well, owing to their solid network together with the gas phase which fills their nanopores. The heat transfer mechanisms within such multi-scale and multi-component nanostructured materials are complicated and the classical heat transfer theory is generally insufficient to predict heat transfer rates in these systems. Figure 2 displays the schematic representation of the mechanisms by which heat can be transferred in a porous material.

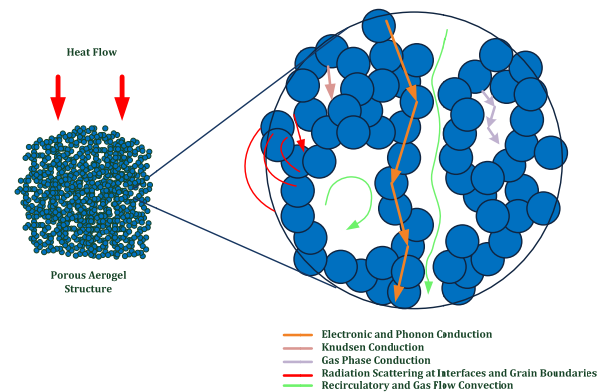


Figure 2: Heat transfer mechanisms in a porous material.

The three main mechanisms which contribute to the heat transfer are conduction, convection and radiation. However, for porous materials several components that contribute to each of these mechanisms differ from that of homogenous media. In the case of conduction, the heat transfer is achieved by electronic conduction along with the phonon conduction of the solid matrix, and by the gas phase conduction that occurs owing to the presence of the gas molecules in the pores, and also by Knudsen conduction that emerges due to

the confinement of the gas molecules within the pores. On the other hand, convective heat transport originates both from the flow of the gas molecules through the interconnected pores and the recirculatory flow of the gas molecules that are confined in the closed pores. Heat transfer by radiation is mainly attained by the scattering from the interfaces and grain boundaries. All of these mechanisms are considered to occur simultaneously that can be regarded as parallel resistances in a circuit; therefore the total thermal conductivity can be analyzed as the sum of conductive, convective and radiative components:

$$\lambda_{total} = \lambda_{conduction} + \lambda_{convection} + \lambda_{radiation} \quad (1)$$

The convective term, $\lambda_{convection}$, is generally ignored for aerogels since the heat transfer due to the flow of the gas molecules within the pores are suppressed owing to the nanosized pores of the aerogel structure.

One of the terms that contribute to the conductive component of thermal conductivity is the solid conduction which strongly depends on the structural parameters of the aerogels such as density, porosity and the interconnectivity of the pores. The solid network conductivity of aerogels, λ_s , is generally calculated using a formula that was developed by Fricke et al. [Fricke, 1992] and Hrubesh et al. [Hrubesh, 1994] which is given by:

$$\lambda_s = \lambda_{s^o} V_s \left(\frac{v_p}{v_d} \right) \quad (2)$$

where λ_s is the solid network conductivity of the aerogels, λ_{s^o} is the intrinsic conductivity of the network material, i.e. silica in the case of silica aerogels, V_s is the volume fraction of the solid, and v_p and v_d are the sound velocities in the porous and dense bodies, respectively. V_s term in fact directly relates the solid thermal conductivity to

the porosity of the material which is simply given by $(1 - V_s)$ [Yoldas, 2000]. With this relation, it can be realized that with increasing porosity, the amount of solid material and thus the contribution of the solid matrix conductivity to the total conductivity are reduced.

Another parameter that contributes to the conductive term of the total thermal conductivity is gaseous conductivity, λ_g , which is given by the Knudsen equation [Lee, 2002]:

$$\lambda_g = \frac{\lambda_g^o V_g}{(1 + \beta K_n)} \quad (3)$$

where λ_g^o is the thermal conductivity of free air, β is a parameter that accounts for the energy transfer between the gas molecules and the solid matrix during the collisions (~ 2) and V_g is the volume fraction of voids – namely porosity. K_n is the Knudsen number which is a characteristic parameter for the heat transfer in porous media describing the flow of gas molecules. For $K_n \gg 1$, the gas molecules are considered to obey the Knudsen flow in which they collide mainly with the pore walls rather than colliding with each other. On the other hand, for $K_n \ll 1$, gas molecules behave like liquid, and thus they frequently collide with each other [Lee, 2002]. Knudsen number is determined by the mean free path of the gas molecules, l_g , and the corresponding pore diameter, ϕ , with the following equation [Fricke, 1992].

$$K_n = \frac{l_g}{\phi} \quad (4)$$

The mean free path is obtained from the kinetic theory of gases and expressed by:

$$l_g = \frac{k_b T}{\sqrt{2} \pi d_g^2 P} \quad (5)$$

with k_b is the Boltzmann constant, d_g is the average size of gas molecules, T and P are temperature and pressure, respectively.

The mean free path of air depends on the temperature and pressure, and has a value

of 70 nm at ambient conditions. Having average pore sizes in a comparable range with the mean free path of the air molecules (1 to 100 nm), aerogel structure confines the gas molecules within the pores and restrains the collisions between them by limiting their motion, and consequently increasing K_n . Therefore, the gaseous thermal conductivity solely comprises the gas molecule-solid collisions, and thus is greatly reduced with fine pore sizes, which is known as the Knudsen effect [Lee, 2002].

For average pore sizes of $D \gg 100$ nm the gaseous conductivity becomes solely a function of the porosity, and decreases when the porosity is decreased. However, for values $D \gg 100$ nm it depends on both the porosity and the average pore size. In that case, the reduction of gaseous thermal conductivity can be accomplished by reducing both the porosity and the pore size [Yoldas, 2000]. The important point is that the porosity can be reduced by increasing the solid network content. However this action will in turn increase the solid thermal conductivity contribution. On the other hand, decreasing the pore size does not have such an adverse effect, hence the most effective way to reduce the thermal conductivity is considered to be the synthesis of aerogels with very fine pore sizes [Yoldas, 2000]. Figure 3 displays the variation of overall thermal conductivity of the silica aerogels with the porosity and average pore size. It is obvious that increasing the porosity decreases the overall thermal conductivity; whereas increasing the average pore diameter causes a rise in the overall thermal conductivity.

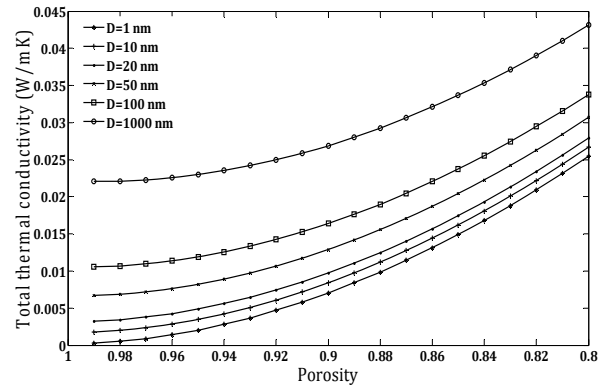


Figure 3: The effect of pore size and porosity on the thermal conductivity of silica aerogels.

For most materials, the heat transfer by radiation is generally ignored by neglecting its contribution to the total heat transfer coefficient in the models. However, radiation term becomes significant for aerogels, since it is affected by the pore structure and effectively scattered by the interfaces and the grain boundaries [Clyne, 2006]. For optically thick materials, the heat transfer by radiation is considered to be a local phenomenon and can be regarded as a diffusion process through a homogenous medium. Under these circumstances, the radiative conductivity which is based on the Rosseland approximation [Zeng, 1995] is given by:

$$\lambda_r = \frac{16 \sigma n^2 T^3}{3 \rho e(T)} \quad (6)$$

where, σ is the Stephan-Boltzmann constant, n is the refractive index, T is the absolute temperature, ρ is the density of the material and $e(T)$ is the mass-specific extinction coefficient which is obtained from the IR-optical measurements of spectral mass specific extinction coefficient. Organic aerogels with thicknesses more than 1 cm exhibit sufficient IR absorbance to be regarded as optically thick materials [Lu, 1992]. However, for silica aerogels there is an IR transmission window over the wavelength range 3-8 μm . This obstacle can be overcome by the use of the strong IR absorbing materials, known as

opacifiers, such as carbon black [Lu, 1995].

It can be realized that the three considerable parameters that mainly controls the total or effective thermal conductivity are the temperature, gas pressure and material density. Density has a determinant role since it defines the pore size of the aerogel with a direct relation to the porosity. However, distinct contributions to total thermal conductivity exhibit different dependencies on density. The solid conduction term increases with increasing density, since increasing density implies additional solid content. On the other hand, increasing density causes a reduction of gaseous conduction term owing to the decreasing porosity. However, the porosity and pore size are closely related and the effects of decreasing porosity on the pore size and pore size distribution should also be considered since pore size is another important parameter that influences the gas filling of the aerogel. All of these coupling effects lead to a distinct behavior of thermal conductivity components with density which is depicted in Figure 4.

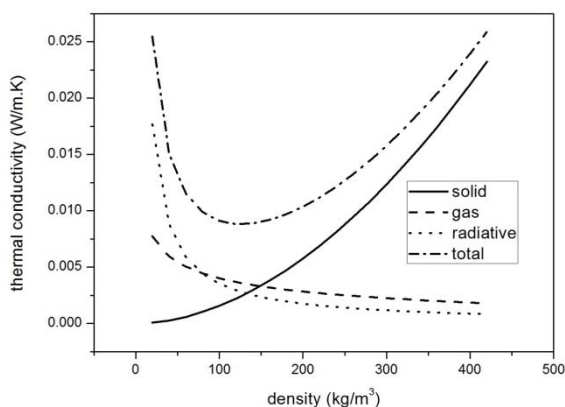


Figure 4: The effect of density on the different mechanisms of the thermal conductivity.

3. AEROGEL COMPOSITES

Many of the recent studies on silica aerogels are associated with the development of composites of silica aerogels with various compounds and polymers such as polyurea [Yin, 2010], di-isocyanates [Meador, 2007], polymethylmetacrylate [Fidalgo, 2007], cyanoacrylates [Boday, 2009], polyvinyl alcohol [Liu, 2002], polystyrene [Nguyen, 2009], etc. The main idea involves the incorporation of these compounds into the aerogel network using various techniques.

There are different ways to incorporate a polymer into the aerogel structure. One way is to add the polymer to the sol mixture before the gelation occurs, i.e. during the hydrolysis or condensation steps of the sol-gel process. With this method the gelation of the silane precursor molecules occur in the presence of the polymers chains. By this way, the polymer chains are distributed between the silica particles which make-up the network resulting in a composite material with a silica phase and a polymer phase. An alternative route involves the reaction of the polymer molecules with the surface groups of the silica aerogel which is carried out after the formation of the solid gel network. The hydroxyl groups of the native silica aerogel surface can in principle participate in such reactions. A more commonly used method is to functionalize the aerogel surface with specific chemical groups. The surface functionalization procedure can be performed during the synthesis by adding the appropriate agents into the sol mixture, or can be carried out as a post-gelation treatment by utilizing surface – OH groups of the already formed silica network. Once attached, the functional surface groups constitute active sites for further reactions and are used for the attachment of the polymers. As a third alternative, polymers can be added to the

sol mixture during the synthesis and can directly participate in the co-condensation reactions with the hydrolyzed precursor molecules. The method thereof requires specific polymers that can undergo co-condensation reactions with $-OH$ groups of the hydrolyzed silane precursors.

In addition chemical vapor deposition and supercritical deposition have also been employed. In most of these techniques the surface chemistry of the silica aerogels becomes the key component of the process since the surface $-OH$ groups are employed for the binding of different chemical groups or polymers.

For the last decade, most of the aerogel studies have focused on the development of aerogels as high performance thermal insulation materials. A wide variety of aerogel based products have been commercialized for insulation applications by companies including Aspen Aerogels, Cabot Aerogels and Airglass. A silica aerogel based blanket is produced by Aspen Aerogels by adding a fibrous matrix to the pre-gel mixture of aerogel which results in a flexible product (Figure 6). This aerogel blanket has a thermal conductivity of 0.0131 W/mK and the product is currently available in the market with a 10 mm thickness [Bardy, 2007]. Aspen Aerogels also produces a variety of flexible aerogel blankets using different fibers and aerogels for both cold and hot climate applications. Aerogels are also potential candidates for windows insulation purposes since they are inherently transparent materials by nature. A monolithic aerogel based window was developed by HILIT⁺ project of European Union (Figure 7) [Schultz, 2008]. The product was obtained with the aid of vacuum glazing technology and had an overall heat loss coefficient (U) of $0.66 \text{ W/m}^2\text{K}$. Currently, two commercial

products for aerogel based daylight systems are available at the market, NanogelTM and Okagel windows, which are developed and manufactured by Okalux and Cabot Aerogel (Figure 5). The aerogel particles produced by Cabot Aerogel were obtained by air drying and by employing the springback effect and thus are not monolithic as can be seen from Figure 5. These products have heat transmittance coefficients of 0.3 and $0.6 \text{ W/m}^2\text{K}$, respectively.

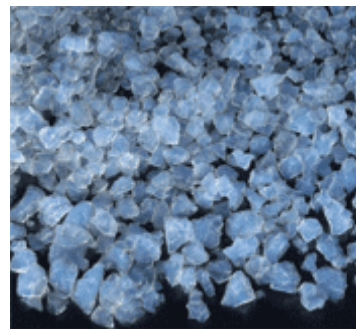


Figure 5: Aerogel Particles, Cabot Aerogel



Figure 6: Aerogel Blankets produced by Aspen Aerogel.



Figure 7: Aerogel window glazing produced by HILIT⁺ project.



Figure 8: Prototype situated at EMPA Campus which is used for weathering tests.

Aerogels have also been intriguing candidates as core materials for vacuum insulation panels (VIPs) which are currently the most promising high performance thermal insulation materials (Figure 8). VIPs are promising candidates for thermal insulation as these materials can achieve high insulation properties with low thicknesses [Baetens, 2010]. In principle, VIPs consist of a core matrix such as fumed silica which is surrounded by a film layer functioning as a barrier. Vacuum is applied in order to evacuate the gas within the material and thus eliminate the gaseous thermal

conductivity. VIPs are currently used in refrigerators and in shipping containers. The thermal conductivity values as low as 0.004 W/mK can be achieved using the VIP panels [Baetens, 2010].

4. CONCLUSION

The high cost of energy as well as intense emissions of green house gases is global problem which is forcing many countries to develop ways to minimize energy consumption. Improvement of current thermal insulation systems in buildings, appliances, manufacturing facilities and transportation will lead to substantial reductions in energy expenditure. Being nano-structured materials, aerogels have potential to replace conventional insulation materials since they have significantly lower thermal conductivities. The superior thermal insulation properties of aerogels emanate from their very low density, highly porous structure and fine pore sizes. Although aerogels and their composites prepared are already in market for industrial purposes, there are some obstacles that should be overcome for more efficient utilization of these materials. One important issue is that the processing costs and time of these materials should be reduced. For instance the aging and supercritical drying steps should be improved in terms of time and efficiency. With more research focused on this subject, the properties of these materials can be exploited utmost. Therefore, understanding the structure and properties of aerogels as well as the fundamentals of heat transfer mechanisms within these highly porous materials is a key requirement which would lead to the improvement and usage of these materials for insulation applications.

REFERENCES

- Kistler, S.S., 1931. Coherent Expanded-Aerogels, *The Journal of Physical Chemistry*, 36(1), p. 52-64.
- Fricke, J., Emmerling, A., 1992. Aerogels - Preparation, Properties, Applications, Structure and Bonding, 77, 37-87.
- Pierre, A.C., Pajonk, G.M., 2002. Chemistry of aerogels and their applications, *Chemical Reviews*, 102, 4243-4265.
- Kartal, A.M., Erkey, C., 2010. Surface modification of silica aerogels by hexamethyldisilazane-carbon dioxide mixtures and their phase behavior, *Journal of Supercritical Fluids*, 53, 115-120.
- Nguyen, B.N., Meador, M.A.B., Medoro, A., Arendt, V., Randall, J., McCorkle, L., Shonkwiler, B., 2010. Elastic Behavior of Methyltrimethoxysilane Based Aerogels Reinforced with Tri-Isocyanate, *Acs Applied Materials & Interfaces*, 2, 1430-1443.
- Meador, M.A.B., Fabrizio, E.F., Ilhan, F., Dass, A., Zhang, G.H., Vassilaras, P., Johnston, J.C., Leventis, N., 2005. Cross-linking amine-modified silica aerogels with epoxies: Mechanically strong lightweight porous materials, *Chemistry of Materials*, 17, 1085-1098.
- Yoldas, B.E., Annen, M.J., Bostaph, J., 2000. Chemical Engineering of Aerogel Morphology Formed under Nonsupercritical Conditions for Thermal Insulation, *Chemistry of Materials*, 12(8), 2475-2484.
- Yin, W., Venkitachalam, S.M., Jarrett, E., Staggs, S., Leventis, N., Lu, H.B., Rubenstein, D.A., 2010. Biocompatibility of surfactant-templated polyurea-nanoencapsulated macroporous silica aerogels with plasma platelets and endothelial cells, *Journal of Biomedical Materials Research Part A*, 92A, 1431-1439.
- Meador, M.A.B., Capadona, L.A., McCorkle, L., Papadopoulos, D.S., Leventis, N., 2007. Structure-property relationships in porous 3D nanostructures as a function of preparation conditions: Isocyanate cross-linked silica aerogels, *Chemistry of Materials*, 19, 2247-2260.
- Fidalgo, A., Farinha, J.P.S., Martinho, J.M.G., Rosa, M.E., Ilharco, L.M., 2007. Hybrid silica/polymer aerogels dried at ambient pressure, *Chemistry of Materials*, 19, 2603-2609.
- Boday, D.J., Stover, R.J., Muriithi, B., Keller, M.W., Wertz, J.T., Obrey, K.A.D., Loy, D.A., 2009. Strong, Low-Density Nanocomposites by Chemical Vapor Deposition and Polymerization of Cyanoacrylates on Aminated Silica Aerogels, *Acs Applied Materials & Interfaces*, 1, 1364-1369.
- Liu, Y., Chen, H., Zhang, L., Yao, X., 2002. Preparation and characterization of porous silica films by a modified base-catalyzed sol-gel process containing PVA: I. The precursor solution synthesis, *Journal of Sol-Gel Science and Technology*, 25, 95-101.
- Nguyen, B.N., Meador, M.A.B., Tousley, M.E., Shonkwiler, B., McCorkle, L., Scheiman, D.A., Palczer, A., 2009. Tailoring Elastic Properties of Silica Aerogels Cross-Linked with Polystyrene, *Acs Applied Materials & Interfaces*, 1, 621-630.
- Bardy, E.R., Mollendorf, J.C., Pendergast, D.R., 2007. Thermal Conductivity and Compressive Strain of Aerogel Insulation Blankets Under Applied Hydrostatic Pressure, *Journal of Heat Transfer*, 129(2), 232-235.
- Schultz, J.M., Jensen, K.I., 2008. Evacuated aerogel glazings, *Vacuum*, 82(7), 723-729.
- Baetens, R., et al., 2010. Vacuum insulation panels for building applications: A review and beyond, *Energy and Buildings*, 42(2), 147-172.
- Fricke, J., et al., 1992. Optimization of Monolithic Silica Aerogel Insulants, *International Journal of Heat and Mass Transfer*, 35(9), 2305-2309.
- Hrubesh, L.W., Pekala, R.W., 1994. Thermal Properties of Organic and Inorganic Aerogels, *Journal of Materials Research*, 9(3), 731-738.
- Lee, O.J., et al., 2002. Determination of mesopore size of aerogels from thermal conductivity measurements, *Journal of Non-Crystalline Solids*, 298(2-3), 287-292.
- Clyne, T.W., et al., 2006. Porous materials for thermal management under extreme conditions. *Philosophical Transactions of the Royal Society a-Mathematical Physical and Engineering Sciences*, 364(1838), 125-146.
- Zeng, S.Q., A. Hunt, R. Greif, 1995. Theoretical Modeling of Carbon Content to Minimize Heat-Transfer in Silica Aerogel, *Journal of Non-Crystalline Solids*, 186, 271-277.
- Lu, X., et al., 1992. Thermal Conductivity of Monolithic Organic Aerogels, *Science*, 255(5047), 971-972.
- Lu, X., et al., 1995. Correlation Between Structure and Thermal-Conductivity of Organic Aerogels, *Journal of Non-Crystalline Solids*, 188(3), 226-234.

NATURAL POROUS LIGHTWEIGHT AGGREGATES AND THEIR INDUSTRIAL FUTURE

Lütfullah GÜNDÜZ

SüleymanDemirelUniversity, Mining Engineering Department, Isparta, TURKEY
a. Corresponding author (lutfullahgunduz@sdu.edu.tr)

ABSTRACT: Pumice, volcanic tuffs, scoria, volcanic slag and diatomite rocks are basically known as natural porous lightweight aggregates and the ecologic materials. Their usage areas are getting world wide based on the chemical components, physico-mechanical characteristics and also the structural formation status. Natural porous lightweight aggregates have been used for centuries in Europe and the world. These natural raw materials can be found in many places around the world, where volcanoes are and have been present. In this paper, Turkish natural porous lightweight aggregates (particularly pumice, volcanic tuffs, scoria, volcanic slag and diatomite rocks), potentials and their industrial future were discussed and the resources of different regions in Turkey were evaluated on behalf of industrial supports.

1. INTRODUCTION

Turkey has actually a great chance as an owner of natural porous lightweight aggregate raw materials. The potential formations of these raw materials can be found in many regions of Turkey and they are already industrially used. Although they have been used successfully in many countries, finding new and improved ways to build with pumice, volcanic tuffs, scoria and diatomite rocks are becoming widespread. Due to their toughness and durability, they have been used as a lightweight aggregate in concrete for over two thousand years.

Improving current technology on innovative composite materials brought the use of natural porous lightweight aggregates as inevitable materials for different industrial areas. For this situation, powder particulates of natural porous lightweight materials are experienced as an important product for the industrial uses. These natural powder particulates also prove very high adding worth to economy of the country. Nowadays these processed materials are

widely used as a basic raw material or an additive material to develop the innovative industrial products.

In this paper, the usage criteria of powder particulates of the natural porous aggregates found in Turkey were discussed for different industrial areas such as developing the nano composites, textile, insulation, hygiene, pharmaceuticals, defence, aeronautics, fire resistant materials etc. and other applications. The pumice stone existence in Turkey was analyzed in a special case for industrial demand.

2. LIGHTWEIGHT AGGREGATES

The classification of lightweight aggregates is based on source, processing methods, and end uses. Natural porous lightweight aggregates include pumice, scoria, volcanic slag and cinders, tuff and diatomite rocks. Manufactured lightweight aggregates are bloated or expanded products commonly obtained by heating certain clays, shales, and slates. Ultralightweights, produced mainly from perlite and vermiculite, are

expanded or exfoliated by heating. Fly ash (produced mainly as a by-product of the combustion of coal and coke in thermal power plants), ground pelletized slag (resulting from metallurgical processes), and condensed silica fume (a by-product of the smelting process used to produce silicon metal and ferrosilicon alloys) are generally classified as supplementary cementing materials because of their pozzolanic characteristics [Vagt, 1994].

Pumice aggregate is a well known and most popular natural porous lightweight aggregate type as an industrial raw material. Its powder form has also large beneficial industrial usage areas in the world. This fact is deeply discussed in the following section with special case for Turkey.

Scoria is also well-known natural porous lightweight aggregate as like pumice. It is a vesicular (bubbly) glassy lava rock of basaltic to andesitic composition ejected from a vent during explosive eruption. The bubbly nature of scoria is due to the escape of volcanic gases during eruption [Gündüz, 2008]. It is typically dark gray to black in color, mostly due to its high iron content (Figure 1). The surface of some scoria may have a blue iridescent color; oxidation may lead to a deep reddish-brown color. The darker color of scoria has made it less useful commercially than pumice. A highly expanded form of scoria is called reticulite, where bubble walls have burst, leaving a three dimensional network of delicate glass threads. One of the main uses of scoria is in the production of lightweight aggregate [Gündüz, 2008]. The scoria is crushed to desired sizes and sold for a variety of uses. Concrete made with scoria typically weighs about 900 to 1700 kg/m³. This is a weight savings compared to concrete made with typical sand and gravel that weighs about 700 to

1500 kg/m³. This savings in weight allows buildings to be constructed with less structural steel. The air trapped and powder form of scoria makes the lightweight composite concrete units a better insulator. Buildings constructed with these lightweight composite products can have lower heating and cooling costs.



Figure 1: A view of scoria aggregate.

Crushed and grained powder (10 to 325 Mesh sizes) scoria is also used to develop roofing units, ground cover materials in landscape projects and insulation materials. Granular scoria is used as a substrate in hydroponic gardening, rip-rap, drainage stone and low-quality road metal. 120 Mesh and the lower size of scoria are preferable used as natural pozzolanic material. Turkey has a great chance to have large scoria regions. Specially, there are very large scoria formations in West and South Anatolia in Turkey. This existence makes a rising industrial potential in the country, especially building and horticulture sectors.

Volcanic slag is a lightweight aggregate and is the basaltic equivalent of volcanic materials, therefore it is also called as basalt lava. It is sometimes called cinders or volcanic cinder [Ritmann, 1976 and Gass *et. al.*,1973]. It is rich in highly vesicles volcanic glass which gives it high porosity and low density [Gündüz, 2008]. Its forms when blobs of gas-charged lava are thrown into the air during an eruption and cool in flight, falling as dark volcanic rock containing

cavities crated by trapped gas bubbles. This raw material is also used in industrial products similar to scoria. In Turkey, volcanic slag aggregate formations are very popular in near ManisaCity, Aegean Region of Turkey and HatayCity, Mediterranean Region of Turkey. Each quarry contains the different colored volcanic slag aggregate in reddish color and in black color.

Tuff is another type of rock consisting of consolidated volcanic ash ejected from vents during a volcanic eruption. Tuff is sometimes called tufa, particularly when used as construction material, although tufa also refers to a quite different rock. Rock that contains greater than 50% tuff is considered tuffaceous. Tuff is technically a sedimentary rock formed by the accumulation of volcanic ash plus pumice or scoria. It is a pyroclastic rock, composed of fine grains less than 2 mm in diameter. Pyroclastic means fire-broken, a name for rocks that have been blown apart by exploding gases. Ash exploded out of a volcano, may fall through the air and settle in beds, called ash-falls when unconsolidated, or tuffs when consolidated [Yasar *et.al.*, 2009]. The ash can vary in composition, for example it may be made up entirely of rock fragments. Tuff formations in Turkey occupy a huge place where volcanoes take part from South to North and from West to East of the country.

Diatomite may resemble chalk or fine-grained volcanic ash beds. But pure diatomite is white or nearly white and quite soft, easy to scratch with a fingernail (Figure 2). When crumbled in water it may or may not turn gritty, but unlike degraded volcanic ash it doesn't turn slippery like clay. On the other hand, diatoms are a major group of algae, and are one of the most common types of phytoplankton. Most diatoms are unicellular, although they can exist as

colonies in the shape of filaments or ribbons. Biochemical sedimentary rocks form from sediment derived by biological processes. This typically occurs in the ocean where a variety of atoms float among the water molecules. Typically only the hard, skeletal parts of an organism are preserved as sediment [<http://geology.about.com>].



Figure 2: A view of diatomite rock.

Diatomite is very useful raw material because silica is strong and chemically inert. It is widely used to filter water and other industrial liquids including foods. It makes excellent fireproof lining and insulation for things like smelters and refiners. It is a very common filler material in paints, foods, plastics, cosmetics, papers and much more. Diatomite is part of many concrete blends and other building materials. In powdered form it is called diatomaceous earth or DE. The microscopic shells injure insects but are harmless to pets and people [<http://geology.about.com>]. Turkey has a great potential of diatomite formations. The estimated potential raw material of diatomite in Turkey is up to 150 Million tones. Industrial use of diatomite in Turkey is recently developing sector. The powder form of diatomite is much valuable than it's granulate forms in terms of composite material products. It is used in composite material structure as a raw or an additive material. Less than 400 mesh size fraction of diatomite is considerably used for armour productions in defense sector. 35 to 325 Mesh size fractions of diatomite powders are preferentially used for producing the fire

resistant materials as additives. The common diatomite reserves in Turkey are shown in Figure 3.

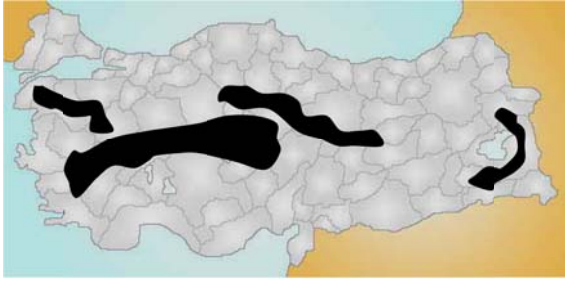


Figure 3. The common diatomite reserves in Turkey.

3. PUMICE STONE INDUSTRY WITH SPECIAL REFERENCE TO TURKEY

Pumice stone formations having an effusive and extremely porous structure are present in various volcanic parts of the world due to the volcanic activities. Turkey has great importance and competitive role in the world with respect to formation type and economical usage of this material. Especially some provinces of Middle and East Anatolia have extremely wide pumice formations. Bitlis, Kayseri, Nevşehir, Niğde, Isparta and Van are the most popular regions among them. Although these formations are known as “pumice”, the volcanic material must be investigated in detail with respect to its physical and structural properties which markedly affect its industrial importance [Gündüz, 2005]. On the other hand, it is possible to see similar formations in some countries, notably in Greece, Italy, Indonesia and China. But, it has been stated that, the formations in these countries, which will be able to use as an economical lightweight aggregate, have different properties than the formation in Turkey from the technical point of view.

Due to increasing trend of using many structural materials in civil engineering applications, materials must have some

compatible properties with appropriate technical values. The different forms of lightweight structural pumice aggregates have been widely used in buildings as a filler material for the last few years because of its desired technical parameters and various advantages such as heat and sound insulation properties [Vikurstaypur, 1988]. Pumice can be classified as natural lightweight aggregate in terms of physical, chemical and inner structure.

Turkey has an important potential of pumice deposits. The pumice deposits were formed by volcanic activities during the late Tertiary to Quaternary period in Central, Eastern Anatolian and Mediterranean regions of Turkey. Acidic pumice which occurs very widespread and is widely used is white-dirty white colour and its bulk density ranges from 0.2-1.0 gr/cm³ [Gündüz *et.al.*, 2001]. Detailed geological studies were carried out for pumice exploration by the General Directorate of MTA and SüleymanDemirelUniversity, Pumice Research Centre throughout Turkey and a total reserve of nine billion m³ was approximately estimated. It is estimated that this potential is 43% of the world total pumice reserves. However, large reserves of young volcanic formations occupy a very characteristic position in the structure of Anatolia. Especially in the Cappadocian region, the pumice is the liparitic composition and it is one of the very important reserves for the raw material source of pumice stones in Turkey [Gündüz, 1998]. The general distribution of the pumice reserves in Turkey is illustrated in Figure 4.

To analyse the technical properties of Turkish pumice stones, a comprehensive research work was carried out for different industrial uses. Twelve different pumice characteristics were determined for the regions in Turkey. It was observed

that pumice varies white colours to dark greyish colour depends on the silica contents. The silica content also affects the pumice specific weight, porosity and the other technical aspects [Gündüz and Ugur, 2004]. To reference this event, a research finding of two different pumice stones, belong to west and middle Anatolian regions, is briefly discusses as follows. According to chemical analyses, the pumice stones are very rich in silica, presents a structure perfectly vitreous, no crystalline structure. Chemical composition of the pumice stones are given in Table 1.

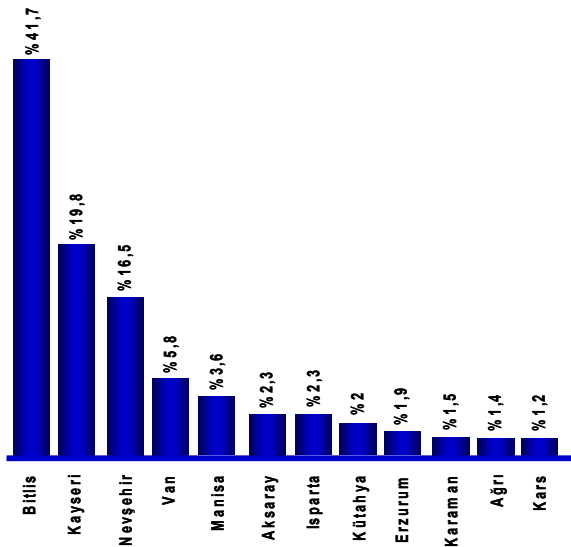


Figure 4: Distribution of pumice reserves in Turkey.

Table 1: Chemical composition of the pumice stone in percent.

Major Element	West Anatolia	MiddleAnatolia
SiO ₂	58 to 64	67 to 75
Al ₂ O ₃	11 to 14	13 to 15,5
Fe ₂ O ₃	1,1 to 1,6	2,7 to 3,2
CaO	1.1 to 1,8	2,8 to 3,0
Na ₂ O	3,0 to 4,0	3,9 to 4,2
K ₂ O	4,0 to 5,2	2.7 to 2,9
MgO	0.28 to 0,37	0.7 to 0,95
TiO ₂	0.05 to 0,08	0,2 to 0.26

The specific unit weight value of the pumice formations varies 2180 – 2210 kg/m³ in west Anatolia and 2290 – 2340 kg/m³ in Middle Anatolia. The unit weight values of the pumice formations were analysed separately according to the basics, stated in BS 812 and DIN 4226 and the parametric findings are given in Table 2. The porosity of pumice samples are also given in Table 3.

Table 2: Unit weight of pumice stones.

Size Fraction, (mm)	Unit Weight, (kg/m ³)	
	West Anatolia	MiddleAnatolia
>32	310-330	210-255
16-32	410-435	270-295
8-16	500-520	325-340
4-8	590-630	365-385
2-4	675-705	420-460
1-2	780-810	480-530
0.5-1	870-930	560-595
0.25-0.5	960-1020	640-690

Table 3: The porosity of pumice stones.

Size Fraction (mm)	West Anatolia	MiddleAnatolia
>32	% 71 ±2	% 88 ±3
16-32	% 69 ±2	% 80 ±4
8-16	% 65 ±3	% 73 ±3
4-8	% 62 ±3	% 68 ±4
2-4	% 59 ±3	% 66 ±3
1-2	% 53 ±2	% 66 ±4
0.5-1	% 50 ±3	% 66 ±3
0.25-0.5	% 46 ±2	% 65 ±3

Pumice is a versatile product, useful for many applications, most notably in the textile, agriculture and the building industries. The usage of pumice in the world and in specifically Turkey and its distribution according to the different industrial sectors is given in Figure 5.

Generally, all the pumice has the same chemical properties depending upon the quarry although its features are slightly

different from the similar acidic rocks. Sometimes, the specific properties of pumice having the same chemical properties based on the usage areas are wanted. One of the most important application of pumice is its use in the denim stonewashing sector which gave a true lift-off to the pumice industry in the middle of the 1980's. Stonewashing denim involves mixing pumice with finished articles of clothing and literally putting the combination through a laundry. That will give clothes a bleaching effect [Gündüz *et.al.*, 2001].

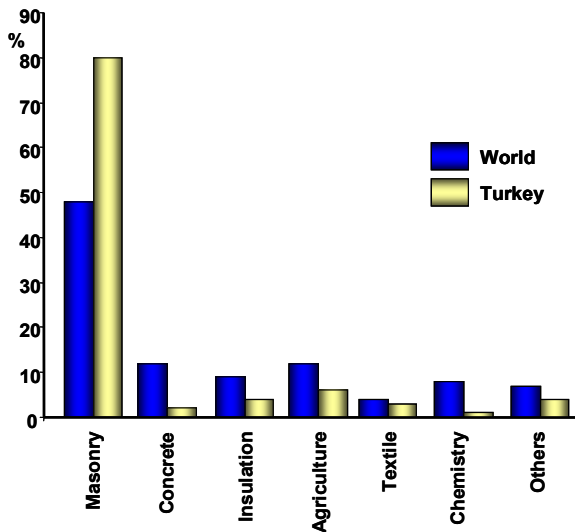


Figure 5: Pumice usage ratios.

Apart from stonewashing, pumice granules in different size fractions are also largely used in agriculture and horticulture for its chemical and physical properties and its being environmentally friendly. It is non-toxic, odourless, 100% inert, and completely inorganic. Acidic pumice stones are not soluble in water, do not degrade in time, neither release nor produce chemical polluting substances. They, being chemically inert, does not allow unwanted chemical reactions, and in comparison to other materials, it is also characterised by a high specific surface which enables it to have a high absorbing power when in the presence of water [Gündüz *et.al.*, 2001].

In order to improve some physical characteristics of agriculture soils primarily with heavy texture, pumice stone can be used as substrate it is also used as growth media for plants without using any soil usually in horticulture particularly under greenhouse conditions. It acts as an insulator in the soil mixture and protects plants from rapid temperature extremes. Pumice retains a high percentage of its weight in absorbed water and waterborne nutrients, making it an excellent buffer [Gündüz *et.al.*, 2001].

The use of pumice in agriculture reduces the weight of clayey grounds, and thanks too the slow and uniform release of water previously absorbed by pumice particles, it also enables to save on the cost of irrigation systems. Many nursery gardner industries and flower growers use pumice gravel in their substrates as it enables a perfect rooting of plants and a very good drainage favouring a natural cultivation cycle. In glasshouse cultivation pumice, retaining the heat, increases the heating system efficiency avoiding energy waste and being environment friendly [Gündüz *et.al.*, 2001].

Acidic pumice products have fundamental characteristics which make them suitable in soil stabilisation, land reclamation (dumps, quarries) and water embankments. Pumice has a low thermal conductivity coefficient, giving it the properties of heat insulation. It is also used to make an aggregative concrete, a product useful for construction [Gündüz *et.al.*, 2001 and Gündüz, 2005]. These properties make pumice suitable for several uses, including: roof insulation and floor insulation.

Apart from the insulation, pumice as a powder form is also used in various fields such as construction, paint manufacture, chemical industry, metal and plastic finishing, dentistry and cosmetics, glass

and mirror polishing, etc. Smooth abrasivity, high porosity, low density, chemical stability and the fact that it is a natural product containing no toxic matter injurious to the environment are many reasons for such a large range of uses for pumice [Gündüz *et.al.*, 2001 and Gündüz, 2005]. Some special usage areas of pumice powder particulates are discussed below.

The mild abrasive and polishing nature of pumice has many diverse abrasive applications. Pumice with a Mohs Hardness of 5.5 to 6.0, together with its wide range of controlled particle sizes, could be used in the most critical abrasive environments [<http://crminerals.com>]. 230 to 325 Mesh (44 to 63 microns) pumice powder particles are mostly used for cleaning lithographic plates. On the other hand, 30 to 325 Mesh (44 to 600 microns) pumice powder particles are mostly used for electroplating and 60 to 325 Mesh (44 to 250 microns) pumice are also used general cleaning and polishing applications. Furthermore, 40 to 325 Mesh (44 to 400 microns) pumice powder are used for pressure blasting (sand blasting) applications and 50 to 325 Mesh (44 to 300 microns) pumice powder are used for vibrating and barrel fishing applications, too.

Chinchilla and other small furry animals should not be bathed in soap and water. Instead, their fur should be cleaned in a manner consistent with their natural instincts, which is to take a dust bath that absorbs the oils and dirt attached to their fur. Fine particles of pumice provide an excellent dust bath. The animal rolls around in the pumice dust, and the pumice attaches to the fur, absorbing oil and dirt [<http://crminerals.com>]. The dust then falls off the fur during normal activity. For this purpose, 30 to 120 Mesh (125 to 600 microns) pumice powder are preferred.

Many porous materials are used as chemical carriers in the chemical process industry. The lightweight, high porosity, and high surface area of pumice powder, together with the fact that it is chemically inert, makes it ideal to serve as a chemical carrier. For this purpose, 6 to 120 Mesh (125 to 3360 microns) pumice particulates are used to be as chemical carriers materials in different industrial applications.

The mild abrasive nature of pumice powder has wide applications in many cleaning products. The combination of mild abrasiveness and controlled particle size allows formulation flexibility in cleaning products including glass and ceramic stove top cleaners, liquid multi-surface cleaners, and hand cleaners [<http://crminerals.com>]. Although 12 micron size of pumice powder is commonly preferred to use in powdered and bar hand cleaners, 30 to 325 Mesh (44 to 600 microns) pumice powder size fraction could be used for the same products. Furthermore, 5 micron size of pumice powder has supply superior performance for liquid hand cleaners. However, 80 to 325 Mesh (44 to 177 microns) pumice powder size fraction could also be used for the similar liquid cleaners. Pumice powder particulates with a variety of size fractions could be used for automobile cleaners, rubbing compounds, waxes and polishes, too.

The use of pumice in cosmetics scrubs is well established. Pumice powder can be used in exfoliating facial, body, and foot scrubs [<http://crminerals.com>]. The pumice particles provide an excellent exfoliating medium, which gently removes dead and rough skin, leaving it fresh and revitalized. The following pumice material size fractions are commonly used in cosmetics scrubs: 325 Mesh (44 microns) for facial scrubs, 30 to 120 Mesh (125 to 600 microns) for foot

scrubs, 80 to 325 Mesh (44 to 177 microns) for exfoliating creams.

Pumice powder pellets are perfectly suited for potpourri and decorative applications [<http://crminerals.com>]. Their lightweight and extremely porous nature makes them ideal for absorbing both color and fragrance. For this purpose, 6 to 120 Mesh (125 to 3360 microns) pumice particulates are used to be as fragrance materials.

The mild abrasive nature of pumice powder makes it an ideal polishing aid to finish acrylic dentures. It is also used in oral hygiene pastes, prophylaxis pastes, and teeth polishing compounds. Pumice powder is used in a water suspension to obtain a smooth surface during polishing. Although 12 micron median particle size of pumice powder is mostly preferred in dental treatments, 30 to 325 Mesh (44 to 600 microns) pumice powder size fraction can be rarely used for the same purposes.

Printed circuit board manufacturing is a complex industry requiring numerous processing steps to produce single or multi-layer printed circuit boards. The abrasive/polishing characteristics of pumice can be used during printed circuit board manufacturing. Brush scrubbing with pumice has been the industry standard for many years. The use of nylon brushes with a suspension of pumice in water results in excellent surface topography. Pumice, with its narrow particle size and Mohs hardness of 5.5 to 6.0, provides uniform abrasion/polishing. During the panel preparation step, the panels are subjected to anti-oxidant baths, cleaners, and pumice scrubs similar to the core preparation. Mechanical scrubbing methods include abrasive brush scrubbing and pumice scrubbing. Brush scrubbing removes a thin layer of surface

copper, thus ensuring a clean surface, but tends to impart stress to a thin core material by deforming it during the scrub. Brush scrubbing can also produce a surface not compatible with fine-line circuit designs [<http://crminerals.com>]. The use of 12 to 44 microns pumice powder size fractions is widespread in this area.

Furniture finishes can be polished to a high or low sheen using the gentle abrasive power of pumice. Pumice powder is used for antiquing and polishing. It is also a key ingredient in French Polishing. The pumice particle size of 325 Mesh (44 microns) is commonly used in hand rubbing satin finishing and gold leafing finishing applications.

Pumice powder is highly recommended for surface finishing and scratch removal prior to the etching and engraving of glass. Due to the particular physical structure of pumice, it provides a smooth but effective abrasive action. The brittle and chemically inert nature of the material is unique [Gündüz *et.al.*, 2001]. It is a natural polishing media, which is ideal for a wide variety of glass treatments such as polishing of toughened and flat glass, crystal, aerospace windscreens, and the newly developed low iron glass. Polishing of crystal with pumice has been a traditional pre-polish glass treatment for many years. The necks and bases of blanks are given particular attention by technicians in the workshop using felt and cork wheels. For these application fields, 80 to 325 Mesh (44 to 177 microns) pumice particulates are unique.

Different grades of pumice particulates can be used for a wide variety of horticulture, turf, and sports turf applications. Most of these applications benefit from the lightweight and porous

nature of pumice [Gündüz *et.al.*, 2001]. The abrasiveness and friability of pumice has a long history of use in the buffing of leather goods. 80 to 325 Mesh (44 to 177 microns) pumice particulates are unique for leather buffing.

Pumice is also a natural polishing media ideal for metal treatments. Due to its unique physical structure, it has a smooth but effective abrasive action suitable for copper treatments. The microscopic action of the pumice particles creates a surface ideal for maximum adhesion of coatings in aluminum extrusions. Pumice leaves metal surfaces smooth with a satin-like finish. It is also used for surface finishing prior to etching and engraving. In the jewelry and silver trade, pumice is recommended as a buffing media [Gündüz *et.al.*, 2001]. It is used in the first stage of polishing, where fine abrasive media is required. Without buffing, the final mirror finish cannot be achieved by polishing technicians. For this abrasive media, although 12 microns median particle size fraction of pumice powder is recommended, 80 to 325 Mesh (44 to 177 microns) pumice powder size are also used.

Different pumice powder sizes are also widely used in the paint and coatings industry. The low density and unique particle morphology of the vitreous pumice imparts many desirable properties to the paint formulation [<http://crminerals.com>]. Pumice has applications in both the body and glaze of pottery. 12 microns median particle size of pumice powder is unique for pottery glazing applications. However, 30 to 325 Mesh (44 to 600 microns) pumice particulates are also occasionally used for this area.

Rubber pumice abrasive wheels are excellent for many cleaning, polishing, and finishing needs. They are made from

natural rubber with imbedded pumice grains that are evenly distributed to assure uniform results. The light abrasive action produces a smooth finish on soft metals. Pumice-Based Erasers are the standard for almost every office/school grade pencil [<http://crminerals.com>]. They will erase the toughest graphite markings, and they are particularly effective on hard papers, such as photocopy paper. Mold Release Agents act as an interface between the mold surface and the material being molded. Many specialty mold release agents incorporate a natural abrasive such as pumice into their mold release compounds.

The porous, lightweight, and surface activity of pumice filtration media provides unique advantages in water treatment processes. Water treatment processes using the pumice powders are as aerobic digestion, anaerobic digestion, clarification, filtration, odor control and sludge treatment.

Pumice is an essential addition in the Sequencing Batch Reactor (SBR) process where inadequate time has been allowed for phase separation to take place. The addition of small amounts of pumice just prior to the settlement stage enhances the settlement of the sludge allowing the water treatment plant to perform up to or beyond design capacity. The anaerobic digestion process destroys/digests organic wastes in the absence of air. This biological process, unlike aerobic digestion which produces CO₂, produces methane gas, CH₄. Pumice acts as a biomass support in this process, typically employed in the treatment of wastes from municipal sludge and industrial wastes from breweries, sugar processing, paper manufacturing, and dairies. The concentration of biomass is significantly increased, growing in ideal conditions on the porous surface of the pumice,

resulting in reduced retention times and higher methane gas generation [<http://crminerals.com>]. Pumice, when added to the raw water, increases the density of the flocs that result from the coagulation process, and accelerates sedimentation. Coagulation occurs when the raw water reacts with the chemical coagulant and the flocks then attach themselves to the pumice particles, giving a ballast effect. Settlement occurs under gravity and the clarified water is recovered from the upper part of the clarifier with the sludge being removed from the bottom. This process is suited to potable water, sewage treatment, and industrial effluent treatment.

Hydrogen sulfide (H₂S) gas is emitted during the treatment of municipal sewage and other industrial organic wastes. Hydrogen sulfide is a highly toxic and malodorous gas, which is severely irritating. When hydrogen sulfide gas is passed through a bed of pumice, the porous nature of pumice efficiently removes the corrosive gas. Oftentimes, odor control with pumice is a cost effective alternative to activated carbon, with the additional benefit that pumice powder is harder than activated carbon, and therefore less subject to mechanical breakage. On the other hand, the safe disposal of sludge derived from the biological treatment of sewage or industrial effluents often requires an additional step of de-watering. De-watering by evaporation, centrifugation, or filtration are the most common methods of dewatering. The addition of pumice to the sludge prior to filtration provides improved de-watering [<http://crminerals.com>]. The porous nature of the pumice produces a more cohesive filter cake that reduces filter cloth blinding, allows greater filter runs with improved filtrate quality, and produces a cake that can be used for agricultural or horticultural purposes.

Pumice powder is also used in composite material structure as a raw material and/or an additive material. The lower size fractions from 270 Mesh pumice are preferably used to make armour plates for defense situations. It could be used for this purpose in developing the armored cars, air crafts, automobiles etc. 60 to 400 Mesh size fractions of pumice powders are preferentially used for producing the fire resistant materials as additives, too.

3. CONCLUSIONS

Well-known natural porous lightweight aggregates are pumice, tuffs, scoria, volcanic slug and diatomite rocks. Because of their nature, usage and producing abilities, they are all ecologic materials. Specifically their powder form sizes are getting world wide and these powder materials are used in different industrial areas as a raw material and/or an additive material. Turkey has great chance to have all these porous lightweight materials. The potential reserves of these lightweight materials in Turkey will take part an important role for industrial future of the world.

REFERENCES

- Gass I.G., Smith P.J., Wilson R.C.L., 1973, Understanding the Earth, Open University Set Book, 383.
- Gündüz L., 1998, Pomza Teknolojisi, (ed.) Cilt I, Isparta.
- Gündüz L., Rota A. ve Hüseyin A., 2001. The Assessment Of Material Characteristics Of Central Anatolian Pumice Stones For Civil Construction Industry With Special Reference To SEM Pumice Stone, 4th International Symposium on Eastern Mediterranean Geology, Isparta, Turkey, 21-25 Mayıs.
- Gündüz L. and Uğur I., 2004, Turkish Pumice How Pumice is Used Depends on Its Chemistry and Physical Structure, Industrial Minerals, May, USA, No:440, p45-49.
- Gündüz L. 2005, İnşaat Sektöründe Bimsblok, Isparta, s928.
- Gündüz L. 2008, Use of quartet blends containing fly ash, scoria, perlite pumice and cement to produce cellular hollow lightweight masonry blocks for non-load bearing walls,

- Construction and Building Materials 22, 747–754.
- Ritmann L., 1976, Volcanoes, Orbis Publishing, LondonUK.
- Vagt, O., 1994. Mineral Aggregates, 32.2 Canadian Minerals Yearbook, Natural Resources Canada, Canada,
- Vikursteypur A., 1988, Ny notkunarsvig (Pumice concrete – New Applications) IBRT Report.
- Yasar E., Tolgay A. and Teymen A., 2009, Industrial Usage of Nevsehir-Kayseri (Turkey) Tuff Stone, World Applied Sciences Journal 7 (3): 271-284.
- <http://geology.about.com>
- <http://crminerals.com>

THE ADVANTAGES OF USING NANO PCC (PRECIPITATED CALCIUM CARBONATE) IN PRODUCTION OF COATED CARTON

M.MÜDÜROĞLU^{1,a}, Z.ARSOY²

1-Adaçal Endüstriyel Mineraller San.Tic.A.Ş., Afyon

2-Adaçal Endüstriyel Mineraller San.Tic.A.Ş., Afyon

a. *Corresponding Author (mmuduroglu@adacal.com.tr)*

ABSTRACT: Precipitated Calcium Carbonate (PCC), produced synthetically from limestone, has superior specifications with high CaCO₃ ratio and low impurities, availability of production in different morphologies and nano size compared to Ground Calcium Carbonate (GCC) and other industrial minerals used as filler in industry. PCC, with these superior specifications, is used as functional filler in many different industries specially abroad such as paper, coatings, plastic, etc.

Considering consumer demand, costs and environmental factors, new improvements which will meet different requirements are needed in carton production. The carton should both have enough resistance to rupture, bursting, tear and at the same time enough liquid absorption, folding endurance for all the process applied during and/or after carton coating. Coating process of the carton surface is very important to improve print quality.

This experimental study has been conducted with adaCAL nano PCC instead of GCC which is used as filler in coating mixture applied on base carton surface. Hiding power, whiteness, ink absorption and physical strength of the coating on carton surface have been examined with the help of SEM (Scanning Electron Microscope) images and an optimum coating mixture formula has been determined for an ideal carton surface.

1.INTRODUCTION

Carton can be recycled and suitable for offset print and that's why it is an indispensable material for use of packaging sector. Functions of carton package can be explained as; to protect the product from exterior effects, to provide the carriage of the product and to increase the demand of consumer by enhancing the product sales appeal. Quality of the carton package is directly related with the visual effects of the print design and quality of each step at printing process. If the physical and chemical properties of the carton is not OK then there is nothing much to do by printer to increase printing quality. First condition of the quality print is to have a carton surface with homogenous/smooth surface and whiteness. It is necessary to have an

optimum coating process to get an optimum printing surface. Hence the ink contacts with coated layer this surface should have optimum specification for printing. Also breaking length, burst and tear strengths, liquid absorption (cob), stiffness should be OK after printing process. During the offset printing on coated carton surface all the problems are faced on interface between coating and ink.

There are different types of cartons produced for different purposes. Uncoated cartons which are commonly used in packaging sector has four layers;

➤ Bottom layer: Interior side of the box. Strong but not well looking. Clean recycled paper pulp is used for production.

➤ Middle layer: Recycled corrugated, Kraft, wood-containing paper and newspapers are used without classification.

➤ Protective top layer: Wood free high grade printing paper pulp is used to hide grey colour coming from middle layer and not to decrease whiteness of top layer.

➤ Top layer: This layer is the strong and well looking exterior part of the package. Therefore it is produced from 100% cellulose pulp(short fiber& long fiber)

1.1. Coating Ingredients

Raw materials used in coating process can be categorized under 3 major topics. These are;

1. Pigments
2. Binders
3. Additives

a. Pigments: Pigment is the basic element for coating mixture which can significantly effect the quality and cost of the coating. Specially white pigments are used in paper and carton coating process. In the formula 80-90% of coating weight are generally pigments which means 70% of coating volume.

Pigments are also classified into 3 groups;

- Basic pigments
- Special pigments
- Additional pigments

Basic pigments:

- Kaolin
- Ground Calcium Carbonate (GCC)
- Talc

Special pigments:

- Gypsum

Additional pigments:

- Precipitated Calcium Carbonate (PCC)
- Calcined kaolin
- Plastic pigments

➤ Aluminium trihydrates

➤ TiO₂

Printing features are improved by using additional pigments. Optical properties (whiteness and opacity), brightness and ink absorption values are improved with these pigments usage (Klass, 2004; Lehtinen, 2000, Mosher, 1952, Zang, 1994 and Sönmez, 2000). The following properties of pigments determine the characteristics of carton coating process (Özden, 2005 and Klass, 2004);

- Particle size and distribution (smaller particle size higher brightness and opacity)
- Particle shape and shape distribution
- Refractive index
- Light scattering and absorption
- Density

b. Binder: Pigment particles are hold together and coating mixture is fixed on carrier board by binder (Bitla, 2002 and Sönmez, 2008). Wax strenght is improved with the increase of binder amount.

c. Additives: A group of material which are used in the formula to get an optimum coating mixture for the process. Additives used in carton coating industry are as follows (Naydowski, 1995; Nilsson, 2007 and Casey, 1960);

- *Anti foam agent*
- *Dispersion agent*
- *Rheology agent*
- *Binder aid*
- *Optical brightener*
- *Lubricants*

2. MATERIAL AND METHOD

This experimental study has been conducted by paper study group at Adacal Ind. Min. Co. using his own laboratory and incorporation with different universities.

In the experiments, adaCAL PCC has been replaced instead of GCC which is used as filler in carton coating formula

and examined for the effects on end product.

Costik	0.3-0.7
Latex	10-15
Thickener	0.1-0.3

2.1. Carton Coating Studies

A standard/average carton coating formula used in the sector is given in Table 2.1.

Table 2.1: Carton coating formula.

Raw Material	Amount (%)
Pigment (CaCO ₃)	85-90
Rheology agent	0.1-0.5

adaCAL PCC has been replaced at different ratio instead of GCC by considering the Table 2.1 as standart formula (Table 2.3). Technical specification of GCC and adaCAL PCC used in the formulas are shown in Table 2.2.

Table 2.2: Technical specification of GCC and adaCAL PCC used in the formulas.

Sample	Whiteness			Particle Size (µm)				Surface area BET (m ² /gr)
	L*	a*	b*	d ₁₀	d ₅₀	d ₉₀	d ₉₇	
GCC	98,65	0,12	1,03	1,16	4,15	9,11	12,05	4,933
adaCAL P1	99,45	0,06	0,56	0,3	0,80	1,1	1,6	9,348
adaCAL B1	99,33	0,05	0,45	1,67	2,63	4,15	4,72	14,068

Table 2.3: Experimental study plan with GCC and adaCAL PCC.

Sample No	Amount(%)	Sample No	Amount(%)
ZA-2013/1 Standart	100 (GCC)	ZA-2013/7	75 (GCC)
			12,5 adaCAL P1(PCC)
			12,5 adaCAL B1(PCC)
ZA-2013/2	75 (GCC)	ZA-2013/8	75 (GCC)
			6,25 adaCAL P1(PCC)
			18,75 adaCAL B1(PCC)
ZA-2013/3	50 (GCC)	ZA-2013/9	50 (GCC)
			36,5 adaCAL P1(PCC)
			13,5 adaCAL B1(PCC)
ZA-2013/4	75 (GCC)	ZA-2013/10	50 (GCC)
			25 adaCAL P1(PCC)
			25 adaCAL B1(PCC)
ZA-2013/5	50 (GCC)	ZA-2013/11	50 (GCC)
			13,5 adaCAL P1(PCC)
			36,5 adaCAL B1(PCC)
ZA-2013/6	75 (GCC)		
		18,75 adaCAL P1(PCC)	
		6,25 adaCAL B1(PCC)	

2.2. Viscosity

It is very important to supply optimum slurry viscosity due to process application conditions. While transfer/pumping problem of the slurry can be seen at higher viscosity, lower viscosity may

cause foaming and splashing during application. All viscosity values of slurries from experimental study have been determined by Brookfield DV-III Ultra instrument at 100 rpm and 24 °C (Figure2.1).

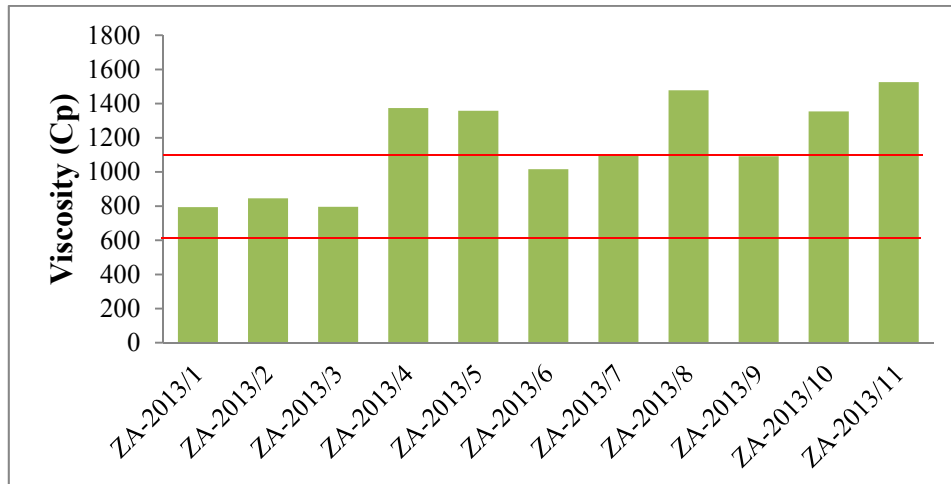
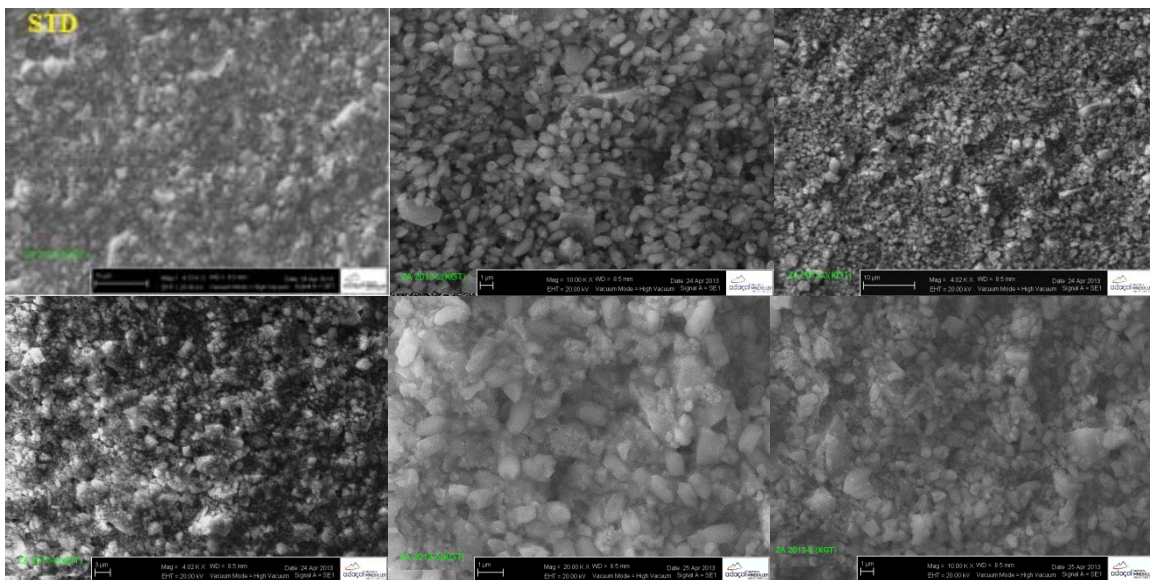


Figure 2.1: Viscosity values of experimental studies.

Viscosity of the slurry has been increased with the addition of adaCAL PCC but still within the application standards 600 – 1100 Cp. Viscosity can be decreased down to more acceptable levels with some improvement (like decreasing the amount of reology agent, etc.) on formula. These improvements will also decrease the product's cost.

2.3. Scanning Electron Microscope (SEM) Photos Of Coated Surfaces

Prepared coating formulas have been applied on carton surface by using a 60 μm applicator. These surfaces were examined for smoothness and material distribution by Scanning Electron Microscope (SEM) (Figure 2.2).



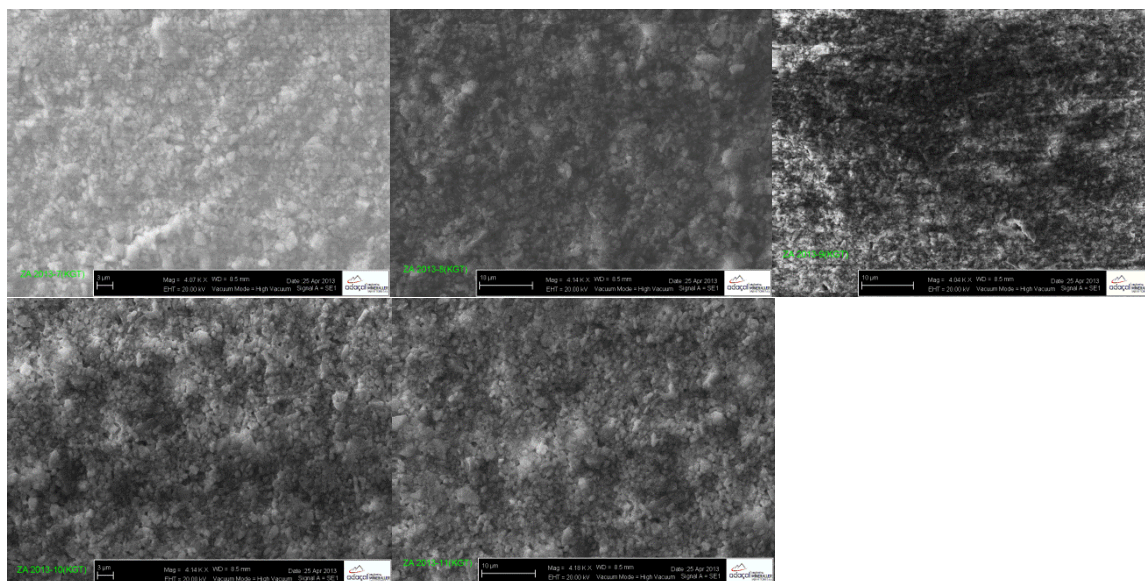


Figure 2.2: SEM photos of coated surfaces.

Table 2.4: Opacity & Porosity values of the prepared formulas.

Sample No	Opacity (%)	Porosity (%)
ZA-2013/1 Std	90.43	87.40
ZA-2013/2	94.61	85.23
ZA-2013/3	94.74	85.90
ZA-2013/4	96.36	84.06
ZA-2013/5	97.74	85.27
ZA-2013/6	93.78	80.14
ZA-2013/7	98.27	84.47
ZA-2013/8	98.48	82.78
ZA-2013/9	99.77	85.58
ZA-2013/10	96.34	84.92
ZA-2013/11	99.83	82.95

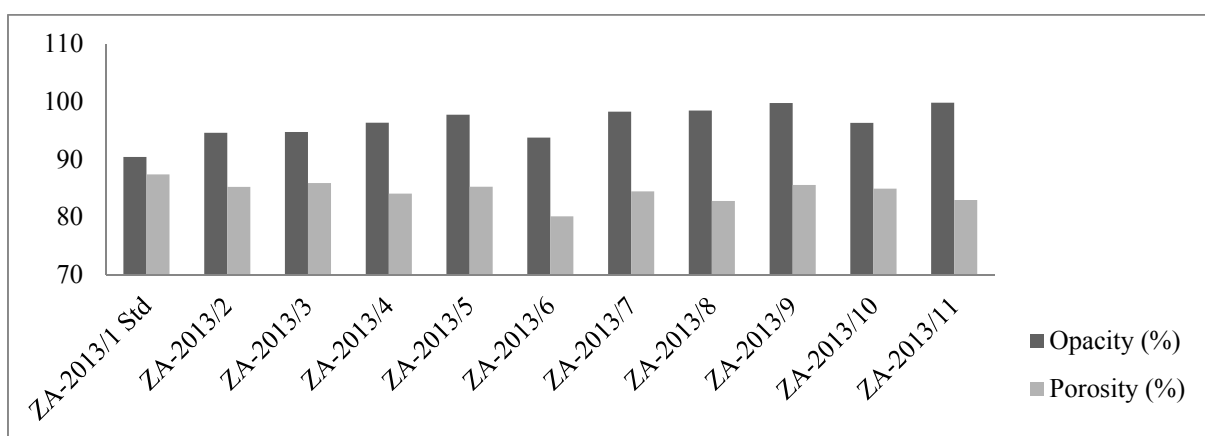


Figure 2.3: Opacity & Porosity values of the prepared formulas.

Ink absorption of carton coating is directly related with opacity and porosity. Maximum opacity and minimum porosity is required for an ideal/optimum carton coating. There is a significant increase on

2.5. Whiteness

White surface of the carton coating improves the printing quality. Therefore, additional pigments (TiO₂, PCC, Calcined kaolin, plastic pigments, etc..) are used in coating formula to improve the printing quality. Whiteness (L) values are improved by adding adaCAL PCC in the formula (Table 2.5).

Table 2.5: Colour Index of the prepared formulas.

Sample No	Colour Index (%)		
	L*	a*	b*
ZA-2013/1 Std	91.27	-0.05	-0.63
ZA-2013/2	92.23	-0.13	-0.43
ZA-2013/3	93.18	-0.19	-0.51
ZA-2013/4	92.30	-0.21	-0.83
ZA-2013/5	94.15	-0.38	-0.9
ZA-2013/6	94.05	-0.2	-0.09
ZA-2013/7	92.17	-0.16	-0.7
ZA-2013/8	91.42	-0.15	-1.01
ZA-2013/9	93.27	-0.19	-0.54
ZA-2013/10	94.26	-0.26	-0.43

Whiteness values are increased with the addition of adaCAL PCC (Table 2.5.)

3. RESULTS

Homogenous white and smooth surface is the first condition of high quality print. Therefore, an optimum coating process is needed to get an ideal printing surface. Hence the ink contacts with coating layer during the printing process, this layer should have optimum features for printing. Pigments are generally 80-95% of the coating weight in the formula. Therefore, coating is the most important step of carton production process. After experimental studies;

opacity values with the use of adaCAL PCC in formulas (Table 2.4.). At the same time high opacity means high whiteness.

- With the use of adaCAL PCC, it is determined that the carton has more homogenous surface due to better dispersion.
- With the use of adaCAL PCC, the coating quality of the carton has been increased and the viscosity of the slurry were maintained within process standards.
- With the use of adaCAL PCC, opacity has been increased and porosity decreased which shows the good conditions for optimum ink absorption were supplied.
- With the use of adaCAL, whiteness values which directly effects the printing quality were also increased.

Finally, adaCAL PCC used as additional pigment in the formula, is increasing the carton coating quality and decreasing the costs with its affordable unit price compared to other pigments.

REFERENCES

- Bitla, S., (2002); Application on Raman Techniques for Paper Coatings, M.s. Thesis, Maine University.
- Casey, J.P., (1960); Selüloz ve Kağıt, Kimyası ve Kimya Teknolojisi, Cilt: 3, Interscience Publishers Inc., Newyork, USA, 1284-1312.
- Klass, C.P., (2004); Introduction to Formulating Coatings for Paperboard, Klas Associates INC., Radnor, PA, 1-4.
- Lehtinen, E., (2000); Pigment Coating and Surface Sizing of Paper, Chapter 4: Coating Pigments – General, Published in Cooperation with The Finnish Paper Engineers Association and TAPPI, Jyväskylä, Finland, 61-66.
- Mosher, R.H., (1952); The Technology of Coated and Processed Papers, Chemical Publishing Co., Inc., New York, USA, 181, 133-145.
- Naydowski, C., (1995); Properties of Calcium Carbonate Pigments, Senior Vice President,

- R & D Technical Service, Plüss – Staufer AG, Oftringen, Switzerland, 1-10.
- Nilsson, K., (2007); Film Formation of Latex in Dry Coating Films, Master Thesis, Karlstad University, Department of Chemical Engineering, Sweden, 4.
- Özden, Ö., (2005); Kağıt yüzey İşlemleri, *Ders Notu*, İstanbul Üniversitesi Orman Endüstri Mühendisliği Bölümü Orman Ürünleri Kimyası ve Teknolojisi Anabilim Dalı, İstanbul, 1-5,
- Sönmez, S., (2008); Kartonun Yüzey Özelliklerinin Değiştirilerek Basılabilirlik Niteliğinin Geliştirilmesi, Marmara Üniversitesi Fenbilimleri Enstitüsü, Matbaa Eğitimi Anabilim Dalı, Doktora Tezi, İstanbul, 220 sf.
- Zang, Y.H. and Aspler, J.S., (1994); The Influence of Coating Structure on The Ink Receptivity and Print Gloss Development of Model Clay Coatings, International Printing and Graphic Art Conference, Canada, 193-199.

RELATION BETWEEN RHEOLOGICAL PROPERTIES AND PORE STRUCTURE OF THE FLY ASH/CEMENT BASED AAC MORTAR AND PRODUCT PROPERTIES

M. Serhat Başpınar^{1a}, Gökhan Görhan², Erhan Kahraman² and İsmail Demir²

1. Afyon Kocatepe University, Technical Education Faculty., Metal Education. Dept., Turkey
2. Afyon Kocatepe University, Engineering Faculty, Department of Electric Engineering, Turkey.
a. Corresponding author (sbaspınar@aku.edu.tr)

ABSTRACT: Fly ash/cement based AAC mortar viscosity changes during the hydration period. When hydration occurs, at the same time Hydrogen gas evolved. Successful pore formation depends on the nucleation, growth and stability of the gas bubbles. However, growth and stability of the gas bubbles depends on the hydrostatic pressure exerted by the mortar. Hydrostatic pressure depend mainly on the viscosity of the mortar. The main objective of this study was to investigate the effect of mortar viscosity on the properties of the fly ash/cement based AAC. Different fly ash/cement ratios and water content mortars were tested by using Viskomat-NT rheometer. Replacement of fly ash with silica fume was also studied. Physical and mechanical properties, pore structure were measured for each series and their relations with starting rheological properties were investigated. It was concluded that, rheological properties of the mortar is important factor for the macrostructure (pore structure, pore size and distribution) of the AAC and rheological properties of the starting mortar can be used as a material design criteria for the designing new foam concretes by using new materials other than conventional AAC raw materials.

1. INTRODUCTION

Aerated concrete is classified as lightweight concrete. It is a kind of either cement or lime mortar in which air-voids are entrapped in the mortar matrix by a suitable aerating agent. The important advantage of aerated concrete is its lightweight, which economizes the design of supporting structures. It has a high degree of thermal insulation and considerable savings in energy and the static loading of the building. Wide range of densities (300-1800 kg/m³) can be produced for several application like structural, partition and insulation purposes. AAC is also a good alternative for the mass utilization of the SiO₂ and CaO rich industrial wastes. Several researchers investigated the partial replacement of waste material instead of quartz rich sand or lime in AAC production. Copper tailings, blast furnace

slag [Huanget *al.* 2012], gasification residues [Holt *et al.* 2005], fly ash from cellulose industry [Hauser *et al.* 1999], coal bottom ash [Kuramaet *al.* 2009] are some examples which were studied by several researchers.

The knowledge of mortars rheology may contribute to understand the behavior of fresh materials and can allow predicting their flow properties. As a consequence, it helps in determining the easy of use for each specific application and since it is a reliable testing method it will help in achieving the optimal formulation and its best properties control. Besides, a relationship is predicted between properties in the fresh and hardened condition, so its use will also help to control the ultimate properties of the mortar. Fresh mortars behave according

to the Bingham model, in which the properties can be expressed by two fundamental rheological parameters, yield stress and viscosity, according to the formula (Figure1):

$$\tau = \tau_0 + \eta\dot{\gamma}$$

where τ (Pa) is the shear stress at shear strain rate $\dot{\gamma}$ (s^{-1}) and τ_0 (Pa) and η (Pa s) are the yield stress value and plastic viscosity, respectively [Tattersal and Banfill, 1983]. The objectives of this work were to investigate the effect of AAC mortar constituents and their relative proportions on the pore structure and properties of the hardened fly ash based AAC. Based on the obtained results it is possible to optimise the AAC mortars composition in order to assure proper working conditions and product properties.

2. EXPERIMENTAL

Fly ash was supplied from one of the thermal power plant in Turkey (Seyitömer TPP). Silica fume was obtained from Antalya-Etibank Ferro-Alloy Production Plant in Turkey. Cement was appropriate to the TS EN 197-1 CEM I (42,5R). Fly ash was classified as F type fly ash according to ASTM C-618. Fly ash and cement have Blaine fineness number of 2564 cm^2/g and 3054 cm^2/g respectively. Fly ash mainly composed from quartz phase and silica fume has almost non-crystalline phase structure.

Mixtures first put into the cylindrical cups of the rotary rheometer. Then the spindle which has a special geometry was put into the mortar. When the spindle starts to turn, rheometer measures the resistance of the mortar to the rotation of the spindle as a rotational torque value. Depending on the selected rotational speed program, torque values were measured. Picture of the rheometer is given in Figure 2.

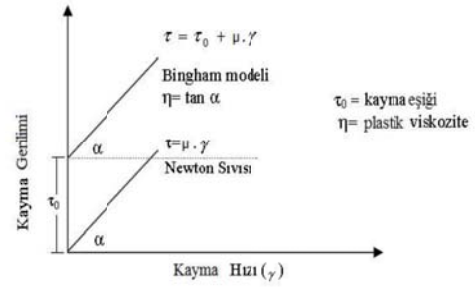


Figure 1: Relation of shear stress and shear rate of Bingham flow and Newtonian flow.



Figure 2: Rheometer and spindle geometry used in the experiments.

During the experiment, depending on the spindle speed (N-shear rate) and time, torque values (Shear stress) were measured. By drawing Torque-speed graph and using the Bingham model (Equation 1.) other rheological properties were determined. For the yield stress g (N mm) and for the plastic viscosity h (N mm min) symbols were used for the determination of rheological properties of the different mortars.

$$T = g + hN \dots \dots \dots \text{Equation (1)}$$

Programming the shear rate vs time is an important point when measuring the rheological properties of the mortar. Due to the sedimentation tendency of the coarser particle in the mortar, experiments should start with high rotational speed. For this reason, a program from higher to lower speed was applied. Applied speed program is given in Figure 3. When determining the test duration, gas evolution period from the aluminum metal was taken into account and therefore 15 minute test time was chosen.

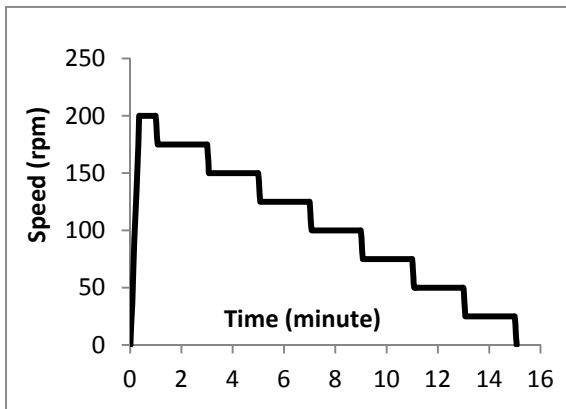


Figure 3: Spindle speed program.

3. RESULTS AND DISCUSSIONS

Rheological measurements showed that when the water amount of the mixture is increased in similar solid content, the yield stress of the mixtures decreased. Increasing water content of the mortar decreased the yield stress at the beginning of the test. However, relation between plastic viscosity and water content was seems to be more complicated. Water/solid ratio of the mixture is directly related with the cement hydration. Water/solid ratio of the mortar was closely effected the viscosity of the mortar system. Depending on the high cement content and low water/solid ratio rheological properties of the mortar changed and more amount of hydration

products occurred. Parallel to the cement amount decrease, yield stress and viscosity values decreased (Figure 4).

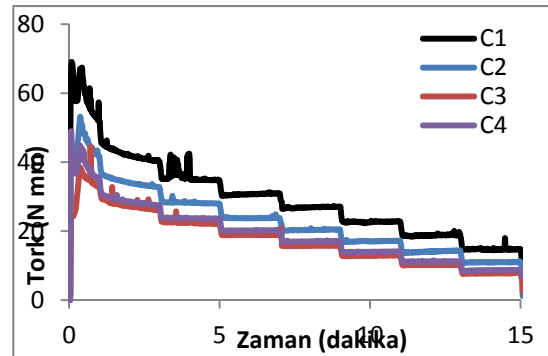


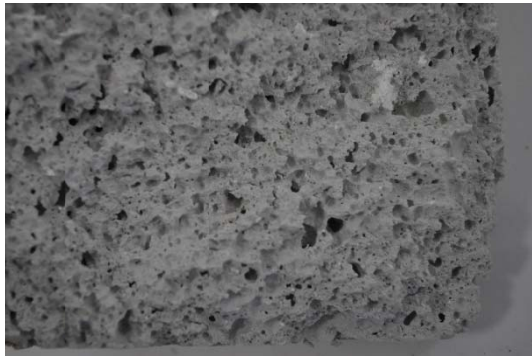
Figure 4: Variaton of the yield stress with composition change of the mortar.

Macroscopic investigations show that when the viscosity of the mortar increased, cell size of the concrete decreased. Figure 5 shows the variation of the cell size depending on the different viscosities. Figure 5a shows the cell size of the sample which has the lowest viscosity in the experiments and Figure 5b shows the cell size of the sample which has the highest viscosity in the experiments.

Figure 6 shows the viscosity and the bulk density variations of the samples. According to the graph, when the viscosity increased the bulk density increased. When comparing the cell structure of the samples with the viscosity vs. bulk density relation, good correlation was obtained. Lower viscosity mortars cannot resist the growth of the gas bubbles and therefore bigger cell structure was observed.

5% Silica fume addition showed the lowest yield stress and viscosity values over the all series of mortars. This behaviour showed that two behaviour of the silica fume effects the rheological properties of the mortar. Silica fume has very small particle size distribution, and these small particles fill the bigger

particles of the mortars and make easier flow of the particles over them. However, excess silica fume resulted in better hydration and finally faster hydration occurred. Faster hydration results in increase in the viscosity and the yield stress.



(a)



(b)

Figure 5: Cell structure of the lowest (a) and highest (b) viscosity samples.

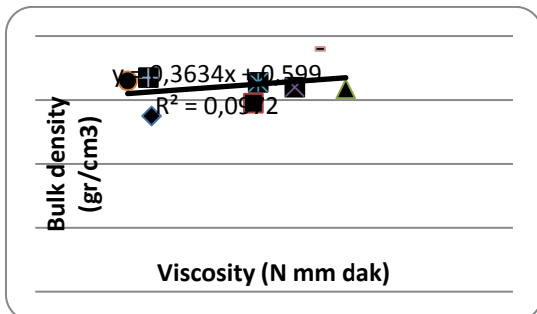


Figure 6: Viscosity vs bulk density variation of the samples.

4. CONCLUSIONS

Experiments showed that cement content, water/solid content of the mortars, addition of active pozzolan have strong effects on the rheological properties of the AAC mortars. Rheological properties of the AAC mortar strongly affect the pore structure of the product.

Acknowledgements: Authors wish to thank to Tübitak (Turkish National Scientific Research Council) which allows the financial support under project number 109M245.

REFERENCES

- Hauser, A., Eggenberger, U., & Mumenthaler, T. (1999) Fly ash from cellulose industry as secondary raw material in autoclaved aerated concrete. *Cement and Concrete Research*, 29, 297–302.
- Holt, E., & Raivio, P. (2005) Use of gasification residues in aerated autoclaved concrete. *Cement and Concrete Research*, 35, 796–802.
- Huang, X., Ni, W., Cui, W., Wang, Z., & Zhu, L. (2012) Preparation of autoclaved aerated concrete using copper tailings and blast furnace slag. *Construction and Building Materials*, 27, 1–5.
- Kurama, H., Topçu, I.B., & Karakurt, C. (2009) Properties of the autoclaved aerated concrete produced from coal bottom ash. *Journal of Materials Processing Technology*, 209, 767–773.
- Tattersal, G. H. and Banfill, P. G., *The Rheology of Fresh Concrete*. Ed. Pitman, London, 1983.

INVESTIGATION ON UTILIZATION OF BIOPLASTICS IN TURKEY

Ezgi Bezirhan¹, H. Duygu Ozsoy^{2,a}

1. Environmental Engineering, Mersin University, Mersin, Turkey

2. Environmental Engineering, Mersin University, Mersin, Turkey

a. Corresponding author (ozsoyhd@gmail.com)

ABSTRACT:In the last decades there has been a significant increase in the amount of plastic wastes all over the world. Increasing environmental concerns/legislative pressure for petroleum-based plastics waste and rapid increases in the cost of petroleum have enabled to the development of bioplastics. “Bioplastics” are polymers made from renewable resources such as corn, sugars, potatoes, etc., and this materials have a wide range of applications in packaging, consumer goods, electronics, transportation, construction, medical and many other fields. The global bioplastics market is thought to be growing at a rate of as much as 20% per year. Total consumption of bioplastics worldwide at an average annual growth rate of 13% from 2009 to 2014. Bioplastics are currently considered the way to go and may be the only alternative in the future as fossil resources become exhausted. Whereas the bioplastics has yet known in recently and bioplastics technology development is in adequate in Turkey. Firms in the plastic industry should to be act in partnership for developing bioplastic technology in Turkey.

1. INTRODUCTION

Plastic materials are currently considered very important materials due to their properties and performance over other materials such as metal and wood [Aguado and Serrano, 1999, Azapagic et al, 2003, Plastics Europe, 2008, Rosato and Rosato, 2003, Alvarez-Chavez et al, 2011]. So plastics are used in a wide range of applications and generated huge amounts of plastic wastes all over the world [Stevens, 2002]. The plastics have caused extensive environmental problems associated with their disposal [Wu, 2009]. Because of environmental pollution problems caused by using plastic made by petrochemicals, the development of environmental friendly materials has attracted extensive interest [Gaspar et al, 2005]. Nowadays, manufacturers and researchers are developing *bioplastic* materials that one of environmental friendly materials. Although the bioplastic utilization and production is known all over the world,

the bioplastic production has just started in Turkey.

The aim of this study emphasizes the importance of the production and use of bioplastic at different application areas.

2. WHAT IS BIOPLASTIC?

Generally, ‘bioplastic’ are made from renewable resources such as corn, sugars, potatoes, etc., and they can be degraded under controlled conditions of biodegradation [Karana, 2012; Sarasa et al., 2009]. There are four types of degradable plastics: photodegradable bioplastics, compostable bioplastics, bio-based bioplastics and biodegradable bioplastics.

Photodegradable bioplastics have light sensitive group incorporated directly into the backbone of the polymer as additives. Extensive ultraviolet radiation (several weeks to months) can disintegrate their polymeric structure rendering them open

to further bacterial degradation. However, landfills lack sunlight and thus they remain non-degraded [El Kadi, 2010].

The Business-NGO Working Group for Safer Chemicals and Sustainable Materials defines *bio-based bioplastics* as “plastics in which 100% of the carbon is derived from renewable agricultural and forestry resources such as corn starch, soybean protein and cellulose” (Business-NGO Working Group for Safer Chemicals & Sustainable Materials, 2007). The US Department of Agriculture defines bio-based plastics as “commercial or industrial goods, (other than feed or food), composed in whole or in significant part of biological products, forestry material, or renewable domestic agricultural materials, including plant, animal or marine materials” (The Biodegradable Products Institute, 2006) [Alvarez-Chavez et al, 2011].

Compostable bioplastics are biologically decomposed during a composting process at a similar rate to other compostable materials and without leaving visible toxic remainders. In order to designate a plastic as bio-compostable, its total biodegradability, its disintegration degree, and the possible eco-toxicity of the degraded material must be determined by means of standard tests (AENOR, 2001; Tuominen et al., 2002) [Sarasa et al., 2009].

Biodegradable bioplastics are fully degraded by microorganism without leaving visible toxic remainders. The term “biodegradable” refers to materials that can disintegrate or break down naturally into biogases and biomass (mostly carbon dioxide and water) as a result of being exposed to a microbial environment and humidity, such as the ones found in soil, hence reducing plastic waste, whereas bio-based sustainable materials (Haugaard et al., 2001;

Lagaron, Gimenez, & Sanchez-Garcia, 2008; Petersen et al., 1999). The fourth types of bioplastics are rather promising because of its actual utilization by microorganism [El Kadi, 2010].

3. THE BIOPLASTIC MARKET

Researchers have developed several tools to assist in decision-making about plastics selection. The plastics pyramid (Figure 1) developed by Thorpe and Van der Naalde in 1998 was an early attempt to visually display the life cycle hazards of different plastics to assist in materials selection. In this pyramid, bioplastic the bottom of the pyramid, indicating they are most preferable, as they are made from renewable resources, and theoretically are biodegradable and compostable [Alvarez-Chavez et al, 2011].

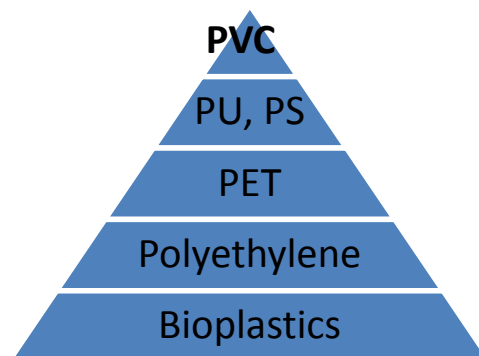


Figure 1: Plastics Pyramid (PVC: Polyvinyl chloride, PU: Polyurethane, PS: Polystyrene, PET: Polyethylene terephthalate)

Since the plastics pyramid was developed, bioplastics are much further along in their commercial development.

Packaging films and containers bioplastics are particularly interesting, since most of these products have a relative short service life and end up in landfills (Figure 2). Biodegradable bioplastic have been found to possess wide range of properties, which find

application in biomedical field like making bone plates and screws, in drug delivery carriers and tissue engineering scaffolds (Marquesa et al., 2002) [Kaith et al, 2010].



Figure 2: Bioplastic spoon

Many countries around the world have already begun to integrate these materials into their technologies. In America, McDonald's is now making biodegradable containers for their fast food. Other companies such as Bayer, DuPont [Iles and Martin, 2013], Dow Cargill, Nike and Danone etc. are also producing biodegradable packaging.

The global bioplastics market is thought to be growing at a rate of as much as 20% per year. Bioplastics approximately 10-15% of the total plastics market and will increase its market share to 25-30% by 2020. The bioplastic market reached over 1 billion US\$ in 2007 and it will be over 10 billion by 2020. More and more companies are entering and investing in this market. New applications and innovations in the automotive and electronics industry lead to market boom.

The Australian Government has paid 1 million dollars to research and develop starch-based bioplastics. Japan has created a biodegradable bioplastic that is made of vegetable oil and has the same strength as traditional plastics. All of these developments have been the world many years ago. However, the bioplastic markets have been developed in Turkey in the last years. Ministry of Environment and Urban Planning recently announced that merchants must use *photodegradable*

bioplastic bags. Approximately 250-300 tonnes of bioplastic materials were imported to Turkey in 2012. In the first half of 2012, the bioplastic producer industry Packberk undertook the bioplastic production in Turkey and now bioplastic materials have only been produced by this industry.

3. RESULT AND DISCUSSION

S.Berkeschin Michigan Univesity reported in March 2005 "Bioplastics: A Rebirth of Plastic". The future of biodegradable plastics show great potential. Here are the advantages of bioplastics materials;

Independence; Bioplastic is made from renewable resources: corn, sugarcane, soy and other plant sources as opposed to common plastics, which are made from petroleum.

Energy efficiency; Production uses less energy than conventional plastics.

Eco-safety; According to the one source, bioplastic also generates fewer greenhouse gasses [Yu and Chen, 2008] and contains no toxins.

The advancement of biodegradable technology has risen in recent years and there are growing signs that the public shows a high amount of curiosity in the product. With the variety of biodegradable plastics available in near future, there will be a place for them current plastics. There certainly are an abundant amount of materials and resources to create and fund more uses for bioplastic in Turkey.

4. CONCLUSIONS

In the future, bioplastics will replace to common plastics. Therefore, a new guide should develop for bioplastic usage and bioplastic waste management both in Turkey and the world. Also labeling legislation may lead to an "eco-label", based on a product's raw material usage,

energy consumption, emissions from manufacture and use.

REFERENCES

- Alvarez-Chavez C. R., Edwards S., Moure-Eraso R.I, Geiser K., 2011, Sustainability of Bio-based Plastics: General Comparative Analysis and Recommendations for Improvement, *Journal of Cleaner Production*, 23 (1): 46-47.
- El-Kadi, S., 2010, *Bioplastic Production From Inexpensive Sources Bacterial Biosynthesis, Cultivation System, Production and Biodegradability*, VDM Publishing House, ABD, 145.
- Gaspar, M., Benko, Z. Dogossy, G., Reczey, K., Czigany, T., 2005, Reducing water absorption in compostable starch-based plastics, *Polymer Degradation and Stability*, 90: 563-569.
- Iles A., Martin A. N., 2013, Expanding bioplastics production: sustainable business innovation in the chemical industry, *Journal of Cleaner Production* 45: 38-49.
- Kaith, B. S., Jindal, R., Jana, A. K., Maiti, M., 2010, Development of corn starch based green composites reinforced with *Saccharum spontaneum* L fiber and graft copolymers – Evaluation of thermal, physico-chemical and mechanical properties, *Bioresource Technology*, 101: 6843–6851.
- Karana E., 2012, Characterization of ‘natural’ and ‘high-quality’ materials to improve perception of bioplastics, *Journal of Cleaner Production* 37: 316-325.
- Lagaron, J. M., Lopez-Rubio, A., 2011, *Nanotechnology For Bioplastics: Opportunities, Challenges and Strategies*, *Trends in Food Science & Technology*, 22(11): 611-617.
- Sarasa, J., Gracia, J. M., Javierre, C., 2008, Study of the biodegradation of a bioplastic material waste, *Bioresource Technology*, 100:3764-3768.
- Stevens, E.S., 2002, *Green Plastics: An Introduction to the New Science of Biodegradable Plastics*, Princeton University Press, ABD, 238.
- Yu, J., Chen L. X. L., 2008, The Greenhouse Gas Emissions and Fossil Energy Requirement of Bioplastics from Cradle to Gate of a Biomass Refinery, *Environ. Sci. Technol.*, 42:6961–6966.
- Wu, C. S., 2009, Renewable resource-based composites of recycled natural fibers and maleated polylactide bioplastic: Characterization and biodegradability”, *Polymer Degradation and Stability* 94: 1076–1084.

THE EFFECT OF THE POROUS BENTONITE-ALCrNi MATERIAL IN THE TURBINE EFFICIENCY PRESERVATION

Mokhtar Bounazef^a, Ali Djeflal, Seif eddine Bendaoudi, El Abbas Adda bedia

Djillali Liabes University, Mechanical Department, Sidi Bel Abbes, Algeria
a. Corresponding author(bounazef@yahoo.com)

ABSTRACT: In order to increase the turbine gas efficiency and its power, the clearances between rotating blades and the interior casing should be as small as possible. To obtain that, one sprays a sacrificial material on the casing by the thermal blowtorch flame-powder process and one obtains a coating layer. During rotation, they scrape the (Al₂O₃.4SiO₂.H₂O-Na-Ca-Mg)-ALCrNi coating and tear off a fine layer in small remains. It creates itself a functional gap between the blades and the casing seal. The combustion gases do not escape through the clearance, and contribute in the power production. The aim of this work is to investigate the behaviour of a particular sacrificial material, the Bentonite-metallic phase and its effect on the turbine blades wear during inter-reaction between them under experimental conditions of operating rotor blades. To determine this problem, we carried out several tests by changing 4 functional parameters. They are the incursion speed within the seal, the linear blades speed, the blades depth incursion inside the casing and the operating temperature. The obtained results are shown in form of graphs and maps, and the comments explain when there are blades wear or material transfer, and the different effects on coating surface.

1. INTRODUCTION

A significant gap between blades and the casing falls the power and the efficiency and increases a fuel consumption of 2.5%. This harmful consequence is valid for the industrial ground turbines and the aircraft gas turbines. This gap is often caused primarily during the rotor and the casing dilatations which are different and secondarily during the start-ups, the stops and the vibrations caused by axial compressor pumping. These phenomena break the blades etancheity plates and create an opening for gases exhaust. One way of improving gas turbines performances consists of minimising the clearances between the rotor blades and the turbine casing, by alteration of etancheity plates by a sacrificial material seal [Mahler, 1972, Wang,1993, Novinski, 1991]. The answer to this problem is the use of an abradable material, which because of its properties

reduces the damages caused by friction. The coating is obtained by the powder spraying with the thermal blowtorch flame-powder (Casto Dyn-DS), and the used parameters are: Oxygen flow is 90 SPLM, Acetylene flow is 45 SPLM, powder flow 65 g/mn, spraying distance is 120 mm. The powder composition is shown in the Table 1.

Table 1: Material composition

Al	Cr	Ni	(Al ₂ O ₃ .4SiO ₂ .H ₂ O-Na-Ca-Mg)
5%	5%	75%	15%

The grains aspect is in the micrography obtained by SEM (Figure 1). The coating seal is mostly composed of metal phase

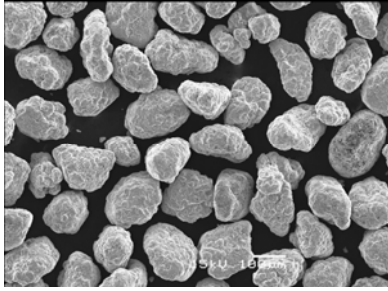


Figure1: Grains aspect of Bentonite-AlCrNi

AlCrNi and self-lubricating phase ($\text{Al}_2\text{O}_3.4\text{SiO}_2.\text{H}_2\text{O}-\text{Na}-\text{Ca}-\text{Mg}$) in high porosities (Figure2) and its characteristics are shown in Table 2

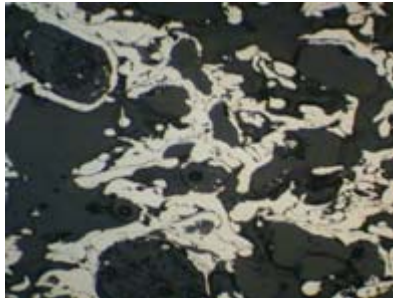


Figure 2: Coating Micrography

Table 2 : Material characteristics

Surf hardness	Micro hardness	Erosion loss	Friction coefficient	% Porosity
51.1 HR15Y	177.17 HK	0.05 g/mn	0.55	64.1 %

The friction is done between blades and the material coating which should not only be soft enough to be scraped easily without causing damages to the blades and the other parts of engine, but also should have high resistance against erosion due to high particles speed in gases flow [Wang, 1996, Schmid *et al.*, 2000, Emery *et al.*, 1983]. Among the other abrasible material characteristics, it is to be machinable and friable to fine remains, to have an oxidation resistance and does not generate warmth during wrenching [Oka *ad all*, 1990, Borel and *all*, 1990]. But this material presents the

harmful property to stick itself on blades top after been scraped. The phenomena of blades wear and abrasible material sticking by coating transfer must be to minimize. The first falls the power, and the second creates mini unbalances and causes a turbulent combustion gases flow. The phenomena understanding is not a easy thing, because several parameters influence these behaviours, such as the linear blades speed, the blade incursion velocity, the incursion depth and the high temperature. In this work, we attempt to evaluate through simulations, using an abrasibility test rig in which we vary successively the 4 parameters. Then, we determine the blades wear degree, the abrasible material displacement and we work out the wear maps for each case. The wear maps are supplemented by the various phenomena which appear on the coating after the friction [Clegg and *all*, 1987, Borel and *all*, 1990, Dorfman and *all*, 1992, Bounazef and *all*, 2004].

2. EXPERIMENTAL PROCEDURE

To carry out the experiments mentioned in first on an abrasible material, it is necessary to have the Sulzer Metco test rig who is used in industry for simulating customers conditions, and allows to try out all alternatives of turbine operating. This equipment which one finds in the aircrafts engines manufacturers is a enough heavy machine for a research laboratories ; its price is very high. Then, with the possibilities which we have, we work out a similar test rig of this machine. We use a manufacturing tools machine with a numerical control by calculator (CNC) (Figure3). In this machine, a principal electrical asynchronous motor, on which we fix a blade piece on the wheel, replaces a rotor turbine; it gives a rotational movement and we obtain with that, the linear friction speed between a

blade and a coating. The thermal motor dilatation and the thermal casing turbine

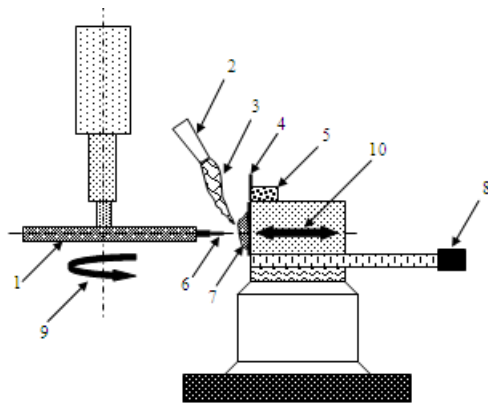


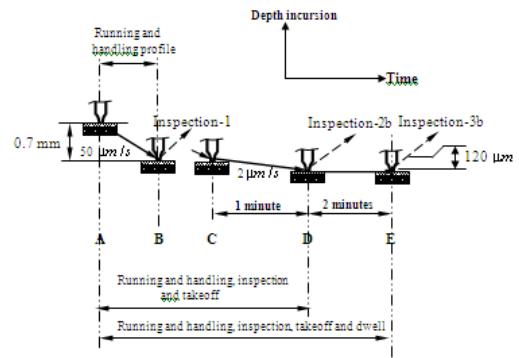
Figure 3: Abradability test rig

Key:

- 1: Wheel
- 2: Blow-pipe
- 3: Flame
- 4: Cutting force sensor
- 5: Thermocouple
- 6: Blade
- 7: Abradable material coating
- 8: Electrical stepper motor
- 9: Linear speed
- 10: Incursion velocity

are obtained in the same time by an electrical stepper motor in test rig, it gives a movement precision of micron thousandth. With stepper motor, we obtain the incursion velocity within coating and the incursion depth inside the spraying material. The coating temperature of the abradable material is obtained with an oxyacetylene blowpipe with which the flame is directed above. The material powder is constituted of complex argillaceous ground compound ($\text{Al}_2\text{O}_3 \cdot 4\text{SiO}_2 \cdot \text{H}_2\text{O} \cdot \text{Na} \cdot \text{Ca} \cdot \text{Mg}$) and metallic phase AlCrNi. It should be noted that the metallic phase wraps the argillaceous phase (bentonite) to avoid to reach its sublimation temperature during spraying. The coating temperature is measured by a thermocouple placed in the coating vicinity. The tangential wrenching stress of the coating particles caused by the blades is measured by a cutting force sensor. The blade piece of TiAlV (% Al: 6.75 ; %V: 4.50) is cut out

from a industrial ground turbine ; it is fixed rigidly on the wheel. We run three types of standard abradability tests (Figure 4). In the first one (test of running and handling profile), we simulate a blade incursion (0.7 mm) inside the ($\text{Al}_2\text{O}_3 \cdot 4\text{SiO}_2 \cdot \text{H}_2\text{O} \cdot \text{Na} \cdot \text{Ca} \cdot \text{Mg}$)-AlCrNi seal at $50 \mu\text{m/s}$ of velocity.



Key:

- Type 1: AB: Test-1
- Type 2: AB: Test-2a ; CD: Test-2b
- Type 3: AB: Test-3a ; CE: Test 3-b

Figure 4 : Standard abradability test

We retrieve the blade for inspection, and make material transfer measurements of the coating on the blade or blade wear (test-1, Figure4). The second type of tests (test of running and handling, inspection and takeoff) is made up of two stages (test-2a, test-2b, Figure4). The first part of second type (test-2a) is similar to the first type (test-1). In the second part (test-2b), we introduce again the blade within the seal during 1 minute with an incursion velocity of $2 \mu\text{m/s}$ and we retrieve it at last for the same inspection that test-1. The third test type (test-3a, test-3b, Figure4) is similar to the second type (test-2a and 2b) with an additional stage (test of running and handling, inspection, takeoff and dwell). After an incursion depth of $120 \mu\text{m}$ obtained by the same part that test-2b, we let the operation continue during 2 minutes at the same depth. It is the blade stabilisation phase. In each stage, it is necessary to respect the 4 parameters values (linear speed, incursion velocity,

incursion depth and temperature). However, in our work, one must vary these values to ascertain their influence on blade wear and the material transfer. To remain under the same working conditions of the standard test of Sulzer Metco, for an initial incursion of 0.7 mm, one keeps the second incursion equal to 120 microns. However, for an initial incursion of 0.6 mm, one uses a second incursion of 103 microns. In the obtained results, the percentage of blade wear or material transfer is calculated compared the initial incursion. Each experiment gives several results of blade wear and $(Al_2O_3, 4SiO_2, H_2O-Na-Ca-Mg)-AlCrNi$ material displacement and some effects on the abradable seal. To show the friction effect of the blade on the coating during the remains wrenching and the phenomena which are generated, we carry out 2 experiments series. In the first (Table3), with a constant temperature of 500 °C in tests couples (T1-T2), (T3-T4), (T5-T6), (T7-T8), we preserve the incursion velocity V_{inc} and the linear speed V_{lin} in each tests couple, and we vary the incursion depth D_{inc} , to determine the change effect on the blades. In the tests couple (T1-T2), we preserve $V_{lin}=400$ m/s and $V_{inc}= 600 \mu m/s$ and we change the incursion depth from 0.6 mm to 0.7 mm. In the tests couple (T3-T4), we have $V_{lin}= 400$ m/s, and with the same change depth of incursion that previously, we use this time V_{inc} equal at $10 \mu m/s$. In the third tests couple (T5-T6), we return to the same values of V_{inc} and D_{inc} that in couple tests (T1-T2), but we use V_{lin} of 200 m/s. In the last tests couple (T7-T8), and compared to the first tests couple (T1-T2), we act simultaneously on the 3 parameters at the same time, we pass to D_{inc} equal at 0.6 mm and 0.7 mm, V_{inc} equal at $60 \mu m/s$, and V_{lin} at 300 m/s. This series of tests couples, is selected thoroughly among so many others to note the 3 parameters effect on blades. In the

second series (Table 4), to note the temperature effect, we carry out experiments with 20°C and 500°C by keeping the 3 other unchanged parameters. The combination of the 2 experiments series, shows the 4 parameters effect then are largely studied, in an isolated or combined way between them.

3. EXPERIMENTAL RESULTS AND DISCUSSION

Let us note that the positive values shown in Tables 3 and 4 indicate the blade wear expressed as percentage of incursion depth. The negative values indicate the material transfer towards the blade, in other words, the blade lengthening. In tests couple (T1-T2), where $V_{lin}= 400$ m/s and $V_{inc}= 600 \mu m/s$, the blade wear decreases from 29.7 for $D_{inc} = 0.6$ mm 3.21 for $D_{inc}= 0.7$ mm (incursion depth), in other words from $178.2 \mu m$ to $22.4 \mu m$. That is confirmed by the tests couple (T5-T6), where the linear speed value is equal to 200 m/s and the same V_{inc} , since blade wear falls from 60.5% ($363 \mu m$) to 51.02% ($357.1 \mu m$) of incursion depth. For the small V_{inc} values, one records a material transfer of the coating towards the blade. In the tests couple (T3-T4), with the increase of the incursion depth from 0.6 mm to 0.7 mm ($V_{inc} = 10 \mu m/s$, $V_{lin} = 400$ m/s), one notices a lengthening increase of the blade from -5.85% ($35.1 \mu m$) to -7.02% ($49.1 \mu m$) depth of incursion. This observation is confirmed by the tests couple (T7-T8) ($V_{inc}=60 \mu m/s$, $V_{lin}=300$ m/s), where one passes from a length increase of -2.7% ($16.2 \mu m$) for $D_{inc}= 0.6$ mm to -4.37% ($30.6 \mu m$) for $D_{inc}= 0.7$ mm. The linear blade speed at the contact point with the abradable seal acts in the same manner that the incursion depth, but in more accentuated way. In experiments (T1-T5), where the incursion velocity is relatively high with $D_{inc}= 0.6$ mm ($V_{inc}= 600 \mu m/s$), one

notices easily that the blade wear falls from 60.5% of D_{inc} (363 μm) for $V_{lin} = 200$ m/s (T5) to 29.7% of D_{inc} (178.2 μm) for $V_{lin}=400$ m/s (T1). In the same way for tests (T2-T6), where $D_{inc} = 0.7$ mm, the wearing tendency of the blade wear is remarkable, since the blade wear falls from 51.02% of 0.7 mm (T6) for $V_{lin}=200$ m/s to 3.21% of 0.7 mm (T2) for $V_{lin}=400$ m/s. Contrary, for relatively low V_{inc} values, it is again the phenomenon of material transfer which appears, as the D_{inc} effect. The experiments (T1-T3) show the passage from a blade wear to a material transfer with 29.7% of D_{inc} for T1 (178.2 μm), and -5.85% of D_{inc} for T3 (35.1 μm). That is true too with T2 and T4 since we note the passage from 3.21% of D_{inc} to -7.02% of D_{inc} . As regards the linear speed effect, its increase reduces considerably the blade wear. All these results are represented in Figure 5.

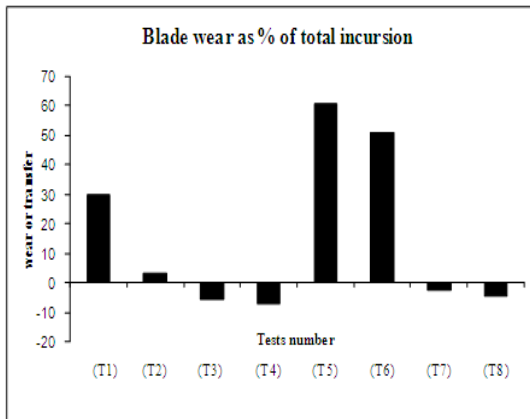


Figure 5 : Blade wear and material transfert (T=500 °C)

In Table 4, the tests couple (T'3-T'9), for $D_{inc} = 0.7$ mm and $V_{inc}=600$ m/s ($T=20$ °C), blade wear decreases from 48.06% of D_{inc} (336.4 μm) to 15.30% of D_{inc} (107.1 μm) with the increase of V_{lin} from 200 m/s to 400m/s. The effect of the incursion velocity gives an opposite result to the 2 first parameters since its increase grows the blade wear. For example, in Table 3,

Table 3 : Tests wear at 500 °C

T=500 °C, $D_{inc}=0.6$ mm $V_{inc}=600 \mu m/s$, $V_{lin}=400$ m/s (T1)	29.7%	T=500 °C, $D_{inc}=0.6$ mm $V_{inc}=600 \mu m/s$, $V_{lin}=200$ m/s (T5)	60.5%
T=500 °C, $D_{inc}=0.7$ mm $V_{inc}=600 \mu m/s$, $V_{lin}=400$ m/s (T2)	3.21%	T=500 °C, $D_{inc}=0.7$ mm $V_{inc}=600 \mu m/s$, $V_{lin}=200$ m/s (T6)	51.02%
T=500 °C, $D_{inc}=0.6$ mm $V_{inc}=10 \mu m/s$, $V_{lin}=400$ m/s (T3)	-5.85%	T=500 °C, $D_{inc}=0.6$ mm $V_{inc}=60 \mu m/s$, $V_{lin}=300$ m/s (T7)	-2.7%
T=500 °C, $D_{inc}=0.7$ mm $V_{inc}=10 \mu m/s$, $V_{lin}=400$ m/s (T4)	-7.02%	T=500 °C, $D_{inc}=0.7$ mm $V_{inc}=60 \mu m/s$, $V_{lin}=300$ m/s (T8)	-4.37%

from test T3 where $V_{inc}=10 \mu m/s$, to test T1 where $V_{inc}=600 \mu m/s$, one records under the same conditions of $D_{inc}=0.6$ mm and $V_{lin}=400$ m/s, an increase in the blade wear. One passes from a blade lengthening (-5.85% of D_{inc}) to a blade wear (29.7% of D_{inc}). It is the same constations that one can observe for the tests couple (T'2-T'4) (from -0.10% to 51.02%) and (T'8-T'10) (from -7.02% to 3.21%) of Ttable 4.

Table 4 : Tests wear at $D_{inc}=0.7$ mm

Tests number	Linear speed m/sec	Incursion velocity $\mu m/s$	% of wear or transfer	Temperature °C
(T'1)	200	10	-1.40%	T=20 °C
(T'2)	200	10	-0.10%	T=500 °C
(T'3)	200	600	48.06%	T=20 °C
(T'4)	200	600	51.02%	T=500 °C
(T'5)	300	60	-3.15%	T=20 °C
(T'6)	300	60	-4.37%	T=500 °C
(T'7)	400	10	-3.00%	T=20 °C
(T'8)	400	10	-7.02%	T=500 °C
(T'9)	400	600	15.30%	T=20 °C
(T'10)	400	600	3.21%	T=500 °C

Two phenomena can appear when the temperature is changed. The first, the material transfer at high linear speed (400 m/s) and low incursion velocity (10 $\mu m/s$) increases (T'7-T'8) from -3.00% of D_{inc} ($T=20$ °C) to -7.02% ($T=500$ °C) of D_{inc} , but it decreases in low linear and incursion velocities (T'1-T'2) from -1.40% of D_{inc} ($T=20$ °C) to -0.10% of D_{inc} ($T=500$ °C). The second phenomenon is the evolution of the blade wear while passing from a low temperature at a high temperature. Let us note that it appears when V_{inc} or V_{lin} are great, as show it the tests couples (T'3-

T'4) and (T'9-T'10) of Table 4. We note that blade wear, when it is carried out under the conditions quoted before, i.e. when the incursion velocity is great ($600 \mu\text{m/s}$) and linear speed is low (200 m/s), increases in value from 48.06% of D_{inc} ($336.4 \mu\text{m}$) at 20°C to 51.02% of D_{inc} ($357.1 \mu\text{m}$) at 500°C . On the contrary, when linear speed and the incursion velocity are high ($V_{\text{inc}} = 600 \mu\text{m/s}$, $V_{\text{lin}} = 400 \text{ m/s}$), the blade wear decreases from 15.30% of D_{inc} ($107.1 \mu\text{m}$) to 3.21% of D_{inc} ($22.4 \mu\text{m}$). The results of temperature effect when $D_{\text{inc}} = 0.7 \text{ mm}$ are represented in Figure 6.

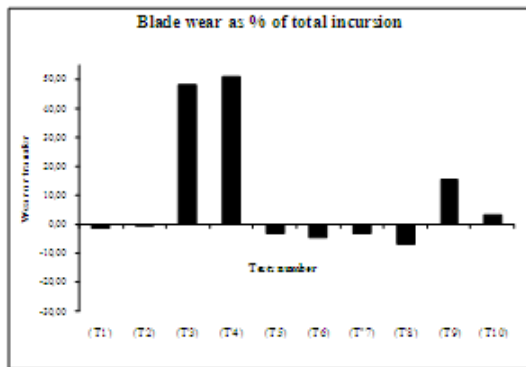


Figure 6: Blade wear and material transfer when $D_{\text{inc}} = .7 \text{ mm}$

In Table 3, there are combinations of two parameters which act in the same direction, they favour or disadvantage blade wear. In tests couple (T5-T7), the reduction effect of the incursion velocity from $600 \mu\text{m/s}$ to $60 \mu\text{m/s}$ and increase of linear speed from 200 m/s to 300 m/s , amplify the result, since one passes from a blade wear of 60.5% of D_{inc} ($363 \mu\text{m}$) to a material transfer of -2.7% of D_{inc} ($16.2 \mu\text{m}$). The most favorable case is seen in the tests couple (T5-T8), since there are at the same time, increase of incursion depth from 0.6 mm to 0.7 mm , reduction of the incursion velocity from $600 \mu\text{m/s}$ to $60 \mu\text{m/s}$ and increase of the linear speed from 200 m/s to 300 m/s . One passes then, from a blade wear of 60.5% ($363 \mu\text{m}$) to a material transfer of -4.37%

($30.5 \mu\text{m}$), we can say a gain of $393.5 \mu\text{m}$. Several phenomena accompany blade wear and material transfer from coating towards the blades during the contact between them. These phenomena are noted visually by optical microscope and measured by a laser roughometer. One can see on the wear map, 4 distinct areas drawn roughly on their limits (Figure 7).

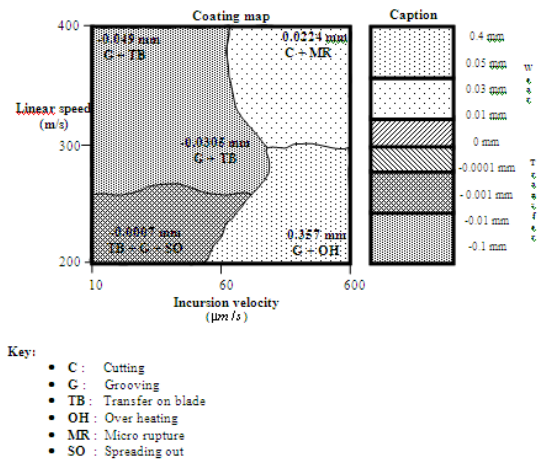


Figure 7 : Wear map of bentonite-NiCrAl

The first zone on the right and bellow, where the blade wear reaches 0.357 mm , one records the grooving and the over heating phenomena on the coating, caused primarily by a very large incursion velocity ($600 \mu\text{m/s}$) and the small linear velocity (200 m/s). The over heating causes a phase shift and changes the coating properties. In the second zone, in map above and on the right, where wear is very tiny (0.0224 mm), one records a material removal by cutting ($V_{\text{inc}} = 600 \mu\text{m/s}$, $V_{\text{lin}} = 400 \text{ m/s}$). That is accompanied by microscopic cracks (micro ruptures) caused by a high incursion velocity ($600 \mu\text{m/s}$) and a high linear speed (400 m/s) in the metals oxides who are encrusted in the metal phase (Figure 2). A high oxides rate of metals weakens the coating. In the third zone, in top and on the left of the wear map, there is a transfer material of -0.049 mm and -0.0305 mm according to V_{inc} and V_{lin} values. In this zone, the

phenomenon of blade transfer is accompanied by a brutal coating wrenching, visible in the grooves form left on surface. On the last zone, in bellow and on the map left, the material transfer is tiny (-0.0007 mm) but it is accompanied by a newspreading out phenomenon and a surface layer crushing of the coating. That occurs at low linear speed (200 m/s) and low incursion velocity (10 $\mu\text{m/s}$). The material does not move on the blade, it is spread out on the surface ;then the coating roughness decreases.

4. CONCLUSION

During the friction between the turbine blades and the coating of an abrasible material sprayed on the casing by the spraying thermal method, the blades wear or the material displacement are inevitable. These two phenomena are harmful, it is necessary to minimize them for the reasons quoted before. The analyses carried out in the various cases of the 4 parameters variation show that to increase the turbine efficiency and its developed power, it is necessary to minimize the running clearances between the blades and the casing by fine particles wrenching of the coating without causing an intensive blades wear and a significant material transfer. To facilitate the various cases analysis quoted before, let us take the most real case, where D_{inc} does not vary (constant parts dilation of turbine) with the same operating temperature (stabilisation phase). One see in Figure 7, that smallest blades wear (0.0224 mm) is obtained when V_{inc} and V_{lin} are great, and smallest material transfer (-0.0007 mm) is obtained when V_{inc} and V_{lin} are small. This abrasible material can be used at the places not exceeding a temperature of 900 °C, i.e. in high pressure stage of turbine. Its wear after several hours does not harm the turbine working. It is eliminated easily by the blades without causing damages on

the parts of turbine and we obtain the functional clearances after friction between the blades and the casing avoiding the gas escape. In each major turbine inspection, it can be replaced it easily with a reasonable cost without changing all the blades line preserved by the low coating hardness.

REFERENCES

- Borel M.O., Miller R.A., Rangswany S., Nicoll A.R., "A new engineered abrasible seal coating properties and performances", Proceeding of the 3rd national thermal spray conference, Long Beach (California), 20 - 25 may 1990.
- Borel M.O., Nicoll, A.R., Schlapfer H.W., Schmid R.K., "The wear mechanisms occurring in abrasible seals of gas turbines", Surface and coatings technology, 1989, pages 117 - 126.
- Bounazef M., Guessasma S., Aitsaadi B., "The wear, deterioration and transformation phenomena of abrasible coating BN-SiAl-Bonding organic element, caused by the friction between the blades and the turbine casing. "Materials Letters 58 (2004), pages 3375-3380
- Clegg M.A., Mehta M.H., "NiCrAl/bentonite thermal spray powder for high temperature abrasible seal," Proceeding of the national thermal spray conference, Orlando Florida 14 - 17 septembre 1987.
- Dorfman M., Novinsky E., Kushner B., Rotolico A., "A high performance alternative to NiCrAl/bentonite for gas turbine abrasible seals", Proceeding of the international thermal spray conference and exposition, Orlando (Florida), 28 may - 5 june 1992.
- Emery A.F., Wolak J., Etemad S., Choi S.R., "An experimental investigation of temperatures due to rubbing at the blade-seal interface in an aircraft compressor", Wear, 91 (1983) 117-130.
- Mahler F.H., Conf Advanced Seal Technology, Rep. PWA-4372, Pratt & Whitney Aircraft, North Haven Connecticut, New Haven Country, USA, 1972.
- Novinski E.R., "The design of thermal sprayed abrasible seal coatings for gas turbine engines", Proceeding of the 4th national thermal spray, conference, Pittsburgh (PA), 4-10 May 1991.
- Oka T., Nakahira H., Norito T., "Basic characteristics of different abrasible coating", conference of international DVS, Essen, Germany, 29 - 31 August 1990.

- Schmid R.K., Ghasnipour F., Dorfman M., Wie X.,
“An overview of compressor abradable thermal spray”, in: c.c. Berndt (Ed), Surface Engineering International Thermal Spray Conference ITSC, May 2000, Montreal Canada, Via Applied Research 2000, page 406.
- Wang H, ”An analysis of turbine blade/abradable seal rubbing”, in: H. Henein and T. Oki (eds.), Proceedings of the first International Conference on Processing materials for Properties, Honolulu County, Hawaii, Minerals, Metals and Materials Society, 1993, pages 1085-1088.
- Wang H, “Criteria for analysis of abradable coatings”, Surface And Coatings Technology, 79 (1996), pages 71-75.

EFFECTS OF DIFFERENT PROCESS CONTROL AGENT ON CHARACTERISTICS OF MECHANICALLY MILLED Al2024 POWDERS

A. Canakci^{1a}, S. Ozkaya¹, F. Erdemir¹, T. Varol¹

1. Metallurgical and Materials Eng. Dept., Karadeniz Technical University, Trabzon, Turkey.
a Corresponding author (aykut@ktu.edu.tr)

ABSTRACT: In this study, the effect of different process control agents (PCA) on particle size, particle morphology and particle hardness produced mechanical milling method was investigated. To evaluate the effects of PCA with increasing milling time, powders have been successfully milled from 0.5h up to 16h. Methanol and stearic acid were used as process control agents to investigate the effect on milled powder properties. The particle size of alloy powders was determined by laser particle size analyzer and the milled powders were characterized by SEM. Microhardness values were obtained for different milling time show that the hardness of powders increase with increasing milling time. The results show that both methanol and stearic acid have different effects on the morphology, particle size and structural behavior of the as milled Al2024 powders. Moreover, it was observed that methanol is earlier than stearic acid for steady state in ductile-ductile milling system.

I. INTRODUCTION

Process variables in MM technique such as milling time, milling speed, ball to powder weight ratio and process control agents (PCAs) have a significant role on the final structure and morphology of the powders [Suryanarayana, 2001; Canakci et al. 2011]. With cold welding, the particles will not be bonded together for interdiffusion while too much cold welding will cause an increase in particle size. Therefore, the balance between cold welding and fracturing is important for successful MM process [Lu and Zhang, 1999]. The balance between these two mechanisms can be controlled by addition of a surface additive, called as PCA, which inhibits cold welding. The type of PCA also plays an important role in the balance [Zhang et al. 1999; Zhu et al. 2010]. There are several kinds of PCAs, for example methanol, stearic acid, hexane, cyclohexane, polyethylene are most common used process control agents in MM process [Juarez et al. 2007]. By adding PCA, particle size can be decreased as a result of inhibited

welding during collisions and increased fracturing process [Pilar et al. 2007].

The aim of this work is to investigate the effect of different process control agents on very fine graded Al2024 powders produced by MM technique.

2. EXPERIMENTAL PROCEDURE

Gas atomized Al2024 powders, with the average particle size of 56 μm were chosen as starting material. The chemical composition of alloy is (in weight percent) of 4.850% Cu, 1.310% Mg, 0.667% Mn, 0.254% Fe, 0.110% Si, 0.079% Zn, 0.033% Cr, 0.008% Ti and balance Al. The milling process was carried out in a planetary ball-mill (Retsch PM 200) at room temperature using tungsten carbide bowl and high argon atmosphere. Alloy was milled up to 16 h with the following parameters; ball to powder charge ratio; 10:1(wt), ball diameter ;10mm, milling speed 400rpm. A total of %2 (wt) of stearic acid or methanol were added to the different

bowls as PCA. To prevent overheating, ball milling experiments were stopped (every 1h) and then resumed when the temperature of the bowl decreased to room temperature. The milled alloy powders were taken out at regular intervals of 0,5 ,1,2,6,10 and 16h for investigating it's properties. The powder sizes of alloys were obtained lazer particle size analyzer (Malvern, model 'Mastersizer Hydro 2000e'), characterization of powders were obtained by scanning electron microscopy. Therefore, the hardness of milled alloys were determined using vickers measurement $HV_{0,1}$.

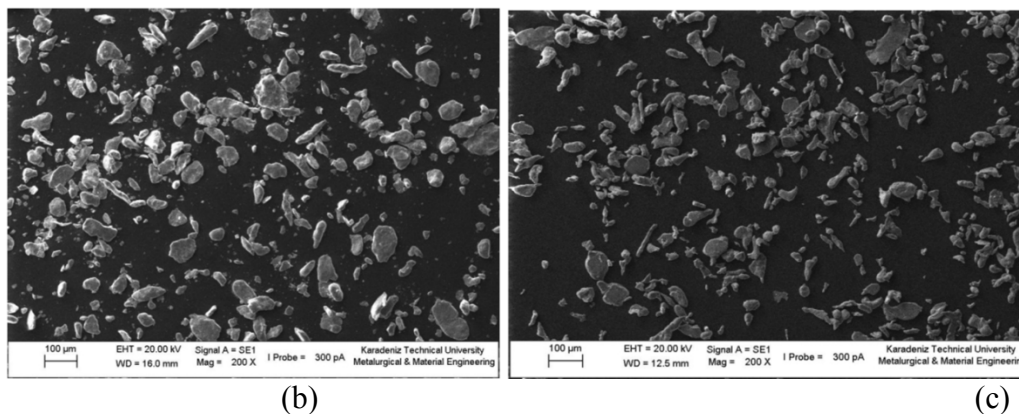
3. RESULTS AND DISCUSSION

3.1. Particle Morphology

The morphologies of the milled Al2024 wt-%2 PCA powders are shown in Fig1. The milling duration changes from 0,5h up to 10 h. When examine the figures, it can be seen that, the effect of methanol on powders starts in early stages of milling. Thus, rapidly changing in powder morphology was obtained. The powder morphology after 0,5h milling

time (Fig.1a) was flake, but after 10h it converted into equiaxial morphology it is because of after 10h powders reach to the steady state. That rapidly changing in powder morphology have an important influence on the powder size that, powder size was decreased quickly [Pilar et al. 2008; Long et al. 2010; Nouri et al. 2010]. On the other hand, stearic acid presented too much lubricant characteristic and powders could not reach to the enough work hardening to be fractured. As indicated in Fig.1 (1h) after 10h milling time, while methanol proceeded through equiaxed morphology, stearic acid has mostly flake shape. When powder morphologies are examined, it can be seen that there is almost no change on powders lubricated with methanol. In other words these powders reach steady state after 10h. But then, the alloy powders lubricated with stearic acid starts fracturing after 10h and at 16h it still continues fracturing.

In conclusion, when compared stearic acid and methanol, methanol is more effective on fracturing and also it gains %40 time, to reach to steady state.



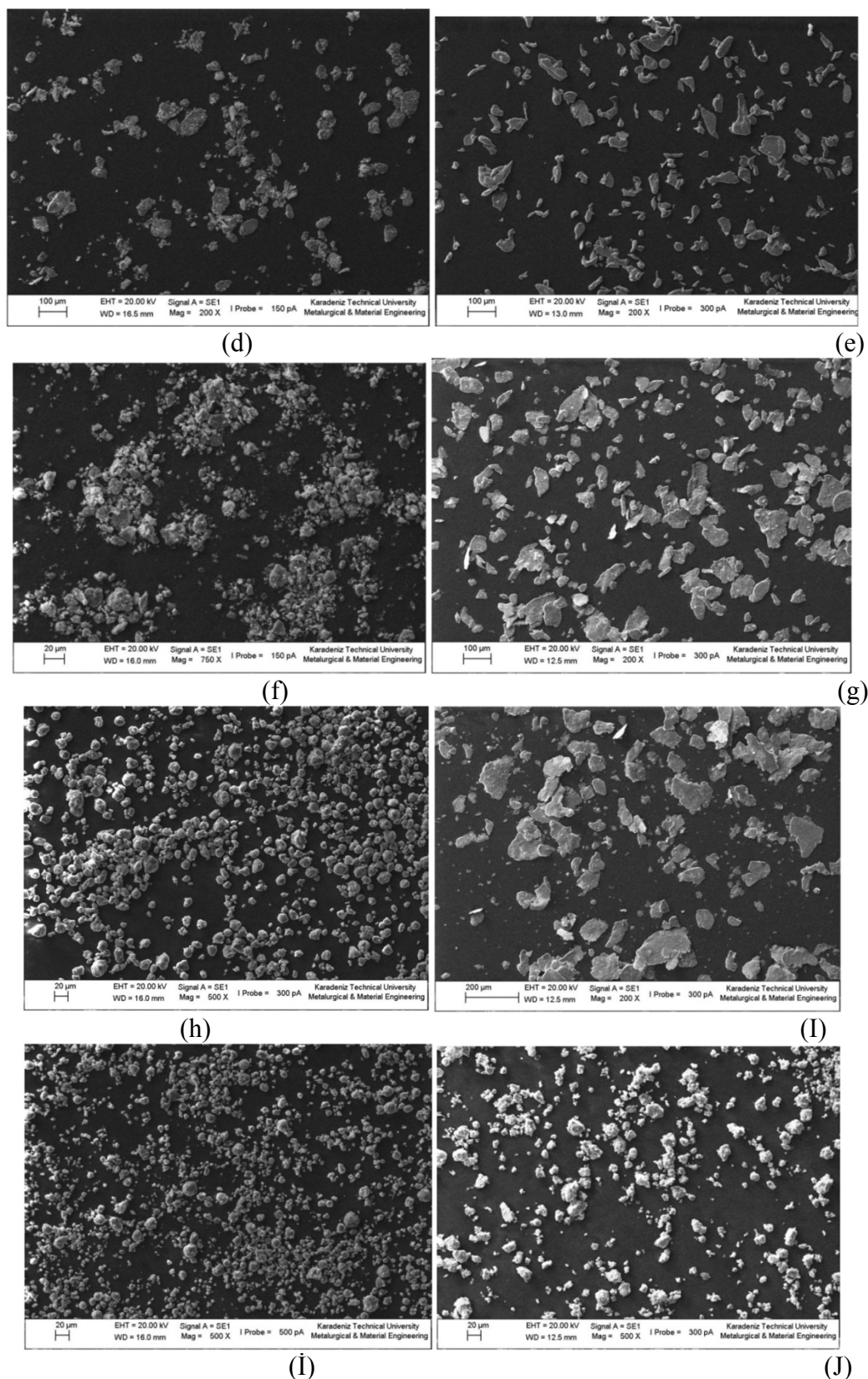


Fig. 1: Powders milled with different process control agent and milling time; (a) Methanol-0.5h, (b) Stearic acid-0.5h, (c) Methanol-1h, (d) Stearic acid-1h, (e) Methanol-6h, (f) Stearic acid-6h, (g) Methanol-10h, (h) Stearic acid-10h, (i) Methanol-16h, (j) Stearic acid-16h.

3.2. Particle Size

Fig.2 shows the measurement of the particle sizes of Al2024 powders for different types of PCA after different MM duration. As shown in figure a large difference in particle size can be observed only for a short MM duration. Up to two hours, while particle size of powder used stearic acid has an increase, particle size has decreased with used to methanol. This may be attributed to the amount of stearic acid is not enough up to two hours to balance between the cold welding and fracturing. The size of the aluminum particles is range from 15-45 μm . In the early stages of ball milling for stearic acid, the coarse particles were soft, and tendency to cold welding and form large particles was high. Thus after 2h of ball milling, powder with stearic acid starts fracturing up to 16h. As it can be seen from the Fig. 2, both stearic acid and methanol comes to steady state that, they are not going on fracturing anymore. When compared these additives, methanol is more effective than stearic acid in this process that methanol reaches steady state %40 earlier than stearic acid.

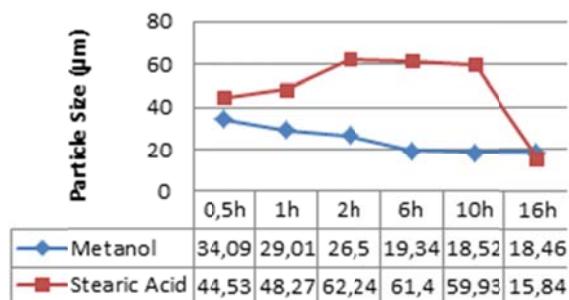


Fig.2 : The change of particle size with increasing milling time

3.3. Microhardness

Figure 3 shows the Vickers hardness of milled powders as a function of milling time and different process control agents. As known, plastic deformation rate and work hardening rate increase with increasing milling time. The hardness of

alloy shows a decidedly upward trend with increasing milling time. In addition, for a given milling time, the hardness of alloy powder milled with methanol higher than that of the powder milled with stearic acid. The reason for difference in hardness can be explained the powders with methanol start fracturing at the beginning of milling. Thus, that powder has more work hardening.

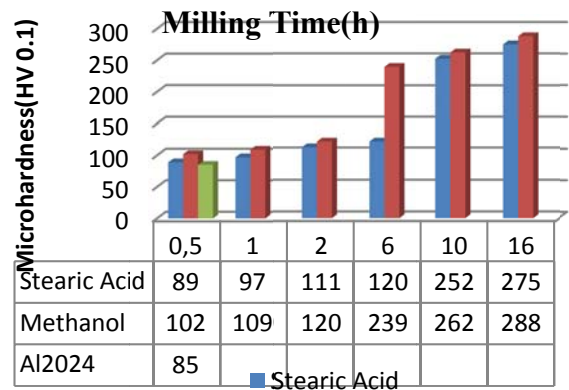


Fig. 3: The change of microhardness with increasing milling time

4. CONCLUSIONS

- 1) The powder sizes increased with increasing milling time in both lubricating additives, but the powders with methanol started fracturing in earlier periods of milling and reached steady state earlier than stearic acid.
- 2) The hardness of powders was increased with increasing milling time and it was shown that, powders with methanol have bigger hardness values than stearic acid.
- 3) Solid lubricators have more efficiency than liquids owing to the that, powders with stearic acid starts fracturing later than methanol.

REFERENCES

- Suryanarayana, C., 2001. Mechanical alloying and milling Progress in Materials Science 46, 1.
- Canakci, A., Varol, T., Nazik, C., 2011. The effect of amount of methanol on the properties of Al-Al₂O₃ composite powders, International 6th Powder Metallurgy proceedings book.
- Lu, L., Zhang, Y.F., 1999. Influence of process control agent on interdiffusion between Al and Mg during mechanical alloying, Journal of Alloys and Compounds, 290, 279.
- Zhang, Y.F., Lu, L., Yap, S.M., 1999. Prediction of the amount of PCA for mechanical milling, Journal of Materials Processing Technology 89-90, 260.
- Zhu, S.G., Wu, C.X., Luo, Y.L., 2010, Effects of stearic acid on synthesis of nanocomposite WC-MgO powders by mechanical alloying, Journal of Materials Science 45, 1817.
- Juarez, R., Sunol, J.J., Berlanga, R., Bonastre, J., Escoda, L., 2007. The effects of process control agents on mechanical alloying behavior of a Fe-Zr based alloy, Journal of Alloys and Compounds 434-435, 472.
- Pilar, M., Sunol, J.J., Bonastre, J., Escoda L., 2007. Influence of process control agents in the development of a metastable Fe-Zr based alloy, Journal of Non-Crystalline Solids 353, 848.
- Pilar, M., Escoda, L., Sunol, J.J. and Greneche, J.M., 2008. Magnetic study and thermal analysis of a metastable Fe-Zr-based alloy: Influence of process control agents, Journal of Magnetism and Magnetic Materials 320, 823.
- Long, B.D., Zuhailawati, H., Umemoto, M., Todaka, Y. and Othman, R., 2010. Effect of ethanol on the formation and properties of a Cu-NbC composite, Journal of Alloys and Compounds 503, 228.
- Nouri, A., Hodgson, P.D. and Wen, C.E., 2010. Effect of process control agent on the porous structure and mechanical properties of a biomedical Ti-Sn-Nb alloy produced by powder metallurgy, Acta Biomaterialia 6, 1630.

FABRICATION OF Fe–Al INTERMETALLIC COATINGS USING MECHANICAL MILLING TECHNIQUE

A. Canakci^{1a}, F. Erdemir¹, T. Varol¹, S. Ozkaya¹

1. Department of Metallurgical and Materials Engineering, Engineering Faculty, Karadeniz Technical University, Trabzon, Turkey.

a Corresponding author (aykut@ktu.edu.tr)

ABSTRACT: In this work, ball milling was used to produce Fe-Al coatings. Steel samples, which were ball-milled with Al powder in a planetary ball-mill, were in the cubic form with 12 mm×12 mm×3 mm dimensions. The repeated substrate-to-ball collisions flattened the Al powders and deposited them onto the surface into a bulk material. Surface morphology and cross-section microstructure of the developed coatings were studied by using scanning electron microscope (SEM). Experimental results showed that the thickness of the aluminum coating on the steel substrate increases with increasing milling time. The surface roughness increases gradually with increasing milling time and particle size. The results revealed that a Fe-Al coating had been formed on the surface of the substrate by formation of Fe-Al intermetallics.

1. INTRODUCTION

In recent years several attempts have been made in order to create the Fe-Al intermetallic coating materials. One aim of these approaches is mechanical alloying technique, in which either a discrete or continuous coating with metal powders is performed to modify the surface properties. Both discrete and continuous coatings by metal powders can be achieved depending on a variety of operating conditions including milling speed, milling time, total charge ratio and ball to powder ratio in a milling vessel [Zhang *et al.*, 2010].

Conventional methods of processing Fe-Al intermetallic, including melting and casting, tradition powder metallurgy, have been investigated till now. In recent years, some efficient methods were reported to fabricate the fine grain size metals and alloys, such as mechanical alloying, spark plasma sintering [He *et al.*, 2006; Paris *et al.*, 2004; Minamino *et al.*, 2000; Suryanarayana, 2001; Kim *et al.*, 2003]. Mechanical alloying method has proved to be an easy tool in order to promote different kinds of solid-state

reactions and to create new materials with peculiar properties. In this study, the fabrication of Fe-Al by mechanical alloying from Al 2024 powders has been investigated. The purpose of this work is to produce the Fe-Al intermetallic coating by mechanical alloying. This work focuses on the effect of mechanical alloying on the properties of Fe-Al intermetallic coatings.

2. EXPERIMENTAL

The coatings were fabricated at three particle sizes of Al 2024 powders: x, y and z μm , respectively. No process control agent was added to these powders. Fig. 1 shows a schematic illustration of the mechanical alloying (MA) method used in the present work. By means of the MA method, Fe-Al coatings were deposited on the substrates. A planetary ball-mill with a 400rpm rotating speed was selected. The vial has a volume of 80 ml and is made of tungsten carbide. The heat-treatment was carried out in an argon environment to prevent oxidation of the coating systems. The samples were placed in the furnace,

which was evacuated of air, filled with argon and heated at $5^{\circ}\text{C min}^{-1}$. The samples were held for 120 min at 600°C and then they were cooled down in the furnace (cooling rate: $5^{\circ}\text{C min}^{-1}$) to minimize the internal stresses. After heat-treatment, the samples were cut with a refine saw and then polished. Scanning electron microscope (SEM) was used to characterize the morphology and microstructure of the coatings. The coating thickness was measured from all sample sides using SEM and the average thickness was calculated for each sample. The composition was analyzed by energy dispersive spectroscopy (EDS). The phases were identified by X-ray diffraction (XRD) analysis with Cu Ka radiation ($\lambda = 1.5405\text{\AA}$, 12 kW). Vickers microhardness test was carried out and a linear profile of microhardness distribution was obtained along the surface of the coating and substrate layers.

3. RESULTS AND DISCUSSION

3.1. Coating morphology

The particles after a short ball-milling time of 1h had not collided sufficiently with the steel surface, although they became slightly work hardened. In other words, for a short milling time the particles were not subjected to an adequate compressive force or kinetic energy input, and therefore, only a minimal coating layer formed on the steel surface [Zadorozhnyy *et al.*, 2011; Tousiet *et al.* 2009; Romankov *et al.*, 2009; Nouri *et al.*, 2011]. Notably, the absence of process control agent (PCA) in the milling process resulted in poor cold welding of powders to the steel surface for a short milling time of 1h, although the milling speed was very low (200 rpm). It should be noted that a process control agent is a surface additive used in the milling process in order to control the balance between the fracturing and cold

welding of particles. The application of PCA to mechanically alloyed powder enables to reduce cold welding and promote fracturing. PCAs adsorb on the surface of the powder particles and minimize cold welding among powder particles, thereby inhibiting agglomeration. It can be observed from the image (Fig. 1), that the deposition progress occurred in both the x-y and z directions. For a milling time of 10h, the coating became denser at a comparatively early stage of the coating process, indicating that increases in the milling time increased the pitch density (Fig. 1). Meanwhile, the powder content increased between the pitch regions. Notably, almost the entire surface was coated with the Al2024 powder after 10h of milling (Fig. 1).

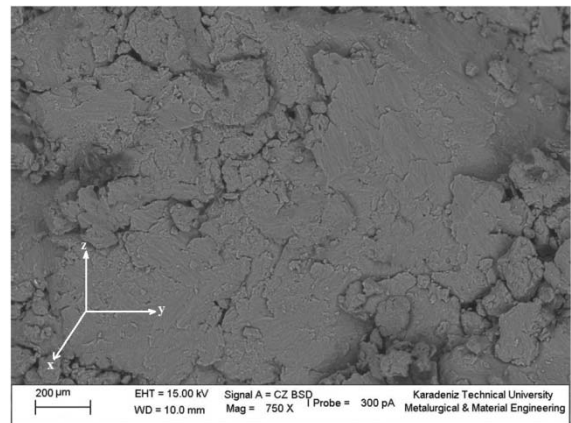


Figure 1. Surface morphology of the coatings after 10h of milling.

3.2. Effect of Milling Time on Coating Thickness

The coating process consisted of three stages: (a) repeated impacts by high energy balls on the substrate wall, sandwiching powders between ball and substrate, (b) cold welding of powders leading to pancake structure of the coated part and (c) delamination of the coated layer. Delamination is a plausible explanation for the observed variability of the coating thickness as a function of milling time.

The average coating thickness was also measured as a function of the milling time. Fig. 2 shows that the average thickness of the coating depended on the milling time. In general, it was observed that the coating thickness increased as a function of milling time. When the milling time was 1h, the steel substrate was covered with a very thin coating layer. For this case, only small Al2024 powders were deposited on the steel substrate. The thickness of the Al coating increased from 0 to 17 μm for the initial milling time (1h). Notably, the steel substrate underwent plastic deformation under the ball-substrate-ball collisions and its edge became slightly deformed. When the milling time was increased to 2h, the energy was sufficient to deposit more Al2024 particles on the steel substrate than after milling for 1h. The thickness of the Al coating increased from 17 to 35 μm for the 2h of milling. The ball-substrate-ball collision per unit time increased with increasing milling time. This increase in the ball-substrate-ball collision frequency resulted in the cold welding of more powder to the substrate, increasing the coating thickness. The thickness of the Fe-Al coatings significantly increased when the milling time was higher than 2h. The coating that had deposited after 4h of milling exhibited rough layer-like morphology, implying that the Fe-Al mixture covered the substrate layer-by-layer. With the increase in milling time from 4h to 10h, the coating formed a denser structure. The mean coating thickness increased to its maximum value at a milling time of 10h. The coating thickness was 66 μm in several places after milling for 10h.

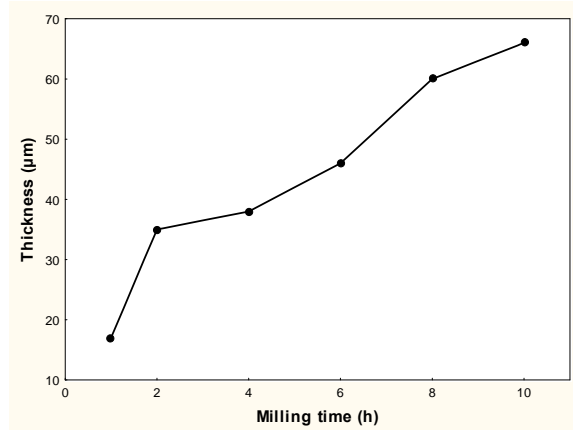


Fig. 2: Coating thicknesses of samples various milling times.

3.3. EDS Analysis

The surface microstructure was refined by ball-substrate-ball collisions in the mechanical alloying process [Nouri et al. 2011]. Ball-powder-ball and ball-substrate-ball collisions, which caused a large amount of structural defects [Tousi et al. 2009] and high local temperatures at the collision surface, resulted in severe plastic deformation of the substrate and the milled powders. The existence of Al in the coating layer, as shown in the EDS analysis, may have happened for the following reasons:

- (1) Ball-substrate-ball impacts caused Al particles to adhere onto the substrate. Then, an Al-rich layer formed on the specimen surface.
- (2) Severe plastic deformation induced high local temperatures, promoting diffusion and the formation of the initial alloy layer.
- (3) Subsequent ball impacts refined the Fe-Al phases in the initial alloy layer, and a new Al layer formed on the substrate's surface.
- (4) Diffusion of Al and Fe occurred between the newly formed Al layer and the initial alloy layer. The inward diffusion of Al was hindered by the coarse-grains of the substrate, while the outward diffusion of Fe was enhanced by the large amount of grain boundaries and defects in the alloy

layer. During heat treatment, on the surface of the sample, different Fe-Al phases were formed as a result of inter-diffusion and reaction between

Fe and Al. In the present work, Fe-Al intermetallics were observed in the coating layer produced by mechanical alloying and are shown in Fig. 3.

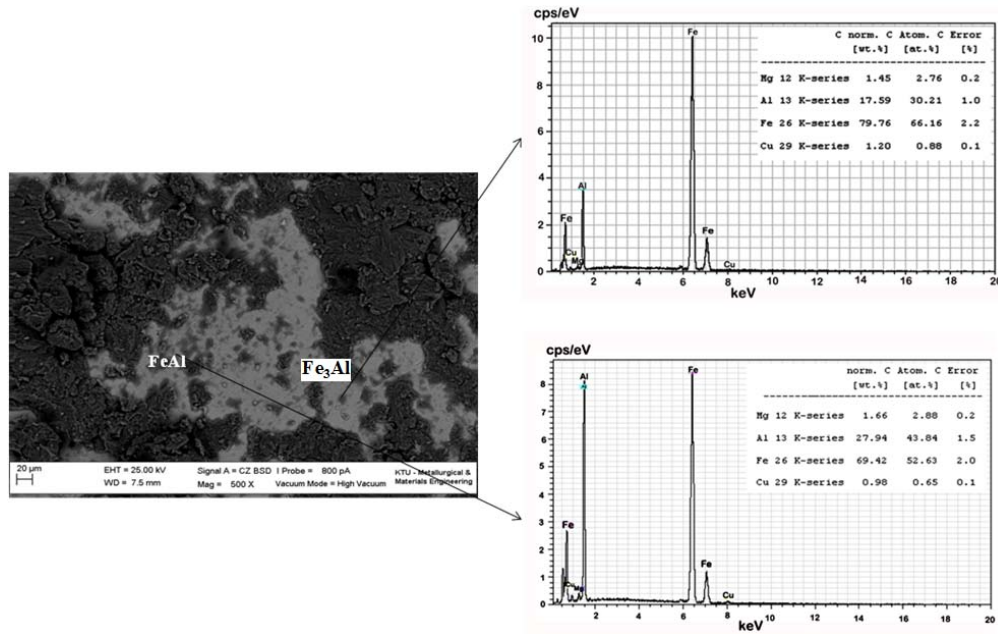


Fig. 3: Elemental spectrum selected from different regions of the SEM image.

4. CONCLUSIONS

The coating thickness and microstructure of Fe-Al coatings fabricated by mechanical alloying technique and heat treatment demonstrated a strong dependence on milling time, heat treatment and chemical composition of the coating and substrate materials. The following optimum MA and heat treatment work conditions were selected to prepare the Fe-Al coatings with intense microstructure, suitable thickness and intermetallic compounds: rotation speed of 200 rpm, milling duration of 10h, with the ball-to-powder weight ratio of 10:1. In this process, repeated ball-substrate-ball collisions cold welded powder particles to a substrate and forged them into a bulk material on the substrate surface. microstructural alteration is determined by the competition between cold-welding and fracturing of particles. Coating thickness increased from 17 to 66 μm with the milling time from 1 to 10h. Fe-Al intermetallic coatings have

been produced with this method at a much lower cost with a much shorter time compared with the conventional processes.

Acknowledgments: The authors are grateful to the Karadeniz Technical University Research Fund for financially supporting this research (No: 2010.112.010.4). The researchers would also like to thank the Gundogdu Exotherm Service for providing the Al2024 powders.

REFERENCES

- Zhang, D., Cai, R., Zhou, Y., Shao, Z., Liao, X.Z., Ma, Z.F., 2010. Effect of milling method and time on the properties and electrochemical performance of LiFePO₄/C composites prepared by ball milling and thermal treatment, *Electrochimica Acta* 55, 2653.
- He, Q., Jia, C. and Meng, Jie., 2006. Influence of iron powder particle size on the microstructure and properties of Fe₃Al intermetallics prepared by mechanical alloying and spark plasma sintering,

- Materials Science and Engineering A 428, 314.
- Paris, S., Gaffet, E., Bernard, F. and Munir, Z.A., 2004. *Scripta Materiala*. 50, 691.
- Minamino, Y., Koizumi, Y. and Tsuji, N., *Science and Technology of Advanced Materials*, 5, 133.
- Suryanarayana, C., 2001. Mechanical alloying and milling, *Progress in Materials Science* 46, 1.
- Kim, J. Satoh, M. and Iwasaki, T., 2003. Mechanical-dry coating of wax onto copper powder by ball milling, *Materials Science and Engineering A* 342, 258.
- Zadorozhnyy, V., Kaloshkin, S., Kaevitser, E. and Romankov, S., 2011. Coating of metals with intermetallics by mechanical alloying, *Journal of Alloys and Compounds*. 509, S507-S509.
- Tousi, S.S., Rad, R.Y., Salahi, E., Mobasherpour I. and Razavi, M. 2009. Production of Al–20 wt.% Al₂O₃ composite powder using high energy milling, *Powder Technology*, 192, 346.
- Romankov, S., Komarov, S.V., Vdovichenko, E., Hayasaka, Y., Hayashi, N. and Kasai, E., 2009. Fabrication of TiN coatings using mechanical milling techniques, *International Journal of Refractory Metals and Hard Materials* 27. 492.
- Nouri, A., Hodgson, P.D. and Wen, C. 2011. Effect of ball-milling time on the structural characteristics of biomedical porous Ti–Sn–Nb alloy, *Materials Science and Engineering C* 31 921.

FABRICATION OF BULK YTTRIA STABILIZED ZIRCONIA-ALUMINA COMPOSITE FILTERS BY DIFFERENT FOAMING METHODS

Burcu Nilgün Çetiner^{1,a}, Özgür Çınar¹

1. University of Marmara, Faculty of Engineering, Dept. Of Metallurgical and Materials Eng., Istanbul, Turkey
a. Corresponding author (nilgun.cetiner@marmara.edu.tr)

ABSTRACT: Macro and microporous yttria stabilized zirconia-alumina composite filters are developed to decrease the casting flaw in order to obtain more purified and less turbulent liquid flow in molten metals. These composites are intended to have light weight, high mechanical strength, large specific surface areas, high porosity, excellent thermal shock resistance, chemical corrosion resistance and high temperature stability in molten metal. In our research we tried several ways of foam production; foaming agents such as H₂O₂, porogens such as PVA (Poly vinyl alcohol) and finally polyurethane foams using like pore templates. After each procedure, samples were sintered at the same temperature (1650 °C). The XRD analysis was performed after the sintering process. The sintered zirconia-alumina composites are characterised by microstructural analysis using SEM and the EDS analysis. The thermal and mechanical behaviours of the zirconia-alumina ceramic filter were decided to be mentioned in another study.

1. INTRODUCTION

Zirconia finding applications as solid oxide fuel cells, catalyst supports, ceramic filters, gas sensors, thermal barriers [Zhang *et al.*, 2011] and as a biomaterial for hip prosthesis, tooth crowns, dental implants due to its high mechanical properties and low toxicity [Matsumoto *et al.*, 2011], its capacity and performance depends mostly on surface and pore characteristics besides its chemical composition and morphology. Even though zirconia porous materials were widely studied for various applications, in general it is quite difficult to produce porous ceramics with a high volume fraction of closed pores owing to a conventional heating technique, i.e. an electric furnace, changing the number and volume fraction of open pores in accordance with those of closed pores during heating regime [Hashimoto *et al.*, 2013]. Several techniques to obtain yttria-stabilized porous zirconia such as sol-gel method, solid state reaction process,

hydrothermal treatments, thermal decomposition, polymeric routes [Zhang *et al.*, 2011], tape casting [Albano *et al.*, 2008], gel casting [Hu *et al.* 2010] methods were utilized. In addition to these procedures, the starch consolidation casting with different amounts of corn starch content (10-50 wt.%) were applied for the production of alumina-zirconia (10-40 wt. %) porous composite [Pabst *et al.*, 2011]. As expected, the microstructure of the porous ZTA (Alumina-zirconia composite ceramics with compositions on the alumina-rich side) composites is primarily determined by the processing route (e.g. the firing temperature), whereas the material composition has a minor influence; however, a change in pore shape has been observed (from convex to concave with increasing zirconia content), which has a certain influence also on the measured pore size. In this study we will study on the production of ZTA composites (60 wt.%)

Alumina and 40 wt% Zirconia) with different foaming methods such as foaming agents such as H₂O₂, porogens such as PVA (Poly vinyl alcohol) and finally polyurethane foams using like pore templates mentioned in [Fidancevska *et al.*,2007]

2. EXPERIMENTAL PROCEDURE

Alumina (Sigma Aldrich) and yttria stabilized zirconia (10 wt.% yttria, Sigma Aldrich) were used as taken, but in order to prepare a batch (ZTA batch) of 60 wt.% zirconia and 40 wt.% alumina (2 wt.% of MgO and 2 wt.% of SiO₂ were used as sintering aids) the appropriate amounts of powders were ball-milled using alumina grinding media (5 mm) –as alumina is harder and more abrasive than zirconia- for 24 h and then dried in a drying oven (Binder). The procedure mentioned in [Fidancevska *et al.*,2007] were modified as summarized in Fig. 1. Porous structures were created using PVA, polyurethane (PU) foams and H₂O₂ as porogen additives, following previous experiments by Fidancevska *et al.*,2007. The porous structure created by using PVA (Polyvinyl alcohol) particles was obtained by embedding of PVA particles in a dense paste composed of 70 wt.% ZTA batch, 10 wt.% PVA, 10 wt.% deflocculant Dolapix CE 64 and the rest (10 wt.%); distilled water (5 wt.%) and H₂O₂ (5 wt.%) mixture After mixing the constituents, the paste was poured into aluminum frames, forming a powder cake with dimensions 10 cm ×5cm×2 cm. In an other method, polyurethane foam was used as substrate which was coated with composite powder (ZTA batch) by slurry dipping using an aqueous based suspension. The foam was squeezed and dipped into the slurry slurry (60 wt.% solid phase, 22 wt.% deflocculant Dolapix CE64 and rest distilled water). The third porous structure was generated using H₂O₂. The slurry was composed of composite Yttria stabilized

zirconia/Alumina powder (ZTA batch) , deflocculant Dolapix CE 64 and nonstabilized H₂O₂ in the ratio (wt.%) 10: 4: 3. After mixing the constituents, the slip was poured into aluminum frames, forming a powder cake with dimensions 10 cm ×5cm×2 cm. The system was dried in a drying oven for 24 h at 130 °C. The sintering was performed under the following conditions: from 40 to 500 °C at a heating rate of 10 °C/min at 500 °C for 3 h, and subsequently with heating from 500 to 1650 °C at a heating rate of 10 °C/min, finally sintering at 1650 °C for 5 h and cooling to room temperature for 24 h.

XRD measurements were carried out using a Rigaku vertical diffractometer with Cu K α radiation, using step size of 0.02° (2 θ), with 2 s intervals and under conditions of 40 mA and 20 kV. The diffraction lines were identified using the program «JADE 6». Scanning electron microscopy (SEM) (Jeol JSM-5910 LV – Low Vacuum Scanning-) and energy dispersive spectroscopy (EDX) (Oxford Inca Energy 200) were used to characterize the microstructure of the ZTA porous composite.

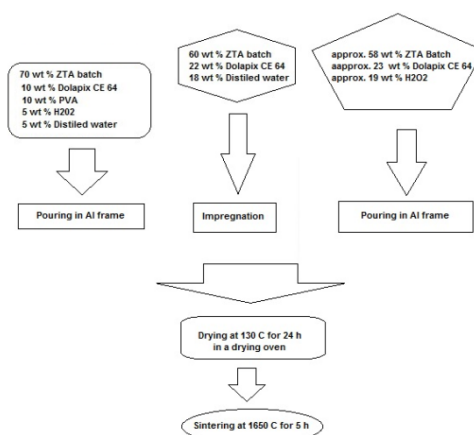


Figure 1: The summary of the experimental procedure.

3. RESULTS AND DISCUSSION

After sintering at 1650 °C, the specimens processed according to procedures

mentioned in Part 2., were cut carefully using a diamond cutting disc (Struers) then prepared for SEM and EDS analysis. Also a group of each type of specimens was reserved for XRD analysis; this group of specimens was cut, crashed and then ground to finer powders. The porous structures obtained after each processes were monitored from macro to increasing micro porosities respectively, in Fig. 2, 3, (PU foam method), Fig.4.,5 (H_2O_2 method), and finally Fig.6 and 7 (PVA method). Table 1, 2 and 3 show the EDS analysis of the points 1 and 2 indicated in each SEM image. The XRD patterns of 3 porous structures were shown in Fig. 8, 9 and 10 from the PU foam method to PVA method, respectively.

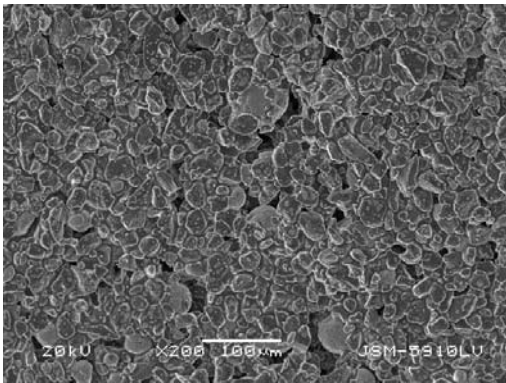


Figure 2: The porous microstructure obtained by the PU foam method. (X200 Magnification)

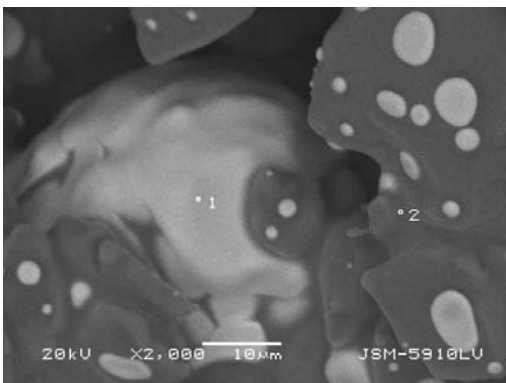


Figure 3: The different phases present in the structure indicated as “1” and “2” points and selected for the EDS analysis

(Back scattered image, X2000 Magnification) [The PU foam method].

Table 1: The EDS analysis of the points 1 and 2. (Processing option : All elements analyzed (Normalised), All results in Weight Percent).

Spectrum	B	O	Al	Zr	Total
Spectrum 1	4.34	36.25	0.63	58.77	100.00
Spectrum 2	-	34.40	65.60	-	100.00

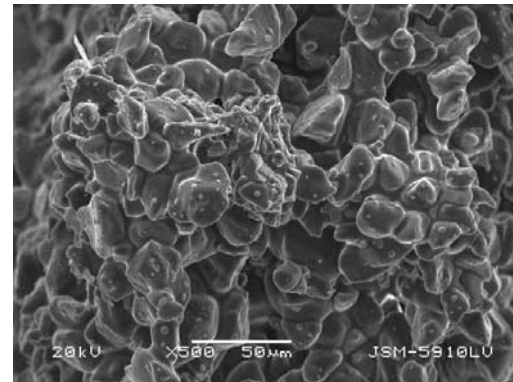


Figure 4: The porous microstructure obtained by the H_2O_2 method. (X500 Magnification)

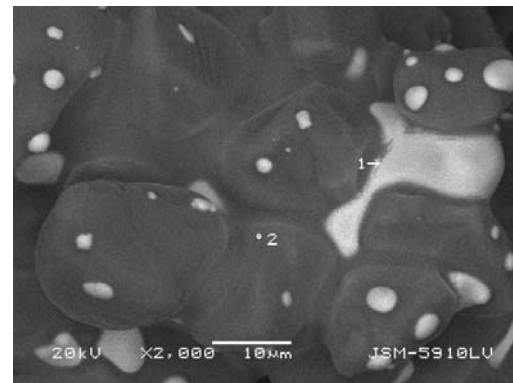


Figure 5: The different phases present in the structure indicated as “1” and “2” points and selected for the EDS analysis (Back scattered image, X2000 Magnification) [The H_2O_2 method].

Table 2: The EDS analysis of the points 1 and 2 of structures obtained by the H₂O₂ method (Processing option : All elements analyzed (Normalised), All results in Weight Percent).

Spectrum	O	Al	Zr	Total
Spectrum 1	24.65	3.11	72.25	100.00
Spectrum 2	36.81	63.19	-	100.00

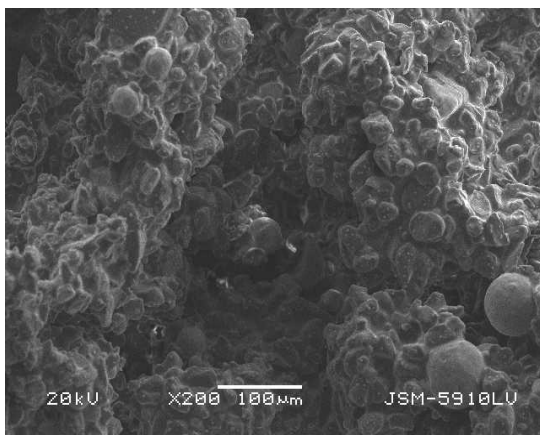


Figure 6: The porous microstructure obtained by the PVA method. (X500 Magnification)

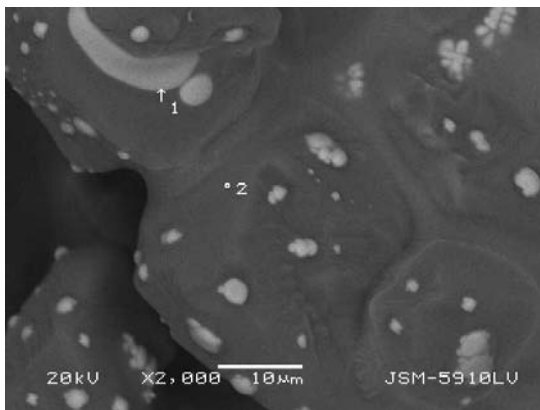


Figure 7: The different phases present in the structure indicated as “1” and “2” points and selected for the EDS analysis (Back scattered image, X2000 Magnification) [The PVA method].

Table 3: The EDS analysis of the points 1 and 2 of structures obtained by the PVA method (Processing option : All elements analyzed (Normalised), All results in Weight Percent).

Spectrum	B	O	Al	Zr	Total
Spectrum 1	1.99	39.10	0.79	58.1	100.00
Spectrum 2	-	34.53	65.47	-	100.00

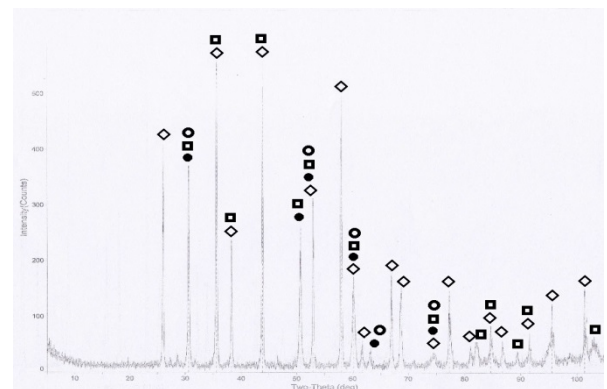


Figure 8: The XRD pattern of the porous structure obtained by the PU foam method. [\diamond ; Alumina and \bullet ; Yttria stabilized Zirconia, \square ; Zirconium silicate ($ZrSiO_4$), \odot ; Magnesium zirconate with formula $2MgO.5ZrO_2$].

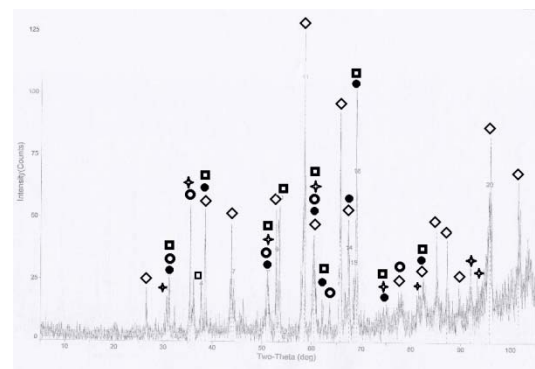


Figure 9: The XRD pattern of the porous structure obtained by the H₂O₂ method. [\diamond ; Alumina and \bullet ; Yttria stabilized Zirconia, \square ; Zirconium silicate ($ZrSiO_4$), \odot ; Magnesium zirconate with formula $2MgO.5ZrO_2$, \star ; Zirconium yttrium oxide].

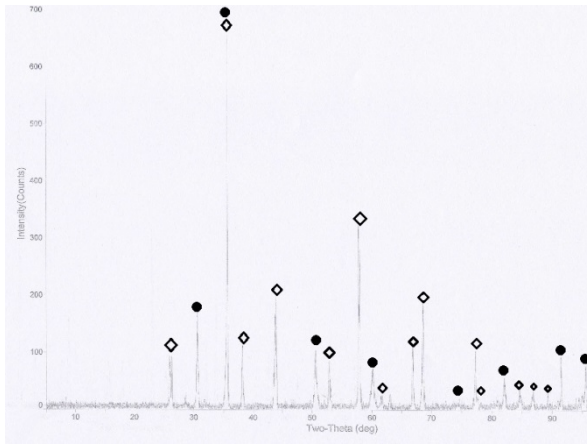


Figure 10: The XRD pattern of the porous structure obtained by the PVA method.

(\diamond ; Alumina and \bullet ; Yttria stabilized Zirconia)

4. CONCLUSION

According to the phase diagrams and reactions between yttria stabilized zirconia and alumina, zirconia and magnesia, zirconia and silica finally alumina-magnesia and alumina-silica, the eutectoid and eutectic points are much more elevated in case of zirconia and alumina and the two other components with alumina, separately in binary phase diagrams so the formation of zirconia-silica and magnesia-zirconia based phases are much more evident as approved by the XRD results and EDS analysis, also the separate phases present in the SEM images. Additionally, the particles of the yttria stabilized zirconia acted as the secondary nucleation sites and formed the preferred nucleation of the phases magnesia and silica which cumulated in these sites, subsequently constituting binary phases. The unreacted and excessive zirconia phase is situated on the alumina-rich matrix as indicated BSE images (Lighter parts). The boron detected in the EDS analysis can be attributed to the contamination during the sample preparation for the SEM and EDS

analysis. The pore sizes created by different foaming methods have tendency to change from coarse and macro pores (the PU foam method) to finer and micro pores (the PVA method).

Acknowledgements: We are thankful to Eng. Dr. Mustafa INAN for his guideness and help during SEM and EDS Analysis, also we wish to express our sincere appreciation to Assoc. Dr. Sinan KESKİN for his support, inspiration, and encouragement throughout our research effort.

REFERENCES

- Albano M.P., Genova L.A., Garrido L.B., Plucknett K., 2008. Processing of porous yttria-stabilized zirconia by tape-casting, *Ceramics International*, 34, 1983.
- Fidancevska E., Ruseska G., Bossert J., Lin Y-M., Boccaccini A.R., 2007. Fabrication and characterization of porous bioceramic composites based on hydroxyapatite and titania. *Materials Chemistry and Physics*, 103, 95.
- Hashimoto S., Umeda T., Hirao K., Kondo H., Zhou Y., Hyuga H., Honda S., Iwamoto Y., 2013. Fabrication and characterization of porous ZrO_2 with a high volume fraction of fine closed pores, *Journal of the European Ceramic Society*, 33,) 61.
- Hu LF., Wang CA., 2010. Effect of sintering temperature on compressive strength of porous yttria-stabilized zirconia ceramics, *Ceramics International*, 36, 1697.
- Matsumoto Junior T., Hyun An S., Ishimoto T., Nakano T., Matsumoto T., Imazato S., 2011. Zirconia-hydroxyapatite composite material with micro porous structure, *Dental Materials*, 27, e205.
- Pabst W., Gregorová E., Sedlá I., Černý M., 2011. Preparation and characterization of porous alumina-zirconia composite ceramics, *Journal of the European Ceramic Society*, 31, 2721.
- Zhang Z., Liu J., Wang F., Kong J., Wang X., 2011. Fabrication of bulk macroporous zirconia by combining sol-gel with calcination processes, *Ceramics International*, 37, 2549

HIGH TEMPERATURE MECHANICAL PROPERTIES OF CEMENT PREPARED BY ADDITION OF WASTE FOUNDRY SAND

Sinem Çevik Üzgür^{1,a}, Tuğba Işıtan¹, Başak Mesci¹, Erhan Tüfenk¹

1. Ondokuz Mayıs University, Materials Science and Engineering, Samsun, Turkey
a. *Corresponding Author*(sinemu@omu.edu.tr)

ABSTRACT: Globally improving industrial technology has severely caused the environmental problems like increasing amount of waste materials. Since there is a serious need to reuse by-products and waste materials generated from industry, solid waste management has become the important concern all over the world. Foundry sand can be used in the foundries several times and it can also be used in cement based materials after it can be no longer used in molds. So spent foundry sand is a by-product of ferrous and non-ferrous metal casting industries. Fly ash, a byproduct of thermal power plants has been reported to improve the mechanical properties and durability of cement. In the present study the influence of fly ash, and spent foundry sand as partial replacement of sand on the elevated temperature mechanical properties of cement is investigated.

1. INTRODUCTION

Automotive, railroad, machinery manufacturing, iron-steel and energy industry which needs materials cast in foundries use large amounts of sand casting depending on the production methods. 65% of the wastes in foundry is foundry sand. Waste foundry sand changes according to using binders. Inorganic binders such as bentonite-clay and organic binders such as furan resins and phenol are used as binders. Due to the reduction of product wastes and conservation of raw materials, recycling and recovery of foundry sand is an effective alternative in order to reduction of environmental impacts. Foundries can reuse sand casting at their own production lines successfully. Recovery and recycling of waste sand can be made by developing in many different industrial methods. There are three kinds of recycling methods are available: thermal, wet and dry mechanical reclamation. In addition, non hazardous solid waste foundry sand used in application such as filling of holes created by abandoned mines and stone, road construction, landscaping, storage

area. There are many applications such as cement, ready-mixed concrete, soil, road and asphalt filler in Europe.

2. PROPERTIES OF WASTE FOUNDRY SAND

Spent Foundry sand is high quality silica sand that is a by product from the production of both ferrous and non ferrous metal castings. Foundries use high quality size-specific silica sands for use in their molding and casting operations. The raw sand is normally of a higher quality than the typical bank run or natural sands used in fill construction sites. In the casting process, molding sands are recycled and reused multiple times. Eventually, however, the recycled sand degrades to the point that it can no longer be reused in the casting process. When it is not possible to further reuse sand in the foundry, it is removed from the foundry and is termed as “spent foundry sand”. The physical and chemical characteristics of foundry sand will depend in great part on the type of casting process and the industry sector from which it originates.

Spent foundry sand consists primarily of silica sand, coated with a thin film of burnt carbon, residual binder (bentonite, sea coal, resins/chemicals) and dust. In Table 1 the chemical composition of the foundry sand can be seen. Depending on the binder and type of metal cast, the pH of spent foundry sand can vary between 4 and 8. It has been reported that some spent foundry sands can be corrosive to metals. In Table 1 the chemical composition of the foundry sand can be seen.

Table 1: The chemical composition of foundry sand (American Foundrymen's Society, 1991) [Siddique and Noumowe, 2008]

Constituent	Value (%)
SiO ₂	87.91
Al ₂ O ₃	4.70
Fe ₂ O ₃	0.94
CaO	0.14
MgO	0.30
SO ₃	0.09
Na ₂ O	0.19
K ₂ O	0.25
TiO ₂	0.15
Mn ₂ O ₃	0.02
SrO	0.03
LOI	5.15
Total	99.87

Spent foundry sand is generally sub angular to round in shape. Green sands are generally black, or gray, and chemically bonded sand is typically a medium tan or off-white color. The grain size distribution of spent foundry sand is uniform, with 85–95% of the material between 0.6 and 0.15mm, 5 to 12% of foundry sand can be smaller than 0.075mm. The physical properties of spent foundry sand can be seen in Table 2.

Foundry sand is produced by different foundry classes. The ferrous foundries (gray iron, ductile iron and steel) produce the most sand, and aluminum, copper, brass and bronze produce the rest. The sands from the brass, bronze and copper foundries are generally not reused. In Table 3 the mechanical properties of spent foundry sand are given.

Table 2: The physical properties of spent foundry sand [Siddique and Noumowe., 2008]

Property	Value
Specific gravity	2.39–2.55
Bulk relative density (kg/m ³)	2589
Absorption (%)	0.45
Moisture content (%)	0.1–10.1
Clay lumps and friable particles	1–44
Coefficient of permeability (cm/s)	10 ⁻³ –10 ⁻⁶
Plastic limit/plastic index	Non-plastic

Table 3: The mechanical properties of spent foundry sand [Benson and Bradshaw 2011]

Property	Results	Relevant Test Method
Micro-Deval Abrasion Loss, % ⁽¹⁾	< 2	ASTM D6928-06
Magnesium Sulfate Soundness Loss, % ⁽²⁾	5–15	ASTM C88-05
Internal friction angle (drained) ^(1,4,5,6)	33° - 43°	ASTM D4767-04 ASTM D 3080
Cohesion intercept (drained), lb/ft ² ^(1,4,5,6)	145–585	ASTM D4767-04 ASTM D 3080
Unconfined compressive strength, lb/ft ² ⁽⁷⁾	482–3968	ASTM D 2166
California Bearing Ratio, % ^(5,7)	4 - 20 average 20	ASTM D1883-05
Resilient Modulus (MR) Regression Coefficients ⁽⁷⁾	K ₁ = 122,000 – 248,000 lb/ft ² K ₂ = 0.44 - 0.56	AASHTO T-294- 94

3. RECYCLING OF WASTE FOUNDRY SAND

Some studies indicated that the incorporation of spent sands into clay bricks reduced the problems related to landfill disposal and minimized the costs of both brick manufacturing and waste sand treatment. Furthermore, the high temperature process required to produce the bricks is hypothesized to stabilize pollutants and decrease leaching. Therefore waste foundry sands can be used in ceramic bricks. That is spent foundry sand can be successfully recycled in brickmaking as a substitute for plasticity-reducing raw materials, such as naturally occurring sands. The percentage of recyclable sand is strongly influenced by the characteristics of the raw materials (both clay and sand) and the brickmaking process (e.g. shaping technique, drying and firing schedule). Performing the appropriate technological and environmental testing is highly recommended prior to re-using unknown foundry sands in ceramic bodies [Alonso-Santurde *et al.*, 2011].

Concrete is the most widely used man made product in the world, and is second only to water as the world's most utilized substance. Concrete is economical, strong, and durable. Throughout the industrial sector, including the concrete industry, the cost of environmental compliance is high. Introduction of use of industrial by-products such as foundry sand, fly ash, bottom ash, and slag can result in significant improvements in overall industry energy efficiency and environmental performance. The presence of finer foundry sand particles in concrete lead to the increase in the water demand, as compared to the regular sand particles.

The use of foundry sand in cement and concrete mixtures is an emerging application area. Various characteristics of foundry sand can affect the quality of concrete produced. Because foundry sand properties vary depending on the source from which the foundry sand was produced, it is important that adequate testing of the sand is performed. Prior to reuse, foundry sand should be screened and crushed to obtain the desired gradation, and magnetic particles should be separated. These processes will remove deleterious materials preventing technical problems when mixing the cement components. Foundry sand from green sand molding is black or gray and may cause finished concrete to have a slightly darker grayish/black tint. A 15 percent or less fine aggregate replacement with foundry sand typically produces a minimal color change.

4. ELEVATED TEMPERATURE RESPONSE OF CONCRETE PRODUCED BY ADDITION OF WASTE FOUNDRY SAND

Self-Compacting-Concrete (SCC) was introduced in 1989 by Professor Ozawa of Japan. Although the use of SCC has many technical and economical advantages, its supply cost could be two

to threetimes higher than that of normal concrete depending upon the composition of the mixture and quality control of concrete produced. Such a high premium has somehow limited SCC application to general construction. For SCC, it is generally necessary to use super-plasticizers in order to obtain high mobility. Adding a large volume of powdered material can eliminate segregation. The powdered materials are fly ash, silica fume, lime stone powder, glass filler, quartzite filler and ground granulated blast furnace slag that can be added to increase the slump of the concrete mix and also to reduce the cost of SCC.

As the use of SCC becomes common, the risk of exposing it to elevated temperatures increases. Influence of elevated temperatures on mechanical properties of concrete is of very much importance for fire resistance studies and also for understanding the behaviour of containment vessels, chimneys, nuclear reactor, pressure vessels during service and ultimate conditions structures like storage tanks for crude oil, hot water, coal gasification, liquefaction vessels used in petrochemical industries, foundation for blast furnace, coal and coke industries, furnace walls, industrial chimney, air craft runways, etc. subjected to elevated temperatures. Concrete structures including walls and pipes may also be exposed to elevated temperatures which may result in significant damage. Hence to predict the response of structure after exposure to elevated temperature, it is essential that the strength properties of concrete subjected to elevated temperature be clearly understood. Variation of compressive strength, split tensile strength, modulus of elasticity, rapid chloride permeability, porosity and mass loss are some of the important properties to be investigated when concrete structures are subjected to

elevated temperatures. Degradation of mechanical behaviour of concrete due to exposure to high temperature has been studied since 1950s in western countries. The rise in temperature of the concrete over 1000°C is enough to destroy the original material. At early stages of heating the evaporable water from concrete is lost over in the range of 20° - 110°C. Above 110°C the cement hydrates decompose, calcium hydroxide is broken down and the calcium carbonate suffers decarbonation. The aggregate also suffers changes, which contributes to the general loss of structure safety. The decrease in compressive strength depends on the aggregate, cement paste and the initial moisture content of the specimen. Some of the studies on SCC subjected to elevated temperature showed both decrease in strength and increase in the risk of spalling or a similar behaviour to that of vibrated concrete [Pathak and Siddique, 2012].

Ghandehari et al. evaluated the residual mechanical properties of high strength concretes after exposure to elevated temperatures by using silica fume, and reported that after heating to 200 °C the strength of all of the concretes slightly improved when compared to strength at 100 °C [Ghandehari *et al.*, 2010].

5. CONCLUSION

Spent foundry sand is waste material from foundries. It exhibits lower unit weight, higher water absorption, and higher percent void compared to regular concrete sand. Spent foundry sand can be used as a replacement for regular sand and/or fly ash in making controlled low strength materials without any significant modification or adjustment. Spent foundry sand could be very conveniently used in making good quality concrete and construction materials. Strength properties of concrete mixtures increase

with the increase in foundry sand contents and also with the age.

REFERENCES

- Alonso-Santurde, R., Andres, A., Viguri, J. R., Raimondo, M., Guarini, G., Zanelli, C., Dondi, M., 2011., Technological behaviour and recycling potential of spent foundry sands in clay bricks, *Journal of Environmental Management*, 92, 994-1002.
- Benson, C. H., Bradshaw, S., 2011., User guideline for foundry sand in green infrastructure construction, *Recycled Materials Resource Center*, USA.
- Ghandehari, M., Ali, B., Mostafa, K., 2010., Residual mechanical properties of high strength concretes after exposure to elevated temperatures, *Journal of Materials in Civil Engineering*, 59-64.
- Pathak, N., Siddique, R., 2012., Effects of elevated temperatures on properties of self-compacting-concrete containing fly ash and spent foundry sand, *Construction and Building Materials*, 34, 512-521.
- Siddique, R., Noumowe, A., 2008., Utilization of spent foundry sand in controlled low-strength materials and concrete, *Resources, Conservation and Recycling*, 53, 27-35.

THE PRODUCTION OF HARD PORCELAIN IN LOW TEMPERATURES

Başak Mesci¹, Sinem Çevik Üzgür^{1,a} and Tuğba Işıtan¹

1. Ondokuz Mayıs University, Materials Science and Engineering, Samsun, Turkey
a. Corresponding Author (sinemu@omu.edu.tr)

ABSTRACT: Hard porcelains are that fired in 1380-1400°C have high energy cost due to high production cost. Porcelains typically have a triaxial composition comprised of about 50% clay, 25% flux and 25% filler. Fired bodies containing these three components result in a grain and bond microstructure, which has large grains or filler (usually quartz) held together by a finer bond or matrix comprised of mullite crystals and a glassy phase. In relation to its raw material composition (clay, quartz and feldspar), porcelain stoneware is considered to be a triaxial porcelain material. In porcelain production, using waste materials can decrease the raw material cost. Using spodumen in hard porcelain body provide the decreasing of the firing temperature without unchanging physical properties of the body. In the present study, the research is mainly about the production of the hard porcelain, the effect of the spodumen on the low temperature production of the porcelain and the waste materials usage in the production of porcelain. Literature review gives the last improvements, which types of waste materials can be used in the porcelain production and how these materials affect the properties of the porcelain and provide the cost savings on the raw material usage.

1. INTRODUCTION

Porcelain is a white, non-porous and partially transparent ceramic material, whose production started in China many centuries ago. Today, porcelain is produced in many countries and its technology is well known. A consistent part of the new studies is related to the substitution of the traditional raw material in the composition (sand, feldspar and kaolin) with others, such as zeolite, corundum, bentonite, etc. glass cullet or waste products. This latter aspect acquires particular importance due to the reduced availability of high quality raw materials [Karamanov *et al.*, 2006]. In Fig.1 the diagram shows the common commercial porcelain compositions [Junkes *et al.*, 2012].

Both bone china and hard porcelain are white and translucent. Bone chinas are highly crystalline materials which are

resistant to edge chipping. Unfortunately, the glazes used on bone chinas tend to be more easily scratched than those on hard porcelains. Hard porcelains are highly glassy and their edges tend to chip easily. They are expected to have lower toughness values and strengths than bone chinas. However, the glazes on hard porcelain, which are rich in silica, are both chemically highly durable and abrasion resistant. Hence, the novel whiteware needed an appearance comparable with bone chinas or hard porcelains, to be chip resistant like bone china and to be coated with a glaze similar to those applied to hard porcelains [Capoglu and Messer, 2004].

Traditional ceramic formulations consist of at least three components that play the three fundamental roles for optimum processing, and hence performance of the final products, kaolin or kaolinitic clay for plasticity, feldspar for fluxing and silica as filler for the structure.

Ceramic processes have long been regarded as ideal to accomplish inertization of potentially hazardous wastes and, given the composition similarities between some wastes and natural raw materials used in ceramics manufacture. This has led to the general acceptance of ceramic industry, particularly the sector dealing with construction materials, as a potentially high consumer of wastes from other industrial sources.

Some wastes often also contain materials that are beneficial for the ceramics manufacture processes and, therefore, promoting industrial wastes to alternative ceramic raw materials is both technically and economically attractive. Recycling and finding reuse alternatives for industrial wastes gain added relevance, and a number of potential applications have been proposed, namely in the production of clay-based bricks, porcelainized tiles, mortars and concrete, ceramic pigments and glass-ceramics to name a few. The waste materials involved range from ore tailings and ornamental stone cuttings to potable and residual water treatment sludges, metal anodizing and other surface treatment sludges, and thermal power plant ashes, and also include agro-industrial and forestry wastes.

In one research study that partial substitution of quartz and kaolin by sandstone dust in a triaxial porcelain composition was found to be beneficial towards improvement in flexural strength and early vitrification at 1115°C. X-ray pattern of stone dust can be shown in Fig. 2. Presence of considerable amount of alkali and alkaline earth minerals in the sandstone dust and clay minerals were responsible for early vitrification. Further, use of such overburden industrial by product reduces the cost of raw

materials and thermal energy without altering the required physico-mechanical properties of ceramic tiles for application in building industries [Halдар and Das., 2012].

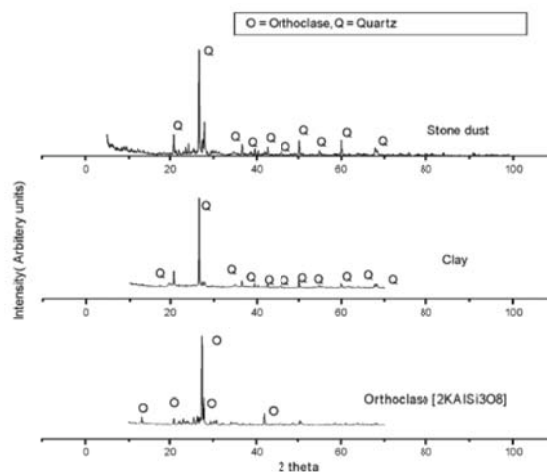


Figure 2: X-ray diffractogram of stone dust, clay and feldspar [Halдар and Das., 2012].

Fly ash has been considered as low cost resource material for alumino-silicate. Fly ash can be used as a partial substitution of clay in the development of ceramic tiles. The reason for this selection is twofold. First, fly ash being a combustion product has very negligible shrinkage, which is an essential criterion for a filler material in porcelain composition. Secondly, as fly ash contains fluxing components, an attempt has been made to utilize this as a partial replacement of feldspar in the composition [Mukhopadhyay *et al.*, 2010]. Moreover high value added products like wear resistant ceramic liner, glass ceramics, synthetic mullite, cenosphere, fly ash–Al matrix composite, wool can be made from fly ash.

Bauxite Residue”, BR, also known as “red mud”, is the main waste generated during the production of alumina by means of the Bayer cycle. In Pontikes *et al.* found that for clay body mixtures with

BR, the initiation of the sintering zone took place at a lower temperature. The firing shrinkage is higher for the mixtures with BR, however does not increase in all cases accordingly with the content of BR. For BR percentage in excess of 40 wt.% and firing temperature higher than 950 °C, low viscosity liquid phase seems to be formed, as indicated by the second shrinkage zone observed in dilatometry. The final mineralogical composition of the mixtures appears to be an assemblage of the clay body mixture and BR [Pontikes *et al.*, 2007].

Junkes *et al.* study suggests that the manufacture of ceramic tiles using only wastes is possible and porcelain-like ceramics can be produced. In this study based on their fluxing character and plasticity, four non-hazardous industrial wastes were selected and characterized: one clay mining tail, the sludge from potable water treatment and two sludges from gneiss and varvite cutting processes. Using the phase diagram of the $\text{SiO}_2\text{--Al}_2\text{O}_3\text{--K}_2\text{O}$ system, four mixtures located within the wastes-defined polygon were formulated, uniaxially pressed and fired for 40 min at 900–1150 °C. The results obtained for the properties of fired samples show that water absorption values below 10% (ceramic tiles) and 3% (porcelain tiles) were reached upon firing at 1100 and 1150 °C, respectively, without firing warpage. Density values were also within the usual range [Junkes *et al.*, 2012].

In another investigation it was considered the possibility to reinforce a standard body mix for porcelain stoneware tiles, by the addition of two alumina powders: a high purity alumina and, calcined bauxite. This choice, overcoming the previously cited problems, allowed to prepare homogeneous particle-dispersed traditional ceramic composites. To decrease the refractoriness, due to

alumina, a stronger fluxing agent was used, by replacing part of the fluxing agent, sodium feldspar, with the same amount of spodumene. The mineral of spodumene was used to partially replace the sodium feldspar in the standard body mix. It contains 97% of α -spodumene and 3% of α -quartz. The chemical composition of spodumene is shown in Table 1. The presence in a silicates body mix of a fluxing agent rich in lithium, as spodumene, promotes the development of a liquid phase, during its firing. That is due to: (i) low melting points of the lithium compounds, (ii) possibility to easily form eutectics and, (iii) high mobility of lithium ion. In their study, part of the fluxing agent of the standard body mix has been replaced with the same amount of spodumene. This resulted in a higher densification at all the tested temperatures in comparison with the standard composition, without spodumene, even when high refractory materials were added. In addition, to the development of a low viscosity liquid phase, the presence of spodumene produces a reduction of shrinkage. As a consequence, the reduced shrinkage favours the dimension stability of fired products that is particularly important for the industrial production of very large pieces.

The presence of spodumene, due to its capability to develop a low viscosity liquid phase, improves the sintering performances of the modified products, reduces porosity and favours the crystallisation of rather elongated needle like mullite. This could have contributed to further increase the mechanical characteristics. Finally it is to be underlined as the presence of spodumene is able to strongly reduce the firing temperature and shrinkage, with positive aspects both from an energetical point of view and for a possible reduce of scraps products [Tucci *et al.*, 2012].

Table 1: Chemical composition, wt. % of spodumene.

P.F.	0.20
SiO ₂	64.00
Al ₂ O ₃	26.00
Fe ₂ O ₃	0.07
CaO	0.05
Li ₂ O	7.60
P ₂ O ₅	0.17
K ₂ O	0.08
Na ₂ O	0.15

3. CONCLUSION

Due to gradual depletion of naturally occurring minerals, there is a strong need to evolve alternate source of raw materials which are abundantly available as overburden wastes. In such attempts, many workers have utilized solid industrial wastes as alternative source of alumino silicate and fluxing mineral by replacing a part of quartz, clay and feldspar in triaxial porcelain composition.

Recycling can help solving important issues related to storage of wastes and simultaneously the preservation of natural raw materials which is fast depleting. To take advantage of this opportunity, wastes must be regarded as possible raw materials and should be carefully characterized in order to predict their behaviour during processing and their effects on the final products. The ceramic industry is one of the largest consumers of natural raw materials but has also the capacity and potential to make significant contributions in solving problems associated with wastes. The use of industrial wastes as alternative raw materials can be considered viable only if the manufacturing process remains essentially unchanged and the quality and characteristics of the product are not unduly affected.

The meaningful utilization of industrial waste materials has been acclaimed world over not only as an economic opportunity, but also as a step towards solving problems of environmental pollution.

REFERENCES

- Capoglu, A., Messer, P. F., 2004., Design and development of a chamotte for use in a low-clay translucent whiteware, *Journal of the European Ceramic Society*, 24, 2067-2072.
- Haldar, M. K., Das, S. K., 2012., Effect of substitution of sand stone dust for quartz and clay in triaxial porcelain composition, *Bull. Mater. Sci.*, 35, 897-904.
- Junkes, J. A., Prates, P. B., Hotza, D., Segadaes, A. M., 2012., Combining mineral and clay-based wastes to produce porcelain-like ceramics: An exploratory study, *Applied Clay Science.*, 69, 50-57.
- Kamseu, E., Leonelli, C., Boccaccini, D. N., Veronesi, P., Miselli, P., Pellacani, G., Melo, U. C., 2007., Characterisation of porcelain compositions using two china clays from Cameroon, *Ceramics International*, 33, 851-857.
- Karamanov, A., Karamanova, E., Ferrari, A. M., Ferrante, F., Pelino, M., 2006., The effect of fired scrap addition on the sintering behaviour of hard porcelain, *Ceramics International*, 32, 727-732.
- Mukhopadhyay, T. K., Ghosh, S., Ghosh, J., Ghatak, S., Maiti, H. S., 2010., Effect of fly ash on the physico-chemical and mechanical properties of a porcelain composition, *Ceramics International*, 36, 1055-1062.
- Pontikes, Y., Nikolopoulos, P., Angelopoulos G. N., 2007., Thermal behaviour of clay mixtures with bauxite residue for the production of heavy-clay ceramics. *Journal of the European Ceramic Society*, 27, 1645-1649.
- Tucci, A., Esposito, L., Malmusi, L., Rambaldi, E., 2007., New body mixes for porcelain stoneware tiles with improved mechanical characteristics, *Journal of the European Ceramic Society*, 27, 1875-1881.
- Tulyaganov, D. U., Agathopoulos, S., Fernandes, H. R., Ferraira, J. F. M., 2004., Synthesis of lithium aluminosilicate glass and glass-ceramics from spodumene material, *Ceramics International*, 30, 1023-1030.
- Youssef, N. F., Abadir, M. F., Shater M. A. O., 1998. Utilization of soda glass (cullet) in the manufacture of wall and floor tiles, *Journal of the European Ceramic Society*, 18/ 12, 1721-1727.

COMPARISONS OF FINE DRY GRINDING OF TWO DIFFERENT POROUS POWDERS: AMORPHOUS SILICA AND DIATOMITE

Vedat Deniz^{1,a}, Yakup Umucu²

1. HititUniversity, Department of Polymer Engineering, Çorum, Turkey

2. SüleymanDemirelUniversity, Mining Engineering, Isparta, Turkey

a. Corresponding author (vedatdeniz@hitit.edu.tr)

ABSTRACT: Powders of amorphous silica and diatomite have recently recognized in the industry. Therefore, the grinding properties of natural amorphous silica and diatomite were studied. Firstly, the Standard Bond Work Index tests were made for the amorphous silica and diatomite samples. Latter, kinetic breakage behaviours of each two sample were studied with the emphasis on a kinetic study in a ball mill. The model parameters (a_T , α , ϕ , γ and β) were compared for the two different porous powder samples. In this investigation, the specific rates of breakage of the diatomite were better than the amorphous silica at the same experimental conditions. The breakage parameters obtained showed that the diatomite is broken faster than amorphous silica. However, although porous samples have different properties with respect to abrasive behavior, the primary breakage of each two porous samples gave close to relative production rate of fines for especially smaller particle sizes. In this study, a relationship between the Bond Work Index and breakage parameters of grinding kinetic on two porous samples was not fully obtained. Reason of this different result is due to different geological origin and properties of internal porosity of porous materials.

1. INTRODUCTION

Porous materials are significant interest due to their wide applications in catalysis, separation, lightweight structural materials, biomaterials and so on. Porous materials (pumice, trass, amorphous silica, diatomite, zeolite, etc.), especially closed pore materials, have been used for a long time for many common purposes, including thermal or acoustic insulators, and construction materials such as light walls. On the other hand, materials required to have open pores are mainly used for industrial purpose, such as catalytic converter filters for exhaust gases, electrolytic membranes, filters, and high efficiency grindstones [Deniz and Onur, 2002; Deniz, 2011].

Diatomite a chalky, sedimentary rock consisting mainly of an accumulation of skeletons remaining from prehistoric diatoms are single-celled, microscopic aquatic plants. The skeletons are

composed of amorphous silica (silicon dioxide, SiO₂), a very durable substance. Besides its amorphous silica content diatomite rocks commonly contain carbonate and clay minerals, quartz and feldspars [Dolley, 1991].

Amorphous silica possessed many physical and chemical properties similar to those of diatomite. Amorphous silica and diatomite particles are used as fillers in the rubber industry, as free-flow and anticaking agents for powder materials and as carriers of liquids, which are used particularly in the manufacture of animal feed and agrochemicals. Moreover, toothpaste, paints, a supplementary cementing and concrete material and silicon rubber represent further important applications [Anderson *et al.*, 2000; Deniz *et al.*, 2003].

In the above-mentioned industries, ultra fine ground of amorphous silica and

diatomite minerals are needed. Depending on the physical properties of the material, i.e. its hardness, brittleness, strength and grindability, the breakage parameters are bound to vary from material to material. The behaviour of porous materials in comminution processes differs substantially from that of non-porous materials. It is strongly affected by the type of porosity, which may be characterized by different void shapes and interconnection degrees [Deniz, 2011].

The grinding process has many variables and some are difficult to understand. The grindability of a material is the only factor used to determine the required size of a grinding machine. Although, Bond grindability test is widely used to estimate power required of an industrial grinding mill. Recently, kinetic model has been mostly used to the design of grinding circuits [Prasher, 1987; Deniz, 2004].

The analysis of grinding in the ball mill uses the concepts of selection and cumulative breakage distribution functions. The selection function (specific rate of breakage) is defined as the fraction by weight of particles of given size i which are selected and broken per unit time of grinding. The value varies with size and denoted by S_i . The cumulative breakage distribution function, B_{ij} , is defined as the fraction by weight of breakage products from size j which fall below size i , where $i \leq j$ [Austin *et al.*, 1984; Deniz, 2004; Deniz, 2011].

The analyses of size reduction in tumbling ball mills, using the concepts of specific rate of breakage and primary daughter fragment distributions, have received considerable attention in years. Austin has reviewed the advantages of this approach and the scale-up of

laboratory data to full-scale mills has also been discussed in a number of papers [Austin, *et al.*, 1981].

This paper presents a comparison of the breakage parameters of diatomite and amorphous silica samples which have different chemical, mineralogical and morphological compositions under the same conditions in a laboratory ball mill.

2. THEORY

Population balance modelling is a widely used tool for the quantitative analysis of comminution processes at the process length scale. The traditional size-discrete form of the population balance equation for batch comminution is linear and assumes first-order breakage kinetics [Austin, 1972].

$$\frac{dw_i(t)}{dt} = -S_i W_i(t) + \sum_{j=1}^{i-1} b_{ij} S_j W_j(t), \quad (1)$$

Thus, the breakage rate of material that is in the top size interval can be expressed as:

$$\frac{-dw_1}{dt} = S_1 w_1(t) \quad (2)$$

Assuming that S_1 does not change with time (that is, a first-order breakage process), this equation integrates to

$$\log(w_1(t)) - \log(w_1(0)) = \frac{-S_1 t}{2.3} \quad (3)$$

where $w_1(t)$ is the weight fraction of the mill hold-up that is of size 1 at time t and S_1 is the specific rate of breakage. The formula proposed by Austin *et al.* (1984) for the variation of the specific rate of breakage S_i with particle size is

$$S_i = a_T X_i^\alpha \quad (4)$$

where X_i is the upper limits of the size interval indexed by i , mm, and a_T and α are model parameters that depend on the properties of the material and the grinding conditions. The value of α is a positive number, which is characteristic of the material (providing the test conditions are in the normal operating range), but the value of a_T varies with the mill conditions.

The cumulative primary breakage distribution (B_{ij}) is also defined in an empirical form [Austin and Luckie, 1972] by

$$B_{i,j} = \phi_j [X_{i-1}/X_j]^\gamma + (1-\phi_j) [X_{i-1}/X_j]^\beta \quad n \geq i > j \quad (5)$$

$$\phi_j = \phi_1 [X_i/X_1]^{-\delta} \quad (6)$$

where X_1 is the top size, and $B_{i,j}$ is the weight fraction of primary breakage products. δ , ϕ_j , γ and β are model parameters that depend on the properties of the material. If $B_{i,j}$ values are independent of the initial size, i.e. dimensionally normalisable, then δ is zero [Austin *et al.*, 1984].

On plotting experimentally determined $B_{i,1}$ values versus x_i on log-log scales, the slope of the lower straight line portion of the curve gives the value of γ , ϕ_j is the intercept of this part of the line extrapolated to x_2 , and β is determined to make the function fit the upper part of the curve. The slope of the lower portion of the $B_{i,j}$ curve can be denoted by γ with smaller values of γ indicating that once particles of a certain size break, they produce many much smaller progeny fragments. Thus γ is a convenient and measurable parameter for characterizing material oriented breakage properties [Makokha and Moys, 2006].

3 EXPERIMENTAL PROCEDURE

3.1 Material and Method

Two samples taken from different regions of Turkey were used as the experimental materials. Amorphous silica was taken from deposits in Isparta (Keçiborlu). Diatomite sample was taken from deposits in Aydın (Karacasu). The chemical properties of samples were presented in Table 1.

Table 1. Chemical composition of porous samples using in experiments.

Oxides (%)	Amorphous Silica	Diatomite
SiO ₂	90.91	89.58
Al ₂ O ₃	0.13	1.77
Fe ₂ O ₃	0.11	0.78
CaO	0.36	0.70
MgO	---	0.22
Na ₂ O	0.07	0.12
K ₂ O	0.06	0.21
SO ₃	0.27	1.61
L.O.I.	4.95	4.99

3.2 Mineralogical and Morphological Analysis

Mineralogical investigations were conducted using polarization microscopy, and a scanning electron microscope (SEM) was used to observe the morphology of two porous samples. SEM images obtained at same magnifications of two samples to make accurate comparisons were shown in Figures 1-4.

Amorphous silica had a SiO₂ content of about 90%, attributed to the presence of quartz and amorphous quartz minerals. The sample using experiments contained high amounts of amorphous silica content. In addition to the amorphous phase, lesser amounts of anatase and opal were also present. Gotit, sulphur, were a minor component of the rock, whereas carbonates such as calcite and dolomite were absent. The examination of the samples with SEM confirmed the

existence of the sponge spicules matrix. In addition, the opaline phase of amorphous silica was determined on the sample with SEM (Figure 1). The predominance of amorphous silica was indicative of transportation and re-deposition of the micro crystal quartz particles (Figure 2).

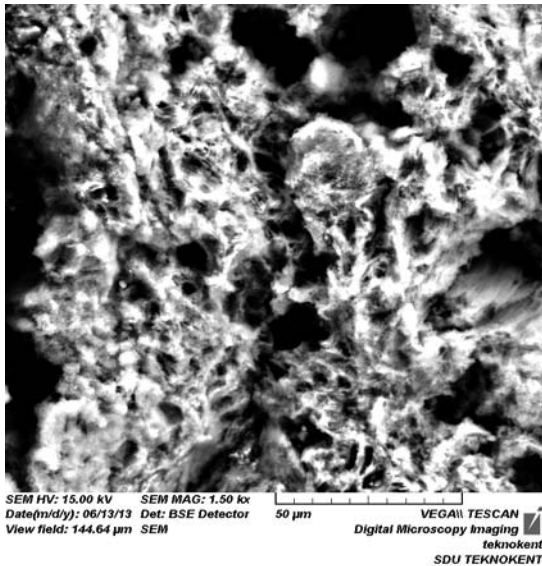


Figure 1: The existence of the sponge spicules matrix in amorphous silica.

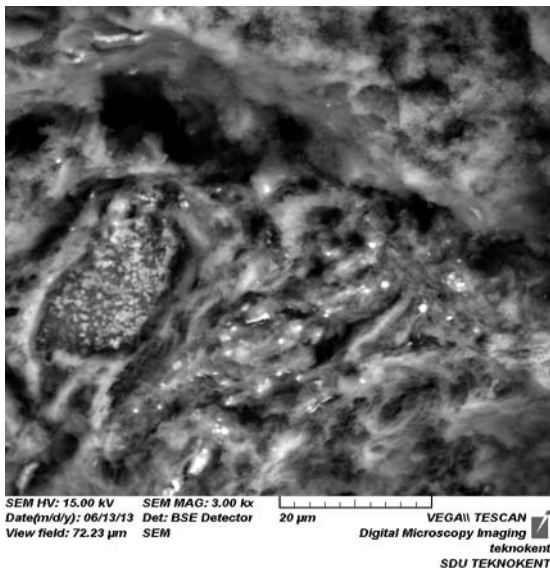


Figure 2: Indicative of transportation and re-deposition of the micro crystal quartz particles in amorphous silica.

The diatomite was found to be pure, amorphous, usually soft and easily friable

with particle size of 5-100 µm. The grains are of the size of very fine dust. The pore walls are made of hundreds of coccoliths that form a poorly cemented mosaic. These coccolith mosaics are mechanically weak and collapse with the changing pore pressure. The porosity is 50-60%, and it is practically impermeable (0.1-5 µm) (Figure 3). It was determined that the diatomite samples were highly with a high water absorption capacity and contained plagioclase, smectite, illite and quartz minerals. The types mainly examined are as follows: *Pinnularia major*, *Cymbella lanceolata*, *Stephanodiscus* sp., *Coscinodiscus* sp., *Amphora ovalis*, *Rhamhoneis augustata* and *Navicula semen*. (Figures 3-4)

The samples of Aydin-Karacasu diatomite deposit have a variety of sizes and shapes with large elongated and disc forms which usually indicate a high quality of filtration crude. Due to its sufficient physical and chemical properties this material should also be suitable for use as light-weight mineral filler in the powder form after general refining processes.



Figure 3: Chalk coccoliths make mechanically weak “mosaic” pore walls.

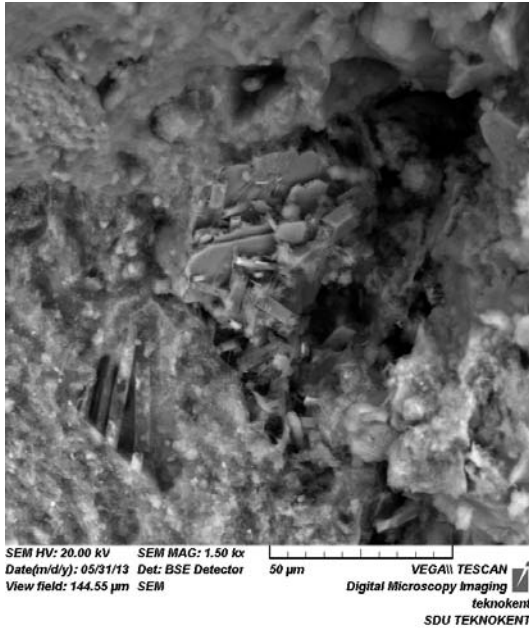


Figure 4: SEM micrographs of close-up view on pores of centric frustules, on centric diatom form, platy diatoms.

3.3. Grinding Tests

Firstly, Standard Bond grindability tests were made for amorphous silica and diatomite samples. Result of tests, the Bond work index values of samples were 12.32 kWh/t and 8.32 kWh/t, respectively. The standard set of grinding conditions used was shown in Table 2, for a laboratory mill of 6283 cm³ volume. Eight particle size fractions (-1.7+1.18, -1.18+0.850, -0.850+0.600, -0.600+0.425, -0.425+ 0.300, -0.300+0.212, -0.212+0.150, -0.150+0.106 mm) were prepared and ground batch wise in a laboratory-scale ball mill for determination of the specific rate of breakage. Each sample was taken out of the mill and a dry sieved product size analysis was carried out.

Table 2: The standard set of grinding conditions

Mill	Diameter	200 mm	
	Length	200 mm	
	Volume	6283 cm ³	
Mill Speed	Critical ^a	101 rpm	
	Operational ($\phi_c = 75\%$)	76 rpm	
Balls	Diameter (mm)	25.4 mm	
	Specific gravity	7.8	
	Quality	Alloy Steel	
	Assumed porosity	40 %	
	Ball filling volume fraction ($J\%$) ^b	20 % ($J = 0.2$)	
Material	Powder gravity, g/cm ³	Amorphous Silica 0.67	Diatomite 0.58
	Interstitial filling ($U\%$) ^d	125 % ($U = 1.25$)	
	Powder filling volume ($f_c\%$) ^c	10 % ($f_c = 0.10$)	

^a Calculated from $N_c = 42.3/\sqrt{D-d}$ (D, d in metres)

^b Calculated from $J = \left(\frac{\text{mass of balls} / \text{ball density}}{\text{mill volume}} \right) \times \frac{1.0}{0.6}$

^c Calculated from $f_c = \left(\frac{\text{mass of powder} / \text{formal bulk density}}{\text{mill volume}} \right)$

^d Calculated from $U = \frac{f_c}{0.4J}$

4. RESULTS AND DISCUSSION

4.1 Determination of SFunction

The first-order plots for various feed size of two porous samples were shown in Figures 5-6. The results indicated that grinding of all size fractions, two samples could be described by the first-order law. In addition, parameters of specific rate of breakage to supply by first-order plots were given in Table 3.

The specific rates of breakage of each mono-size fraction, that exhibited first-order grinding kinetic behavior, were determined from the slope of straight-line of the first-order plots. In Figure 7, S_i values of the two samples used were given as a function of time.

The two samples demonstrated entirely different characteristics in the selection function. As the feed sizes increase, the S_i values increased proportionally for two minerals.

The values of the estimated values of a_T and α for two samples were given in Table 3. From the Table 3, with very large rates of disappearance of the top size interval and higher α values, diatomite given higher breakage rates for particles of all size ranges, while amorphous silica is resulted insignificantly lower breakage rates for fine particle sizes.

The a_T value is 2.68 min^{-1} for the amorphous silica, while the a_T value is 6.04 min^{-1} with for the diatomite when ground with the ball diameter of 25.4 mm at the same conditions. From a_T values experimentally obtained, grinding was faster for the diatomite than amorphous silica.

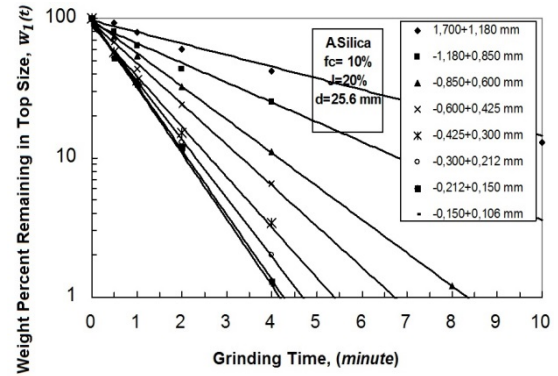


Figure 5: First-order plots for amorphous silica

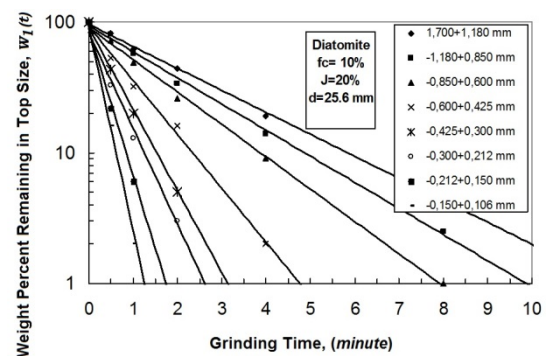


Figure 6: First-order plots for diatomite

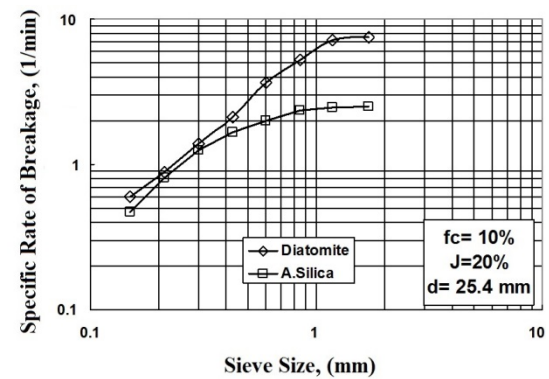


Figure 7: Variation of specific rates of breakage with particle size for porous materials

4.2 Determination of BFunction

The slope of the lower portion of the $B_{i,j}$ curve denoted by γ is also a convenient and measurable parameter for characterizing material oriented breakage properties. It characterizes the relative amount of fines produced from the breakage of the top size material and therefore directly relates to the efficiency of the grinding process. A higher value of

γ implies that the progeny fragments are coarser, i.e., their size is closer to the size of the parent material being broken and that grinding is taking place at a slow rate. On the other hand, a lower value of γ would imply more effective breakage action with high production of fines. [Shah and Austin, 1983].

By definition, the values of B were determined from the size distributions at short grinding times. The parameters were determined according to the B_{II} method [Prasher, 1987], and Table 3 shows the fitted values, while their graphical representation was given in Figure 8. Every two porous samples showed a typical normalised behavior, and the progeny distribution did not depend on the particle size, and it followed that the parameter δ was zero. Model parameters supply by cumulative distribution and these parameters were given in Table 3.

The B curves for diatomite grinding were essentially the same as those of the amorphous silica grinding. However, the B_{ij} values of amorphous silica were different from the diatomite whose γ value of amorphous silica was smaller than that of diatomite indicating that smaller γ values mean that more fines were produced in the amorphous silica grinding. On the other hand, diatomite (8.32 kWh/t) easier grinding than

amorphous silica (12.82 kWh/t) in terms of Bond work index values (W_i). The reason of this, amorphous silica had more abrasive minerals such as sanidine, pyroxene and feldspar than the diatomite. Addition, diatomite had larger pore length and pore diameter than the amorphous silica (Figures 1-2), and according to amorphous silica, pores in matrix of diatomite were each interdependent (Figures 3-4). In addition, higher values of ϕ and β for the diatomite further showed the rapid grinding of diatomite compared to amorphous silica especially at sizes close to feed size. As it supports, diatomite (12.32 kWh/t) was easy grinding than the amorphous silica in terms of the Bond work index values (W_i).

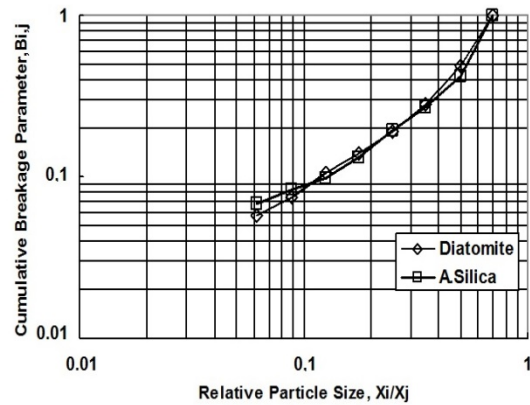


Figure 8: Cumulative breakage distribution functions for porous materials

Table 3: Bond's work index values and characteristic breakage parameters of samples

Material	W_i kWh/ton	$S_i(0.150-0.106 \text{ mm})$ (min^{-1})	a_T (min^{-1})	α	γ	ϕ_i	β
Amorphous Silica	8.32	0.462	2.68	1.248	0.612	0.368	2.325
Diatomite	12.32	0.611	6.04	1.222	0.856	0.617	3.092

5. CONCLUSIONS

Although amorphous silica and diatomite have different Bond work index values with 12.32 and 8.32 g/rev, respectively,

they have demonstrated entirely close characteristics in some selection and breakage parameters.

The Bond's equation applies for the calculation of the mill power of large industrial (cylindrical) ball mills, where the mass of the grinding media in the mill is much larger than that of the material being ground. It does not include any term for the influence of the mill power in grinding, even though takes into account the movement of the charge, and hence the mill power, the rheological behavior. Thus, the Bond grindability value alone does not define the breakage action. Whereas, breakage parameters of kinetic grinding models are more expressed than the Bond model for define of grinding process.

The values of the primary daughter fragment distributions and the values of a_T in $S_i = a_T X_i^a$ were different in amorphous silica and diatomite. As the values of S_i or a_T increased, very fast breakage was observed in the undersize of the original particle size. It can be seen from experimentally obtained a_T values that grinding is faster for diatomite ($a_T = 6.04$) than that of amorphous silica ($a_T = 2.68$).

Since diatomite has more porosity than that of amorphous silica, the breakage of the top size showed acceleration for diatomite ($\phi = 0.617$), and deceleration for amorphous silica ($\phi = 0.368$). Even if, mineralogical analysis shows amorphous silica is more abrasive. Since amorphous silica has a greater content in abrasive materials than diatomite, the primary breakage of amorphous silica gave the lower relative production rate of fines ($\gamma = 0.612$), while diatomite yielded a greater proportion of fines ($\gamma = 0.856$).

Furthermore, effect of porosity on breakage approach of porous materials is not clear. This study showed that grinding kinetic parameters could be different for porous materials with different mineralogical and morphological properties. Therefore, it has appeared that

the grinding kinetics for each material must be evaluated to lower the energy costs in the grinding process.

REFERENCES

- Anderson, D., Roy, A., Seals, R.K., Cartledge, F.K., Akhter H. and Jones S.C., 2000. A preliminary assessment of the use of an amorphous silica residual as a supplementary cemetery cementing material, *Cement and Concrete Research*, 30, 473-445.
- Austin, L.G., 1972. A review introduction to the description of grinding as a rate process. *Powder Technol.* 5, 1-7.
- Austin, L.G., Luckie P.T., 1972. Methods for determination of breakage distribution parameters. *Powder Technol.* 5, 215-222.
- Austin, L.G., Bagga, R., Çelik, M., 1981. Breakage properties of some materials in a laboratory ball mill. *Powder Technol.* 28, 235-241.
- Austin, L.G., Klimpel, R.R., Luckie, P.T., 1984. *Process engineering of size reduction: ball milling*, S.M.E., A.I.M.E., New York, USA.
- Deniz, V., Onur. T., 2002. Investigation of the breakage kinetic of pumice samples as dependent on powder filling in a ball mill. *Int. J. Miner. Process.* 67, 71-78.
- Deniz, V., Sütçü, N., Umucu, Y., 2003. The effect of circulation load and test sieve size on the Bond work index based on natural amorphous silica. *Proceedings of 18th International Mining Congress and Exhibition of Turkey*. 517-522.
- Deniz, V., 2004. Relationships between Bond's grindability (G_{bg}) and breakage parameters of grinding kinetic on limestone. *Powder Technol.* 109, 208-213.
- Deniz, V., 2011. Comparison with some porous materials and the effects of powder filling on breakage parameters of diatomite in dry ball milling, *Part. Sci. Technol.* 29, 428-440.
- Dolley, T. P. 1991. Diatomite. *Ceramics Bulletin* 70(5): 860.
- Makokha, A., Moys, M.H., 2006. Towards optimising ball-milling capacity: effect of lifter design, *Miner. Eng.* 19, 1439-1445.
- Prasher, C.L., 1987. *Crushing and grinding process handbook*, John Wiley & Sons, Chichester, U.K.
- Shah, I., Austin, L.G., 1983. Breakage rates and size distributions in dry ball milling for fine sizes, *Ultrafine Grinding and Separation of Industrial Minerals* (Ed.: S.G. Malghan), AIME, New York, USA, pp. 9-19.

EVALUATION OF PHOSPHOGYPSUM POWDER AS AN ADDITIVE IN THE PRODUCTION OF PLASTER

Tugba Işıtan^{1,a}, Sinem Cevik Uzgur², Başak Mesci³ and Elif Odabaş⁴

1,2,3,4 Materials Science and Engineering, Ondokuz Mayıs University, Samsun/ TURKEY
a. Tuğba Işıtan (tugba.isitan@omu.edu.tr)

ABSTRACT: In the light of the development in technology, materials used in construction industry and applications techniques are increasingly taking relevant shape. Today, the main expected economic developments in the industry, depending on the fitness for purpose, is to be more economical and more aesthetic. In order to meet these type expectations, more technical development and more diversity obtained in building materials industry. Concrete and cement mortar which is the main materials of construction industry doped with various additive materials gain the relevant properties. But, nowadays traditional plaster mortar production do not meet the desired specifications. For instance, after a rough application is made on the structure, the plaster mortar applications are to be difficult to hold on to the surface. Nowadays, construction materials technology have alternative solutions for this problem. Due to various additives to plaster mortars, the surface is making suitable for plaster applications. These additives can be some industrial wastes. In this study, usage of powder phosphogypsum which is obtained in production of phosphoric acid as by product or as a waste, is investigated as an additive for plaster mortar.

Key words: Mechanical strength, phospho-gypsum, plaster, porosity

1. INTRODUCTION

Today, parallel to the economical developments the expected features from structures are expediency, being economical and visual esthetic. Due to past and present of the growing population and developing technology it requires less time for construction period. To achieve this purpose different techniques are generated and researched. the results of all these endeavors urged more esthetic and perfect structures. Mortar and concrete which are one of the main materials of ferroconcrete structures can be doped with various additives to get the desired features. Traditional plaster and mortar cannot afford today's developments.

Applications made after the rough mortar and plaster applied to structures made it difficult to attach to the surface. To overcome these problems, the addition of polymer or different additives mortures to

surface coating applications is optimized. In this study we focused on this subject industrial waste is used as an additive.

In this study, usage of powder phosphogypsum which is obtained in production of phosphoric acid as by product or as a waste, is investigated as an additive for plaster mortar.

1.1. Plaster

Plaster is a covering based on mortar used for inner and outer surfaces and on ceilings at specific thickness (Eriç, 1992).



Figure 1: Plaster

Plaster makes the surfaces applied smooth. It protects the building from outer effects.

1.2. Layers of Plaster

Plaster is a structure component. Plaster mortars choices are sand, pebbles, crushed rocs etc. The bindings are limes, cement and synthetics. These mortars are named according to their applications. It divides in two groups: rough plaster and finish plaster (Tuna, 1998). Rough plaster is made of rough sands and is firstly applied plaster to the surface. Finished plaster is made of sieved sand and applied secondly.

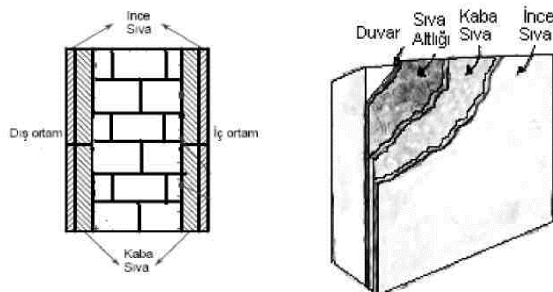


Figure 2: Layer of plaster (Tuna, 1998)

1.3. Various Additives Materials Added to Plaster

According to Turatsinze et al. (2005), tires obtained from worn car tires are

added to mortars instead of aggregate. In this study cement, sand, water and plasticizer came into being as a mixture and 20%-30% of sand volume tires added. It is determined that compressive and flexural strengths are decreased and also decreased elasticity module and macro cracks were decreased compared to the control group.

Miller and Baradan (2005) examined the effects of puzzolanic plaster on the wall. In this study, hydrated lime, cement and fly ash samples were prepared by mixing. It was observed that increased compressive strength which the samples of preparing with lime, cement and fly ash by mixing process.

Bochen et al. (2005) investigated the porous structure of the surface plasters. Because of the different climatic conditions, the amount of porosity increased in the outer surfaces of the building with respect to time. According to natural and accelerated tests results, depending on the time between the values of 9.62% to 6.50% concluded that porosity was increased.

1.4. Phosphogypsum

Powder phosphogypsum is obtained in production of phosphoric acid as by product or as a waste.



Figure 3: Phosphogypsum ($\text{CaSO}_4 \cdot 2\text{H}_2\text{O}$)

Phosphogypsum which is a waste material, is usually stored in open fields and cause of environmental pollution.

In recent studies, phosphogypsum is used in the construction industry and also as

raw material for production of cement and clinker industry. Moreover, it can be used for artificial aggregates production.

Table 1: Chemical and physical properties of Phosphogypsum

Chemical Properties	Physical Properties
CaSO ₄ 2H ₂ O 95,0	Specific weight 2,40
P ₂ O ₅ 0,50	
F 1,35	

3. RESULT AND DISCUSSION

If we look at the studies about the phosphogypsum powder as an additive in the production of plaster according to Turabi *et al.*,(2006), phosphogypsum is used in the road and the stabilization of the road. Phosphogypsum was added at different rates (%0.5, 10, 15) in the mortars. After experimental methods, increased amount of dry unit weights was observed which are samples of ground. In another study (Singh, 2004), phosphogypsum was studied on the setting time, strength development and microstructure of the selenite gypsum plaster. According to the test results, the compressive strength of the hardened selenite plaster was maximum. The other properties of plaster like setting time, bulk density and workability were normal.

4. CONCLUSION

Phosphogypsum is added to plaster. As a result of this process porosity ratio was gradually decreased. Depending on this process compressive strength was increased. One of the biggest problems in the environmental problems of today. Such as recycling of waste is a major problem. Wastes re-evaluated different forms.

Used in various sectors such as industrial waste phosphogypsum is also important for the environment. In this way, both

protection of the environment and contributes to the country economy.

REFERENCES

- Bochen J., Gil S.,Sczwabowski J., 2005. Influence of ageing process on porosity changes of the external plasters, *Cement and Concrete Composites*, 27, 769-775.
- Eriç M., 1992. Plaster applications and problems of the structure, *Journal of Construction*, 70-73, İstanbul.
- Tuna G., 1998. Determination of the problems occuret of plaster of external buildings facades and solution suggestions, Msc Thesis, Yıldız Teknik University.
- Turabi A., Okucu A., Değirmenci N., 2002. Investigation use of phosphogypsum stabilization materials, IV. Congress of Engineering and Architecture, Balıkesir.
- Turatsinze A., Bonnet S., Granju J.L., 2005. Materials characterization of cement-based mortar incorporating rubber aggregates from recycled worn tyres, *Building and Environment*, 40, 221-226.
- Singh M., 2004. Role of phosphogypsum impurities on strength and microstructure of selenite plaster, *Construction and Building Materials*, 19, 480-486.

UTILIZATION OF ACTIVATED GBFS AND PERLITE IN POROUS LIGHTWEIGHT COMPOSITE MATERIAL

Cenk Karakurt^{1,a}, Abdullah Demir², Mehmet Canbaz³, Mehmet Uğur Toprak²

1 Bilecik Şeyh Edebali University, Department of Civil Engineering, 11210, Bilecik, Turkey

2 Dumlupınar University, Department of Civil Engineering, 43100, Kütahya, Turkey

3 Eskişehir Osmangazi University, Department of Civil Engineering, 26480, Eskişehir, Turkey

a. Corresponding author (cenk.karakurt@bilecik.edu.tr)

ABSTRACT: The perlite aggregate has been used widely in lightweight concrete production. The expanded and raw perlite can be used as lightweight insulation material due to its high porosity. The light weight concretes are utilized in structures in order to reduce the own weight of the structure thus reducing the earthquake force which affects on the structure. The ground granulated blast furnace slag (GBFS) can be activated by using such activators like alkalis, lime and calcium sulfate. Therefore, it becomes an alternative binder against cement. In this study, GBFS is used as binder by plaster activation and lime. In lightweight composite production, GBFS and expanded perlite with silica sand was used as binding phase and aggregate respectively. The produced specimens were cured in different regimes as air curing, and steam curing. The physical and mechanical properties of the specimens were determined by experimental studies at early and further ages. Also the insulation properties of the composite specimens were obtained by thermal conductivity tests. According to test results, the unit weights and the strength properties of the specimens were decreased.

1. INTRODUCTION

Fly ash, granulated blast furnace slag, and silica fume are the industrial wastes which utilize in concrete mixtures as mineral additives. These admixtures especially increase the durability properties of hardened concrete [Tokyay, 2013; Uysal, 2013]. The new, technically improved binders are improved by activating these industrial wastes. According to some studies it is determined that the drying shrinkage of alkali activated metakaolin and silica fume mortars are reduced [Aydın *et.al.*, 2013]. The mixtures produced with fly ash cements and anhydrate of calcium sulfate and gypsum mixtures as activator showed that the anhydrite is effective on early age strengths and gypsum is effective at later ages [Poon *et.al.*, 2001]. The high temperature resistance of sodium silicate activated fly ash mixtures are higher than Portland cement composites [Rashad *et.al.*, 2011]. The

type of fly ash is effective on activation with gypsum [Sadique *et.al.*, 2013]. The sulfate effect increase the activation of fly ash [Criado *et.al.*, 2010]. It is found that utilization of geopolymers obtained by activation of granulated blast furnace slag with sodium hydroxide showed lower radiation transferring and this material suggested that for radiation shielding [Binici *et.al.*, 2011]. Also it is found that the alkali activated blast furnace slags increase the durability against thermal and chemical effects [Topçuet *et.al.*, 2008; 2008^a; 2009]. The bottom ash can be use for lightweight mortar production by activation of sodium silicate and sodium hydroxide [Topçuet *et.al.*, 2009^a]. The compressive strength of bricks produced by activation of fly ash by sodium hydroxide can reach 60 MPa [Zeybek, 2009].

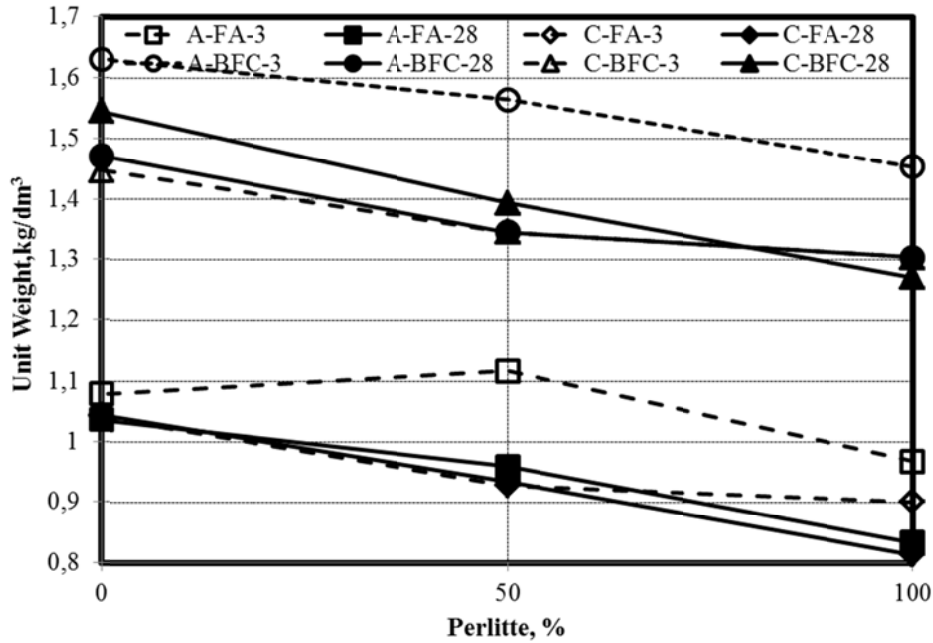


Figure 1: Unit weight test results.

2. MATERIALS AND METHODS

2.1. Materials

The specimens are produced with blast furnace slag obtained from Erdemir Steel Factory, fly ash from Soma Thermal

2.2. Methods and Results

The ratio of gypsum, fly ash-slag and lime used as 0.1:0.7:0.2 respectively. The ultrasound pulse velocity (UPV) results varied between 1.2-2.7 km/sec. It is found that perlite do not change the UPV

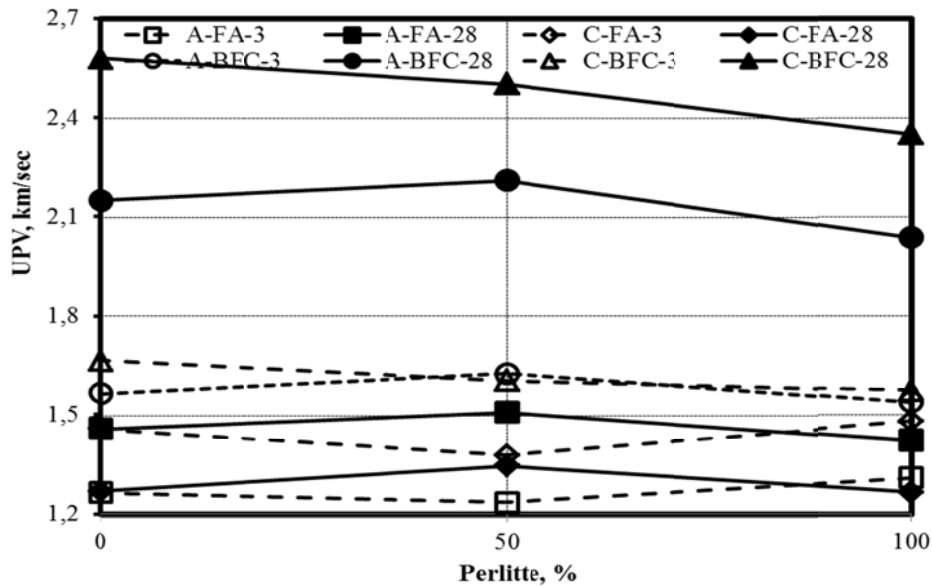


Figure 2: UPV test results.

Power Plant, gypsum of Atışkan Gypsum Factory, standard Rilem sand according to TS EN 196-1, expanded perlite from

Genper, lime from Adaçal lime factory and Eskişehir tap water.

results significantly but blast furnace slag increase the UPV results at later ages. This behaviour is related with the filling effect of furnace slag at later ages due to the pozzolanic reaction of this material.

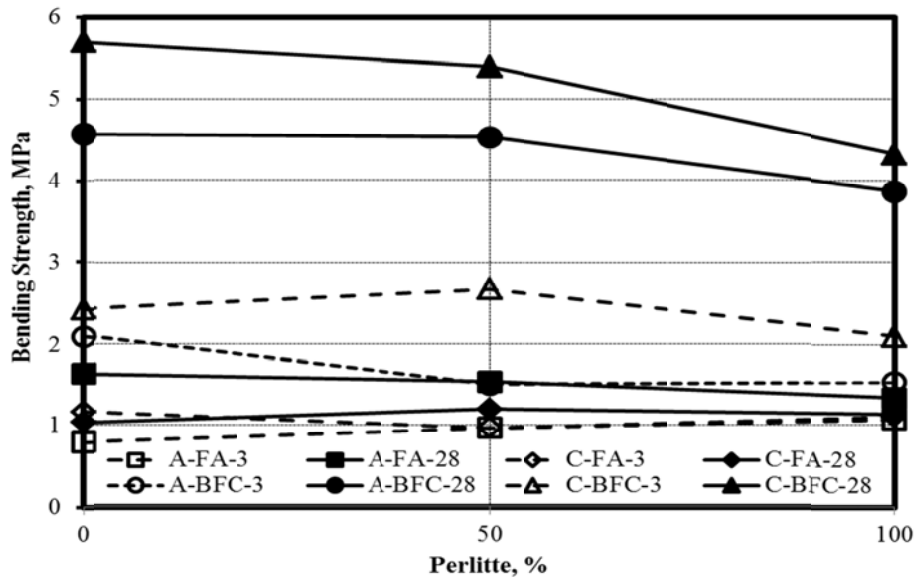


Figure 3: Effect of perlite on bending strength.

The bending strength of perlite used mineral activated specimens are shown in Figure 3. According to Figure 3 the bending strength of fly ash specimens quite low. The best bending strength values were obtained with blast furnace specimens. The strength values of 28 day specimens are two times higher than 3 days strengths. It is seen that the bending strength values of specimens cured in

curing cabinet higher. The compressive strength results of activated perlite specimens are shown in Figure 4. As seen from Figure 4 the higher compressive strength results were obtained with blast furnace slag specimens as bending strength results. The strengths were reduced with air curing and increase of perlite ratio. The water absorption test results by weight is shown in Figure 5.

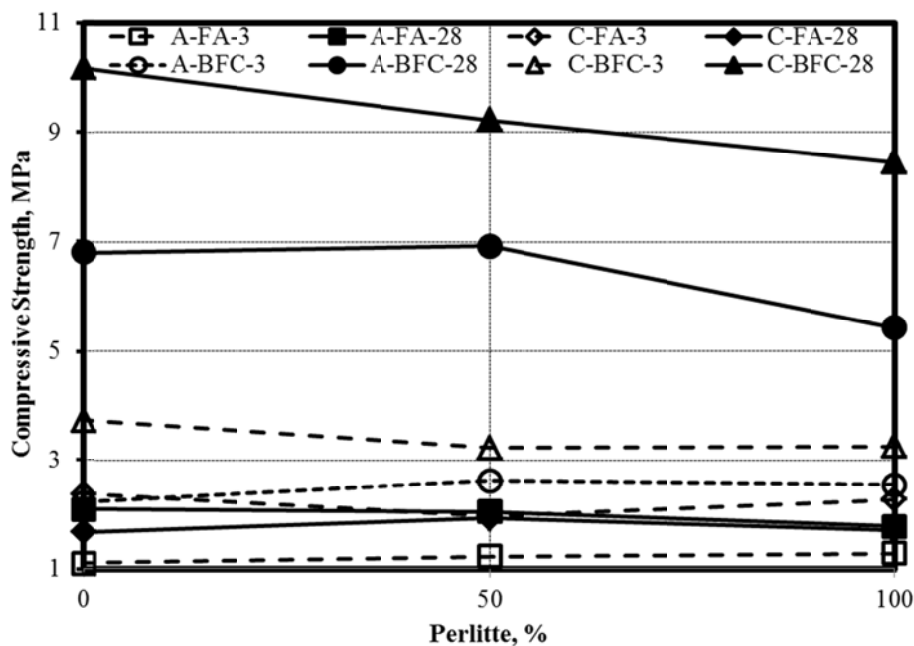


Figure 4: Effect of perlite on compressive strength.

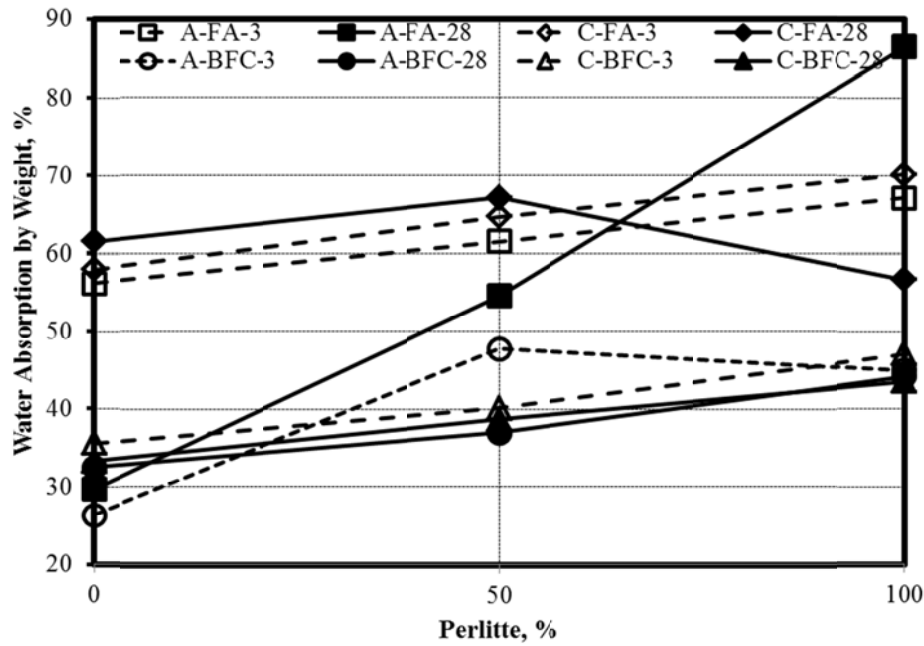


Figure 5: Effect of perlitte on water absorption.

As seen from Figure 5 the water absorption of alkali activated fly ash specimens reach 50% absorption ratio and the variation showed irregular behavior at later ages due to the perlitte content. The water absorption ratios of blast furnace slag used specimens are lower than 50%. Also the water absorption increase with the increase of perlitte ratio. The capillary water

absorption coefficients of specimens are shown in Figure 6. According to Figure 6 the capillarity coefficient variation showed irregular behaviour with the increase of the perlitte content. These results showed that the capillarity of the mortar specimens increase with the increase of perlitte ratio.

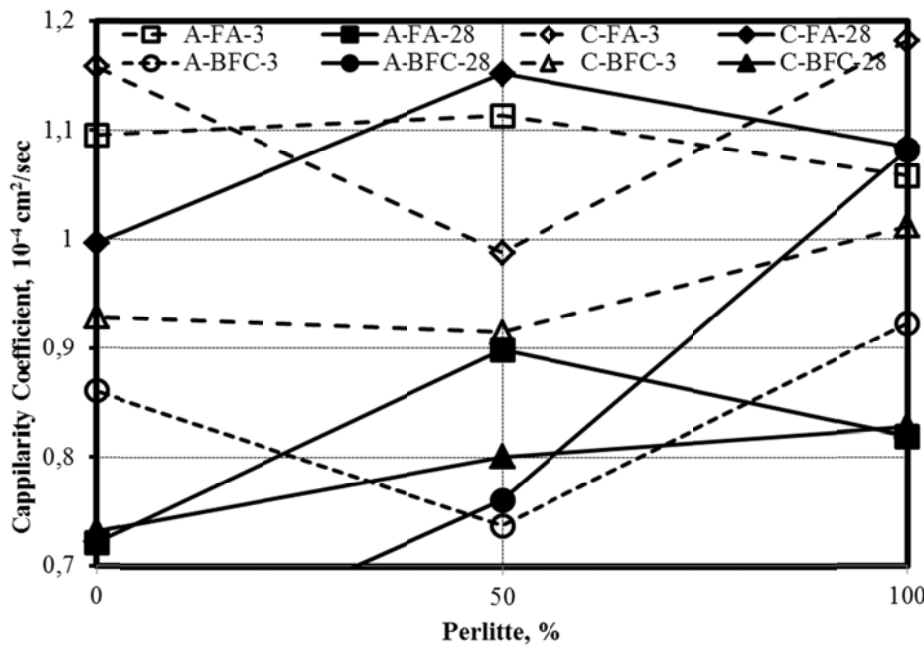


Figure 6: Effect of perlitte on capillarity.

4. CONCLUSIONS

According to test results the gypsum activated blast furnace slag used specimens the unit weight, ultrasound pulse velocity, flexural and compressive strength results are higher than the fly ash activated specimens. On the other hand the water absorption and capillarity properties of blast furnace slag specimens showed lower ratios when compared with fly ash specimens.

The unit weight and strength properties of specimens are reduced with the increase of perlite usage. It is suggested that utilization of perlite with activated fly ash specimens can be used when lightness is important. However, the alkali activated blast furnace slag used mortars can be used for higher strengths.

REFERENCES

- Aydın, S., ve Baradan, B., 2013. Mineral ve Kimyasal Katkıların Alkalilerle Aktive Edilmiş Harçların Özelliklerine Etkisi, Beton2013, THBB, İstanbul, ss. 200-209.
- Binici, H., Eken, M., ve Aksoğan, O., 2012. Cüruf, Uçucu Kül, Silis Kumu ve Pomza Esaslı Geopolimerlerin Fiziksel, Mekanik ve Radyasyon Geçirgenlik Özellikleri, Yapı Teknolojileri Elektronik Dergisi Cilt: 8, No: 2, 2012 (12-25).
- Criado, M., Jiménez A.F., and Palomo, A., 2010. Effect of Sodium Sulfate on the Alkali Activation of Fly Ash, Cement & Concrete Composites 32 (2010) 589–594.
- Poon, C.S., Kou, S.C., Lam, L., and Lin Z.S., 2001. Activation of Fly Ash/Cement Systems Using Calcium Sulfate Anhydrite, CCR, 31, 2001, pp. 873-881.
- Rashad, A.M., and Zeedan S.R., 2011. The Effect of Activator Concentration on the Residual Strength of Alkali-Activated Fly Ash Pastes Subjected to Thermal Load, Construction and Building Materials 25 (2011) 3098–3107.
- Sadique, M., Al-Nageim, H., Atherton W., Seton, L., and Dempster, N., 2013. Mechano-chemical Activation of High-Ca Fly Ash by Cement Free Blending and Gypsum Aided Grinding, Construction and Building Materials 43 (2013) 480–489.
- Tokuy, M., 2013. Betonda UK, GYFC ve SD'nin Rolü: Mevcut Bilgi Birikimi, Beton2013, THBB, İstanbul, ss. 201-238.
- Topçu, İ.B., ve Canbaz, M., 2008. Alkali Aktive Edilmiş Yüksek Fırın Cürüflü Harçlarda Asit Etkisi, Dumlupınar Üniversitesi, Fen Bilimleri Enstitüsü Dergisi, sayı 16, 2008, ss. 69-80.
- Topçu, İ.B., ve Canbaz, M., 2008^a. Alkali Aktive Edilmiş Yüksek Cürüflü Harçlarda Donma Çözülme, Eskişehir Osmangazi Üniversitesi Mühendislik Mimarlık Fakültesi Dergisi Cilt:XXI, Sayı:2, 2008, ss.1-16.
- Topçu, İ.B., Canbaz, M., ve Sarıdemir, M., 2009. Kimyasal Etkide Kalmış AAYFC'li Harcın Dayanımının YSA ve BM Kullanılarak Tahmini, Eskişehir Osmangazi Üniversitesi Mühendislik Mimarlık Fakültesi Dergisi Cilt:XXII, Sayı:3, 2009, ss.123-133.
- Topçu, İ.B., ve Toprak, M.U., 2009^a. Alkalilerle Aktive Edilen Taban Küllü Hafif Harç Üretimi, Eskişehir Osmangazi Üniversitesi Mühendislik Mimarlık Fakültesi Dergisi Cilt:XXII, Sayı:2, 2009, ss. 153-162.
- Uysal, M., 2013. Mineral Katkılı Betonların Donma-Çözülme Etkisi Altındaki Davranışının İncelenmesi, Beton2013, THBB, İstanbul, ss. 290-300.
- Zeybek, O., 2009. Uçucu Kül Esaslı Geopolimer Tuğla Üretimi, Anadolu Üniversitesi, Fen Bilimleri Enstitüsü, Yüksek Lisans Tezi, 2009, s. 87.

TECHNICAL PROPERTIES OF SEPIOLITE FIBER-REINFORCED AAC

Taner Kavas^{1,a}, A. Doğan Soyal², Recep Uysal², Uğur Uzgan² and Abdullah Tan³

1. AKU, Faculty of Engineering, Department of Material Sci. and Engineering, Afyonkarahisar, Turkiye
2. AKG, Gazbeton Enterprises of Industry and Trade Inc., Department of R&D, İzmir, Turkiye
3. AKG, Gazbeton Enterprises of Industry and Trade Inc., Department of R&D, Kirikkale, Turkiye
a. Taner Kavas (tkavas@aku.edu.tr)

ABSTRACT: In this study, technical properties that sepiolite mineral (SM) added to the structure of Autoclaved Aerated Concrete (AAC) were investigated by means of various characterization techniques. For this purpose, mud receipts of R₀, R₁, R₃, R₅ were prepared with addition of sepiolite (in ratio of 0, 1, 3, and 5 wt.%) to raw material mixture containing cement, lime, silica sand, gypsum, aluminum and mixing water. Sufficient amount of casting mud were produced from prepared receipts. Specimens were shaped in metal molds by slip casting techniques with addition of an aqueous solution of aluminum during mixing of mud to obtain homogeneity. The shaped samples were autoclaved at 200°C and 12 bar pressure for 4.5 hours after sufficient cutting hardness. Mechanical (compressive strength), chemical (XRF), mineralogical (XRD) and micro-structural (SEM) analyses were carried out. The experimental results provided that the sepiolite mineral addition up to 5 wt.% to a standard AAC improves mechanical properties, decreases density and increases A factor of final sepiolite fiber reinforced autoclaved aerated concrete structure.

Keywords: Sepiolite, Additive, AAC, Mineralization

1. INTRODUCTION

Autoclaved aerated concrete (AAC) is a well-known lightweight concrete (Karakurt, *et al.*, 2010) and its engineering properties are currently being investigated. In this work, the technical and structural properties of sepiolite fiber-reinforced Autoclaved Aerated Concrete (SFRAAC) were studied. As it known AAC is not a new building material or system. It is manufactured by combining sand, lime, cement, gypsum, water, expansion agent that reacts with the other ingredients to form the porous microstructure and many different kind of additive materials to enhance its engineering properties. These additive materials could be separated into two main groups which are called as non-hydraulic and hydraulic. Properties of these two groups are very different and both of them could increase plastic strength of mud and mechanical

(compressive/flexural) strength of final products (Laukaitis, *et al.*, 2009). However, it was reported in literature that some non-hydraulic additives are not appropriate for reinforced AAC such as carbon, polypropylene, basalt and kaolin fiber, although they are suitable for conventional concrete materials (Li, 2011). On the other hand, hydraulic additives like sepiolite, fly/bottom ash act as a set accelerator in mixture of raw materials when they react with water. Their high water demand especially depends on crystal structure and surface area value. Sepiolite is a naturally occurred clay mineral. It is also microcrystalline-hydrated magnesium silicate (with foreign ions) with $\text{Si}_{12}\text{Mg}_8\text{O}_{30}(\text{OH})_4(\text{H}_2\text{O})_{48}\text{H}_2\text{O}$ the unit cell formula (Kavas, *et al.*, 2004). It exhibits a micro-fibrous morphology with a particle length of 2-10 μm structurally

(Gómez, et al., 2006). It is formed by an alternation of blocks and tunnels which grow up in the fiber direction.

2. EXPERIMENTAL STUDY

The SFRAAC mixture was produced by using cement, lime, sand mud consist of sand and water, gypsum, aluminum suspension, mixing water and sepiolite in ratio 0, 1, 3, and 5 wt.% of total solid raw materials. Sepiolite raw material sample used in this study was taken from Sivrihisar/Eskişehir/Turkey region. The mineralogical analyses of sepiolite samples were determined by X-ray diffraction (XRD) analysis. Chemical analysis of sepiolite was also carried out by using a X-ray fluorescence (XRF) unit (Thermo Advant'XP). After grinding of sepiolite up to a range of 250-500 µm, raw material mixtures were prepared by taking enough amounts of quartz, lime, cement, sand, gypsum, aluminum, mixing water and 1-5% sepiolite by weight. Four different groups were constituted. These groups were named as R₀, R₁, R₃ and R₅, respectively. The control group (R₀) did not contain any sepiolite additive. After mixing process sufficient amount of casting mud consisting of all raw materials were produced. Samples were shaped in metal molds by slip casting method. Molded samples were subjected into the two curing cycles. At the first step, green samples were kept in pre-curing line at 52°C for 4.5 h to obtain enough hardness and volume stability. After first curing step, samples which have sufficient cutting hardness cut into desired dimensions and then autoclaved. Curing has been used to accelerate the strength development of samples. At the end of second curing step, autoclave was allowed to cool down till room temperature slowly to prevent the detrimental effects of thermal stress on mechanical properties of the final products. Representative samples were taken from each group and mechanical

(comprehensive strength), density, A factor which shows quality degree of products, and micro-structural (SEM) analyses were performed by different techniques.

3. RESULTS AND DISCUSSION

3.1. Chemical Analyses

The chemical analyses obtained from XRF results that identify the main oxide compositions of sepiolite are given in Table 1. The details of the chemical analyses can be found elsewhere (Kavas, et al., 2004). When Table 1 is examined, the major oxide of sepiolite is SiO₂. And other important oxides are CaO and MgO. The chemical analyses result is also revealed that impurities are Al₂O₃, Fe₂O₃, K₂O, SO₃ and Na₂O. The remarkable increase in sepiolite is due to the crystal water.

Table 1: Chemical Analysis of Sepiolite

Si O ₂	Al ₂ O ₃	Fe ₂ O ₃	Ca O	Mg O	SO ₃	K ₂ O	Na ₂ O	LO I
35. 6	2.9	1.4	13. 1	18. 6	0.5	0.6	0.1	26. 4

3.2. Mineralogical Analyses

The mineralogical analyses result of sepiolite with X-ray diffraction (XRD) technique is revealed that dolomite is the main associated impurity with traces of quartz, calcite and clay minerals.

3.3. Microstructural Analyses

An examination of the microstructural development of SFRAAC (R₅) taken as a reference specimen has been conducted by means of SEM. The results which were obtained from different conditions and points of samples are presented Fig. 1-3. Fig.1 shows that the microstructure has uniform micro and macro pores. The micropores which are under the diameter of 50-60 µm are not clearly determined at this magnification. But, macropores which are formed due to the expansion of

mass during chemical reaction are more than 250 μm in generally.

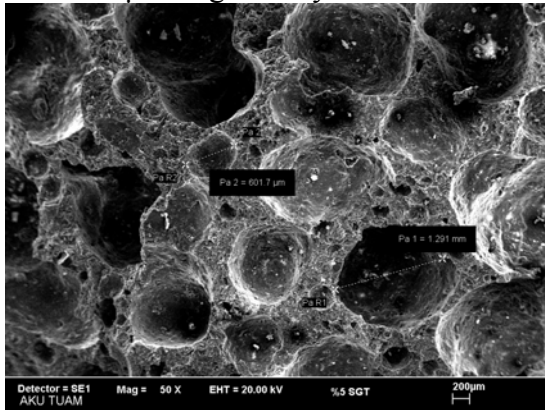


Figure 1: SEM image of SFRAAC (R_5).

On the other hand, it can be clearly seen in both Fig.2 and Fig.3 that reticulated structures were occurred by addition of sepiolite fiber to standard AAC structure. These nested hydrated crystal structures which consist of needle like sepiolite crystal and tobermorite, a calcium silicate hydrate crystal, give the desired mechanical properties to the final products (SFRAAC).

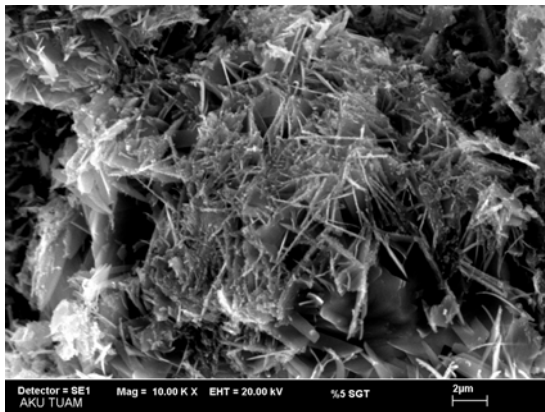


Figure 2: SEM image of tobermorite and hydrated sepiolite fiber in R_5 .

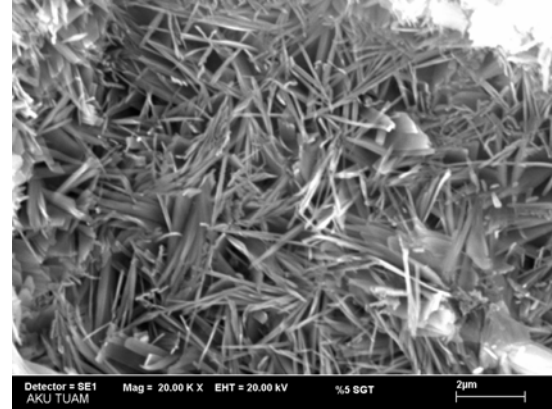


Figure 3: SEM image of sepiolite fiber in the matrix of R_5 .

3.4. Mechanical, Physical Properties and A Factor

Comprehensive strength, dry density and A factor results of all groups are given in Table 2. The results taken from experimental study shows that mechanical properties improve with the addition of sepiolite up to 5 wt.%. When compared to the dry density values of sample, R_5 is the lowest one. Because sepiolite fiber addition to the standard AAC raw materials mixture leads to more porous occurrence in the final product structure. As a result of lowest density and highest comprehensive strength value, A factor is getting better.

Table 2: Mechanical, Physical and A Factor Values of R_5 Group Samples.

Group	Comprehensive Strength (N/mm^2)	Dry Density (kg/m^3)	A Factor
R_0	1,93	381	830,97
R_1	1,87	376	826,70
R_3	2,09	385	881,26
R_5	2,04	377	897,07

4. CONCLUSIONS

This experimental study demonstrated that sepiolite can be used as a replacement material in the production of AAC. With addition of this main come out the following conclusions can also be drawn from this study.

1. The addition of sepiolite in proportion of 5% by wt. to standard AAC receipt increases fiber structure occurrence in main matrix due to hydraulic behavior of sepiolite.

2. As seen from physical and mechanical test results taken from experimental study, comprehensive strength of samples are increased by adding sepiolite although the dry densities are decreased.

3. A factor value of R_3 is the highest between sample groups owing to low density and high comprehensive strength.

4. According to the come outs of this experimental study sepiolite could be used in different proportion (5% wt.) as replacement/additive materials in production of AAC material.

ACKNOWLEDGEMENT

The authors wish to express their gratitude and thanks to the AKG Gazbeton Enterprises of Industry and

Trade Inc. for its support during experimental study.

REFERENCES

- Nohales, A., Solar, L., Porcar, I., Vallo, C.I., Gómez, C.M., 2006. Morphology, flexural, and thermal properties of sepiolite modified epoxy resins with different curing agents, *European Polymer Journal*, 42 (11), 3093.
- Karakurt, C., Kurama, H., Topcu, I. B., 2010. Utilization of natural zeolite in aerated concrete production, *Cement and Concrete Composites*, 32, 1.
- Kavas, T., Sabah, E., Celik, M. S., 2004. Structural properties of sepiolite-reinforced cement composite, *Cement and Concrete Research*, 34 (11), 2135.
- Laukaitis, A., Keriene, J., Mikulskis, D., Sinica, M., Sezemanas, G., 2009. Influence of fibrous additives on properties of aerated autoclaved concrete forming mixtures and strength characteristics of products, *Construction and Building Materials*, 23(9), 3034.
- Li, M., 2011. A discussion of "Influence of fibrous additives on properties of aerated autoclaved concrete forming mixtures and strength characteristics of products, 25, 2169.

BIO-PITCH: A NOVEL PRECURSOR FOR CARBON FOAM PRODUCTION

Murat Kılıç^{1,a} and Ayşe Eren Pütün²

1. Anadolu University, Faculty of Engineering, Department of Chemical Engineering,
26480 Eskişehir, TURKEY

2. Anadolu University, Faculty of Engineering, Department of Chemical Engineering,
26480 Eskişehir, TURKEY

a. Corresponding author (mkilic3@anadolu.edu.tr)

ABSTRACT: Generally carbon foams were fabricated by using raw coal, coal tar pitch, petroleum pitch, synthetic pitch from organics such as AR pitch, and polymeric foams. It is obvious that most of the precursors, used for obtaining mesophase pitches are usually belong to the fossil fuel resources or fossil fuel derived materials. On the other hand, biomass pyrolysis oil (tar) with its aromatic hydrocarbon content seems to be an effective and alternative mesophase pitch precursor for producing carbon foam. Therefore, this study was focused on to determine the possible usage of biomass tar for carbon foam production. It is believed that production of carbon foam from bio-pitch will be less expensive and easier to obtain than fossil fuel derived pitches.

Keywords: Carbon foam, biomass, pyrolysis, tar, bio-pitch.

1. INTRODUCTION

Walter D. Ford was first obtained the organic foam in the late 60's [Ford, 1964]. After James Klett's discovery in 1997, the carbon foams have become popular among the carbon materials because of their potential application [Klett, 1998 and 2000, Klett *et al.*, 2000]. Carbon foam is a sponge like carbon material owing certain properties, such as light weight (0.2-0.8 g/cm³), high-temperature tolerance (up to 3000 °C in inert atmosphere), high strength (up to ~ 20 MPa, compression), large external surface area with open cell structure, and adjustable thermal and electrical conductivity [Chen *et al.*, 2006].

Carbon foams were fabricated by using raw coal, coal tar pitch, petroleum pitch, synthetic pitch from organics such as AR pitch, and polymeric foams. Among them, fossil pitches have been largely investigated as carbon foam precursors mainly because of being cheaper than the other materials. However, the decline in tar supply and introduction of rigorous

environmental regulations have affected the production and consumption of these pitches. Nowadays, studies for investigation of alternative precursors are in increasing attention. On the other hand biomass pyrolytic oil, tar, should be an effective alternative precursor for mesophase pitch production. Because, it is a complex mixture of condensable hydrocarbons, which includes single ring to 5-ring aromatic compounds along with other oxygen-containing hydrocarbons and complex polycyclic aromatic hydrocarbon (PAH) [Li and Suzuki, 2009].

With the above considerations, this study was focused on to determine the possible usage of biomass tar to obtain bio-pitch for carbon foam production. It is believed that production of bio-pitch and also carbon foam from biomass tar will be less expensive and easier to obtain than fossil fuel derived pitches.

2. EXPERIMENTAL

2.1. Raw Materials

Lignin is the second most abundant biomass component and the only renewable aromatic resource in nature [Nowakowski *et al.*, 2010]. Due to its aromatic nature lignin is a potential source of aromatic hydrocarbons and is attracting an increasing attention for conversion into valuable products. It is known from the literature that woody biomass types have higher lignin content than the other biomass types. The proportions and chemical composition of lignin and hemicellulose are different in softwoods and hardwoods, while cellulose is a uniform component of all woods. Hardwoods have a higher proportion of cellulose, hemicellulose, and extractives than softwoods, but softwoods have a higher proportion of lignin [Telmo and Lausada, 2011].

In this study seven different biomass samples were used for obtaining aromatic content rich tar via pyrolysis. Raw materials were pine tree (PT) as softwood biomass, oak tree (OT) as hardwood biomass, hazelnut (HS) and almond (AS) shells as high lignin content fruit shells, pine sawdust (PS) and pinecone (PC) as industrial and forest waste biomass. Table 1 shows the physical and chemical properties of raw materials. It is shown that low ash and higher volatile content indicates that the raw materials are suitable for pyrolysis.

2.2. Preparation of Bio-oils

Pyrolysis experiments of raw materials for tar production were carried out in a fixed-bed Heinze retort under nitrogen (N_2) flow of 100 mL min^{-1} using a heating rate of $10 \text{ }^\circ\text{C min}^{-1}$. To determine the suitable temperature, experiments were conducted by using different reaction temperatures ranging between $300\text{-}700 \text{ }^\circ\text{C}$. Tar yields were determined gravimetrically by weighing the products.

Aromatic hydrocarbon content of tars was determined by using $^1\text{H-NMR}$ analysis.

2.3. Preparation of Bio-pitches

Tars, obtained from pyrolysis of biomass samples are consist of aliphatic and aromatic hydrocarbon mixtures. Aromatic hydrocarbon fraction should be separate from the tar to produce mesophase bio-pitch precursors for carbon foam production. Therefore, tars were vacuum distilled to obtain bio-pitch. Generally, fossil pitches were produced at a temperature range of $350\text{-}450 \text{ }^\circ\text{C}$ and a vacuum pressure of under 50 mbar. This temperature range is too high for bio-oils, because of the high oxygen content. According to the temperature-pressure nomograph the appropriate temperature range for bio-oil were determined between $150\text{-}250 \text{ }^\circ\text{C}$. Different vacuum pressures (100-700 mbar) and treatment times (1-8 h) were used. Yields were calculated from the initial weight of pitch and the weight remaining after distillation.

2.4. Characterization of Bio-pitches

The softening point of the bio-pitches were determined using a Mettler Toledo instrument, according to the ASTM D3104 standard. The carbon, hydrogen, and nitrogen contents of the samples were determined using a LECO-CHN-628 elemental analyzer. The oxygen content was determined from the difference. The toluene and quinolone insoluble content was determined according to the ASTM D4312 and ASTM D2318. Ash content of bio-pitches were determined according to the ASTM D2415. High heating values (HHV) of samples were determined by using Dulong's formula. A SETERAM-LABSYS evo thermogravimetric analyzer (TGA) was used to determine the weight loss curves of bio-pitches. About 5-15 mg of sample was heated under $100 \text{ mL min}^{-1} N_2$ flow at heating

rate of 10 °C min⁻¹ from room temperature to 1000 °C in TGA. **3.**

RESULTS AND DISCUSSION

Hazelnut shell, oak tree and pine sawdust tars were found the appropriate raw materials for bio-pitch production according to the data obtained from pyrolysis experiments. Optimum pyrolysis temperature were determined as 400 °C for raw materials. Bio-oil yields of HS, OT, and PS 400 °C were found as 24.2 %, 22.2 %, and 25.4 %, respectively. Moreover, aromatic hydrocarbon contents of these tars were 31.4 %, 29.4 %, and 25.7 %, respectively.

Properties of bio-pitches obtained from vacuum distillation of HS, OT, and PS at 200 °C/8h, using different vacuum pressures are given in Table 2. Samples were labeled according to their corresponding vacuum pressure. The softening point of bio-pitch samples ranged from 83 to 203 °C. The increase in softening point is a result of decreasing vacuum pressure. Low vacuum pressures lead to remove more aliphatic hydrocarbon from the tar, leading an aromatic hydrocarbon content rich pitch. Also Pitch yield decreased with

decreasing vacuum pressure, because of aliphatic hydrocarbon removal from the tar. Ash content in bio-pitch was very low due to the low ash content in the raw materials. Ash content was below 1.0 % which can be acceptable as a negligible concentration. Densities, determined by using Helium pycnometry, were in the range of between 1.32 and 1.41 g cc⁻¹. Elemental analyses results showed that carbon content of bio-pitch samples were about 70.0 %, hydrogen content about 6.0 %, nitrogen content below 1.0 %, and oxygen content about 20.0 %. Similar results are found in some studies from the literature [Rocha *et al.*, 2002, Prauchner *et al.*, 2004].

Properties of bio-pitches have been compared with other reported studies from the literature and presented in Table 3. The experimental data of the present study are comparable with reported values and was found to be compatible with that reported studies.

Table 1: Characteristics of raw materials

<i>Proximate analysis (%)</i>	PT	OT	HS	AS	PS	PC
Moisture	7.27	7.13	8.13	6.54	5.98	7.67
Ash	0.82	0.96	0.61	2.29	1.27	1.09
Volatiles	76.02	77.79	73.64	72.33	76.77	75.00
Fixed C*	15.89	14.12	17.62	18.84	15.98	15.24
<i>Component analysis (%)</i>						
Extractive	3.07	1.53	0.25	7.52	0.21	2.95
Lignin	33.40	27.75	43.07	20.34	30.04	29.89
Hemicellulose	29.51	27.35	25.33	31.23	27.28	33.47
Cellulose**	33.20	42.41	30.84	38.62	41.20	32.60

*,** By difference

Table 2: Properties of bio-pitches

	Pitch Yield (%)	Softening Point (°C)	Density (g/cc)	C (%)	H (%)	N (%)	O (%)	HHV (MJ/kg)	Ash (%)
<i>Hazelnut shell</i>									
HS-P700	75.2	84.5	1.33	69.35	6.05	0.56	24.04	20.22	0.20
HS-P500	57.9	107.6	1.37	69.60	5.96	0.58	23.86	20.32	0.26
HS-P300	36.5	145.0	1.38	71.55	5.92	0.65	21.88	21.33	0.77
HS-P100	26.3	203.0	1.40	71.67	5.90	0.71	21.72	21.39	0.87
<i>Oak tree</i>									
OT-P700	75.3	92.8	1.32	67.64	6.12	0.32	25.92	19.31	< 0.01
OT-P500	50.2	125.1	1.34	68.25	6.13	0.34	25.28	19.63	< 0.01
OT-P300	50.1	125.2	1.39	68.95	6.16	0.32	24.57	20.01	< 0.01
OT-P100	45.6	125.8	1.41	69.31	6.22	0.32	24.15	20.21	< 0.01
<i>Pine sawdust</i>									
PS-P700	62.2	83.3	1.32	68.57	6.20	0.62	24.61	19.88	0.39
PS-P500	54.9	98.6	1.35	69.15	6.25	0.66	23.94	20.20	0.23
PS-P300	40.3	128.5	1.36	69.61	6.28	0.78	23.33	20.47	0.10
PS-P100	30.1	141.3	1.39	70.90	6.31	0.88	21.91	21.17	0.08

Table 3: Properties of various pitches from the literature

Pitch Sample	Softening Point (°C)	Density (g cc ⁻¹)	Ash (%)	C (%)	H (%)	N (%)	O (%)	Reference
Biopitch #03	108.0	1.24-1.26	0.2	70.50	6.30	0.70	22.60	[Rocha <i>et al.</i> , 2002]
Biopitch 250°C/4h	112.0	-	1.10	71.60	6.00	-	22.90	[Prauchner <i>et al.</i> , 2004]
Oil shale/Asphaltite pitch	136.0	-	-	81.90	7.30	2.40	4.40	[Apak <i>et al.</i> , 2002]
Coal tar pitch	116.0	-	-	93.28	4.17	0.96	0.51	[Perez <i>et al.</i> , 2004]
Petroleum pitch	127.0	-	-	91.90	5.39	0.19	0.97	[Kershaw and Black, 1993]
HS-P100	203.0	1.40	0.87	71.67	5.90	0.71	21.72	This study
OT-P100	125.8	1.41	< 0.01	69.31	6.22	0.32	24.15	This study
PS-P100	141.3	1.39	0.08	70.90	6.31	0.88	21.91	This study

4. CONCLUSIONS

Pitch based carbon foam with unique properties has getting increased attention due to its potential use in numerous industries. In this study possible usage of biomass pyrolysis liquid product tar for mesophase pitch-based carbon foam production has been reported. Detailed characterization studies and literature comparison bio-pitch, produced from biomass tar, can be used effectively as an alternative and economic precursor for

carbon foam production. Bio-pitch has the potential to reduce the cost of pitch and carbon foam production.

Acknowledgements: The authors would like to thank “Anadolu University Scientific Research Council” for the financial support of this work through the projects 1106F117 and 1110F155.

REFERENCES

- Apak E., Yardim M.F., Ekinçi E., 2002. Preparation of carbon fiber precursors from the pyrolysis and copyrolysis of Avgamasya asphaltite and Göynük oil shale: vacuum distillation and hexane extraction. *Carbon*, 40, 1331.
- Chen C., Kennel E.B., Stiller A.H., Stansberry P.G., Zondlo J.W., 2006. Carbon foam derived from various precursors. *Carbon*, 44, 1535.
- Ford W.D., 1964. Methods of making cellular refractory thermal insulating material. US Patent: 3,121,050.
- Kershaw J.R. and Black K.J.T., 1993. Structural characterization of coal-tar and petroleum pitch. *Energy & Fuels*, 7, 420.
- Klett J.W., 1998. High thermal conductivity, mesophase pitch-derived carbon foam, Proceedings of the 43rd International SAMPE Symposium, Part 1 (of 2), Anaheim, California, U.S.A., May 31-June 4.
- Klett J.W., 2000. Process for making carbon foam. US Patent: 6,033,506.
- Klett J., Hardy R., Romine E., Walls C., Burchell T., 2000. High-thermal-conductivity mesophase-pitch-derived carbon foams: effect of precursor on structure and properties. *Carbon*, 38, 953.
- Li C., Suzuki K., 2009. Tar property, analysis, reforming mechanism and model for biomass gasification-An overview. *Renewable & Sustainable Energy Reviews*, 13, 594.
- Nowakowski D.J., Bridgwater A.V., Elliott D.C., Meier D., Wild P., 2010. Lignin fast pyrolysis: Result from an international collaboration. *Journal of Analytical and Applied Pyrolysis*, 88, 53.
- Perez M., Granda M., Santamaria R., Morgan T., Menendez R., 2004. A thermoanalytical study of the co-pyrolysis of coal-tar pitch and petroleum pitch. *Fuel*, 83, 1257.
- Prauchner M.J., Pasa V.M.D., Otani C., Otani S., Menezes S.M.C., 2004. Eucalyptus tar pitch pretreatment for carbon material processing. *Journal of Applied Polymer Science*, 91, 1604.
- Rocha J.D., Coutinho A.R., Luengo C.A., 2002. Biopitch produced from Eucalyptus wood pyrolysis liquids as a renewable binder for carbon electrode manufacture. *Brazilian Journal of Chemical Engineering*, 19, 127.
- Telmo C., Lousada J., 2011. The explained variation by lignin and extractive contents on higher heating value of wood. *Biomass and Bioenergy*, 35, 1663.

PRODUCTION OF POROUS CERAMIC MATERIAL FROM KAOLIN DOPED PORCELAIN POLISHING WASTE

Derya Kirsever^{1,a}, Nil Toplan¹ and H.Özkan Toplan¹

1. Sakarya University, Department of Metallurgical and Materials Engineering, Sakarya, TURKEY
a. Corresponding author (dkirsever@sakarya.edu.tr)

ABSTRACT:The possibility of recycling residues, coming from the industrial polishing process of porcelain stoneware tiles, by the addition of kaolin to the raw materials was studied. Mixtures of polishing porcelain stoneware waste and kaolin were prepared at different compositions (up to wt. 10 % kaolin) and sintered at different temperatures (up to 1175⁰C). TG-DTA analysis of powder mixtures was performed. The sintered samples were also characterized to determine expansion and bulk density of the sintered samples. Microstructural analyses were characterized by scanning electron microscopy-energy dispersive spectroscopy.

1. INTRODUCTION

As compared with other classes of tiles, porcelain stoneware tiles exhibit excellent physical and mechanical properties [García-Ten et al., 2012]. The typical composition contains 25-30 wt% of kaolin and ball clays, 50-60 wt% feldspars and 5-10 wt% of quartz sand. Their aesthetic and performances are enhanced by surface polishing. On the other hand, the industrial polishing process causes an important environmental problem, due to the polishing porcelain stoneware residues in form of mud [Rambaldi et al., 2007].

Porcelain tile polishing sludges are essentially mix of water, very fine debris of the specific porcelain body and residue of the abrasive particles as magnesite, silicon carbide and diamond [Bernardin et al., 2006; Rambaldi et al., 2007]. According to EU regulations, the polishing porcelain stoneware residues (PPR) are not applicable to be land-filled due to environmental impact and an increasing of the industrial costs [Colombo et al., 2003; Rambaldi et al., 2007].

The aim of the research is to assess the possibility to recycle the polishing porcelain stoneware residues, in the production of porous ceramic material. In addition, kaolin increases plasticity and facilitates to form to the material.

2. EXPERIMENTAL DETAILS

The chemical compositions of PPR [Duratiles Co., Turkey] and kaolin [Kalemaden Co., Turkey] were given in Table 1. Three different compositions were studied, as mentioned Table 2. The compositions were ball milled in water with 3 mm Al₂O₃ balls in a polyethylene bottle for 2 hours.

The compositions were dried at 100⁰C for 24 hours and pressed (1 ton/cm²) in square specimens (2.5x2.5 cm²). The compacts were sintered during 30, 60, 120 and 180 min at 1100, 1125, 1150 and 1175⁰C with 10⁰C/ min heating rate.

The morphology of samples were observed by using Joel 6060 LV scanning electron microscope (SEM). Differential thermal analysis (DTA) and

Table 1: Chemical composition (wt%) of the polishing stoneware residues (PPR) and kaolin.

	SiO ₂	Al ₂ O ₃	Fe ₂ O ₃	CaO	K ₂ O	Na ₂ O	MgO	ZrO ₂	TiO ₂	LOI
PPR	64,63	18,28	0,616	1,613	1,0	4,94	3,4	1,95	0,462	2,94
Kaolin	52.12	33.83	0.55	0.15	0.13	0.01	0.05	-	0.45	12.45

thermogravimetry (TG) measurements were performed in air at a heating rate 10⁰C/min by using TA Instruments SDTQ 600. After sintering, bulk density and expansion (%) of the expanded samples were calculated by Eq.1 and Eq.2, respectively.

$$\text{Expansion (\%)} = \frac{h_0 - h_p}{h_0} \times 100 \quad \text{Eq.1}$$

$$\text{Bulk density} = M/V \quad \text{Eq.2}$$

h₀ is the height of sample after pressing and h_p is the height of sample after sintering (mm). M is mass of sample (g.) and V is volume of sample (cm³).

Table 2: Compositions studied

Code	Composition (wt %)		
	K-5	K-10	K-20
PPR	95	90	80
Kaolin	5	10	20

3. RESULTS AND DISCUSSION

Expansion (%) vs sintering time curves are shown in Fig. 1 for K-5, K-10 and K-20 samples after sintering at 1100, 1125, 1150 and 1175⁰C. All samples presents a great and continuous expansion. This is due the presence of SiC particles coming from polishing process. Furthermore, expansion (%) increases for K-5, K-10 and K-20 samples with sintering temperature. But, expansion (%) decreases with the kaolin additions. After sintering at 1175⁰C for 180 min, K-5 sample shows the firing expansion of 283,8 % .

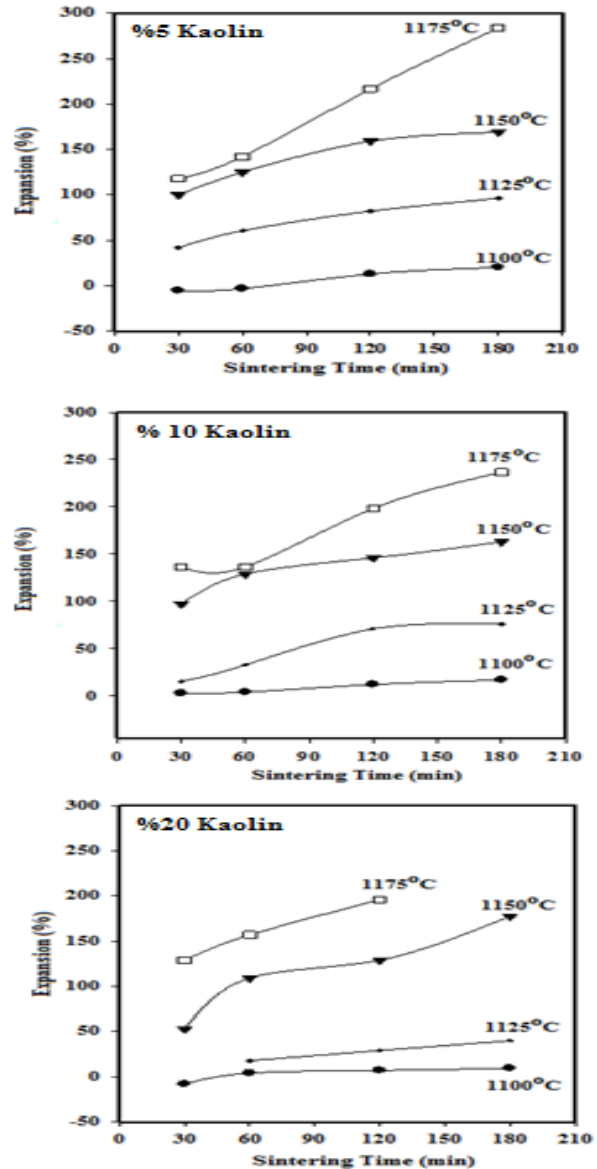


Figure 1: Expansion (%) curves of all samples.

Bulk density vs sintering time curves are given in Fig. 2 for K-5, K-10 and K-20 samples. It is obvious that bulk density of samples decreases while sintering time increases. Also, the bulk density decreases with sintering temperature. On the other hand, the bulk density of all

samples decrease with the kaolin additions. The sample with 5 % wt kaolin addition has very low bulk density ($0,22 \text{ g/cm}^3$) after sintering at 1175°C for 180 min.

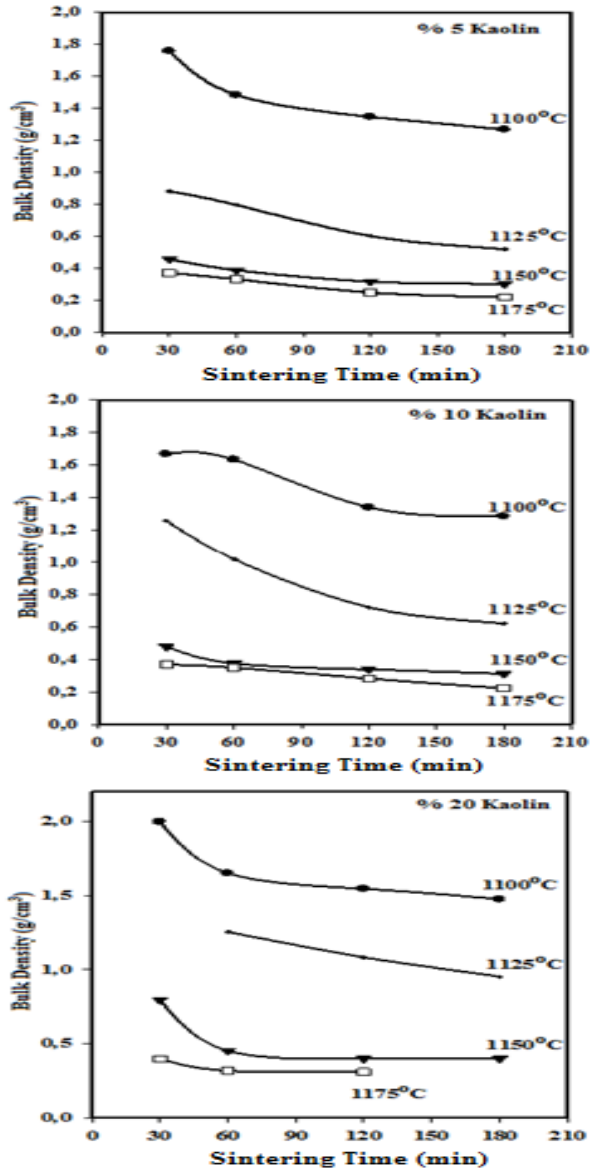


Figure 2: Bulk density of all samples.

The SEM micrographs of all samples are shown in Fig.3. The samples have big, closed and rounded pores. It is obvious that pore size decreases with kaolin addition. The presence of SiC particles in PPR powder coming from polishing process is a reason in pore formation.

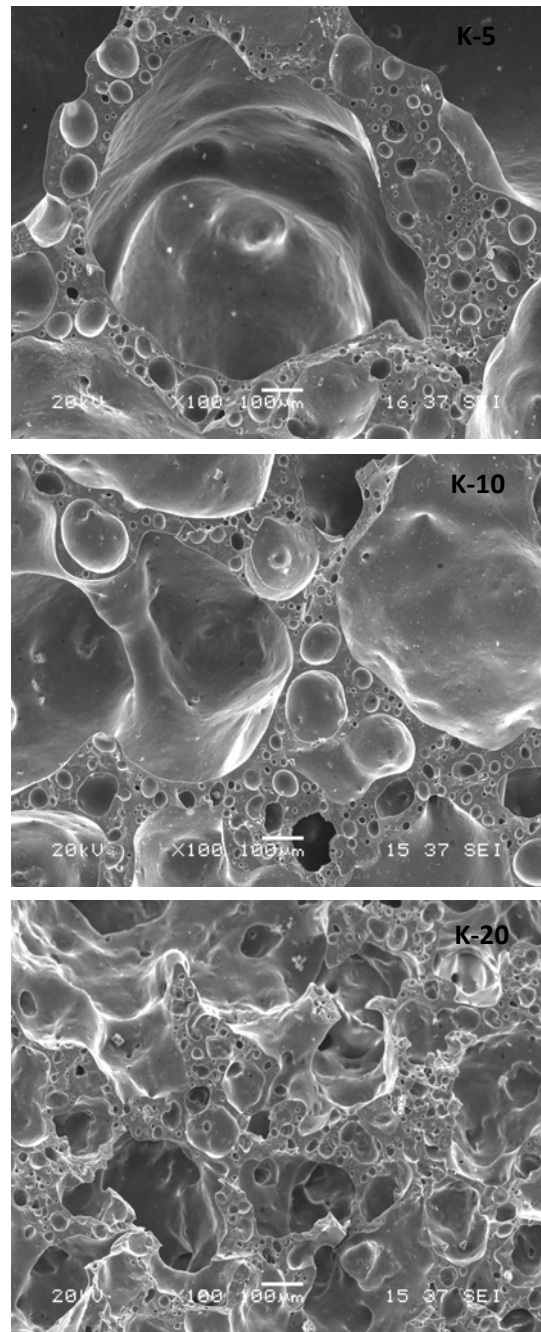


Figure 3: SEM micrographs of all samples sintered at 1150°C for 60 min.

DTA and TG analysis of K-5 sample is given in Fig. 4. The weight loss of first step at low temperatures ($30\text{-}150^\circ\text{C}$) is about 1.0 wt %, corresponding to the first endothermic peak is the evaporation of adsorbed water. The second endothermic peak at 491°C with weight loss is related to the dehydration of kaolin (Chen et al., 2004).

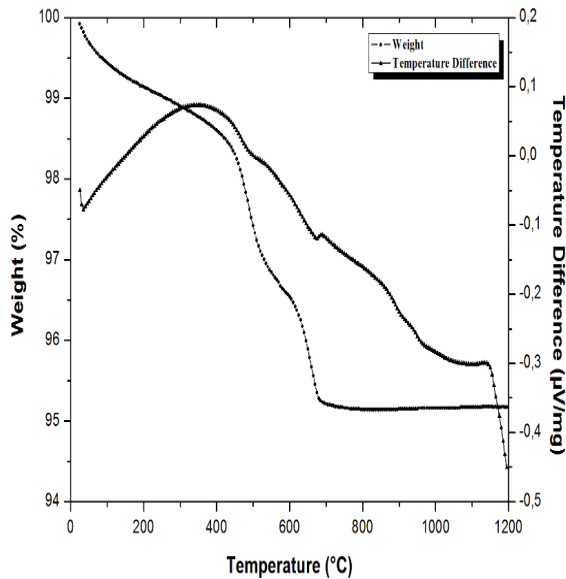


Figure 4: DTA-TG curves of K-5 sample.

The third endothermic peak at around 671°C is attributed to decomposition of magnesite. On the other hand, the weight loss does not change significantly during the heating temperature at above 1100°C . The exothermic peak at around 1142°C can be due to the decomposition of moissanite (SiC) (Rambaldi et al., 2007) or the formation of mullite.

4. CONSLUSION

In this study, the production of porous ceramics from porcelain tile polishing residues was investigated. The reduction of the bulk density is related to the presence of SiC particles coming from polishing process.

All samples show great expansion after sintering. Also, the expansion occurs by the presence of closed pores in the microstructure of all samples. The addition of 5 % wt of kaolin is enough in pore formation, density reduction and increasing expansion.

REFERENCES

- Bernardin, A.M., Silva, M.J.d. and Riella, H.G., 2006. Characterization of cellular ceramics made by porcelain tile residues. *Materials Science and Engineering: A*, 437(2): 222-225.
- Chen, Y.-F., Wang, M.-C. and Hon, M.-H., 2004. Phase transformation and growth of mullite in kaolin ceramics. *Journal of the European Ceramic Society*, 24(8): 2389-2397.
- Colombo, P., Brusatin, G., Bernardo, E. and Scarinci, G., 2003. Inertization and reuse of waste materials by vitrification and fabrication of glass-based products. *Current Opinion in Solid State and Materials Science*, 7(3): 225-239.
- García-Ten, J., Saburit, A., Bernardo, E. and Colombo, P., 2012. Development of lightweight porcelain stoneware tiles using foaming agents. *Journal of the European Ceramic Society*, 32(4): 745-752.
- Rambaldi, E., Esposito, L., Tucci, A. and Timellini, G., 2007. Recycling of polishing porcelain stoneware residues in ceramic tiles. *Journal of the European Ceramic Society*, 27(12): 3509-3515.

UTILIZATION OF POLISHING PORCELAIN STONEWARE WASTE WITH TALC ADDITION IN THE PRODUCTION OF POROUS CERAMIC BODIES

Derya Kirsever^{1,a}, Nil Toplan¹ and H.Özkan Toplan¹

1. Sakarya University, Department of Metallurgical and Materials Engineering, Sakarya, TURKEY
a. Corresponding author (dkirsever@sakarya.edu.tr)

ABSTRACT:The present work aimed at studying the utilization of wastes from polishing to produce porcelain stoneware. Mixtures containing polishing porcelain stoneware waste and talc were prepared at different compositions (up to 10 wt.% talc). The powder mixtures were compressed in a hydraulic press and sintered at different temperatures as 1100, 1125 and 1150°C. SEM, XRD, and TG-DTA analysis of the sintered samples were performed. Also, the sintered samples were also characterized to determine expansion (%) and water absorption (%) of the sintered samples.

1. INTRODUCTION

Porcelain stoneware is very high density ceramic material (water absorption < 0.5%), made up of crystalline phases surrounded in a glassy matrix (Cavalcante et al., 2004). Porcelain stoneware tiles have attractive technical properties such as good flexural strength, surface hardness, high surface abrasion resistance and fracture toughness as compared with other classes of tiles (Tucci et al., 2004).

The typical composition of porcelain stoneware tile contains 40-50 wt.% kaolin clay, 35-45 wt.% feldspar and 10-15 wt.% quartz (Martín-Márquez et al., 2008). The crystalline phases of porcelain stoneware tile constitute quartz and mullite in glassy matrix. Quartz is the major crystalline phase (30 wt%) compared to mullite (up to 8%) in the fired body (Sánchez et al., 2006).

In recent years, there has been a strong increase in the production of polished porcelain tiles. The polishing process obtains smooth, glazed surface as compared with unpolished tiles (Sánchez et al., 2006). But, an environmental problem occurs due to polishing porcelain stoneware residues, PPR, in

form of mud (Rambaldi et al., 2007). This mud includes residues of the porcelain stoneware tile and abrasive particles as magnesite, silicon carbide and diamond (Bernardin et al., 2006; Rambaldi et al., 2007)

The objective of the present research is to study the substitution of talc to PPR powder for the manufacturing of low density ceramics that can be used as building materials due to their thermal and acoustic properties.

2. EXPERIMENTAL DETAILS

The chemical compositions of PPR (Duratiles Co., Turkey) and talc (Kalemaden Co., Turkey) were given in Table 1. Three different compositions were studied, as mentioned Table 2. The compositions were ball milled in water with 3 mm Al₂O₃ balls in a polyethylene bottle for 2 hours.

The compositions were dried at 100°C for 24 hours and pressed (1 ton/cm²) in cylindrical specimens (2.5 cm diameter). The compacts were sintered during 30, 60, 90 min at 1100, 1125, 1150 with 10°C/min heating rate.

Table 1: Chemical composition (wt%) of the polishing stoneware residues (PPR) and talc.

	SiO ₂	Al ₂ O ₃	Fe ₂ O ₃	CaO	K ₂ O	Na ₂ O	MgO	ZrO ₂	TiO ₂	LOI
PPR	64,63	18,28	0,616	1,613	1,0	4,94	3,4	1,95	0,462	2,94
Talc	63	0.40	0.25	0.40	0.04	0.08	30,0	-	0.40	4.83

The crystalline phases were analysed by X-ray diffraction analysis (XRD) using Rigaku Ultima X-ray diffractometer and Cu K_α radiation. Specimen microstructure was characterised by using Joel 6060 LV scanning electron microscope SEM-EDS. Differential thermal analysis (DTA) and thermogravimetry (TG) measurements were performed in air at a heating rate 10⁰C/min by using TA Instruments SDTQ 600. After sintering, the expanded samples of all compositions were determined water absorption (%) and expansion (%) by formula (1) and (2), respectively.

$$\text{Water Absorption}(\%) = (M_2 - M_1) / M_1 \quad (1)$$

$$\text{Expansion}(\%) = (h_0 - h_p) / h_0 \times 100 \quad (2)$$

M₂ is the weight of specimens after soaking in water for 24 h and M₁ is the weight of specimens before soaking (g). h₀ is the height of sample after pressing and h_p is the height of sample after sintering (mm).

Table 2: Compositions studied

Code	Composition (wt %)		
	T-1	T-2	T-3
PPR	97,5	95	90
Talc	2,5	5	10

3. RESULTS AND DISCUSSION

Fig.1 shows the XRD patterns of T-1, T-2, T-3 samples as sintered at 1150⁰C for 30 min. (R: Rutile, TiO₂; K: Kyanite,

Al₂SiO₅; Q: Quartz, SiO₂; S: SiO₂; M: Mullite, Al₆Si₂O₁₃) As a result, quartz, SiO₂ and kyanite are the major phases of all samples sintered at 1150⁰C for 30 min. Also, amorphous phase is observed in XRD patterns due to glass melting. The silicon carbide (SiC) was not identified due to decomposition of the silicon carbide into silica and carbon dioxide at above 1000⁰C.

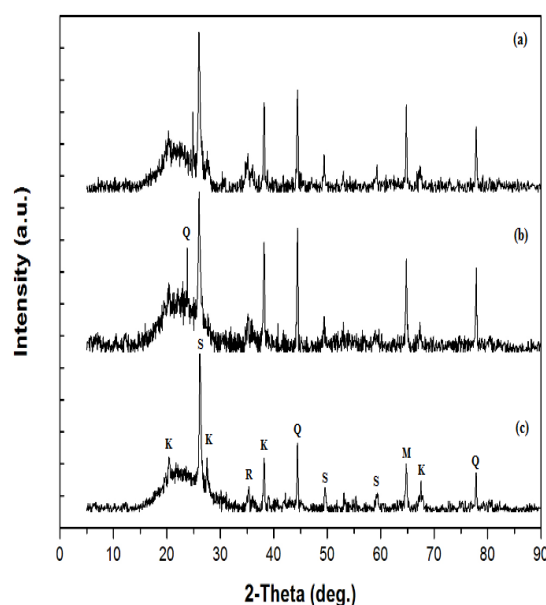


Fig.1 XRD patterns of T-1 (c), T-2 (b), T-3 (a) were sintered at 1150⁰C for 30 min.

The microstructure of T-1, T-2 and T-3, sintered at 1150⁰C for 60 min is presented in Fig.2. The pore are large, spherical and closed. It is clear that pore size increases with talc addition. The decomposition of SiC particles coming from polishing process at above 1000⁰C causes pore formation. Therefore, the

product can present good thermal and acoustic insulation

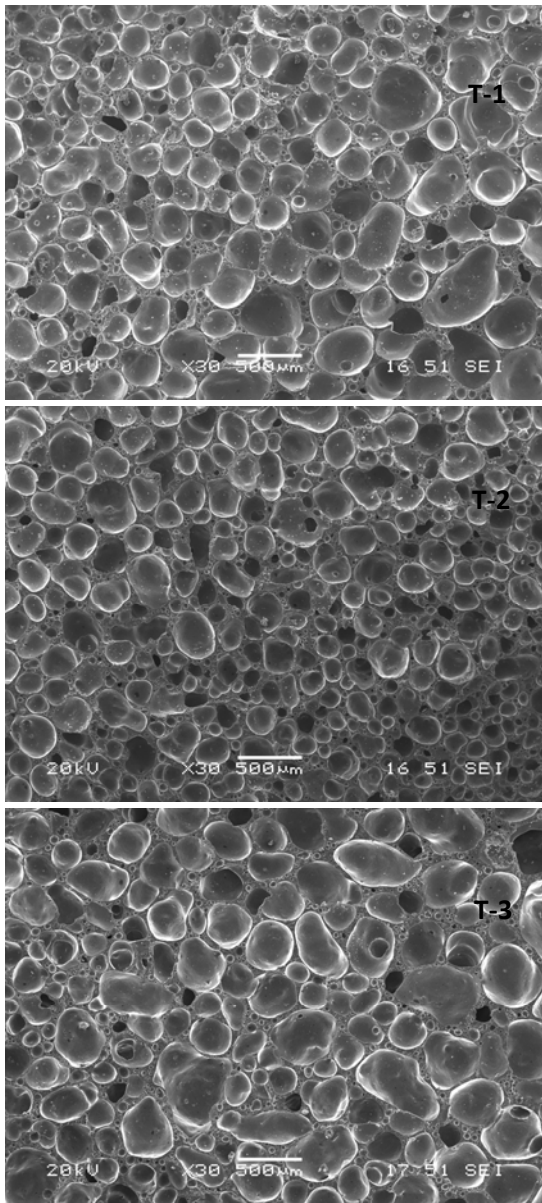


Figure 2: SEM micrographs of all samples sintered at 1150°C for 60 min.

Expansion (%) vs sintering time curves are shown in Fig. 3 for T-1, T-2 and T-3 samples after sintering at 1100, 1125, 1150°C. Expansion (%) of all samples increases with sintering temperature and talc addition. This is due the dissociation of SiC particles coming from polishing process.

Accordingly, T-3 sample with 10 % wt shows the firing expansion of 82,43 % at 1150°C for 90 min. This feature does not allow the use of this kind of residue in the production of dense tiles, as the porcelain tiles. The product expansion and density reduction is obtained by the presence of closed pores in the microstructure of the samples. The glass melting at the same time of SiC decomposition into silica and carbon dioxide at above 1000°C results in a product that permanently holds gas, then closed pores occurs during cooling process (Pereira et al., 2008).

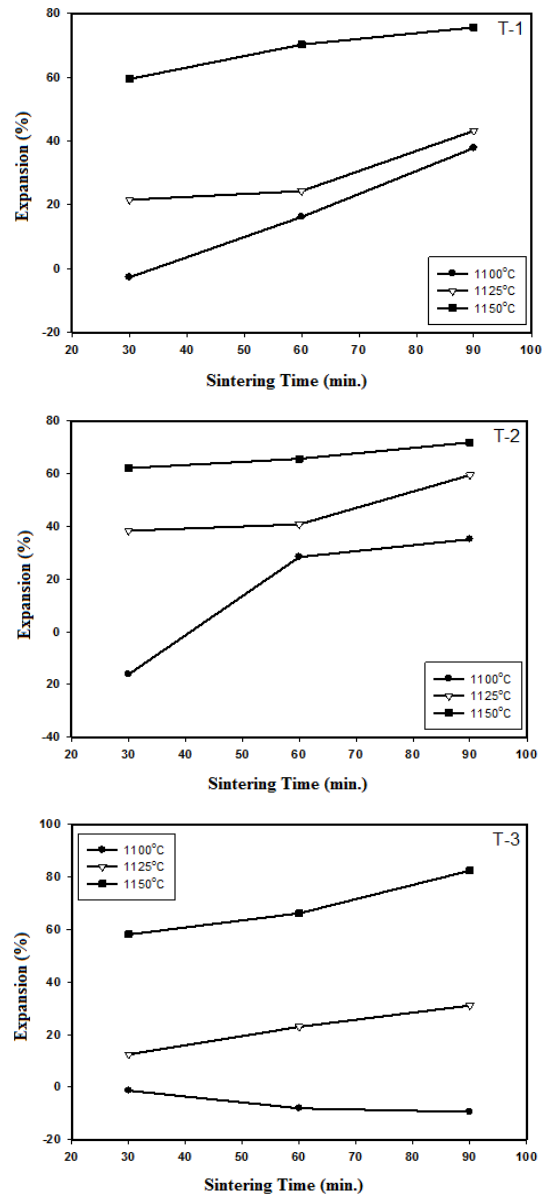


Figure 3: Expansion (%) curves of all samples.

Water absorption of all samples were determined and the results are presented in Fig. 4. Water absorption (%) decreases with sintering time and sintering temperature for T-1, T-2 and T-3 samples. In addition, T-3 sample with 10 % wt shows higher water absorption of 4,6 % at 1100°C for 30 min.

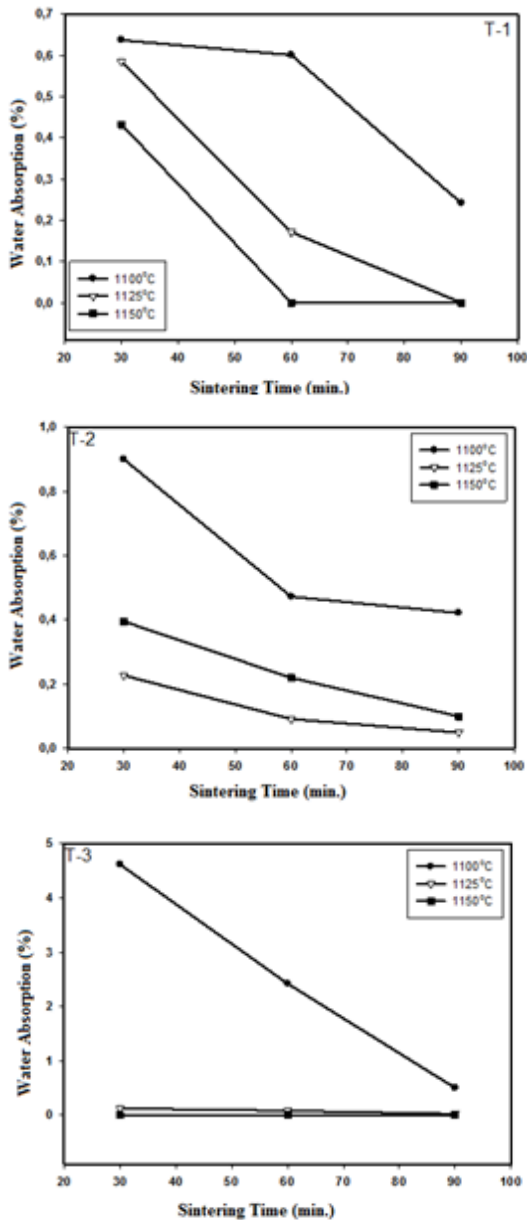


Figure 4: Water absorption (%) curves of all samples.

DTA and TG analysis of T-2 sample is shown in Fig. 5. The weight loss at the

first stage at low temperature (30-150°C) is related to the evaporation of the adsorbed water molecules with endothermic reaction. Endothermic peaks at 348 and 484°C can be due to thermal decompositions of the organic substances in the PPR (Rambaldi et al., 2007). Also, endothermic peak at 636°C is indicated decomposition of magnesite. The weight loss does not change significantly at above 1100°C. Therefore, the exothermic peak at around 1114°C can be related to the decomposition of moissanite (SiC) (Rambaldi et al., 2007) or the formation of mullite (Chen et al., 2004).

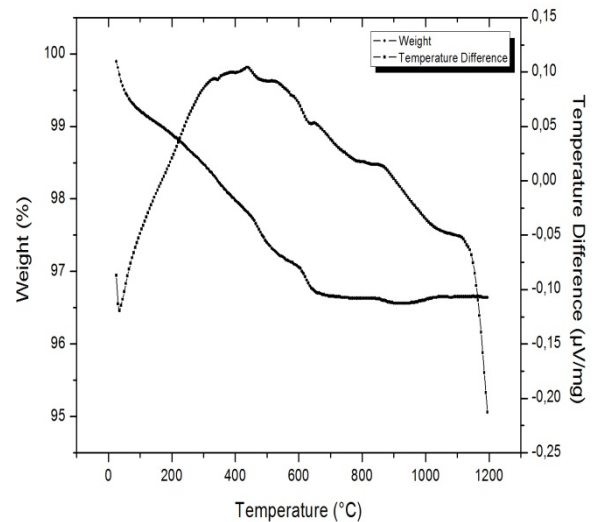


Figure 5: DTA-TG curves of T-2 sample.

4. CONSLUSIONS

It is possible to use porcelain polishing residues (PPR) for production of porous ceramics with low density. Porous ceramics can be used in the building industry due to their good acoustic and thermal insulation.

Water absorption (%) decreases with sintering time and sintering temperature for all samples. Also, expansion occurs by the presence of closed pores in the microstructure of the samples.

Finally, the addition of 10 % wt of talc is enough in pore formation and increasing expansion.

REFERENCES

- Bernardin, A.M., Silva, M.J. and Riella, H.G., 2006. Characterization of cellular ceramics made by porcelain tile residues. *Materials Science and Engineering: A*, 437(2): 222-225.
- Cavalcante, P.M.T. et al., 2004. The influence of microstructure on the performance of white porcelain stoneware. *Ceramics International*, 30(6): 953-963.
- Chen, Y.-F., Wang, M.-C. and Hon, M.-H., 2004. Phase transformation and growth of mullite in kaolin ceramics. *Journal of the European Ceramic Society*, 24(8): 2389-2397.
- Martín-Márquez, J., Rincón, J.M. and Romero, M., 2008. Effect of firing temperature on sintering of porcelain stoneware tiles. *Ceramics International*, 34(8): 1867-1873.
- Pereira, A.S., Felisberto, D.S., Luckmann, G., Daros, M.T. and Bernardin, A.M., 2008. Cellular ceramics made from porcelain tile polishing residues: Effect of soaking time. *Proc. Qualicer*: 83-87.
- Rambaldi, E., Esposito, L., Tucci, A. and Timellini, G., 2007. Recycling of polishing porcelain stoneware residues in ceramic tiles. *Journal of the European Ceramic Society*, 27(12): 3509-3515.
- Sánchez, E. et al., 2006. Porcelain tile microstructure: Implications for polished tile properties. *Journal of the European Ceramic Society*, 26(13): 2533-2540.
- Tucci, A., Esposito, L., Rastelli, E., Palmonari, C. and Rambaldi, E., 2004. Use of soda-lime scrap-glass as a fluxing agent in a porcelain stoneware tile mix. *Journal of the European Ceramic Society*, 24(1): 83-92.

MAGNESIA BASED CASTABLE REFRACTORY PRODUCTION AND UTILIZATION AREAS

Hande Marulcuoğlu¹, C. Betül Emrullahoğlu Abi²

¹Ondokuz Mayıs University, Engineering Faculty, Materials Science and Engineering Department

²Afyon Kocatepe University, Engineering Faculty, Materials Science and Engineering Department

ABSTRACT: The percentage of unshaped refractory usage in iron-steel, cement, metal industries and refuse incineration plants have increased in recent years. For castable refractories, the aim is to obtain maximum packing with low porosity via using optimum particle size distribution by means of thixotropic colloidal systems found in the structure. Of late years, investigations about the development and utilization of MgO based self flowing alkaline castables have been carried out. The real reason why MgO is preferred is the high melting point and widespread occurrence of this oxide within the refractory oxides. Nowadays, the area of usage of self flowing castables include metallurgical crucibles knitted products, process, and transport crucibles, melting plants, high-temperature plants of cement / lime industry.

1. INTRODUCTION

Refractory materials in general are defined as materials that can withstand high temperatures. [Böcek, 2011]. Refractories main task is expected to rise out of the system to prevent the temperature industrial process environment. At the same time, protects the system to provide continuity of the operation. In carrying out this task, they be based on mechanical, chemical and thermal strain [Başpınar, 2005].

Castable is made of a granular and powdered refractory material and adding a certain amount of binding agent and water together to form a construction suitable for the casting method, and can be hardened without heating. Non amorphous refractory composed of refractory aggregate powders, binders, additives, water or other liquid material is generally in the use of the site by pouring, vibration or tamping method of pouring molding, use can also be made of prefabricated parts.

Usually the main components of castable refractories produced with the traditional cast method may be considered as

aggregates, hydraulic binder, high duty alumina cement, water and the dispersant. With additions of reactive alumina and micro silica beads, high packaging known as a super-slim packaging can be obtained and the rheological properties of the material, as well as service temperature performance of the material can be increased [Durmuş, 1998].

There is a trend to increase the use of unshaped refractory castables in various industries like steel-making, cement production, energy production and waste incineration. Quality improvement is needed particularly to design durable parts or structures based on these materials [Marzagui and Cutard, 2004]. Consumption rate of unshaped refractories in iron-steel and metal industry, cement and waste incineration has been increasing rapidly in recent years. Quality requirement of these products is also increasing. Advantages of using unshaped refractories include economy, easy application to thin sections, complex shapes, and regions that are difficult to reach. It is also possible to use it on the damaged

refractory lining as a repair mortar [Bugajski and Schwaiger, 1996].

The effect of mold in the shape of the gravity spread only castable refractories can rheological properties. Thanks to this feature, a new research has gained importance and has been the subject for the producers. [Gül, 2002]. Castable refractories spontaneous flow properties due to the physical and chemical characteristics of the mixture. The interaction between the particles must be minimized for better fluidity. For this to occur should be a uniform distribution of particles in suspension. In this place, Besides the type and quality of dispersant, It is also important to dust particle size used powder [Durmuş, 1988].

Particle size distribution of the self-flowing castable products should be designed so as to limit coarse particle interaction. Coarse particle fraction takes place in the well-liquidified binder matrix, which acts as a lubricant. Such behavior of liquidified mixes can only be reached by using high packing density particle structure. High packing density is essential for self-flowing castables. This affects the flow behavior and properties of concrete [Watanabe *et al.*, 1989].

For a number of years, self-flowing castables have been used to line high-temperature plants, especially in the area of metallurgy. The initial development of self-flowing bodies was the process engineering optimisation of castables that were densified by pneumatic or electric vibrators. Castables are thixotropic bodies, that can be fluidised by vibration. If a thixotropic castables is liquefied by an overdose of the mixing water, which can be necessary for the filling in of narrow gaps or other difficult to reach areas. This can lead to a de-mixing due to the inhomogeneous distribution of the

fine and coarse grains. As a result, self-flowing refractory castables were developed which need no mechanical densification assistance in order to achieve the appropriate processing consistency and the corresponding parametric values of the thixotropic castables. Essential for the self-flowing properties of the castables often is the regulation of the dilatant rheological behaviour [Schulle *et al.*, 2001].

As major varieties of unshaped refractory castables in addition to the common characteristics without firing can be directly used, many species of the unshaped refractory production processes are relatively simple and do not require special equipment, a high degree of mechanization, the construction of the most simple, high material utilization, in addition to the general high temperature strength, can be made of prefabricated kiln the spin-workers on-site installation, such as continuous casting in the middle of the tank with the refractory castable weir plate preform install.

Raise the ratio of unshaped refractory, refractory castable is bound to the rapid development, at the same time the increase in the variety will also be a corresponding increase in quality, the focus will continue the development of low cement, ultra low cement and cement refractory castable selection the homogenizing and quality of raw materials and special aggregates to improve the basic components combined resource conditions, research and promotion of the use of fiber reinforced refractory castable and artesian refractory castable, application of various additives to improve the performance of the refractory castable In addition, the development of dedicated castable (such as iron trough, ladle lining, etc.) as well as with special functional materials (such as wear-resistant, acid and alkali

resistant, high-strength insulation, high strength and high thermal conductivity characteristics), in the production and application of technology to improve production equipment and construction of ancillary equipment [http://www.hotwikipedia.us/Wikipedia-1513037-Refractory-castable.html].

Magnesium oxide (MgO) or magnesia is one of the most important raw materials in the refractory industry. Because of its high refractoriness (melting point of 2800 °C) and corrosion resistance, the presence of this oxide in refractory compositions promotes an increase in the performance of pre-shaped linings for steel production [Salomão *et al.*, 2007]. In addition, there are plenty of refractory oxides. Especially, Magnesia is an extremely important material for the steel industry. The importance of magnesia results from high refractoriness, hydration resistance, chemical stability, the high temperature and alkaline environments..

The area of usage of magnesia based castable refractory include electric arc furnaces, dust collection systems, blast furnace stoves, isolation of LPG tanks, melting pot plants, pot furnaces, the base of basic open-hearth steel furnaces etc. used in places that require such high temperature resistance.

2. CONCLUSIONS

Changing the magnesia grain size of magnesia castables completely affected the phase development at high temperatures and their distribution throughout the castable. As shown in Figure 1, selecting the magnesia grain size is a key issue to magnesia castables design, as it affects the castable microstructure after firing.

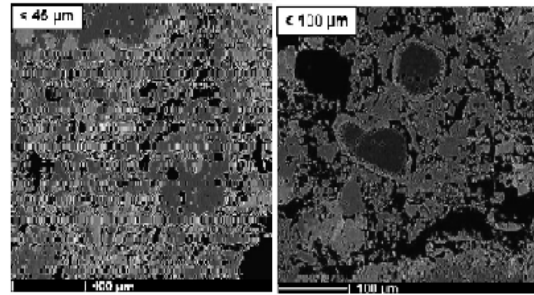


Figure 1: Microstructures of castables containing different MgO grain sizes (<45 and <100_μm), after firing at 1500 °C for 5 h [Braulio *et al.*, 2008].

The creep resistance is better for the sample containing the fine MgO source, as fewer cracks develop. Nevertheless, compositions presenting coarse MgO grains might present better thermal shock damage resistance, due to the great number of pores. The sample containing the coarse MgO grain showed reduced mechanical strength (Fig.2a) and an increase in the apparent porosity (Fig.2b) from 1300 to 1500 °C, which is the temperature range where spinel and CA6 are developed. [Braulio *et al.*, 2008].

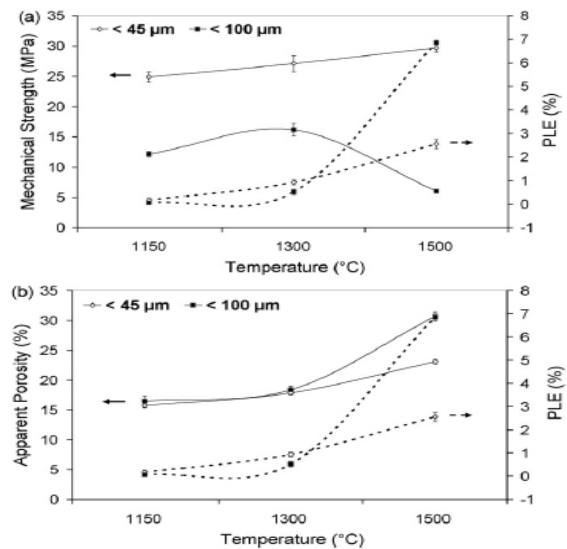


Figure 2: (a) Mechanical strength versus permanent linear expansion (PLE). (b) apparent porosity × PLE of castables containing different MgO grain sizes (<45 and <100_μm).

As magnesia castables are commonly used in steel ladles, they are fired under mechanical constraining. This could improve the thermo-mechanical behavior, due to the development of a toughening mechanism [Braulio *et al.*, 2008].

Castable refractories are produced with the use of microsilica. It has been demonstrated that it is possible to utilise the MgO-SiO₂ bond to make castables that both exhibit good flow, controlled setting characteristics, and attractive hot properties. Approximately 6% microsilica seems to be essential in the make up of these castables giving good placement properties and also slag resistance [Ødegård *et al.*, 2004].

Through specific use of dispersant agents, the hydration tendency of magnesia can be effectively stopped [Schulle *et al.*, 2001].

The thermal shock resistance can be considered good due to the spinel content in the matrix [Schulle *et al.*, 2001].

The use of self-flowing bodies seems to be possible at temperatures considerably above 1500°C [Schulle *et al.*, 2001].

Magnesia hydration and the apparent volumetric expansion were significantly affected by the nature and the content of the binder used in the castable compositions. It was observed that magnesia hydration resulted in less intense damages in compositions with low (1.5–3 wt.%) and high (12 wt.%) calcium aluminate cement contents. In the first case, because the low calcium aluminate cement content did not increase the castables' pH so intensively, the driving force for magnesia hydration was reduced and, additionally, the extra volume generated by the MgO hydration could be suitably accommodated. For the 12 wt.% calcium aluminate cement, the

high mechanical strength developed minimized the damages caused by the magnesia hydration. The compositions with the calcium aluminate cement contents 6–9 wt.% range presented the highest levels of damage caused by a combination of high pH, lower porosity and intermediate values of mechanical strength, resulting in a high magnesia hydration degree and not high enough mechanical strength to restrict the volumetric expansion (Fig 3). Due to the drawbacks pointed out as a result of either the low or high calcium aluminate cement amounts, it is reasonable to consider that the calcium aluminate cement content control should be applied in combination with other magnesia anti hydration techniques in order to attain better results [Salomão and Pandolfelli, 2009].

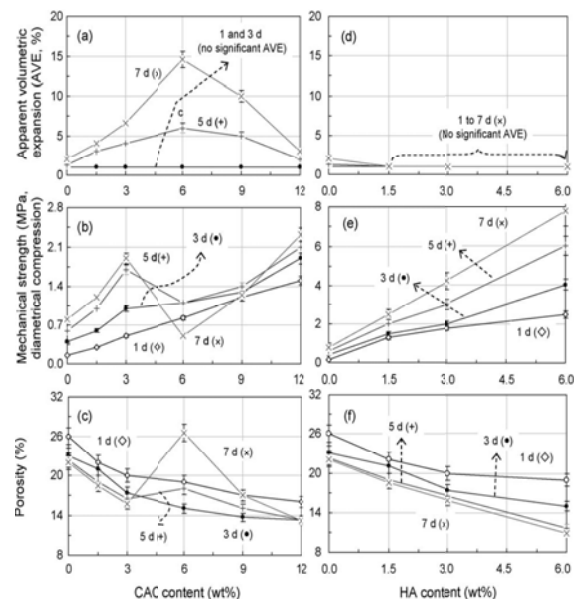


Figure 3: Effect of different calcium aluminate cement (CAC) on castables' apparent volumetric expansion (a and d), mechanical strength (b and e) and porosity (c and f).

REFERENCES

Başpınar S.M., 2005. Müllit Refractories in the linker phase optimization, Anadolu

- University, Graduate School of Sciences, PhD Thesis, Eskişehir.
- Böcek E., 2011. Refractory materials, Cumhuriyet University, Faculty of Science, Department of Chemistry, Sivas.
- Braulio M.A.L., Bittencourt L.R.M., Pandolfelli V.C., 2008. Magnesia grain size effect on in situ spinel refractory castables, *Journal of the European Ceramic Society*, 28, 2845-2852.
- Bugajski M., Schwaiger R., 1996. Self-flowing castables-a new type of unsahped refractory products, *Veitsch-Radex Rundsch*, Austria, 1,44-52.
- Durmuş Ç., 1998. Alumina based castables development, Istanbul Technical University, Faculty of Science, Master Thesis, İstanbul.
- Gül E., 2002. SiC based castable refractories production, Afyon Kocatepe University, Faculty of Engineering, undergraduate thesis, Afyon.
- <http://www.hotwikipedia.us/Wikipedia-1513037-Refractory-castable.html>.
- Marzagui H., Cutard T., 2004. Characterisation of microstructural evolution in refractory castables by in situ high temperature ESEM, *Journal of Materials Processing Technology*, 155-156, 1474-1486.
- Odegard C., Myhre B., Zhou N. and Zhang S., 2004. Flow and properties of MgO based castables, XXXII Congreso Alafar, Guatemala.
- Salomão R., Pandolfelli V.C., 2009. The role of hydraulic binders on magnesia containing refractory castables: Calcium aluminate cement and hydratable alumina, *Ceramics International*, 35, 3117-3124.
- Salomão R., Bittencourt L.R.M. and Pandolfelli V.C., 2007. A novel approach for magnesia hydration assessment in refractory castables, *Ceramics International*, 33, 803-810.
- Schulle W., Ulbricht J. and Altun A., 2001. Investigations in the development of self-flowing basic castables, *Ceramic Forum International/Bericheder Deutshen Keramicshen Gesellschaft*, 78 (5), 39-42.
- Watanabe K., Ischikawa M. and Wakamuts M., 1989. Rheology of castables refractories, *Taikabutsu Overseas*, 9 (1), 41-53.

CEMENT-BASED COMPOSITES MODIFIED LOW BASIC CLINKERS

Gulrukh Begjanova¹, Atabek Begjanov¹, Sayibjan Negmatov¹, Nigmat Ruziev¹

1. State Unitary Enterprise "Fan va Taraqqiyot", Tashkent State Technical University, Uzbekistan
a. Corresponding author: (polycomfi2005@rambler.ru)

ABSTRACT:In work are presented results of the studies on revealing the regularities physico-chemical conversions in raw materials mixture under their heat processing, the sequence of the process of the formation clinker mineral on comparatively low temperature to stage. To account of the high reactionary ability raw materials mixtures process is terminated at the 1350⁰ that on 100⁰C lower, the temperature burning traditional raw materials charge. Clinker are a product dominating of the composition, on their shaping in determined degree affects the condition of the cooling: water cooling promotes the stabilizations of the structure high temperature forms 2s. Due to more high contents C₃A and S₄AF cements create the optimum structure, providing strong artificial conglomerate. The Installed dependency "composition-structure-toughness".

Is it For the first time designed efficient compositions binding composition, on toughness not yielding traditional portland cement, by introductions to composition at grind additives from. The Revealed regularities corrolations dependencies "composition - a structure - a characteristic" when repeating over and over again designed composition.

1. OBJECT AND TECHNIQUE OF RESEARCHES

The problem of optimisation of process of synthesis portlandtsementny clinker is actual for the world industry, first of all, from positions of level recession of emission of carbonic gas in atmosphere that dictates necessity of reduction of a share a carbonate of containing raw materials as a part of raw mixtures, and also decrease in the expense of organic fuel on roasting clinker in industrial furnaces for what it is necessary to develop and introduce in cement manufacture low-termical compounds of raw mixtures and to organize release high-filled (low-brick) cements with the greatest possible quantity of active mineral additives and with the low maintenance expensive clinker a component. The solution of a problem of economy of power resources and development essentially new the low-power-intensive technologies of roasting of the cement raw mixtures providing low level of

emissions of carbonic gas, becomes possible with development of the production technology of cement on a basis clinker from raw mixtures with the lowered basicity [Larbi et al., 2009].

At calculation four-componential the low-main raw mixtures limestone and the clay shale's of the Karmaninsky deposit correcting additives– ferriferous ore of the Chimkurgansky deposit and ash Angrensky TES are used. For drawing up low-termical raw mixtures calculation led at values SF=0,75; 0,78; 0,80; 0,83; 0,85. Values p and r have been accepted same, as at a factory raw mixture. As base for comparison the technology of reception portlandtsementn clinker on Open Society "Kizilkumcement" where raw fusion mixture Singular fusion mixture plural fusion mixtures pays off at values SF=0,92 is accepted; $p=2,20$ and $r=1,15$ (a compound № 6). The Chemical compound of used materials led of 100%, is introduced to Table 1.

Table 1: The chemical compound of used materials ledof 100 %

Materials	The maintenance oxides, %							
	SiO ₂	Al ₂ O ₃	Fe ₂ O ₃	CaO	MgO	SO ₃	Ppp	The sum
Limestone	0,46	0,16	0,14	55,76	0,65	-	42,86	100,00
Clayshales	65,63	14,14	6,5	4,59	3,56	-	5,37	100,00
Ash	52,28	17,72	9,42	6,93	1,82	-	11,82	100,00
Ferruterous ore	33,7	4,02	41,54	5,92	5,03	1,82	7,97	100,00

Under the settlement data, the maintenance of CaO in the low-main raw mixtures on 0,09-1,16% is less, than in a factory raw mixture, and this difference that above, than is less value *SF*. Maintenance SiO₂ in the low-main raw mixtures on 0,86-2,18 %; Al₂O₃ 0,21 0,49 %, and Fe₂O₃ 0,07-0,43% above, than in a factory raw mixture. These factors, as a rule, should cause to lead process of their roasting at rather low temperatures, and a little raised maintenance Fe₂O₃ should affect positively chilling effect of roasting and formation four-calcic alymoferrite

(C₄AF). With increase in value *SF* from 0,75 to 0,85 maintenance C₃S increases (from 22,60 to 46,47 % against 65,5 % factory clinkers), and C₂S on the contrary, with growth *SF* decreases (from 52,40 to 25,05 %). Hence, the silicate part the low-main clinkers is characterized mainly belit by a compound, in them maintenance C₃A and C₄AF higher, than in industrial alitovy clinkers that should accelerate hydration process belit a component clinker and rate a set of durability of a cement stone in initial terms curing (Table 2).

Table 2: Settlement mineralogical compound the low-main clinkers

№	Values			The maintenance oxides, %					
	<i>SF</i>	<i>N</i>	<i>p</i>	C ₃ S	C ₂ S	C ₃ A	C ₄ AF	The other	Σ
1	0,75	2,20	1,15	22,60	52,40	6,90	15,40	2,7	100,00
2	0,78	2,20	1,15	28,90	46,80	6,80	15,30	2,2	10,00
3	0,80	2,20	1,15	34,76	40,70	6,68	15,02	2,84	100,00
4	0,83	2,20	1,15	42,15	34,36	6,52	14,68	2,29	100,00
5	0,85	2,20	1,15	46,47	25,05	6,48	14,47	7,53	100,00
6	0,92	2,20	1,15	65,50	14,74	6,08	13,68	-	100,00

The limestone maintenance in the low-main raw mixtures makes 72,42-74,55 % of % that on 1,0÷3,13 it is less than %, than in a factory raw mixture. At low values SF (0,75-0,80) maintenance of clay shales in skilled mixtures increases on 0,24÷0,42%. With increase of its value to 0,83-0,85 their maintenance decreases on 0,09-0,35. In skilled raw mixtures, with increase SF the maintenance ferruterousmineralizer from 1,3-1,6 % decreases, and ash (tab. 3) increases on 2,96÷3,62 %. Such

distinction in componental and a chemical compound of raw mixtures for reception the low-main clinker dictates necessity of detailed studying of their reactionary ability for the purpose of definition of optimum temperature of endof process clinker-main at their roasting, a phase compound of products of roasting and a structural structure of mineral phases clinker.

By datathe X-ray phase the analysis, fullmastering oxides calcium

Table 3: Material compound of raw mixtures

№	Settlement parametres			Parity of ingredients, masses. %			
	SF	n	p	Limestone	The clay Shales	Ferruterousor e	Ash TЭC
1	0,75	2,2	1,15	72,42	16,69	3,76	7,13
2	0,78	2,2	1,15	72,98	16,27	3,69	7,06
3	0,80	2,2	1,15	73,53	16,09	3,61	6,76
4	0,83	2,2	1,15	74,15	15,76	3,52	6,57
5	0,85	2,2	1,15	74,55	15,50	3,47	6,47
6	0,92	2,2	1,15	75,55	15,85	5,09	3,51

And process end mineralogenesisat roasting the low-main raw mixtures with $SF=0,75$ occurs at temperature 1350°C, and above - at 1380-1400°C (fig. 1). On diffract gram the raw mixtures burnt at this temperature, the line of CaO_{free} at $d/n=0,492$ nm is absent. With reduction

SF the configuration the diffraction reflexions clinkers minerals has changed towards strengthening of reflexes $\beta-S_2S$, it has more ordered structure that testifies to accurate crystallization clinkers minerals. On a structural structure of grains of minerals the low-main clinkers essential influence renders a cooling regime: at air cooling they are characterized by a structural variety: along with small agglomerations of roundish grains belit the grains formed, probably, owing to transition $\beta-S_2S$ in α' -updating (fig. 2) predominate the scaly form. Water cooling promotes stabilization $\beta-S_2S$ thanks to what the microstructure the low-main clinker takes a form of in regular intervals distributed fine-grained mass consisting of grains belit of the roundish form, bordered glass phase, are observed dissolved in glass

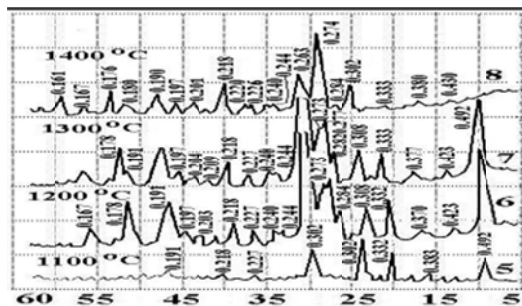


Fig. 1: The diffract gram sinter, burnt at temperatures 1100°C(5); 1200°C(6); 1300°C(7); 1400°C(8) raw mixtures with $SF=0,83$.

phase cubic, the hexagonal and sharp:
And - on air, - in water.

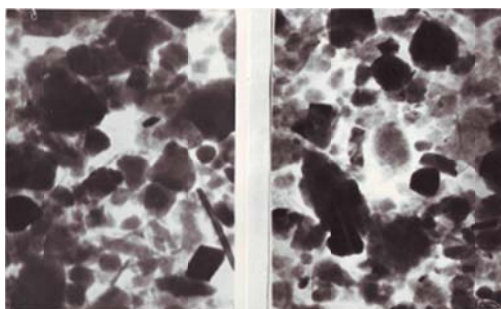


Figure 2: Electronic micro photos from a surface скола the low-main clinker with SF=0,85, burnt at 1380°C. Cooling

Shapeless grains alite, and also чешуеобразные grains – products of surface hydration C₃A. These results well correlate with the data of authors [Savelyev et al., 1991; Kurdowski, 1997], mineral phases marking the big variety the low-main clinker depending on presence of modifiers, roasting and cooling conditions, and also possibility of partial transition β-S₂S in α – modifications [Sudakas et al., 1986; Rjumpler et al., 1980]. Deficiency of structure of minerals the low-main clinker water cooling predetermines their high enough hydration and hydraulic activity. Hence, it is possible to establish the fact of positive influence of sharp cooling in water on structure formation the low-main clinker in respect of

accurate crystallization and structural orderliness of minerals that is important for increase of hydraulic activity of cements on its basis.

REFERENCES

- Касими Larbi, Simon-Masseron Anzhelika, Salem Suriya, etc. Synthesis belite cement of clinker with high hydraulic activity/Cem. And Concr. Res. 2009. 39. № 7. – Pages 559-565.
- Savelyev V. G, Abakumov A.V., etc. phase-main at the low-temperature synthesis belite with additives of salts//Tr. MHTI «Is amorphous-crystal materials: synthesis, structure, properties, application». – TH. 1991. - Pages 140 - 145.
- Kurdowski W., Duszar S., Trybalska B. Belite produced by means of low temperature is//Gem and concr. Res. 1997. 27J1. - THE RIVER 51-62.
- Sudakas L.G., Sokolov H.A., Etc. the Compound and a condition of mineral phases in the low-main clinker//Works SII cement. executed. 89. - TH. 1986. – Pages 88-93.
- ШтаркЙ, Rjumpler K, Müller A, etc. About active belite cement//Silikattechnik. 1980. № 2. 1980. № 6. – Pages 18-20, 29-31.

RESEARCH AND DEVELOPMENT OF COMPOSITE POWDER POLYMER MATERIALS AND PRODUCTION OF COTTON MACHINE PARTS ON THEIR BASES

Nadira Abed-Negmatova¹, Giyas Gulyamov¹, Sayibzhan Negmatov¹, Jakhongir Negmatov¹, Shukhrat Bozorboev¹, Sherzod Eminov¹, Nurillo Ikramov¹

1. State Unitary Enterprise "Fan va Taraqqiyot", Tashkent State Technical University, Uzbekistan
Corresponding author: (polycomft2005@rambler.ru)

ABSTRACT: Study analysis of the effect of different fillers on physical, mechanical and tribological properties of the compositions shows that glass, wollastonite, cotton lint, cement increase the coefficient of friction and reduce the wear rate. Graphite, carbon black, kaolin, talc reduce the coefficient of friction, but increase the wear of composite materials, improves thermal and electrical conductivity, and thus, lower the temperature and amount of static electricity in area of friction pairs contact. Researched that best physical, mechanical and tribological properties of the interaction with cotton composite polymeric materials are fillers with mineral fillers and Carbon-Graphite. Studied that for minimum value of the coefficient of friction best content of fillers is: 5-30 mass part of carbon, graphite, 10-30 m.p of talc, kaolin. For minimum wear rate during friction with cotton fillers' optimal content is: 10-40 m.p. of fiber, lint, wollastonite, cement, 5-15 m.p. of kaolin and talc. Considering researched studies we designed antifriction and anti-friction wear-resistant polyethylene compositions of functional purpose for details of the working bodies of cotton processing machinery.

1. OBJECTS AND RESEARCH TECHNIQUE

The industrial sample - polyethylene of high density (HDPE) of the I-0754 brand with a density of 0,954 g/cm³ and the indicator of fluidity of fusion (IFF) of 6,70 g / 10min, potentially meeting the general and special demands made to materials, taking into account a functional purpose and service conditions of working bodies of cotton processing machines and mechanisms, the low cost, technological effectiveness and not deficiency is chosen as object of research.

As a filler the following powdery mineral substances of the various chemical nature and dispersion are applied: talc, kaolin, cement, wollastonite; the carbon and graphite - soot, graphite; the fibrous - fiber glass, cotton lint. The choice of these fillers is caused by their availability and

considerable low cost. However each substance has the shortcomings and advantages. By pilot studies [Gulyamov, 2005] it is established that fiber glass, wollastonite and cotton lint increase coefficient of friction and reduce intensity of wear. Graphite, soot, kaolin and talc reduce friction coefficient, but increase wearability of composite materials, and also improve warm and conductivity and, thereby, reduce temperature and size of a charge of the static electricity, arising in a zone of friction of contacting couples. And, efficiency of these substances, especially fibrous, is considerably shown at their smaller contents, - is at the smaller content of fiber glass considerably intensity of wear decreases, and at further increase in their contents intensity of wear of composite materials decreases a little, but the friction coefficient sharply

increases. The most effective decrease in coefficient of friction of composite materials with a counterbody (cotton raw) is observed at soot and graphite introduction.

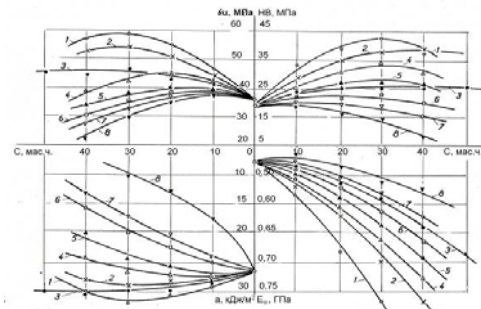
The main physicommechanical properties (a breaking stress in bending $\sigma_{и}$, the flexural modulus $E_{и}$, impact resilience a , Brinell hardness H_B) samples are determined by the standard methods - state standards. Complex of tribotechnical properties (friction coefficient, intensity of wear, temperature in a friction zone with cotton raw $T_{тп}$, the size of charges of static electricity of Q) compositions at interaction with version cotton raw Tashkent-3, the 1st grade, humidity of 8,2% are defined on disk tribometer equipped with the device for measurement of linear wear in compliance with GOST 23.223-97.

2. RESULTS OF RESEARCHES AND THEIR DISCUSSION

For receiving compositions of optimum structures on the basis of PP and HDPE researches on studying of dependences of the main physicommechanical and tribotechnical properties of polymers from a look and the maintenance of powder mineral, carbon and graphite and fibrous fillers are conducted.

The analysis of the obtained experimental data (fig. 1) showed that introduction in HDPE of fillers – fiber glass, cotton lint, wollastonite and cement till 20-30 masses. h. conducts to increase of breaking stress in bending $\sigma_{и}$ of compositions to a maximum (68,5; 53,5; 47,2; 45,0 MPas). The further increase in the maintenance of these fillers is accompanied by gradual reduction of $\sigma_{и}$. At introduction in HDPE of talc, a kaolin, soot and graphite $\sigma_{и}$ decreases with increase in their contents. However $\sigma_{и}$ remains quite high at the compositions filled till 15-20 masses. h. talc (39,0 MPas), kaolin (40,0

MPas) and till 5-10 masses. h. soot and graphite (38,0; 36,5 MPas, respectively).



$\sigma_{и}$ - breaking stress in bending; HB – Brinell hardness;
 a – impact resilience; $E_{и}$ – flexural modulus; C – fillers content

Figure 1. Dependences of physico-mechanical properties of composite polyethylene materials on a type and content of fillers: 1– fiber glass, 2 – cotton lint, 3 – wollastonite, 4 – cement, 5 – kaolin, 6 – talc, 7 – graphite, 8 – soot

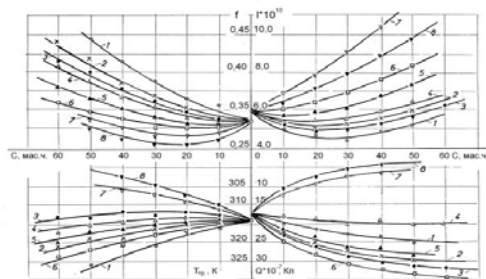
Impact resilience a of compositions with the content of fiber glass, cotton lint, wollastonite up to 30 masses. h. (33,5; 27,2; 22,5 MPas), cement to 10 ... 15 masses. h. (23,5 kJ/sq.m) increases, and then decreases. At introduction of other fillers the impact resilience of composition gradually decreases with increase in the maintenance of fillers.

Hardness HB of compositions with introduction of fiber glass, cotton lint, cement, a kaolin up to 30 masses. h. (44,1; 38,2; 33,5; 26,2 MPas), talc, soot and graphite to 10 ... 15 masses. h. (23,2; 20,0; 17,3 MPas) increase, and then decrease is observed. The flexural modulus $E_{и}$ of composition with increase in the content of fillers gradually raises.

The increase in the flexural strength up to certain filler content, apparently due to its accumulation in the inter-spherulitic areas where it gets as the center in the course of crystallization. Decrease in durability of compositions at big filling is apparently caused by that presence of a

large number of a filler between polymer macromolecules weakens energy of their intermolecular interaction a little, accelerating process of destruction of composition.

The coefficient of friction of f of polymeric composition (Fig. 2) with increase in the content of fiber glass, cotton lint, wollastonite and cement grows. At introduction of a kaolin, talc, graphite and soot in composition structure within 15 ... 20 masses. h. decrease in coefficient of friction (0,31 is observed; 0,30; 0,285; 0,265) and then – increase with increase in the maintenance of a filler.



f – Coefficient of friction; I – wearrate; T_{mp} - the temperature in the friction zone; Q - value of the charge of static electricity in the area of friction; C – filler content

Figure 2. Dependences of tribo-technical properties of composite polyethylene materials on a type and content of fillers ($P = 0,02$ MPas, $V = 2,0$ m/s, $W = 8,2\%$): 1 - fiber glass, 2 – cotton lint, 3 – wollastonite, 4 – cement, 5 – kaolin, 6 – talc, 7 – graphite, 8 – soot

Decrease in coefficient of friction of the composition, filled with powdery talc and a kaolin, is connected with their lamellar structure and a fine dispersion at the compositions filled with soot and graphite, – with rather low size of heat conductivity, low specific superficial resistance and static characteristic. Growth of coefficient of friction of composition with cotton raw at the big maintenance of a powder filler is

connected with increase in a roughness of their surface at the expense of an agregatization of a filler and in certain extent of decrease in physicomechanical characteristics of the high-filled materials due to rather low adhesion between a polymeric matrix and filler particles.

The analysis of results of research of change of intensity of linear wear (Fig. 2) of composite polyethylene materials at friction with cotton raw shows that with increase in the maintenance of a kaolin and talc to 10 ... 20 masses. h. intensity of wear ($6,2 \cdot 10^{10}$) doesn't change almost, despite some increase in coefficient of friction. Introduction of powder graphite and soot increases intensity of wear that correlates with change of coefficient of friction. The increase in intensity of wear of compositions at increase in the content of soot and graphite is explained by decrease in hardness and increase of fragility of a material.

High resistance to wear the compositions filled with fiber glass, lint, powdery wollastonite and cement possess. At these compositions with increase in the maintenance of a filler intensity of wear decreases to a minimum ($4,5 \cdot 10^{10}$; $5,2 \cdot 10^{10}$; $4,8 \cdot 10^{10}$; $5,5 \cdot 10^{10}$, respectively), and the friction coefficient grows in a certain degree. As a result of the conducted researches the fillers which increase in the contents leads to decrease in coefficient of friction and intensity of wear of compositions at friction with cotton raw are defined.

It is established that for receiving the minimum coefficient of friction of composition the following maintenance of fillers is optimum: soot and graphite of 5-30 masses. h. talc of 10 - 30 masses. h. kaolin of 10 - 30 masses. h. For obtaining the minimum intensity of wear of composition the maintenance of fillers – 10 - 40 masses is optimum. h. fiber glass,

lint, wollastonite both cement and 5 - 15 masses. h. kaolin and talc.

For an explanation of processes of interaction in system polymer-cotton besides the analysis of changes of coefficient of friction and intensity of wear of composites researches of temperature and a charge of the static electricity, arising in a friction zone were conducted. As these factors can lead to decline in production of machines and mechanisms, to fire emergence, etc.

Apparently from results of researches (Fig. 2) polyethylene compositions at friction with cotton raw, with introduction of fillers of graphite, soot and wollastonite till 30-40 masses. h. temperature in a zone of friction decreases (305,0; 302,5; 312,0 K, respectively), and with introduction of fillers of cotton lint, fiber glass, talc and a kaolin the increase in temperature (319,0 is observed; 323,5; 320,0; 316,5K, respectively).

From results of pilot studies it is visible that in the course of friction electric charges arise and collect. As a result of it intensity and electric forces in a double electric layer increase that, probably, leads to increase in total friction force.

At increase in the content of talc and a kaolin and polyethylene compositions extent of their electrization raises, the size of charges at 40 masses. h. it is equal $26,7 \cdot 10^{-7}$ and $31,3 \cdot 10^{-7}$ C, respectively. It speaks, probably, that talc considerably improves electroinsulating properties of compositions, increases electric resistance and reduces ways of leakage of the charges which were formed at friction of static electricity. Composition filling by graphite and soot causes strong decrease in size of a charge of static electricity at friction them with cotton raw ($6,0 \cdot 10^{-7}$; $5,0 \cdot 10^{-7}$ C, respectively).

Thus, analyzing results of research, it is possible to draw conclusions that the friction coefficient, intensity of wear, size of a charge of static electricity and temperature in a zone of friction of composite polymeric materials with cotton raw depend on a look, the nature and the maintenance of fillers. It is established that at introduction in composite polymeric materials of powder mineral fillers their coefficient of friction with cotton raw considerably increases, temperature and size of a charge of static electricity in a friction zone, decreases intensity of wear. Introduction of other fillers leads to change of temperature and a charge of static electricity in a friction zone with cotton raw.

The analysis of researches of physicommechanical and tribotechnical characteristics of composites showed that when developing antifrictional and antifrictional and wearproof compositions can be applied various mineral (talc, a kaolin, cement, wollastonite), carbon and graphite (soot and graphite) and fibrous (fiber glass, cotton lint) fillers. As at introduction in composition of fillers separately the last not always provide overall performance of knots of friction of machines because of their some shortcomings, for fuller realization of advantages of each filler the system of fillers which gives to a material a complex of necessary properties was entered into structure of composition.

As a result of the conducted researches it is revealed that for the minimum value of coefficient of friction of composition the optimum maintenance of fillers makes, masses. h: for soot and graphite 5-30. talc 10-30, kaolin 10-30. For the minimum value of intensity of wear of composition at friction with cotton raw the optimum maintenance of fillers are 10-40 masses. h. fiber glasses, lint, wollastonite and cement, 5-15 masses. h. kaolin and talc.

When designing antifrictional and wearproof polyethylene materials requirements of the minimum coefficient of friction and the minimum intensity of wear were considered

On the basis of the aforesaid, we developed antifrictional And) and antifrictional and wearproof (AW) polyethylene (PE) the composite materials (CM) on the basis of polyethylene of the high density, possessing the good mechanical durability, high wear resistance and in low coefficient of friction in comparison with steel (Table 1). They quite meet the functional demands made to materials of

details of working bodies of means of mechanization of the cotton processing industry and can be recommended for their production.

Physicomechanical and tribotechnical properties are given in the table developed antifrictional and antifrictional and wearproof polyethylene compositions (AWPE-Pe+soot + kaolin) and antifrictional wear-resistant polyethylene compositions (AWRPE – PE + cotton lint + graphite + kaolin). Apparently from the table data, the developed composite materials have rather high mechanical properties.

Table 1. Physicomechanical and tribotechnical properties of the developed antifrictional and antifrictional and wearproof composite materials on the basis of HDPE

Indicators	AWPE -1	AWPE -2	AWRPE -1	AWRPE -2
breaking stress in bending, σ_n MPa	33,4	35,5	40,9	37,8
Impact resilience, a kJ/sq.m	17,5	21,3	27,3	23,0
Brinell hardness, HB , MPa	55,1	58,4	51,5	49,3
Flexural modulus, E_n GPa	0,62	0,65	0,75	0,71
Coefficient of friction f (at $P=0,02$ of MPa, $V=2,0$ of m/s, $W=8,2\%$)	0,28	0,29	0,32	0,35
Wearrate $I \cdot 10^{10}$ (at $P=0,02$ of MPa, $V=2,0$ m/s, $W=8,2\%$)	6,7	6,5	5,3	5,6
Temperature in a friction area, T_f , K	321	315	313	316
Value of the charge of static electricity in the area of friction, $Q \cdot 10^{-7}$ C	23,7	20,3	16,7	20,2

Note: P -specific pressure, V -sliding speed, W -humidity of cotton raw

On the basis of the received results were manufactured the operating parts details of cotton processing machines and mechanisms with the set geometrical parameters were cast and production tests are carried out.

The analysis of data shows that application of antifrictional and antifrictional and wearproof polymeric composite materials as

materials for the developed new design of details of operating parts of cotton processing machines and the mechanisms working in the conditions of frictional interaction with cotton - a raw leads to increase of productivity of machines for 12-16% and to decrease in power consumption for 7-18%, damages of cotton fibers and a crushing of seeds, and also eliminations of

possible fire of cotton - a raw and education having reeled up fibers on surfaces of details.

3. CONCLUSIONS

Thus, as a result of complex analyses of the conducted researches the optimum maintenance of the fillers, providing receiving optimum structures of developed composite polymeric materials of a functional purpose with the set properties for details of rubbing couples of knots of friction of working bodies of machines and mechanisms of hlopkoochistitelny plants and allowing to increase their working capacity and durability is revealed.

It is established that the best physicommechanical and tribotechnical properties at interaction with cotton raw have the composite polymeric materials filled with carbon and graphite and mineral fillers that is connected with improvement of conditions of contact interaction at the expense of increase electro - and heat conductivity of compositions agrees molecular mechanical electric theory of interaction in the system polymer-cotton offered by the academician of AN of RUZ S. S. Negmatovs. It is thus shown that mineral fillers like talc, a kaolin, having lamellar structure, reduce friction coefficient, but increase intensity of wear of composite polymeric materials. Effective decrease in wear of composite polymeric materials is observed at introduction of fillers of the fibrous type providing high durability of composite materials.

REFERENCES

- Negmatov S. S. Bases of processes of contact interaction of composite polymeric materials with a fibrous mass. Tashkent: Fan, 1984. – 296 pages.
- Gulyamov G. Antifrictional and antifrictional and wearproof polymeric composite materials on the basis of polyolefins//Composite materials, 2005, No. 3, page 37-39.

RESEARCH AND DEVELOPMENT OF NEW POWDER COLORIFIC COMPOSITIONS BASED ON SALTS OF POLYVALENT METALS FOR DYEING THE NATURAL AND SYNTHETIC FIBERS AND TEXTILE MATERIALS ON THEIR BASES

Sayibjan Negmatov¹, Shokhista Rasulova¹, Won Cheol Lee¹, Valeriy Kim¹,
Jakhongir Negmatov¹, Malika Negmatova¹, Shirin Abed¹

1. State Unitary Enterprise "FanvaTaraqiyot", Tashkent State Technical University, Uzbekistan
Corresponding author: (polycomfi2005@rambler.ru)

ABSTRACT: On the basis of comprehensive studies were designed the optimum compositions of powder colorific compositions based on salts of polyvalent metals for protein and polyamide and cellulosic fibers and fabric dyeing technology based on them. Powder colorific compositions for textiles based on protein, cellulose and polyamide fibers, due to their interaction with the fiber, help creating salt, coordination and covalent connections and creating the coloring on fibers, which has a high resistance to various physical and chemical effects.

Dyeing of protein, polyamide and cotton fibers with colorific composition is carried out in an acidic environ at pH 3-4. At the boiling temperature reaches its equilibrium in the case of dyeing textile materials based on protein fibers for 2-3 minutes, cotton fabrics - 6-7 minutes, polyamide for 35-40 minutes. The obtained colorings are characterized by high resistance to various physical and chemical factors: washing, dry cleaning, abrasion and light.

1. INTRODUCTION

The modern theoretical views in the field of dyeing the fiber material by various dyes are based on a functional dependence between the affinity values determined in the basic by the nature of the spraying dyeing material and the diffusion coefficient, which at this temperature for the same fiber depends on the geometrical dimensions of the compound which give the color and on rate of dyeing. With the decrease of affinity and an increase in the diffusion coefficient the increase of dyeing rate is observed.

The chemical structure of the fibrous polymer has an important influence on the fixation of dyes because the functional groups of elemental link, the ending groups of macromolecules, other circuit elements of main valency and the

branch groups are the potential centers on which the physical and the chemical sorption of dyes is occurred.

Depending on the structure of potential active centers and structure of the dye can be implemented a wide range of interaction forces between them, from the physical intermolecular to the covalent chemical. Fixing fibers by dyes, as one of the main stages, include the diffusion of the dye into the fiber. Together with that the geometric size of the molecule or compound's ion which imparts color is very important, because it largely determines the rate of diffusion into the fiber.

Due to the above stated in terms of effectiveness, the greatest interest is the way of dyeing and printing through the synthesis of the dye on the fiber, where

the molecules of the initial compounds have almost no affinity to the fiber, which determines the possibility of using the same pigment forming compounds for dyeing different nature fibers, and due to the small geometric dimensions, show high values of diffusion coefficients into the fibrous substrate.

One of the ways to modify the natural and chemical fibers is the input to the polymer substrate of different compounds contributing to the formation of nanostructures. In the last decade, researchers focus on the development of studies in the field of obtaining nanostructures. This is due to the fact that small inclusion in the polymer matrix of other compounds of organic or inorganic nature at nano dimensions is greatly improve the physical, chemical and mechanical properties.

The requirement to obtain colors with high strength to various physical and chemical factors creates the need for development of such pigment forming systems that can form the strong chemical bonds with polymer substrate. Selected half-finished products, composing the dye compositions should also comply with the requirements complex: easy enough diffusion into the fiber and sorption on the inner surface, high reaction rate, resulting in coloration of textile material; rather mild reaction conditions that do not lead to the destruction of the fiber. These requirements met by different half-finished products and final products of their reactions, some of which are azoic dyes.

Azoic dyes are synthesized directly on the fiber during dyeing and printing which is the result of the azo coupling reaction between azocompounds (phenols, naphthols, and azotols) and

diazocompounds, which are the primary aromatic amines.

2. SUBJECT AND METHODS OF RESEARCH

The subject of research was protein fiber, nylon fabric, cotton fabric, alkali and polyvalent metals salts, aromatic hydroxy compounds. The study of the physicochemical properties of the fibers and materials structure carried out by IR spectroscopy, spectrophotometry, chelatometry, pH analysis, X-ray diffraction, electron microscopy and other physical and chemical methods of analysis.

3. RESEARCH RESULTS AND THEIR DISCUSSION

Protein fibers are high-molecular compounds, constructed mainly of acyclic, carboxylic and heterocyclic amino acids. The presence of amino acids in the protein fibers containing aromatic rings (tyrosine, tryptophan) allows the formation of complex compounds chelate type with polyvalent metal ions. Protein fibers consists of the remnants of α -amino acids and, therefore, contain a large number of amino and carboxyl groups. In addition to the groups located at the ends of the polypeptide chain the fibroin consists of a large number of residues diamino- and dicarboxylic acids. These acid residues contain in side radicals also free amino and carboxyl groups capable to a reaction of nucleophilic and electrophilic substitution. The combination of phenols with diazotized proteins may contribute to giving the color to a fiber.

On the other hand, amines as well as carbonyls have the property of forming coordination bonds. With polyvalent metals cations such as iron, nickel, cobalt, copper, having their own chromophoric properties, they form colored complexes. By the action of nitric

acid on the protein fibers all amino groups are changing. Not excluded the possibility of a transition part of the amino groups in the azo group and further interaction with metal cations with complexes formation. The presence of hydroxyl or amino groups in the o-position to the azo group promotes the formation of stable complex compounds.

In articles [Abdurakhmanova *et al.*, 2001] has been informed about the development of dye compositions based on derivatives of phenol, which can color the protein fibers. Dyeing compositions include phenol derivatives, salts of polyvalent metals, sodium nitrite. Sodium nitrite in the dye composition contributes diazotization of amino groups and the transition of phenols in nitrosophenol forming colored complex compounds with transition metal cations.

Getting the metal complexes in the polymer matrix of protein fibers held in a known manner of the formation of complex compounds of polyvalent metal cations with phenol derivatives. Protein fibers were treated at the boiling point for 2-3 min in a solution containing a water-soluble polyvalent metal salt, phenol and sodium nitrite. The molecules of these compounds are virtually no affinities to the fiber and because of the small geometric dimensions show high diffusion coefficients in the fibrous substrate. Equally important is the fact of

the presence of the amino and carboxyl groups in fiber capable of forming complex compounds or associate fiber with the formed complex by strong, covalent bonds.

Dyeing the protein fibers by dye composition is carried out in an acidic medium at pH = 3-4. At boiling temperature the dyeing reaches equilibrium within 2-3 min (Figure 1).

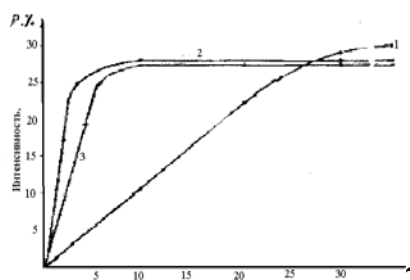


Figure 1. Kinetics of dyeing different fibers by dye compositions based on salts of $\text{Fe}_2(\text{SO}_4)_3$: 1- nylon, 2- silk, 3-cotton.

The input of metal complexes on the basis of cations of copper, iron, nickel, cobalt to the protein fibers is contribute to the intense colors of fiber, resistant against various physical and chemical factors: the wet treatments, to organic solvents, to light and abrasion.

Table 1 shows the color tones of natural and synthetic fibers, dyed by dyeing powder compositions based on resorcinol.

Table 1. The color tones are obtained on different fibers with powdered dye compositions.

Input polyvalent metals cations	Fiber nature	Color tone of obtained coloration
Fe ³⁺	Natural silk, Cotton, Nylon	From green to black Green From green to black
Co ²⁺	Natural silk, Cotton, Nylon	From orange to burgundy Orange From orange to burgundy
Cu ²⁺	Natural silk, Cotton, Nylon	Brown, Brown, Brown
Ni ²⁺	Natural silk, Cotton, Nylon	From mustard to brown Mustard From mustard to brown

Based on the conducted studies, it was concluded that the developed dye composition can be applied to any dyeing fibers in the presence of the primary amino groups in polymer substrate. The presence of ending primary amino groups in polyamide fiber allows the direct synthesis of colored compounds in the fiber by diazotization of primary amines with their transformation into a diazonium salt capable to interact with phenols, aromatic amines and some other compounds with free o-and p-positions with formation azo dyes in conjunction of arilazogroup to a carbon atom. The presence of the hydroxyl group in o-position to the azo group leads to the formation of chelate bond, which contributes to stable complexes. This conclusion was confirmed by dyeing of polyamide fibers by dye compositions.

By spectrophotometric studies of solutions of polyamide and protein fibers has been found the formation of colored complex compounds in polymer substrate. By X-ray diffraction and electron microscopy was determined the even distribution of complexes (nano) particles in the fiber volume.

One of the shortcomings of nylon fibers is low lightfastness. It has been found that the input of the compositions into the fiber contributes to its light stability.

The chemical structure of polymers has a significant effect on the fixation of the input compounds because the functional groups of building blocks, the end groups of the macromolecules and other elements of the main valences circuit and side groups are potential active centers, on which the physical and chemical adsorption of the compounds can occur.

One of the end groups of polyamide macromolecules is an amino group that makes possible to apply the developed dye composition for dyeing it. Due to the dense packing of the structural elements, the rate of dyeing of polyamide textile materials is lower than the other studied fibers. Dyeing of polyamide fibers at the boiling temperature reaches its equilibrium after 35-40 minutes (Figure 1).

The possibility of using the developed dye compositions for dyeing cellulose textile materials has been studied. [Madjidova and Rasulova, 2009] For which, by modifying the cellulose (cotton) fibers by alkoxysilane the aminated cellulose textile materials obtained: cotton fabric with a degree of substitution of $\gamma = 16,1$.

Dyeing of cellulose materials was carried out in an acidic medium at pH= 4.3 at the boiling point. The dyeing of cotton jersey reaches its equilibrium value during 6-7 minutes. However, the amount of evenly

sorbed dye in the case of cotton fiber dyeing is higher, as evidenced by the intensity of the colors obtained. Apparently, the formation of colored complex compounds in the structure of the fiber is happened not only intramolecularly but also intermolecularly; and the small distance between the structural elements of the cotton fiber contribute to the formation of more intermolecular colored structures. One of the shortcomings of the cellulose fibers are the low elasticity, low shape stability. Modification of cellulose fibers by silanes followed by input of developed compositions increase the elasticity; improve the physical and mechanical properties.

The high permanence of the obtained colors to different physical and chemical factors has been determined (Table 2).

Polyvalent metals (iron, cobalt, and nickel, copper) cations with phenols form colored complex compounds. The carried out modifications contributes to the dyeing of polymeric substrate. Due to the fact that the compositions based on phenols and metal salts have small geometric dimensions and have no affinity to fibers a high rate of dyeing and dyeing ability by the same composition of the different nature of the fibers has been established. Dyeing at boiling temperature reaches its equilibrium in the case of dyeing the textile materials based on protein fibers for 2-3 minutes, cotton fabrics - 6-7 minutes, polyamide for 35-40 minutes.

Table 2. Color permanence of different fibers, dyed by powder dye compositions

No.	Material type	Input salt	Color tone	Color permanence, points				
				To light	To wash	To organic salt solution	To abrasion	
							dry	wet
1	Natural silk Cotton jersey Nylon	Ni ²⁺	Dark brown	4	5/5/5	5/5/5	5	4
3	Natural silk Cotton jersey Nylon	Cu ²⁺	brown	5	5/5/5	5/5/5	5	4
4	Natural silk Cotton jersey Nylon	Fe ³⁺	green	4	5/5/5	5/5/5	5	4
5	Natural silk Cotton jersey Nylon	Co ²⁺	orange	5	5/5/5	5/5/5	5	4

The mechanism of color formation on various fibers by means of dye compositions has been studied by IR spectroscopy. Based on the obtained data has been suggested the following mechanism for the dyeing of textile materials based on the different nature of the fibers: by the action of sodium nitrite in acid medium the phenol derivatives transfers to dinitrosophenols that with polyvalent metal cations form colored

complexes interacting with diazotized groups of different fibers. Consequently, the structural elements of fibers are part of the resulting colored structures that explains the high strength properties of obtained colors to the different physical and chemical impacts.

The high permanence of obtained colors to light, in contrast to the colors of azoic dyes is explained by the presence of

polyvalent metal cations in the dye composition.

4. CONCLUSIONS

Based on the conducted studies were developed the optimum compositions of powder dye compositions based on salts of polyvalent metals for protein, polyamide and cellulose fibers and fabric dyeing technology based on them.

The dye compositions for textile materials based on protein, cellulose and

polyamide fibers, due to their interaction with the fiber contribute to the formation of salt, covalent and coordinate bonds and the formation of the color on fibers, with high resistance to the various physical and chemical effects.

Thus, the carried out study showed that by powdered dye composition can be colored the protein, polyamide and cellulose fibers.

REFERENCES

- Abdurakhmanova Sh.G., Negmatov S.S., Madjidova Sh.G., Sagdiyeva F.G., Babazhanova M.A./ The method of dyeing the textile materials // Patent RU № IDP 04924.
- Abdurakhmanova Sh.G, Madjidova Sh.G., Babazhanova M.A./ Development of composite structures and dyeing the

- protein fibers by them // Composite Materials, 2001. - № 1. - C.28-32.
- Madjidova Sh.G., Rasulova Sh.N./ Development of technology for the amination of cotton fiber. // Materials of the Republican Interuniversity Scientific Conference of Young Scientists. "Nanocomposite materials." 2009. p.176

RESEARCH AND DEVELOPMENT OF TECHNOLOGIES OF OBTAINING THE MECHANICALLY ACTIVATED POWDER BASED ON NATURAL INGREDIENTS AND DUNE SAND FOR PRODUCTION OF SEALING COMPOSITE CEMENTS AND COMPOSITE MATERIALS FOR VARIOUS PURPOSES

Sayibjan Negmatov¹, Kakhramon Inoytov¹, Lochin Oblakulov¹, Shukhrat Bozorboyev¹, Bahodir Sobirov¹, Jahongir Negmatov¹, Dilshod Makhkamov¹, Rustam Soliev¹, Mahammadjon Tursunov¹

1. SUE "Science and Progress" Toshkent State Technical University, Tashkent, Uzbekistan, *Corresponding author: (polycomft2005@rambler.ru)*

ABSTRACT: Based on comprehensive research we developed mechanoactivated technology and created installation - dismembrator based on impact-splitting-abrasive method for dispersing and natural dune sand, providing reception of powdered ingredients with a high degree of dispersion - up to 30-90 microns, developed surface area and their use in production of non-hardened and vibration reducing mastics and sealants for building designs of windows, sealing cracks of asphalt roads, filling the joints of concrete roads, composite coating of asphalt roads, and other industries.

Study of the effect of mechanical activation and natural dune sand on the mechanical properties of composite cements and asphalt surfaces shows that when they are activated by dismembrator installation achieved increase in compressive strength and shear in half and according to their durability..

1. OBJECT AND TECHNIQUE OF RESEARCHES

Objects researches are bitumen's of marks BN-90/10 (BNI-V), BN-70/30 (BNI-IV), a rubber crumb, gossipolovy pitch, hydrolytic ligin secondary polyethylene polyvinylchloride, extinguished lime, basalt fibrous filling compound and activated small-dispers wollastonity, Chinaz and Chirchik river, Jazjavansky and Jangierysky barkhan sand and compositions on their basis. At definition of physical and chemical, mechanical and operational properties of the developed composite materials for the asphalt concrete coverings and hermetic sealing of their deformation seams and cracks with use of local and secondary raw materials and mechanical activated mineral components, definition of temperature of a softening, an extensibility at 250C, depths permeation needles-penetration, disabilities of

coupling with concrete, water absorption and other physic mechanical properties developed composite hermetic materials have been used corresponding operating state standard and devices.

Considering importance of a problem, we had been conducted complex researches in area mechanical activation, the technology is developed mechanical activation and installation - dismembration, based on a with great dispatch-cleave-using up way for dispergation natural and barkhan the sand providing reception the powdery of components with high dispersion - to 30-90 micron, by the developed specific surface and possibility of their use in manufacture not hardening, vibro-absorption and hermetic mastics for building designs of windows, hermetic sealing of cracks the asphalt concrete

roads, filling of deformation seams of concrete roads, composite materials for a covering the asphalt concrete roads and other industries has been created.

2. RESULTS OF RESEARCHES AND THEIR DISCUSSION

As a result of the spent researches, first of all, have been defined initial chemical and mineralogical structure of local natural sand. For this purpose we had been chose basically local natural sand of four deposits: Chirchik (river), Chinaz (river), Jazjavansky and Jangiersky (barkhan). They differ on mineralogical and granulometric to structures and as,

modeling samples, allow to draw preliminary conclusions on possibility of application local natural, including, barkhan sand for manufacture hermetic composite mastics and composite materials.

In tables 1 and 2 results of researches of chemical and mineralogical structures of local natural sand are presented.

Table 1. Chemical compound of local natural sand

Chemical compound	Deposits of natural sand			
	The Chirchiksky	The Jazjavansky	The Jangiersky	The Chinazsky
SiO ₂	87,01	75,76	78,95	83,34
Al ₂ O ₃	4,8	5,8	5,1	5,2
TiO ₂	0,31	0,32	0,28	0,32
Fe ₂ O ₃	0,18	0,20	0,21	0,20
CaO	3,1	2,8	2,5	2,6
MgO	1,8	2,1	2,2	2,3
K ₂ O	1,24	2,8	1,7	1,29
Na ₂ O	0,28	0,32	0,36	0,29
PPP	1,28	9,8	8,7	4,66

Table 2. Mineralogical structure of local natural sand

Structures	Deposits of natural sand			
	The Chirchiksky	The Jazjavansky	The Jangiersky	The Chinazsky
Quartz and siliceous fragments	83,1	71,67	71,47	81,55
Calcite and feldspars	8,65	20,91	20,57	12,83
Clay and other minerals	2,25	7,42	7,96	5,62

From tables it is visible that both on chemical, and on mineralogical to structures barkhan sand essentially differ from the river.

From the analysis of the given tables natural barkhan sand can be grouped in the greatest quantity of the basic minerals which consist of silicates, calcite, field spars and other clay minerals. Such conditional grouping allows to carry out scientifically - well-founded approach at

physical and mechanical chemical updating of natural sand for the asphalt concrete coverings.

The specific area of a surface of sand, i.e. the total area of a surface of grains of the sand, having on 0.0022 ft (1 Gramm), depends on the size of grains (with reduction of the sizes of grains increases), its structure and character of a surface. The most exact method is definition of a specific surface on mineral. By small-

container means of size of a specific surface it is possible to estimate indirectly change of a roughness of a surface of the grains which size is one of the main criteria mechanical activation. Besides, under equal other conditions, on change of bulk density it is possible to predict

size of the specific surface which definition is connected with big enough time and expenditures of labour.

Superficial and volume properties of local natural sand which are presented in table 3 are defined.

Table 3. Superficial and volume properties of local natural sand

Deposits of natural sand	Specific surface, sm ² /g	Bulk density, kg/m ³	Density, Kg/m ³
The Chirchiksky	382	1452	2345
The Jazjavansky	418	1486	2286
The Jangiersky	402	1482	2312
The Chinazsky	396	1461	2324
The rest on a sieve № 014			

Mechanical activation natural sand carried out on dismembration to installation NTC « Fan va tarakkiet», developed Candidate of Technical Sciences. Negmatovym N.S. [Negmatov, 2012].

Based on an dispatch-cleave-using up way. For an establishment of an optimum technological mode we made experiments on activation of the chosen natural sand.

Considering that these sand fine-grained enough, for activation of their surface chose using up principle of work of installation at various loadings. For this purpose loading dismembrator was carried out sand in the portions from 1 to 5 kg a minute with an interval by of 1 kg. The backlash between fingers of a rotor and craropa dismembrator made 0,2 mm. More low in table 4 results mechanical activated natural sand are presented.

Table 4. Influence of a mode of loading on mechanical activated natural sand

Change of properties of sand of various deposits	Influence of a mode of loading on mechanical activated natural sand, at loading, kg					
	0	1	2	3	4	5
The Chirchiksky						
The rest on a sieve №014, %	22,5	20,2	19,3	16,5	16,8	17,2
Bulk density, kg/m ³	1452	1424	1414	1388	1392	1396
Specific surface, sm ² /g	382	400	460	550	420	425
The Jazjavansky						
The rest on a sieve №014, %	26,5	22,1	18,4	15,0	15,2	15,1
Bulk density, kg/m ³	1486	1438	1421	1401	1405	1416
Specific surface, sm ² /g	418	430	445	506	440	435
The Jangiersky						
The rest on a sieve № 014, %	18,6	14,1	12,9	8,3	8,4	9,2
Bulk density, kg/m ³	1482	1452	1446	1398	1402	1424
Specific surface, sm ² /g	402	415	435	460	424	420
The Chinazsky						
The rest on a sieve № 014, %	2,4	1,8	1,4	1,0	1,1	1,2
Bulk density, kg/m ³	1461	1442	1405	1395	1398	1402
Specific surface, sm ² /g	396	405	426	455	440	436

Proceeding from the received data, for optimum quantity of loading dismembrator at an operating mode of 1500 rpm and a backlash between a rotor and casing 0,2 mm it is possible to accept 3 kg/minutes Thus hour productivity dismembrator will make 180 kg mechanical activated sand at an o'clock.

As a result of researches the form of particles initial and mechanical activated sand depending on a method and a processing mode has been defined. More low in drawing forms of the initial and crushed sand are schematically presented.

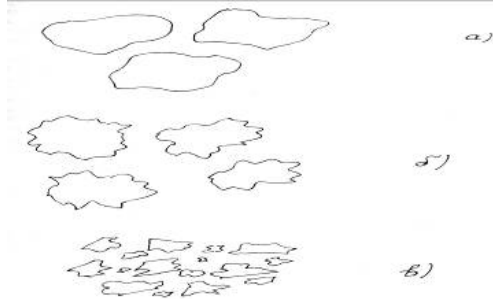


Fig. 1. The modeling scheme of morphological changes of the form of particles and a relief of surfaces of natural sand at processing in dismembration the activator

Initial (natural, with окатанной a surface) the form of particles; the form of particles at a with great dispatch-using up mode; the form of particles at a with great dispatch-cleave-using up mode

Further results of complex research and the analysis of operational properties of composite materials with use mechanical activated natural sand and components from a waste fat and oil the hydrolytic industry, and also working out of effective composite materials on a basis mechanical activated local natural sand and a waste of manufactures for the asphalt concrete coverings of highways are resulted.

On the basis of the spent complex researches optimum compounding the asphalt concrete coverings with use natural river and barkhan mechanical activated sand instead of mineral наполнителей which are imported till now from Russia, Ukraine, Germany are developed, etc.

In Table 5 optimum structures of the developed compoundings the asphalt concrete coverings are resulted.

Table 5. Compoundings the asphalt concrete coverings

Structure coverings	GOST 9128-97	The developed structures, mac. %			
		Chirchik	Chinaz	Jazjavan	Jangier
Bitumen BND 60-90	6	-	-	-	-
Bitumen BND 60-90 + ГС (7 % from bitumen weight)	-	6,042	6,042	6,042	6,042
Rubble	45	45	45	45	45
Sand not activated	41	41,058	41,058	41,058	41,058
Mineral filler	8	-	-	-	-
Mechanical activated sand	-	8	8	8	8
Total	100	100	100	100	100

From the received data it is visible that the asphalt concrete the coverings received with use mechanical activated of components on the basis of natural and barkhan of sand instead of mineral filler,

modified gossipolovy pitch and bitumen BND 60/90, on all indicators of physic mechanical characteristics completely meet the requirements of Specifications Tsh 14-20; 2004.

Results of the spent complex researches give the grounds to make the conclusion about possibility of successful use specified mechanical activated components on the basis of sand in manufacture the asphalt concrete coverings on a large scale instead of mineral filler which is brought from abroad. Besides, by us on the basis of the spent complex researches about influence of technology factors of cooking of

mastic and various components on its properties, are developed a number of the compounding, allowing receiving hermetical composite mastics with in advance set technological and physic mechanical properties.

Compounding and structures of the developed mastics are resulted in table 6 and 7.

Table 6. The developed compounding hermetical composite mastics on the basis of a local source of raw materials

The name of components	The maintenance of components, mass hours, for mastics of marks				
	MBRG-80	MBRG-90	MBRG-100	MBRG-110	MBRG-120
Bitumen BN-90/10 (BNI-V)	40	38,0	38,0	35,3	30,2
Bitumen BN-70/30 (BNI-IV)	23	22,0	21,7	20,2	20,2
Gossipolovy pitch	23	22,0	21,7	20,2	20,2
Rubber crumb	11,5	14,2	13,2	14,0	16,2
The fine-fibered mineral filler	2,5	2,7	3,2	3,1	4,1
Lime the slaked	-	1,1	2,2	3,1	3,1
Activated filler a mineral origin (ANPM)	-		-	4,1	6,0

Apparently from given tables 6 and 7, by selection of corresponding components with the subsequent change of their parities it is possible to create composite hermetical materials with in advance set properties. In particular, at the maintenance of bitumens of 55 mass parts, gossipolovy pitches 20, a rubber crumb 10-13, fine-fibered mineral filler 2-3 and slaked to exhaust 1-2 mass parts, turn out hermetical the composite materials, capable to be maintained in intervals of temperatures from -22 to 100 °C. At change of the maintenance of bitumens from 55 to 50 mass hour and maintenance preservation gossipolovy pitches at level 20 mass hour with the subsequent change of the maintenance of a rubber crumb from 14 to 16 mass hour fibrous filler within 3-4 mass hour and addition activated filler a mineral origin 4-6 mass hour parts, turn out hermetical composite materials + capable to be

maintained in intervals of temperatures from -22-25 to +110-1200C.

3. CONCLUSIONS

By research it is established that mechanical activated natural and barkhan sand considerably influence mechanical properties of composite mastics and the asphalt concrete coverings, the strength increase is reached at compression and shift in one and a half time and according to their durability. Improvement of properties hermetical waterproofing mastics and composite materials at mechanical activated natural sand on dismembration to the installation realising with great dispatch-cleave-using up effect, occurs not only at the expense of increase in a specific surface dispergation particles and submicroroughnesses their surfaces but also at the expense of polarisation of particles at the molecular level,

accompanied by occurrence heterogeneous dipolar the moments which promote improvement of adhesive

properties with formation of chemical bonds (hydrogen) both cation-active, and anion-active substances.

Table 7. Physical mechanical indicators hermetical composite mastics

The name of indicators	Definition method	Values of indicators for mastics of marks				
		MBRG-80	MBRG-90	MBRG-100	MBRG-110	MBRG-120
Parametres	Visually, absence of extraneous inclusions, uniformity	Extraneous inclusions are absent, weight homogeneous				
Softening temperature on KiSh, °C, Not less	GOST 26589	80	90	100	115	125
Fragility temperature on Fraasu, °C, Not above	GOST 11507	-18	-20	22	23	25
Extensibility at 25 °C, sm, Not less	GOST 11056	4,0	3,8	3,5	3,0	3,0
Durability of coupling with concrete, MPa, not less	THAT Republic of Uzbekistan 14.04.2004.	0,4	0,45	0,5	0,7	0,9
Depth Penetrations needles, mm ⁻¹ at temperature 25 °C, (penetration), Not less	GOST 11501	30,0	0,27	25,0	15,0	10,0
Water absorption for 24 hour, No more, than %	0,2	0,15	0,16	0,17	0,19	0,2

REFERENCES

Negmatov S.S., Sobirov B. B., Inojatov K.M., Salimsakov J.A. «Composite the asphalt concrete materials for a covering of roads», Tashkent – «Fan va tehnologiya»-2012.

Negmatov S.S., Sobirov B. B., Abdullaev A.H., Rakhmonov B. Sh, Inojatov K.M., Salimsakov J.A.«the Modified bitumen

compositions multipurpose appointment» Tashkent – «Fan va tehnologiya»-2012.

Negmatov S.S., Sobirov B. B., Rakhmonov B. Sh, Salimsakov J.A. «Bases creation hermetical composite materials for roads, bridges and airdromes» Tashkent – «Fan va tehnologiya»-2012.

Sobirov B. B. «Working out of effective structures and technology of composite materials for the asphalt concrete roads» the Dissertation Tashkent-2010.

RESEARCH AND DEVELOPMENT OF TECHNOLOGIES OF OBTAINING THE COMPOSITE METAL MATERIALS FROM POWDER POOR AND OFF-BALANCED ORES

Soyibjon Negmatov¹, Aminjon Bozorov¹, Fakhridin Rakhimov¹, Hasan Sharipov¹, Mahmudjon Yakubov¹, Jahongir Negmatov¹, Mahammadjon Tursunov¹

1. SUE "Science and Progress" Tashkent State Technical University, Tashkent, Uzbekistan,
Corresponding author: (polycomfi2005@rambler.ru)

ABSTRACT: Based on research results we developed small volume technology for obtaining ferromanganese and ferromolybdenum by restoring (enrichment) of powdered manganese ore and molybdenum cakes.

We calculated and chose reagents, necessary equipment, material flow for modeling the hydrometallurgical process, we conducted and established consistent pattern of thermal studies and on their base developed a new way to extract the ferroalloys from powdered poor and off-balance ores, developed optimal technological mode of furnaces, which are fundamentally different from existing ones.

The developed technology of ferroalloys will provide the alloying component for metallurgical and engineering industry sectors.

1. THE OBJECT AND METHOD OF STUDY

The study is dumping cakes molybdenum production Uzbek Refractory and high temperature metal ash from the boilers of power plants running on heavy fuel oil and powdered poor and off-balance ores of molybdenum, tungsten, manganese and vanadium.

The chemical and mineralogical composition of the residues from the classical chemical analysis was performed. The metal content was determined by atomic absorption spectrometer. To determine the mineralogical composition of the studied diffraction patterns of the original cakes and processed products. Radiographs were obtained on a DRON-2, 0 with CuK α - radiation in the range of $2\theta = 2-40^\circ$. In deciphering the use of U.S. roster ASTM.

To identify the products of processing methods used infrared spectroscopy.

IR spectra were recorded on an IR spectrometer in the frequency range of 400-4000 cm⁻². This technique used in compressing the substance KBg tablets.

Dumping cakes molybdenum production Uzbek Refractory and Heat Resistant Metals, contain significant amounts of molybdenum (3-5%) and can significantly expand the raw material base for the production of these metals. These studies focus on the development of technologies for processing molybdenum dump cakes, ash from the boilers of power plants running on heavy fuel oil and powdered poor and off-balance ores of molybdenum, tungsten, manganese and vanadium.

During the study involved the use not only of gravity and flotation concentration methods, as well as new ways of pyrometallurgical processing of the above-mentioned raw materials.

The study was performed, the chemical and mineralogical composition of dump cakes molybdenum production and off-poor ores and bottom ash from burning fuel oil in power plants, to determine the content of rare and precious metals. It is shown that their involvement in the production will partially solve the problem of idle load capacity Uzbek Refractory and Heat Resistant Metal. Recycling of waste and ore is cost effective in the current conjuncture of prices for rare and precious metals. A flow chart of cakes and processing of ores to produce Ferro manganese and vanadium as needed metallurgists Uzbekistan.

Dumping cakes plants receiving molybdenum and tungsten products to date have a high content of these elements. Cakes after baking and ammoniacal leach containing from 2 to 5% molybdenum, tungsten and the same or up to 20% of their contents in the starting materials. In the soluble components contained in Kekaha insoluble and water-soluble ammonium compound in these cells. Thus, ammoniacal leaching cakes are products containing up to 50% of molybdenum and tungsten in the oxidized forms.

There are several schemes for extracting these elements of cakes:

- Pyro-hydrometallurgical,
- Acid,
- Soda-hypochlorite,
- Chlorine-soda,
- Electrochemical leaching.

The same pattern podshihtovyvayut soda cakes, roasted and then leached with water. [Vorobyov, 1968]. Elements of the ferric chloride solution is precipitated.

According to another method [Basco, 1968], a material containing molybdenum and tungsten are mixed with sodium nitrate and sodium carbonate were placed

in a container with a lid, heated to 300-400 ° C and leached with water spec compound precipitated from the solution of these elements.

Treatment middlings, waste containing nickel, iron, sulfur, molybdenum and tungsten as impurities, is produced by milling the product, its mixing with the alkali metal compounds, such as NaOH, Na₂S Na₂CO₃ mixtures thereof in a ratio of 20:1 to 30:1 . Next, after wetting, briquetting or pelletizing them fired at 540-870 ° C.

Fired pellets rapidly cooled in water and the resulting pulp is treated to convert the molybdenum and tungsten in solution, separated from the residue and sent to their isolation. More than 80% of alkali metal compounds introduced into the mixture in the dry state, and the rest of salts dissolved in the water going to wet the mixture. [Kholmogorov, 1971].

The use of nitric acid for opening cakes has a number of advantages over other methods:

- The lack of dust emission products to the atmosphere;
- Exclusion of harmful discharges solutions;
- The mother liquors are recycled to sulfoammiachnuyu valuable nitrate fertilizer.

The interaction of molybdenite and wolframite with nitric acid is formed hydroxyl that envelop the particles concentrate leaching process slows down. Introduction to the leach solution lennogo – determined amount of sulfuric acid [Vorobyov, 1968], contributes to the stabilization and retention of molybdenum and tungsten in solution by forming complexes sulfate. Nitrogen-sulfuric acid concentrates for hydrometallurgical processing option involves the use of extraction and

adsorption processes for extraction. The use of sorption technology allows selective extract molybdenum and tungsten from the rich and the poor solutions.

In a method combining flotation concentration and hydrometallurgy, taking into account the good solubility in a medium soda difficult filtered oxygenated compounds of molybdenum and copper. The most technologically is a scheme providing for a preliminary soda leaching dump cakes, followed by flotation recovery of insoluble sulfides Na_2CO_3 easily filterable MoS_2 and CuS .

A method for obtaining the pure compounds of molybdenum and tungsten from waste [Rezvanov, 1972; Cartilage and Kochetkova, 1968], comprising treating them with mineral acids, acidic separation of molybdenum and tungsten containing solution or an acidic solution of starting use of these elements - the waste production. There is also the introduction of iron into it an alkali reagent additive reagent extract obtained slurry under stirring, filtration, washing, drying and calcination of the precipitate with blowing air.

A method of extraction and separation of copper and molybdenum, molybdenum-copper concentrate and intermediate products consisting [Patent number 55773, 1938] in the processing solution concentrate calcined soda in an autoclave (2.5-5%) at a temperature of 170-200 ° C for 2-3 hours. Thus molybdenum into solution, which was subsequently recovered by means of a calcium chloride CaMoO_4 .

A process for recovering molybdenum from molybdenum concentrates calcine is leached with the addition of ammonia solutions of ammonium carbonate [Patent number 2328250, 1939].

To obtain pure powder of Mo concentrates containing 90-95% Mo, a scheme comprising Mo to MoO_3 roasting, leaching solution and NH_3 (NH_3) MoO_4 cleaning solution of copper and other impurities precipitate out of solution Mo in an autoclave in the presence of a catalyst complex salt containing 60% Mo and salt recovery Hg at a temperature of 982 ° C [Paidassi, 1951].

To remove any impurities calcined molybdenum concentrate containing molybdenum trioxide, treated with aqueous ammonium hydroxide. Thus molybdenum remains in the insoluble solid residue. This method provides a higher purity of molybdenum trioxide, 99% of all impurities contained in the raw material [Iarrs, 1958].

A process for recovering molybdenum from materials containing these metals include firing material in the presence of calcium compounds, such as burnt lime to produce calcine containing calcium molybdate (CaMoO_4) calcine is leached with acid at pH 1. As a result, a solution containing a molybdenum compound dissolved. Alternately, calcium calcine is leached with water, and the resulting slag is subjected to leaching acid solution is filtered and washed to remove insoluble residue, and then treated in known manner for separation and recovery of molybdenum from the filtrate [Argali, 1944].

Based on the results of exploratory research we have developed and proposed hydrometallurgical technology for extraction of molybdenum from dump cakes. Molybdenum cake is leachable in Pachuca, equipped with nets to separate the phases of the sorbent. To leach solutions used soda 75-100 g / l of ammonia or 50-75 g / l. The process is conducted at ambient temperature for 4

hours. Leach slurry enters the filtration on the disc filter. The resulting cake with contents of 0.3-0.5% molybdenum, gold, 20-30 g / t Cu 0.1-0.2%, silica 45-50% is mixed with other fluxing materials DM.1U, kneaded and fed at the copper smelter. After direct leaching solution contains 10-15 g / l of molybdenum, 10-12 mg / l of rhenium. To obtain a greater concentration of the solution fed to the leaching turnover of 50-70% of its volume. After it reached to the production solution concentration of molybdenum and 40 g / l. Removing a

85-90% solution of molybdenum, rhenium -70-75%). Produktcionnyj solution (25-50%) of the original volume supplied to the reactor with a stirrer in the precipitation of calcium molybdate mortar. The resulting slurry is filtered. The output of sediment is 60-80 kg per 1 ton of raw cake. The table below summarizes the results of laboratory heats.

Table 1. Results of laboratory heats

Consumption,% by weight of metal						Metal %					cinder	
Sbozhennye plate	NiO	Fe ₂ O ₃	Na ₂ SiO ₃	CaO	SiO ₂	Ni	Fe	Cr	W	Mo	WO ₃	MoO ₃
Metallic waste (average composition)						29,9	44,0	45,0	5,2 U	3,27	no	
		50	26			44,1	45,3	0,78	1,89	2,8	3,78	0,21 0,21
		60	26			34,7	62,1	traces	0,10	3,13	4,86	0,21
		80	26			36,0	58,2		traces	2,73	6,55	0,66
		100	26			46,4	49,3			1,66	5,16	0,75
	74					72,0	24,9		0,75	2,28	5,49	1,40
	118		20			91,1	7,2		traces	0,11	no	no
	74 100	38		12		85,7	14,1			0,16	4,63	3,50 1,40
	100	100	100			86,6	13,8			Следы	1,50	1,40
Metallic waste (average composition)						58,7	10,0	19,0	9,1	4,8	no	no
	74	38		12		77,3	17,3	traces		0,33	7,06	4,20
	100	100	25			85,7	10,4			0,04	5,17	2,60
136				13	13	75,3	23,6			0,24	-	-
200	1			13	13	76,	21,30			0,40	-	-

These laboratory experiments showed (table) that can completely oxidize Fe₂O₃ chromium and tungsten having a higher affinity for oxygen than iron, and to maximize the oxidation of Mo should be used NiO. introduction which, moreover, allows to increase the nickel content in the nickel alloy. The most efficient oxidation of molybdenum,

nickel at a concentration achieved in the final alloy of nickel greater than 80%.

Thus, the results of laboratory studies on the processing of oxide ores of the poor and of metal complex alloys based on iron-nickel-containing tungsten, molybdenum and chromium, have shown that the use of low-iron and Fe-free solid oxidizers can get conditioned nickel alloy

suitable for further processing of tungsten - molybdenum slag.

2. CONCLUSION

Based on the research the technology for production of tungsten molybdenum, manganese and vanadium alloys from poor oxidized ores, iron and steel industry wastes and residues from sludge depositories of Uzbek Refractory and Heat Resistant Metal. Technology for producing molybdenum tungsten, manganese and alloys vanadivyh is based on the reduction of molybdenum,

tungsten, manganese and vanadium from waste iron and steel industry.

The research supporting the possibility of recovery and separation of molybdenum from cakes of metallurgical slag on the developed technology. When using natural gas to recover metals must be pyrolyzed. Pyrolysis is carried out effectively melts containing reducing metal oxides.

REFERENCES

- Sharipov, Kh.T.. Aspects and content of Integrated processing of ores and other raw materials containing rare metals. "Rhenium, molybdenum, tungsten". Prospects for production and Industrial applications International Scientific and Practical conference Moskow, 1998, p.81.
- Sharipov X.T. Problems processing man-made materials in metallurgy of non-ferrous metals. II Scientific-Technical Conference "New inorganic materials." Tashkent, 1999 1 page
- Fundamentals of Metallurgy. "Metallurgy", that is, IY, 1967, p 62.
- Vorobyov VP etc. "The study of polymerization of molybdenum in kistryrastvorah" ZhNHvyp. 10. 1968.
- Basco AK Molybdenum and other polyanions in acidic solutions ZHNNH MY. 1. 1968.
- Kholmogorov AG, Makarov MK Scientific papers of the Siberian Scientific Research and Design Institute of ferrous metallurgy. MY. 4. 1971.
- Rezvanov., GF. Sulfuric acid processing circuit poor copper and molybdenum concentrates. Bulletin «Non-Ferrous Metals», 1972, № 3.
- Cartilage., SV, Kochetkova, EA. Electrochemical oxidation of sulfide molybdenum products. "Non-Ferrous Metals", 1968, № 8.
- Patent number 55773, which states in 1938. published in 1939, KI Masletsky.
- Patent number 2328250, announced in 1939. published in 1941 31. Patent number 3196004.
- Paidassi, J. - "Ind. Guim", 1951. v. 10 (10), p. 5.
- Iarrs K. - "Metalloberplache", 1958. Bd. 8a, S.
- Argali VI, Traevsky K.M. - "Journal of Theoretical Physics", 1944, v. 14, p. 132.

RESEARCH AND DEVELOPMENT OF COMPOSITE POWDER MATERIALS BASED INDUSTRIAL WASTES FOR USE IN DRILLING OF OIL AND GAS WELLS

Komila Negmatova¹, Soyibjon Negmatov¹, Bakhrom Mamanov¹, GapporRahmonberdiev¹, Jakhongir Negmatov¹, Nodir Kobilov¹, Malika Negmatova¹

1. State Unitary Enterprise "Fan va Taraqqiyot", Tashkent State Technical University, Uzbekistan
Corresponding author: (polycomft2005@rambler.ru)

ABSTRACT: First time it was developed and scientifically substantiated the possibility of creating of effective composite powder formulations of chemicals reagents for drilling fluids and production their technology, using local raw materials and waste production of nitric acid – “nedopal”, non-ferrous metals – “alyumak” and modified powder gossypol resin - CPGR.

We discovered the pattern of the influence of ingredients of composite compositions of chemical reagents on the physical and chemical processes, which lead to an increase of technological and operational characteristics of drilling fluids, and allow perform the drilling operations in complicated geological and technical conditions.

We developed optimum composition of composite chemical reagents type CCR for drilling fluids and found that they exhibit surface-active properties. The expediency of using the developed new composite chemicals in drilling muds instead of expensive imported was shown, both in fresh and in high mineral formation water. It increases the possibility of drilling operations without complications and accidents.

1. OBJECT AND TECHNIQUE OF RESEARCHES

Objects of research are: *Na*-carboxymethylcellulose – *Na*-CMC, polyacrylamide (PAA) and ferrokhlorsulfanat-1 (FHL-1) received on the basis of production wastes of alcohol – a lignin, and cotton oil (Gossypol resin), the caustic soda and sodium carbonate, green coke - withdrawal of production of nitric acid of the “Ferganaazot” enterprise, gossypol resin - withdrawal of oil and fat production, alyumak – withdrawal of the Tashkent plant on preparation and processing of non-ferrous metals waste scrap and neftabad red clay.

Physical and chemical properties of ingredients determined by methods of the chemical, X-ray phase, differential and

thermal analysis. Technical characteristics (density, g/cm³; viscosity, with; water return, cm³/30 min.; degree of tension of shift – CHC₁₀, mg/cm²; hydrogen indicator - pH) developed composite compositions of chemical reagents and drill muds were determined by methods, devices and installations according to requirements of the corresponding state standard specifications accepted in the CIS.

2. RESULTS OF RESEARCHES AND THEIR ANALYSIS

Set of the conducted researches on identification of influence of concentration of such reagents as CMC, PAA, CPGR, FHL-1 and volume of the contents of **green coke** in solution, testifies that by selection of the corresponding concentration and amount

of these reagents it is possible to receive as facilitated, i.e. with a density up to $0,9 \text{ g/cm}^3$, and average weighted, i.e. with a density up to $1,25 \text{ g/cm}^3$ and more. That CMC and CPGR reagents are the most available and CPGR rather cheap, further we developed composite chemical reagents with use of these reagents and green coke for receiving the drill muds, capable to be operated under various geological specifications of drilling of oil and gas wells.

On the basis of results of researches and their analysis a number of compoundings and technology of receiving the effective composite chemical reagents used for preparation of drill muds, capable to be operated under various geological specifications of drilling of the necessary quality was developed. It was established that at creation of effective compoundings of composite chemical reagents it is important to use CPGR. As initial raw materials for its production as showed our researches, gossypol resin - withdrawal of oil and fat production after modification with the caustic soda and sodium carbonate can serve. Further it was shown that for a final decision of a problem it is extremely important to use waste of productions of processing of secondary non-ferrous metals – alyumak, and also green coke, being withdrawal of plants of chemical fertilizers, with a carboxymethylcellulose CMC additive. Dependences of physical and chemical and technological properties of 10% drill muds received with use of CPGR and CMC reagents are given in Fig. 1, prepared on the mineralized water of a field Northern Berdakh. In numerator - the content of CMC, in denominator the content of CPGR

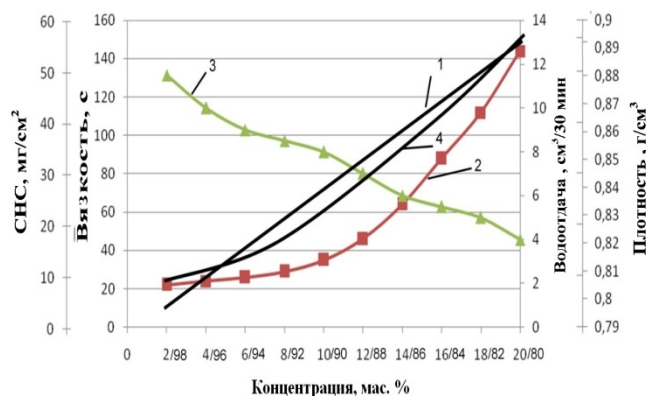


Fig. 1. Dependence of density (1), viscosity (2), water return (3) and CHC_{10} (4) from CPGR and CMC ratio

From a course of curve Fig. 1 it is visible that 10% drill muds, depending on a ratio of CPGR and CMC and their contents, have various physical and chemical and technological properties. It is easy to notice that with increase in quantity of CPGR in drill mud it is observed the decrease in all physical and chemical and technological indicators, except a water return indicator. At increase in quantity of CMC inverse relationship, i.e. growth of the specified indicators is observed. So, at change of a ratio of CPGR and CMC from 2/98 to 20/80 density of drill muds viscosity – from 22 to 144 lies within $0,8 - 0,89 \text{ g/cm}^3$, with, water return decreases from 11,5 to 4,0 $\text{cm}^3/30$ of mines and CHC – from 10 to 56 mg/cm^2 .

From these compoundings that which contain CPGR from 86 to 92% and CMC from 8 to 14% are the most acceptable. At the content of CMC as a part of composition from 2 to 6% and CHC of 10% - drill mud rather low also are incapable to provide viscosity of full emission of boring slime. At the concentration stated above water return quite high that increases permeability of drill mud in layer, naturally enough, its expense will be considerable.

At increase in the content of CMC in composition from 6 to 14% all technological indicators of drill muds are normalized and they can be applied when drilling oil and gas wells at a driving of layers with abnormally low sheered pressure. With a further growth of quantity of CMC more than 14% in spite of the fact that density and CHC increase, and water return decreases, the increase in values of viscosity leads to decrease in speed of drilling and labor productivity, especially when drilling wells with abnormally low sheered pressure.

Therefore, it is possible to conclude that depending on conditions of drilling it is possible to choose the necessary structure from again developed compoundings for practical use.

In table 1 the optimum compositions of the developed composite chemical reagents CCR-1, and are given in table 2 their physical and chemical and technological properties.

Table 1. Optimum compositions of the developed composite chemical reagents of CCR-1 type

Ingredients	CCR -1-1	CCR -1-2	CCR -1-3	CCR -1-4	CCR -1-5
	Content of ingredients, weight.h				
Composite powdery gossypol resin – CPGR*	92	90	88	86	84
Sodium-carboxymethyl cellulose – Na-CMC	8,0	10,0	12,0	14,0	16,0

* - CPGR consists of the Gossypol resin, the caustic soda and sodium carbonate and alyumak.

Further we investigated dependences of physical and chemical and technological properties of the drill muds received with use of CPGR and CMC. Their

characteristic indicators, depending on a quantitative ratio of green coke, were given earlier in Fig. 1.

Table 2. Physical and chemical and technical characteristics 10% drill muds on the basis of the developed composite chemical reagents of the CCR-1 type

Characteristics of boring solutions	CCR -1-1	CCR -1-2	CCR -1-3	CCR -1-4	CCR -1-5
Appearance	powder of dark brown color				
Water solubility (10% water solution)	dissolved in water				
Density, γ , g/cm ³	0,83	0,84	0,85	0,86	0,87
Conditional viscosity of 10% of water solution on CIIB -5, T, with, not less than	29	35	46	64	88
Water return of 10% of water solution on the device BM-6, V, cm ³ /30min	8,5	8	7	6	5,5
Static stress of shift, CHC, 1/10min, mg/cm ²	18	23	28	34	41
Hydrogen indicator, pH	9	9	9	9	9
Thickness of a crust, mm	traces	traces	traces	traces	traces

Results of physical and chemical and technological researches of properties of drill muds are given in fig. 2 on the basis of the developed composite chemical reagents consisting of CPGR, CMC and green coke in certain ratios.

Apparently from the obtained data, 10% drill muds, depending on a ratio of CPGR, CMC and green coke, have various physical and chemical and technological properties. Thus, with increase in quantity of green coke, unlike the data provided in table 2, all indicators, except a water return indicator, tend to increase in process of increase in quantity of green coke in a compounding of the developed composite chemical reagents. At increase in quantity of green coke from 5 to 45% density of drill muds increases from 0,82 to 1,18 g/cm³, viscosity increases from 22,5 to 118, water return decreases from 12 to 5 cm³/30 of mines, and CHC increases from 11 to 50 mg/cm³.

The analysis of the data provided on Fig. 2, shows that the compositions containing in the structure of CPGR from 82 to 88%, CMC from 12 to 18% and green coke from 30 to 45% can be applied as composite reagent of drill muds when drilling oil and gas wells with abnormally average sheeted pressure as for passing of layers with average sheeted pressure the drill muds having density not less than 1,05 g/cm³ with the corresponding

viscosity, are, as a rule, used by water return and CHC.

Optimum structures and the main physical and chemical properties of the developed composite chemical reagents of the CCR-2 type are given in tables 3 and 4.

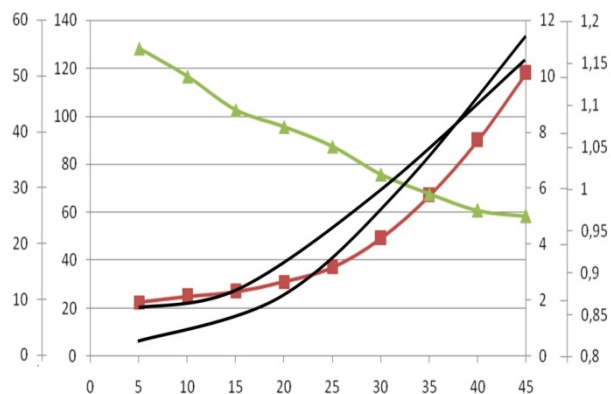


Fig. 2. Dependence of density [Negmatova, *et al.*, 2011], viscosity [Negmatova, *et al.*, 2011], water return [Rahmonberdiev, *et al.*, 2012] and CHC₁₀ [Negmatova, *et al.*, 2012] drill muds received with use of CPGR and CMC, (which contents is given in fig. 1) from a quantitative ratio of green coke.

Comparing the data provided on Fig. 1 and 2, and in tables 2 and 4, it should be noted that in increase in viscosity, water return and CHC the main role is played by CMC. Existence of green coke promotes generally to increase of density of drill muds.

Table 3 Optimum compositions of the developed composite chemical reagents of the CCR-2 type

Ingredients	CCR -2-1	CCR -2-2	CCR -2-3	CCR -2-4	CCR -2-5
	Content of ingredients, weight part				
Total amount (CCR -1)	100	100	100	100	100
Grren coke (CaCO ₃ , Na ₂ O)	20,0	25,0	30,0	35,0	40,0

Table 4 Physical and chemical and technical characteristics of 10% drill muds on the basis of the developed composite chemical reagents of the CCR-2 type

Characteristics of drill muds	CCR -2-1	CCR -2-2	CCR -2-3	CCR -2-4	CCR -2-5
Density, γ , g/cm ³	0,88	0,92	0,97	1,05	1,11
Conditional viscosity of 10% of water solution on CIIB -5, T, s, not less than	31	37	49	67	90
Water return of 10% of water solution on the device BM -6, V, cm ³ /30min	8,2	8	6,5	5,8	5,2
Static stress of shift, CHC, 1/10 min., mg/cm ²	20	25	30	37	44
Hydrogen indicator, pH	12	12	12	12	12
Thickness of a crust, mm	0,1	0,3	0,6	0,8	1,0

Proceeding from set of conducted researches of dependence of density, viscosity, water return and CHC of 10% drill muds with a various ratio of CPGR with CMC and with various number of the contents of green coke, it is necessary to conclude that by selection of the corresponding ratio of CPGR from CMC and quantity of green coke it is possible to receive drill muds with the demanded physical and chemical and technological properties, capable to be operated when drilling oil and gas wells in it is complicated - geological conditions and passing of layers, both with low, and with average sheeted pressure.

Operational properties of the developed composite chemical reagents like CCR were investigated. It is known that the main operational properties of drill muds is properties surface-active emulsifying, rheological, filtrational and inhibiting them. In this regard, we in this section investigated operational properties of the developed composite chemical reagents like CCR [Negmatova, *et al.*, 2011; Negmatova, *et al.*, 2011].

It is known that superficial properties of drill muds in many respects predetermine efficiency of their use when drilling oil and gas wells under various geological specifications and opening of the productive horizons.

In this plan the composite chemical reagent of the CCR-1 type developed by us and drill muds on its basis possess surface-active properties. It is confirmed by that CCR-1 is dissolved both in cold,

and in hot water in any ratios, ability of various concentration of reagent to reduce filtrational properties of solution and manifestation of stabilizing activity in relation to low-clay, cretaceous and calcareous solutions.

3. CONCLUSIONS

For the first time it is developed also the scientific possibility of creation of effective powdery composite compositions of chemical reagents for drill muds and technology of their production with use of local raw material resources and withdrawal of production of nitric acid - green coke, non-ferrous metals – alyumak and the modified powdery gossypol resin - CPGR is proved.

The main consistent patterns of influence of ingredients of composite compositions of chemical reagents on the physical and chemical processes proceeding between them, bringing to increase of technical and operational characteristics on drill muds, and allowing carrying out drilling operations in the complicated geological specifications are determined.

Optimum compositions of composite chemical reagents like CCR are developed for drill muds and is established that they show surface-active properties.

Researches of emulsifying properties of the developed composite compositions of chemical reagents specify that, thanks to their increased superficial activity, they are adsorbed on surfaces of alyumak, green coke and red clay with formation of aggregatively stable emulsions and suspensions which is consistent with the theory of mono-molecular adsorption of American Scientists Langmuir.

It is established that introduction in drill mud of the developed composite compositions of chemical reagents, thanks to their good solubility in water, to manifestation of hydrophobic ability and high greasing effect, and also at the expense of good physical and chemical interaction with the components which are a part of compositions, promotes manifestation of synergetic effect, decrease in coefficient of a filtration and crust forming that provides high stabilizing action on properties of drill muds, improves coating quality of drilling cuttings from under a bore bit, provides good washing of a face of a well, and also increases the mechanical speed of drilling for 10-15%, increases opening of the productive horizons by oil and gas for 30-35%, and also provides ecological harmlessness for environment.

Expediency of application of the developed new composite chemical reagents is shown at preparation of drill muds instead of expensive imported, both in fresh, and in highly mineralized reservoir water. It is established that thus there is possible a carrying out drilling

operations without complications and accidents.

REFERENCES:

- Negmatova K.C. Sharifov G.N. Isakov Sh.S. Negmatov S.S. Sobirov A.B. Rahimov Kh.K. Polymer reagents for stabilization of drilling mud, used in the process of drilling of oil wells//European polymer congress 2011. XII congress of the specialized group of polymers. Congress program, june 26-july 1, 2011, Granada, Spain, p. 018 .
- Negmatova K.S. Salimsakov Yu.A. Sharifov G. N., Kobilov N. S., Haydarov Zh.M. Effective composite chemical reagents and drill muds on their basis, being applied with various sheeted pressure//the Academic magazine of Western Siberia. Natural sciences: Achievements of a new eyelid, 2011. - No. 2. – Page 63-64.
- Rahmonberdiev G. Murodov M.M. Negmatova K.S. Negmatov S.S. Lysenko A.M. Effective technology of obtaining the carboxymethyl cellulose from annual plants//Materials Science and Engineering Application II. (ICMSEA 2012), January 7-8, 2012. - Xi'an, China. River 541-543.
- Negmatova K.S. Isakov Sh.S. Kobilov N.S. Negmatova M.I. Haydarov J.M. Sobirov B.B. Negmatov S.S. Effective composite chemical reagents based on organic and inorganic ingredients for drilling fluids used in the process of drilling oil wells//Materials Science and Engineering Application II. (ICMSEA 2012), January 7-8, 2012. - Xi'an, China. R.544-547.
- Rahmonberdiev, G., Murodov, M., Negmatova, K, Negmatov, S and Lysenko, A., Effective Technology of Obtaining The Carboxymethyl Cellulose From Annual Plants//Trans Tech Publication Advanced Materials Research Vol. 413 (2012). - Switzerland. River 541-543
- Negmatova, K, Isakov, S, Kobilov, N., Negmatova, M., Negmatov, J., Haydarov, J., Sharifov, G., Rahimov. S., Effective Composite Chemical Reagents Based On Organic And Inorganic Ingredients For Drilling Fluids Used In The Process Of Drilling Oil Wells//Advanced Materials Research Vol. 413 (2012). Trans Tech Publications, Switzerland. River 544-547.

PRODUCTION OF COPPER FOAM BY CARBAMIDE SPACE HOLDER

Mohammad HoseinShahzeydi¹, MasoudPanjepour^{1,a}

1. Isfahan university of technology, Department of materials, Isfahan, Iran
a. Corresponding author (panjepour@cc.iut.ac.ir)

ABSTRACT: Today metallic foams have known as one of the most widely used materials in the aerospace industries. Characteristics such as high thermal conductivity, low density and good specific strength caused that manufacturing methods of foams expand which one of these methods is powder metallurgy. In this study the production and characterization of copper foam by method of powder metallurgy using carbamide space holder were investigated. However for production of copper foam with different porosity of 50, 60 and 70 vol. %, the powder mixture of copper- carbamide (with different value of carbamide) were compressed under 300 MPa. Then the prepared samples were sintered at 800 °C for 2 hrs. After removing of carbamide from samples during sintering process the pore structure in the copper foam studied by optical microscopy. Finally the result of quantity evaluations were shown that the volume percent, distribution and size of pores in the copper foam strongly were depended to value and size of carbamide in initial powder mixture.

1. INTRODUCTION

Metallic foams have recently attracted more attention in industries because of their unique properties of mechanical, acoustic, thermal, electrical, and chemical. These special materials have low density, good specific strength, high impact energy absorption, excellent sound absorption, and high thermal conductivity. According to the connectivity of cells, metallic foams categorized as either closed- or open-celled. Studies have shown that most application, such as filtration, separation, heat exchanging, and sound or energy absorption require open-celled foams. Thus, open-celled foams have wider applications than closed-celled foams [Zhao *et al.*, 2004; Banhart, 2001].

Among metallic foams, Cu foams have many application and properties. These foams are used in electrical industries, fuel cells, and heat exchangers (such as heat exchanger sused for the cooling of computer microprocessors).Up to now,

numerous techniques have been developed to produce Cu foams, such as directional solidification, electrodeposition or vapor deposition, and powder metallurgy [Banhart, 2001]. Directional solidification is especially suitable for producing Cu foams with low porosity and low open cell. Therefore, this method used to produce Cu foams with special applications [Banhart, 2001; Nakajima *et al.*, 2001]. For electro deposition and vapor deposition, however, there are still some restrictions in porosity percentage, size and shape of pores, lead to little use of this method for producing Cu foams [Banhart, 2001].

One of the newest and most widely used methods of producing copper foam with controlled cell shape, cell size, and porosity percentage is powder metallurgy [Zhao *et al.*, 2005].Zhao and Sun have developed a technique for producing open-celled Al foams via powder metallurgy, known as the sintering and dissolution process (SDP) [Zhao and Sun, 2001]. This technique uses

NaCl powder as space holder. The main limitations of SDP are that it is time consuming to eliminate NaCl completely and any residual NaCl can lead to contamination or corrosion of the base metal. Zhao et al. developed a technique for producing open-celled Cu foams with high porosity percentage (up to 80%), known as the lost carbonate sintering (LCS). This technique uses K_2CO_3 powder as space holder. Two main limitation of this technique are time-consuming of space holder removing and shrinkage of foams in sintering stage [Zhao *et al.*, 2005]. Parvanian et al. studied on the mechanical behavior of the open pore copper foams produced with LCS technique. They found that mechanical pre-activation of copper powder, and thus changing its morphology could enhance the structural integrity of foams and thus their mechanical strength [Parvanian and Panjepour, 2013].

Therefore, the aims of this study are production of copper foam by method of powder metallurgy using carbamide space holder, and investigation the relationship between porosity percentage and size of cells in Cu foams with volume percentage and size of carbamide in initial powder mixture.

2. EXPERIMENTAL PROCEDURE

2.1. Raw Materials

The raw materials used in this study are Cu powder with a purity of <99.9% to produce main framework of the foam and carbamide ($CO(NH_2)_2$) granulates as the space holder. To improve the mechanical properties of the foams, Cu powders was grinded in planetary ball mill with rotating speed of 350 rpm and BPP of 5, for 4 hours. Typical morphology of Cu powders after grinding and carbamide granulates is shown in Figure 1. It can be seen that the

Cu powders are irregularly shaped with size of 2-67 μm and the carbamide granulates are spherical with size of 0.9-1.4 mm.

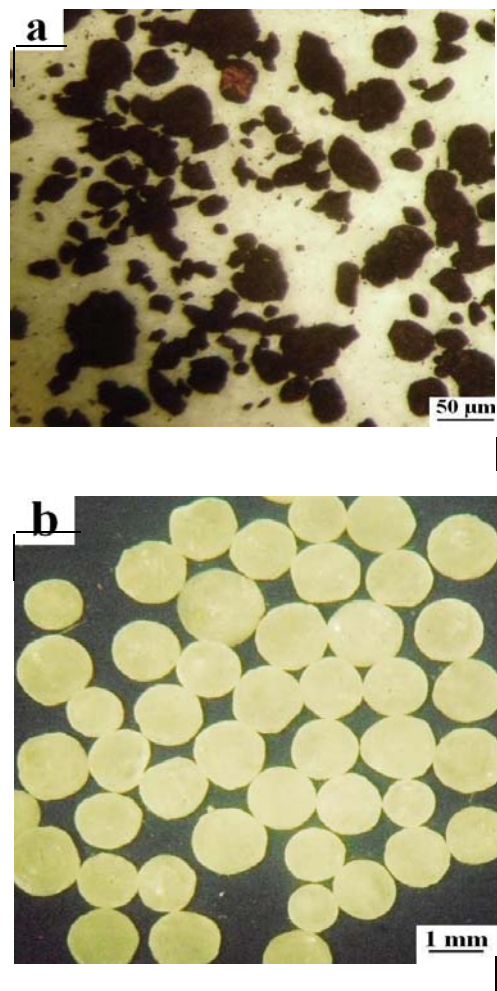


Figure 1: Microscopic image of (a) Cu powder after grinding, (b) spherical carbamide granulates.

2.2. Foam Preparation

In order to prepare the foams, the copper powder with 50, 60, and 70 volume percent of carbamide were mixed. During the mixing operation, 1 wt% ethanol was added to the mixture as binder. The mixture was uniaxially pressed at 300 MPa pressure in a steel mold with a dimensions of $30 \times 30 \times 7 \text{ mm}^3$. The carbamide

granulates were removed from green compact by immersing samples in distilled water bath at 25 °C for 1 hour. Finally for increasing the strength of the samples and remove the remaining carbamide, samples were sintered at 850 °C for 2 hours. Figure 2 has shown the profile of heating samples to sintering temperature. Sample holding at temperatures below 850 °C have been down to reduce thermal shock damage to the samples.

2.3. Characterization of Foams

The structure of foams was studied by optical microscopy (OM). X-ray diffraction (XRD) analysis was performed to explain the final crystal structure of the Cu foams. For the XRD study a Philips Xpert MPD instrument with 20 kV and CuK α radiation was used. In order to measure the density (ρ_f), total porosity (ϵ_t), and open porosity (ϵ_o) of foams, the standard ASTM C20 Was used. First, dry produced foams were

weighed in air with accuracy of 0.01 g (w_1). Then the foams were immersed in boiling water for 1 hour and then foams were weighed in air and then foams were weighed in air immediately (w_2). Finally, the foams were immersed in water and during immersing the immersed weight of foams were measured (w_3). Density of foams (ρ_f) was calculated by the following equation:

$$\rho_f = \frac{W_1}{W_2 - W_3} \quad (1)$$

Also the total porosity (ϵ_t) and open porosity (ϵ_o) of foams was calculated by (2) and (3) respectively. ρ_s in equation (2) is bulk density of Cu (8.94 g/cm³).

$$\epsilon_t \% = \left(1 - \frac{\rho_f}{\rho_s}\right) \times 100 \quad (2)$$

$$\epsilon_o \% = \left(\frac{W_2 - W_1}{W_2 - W_3}\right) \times 100 \quad (3)$$

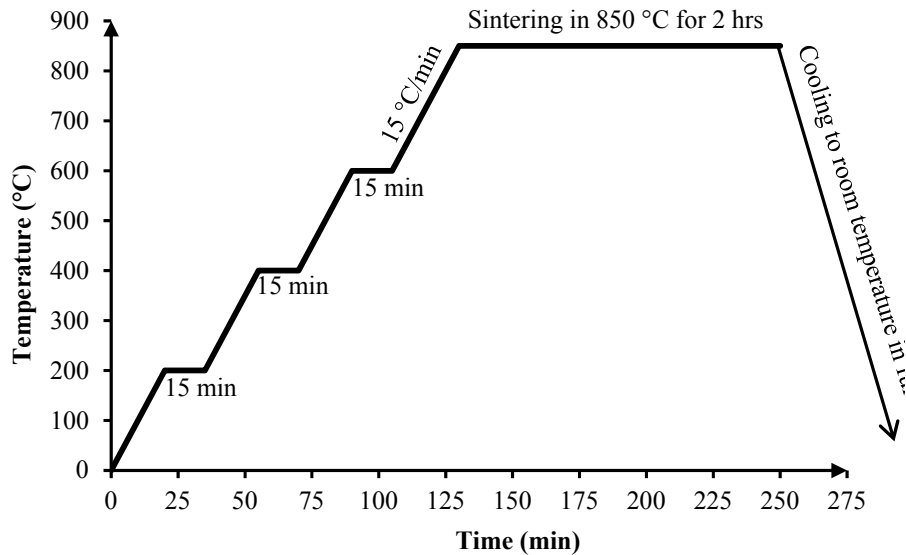


Figure 2: Heating profile of samples to sintering temperature.

3. RESULTS AND DISCUSSION

3.1. Porosity of Foams

Figure 3 shows the relationship between the porosity percentage of the foams and volume fraction of the carbamide in initial powder mixture. According to this figure, it is clear that porosity percentage of the foams is 0.3-4.6% higher than the initial volume fraction of carbamide. This increasing in porosity percentage is because of the decomposition of residual carbamide in green compacts during the sintering process and increasing of the cell sizes. The decomposition reaction of carbamide has shown in (4) [Chen and Isa, 1998]. The H₂O in (4) refers to absorbed water in the carbamide.

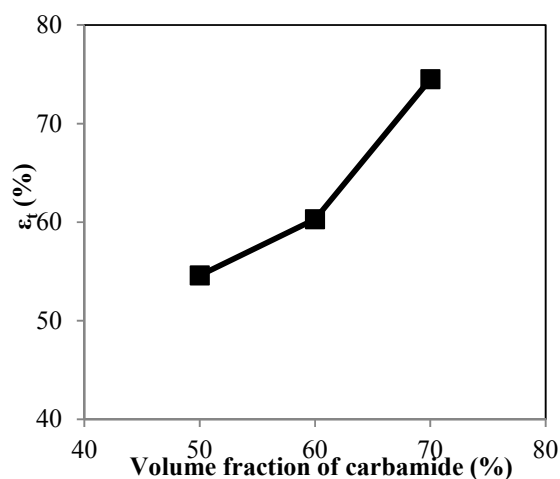
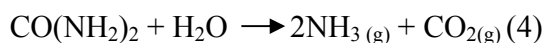


Figure 3: Relationship between volume fraction of carbamide in initial powder mixture and porosity in the final Cu foams.

Density, total porosity, open porosity, and closed porosity of foams are given in Table 1. This table indicates that increasing of the volume fraction of carbamide lead to

increasing in percentage of closed porosity of foams.

Table 1: Density and porosity of Cu foams.

Vol. fraction of carbamide	ρ_f (g/cm ³)	ϵ_t (%)	ϵ_o (%)	ϵ_c (%)
50	4.06	54.6	27.6	27
60	3.55	60.3	29.6	30.7
70	2.28	74.5	34.3	40.2

3.2. Structure of Foams

XRD pattern of Cu foams indicated the presence of only copper in the foams (Figure 4). Therefore, carbamide is completely removed from foams.

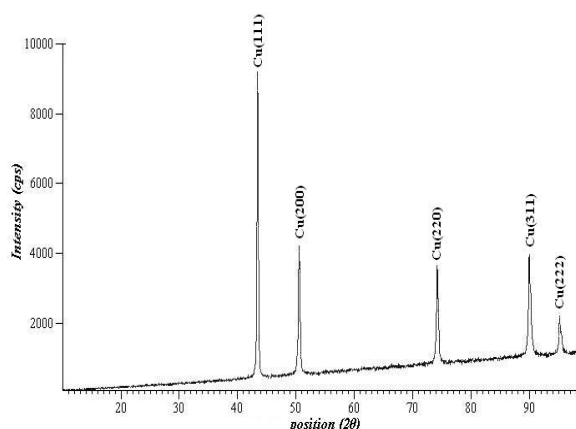


Figure 4: X-ray diffraction pattern for copper foam having 70% porosity.

Figure 5 shows the typical morphologies of the Cu foams with porosity of 74.5%, 60.3%, and 54.6%. Figure 5 indicates that with the increase of porosity, distribution of pores have been uniform. Non-uniformity distribution of pores is because of high density difference between Cu and carbamide. Difference between density of Cu and carbamide causes non-uniformity distribution of the powder mixture as well as the non-uniformity distribution of pores

in foam. Therefore this method has no ability to control the distribution of pores in the foams [Medraj et al., 2007]. Figure 6 shows the failure section of Cu foam with porosity of 74.5%. As seen in

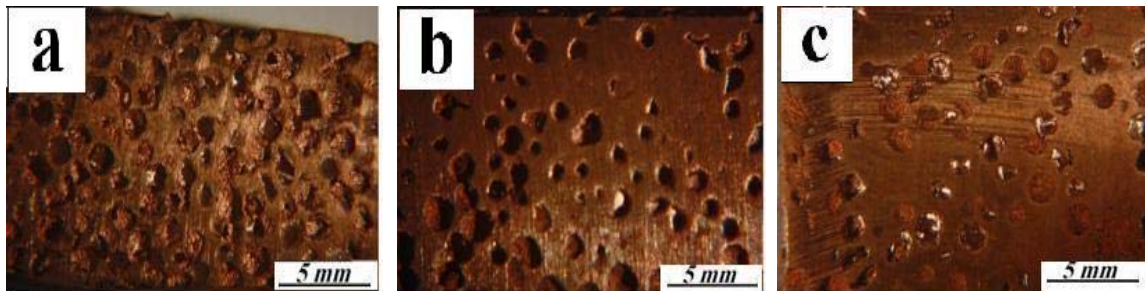


Figure 5: Surface Morphologies of Cu foams with a porosity of: (a) 74.5%, (b) 60.3%,

Figure 6, the cell size of the foams is in range of 1-1.6 mm. Increasing size of the cells is because of the decomposition of residual carbamide in green compacts during the sintering process.

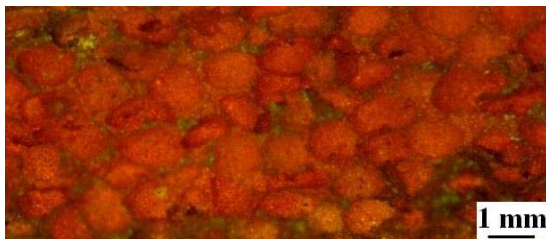


Figure 6: Failure sections of Cu foam with porosity of 74.5 %.

4. CONCLUSIONS

In this study, Cu foams with porosity in the range of 50-70% and cell sizes in the range of 1-1.6 mm have been produced by powder metallurgy method using carbamide space holder. Decomposition of residual carbamide in green compact during the sintering process caused the porosity of foams be 0.3-4.6% higher than the theoretical porosity. Also the result of quantity evaluations were shown that the distribution of pores in the foams strongly was depended to value of carbamide in initial powder mixture.

REFERENCES

- ASTM C20, standard test methods for apparent porosity, water absorption, apparent specific gravity, and bulk density of burned refractory brick and shapes by boiling water.
- Banhart, J., 2001, Manufacture, characterisation and application of cellular metals and metal foams, *Progress in Materials Science*, 46, 559.
- Chen, J.P., Isa, K., 1998, Thermal decomposition of urea and urea derivatives by simultaneous TG/ (DTA)/ MS, *Mass Spectrom. Soc. Jpn.*, 46, 299.
- Medraj, M., Baril, E., Loya, V., Lefebvre, L.P., 2007, the effect of microstructure on the permeability of metallic foams, *Materials science*, 42, 4372.
- Nakajima, H., Hyun, S.K., Ohashi, K., 2001, Fabrication of porous copper by unidirectional solidification under hydrogen and its properties, *colloids surface A: physicochemical and engineering aspects*, 179, 209.
- Parvanian, A.M., Panjepour, M., 2013, Mechanical behavior improvement of open-pore copper foams synthesized through space holder technique, *Materials and design*, 49, 834.
- Zhao, Y.Y., Sun, D.X., 2001, A novel sintering-dissolution process for manufacturing Al foams, *Scripta Materialia*, 44, 105.
- Zhao, Y.Y., Fung, T., Zhang, L.P., Zhang, F.L., 2005, Lost carbonate sintering process for manufacturing metal foams, *Scripta Materialia*, 52, 295.

THE EFFECTS OF POROSITY RATIO OF THE WELDED TUFFS ON SOUND AND HEAT INSULATION

Murat SERT^{1,a}, Sevgi GÜRCAN¹ and H. Tarık ÖZKAHRAMAN²

1. Afyon Kocatepe University, Mining Engineer Department, Afyonkarahisar, Turkey

2. Suleyman Demirel University, Mining Engineer Department, Isparta, Turkey

a. Corresponding author (msert@aku.edu.tr)

ABSTRACT: Welded tuffs have long been used in the construction business. These stones were focused on as choice during the periods when the technology was undeveloped due to their characteristics as ability of being processed easily, lightweight and insulation properties. Such constructions as churches and mosques where the welded tuffs have been used as the basic structural member have been subsisted for hundreds of years.

Welded tuff is a kind of a volcanic rock with lots of pores. Such pores are observed to be in small circular shapes in general and joined to one another with small deformations.

In this study, the relationships between porosity ratios, mineralogical - petrographical properties and sound and heat permeability values of eight different types of welded tuffs from Nevsehir region are evaluated. In addition, their usability in the different industrial fields is studied comparing them to less porous massive mass natural stones.

1. INTRODUCTION

Welded tuffs are light colored and light weight sedimentary porous volcanic ash in various sizes deposited after volcanoes erupted. They deposited on top of each other depending on the time of eruption by climatic effects. (Bilgin and Sargın, 2003). In the literature, they are named as volcanic tuff, tuff stone, welded tuff, sedimentary stone and they belong to natural stone category. Welded tuff is a building construction material used in the construction industry for many years. They are used mostly in the construction sector in building industry for wall cladding in outside exterior of buildings, at floor covering, and in masonry walls for decorative purposes due to having a wide range of color.

The use of welded tuffs in the building sector has an economic advantage besides its visual richness. The most important of these is its higher rate of heat and sound insulation in buildings when the building is covered by exterior wall cladding.

Therefore tuff stone is a good heat insulator due to having a high degree of porosity. The amount of heat energy conserved by using tuff stone in external walls of buildings is determined by Ozkahrman and Bolatturk, (Ozkahrman and Bolatturk, 2003).

It is found that the inner molecular structure of the media was the most important parameter that affects the transmission speed of heat and sound waves (Fenokulu, 2013). Heat waves radiate from its source without a media for transmission unlike sound waves that requires a medium for transmission. Heat waves travels in space.

Each substance have different transmission rate due to different inner structure that contains pores and voids. The heat transmission rate is higher if the inner structure is more compact and dense.

Heat insulation means to prevent or completely reduce heat exchange between two different media that has

different temperatures. Similarly, sound insulation means to stop or prevent sound transmission between to different media.

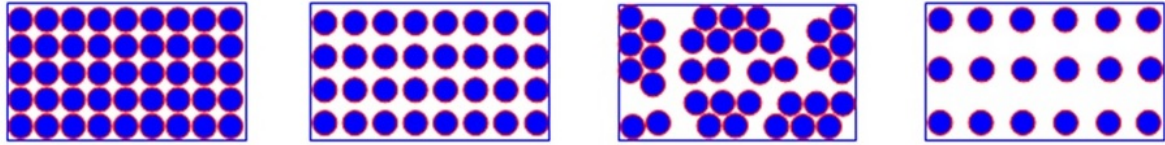


Figure 1: Arrangement of the particles that make up the substance forms

The heat and sound conductivity decreases with increasing spacing of the particles, when heat and sound conductivity is considered. The amount of voids and pores between the particles affect isolation. Isolation reduces with increasing porosity, (Fig.1).

In this study, porosity, heat and sound transmission rates of welded tuffs of Nevşehir region is determined by the standard tests in the laboratory and the results are compared with each other. At the end of this study very useful information is gathered which is very important in building construction industry.

2. METHOD AND MATERIALS USED

2.1. Properties of the Tuffs Used in Tests

Eight different welded tuff samples is used in the tests that are collected from operated quarries in Nevşehir region in Turkey. The mineralogical – petrographical properties of tuff stones is determined by polarisan microscope. The porosity is determined according to TS EN 1936 standard. In addition thermal conductivity and P-wave velocity tests are made on welded tuffs to determine the relation between porosity and thermal conductivity values. The results of porosity, thermal conductivity and P-wave velocity measurements of tuff samples used in the study is given in Table 1.

Table 1: The results of porosity, Thermal conductivity and P-wave velocity measurements of eight different tuff samples

Name of the Stone	Tuff							
	Tuff 1	Tuff 2	Tuff 3	Tuff 4	Tuff 5	Tuff 6	Tuff 7	Tuff 8
Porosity, %	32,7	33,2	32,8	51,1	46,5	43,3	56,5	45
Thermal conductivity (W/m.K), k (λ)	0,5	0,47	0,51	0,3	0,39	0,35	0,25	0,37
P-wave velocity, (m/s)	3000	2700	1950	2250	2100	2200	1800	2400

2. RESULTS AND DISCUSSION

3.1. The Relation Between Thermal Conductivity And Porosity

Thermal conductivity change with porosity is studied for welded tuff samples that are collected from operated quarries in Nevşehir region and given in Fig.2. The porosity is 56.5% against

thermal conductivity value of 0.25 (W/m.K) in tuff sample 7. The porosity is 32.7% against thermal conductivity value of 0.5 (W/m.K) in tuff sample 1. It is found that thermal conductivity reduces with increasing porosity. Therefore there is a direct relationship between thermal conductivity value and percentage of porosity.

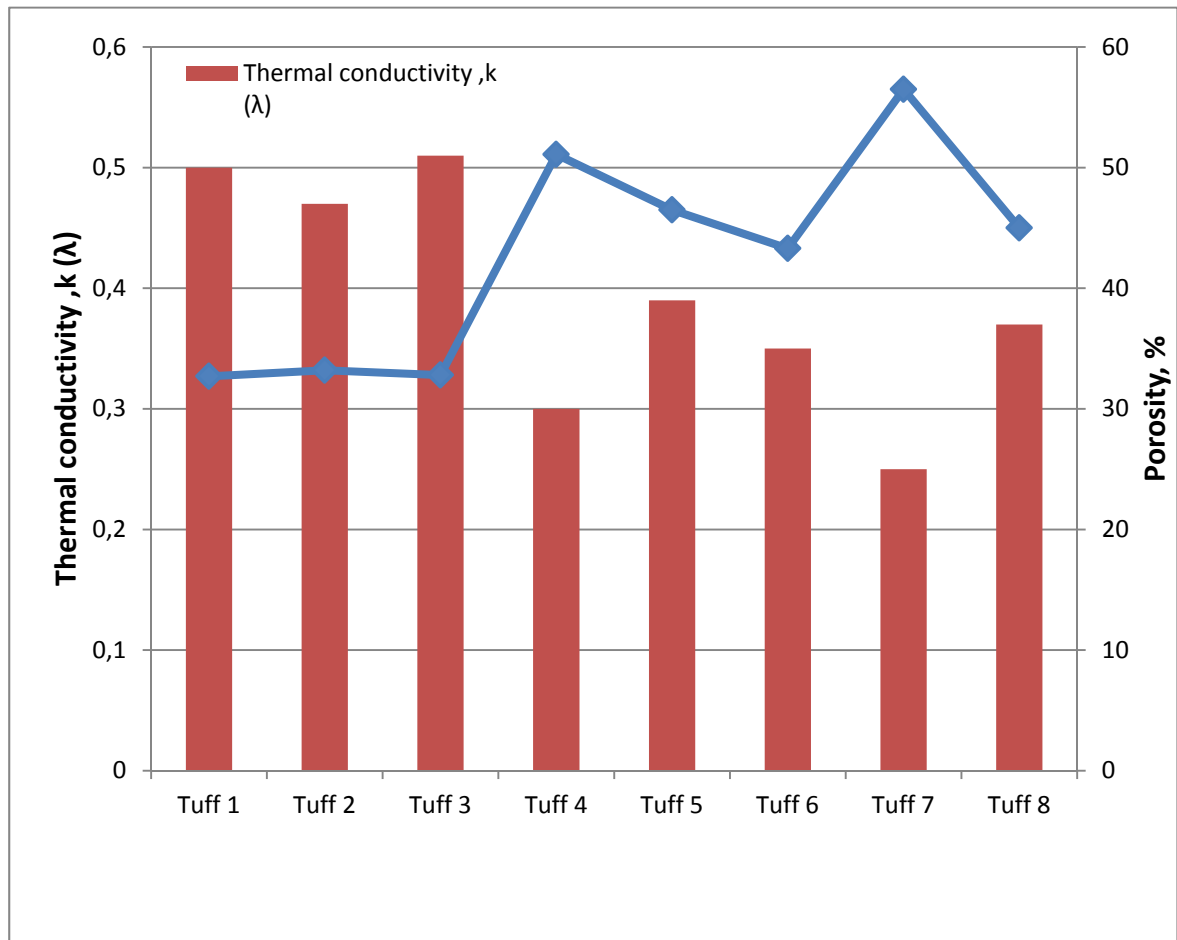


Figure 2: The relation between thermal conductivity and porosity

3.2. The Relation Between Thermal Conductivity and Porosity

The variation in the sound isolation of welded tuffs is studied for different porosity values. The determined porosity value is 56,5% against P-wave

velocity of 1800 m/s for tuff 7 sample. Where as porosity is 32,7%, against P-wave velocity of 3000 m/s for tuff 1 sample. Therefore as porosity increases P-wave velocity decreases.

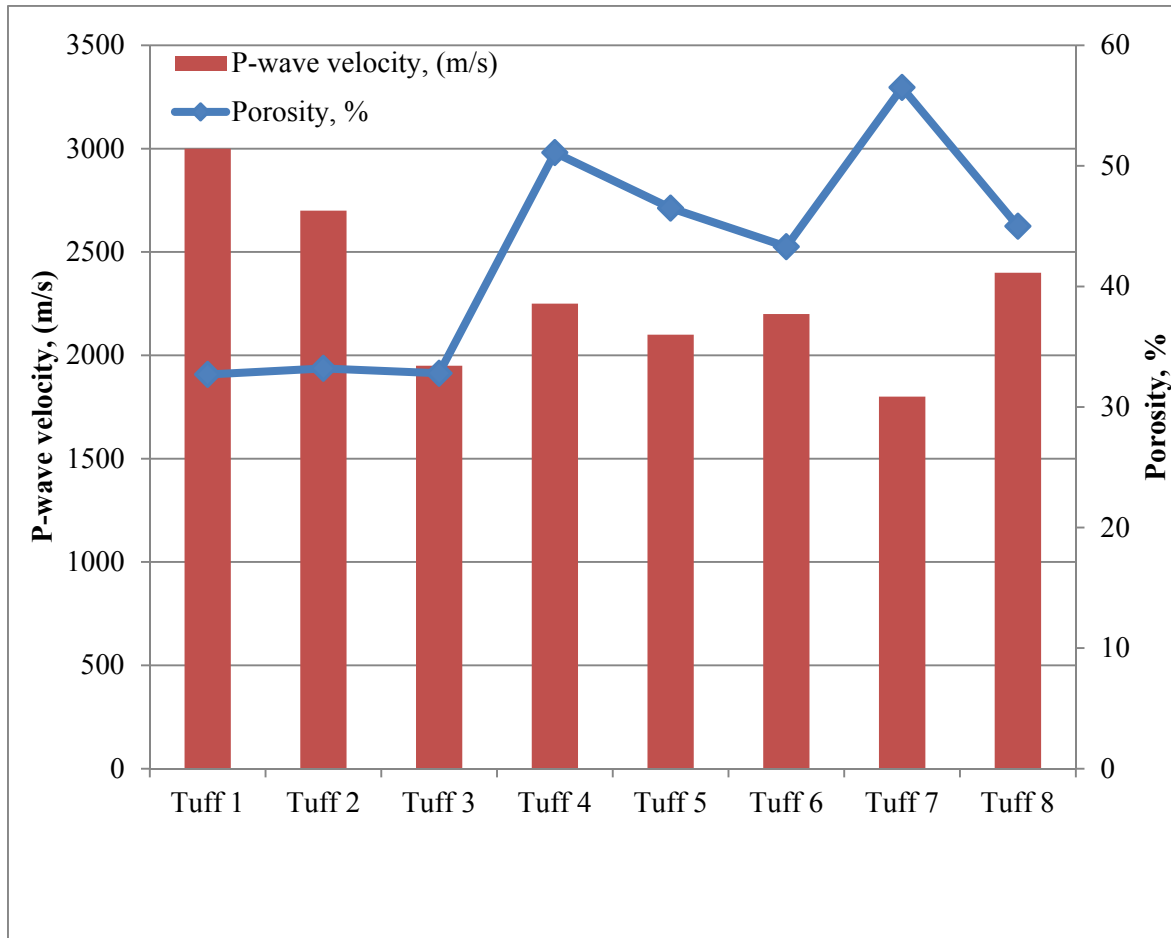


Figure 3: The relation between P-wave velocity and porosity

P-wave velocity values are low in porous rocks that mean it travels more slowly in porous rocks. Therefore sound isolation property of porous rocks is more than compact rocks.

3.3. Mineralogical and Petrographical Properties

The porous structure is found to be due to phenocrystals by mineralogical and petrographical properties. The feldspars are decomposed by weathering action from phenocrystals and transformed to clay minerals by forming kaoline (china clay). The matrix which surrounds this

phenocrystals has a unstable crystal structure. The porosity in this stones is produced by environmental effects according to mineralogical structure of the tuffs not from sudden cooling in magmatic stones or due to metamorphism. They contain 15% zeolite mineral (Ozkahraman HT., Bolatturk A., 2006). There is high volume of pores in zeolites and make up 50% of their total volume (Wikipedia, 2013). This high value of porosity increases the total porosity of welded tuffs as well.

4. RESULTS

In this study, the relation between thermal conductivity, P wave velocity values and porosity is studied for welded tuff samples taken from different stone quarries at Nevsehir region. The main results obtained from this research;

- The thermal conductivity reduces as porosity increases as a result of experimental studies.
- The P-wave velocity increases with the decrease in the rate of porosity.
- Their porosity change with the amount of zeolite they contain.
- Therefore tuff stone is a good heat insulator due to having a high degree of porosity compared to other natural stones (marble, granite etc.)

REFERENCES

Bilgin A., Sargin S., Building stones and environmental interaction in Isparta (Turkey) region, In: International symposium on Industrial Minerals and Building Stones (IMBS), İstanbul, 2003.

<http://www.fenokulu.net/portal/Sayfa.php?Git=KonuKategorileri&Sayfa=KonularKonuYazdir&KonuID=518>, Date of access: 15.05.2013

<http://tr.wikipedia.org/wiki/Zeolit>, date of Access: 16.05.2013

Ozkahraman H.T., Bolatturk A., The use of tuff stone cladding in buildings for energy conservation, Construction and Building Materials 20 (2006) 435-440.

Özkahraman H.T., Bolattürk A., 2003. "Bina yapımında köyke taşı (kaynaklanmış tuf) kullanılmasının enerji tasarrufundaki önemi", Türkiye IV.üncü Mermer Sempozyumu, Sayfa 49-60, AFYONKARAHİSAR

USING OF PHOTOLUMINESCENT TILE FOR EVACUATION OF THE BUILDINGS DURING ELECTRICAL FAILURE

Neslihan TAMSÜ¹, Ayse TUNALI¹

¹Eczacibasi Building Products Co. Vitra Innovation Center Bozuyuk/Bilecik-Turkey
a. Corresponding author (neslihan.tamsu@eczacibasi.com.tr)

ABSTRACT: Photoluminescent pigments could be successfully applied on the wall tiles, floor tiles and porcelain tiles as well as glass substrates (glass mosaics, borders, and cutted glass with various designs). For this applications, these products can be used for different purposes. In this study, these pigments are applied on the ceramic tiles and glass mosaics/tiles with traditional ceramic production line. These products are intended to provide guidance in the event of a power failure. With this study also aimed to prevent potential accidents and injury during evacuation of building

1. INTRODUCTION

The term “luminescence” originates from the Latin word “lumen”, which means light and the literal translation from Latin is “weak glow”. It was introduced into the scientific literature by Eilhardt Wiedemann, a German physicist, in 1888 [Wiedemann, 1988]. Luminescence, which includes both fluorescence and phosphorescence in which the electronic state of a solid is excited by an external energy and the absorbed energy is given off as visible light. Light is comprised of photons, which are quantized waves exhibiting some of the properties of particles, i.e., wave-particle duality [Zukauskas et al., 2002, Kaya et al., 2012]. Photoluminescence (PL) is excited by electromagnetic radiation with short-wavelengths such as ultraviolet light. Inorganic luminescent materials can be divided in two classes [Gribkoskii, 1988]: i) those that absorb light (pigmented) and ii) those that absorb the energy and emit light (phosphors and solid state lasers). In both cases, certain amounts of transition and/or lanthanide ion(s) are incorporated to control the absorption and emission

characteristics of that solid. Phosphors in the strontium aluminates system activated with europium (Eu) and dysprosium (Dy) has a wide range of industrial applications such as phosphor host compounds [Cho et al., 2003, Kong et al., 2003], glazes, pigments [Alarcon et al., 1985], electrical insulators [Lepkova et al., 1980], and it is an important component in glass ceramics [Strands, 1986]. When these structure compared to the classical sulphur phosphors, they are superior because of their high radiation intensity, color purity, long emission duration, chemical stability and because they are reliable and have no radiation [Kaya et al., 2012]. In this present study, In this study, these pigments are applied on the ceramic tiles with traditional ceramic production line. These products are intended to provide guidance in the event of a power failure. With this study also aimed to prevent potential accidents and injury during evacuation of building.

2. EXPERIMENTAL PROCEDURE

In this study, SrAl₂O₄ phosphorescent pigments with long-term phosphorescence

which bluish-green denoted as (S) and yellowish-green denoted as (Y), were used in wall tile vetrosa applications. The chemical analysis of the pigments was shown in Table 1.

Table 1: Chemical compositions of the phosphorescent pigments.

Compositions	(S)	(Y)
SiO ₂	32.55	0.11
SrO	53.29	46.29
Eu ₂ O ₃	0.38	0.49
Fe ₂ O ₃	0.20	0.20
MgO	11.70	-
Dy ₂ O ₃	0.64	0.84
CaO	-	0.08

After firing, obtained fritted surfaces' after glow property was measured by using Photometer (LS-100, Konica, Minolta). After glow property was determined considering the glowness of the sample in darkness versus time.

3. RESULTS AND DISCUSSION

Tests on wall tile vetrosa applications were carried out for pigments derived in the last stage of the study. Phosphorescent pigment added vetrosa frit with same proportions was applied on glazed tile bodies and third firing was carried out. In the case of emergency situation, first half hour is quite critical in the event of a power failure, for this reason photoluminescent tiles must show glow in the dark in this period. Therefore, pigmented surfaces glowness in order to understand whether it is suitable of use in an emergency exit measured in the dark. Figure 1 shows the after glow property of the photoluminescent tile, which were excited under light for 5 minutes, versus time in the darkness. Based on this graph (Figure 1), the tiles, for first 5 minutes shows 250 mcd intensity, after 40 minutes this value decreases to 30 mcd. The minimum light detection intensity

value in the darkness for human eyes is 0,32 mcd. Therefore, developed tiles can be used for emergency exits readily.

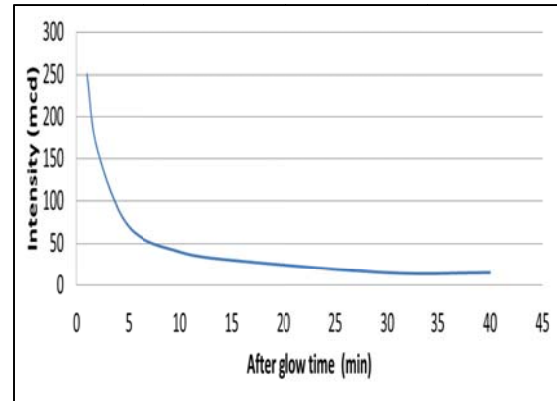


Figure 1: After glow property of the tiles versus time in the darkness.

The photographs of tiles produced using the optimum parameters derived as a result of the studies are given in Figure 2.



Figure 2: Images of produced photoluminescent tiles in dark

4. CONCLUSIONS

Phosphorescent pigment added vetrosa frit with same proportions was applied on glazed tile bodies and third firing was carried out. According to the analyses, it has been found that newly developed photoluminescent tiles can be successfully applied to emergency exits and signs.

REFERENCES

- Wiedemann. G., Annual Physical Chemistry, v.34, (1888) p.446.
- A. Zukauskas, M.S., Shur, and R. Gaska, "Introduction to Solid-State Lighting", John Wiley & Sons, New York, (2002).
- Kaya Yesilay S. and B. Karasu "Glass and Ceramics with Phosphorescent Ability", Ceramics Technical, No: 34, 94-99, May 2012.
- V.P. Gribkoskii, (1998) "Theory of Luminescence", Luminescence of Solids, ed. by D.R. Vij (Plenum Press, New York), pp. 1 – 43.
- T.H. Cho, and H.J. Chang, Ceramics International, v.29, (2003) p. 611.
- Y.C. Kang, and H.D. Park, Applied Physics A, v.77, (2003), p. 529.
- J. Alarcon, P. Escribano, and R. Maria Martin, British Ceramics Transactions J., v.84, (1985) p. 170.
- D. Lepkova, A. Nenov, L. Pavlova, and I. Ivalnov, Stroit.Materi.Silik.Promst. v.21, (1980) p. 18.
- Z. Strands, "Glass Science and Technology", v.8, (1986) p. 101.Elsevier, Amsterdam.

SILICA BASED SHEAR THICKENING FLUIDS (STFs) FOR PERSONAL PROTECTION

Sema Yıldız¹, Oylum Çolpankan¹, Fikret Şenel², Metin Tanoğlu^{3,a}

1. Izmir Institute of Technology, Materials Science and Engineering Department, Urla-Izmir, Turkey
2. BARIŞ Electrical Industry Inc., Havaalanı Yolu 23. Km, Akyurt, 06750, Ankara, Turkey
3. Izmir Institute of Technology, Mechanical Engineering Department, Urla-Izmir, Turkey
 - a. Corresponding author (metintanoglu@iyte.edu.tr)

ABSTRACT: Shear thickening phenomenon is a non-Newtonian fluid behavior which takes place in concentrated colloidal suspensions and described as the increase in viscosity with increasing applied shear stress or shear rate. Due to this unique property, shear thickening fluids (STFs) have attracted attention for using in impact resistance applications. In this study, fumed silica nanoparticles/Polyethylene glycol (PEG) suspensions were prepared by a sonochemical method with various concentrations of silica particles and containing PEG 200 and PEG 300 which are 200 and 300 g/mole molecular weight, respectively. Rheological behaviour of the prepared STFs were investigated by a (TA AR2000ex) rheometer to investigate the effect of silica concentration and PEG molecular weight on the behaviour of the liquids. Characterization of nano-sized silica particles were carried out by means of scanning electron microscopy (SEM) and X-ray diffraction (XRD) whereas PEG's were analyzed by differential scanning calorimetry (DSC), thermogravimetric analysis (TGA) and STFs by TGA and SEM.

1. INTRODUCTION

According to the Newton's law, liquids can be categorized into two groups according to their behaviour under shear stress; Newtonian and non-Newtonian. For most fluids shear stress is proportional to the deformation rate. They follow Newton's law with the constant viscosity [Lomakin *et al.*, 2011]. However, concentrated colloidal dispersions do not show a constant viscosity under shear stress, shear stress is not proportional to the shear rate, and they are called as non-Newtonian fluids [Kalman *et al.*, 2009].

Shear thickening is a non-Newtonian flow behavior and defined in the British Standard Rheological Nomenclature as the increase of viscosity with increase in shear rate [Barnes, 1989].

In recent years, shear thickening fluid (STF) has attracted great interest and it has been started to use within the systems

such as adhesives and sealants, flame resistant clothing, body armor (bullet or stab proof), motorcycle protective clothing etc. [Suhaimi *et al.*, 2009].

The shear thickening fluids consist of two phase; nano-scale particles such as silica [Kang *et al.*, 2012], [Lee *et al.*, 2003], calcium carbonate [Wetzel *et al.*, 2004], PMMA particles [Kalman *et al.*, 2007], and medium fluid in which the particles are dispersed such as polypropylene glycol (PPG) [Kagei *et al.*, 2005], polyethylene glycol (PEG) etc. [Hassan *et al.*, 2010].

In this study, fumed silica nanoparticles/ Polyethylene glycol (PEG) suspensions were prepared by a sonochemical method with various concentrations of silica particles and PEG 200 and PEG 300 which are 200 and 300 g/mole molecular weight, respectively. The microstructural characterization of silica nanoparticles, STF containing 30wt.% silica-PEG 300 were performed by using SEM. The steady-shear rheological properties of STFs were investigated using a rotational rheometer. Silica nanoparticles crystallinity was carried out by means of XRD, thermal behavior of PEGs was analyzed by DSC whereas STFs and PEGs behavior were analyzed by TGA.

2. EXPERIMENTAL PROCEDURE

2.1. Materials

Fumed silica nanoparticles and polyethylene glycol (PEG) (200 g/mole and 300g/mole) were used as a filler material and as a medium fluid, respectively. In order to obtain stable dispersion ethyl alcohol was used.

2.2. Synthesis of Shear Thickening Fluid

The sonochemical method was used to synthesize shear thickening fluid. In this technique a variety of weight percentages of silica nanoparticles were added to PEG and they were blended in excess amount of ethyl alcohol for 8 hours. After obtaining the solution of the STF, the solution was held in an air-circulating oven at ethyl alcohol evaporation temperature (79 °C) in order to evaporate all ethyl alcohol in the reaction mixture. After all ethyl alcohol are removed, STF was grinded in a agate mortar and in order to eliminate the bubbles, STF was placed in a vacuum pump for several hours until no bubbles were observed.

2.3. Characterization

The steady-shear rheological properties of STFs were investigated by using a rotational rheometry TA 2000ex at 25 °C in order to investigate the effect of silica concentration and PEG molecular weight on the rheological behaviour of the liquids.

Microstructural characterization of silica nanoparticles and STF containing 30 wt.% of silica-PEG 300 were performed by using Phillips™ XL-30S FEG Scanning Electron Microscopy (SEM).

The crystallinity of silica nanoparticles was characterized by X-ray Diffraction (XRD) analysis using a Phillips™ Xpertdiffractometer over a 2 θ -range of 5° - 70°.

For the evaluating thermal behaviour of PEGs TA Instruments Q10 Differential Scanning Calorimetry (DSC) was used. The experiments were carried out from -40 °C to 400 °C.

Thermal gravimetric analysis (TGA) was conducted to determine the decomposition behaviour of neat PEG and the weight percentage of silica and polyethylene glycol in prepared STF sample with Perkin Elmer Diamond Thermo Gravimetric Analyzer (TGA). The experiments were carried out from 30 °C to 800 °C.

3. RESULTS AND DISCUSSIONS

3.1. Rheological Properties

In STFs viscosity is firstly decreases at low shear rates and a sharp increase follows this behavior when shear rate reaches a critical value. The main reason of dramatic increase in viscosity of shear thickening fluids is the hydrocluster formation which occurs when shear rate reaches its critical value. As it can be seen in Figure 1. STFs which have concentration in the range of

10-30 wt % enters a shear thinning region by a slight decrease in their viscosity.

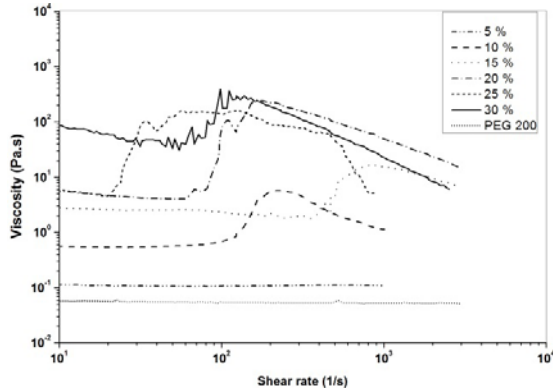


Figure 1: Steady shear viscosity as a function of shear rate for STF composed of PEG 200 at varying weight fractions.

Figure 1 also shows that fumed silica concentration affects the increment in viscosity value. When silica concentration increased from 10% to 30 wt%, viscosity gradually increases. Maximum viscosity was obtained about 400 Pa.s at 30 wt% concentration, and its critical shear rate is determined as 50 1/s. It seems that friction between fumed silica particles increases with increasing concentration. On the other hand, 5% fumed silica containing STF does not show a viscosity change with increasing shear rate. It can be attributed to the low concentration, because to observe a shear thickening effect, amount of silica in the medium fluid should reach a certain value to induce hydrocluster formation.

The steady-shear viscosity graph of STF containing PEG 300 is shown in Figure 2. This graph indicates a similar trend in viscosity as in Figure 1. Viscosity values at concentrations from 5 wt% to 30 wt % increases to higher values and more orderly compared to STF containing PEG 200. The maximum viscosity value is 1241 Pa.s, and it was obtained at about 11/s shear rate for STF at 30 wt % concentration. There is

a general decrease in onset of shear thickening with increasing fumed silica concentrations.

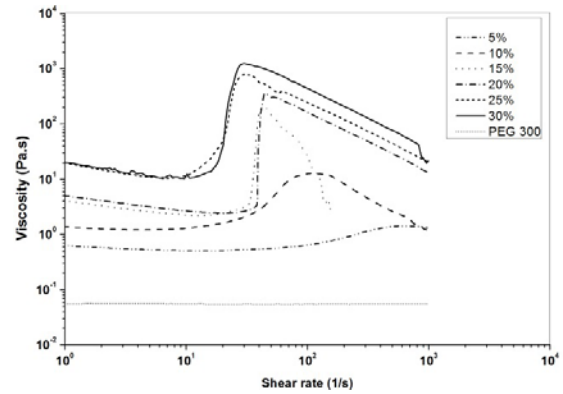


Figure 2: Steady shear viscosity as a function of shear rate for STF composed of PEG 300 at varying weight fractions.

3.2. Microstructural Features

The XRD pattern of the fumed silica nanoparticles is shown in Figure 3. The characteristic peak for silica was revealed at the diffraction angle of about 23 °C. As seen in the figure, silica shows a broad peak that indicates a relatively high fracture of amorphous phases with the silica structure.

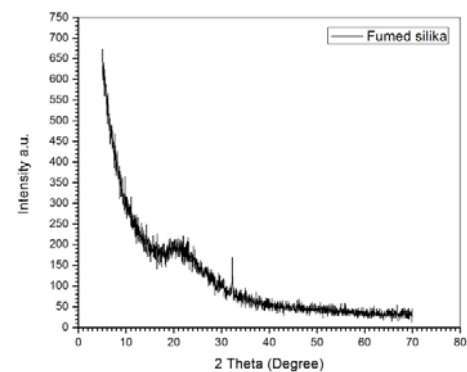


Figure 3: XRD pattern of fumed silica nanoparticles.

SEM images of fumed silica nanoparticles at 100000x magnification and STF containing 30wt % fumed silica – 70wt % PEG 300 at 50000x magnification are shown in Figures 4 and 5, respectively. Silica nanoparticles are spherical shaped and well dispersed. SEM image of the STF represents that PEG 300 and silica particles well interacts with each other and exhibits a good homogeneity.

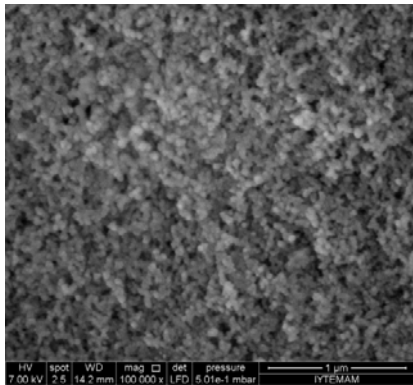


Figure 4: SEM image of fumed silica nanoparticles

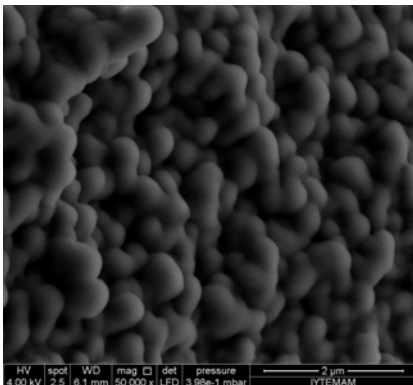


Figure 5: SEM image of STF containing 30 wt % fumed silica – 70 % PEG 300.

3.3. Thermal Properties

Figure 6 shows typical thermogravimetric analysis (TGA) weight loss curves of neat PEG and STFs with PEG 300. Test results show that there are two weight loss stages.

The first weight loss was observed to start at around 160 °C due to the evaporation of the PEG. The PEG decomposes at around 260 °C where a major weight loss stage is noticed as seen in TGA curves. The remaining sample residue is silica and these values are closer to the actual values.

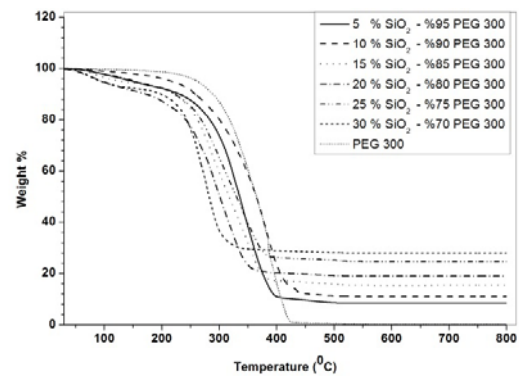


Figure 6: TGA graph for neat PEG and prepared STF sample with PEG 300.

Differential Scanning Calorimetry (DSC) test was performed under nitrogen atmosphere between -40-400 °C. Melting temperature of PEG 300 was found as -16.02 °C. This value seems low, but PEG 300 is liquid at room temperature. Also, the glass transition temperature (T_g) of PEG 300 is determined as 110 °C.

4. CONCLUSION

Silica based STFs with PEG 200 and PEG 300 were developed successfully and their steady-shear rheological characterization was determined. As the concentration increased, the shear thickening effect was observed more significantly. The maximum viscosity was obtained at 30 wt % concentration of fumed silica for both PEG 200 and PEG 300. Maximum viscosity values were determined as 400 Pa.s and 1241 Pa.s for PEG 200 and PEG 300, respectively. However, the highest viscosity values was found for PEG 300 at

the same concentrations rather than PEG 200. Also, it was observed that there is a general trend of onset of shear thickening decreases with increasing concentration. Tg of PEG 300 was obtained as 110 °C as a result of DSC analysis. SEM images indicates that sonochemical method improves the dispersion of fumed silica particles in STFs. TGA test result of STFs with PEG 300 indicates the weight loss % of fluids and the weight fraction of residual silica. The actual values and the remaining silica values are closer together.

Acknowledgements: The authors gratefully acknowledge the support of BARIŞ Electrical Industry Inc. and Undersecretariat for Defence Industries of Turkey (SSM).

REFERENCES

- Barnes, H.A. 1989. Shear thickening(dilatancy) in suspensions of nonaggregating solid particles dispersed in newtonian liquids, *Journal of Rheology*, 33(2), 329.
- Hassan, T. A., Rangari, V. K., Jeelani, S. 2010. Sonochemical synthesis and rheological properties of shear thickening silica dispersions. *Ultrasonics Sonochemistry*, 17(5), 947.
- Kagei, N., Kanie, D. and Kawaguchia, M., 2005. Viscous fingering in shear thickening silica suspensions. *PHYSICS OF FLUIDS* 17, 054103.
- Kalman, D. P., Schein, J. B., Houghton, J. M., Laufer, C. H. N. and Wetzel, E. D. 2007. Polymer Dispersion Based Shear Thickening Fluid-Fabrics For Protective Applications, presented at the SAMPE 2007, June 3-7, 2007.
- Kalman, Dennis P., Merrill, R. L., Wagner N. J. and Wetzel, E. D. 2009. Effect of Particle Hardness on the Penetration Behavior of Fabrics Intercalated with Dry Particles and Concentrated Particle-Fluid Suspensions, *ACS applied materials & interfaces*, 1(11), 2602.
- Kang, T. J., Kim, C. Y. and Hong, K. H. 2012. Rheological Behavior of Concentrated Silica Suspension and Its Application to Soft Armor, *Journal of Applied Polymer Science*, 124, 1534.
- Lee, Y. S., Wetzel, E. D. and Wagner, N. J. 2003. The ballistic impact characteristics of Kevlar woven fabrics impregnated with a colloidal shear thickening fluid, 38, 2825.
- Lomakin, E. V., Bragov, P. A. A. M., Lomunov, A. K., Konstantinov, A. Y., Kolotnikov, M. E., Antonov, F. K. and Vakshtein, M. S. 2011. Investigation of impact resistance of multilayered woven composite barrier impregnated with the shear thickening fluid, *Archive of Applied Mechanics*, 81(12), 2007.
- Suhaimi, M. S., Mohamed, R. and Faiza, M. A. 2009. Effect of polymer microsphere incorporation on impact performance of STF cotton fabric composite, presented at the 9th National National Symposium on Polymeric Materials, December 14-16, 2009.
- Wetzel, E. D., Lee, Y. S. Egres, R. G., Kirkwood, K. M., Kirkwood, J. E., and Wagner, N. J. 2004. The Effect of Rheological Parameters on the Ballistic Properties of Shear Thickening Fluid (STF)-Kevlar Composites, presented at the NUMIFORM 2004, June 13-17, 2004.

ENERGY EFFECTIVE GRANULE PREPARATION IN PORCELAIN TILE PRODUCTION

Ayşe Tunalı^{1,a} and Neslihan Tamsü Selli^{1,a}

1. Eczacıbaşı Building Product Co., Vitra Innovation Centre, Bilecik, Turkey

a. Corresponding authors: ayse.tunali@eczacibasi.com.tr; neslihan.tamsu@eczacibasi.com.tr

ABSTRACT:In this study, the effect of polymeric dispersant was investigated in ceramic powder blend of porcelain tile to determine the best dispersing formulation. The aim is to outperform the currently used dispersing formulation (sodium silicate) in order to directly save energy and production time (higher slurry solids at same viscosity). Polymeric dispersant was tested in formulation with sodium silicate at different ratios. Finally, by using 0,25% dispersing agent in the ratio of 90% sodium silicate to 10% polymeric dispersant the best value was achieved. Compared to the current dispersant system it allows increasing the solids by 2% (from 65% for the current dispersing system to 67% with polymeric dispersant.) By increasing the solid ratio, the energy spent for preparation of granule in spray drier is decreased.

1. INTRODUCTION

At present, in the ceramic tile industry, world clay consumption is of the order of two dozen million tons/year. From a technological viewpoint, much of the ceramic production sector works with a technology based on unit operations that use these raw materials in aqueous suspension [Avgustinik, 1983].

Ceramic suspension is formed by blending raw materials such as clay, feldspar, and quartz with water. After blending, it is grounded in a ball mill to get the ceramic slurry. Generally solid ratio of ceramic slurry is 65%. After the formation of ceramic slurry, the material which will soon be made into ceramic tile is now put into a spray dryer and heated at high temperature.

Specifically in the ceramic tile industry, spray dryer process is used to evaporate the water added to aid the grinding process of the raw material and to homogenize the additives. The main advantage of adapting such a process is the resulting powder flowability, since the granules obtained keep the spherical shape of atomized droplets; the quality of the final product is directly affected by

the granule sphericity, while transportation and compaction are improved [Favalli et al., 2002].

When the body slip is heated, it is transformed into granule which contains moisture of about 6% in spray drier. Processing cost per unit of granulated product are reduced significantly when the slurry has a high solids loading and relatively less water must be eliminated [Reed, 2000].

With regard to the economic aspects, there is a conflicting feature, since increasing solids content in a clay suspension significantly reduces its flowability. The clay particles are in colloidal suspension, and hence subject to mutual attraction interactions that increase considerably with the rise in solids content. Such an effect negatively affects suspension flowability, as the formation of “contacts” between particles hinders liquid flow as a whole. The optimisation of a ceramic suspension therefore depends on introducing substances that eliminate interparticle attractions as far as possible, i.e. which have a diluting effect on the suspension. These substances are chemical additives

known as deflocculants [Pozzi and Galassi, 1994; Ravagioli, 1989; Pellacani and Manfredini, 1986; Manfredini et al., 1990; Tadros, 1985; Rodrigues Neto et al., 2002].

Silicates and polyphosphates have been most widely used materials for deflocculating suspensions of ceramic bodies in Turkey. Silicates (generally liquid sodium metasilicates) are very cheap dispersants but have limited action. Polyphosphates (generally sodium tripolyphosphates) are more expensive than silicates but also more efficient deflocculants.

In recent years, liquid organic compounds (mainly acrylic acid polymers) were being used in some country such as Italy and Brazil [Ballester, 2000]. It was reported that polymeric dispersants (polyacrylates) are also expensive, but are the most efficient dispersant, lowering viscosity and improving thixotropy.

The ultimate goal of this study is to increase the solid content as much as possible while maintaining adequate slurry flow properties. For this purpose, a combination of silicate and polymeric dispersant was as a cost effective way of granule preparation for porcelain tile production. The trials were carried out at Vitra Karo San. ve Tic. A.Ş., a ceramic tile company located in Bilecik, Turkey. The energy saving of such combination obtained were quantified and other results such as viscosity and density of the slurry were also discussed.

2. MATERIALS AND METHODS

Characteristics of commercial industrial slurry are shown in Table 1. In this study porcelain tile body composition was prepared by using industrial raw materials. The batches were prepared according to the commercial recipe of Vitra Karo Tile Company.

Table 1: Characteristics of industrial slurry

Slip density	1690-1710 g/l
Solid ratio	65%
Deflocculant dosage	0,3 dry/dry
Viscosity Ford Cup n° 4	25-35 sec

Standard (commercial) porcelain tile recipe (STD) comprised of 65% solid ratio was ground by a wet technique through an alumina ball mill using sodium silicate at a rate of 0,3 (dry/dry). Then new recipes (PD-10, PD-20, PD-30) which enable polymeric dispersant to be used as a replacement of sodium silicate as a deflocculant and rational analysis of these recipes are given in Table 2.

Table 2: Prepared slurries

	STN	PD-10	PD-20	PD-30
Slurry ratio %	65	68	68	68
dispersant ratio (sodium silicate/polymeric dispersant)	100/0	90/10	80/20	70/30
Dispersant dosage (%dry/dry)	0,3	0,4	0,4	0,4

These new recipes comprised of 68% solid ratio were ground again by a wet technique through an alumina ball mill using deflocculant (sodium silicate together with polymeric one) at a rate of 0,4%. All of the batches were milled up to achieving 1-2% residue on the 45 µm sieve. Slip density was measured by using metal pycnometer. Flow time of slurries (viscosity) was measured by using 4 mm Ford cup.

3. RESULTS AND DISCUSSION

Viscosity of the prepared slurries (Table 1) is seen in Figure 1. Viscosity of the standard slurry is 33 sec. at %65 solids (1690 g/l density), with 0,3% sodium silicate. At 68% solids (1740 g/l density), with 0,4% dispersant, increasing the part of polymer dispersant in the ratio silicate/polymer, improves slurry viscosity, however too much polymer dispersant necessary to get a reasonable viscosity, which will not be acceptable in terms of cost.

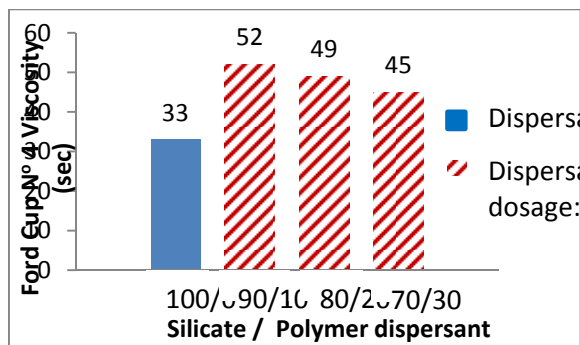


Figure 1: Viscosity of the prepared recipes

With regard to the economic aspects, silicate/polymer ratio was chosen as 90/10. After that, all of the recipes was prepared by considering this ratio: Different dispersant dosage (0,50 - 0,40 - 0,35 - 0,30 - 0,25 - 0,20) was tried for different solid ratio (68% - 67,5% - 67% - 65%). Density and the viscosity of the slurries are shown in Figure 2.

In terms of characteristics of industrial slurry (Table 1), 1720 g/l slip density is most suitable one among the recipes given in Figure 2. It can be concluded that 0,25 dispersant dosage gives the acceptable viscosity value with 67% solid ratio.

4. CONCLUSIONS

The dispersing system containing 90 sodium silicate/10 polymer dispersant (expressed as solids) dosed at 0,25% (as

solids) allows preparing a slurry at 67% solids (1720 g/l density), which is not reachable by sodium silicate alone.

This higher solid slurry makes possible saving energy and production time in spray drier by decreasing the water amount that should be evaporated during granulation process.

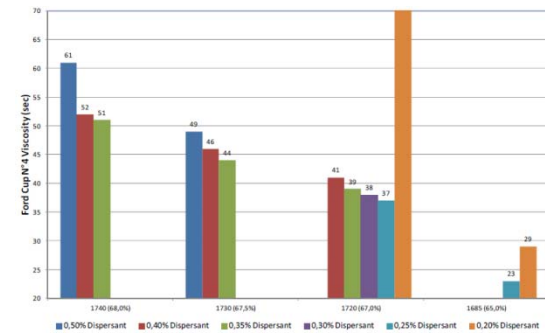


Figure 2: Viscosity of the slurries prepared by 90/10 silicate/polymer dispersant ratio.

Acknowledgements: The authors would like to thank Mr. Vedat Bayrak and Mr. Hidayet Özdemir for their help and fruitful discussion throughout this study.

REFERENCES

- Avgustinik, A.I., 1983. Cerámica, 2nd Edition, Reverté S.A., Barcelona, Spain.
- Favalli, R.C., Pimenta, M.M. and Paschoal, J.O.A., 2002. Numerical Simulation of Spray Dryers, Qualicer, Spain, P.GI-3.
- Manfredini, T., Pellacani, G.C. and Pozzi, P., 1985. Applied Clay Science, 193.
- Pellacani, G.C. and Manfredini, T., 1986. Cera murgia. 16, 1, 30.
- Pozzi, P. and Galassi, C., 1994. La Reologia dei Materiali Ceramici Tradiz ionali, Eacnza Editrice S.p.A., Italy.
- Reed, J.S., 2000. From Batch to Pressed Tile: Mechanics and System Microstructural Changes, Qualicer, Spain, Con-23.
- Ravagioli, A., 1989. Reologia Ceramica Applicat e. Faenza Editrice S.p .A., Italy.
- Rodrigues Neto, J.B., Novaes de Oliveria, A.P., Alarcon, O.E., Pozzi, P. And Andreola, F. 2002, Comparative Study of Deflocculation Mechanism in Colloidal Clay Suspensions, Qualicer, Spain, P.GI-283.
- Tadros, T.F., 1985. Chemistry and Industry, 4, 210.

EFFECT OF USAGE OF FLY ASH AND SILICA FUME AT CONCRETE PRODUCTION OVER QUALITY AND COST OF CONCRETE

Süleyman Uluöz^{1,a}, Selahattin Düzbasan², Erol Yakıt³, Tolga Uluöz⁴

- 1.İlgaz Cons. Trade Ştd Co, Quality Control Manager , Adana, Turkey
- 2.İlgaz Cons. Trade Ştd Co, General Manager , Ankara,Turkey
- 3.Railone İlgaz Sleeper Factory, General Manager, Polatlı – Ankara, Turkey
4. Politechnika Warszawska , Faculty of Civil Engineering, Warsaw, Poland
a. Corresponding author 1 (uluozsuleyman@hotmail.com)

ABSTRACT: While it is one of the biggest problems of plant managers to dispose fly ash which emerges during the activities of thermal plants, fly ash and silica fume have been started to be used as a result of R&D studies performed in building sector and so the production cost has been decreased and quality of concrete has been increased. In production of 1 ton CEM I cement, approximately 900 kg CO₂ gas emerges. So there is a positive effect over environmental pollution of usage of fly ash and silica fume in cement and concrete production.

Silica fume particle is 100 times finer than cement so silica fume is preferred especially in marine structures. By this means, silica fume enters into cavities which are not filled by concrete and so no other chemical substances inside sea water can enter into concrete, corrosion of reinforced concrete is prevented. In production of 202 ea precast beam for terminal structure at Yumurtalık section of BTC (Baku Tbilisi Ceyhan Raw Oil Pipe Line), 112,8 ton silica fume and 24 ton super plasticizer concrete chemical including naphthalene sulphionate group so these precast beams have not been affected from sea water.

1. INTRODUCTION

Environmental pollution increases rapidly in parallel with industrialization. In order to prevent environmental pollution due to industrialization, it is required to utilize wastes. Wastes of thermal plants and ferro - chromium plants cause environmental pollution. Considering that approximately 15 million ton fly ash has been emitted from thermal plants which are currently active in Turkey during year of 2012, the negative effect of fly ash over environment shall be clearly understood. Since grain size of fly ash and silica fume emitted from thermal plant and ferro chromium plants are smaller than grain size of cement, they have been started to be used in production of cement and concrete since

1930 at the end of performed R&D studies.

2. FLY ASH

Fly ash is an important byproduct collected by cyclone or electro filters after being carried by chimney gases occur as a result of coal burning in Thermal Plants. Fly ash particles which have size of 0,5 - 150 micron are glassy spherical shaped particles and small spheres are inside bigger spheres as shown in Figure 1.

Inside the fly ash, there are available SiO₂, Al₂O₃, Fe₂O₃ and CaO as main oxides and MgO, SO₃, alkali oxides are available as minor components and depending on amounts of them, type of fly ash is determined. Fly ashes are

separated into F and C class according to ASTM C 618 standard [Türker *et al.*, 2007]

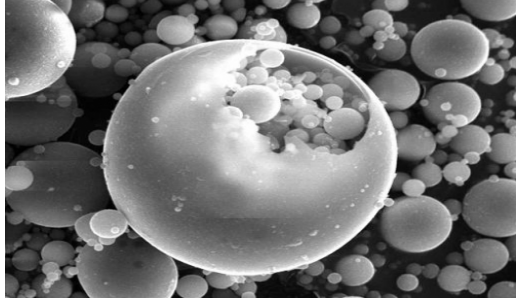


Figure 1: View of fly ash.

At thermal plants which have been built to decrease the energy deficit of Turkey, there occur approximately 15 million m³ fly ash waste. Since fly ashes are kept inside chimneys, air and soil pollution which are two of the biggest problems of present can be prevented to some degree.

2.1. Usage of Fly Ash at Cement Production

Cement production is the biggest sector causing air pollution and in production of 1 ton CEM I cement, approximately 900 kg CO₂ gas emerges. At Cement Plants, fly ashes at 21 - 35 %, 6 - 20 % rates are placed inside clinker and then special cements of CEM II (A-P, B-P, A-Q, B-Q) class used for different purposes are produced [TS EN 197-1]. At cement factories which are members of TÇMB, within year of 2012, 476.036 ton fly ash has been used in production of 63.879.050 ton cement.

2.2. Usage of Fly Ash at Concrete Production

Within year of 2012, 93.050.000 m³ concrete production has been performed in 980 ea Ready Mixed Concrete Plant of 540 ea companies active in Turkey. Service life of concrete structures is approximately 50 - 60 years.

In case of air cavity ratio is higher in concrete used at structures, chlorine,

sulphate and oxygen entering inside the concrete structure shall be more and this shall expedite corrosion of structural steel so structure shall become out of use. Fly ash increases the resistance of concrete, decreases permeability of concrete, increases resistance against freezing - thaw effect, decreases corrosion of reinforcement of the structure, prevents desorption in concrete and segregation, increases processability, decreases hydration heat of concrete so prevents occurrence shrinking cracks and increases resistance of concrete against waters with chemical contents.

2.3. Effect of Usage of Fly Ash in Concrete Cost

Fly ash used in concrete production both increases the quality of concrete and decreases production cost. At TS EN 206-1 standard which is in force about usage of fly ash in concrete production it has been determined as “fly ash / cement $\leq 0,33$ by mass” [TS EN 206-1]. So, it is possible to use fly ash at approximately 20 - 30 % of CEM I class cement. As a result, the production cost of concrete is decreased significantly by using fly ash with 15 TL / ton unit price instead of CEM I cement with 138 TL / ton unit price.

3. SILICA FUME

Silica fume is a gray colored dust obtained as a result of reduction of quartzite silisium with a high concentration or ferro silisium alloy by coke at electrical arc ovens [Yeğınobalı 2007]. Silica fume is mostly, spherical structure and is 100 times smaller than cement particles and sizes of particles are smaller than 0.1 μm . While specific surface of cement is approximately 3000 cm² / gr, specific surface of silica fume is in between 200.000 - 300.000 cm² / gr.

3.1. Usage of Silica Fume at Cement Production

During cement production, silica fume at 6 - 10 % rate is placed inside clinker and then special purpose cement of CEM II portland silica fume cement (CEM II / A-D) are produced [TS EN 197-1]. At cement factories which are members of TÇMB, within year of 2012, 19.776 ton silica fume has been used in production of 63.879.050 ton cement.

3.2. Usage of Silica Fume at Concrete Production

The weakest section of concrete is cement paste interim surface with bigger aggregate particles. Since water accumulated in between bigger aggregate particles during perspiration of concrete shall increase water / cement ratio, cavity percentage in concrete shall increase. Since used silica fume is 100 times thinner than cement, it fills out cavities so interim surface of aggregate with cement is getting stronger.

Whenever silica fume is used together with super plasticizer additives in concrete production, it becomes possible to produce highly resistant concrete besides positive effects of fly ash over concrete quality. *At the contest of "Highly Resistant Concrete Sample Production" within year of 1990 under the scope of IInd National Concrete Congress, Süleyman Uluöz and his team which has participated in the contest on behalf of DSİ have obtained a concrete resistance of 1423 kg/cm² over concrete sample which has been produced by using 350 kg cement, 1 % super plasticizing concrete chemical and 10 % silica fume and have been first of the contest.*

4. USAGE OF SILICA FUME AT MARINE STRUCTURES

Prefabricated beams produced for terminal structure at Yumurталık section of Baku Tbilisi Ceyhan Raw Oil Pipe

Line Project shall be used inside sea water. In order the beam concrete and reinforcement inside not to be affected from chemical substances inside sea water, it has been planned to minimize air voids inside concrete and in order to provide this purpose, it has been decided to use silica fume which is 100 times thinner than cement during the production. Studies Performed Before Commencing Production;

At 1st Phase; before commencing precast beam production, the following conformances have been verified; conformance of aggregate with TS 706 EN 12620 standard, conformance of cement with TS EN 197-1 standard and conformance of mixture water with TS EN 1008 standard.

At 2nd Phase; concrete design studies have been performed by using silica fume which is in conformance with ASTM C 618, ASTM C 1240 / 95 and synthetic polymer based concrete chemical with water reducer at high rate and which is in conformance with ASTM C- 494 Type A and F at different ratios [Uluöz *et al.*,2005]. Regarding the obtained test results, it has been decided to use concrete design given in Table 1 at precast beam production.

Table 1:Concrete design used at precast beam production.

Concrete components		Weight For
River sand		770 kg / m ³
Broken aggregate	16 mm	410 kg /m ³
	8 mm	668 kg / m ³
Silica fume		32 kg / m ³
Cement		420 kg / m ³
Super Plasticizer		5,87 kg / m ³
Mixture water		154 kg / m ³

4.1. Effect of Usage of Silica Fume in Concrete Quality

In order to determine the effect performed by silica fume over quality of concrete; beam samples with 15 x 15 x 70 cm dimensions and with 15 cm cube from replicate concrete having same concrete component amounts and consistency but without micro silica and concrete which shall be used in production of concrete beam have been taken. After the samples have been subjected to steam and water sure under the same conditions; tests of unit volume weight, water absorption, pressure resistance, splitting strength, bending resistance, pressurized permeability according to DIN 1048 standard and fast chlorine permeability according to ASTM C 1202 standard have been performed.

As can be seen from test results given in Table 2, silica fume usage in precast beam concrete which shall be in contact with sea water has positively increased the concrete quality. At Figure 2 pressurized water permeability test has been given.

Table 2: Comparison of concrete with silica fume by replicate sample.

Name of experiment	Test result	
Unit weight kg/m ³	S	2.420
	M	2.390
Pressure resistance Mpa	S	65,6
	M	52,0
Water absorption %	S	1,7
	M	2,8
Pressurized permeability mm	S	12,7
	M	20,5
Fast chlorine permeability columb	S	375
	M	664
S: With silica fume M: Without silica fume		



Figure 2: Pressurized water permeability test

4.2. Production of Prefabricated Beam Which Shall be Used in Sea Water

For 4.085,809 m³ concrete which has been used in production of 202 ea precast beams of which lengths are changing in between 8,38 and 24,2 m in the project; 1720 ton CEM I PÇ 42,5 cement, 112,8 ton silica fume and 24 ton super plasticizer concrete chemical including naphthalene sulphonate group have been used. For cement and micro silica to be used in production, 2 ea Storage Bins with 75 ton capacity each have been bought.

Concrete used in production of prefabricated concrete beam has been prepared in concrete plant equipped by computer hardware. [Uluöz *et al.*, 2005]

After reinforcement has been placed in prepared production forms, concrete has been provided to be placed inside the form by operating surface vibrators mounted over the mold while the prepared concrete is poured inside the form. Steam cure has been applied until the environment temperature becomes 65 °C, 3 hours later the steam cure halls are closed and precast beams have been removed out of form 3 hours after a 5 hour steam cure at this temperature and they have been delivered to stock area then to Adana Yumurtalık at which the installation shall be made. At Figure 3-10 stages of production of precast beam which shall be used in marine structures has been given.



Figures 3, 4: Precast beam production.



Figures 5, 6: Precast beam delivery.



Figures 7, 8: Precast beam installation.



Figures 9, 10: Precast beam installation.

5. CONCLUSION

Due to the usage of fly ash which are emitted from thermal plants and of silica fume which are emitted from ferro chromium plants in production of cement and concrete;

- Cost of cement and concrete production has been decreased.

- Special cement types which are used for different purposes in cement sector have been produced.
- Since concrete quality in buildings have been increased, service life of these buildings have been extended.
- Corrosion of reinforcement by chemical materials included in sea water has been prevented.
- Amount of CO₂ emitted from cement factories have been significantly decreased.
- While managers of thermal plants and ferro chromium plants were thinking about disposal of wastes, fly ash and silica fume have been started to be sold as by product.

Acknowledgement:

Authors acknowledge Kürşat Onur from TSE, Kerem Erşen from TÇMB, Mustafa Taştepe from ÇİMSA and Hakan Özbebek from OYAK Concrete Regional Directorate of Mediterranean due to their contributions in this article.

REFERENCES

- TS EN 197-1
 TS EN 206-1
 Turker,P., Erdoğan,B., Katnaş,F., Yeğinoğlu,A., 2007, Classification of Fly Ashes in Turkey and Their Specifications, Ankara,Turkey.
 Uluöz,S.,Düzbasan,S.,Yakıt,E.,2005, Usage of Micro Silica in Marine Structures, 6th National Concrete Congress Book, Istanbul, Turkey Page 191-200.
 Yeğinoğlu,A.,2007,Usage in Concrete With Cement and Silica Fume, Ankara, Turkey.

THE EFFECT OF WASTE MARBLE POWDER ON THE FRESH STATE AND MECHANICAL PROPERTIES OF SELF-COMPACTING MORTARS

Çağlar Yalçinkaya^a, Ahsanollah Beglarigale and Halit Yazıcı

Dokuz Eylül University, Department of Civil Engineering, İzmir, Turkey
a. Corresponding author (caglar.yalcinkaya@deu.edu.tr)

ABSTRACT: Self-Compacting Mortar (SCM) is a relatively new repair material. This type of mortar may be preferred for narrow sections of reinforced concrete structures due to lack of coarse aggregate and its self-compacting behavior. However, it needs higher cementitious and fine materials to enhance segregation resistance. Marble powder (MP) as an industrial solid waste can be utilized in concrete products. The main goal of this study is to demonstrate the possibility of using waste marble powder as a substitute rather than crushed aggregates in SCM production. For this purpose, crushed limestone sand was replaced with MP up to 30%. Mini slump-flow and V-funnel experiments were performed at fresh state. Moreover, rheology of mixtures has been investigated. Compressive and flexural strengths were determined under standard and steam curing conditions. Results showed that MP can be used up to 20% volume of fine aggregate without remarkable workability loss. Moreover, mechanical properties were not significantly affected by MP substitution. In addition, water curing provided higher strengths compared to steam curing.

1. INTRODUCTION

The marble used for decorative purposes are prepared by sawing, shaping, and polishing. Stocking of the marble powder (MP) which is come out during the preparing process is one of the problems worldwide nowadays. Turkey (40% of total marble reserve in the world), Belgium, USA, Sweden, Belgium, Greece, Spain, Portugal, Italy, Egypt, Portugal and France are the countries which have remarkable marble reserve. As regards Turkey has about 5000 marble processing plants and producing 7,000,000 tons of marble, stoking millions tons of waste MP is seems impossible [Onargan et al., 2006].

Cement based composites have potential for recycling waste materials. Industrial by-products such as blast furnace slag, fly ash, and silica fume are being used as filler materials in self-compacting concrete (SCC) and self-compacting mortar (SCM). In recent years some researchers have dealt with utilization of

waste MP as filler in SCC. Many studies showed the positive effect of filler material used in SCC such as improving workability, reducing cement content, recycling by-products, economical benefits, and producing impermeable concrete [Pope and Schutter, 2005].

SCM is a specially designed very flowable mortar without leading segregation and bleeding that can cast into narrow and deep sections for repair purposes. The main goal of this study is to demonstrate the possibility of using waste MP as a substitute rather than crushed limestone aggregates (CLA) in SCM production. For this purpose, crushed limestone sand was replaced with MP up to 30% (by volume). The influences of the replacement on the rheology of SCM have been investigated. Fresh (mini slump-flow value and V-funnel time) and hardened properties (flexural and compressive strength) of cement mortars incorporating waste MP have been determined.

2. EXPERIMENTAL

2.1. Materials and Mix Design

An ordinary Portland cement (CEM I 42.5R) produced by Denizli Cement Company has been used at all SCM mixtures. The Bogue composition of cement was: C₃S (62%), C₂S (6%), C₃A (5%), C₄AF (12%). The Blaine surface area and specific gravity values of cement were 369 m²/kg and 3.1, respectively. Crushed limestone aggregate (CLA) with a maximum size of 5 mm was used as fine aggregates. The specific gravity and water absorption of CLA are 2.62 and 1%, respectively. A waste MP originated from İzmir region with a size of 1 – 250 µm was used. The specific gravity of MP is 2.75. The sieve analysis of crushed aggregate and MP is given in Figure 1. Chemical composition of MP is shown in Table 1.

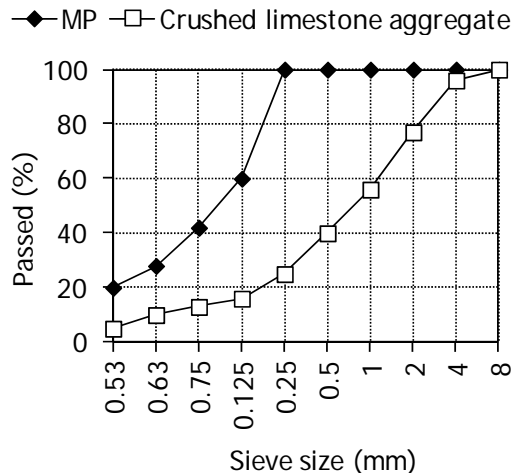


Figure 1: Sieve analysis of MP and CLA.

Table 1: Chemical composition of MP.

Chemical Composition	(%)
CaO	31.10
MgO	21.04
Fe ₂ O ₃	0.03
SiO ₂	0.22
Al ₂ O ₃	0.02
Na ₂ O and K ₂ O	<0.01

The selected MP dosages were 10, 20 and 30% by volume of CLA, due to the fact

that upper dosages caused sharp workability decrease. Minimum slump-flow diameter was targeted 200 mm to achieve self-compacting behavior. The water/cement ratio (W/C) and cement dosage of SCMs were kept constant to 0.50 and 500 kg/m³, respectively. For each mixture, a constant amount of finely grounded limestone powder (LP) from Öztüre Muğla Factory (100 kg/m³) was used to enhance deformability and segregation resistance. The Blaine surface area and specific gravity values of LP were 440 m²/kg and 2.65, respectively. A new generation polycarboxylate based superplasticizer (SP) was used in this study. Neat mortar without MP was designed to give a slump-flow diameter of 260±10 mm. Thus, SP dosage was kept constant at 1% by weight of cement. Mix proportions are presented in Table 2. In Table 2, for instance, “MP20” shows 20% MP replacement by volume of CLA.

Table 2: Mix Proportions.

kg/m ³	MP0	MP10	MP20	MP30
Water	250	250	250	250
Cement	500	500	500	500
LP	100	100	100	100
CLA*	1381	1256	1102	963
MP	0	132	292	439
SP	5	5	5	5

*CLA in saturated surface dry condition

2.2. Test Methods

A Hobart mixer was used to prepare fresh mixtures. All dry particles were mixed for 1 min. Then, water – one quarter SP solution was added to dry mixture. The mortar was mixed for 3 min at low rotation speed and 3 min at high rotation speed with remaining SP. After mixing, mini V-funnel (for flow time) and slump-flow tests were immediately applied in accordance with EFNARC [2005].

The rheological properties of the SCMs were measured on the same mixtures as

mini V-funnel and slump-flow tests. Anton Paar Physica MCR 51 rheometer was used. It was equipped with a ball measuring system. Measurements were conducted at a constant temperature ($20^{\circ}\text{C}\pm 1$) by way of a water circulation system assembled to the rheometer container. Details about the testing system can be found in Felekoğlu et al. [2012]. It is possible to obtain any shear rate protocol with using software of rheometer. A flow curve with shear rates up to 35 s^{-1} was recorded. In this study, a five interval shear rate protocol was used. Rheometer and the protocol can be seen in Figure 2 and Figure 3, respectively. First interval was applied to obtain the same history for all SCM mixtures. Yield stresses and plastic viscosities were calculated from 2-5th intervals according to the Bingham flow model:

$$\tau = \tau_y + \eta\dot{\gamma} \quad (1)$$

where τ is the shear stress (Pa), τ_y is the yield stress (Pa), η is the plastic viscosity, $\dot{\gamma}$ is the shear stress (s^{-1}).

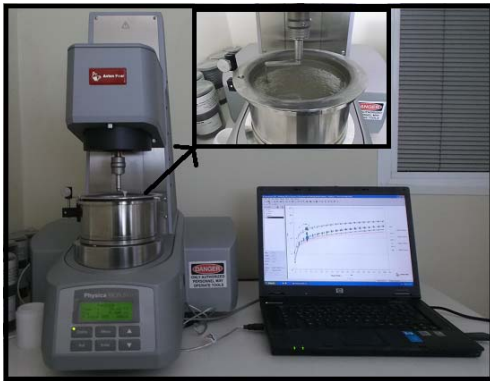


Figure 2: Rheometer.

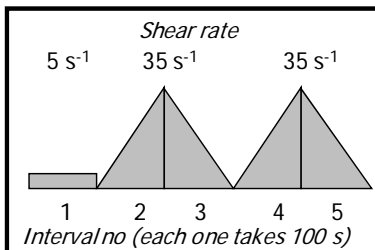


Figure 3: Shear rate protocol.

After workability tests, fresh SCMs were cast into $40\times 40\times 160$ mm prismatic moulds without any vibration or compaction. Steam and water curing were applied to determine mechanical (flexural and compressive strengths) properties. Specimens were kept in an automatic curing machine subsequent to casting for applying steam curing under 100°C . The treatment duration was 12 h. The heat treat cycle applied is illustrated schematically in Figure 4. For water curing, all prismatic specimens were demoulded and submerged in lime-saturated water at 20°C subsequent to 24h curing in a cabinet with $20\pm 1^{\circ}\text{C}$ and $98\pm 2\%$ relative humidity. Flexural and compressive strength tests were performed according to ASTM C348 and C349 standards. Three specimens were tested for flexural strength. Compressive strength tests were applied on two pieces left from flexural tests.

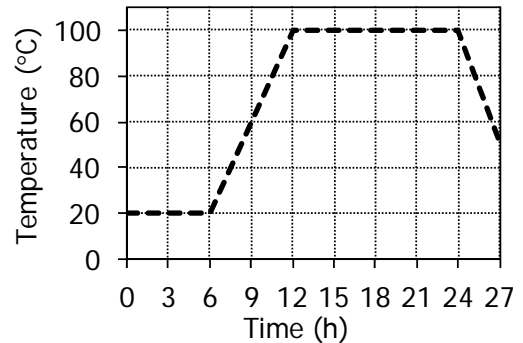


Figure 4: Heat treat cycle applied.

3. RESULTS and DISCUSSION

3.1. Fresh State Properties

The results of spread flow and V-funnel tests are presented in Figure 5. It was observed that replacement of MP up to 20% slightly increased the flow times. In addition, slump-flow values were very close to each other (250 ± 10 mm). However, increasing MP volume up to 30% prolonged the V-funnel flow time from 12 s to 30 s. It decreased also slump-flow diameter to 200 mm.

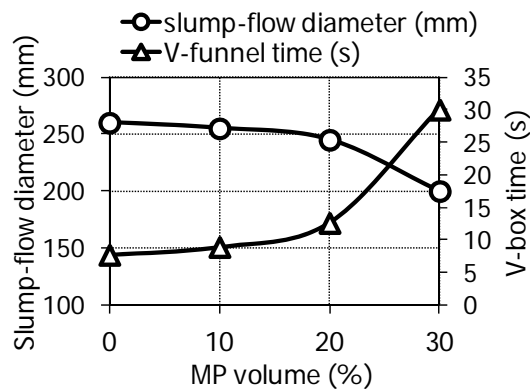


Figure 5: workability test results.

Flow curves (shear rate- $\dot{\gamma}$ vs. shear stress- τ) obtained by rheometer are exhibited in Figure 6. Data of 5th interval was used to draw these curves. Nevertheless, thixotropy measured by the hysteresis area between the up and the down curves of all intervals was very limited. This can be attributed to high segregation resistance of the mixtures. Because of the ball measuring system of rheometer, drag resistance of the ball buried in the sample and flow curves are very sensitive to segregation and bleeding. Thus, shear rate protocol in Figure 3 containing up and down slopes can indicate segregation tendency during the test. It can be said from Figure 5, an increase in MP volume shifted the curves up.

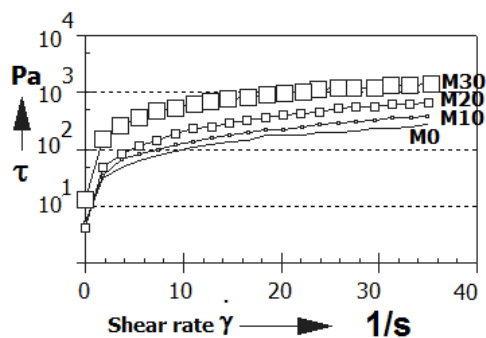


Figure 6: Flow curves.

Rheological parameter vs. MP volume graphs are given in Figure 7. It was observed that increasing the MP volume from 20% to 30% resulted in a significant increase in plastic viscosity similar to V-

funnel test results. Yield stresses for all mixtures were less than 15 Pa, implying self-compacting behavior. A linear relation between V-funnel time and the viscosity and also flow diameter and yield stresses with a high correlation ratio (>0.99) were obtained. Domone and Jin [1999] showed that spread-flow value and V-funnel time are closely related to the Bingham constants of yield stress and plastic viscosity. Güneysi et al. [2009] reported that the utilization of waste MP increase the V-funnel flow time, setting times and viscosity of SCM, while it decrease the hardened characteristics. Increase in Bingham constants with an increase in MP volume can be attributed to two different factors: a) surface area was increased by means of incorporating finer powders. b) MP particles can be well dispersed and increased the cohesiveness in mortar case compared to sand particles. It is obvious from Figure 8 that higher viscosity of M30 mixture caused higher pore concentration of the moulded surface.

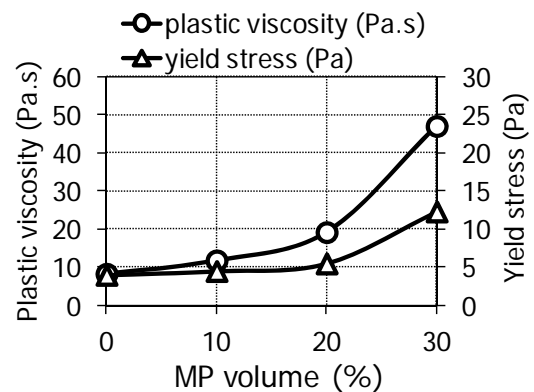


Figure 7: Flow curves.



Figure 8: Surface appearances.

3.2. Mechanical Properties

Compressive and flexural strengths obtained by water (W) and steam (S) curing can be seen in Figure 9. Compressive strengths and flexural strengths under water curing were 55 ± 1.5 and 11 ± 0.5 MPa, respectively. The same values obtained by water curing were 36 ± 0.8 and 8.5 ± 0.5 MPa, respectively. MP replacement slightly increased compressive strengths (up to 4%) under water curing. Above all, steam curing, in comparison with water curing, decreased the compressive and flexural strengths up to 37% and 33%, respectively. This marked reduction may be attributed to rapid hydration under 100°C steam curing. Formation of dense hydrated phases around the unhydrated cement particles may hinder further hydration. The non uniform distribution of hydration products also leads to larger pores in the microstructure [Barnett et al., 2006]. On the other hand, shrinkage induced micro cracks due to high temperature may reduce flexural performance.

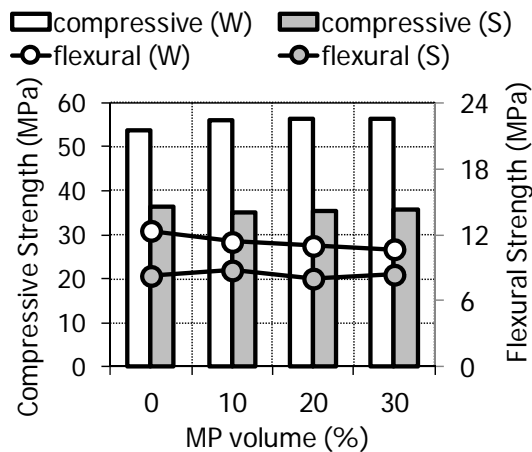


Figure 9: Mechanical properties.

4. CONCLUSIONS

Based on the test results the following results have been obtained;

- An increase of the MP volume leads to an increase of the rheological parameters.

- Rheological parameters were well correlated with the mini V-funnel and slump-flow test results ($R^2 > 0.99$).
- It was possible to replace crushed limestone aggregate with waste MP up to 20% without significant workability and strength loss at a constant W/C ratio and SP dosage.
- Due to rapid and inadequate hydration, mechanical performance of SCMs under steam curing was lower compared to water curing application.

REFERENCES

- Barnett, M.N., Soutsos, S.G., Millard, J.H. Bungey, S.J., 2006. Strength Development of Mortars Containing Ground Granulated Blast-Furnace Slag: Effect of Curing Temperature and Determination of Apparent Activation Energies, *Cement and Concrete Research*, 36, 434.
- Domone, P.J., Jin, P., 1999. Properties of Mortar for Self-Compacting Concrete. First International Rilem Symposium on SCC, Stockholm: RILEM Publications, SARL, 109.
- EFNARC. 2005. The European Guidelines for Self-Compacting Concrete: Specification, Production and Use.
- Felekoğlu, B., Felekoğlu, K.T., Yalçinkaya, Ç., Baradan, B., 2012. Influence of Styrene Acrylate and Styrene Butadiene Rubber on Fresh and Mechanical Properties of Cement Paste and Mortars, 7th Asian Symposium on Polymers in Concrete, ITU, İstanbul, Turkey, 145.
- Güneyisi, E., Gesoğlu, M., Özbay, E., 2009. Effects of Marble Powder and Slag on the Properties of Self-Compacting Mortars. *Materials and Structures*, 42, 813.
- Onargan, T, Kose, H, Deliormanlı, A.H., 2006. Marble. Union of Chambers of Turkish Engineers and Architects (UCTEA), Chamber of Mining Engineers of Turkey [in Turkish].
- Poppe, A.M., Schutter, G.D., 2005. Cement Hydration in the Presence of High Filler Contents, *Cement and Concrete Research*, 35(12), 2290.

TRIBOLOGICAL AND THERMO-MECHANICAL PROPERTIES OF GLASS FIBER REINFORCED COMPOSITES CONTAINING TUNGSTEN BASED NANOFILLERS

Kazım Karal¹, Metin Tanoğlu^{2,a}, Vefa Ezirmik³, M.Lütfi Öveçoğlu³, Mustafa Ürgen³

İzmir Institute of Technology

¹ Material Science and Engineering Program

² Mechanical Engineering Department

Gülbahçe Campus, 35437 Urla, İzmir, Turkey

³ Istanbul Technical University, Department of Metallurgical and Materials Engineering

34469, Maslak, İstanbul, Turkey

a. Corresponding Author: Metin Tanoğlu

ABSTRACT: In this study, quadriaxial non-crimp glass fiber reinforced epoxy composites were prepared with the addition of tungsten based nanostructured powders produced by mechanical alloying. The powders were incorporated into matrix resin to apply on one side of the laminates as a relatively thin surface layer. Laminates were manufactured with hand lay-up technique and cured under compression. The effects of the nanostructured additives on the tribological and thermo-mechanical properties of fiber reinforced epoxy composites were investigated. It was found that tungsten based powder loading has no significant effect on the flexural properties of laminates. The significant improvement on the wear resistance of the composites was observed with the addition of 3 wt. % W-SiC-C (mechanically alloyed for 24 h) powder onto composite surface. The worn surfaces were examined with scanning electron microscopy (SEM) and the results revealed that wear mechanisms are altered due to the presence of nanoparticles in the matrix. Incorporation of nanoparticles improved the thermo-mechanical properties of composite laminates.

1. INTRODUCTION

Fiber reinforced composites are high-performance structural materials applied in wide application areas such as for automotive, marine, aerospace, and defence. The common materials systems used to fabricate those composites include fibers of carbon, glass and aramid and polymers such as epoxy and vinyl-ester resins. In their applications, polymer composites are frequently employed as sliding elements in which the friction and wear behaviour of the material is critical. In addition to high mechanical properties and low specific weight, the material is expected to provide high wear resistance [1,2]. The wear resistance of the polymers can be enhanced by the incorporation of fibers, inorganic particles and solid lubricants.

Epoxy resins are widely used in industrial applications due to their high mechanical and adhesion characteristics and good solvent and chemical resistance, together with their durability in a wide range of temperatures without the emission of volatile by products.

Epoxy resins are modified by adding mineral fillers, flexibilizers, viscosity reducers, colorants, thickeners, accelerators, adhesion promoters, etc. to reduce costs, to improve performance, and processing convenience. In order to improve the friction and wear behaviour of an epoxy material, one of the traditional concepts is to reduce its adhesion to the counterpart material and to enhance its hardness, stiffness and compressive strength. This was attempted to be achieved by using special fillers that

exhibit a good compatibility with liquid epoxy resins[4].

Fillers can improve the electrical and thermal conductivity, wear resistance, corrosion-resistance of plastics [1,5]. Use of nanoparticles as fillers is attracting a great attention due to their unique characteristics [6].

In the recent years, for improving the tribological performance of the matrices various nanoparticulate filled polymer composites were developed and investigated. In comparison with the conventional microscaled particles, nanoparticles proved to have some special advantages for tribological applications: (1) lower abrasiveness due to its reduced angularity; (2) a remarkable reinforcing effect, i.e., the enhanced modulus, strength, and toughness simultaneously; (3) better adhesion between the nanoparticles and the matrix due to its higher specific areas; and (4) a lower content of filler needed [7-8].

It is known that if the nanoparticles are well dispersed in the surrounding polymer matrix, nanoparticules are effective and a considerable improvement of the mechanical and tribological properties can be achieved at very low filler volume content. Otherwise, nanoparticles in general tend to agglomerate because of their high specific surface area [9]. High shear mixing technique, direct incorporation using chemical methods and ultrasound vibration has been applied to obtain better nanoparticle dispersion [2].

It has been revealed by various applications that nanofillers act as effective reinforcement in polymer matrices for the improvement of the mechanical properties.

B. Wetzel et al. [2] investigated the influence of various amounts of micro- and nano-scale particles (calcium silicate CaSiO_3 , 4–15 μm , alumina Al_2O_3 , 13 nm) on the impact energy, flexural strength, dynamic mechanical thermal properties and block-on-ring wear behavior. It was found that the combination of nanoparticles with conventional microparticles induces synergistic effects to obtain wear resistance with much higher values. The addition of alumina nanoparticles simultaneously improved stiffness, impact energy and failure strain at low filler contents (1–2 vol. %) while, a slight improvement of the wear resistance at 2 vol. % Al_2O_3 was observed.

There is limited work published in the literature on the investigation of tribological behaviour of the nanoparticle reinforced composite systems. Moreover, to our knowledge, there is no work published on the preparation and characterization of tungsten particle added composite systems.

The objectives of the present study are; a) development of tungsten based nanoparticle added epoxy suspensions with a good dispersion, b) fabrication of glass fiber reinforced composites using nanocomposite suspensions as a matrix, c) characterization of the effect of filler type and content on the tribological, mechanical and thermo-mechanical properties of prepared composite laminates. Tungsten and tungsten based nanoparticles used in this study were mechanically alloyed in a high energy ball mill. In that manner, the tungsten based nanostructured powders were incorporated into epoxy resin to obtain suspensions. The prepared suspensions were used and composite laminates with and without fillers were fabricated by hand lay-up technique. As an innovative approach, single top surface of the

composite laminates were impregnated with epoxy suspensions to obtain functionalized surfaces. The specific wear rate, friction coefficient and flexural properties of the composite laminates were measured to evaluate the effects of the particles on the tribological and mechanical properties. By utilizing dynamic mechanical analyser (DMA), thermo-mechanical properties of the composites were investigated. The worn surfaces of specimens were investigated through scanning electron microscopy (SEM) to reveal the wear mechanisms. The structure of tungsten based powders was investigated through X-ray diffraction (XRD). The void contents and the structure of nanocomposites and laminates were examined based on optical microscopy and SEM, respectively.

2. EXPERIMENTAL PROCEDURE

2.1. Materials

Bisphenol A-Epichlorhydrin based epoxy resin and its polyamine based curing agent provided from Aero Enercon Company were used for this study. Micron-sized pure tungsten powders (about 3-5 μm) and three types of nanostructured tungsten powders were incorporated into the epoxy resin matrix to fabricate four different composites comprising nanofillers. The incorporated powders are; a) W, b) W – 2 wt.B₄C – 1 wt.%C (now hereafter referred as W-B₄C-C 10h) mechanically alloyed for 10 hours, c) W – 10 wt.SiC – 1 wt.%C (now hereafter referred as W-SiC-C 6h) mechanically alloyed for 6 hours, d) W–10 wt.SiC–1 wt.%C (now hereafter referred as W-SiC-C 24h) mechanically alloyed for 24 hours. Tungsten based nanostructured powders including W, W-B₄C-C (10 hours milling), W-SiC-C (6 hours milling), W-SiC-C (24 hours milling)

were obtained to incorporate into epoxy resin. 0°/+45°/90°/-45° quadriaxial stitched non-crimp glass fibers (Metyx, Telateks Inc.) were used as reinforcement constituent to fabricate fabric reinforced composite panels with nano-filler modified epoxy matrix.

2.2. Preparation of Fiber Reinforced Composites with Nanoparticles

The resin suspensions containing various types of tungsten based nanopowders were prepared as described in details in our previous study. The prepared suspensions were used as a matrix to manufacture thick composite laminates by hand lay up technique. The procedure involves laying multiple plies on top of one another while spreading the resin between the adjacent fabrics in a mold. Prior to composite processing, mold surface was coated with a release agent in order to ease the peeling of the tool. As an innovative approach of this processing technique, on one side of the composites, the top layers of the laminates were impregnated with epoxy resin suspensions containing nanopowders, whereas rest of composite layers were wet using epoxy resin without powder addition as sketched in Figure 1. The corresponding composites were then allowed to cure at room temperature followed by post curing at 80 and 150° C for 1 h and 2 h, respectively.

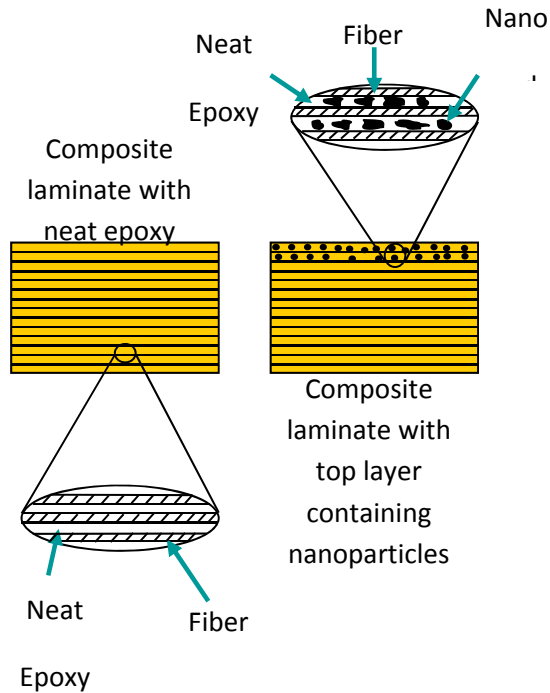


Figure 1: Illustration of fiber reinforced composite laminates with and without fillers

2.3. Wear and Hardness Test

The pin-on-disk wear test technique was conducted using the tribometer (CSM instruments) in order to determine the effect of tungsten based nanopowders on the friction coefficient and specific wear rate of the resultant composites. Cylindrical test specimens were prepared by sectioning from larger composite laminates. In this wear test technique, 52100 steel balls with a diameter of 6 mm were used as the stationary pin material. A linear speed of 10 cm/s, with load of 4 N and wear track radius of 7.1 mm, a total linear distance of 500 m were used during the wear testing under laboratory conditions. Friction coefficient values were determined by the tribometer, as the ball was sliding on the specimens. After a wear test was performed, 3D profilometer (Veeco Wyko™ NT 1100) was used to monitor the amount of volume loss from specimens and surface topography. The specific wear rate (WS) of the material

was calculated based on the loss in volume, the normal load, and the sliding distance.

Surface hardness values of the test specimens were measured by Shimadzu™ micro hardness tester with a Vickers indenter under a load of 1 kg for 15 seconds. Results of hardness tests were averaged out of 5 successive indentations.

3. RESULTS AND DISCUSSION

3.1 Microstructure of Tungsten based Powders

XRD patterns of tungsten (W) and mechanically alloyed tungsten based powders are shown in Figure 2. For W-SiC-C powders, with the increasing time (from 6 h to 24 h) of mechanical alloying, peaks are broadened and heights of peaks are decreased, which are due to refining of grain size and increasing of internal strain resulted during mechanical alloying.

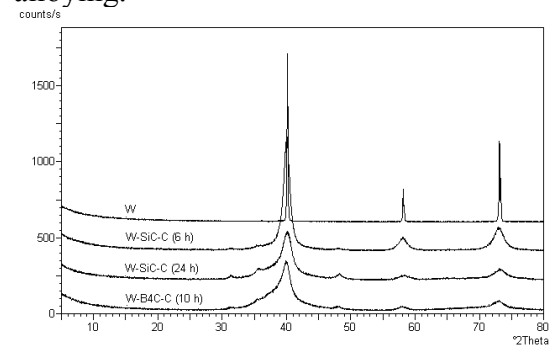


Figure 2: XRD patterns of a) W, b) W-SiC-C 6h, c) W-SiC-C 24h, and d) W-B₄C-C 10 h powder

As a result, average particle sizes of W-SiC-C (6h), W-SiC-C (24h), and W-B₄C-C (10h) were found to be 202 nm, 105 nm and 663 nm, respectively. Also, the images of 6h and 24h mechanically alloyed W-SiC-C powders show that the particle sizes of powders are decreasing with the increasing time of mechanical alloying. As observed in SEM, while the particle size of the powders becomes

smaller, more volume of agglomerates occupy within micro-structures.

3.2 Tribological Properties

The specific wear rates of non-crimp glass fabric reinforced composites (FRCs) without filler addition and those incorporated with W, W-SiC-C 6h, W-SiC-C 24h, and W-B₄C-C 10 h powder as 3 and 5 wt.% of the composites are illustrated in Figures 4 and 5, respectively. As seen in the same figures, incorporation of fillers into the surface layer of fiber reinforced composites improves the wear resistance. It was found that, at 3 wt. % of powder additions, all of the specimens exhibited improved wear resistance since they showed lower wear rates as compared to those with neat composites. Among different types of the powders, addition of 3 wt. % of W-SiC-C (24h) exhibited the highest improvement (approximately 2.5 times better wear rate than neat composites) on the wear rate. On the other hand, W and W-SiC-C (6h) exhibited relatively close values with neat composites.

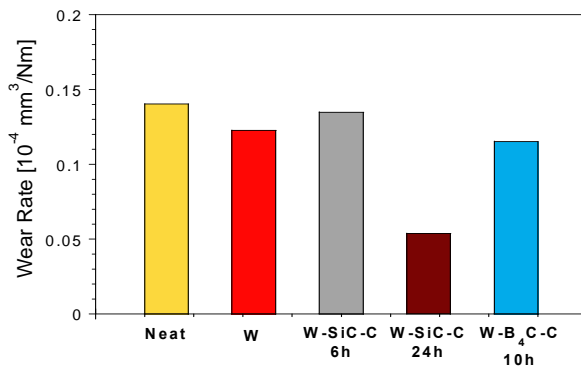


Figure 3: Comparison of the specific wear rates of fiber reinforced nanocomposites containing 3 wt. % of tungsten-based powders

With the increase of powder content from 3 wt % to 5 wt %, it was observed that the wear rate of the composite system that contains W-SiC-C 24h is further reduced. However, the wear rate of the

composites containing W was found to be increased even above the value of composites with neat epoxy. The wear rate for composite containing W-B₄C-C and W-SiC-C 6h remained close to the values for composites with neat epoxy.

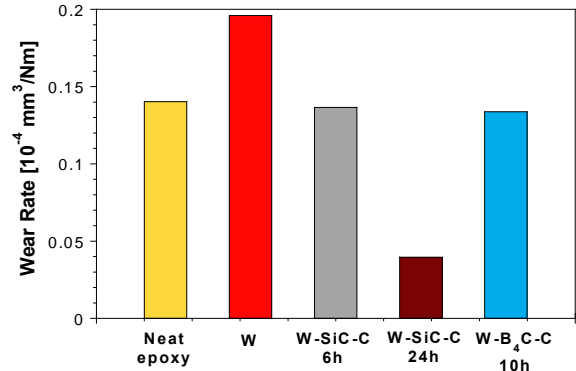


Figure 4: Comparison of the specific wear rates of fiber reinforced nanocomposites containing 5 wt. % of tungsten-based powders

Contrary to wear rates, composite laminates without filler addition (neat epoxy) neat epoxy exhibited almost the lowest friction coefficient values. This might be due to the fact that it does not contain hard particles, thus wear debris of neat epoxy produced during the sliding is softer as compared with other composites and this soft wear debris has lower resistance to sliding. Of all specimens, the composite containing W-SiC-C (2h milling) exhibited the highest friction coefficient values for both 3 and 5 wt. % contents. These results also associate well with the wear rate values.

The topographic image of fiber reinforced composite (FRC) and 5 wt. % W-SiC-C (24h) powder incorporated FRC taken from 3-D profilometer after wear test is illustrated in Figure 5. By comparing worn surfaces of the composites with or without nanofillers, it was observed that the depth of the wear groove is higher for the composite without nanofillers. This is in association with wear rate values. W-SiC-C (24h)

powder has the highest volume fraction within epoxy resin because of its relatively lower density as compared to other powders used in this study. This may be also important factor on why nanocomposite containing W-SiC-C (24h) exhibited an enhanced wear resistance than those with other powders.

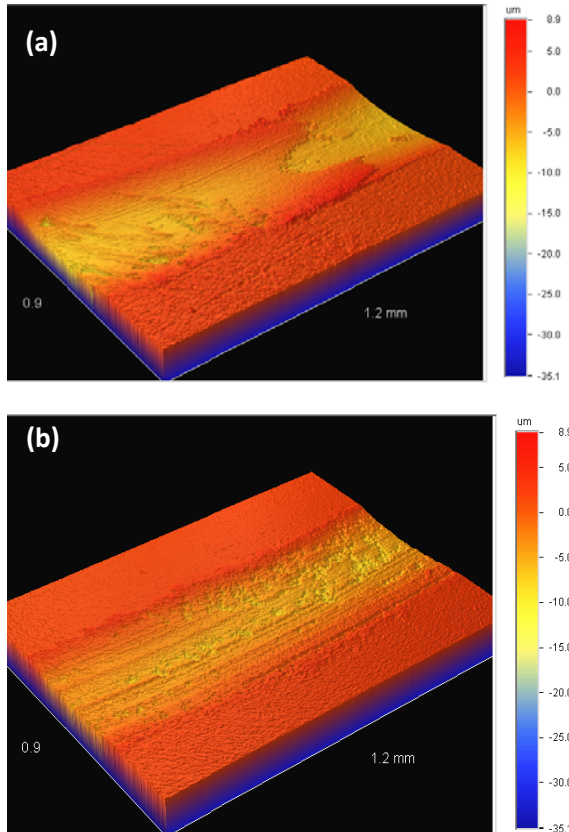
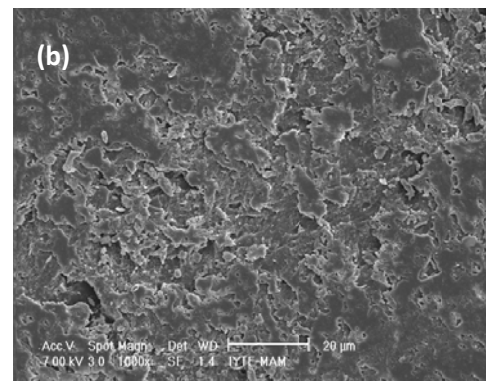
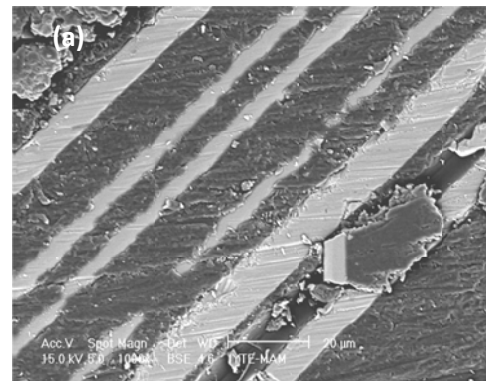


Figure 5: The surface topography for worn surfaces of non-crimp fabric reinforced prepared with (a) neat epoxy (b) epoxy nanocomposite containing 5 wt.% W-SiC-C (24h) powder

Figure 6 illustrates SEM surface images of worn surfaces of glass fabric reinforced composites containing epoxy matrix with and without particle additions. As seen from SEM images, fiber grinding and breakage was observed in composites without fillers after wear test. However, an increased surface roughness was observed. Thus, on the basis of Figure 8, fatigue wear

mechanism seems to be the dominative wear mechanism for the FRPs of the present investigation. This mechanism is based on the sub-surface cracks nucleation due to shear deformation of the softer surface induced by the traction of the harder asperities[4]. Quintelier et al. [6] studied the importance of the fiber orientation on wear properties for the fiber reinforced polyester composites. They observed some wear mechanisms such as fiber-matrix debonding, which consists of two parts. The first one is the fiber-matrix debonding where matrix material is removed nearby the fibers. The second one is exposing the fiber, where matrix material above an underlying fiber is removed. The fiber-matrix debonding is dependent on the fiber orientation, mainly in the direction of the fiber. In the parallel orientation, this is due to the characteristics of the fiber, where the fibers move aside into direction parallel to applied load. In the perpendicular orientation, this is due to the possible bending of the fibers.



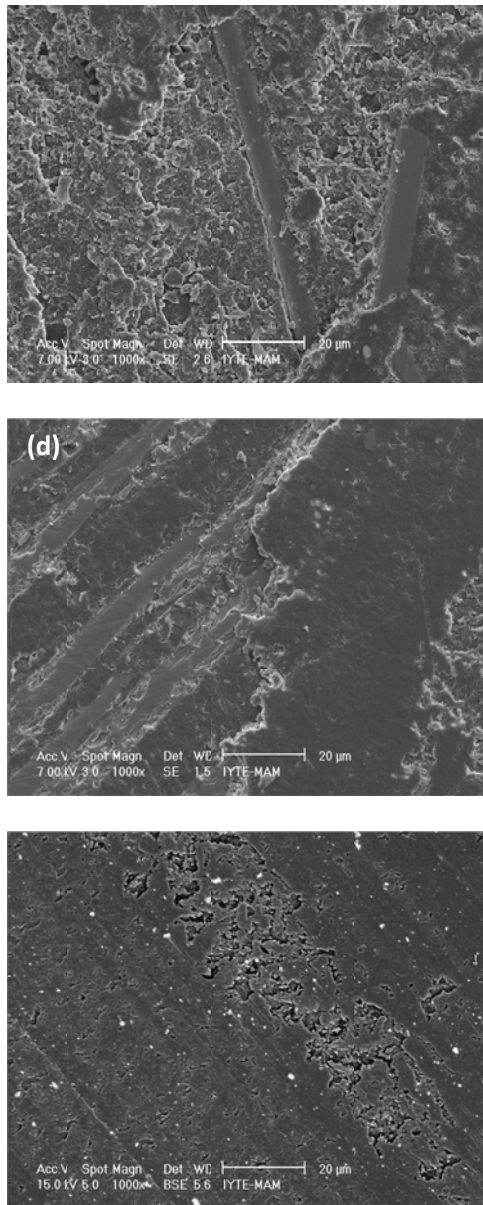


Figure 6: SEM images of worn surfaces of glass fabric reinforced composites containing epoxy matrix with (a) without powder addition (neat epoxy), (b) 3wt.% W, (c) 3 wt. % W-SiC-C (24h), (d) 5wt.% W and (e) 5 wt. % W-SiC-C (24h)

3.3 Microhardness

Surface hardness is principally regarded as one of the most important factor that govern the wear resistance of materials [7]. Vickers microhardness values, H_v , of the composites were measured. As mentioned in our previous study, the hardness values and wear resistance properties are related to each other. The composite containing 5 wt. % of W-SiC-

C (24h) has the highest hardness value, thus resulting in the lowest wear rate value.

3.4 Thermo-mechanical Properties

The effects of fiber reinforcement and nanofiller additives on the thermomechanical properties of epoxy matrix composites were evaluated by DMA. The dynamic storage modulus (E') and $\tan \delta$ versus temperature for FRCs prepared with neat epoxy and nanocomposites containing 3 and 5 wt. % powder are shown in Figures 10 and 11, respectively. The composite laminates with neat epoxy exhibited a storage modulus value of 7 GPa. It was found that the addition of 3 and 5 wt. % of particles on the surface of laminates increase the E' values. The improvement was found to be the highest with 3 wt. % W particle addition (E' values change from 7 to 11 GPa). However, note that nanoparticles are incorporated on one side of laminates as surface layer. Also, note that both fibers and nanoadditives are expected to have effect on storage modulus, the fiber is the dominant reinforcement constituents as compared with nanofiller to enhance the thermomechanical properties of epoxy composite.

4. CONCLUSIONS

In the present study, the effects of tungsten based powders on the tribological, mechanical and thermal properties of quadriaxial stitched non-crimp glass fibers reinforced epoxy composites were investigated. Tungsten based powders obtained from mechanical alloying at various milling times exhibit different particle size distributions. With the incorporation of tungsten based powders into epoxy resin, resin suspensions containing 3 and 5 wt. % of various types of powders including W, W-SiC-C (6 and 24 h milled), W-B₄C-C (10 h) were obtained and these

suspensions were used as a matrix to manufacture fiber reinforced epoxy composites. Fabric reinforced composites were successfully fabricated utilizing tungsten based powder modified epoxy resin as matrix materials by conducting hand lay-up technique. It was found that incorporation of fillers into the surface layer of fiber reinforced composites improves wear resistance.

Acknowledgments

The authors acknowledge TÜBİTAK of Turkey for financial support for MAG 105M065 project.

REFERENCES

- [1] L. Chang, Z. Zhang, Tribological properties of epoxy nanocomposites: II. A combinative effect of short carbon fibre and nano-TiO₂, *Wear*, submitted for publication.
- [2] L. Chang, Z. Zhang, C. Breidt, K. Friedrich, Tribological properties of epoxy nanocomposites. I. Enhancement of the wear resistance by nano-TiO₂ particles, *Wear* 258 (1–4) (2005) 141–148.
- [3] F.H. Chowdhury, M.V. Hosur, S. Jeelani. Studies on the flexural and thermomechanical properties of woven carbon/nanoclay-epoxy laminates. *Materials Science and Engineering A* 421 (2006) 298–306
- [4] Z. Zhang, C. Breidt, L. Chang, F. Hauptert, K. Friedrich, Enhancement of the wear resistance of epoxy: short carbon fibre, graphite, PTFE and nano-TiO₂, *Composites A* 35 (2004) 1385–1392.
- [5] Paul D. Bloom, K.G. Baikerikar, James W. Anderegg, Valerie V. Sheares. Fabrication and wear resistance of Al-Cu-Fe quasicrystal-epoxy composite materials. *Materials and Engineering A* 360 (2003) 46–57.
- [6] Xing XS, Li RKY. Wear behavior of epoxy matrix composites filled with uniform sized sub-micron spherical silica particles. *Wear* 2004; 256:21–26.
- [7] Zhang MQ, Rong MZ, Yu SL, Wetzel B, Friedrich K. Effect of particle surface treatment on the tribological performance of epoxy based nanocomposites. *Wear* 2002; 253:1086–1093.
- [8] Guijun Xian, Rolf Walter, Frank Hauptert. A Synergistic Effect of Nano-TiO₂ and Graphite on the Tribological Performance of Epoxy Matrix Composites. 2006

NATURAL JUGLON DYE AS A PHOTSENSITIZER FOR DYE-SENSITIZED SOLAR CELLS

Seçkin Akın^{1,a}, Cafer Akyürek², Hasan Akış³ and Savaş Sönmezoğlu⁴

1. Department of Physics, Faculty of Kamil Özdağ Science, Karamanoğlu Mehmetbey University, Karaman, Turkey
 2. Karamanoğlu Mehmetbey University, Vocational High School of Technical Sciences, Department of Food Technology, Karaman, Turkey,
 3. Karamanoğlu Mehmetbey University, Vocational High School of Technical Sciences, Department of Carpets and Kilims, Karaman, Turkey,
 4. Department of Materials Science and Engineering, Faculty of Engineering, Karamanoğlu Mehmetbey University, Karaman, Turkey
- a. Corresponding author (seckinakin@kmu.edu.tr)

ABSTRACT: Juglon dye was obtained from the shell of walnut fruit using by hot extraction method, and used in the production of TiO₂ based dye-sensitized solar cell. When the obtained optical analysis measurements are examined, it is seen that TiO₂ absorbed with Juglon dye has a higher absorption coefficient than pure TiO₂. It seems that these phenomena were related to electrical surface-state modifications induced by dye molecules. DSSC is formed with combining of FTO/TiO₂/Juglon working electrode and FTO/Platinum counter-electrode layers in the form of a sandwich. The performance was for Juglon dye with a solar energy conversion efficiency of 0.945%, with a fill factor of 54.5% using an incident irradiation of 100 mW/cm² at room temperature. As a result, Juglon dye-sensitized solar cell produced in this study is also available in commercial potential due to having a simple and inexpensive production method.

1. INTRODUCTION

Dye sensitized solar cells (DSSCs) are recognized as viable alternatives to conventional silicon-based solar cells, due to low production cost, including a vast range of semiconducting materials and produced by using simple fabrication processes [O'Regan and Grätzel, 1991; Grätzel, 2001]. Moreover, compared with Ru based dyes, metal-free natural dyes have many advantages, including better environmental compatibility, a simple manufacturing process, lower toxicity and low fabrication costs [Thomas *et al.*, 2011].

Here, we describe the extraction of juglon dye from the walnut (*Juglans Regia L.*) fruit using a hot water method. Then, TiO₂ based DSSC solar cell has been fabricated by using this extracted natural dye, iodine liquid as an electrolyte.

2. EXPERIMENTAL

Fresh juglon plants were washed with water and dried. Then, the dried plants were subjected to a grinding mill and 10 g of the ground material placed in 100 ml of distilled water and immersed in hot water (50°C) as an extracting solvent for 24 h.

The working electrode was prepared by depositing TiO₂ film onto ultrasonically cleaned FTO conducting glass. TiO₂ nanopowder paste was spread uniformly on the substrate by sliding a glass rod on a hot plate at 150 °C for 20 min then immersed into the dye solution at room temperature for 24 h.

At the same time, to prepare counter electrode, a 5 mM chloroplatinic acid hexahydrate [H₂PtCl₆.6H₂O] in 2-propanol [C₃H₈O] was spread uniformly

onto FTO conducting glass by spin coating system.

The platin-coated counter electrode was placed so that the conductive side of the counter electrode faces the TiO₂ film. The I⁻/I₃⁻ electrolyte solution (0.05 M iodine mixed with 10 ml ethylene glycol and 0.05 M potassium iodide) was placed at the plate edges and liquid was drawn into the space between the electrodes by capillary action. Thus, juglon sensitizers based DSSCs were obtained.

Ultraviolet (UV)-visible absorption measurements of dye solution and photoanode were carried out by using UV-3600 spectrophotometer (Shimadzu). The current-voltage (I-V) curve was recorded with a Keithley 4200 SCS source meter. The light source was a 300 W xenon arc lamp with a filter to simulate the AM 1.5 Solar Light XPS 300 solar spectrum using a standard solar irradiation of 100 mW.cm⁻². The wavelength-dependent incident photon to charge carrier efficiency (IPCE) was measured using an Enlitech QE-R system with a 75 W xenon arc lamp source.

3. RESULTS AND DISCUSSION

3.1. Spectral Characterizations

The absorption spectrum of dye and photoanode is shown in Figure 1. Results show that dye has a wider absorption spectra than TiO₂ alone. Moreover, dye exhibits an absorption peak in the visible region with maxima at ~370 nm.

The absorption spectra obtained for photoanodes follow the same trend as the natural dyes. Furthermore, the UV-vis result demonstrate that juglon immersed TiO₂ shows a strong absorbance in the UV region close to the visible light region of the solar spectrum.

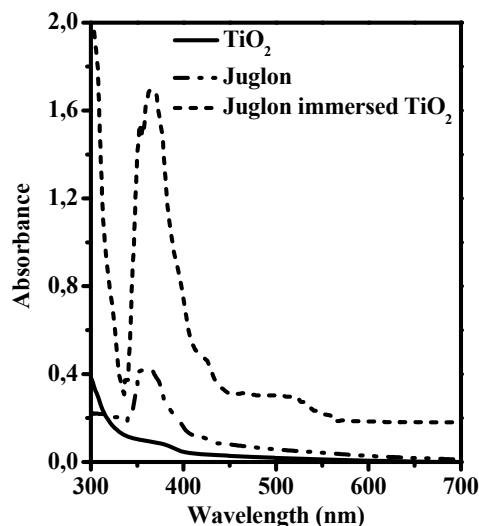


Figure 1: The absorbance of extracted juglon dye and dye doped photoanode.

3.2. Photovoltaic Performance of DSSCs

The photovoltaic properties of the DSSCs sensitized by juglon dye were studied using I-V curves (Figure 2). Juglon sensitizer based DSSC has a fill factor (FF) of 54.5% and a power conversion efficiency of $\eta = 0.945\%$. This results are better than the other natural dyes (such as perilla, begonia, mangosteen, quercetin, alizarin, luteolin, etc.) based DSSCs [Huizhi *et al.*, 2011; Sofyan *et al.*, 2013; Sönmezoğlu *et al.*, 2012]. This can be caused by the absorbing ability of juglon and binding ability of juglon to the TiO₂ structure.

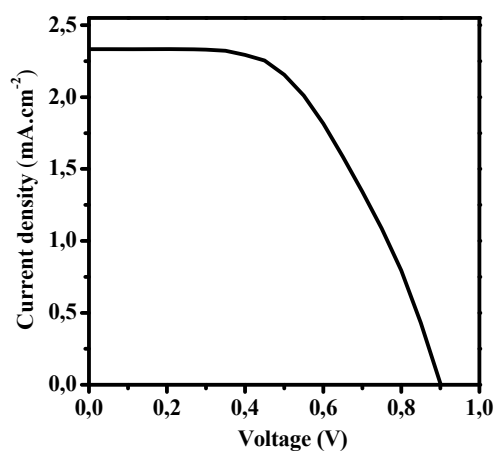


Figure 2: The photovoltaic characteristics. The incident photon to current conversion efficiency (IPCE) spectrum of juglon sensitizer based DSSC is shown in Figure

3. The IPCE spectrum peaks in the range from 300 to 600 nm which are well match the results of the UV-vis absorption spectra. It is also in perfect agreement with the measured short-circuit photocurrents.

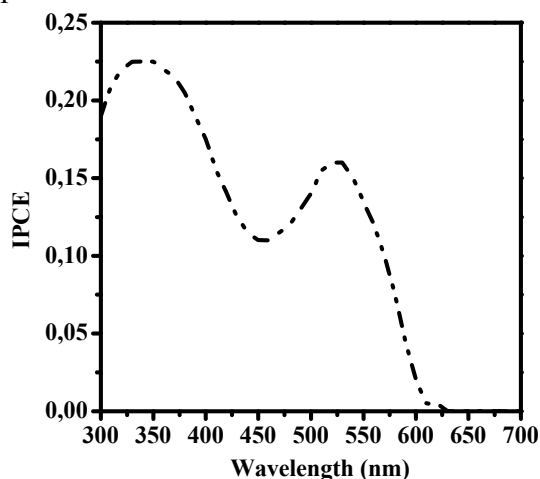


Figure 3: The IPCE spectra of DSSC.

4. CONCLUSIONS

In conclusion, we found that: (i) dye sensitizer greatly increases the absorption of TiO_2 in the visible range (which dominates the terrestrial solar spectrum), (ii) Juglon as a sensitizer provides a comparable power conversion efficiency, (iii) These results demonstrate that juglon dye is a convenient alternative to achieve highly efficient DSSCs..

Acknowledgements: This work is supported by the Scientific Research Commission of Karamanoğlu Mehmetbey University under Project No. 28-M-12.

REFERENCES

- Grätzel, M., 2001. Photoelectrochemical Cells, *Nature*, 414, 338.
- Huizhi, Z., Liqiong, W., Yurong, G. and Tingli, M., 2011. Dye-Sensitized Solar Cells Using 20 Natural Dyes as Sensitizers, *Journal of Photochemistry and Photobiology A: Chemistry*, 219, 188.
- O'Regan, B. and Grätzel, M., 1991. A Low-Cost, High-Efficiency Solar Cell Based on Dye-Sensitized Colloidal TiO_2 Films, *Nature*, 353, 37.
- Sofyan, A.T., Taher, M.E., Hatem, S.E. and Monzir, S.A.L., 2013. Dye-Sensitized Solar

Cells Using Fresh and Dried Natural Dyes, *International Journal of Materials Science and Applications*, 2, 37.

- Sönmezoğlu, S., Akyürek, C. and Akin, S., 2012. High-Efficiency Dye-Sensitized Solar Cells Using Ferrocene-Based Electrolytes and Natural Photosensitizers, *Journal of Physics D: Applied Physics*, 45, 425101.
- Thomas, K.R.J., Singh, P., Baheti, A., Hsu, Y.C., Ho, K.C. and Lin, J.T., 2011. Electro-Optical Properties of New Anthracene Based Organic Dyes for Dye-Sensitized Solar Cells, *Dyes and Pigments*, 91, 33.

SIMPLE SILICON VAPOR ETCHING TECHNIQUE TO FORM THIN SiO_x/Si/SiO_x STRUCTURES

Selma Aouida^{1,a}, Nassima Ennajeh², Nesrine Bachtouli³ and Brahim Bessais⁴

1, 2, 3, 4. Photovoltaic Laboratory, Research and Technology Centre of Energy, Borj-Cedria Science and Technology Park, BP 95, 2050 Hammam-Lif, Tunisia

a. Salma Aouida (salma.aouida@crtten.rnrt.tn)

ABSTRACT: Chemical vapor etching (CVE) of silicon substrate transform silicon crystalline structure to hexafluorosilicates ((NH₄)₂SiF₆) crystalline white powder. The transformed silicon can vary from a few micrometers to the total substrate thickness. The analysis of the silicon/(NH₄)₂SiF₆ interface by infrared investigation reveals a SiO_x structure, which presents an intermediate state in silicon transformation. The CVE of double side silicon substrate generates SiO_x/Si/SiO_x structures. The shape and the thickness of these structures can be easily defined by the masked silicon surface and the experimental CVE conditions. In this work we present the reaction mechanism and the kinetic study of the CVE of silicon substrate in particular conditions. We establish that this etching technique is sensitive to the temperature and the chemical vapor composition. The vapor composition varies during the reaction progress and lead to different etching rates in the same experimental conditions. Cross-sectional scanning electron microscopy (SEM) images show a thin SiO_x layer of about 300 nm sandwiched between silicon bulk and (NH₄)₂SiF₆ powder.

1. INTRODUCTION

Chemical etching of silicon wafer is the most commonly used step when manufacturing silicon semiconductor [Kern, 1990]. Acidic and alkaline solutions have been used as wet etching silicon surface. The etched silicon surface can be polished, roughened or porous; this depends on the affinity between the etch strong and the bonding energy of silicon atoms in the crystal structure. Alkaline solutions as NaOH, KOH, TMAH..., lead to pyramidal textures [Bachtouli *et al.*, 2012]; electrochemical etching in HF based solution give rise to porous silicon structures [Canham; 1990], stain etching in HF, HNO₃, H₂O mixture generates thin porous silicon layers [Schirone *et al.*, 2000; Ben Hander *et al.*, 2003].

The main of these etching process is the dissolution of silicon atoms which are oxidized to Si⁴⁺ state and form Si(OH)₄ compound in alkaline solutions and

H₂SiF₆ in acidic solutions. Chemical Vapor Etching (CVE) based on HF/HNO₃ mixture forms thin porous silicon layers and/or hexafluorosilicates ((NH₄)₂SiF₆) crystalline white powder [Saadoun *et al.*, 2003; Aouida *et al.*, 2005]. This powder presents different properties, which have been studied in previous work [Aouida *et al.*, 2006; Saadoun *et al.*, 2002; Kalem, 2008].

In this communication we focus on the silicon/(NH₄)₂SiF₆ interface and on the sensibility of reaction kinetics to temperature and vapour composition. Infrared spectroscopy in attenuated total reflexion mode (ATR) and Scanning electron microscopy (SEM) investigations have been realized to characterize silicon/(NH₄)₂SiF₆ interface.

2. EXPERIMENTAL

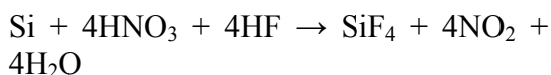
CVE based on HF/HNO₃ vapour mixture generated from solutions (HF/HNO₃:3/1) and (HF/HNO₃:6/1) volumes mixtures have been used to groove solar grade

silicon wafers presenting the following characteristics: (100) orientation, boron doped with a resistivity of about 1-3 ohm.cm. The silicon samples used for kinetic study have a square form of side 1 cm, a thickness of 200 μm and the etched zone is a circle of diameter 0.5 cm. The kinetic control have been studied for two experimental temperatures 40°C and 50°C. We determine the etched thickness versus etching time using a digital palmer instrument. Nicolet Magna FTIR spectrometer with a resolution of 4 cm⁻¹ in ATR mode is used to characterize silicon/(NH₄)₂SiF₆ interface.

3. RESULTS AND DISCUSSIONS

3.1 Chemical Vapour Etching Mechanism

Chemical etching of silicon semiconductor using HF/HNO₃ chemical solutions consists on silicon oxidation step followed by silicon dissolution. The first step is governed by HNO₃ compound and the HF permit the dissolution of oxidized silicon. The total reaction can be summarized as:



Both SiF₄ and NO₂ are in gas state. In aqueuse solution rich on HF (stain etching), they dissolve and may form H₂SiF₆ and HNO₃, respectively. In vapor etching conditions, NO₂ gas is able to oxidize Si atoms and to be reduced on NH₄⁺, leading to the formation of (NH₄)₂SiF₆ powder. The corresponding reaction can be summarized as [Heimann *et al.*, 1984]:

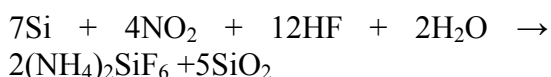


Figure 1 presents a SEM image of vapor etched silicon sample (350μm thick) showing the potentiel of acid vapor to transform isotropically silicon crystal on powder; once the reaction is set off, it

will stop only if the total silicon thickness is transformed or with a control of the reaction time.

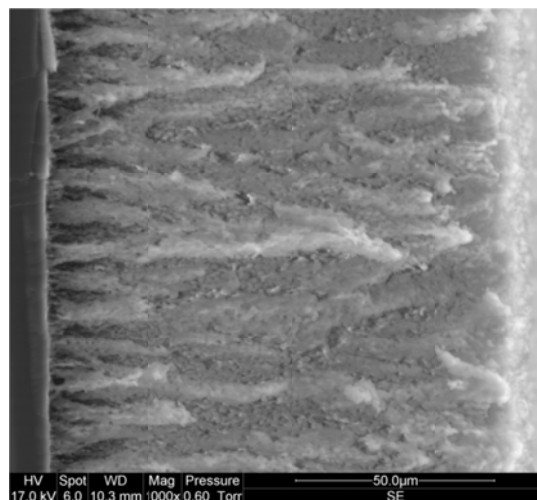


Figure 1: Cross-sectional SEM image of HF/HNO₃ vapor etched silicon sample (350 μm thick).

3.2 Silicon/(NH₄)₂SiF₆ Interface Analysis

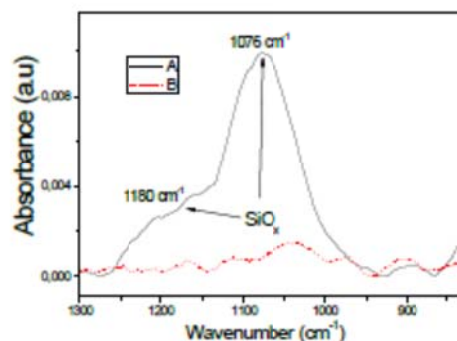


Figure 2: Infrared spectra of silicon/(NH₄)₂SiF₆ interface; (A) before and (B) after immersion in HF diluted solution.

Infrared spectroscopy in ATR-FTIR mode using ZnSe crystal, permits the analysis of thin surface layer. Figure 2 presents infrared spectra of CVE silicon sample without (NH₄)₂SiF₆ powder. Spectrum (A) presents absorption bands at 1180 cm⁻¹ and 1076 cm⁻¹, related to SiO_x layer. These absorption bands disappear after immersion in HF diluted solution, Spectrum (B).

Figure 3 presents SEM image of silicon/(NH₄)₂SiF₆ interface. A thin oxide layer of about 300 nm is detected between silicon bulk and (NH₄)₂SiF₆.

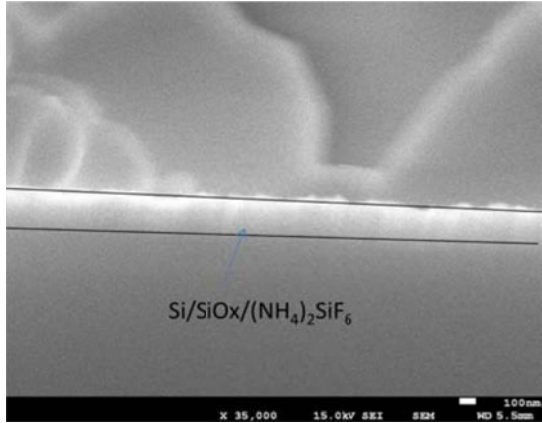


Figure 3: SEM image of Si/SiO_x/(NH₄)₂SiF₆ structure.

3.3 Kinetic Study

To perform kinetic study we determine the etched thickness versus time using a digital palmer instrument. We found that the silicon CVE kinetic presents a linear behaviour with different etching rates. Figures 4-6 present kinetic results associated to the following experimental conditions: HF/HNO₃ = 3/1 at 40°C, HF/HNO₃ = 3/1 at 50°C and HF/HNO₃ = 6/1 at 40°C, respectively.

CVE of silicon sample, using solution composed of HF/HNO₃ = 3/1 volumes mixture, presents two etching rates (k_1 , k_2). At solution temperature $T = 40^\circ\text{C}$, ($k_1 = 1.36 \mu\text{m}\cdot\text{min}^{-1}$, $k_2 = 0.75 \mu\text{m}\cdot\text{min}^{-1}$). At solution temperature $T = 50^\circ\text{C}$, k_1 increases to $1.8 \mu\text{m}\cdot\text{min}^{-1}$ and k_2 slightly increases to $0.76 \mu\text{m}\cdot\text{min}^{-1}$ (Fig. 4 et 5).

The existence of double etching rate in the same experimental conditions is associated to the variation of vapour composition with the reaction progress. The increase of k_1 and k_2 with temperature is also attributed to vapour composition which is more concentrated at high temperatures.

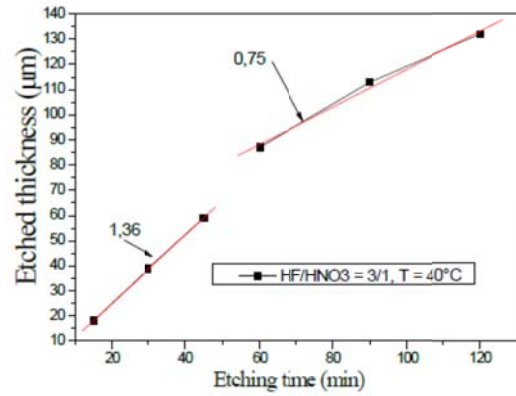


Figure 4: Kinetic results of silicon CVE based on HF/HNO₃ = 3/1 at 40°C.

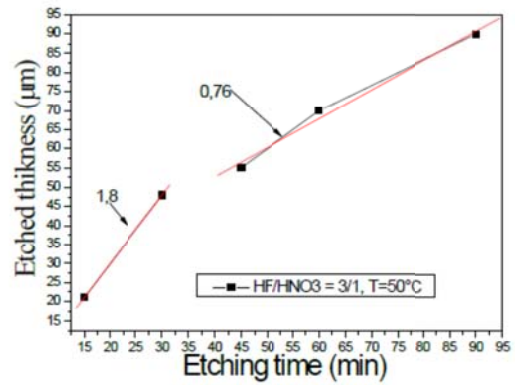


Figure 5: Kinetic results of silicon CVE based on HF/HNO₃ = 3/1 at 50°C.

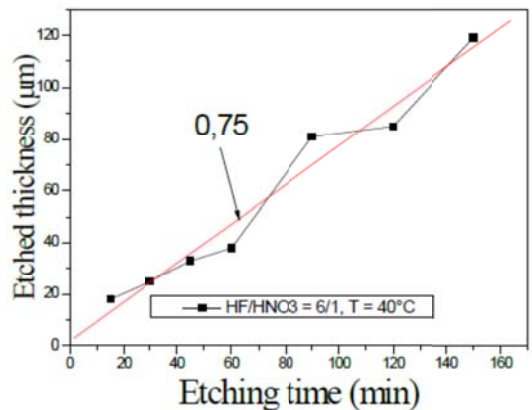


Figure 6: Kinetic results of silicon CVE based on HF/HNO₃ = 6/1 at 40°C.

CVE of silicon sample, using solution composed of HF/HNO₃ = 6/1 volumes mixture, presents a linear kinetic with simple etching rate $k = 0.75 \mu\text{m}\cdot\text{min}^{-1}$ at $T = 40^\circ\text{C}$ (Figure 6) and $k = 1.01 \mu\text{m}\cdot\text{min}^{-1}$

¹ at $T = 50^{\circ}\text{C}$ (not presented). This experimental result highlights the vapour composition role. In fact by comparing $\text{HF}/\text{HNO}_3 = 6/1$ with $\text{HF}/\text{HNO}_3 = 3/1$, the amount of HF used to form $(\text{NH}_4)_2\text{SiF}_6$ may be enough to the total reaction progress.

3.4 CVE of Double Side Silicon Substrate

By considering kinetic behaviour of silicon CVE, we are able to form thin $\text{SiO}_x/\text{Si}/\text{SiO}_x$ structures. Figure 7 presents our first results. A thin silicon layer of about $30\ \mu\text{m}$ in sandwich two thick $(\text{NH}_4)_2\text{SiF}_6$ powder.

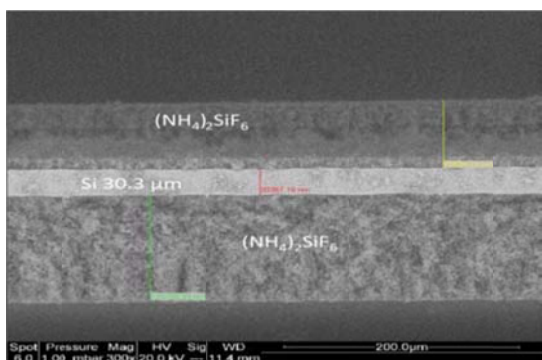


Figure 7: SEM image of silicon sample double side CVE.

4. CONCLUSIONS

In this communication, silicon CVE based on HF/HNO_3 solutions is presented. This chemical etching technique generates $(\text{NH}_4)_2\text{SiF}_6$ powder. The analysis of $\text{Si}/(\text{NH}_4)_2\text{SiF}_6$ interface leads to SiO_x thin layer. Kinetic studies highlight the effect of temperature and vapour composition. Using this simple method we perform $\text{SiO}_x/\text{Si}/\text{SiO}_x$. The annealing process of obtained structures may generate stable $\text{SiO}_2/\text{Si}/\text{SiO}_2$ structures.

Acknowledgements: The authors acknowledge the help in SEM image production, provided by Pr. My Ali El Khakani, Institut National de la

Recherche Scientifique (INRS), 1650, Blvd. Lionel-Boulet, Varennes, Québec J3X 1S2, 6 Canada.

REFERENCES

- Aouida, S., Saadoun, M., Ben Saad, K. and Bessais, B., 2005. Structural and luminescence properties of vapour-etched porous silicon, *phys. stat. sol. (c)* 2, No. 9, 3409.
- Aouida, S., Saadoun, M., Ben Saad, K. and Bessais, B., 2006. Phase transition and luminescence properties from vapor etched silicon, *Thin Solid Films* 495, 357.
- Bachtouli, N., Aouida, S., Hadj Laajimi, R., Boujmil, M.F. and Bessais, B., 2012. Implications of alkaline solutions-induced etching on optical and minority carrier lifetime features of monocrystalline silicon, *Applied Surface Science*, 258, 8889.
- Ben Hander, F.A., Moreno, J. D., Marcos M. L., and González Velasco J., 2003. Electrochemical Behaviour of Porous Silicon Layers Prepared by Stain Etching Processes, *J. New. Mat. Electrochem. Systems* 6, 129.
- Canham, L., 1990. Silicon quantum wire array fabrication by electrochemical and chemical dissolution of wafers, *Appl. Phys. Lett.* 57, 1046.
- Heimann R. B., Ives M.B., (1984), The effect of deposition mechanism on the composition of surface films on silicon, *Thin Solid Films*, 112, 329.
- Kalem, S., 2008. Self-organization of ammonium silicon hexafluoride complex low-dimensional structures on Silicon, *Superlattices and Microstructures*, 44, Issues 4–5, 705.
- Kern, W., 1990. The Evolution of Silicon Wafer Cleaning Technology, *J. Electrochem. Soc.*, Vol. 137, No. 6, 1887.
- Saadoun, M., Mliki, N., Kaabi, H., Daoudi, K., Bessais, B., Ezzaouia, H., Bennaceur, R., 2002. Vapour-etching-based porous silicon: a new approach, *Thin Solid Films* 405, 29.
- Saadoun, M., Bessais, B., Mliki, N., Ferid, M., Ezzaouia, H. and Bennaceur, R., 2003. Formation of luminescent $(\text{NH}_4)_2\text{SiF}_6$ phase from vapour etching-based porous silicon, *Appl. Surf. Sci.* 210, 240.
- Schirone, L., Sotgiu, G. and Montecchi, M., 2000. Towards the Morphology Control of Stain Etched Porous Silicon, *Journal of Porous Materials* 7, 405.

AUTHOR INDEX

A

Abatay, E.	611
Abdullaeva, R.	98
Abed, S.	877
Abi, C.B.E.	862
Açıklan, A.	620
Adda Bedia, E.A.	796
Ağtaş, G.	539
Akar, S.T.	438
Akar, T.	438,467
Akbay, E. Ö.	105,109
Akın, S.	342, 939
Akiş, H.	939
Akpınar, G.	180
Aktuğ, S.L.	42
Allen, E.H.	2
Akyürek, C.	939
Alshathly, M.	586
Altıntaş, Z.K.	288
Altıntaş, E.	417
Altuğ, G.S.	114
Ambrosone, G.	16
Angın, D.	417
Aouida, S.	942
Argibay, E.C.	629
Ari, A.G.	438
Armatas, G.S.	268
Arslanoğlu, A.	611
Arsoy, Z.	781
Artoni, R.	752
Asharif, A.	366, 656
Asman, G.	563
Aşık, E.E.	237
Ata, A.	391
Ataefard, M.	348
Atik, E.	180
Aydın, M.	145
Aydın, İ.	635
Aygun, S.S.	572
Azadmehr, A.R.	216

B

Babakhanova, Mad.	242
Babakhanova, Muk.	242
Bachtouli, N.	942
Badrossamay, M.	92
Bafghi, H.F.	348
Bağirov, H.	602
Bahçeci, E.	68
Baia, L. V.	422
Bâlc, N.	506
Balköse, D.	624
Bandosz, T.J.	433
Basa, D.K.	16
Basim, G.B.	534
Başarı, E.	651
Başpınar, M.S.	119,133,171,788
Baştan, F. E.	539
Baştürk, S.B.	123,128
Baydaroğlu, F.	387,391
Bayesteh, H.	674, 713
Bayrakçeken, H.	133
Bayrakdar, H.	137,139,142
Bayram, C.	525
Bayramoğlu, S.	42
Begjanov, A.	867

Begjanova, G.	867
Beglarigale, A.	926
Beker, U.	463
Beköz, N.	47,52
Belogorlov, A.	638
Bendaoudi, S.E.	796
Bessais, B.	942
Bezirhan, E.	792
Bıyık, S.	145
Bican, O.	155
Bichara, D. A.	569
Boboia, S.	160
Bor, Ş.	237
Borisenko, V.	366
Bounazef, M.	796
Bozorboyev, S.	871, 883
Bozorov, A.	889
Breza, A.	263
Broom, D.P.	397
Budak, A.	659
Buytoz, S.	82

C

Canakci, A.	58,150,722,804, 809
Canbaz, M.	839
Capar, G.	572
Celik, S.	438
Chaliampalias, D.	263
Chernyak, I.N.	472
Chernyakova, R. M.	511
Chiaro, S.S.X.	422
Cilasun, N.S.	155
Civan, A.	371
Cojocar, I.	160
Colombo, P.	9
Cora, Ö.N.	732
Coscia, U.	16
Ctibor, P.	207
Culha, M.	164
Cuvalci, H.	58

Ç

Çakmakkaya, M.	168,171,186
Çalın, R.	155
Çelebi, H.	248
Çelik, E.	175
Çelik, H.	77
Çetinel, H.	635
Çetiner, B. N.	336,339,345,814
Çetiner, D.	258
Çınar, Ö.	814
Çırak, T.	525
Çivi, C.	180
Çiçekli, A.E.	306
Çolak, F.	186
Çolpankan, O.	913

D

Dabrowski, J.R.	577
Davydova, N.	581
Demir, A.	839
Demir, İ.	788
Demirbilek, M.	525
Demirkılıç, G.	109

Demirtaş, A.	42,109
Deniz, V.	828
Denkbaş, E.B.	525
Depci, T.	646
Deptula, P.	577
Dinçkal, Ç.	727
Divriklioğlu, M.	467
Djeffal, A.	796
Doğu, T.	361
Donat, E.	331
Dönerci, A.	620
Dumitrescu, L. S.	160
Durdu, S.	42,63,258
Đurić, Z.	545
Đuriš, J.	545
Durukan, S.	651
Düzbasan, S.	921

E

Ekelik, T.	686
Elsayed, A.	190
Elsharkawy, E.	586
Eminov, S.	871
Emrullahoğlu Abi, B.	862
Ennajeh, N.	942
Erdemir, F.	58, 804, 809
Eremin, Y.	638
Erkey, C.	762
Erkmen, Z. E.	336,339,345
Ermış, A. E.	559
Erol, A.	171,331
Erol, Ü.S.	382
Ersoy, E.	68
Ertuğ, B.	336,339,345
Ertürk, A.T.	195
Eski, Ö.	82
Eugen, V.	222
Ezirmik, V.	931

F

Fakin, T.	73
Figueiredo, M. A. G.	422
Frangis, N.	263
Fritsching, U.	664

G

Gaponenko, N.	366,656
Geçit, M.R.	572
Gerçeker, D.	371
Girgin, İ.	693
Gökçe, H.	336,339,345
Gönen, M.	659
Görhan, G.	788
Grekhov, A.	638
Guller, A. E.	606
Gunduz, L.	770
Gulyamov, G.	871
Gupta, C.	569i
Güllü, M.	382
Gülsoy, H.Ö.	114
Gülşen, H. E.	449
Günel, O.	301
Güner, F.	732

Gürcan, S.	905
Güvercin, S.	686
Güy, N.	377

H

Hadavand B.S.	348
Hamamcı Alışır, S.	306
Handa, M.	669
Harabas, K.	274
Harsa, Ş.	616
Hasimoğlu, A.	387
Helal, M.	586
Hernández, M.	593
Hilmioglu, N.D.	253,297
Hornig, N.	664
Hoseini, S.R.	227
Huck-Jones, D.	39

I

Ibrić, S.	545
Ilyushchenko, A.F.	472
Ikramov, N.	871
Inoytov, K.	883
Isakov, S.	475
Isgor, B.S.	550i
Isgor, Y.G.	550
Islak, S.	77,82,175
Islamov, D.	98
Işıtan, T.	819, 823, 836

J

Jussipbekov, U. Z.	511
----------------------------	-----

K

Kadkhodaei, M.	92
Kaghazchi, T.	443
Kahraman, E.	788
Kalay, Ş.	164
Kanaltı, G.	502
Kaptsevich, V.M.	472
Kara, R.	186
Karaduman, A.	382
Karahan, T.	114
Karakurt, C.	839
Karal, K.	931
Karamahmut, N.	486
Kassem, H.	737
Kaučić, V.	73
Kavas, T.	844
Kaya, C.	352
Kaya, F.	352
Kayalar, A.Ş.	651
Kazanin, I.	697
Khaydukov, E. V.	278, 606
Khokhlov, A.	581
Khoroshko, L.	366, 656
Kıdır, N.D.	620
Kılıç, E.	325
Kılıç, M.	88,452, 848
Kır, D.	77,82,175
Kırsever, D.	853, 857
Kikuchi, M.	555

Kim, K. S.	199
Kim, V.	877
Klekotka, M.	577
Kobilov, N.	894
Koku, H.	202
Koltka, S.	686
Kortov, V.	656
Koskinen, J.	488
Kosoglu, G.	263
Kotlan, J.	207
Koyuncu, G.	449
Kozlowski, M.	212,598
Krstić, M.	545
Krutko, E.	366
Kul, A.R.	646
Kulak, A.	366
Kumbur, H.	449
Kusin, R.A.	472
Kutbay, I.	42,63
Kürkan, H.	417

L

Laukhina, E.	581
Lebiga, V.	697
Lee, W.C.	877
Lembovich, A.I.	472
Levoguer, C.L.	39
Li, K.	572
Lima, E.	593
Lin, C.L.	25
Ling, D.	569
Linnik, O.	366
Lioutas, C.	263
Longloilert, R.	320

M

Macyszyn, J.	212,598
Mahaninia, M.H.	443
Makein, L.	39
Makhkamov, D.	883
Mamanov, B.	894
Marulcuoğlu, H.	862
Meissner, D.	405
Melin, K.	488
Meledina, M.	366
Meratian, M.	746
Mertgenç, E.	186
Mesci, B.	819,823, 836
Mikuriya, M.	669
Miller, J.D.	25, 646
Mirghasemi, A.A.	674,713
Misiewicz, J.	656
Mohamadi, F.	216
Molchan, I.	656
Moldovan, M.	160,222
Movahedi, N.	227
Muduroglu, M.	781
Muratoglu, O. K.	569

N

Nacar, F.	559
Nakanishi, Y.	669
Nakashima, Y.	232
Nakaş, G.İ.	237

Nalbant, B.	611
Nechaev, A. V.	278, 606
Negmatov, J.	242, 475, 871, 877, 883, 889, 894
Negmatova, K.	475,894
Negmatova, M.	242, 877, 894
Negmatova, N.A.	871
Negmatov, S.	98,242,475, 867, 871,877, 883,889, 894
Nergiz, N. T.	248
Nguyen, D.T.	199
Nigiz, F. U.	253,297
Noberi, C.	352
Norberg, P.	457
Nosirova, L.	242

O

Oblakulov, L.	883
Odabaş, E.	836
Oktay, E.	47
Olcay, A. N.	502,680
Onal, Y.	646
Orekhovskaya, T.	366
Oshima, S.	555
Ouchi, K.	669
Ozatay, O.	263
Ozdemir, Z.	534
Ozeki, K.	555
Ozkan, F.C.	520,642
Ozkaya, S.	58, 804, 809
Ozsahin, S.	722
Ozsoy, H.D.	792

Ö

Öksüz, K. E.	602
Önal, E.	481
Önal, I.	371
Öveçoğlu, M. L.	336,339,345, 931
Öz, N.	105
Özacar, M.	377
Özbay, N.	481
Özbek, S.	114
Özbek, Y.Y.	539
Özçatalbaş, Y.	68
Özdemir, E.	387,391
Özdemir, O.	686
Özdemir, Ö. D.	486
Özdenkci, K.	488, 514
Özkahraman, H.T.	905
Özkal, B.	258, 494
Özmen, T.	611
Özsin, G.	88,452
Öztürk, M.	292

P

Pak, A.	697
Pala, Z.	207
Panchenko, V. Y.	278, 606
Panjepour, M.	746, 900
Parvin, N.	216
Pasinli, A.	635
Pastukhova, E.	638
Pişkin S.	486
Podhorodecki, A.	656
Polat, H.	502,514, 559, 680

Polat, M.	502, 514, 559, 680
Polatoglu, İ.	520
Polychroniadis, E.	263
Pomonis, P.J.	268
Pordan, D.	222
Prejmerean, C.	222
Prisbrey, K.A.	646
Prislopskii, S.	656
Prodan, D.	160
Pul, M.	155
Pustovarov, V.	656
Pütün, A. E.	88,452,848
Pütün, E.	88,452

Q

Quintela, A.L.	629
------------------------	-----

R

Rahmonberdiev, G.	475, 894
Rajabov, A.	475
Rakhimov, F.	889
Randolph, M. A.	569i
Rasulova, S.	877
Ravari, M.R.K.	92
Rezaei, R.	92
Richter, J.	274
Ristić, A.	73
Rivas, J.	629
Ruchay, N.S.	472
Rudenko, M.	656
Ruziev, N.	867

S

Sabah, E.	686
Sanli, D.	762
Santomaso, A. C.	752
Saplontai, M.	506
Saplontai, V.	160, 506
Saplontai-Pop, A.	222
Saraç, F. E.	315
Sarada, K.V.	488
Sarkisov, L.	703
Saroşi, C.	222
Savelyev, A. G.	278
Selli, N.T.	918
Semchishen, V. A.	278, 606
Seminogov, V. N.	606
Senturk, H.B.	569
Seredych, M.	433
Sergeev, V.	581
Sert, M.	905
Sezer, U.A.	550
Sezgin, Y.	494
Shahzeydi, M.H.	900
Sharifov, G.	475
Sharipov, H.	889
Shodiev, K.	242
Silahşor, B.	602
Simsek, E.B.	463
Sinitsyna, O.	581
Siretli, Ç.	514
Sjöström, C.	457

Skarlatos, Y.	263
Smirnova, N.	366
Sobirov, B.	242, 883
Sofuoğlu, H.	732
Sokolov, V. I.	278,606
Soleimani, M.	443
Soliev, R.	883
Souza, W. C.	422
Soyal, A. D.	844
Sönmezoğlu, S.	342,939
Stephens, S.	757
Sultanbayeva, G. S.	511

Ş

Şahin, Ş.	283,288
Şahin, T.	195,283,288
Şahin, R.Z.Y.	481
Şenel, F.	913

T

Talaş, Ş.	168
Tamsü, N.	910
Tan, A.	844
Tanaka, H.	669
Tanoglu, M.	123,128, 611, 913, 931
Tarhan, Ö.	616
Taşkın, M.	563
Taşlıçukur, Z.	114
Terzioğlu, P.	292
Tezel, F. H.	757
The Nguyen, D.	199
Thompson, G.	656
Toplan, H.Ö.	853, 857
Toplan, N.	853,857
Toprak, M.U.	839
Traş, Z.F.	502
Truşcă, R.	506
Tsaousi, E.T.	268
Tulyaganova, V.	98
Tuna, A.Ö.A.	463
Tunalı, A.	910, 918
Tuncel, A.	35
Tunçal, T.	494
Tursunov, M.	883, 889
Tüfenk, E.	819
Tüken, T.	620
Twumasi, E.	457

U

Uçar, Y.	620
Ugur, B.	757
Uluöz, S.	921
Uluöz, T.	921
Umucu, Y.	828
Uribarri,L.A.	2
Uslu, O.	494
Usta, M.	42,63,258
Usta, Y.	301
Uysal, R.	844
Uzgan, U.	844
Uzgun, S.C.	819, 823,836
Uzun, İ.	354

Ü	
Ünal, U.	310,315
Ürgen, M.	931
Üstel, F.	539

V	
Vargas, A.G.	593
Varol, T.	58,150, 722, 804,809
Volkov, A.	638
Volpato, S.	752
Vukosavljević, B.	545

W	
Willen, U.	39
Wongkasemjit, S.	320

Y	
Yakar, A.	693
Yakit,E.	921
Yakimovich, N.N.	472
Yakubov, M.	889
Yalcın, E.D.	58
Yalçınkaya, Ç.	926
Yargıç, A. Ş.	481
Yavuz, İ.	133
Yazhanov, D.	105

Yazıcı, H.	926
Yerkesikli, A.G.	642
Yeşilyurt, M.K.	354
Yetgin, S.	624
Yıldırım, V.	602
Yıldız, S.	913
Yılmaz, C.	310
Yılmaz, H.	602
Yılmaz, M. S.	486
Yılmaz, S.	325
Yılmaz, Z.	164
Yiğit, Z.V.	391
Yoshioka, D.	669
Yönetken, A.	171,331
Yulchieva, S.	98
Yushkin, A.	638
Yücel, S.	292

Z	
Zafari, M.	746
Zhao, Y.	433
Zhong, Q.	433
Zhukovskiy, M.	366
Zinovyev, V.	697
Zvyagin, A. V.	278, 606